

## Mechanical Behavior of Materials

A balanced mechanics-materials approach and coverage of the latest developments in biomaterials and electronic materials, the new edition of this popular text is the most thorough and modern book available for upper-level undergraduate courses on the mechanical behavior of materials. Kept mathematically simple and with no extensive background in materials assumed, this is an accessible introduction to the subject.

New to this edition:

Every chapter has been revised, reorganised and updated to incorporate modern materials whilst maintaining a logical flow of theory to follow in class.

Mechanical principles of biomaterials, including cellular materials, and electronic materials are emphasized throughout.

A new chapter on environmental effects is included, describing the key relationship between conditions, microstructure and behavior.

New homework problems included at the end of every chapter.

Providing a conceptual understanding by emphasizing the fundamental mechanisms that operate at micro- and nano-meter level across a wide-range of materials, reinforced through the extensive use of micrographs and illustrations, this is the perfect textbook for a course in mechanical behavior of materials, in mechanical engineering, and materials science.

**Marc Meyers** is a Professor in the Department of NanoEngineering and Mechanical and Aerospace Engineering at the University of California, San Diego. A Co-Founder and Co-Chair of the EXPLOMET Conferences, he has authored numerous texts and won international awards, including the Humboldt Senior Scientist Award (Germany), the TMS Distinguished Scientist/Engineer Awards (USA), and the Lee Hsun Award (China).

**Krishan Chawla** is a Professor in the Department of Materials Science and Engineering, University of Alabama at Birmingham. He is a Fellow of ASM International, Editor of *International Materials Reviews*, and has worked at various institutions in the Americas and Europe. He has authored several others texts and won numerous awards for his research and teaching.



---

# **Mechanical Behavior of Materials**

Marc André Meyers

*University of California, San Diego*

Krishan Kumar Chawla

*University of Alabama at Birmingham*



**CAMBRIDGE**  
UNIVERSITY PRESS

CAMBRIDGE UNIVERSITY PRESS  
Cambridge, New York, Melbourne, Madrid, Cape Town, Singapore, São Paulo, Delhi

Cambridge University Press  
The Edinburgh Building, Cambridge CB2 8RU, UK

Published in the United States of America by Cambridge University Press, New York  
[www.cambridge.org](http://www.cambridge.org)  
Information on this title: [www.cambridge.org/9780521866750](http://www.cambridge.org/9780521866750)

© Cambridge University Press 2009

This publication is in copyright. Subject to statutory exception  
and to the provisions of relevant collective licensing agreements,  
no reproduction of any part may take place without  
the written permission of Cambridge University Press.

First published in 1998 by Prentice-Hall  
Second edition 2009 Cambridge University Press

Printed in the United Kingdom at the University Press, Cambridge

*A catalogue record for this publication is available from the British Library*

ISBN 978-0-521-86675-0 hardback

---

Cambridge University Press has no responsibility for the persistence or accuracy of URLs for external or third-party Internet websites referred to in this book and does not guarantee that any content on such websites is, or will remain, accurate or appropriate.

---

Lovingly dedicated to the memory of my parents,  
Henri and Marie-Anne.

*Marc André Meyers*

Lovingly dedicated to the memory of my parents,  
Manohar L. and Sumitra Chawla.

*Krishan Kumar Chawla*

We dance round in a ring and suppose.  
But the secret sits in the middle and knows.

*Robert Frost*

---

# Contents

<i>Preface to the First Edition</i>	<i>page</i> xvii
<i>Preface to the Second Edition</i>	xxi
<i>A Note to the Reader</i>	xxiii

---

<b>Chapter I</b> Materials: Structure, Properties, and Performance	1
1.1 Introduction	1
1.2 Monolithic, Composite, and Hierarchical Materials	3
1.3 Structure of Materials	15
1.3.1 Crystal Structures	16
1.3.2 Metals	19
1.3.3 Ceramics	25
1.3.4 Glasses	30
1.3.5 Polymers	31
1.3.6 Liquid Crystals	39
1.3.7 Biological Materials and Biomaterials	40
1.3.8 Porous and Cellular Materials	44
1.3.9 Nano- and Microstructure of Biological Materials	45
1.3.10 The Sponge Spicule: An Example of a Biological Material	56
1.3.11 Active (or Smart) Materials	57
1.3.12 Electronic Materials	58
1.3.13 Nanotechnology	60
1.4 Strength of Real Materials	61
Suggested Reading	64
Exercises	65
<b>Chapter 2</b> Elasticity and Viscoelasticity	71
2.1 Introduction	71
2.2 Longitudinal Stress and Strain	72
2.3 Strain Energy (or Deformation Energy) Density	77
2.4 Shear Stress and Strain	80
2.5 Poisson's Ratio	83
2.6 More Complex States of Stress	85
2.7 Graphical Solution of a Biaxial State of Stress: the Mohr Circle	89
2.8 Pure Shear: Relationship between $G$ and $E$	95
2.9 Anisotropic Effects	96
2.10 Elastic Properties of Polycrystals	107
2.11 Elastic Properties of Materials	110
2.11.1 Elastic Properties of Metals	111
2.11.2 Elastic Properties of Ceramics	111
2.11.3 Elastic Properties of Polymers	116
2.11.4 Elastic Constants of Unidirectional Fiber Reinforced Composite	117

2.12	Viscoelasticity	120
2.12.1	Storage and Loss Moduli	124
2.13	Rubber Elasticity	126
2.14	Mooney-Rivlin Equation	131
2.15	Elastic Properties of Biological Materials	134
2.15.1	Blood Vessels	134
2.15.2	Articular Cartilage	137
2.15.3	Mechanical Properties at the Nanometer Level	140
2.16	Elastic Properties of Electronic Materials	143
2.17	Elastic Constants and Bonding	145
	Suggested Reading	155
	Exercises	155

---

<b>Chapter 3</b>	<b>  Plasticity</b>	161
------------------	---------------------	-----

3.1	Introduction	161
3.2	Plastic Deformation in Tension	163
3.2.1	Tensile Curve Parameters	171
3.2.2	Necking	172
3.2.3	Strain Rate Effects	176
3.3	Plastic Deformation in Compression Testing	183
3.4	The Bauschunger Effect	187
3.5	Plastic Deformation of Polymers	188
3.5.1	Stress-Strain Curves	188
3.5.2	Glassy Polymers	189
3.5.3	Semicrystalline Polymers	190
3.5.4	Viscous Flow	191
3.5.5	Adiabatic Heating	192
3.6	Plastic Deformation of Glasses	193
3.6.1	Microscopic Deformation Mechanism	195
3.6.2	Temperature Dependence and Viscosity	197
3.7	Flow, Yield, and Failure Criteria	199
3.7.1	Maximum-Stress Criterion (Rankine)	200
3.7.2	Maximum-Shear-Stress Criterion (Tresca)	200
3.7.3	Maximum-Distortion-Energy Criterion (von Mises)	201
3.7.4	Graphical Representation and Experimental Verification of Rankine, Tresca, and von Mises Criteria	201
3.7.5	Failure Criteria for Brittle Materials	205
3.7.6	Yield Criteria for Ductile Polymers	209
3.7.7	Failure Criteria for Composite Materials	211
3.7.8	Yield and Failure Criteria for Other Anisotropic Materials	213
3.8	Hardness	214
3.8.1	Macroindentation Tests	216
3.8.2	Microindentation Tests	221
3.8.3	Nanoindentation	225
3.9	Formability: Important Parameters	229
3.9.1	Plastic Anisotropy	231

---

3.9.2	Punch-Stretch Tests and Forming-Limit Curves (or Keeler-Goodwin Diagrams)	232
3.10	Muscle Force	237
3.11	Mechanical Properties of Some Biological Materials	241
	Suggested Reading	245
	Exercises	246
<b>Chapter 4   Imperfections: Point and Line Defects</b>		251
4.1	Introduction	251
4.2	Theoretical Shear Strength	252
4.3	Atomic or Electronic Point Defects	254
4.3.1	Equilibrium Concentration of Point Defects	256
4.3.2	Production of Point Defects	259
4.3.3	Effect of Point Defects on Mechanical Properties	260
4.3.4	Radiation Damage	261
4.3.5	Ion Implantation	265
4.4	Line Defects	266
4.4.1	Experimental Observation of Dislocations	270
4.4.2	Behavior of Dislocations	273
4.4.3	Stress Field Around Dislocations	275
4.4.4	Energy of Dislocations	278
4.4.5	Force Required to Bow a Dislocation	282
4.4.6	Dislocations in Various Structures	284
4.4.7	Dislocations in Ceramics	293
4.4.8	Sources of Dislocations	298
4.4.9	Dislocation Pileups	302
4.4.10	Intersection of Dislocations	304
4.4.11	Deformation Produced by Motion of Dislocations (Orowan's Equation)	306
4.4.12	The Peierls-Nabarro Stress	309
4.4.13	The Movement of Dislocations: Temperature and Strain Rate Effects	310
4.4.14	Dislocations in Electronic Materials	313
	Suggested Reading	316
	Exercises	317
<b>Chapter 5   Imperfections: Interfacial and Volumetric Defects</b>		321
5.1	Introduction	321
5.2	Grain Boundaries	321
5.2.1	Tilt and Twist Boundaries	326
5.2.2	Energy of a Grain Boundary	328
5.2.3	Variation of Grain-Boundary Energy with Misorientation	330
5.2.4	Coincidence Site Lattice (CSL) Boundaries	332
5.2.5	Grain-Boundary Triple Junctions	334

5.2.6	Grain-Boundary Dislocations and Ledges	334
5.2.7	Grain Boundaries as a Packing of Polyhedral Units	336
5.3	Twinning and Twin Boundaries	336
5.3.1	Crystallography and Morphology	337
5.3.2	Mechanical Effects	341
5.4	Grain Boundaries in Plastic Deformation (Grain-size Strengthening)	345
5.4.1	Hall-Petch Theory	348
5.4.2	Cottrell's Theory	349
5.4.3	Li's Theory	350
5.4.4	Meyers-Ashworth Theory	351
5.5	Other Internal Obstacles	353
5.6	Nanocrystalline Materials	355
5.7	Volumetric or Tridimensional Defects	358
5.8	Imperfections in Polymers	361
	Suggested Reading	364
	Exercises	364

---

<b>Chapter 6</b>	<b>Geometry of Deformation and Work-Hardening</b>	369
------------------	---	-----

6.1	Introduction	369
6.2	Geometry of Deformation	373
6.2.1	Stereographic Projections	373
6.2.2	Stress Required for Slip	374
6.2.3	Shear Deformation	380
6.2.4	Slip in Systems and Work-Hardening	381
6.2.5	Independent Slip Systems in Polycrystals	384
6.3	Work-Hardening in Polycrystals	384
6.3.1	Taylor's Theory	386
6.3.2	Seeger's Theory	388
6.3.3	Kuhlmann-Wilsdorf's Theory	388
6.4	Softening Mechanisms	392
6.5	Texture Strengthening	395
	Suggested Reading	399
	Exercises	399

---

<b>Chapter 7</b>	<b>Fracture: Macroscopic Aspects</b>	404
------------------	--------------------------------------	-----

7.1	Introduction	404
7.2	Theoretical Tensile Strength	406
7.3	Stress Concentration and Griffith Criterion of Fracture	409
7.3.1	Stress Concentrations	409
7.3.2	Stress Concentration Factor	409
7.4	Griffith Criterion	416
7.5	Crack Propagation with Plasticity	419
7.6	Linear Elastic Fracture Mechanics	421
7.6.1	Fracture Toughness	422

---

7.6.2	Hypotheses of LEFM	423
7.6.3	Crack-Tip Separation Modes	423
7.6.4	Stress Field in an Isotropic Material in the Vicinity of a Crack Tip	424
7.6.5	Details of the Crack-Tip Stress Field in Mode I	425
7.6.6	Plastic-Zone Size Correction	428
7.6.7	Variation in Fracture Toughness with Thickness	431
7.7	Fracture Toughness Parameters	434
7.7.1	Crack Extension Force $G$	434
7.7.2	Crack Opening Displacement	437
7.7.3	$J$ Integral	440
7.7.4	R Curve	443
7.7.5	Relationships among Different Fracture Toughness Parameters	444
7.8	Importance of $K_{Ic}$ in Practice	445
7.9	Post-Yield Fracture Mechanics	448
7.10	Statistical Analysis of Failure Strength	449
	Appendix: Stress Singularity at Crack Tip	458
	Suggested Reading	460
	Exercises	460
<b>Chapter 8</b>	<b>Fracture: Microscopic Aspects</b>	466
8.1	Introduction	466
8.2	Fracture in Metals	468
8.2.1	Crack Nucleation	468
8.2.2	Ductile Fracture	469
8.2.3	Brittle, or Cleavage, Fracture	480
8.3	Fracture in Ceramics	487
8.3.1	Microstructural Aspects	487
8.3.2	Effect of Grain Size on Strength of Ceramics	494
8.3.3	Fracture of Ceramics in Tension	496
8.3.4	Fracture in Ceramics Under Compression	499
8.3.5	Thermally Induced Fracture in Ceramics	504
8.4	Fracture in Polymers	507
8.4.1	Brittle Fracture	507
8.4.2	Crazing and Shear Yielding	508
8.4.3	Fracture in Semicrystalline and Crystalline Polymers	512
8.4.4	Toughness of Polymers	513
8.5	Fracture and Toughness of Biological Materials	517
8.6	Fracture Mechanism Maps	521
	Suggested Reading	521
	Exercises	521
<b>Chapter 9</b>	<b>Fracture Testing</b>	525
9.1	Introduction	525
9.2	Impact Testing	525
9.2.1	Charpy Impact Test	526

9.2.2	Drop-Weight Test	529
9.2.3	Instrumented Charpy Impact Test	531
9.3	Plane-Strain Fracture Toughness Test	532
9.4	Crack Opening Displacement Testing	537
9.5	J-Integral Testing	538
9.6	Flexure Test	540
9.6.1	Three-Point Bend Test	541
9.6.2	Four-Point Bending	542
9.6.3	Interlaminar Shear Strength Test	543
9.7	Fracture Toughness Testing of Brittle Materials	545
9.7.1	Chevron Notch Test	547
9.7.2	Indentation Methods for Determining Toughness	549
9.8	Adhesion of Thin Films to Substrates	552
	Suggested Reading	553
	Exercises	553

---

<b>Chapter 10</b>	<b>Solid Solution, Precipitation, and Dispersion Strengthening</b>	558
10.1	Introduction	558
10.2	Solid-Solution Strengthening	559
10.2.1	Elastic Interaction	560
10.2.2	Other Interactions	564
10.3	Mechanical Effects Associated with Solid Solutions	564
10.3.1	Well-Defined Yield Point in the Stress-Strain Curves	565
10.3.2	Plateau in the Stress-Strain Curve and Lüders Band	566
10.3.3	Strain Aging	567
10.3.4	Serrated Stress-Strain Curve	568
10.3.5	Snoek Effect	569
10.3.6	Blue Brittleness	570
10.4	Precipitation- and Dispersion-Hardening	571
10.5	Dislocation-Precipitate Interaction	579
10.6	Precipitation in Microalloyed Steels	585
10.7	Dual-Phase Steels	590
	Suggested Reading	590
	Exercises	591

---

<b>Chapter 11</b>	<b>Martensitic Transformation</b>	594
11.1	Introduction	594
11.2	Structures and Morphologies of Martensite	594
11.3	Strength of Martensite	600
11.4	Mechanical Effects	603
11.5	Shape-Memory Effect	608
11.5.1	Shape-Memory Effect in Polymers	614
11.6	Martensitic Transformation in Ceramics	614
	Suggested Reading	618
	Exercises	619

---

<b>Chapter 12   Special Materials: Intermetallics and Foams</b>	
12.1 Introduction	621
12.2 Silicides	621
12.3 Ordered Intermetallics	622
12.3.1 Dislocation Structures in Ordered Intermetallics	624
12.3.2 Effect of Ordering on Mechanical Properties	628
12.3.3 Ductility of Intermetallics	634
12.4 Cellular Materials	639
12.4.1 Structure	639
12.4.2 Modeling of the Mechanical Response	639
12.4.3 Comparison of Predictions and Experimental Results	645
12.4.4 Syntactic Foam	645
12.4.5 Plastic Behavior of Porous Materials	646
Suggested Reading	650
Exercises	650
<b>Chapter 13   Creep and Superplasticity</b>	653
13.1 Introduction	653
13.2 Correlation and Extrapolation Methods	659
13.3 Fundamental Mechanisms Responsible for Creep	665
13.4 Diffusion Creep	666
13.5 Dislocation (or Power Law) Creep	670
13.6 Dislocation Glide	673
13.7 Grain-Boundary Sliding	675
13.8 Deformation-Mechanism (Weertman–Ashby) Maps	676
13.9 Creep-Induced Fracture	678
13.10 Heat-Resistant Materials	681
13.11 Creep in Polymers	688
13.12 Diffusion-Related Phenomena in Electronic Materials	695
13.13 Superplasticity	697
Suggested Reading	705
Exercises	705
<b>Chapter 14   Fatigue</b>	713
14.1 Introduction	713
14.2 Fatigue Parameters and S–N (Wöhler) Curves	714
14.3 Fatigue Strength or Fatigue Life	716
14.4 Effect of Mean Stress on Fatigue Life	719
14.5 Effect of Frequency	721
14.6 Cumulative Damage and Life Exhaustion	721
14.7 Mechanisms of Fatigue	725

---

14.7.1	Fatigue Crack Nucleation	725
14.7.2	Fatigue Crack Propagation	730
14.8	Linear Elastic Fracture Mechanics Applied to Fatigue	735
14.8.1	Fatigue of Biomaterials	744
14.9	Hysteretic Heating in Fatigue	746
14.10	Environmental Effects in Fatigue	748
14.11	Fatigue Crack Closure	748
14.12	The Two-Parameter Approach	749
14.13	The Short-Crack Problem in Fatigue	750
14.14	Fatigue Testing	751
14.14.1	Conventional Fatigue Tests	751
14.14.2	Rotating Bending Machine	751
14.14.3	Statistical Analysis of S-N Curves	753
14.14.4	Nonconventional Fatigue Testing	753
14.14.5	Servohydraulic Machines	755
14.14.6	Low-Cycle Fatigue Tests	756
14.14.7	Fatigue Crack Propagation Testing	757
	Suggested Reading	758
	Exercises	759
<hr/> <b>Chapter 15   Composite Materials</b>		765
15.1	Introduction	765
15.2	Types of Composites	765
15.3	Important Reinforcements and Matrix Materials	767
15.3.1	Microstructural Aspects and Importance of the Matrix	769
15.4	Interfaces in Composites	770
15.4.1	Crystallographic Nature of the Fiber-Matrix Interface	771
15.4.2	Interfacial Bonding in Composites	772
15.4.3	Interfacial Interactions	773
15.5	Properties of Composites	774
15.5.1	Density and Heat Capacity	775
15.5.2	Elastic Moduli	775
15.5.3	Strength	780
15.5.4	Anisotropic Nature of Fiber Reinforced Composites	783
15.5.5	Aging Response of Matrix in MMCs	785
15.5.6	Toughness	785
15.6	Load Transfer from Matrix to Fiber	788
15.6.1	Fiber and Matrix Elastic	789
15.6.2	Fiber Elastic and Matrix Plastic	792
15.7	Fracture in Composites	794
15.7.1	Single and Multiple Fracture	795
15.7.2	Failure Modes in Composites	796
15.8	Some Fundamental Characteristics of Composites	799
15.8.1	Heterogeneity	799

---

15.8.2 Anisotropy	799
15.8.3 Shear Coupling	801
15.8.4 Statistical Variation in Strength	802
15.9 Functionally Graded Materials	803
15.10 Applications	803
15.10.1 Aerospace Applications	803
15.10.2 Nonaerospace Applications	804
15.11 Laminated Composites	806
Suggested Reading	809
Exercises	810
<b>Chapter 16   Environmental Effects</b>	<b>815</b>
16.1 Introduction	815
16.2 Electrochemical Nature of Corrosion in Metals	815
16.2.1 Galvanic Corrosion	816
16.2.2 Uniform Corrosion	817
16.2.3 Crevice corrosion	817
16.2.4 Pitting Corrosion	818
16.2.5 Intergranular Corrosion	818
16.2.6 Selective leaching	819
16.2.7 Erosion-Corrosion	819
16.2.8 Radiation Damage	819
16.2.9 Stress Corrosion	819
16.3 Oxidation of metals	819
16.4 Environmentally Assisted Fracture in Metals	820
16.4.1 Stress Corrosion Cracking (SCC)	820
16.4.2 Hydrogen Damage in Metals	824
16.4.3 Liquid and Solid Metal Embrittlement	830
16.5 Environmental Effects in Polymers	831
16.5.1 Chemical or Solvent Attack	832
16.5.2 Swelling	832
16.5.3 Oxidation	833
16.5.4 Radiation Damage	834
16.5.5 Environmental Crazing	835
16.5.6 Alleviating the Environmental Damage in Polymers	836
16.6 Environmental Effects in Ceramics	836
16.6.1 Oxidation of Ceramics	839
Suggested Reading	840
Exercises	840
<i>Appendices</i>	843
<i>Index</i>	851



---

## Preface to the First Edition

Courses in the mechanical behavior of materials are standard in both mechanical engineering and materials science/engineering curricula. These courses are taught, usually, at the junior or senior level. This book provides an introductory treatment of the mechanical behavior of materials with a balanced mechanics-materials approach, which makes it suitable for both mechanical and materials engineering students. The book covers metals, polymers, ceramics, and composites and contains more than sufficient information for a one-semester course. It therefore enables the instructor to choose the path most appropriate to the class level (junior- or senior-level undergraduate) and background (mechanical or materials engineering). The book is organized into 15 chapters, each corresponding, approximately, to one week of lectures. It is often the case that several theories have been developed to explain specific effects; this book presents only the principal ideas. At the undergraduate level the simple aspects should be emphasized, whereas graduate courses should introduce the different viewpoints to the students. Thus, we have often ignored active and important areas of research. Chapter 1 contains introductory information on materials that students with a previous course in the properties of materials should be familiar with. In addition, it enables those students unfamiliar with materials to “get up to speed.” The section on the theoretical strength of a crystal should be covered by all students. Chapter 2, on elasticity and viscoelasticity, contains an elementary treatment, tailored to the needs of undergraduate students. Most metals and ceramics are linearly elastic, whereas polymers often exhibit nonlinear elasticity with a strong viscous component. In Chapter 3, a broad treatment of plastic deformation and flow and fracture criteria is presented. Whereas mechanical engineering students should be fairly familiar with these concepts, (Section 3.2 can therefore be skipped), materials engineering students should be exposed to them. Two very common tests applied to materials, the uniaxial tension and compression tests, are also described. Chapters 4 through 9, on imperfections, fracture, and fracture toughness, are essential to the understanding of the mechanical behavior of materials and therefore constitute the core of the course. Point, line (Chapter 4), interfacial, and volumetric (Chapter 5) defects are discussed. The treatment is introductory and primarily descriptive. The mathematical treatment of defects is very complex and is not really essential to the understanding of the mechanical behavior of materials at an engineering level. In Chapter 6, we use the concept of dislocations to explain work-hardening; our understanding of this phenomenon, which dates from the 1930s, followed by contemporary developments, is presented. Chapters 7 and 8 deal with fracture from a macroscopic (primarily mechanical) and a microstructural viewpoint, respectively. In brittle materials, the fracture strength under

tension and compression can differ by a factor of 10, and this difference is discussed. The variation in strength from specimen to specimen is also significant and is analyzed in terms of Weibull statistics. In Chapter 9, the different ways in which the fracture resistance of materials can be tested is described. In Chapter 10, solid solution, precipitation, and dispersion strengthening, three very important mechanisms for strengthening metals, are presented. Martensitic transformation and toughening (Chapter 11) are very effective in metals and ceramics, respectively. Although this effect has been exploited for over 4,000 years, it is only in the second half of the 20th century that a true scientific understanding has been gained; as a result, numerous new applications have appeared, ranging from shape-memory alloys to maraging steels, that exhibit strengths higher than 2 GPa. Among novel materials with unique properties that have been developed for advanced applications are intermetallics, which often contain ordered structures. These are presented in Chapter 12. In Chapters 13 and 14, a detailed treatment of the fundamental mechanisms responsible for creep and fatigue, respectively, is presented. This is supplemented by a description of the principal testing and data analysis methods for these two phenomena. The last chapter of the book deals with composite materials. This important topic is, in some schools, the subject of a separate course. If this is the case, the chapter can be omitted.

This book is a spinoff of a volume titled *Mechanical Metallurgy* written by these authors and published in 1984 by Prentice-Hall. That book had considerable success in the United States and overseas, and was translated into Chinese. For the current volume, major changes and additions were made, in line with the rapid development of the field of materials in the 1980s and 1990s. Ceramics, polymers, composites, and intermetallics are nowadays important structural materials for advanced applications and are comprehensively covered in this book. Each chapter contains, at the end, a list of suggested reading; readers should consult these sources if they need to expand a specific point or if they want to broaden their knowledge in an area. Full acknowledgment is given in the text to all sources of tables and illustrations. We might have inadvertently forgotten to cite some of the sources in the final text; we sincerely apologize if we have failed to do so. All chapters contain solved examples and extensive lists of homework problems. These should be valuable tools in helping the student to grasp the concepts presented.

By their intelligent questions and valuable criticisms, our students provided the most important input to the book; we are very grateful for their contributions. We would like to thank our colleagues and fellow scientists who have, through painstaking effort and unselfish devotion, proposed the concepts, performed the critical experiments, and developed the theories that form the framework of an emerging quantitative understanding of the mechanical behavior of materials. In order to make the book easier to read, we have opted to minimize the use of references. In a few places, we have placed them

in the text. The patient and competent typing of the manuscript by Jennifer Natelli, drafting by Jessica McKinnis, and editorial help with text and problems by H. C. (Bryan) Chen and Elizabeth Kristofetz are gratefully acknowledged. Krishan Chawla would like to acknowledge research support, over the years, from the US Office of Naval Research, Oak Ridge National Laboratory, Los Alamos National Laboratory, and Sandia National Laboratories. He is also very thankful to his wife, Nivedita; son, Nikhilesh; and daughter, Kanika, for making it all worthwhile! Kanika's help in word processing is gratefully acknowledged. Marc Meyers acknowledges the continued support of the National Science Foundation (especially R. J. Reynik and B. MacDonald), the US Army Research Office (especially G. Mayer, A. Crowson, K. Iyer, and E. Chen), and the Office of Naval Research. The inspiration provided by his grandfather, Jean-Pierre Meyers, and father, Henri Meyers, both metallurgists who devoted their lives to the profession, has inspired Marc Meyers. The Institute for Mechanics and Materials of the University of California at San Diego generously supported the writing of the book during the 1993–96 period. The help provided by Professor R. Skalak, director of the institute, is greatly appreciated. The Institute for Mechanics and Materials is supported by the National Science Foundation. The authors are grateful for the hospitality of Professor B. Ilschner at the École Polytechnique Fédérale de Lausanne, Switzerland during the last part of the preparation of the book.

Marc André Meyers  
*La Jolla, California*

Krishan Kumar Chawla  
*Birmingham, Alabama*



---

## Preface to the Second Edition

The second edition of *Mechanical Behavior of Materials* has revised and updated material in every chapter to reflect the changes occurring in the field. In view of the increasing importance of bioengineering, a special emphasis is given to the mechanical behavior of biological materials and biomaterials throughout this second edition. A new chapter on environmental effects has been added. Professors Fine and Voorhees<sup>1</sup> make a cogent case for integrating biological materials into materials science and engineering curricula. This trend is already in progress at many US and European universities. Our second edition takes due recognition of this important trend. We have resisted the temptation to make a separate chapter on biological and biomaterials. Instead, we treat these materials together with traditional materials, viz., metals, ceramics, polymers, etc. In addition, taking due cognizance of the importance of electronic materials, we have emphasized the distinctive features of these materials from a mechanical behavior point of view.

The underlying theme in the second edition is the same as in the first edition. The text connects the fundamental mechanisms to the wide range of mechanical properties of different materials under a variety of environments. This book is unique in that it presents, in a unified manner, important principles involved in the mechanical behavior of different materials: metals, polymers, ceramics, composites, electronic materials, and biomaterials. The unifying thread running throughout is that the nano/microstructure of a material controls its mechanical behavior. A wealth of micrographs and line diagrams are provided to clarify the concepts. Solved examples and chapter-end exercise problems are provided throughout the text.

This text is designed for use in mechanical engineering and materials science and engineering courses by upper division and graduate students. It is also a useful reference tool for the practicing engineers involved with mechanical behavior of materials. The book does not presuppose any extensive knowledge of materials and is mathematically simple. Indeed, Chapter 1 provides the background necessary. We invite the reader to consult this chapter off and on because it contains very general material.

In addition to the major changes discussed above, the mechanical behavior of cellular and electronic materials was incorporated. Major reorganization of material has been made in the following parts: elasticity; Mohr circle treatment; elastic constants of fiber reinforced composites; elastic properties of biological and of biomaterials; failure criteria of composite materials; nanoindentation technique and its use in extracting material properties; etc. New solved and

---

<sup>1</sup> M. E. Fine and P. Voorhees, "On the evolving curriculum in materials science & engineering," *Daedalus*, Spring 2005, 134.

chapter-end exercises are added. New micrographs and line diagrams are provided to clarify the concepts.

We are grateful to many faculty members who adopted the first edition for classroom use and were kind enough to provide us with very useful feedback. We also appreciate the feedback we received from a number of students. MAM would like to thank Kanika Chawla and Jennifer Ko for help in the biomaterials area. The help provided by Marc H. Meyers and M. Cristina Meyers in teaching him the rudiments of biology has been invaluable. KKC would like thank K. B. Carlisle, N. Chawla, A. Goel, M. Koopman, R. Kulkarni, and B. R. Patterson for their help. KKC acknowledges the hospitality of Dr. P. D. Portella at Federal Institute for Materials Research and Testing (BAM), Berlin, Germany, where he spent a part of his sabbatical. As always, he is grateful to his family members, Anita, Kanika, Nikhil, and Nivi for their patience and understanding.

Marc André Meyers  
*University of California, San Diego*

Krishan Kumar Chawla  
*University of Alabama at Birmingham*

---

## A Note to the Reader

Our goal in writing *Mechanical Behavior of Materials* has been to produce a book that will be the pre-eminent source of fundamental knowledge about the subject. We expect this to be a guide to the student beyond his or her college years. There is, of course, a lot more material than can be covered in a normal semester-long course. We make no apologies for that in addition to being a classroom text, we want this volume to act as a useful reference work on the subject for the practicing scientist, researcher, and engineer.

Specifically, we have an introductory chapter dwelling on the themes of the book: structure, mechanical properties, and performance. This section introduces some key terms and concepts that are covered in detail in later chapters. We advise the reader to use this chapter as a handy reference tool, and consult it as and when required. We strongly suggest that the instructor use this first chapter as a self-study resource. Of course, individual sections, examples, and exercises can be added to the subsequent material as and when desired.

Enjoy!



---

# Chapter I

## Materials: Structure, Properties, and Performance

### 1.1 | Introduction

Everything that surrounds us is matter. The origin of the word matter is *mater* (Latin) or *matri* (Sanskrit), for *mother*. In this sense, human beings anthropomorphized that which made them possible – that which gave them nourishment. Every scientific discipline concerns itself with matter. Of all matter surrounding us, a portion comprises materials. What are materials? They have been variously defined. One acceptable definition is “matter that human beings use and/or process.” Another definition is “all matter used to produce manufactured or consumer goods.” In this sense, a rock is not a material, intrinsically; however, if it is used in aggregate (concrete) by humans, it becomes a material. The same applies to all matter found on earth: a tree becomes a material when it is processed and used by people, and a skin becomes a material once it is removed from its host and shaped into an artifact.

The successful utilization of materials requires that they satisfy a set of properties. These properties can be classified into thermal, optical, mechanical, physical, chemical, and nuclear, and they are intimately connected to the structure of materials. The structure, in its turn, is the result of synthesis and processing. A schematic framework that explains the complex relationships in the field of the mechanical behavior of materials, shown in Figure 1.1, is Thomas’s iterative tetrahedron, which contains four principal elements: mechanical properties, characterization, theory, and processing. These elements are related, and changes in one are inseparably linked to changes in the others. For example, changes may be introduced by the synthesis and processing of, for instance, steel. The most common metal, steel has a wide range of strengths and ductilities (*mechanical properties*), which makes it the material of choice for numerous applications. While low-carbon steel is used as reinforcing bars in concrete and in the body of automobiles, quenched and tempered high-carbon steel is used in more critical applications such as axles and gears. Cast iron, much more brittle, is used in a variety of applications, including automobile

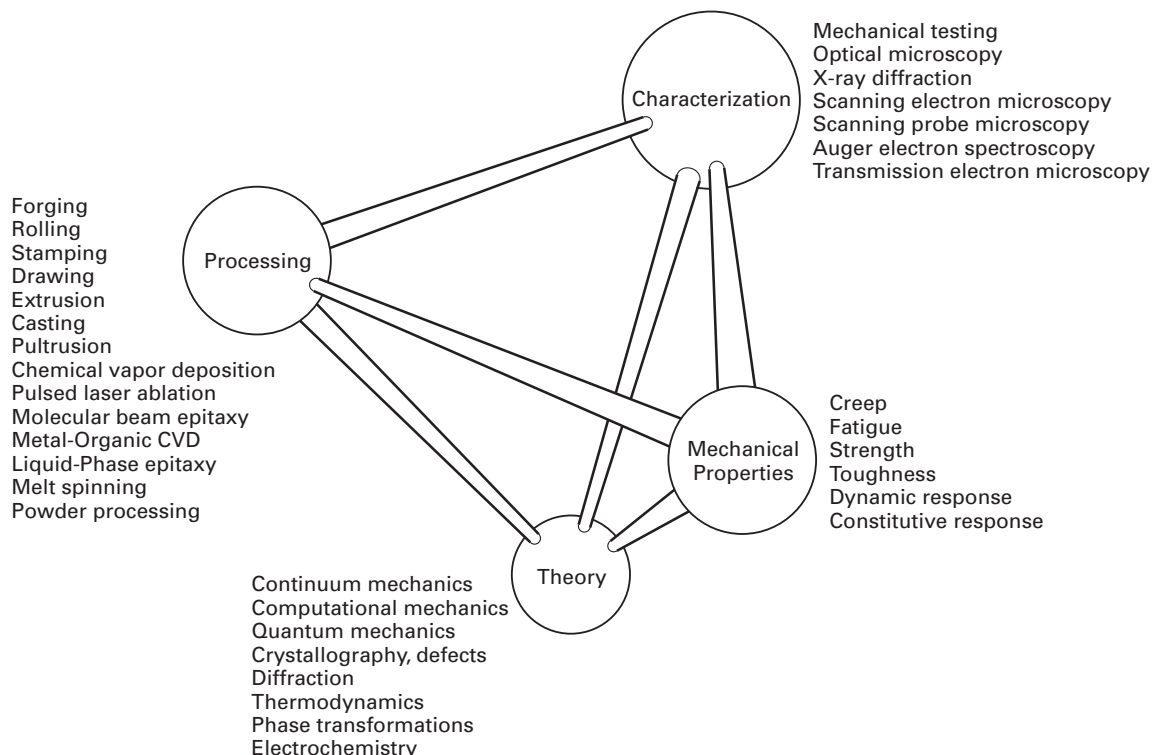


**Fig. I.1** Iterative materials tetrahedron applied to mechanical behavior of materials. (After G. Thomas.)

engine blocks. These different applications require, obviously, different mechanical properties of the material. The different properties of the three materials, resulting in differences in performance, are attributed to differences in the internal structure of the materials. The understanding of the structure comes from *theory*. The determination of the many aspects of the micro-, meso-, and macrostructure of materials is obtained by *characterization*. Low-carbon steel has a primarily ferritic structure (body-centered cubic; see Section 1.3.1), with some interspersed pearlite (a ferrite–cementite mixture). The high hardness of the quenched and tempered high-carbon steel is due to its martensitic structure (body-centered tetragonal). The relatively brittle cast iron has a structure resulting directly from solidification, without subsequent mechanical working such as hot rolling. How does one obtain low-carbon steel, quenched and tempered high-carbon steel, and cast iron? By different *synthesis* and *processing* routes. The low-carbon steel is processed from the melt by a sequence of mechanical working operations. The high-carbon steel is synthesized with a greater concentration of carbon (>0.5%) than the low-carbon steel (0.1%). Additionally, after mechanical processing, the high-carbon steel is rapidly cooled from a temperature of approximately 1,000 °C by throwing it into water or oil; it is then reheated to an intermediate temperature (tempering). The cast iron is synthesized with even higher carbon contents (~2%). It is poured directly into the molds and allowed to solidify in them. Thus, no mechanical working, except for some minor machining, is needed. These interrelationships among

structure, properties, and performance, and their modification by synthesis and processing, constitute the central theme of materials science and engineering. The tetrahedron of Figure 1.1 lists the principal processing methods, the most important theoretical approaches, and the most-used characterization techniques in materials science today.

The selection, processing, and utilization of materials have been part of human culture since its beginnings. Anthropologists refer to humans as “the toolmakers,” and this is indeed a very realistic description of a key aspect of human beings responsible for their ascent and domination over other animals. It is the ability of humans to manufacture and use tools, and the ability to produce manufactured goods, that has allowed technological, cultural, and artistic progress and that has led to civilization and its development. Materials were as important to a Neolithic tribe in the year 10,000 BC as they are to us today. The only difference is that today more complex synthetic materials are available in our society, while Neolithic tribes had only natural materials at their disposal: wood, minerals, bones, hides, and fibers from plants and animals. Although these naturally occurring materials are still used today, they are vastly inferior in properties to synthetic materials.

## 1.2 Monolithic, Composite, and Hierarchical Materials

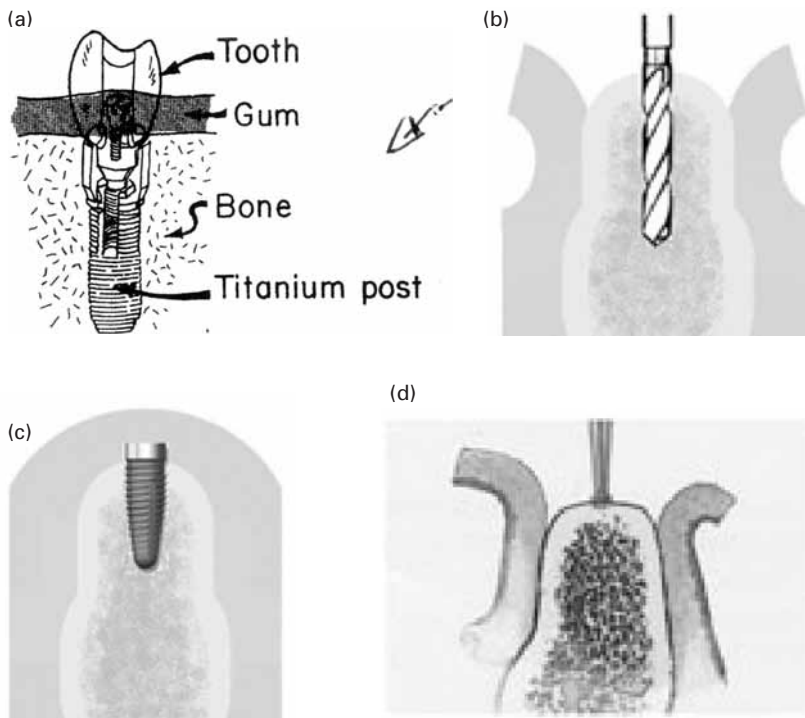
The early materials used by humans were natural, and their structure varied widely. Rocks are crystalline, pottery is a mixture of glassy and crystalline components, wood is a fibrous organic material with a cellular structure, and leather is a complex organic material. Human beings started to synthesize their own materials in the Neolithic period: ceramics first, then metals, and later, polymers. In the twentieth century, simple monolithic structures were used first. The term *monolithic* comes from the Greek *mono* (one) and *lithos* (stone). It means that the material has essentially uniform properties throughout. Microstructurally, monolithic materials can have two or more phases. Nevertheless, they have properties (electrical, mechanical, optical, and chemical) that are constant throughout. Table 1.1 presents some of the important properties of metals, ceramics, and polymers. Their detailed structures will be described in Section 1.3. The differences in their structure are responsible for differences in properties. Metals have densities ranging from 3 to 19 g/cm<sup>-3</sup>; iron, nickel, chromium, and niobium have densities ranging from 7 to 9 g/cm<sup>-3</sup>; aluminum has a density of 2.7 g/cm<sup>-3</sup>; and titanium has a density of 4.5 g/cm<sup>-3</sup>. Ceramics tend to have lower densities, ranging from 5 g/cm<sup>-3</sup> (titanium carbide; TiC = 4.9) to 3 g/cm<sup>-3</sup> (alumina; Al<sub>2</sub>O<sub>3</sub> = 3.95; silicon carbide; SiC = 3.2). Polymers have the lowest densities, fluctuating around 1 g cm<sup>-3</sup>. Another marked difference among these

**Table 1.1** Summary of Properties of Main Classes of Materials

Property	Metals	Ceramics	Polymers
Density (g/cm <sup>3</sup> )	from 2 to 20	from 1 to 14	from 1 to 2.5
Electrical conductivity	high	low	low
Thermal conductivity	high	low	low
Ductility or strain-to-fracture (%)	4–40	<1	2–4
Tensile strength (MPa)	100–1,500	100–400	—
Compressive strength (MPa)	100–1,500	1,000–5,000	—
Fracture toughness (MNm <sup>-3/2</sup> )	10–30	1–10	2–8
Maximum service temperature (°C)	1,000	1,800	250
Corrosion resistance	low to medium	superior	medium
Bonding	metallic (free-electron cloud)	ionic or covalent	covalent
Structure	mostly crystalline (Face-centered cubic; FCC) Body-centered cubic; BCC Hexagonal closed packed; HCP)	complex crystalline structure	amorphous or semicrystalline polymer

three classes of materials is their ductility (ability to undergo plastic deformation). At room temperature, metals can undergo significant plastic deformation. Thus, metals tend to be ductile, although there are a number of exceptions. Ceramics, on the other hand, are very brittle, and the most ductile ceramics will be more brittle than most metals. Polymers have a behavior ranging from brittle (at temperatures below their glass transition temperature) to very deformable (in a nonlinear elastic material, such as rubber). The fracture toughness is a good measure of the resistance of a material to failure and is generally quite high for metals and low for ceramics and polymers. Ceramics far outperform metals and polymers in high-temperature applications, since many ceramics do not oxidize even at very high temperatures (the oxide ceramics are already oxidized) and retain their strength to such temperatures. One can compare the mechanical, thermal, optical, electrical, and electronic properties of the different classes of materials and see that there is a very wide range of properties. Thus, monolithic structures built from primarily one class of material cannot provide all desired properties.

In the field of biomaterials (materials used in implants and life-support systems), developments also have had far-reaching effects. The mechanical performance of implants is critical in many applications, including hipbone implants, which are subjected to high stresses, and endosseous implants in the jaw designed to serve as the base for



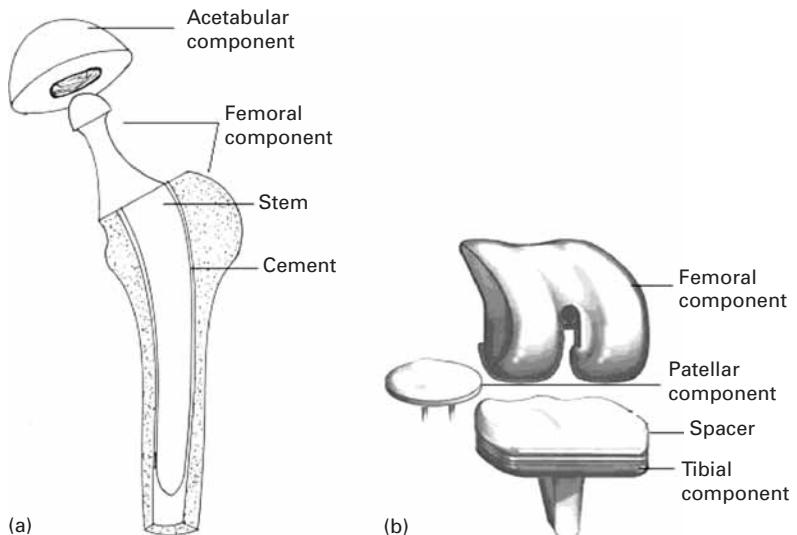
teeth. Figure 1.2 (a) shows the most successful design for endosseous implants in the jawbone. With this design, the tooth is fixed to the post and is effective. A titanium post is first screwed into the jawbone and allowed to heal. The tooth is then fixed to the post, and is effectively rooted into the jaw. The insertion of endosseous implants into the mandibles or maxillae, which was initiated in the 1980s, has been a revolution in dentistry. There is a little story associated with this discovery. Researchers were investigating the bone marrow of rabbits. They routinely used stainless steel hollow cylinders screwed into the bone. Through the hole, they could observe the bone marrow. It so happened that one of these cylinders was made of titanium. Since these cylinders were expensive, the researchers removed them periodically, in order to reuse them. When they tried to remove the titanium cylinder, it was tightly fused to the bone. This triggered the creative intuition of one of the researchers, who said “What if . . . ?”

Figure 1.2(c) shows the procedure used to insert the titanium implant. The site is first marked with a small drill that penetrates the cortical bone. Then successive drills are used to create the orifice of desired diameter (Figure 1.2(d)). The implant is screwed into the bone and the tissue is closed (Figure 1.2(c)). This implant is allowed to heal and fuse with the bone for approximately six months. Chances are that most readers will have these devices installed sometime in their lives.

Hip- and knee-replacement surgery is becoming commonplace. In the USA alone between 250,000 and 300,000 of each procedure are carried out annually. The materials of the prostheses have an

**Fig. 1.2** (a) Complete enclosures implant, (b) A hole is drilled and (c) a titanium post is screwed into jawbone. (d) Marking of site with small drill. (Courtesy of J. Mahooti.)

**Fig. 1.3** (a) Total hip replacement prosthesis; (b) total knee replacement prosthesis.



important bearing on survival probability. Typical hip and knee prostheses are shown in Figure 1.3.

The hip prosthesis is made up of two parts: the acetabular component, or socket portion, which replaces the acetabulum; the femoral component, or stem portion, which replaces the femoral head.

The femoral component is made of a metal stem with a metal ball on the extremity. In some prostheses a ceramic ball is attached to the metal stem. The acetabular component is a metal shell with a plastic inner socket liner made of metal, ceramic, or a plastic called ultra-high-molecular-weight polyethylene (UHMWP) that acts like a bearing. A *cemented* prosthesis is held in place by a type of epoxy cement that attaches the metal to the bone. An *uncemented* prosthesis has a fine mesh of holes on the surface area that touches the bone. The mesh allows the bone to grow into the mesh and become part of the bone. Biomaterial advances have allowed experimentation with new bearing surfaces, and there are now several different options when hip-replacement surgery is considered.

The metal has to be inert in the body environment. The preferred materials for the prostheses are Co-Cr alloys (Vitalium) and titanium alloys. However, there are problems that have not yet been resolved: the metallic components have elastic moduli that far surpass those of bone. Therefore, they “carry” a disproportionate fraction of the load, and the bone is therefore unloaded. Since the health and growth of bone is closely connected to the loads applied to it, this unloading tends to lead to bone loss.

The most common cause of joint replacement failure is wear of the implant surfaces. This is especially critical for the polymeric components of the prosthesis. This wear produces debris which leads to tissue irritation. Another important cause of failure is loosening of the implant due to weakening of the surrounding bone. A third source of failure is fatigue.

*Biocompatibility* is a major concern for all implants, and ceramics are especially attractive because of their (relative) chemical inertness. Metallic alloys such as Vitalium® (a cobalt-based alloy) and titanium alloys also have proved to be successful, as have polymers such as polyethylene. A titanium alloy with a solid core surrounded by a porous periphery (produced by sintering of powders) has shown considerable potential. The porous periphery allows bone to grow and affords very effective fixation. Two new classes of materials that appear to present the best biocompatibility with bones are the Bioglass® and calcium phosphate ceramics. Bones contain calcium and phosphorus, and Bioglass® is a glass in which the silicon has been replaced by those two elements. Thus, the bone “perceives” these materials as being another bone and actually bonds with it. Biomechanical properties are of great importance in bone implants, as are the elastic properties of materials. If the stiffness of a material is too high, then when implanted the material will carry more of the load placed on it than the adjacent bone. This could in turn lead to a weakening of the bone, since bone growth and strength depends on the stresses that the bone is subjected to. Thus, the elastic properties of bone and implant should be similar. Polymers reinforced with strong carbon fibers are also candidates for such applications. Metals, on the other hand, are stiffer than bones and tend to carry most of the load. With metals, the bones would be shielded from stress, which could lead to bone resorption and loosening of the implant.

Although new materials are being developed continuously, monolithic materials, with their uniform properties, cannot deliver the range of performance needed in many critical applications. Composites are a mixture of two classes of materials (metal-ceramic, metal-polymer, or polymer-ceramic). They have unique mechanical properties that are dependent on the amount and manner in which their constituents are arranged. Figure 1.4(a) shows schematically how different composites can be formed. Composites consist of a matrix and a reinforcing material. In making them, the modern materials engineer has at his or her disposal a very wide range of possibilities. However, the technological problems involved in producing some of them are immense, although there is a great deal of research addressing those problems. Figure 1.4(b) shows three principal kinds of reinforcement in composites: particles, continuous fibers, and discontinuous (short) fibers. The reinforcement usually has a higher strength than the matrix, which provides the ductility of the material. In ceramic-based composites, however, the matrix is brittle, and the fibers provide barriers to the propagating cracks, increasing the toughness of the material.

The alignment of the fibers is critical in determining the strength of a composite. The strength is highest along a direction parallel to the fibers and lowest along directions perpendicular to it. For the three kinds of composite shown in Figure 1.4(b), the polymer matrix plus (aramid, carbon, or glass) fiber is the most common combination if no high-temperature capability is needed.

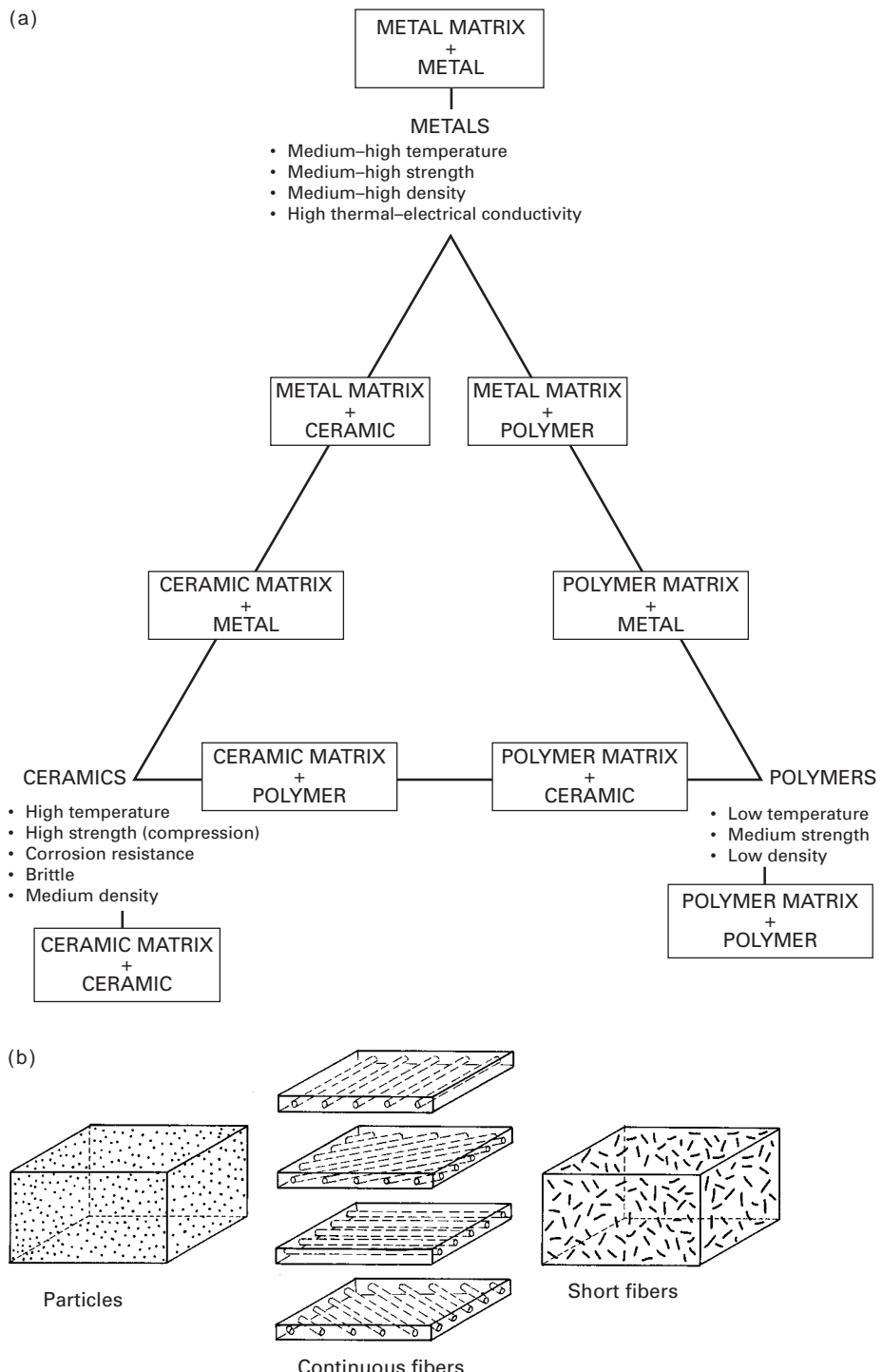


**Fig. 1.4** (a) Schematic representations of different classes of composites. (b) Different kinds of reinforcement in composite materials. Composite with continuous fibers with four different orientations (shown separately for clarity).

**Table 1.2** Specific Modulus and Strength of Materials Used in Aircraft

Material	Elastic Modulus	Tensile Strength
	Density (GPa/g · cm <sup>-3</sup> )	Density (MPa/g · cm <sup>-3</sup> )
Steel (AISI 4340)	25	230
Al (7075-T6)	25	180
Titanium (Ti-6Al-4V)	25	250
E Glass/Epoxy composite	21	490
S Glass/Epoxy composite	47	790
*Axamid/Epoxy composite	55	890
HS (High Tensile Strength) Carbon/Epoxy composite	92	780
HM (high modulus) Carbon/Epoxy composite	134	460

Composites are becoming a major material in the aircraft industry. Carbon/epoxy and aramid/epoxy composites are being introduced in a large number of aircraft parts. These composite parts reduce the weight of the aircraft, increasing its economy and payload. The major mechanical property advantages of advanced composites over metals are better stiffness-to-density and strength-to-density ratios and greater resistance to fatigue. The values given in Table 1.2 apply to a unidirectional composite along the fiber reinforcement orientation. The values along other directions are much lower, and therefore the design of a composite has to incorporate the anisotropy of the materials. It is clear from the table that composites have advantages over monolithic materials. In most applications, the fibers are arranged along different orientations in different layers. For the central composite of Figure 1.4(b), these orientations are 0°, 45°, 90°, and 135° to the tensile axis.

Can we look beyond composites in order to obtain even higher mechanical performance? Indeed, we can: Nature is infinitely imaginative.

Our body is a complex arrangement of parts, designed, as a whole, to perform all the tasks needed to keep us alive. Scientists are looking into the make-up of soft tissue (skin, tendon, intestine, etc.), which is a very complex structure with different units active at different levels complementing each other. The structure of soft tissue has been called a *hierarchical* structure, because there seems to be a relationship between the ways in which it operates at different levels. Figure 1.5 shows the structure of a tendon. This structure begins with the tropocollagen molecule, a triple helix of polymeric protein chains. The tropocollagen molecule has a diameter of approximately

**Fig. 1.5** A model of a hierarchical structure occurring in the human body. (Adapted from E. Baer, *Sci. Am.* 254, No. 10 (1986) 179.)

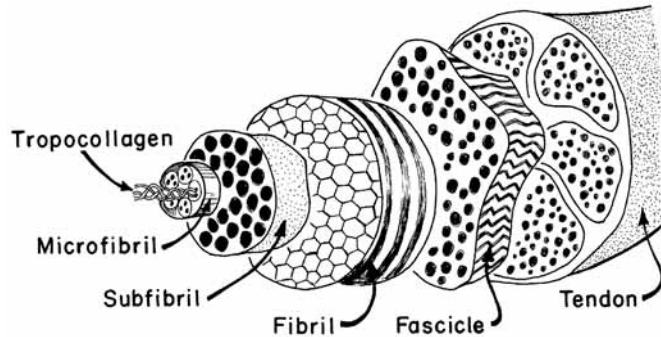
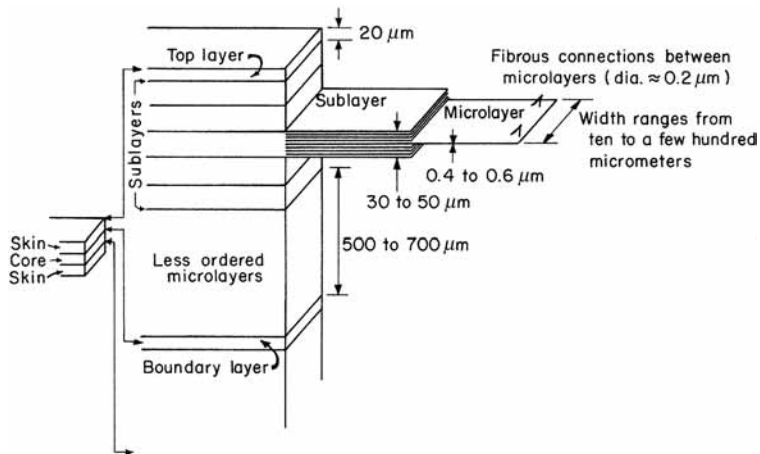


**Fig. 1.6** Schematic illustration of a proposed hierarchical model for a composite (not drawn to scale). (Courtesy of E. Baer.)



1.5 mm. The tropocollagen organizes itself into microfibrils, subfibrils, and fibrils. The fibrils, a critical component of the structure, are crimped when there is no stress on them. When stressed, they stretch out and then transfer their load to the fascicles, which compose the tendon. The fascicles have a diameter of approximately 150–300 μm and constitute the basic unit of the tendon. The hierarchical organization of the tendon is responsible for its toughness. Separate structural units can fail independently and thus absorb energy locally, without causing the failure of the entire tendon. Both experimental and analytical studies have been done, modeling the tendon as a composite of elastic, wavy fibers in a viscoelastic matrix. Local failures, absorbing energy, will prevent catastrophic failure of the entire tendon until enormous damage is produced.

Materials engineers are beginning to look beyond simple two-component composites, imitating nature in organizing different levels of materials in a hierarchical manner. Baer<sup>1</sup> suggests that the study of biological materials could lead to new hierarchical designs for composites. One such example is shown in Figure 1.6, a layered structure of liquid-crystalline polymers consisting of alternating core and skin layers. Each layer is composed of sublayers which, in their

<sup>1</sup> E. Baer, *Sci. Am.* 254, No. 10 (1986) 179.

turn, are composed of microlayers. The molecules are arranged in different arrays in different layers. The lesson that can be learned from this arrangement is that we appear to be moving toward composites of increasing complexity.

### Example 1.1 | (Design problem)

Discuss advanced materials used in bicycle frames.

This is a good case study, and the instructor can “pop” similar questions on an exam, using different products. For our specific example here, we recommend the insightful article by M. F. Ashby, *Met. and Mat. Trans.*, A 26A (1995) 3057. Ashby states that “Materials and processes underpin all engineering design.”



**Fig. E1.1** Bending moments ( $M_1$  and  $M_2$ ) and torsional torques ( $T_1$  and  $T_2$ ) generated in bicycle frame by forces  $F_1$  and  $F_2$  applied to pedals.

Figure E1.1 shows a bicycle, with forces  $F_1$  and  $F_2$  applied to the frame by the pedals. These forces produce bending moments and torsions in the frame tubes. In bicycle frames, weight and stiffness are the two primary requirements. Stiffness is important because excessive flexing of the bicycle upon pedaling absorbs energy that should be used

to propel the bicycle forward. This requires the definition of new properties, because just the strength or endurance limit (the stress below which no failure due to fatigue occurs) and Young's modulus (defined in Chapter 2) are not sufficient. In conversations, we always say that aluminum bicycles are "stiffer" than steel bicycles, whereas steel provides a more "cushioned" ride. An aluminum bicycle may indeed be stiffer than a steel bicycle, although  $E_{st}$  ( $= 210$  GPa)  $\approx 3 E_{A1}$  ( $= 70$  GPa). We will see shortly how this can happen and what is necessary for it to occur. The forces  $F_1$  and  $F_2$  cause bending moments ( $M_1$  and  $M_2$ ), respectively. The bending stresses in a hollow tube of radius  $r$  and thickness  $t$  are<sup>2</sup>

$$\sigma = \frac{Mr}{I},$$

where  $I$  is the moment of inertia,  $M$  the bending moment, and  $r$  the radius of the tube. Setting  $\sigma = \sigma_e$ , the endurance limit, and substituting the expression for the moment of inertia  $I = \pi r^3 t$ , we obtain the thickness of the tube,  $t$ , from:

$$M = \frac{\sigma_e \pi^3 t}{r}.$$

From strength considerations, the mass per unit length of the bicycle frame is

$$\frac{m}{L} = 2\pi r t \rho = \frac{2M}{r} \left( \frac{\rho}{\sigma_e} \right), \quad (\text{E1.1.1})$$

where  $\rho$  is the density of the frame. Now, the radius of curvature  $\rho'$  of a circular beam under bending is given by the Bernoulli-Euler equation,

$$\frac{1}{\rho'} = \frac{d^2 v}{dx^2} = \frac{M}{EI},$$

where  $v$  is the deflection of the beam. Substituting for  $I$ , we obtain

$$\frac{1}{\rho'} = \frac{M}{E \pi r^3 t}, \text{ or } \pi r t = \frac{M \rho'}{r^2 E}.$$

From bending considerations, the mass per unit length is

$$\frac{m}{L} = 2\pi r t \rho = \frac{2M \rho'}{r^2} \left( \frac{\rho}{E} \right) \quad (\text{E1.1.2})$$

A similar expression can be developed for the torsion, which is important in pedaling. The torsion is shown in Figure E1.2 as  $T_1$  and  $T_2$ . Since  $M$ , the applied moment, is given by the weight of cyclist, it is constant for each frame. Likewise, the maximum curvature  $1/\rho'$  can be fixed. The quantity  $m/L$  has to be minimized for both strength and stiffness considerations. Ashby accomplished this by plotting  $(\sigma_e/\rho)$  and  $(E/\rho)$ , whose reciprocals appear in Equations (E1.1.1) and (E1.1.2), respectively. (See Figure E1.2.) The computations assume a constant  $r$ , but

---

<sup>2</sup> Students should consult their notes on the mechanics of materials or examine a book such as *Engineering Mechanics of Solids*, by E. P. Popov (Englewood Cliffs, NJ: Prentice Hall, 1990).

varying tube thickness  $t$ . The most common candidate metals (steels, titanium, and aluminum alloys) are closely situated in the figure. The expanded window in this region shows a clearer separation of the various alloys. Continuous carbon fiber reinforced composites (CFRPs) are the best materials, and polymers and glass/fiber reinforced polymer composites (GFRPs) have insufficient stiffness. By relaxing the requirement of constant  $r$  and allowing different tube radii, the results are changed considerably. This example illustrates how material properties enter into the design of a product and how compound properties ( $E/\rho$ ,  $\sigma/\rho$ ) need to be defined for a specific application. It can be seen from Equations (E1.1.1) and (E1.1.2) that strength scales with  $r$  and stiffness with  $r^2$ . By varying  $r$ , it is possible to obtain aluminum bicycle frames that are stiffer than steel. Now the student is prepared to go on a bike ride!

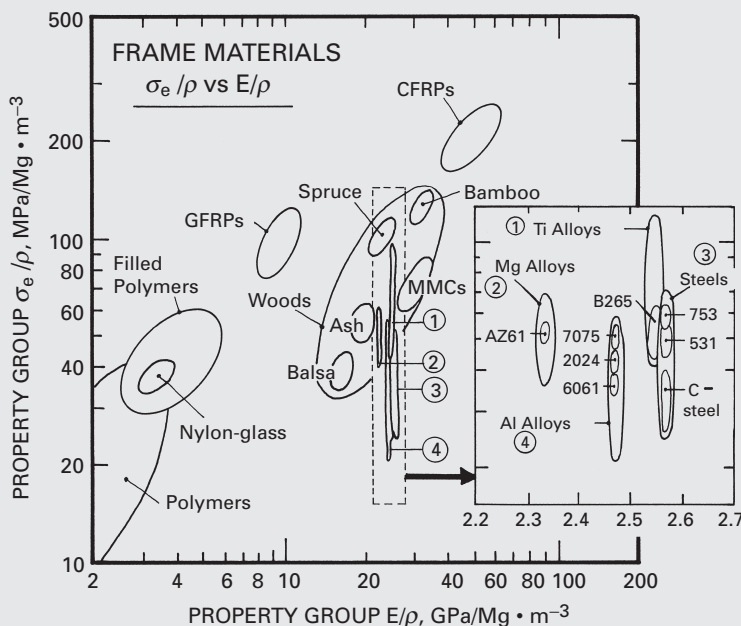


**Fig. E1.2** Normalized strength ( $\sigma_e/\rho$ ) versus normalized Young's modulus ( $E/\rho$ ) for potential bicycle frames. (Adapted from M. F. Ashby, *Met. and Mat. Trans.*, **A26** (1995) 3057.)

### Example 1.2

Suppose you are a design engineer for the ISAACS bicycle company. This company traditionally manufactures chromium-molybdenum (Cr-Mo) steel frames. The racing team is complaining that the bicycles are too “soft” and that stiffer bicycles would give them a competitive edge. Additionally, the team claims that competing teams have aluminum bikes which are considerably lighter. You are asked to

redesign the bikes, using a precipitation hardenable aluminum alloy (7075 H4).

- Calculate the ratio of the stiffness of the two bikes if the tube diameters are the same.
- What would you do to increase the stiffness of the two bikes?
- If the steel frame weighs 4 kg, what would the aluminum frame weigh? State your assumptions.

Given:

	$\sigma_e$ (MPa)	$\rho$ (kg/m <sup>3</sup> )	$E$ (GPa)	$G$ (GPa)
7075 Al	500	2700	70	27
4340 Steel	1350	7800	210	83

Steel tube diameter,  $2r = 25$  mm

Wall thickness,  $t = 1.25$  mm

**Solution:** The mass per unit length, from strength considerations, is

$$\frac{m}{L} = 2\pi rt\rho = \frac{2M}{r} \left( \frac{\rho}{\sigma_e} \right).$$

The mass per unit length, from bending considerations, is

$$\frac{m}{L} = 2\pi rt\rho = \frac{2M\rho'}{r^2} \left( \frac{\rho}{E} \right).$$

where  $\rho'$  is the radius of curvature and  $M$  is the bending moment applied by cyclist.

The radius of curvature  $\rho'$  is a good measure of the stiffness; the larger  $\rho'$ , the higher is the stiffness, for a fixed  $M$ .

- $r_{Al} = r_{St} = 12.5$  mm.

For the two metals, we have:

	Steel	Aluminum
$\rho/\sigma_e$	5.77	5.4
$\rho/E$	37.14	38.57

The mass-to-length ratios are

$$\frac{\left(\frac{m}{L}\right)_{St}}{\left(\frac{m}{L}\right)_{Al}} = \frac{\frac{2M}{r} \left( \frac{\rho}{\sigma_e} \right) |_{St}}{\frac{2M}{r} \left( \frac{\rho}{\sigma_e} \right) |_{Al}} = 1.06.$$

For the same weight, we calculate the ratio of the radii of curvature from bending:

$$1.06 \frac{\rho'_{Al}}{\rho'_{St}} = \frac{\left(\frac{\rho}{E}\right)_{St}}{\left(\frac{\rho}{E}\right)_{Al}} = 0.96,$$

$$\frac{\rho'_{Al}}{\rho'_{St}} = \frac{0.96}{1.06} = 0.91.$$

Thus, the stiffness is approximately the same for each metal.

(b) We increase diameter of the tubes. This is possible because the wall thickness of aluminum bikes is approximately three times the wall thickness of steel bikes.<sup>3</sup> For instance, we can increase the diameter to 50 mm!<sup>4</sup>

(c) Let us assume that, for aluminum,  $2r_{Al} = 50$  mm. Then

$$\frac{\left(\frac{m}{L}\right)_{St}}{\left(\frac{m}{L}\right)_{Al}} = x = \frac{\frac{2M\rho'_{St}}{r_{St}^2} \left(\frac{\rho}{E}\right)_{St}}{\frac{2M\rho'_{Al}}{r_{Al}^2} \left(\frac{\rho}{E}\right)_{Al}},$$

$$x \frac{\rho'_{Al} r_{St}^2}{\rho'_{St} r_{Al}^2} = \frac{\left(\frac{\rho}{E}\right)_{St}}{\left(\frac{\rho}{E}\right)_{Al}}.$$

Going back to the strength equation, we obtain

$$x = \frac{\left(\frac{m}{L}\right)_{St}}{\left(\frac{m}{L}\right)_{Al}} = \frac{\frac{2M}{r_{St}} \left(\frac{\rho}{\sigma_e}\right)_{St}}{\frac{2M}{r_{Al}} \left(\frac{\rho}{\sigma_e}\right)_{Al}} = 2 \frac{5.77}{5.4} = 2.14.$$

If the total weight of the steel frame is 4 kg, then

$$\frac{w_{Al}}{w_{St}} = \frac{\left(\frac{m}{L}\right)_{Al}}{\left(\frac{m}{L}\right)_{St}} \cdot w_{St} = \frac{4}{2.14} = 1.86.$$

The stiffness ratio will be

$$\frac{\rho'_{Al}}{\rho'_{St}} = \frac{1}{x} \frac{r_{Al}^2}{r_{St}^2} \frac{\left(\frac{\rho}{E}\right)_{St}}{\left(\frac{\rho}{E}\right)_{Al}} = \frac{4}{2.14} \frac{37.14}{38.54} = 1.80,$$

or

$$\rho'_{Al} = 1.8 \rho'_{St}.$$

The aluminum bike is almost twice as stiff!

## 1.3 | Structure of Materials

The *crystallinity*, or periodicity, of a structure, does not exist in gases or liquids. Among solids, the metals, ceramics, and polymers may or may not exhibit it, depending on a series of processing and composition parameters. Metals are normally crystalline. However, a metal cooled at a superfast rate from its liquid state – called *splat cooled* – can have an amorphous structure. (This subject is treated in greater detail in Section 1.3.4.) Silicon dioxide ( $SiO_2$ ) can exist as amorphous (fused silica) or as crystal (crystoballite or trydimite). Polymers consisting of molecular chains can exist in various degrees of crystallinity.

Readers not familiar with structures, lattices, crystal systems, and Miller indices should study these subjects before proceeding with

<sup>3</sup> Since the wall thickness is larger, we can produce larger tube diameters without danger of collapse by buckling.

<sup>4</sup> A 50-mm steel tube would have walls that would be exceedingly thin; indeed, it could be dented by pressing it with the fingers.

the text. Most books on materials science, physical metallurgy, or X-rays treat the subjects completely. A brief introduction is presented next.

### 1.3.1 Crystal Structures

To date, seven crystal structures describe all the crystals that have been found. By translating the unit cell along the three crystallographic orientations, it is possible to construct a three-dimensional array. The translation of each unit cell along the three principal directions by distances that are multiples of the corresponding unit cell size produces the crystalline lattice.

Up to this point, we have not talked about atoms or molecules; we are just dealing with the mathematical operations of filling space with different shapes of blocks. We now introduce atoms and molecules, or “repeatable structural units.” The unit cell is the smallest repetitive unit that will, by translation, produce the atomic or molecular arrangement. Bravais established that there are 14 space lattices. These lattices are based on the seven crystal structures. The points shown in Figure 1.7 correspond to atoms or groups of atoms. The 14 Bravais lattices can represent the unit cells for all crystals. Figure 1.8 shows the indices used for directions in the cubic system. The same symbols are employed for different structures. We simply use the vector passing through the origin and a point  $(m, n, o)$ :

$$\mathbf{V} = m\mathbf{i} + n\mathbf{j} + o\mathbf{k}.$$

When the direction does not pass through the origin, and we have the head of the vector at  $(m, n, o)$  and the tail at  $(p, q, r)$ , the vector  $\mathbf{V}$  is given by:

$$\mathbf{V} = (m - p)\mathbf{i} + (n - q)\mathbf{j} + (o - r)\mathbf{k}.$$

The notation used for a direction is

$$[m \ n \ o].$$

When we deal with a family of directions, we use the symbol  $\langle m \ n \ o \rangle$ .

The following family encompasses all equivalent directions:

$$\begin{aligned} \langle m \ n \ o \rangle \Rightarrow & [m \ n \ o], [m \ o \ n], [o \ m \ n], [o \ n \ m], [n \ m \ o], [m \ \bar{n} \ o], \\ & [m \ o \ \bar{n}], [o \ m \ \bar{n}], [o \ \bar{n} \ m], [\bar{n} \ m \ o], \dots \end{aligned}$$

A direction not passing through the origin can be represented by

$$[(m - p)(n - q)(o - r)].$$

Note that for the negative, we use a bar on top. For planes, we use the Miller indices, obtained from the intersection of a plane with the coordinate axes. Figure 1.9 shows a plane and its intercepts. We take the inverse of the intercepts and multiply them by their common

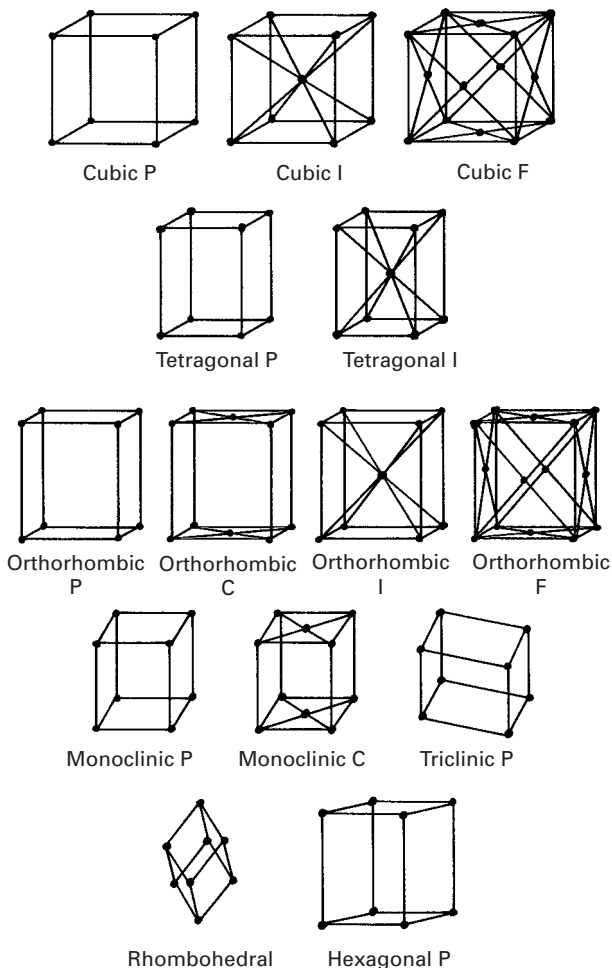


**Fig. 1.7** The 14 Bravais space lattices (P = primitive or simple; I = body-centered cubic; F = face-centered cubic; C = base-centered cubic).

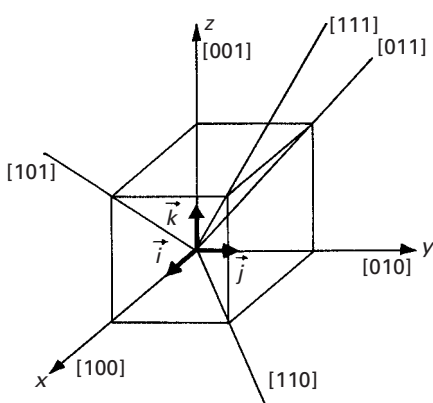


**Fig. 1.8** Directions in a cubic unit cell.

**Fig. 1.9** Indexing of planes by Miller rules in the cubic unit cell.

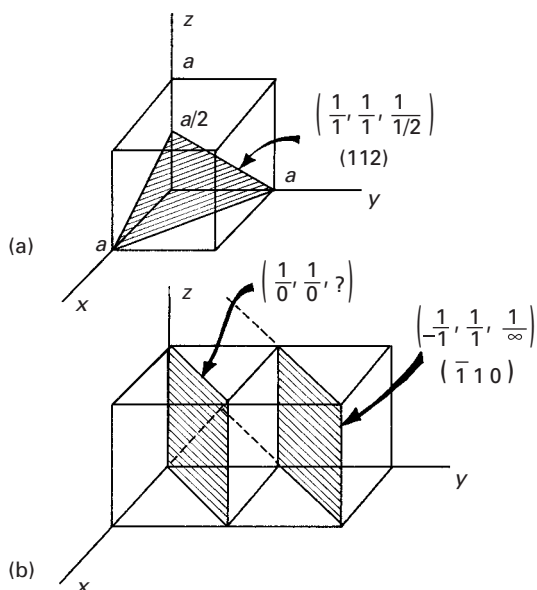
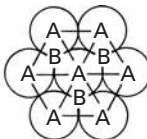
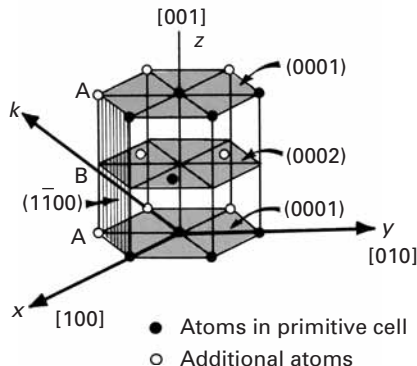


**Fig. 1.10** Hexagonal structure consisting of a three-unit cell.



Stacking of (0002) planes



denominator so that we end up with integers. In Figure 1.9 (a), we have

$$\frac{1}{1}, \frac{1}{1}, \frac{1}{1/2} \Rightarrow (112).$$

Figure 1.9(b) shows an indeterminate situation. Thus, we have to translate the plane to the next cell, or else translate the origin. The indeterminate situation arises because the plane passes through the origin. After translation, we obtain intercepts  $(-1, 1, \infty)$ . By inverting them, we get  $(\bar{1} 10)$ . The symbol for a family of planes is  $\{m n o\}$ .

For hexagonal structures, we have a slightly more complicated situation. We represent the hexagonal structure by the arrangement shown in Figure 1.10. The atomic arrangement in the basal plane is shown in the top portion of the figure. Often, we use four axes ( $x$ ,  $y$ ,  $k$ ,  $z$ ) with unit vectors ( $\vec{i}$ ,  $\vec{j}$ ,  $\vec{k}$ ,  $\vec{l}$ ) to represent the structure. This is mathematically unnecessary, because three indices are sufficient to represent a direction in space from a known origin. Still, the redundancy is found by some people to have its advantages and is described here. We use the intercepts to designate the planes. The hatched plane (prism plane) has indices

$$\frac{1}{1}, \frac{1}{-1}, \frac{1}{\infty}, \frac{1}{\infty}.$$

After determining the indices of many planes, we learn that one always has

$$h + k = -i.$$

Thus, we do not have to determine the index for the third horizontal axis. If we use only three indices, we can use a dot to designate the fourth index, as follows:

$$(1\bar{1}\cdot 0).$$

For the directions, we can use either the three-index notation or a four-index notation. However, with four indices, the  $h + k = -i$  rule will not apply in general, and one has to use special “tricks” to make the vector coordinates obey the rule.

If the indices in the three-index notation are  $h'$ ,  $k'$ , and  $\ell'$ , the four index notation of directions can be obtained by the following simple equations;

$$h = \frac{1}{3}(2h' - k')$$

$$k = \frac{1}{3}(2k' - h')$$

$$i = -\frac{1}{3}(h' + k')$$

$$\ell = \ell'$$

It can be easily verified that  $h + k = -i$ . Thus, the student is equipped to express the directions in the four-index notation.

### 1.3.2 Metals

The metallic bond can be visualized, in a very simplified way, as an array of positive ions held together by a “glue” consisting of electrons. These positive ions, which repel each other, are attracted to the “glue,” which is known as an electron gas. Ionic and covalent bonding, on the other hand, can be visualized as direct attractions between atoms. Hence, these types of bonding – especially covalent

### Example 1.3 |

Write the indices for the directions and planes marked in Figure E1.3.

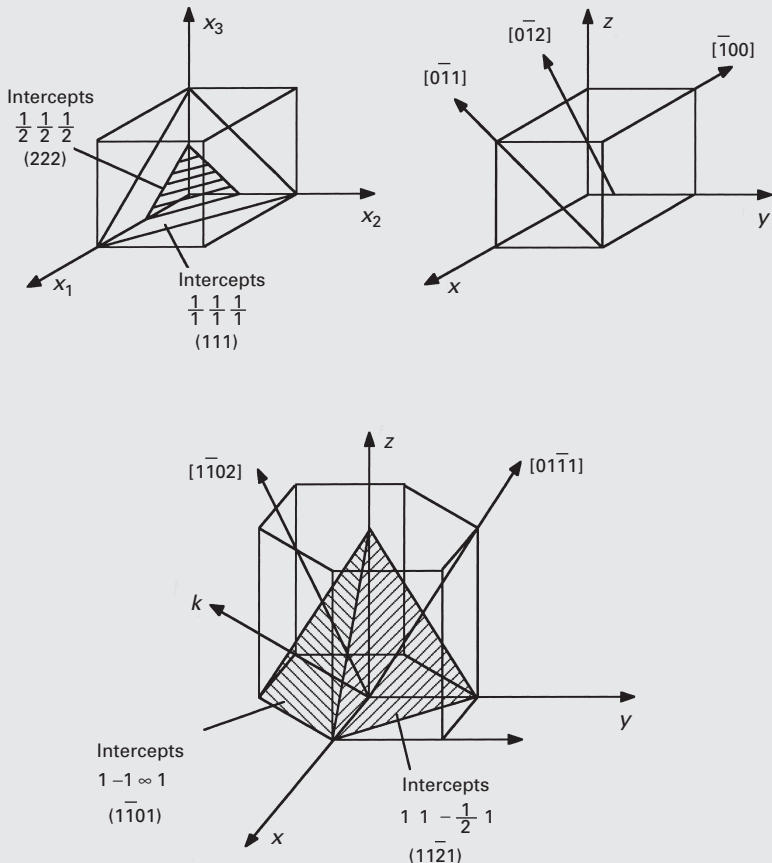
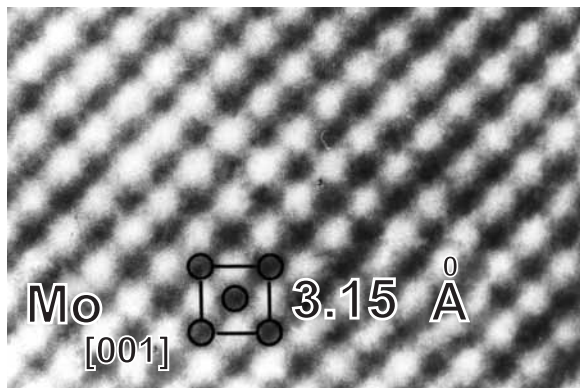


Fig. E1.3

bonding – are strongly directional and determine the number of neighbors that one atom will have, as well as their positions.

The bonding – and the sizes of the atoms in turn – determines the type of structure a metal has. Often, the structure is very complicated for ionic and covalent bonding. On the other hand, the directionality of bonding is not very important for metals, and atoms pack into the simplest and most compact forms; indeed, they can be visualized as spheres. The structures favored by metals are the face-centered cubic (FCC), body-centered cubic (BCC), and hexagonal close-packed (HCP) structures. In the periodic table, of the 81 elements to the left of the Zindl line, 53 have either the FCC or the HCP structure, and 21 have the BCC structure; the remaining 8 have other structures. The Zindl line defines the boundary of the elements with metallic character in the table. Some of them have several structures, depending on temperature. Perhaps the most



**Fig. 1.11** Transmission electron micrograph of atomic resolution of (001) plane in molybdenum showing body-centered cubic arrangement of atoms. (Courtesy of R. Gronsky.)

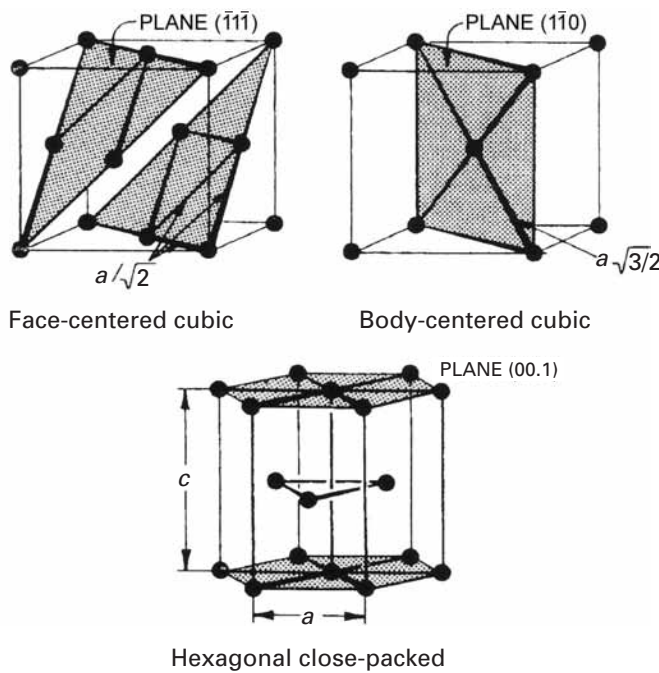


**Fig. 1.12** Most closely packed planes in (a) FCC; (b) BCC; (c) HCP.

complex of the metals is plutonium, which undergoes six polymorphic transformations.

Transmission election microscopy can reveal the positions of the individual atoms of a metal, as shown in Figure 1.11 for molybdenum. The regular atomic array along a [001] plane can be seen. Molybdenum has a BCC structure.

Figure 1.12 shows the three main metallic structures. The positions of the atoms are marked by small spheres and the atomic planes by dark sections. The small spheres do not correspond to the scaled-up size of the atoms, which would almost completely fill the available space, touching each other. For the FCC and HCP structures, the co-ordination number (the number of nearest neighbors of an atom) is 12. For the BCC structure, it is 8.

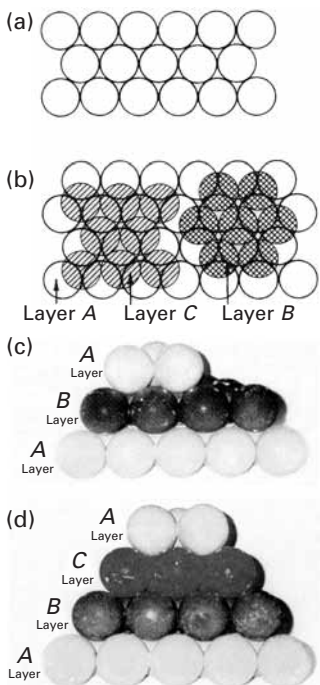


**Fig. 1.13** (a) Layer of most closely packed atoms corresponding to (111) in FCC and (00.1) in HCP. (b) Packing sequence of most densely packed planes in AB and AC sequence. (c) Photograph of ball model showing the ABAB sequence of the HCP structure. (d) Photograph of ball model showing the ABCABC sequence of the FCC structure.

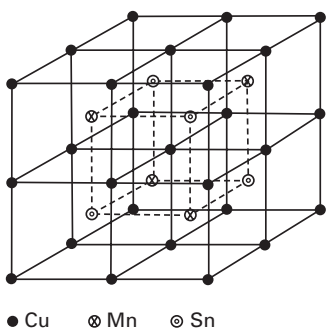


**Fig. 1.14**  $\beta$ -ordered phase in Heusler alloys ( $\text{Cu}_2\text{MnSn}$ ). (Reprinted with permission from M. A. Meyers, C. O. Ruud, and C. S. Barrett, *J. Appl. Cryst.*, 6 (1973) 39.)

The planes with the densest packing are indicated in the figure. They are (111), (110), and (00.1) for the FCC, BCC, and HCP structures, respectively. These planes have an important effect on the directionality of deformation of the metal, as will be seen in chapters 4 and 6. The distances between the nearest neighbors are also indicated in the figure. The reader should try to calculate them as an exercise. These distances are  $a\sqrt{2}$ ,  $(a\sqrt{3}/2)$ , and  $a$  for the FCC, BCC, and HCP structures, respectively.

The similarity between the FCC and HCP structures is much greater than might be expected from looking at the unit cells. Planes (111) and (00.1) have the same packing, as may be seen in Figure 1.13. This packing, the densest possible of coplanar spheres, is shown in Figure 1.13(a). The packing of a second plane similar to, and on top of, the first one (called A) can be made in two different ways; Figure 1.13(b) indicates these two planes by the letters B and C. Hence, either alternative can be used. A third plane, when placed on top of plane B, would have two options: A or C. If the second plane is C, the third plane can be either A or B. If only the first and second layers are considered, the FCC and HCP structures are identical. If the position of the third layer coincides with that of the first (the ABA or ACA sequence), we have the HCP structure. Since this packing has to be systematically maintained in the lattice, one would have ABABAB . . . or ACACAC . . . In case the third plane does not coincide with the first, we have one of the two alternatives ABC or ACB. Since this sequence has to be systematically maintained, we have ABCAB-CABC . . . or ACBACBACB . . . This stacking sequence corresponds to the FCC structure. We thus conclude that the only difference between the FCC and HCP structures (the latter with a theoretical  $c/a$  ratio of 1.633) is the stacking sequence of the most densely packed planes. The difference resides in the next neighbors and in the greater symmetry of the FCC structure.

Figures 1.13(c) and (d) show photographs of ideal ball stackings. The ABA . . . sequence of layers, characteristic of HCP structure (Figure 1.13(c)) is compared with the ABCA . . . sequence for the FCC structure (Figure 1.13(d)).

In addition to the metallic elements, intermediate phases and intermetallic compounds exist in great numbers, with a variety of structures. For instance, the beta phase in the copper–manganese–tin ( $\text{Cu}-\text{Mn}-\text{Sn}$ ) system exhibits a special ordering for the composition  $\text{Cu}_2\text{MnSn}$ . The unit cell (BCC) is shown in Figure 1.14. However, the ordering of the Cu, Mn, and Sn atoms creates a superlattice composed of four BCC cells. This superlattice is FCC; hence, the unit cell for the ordered phase is FCC, whereas that for the disordered phase has a BCC unit cell. This ordering has important effects on the mechanical properties and is discussed in Chapter 11.

Table 1.3 lists some of the most important intermetallic compounds and their structures. Intermetallic compounds have a bonding that is somewhat intermediate between metallic and ionic/covalent bonding, and have properties that are most desirable for high-temperature applications. Nickel and titanium aluminides are

**Table 1.3** Some Important Intermetallic Compounds and Their Structure

Compound	Melting Point (°C)	Type of Structure
$\text{Ni}_3\text{Al}$	1,390	$\text{Ll}_2$ (ordered FCC)
$\text{Ti}_3\text{Al}$	1,600	$\text{DO}_{19}$ (ordered hexagonal)
$\text{TiAl}$	1,460	$\text{Ll}_0$ (ordered tetragonal)
$\text{Ni-Ti}$	1,310	$\text{CsCl}$
$\text{Cu}_3\text{Au}$	1,640	$\text{B}_2$ (ordered BCC)
$\text{FeAl}$	1,250–1,400	$\text{B}_2$ (ordered BCC)
$\text{NiAl}$	1,380–1,638	$\text{B}_2$ (ordered BCC)
$\text{MoSi}_2$	2,025	$\text{C}11_b$ (tetragonal)
$\text{Al}_3\text{Ti}$	1,300	$\text{DO}_{22}$ (tetragonal)
$\text{Nb}_3\text{Sn}$	2,134	$\text{A}15$
$\text{Nb}_5\text{Si}_3$	2,500	(tetragonal)

candidates for high-temperature applications in jet turbines and aircraft applications.

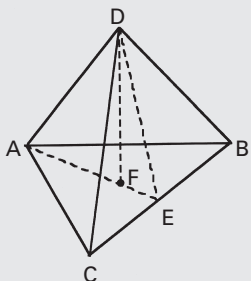
**Example 1.4**

Determine the ideal  $c/a$  ratio for the hexagonal structure.

**Solution:** The atoms in the basal A plane form a closely packed array, as do the atoms in the B plane going through the mid plane. If we take three atoms in the basal plane, with an atom in the B plane resting among them, we have constructed a tetrahedron. The sides of the tetrahedron are  $2r = a$ , where  $r$  is the atomic radius. The height of this tetrahedron is  $c/2$ , since the distance between planes is  $c$ . Hence, the problem is now reduced to finding the height,  $c/2$ , of a regular tetrahedron. In Figure E1.4, we have

$$DF = \frac{c}{2},$$

$$AB = AC = BC = AD = DB = DC = a.$$

**Fig. E1.4**

For triangle  $AEC$ ,

$$AE^2 + EC^2 = AC^2,$$

$$AE = \sqrt{a^2 - \frac{a^2}{4}} = \frac{a}{2}\sqrt{3}.$$

For triangle  $DFE$ ,

$$EF^2 = DF^2 = DE^2.$$

But

$$EF = \frac{1}{3}AE = \frac{a}{6}\sqrt{3},$$

$$DE = AE = \frac{a}{2}\sqrt{3},$$

$$DF = \left(\frac{3a^2}{4} - \frac{3a^2}{36}\right)^{1/2},$$

$$\frac{c}{2} = a\left(\frac{2}{3}\right)^{1/2},$$

$$\frac{c}{a} = 2\left(\frac{2}{3}\right)^{1/2}.$$

Thus,

$$\boxed{\frac{c}{a} = 1.633.}$$

### Example 1.5 |

If the copper atoms have a radius of 0.128 nm, determine the density in FCC and BCC structures.

(i) In FCC structures,  $4r = \sqrt{2}a_0$

$$a_0 = \frac{4}{\sqrt{2}}r = \frac{4}{\sqrt{2}} \times 0.128 \text{ nm}$$

$$a_0 = 0.362 \text{ nm}$$

There are 4 atoms per unit cell in FCC. Atomic mass (or weight) of copper is 63.54 g/g.mol. So, density of copper ( $\rho$ ) in FCC structures is

$$\rho = \frac{63.54 \times 4}{(0.362 \times 10^{-7})^3 \times (6.02 \times 10^{23})} = 8.89 \text{ g/cm}^3$$

↑  
Avogadro's number

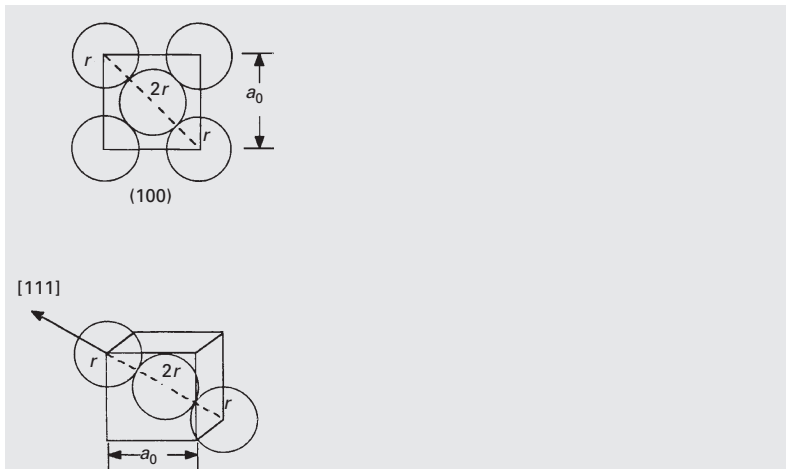
(ii) In BCC structures,  $4r = \sqrt{3}a_0$

$$a_0 = \frac{4}{\sqrt{3}}r = \frac{4}{\sqrt{3}} \times 0.128 \text{ nm}$$

$$a_0 = 0.296 \text{ nm}$$

There are 2 atoms per unit cell in BCC structures.

$$\rho = \frac{63.54 \times 2}{(0.296 \times 10^{-7})^3 \times (6.02 \times 10^{23})} = 8.14 \text{ g/cm}^3$$

**Fig. E1.5**

The stable form of Cu is FCC. Only under unique conditions, such as Cu precipitates in iron, is the BCC form stable (because of the constraints of surrounding material).

### 1.3.3 Ceramics

The name ceramic comes from the Greek KERAMOS (pottery). The production of pottery made of clay dates from 6500 BC. The production of silicate glass in Egypt dates from 1500 BC. The main ingredient of pottery is a hydrous aluminum silicate that becomes plastic when mixed, in fine powder form, with water. Thus, the early utilization of ceramics included both crystalline and glassy materials. Portland cement is also a silicate ceramic; by far the largest tonnage production of ceramics today – glasses, clay products (brick, etc.), cement – are silicate-based.

However, there have been dramatic changes since the 1970s and a wide range of new ceramics has been developed. These new ceramics are finding applications in computer memories (due to their unique magnetic applications), in nuclear power stations ( $\text{UO}_2$  fuel rods), in rocket nose cones and throats, in submarine sonar units (piezoelectric barium titanate), in jet engines (as coatings to metal turbine blades) as electronic packaging components ( $\text{Al}_2\text{O}_3$ ,  $\text{SiC}$  substrates), as electro-optical devices (lithium niobate, capable of transforming optical into electrical information and vice versa), as optically transparent materials (ruby and yttrium garnet in lasers, optical fibers), as cutting tools (boron nitride, synthetic diamond, tungsten carbide), as refractories, as military armor ( $\text{Al}_2\text{O}_3$ ,  $\text{SiC}$ ,  $\text{B}_4\text{C}$ ), and in a variety of structural applications.

The structure of ceramics is dependent on the character of the bond (ionic, covalent, or partly metallic), on the sizes of the atoms, and on the processing method. We will first discuss the crystalline

### Example 1.6 |

Sketch the 12 members of the  $\langle 110 \rangle$  family for a cubic crystal. Indicate the four  $\{111\}$  planes. You may use several sketches.

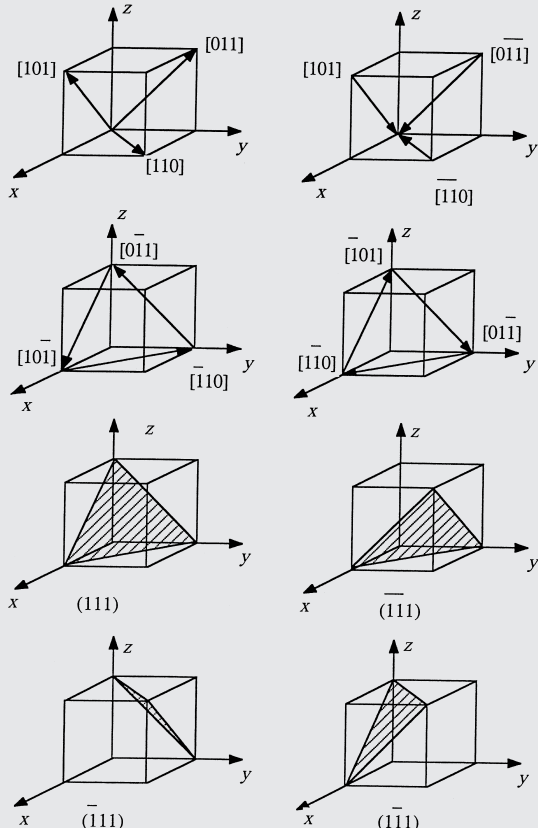


**Fig. EI.6**

ceramics. Transmission electron microscopy has reached the point of development where we can actually image individual atoms, and Figure 1.15 shows a beautiful picture of the zirconium atoms in  $ZrO_2$ . The much lighter oxygen atoms cannot be seen but their positions are marked in the electron micrograph. By measuring the atomic distances along two orthogonal directions, one can see that the structure is not cubic, but tetragonal. The greater complexity of ceramics, in comparison to metallic structures, is evident from Figure 1.15. Atoms of different sizes have to be accommodated by a structure, and bonding (especially covalent) is highly directional. We will first establish the difference between ionic and covalent bonding.

The electronegativity value is a measure of an atom's ability to attract electrons. Compounds in which the atoms have a large difference in electronegativity are principally ionic, while compounds with the same electronegativity are covalent. In ionic bonding one

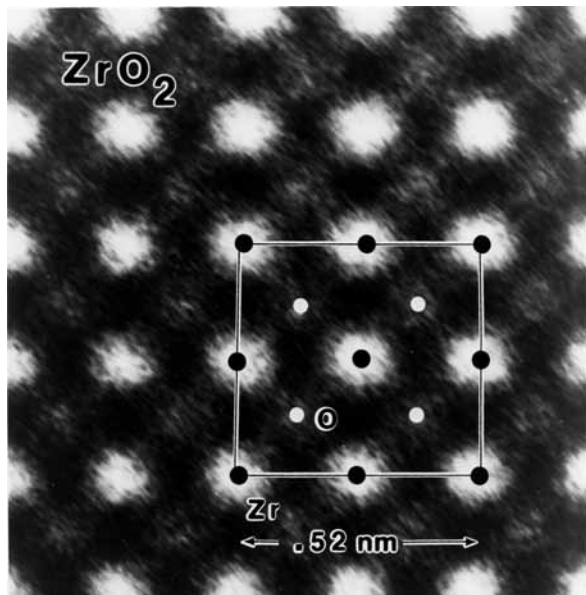


**Fig. 1.15** Transmission electron micrograph of  $\text{ZrO}_2$  at high resolution, showing individual Zr atoms and oxygen sites. (Courtesy of R. Gronsky.)

atom loses electrons and is therefore positively charged (cation). The atom that receives the electrons becomes negatively charged (anion). The bonding is provided by the attraction between positive and negative charges, compensated by the repulsion between charges of equal signs. In covalent bonding the electrons are shared between the neighboring atoms. The quintessential example of covalent bonding is diamond. It has four electrons in the outer shell, which combine with four neighboring carbon atoms, forming a tridimensional regular diamond structure, which is a complex cubic structure. Figure 1.16 shows the diamond structure. The bond angles are fixed and equal to  $70^\circ 32'$ . The covalent bond is the strongest bond, and diamond has the highest hardness of all materials. Another material that has covalent bonding is SiC.

As the difference of electronegativity is increased, the bonding character changes from pure covalent to covalent-ionic, to purely ionic. Ionic crystals have a structure determined largely by opposite charge surrounding an ion. These structures are therefore established by the maximum packing density of ions. Compounds of metals with oxygen ( $\text{MgO}$ ,  $\text{Al}_2\text{O}_3$ ,  $\text{ZrO}_2$ , etc.) and with group VII elements ( $\text{NaCl}$ ,  $\text{LiF}$ , etc.) are largely ionic. The most common structures of ionic crystals are presented in Figure 1.17. Evidently, one has more complex structures in ceramics than in metals because the combinations possible between the elements are so vast.

Ceramics also exist in the glassy state. Silica in this state has the unique optical property of being transparent to light, which is used technologically to great advantage. The building blocks of silica in crystalline and amorphous forms are the silica tetrahedra. Silicon bonds to four oxygen atoms, forming a tetrahedron. The oxygen atoms bond to just two silicon atoms. Numerous structures are possible, with

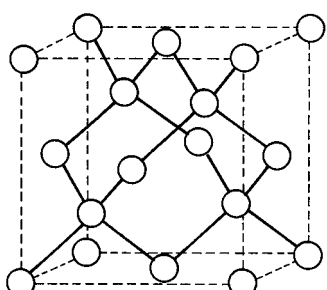
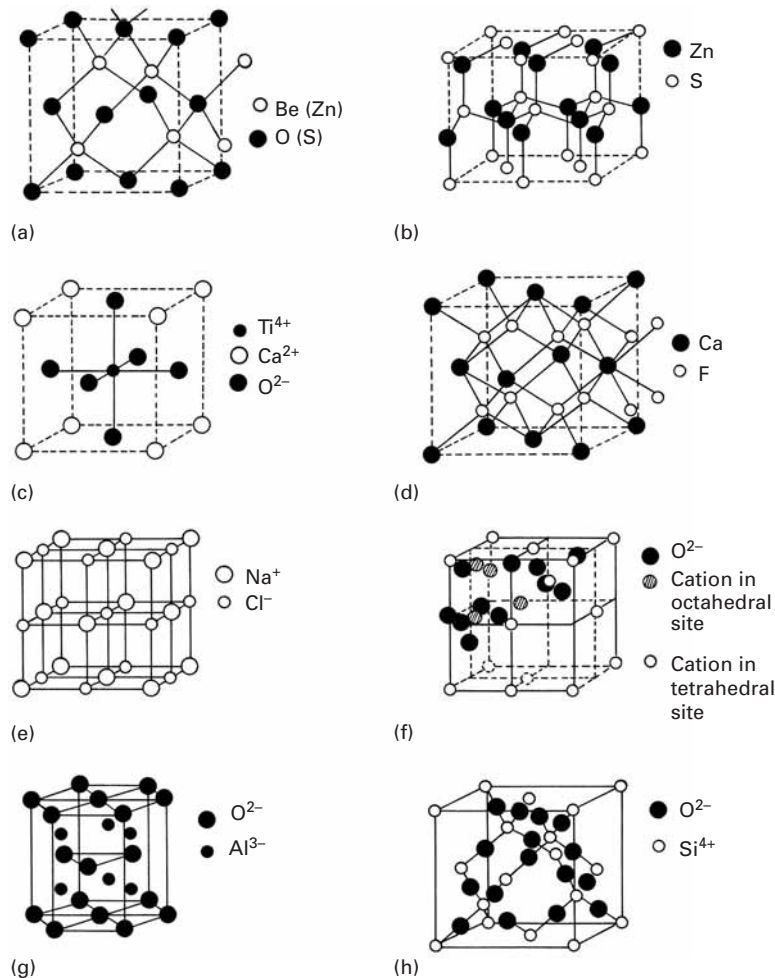


**Fig. 1.16** Crystal structure of diamond.

**Fig. 1.17** Most common structures for ceramics. (a) Zinc blende ( $\text{ZnS}$ ,  $\text{BeO}$ ,  $\text{SiC}$ ). (b) Wurtzite ( $\text{ZnS}$ ,  $\text{ZnO}$ ,  $\text{SiC}$ ,  $\text{BN}$ ). (c) Perovskite ( $\text{CoTiO}_3$ ,  $\text{BaTiO}_3$ ,  $\text{YCu}_2\text{Ba}_3\text{O}_{7-x}$ ). (d) Fluorite ( $\text{ThO}_2$ ,  $\text{UO}_2$ ,  $\text{CeO}_2$ ,  $\text{ZrO}_2$ ,  $\text{PuO}_2$ ). (e)  $\text{NaCl}$  ( $\text{KCl}$ ,  $\text{LiF}$ ,  $\text{KBr}$ ,  $\text{MgO}$ ,  $\text{CaO}$ ,  $\text{VO}$ ,  $\text{MnO}$ ,  $\text{NiO}$ ). (f) Spinel ( $\text{FeAl}_2\text{O}_4$ ,  $\text{ZnAl}_2\text{O}_4$ ,  $\text{MoAl}_2\text{O}_4$ ). (g) Corundum ( $\text{Al}_2\text{O}_3$ ,  $\text{Fe}_2\text{O}_3$ ,  $\text{Cr}_2\text{O}_3$ ,  $\text{Ti}_2\text{O}_3$ ,  $\text{V}_2\text{O}_3$ ). (h) Crystobalite ( $\text{SiO}_2$  – quartz). The  $\text{CsCl}$  structure, which has one  $\text{Cs}^+$  surrounded by four  $\text{Cl}^-$  ions in cube edges, is not shown.



different arrangements of the tetrahedra. Pure silica crystallizes into quartz, crystobalite, and trydimite. Because of these bonding requirements, the structure of silica is fairly open and, consequently, gives the mineral a low density. Quartz has a density of  $2.65 \text{ g/cm}^{-3}$ , compared with  $3.59 \text{ g/cm}^{-3}$  and  $3.92 \text{ g/cm}^{-3}$ , for  $\text{MgO}$  and  $\text{Al}_2\text{O}_3$ , respectively. The structure of crystobalite (Figure 1.17 (h)) shows clearly that each Si atom (open circle) is surrounded by four oxygen atoms (filled circles), while each oxygen atom binds two Si atoms. A complex cubic structure results. However, an amorphous structure in silica is more common when the mineral is cooled from the liquid state. Condensation of vapor on a cold substrate is another method by means of which thin, glassy films are made. One can also obtain glassy materials by electro-deposition, as well as by chemical reaction. Chapter 3 describes glassy metals in greater detail. Figure 1.18 provides a schematic representation of silica in its crystalline and glassy forms in an idealized two-dimensional pattern. The glassy state lacks long-range ordering; the three-dimensional silica tetrahedra arrays lack both symmetry and periodicity.

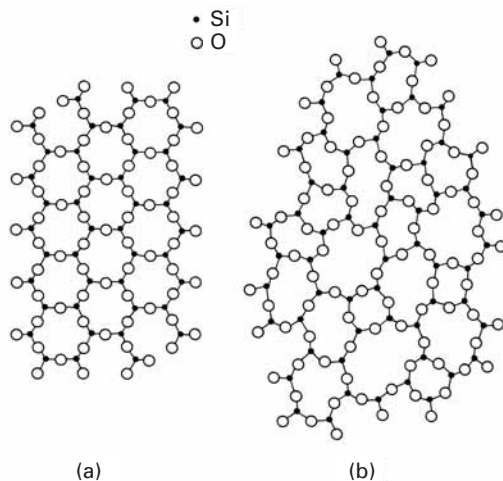


**Fig. 1.18** Schematic representation of (a) ordered crystalline and (b) random-network glassy form of silica.

---

### Example 1.7

Determine the C-C-C-bonding angle in polyethylene.

The easiest manner to visualize the bonding angle is to assume that one C atom is in the center of a cube and that it is connected to four other C atoms at the edges of the cube. (See Figure E1.7.) Suppose all angles are equal to  $\alpha$ .

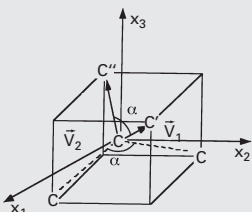


Fig. E1.7

The problem is best solved vectorially. We set the origin of the axes at the center of the carbon atom and have

$$\vec{V}_1 = \frac{1}{2}\vec{i} + \frac{1}{2}\vec{j} + \frac{1}{2}\vec{k},$$

$$\vec{V}_2 = \frac{1}{2}\vec{i} + \frac{1}{2}\vec{j} + \frac{1}{2}\vec{k}.$$

The angle between two vectors is (see Chapter 6 or any calculus text)

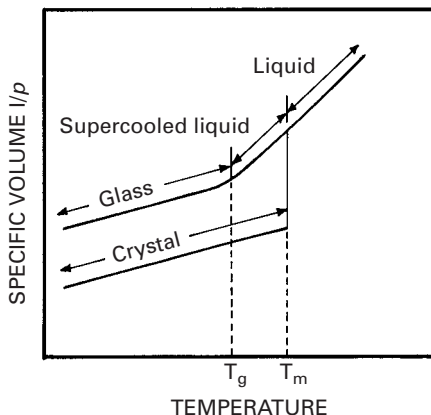
$$\cos \alpha = \frac{\frac{1}{2} \left(-\frac{1}{2}\right) + \frac{1}{2} \left(-\frac{1}{2}\right) + \frac{1}{2} \cdot \frac{1}{2}}{\sqrt{\frac{1}{4} + \frac{1}{4} + \frac{1}{4}} \cdot \sqrt{\frac{1}{4} + \frac{1}{4} + \frac{1}{4}}} = -\frac{1}{3}.$$

so

$$\alpha = 109.47^\circ$$

(Note: When we have double bonds, the angle is changed.)

**Fig. 1.19** Specific volume (inverse of density) as a function of temperature for glassy and crystalline form of a material.



### 1.3.4 Glasses

As described earlier, glasses are characterized by a structure in which no long-range ordering exists. There can be short-range ordering, as indicated in the individual tetrahedral arrays of  $\text{SiO}_4^{-4}$  in Figure 1.18, which shows both the crystalline and glassy forms of silica. Over distances of several atomic spacings, the ordering disappears, leading to the glassy state. It is possible to have glassy ceramics, glassy metals, and glassy polymers.

The structure of glass has been successfully described by the Zachariasen model. The Bernal model is also a successful one. It consists of drawing lines connecting the centers of adjacent atoms and forming polyhedra. These polyhedra represent the glassy structure of glass. Glassy structures represent a less efficient packing of atoms or molecules than the equivalent crystalline structures. This is very easily understood with the “suitcase” analog. We all know that by throwing clothes randomly into a suitcase, the end result is often a major job of sitting on the suitcase to close it. Neat packing of the same clothes occupies less volume. The same happens in glasses. If we plot the inverse of the density (called *specific volume*) versus temperature, we obtain the plot shown in Figure 1.19. Contraction occurs as the temperature is lowered. If the material crystallizes, there is a discontinuity in the specific volume at the melting temperature  $T_m$ . If insufficient time is allowed for crystallization, the material becomes a supercooled liquid, and contraction follows the liquid line. At a temperature  $T_g$ , called the *glass transition temperature*, the supercooled liquid is essentially solid, with very high viscosity. It is then called a glass. This difference in specific volume between the two forms is often referred to as *excess volume*.

In ceramics, reasonably low cooling rates can produce glassy structures. The regular arrangement of the silica tetrahedra of Figure 1.18(a) requires a significant amount of time. The same is true for polymeric chains, which need to arrange themselves into regular

crystalline arrangements. For metals, this is more difficult. Only under extreme conditions it is possible to obtain solid metals in a noncrystalline structure. Figure 1.20 shows a crystalline and a glassy alloy with the same composition. The liquid state is frozen in, and the structure resembles that of glasses. It is possible to arrive at these special structures by cooling the alloy at such a rate that virtually no reorganization of the atoms into periodic arrays can take place. The required cooling rate is usually on the order of  $10^6$  to  $10^8$  K/s<sup>-1</sup>. It is also possible to arrive at the glassy state by means of solid-state processing (very heavy deformation and reaction) and from the vapor.

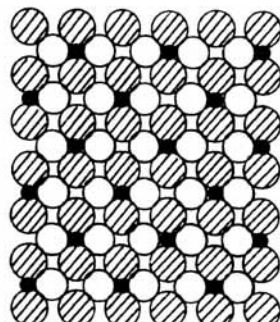
The original technique for obtaining metallic glasses was called splat cooling and was pioneered by Duwez and students.<sup>5</sup> An alloy in which the atomic sizes are quite dissimilar, such as Fe–B, is ideal for retaining the “glassy” state upon cooling. This technique consisted of propelling a drop of liquid metal with a high velocity against a heat-conducting surface such as copper. The interest in these alloys was mainly academic at the time. However, the unusual magnetic properties and high strength exhibited by the alloys triggered worldwide interest, and subsequent research has resulted in thousands of papers. The splat-cooling technique has been refined to the point where 0.07- to 0.12-mm-thick wires can be ejected from an orifice. Production rates as high as 1,800 m/min can be obtained. Sheets and ribbons can be manufactured by the same technique. An alternative technique consists of vapor deposition on a substrate (sputtering). This seems a most promising approach, and samples with a thickness of several millimeters have been successfully produced.

### 1.3.5 Polymers

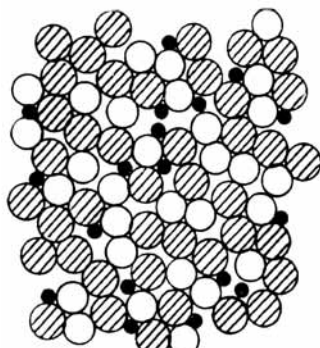
From a microstructural point of view, polymers are much more complex than metals and ceramics. On the other hand, they are cheap and easily processed. Polymers have lower strengths and moduli and lower temperature-use limits than do metals or ceramics. Because of their predominantly covalent bonding, polymers are generally poor conductors of heat and electricity. Polymers are generally more resistant to chemicals than are metals, but prolonged exposure to ultraviolet light and some solvents can cause degradation of a polymer’s properties.

#### Chemical Structure

Polymers are giant chainlike molecules (hence, the name *macromolecules*), with covalently bonded carbon atoms forming the backbone of the chain. Polymerization is the process of joining together many monomers, the basic building blocks of polymers, to form the



(a)

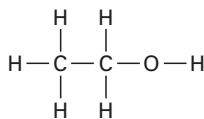


(b)

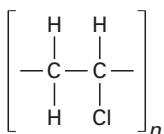
**Fig. 1.20** Atomic arrangements in crystalline and glassy metals. (a) Crystalline metal section. (b) Glassy metal section. (Courtesy of L. E. Murr.)

<sup>5</sup> W. Klement, R. H. Willens, and P. Duwez, *Nature*, 187 (1960) 869.

chains. For example, the ethyl alcohol monomer has the chemical formula



The monomer vinyl chloride has the chemical formula  $\text{C}_2\text{H}_3\text{Cl}$ , which, on polymerization, becomes polyvinyl chloride (PVC). The structural formula of polyvinyl chloride is represented by



where  $n$  is the degree of polymerization.

### Types of Polymers

The difference in the behavior of polymers stems from their molecular structure and shape, molecular size and weight, and amount and type of bond (covalent or van der Waals). The different chain configurations are shown in Figure 1.21. A *linear polymer* consists of a long chain of atoms with attached side groups (Figure 1.21(a)). Examples include polyethylene, polyvinyl chloride, and polymethyl methacrylate. Note the coiling and bending of the chain. *Branched polymers* have branches attached to the main chain (Figure 1.21(b)). Branching can occur with linear, cross-linked, or any other types of polymers. A *cross-linked polymer* has molecules of one chain bonded with those of another (Figure 1.21(c)). Cross-linking of molecular chains results in a three-dimensional network. It is easy to see that cross-linking makes sliding of molecules past one another difficult, resulting in strong and rigid polymers. *Ladder polymers* have two linear polymers linked in a regular manner (Figure 1.21(d)). Not unexpectedly, ladder polymers are more rigid than linear polymers.

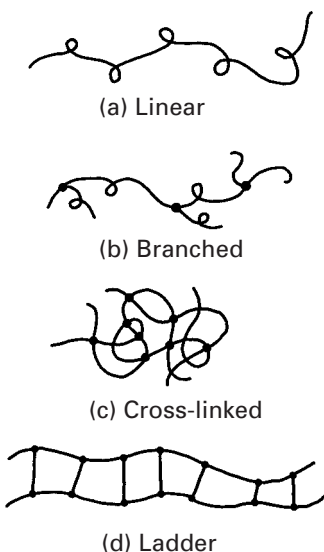


**Fig. 1.21** Different types of molecular chain configurations.

Yet another classification of polymers is based on the type of the repeating unit (see Figure 1.22.) When we have one type of repeating unit – for example, *A* – forming the polymer chain, we call it a *homopolymer*. *Copolymers*, on the other hand, are polymer chains having two different monomers. If the two different monomers, *A* and *B*, are distributed randomly along the chain, then we have a *regular*, or *random*, copolymer. If, however, a long sequence of one monomer *A* is followed by a long sequence of another monomer *B*, we have a *block copolymer*. If we have a chain of one type of monomer *A* and branches of another type *B*, then we have a *graft copolymer*.

Tacticity has to do with the order of placement of side groups on a main chain. It can provide variety in polymers. Consider a polymeric

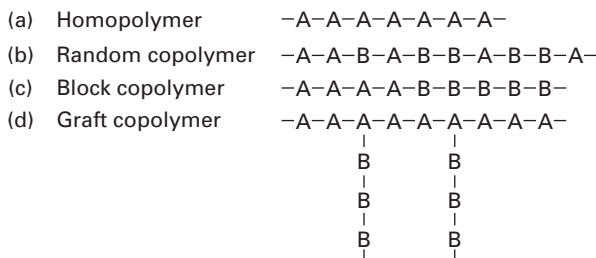


**Fig. 1.22** (a) Homopolymer: one type of repeating unit.  
 (b) Random copolymer: two monomers, A and B, distributed randomly.  
 (c) Block copolymer: a sequence of monomer A, followed by a sequence of monomer B.  
 (d) Graft copolymer: Monomer A forms the main chain, while monomer B forms the branched chains.

backbone chain having side groups. For example, a methyl group ( $\text{CH}_3$ ) can be attached to every second carbon atom in the polypropylene chain. By means of certain catalysts, it is possible to place the methyl groups all on one side of the chain or alternately on the two sides, or to randomly distribute them in the chain. Figure 1.23 shows tacticity in polypropylene. When we have all the side groups on one side of the main chain, we have an *isotactic* polymer. If the side groups alternate from one side to another, we have a *syndiotactic* polymer. When the side groups are attached to the main chain in a random fashion, we get an *atactic* polymer.

### Thermosetting Polymers and Thermoplastics

Based on their behavior upon heating, polymers can be divided into two broad categories:

- (i) thermosetting polymers,
- (ii) thermoplastics.

When the molecules in a polymer are cross-linked in the form of a network, they do not soften on heating. We call these cross-linked polymers *thermosetting* polymers. Thermosetting polymers decompose upon heating. Cross-linking makes sliding of molecules past one another difficult, which produces a strong and rigid polymer. A typical example is rubber cross-linked with sulfur, i.e., vulcanized rubber. Vulcanized rubber has 10 times the strength of natural rubber. Common examples of thermosetting polymers include phenolic, polyester, polyurethane, and silicone. Polymers that soften or melt upon heating are called *thermoplastics*. Suitable for liquid flow processing, they are mostly linear polymers – for example, low- and high-density polyethylene and polymethyl methacrylate (PMMA).

Polymers can have an amorphous or partially crystalline structure. When the structure is amorphous, the molecular chains are arranged randomly, i.e., without any apparent order. Thermosetting polymers, such as epoxy, phenolic, and unsaturated polyester, have an amorphous structure. Semicrystalline polymers can be obtained by using special processing conditions. For example, by precipitating a polymer from an appropriate dilute solution, we can obtain small, platelike crystalline lamellae, or crystallites. Such solution-grown polymer crystals are characteristically small. Figure 1.24 shows a transmission electron micrograph of a lamellar crystal of poly-

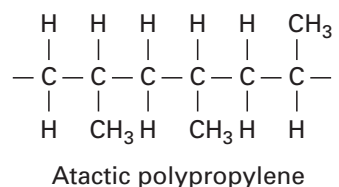
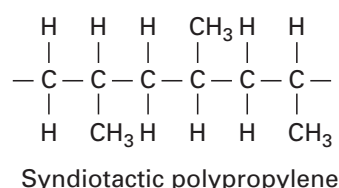
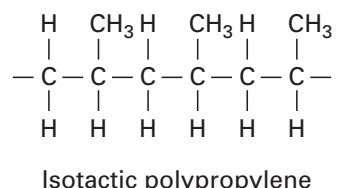
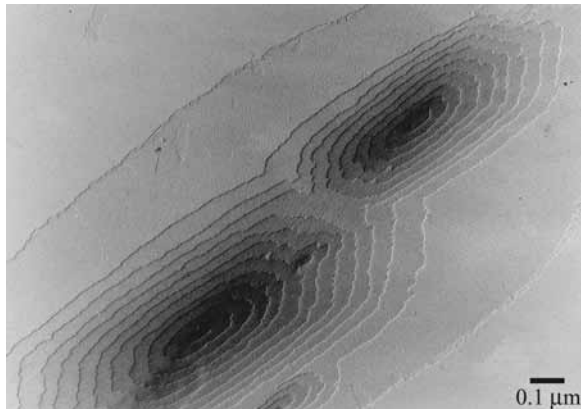


**Fig. 1.23** Tacticity, or the order of placement of side groups.

**Fig. 1.24** Electron micrograph of a lamellar crystal showing growth spirals around screw dislocations. (Courtesy of H. D. Keith.)



( $\epsilon$ -caprolactone). Note the formation of new layers of growth spirals around screw dislocations. The screw dislocations responsible for crystal growth are perpendicular to the plane of the micrograph. Polymeric crystals involve molecular chain packing, rather than the atomic packing characteristic of metals. Molecular chain packing requires a sufficiently stereographic regular chemical structure. Solution-grown polymeric crystals generally have a lamellar form, and the long molecular chains crystallize by folding back and forth in a regular manner. Lamellar polymeric crystals have straight segments of molecules oriented normal to the lamellar panes. Figure 1.25 depicts some important chain configurations in a schematic manner. The flexible, coiled structure is shown in Figure 1.25(a), while the chain-folding configuration that results in crystalline polymers is shown in Figure 1.25(b). Under certain circumstances, one can obtain an extended and aligned chain structure, shown in Figure 1.25(c). Such a structure, typically obtained in fibrous form, has very high strength and stiffness. A semicrystalline configuration called a fringed micelle structure is shown in Figure 1.25(d). Almost all so-called semicrystalline polymers are, in reality, mixtures of crystalline and amorphous regions. Only by using very special techniques, such as solid-state polymerization, is it possible to prepare a 100% crystalline polymer. Polydiacetylene single crystals in the form of lozenges and fibers have been prepared by solid-state polymerization.

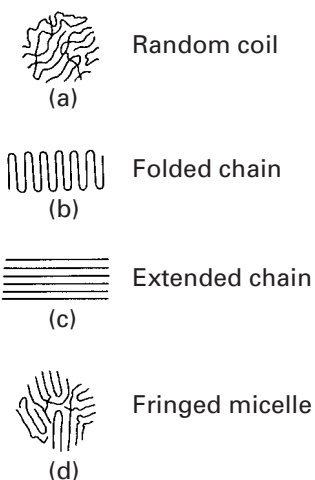


**Fig. 1.25** Some important chain configurations. (a) A flexible, coiled chain structure. (b) A folding chain structure. (c) An extended and aligned chain structure. (d) A fringed micelle chain structure.

Partially crystallized, or semicrystalline, polymers can also be obtained from melts. Generally, because of molecular chain entanglement, the melt-formed crystals are more irregular than those obtained from dilute solutions. A characteristic feature of melt-formed polymers is the formation of *spherulites*. When seen under cross-polarized light in an optical microscope, the classical spherulitic structure shows a Maltese cross pattern. (See Figure 1.26(a).) Figure 1.26(b) presents a schematic representation of a spherulite whose diameter can vary between a few tens to a few hundreds of micrometers. Spherulites can nucleate at a variety of points, as, for

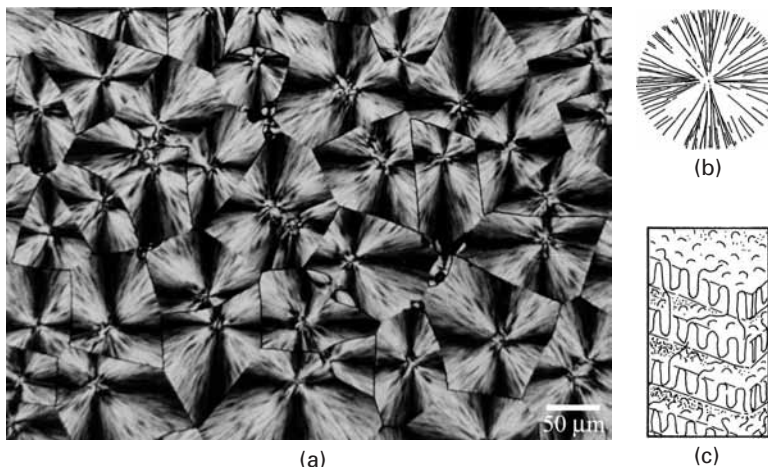


**Fig. 1.26** Spherulitic structures.

(a) A typical spherulitic structure in a melt-formed polymer film. (Courtesy of H. D. Keith.) (b) Schematic of a spherulite. Each spherulite consists of an assembly of radially arranged narrow crystalline lamellae. (c) Each lamella has tightly packed polymer chains folding back and forth. Amorphous regions fill the spaces between the crystalline lamellae.

example, with dust or catalyst particles, in a quiescent melt and then grow as spheres. Their growth stops when the neighboring spherulites impinge upon each other. Superficially, the spherulites look like grains in a metal. There are, however, differences between the two. Each grain in a metal is a single crystal, whereas each spherulite in a polymer is an assembly of radially arranged, narrow crystalline lamellae. The fine-scale structure of these lamellae, consisting of tightly packed chains folding back and forth, is shown in Figure 1.26(c). Amorphous regions containing tangled masses of molecules fill the spaces between the crystalline lamellae.

### Degree of Crystallinity

The *degree of crystallinity* of a material can be defined as the fraction of the material that is fully crystalline. This is an important parameter for semicrystalline polymers. Depending on their degree of crystallinity, such polymers can show a range of densities, melting points, etc. It is worth repeating that a 100% crystalline polymer is very difficult to obtain in practice. The reason for the difficulty is the long chain structure of polymers: some twisted and entangled segments of chains that get trapped between crystalline regions never undergo the conformational reorganization necessary to achieve a fully crystalline state. Molecular architecture also has an important bearing on a polymer's crystallization behavior. Linear molecules with small or no side groups crystallize easily. Branched chain molecules with bulky side groups do not crystallize as easily. For example, linear, high-density polyethylene can be crystallized to 90%, while branched polyethylene can be crystallized only to about 65%. Generally, the stiffness and strength of a polymer increase with the degree of crystallinity.

Like crystalline metals, crystalline polymers have imperfections. It is, however, not easy to analyze these defects, because the topological connectivity of polymer chains leads to large amounts and

numerous types of disorder. Polymers are also very sensitive to damage by the electron beam in TEM, making it difficult to image them. Generally, polymer crystals are highly anisotropic. Because of covalent bonding along the backbone chain, polymeric crystals show low-symmetry structures, such as orthorhombic, monoclinic, or triclinic. Deformation processes such as slipping and twinning, as well as phase transformations that take place in monomeric crystalline solids, may also occur in polymeric crystals.

### Molecular Weight and Distribution

Molecular weight is a very important attribute of polymers, especially because it is not so important in the treatment of nonpolymeric materials. Many mechanical properties increase with molecular weight. In particular, resistance to deformation does so. Of course, concomitant with increasing molecular weight, the processing of polymers becomes more difficult.

The molecular weight of a polymer is given by the product of the molecular weight of the repeat unit (the “*mer*”) and the number of repeat units. The molecular weight of the ethylene repeat unit ( $-\text{CH}_2\text{--CH}_2-$ ) is 28. We write the chemical formula: H ( $-\text{CH}_2\text{--CH}_2-$ )<sub>*n*</sub> H. If *n*, the number of repeat units, is 10,000, the high-density polyethylene will have a molecular weight of 280,002. In almost all polymers, the chain lengths are not equal, but rather, there is a distribution of chain lengths. In addition, there may be more than one species of chain in the polymer. This makes for different parameters describing the molecular weight.

The number-averaged molecular weight ( $M_n$ ) of a polymer is the total weight of all of the polymer’s chains divided by the total number of chains:

$$M_n = \sum N_i M_i / \sum N_i,$$

where  $N_i$  is the number of chains of molecular weight  $M_i$ .

The weight-averaged molecular weight ( $M_w$ ) is the sum of the square of the total molecular weight divided by the total molecular weight. Thus,

$$M_w = \sum N_i M_i^2 / \sum M_i N_i.$$

Two other molecular weight parameters are

$$M_z = \sum N_i M_i^3 / \sum N_i M_i^2,$$

and

$$M_v = \left[ \sum N_i M_i^{(1+a)} / \sum N_i M_i \right]^{1/a},$$

where *a* has a value between 0.5 and 0.8.

Typically,  $M_n : M_w : M_z = 1:2:3$ . Figure 1.27 shows a schematic molecular weight distribution curve with various molecular weight parameters indicated. Molecular weight distributions of the same polymer

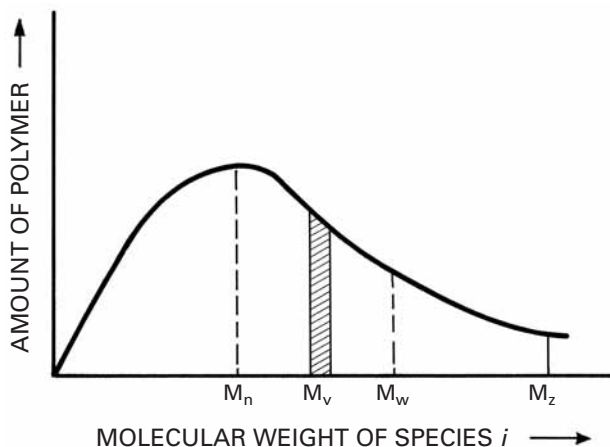


**Fig. 1.27** A schematic molecular weight distribution curve. Various molecular weight parameters are indicated.

obtained from two different sources can be very different. Also, molecular weight distributions are not necessarily single peaked. For single-peaked distributions,  $M_n$  is generally near the peak – that is, the most probable molecular weight. The weight-averaged molecular weight,  $M_w$ , is always larger than  $M_n$ . The molecular weight characterization of a polymer is very important. The existence of a very high-molecular-weight tail can make processing very difficult because of the enormous contribution of the tail to the melt viscosity of a polymer. The low end of the molecular weight distribution, however, can be used as a plasticizer.

It is instructive to compare some monomers with low- and high-molecular-weight polymers. A very common monomer is a molecule of water,  $H_2O$ , with a molecular weight of 18. Benzene, on the other hand, is a low-molecular-weight organic solvent; its molecular weight is 78. By contrast, natural rubber has a molecular weight of about  $10^4$ , and polyethylene, a common synthetic polymer, can have a molecular weights greater than this. Polymers having such large molecular weights are sometimes called *high polymers*. Their molecular size is also very great.

### Example 1.8

A polymer has three species of molecular weights:  $3 \times 10^6$ ,  $4 \times 10^6$ , and  $5 \times 10^6$ . Compute its number-averaged molecular weight  $M_n$  and weight-averaged molecular weight  $M_w$ .

**Solution:** For the number-averaged molecular weight, we have

$$M_n = \frac{\sum N_i M_i}{\sum N_i}$$

$$= \frac{3 \times 10^6 + 4 \times 10^6 + 5 \times 10^6}{3} = 4 \times 10^6.$$

The weight-averaged molecular weight is

$$\begin{aligned} M_w &= \frac{\sum N_i M_i^2}{\sum N_i M_i} \\ &= \frac{(3 \times 10^6)^2 + (4 \times 10^6)^2 + (5 \times 10^6)^2}{3 \times 10^6 + 4 \times 10^6 + 5 \times 10^6} \\ &= \frac{50 \times 10^{12}}{12 \times 10^6} = 4.17 \times 10^6. \end{aligned}$$

### Example 1.9 |

Estimate the molecular weight of polyvinyl chloride with degree of polymerization,  $n$ , equal to 800.

**Solution:** The molecular weight of each *mer* of polyvinyl chloride ( $C_2H_3Cl$ ) is

$$2(12) + 3(1) + 35.5 = 62.5.$$

For  $n = 800$ , the molecular weight is  $800 \times 62.5 = 50,000$  g/mol.

### Example 1.10 |

Discuss how a polymer's density changes as crystallization proceeds from the melt.

**Answer:** The density increases and the volume decreases as crystallization proceeds. This is because the molecular chains are more tightly packed in the crystal than in the molten or noncrystalline polymer. This phenomenon is, in fact, exploited in the so-called *density* method to determine the degree of crystallinity.

## Quasi Crystals

Quasi crystals represent a new state of solid matter. In a crystal, the unit cells are identical, and a single unit cell is repeated in a periodic manner to form the crystalline structure. Thus, the atomic arrangement in crystals has positional and orientational order. Orientational order is characterized by a rotational symmetry; that is, certain rotations leave the orientations of the unit cell unchanged. The theory of crystallography holds that crystals can have twofold, threefold, fourfold, or sixfold axes of rotational symmetry; a fivefold rotational symmetry is not allowed. A two-dimensional analogy of this is that one can tile a bathroom wall using a single shape of tile if and only if the tiles are rectangles (or squares), triangles, or hexagons, but not if the tiles are pentagons. One may obtain a glassy structure by rapidly cooling a vapor or liquid well below its melting point, until the disordered atomic arrangement characteristic of the vapor or liquid state gets frozen in. The atomic packing in the glassy state is

dense but random. This can be likened to a mosaic formed by taking an infinite number of different shapes of tile and randomly joining them together. Clearly, the concept of a unit cell will not be valid in such a case. The atomic structure in the glassy state will have neither positional nor orientational order.

Quasi crystals are not perfectly periodic, but they do follow the rigorous theorems of crystallography. They can have any rotational symmetry axes which are prohibited in crystals. It is worth reminding the reader that a glassy structure shows an electron diffraction pattern consisting of diffuse rings for all orientations. A crystalline structure has an electron diffraction pattern that depends on the crystal symmetry.

Schectman et al. discovered that a rapidly solidified (melt-spun) aluminum-manganese alloy showed fivefold symmetry axis.<sup>6</sup> They observed a metastable phase that showed a sharp electron diffraction pattern with a perfect icosahedral symmetry. (Remember that sharp electron diffraction patterns are associated with the orderly atomic arrangement in crystals and icosahedral symmetry is forbidden in crystals.) At first, this was thought to be a paradox. However, some very careful and sophisticated electron microscopy work showed conclusively that it was indeed an icosahedral (twentyfold) symmetry. Al-Mn alloys containing 18 to 25.3 weight percent Mn examined by transmission electron microscopy showed the same anomalous diffraction. In particular, Al-25.3 wt% Mn alloy consisted almost entirely of one phase which has a composition close to  $\text{Al}_6\text{Mn}$ . The selected area diffraction pattern of  $\text{Al}_6\text{Mn}$  showed a fivefold symmetry. This new kind of structure is neither amorphous nor crystalline; rather, the new phase in this alloy had a three-dimensional icosahedral symmetry.

Perhaps, it would be in order for us to digress a bit and explain this icosahedral symmetry. *Icosahedral* means twenty faces. An icosahedron has twenty triangular faces, thirty edges, and twelve vertices. Consider the two-dimensional case. As pointed out earlier, one can tile a bathroom wall without leaving an open space (a *crack*) by hexagons. Three hexagons can be tightly packed without leaving a crack. Three pentagons, however, cannot be tightly packed. The reader may try this out. In three dimensions, four spheres pack tightly to form a tetrahedron. Twenty tetrahedrons can, with small distortions, fit tightly into an icosahedron. Icosahedrons have fivefold symmetry (five triangular faces meet at each vertex) and they *cannot* fit together tightly, i.e., complete space filling is not possible with them. An icosahedron, therefore, cannot serve as a unit cell for a crystalline structure. Therefore, structures, are known as quasi crystals.

### 1.3.6 Liquid Crystals

A liquid crystal is a state of matter that shares some properties of liquids and crystals. Like all liquids, liquid crystals are fluids; however, unlike ordinary liquids, which are isotropic, liquid crystals can be anisotropic. Liquid crystals are also called *mesophases*. The liquid

<sup>6</sup> D. Schectman, I. A. Blech, D. Gratias, and J. W. Cahn, *Phys. Rev. Lett.*, 53 (1984) 1951.

crystalline state exists in a specific temperature range, below which the solid crystalline state prevails and above which the isotropic liquid state prevails. That is, the liquid crystal has an order between that of a liquid and a crystalline solid. In a crystalline solid, the atoms, ions, or molecules are arranged in an orderly manner. This very regular three-dimensional order is best described in terms of a crystal lattice. Because of a different periodic arrangement in different directions, most crystals are anisotropic. Now consider a crystal lattice with rod-shaped molecules at the lattice points. In this case, we now have, in addition to a positional order, an orientational order. An analogy that is used to qualitatively describe the order in a liquid crystal is as follows: If a random pile of pencils is subjected to an external force, it will undergo an ordering process very much akin to that seen in liquid crystals. The pencils, long and rigid, tend to align themselves, with their long axes approximately parallel. By far the most important characteristic of liquid crystals is that their long molecules tend to organize according to certain patterns. The order of orientation is described by a directed line segment called the *director*. This order is the source of the rather large anisotropic effect in liquid crystals, a characteristic that is exploited in electrooptical displays or the so-called liquid-crystal displays. Another important application of liquid crystals is the production of strong and stiff organic fibers such as aramid fiber, in which a rigid, rodlike molecular arrangement is provided by an appropriate polymer solution in the liquid crystalline state.<sup>7</sup> When a polymer manifests the liquid crystalline order in a solution, we call it a *lyotropic* liquid crystal, and when the polymer shows the liquid crystalline state in the melt, it is called a *thermotropic* liquid crystal. The three types of order in the liquid crystalline state are nematic, smectic, and cholesteric, shown schematically in Figure 1.28. A nematic order is an approximately parallel array of polymer chains that remains disordered with regard to end groups or chain units; that is, there is no positional order along the molecular axis. Figure 1.28(a) shows this type of order, with the director vector  $n$  as indicated. In smectic order, we have one-dimensional, long-range positional order. Figure 1.28(b) shows smectic-A order, which has a layered structure with long-range order in the direction perpendicular to the layers. In this case, the director is perpendicular to the layer. Other more complex smectics are B, C, D, F, and G. The director in these may not be perpendicular to the layer, or there may exist some positional order as well. Cholesteric-type liquid crystals, shown in Figure 1.28(c), have nematic order with a superimposed spiral arrangement of nematic layers; that is, the director  $n$ , pointed along the molecular axis, has a helical twist.

### 1.3.7 Biological Materials and Biomaterials

The mechanical properties of biological materials are, of course, of great importance, and the design of all living organisms is optimized

---

<sup>7</sup> See K. K. Chawla, *Fibrous Materials* (Cambridge, U.K.: Cambridge University Press, 1998).

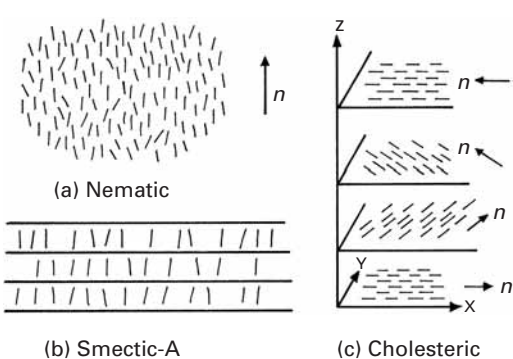
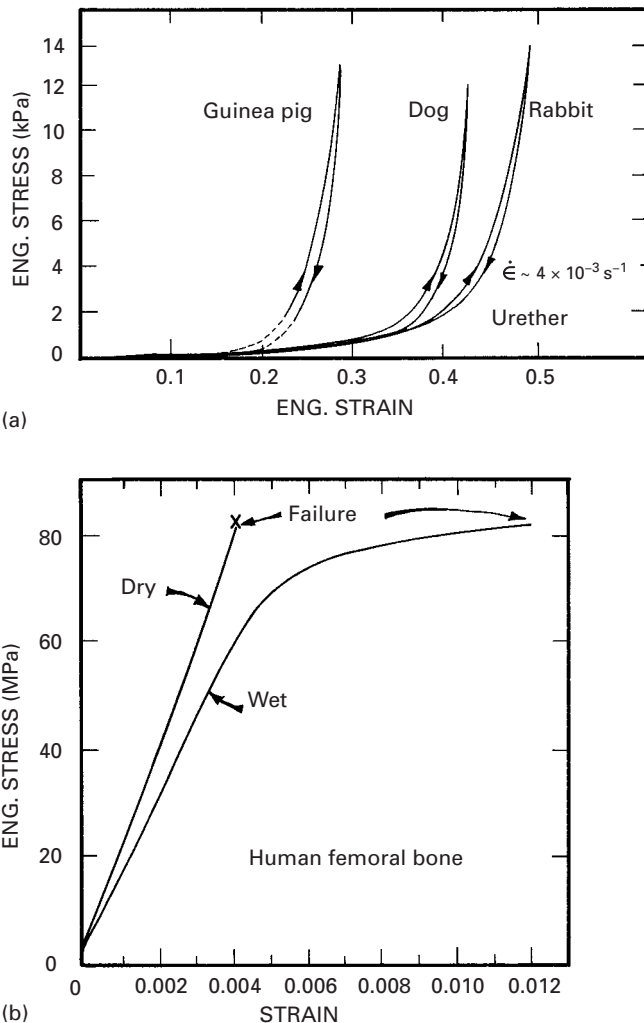


**Fig. 1.28** Different types of order in the liquid crystalline state.

for the use of these properties. Biological materials cover a very broad range of structures. The common feature is the hierarchical organization of the structure, so that failure at one level does not generate catastrophic fracture: The other levels in the hierarchy “take up” the load. Figure 1.29 demonstrates this fact. Figure 1.29(a) shows the response of the urether of three animals: guinea pig, dog, and rabbit. This muscle is a thick-walled cylindrical tube that has the ability to contract until the closure of the inner hole is complete. With a nonlinear elastic mechanical response, the urether is not unlike other soft tissues in that regard: its stiffness increases with loading, and the muscle becomes very stiff after a certain strain is reached. The unloading and loading responses are different, as shown in the figure, and this causes a hysteresis. Increases in length of 50% can be produced. Bone, on the other hand, is a material with drastically different properties: its strength and stiffness are much higher, and its maximum elongation is much lower. The structure of bones is quite complex, and they can be considered composite materials. Figure 1.29(b) illustrates the strength (in tension) of dry and wet bone. The maximum tensile strength is approximately 80 MPa, and Young’s modulus is about 20 GPa.

The abalone shell and the shells of bivalve molluscs are often used as examples of a naturally occurring laminated composite material. These shells are composed of layers of calcium carbonate, glued together by a viscoplastic organic material. The calcium carbonate is hard and brittle. The effect of the viscoplastic glue is to provide a crack-deflection layer so that cracks have difficulty propagating through the composite. Figure 1.30 shows cracks that are deflected at each soft layer. The toughness of this laminated composite is vastly superior to that of a monolithic material, in which the crack would be able to propagate freely, without barriers. The effect is shown at two scales: the mesoscale and the microscale. At the mesoscale, layers of calcium carbonate have a thickness of approximately 500  $\mu\text{m}$ . At the microscale, each calcium carbonate layer is made up of small brick-shaped units (about  $0.5 \times 7.5 \mu\text{m}$  longitudinal section), glued together with the organic matter. The formation of this laminated composite results in a fracture toughness and strength

**Fig. 1.29** Stress-strain curves for biological materials. (a) Urether. (After F. C. P. Yin and Y. C. Fung, *Am. J. Physiol.* 221 (1971), 1484.) (b) Human femur bone. (After F. G. Evans, *Artificial Limbs*, 13 (1969) 37.)



(about  $4 \text{ MPa/m}^{1/2}$  and approximately 150 MPa, respectively) that are much superior to those of the monolithic  $\text{CaCO}_3$ . The composite also exhibits a hierarchical structure; that is, the layers of  $\text{CaCO}_3$  and organic glue exist at more than one level (at the micro- and mesolevels). This naturally occurring composite has served as inspiration for the synthesis of  $\text{B}_4\text{C}-\text{Al}$  laminate composites, which exhibit a superior fracture toughness.<sup>8</sup> In these synthetic composites, there is a 40% increase in both fracture toughness and strength over monolithic  $\text{B}_4\text{C}-\text{Al}$  cermets. *Biomimetics* is the field of materials science in which inspiration is sought from biological systems for the design of novel materials.

Another area of biomaterials in which mechanical properties have great importance is bioimplants. Complex interactions between the

<sup>8</sup> M. Sarikaya, K. E. Gunnison, M. Yasrebi, and I. A. Aksay, *Mater. Soc. Symp. Proc.*, 174 (1990) 109.

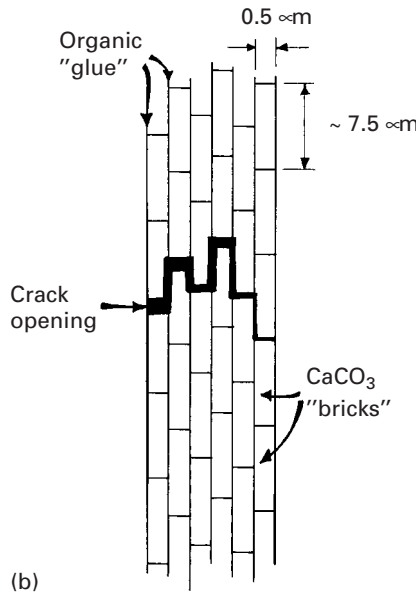
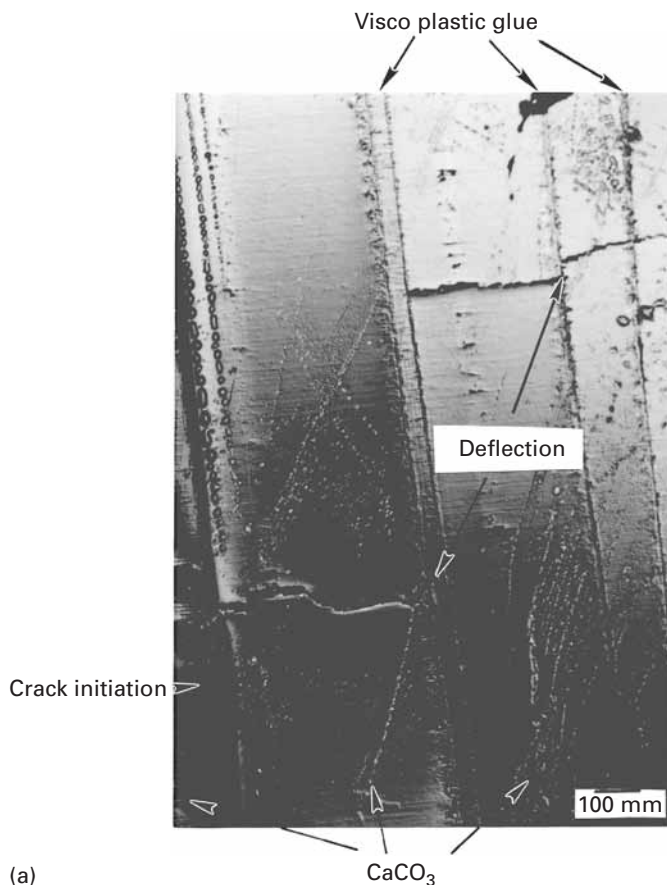


**Fig. 1.30** (a) Cross section of abalone shell showing how a crack, starting at left, is deflected by viscoplastic layer between calcium carbonate lamellae (mesoscale). (b) Schematic drawing showing arrangement of calcium carbonate in nacre, forming a miniature "brick and mortar" structure (microscale).

musculoskeletal system and these implants occur in applications where metals and ceramics are used as replacements for hips, knees, teeth, tendons, and ligaments. The matching of material and bone stiffness is important, as are the mechanisms of bonding tissue to these materials. The number of scientific and technological issues is immense, and the field of bioengineering focuses on these.

### 1.3.8 Porous and Cellular Materials

Wood, cancellous bone, styrofoam, cork, and insulating tiles of the Space Shuttle are examples of materials that are not compact; their structure has air as a major component. The great advantage of cellular structures is their low density. Techniques for making foam metals, ceramics, and polymers have been developed, and these cellular materials have found a wide range of applications, in insulation, in cushioning, as energy-absorbing elements, in sandwich panels for aircraft, as marine buoyancy components, in skis, and more.

The mechanical response of cellular materials is quite different from that of bulk materials. The elastic loading region is usually followed by a plateau that corresponds to the collapse of the pores, either by elastic, plastic buckling of the membranes or by their fracture. The third stage is an increase in the slope, corresponding to final densification. Figure 1.31(a) shows representative curves for polyethylene with different initial densities. The plateau occurs at different stress levels and extends to different strains for different initial densities. The bulk (fully dense) polyethylene is shown for comparison purposes. Cellular mullite, an alumina-silica solid solution, exhibits a plateau marked by numerous spikes, corresponding to the breakup of the individual cells (Figure 1.31(b)). Materials with initial densities as low as 5% of the bulk density are available as foams. Figure 1.31(c) shows a very important use of foams: Sandwich structures, composed of end sheets of solid material in which a foam forms the core region, have numerous applications in the aerospace industry. The foam between the two panels makes them more rigid; this is accomplished without a significant increase in weight.

There are many biological examples of sandwich structures. The toucan beak (Figure 1.32(a)) is a structure with very low density ( $0.04 \text{ g cm}^{-3}$ ) that consists of an external layer of compact keratin. Figure 1.32(b) shows the keratin layer. It is composed of superimposed scales. The inside of the toucan beak is a cellular material with extremely low density, Figure 1.33(b). The function of the cellular material is to provide structural rigidity to the system. In the absence of this foam, the external shell would buckle easily. Hence the toucan can fly without taking a nose dive.

As examples of foams in synthetic and naturally occurring materials, we show in Figure 1.33 two structures. Figure 1.33(a) shows an open-celled aluminum foam. We sectioned the beak of the toucan and observed that the inside is composed of a foam with similar length scale. Nature uses foams for the same purposes we do: to provide

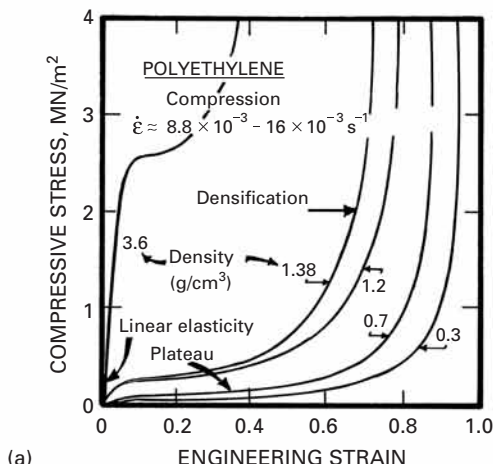
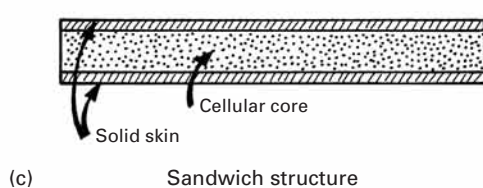
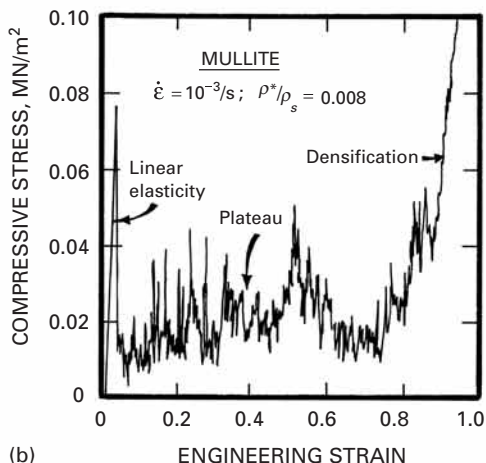


**Fig. 1.31** Compressive stress-strain curves for foams. (a) Polyethylene with different initial densities. (b) Mullite with relative density  $\rho^*/\rho_s = 0.008$ . (Adapted from L. J. Gibson and M. F. Ashby, *Cellular Solids: Structure and Properties* (Oxford, U.K.: Pergamon Press, 1988), pp. 124, 125.) (c) Schematic of a sandwich structure.

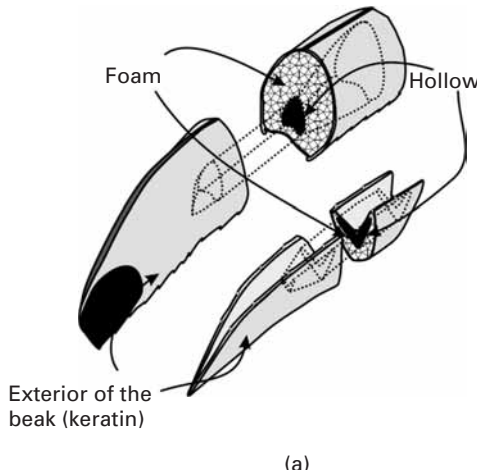


rigidity to structures with the addition of minimal weight. In Chapter 12 we give a detailed analysis of stresses involved in foams.

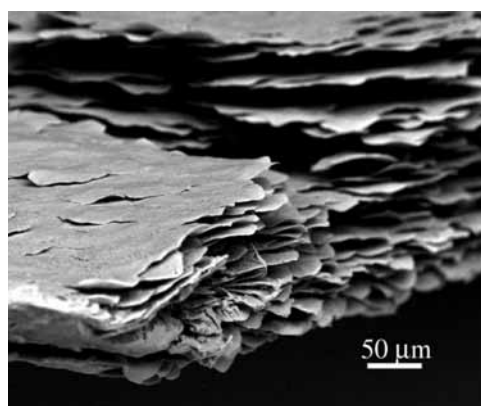
### 1.3.9 Nano- and Microstructure of Biological Materials

Biological materials are more complex than synthetic materials. They form complex arrays, hierarchical structures, and are often multifunctional, i.e., one material has more than one function. For

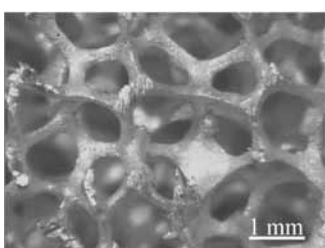
**Fig. 1.32** (a) Toucan beak; (b) external shell made of keratin scales. (Courtesy of Y. Seki.)



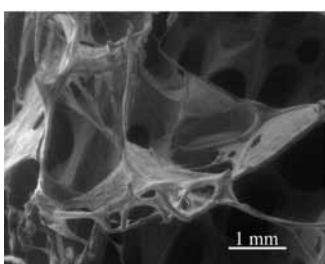
(a)



(b)



(a)



(b)

**Fig. 1.33** Cellular materials: (a) synthetic aluminium foam; (b) foam found in the inside of toucan beak. (Courtesy of M. S. Schneider and K. S. Vecchio.)

example, bone has a structural function and serves as a producer of red blood cells (in marrow). We classify biological materials, from the mechanical property viewpoint, into soft and hard. Hard materials provide the skeleton, teeth, and nails in vertebrates and the exoskeleton in arthropods. Soft biological materials build skin, muscle, internal organs, etc. Table 1.4 provides the distribution (on a weight percentage) of different constituents of the body.

Here are some examples of “hard” biological materials:

- Calcium phosphate (hydroxyapatite- $\text{Ca}_{10}(\text{PO}_4)_6(\text{OH})_2$ ): teeth, bone
- Chitin: nails
- Keratin: bird beaks, horn, hair
- Calcium carbonate (aragonite): mollusc shells, some reptile eggs  
(calcite): bird’s eggs, crustaceans, molluscs
- Amorphous silica ( $\text{SiO}_2(\text{H}_2\text{O})_n$ ): spicules in sponges
- Iron oxide (Magnetite –  $\text{Fe}_3\text{O}_4$ ): teeth in chitons (a weird-looking marine worm), bacteria.

**Table 1.4** Occurrence of Different Biological Materials in the Body

Biological Material	Weight Percentage in Human Body
Proteins	17
Lipids	15
Carbohydrates	1
Minerals	7
DNA, RNA	2
Water	58

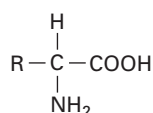
Of the above, iron oxide, calcium phosphate, silica, and iron oxide are minerals. Chitin and keratin are proteins.

Figure 1.34(a) shows the atomic arrangement of the calcium, phosphorus, and oxygen atoms in hydroxyapatite. The unit cell is quite complex and consists of four primitive hexagonal cells juxtaposed. We should remember that the hexagonal cell is composed of three primitive cells, brought together at their  $120^\circ$  angles ( $3 \times 120 = 360$ ). In the case of the hydroxyapatite unit cell, there are four unit cells: two at the  $60^\circ$  angle and two at the  $120^\circ$  ( $2 \times 60 + 2 \times 120 = 360$ ).

Figure 1.34(b) shows the aragonitic form of calcium carbonate. Aragonite has the orthorhombic structure. However, it is important to recognize that the minerals do not occur in isolation in living organisms. They are invariably intimately connected with organic materials, forming complex hierarchically structured composites. The resulting composite has mechanical properties that far surpass those of the monolithic minerals. Although we think of bone as a cellular mineral, it is actually composed of 60% collagen (on a volume percentage basis) and 30–40% hydroxyapatite (on a weight basis). If the mineral is dissolved away, the entire collagen framework is retained.

The principal organic building blocks in living organisms are the proteins. The word comes from Greek (*Proteios*) which means “of first rank” and indeed proteins play a key role in most physiological processes. The soft tissues in the body are made of proteins. As seen above, they are also an important component of biominerals. In order to fully understand proteins, we have to start at the atomic/molecular level, as we did for polymers.

Actually, proteins can be conceived of as polymers with a greater level of complexity. We start with amino acids, which are compounds containing both an amine ( $-\text{NH}_2$ ) and a carboxyl ( $-\text{COOH}$ ) group. Most of them have the following structure, where R stands for a radical:



**Fig. 1.34** Atomic structure of hydroxyapatite: (a) small white atoms (P), large gray atoms (O), black atoms (Ca). (b) Atomic structure of aragonite: large dark atoms (Ca), small gray atoms (C), large white atoms (O).

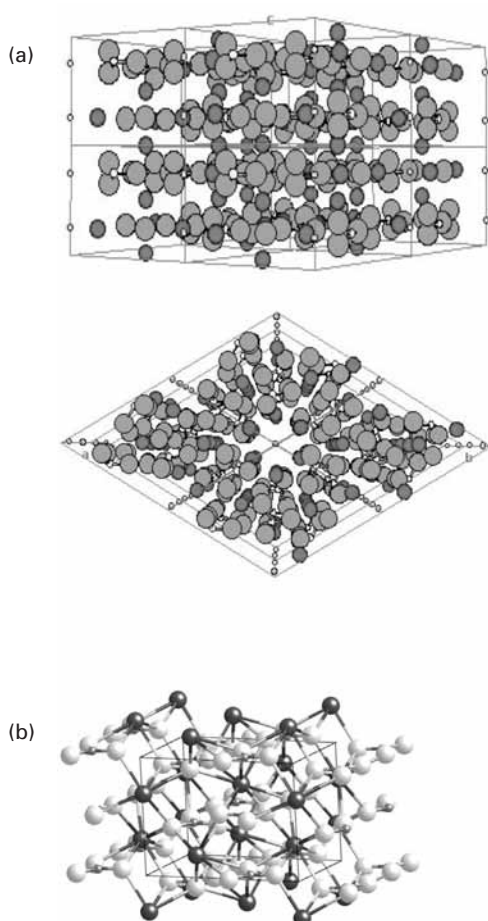


Table 1.5 shows eight main amino acids. There are currently 20 amino acids in proteins. In addition to these eight, we have the following: aspartic acid, glycine, methionine, asparagine, glutamine, arginine, threonine, valine, tyrosine, isoleucine, phenylalanine, and tryptophan.

In DNA, the four amino acids present are designated by the letters ACTG: adenine, cytosine, thymine, and guanine. In both DNA and proteins, these amino acids combine themselves by forming links between the carboxyl group of one amino acid and the amino group of another. These linear chains, similar to polymer chains, are called polypeptide chains. The polypeptide chains acquire special configurations because of the formation of bonds (hydrogen, van der Waals, and covalent bonds) between amino acids on the same or different chains. The two most common configurations are the alpha helix and the beta sheet. Figure 1.35(a) shows how an alpha helix is formed. The NH and CO groups form hydrogen bonds between them in a regular pattern, and this creates the particular conformation of the chain that is of helical shape. One such bond is shown in Figure 1.35(a). In

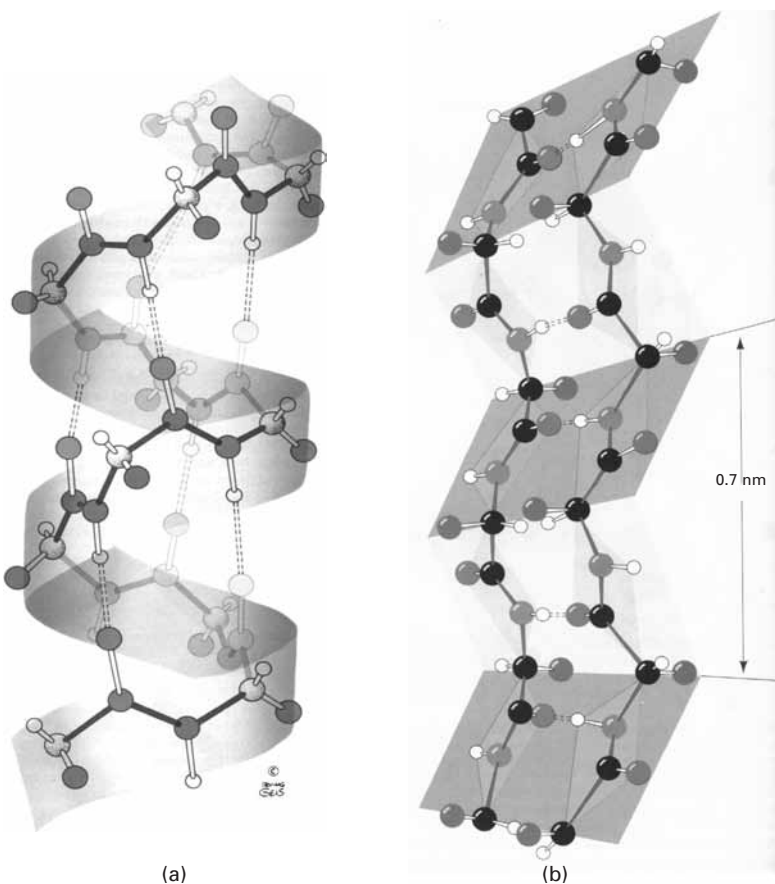
**Table 1.5** Eight Amino Acids Found in Proteins

Name	Chemical Formula
Alanine	$\begin{array}{c} \text{H} & \text{O} \\   &   \\ \text{CH}_3 - \text{C} - \text{C} - \text{OH} \\   \\ \text{NH}_2 \end{array}$
Leucine	$\begin{array}{c} \text{CH}_3 & & \text{O} \\ & \diagdown &   \\ & \text{CH} & \text{C} - \text{COOH} \\ & / \diagup &   \\ \text{CH}_3 & & \text{NH}_2 \end{array}$
Phenylalanine	$\begin{array}{c} \text{CH} = \text{CH} & & \text{H} \\ & \diagdown &   \\ & \text{CH} & \text{C} - \text{CH}_2 - \text{C} - \text{COOH} \\ & / \diagup &   \\ \text{CH} & & \text{NH}_2 \end{array}$
Proline	$\begin{array}{c} \text{H} \\   \\ \text{CH}_2 - \text{CH}_2 - \text{C} - \text{COOH} \\   \\ \text{CH}_2 - \text{N} - \text{H} \end{array}$
Serine	$\begin{array}{c} \text{H} \\   \\ \text{H} - \text{O} - \text{CH}_2 - \text{C} - \text{COOH} \\   \\ \text{NH}_2 \end{array}$
Cysteine	$\begin{array}{c} \text{H} \\   \\ \text{H} - \text{S} - \text{CH}_2 - \text{C} - \text{COOH} \\   \\ \text{NH}_2 \end{array}$
Glutamate	$\begin{array}{c} \text{O} \\    \\ \text{O} - \text{C} - \text{CH}_2 - \text{CH}_2 - \text{C} - \text{COOH} \\   \\ \text{NH}_2 \end{array}$
Lysine	$\begin{array}{c} \text{H} \\   \\ \text{NH}_3 - \text{CH}_2 - \text{CH}_2 - \text{CH}_2 - \text{CH}_2 - \text{C} - \text{COOH} \\   \\ \text{NH}_2 \end{array}$

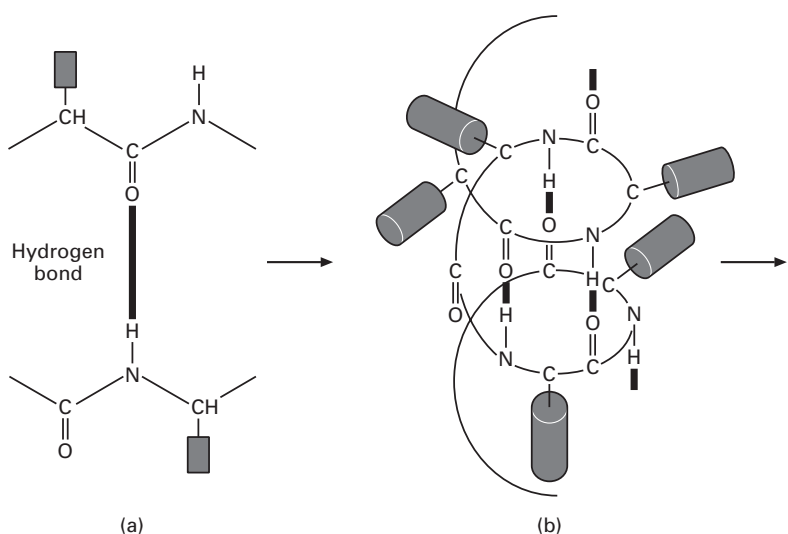
Figure 1.35(b) several hydrogen bonds are shown, causing the polypeptide chain to fold. The radicals stick out. This is shown in a clear fashion in Figure 1.36(a). The hydrogen bonds are also shown.

Another common conformation of polypeptide chains is the beta sheet. In this conformation, separate chains are bonded. Figure 1.36(b) shows two anti-parallel chains that are connected by hydrogen bonds. We can see that the radicals (large grey balls) of two adjacent chains stick out of the sheet plane on opposite sides. Successive chains can bond in such a fashion, creating pleated sheets.

**Fig. I.35** (a) Structure of alpha helix; dotted double lines indicate hydrogen bonds. (b) Structure of beta sheet with two anti-parallel polypeptide chains connected by hydrogen bonds (double-dotted lines).



**Fig. I.36** (a) Hydrogen bond connecting a CO to an NH group in a polypeptide. (b) Successive hydrogen bonds on same polypeptide chain leading to formation of a helical arrangement. (Adapted from A. Vander, J. Sherman, D. Luciano, *Human Physiology*, 8th ed. (New York: McGraw Hill, 2001).)



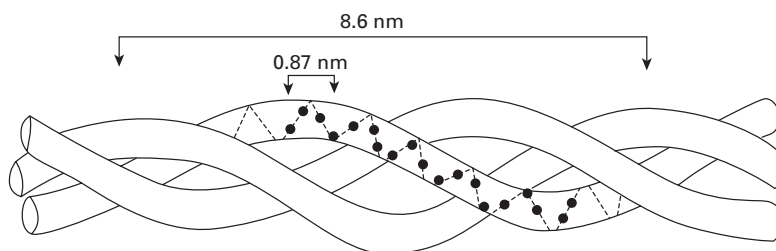


**Fig. 1.37** Triple helix structure of collagen. (Adapted from Y. C. Fung, *Biomechanics: Mechanical properties of Living Tissues* (Berlin: Springer, 1993).)

We describe below the most important proteins: collagen, actin, myosin, elastin, resilin and abductin, keratin, cellulose and chitin.

### Collagen

Collagen is a rather stiff and hard protein. It is a basic structural material for soft and hard bodies; it is present in different organs and tissues and provides structural integrity. Fung<sup>9</sup> compares it to steel, which is the principal load-carrying component in structures. In living organisms, collagen plays the same role: it is the main load-carrying component of blood vessels, tendons, bone, muscle, etc. In rats, 20% of the proteins are collagen. Humans are similar to rats in physiology and behavior, and the same proportion should apply. Figure 1.37 shows the structure of collagen. It is a triple helix, each strand being made up of sequences of amino acids. Each strand is itself a left-handed helix with approximately 0.87 nm per turn. The triple helix has a right-handed twist with a period of 8.6 nm. The dots shown in a strand in Figure 1.37 represent glycine and different amino acids. There are over 10 types of collagen, called Type I, II, X, etc. Fiber-forming collagens organize themselves into fibrils, Figure 1.38. Figure 1.38(c) is a transmission electron micrograph of tendon fibrils. Each fibril has transverse striations, which are spaced approximately 68 nm apart. These striations are caused by the staggering of the individual collagen molecules. This staggering is represented in a schematic manner in Figure 1.38(b). The length of each collagen molecule is 4.4 times the distance of stagger, 68 nm. This is equal to 300 nm. The diameter of the fibrils varies between 20 and 40 nm.

Fibrils, in turn, arrange themselves into fibers. Fibers are bundles of fibrils with diameters between 0.2 and 12  $\mu\text{m}$ . In tendons, these fibers can be as long as the entire tendon. In tendons and ligaments, the collagen fibers form primarily one-dimensional networks. In skin, blood vessels, intestinal mucosa and the female vaginal tract, the fibers organize themselves into more complex patterns leading to two- and three-dimensional networks.

The hierarchical organization of a tendon starts with tropocollagen (a form of collagen), and moves up, in length scale, to fascicles. There is a crimped, or wavy structure shown in the fascicles that

<sup>9</sup> Y. C. Fung, *Biomechanics: Mechanical Properties of Living Tissues* (Berlin, Springer, 1993)

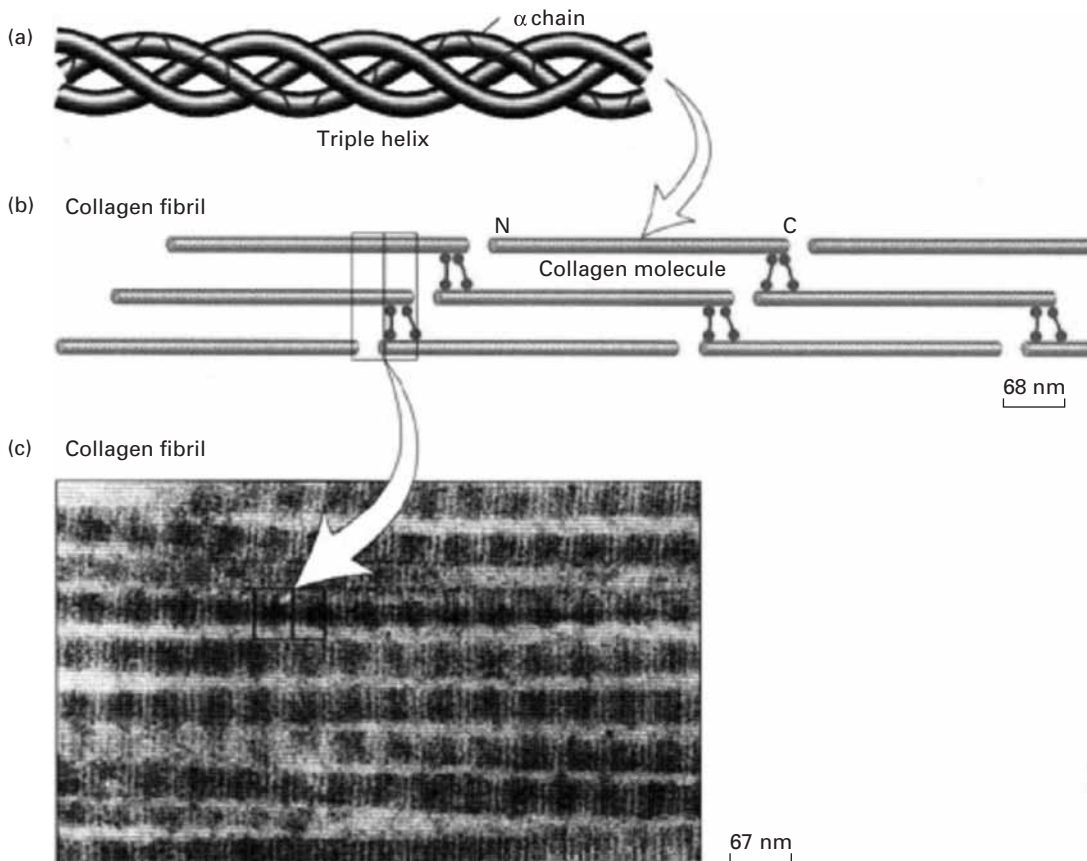


**Fig. 1.38** Hierarchical organization of collagen, starting with triple helix, and going to fibrils. (From H. Lodish et al., *Molecular Cell Biology*, 4th ed. (New York, W.H. Freeman & Company, 1999).)

has an important bearing on the mechanical properties. Figure 1.39 shows an idealized representation of a wavy fiber. Two parameters define it: the wavelength  $2l_0$  and the angle  $\theta_0$ . Typical values for the Achilles tendon of a mature human are  $l_0 = 20\text{--}50 \mu\text{m}$  and  $\theta_0 = 6\text{--}8^\circ$ . These bent collagen fibers stretch out in tension. When the load is removed, the waviness returns. When the tendon is stretched beyond the straightening of the waviness, damage starts to occur. Figure 1.40 shows a schematic stress-strain curve for tendons. The tendon was stretched until rupture. There are essentially three stages:

- Region I: toe part, in which the slope rises rapidly. This is the physiological range in which the tendon operates under normal conditions.
- Region II: linear part, with a constant slope.
- Region III: slope decreases with strain and leads to failure.

The elastic modulus of collagen is approximately 1 GPa and the maximum strain is in the 10–20% range. Cross-linking increases with age, and collagen becomes less flexible.

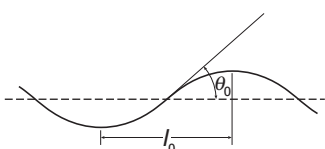


**Fig. 1.39** Idealized configuration of a wavy collagen fiber.

### Actin and Myosin

These are the principal proteins of muscles, leukocytes (white blood cells), and endothelial cells. Muscles contract and stretch

through the controlled gliding/grabbing of the myosin with respect to the actin fibers. Figure 1.41(a) shows an actin fiber. It is composed of two polypeptides in a helical arrangement. Figure 1.41(b) shows the myosin protein. It has little heart-shaped “grapplers” called cross-bridges. The tip of the cross-bridges bind and unbind to the actin filaments. Figure 1.41(c) shows the myosin and actin filaments, and the cross-bridges at different positions. The cross-bridges are hinged to the myosin and can attach themselves to different positions along the actin filaments as the actin is displaced to the left. Thus, the muscles operate by a micro-telescoping action of these two proteins.

Figure 1.42 shows how the filaments organize themselves into myofibrils. Bundles of myofibrils form a muscle fiber. The Z line represents the periodicity in the myosin–actin units (that are called sarcomeres) and is approximately equal to 3  $\mu\text{m}$  in the stretched configuration. It shortens when the muscle is contracted. This gives the muscle a striated pattern when observed at high magnification. They resemble a coral snake in the microscope. Myofibrils have a diameter of approximately 1–2  $\mu\text{m}$ .

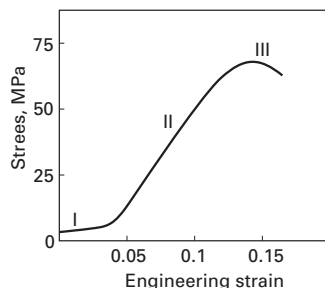


**Fig. 1.40** Stress–strain curve of collagen with three characteristic stages.

### Elastin

Elastin is found in skin, walls of arteries and veins, and lung tissue. A prominent place is in the “*ligamentum nuchae*,” a long ligament that runs along the top of the neck in horses and is constantly under tension. Other vertebrates have it too, but it is less pronounced. In this manner, the horse can keep the head up without using muscles. The “*ligamentum nuchae*” plays a role similar to the cables in a suspension bridge. It is a rather robust cylinder.

### Resilin and Abductin

They are found in arthropods. They have properties similar to those of elastin, but occur in totally different animals and have a different structure.

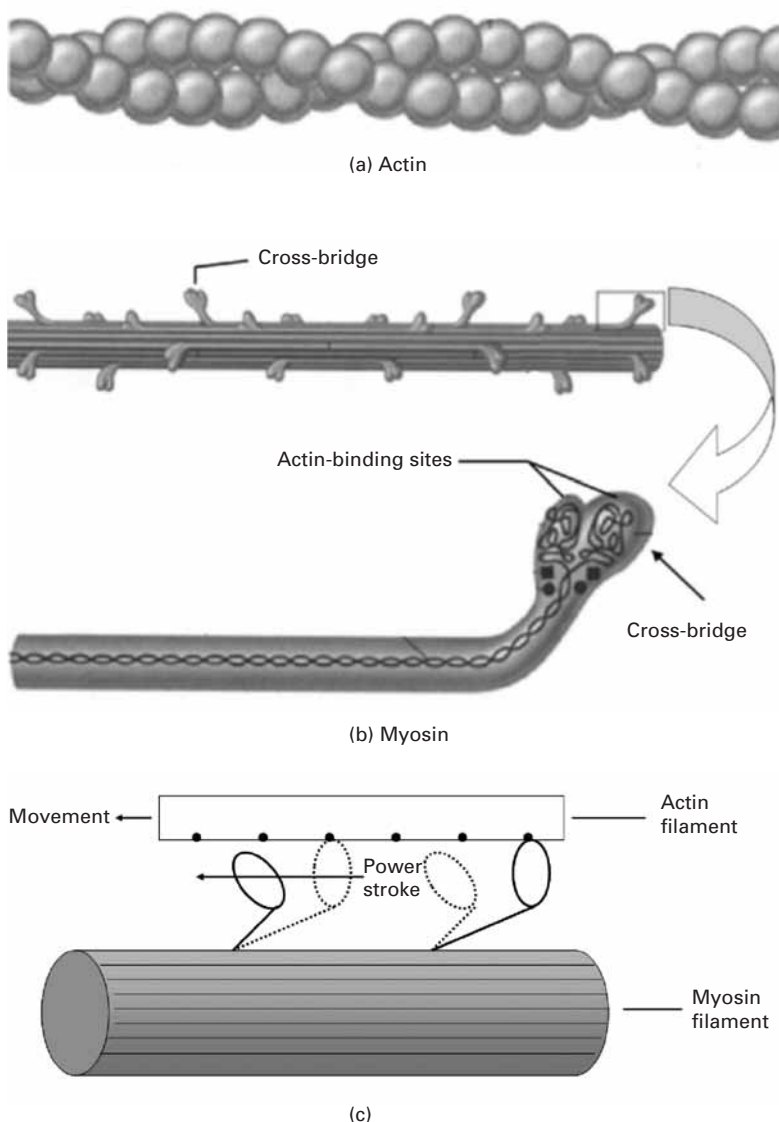
### Keratin

Keratin is found in hair, horn, bird beaks and feathers, and whale baleen. The toucan beak presented in Section 1.3.8 is made of keratin. It has a structure similar to collagen (three interwoven helices). These helices combine themselves to form microfibrils with a diameter of 8 nm. Interestingly, it undergoes a phase transformation under tensile load, which increases its elongation.

### Cellulose

Cellulose is the most abundant biological structural material, and is present in wood (which is a composite of cellulose and lignin) and cotton (almost pure cellulose). Cellulose is a cross-linked crystalline polymer. Its basic building block is a fibril with 3.5 nm diameter and 4 nm periodicity.

**Fig. 1.41** Molecular structure of (a) actin and (b) myosin; (c) action of cross-bridges when actin filament is moved to left with respect to myosin filament; notice how cross-bridges detach themselves, then reattach themselves to actin.



### Chitin

Chitin is a polysaccharide found in many invertebrates. The exoskeleton of insects is made of chitin.

### Silk

Silk is composed of two proteins: fibroin (tough strands) and sericin, a gummy glue. The mechanical properties (strength and maximum elongation) can vary widely, depending on the application intended by the animal. For instance, among the silks produced by spiders are: dragline and spiral. Dragline, used in the radial components of the web, is the structural component, and has high tensile strength (600 MPa) and a strain at failure of about 6%. The spiral tangential

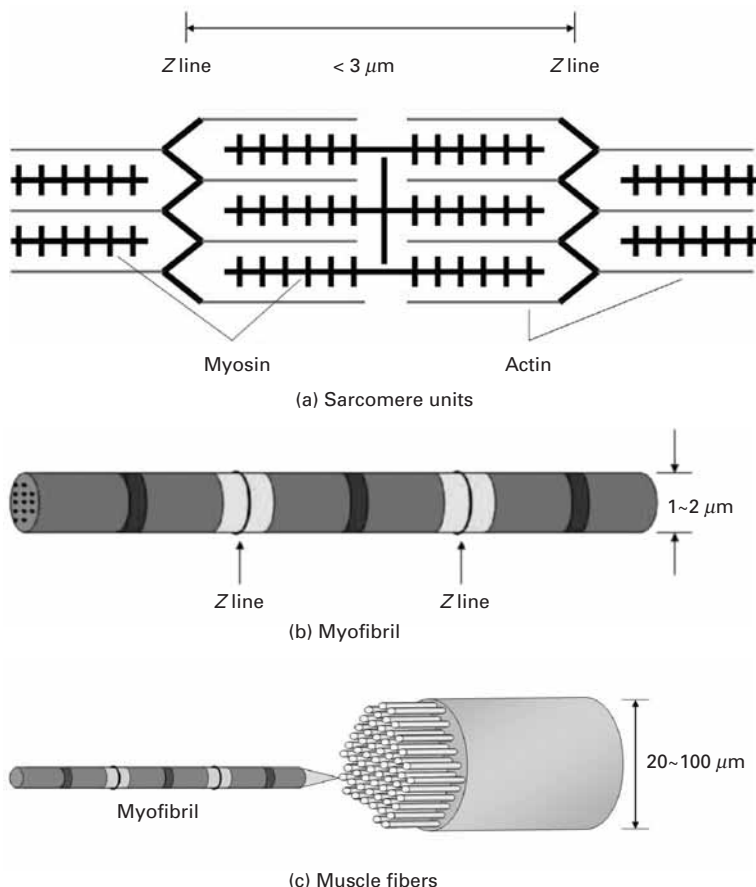


**Fig. 1.42** Structure of muscle, from (a) the sarcomere units, to (b) myofibril, and finally to (c) fibers.

components are intended to capture prey, and are “soft” and “sticky.” The strain at failure in this case can exceed 16, i.e. 1,600%.

### Example 1.11 |

Determine the maximum strain that the collagen fibers can experience without damage if their shape is as given in Figure 1.39 with a ratio between amplitude and wavelength of 0.2

We can assume a sine function of the form:

$$y = k \sin 2\pi x/\lambda.$$

The maximum of  $y$  is reached when  $x = \pi/4$ .

Hence:

$$y_{\max} = k = \lambda/5.$$

We can integrate over the length of the sine wave from 0 to  $2\pi$ . However, this will lead to an elliptical integral of difficult solution. A simple approximation is to consider the shape of the wavy protein as an ellipse with major axis  $2a$  and minor axis  $2b$ . The circumference is given by the

approximate expression (students should consult a mathematics text to obtain this expression):

$$L \approx \pi \left[ \frac{3}{2} (a + b) - (ab)^{1/2} \right].$$

In the sine function, we have two arms, one positive and one negative. Their sum corresponds, in an approximate manner, to the circumference of the ellipse. The strain is equal to:

$$\varepsilon = \frac{L - 4a}{4a} = \frac{\pi \left[ \frac{3}{2} (a + b) - (ab)^{1/2} \right] - 4a}{4a}.$$

Thus:

$$\varepsilon = \frac{\pi}{4} \left[ \frac{3}{2} \left( 1 + \frac{b}{a} \right) - \left( \frac{b}{a} \right)^{1/2} \right] - 1.$$

The following ratio is given:

$$\frac{b}{2a} = 0.2 \quad \text{and} \quad \frac{b}{a} = 0.4.$$

The corresponding strain is:

$$\varepsilon = 0.53.$$

Beyond this strain, the collagen will break.

### 1.3.10 The Sponge Spicule: An Example of a Biological Material

Marine sponges have long tentacles that are called spicules. These spicules act as antennas, which are subjected to marine currents and other stresses. These long silica rods have properties that dramatically exceed the strength of synthetic silica. Figure 1.43 shows the flexure strength of both spicule and synthetic silica. The difference in flexure strength between sponge spicule and synthetic silica is remarkable. The synthetic silica fractures at a relatively low stress of 200 MPa compared to the yield stress of the spicule at 870 MPa. The area under the stress-strain curve gives a reasonable idea of the toughness. Clearly the toughness of the spicule is many times higher than that of synthetic silica. As evidenced by Figure 1.43, failure does not occur catastrophically in the spicule. Instead, the spicule fails “gracefully,” which is a considerable advantage.

Figure 1.44 shows the microstructure of a fracture surface. The spicule consists of many concentric layers. This onion-like structure is responsible for the strengthening effect observed. When stress is applied to a silica rod, a crack will initiate at the weakest point in the material and propagate through the silica rod in a catastrophic manner. In contrast, crack propagation in the spicule will be arrested at each interface. This type of “graceful” failure is extremely useful. We can truly learn and apply this lesson from nature to modern material applications.

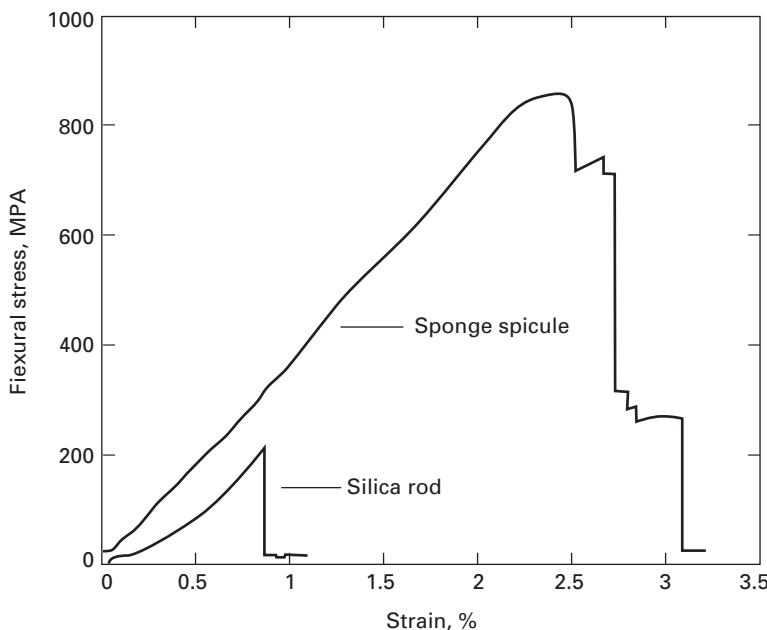


**Fig. 1.43** Stress-deflection responses of synthetic silica rod and sponge spicule in flexure testing. (Courtesy of M. Sarikaya and G. Mayer.)

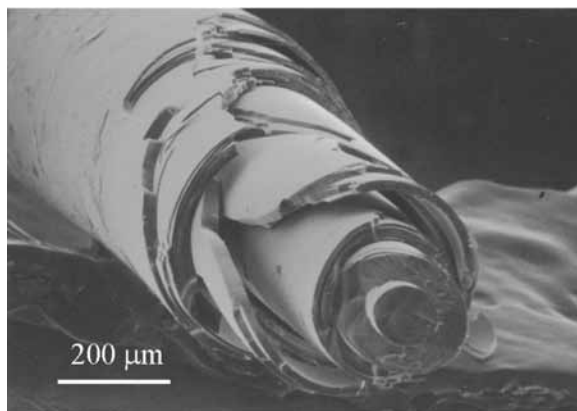


**Fig. 1.44** SEM of fractured sponge spicule showing two-dimensional onion-skin structure of concentric layers. (Courtesy of G. Mayer and M. Sarikaya.)

### 1.3.11 Active (or Smart) Materials

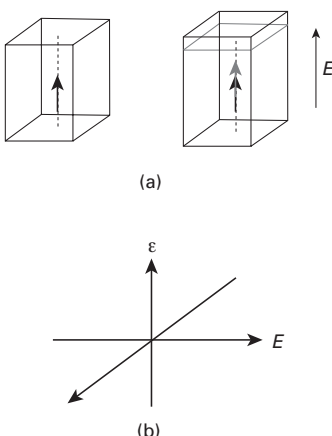
Technology puts greater and greater demand on materials and there is a constant push to develop materials with enhanced capabilities. The term *multifunctional materials* has been coined to describe materials with more than one capability. This is inspired by nature, where materials often have more than one function. For example, the trunk of a tree is at the same time a structural component and a carrier for the sap. Bones have a structural as well as a red-blood-producing function.

Another category of advanced materials are *active materials*. They are also called “smart” materials. Active materials have responses that can be used in all kinds of devices. Given below are the main classes of active materials.

- Shape memory alloys: The most common is a NiTi alloy known as Nitinol. It can undergo strains of 1–5% through a martensitic transformation that is reversible. A detailed description of these alloys is given in Chapter 11. There are numerous applications through two effects: the shape memory effect and the superelastic (or pseudoelastic) effect: dental braces, stents, etc. They are presented in Chapter 11.
- Magnetorheological materials: These materials exhibit a viscosity that depends on an externally applied magnetic field. The suspension system of a US-made luxury automobile uses this material. The stiffness can be adjusted by varying the magnetic field.
- Piezoelectric ceramics and ferroelectricity:<sup>10</sup> These materials generate an electric field when strained. Conversely, if an electric current is passed through them, they change their dimension. Barium titanate, lead zirconate titanate ( $Pb(Zr, Ti)O_3$ ) are examples. They have the perovskite structure with composition  $ABO_3$ , where A and B are metals. They are characterized by a linear strain-electric field response. The maximum strain is on the order of 0.2%. Applications include vibration control, micropositioning devices, ultrasonics, and non-destructive evaluation.

It is a property of ferroelectrics to exhibit polarization in the absence of an electric field. Polarization is defined as dipole moment per unit volume or charge per unit area on the surface. The material is divided into domains, which are regions with uniformly oriented polarization. Ferroelectrics are characterized by a linear relationship between stress  $\sigma$  and polarization  $P$ :

$$P = d\sigma.$$



There is a converse relationship between strain  $\epsilon$  and electric field,  $E$ :

$$\epsilon = dE,$$

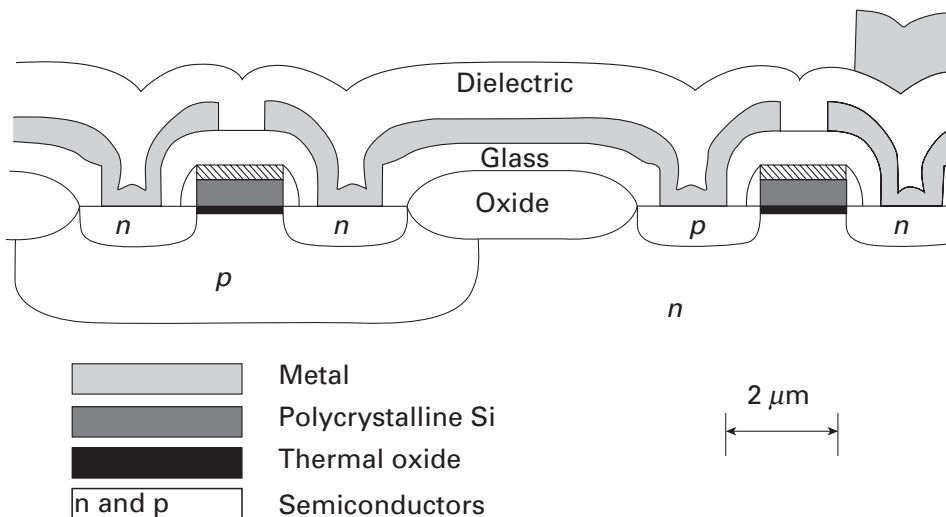
where  $d$  is called the polarizability tensor. Figure 1.45(a) shows how the application of an externally applied electric field  $E$  results in a change in length of the specimen. Figure 1.45(b) shows the linear relationship between the strain and the field. This is a property of ferroelectric crystals, certain noncentrosymmetric crystals (e.g. quartz,  $ZnO$ ), textured polycrystals, and polycrystals with a net spontaneous polarization. Applications include adaptive optics, active rotors and control surfaces, robotics, and MEMS/NEMS (microelectromechanical systems/nanoelectromechanical systems) actuators.

**Fig. 1.45** (a) Effect of applied field  $E$  on dimension of ferroelectric material. (b) Linear relationship between strain and electric field. (Courtesy of G. Ravichandran.)

### 1.3.12 Electronic Materials

Electronic materials are composed, for the most part, of thin films arranged in several layers and deposited on a substrate. The most

<sup>10</sup> K. Bhattacharya and G. Ravichandran, *Acta Mater.*, 51 (2003) 5941.



common substrate is monocrystalline silicon (the silicon wafer). Integrated circuits form the heart of modern computers and the silicon chip is a primary example. Figure 1.46 shows a schematic of the materials and structure used in a CMOS (complementary metal oxide semiconductor) transistor device. The  $pn$  junctions form transistors. The substrate is silicon, which in this case is  $n$  doped. The thin film layers are vapor deposited and there are a number of mechanical aspects that are of considerable importance. In Figure 1.46, we have monocrystalline and polycrystalline silicon, oxide, glass, metal, and a dielectric passivation layer.

The thin films deposited on the substrate have dimensions of a few nanometers to a few micrometers. These films may be under residual stresses as high as 500 MPa. These stresses are due to:

- Thermal expansion coefficient effects. When the film cools it contracts. The thermal expansion coefficients of the different layers can be different, creating internal stresses.
- Phase transformations. The phases in thin films are often non-equilibrium phases.

There are a number of mechanical problems associated with these stresses. Dislocations at the interface between substrate and thin film, cracking of the passivation layer, bending of the substrate/thin film system are a few examples. We will briefly describe these effects in chapters 2, 6, 9, and 13.

Magnetic hard disks are also made of thin films. The aluminum disk, upon which a thin layer of magnetic material is deposited, rotates at surface velocities approaching 80 km per hour, while the “head” flies aerodynamically over it. The distance between head and disk is as low as 0.3  $\mu\text{m}$ . Some of the mechanical problems are friction, wear, and the unavoidable collisions between disk and head.

**Fig. 1.46** Cross section of a complementary metal-oxide semiconductor (CMOS). (Adapted from W. D. Nix, *Met. Trans.*, 20A (1989) 2217.)

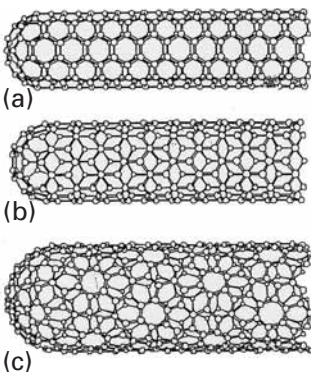


**Fig. 1.47** Three configurations for single wall carbon nanotubes: (a) armchair; (b) “zig-zag”; (c) chiral. (Adapted from M. S. Dresselhaus, G. Dresselhaus, and R. Saito, *Carbon*, 33 (1995) 883.)

### 1.3.13 Nanotechnology<sup>11,12</sup>

Nanotechnology refers to the structure and properties of materials and devices at the nanometer level. Developments in synthesis and characterization methods have resulted in materials that are designed from the “bottom up,” rather than from the “top down.” These terms were first used by the famous physicist Richard Feynman. The traditional method used in the design of new materials is to develop synthesis and processing techniques at the macro-scale, and then to carry out detailed characterization at the micrometer and nanometer scale. The new approach is to start with atoms, then assemble them into small arrays and characterize their structure and properties at that level. This approach was led by the semiconductor revolution. As the sizes of devices become smaller, we approach atomic dimensions. At that level, it is being found that many materials possess unique properties. Many biological processes also use the bottom-up approach. Atoms aggregate themselves into molecules and complex arrays through genetic messages. The atoms come together and self-organize themselves into complex arrays of amino acids, which in their turn form proteins. It is hoped that we will be able to fully harness this approach in the future. There are already applications of nanotechnology in the marketplace.

A material that is showing great potential because of unique characteristics is the carbon nanotube. The first nanotube was produced in Japan by S. Iijima. One can envisage a carbon nanotube by rolling a single layer of carbon atoms into a hollow cylinder. The ends can be semi-spherical caps (one half of a “Buckyball”). There are three morphologies for carbon nanotubes, shown in Figure 1.47: armchair, zig-zag, and chiral. They differ in the following:

- Armchair: the hexagons have the “pointy” side perpendicular to cylinder axis.
- Zig-Zag: the hexagons have the pointy side aligned with the cylinder axis.
- Chiral: The hexagons are inclined with respect to the cylinder axis, and the carbon sheet wraps itself helically around cylinder.

These carbon nanotubes have typically a diameter between 5 and 20 nm and length between 1 and 100  $\mu\text{m}$ . They have outstanding mechanical properties, since they are based on the C-C bond, the strongest in nature. There are varying estimates of their strength, and values between 45 and 200 GPa are quoted. This would make them the strongest material known, ranking with diamond. Although the nanotubes are very short, one can envisage a day where continuous

<sup>11</sup> C. P. Poole and F. J. Owens, *Introduction to Nanotechnology* (Hoboken, NJ, Wiley-Interscience, 2003).

<sup>12</sup> M. Ratner and D. Ratner, *Nanotechnology* (Englewood Cliffs, NJ, Prentice Hall, 2003).

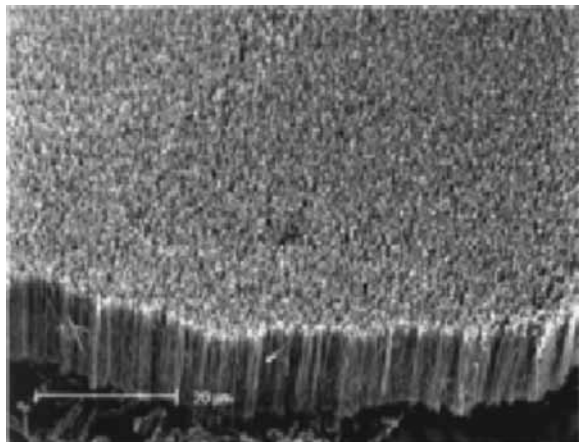


**Fig. 1.48** Array of parallel carbon nanotubes grown as a forest. (From R. H. Baughman, A. A. Zakhidov and W. A. de Heer, *Science*, 297 (2002) 787.)

nanotubes are manufactured. Their incorporation as reinforcements in composites presents a bright prospect.

Figure 1.48 shows how arrays of parallel carbon nanotubes can be produced. The individual nanotubes, approximately 10  $\mu\text{m}$  in length, form a dense forest. The carbon nanotube is only one example of nanotechnology. The mechanical properties of metals are significantly increased when their grain size is reduced to the nanometer range. This topic, nanostructured materials, is treated in Chapter 5.

## 1.4 | Strength of Real Materials

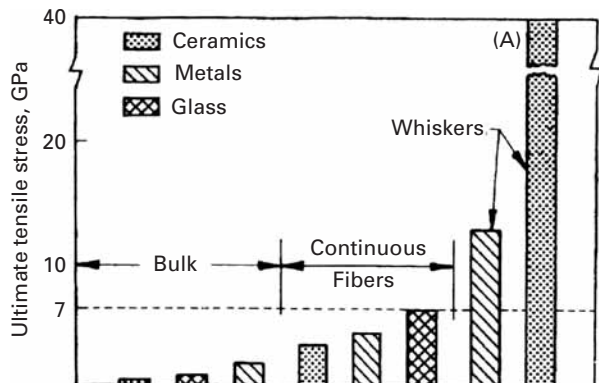
Materials deform and fail through defects. These defects (cracks, point defects, dislocations, twins, martensitic phase transformations, etc.) are discussed in chapters 4 through 8. The two principal mechanisms are crack growth and dislocations and plastic flow.

*Crack growth:* Real materials can have small internal cracks, at whose extremities high-stress concentrations are set up. Hence, the theoretical cleavage strength can be achieved at the tip of the crack at applied loads that are only a fraction of that stress. Griffith's theory (see Chapter 7) explains this situation very clearly. These stress concentrations are much lower in ductile materials, since plastic flow can take place at the tip of a crack, blunting the crack's tendency to grow.

*Dislocations and plastic flow:* Before the theoretical shear stress is reached, dislocations are generated and move in the material; if they are already present, they start moving and multiply. These dislocations are elementary carriers of plastic deformation and can move at stresses that are a small fraction of the theoretical shear stress. They will be discussed in detail in Chapter 4.

In sum, cracks prevent brittle materials from obtaining their theoretical cleavage stress, while dislocations prevent ductile materials from obtaining their theoretical shear stress.

**Fig. 1.49** Theoretical strength of tridimensional materials, continuous fibers, and whiskers. The strength of the SiC whisker produced by the Philips Eindhoven Laboratory is indicated by (A).



To achieve the theoretical strength of a crystalline lattice, there are two possible methods: (1) eliminating all defects and (2) creating so many defects, that their interactions render them inoperative. The first approach has yielded some materials with extremely high strength. Unfortunately, this has been possible only in special configurations called "whiskers." The second approach is the one more commonly pursued, because of the obvious dimensional limitations of the first; the strength levels achieved in bulk metals have steadily increased by an ingenious combination of strengthening mechanisms, but are still much lower than the theoretical strength. Maraging steels with useful strengths up to 2 GPa have been produced, as have patented steel wires with strengths of up to 4.2 GPa; the latter are the highest strength steels.

Figure 1.49 compares the ambient-temperature strength of tridimensional, filamentary, and whisker materials. The whiskers have a cross-sectional diameter of only a few micrometers and are usually monocrystalline (although polycrystalline whiskers have also been developed). Whiskers are one of the strongest materials developed by human beings. The dramatic effect of the elimination of two dimensions is shown clearly in Figure 1.49. The strongest whiskers are ceramics. Table 1.5 provides some illustrative examples. Iron whiskers with a strength of 12.6 GPa have been produced, compared with 2 GPa for the strongest bulk steels. The value 12.6 GPa is essentially identical to the theoretical shear stress, because the normal stress is twice the shear stress. In general, FCC whiskers tend to be much weaker than BCC whiskers and ceramics. For instance, Cu whiskers have a strength of about 2 GPa. This is consistent with the much lower theoretical shear strength exhibited by copper whiskers. It turns out that silver, gold, and copper have  $\tau_{\max}/G$  ratios of 0.039 (see chapter 4). Hence, they are not good whisker materials. Figure 1.50 shows a stress-strain curve for a copper whisker. The specimen had a length between 2 and 3 mm and a cross-sectional diameter of 6.8  $\mu\text{m}$ . The stress drops vertically after the yield point, with a subsequent plateau corresponding to the propagation of a Lüders band.

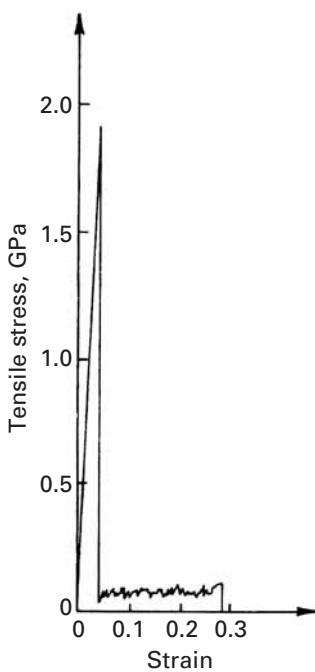


**Fig. 1.50** Stress-strain curve of a copper whisker with a fiber direction  $<100>$ . The whisker diameter is 6.8  $\mu\text{m}$ . (Adapted with permission from K. Yoshida, Y. Goto, and M. Yamamoto, *J. Phys. Soc. Japan*, 21 (1966) 825.)

**Table 1.6** Tensile Strength of Whiskers at Room Temperature\*

Material	Maximum Tensile Strength (GPa)	Young's Modulus (GPa)
Graphite	19.6	686
$\text{Al}_2\text{O}_3$	15.4	532
Iron	12.6	196
SiC	20–40	700
Si	7	182
AlN	7	350
Cu	2	192

\*Adapted with permission from A. Kelly, *Strong Solids* (Oxford, U.K.: Clarendon Press, 1973), p. 263.

In the elastic range, the curve deviates slightly from Hooke's law and exhibits some temporary inflections and drops (not shown in the figure). In many cases, for both metals and nonmetals, failure occurs at the elastic line, without appreciable plastic strain. When plastic deformation occurs, as, for example, in copper and zinc, a very large yield drop is observed. Although the strength of whiskers is not completely understood, it is connected to the absence of dislocations. It is impossible to produce a material virtually free of dislocations – in other words, perfect. However, for whiskers, dislocations can easily escape out of the material during elastic loading. Their density and mean free path are such that they will not interact and produce other sources of dislocation. Hence, the yield point is the stress required to generate dislocations from surface sources. The irregularities observed in the elastic range indicate that existing dislocations move and escape out of the whisker. At a certain stress, the whisker becomes essentially free of dislocations. When the stress required to activate surface sources is reached, the material yields plastically, or fails.

### Example 1.12

Calculate the stresses generated in a turbine blade if its cross-sectional area is  $10 \text{ cm}^2$  and the mass of each blade is  $0.2 \text{ kg}$ .

This is an example of a rather severe environment where the material properties must be predicted with considerable detail. For example, the blade may be in a jet engine. Figure E1.12 shows a section of the compressor stage of a jet. The individual blades are fixed by a dovetail arrangement to the turbine vanes. Assume a rotational velocity  $\omega = 10,000 \text{ rpm}$  and a mean radius  $R = 0.5 \text{ m}$ . The centripetal acceleration in the bottom of each turbine blade is

$$a_c = \omega^2 R = \left[ 10,000 \times \frac{1}{60} \times 2\pi \right]^2 \times 0.5 = 5.4 \times 10^5 \text{ m/s}^2.$$

The stress that is generated is

$$\sigma = \frac{F}{A} = \frac{ma_c}{A} = \frac{0.2 \times 5.4 \times 10^5}{10 \times 10^{-4}} = 100 \text{ MPa},$$

where  $F$  is the centripetal force and  $A$  is the cross-sectional area. This stress of 100 MPa is significantly below the flow stress of nickel-based superalloys at room temperature, but can be quite significant at higher temperatures.

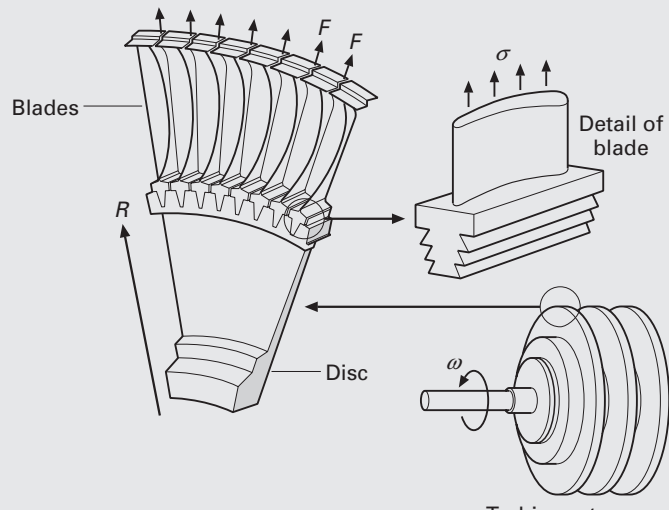


**Fig. E1.12** Turbine blade subjected to centripetal force during operation.

## Suggested Reading

### Materials in General

- J. F. Shackelford. *Introduction to Materials Science for Engineers*, 4th ed. Upper Saddle River, NJ: Prentice Hall, 1996.
- W. F. Smith. *Principles of Materials Science and Engineering*, 3rd ed. New York, NY: McGraw Hill, 1996.
- D. R. Askeland and P. Phule. *The Science and Engineering of Materials*, 4th ed. Pacific Grove, CA: Thomson, 2003
- W. D. Callister Jr. *Materials Science and Engineering*, 4th ed. New York, NY: Wiley, 2003

### Metals

- C. S. Barrett and T. B. Massalski. *Structure of Metals*, 3rd rev. ed. Oxford: Pergamon, 1980.
- M. A. Meyers and K. K. Chawla. *Mechanical Metallurgy*. Englewood Cliffs, NJ: Prentice-Hall, 1984.

### Ceramics

- W. D. Kingery, H. K. Bowen, and D. R. Uhlmann. *Introduction to Ceramics*, 2nd ed. New York, NY: J. Wiley, 1976.
- Y.-M. Chiang, D. Birnie III, and W. D. Kingery, *Physical Ceramics*, New York, NY: J. Wiley, 1997.

## Polymers

- D. C. Bassett. *Principles of Polymer Morphology*. Cambridge, U.K.: Cambridge University Press, 1981.
- A. Hiltner (ed.). *Structure-Property Relationships of Polymeric Solids*. New York, NY: Plenum Press, 1983.
- R. J. Young. *Introduction to Polymers*. London: Chapman & Hall, 1986.
- B. Wunderlich. *Macromolecular Physics, Vol. 1: Crystal Structure*. New York, NY: Academic Press, 1973.
- B. Wunderlich. *Macromolecular Physics, Vol. 2: Crystal Nucleation*. New York, NY: Academic Press, 1976.

## Composite Materials

- K. K. Chawla. *Composite Materials: Science & Engineering*. 2nd ed. New York, NY: Springer, 1998.
- K. K. Chawla. *Ceramic Matrix Composites*, 2nd ed. Boston, MA: Kluwer, 2003
- N. Chawla and K. K. Chawla. *Metal Matrix Composites*, New York, NY: Springer, 2006.

## Liquid Crystals

- A. Ciferri, W. R. Krigbaum, and R. B. Meyer, eds. *Polymer Liquid Crystals*. New York, NY: Academic Press, 1982.

## Biomaterials

- M. Elices (ed.). *Structural Biological Materials*, Amsterdam: Pergamon, 2000.
- J. F. V. Vincent. *Structural Biomaterials*. Princeton, NJ: Princeton University Press, 1991.
- Y. C. Fung. *Biomechanics: Mechanical Properties of Living Tissues*. New York, NY: Springer, 1981.

## Cellular Materials

- L. J. Gibson and M. F. Ashby. *Cellular Solids: Structure and Properties*. Oxford, U.K.: Pergamon Press, 1988.

## Electronic Materials

- W. D. Nix. Mechanical Properties of Thin Films, *Met. Trans.*, 20A (1989) 2217.
- L. B. Freund and S. Suresh. *Thin Film Materials: Stress, Defect Formation and Surface Evolution*. Cambridge, U.K.: Cambridge University Press, 2003

## Exercises

**1.1** A jet turbine rotates at a velocity of 7,500 rpm. Calculate the stress acting on the turbine blades if the turbine disc radius is 70 cm and the cross-sectional area is 15 cm<sup>2</sup>. Take the length to be 10 cm and the alloy density to be 8.5 g/cm<sup>3</sup>.

**1.2** The material of the jet turbine blade in Problem 1.1, Superalloy IN 718, has a room-temperature yield strength equal to 1.2 GPa; it decreases with temperature as

$$\sigma = \sigma_0 \left( 1 - \frac{T - T_0}{T_m - T_0} \right),$$

where  $T_0$  is the room temperature and  $T_m$  is the melting temperature in K ( $T_m = 1,700$  K). At what temperature will the turbine flow plastically under the influence of centripetal forces?

**1.3**

- (a) Describe the mechanical properties that are desired in a tennis racket, and recommend different materials for the different parts of the racket.
- (b) Describe the mechanical properties that are desired in a golf club, and recommend different materials for the different parts of the club.

**1.4** On eight cubes that have one common vertex, corresponding to the origin of axes, draw the family of {111} planes. Show that they form an octahedron and indicate all <110> directions.

**1.5** The frequency of loading is an important parameter in fatigue. Estimate the frequency of loading (in cycles per second, or Hz) of an automobile tire in the radial direction when the car speed is 100 km/h and the wheel diameter is 0.5 m.

**1.6** Indicate, by their indices and in a drawing, six directions of the <112> family.

**1.7** The density of Cu is 8.9 g/cm<sup>3</sup> and its atomic weight (or mass) is 63.546. It has the FCC structure. Determine the lattice parameter and the radius of atoms.

**1.8** The lattice parameter for W(BCC) is  $a = 0.32$  nm. Calculate the density, knowing that the atomic weight (or mass) of W is 183.85.

**1.9** Consider the unit cell of the CsCl which has NaCl structure. The radius of Cs<sup>+</sup> is 0.169 nm and that of Cl is 0.181 nm. (a) Determine the packing factor of the structure, assuming that Cs<sup>+</sup> and Cl<sup>-</sup> ions touch each other along the diagonals of the cube. (b) Determine the density of CsCl if the atomic weight of Cs is 132.905 and of Cl is 35.453.

**1.10** MgO has the same structure as NaCl. If the radii of O<sup>2-</sup> and Mg<sup>2+</sup> ions are 0.14 nm and 0.070 nm, respectively, determine (a) the packing factor and (b) the density of the material. The atomic weight of O<sub>2</sub> is 16 and that of Mg is 24.3.

**1.11** Germanium has the diamond cubic structure with interatomic spacing of 0.245 nm. Calculate the packing factor and density. (The atomic weight of germanium is 72.6.)

**1.12** The basic unit (or mer) of polytetrafluoroethylene (PTFE) or Teflon is C<sub>2</sub>F<sub>4</sub>. If the mass of the PTFE molecule is 45,000 amu, what is the degree of polymerization?

**1.13** Using the representation of the orthorhombic unit cell of polyethylene (see Figure E1.13), calculate the theoretical density. How does this value compare with the density values of polyethylene obtained in practice?

**1.14** A pitch blend sample has five different molecular species with molecular masses of  $0.5 \times 10^6$ ,  $0.5 \times 10^7$ ,  $1 \times 10^7$ ,  $4 \times 10^7$ , and  $6 \times 10^7$ . Compute the number-averaged molecular weight and weight-averaged molecular weight of the sample.

**1.15** Different polymorphs of a material can have different mechanical properties. Give some examples.

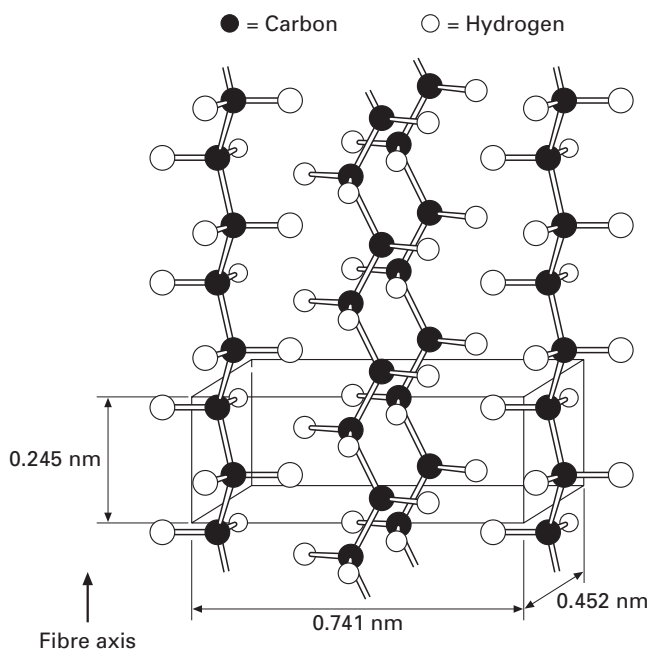


**Fig. E1.13** Crystalline form of polyethylene with orthorhombic unit cell.

1.16 What are smart materials? Give some examples.

1.17 What are glass-ceramics? Explain their structure and properties. (Hint: Think of Corning ware.)

1.18 Explain how the scale of microstructure can affect the properties of a material. Use steel, an alloy of iron and carbon as an example.

1.19 For a cubic system, calculate the angle between

- (a) [100] and [111],
- (b) [111] and [112],
- (c) [112] and [221].

1.20 Recalculate the bicycle stiffness ratio for a titanium frame. (See Examples 1.1 and 1.2) Find the stiffness and weight of the bicycle if the radius of the tube is 25 mm. Use the following information:

Alloy: Ti—6% Al—4% V,

$$\sigma_y = 1,150 \text{ MPa},$$

$$\text{Density} = 4.5 \text{ g/cm}^3,$$

$$E = 106 \text{ GPa},$$

$$G = 40 \text{ GPa}.$$

1.21 Calculate the packing factor for NaCl, given that  $r_{\text{Na}} = 0.186 \text{ nm}$  and  $R_{\text{Cl}} = 0.107 \text{ nm}$ .

1.22 Determine the density of BCC iron structure if the iron atom has a radius of 0.124 nm.

1.23 Draw the following direction vectors in a cubic unit cell:

- a [100] and [110], b [112], c [1̄10], d [3̄21].

**1.24** Calculate the stress generated in a turbine blade if its cross-sectional area is  $0.002 \text{ m}^2$  and the mass of each blade is 0.5 kg. Assume that the rotational velocity  $\omega = 15,000 \text{ rpm}$  and the turbine disk radius is 1 m.

**1.25** Suppose that the turbine blade from the last problem is part of a jet turbine. The material of the jet turbine is a nickel-based superalloy with the yield strength,  $\sigma_y = 1.5 \text{ GPa}$ ; it decreases with temperature as

$$\sigma = \sigma_0[(1 - (T - T_0))/(T_m - T_0)],$$

where  $T_0 = 293 \text{ K}$  is the room temperature and  $T_m = 1,550 \text{ K}$  is the melting temperature. Find the temperature at which the turbine will flow plastically under the influence of centripetal forces.

**1.26** Calculate the lattice parameter of Ni(FCC) knowing that the atomic diameter of nickel is 0.249 nm.

**1.27** A jet turbine blade, made of MARM 200 (a nickel-based superalloy) rotates at 10,000 rpm. The radius of the disk is 50 mm. The cross-sectional area is  $20 \text{ cm}^2$  and the length of the blade is equal to 12 cm. The density of MARM 200 is  $8.5 \text{ g/cm}^3$ .

- (a) What is the stress acting on the turbine blade in MPa?
- (b) If the room temperature strength of MARM 200 is equal to 800 MPa, what is the maximum operational temperature in kelvin?

The yield stress varies with temperature as:

$$\sigma = \sigma_0 \left[ 1 - \left( \frac{(T - T_0)}{(T_m - T_0)} \right)^m \right],$$

where  $T_m$  is the melting temperature ( $T_m = 1,700 \text{ K}$ ) and  $T_0$  is the room temperature;  $m = 0.5$ .

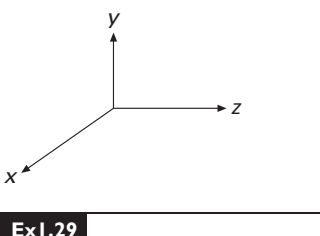
**1.28** Generate a three-dimensional unit cell for the intermetallic compound AuCu<sub>3</sub> that has a cubic structure. The Au atoms are at the cube corners and the Cu atoms at the center of the faces. Given:

$$\begin{aligned} r_{\text{Cu}} &= 0.128 \text{ nm} \quad \text{A.N.}_{\text{Cu}} = 63.55 \text{ amu} \\ r_{\text{Au}} &= 0.144 \text{ nm} \quad \text{A.N.}_{\text{Au}} = 196.97 \text{ amu} \end{aligned}$$

- (a) Find the lattice parameter in nanometers.
- (b) What is the atomic mass of the unit cell in grams?
- (c) What is the density of the compound in  $\text{g/cm}^3$ ?

**1.29** Draw the following unit cells with the planes (one plane per cube with the coordinate axes shown below):

- (a)  $(\bar{1}01)$ ,
- (b)  $(1\bar{1}1)$ ,
- (c)  $(0\bar{1}2)$ ,
- (d)  $(301)$ .



**1.30** Show how the atoms pack in the following planes by drawing circles (atoms) in the appropriate spots:

- (a)  $(111)$  in FCC,
- (b)  $(110)$  in FCC,
- (c)  $(111)$  in BCC,
- (d)  $(110)$  in BCC.

1.31 BET is a technique for measuring the surface area of particles, which is of obvious importance in nanomaterials. Describe this technique. Don't forget to mention what the acronym BET stands for.

1.32 "Tin plate" is one of the largest tonnage steel products. It is commonly used for making containers. If it is a steel product why is it called tin plate?

1.33 Using Figure 1.7, list the important symmetry operations in the following crystal systems:

- (a) Triclinic,
- (b) Monoclinic,
- (c) Orthorhombic.

1.34 The only possible rotation operations that can be used to define crystal systems are rotations of type  $n = 1, 2, 3, 4$ , and  $6$ . Using other values of  $n$  will result in unit cells which, when joined together, will not fill all space. Demonstrate this by giving a simple mathematical proof. (*Hint:* consider two lattice points separated by a unit translation vector.)

1.35 Calculate the APF (atomic packing factor) for BCC and FCC unit cells, assuming the atoms are represented as hard spheres. Do the same for the diamond cubic structure.

1.36 Draw the following crystallographic planes in BCC and FCC unit cells along with their atoms that intersect the planes:

- (a) (101),
- (b) (110),
- (c) (441),
- (d) (111),
- (e) (312).

1.37 A block copolymer has macromolecules of each polymer attached to the other as can be seen in Figure 1.22(c). The total molecular weight is 100,000 g/mol. If 140 g of A and 60 g of B were added, determine the degree of polymerization for each polymer. A: 56 g/mol; B: 70 g/mol.

1.38 Sketch the following planes within the unit cell. Draw one cell for each solution. Show new origin and ALL necessary calculations.

- (a) (0 $\bar{1}\bar{1}$ ),
- (b) (102),
- (c) (002),
- (d) (1 $\bar{3}$ 0),
- (e) ( $\bar{2}$ 12),
- (f) (3 $\bar{1}\bar{2}$ ).

1.39 Sketch the following directions within the unit cell. Draw one cell for each solution. Show new origin and ALL necessary calculations.

- (a) [101],
- (b) [0 $\bar{1}$ 0],
- (c) [12 $\bar{2}$ ],
- (d) [301],
- (e) [ $\bar{2}$ 01],
- (f) [2 $\bar{1}$ 3].

**1.40** Suppose we introduce one carbon atom for every 100 iron atoms in an interstitial position in BCC iron, giving a lattice parameter of 0.2867 nm. For the Fe–C alloy, find the density and the packing factor.

Given:

Atomic mass of C = 12,

Atomic mass of Fe = 55.89,

$a(\text{Fe}) = 0.2867 \text{ nm}$ ,

Avogadro's number,  $N = 6.02 \times 10^{23}$ .

**1.41** Determine the maximum length of a polymer chain made with 1,500 molecules of ethylene, knowing that the carbon bond length is 0.13 nm.

---

## Chapter 2

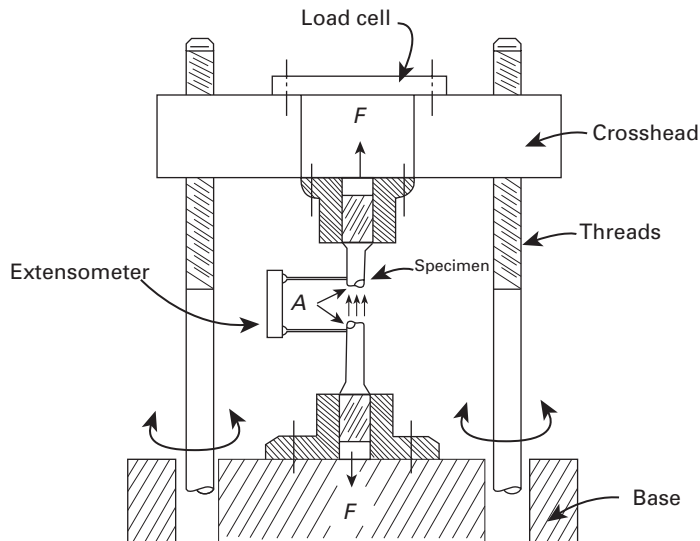
# Elasticity and Viscoelasticity

---

### 2.1 | Introduction

Elasticity deals with elastic stresses and strains, their relationship, and the external forces that cause them. An *elastic strain* is defined as a strain that disappears instantaneously once the forces that cause it are removed. The theory of elasticity for Hookean solids – in which stress is proportional to strain – is rather complex in its more rigorous treatment. However, it is essential to the understanding of micro- and macromechanical problems. Examples of the former are stress fields around dislocations, incompatibilities of stresses at the interface between grains, and dislocation interactions in work hardening; examples of the latter are the stresses developed in drawing, and rolling wire, and the analysis of specimen-machine interactions in testing for tensile strength. This chapter is structured in such a way as to satisfy the needs of both the undergraduate and the graduate student. A simplified treatment of elasticity is presented, in a manner so as to treat problems in an undergraduate course. Stresses and strains are calculated for a few simplified cases; the tridimensional treatment is kept at a minimum. A graphical method for the solution of two-dimensional stress problems (the Mohr circle) is described. On the other hand, the graduate student needs more powerful tools to handle problems that are somewhat more involved. In most cases, the stress and strain systems in tridimensional bodies can be better treated as tensors, with the indicial notation. Once this tensor approach is understood, the student will have acquired a very helpful visualization of stresses and strains as tridimensional entities. Important problems whose solutions require this kind of treatment involve stresses around dislocations, interactions between dislocations and solute atoms, fracture mechanics, plastic waves in solids, stress concentrations caused by precipitates, the anisotropy of individual grains, and the stress state in a composite material.

**Fig. 2.1** Sketch of screw-driven tensile-strength testing machine.



## 2.2 | Longitudinal Stress and Strain

Figure 2.1 shows a cylindrical specimen being stressed in a machine that tests materials for tensile strength. The upper part of the specimen is screwed to the crosshead of the machine. The coupled rotation of the two lateral screws causes the crosshead to move. The load cell is a transducer that measures the load and sends it to a recorder; the increase in length of the specimen can be read by strain gages, extensometers, or, indirectly, from the velocity of motion of the crosshead. Another type of machine, called a servohydraulic machine, is also used. Assuming that at a certain moment the force applied on the specimen by the machine is  $F$ , there will be a tendency to “stretch” the specimen, breaking the internal bonds. This breaking tendency is opposed by internal reactions, called stresses. The best way of visualizing stresses is by means of the method of analysis used in the mechanics of materials: The specimen is “sectioned,” and the missing part is replaced by the forces that it exerts on the other parts. This procedure is indicated in the figure. In the situation shown, the “resistance” is uniformly distributed over the normal section and is represented by three modest arrows at A. The normal stress  $\sigma$  is defined as this “resistance” per unit area. Applying the equilibrium-of-forces equation from the mechanics of materials to the lower portion of the specimen, we have

$$\begin{aligned}\sum F &= 0 \\ F - \sigma A &= 0 \\ \sigma &= \frac{F}{A}.\end{aligned}\tag{2.1}$$

This is the internal resisting stress opposing the externally applied load and avoiding the breaking of the specimen. The following

stress convention is used: Tensile stresses are positive and compressive stresses are negative. In geology and rock mechanics, on the other hand, the opposite sign convention is used because compressive stresses are much more common.

As the applied force  $F$  increases, so does the length of the specimen. For an increase  $dF$ , the length  $l$  increases by  $dl$ . The normalized (per unit length) increase in length is equal to

$$d\varepsilon = \frac{dl}{l},$$

or, upon integration,

$$\varepsilon = \int_{l_0}^{l_1} \frac{dl}{l} = \ln \frac{l_1}{l_0}, \quad (2.2)$$

where  $l_0$  is the original length. This parameter is known as the *longitudinal true strain*.

In many applications, a simpler form of strain, commonly called *engineering* or *nominal strain*, is used. This type of strain is defined as

$$\varepsilon_n = \varepsilon_e = \frac{\Delta l}{l_0} = \frac{l_1}{l_0} - 1. \quad (2.2a)$$

In materials that exhibit large amounts of elastic deformation (rubbers, soft biological tissues, etc.) it is customary to express the deformation by a parameter called "stretch" or "stretch ratio." It is usually expressed as  $\lambda$ :

$$\lambda = \varepsilon_e + 1.$$

Hence, deformation starts at  $\lambda = 1$ .

When the strains are reasonably small, the engineering (or nominal) and true strains are approximately the same. We will use subscripts  $t$  for true values and  $e$  for engineering values. It can be easily shown that

$$\varepsilon_t = \ln(1 + \varepsilon_e). \quad (2.2b)$$

The elastic deformation in metals and ceramics rarely exceeds 0.005, and for this value, the difference between  $\varepsilon_t$  and  $\varepsilon_e$  can be neglected.

In a likewise fashion, a *nominal* (or *engineering*) stress is defined as

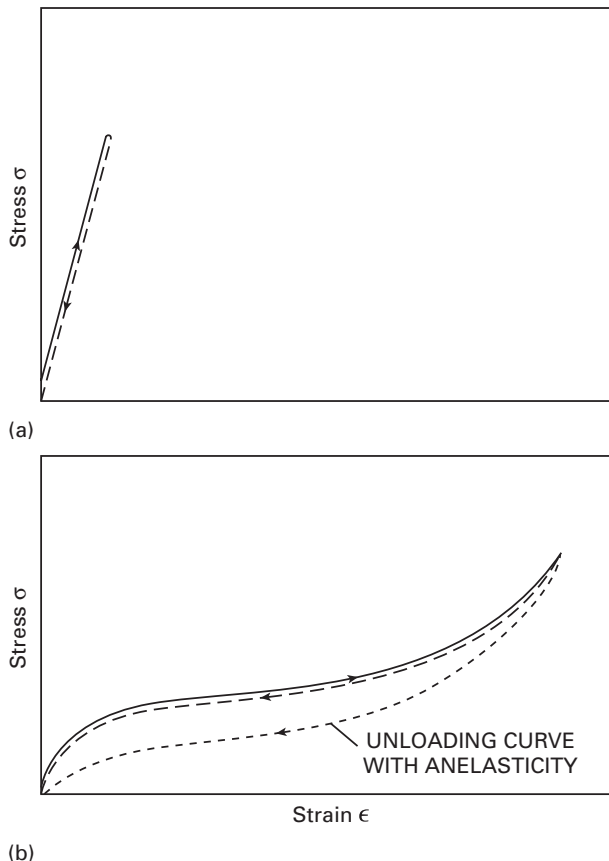
$$\sigma_e = \frac{F}{A_0}, \quad (2.2c)$$

where  $A_0$  is the original area of cross-section.

The relationship between the true stress and the engineering stress is

$$\frac{\sigma_t}{\sigma_e} = \frac{A_0}{A}.$$

**Fig. 2.2** Stress-strain curves in an elastic regimen. (a) Typical curve for metals and ceramics. (b) Typical curve for rubber.



During elastic deformation, the change in cross-sectional area is less than 1% for most metals and ceramics; thus  $\sigma_e \cong \sigma_t$ . However, during plastic deformation, the differences between the true and the engineering values become progressively larger. More details are provided in Chapter 3 (Section 3.1.2).

The sign convention for strains is the same as that for stresses: Tensile strains are positive, compressive strains are negative. In Figure 2.2, two stress-strain curves (in tension) are shown; both specimens exhibit elastic behavior. The solid lines describe the loading trajectory and the dashed lines describe the unloading. For perfectly elastic solids, the two kinds of lines should coincide if thermal effects are neglected. The curve of Figure 2.2(a) is characteristic of metals and ceramics; the elastic regimen can be satisfactorily described by a straight line. The curve of Figure 2.2(b) is characteristic of rubber;  $\sigma$  and  $\epsilon$  are not proportional. Nevertheless, the strain returns to zero once the stress is removed. The reader can verify this by stretching a rubber band. First, you will notice that the resistance to stretching increases slightly with extension. After considerable deformation, the rubber band “stiffens up,” and further deformation will eventually lead to rupture. The whole process (except failure) is elastic. A

conceptual error often made is to assume that elastic behavior is always linear; the rubber example shows very clearly that there are notable exceptions. However, for metals, the stress and strain can be assumed to be proportional in the elastic regimen; these materials are known as Hookean solids. For polymers, viscoelastic effects are very important. Viscoelasticity results in different trajectories for loading and unloading, with the formation of a hysteresis loop. The area of the hysteresis loop is the energy lost per unit volume in the entire deformation cycle. Metals also exhibit some viscoelasticity, but it is most often neglected. Viscoelasticity is attributed to time-dependent microscopic processes accompanying deformation. An analogy that applies well is the attachment of a spring and dashpot. The spring represents the elastic portion of the material, the dashpot the viscoelastic portion.

In 1678, Robert Hooke performed experiments that demonstrated the proportionality between stress and strain. He proposed his law as an anagram – “ceiiinosssttuv,” which rearranged, forms the Latin *Ut tensio sic vis*. The meaning is “As the tension goes, so does the stretch.” In its most simplified form, we express this law as

$$E = \frac{\sigma}{\varepsilon}, \quad (2.3)$$

where  $E$  is Young's modulus. For metals and ceramics,  $E$  has a very high value – for example, 210 GPa for iron. Chapter 4 devotes some effort to the derivation of  $E$  for materials from first principles.  $E$  depends mainly on the composition, crystallographic structure, and nature of the bonding of elements. Heat and mechanical treatments have little effect on  $E$ , as long as they do not affect the former parameters. Hence, annealed and cold-rolled steel should have the same Young's modulus; there are, of course, small differences due to the formation of the cold-rolling texture.  $E$  decreases slightly with increases in temperature.

In monocrystals,  $E$  shows different values for different crystallographic orientations. In polycrystalline aggregates that do not exhibit any texture,  $E$  is isotropic: It has the same value in all directions. The values of  $E$  given in tables (e.g., Tables 2.3–2.5 later in this chapter) are usually obtained by dynamic methods involving the propagation of elastic waves, not from conventional stress-strain tests. An elastic wave is passed through a sample; the velocities of the longitudinal and shear waves,  $V_\ell$  and  $V_s$ , respectively, are related to the elastic constants by means of the following mathematical expressions ( $\rho$  is the density,  $E$  is Young's modulus, and  $G$  is the shear modulus).<sup>1</sup>

$$V_\ell = \sqrt{\frac{E}{\rho}} \quad V_s = \sqrt{\frac{G}{\rho}}$$

<sup>1</sup> For more details, see M. A. Meyers, *Dynamic Behavior of Materials* (New York: Wiley, 1994).

### Example 2.1

Calculate the material properties  $E$ ,  $G$ , and  $\nu$  of SiC, given the graphs of the longitudinal and shear sound velocities obtained using ultrasonic equipment. (See Figure E2.1). Here,  $\rho = 3.18 \times 10^3 \text{ kg/m}^3$  and the length of specimen is  $L = 4 \text{ mm}$ .

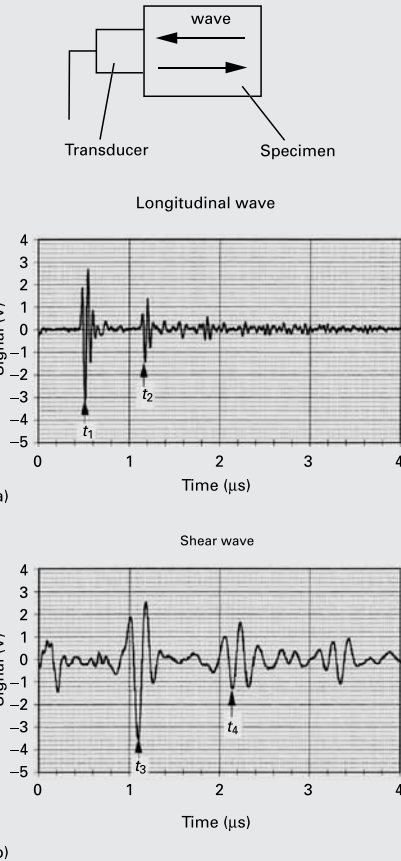


**Fig. E2.1**

**Solution:** We take equivalent peaks, marked by arrows, in sequential signal packets. We must remember that the pulse reflects at the free surface, and therefore, we have to take twice the length of the pulse. We have

$$V_\ell = \frac{2L}{t_2 - t_1} = \frac{2 \times 4 \times 10^{-3}}{(1.16 - 0.52) \times 10^{-6}} = 12.5 \times 10^3 \text{ m/s},$$

$$V_\ell = \sqrt{\frac{E}{\rho}},$$

$$E = \rho V_\ell^2 = 3.18 \times 10^3 \times (12.5 \times 10^3)^2 = 496.9 \times 10^9 \text{ Pa} = 496.9 \text{ GPa},$$

$$V_s = \frac{2L}{t_4 - t_3} = \frac{2 \times 4 \times 10^{-3}}{(2.15 - 1.10) \times 10^{-6}} = 7.62 \times 10^3 \text{ m/s}$$

$$V_s = \sqrt{\frac{G}{\rho}},$$

$$G = \rho V_s^2 = 3.18 \times 10^3 \times (7.62 \times 10^3)^2 = 184.6 \times 10^9 \text{ Pa} = 184.6 \text{ GPa}.$$

Since, according to Table 2.2,

$$G = \frac{E}{2(1 + \nu)},$$

where  $\nu$  is Poisson's ratio, as explained in Section 2.4, it follows that

$$\nu = \frac{E}{2G} - 1 = \frac{496.9}{2 \times 184.6} - 1 = 0.346.$$

(Note: The preceding calculations were conducted assuming uniaxial stress and without the dispersion correction; hence, the results are only approximate.)

A correct equation for the elastic modulus would be

$$V_\ell = \sqrt{\frac{\bar{E}}{\rho}}, \quad \bar{E} = \frac{(1 - \nu)}{(1 + \nu)(1 - 2\nu)} E.$$

This is because the length of the pulse is much shorter than the lateral dimension of the specimen, and therefore, the specimen is stressed in uniaxial strain.<sup>2</sup>

## 2.3 Strain Energy (or Deformation Energy) Density

When work is done on a body, its dimensions change. The work done ( $W$ ) is converted into heat ( $Q$ ) and an increase in internal energy ( $U$ ) of the body. We can write as per the first law of thermodynamics

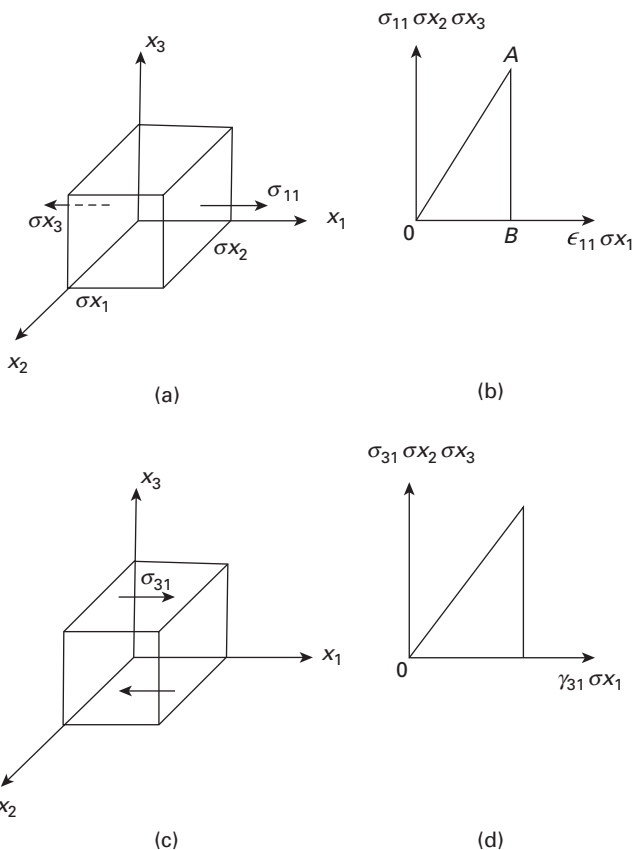
$$dU = dQ - dW.$$

For most solids, the elastic work produces an insignificant amount of heat. Hence, the work done on a body during deformation is converted into internal energy, which is stored in the deformed material and we call it strain energy or strain energy density when referring to the stored strain energy per unit volume. In elastic springs the energy is stored, while in a damping element the energy is dissipated as heat. Quite frequently, in mechanics, we use the principle of minimization of energy to arrive at useful expression.

Consider an elemental cube under uniaxial tension,  $\sigma_{11}$ , as shown in Fig. 2.3(a). The work done is given by product of force and change in length. Figure 2.3(b) shows the plot of tensile force vs. displacement, where we have converted the stress into force and strain into

<sup>2</sup> The interested student can obtain more information in M. A. Meyers, *Dynamic Behavior of Materials* (New York: Wiley, 1994).

**Fig. 2.3** (a) Cube under a tensile stress,  $\sigma_{11}$ . (b) Tensile force vs. displacement. (c) Cube under a shear stress,  $\sigma_{31}$ . (d) Shear force vs. displacement.



displacement. The work done is the area under the force vs. displacement curve:

$$\text{Total work done} = \frac{1}{2}[\sigma_{11}(\sigma x_2 \sigma x_3) \varepsilon_{11} \sigma x_1] = \frac{1}{2}[\sigma_{11} \varepsilon_{11} (\sigma x_1 \sigma x_2 \sigma x_3)],$$

where  $\sigma_{11}$  is the tensile stress component in direction 1,  $\varepsilon_{11}$  is the corresponding tensile strain,  $\sigma x_1$ ,  $\sigma x_2$  and  $\sigma x_3$  are the lengths of side of the cube.

The work done per unit volume is

$$W_{11} = \frac{1}{2} \sigma_{11} \varepsilon_{11}.$$

We can obtain similar expressions for the work done by other stress components. The reader can show that for the shear stress,  $\sigma_{31}$ , the work done per unit volume (see Figure 2.3(c) and (d)) is given by

$$W_{31} = \frac{1}{2} \sigma_{31} \gamma_{31},$$

where  $\sigma_{31}$  and  $\gamma_{31}$  are the shear stress and shear strain components, respectively, acting in direction 3.

Using the principle of superposition, i.e., combining the results for two or more stresses (or strains), we can write for the total work done per unit volume or the strain energy density as

$$W = \frac{1}{2}(\sigma_{11}\varepsilon_{11} + \sigma_{22}\varepsilon_{22} + \sigma_{33}\varepsilon_{33} + 2\sigma_{12}\gamma_{12} + 2\sigma_{23}\gamma_{23} + 2\sigma_{31}\gamma_{31}).$$

In more compact indicial notation, we can write

$$U = W = \frac{1}{2}\sigma_{ij}\varepsilon_{ij},$$

where the subscripts  $i$  and  $j$  represent the plane normal on which the stress is acting and the direction in which the stress is acting, respectively. This notation is explained in Section 2.9. The units of strain energy density are  $\text{J/m}^3$  or  $\text{N}\cdot\text{m}/\text{m}^3$ , or  $\text{N}/\text{m}^2$ . The last one is the same as the units of stress. It should not cause any confusion if the reader will recall that the strain is a dimensionless quantity. Note that strain energy density is a scalar quantity, hence no indexes.

For a linearly elastic solid under a uniaxial stress we can use the Hooke's law ( $\sigma_{ij} = E\varepsilon_{ij}$ ) to obtain an alternate expression for the strain energy density:

$$U = W = \frac{1}{2}\sigma_{ij}\varepsilon_{ij} = \frac{1}{2}E\varepsilon_{ij}^2 = \frac{1}{2E}\sigma_{ij}^2.$$

One can extend the concept of elastic strain energy density to region of inelastic behavior by defining the strain energy density as the area under the stress-strain curve of a material. Sometimes, we take this area under the stress-strain curve as a measure of the toughness of a material.

### Example 2.2

A bar of a material with Young's modulus,  $E$ , length,  $L$ , and cross-sectional area,  $A$ , is subjected to an axial load,  $P$ . Derive an expression for strain energy stored in the bar.

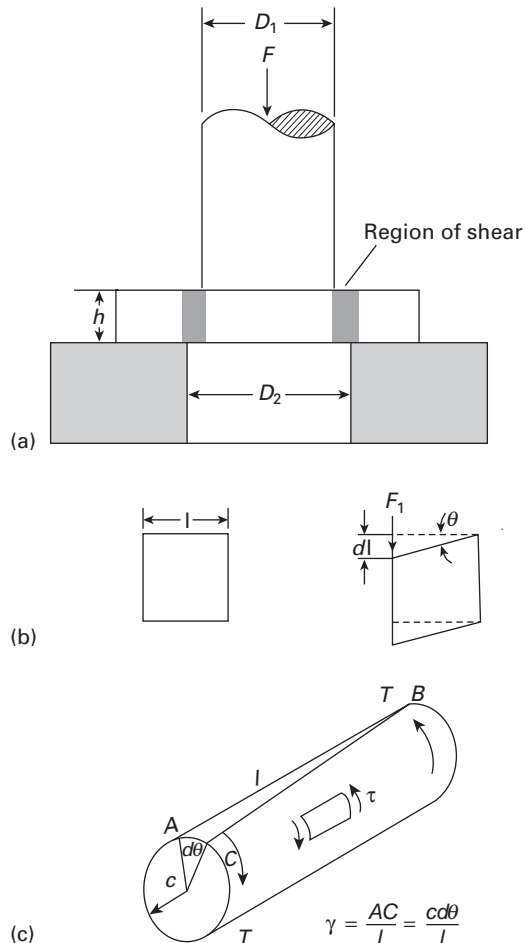
**Solution:** In order to determine the total elastic strain energy stored in a body under a general stress,  $\sigma$ , we need to integrate the elastic strain energy density over the original volume of the material. Thus, the total elastic strain energy for a material of volume  $V$ , can be written as

$$U_{\text{total}} = \int_V \frac{\sigma^2}{2E} dV.$$

For the simple case of a tensile force  $P$  acting on an area,  $A$ , we can write this as

$$U_{\text{total}} = \int_0^L \frac{P^2}{2EA^2} dx = \frac{P^2 L}{2EA^2}.$$

**Fig. 2.4** (a) Specimen subjected to shear force. (b) Strain undergone by small cube in shear region. (c) Specimen (cylinder) subjected to torsion by a torque  $T$ .



## 2.4 | Shear Stress and Strain

Imagine the loading arrangement shown in Figure 2.4(a). The specimen is placed between a punch and a base having a cylindrical orifice; the punch compresses the specimen. The internal resistance to the external forces now has the nature of a shear. The small cube in Figure 2.4(b) was removed from the region being sheared (between punch and base). It is distorted in such a way that the perpendicularity of the faces is lost. The shear stresses and strains are defined as

$$\tau = \frac{F}{A}, \quad \gamma = \frac{dl}{l} = \tan \theta \cong \theta. \quad (2.4)$$

The sign convention for shear stresses is given in Section 2.6. The area of the surface that undergoes shear is

$$A \cong \pi \left( \frac{D_1 + D_2}{2} \right) h.$$

The average of the two diameters is taken because  $D_2$  is slightly larger than  $D_1$ .

A mechanical test commonly used to find shear stresses and strains is the torsion test. The equations that give the shear stresses and strains in terms of the torque are given in texts on the mechanics of materials. Figure 2.4(c) shows a cylindrical specimen subjected to a torque  $T$ . The relationship between the torque and the shear stresses that are generated is given by<sup>3</sup>

$$\tau_{\max} = \frac{Tc}{J},$$

where  $c$  is the radius of the cylinder and  $J = \pi c^4/2$  is the polar moment of inertia. Tubular specimens are preferred over solid cylinders because the shear stress can be approximated as constant over the cross section of the cylinder. For a hollow cylinder with  $b$  and  $c$  as inner and outer radii, respectively, we subtract out (the hollow part to obtain)

$$J = \frac{\pi c^4}{2} - \frac{\pi b^4}{2}.$$

For metals, ceramics, and certain polymers (the Hookean solids), the proportionality between  $\tau$  and  $\gamma$  is observed in the elastic regimen. In analogy with Young's modulus, a transverse elasticity, called, the *rigidity*, or *shear modulus*, is defined as

$$G = \frac{\tau}{\gamma}. \quad (2.5)$$

$G$ , which is numerically less than  $E$ , is related to  $E$  by Poisson's ratio, discussed in Section 2.5. Values of  $G$  for different materials are given in Table 2.5; it can be seen that  $G$  varies between one-third and one-half of  $E$ .

### Example 2.3

A cylindrical steel specimen (length = 200 mm, diameter = 5 mm), is subjected to a torque equal to 40 N · m.

- (a) What is the deflection of the specimen end, if one end is fixed?
- (b) Will the specimen undergo plastic deformation?

Given:

$$E = 210 \text{ GPa},$$

$$\nu = 0.3,$$

$$\sigma_y = 300 \text{ MPa} \text{ (tensile yield stress).}$$

<sup>3</sup> See E. P. Popov, *Engineering Mechanics of Solids* (Englewood Cliffs, NJ: Prentice Hall, 1990).

*Solution:*

$$(a) \quad \tau_{\max} = \frac{T \cdot c}{J}. \quad (1)$$

Given

$$T = 40 \text{ N}\cdot\text{m}, \quad c = \frac{d}{2} = 2.5 \text{ mm}.$$

To calculate  $\tau_{\max}$ , we need to know  $J$ :

$$J = \pi \frac{c^4}{2}. \quad (2)$$

Substitute (2) into (1).

$$\begin{aligned} \tau_{\max} &= \frac{T \cdot c}{\pi \left( \frac{c^4}{2} \right)} = \frac{2T}{\pi c^3} = \frac{2 \cdot 40}{\pi \cdot (2.5)^3} \frac{\text{N}\cdot\text{m}}{\text{mm}^3} \\ &= 1630 \text{ MPa} \\ &= 1.63 \text{ GPa}. \end{aligned}$$

Shear stress and shear strain are related as

$$\tau = G \gamma.$$

$G$  can be calculated from  $E$  and  $\nu$ .

$$G = \frac{E}{2(1 + \nu)} = \frac{210}{2(1 + 0.3)} = 81 \text{ GPa},$$

$$\gamma = \frac{\tau_{\max}}{G} = \frac{1.63}{81} = 0.02.$$

But,

$$\gamma = \frac{c\theta}{L},$$

where  $\theta$  is the angle of rotation.

Torsional deflection = angle of rotation

$$\begin{aligned} &= \frac{\gamma L}{c} \\ &= \frac{0.02 \times 200}{2.5} = 1.6 \text{ radians}. \end{aligned}$$

$$(b) \quad \tau_{\max} = 1.63 \text{ GPa}.$$

The shear stress required to cause permanent deformation is related to the yield stress as follows:

$$\tau_y = \frac{\sigma_y}{2}.$$

When the stress is  $\sigma_y$ ,

$$\tau_y = \frac{300}{2} = 150 \text{ MPa}.$$

But from (a),  $\tau_{\max} = 1.63 \text{ GPa} > 150 \text{ MPa}$ . Therefore, the specimen will undergo plastic deformation.

**Example 2.4**

What is the strain energy density in a low-carbon steel sample loaded to its elastic limit of 500 MPa?

**Solution:** Take  $E$  for a low-carbon steel to be 210 GPa. For such a material under a stress  $\sigma$ , we have a strain energy density given by

$$\begin{aligned} U &= \frac{1}{2} \frac{\sigma^2}{E} = \frac{1}{2} \frac{(500 \times 10^6)^2}{210 \times 10^9} \\ &= 595 \text{ kJ/m}^3. \end{aligned}$$

## 2.5 | Poisson's Ratio

A body, upon being pulled in tension, tends to contract laterally. The cube shown in Figure 2.5 exhibits this behavior. The stresses are now defined in a tridimensional body, and they have two indices. The first indicates the plane (or the normal to the plane) on which they are acting; the second indicates the direction in which they are pointing. These stresses are schematically shown acting on three faces of a unit cube in Figure 2.5(a). The normal stresses have two identical subscripts:  $\sigma_{11}$ ,  $\sigma_{22}$ ,  $\sigma_{33}$ . The shear stresses have two different subscripts:  $\sigma_{12}$ ,  $\sigma_{13}$ ,  $\sigma_{23}$ . These subscripts refer to the reference system  $0x_1x_2x_3$ . If this notation is used, both normal and shear stresses are designated by the same letter, lower case sigma. On the other hand, in more simplified cases where we are dealing with only one normal and one shear stress component,  $\sigma$  and  $\tau$  will be used, respectively; this notation will be maintained throughout the text. In Figure 2.5, the stress  $\sigma_{33}$  generates strains  $\varepsilon_{11}$ ,  $\varepsilon_{22}$ ,  $\varepsilon_{33}$ . (The same convention is used for stresses and strains.) Since the initial dimensions of the cube are equal to 1, the changes in length are equal to the strains. Poisson's ratio is defined as the ratio between the lateral and the longitudinal strains. Both  $\varepsilon_{11}$  and  $\varepsilon_{22}$  are negative (signifying a decrease in length), and  $\varepsilon_{33}$  is positive. In order for Poisson's ratio to be positive, the negative sign is used. Hence,

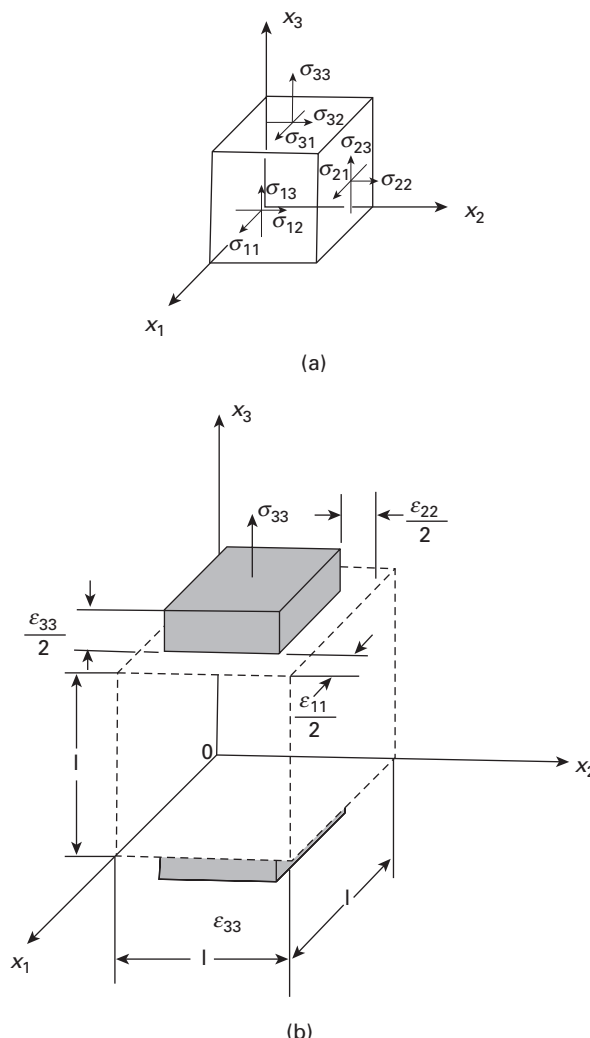
$$\nu = -\frac{\varepsilon_{11}}{\varepsilon_{33}} = -\frac{\varepsilon_{22}}{\varepsilon_{33}} \quad (2.6)$$

In an isotropic material,  $\varepsilon_{11}$  is equal to  $\varepsilon_{22}$ . We can calculate the value of  $\nu$  for two extreme cases: (1) when the volume remains constant and (2) when there is no lateral contraction. When the volume is constant, the initial and final volumes,  $V_0$  and  $V$ , respectively, are equal to

$$V_0 = 1,$$

$$V = (1 + \varepsilon_{11})(1 + \varepsilon_{22})(1 + \varepsilon_{33}).$$

**Fig. 2.5** (a) Unit cube in body subjected to tridimensional stress; only stresses on the three exposed faces of the cube are shown. (b) Unit cube being extended in direction  $Ox_3$ .



Neglecting the cross products of the strains, because they are orders of magnitude smaller than the strains themselves, we have

$$V = 1 + \varepsilon_{11} + \varepsilon_{22} + \varepsilon_{33}.$$

Since \$V=V\_0\$,

$$\varepsilon_{11} + \varepsilon_{22} + \varepsilon_{33} = 0.$$

For the isotropic case, the two lateral contractions are the same (\$\varepsilon\_{11} = \varepsilon\_{22}\$). Hence,

$$2\varepsilon_{11} = -\varepsilon_{33}. \quad (2.7)$$

Substituting Equation 2.7 into Equation 2.6, we arrive at

$$\nu = 0.5.$$

For the case in which there is no lateral contraction,  $\nu$  is equal to zero. Poisson's ratio for metals is usually around 0.3. (See Table 2.5.) The values given in the table apply to the elastic regimen; in the plastic regimen,  $\nu$  increases to 0.5, since the volume remains constant during plastic deformation.

Poisson's ratio for cork (and other cellular materials) is about 0.2, which means that we can push cork into a glass bottle without expanding the bottle. The student should try to do this with a rubber stopper ( $\nu \sim 0.5$ )!

It is possible to establish the maximum and minimum for Poisson's ratio. We know that  $G$  and  $E$  are positive. This is a consequence of the positiveness and definiteness of the strain energy function (a subject that we will not treat here – in simple words, the unloaded state of the body is the lowest energy state).

In the equation below:

$$G = \frac{E}{2(1 + \nu)}$$

we set:

$$E, G \geq 0.$$

Thus:

$$\frac{G}{E} = \frac{1}{2(1 + \nu)} \geq 0$$

This leads to:

$$\nu \geq -1.$$

The lower bound for Poisson's ratio is obtained by deforming a body and assuming that its volume remains constant, as was done earlier in this section. Thus:

$$0.5 \geq \nu \geq -1.$$

## 2.6 | More Complex States of Stress

The relationships between stress and strain described in sections 2.2 and 2.4 are unidimensional or uniaxial stress states, and do not apply to bidimensional and tridimensional states of stress. The most general state of stress can be represented by the unit cube of Figure 2.5(a). The generalized Hooke's law (as the set of equations relating tridimensional stresses and strains is called) is derived next, for an isotropic solid. It is assumed that shear stresses can generate *only* shear strains. Thus, the longitudinal strains are produced exclusively by the normal stresses.  $\sigma_{11}$  generates the following strain:

$$\varepsilon_{11} = \frac{\sigma_{11}}{E}. \quad (2.8)$$

Since  $v = -\varepsilon_{22}/\varepsilon_{11} = -\varepsilon_{33}/\varepsilon_{11}$  for stress  $\sigma_{11}$ , we also have

$$\varepsilon_{22} = \varepsilon_{33} = -\frac{v\sigma_{11}}{E}.$$

The stress  $\sigma_{22}$ , in its turn, generates the following strains:

$$\varepsilon_{22} = \frac{\sigma_{22}}{E} \quad \text{and} \quad \varepsilon_{11} = \varepsilon_{33} = -\frac{v\sigma_{22}}{E}. \quad (2.9)$$

For  $\sigma_{33}$ ,

$$\varepsilon_{33} = \frac{\sigma_{33}}{E} \quad \text{and} \quad \varepsilon_{11} = \varepsilon_{22} = -\frac{v\sigma_{33}}{E}. \quad (2.10)$$

In this treatment, the shear stresses generate only shear strains:

$$\gamma_{12} = \frac{\sigma_{12}}{G}, \quad \gamma_{13} = \frac{\sigma_{13}}{G}, \quad \gamma_{23} = \frac{\sigma_{23}}{G}.$$

The second simplifying assumption is called the “principle of superposition.” The total strain in one direction is considered to be equal to the sum of the strains generated by the various stresses along that direction. Hence, the total  $\varepsilon_{11}$  is the sum of  $\varepsilon_{11}$  produced by  $\sigma_{11}$ ,  $\sigma_{22}$ , and  $\sigma_{33}$ . Adding strains from Equations 2.8 through 2.10, we obtain the generalized Hooke’s law:

$$\begin{aligned} \varepsilon_{11} &= \frac{1}{E} [\sigma_{11} - v (\sigma_{22} + \sigma_{33})]. \\ \varepsilon_{22} &= \frac{1}{E} [\sigma_{22} - v (\sigma_{11} + \sigma_{33})]. \\ \varepsilon_{33} &= \frac{1}{E} [\sigma_{33} - v (\sigma_{11} + \sigma_{22})]. \\ \gamma_{12} &= \frac{\sigma_{12}}{G}, \quad \gamma_{13} = \frac{\sigma_{13}}{G}, \quad \gamma_{23} = \frac{\sigma_{23}}{G}. \end{aligned} \quad (2.11)$$

Applying these equations to a hydrostatic stress situation ( $\sigma_{11} = \sigma_{22} = \sigma_{33} = -p$ ), we can see perfectly that there are no distortions in the cube ( $\gamma_{12} = \gamma_{13} = \gamma_{23} = 0$ ) and that  $\varepsilon_{11} = \varepsilon_{22} = \varepsilon_{33}$ .

The triaxial state of stress is difficult to treat in elasticity (and even more difficult in plasticity). In the great majority of cases, we try to assume a more simplified state of stress that resembles the tridimensional stress. This is often justified by the geometry of the body and by the loading configuration. The example discussed in Section 2.2 is the simplest state (uniaxial stress). It occurs when beams are axially loaded (in tension or compression). In sheets and plates (where one dimension can be neglected with respect to the other two), the state of stress can be assumed to be bidimensional. This state of stress is also known as *plane stress*, because normal stresses (normal to the surface) are zero at the surface, as are shear stresses (parallel to the surface) at the surface. In Figure 2.5(a), one would be left with  $\sigma_{11}$ ,  $\sigma_{12}$ ,  $\sigma_{22}$  if  $0x_1x_2$  were the plane of the sheet. Since the sheet is thin, there is no space for buildup of the stresses that are zero at the surface. The

solution to this problem is approached graphically in Section 2.7. The opposite case, in which one of the dimensions is infinite with respect to the other two, is treated under the assumption of plane strain. If one dimension is infinite, strain in it is constrained; hence, one has two dimensions left. This state is called *bidimensional* or, more commonly, *plane strain*. It also occurs when strain is constrained in one direction by some other means. A long dam is an example in which deformation in the direction of the dam is constrained. Yet another state of stress is pure shear, when there are no normal stresses.

### Example 2.5

Consider a plate under uniaxial tension that is prevented from contracting in the transverse direction. Find the effective modulus along the loading direction under this condition of plane strain.

**Solution:** Take

$$E = \text{Young's modulus}, \quad v = \text{Poisson's ratio}$$

Let the loading and transverse directions be 1 and 2, respectively. There is no stress normal to the free surface, i.e.,  $\sigma_3 = 0$ . Although the applied stress is uniaxial, the constraint on contraction in direction 2 results in a stress in that direction also. The strain in direction 2 can be written in terms of Hooke's law as

$$\varepsilon_2 = 0 = (1/E)[\sigma_2 - v\sigma_1].$$

Thus,  $\sigma_2 = v\sigma_1$ .

In direction 1, we can write, for the strain,

$$\begin{aligned} \varepsilon_{11} &= (1/E)[\sigma_1 - v\sigma_2] = (1/E)[\sigma_1 - v^2\sigma_1] \\ &= (\sigma_1/E)(1 - v^2). \end{aligned}$$

Hence, the plane strain modulus in direction 1 is

$$E' = (\sigma_1/\varepsilon_1) = E/(1 - v^2).$$

If we take  $v = 0.33$ , then the plane strain modulus  $E' = 1.12E$ .

### Example 2.6

An isotropic, linear, elastic material is compressed by a force  $P$  by means of a punch in a rigid die. The material has a Young's modulus  $E$  and a Poisson's ratio  $v$ . The displacement of the material is  $\Delta$ , and the cavity has a height  $h$  and a square base of side  $a$ . (See Figure E2.6.)

Determine the stress and strain components. Also, determine the relationship between  $P$  and the displacement  $\Delta$  of the material.

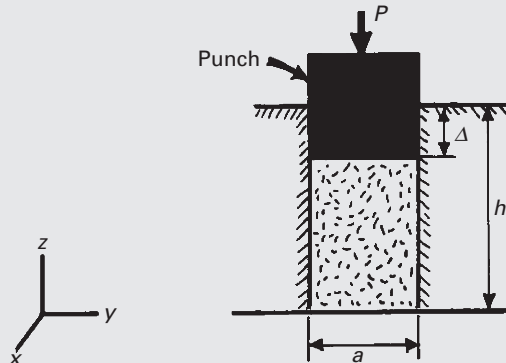


**Fig. E2.6**

**Solution:** This is a three-dimensional problem. There are no shear strains, and the only nonzero normal strain component is  $\varepsilon_z$ , the strain in the  $z$ -direction. The normal strains in the  $x$ - and  $y$ -directions are zero, because the rigid die does not allow deformation in these directions. However, the stress components in these directions are not zero. We use the generalized Hooke's law to obtain the three stress components. We can write, for the strain components,

$$\varepsilon_z = -\Delta/h, \quad \varepsilon_x = \varepsilon_y = \varepsilon_{xy} = \varepsilon_{yz} = \varepsilon_{zx} = 0.$$

Now we can write the following constitutive relationships by inverting Equation 2.11) and using  $x$ ,  $y$ , and  $z$  instead of 1, 2, and 3:

$$\begin{aligned}\sigma_x &= E / [(1 + v)(1 - 2v)] [(1 - v)\varepsilon_x + v(\varepsilon_y + \varepsilon_z)] \\ &= E / [(1 + v)(1 - 2v)] \cdot [0 + v(-\Delta/h)],\end{aligned}$$

or

$$\sigma_x = -[E v / (1 + v)(1 - 2v)] [\Delta/h].$$

Similarly,

$$\begin{aligned}\sigma_y &= E / [(1 + v)(1 - 2v)] [(1 - v)\varepsilon_y + v(\varepsilon_x + \varepsilon_z)] \\ &= E / [(1 + v)(1 - 2v)] \cdot [0 + v(-\Delta/h)],\end{aligned}$$

or

$$\sigma_y = -E v / [(1 + v)(1 - 2v)] [\Delta/h].$$

Finally,

$$\begin{aligned}\sigma_z &= E / [(1 + v)(1 - 2v)] [(1 - v)\varepsilon_z + v(\varepsilon_y + \varepsilon_x)] \\ &= E / [(1 + v)(1 - 2v)] \cdot [1 - v(-\Delta/h) + 0],\end{aligned}$$

or

$$\sigma_z = -E(1 - v) / [(1 + v)(1 - 2v)] [\Delta/h].$$

The load-displacement relationship is obtained by writing

$$P = \sigma_z a^2,$$

$$\sigma_z = P/a^2 = -E(1-\nu)/[(1+\nu)(1-2\nu)][\Delta/h],$$

or

$$P = -E a^2(1-\nu)(\Delta/h)/[(1+\nu)(1-2\nu)].$$

Note the linear relationship between  $P$  and  $\Delta$ , as it should be because the material in the cavity is linear elastic.

## 2.7 Graphical Solution of a Biaxial State of Stress: the Mohr Circle

There are two common graphical methods to obtain the stresses in a general orientation from  $\sigma_{11}$ ,  $\sigma_{12}$ , and  $\sigma_{22}$ . These methods are similar and are a graphical representation of the equations below, that can be found in any mechanics of materials text:

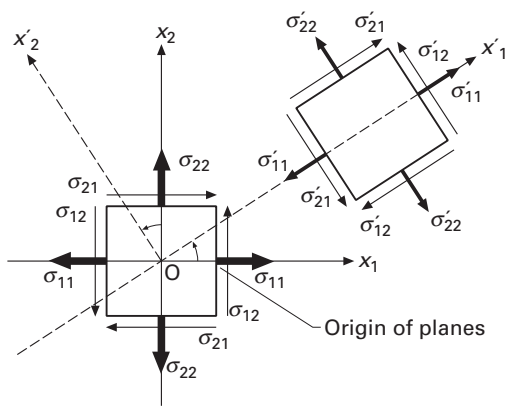
$$\sigma'_{11} = \frac{\sigma_{11} + \sigma_{22}}{2} + \frac{\sigma_{11} - \sigma_{22}}{2} \cos 2\theta + \sigma_{12} \sin 2\theta,$$

$$\sigma'_{12} = -\frac{\sigma_{11} - \sigma_{22}}{2} \sin 2\theta + \sigma_{12} \cos 2\theta$$

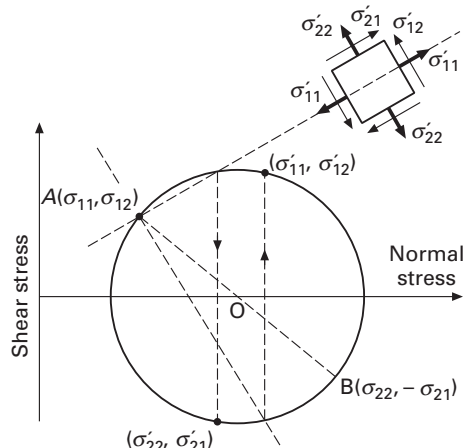
The angle  $\theta$  can be eliminated from the two equations above, leading to a quadratic equation that represents a circle. We present below two graphical methods to obtain the values of normal and shear stresses in any orientation, as well as the maximum normal and shear stresses.

Figure 2.6(a) shows a biaxial (or bidimensional) state of stress. The graphical scheme developed by O. Mohr allows the determination of the normal and shear stresses in any orientation in the plane. The reader should be warned, right at the onset, that a *change in sign convention* for the shear stresses has to be introduced here. The former sign convention – positive shear stresses pointing toward the positive direction of axes in faces shown in Figure 2.5(a) – has to be *temporarily abandoned* and the following convention adopted: Positive shear stresses produce counterclockwise rotation of a cube (or square), and negative shear stresses produce clockwise rotation. The sign convention for normal stresses remains the same. Figure 2.6(b) shows Mohr's construction. The normal stresses are plotted on the abscissa, while the shear stresses are plotted on the ordinate axis. Point A in the diagram corresponds to a state of stress on the face of the cube perpendicular to  $Ox_1$ ; point B represents the state of stress on the face perpendicular to  $Ox_2$ . From A and B, we construct a circle with center in the axis of the abscissa and passing through A and B. The center is the point where the segment AB intersects the abscissa. Note that the center occurs at  $(\sigma_{11} + \sigma_{22})/2$ . The stress states for all orientations of the cube (in the same plane) correspond to points diametrically

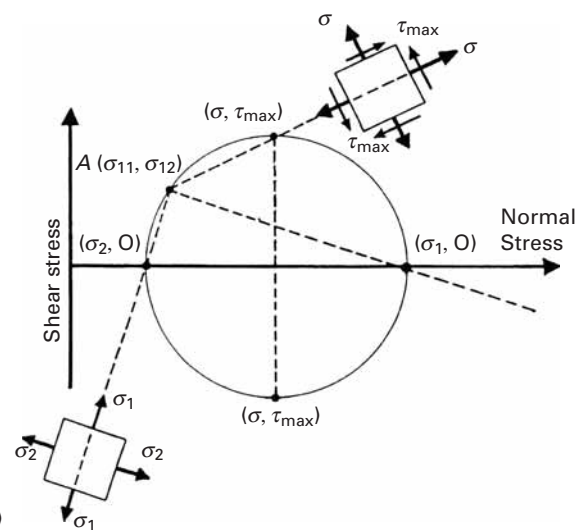
**Fig. 2.6** (a) Biaxial (or bidimensional) state of stress. (b) Mohr circle and construction of general orientation  $0x'_1x'_2$ . (c) Mohr circle and construction of principal stresses and maximum shear stresses (Method I).



(a)



(b)



(c)

opposed in Mohr's circle. Hence, we can determine the state of stress for any orientation.

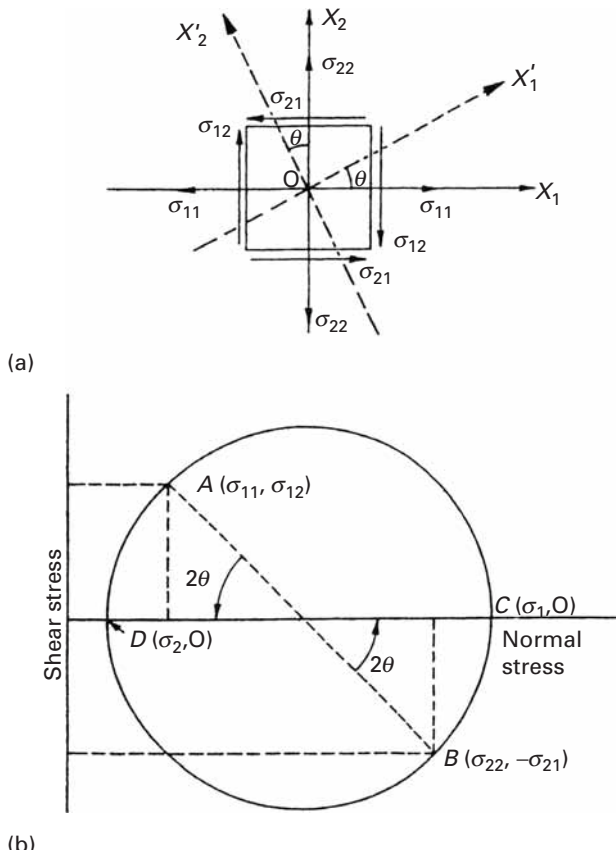
Method I is as follows: Point A (the stress system on the right-hand of the cube face) is called the "origin of planes." We will always start from it on the Mohr circle. We solve two problems.

First, we determine the stresses on a general coordinate direction  $Ox'_1$ ,  $Ox'_2$ . This is shown in Figure 2.6(b). Lines are drawn through A (the origin of planes) parallel to  $Ox'_1$  and  $Ox'_2$ . We seek the intersection of the axes with the circle. We draw lines perpendicular to the normal stress axis and find the new intersection. Thus,  $(\sigma'_{11}, \tau'_{12})$  represents stresses on the face perpendicular to  $Ox'_1$ , and  $(\sigma'_{22}, \tau'_{12})$  represents stresses on face perpendicular to  $Ox'_2$ . These stresses are drawn in Figure 2.6(b). Remember that the clockwise–counterclockwise convention has to be used and that shear stresses are such that the summation of moments is zero.

Now we determine the maximum normal stresses (principal stresses) and maximum shear stresses. From point A (the origin of planes), we draw lines to the points corresponding to the maximum and minimum principal stresses (Figure 2.6(c)). Notice that these planes make an angle of  $90^\circ$ . Since we are on a normal stress axis, the intersection of the perpendicular to this axis corresponds to the initial point. We draw a square and place the stresses  $(\sigma_1, \sigma_2)$  on the square. This represents the orientation and values of the principal stresses. For the maximum shear stresses, we repeat the procedure ( $\tau_{\max} = (\sigma_1 - \sigma_2)/2$ ). At points of intersection, (Figure 2.6(c)), we go to the opposite intersection with respect to the normal stress axis and obtain the values. We draw these on the square, with the convention that clockwise is positive. This represents the maximum shear stress value and orientation. Note that the normal stresses for this orientation (and the one  $90^\circ$  from it) are nonzero. Note also that  $\tau_{\max}$  occurs in orientations that make  $45^\circ$  with the principal stress orientations.

In Method II the sign convention for the shear stresses is the same: clockwise positive, counterclockwise negative. Again, the normal stresses are plotted in the abscissa and the shear stresses in the ordinate. Point A in the diagram corresponds to a state of stress on the face of the cube perpendicular to  $Ox_1$ : point B represents the state of stress on the face perpendicular to  $Ox_2$ . From A and B we construct a circle with center in the axis of the abscissa and passing through A and B. The center is the point where the segment AB intersects the abscissa. The stress states for all orientations of the square (in the same plane) correspond to points diametrically opposed in Mohr's circle. Hence we can determine the state of stress for any orientation. The rotations in the square (real rotations) and in Mohr's circle have the same sense: however a rotation of  $\theta$  in the square corresponds to  $2\theta$  in Mohr's circle. For instance, a rotation of  $2\theta$  in the counterclockwise direction leads to a state of stress defined by C and D in Mohr's circle. The shear stresses are zero for this orientation and the

**Fig. 2.7** (a) Biaxial (or bidimensional) state of stress; (b) Mohr circle construction (Method II).



normal stresses are called *principal* stresses. One subscript is sufficient to designate the stresses in these special orientations:  $\sigma_1, \sigma_2, \sigma_3$ . We use the convention  $\sigma_1 > \sigma_2 > \sigma_3$ . In Figure 2.7(a) a rotation of only  $\theta$  was done in the same counterclockwise sense, leading to the same principal stresses. The orientations  $Ox_1$  and  $Ox_2$  are called *principal axes* (or directions). The curious reader should consult a mechanics of materials text, such as E. P. Popov, *Engineering of Solids* (Upper Saddle River, NJ: Prentice Hall, 1999).

### Example 2.7

Elisabeth S., a bright, but somewhat nerdy, graduate student, went skiing in her brand-new boots. She had an unfortunate mishap on the slopes, and her right ski twisted beyond the strength of her femur, resulting in a fracture. The doctor took some X-rays and informed Elisabeth that she had a “spiral fracture.” This triggered a spirited dialogue between Elisabeth and the doctor. Elisabeth claims that her fracture (“peaking” through the ruptured skin) is helical. With whom do you agree? Why? Show, using your knowledge of engineering, what is the

maximum torque? The tensile strength of bone is 80 MPa and the diameter of the femur is 25 mm.

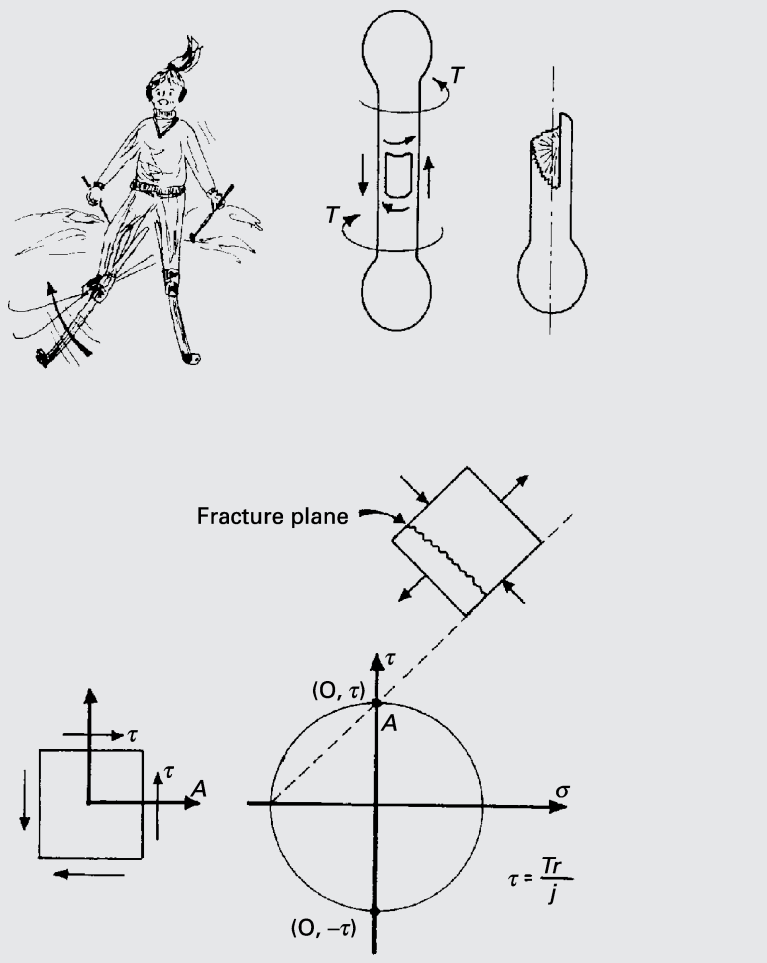


**Fig. E2.7**

The Mohr circle construction (see Figure E2.7) shows that the torsion  $T$  applied to the bone leads to a state of simple shear in the cross section. If the material were ductile, the failure plane would be the plane of maximum shear. Since bone is brittle, however, failure will occur along the surface where the tensile stresses are maximum. This surface is at an angle of  $45^\circ$  with the cross-sectional plane. Thus, the fracture is helical, and not spiral. (Students should repeat this analysis by using a piece of chalk and subjecting it to torsion.) The maximum torque that the bone will withstand is

$$T = \frac{\tau J}{r},$$

where  $J$  is the polar moment of inertia. (The student should consult a text on the mechanics of materials). Now, since  $\tau_{\max} = \sigma_{1\max}$ , it follows

that  $\tau_{\max} = 80 \text{ MPa}$ . Also,

$$J = \frac{\pi d^4}{32}.$$

Thus,

$$T = \frac{\tau_{\max} \pi d^3}{16} = 245 \text{ N}\cdot\text{m}.$$

The weight of a normal person is 750 N. Here is a ski tip, then: A distance of 1 meter from the axis of the leg can easily generate a torque of sufficient magnitude for a helical bone fracture to occur. Skiers, beware!

### Example 2.8 |

A state of stress is given by

$$\sigma_{11} = 350 \text{ MPa},$$

$$\sigma_{12} = 70 \text{ MPa},$$

$$\sigma_{22} = 210 \text{ MPa}.$$

Determine the principal stresses, the maximum shear stress, and their angle with the given direction by the Mohr circle.

**Solution:** Figure E2.8 shows the desired quantities.

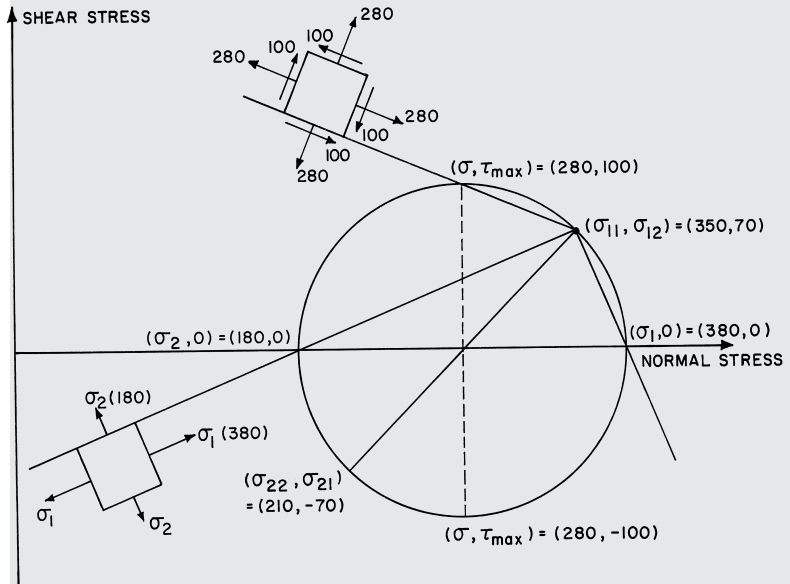
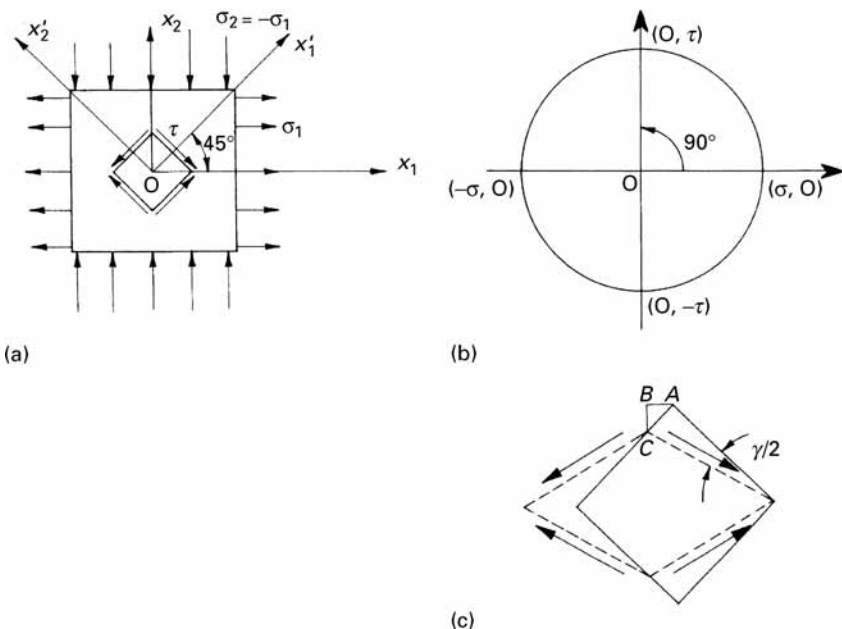


Fig. E2.8



**Fig. 2.8** Pure shear.

## 2.8 | Pure Shear: Relationship between $G$ and $E$

There is a special case of bidimensional stress in which  $\sigma_{22} = -\sigma_{11}$ . This state of stress is represented in Figure 2.8(a). It can be seen that  $\sigma_{12} = 0$ , implying that  $\sigma_{11}$  and  $\sigma_{22}$  are principal stresses. Hence, we can use the special subscripts for principal stresses and write  $\sigma_2 = -\sigma_1$ . In Mohr's circle of Figure 2.8(b), the center coincides with the origin of the axes. We can see that a rotation of  $90^\circ$  (on the circle) leads to a state of stress in which the normal stresses are zero. This rotation is equivalent to a  $45^\circ$  rotation in the body (real space). The magnitude of the shear stress at this orientation is equal to the radius of the circle. Hence, the square shown in Figure 2.8(c) is deformed to a lozenge under the combined effect of the shear stresses. Such a state of stress is called *pure shear*.

It is possible, from this particular case, to obtain a relationship between  $G$  and  $E$ ; furthermore, the relationship has a general nature. The strain  $\varepsilon_{11}$  is, for this case,

$$\varepsilon_{11} = \frac{1}{E} (\sigma_1 - v \sigma_2) = \frac{\sigma_1}{E} (1 + v). \quad (2.12)$$

We have, for the shear stresses (using the normal, and not the Mohr, sign convention),

$$\tau = -\sigma_1. \quad (2.13)$$

But we also have,

$$\tau = G \gamma. \quad (2.14)$$

Substituting Equations 2.13 and 2.14 into Equation 2.12 yields

$$\varepsilon_{11} = -\frac{G\gamma}{E}(1+\nu).$$

It is possible, by means of geometrical considerations on the triangle ABC in Fig. 2.8(c), to show that

$$2\varepsilon_{11} = -\gamma.$$

The reader should do this, as an exercise. Hence,

$$G = \frac{E}{2(1+\nu)}.$$

Consequently,  $G$  is related to  $E$  by means of Poisson's ratio. This theoretical relationship between  $E$  and  $G$  is in good agreement with experimental results. For a typical metal having  $\nu = 0.3$ , we have  $G = E/2.6$ . The maximum value of  $G$  is  $E/2$ .

The state of *simple shear* should not be confused with *pure shear*; simple shear involves an additional rotation, so that two faces remain parallel after deformation.

## 2.9 | Anisotropic Effects

Figure 2.5 shows that a general stress system acting on a unit cube has nine components and is a symmetrical tensor. (The off-diagonal components are equal, i.e.,  $\sigma_{13} = \sigma_{31}$ ,  $\sigma_{12} = \sigma_{21}$ , and  $\sigma_{23} = \sigma_{32}$ .) We can therefore write

$$\begin{pmatrix} \sigma_{11} & \sigma_{12} & \sigma_{13} \\ \sigma_{21} & \sigma_{22} & \sigma_{23} \\ \sigma_{31} & \sigma_{32} & \sigma_{33} \end{pmatrix} = \begin{pmatrix} \sigma_{11} & \sigma_{12} & \sigma_{13} \\ \sigma_{12} & \sigma_{22} & \sigma_{23} \\ \sigma_{13} & \sigma_{23} & \sigma_{33} \end{pmatrix}.$$

When the unit cube in Figure 2.5 is rotated, the stress state at that point does not change; however, the components of the stress change. The same applies to strains. A general state of strain is described by

$$\begin{pmatrix} \varepsilon_{11} & \varepsilon_{12} & \varepsilon_{13} \\ \varepsilon_{21} & \varepsilon_{22} & \varepsilon_{23} \\ \varepsilon_{31} & \varepsilon_{32} & \varepsilon_{33} \end{pmatrix} = \begin{pmatrix} \varepsilon_{11} & \varepsilon_{12} & \varepsilon_{13} \\ \varepsilon_{12} & \varepsilon_{22} & \varepsilon_{23} \\ \varepsilon_{13} & \varepsilon_{23} & \varepsilon_{33} \end{pmatrix}.$$

We can also use a matrix notation for stresses and strains, replacing the indices by the following:

$$11 \rightarrow 1 \quad 12 \rightarrow 5$$

$$22 \rightarrow 2 \quad 13 \rightarrow 5$$

$$33 \rightarrow 3 \quad 12 \rightarrow 6$$

$$\begin{pmatrix} 11 & 12 & 13 & 1 & 6 & 5 \\ \searrow & \nearrow & \uparrow & \searrow & \nearrow & \uparrow \\ 22 & 23 & 33 & = & 2 & 4 \\ \searrow & \nearrow & \uparrow & & \searrow & \uparrow \\ & & 33 & & & 3 \end{pmatrix}$$

We now have the stress and strain, in general form, as

$$\begin{pmatrix} \sigma_1 & \sigma_6 & \sigma_5 \\ \sigma_6 & \sigma_2 & \sigma_4 \\ \sigma_5 & \sigma_4 & \sigma_3 \end{pmatrix} \quad \text{and} \quad \begin{pmatrix} \varepsilon_1 & \varepsilon_6/2 & \varepsilon_5/2 \\ \varepsilon_6/2 & \varepsilon_2 & \varepsilon_4/2 \\ \varepsilon_5/2 & \varepsilon_4/2 & \varepsilon_3 \end{pmatrix}.$$

It should be noted that  $\varepsilon_1 = \varepsilon_{11}$ ,  $\varepsilon_2 = \varepsilon_{22}$ , and  $\varepsilon_3 = \varepsilon_{33}$ , but

$$\varepsilon_4 = 2\varepsilon_{23} = \gamma_{23},$$

$$\varepsilon_5 = 2\varepsilon_{13} = \gamma_{13},$$

$$\varepsilon_6 = 2\varepsilon_{12} = \gamma_{12}.$$

These differences in notation are important to preserve the equations (see shortly) that relate stresses to strains.

The foregoing transformation is easy to remember: One proceeds first along the diagonal ( $1 \rightarrow 2 \rightarrow 3$ ) and then back ( $4 \rightarrow 5 \rightarrow 6$ ). It is now possible to correlate the stresses and strains for a general case, in which the elastic properties of a material are dependent on its orientation. We use two elastic constants:  $C$  (stiffness) and  $S$  (compliance), or

$C \rightarrow$  Stiffness

$S \rightarrow$  Compliance.

Symbols are inverted to render treatment more confusing!

We have

$$\begin{pmatrix} \sigma_1 \\ \sigma_2 \\ \sigma_3 \\ \sigma_4 \\ \sigma_5 \\ \sigma_6 \end{pmatrix} = \begin{pmatrix} C_{11} & C_{12} & C_{13} & C_{14} & C_{15} & C_{16} \\ C_{21} & C_{22} & C_{23} & C_{24} & C_{25} & C_{26} \\ C_{31} & C_{32} & C_{33} & C_{34} & C_{35} & C_{36} \\ C_{41} & C_{42} & C_{43} & C_{44} & C_{45} & C_{46} \\ C_{51} & C_{52} & C_{53} & C_{54} & C_{55} & C_{56} \\ C_{61} & C_{62} & C_{63} & C_{64} & C_{65} & C_{66} \end{pmatrix} \begin{pmatrix} \varepsilon_1 \\ \varepsilon_2 \\ \varepsilon_3 \\ \varepsilon_4 \\ \varepsilon_5 \\ \varepsilon_6 \end{pmatrix}$$

In short notation, noting that repeated indices in one term imply summation, we have:

$$\sigma_i = C_{ij}\varepsilon_j,$$

$$\varepsilon_i = S_{ij}\sigma_j.$$

The elastic stiffness and compliance matrices are symmetric, and the 36 components ( $6 \times 6$ ) are reduced to 21. We now apply this general expression to crystals having different structures and, therefore, different symmetries to obtain successive simplifications. In the isotropic case, the elastic constants are reduced from 21 to 2.

The different crystal systems can be characterized exclusively by their symmetries. The proof of this is beyond the scope of the book; however, it is sufficient to say that the cubic system can be perfectly described by four threefold rotations. The seven crystalline systems can be perfectly described by their axes of rotation.

Table 2.1 presents the different symmetry operations defining the seven crystal systems. For example, a threefold rotation is a rotation of  $120^\circ$  ( $3 \times 120^\circ = 360^\circ$ ); after  $120^\circ$ , the crystal system comes to a position identical to the initial one. The hexagonal system

**Table 2.1** Minimum Number of Symmetry Operations in Various Systems

System	Rotation
Triclinic	None (or center of symmetry)
Monoclinic	1 twofold rotation
Orthorhombic	2 perpendicular twofold rotations
Tetragonal	1 fourfold rotation around [001]
Rhombohedral	1 threefold rotation around [111]
Hexagonal	1 sixfold rotation around [0001]
Cubic	4 threefold rotations around <111>

exhibits a sixfold rotation around the  $c$  axis; after each  $60^\circ$ , the structure superimposes upon itself. In terms of a matrix, we have the following:

$$\begin{array}{c}
 \text{Orthorhombic} \\
 \left[ \begin{array}{cccccc} 11 & 12 & 13 & 0 & 0 & 0 \\ . & 22 & 23 & 0 & 0 & 0 \\ . & . & 33 & 0 & 0 & 0 \\ . & . & . & 44 & 0 & 0 \\ . & . & . & . & 55 & 0 \\ . & . & . & . & . & 66 \end{array} \right], \quad \text{Tetragonal} \\
 \left[ \begin{array}{cccccc} 11 & 12 & 13 & 0 & 0 & 16 \\ . & 11 & 13 & 0 & 0 & -16 \\ . & . & 33 & 0 & 0 & 0 \\ . & . & . & 44 & 0 & 0 \\ . & . & . & . & 44 & 0 \\ . & . & . & . & . & 66 \end{array} \right], \\
 \text{Hexagonal} \\
 \left[ \begin{array}{cccccc} 11 & 12 & 13 & 0 & 0 & 0 \\ 11 & 13 & 0 & 0 & 0 & 0 \\ 33 & 0 & 0 & 0 & 0 & 0 \\ 44 & 0 & 0 & 0 & 0 & 0 \\ 44 & 0 & 0 & 0 & 0 & 0 \\ x & & & & & \end{array} \right] \quad \text{where} \\
 x \rightarrow 2(S_{11} - S_{12}), \quad \text{or} \\
 x \rightarrow \frac{1}{2}(C_{11} - C_{12}).
 \end{array}$$

Laminated composites made by the consolidation of prepregged sheets, with individual plies having different fiber orientations, have orthotropic symmetry with nine independent elastic constants. Orthotropic symmetry is analogous to orthorhombic symmetry: there are three mutually perpendicular axes of symmetry, and the elastic constants along these three axes are different. For the Cubic system, the elastic matrix is the following configuration:

$$\left[ \begin{array}{cccccc} 11 & 12 & 12 & 0 & 0 & 0 \\ . & 11 & 12 & 0 & 0 & 0 \\ . & . & 11 & 0 & 0 & 0 \\ . & . & . & 44 & 0 & 0 \\ . & . & . & . & 44 & 0 \\ . & . & . & . & . & 44 \end{array} \right].$$

The number of independent elastic constants in a cubic system is three.

For isotropic materials (most polycrystalline aggregates can be treated as such):

$$C_{44} = \frac{C_{11} - C_{12}}{2}. \quad (2.15)$$

The stiffness matrix is

$$\begin{bmatrix} C_{11} & C_{12} & C_{12} & 0 & 0 & 0 \\ . & C_{11} & C_{12} & 0 & 0 & 0 \\ . & . & C_{11} & 0 & 0 & 0 \\ . & . & . & \frac{C_{11} - C_{12}}{2} & 0 & 0 \\ . & . & . & . & \frac{C_{11} - C_{12}}{2} & 0 \\ . & . & . & . & . & \frac{C_{11} - C_{12}}{2} \end{bmatrix} \quad (2.16)$$

For anisotropic systems, Equation 2.15 does not apply, and we define an anisotropy ratio (also called the Zener anisotropy ratio, in honor of the scientist who introduced it):

$$A = \frac{2C_{44}}{C_{11} - C_{12}} \neq 1. \quad (2.17)$$

Some metals have high anisotropy ratios, whereas others, such as aluminum and tungsten, have values of  $A$  very close to 1. For the latter, even single crystals are almost isotropic.

For the elastic compliances, we have, for the isotropic case:

$$\begin{bmatrix} S_{11} & S_{12} & S_{12} & 0 & 0 & 0 \\ . & S_{11} & S_{12} & 0 & 0 & 0 \\ . & . & S_{11} & 0 & 0 & 0 \\ . & . & . & 2(S_{11} - S_{12}) & 0 & 0 \\ . & . & . & . & 2(S_{11} - S_{12}) & 0 \\ . & . & . & . & . & 2(S_{11} - S_{12}) \end{bmatrix}. \quad (2.18)$$

Hence, for the cubic system, the 81 components of the elastic constants have been reduced to three independent ones while for the isotropic case, only two independent elastic constants are needed. However, it is not under this form that the elastic constants are usually known.

Table 2.2 gives the various equations interrelating the foregoing parameters.

The relationships between stresses and strains for isotropic materials become

$$\varepsilon_1 = S_{11}\sigma_1 + S_{12}\sigma_2 + S_{12}\sigma_3 = \frac{1}{E} [\sigma_1 - \nu(\sigma_2 + \sigma_3)],$$

$$\varepsilon_2 = S_{12}\sigma_1 + S_{11}\sigma_2 + S_{12}\sigma_3 = \frac{1}{E} [\sigma_2 - \nu(\sigma_1 + \sigma_3)],$$

$$\varepsilon_3 = S_{12}\sigma_1 + S_{12}\sigma_2 + S_{11}\sigma_3 = \frac{1}{E} [\sigma_3 - \nu(\sigma_1 + \sigma_2)],$$

**Table 2.2** Relations among the Elastic Constants for Isotropic Materials

Elastic Constants	In Terms of:				
	$E, \nu$	$E, G$	$K, \nu$	$K, G$	$\lambda, \mu$
$E$	$= E$	$= E$	$= 3(1-2\nu)K$	$= \frac{9K}{1+3K/G}$	$= \frac{\mu(3+2\mu/\lambda)}{1+\mu/\lambda}$
$\nu$	$= \nu$	$= -1 + \frac{E}{2G}$	$= \nu$	$= \frac{1-2G/3K}{2+2G/3K}$	$= \frac{1}{2(1+\mu/\lambda)}$
$G$	$= \frac{E}{2(1+\nu)}$	$= G$	$= \frac{3(1-2\nu)K}{2(1+\nu)}$	$= G$	$= \mu$
$K$	$= \frac{E}{3(1-2\nu)}$	$= \frac{E}{9-3E/G}$	$= K$	$= K$	$= \lambda + \frac{2\mu}{3}$
$\lambda$	$= \frac{E\nu}{(1+\nu)(1-2\nu)} = \frac{E(1-2G/E)}{3-E/G}$	$= \frac{3K\nu}{1+\nu}$	$= K - \frac{2G}{3}$	$= \lambda$	
$\mu$	$= \frac{E}{2(1+\nu)}$	$= G$	$= \frac{3(1-2\nu)K}{2(1+\nu)}$	$= G$	$= \mu$

$$\varepsilon_4 = 2(S_{11} - S_{12})\sigma_4 = \frac{1}{G}\sigma_4,$$

$$\varepsilon_5 = 2(S_{11} - S_{12})\sigma_5 = \frac{1}{G}\sigma_5,$$

$$\varepsilon_6 = 2(S_{11} - S_{12})\sigma_6 = \frac{1}{G}\sigma_6.$$

Expressing the strains as function of the stresses, we have

$$\sigma_1 = C_{11}\varepsilon_1 + C_{12}\varepsilon_2 + C_{12}\varepsilon_3 = (2\mu + \lambda)\varepsilon_1 + \lambda\varepsilon_2 + \lambda\varepsilon_3,$$

$$\sigma_2 = C_{12}\varepsilon_1 + C_{11}\varepsilon_2 + C_{12}\varepsilon_3 = \lambda\varepsilon_1 + (2\mu + \lambda)\varepsilon_2 + \lambda\varepsilon_3,$$

$$\sigma_3 = C_{12}\varepsilon_1 + C_{12}\varepsilon_2 + C_{11}\varepsilon_3 = \lambda\varepsilon_1 + \lambda\varepsilon_2 + (2\mu + \lambda)\lambda\varepsilon_3,$$

$$\sigma_4 = \frac{1}{2}(C_{11} - C_{12})\varepsilon_4 = \mu\varepsilon_4,$$

$$\sigma_5 = \frac{1}{2}(C_{11} - C_{12})\varepsilon_5 = \mu\varepsilon_5,$$

$$\sigma_6 = \frac{1}{2}(C_{11} - C_{12})\varepsilon_6 = \mu\varepsilon_6.$$

Note that  $\mu = G$ .

The elastic compliance matrix for isotropic materials is directly obtained from the generalized Hooke law:

$$\begin{pmatrix} \varepsilon_1 \\ \varepsilon_2 \\ \varepsilon_3 \\ \varepsilon_4 \\ \varepsilon_5 \\ \varepsilon_6 \end{pmatrix} = \begin{pmatrix} 1/E & -\nu/E & -\nu/E & 0 & 0 & 0 \\ & 1/E & -\nu/E & 0 & 0 & 0 \\ & & 1/E & 0 & 0 & 0 \\ & & & 1/G & 0 & 0 \\ & & & & 1/G & 0 \\ & & & & & 1/G \end{pmatrix} \begin{pmatrix} \sigma_1 \\ \sigma_2 \\ \sigma_3 \\ \sigma_4 \\ \sigma_5 \\ \sigma_6 \end{pmatrix}.$$

The elastic stiffness matrix is obtained in a similar manner:

$$\begin{pmatrix} \sigma_1 \\ \sigma_2 \\ \sigma_3 \\ \sigma_4 \\ \sigma_5 \\ \sigma_6 \end{pmatrix} = \begin{pmatrix} 2\mu + \lambda & \lambda & \lambda & 0 & 0 & 0 \\ & 2\mu + \lambda & \lambda & 0 & 0 & 0 \\ & & 2\mu + \lambda & 0 & 0 & 0 \\ & & & \mu & 0 & 0 \\ & & & & \mu & 0 \\ & & & & & \mu \end{pmatrix} \begin{pmatrix} \varepsilon_1 \\ \varepsilon_2 \\ \varepsilon_3 \\ \varepsilon_4 \\ \varepsilon_5 \\ \varepsilon_6 \end{pmatrix}.$$

From the product of these two matrices ( $= I$ ) we can obtain some of the relations in Table 2.2.

By comparing the terms of the elastic compliance and stiffness matrices for isotropic materials with the matrices in Equations 2.16 and 2.17, one can obtain the following relationships: Young's modulus:

$$E = \frac{1}{S_{11}}. \quad (2.19)$$

Rigidity or shear modulus:

$$G = \frac{1}{2(S_{11} - S_{12})}.$$

Compressibility ( $B$ ) and bulk modulus ( $K$ ):

$$B = \frac{1}{K} = \frac{\varepsilon_{11} + \varepsilon_{22} + \varepsilon_{33}}{-\frac{1}{3}(\sigma_{11} + \sigma_{22} + \sigma_{33})}.$$

Poisson's ratio:

$$\nu = -\frac{S_{12}}{S_{11}}.$$

Lamé's constants:

$$\mu = C_{44} = \frac{1}{2} (C_{11} - C_{12}) = \frac{1}{S_{44}} = G,$$

$$\lambda = C_{12}.$$

A great number of materials can be treated as isotropic, although they are not microscopically so. The individual grains exhibit the

crystalline anisotropy and symmetry, but when they form a polycrystalline aggregate and are randomly oriented, the material is macroscopically isotropic (i.e., the elastic constants are the same in all directions). Often, a material is not completely isotropic; if the elastic modulus  $E$  is different along three perpendicular directions, the material is orthotropic; composites are a typical case.

In a cubic material, the elastic moduli can be determined along any orientation, from the elastic constants, by application of the following equation:

$$\frac{1}{E_{ijk}} = S_{11} - 2 \left( S_{11} - S_{12} - \frac{1}{2} S_{44} \right) \\ \times (\ell_{i1}^2 \ell_{j2}^2 + \ell_{j2}^2 \ell_{k3}^2 + \ell_{i1}^2 \ell_{k3}^2), \quad (2.20)$$

where  $E_{ijk}$  is the Young's modulus, respectively, in the  $[ijk]$  direction;  $\ell_{i1}$ ,  $\ell_{j2}$ , and  $\ell_{k3}$  are the direction cosines of the direction  $[ijk]$ .

The expression for the shear modulus is a little more complicated than that for Young's modulus, because it involves a direction of shear and a plane of shear. The Young's modulus, on the other hand, involves only a direction (the direction of extension or compression). The plane normal is the same as the direction. The shear modulus on the cube face planes  $\{100\}$  is equal to:

$$G_0 = \frac{1}{S_{44}}.$$

This shear modulus is the same, for any direction in these planes. In the  $\{111\}$  planes, on the other hand, the shear modulus varies with direction. For shear along  $[110]$ , it is equal to:

$$G_1 = \frac{3}{S_{44} + 4(S_{11} - S_{12})}.$$

For isotropic materials,

$$S_{44} = 2(S_{11} - S_{12})$$

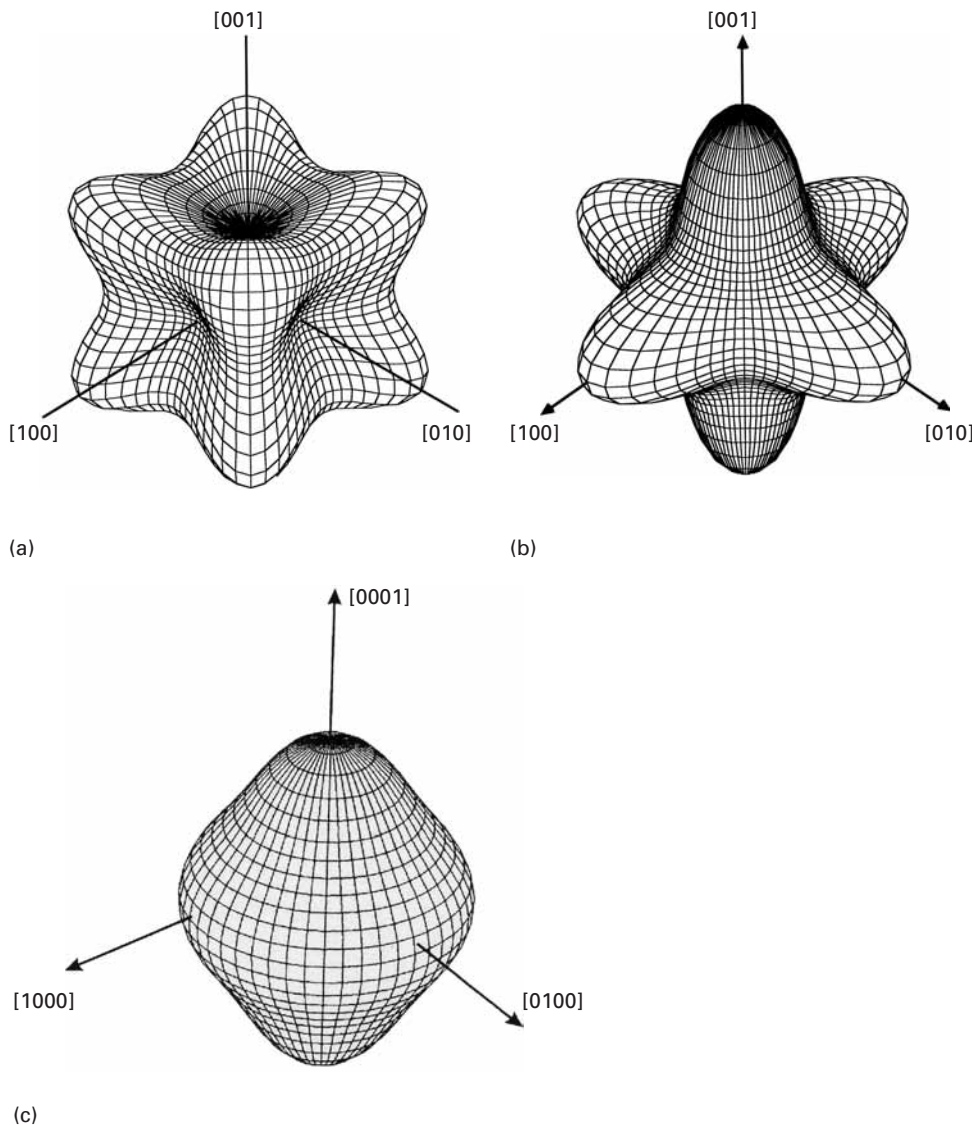
and

$$G = 1/S_{44}$$

for all orientations. For example, for copper  $S_{11} = 1.498$ ,  $S_{12} = -0.629$ ,  $S_{44} = 1.329 (\times 10^{-2} \text{ GPa}^{-1})$ ;  $G_0 = 75.4 \text{ GPa}$ ,  $G_1 = 30 \text{ GPa}$ .

Figure 2.9(a) illustrates the dependence on orientation of elastic Young's modulus for copper. The  $[100]$ ,  $[010]$ , and  $[001]$  directions are “softer,” whereas the  $[111]$ ,  $[1\bar{1}\bar{1}]$ , and  $[1\bar{1}\bar{1}]$  directions are stiffer. For cubic zirconia (Figure 2.9(b)), the opposite occurs: The coordinate axes correspond to the stiff directions. These diagrams illustrate very well the importance of anisotropy of elastic properties. For a cubic material that has the same Young's modulus along all directions (an isotropic material), we have the relationship

$$2(S_{11} - S_{12}) = S_{44}. \quad (2.21)$$



The tridimensional picture in Figure 2.9(c) shows anisotropy of Young's modulus in the hexagonal structure in a clearer fashion. This corresponds to zirconium. The isotropy of  $E$  in the basal plane is responsible for the “flying saucer” aspect of the polar plot.

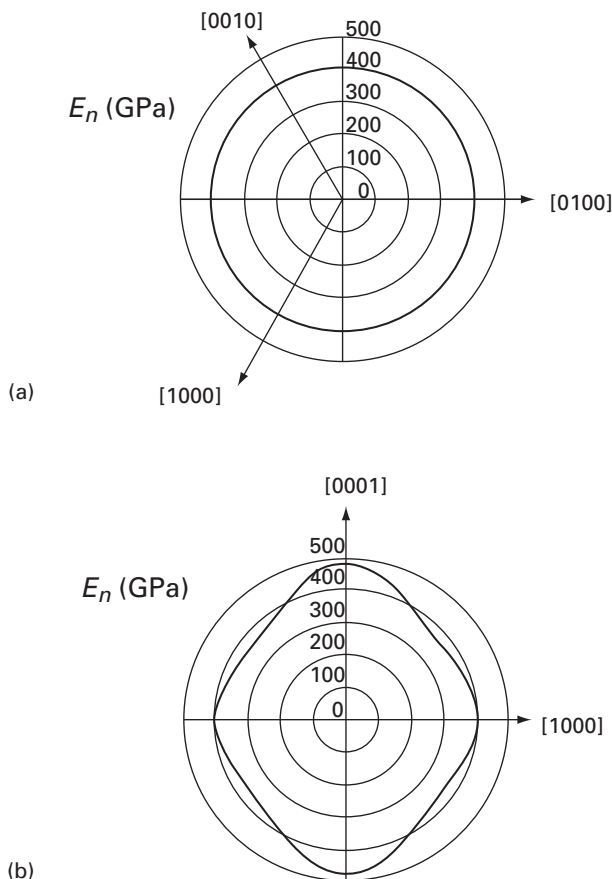
For hexagonal crystals, the Young's modulus is isotropic in the basal plane, but varies if one moves toward the  $c$  axis. The Young's modulus is given by:

$$\frac{1}{E} = (1 - l_3^2)S_{11} + l_3^4 S_{33} + l_3^2(1 - l_3^2)(2S_{13} + S_{44}),$$

where  $l_3$  is the cosine of the angle with the basal plane. Figure 2.10 shows the variation of  $E$  with orientation for SiC. It is constant and equal to 400 GPa in the basal plane. (Fig. 2.10(a)). In the  $c$  direction, it rises to 465 GPa (Figure 2.10(b)).

**Fig. 2.9** Dependence on orientation of Young's modulus for monocrystalline (a) copper; (b) cubic zirconia. (Courtesy of R. Ingel.) (c) Tridimension polar plot for zirconium. (Courtesy of J. M. Gebert.)

**Fig. 2.10** Variation of effective  $E$  for silicon carbide as a function of orientation; (a) basal plane; (b) perpendicular to basal plane.  
 (From C. J. Shih, M. A. Meyers, V. F. Nesterenko and S. J. Chen, *Acta Mater.*, 48 (2000) 2399.)



In Section 2.5 we defined the Poisson's ratio for isotropic materials. In anisotropic materials, we define Poisson's ratio in a similar manner. It is the magnitude of the ratio between the lateral and longitudinal strain (the direction along which the stress is applied). In the anisotropic case, the Poisson's ratio will depend on orientation and for each loading direction we have more than one Poisson's ratio. It is quite rare to find materials with negative Poisson's ratios. This did not deter Lubarda and Meyers<sup>4</sup> from finding one. Monocrystalline zinc, an HCP metal, has a negative Poisson's ratio in a certain orientation. In anisotropic materials, Poisson's ratio varies (as do all elastic constants) with orientation. We define  $\theta$  as the angle with the basal plane. Figure 2.11 shows the variation of  $\nu_{\ell n}$  (there is another Poisson's ratio in this case:  $\nu_{mn}$ ) with  $\theta$ . For  $\theta$  less than  $18^\circ$ , it is negative. It should be noted that for most HCP metals this negative regimen does not exist.

<sup>4</sup> V. A. Lubarda and M. A. Meyers, *Scripta Mater.*, 40 (1999) 975.

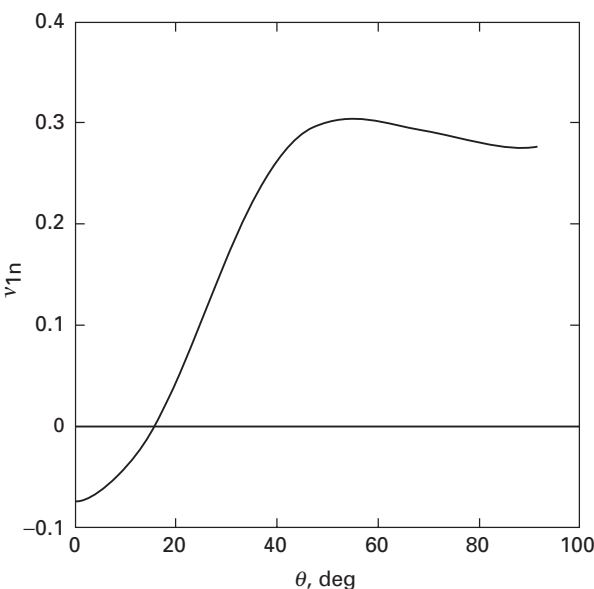


**Fig. 2.11** Variation in Poisson's ratio  $v_{1n}$  in direction 1 due to stress applied along direction  $n$ , making an angle  $\theta$  with the basal plane of the zinc (HCP) crystal.

### Example 2.9

A hydrostatic compressive stress applied to a material with cubic symmetry results in a dilation of  $-10^{-5}$ . The three independent elastic constants of the material are  $C_{11} = 50 \text{ GPa}$ ,  $C_{12} = 40 \text{ GPa}$ , and  $C_{44} = 32 \text{ GPa}$ . Write an expression for the generalized Hooke's law for this material, and compute the applied hydrostatic stress.

**Solution:** Dilation is the sum of the principal strain components:

$$\varepsilon = \varepsilon_1 + \varepsilon_2 + \varepsilon_3 = -10^{-5}.$$

Cubic symmetry implies that

$$\varepsilon_1 = \varepsilon_2 = \varepsilon_3 = -3.33 \times 10^{-6}$$

and

$$\varepsilon_4 = \varepsilon_5 = \varepsilon_6 = 0.$$

From Hooke's law,

$$\sigma_i = C_{ij}\varepsilon_j$$

and

$$\sigma_1 = C_{11}\varepsilon_1 + C_{12}\varepsilon_2 + C_{13}\varepsilon_3.$$

The applied hydrostatic stress is (see p. 98)

$$\begin{aligned}\sigma_p &= \sigma_1 = (50 + 40 + 40)(-3.33)10^3 \text{ Pa} \\ &= -130 \times 3.33 \times 10^3 \text{ Pa} \\ &= -433 \text{ kPa.}\end{aligned}$$

### Example 2.10

From the elastic stiffnesses for a cubic material, Nb ( $C_{11} = 242$  GPa;  $C_{12} = 129$  GPa;  $C_{44} = 286$  GPa), find the elastic compliances.

The relationship between stiffnesses and compliances is given by the product of their two matrices, which is an identity matrix:

$$\begin{pmatrix} S_{11} & S_{12} & \dots & S_{16} \\ S_{21} & S_{22} & \dots & S_{26} \\ \vdots & & & \\ \vdots & & & \\ S_{61} & S_{62} & \dots & S_{66} \end{pmatrix} \begin{pmatrix} C_{11} & C_{12} & \dots & C_{16} \\ C_{21} & C_{22} & \dots & C_{26} \\ \vdots & & & \\ \vdots & & & \\ C_{61} & C_{62} & \dots & C_{66} \end{pmatrix} = (I).$$

For materials with cubic symmetry,

$$\begin{pmatrix} S_{11} & S_{12} & S_{12} & 0 & 0 & 0 \\ S_{12} & S_{11} & S_{12} & 0 & 0 & 0 \\ S_{12} & S_{12} & S_{11} & 0 & 0 & 0 \\ 0 & 0 & 0 & S_{44} & 0 & 0 \\ 0 & 0 & 0 & 0 & S_{44} & 0 \\ 0 & 0 & 0 & 0 & 0 & S_{44} \end{pmatrix} \begin{pmatrix} C_{11} & C_{12} & C_{12} & 0 & 0 & 0 \\ C_{12} & C_{11} & C_{12} & 0 & 0 & 0 \\ C_{12} & C_{12} & C_{11} & 0 & 0 & 0 \\ 0 & 0 & 0 & C_{44} & 0 & 0 \\ 0 & 0 & 0 & 0 & C_{44} & 0 \\ 0 & 0 & 0 & 0 & 0 & C_{44} \end{pmatrix} = (I).$$

All the off-diagonal terms of the identity matrix are zero. The diagonal terms are equal to 1.

Row 1 and column 1 give

$$S_{11}C_{11} + S_{12}C_{12} + S_{12}C_{12} = 1. \quad (1)$$

From row 6 and column 6, we have

$$S_{44}C_{44} = 1.$$

Therefore,

$$S_{44} = \frac{1}{C_{44}}.$$

Row 1 and column 2 yield

$$S_{11}C_{12} + S_{12}C_{11} + S_{12}C_{12} = 0. \quad (2)$$

From equations 1 and 2, we get, for row 1 and column 1,

$$S_{12} = \frac{-C_{12}}{C_{11}^2 + C_{11}C_{12} - 2C_{12}^2} = \frac{-C_{12}}{(C_{11} + 2C_{12})(C_{11} - C_{12})}. \quad (3)$$

Substituting Equation 3 into Equation 1 yields

$$S_{11} = \frac{1}{C_{11}} + \frac{2C_{12}^2}{C_{11}(C_{11} + 2C_{12})(C_{11} - C_{12})} = \frac{C_{11} + C_{12}}{(C_{11} + 2C_{12})(C_{11} - C_{12})}$$

Thus,

$$\begin{aligned} S_{44} &= 3.5 \times 10^{-3} \text{ GPa}^{-1}, \\ S_{12} &= -0.22 \times 10^{-2} \text{ GPa}^{-1}, \\ S_{11} &= 0.66 \times 10^{-2} \text{ GPa}^{-1}. \end{aligned}$$

These values are fairly close to the values given in Table 2.4 (p. 112).

## 2.10 | Elastic Properties of Polycrystals

The elastic constants of materials are determined by the bonding between the individual atoms. While monocrystals have the elastic properties dictated by the crystalline symmetry, most metals and ceramics are polycrystalline. In polycrystals, the properties are determined from the individual grains by an averaging process.

In a polycrystalline aggregate, the deformation of one grain is not independent of the deformation of its neighbor. The compatibility requirements are such that we have to apply either one of two simplifying assumptions:

1. The local strain is equal to the mean strain (all grains undergo the same strain); this is called the *Voigt average*. The Young's modulus and shear moduli can then be obtained from:

$$E = \sum E_i V_i \quad \text{and} \quad G = \sum G_i V_i,$$

where  $E_i$ ,  $G_i$  and  $V_i$  represent the Young's modulus, shear modulus, and volume fraction, respectively, of grains of different orientations. One possible form attributed to Hill<sup>5</sup> is:

$$\begin{aligned} E &= \frac{1}{5} (3F + 2G^* + H) \\ G &= \frac{1}{5} (F + 4G^* - 2H) \end{aligned}$$

where

$$F = \frac{1}{2} (C_{11} + C_{22} + C_{33}),$$

$$G^* = \frac{1}{3} (C_{12} + C_{23} + C_{13}),$$

$$H = \frac{1}{3} (C_{44} + C_{55} + C_{66}).$$

We use  $G^*$  instead of  $G$  to avoid confusion with shear modulus,  $G$ .

2. The local stress is equal to the mean stress (all grains are under the same stress); this is called the *Reuss average*:  $\frac{1}{E} = \sum \frac{V_i}{E_i}$ . This provides

<sup>5</sup> R. Hill, Proc. Phys. Soc., A65 (1952) 349.

a lower bound. The inverse of the Young's modulus is then

$$\frac{1}{E} = \frac{1}{5} (3F' + 2G' + H')$$

where:  $F' = \frac{1}{3} (S_{11} + S_{22} + S_{33})$ ,

$$G' = \frac{1}{3} (S_{12} + S_{23} + S_{13}),$$

$$H' = \frac{1}{3} (S_{44} + S_{55} + S_{66}).$$

The actual stress and strain configuration is probably between the two assumptions. There are more advanced methods, such as the Hashin-Shtrikman upper and lower bound method; however, this will not be treated here. The above equation assumes a distribution of orientation of grains within the polycrystalline aggregate.

### Example 2.11 |

Determine the Young's moduli along [100], [110], and [111] for copper, tungsten, and ZrO<sub>2</sub>. We use Equation 2.20:

$$\frac{1}{E_{ijk}} = S_{11} - 2 \left( S_{11} - S_{12} - \frac{1}{2} S_{44} \right) \times (l_{i1}^2 l_{j2}^2 + l_{j2}^2 l_{k3}^2 + l_{i1}^2 l_{k3}^2).$$

The direction cosines are as follows:

	$l_{i1}$	$l_{j2}$	$l_{k3}$	$(l_{i1}^2 l_{j2}^2 + l_{j2}^2 l_{k3}^2 + l_{i1}^2 l_{k3}^2)$
[100]	1	0	0	0
[110]	$\sqrt{2}/2$	$\sqrt{2}/2$	0	1/4
[111]	$1/\sqrt{3}$	$1/\sqrt{3}$	$1/\sqrt{3}$	1/3

The compliances for Cu and W are given in later in this chapter Table 2.4; Table 2.6 provides the stiffnesses for cubic ZrO<sub>2</sub>. We have:

W	Cu
$S_{11} = 0.257 \times 10^{-2} \text{ GPa}^{-1}$	$S_{11} = 1.498 \times 10^{-2} \text{ GPa}^{-1}$
$S_{44} = 0.66 \times 10^{-2} \text{ GPa}^{-1}$	$S_{44} = 1.326 \times 10^{-2} \text{ GPa}^{-1}$
$S_{12} = -0.073 \times 10^{-2} \text{ GPa}^{-1}$	$S_{12} = -0.629 \times 10^{-2} \text{ GPa}^{-1}$

This yields

$$\text{Cu : } E_{100} = 66 \text{ GPa}, \quad E_{110} = 130 \text{ GPa}, \quad E_{111} = 191 \text{ GPa},$$

$$\text{W : } E_{100} = E_{110} = E_{111} = 389 \text{ GPa}.$$

For ZrO<sub>2</sub>, we have to use the equations derived in Example 2.10 to obtain the elastic compliances:

$$C_{11} = 410 \text{ GPa}, \quad C_{12} = 110 \text{ GPa}, \quad C_{44} = 60 \text{ GPa},$$

$$S_{44} = \frac{1}{C_{44}} = 1.6 \times 10^{-2} \text{ GPa}^{-1},$$

$$S_{12} = \frac{-C_{12}}{(C_{11} + 2C_{12})(C_{11} - C_{12})} = -0.058 \times 10^{-2} \text{ GPa}^{-1},$$

$$S_{11} = \frac{1}{C_{11}} + \frac{C_{12}^2}{C_{11}(C_{11} + 2C_{12})(C_{11} - C_{12})} = 0.275 \times 10^{-2} \text{ GPa}^{-1}.$$

These yield

$$E_{100} = 363.5 \text{ GPa}$$

$$E_{110} = 196.7 \text{ GPa},$$

$$E_{111} = 171 \text{ GPa}.$$

### Example 2.12 |

Determine the elastic anisotropy ratios of Ag, Al, Cu, Ni, Fe, Ta, and W. Which one of these metals has the greatest dependence on orientation for Young's modulus? Which one has the smallest?

**Solution:** First, we have

$$A = \frac{2C_{44}}{C_{11} - C_{12}}.$$

From Table 2.3 (later on), we obtain the following results:

$$\text{Ag : } A = \frac{46.1 \times 2}{124 - 93.4} = 3.01.$$

$$\text{Al : } A = \frac{28.5 \times 2}{108.2 - 61.3} = 1.22.$$

$$\text{Cu : } A = \frac{75.4 \times 2}{168.4 - 121.4} = 3.21.$$

$$\text{Ni : } A = \frac{124.7 \times 2}{246.5 - 147.3} = 2.51.$$

$$\text{Fe : } A = \frac{116.5 \times 2}{228 - 132} = 2.43.$$

$$\text{Ta : } A = \frac{82.5 \times 2}{267 - 161} = 1.56.$$

$$\text{W : } A = \frac{151.4 \times 2}{501.0 - 198} = 1.00.$$

Copper has the highest and W the lowest anisotropy ratio. Elastic properties should therefore be most orientation-dependent for Cu and orientation-independent for W.

### Example 2.13 |

Determine the Young's modulus for polycrystalline iron, using Reuss's and Voigt's averages. From Tables 2.3 and 2.4, we get the elastic stiffnesses and compliances:

$$C_{11} = 228 \text{ GPa}, \quad S_{11} = 0.762 \times 10^{-2} \text{ GPa}^{-1},$$

$$C_{44} = 116.5 \text{ GPa}, \quad S_{44} = 0.858 \times 10^{-2} \text{ GPa}^{-1},$$

$$C_{12} = 312 \text{ GPa}, \quad S_{12} = -0.279 \times 10^{-2} \text{ GPa}^{-1}.$$

Voigt method:

We first calculate the parameters, taking into account cubic symmetry:

$$F = \frac{1}{3} (C_{11} + C_{22} + C_{33}) = C_{11},$$

$$G^* = \frac{1}{3} (C_{12} + C_{23} + C_{13}) = C_{12},$$

$$H = \frac{1}{3} (C_{44} + C_{55} + C_{66}) = C_{44}.$$

Then:

$$E = \frac{1}{5} (3F + 2G^* + H) = \frac{1}{5} (3C_{11} + 2C_{12} + C_{44})$$

$$E = 186.5 \text{ GPa.}$$

Reuss method:

$$F' = \frac{1}{3} (S_{11} + S_{22} + S_{33}) = S_{11},$$

$$G' = \frac{1}{3} (S_{12} + S_{23} + S_{13}) = S_{12},$$

$$H' = \frac{1}{3} (S_{44} + S_{55} + S_{66}) = S_{44},$$

$$\frac{1}{E} = \frac{1}{5} (3F' + 2G' + H') = \frac{1}{5} (3S_{11} + 2S_{12} + S_{44}),$$

$$= 0.517 \times 10^{-2}.$$

So

$$E = 193 \text{ GPa.}$$

## 2.11 | Elastic Properties of Materials

Figure 2.12 presents a comparison of the elastic constants of different classes of materials. At the top, we have diamond (with covalent bonding). For metals, there is a correlation between the melting point (indicative of the bonding energy between atoms) and the Young's modulus. Thus, the metals with the highest bonding energies have the highest melting points, interatomic forces, and Young's modulus. The ranking of the metals in the second column of the figure shows this relationship; at the top are osmium and tungsten, and at the bottom is lead. The third column of the figure shows the polymers, which have elastic constants that are much lower than those of the metals. The composites in the last column show a wide variation in elastic constants. The carbon-fiber reinforced polymers (CFRPs) can have a very high modulus.

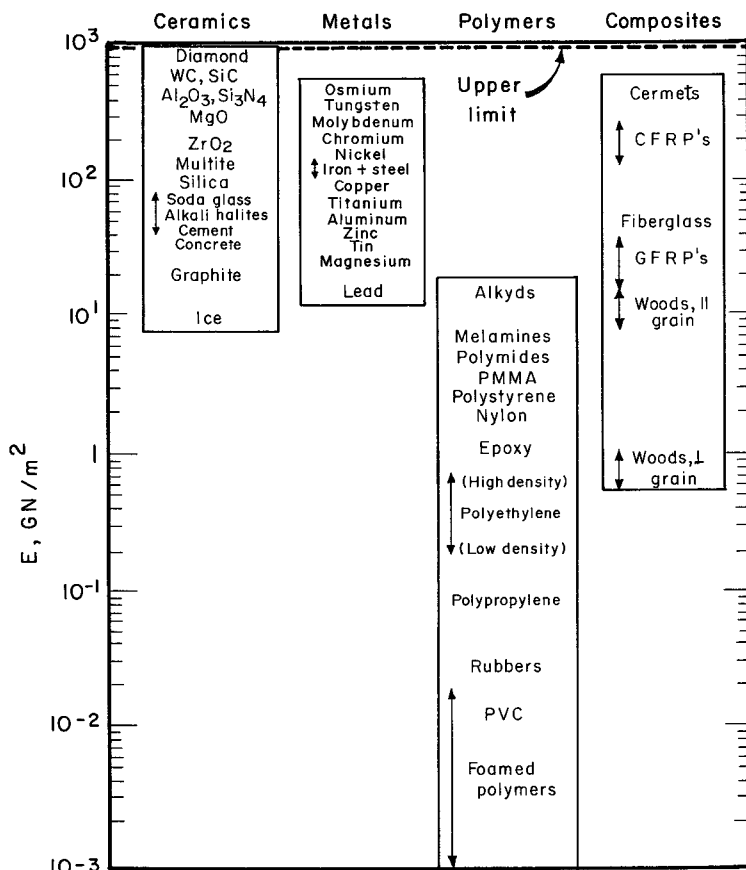


**Fig. 2.12** Bar chart of data for Young's moduli. (Adapted from M. F. Ashby and D. R. H. Jones, *Engineering Materials* (Oxford: Pergamon Press, 1980), p. 32.)

### 2.11.1 Elastic Properties of Metals

Tables 2.3 and 2.4 give the elastic stiffnesses and compliances, respectively, of metallic monocrystals. One of the most complete compilations of elastic constants for crystals is that by Simmons and Wang. (See suggested reading.) The elastic constants for a number of polycrystalline metals are given in Table 2.5. We can also determine the polycrystalline (isotropic) elastic constants from the monocrystalline ones, using equations given earlier.

### 2.11.2 Elastic Properties of Ceramics

The elastic properties of ceramic monocrystals possess the symmetry of the crystal (see Table 2.6). As an example, consider the stiffnesses and compliances for MgO at room temperature. Magnesia is a cubic crystal, and alumina has the rhombohedral structure. The corresponding Young and shear moduli, computed along the three crystallographic axes of the monocrystal from Equation 2.20 are given in Table 2.7. Table 2.8 presents the elastic moduli for a number of ceramics and glasses. The largest elastic constant is that for diamond and is equal to 1,000 GPa. This is due to the C-C bonds, as is explained in Chapter 4.

**Table 2.3** | Elastic Stiffnesses of Monocrystals at Ambient Temperature (GPa)

Element	Structure	$C_{11}$	$C_{44}$	$C_{12}$	$C_{33}$	$C_{66}$	$C_{13}$	$C_{14}$
Ag	FCC	124.0	46.1	93.4				
Al	FCC	108.2	28.5	61.3				
Au	FCC	186.0	42.0	157.0				
Cu	FCC	168.4	75.4	121.4				
Ni	FCC	246.5	124.7	147.3				
Pb	FCC	49.5	14.9	42.3				
Fe	BCC	228.0	116.5	132.0				
Mo	BCC	460.0	110.0	176.0				
Ta	BCC	267.0	82.5	161.0				
W	BCC	501.0	151.4	198.0				
Co	HCP	307.0	75.3	165.0	358.1		103.0	
Zn	HCP	161.0	38.3	34.2	61.0		50.1	
Ti	HCP	162.4	46.7	92.0	180.7	69.0		
Be	HCP	292.3	162.5	26.7	336.4	14.0		
Zr	HCP	143.4	32.0	72.8	164.8	65.3		
Mg	HCP	59.7	16.7	26.2	61.7	21.7		
Sn	Tetragonal	73.5	22.0	23.4	87.0	22.6	28.0	
In	Tetragonal	44.5	06.6	39.5	44.4	12.2	40.5	
Hg	Rhombohedral	36.0	12.9	28.9	50.5		30.3	05.0

**Table 2.4** | Elastic Compliances for Monocrystalline Metals at Ambient Temperature ( $10^{-2}$  GPa $^{-1}$ )

Element	Structure	$S_{11}$	$S_{44}$	$S_{12}$	$S_{23}$	$S_{13}$
Ag	FCC	2.29	2.17	-0.983		
Al	FCC	1.57	3.51	-0.568		
Au	FCC	2.33	2.38	-1.065		
Cu	FCC	1.498	1.326	-0.629		
Ni	FCC	0.734	0.802	-0.274		
Pb	FCC	9.51	6.72	-4.38		
Fe	BCC	0.762	0.858	-0.279		
Mo	BCC	0.28	0.91	-0.078		
Nb	BCC	0.69	3.42	-0.249		
Ta	BCC	0.685	1.21	-0.258		
W	BCC	0.257	0.66	-0.073		
Be	HCP	0.348	0.616	-0.030	0.298	-0.031
Mg	HCP	2.20	6.1	-0.785	1.97	-0.50
Ti	HCP	0.958	2.14	-0.462	0.698	-0.189
Zr	HCP	1.013	3.13	-0.404	0.799	-0.241

The elastic moduli of ceramics are strongly dependent on porosity. Ceramics are porous owing to their fabrication, and one should be aware of the effect of porosity. Figure 2.13 shows the variations in the Young modulus of alumina with volume fraction of pores. For 10% porosity (a common value for commercial alumina), the Young's modulus is decreased by 20%.

The change in Young's modulus with porosity has been empirically expressed by Wachtman and MacKenzie,<sup>6</sup>

$$\boxed{E = E_0(1 - f_1 p + f_2 p^2)} \quad (2.22)$$

where  $p$  is the porosity and  $f_1$  and  $f_2$  are constants. For spherical voids, MacKenzie found that  $f_1$  and  $f_2$  are equal to 1.9 and 0.9, respectively, for a Poisson's ratio of 0.3. The data of Coble and Kingery<sup>7</sup> may be compared with the prediction of Equation 2.22. If one assumes the law of mixtures for the porosity, then, as a first approximation, one has

$$E = E_A(1 - f_B) + E_B f_B, \quad (2.23)$$

where  $f$  is the volume fraction of a phase and the subscripts  $A$  and  $B$  denote the two phases.

However, if phase  $B$  is the pore and denoting the pore fraction by  $p$ , one has

$$E = E_0(1 - p). \quad (2.24)$$

For relatively low porosity, the quadratic term in Equation 2.22 can be neglected, leaving

$$E = E_0(1 - 1.9p). \quad (2.25)$$

If  $E$  varied linearly with  $p$ , the form would be  $E = E_0(1 - p)$ . Thus, the physical significance of MacKenzie's equation is that porosity has an effect of  $E$  equal to approximately double the volume of pores.

Another effect of considerable importance on Young's modulus for ceramics is the presence of microcracks, which decrease the stored elastic energy and reduce the effective Young's modulus. Figure 2.14 shows schematically how the presence of microcracks would affect the slope of the stress-strain curve. The initial slope,  $E_0$ , is decreased by microcracking. Microcracks can also form during the cooling of the ceramic due to thermal expansion (or contraction) anisotropy. Different grains contract by different amounts along different orientations, resulting in a buildup of elastic stress in the boundary area. Elastic stress can generate microcracks. Similarly, the anisotropy of elastic constants can generate elastic stress concentrations at the grain boundaries, where the neighboring grains undergo different strains (due to differences in crystallographic orientation). The change in the Young's modulus with microcracking has been computed by a

<sup>6</sup> See J. B. Wachtman, in *Mechanical and Thermal Properties of Ceramics*, ed. J. B. Wachtman, NBS Special Publication 303, NBS Washington, 1963, p. 139; and J. K. MacKenzie, *Proc. Phys. Soc.*, B63 (1950) 2.

<sup>7</sup> R. L. Coble and W. D. Kingery, *J. Am. Cer. Soc.* 39 (1956) 377.

**Table 2.5** | Elastic and Shear Moduli and Poisson Ratios for Polycrystalline Metals<sup>a</sup>

Metal (20°C)	E (GPa)	G (GPa)	$\nu$
Aluminum	70.3	26.1	0.345
Cadmium	49.9	19.2	0.300
Chromium	279.1	115.4	0.210
Copper	129.8	48.3	0.343
Gold	78.0	27.0	0.440
Iron	211.4	81.6	0.293
Lead	16.0	5.5	0.450
Magnesium	44.7	17.3	0.291
Nickel	199.5	76.0	0.312
Niobium	104.9	37.5	0.397
Silver	82.7	30.3	0.367
Tantalum	185.7	69.2	0.342
Titanium	115.7	43.8	0.321
Tungsten	411.0	160.6	0.280
Vanadium	127.6	46.7	0.365

<sup>a</sup> Adapted with permission from R. W. Hertzberg, *Deformation and Fracture Mechanics of Engineering Material*, New York: John Wiley, 1976, p. 8.

**Table 2.6** | Elastic Constants for Ceramics ( $S_{ij}$  in  $10^{-10}$  Pa $^{-1}$ ;  $C_{ij}$  in GPa)

Material	$C_{11}$	$C_{12}$	$C_{44}$	$C_{13}$	$C_{33}$	$S_{11}$	$S_{12}$	$S_{44}$
MgO	289.2	88.0	154.6			4.03	-0.94	6.47
Al <sub>2</sub> O <sub>3</sub>	497.1	162.3	147.7	117	502			
ZrO <sub>2</sub>	410	110	60					
MgAl <sub>2</sub> O <sub>4</sub>	279	153	153			5.83	-2.08	6.54
TiC	513	106	178	0.2	2.1	-0.36	5.61	
Diamond	1076	125	576					
LiF	112	46	63					
NaCl	49	13	13					
ThO <sub>2</sub>	367	106	797			3.13	-0.70	12.5
LiO <sub>2</sub>	395	121	64.1			2.96	-0.70	15.6
SiC (hexagonal)	500	186	168	176	521			
SiC (cubic)	352	140	233					

number of investigators. The formulations give predictions that vary with the orientation of the cracks with respect to the tensile axis, among other parameters. An expression developed by Salganik<sup>8</sup> is

$$\boxed{\frac{E}{E_0} = \left[ 1 + \frac{16(10 - 3\nu_0)(1 - \nu_0^2)}{45(2 - \nu_0)} Na^3 \right]^{-1} = (1 + ANa^3)^{-1}}, \quad (2.26)$$

<sup>8</sup> R. L. Salganik, *Izv. Akad. Nauk SSR Mekh. Tverd. Tela*, 8 (1973) 149.

**Table 2.7** | Orientation Dependence of Young's Modulus and Shear Modulus for MgO and Al<sub>2</sub>O<sub>3</sub> at 25 °C

Crystal Orientation	Young's Modulus, Al <sub>2</sub> O <sub>3</sub> (GPa)	Young's Modulus, MgO (GPa)	Shear Modulus, MgO (GPa)
<100>	299	248.2	154.6
<110>	330	316.4	121.9
<111>	344	348.9	113.8

where  $E$  is the Young's modulus of the cracked ceramic,  $v_0$  and  $E_0$  are, respectively, Poisson's ratio and Young's modulus of the uncracked material,  $a$  is the radius of a mean crack, and  $N$  is the number of cracks per unit volume. The factor

$$A = \frac{16(10 - 3v_0)(1 - v_0^2)}{45(2 - v_0)} \quad (2.27)$$

varies between 1.77 and 1.5 when  $v_0$  varies between 0 and 0.5. To a first approximation, one can say that

$$\frac{E}{E_0} = [1 + 1.63 Na^3]^{-1}. \quad (2.28)$$

O'Connell and Budiansky arrived at a slightly different expression:<sup>9</sup>

$$\frac{E}{E_0} = 1 - \frac{16(10 - 3v)(1 - v^2)}{45(2 - v)} f_s. \quad (2.29)$$

Here,  $f_s$  is defined as the volume fraction of cracks. (i.e., the number of cracks per unit volume,  $N$ , multiplied by the cube of the mean crack radius,  $a^3$ ) and  $v$  is Poisson's ratio of the porous material, which is related to Poisson's ratio of the fully dense material by

$$v = v_0 \left(1 - \frac{16f_s}{9}\right). \quad (2.30)$$

By applying the same approximation as in Salganik's equation, we arrive at

$$\frac{E}{E_0} = 1 - 1.63 Na^3.$$

(2.31)

Note that  $Na^3$  is a measure of the fraction of the material that is under the effect of the cracks. Figure 2.15 shows the effect of microcracks on the Young's modulus of alumina. This effect is substantial. For  $f_s = 0.1$ , the Young's modulus is reduced by 20%. Both Salganik's and O'Connell and Budiansky's predictions are plotted, and it can be seen that they are in fairly close agreement for values of  $f_s$  smaller than 0.1. For higher values, O'Connell and Budiansky's equation predicts a more rapid decrease in  $E$ .

<sup>9</sup> R. J. O'Connell and B. Budiansky, *J. Geol. Res.* 79 (1974) 5412.

**Table 2.8** Modulus of Elasticity of Some Ceramic Materials

Material	$E$ (GPa)
Aluminum oxide crystals	378
Sintered alumina*	365
Alumina porcelain (90–95% $\text{Al}_2\text{O}_3$ )	365
Sintered beryllia	310
Hot-pressed boron nitride*	82.7
Hot-pressed boron carbide*	289
Graphite*	9
Sintered magnesia*	210
Sintered molybdenum silicide*	406
Sintered spinel*	238
Dense silicon carbide (cubic or hexagonal)	280–510
Sintered titanium carbide*	310
Sintered stabilized zirconia*	152
Silica glass	72.3
Vycor glass	72.3
Pyrex glass	68.9
Superduty fire-clay brick	96.4
Magnesite brick	172.2
Bonded silicon carbide**	345
Silicon nitride	320–365
Aluminum nitride	
Mullite (aluminosilicate) porcelain	69
Steatite (magnesia aluminosilicate)	69
Diamond	450–650
Tungsten carbide	400–530
Cobalt/tungsten carbide cermets	379
Titanium dioxide	290
Titanium diboride	440

\* (c. 5% porosity).

\*\* (c. 20% porosity).

Adapted from W. D. Kingery, H. K. Bowen, and D. R. Uhlmann, *Introduction to Ceramics*, 2nd ed., (New York: John Wiley, 1976) p. 3.

### 2.11.3 Elastic Properties of Polymers

Polymers have elastic constants that range from the lower end of the metallic elastic constants to values even lower by several orders of magnitude. As an example, melamines have elastic constants of 6–7 GPa ( $E$  (lead) = 14 GPa), while the elastic constant of polymeric foams is between 3 and 10 MPa. Table 2.9 lists the elastic constants of a number of polymers. The bar chart of Figure 2.12 provides a comparison of the elastic constants of the different classes of materials. The elastic behavior of polymeric materials is more difficult to describe than that of metals or ceramics, because it is strongly dependent on both temperature and time. This behavior, called *viscoelastic* or *anelastic*, is described separately in Section 2.12. Here we merely introduce the

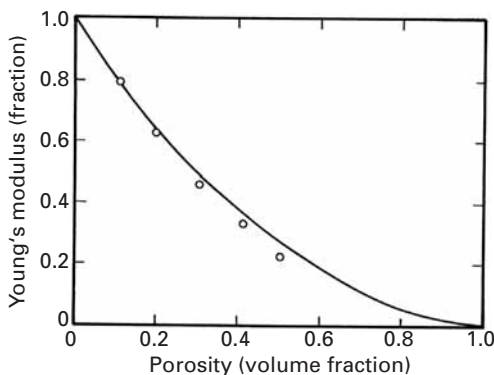


**Fig. 2.13** Effect of porosity on elastic modulus of alumina. Circles represent experimental measurements. (After R. L. Coble and W. D. Kingery, *J. Am Ceram Soc.*, 39 (1956) 377.)

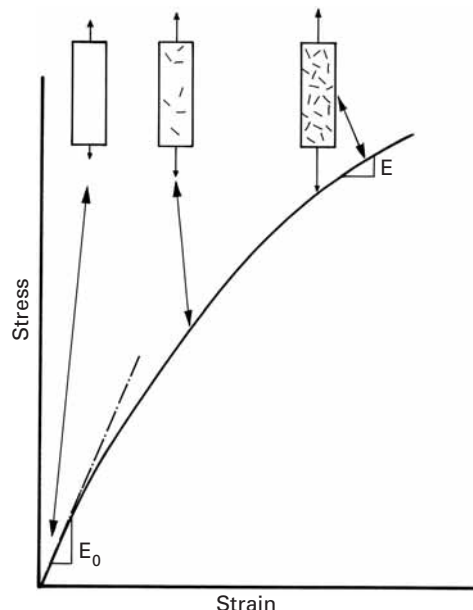


**Fig. 2.14** Effect of microcracks on Young's modulus for ceramics.

subject briefly. In most polymers, there are dramatic changes in  $E$  between  $20^\circ\text{C}$  and  $200^\circ\text{C}$ ; for most metals and ceramics, the changes in  $E$  in this range can be neglected. The glass transition temperature  $T_g$  plays an important role in polymers. Above  $T_g$ ,  $E$  is considerably low, and the behavior of the polymer can be described as rubbery and viscous. Below  $T_g$ , the modulus of elasticity is considerably higher, and the behavior is closer to linear elastic. Figure 2.16 shows schematically the elastic behavior of a linear polymer as a function of temperature. The modulus of elasticity ranges from  $10^3$  to  $10^{-1}$  MPa.

#### 2.11.4 Elastic Constants of Unidirectional Fiber Reinforced Composite

An orthotropic material has three mutually perpendicular axes of symmetry, which reduces the number of independent elastic

**Fig. 2.15** Comparison of predictions of Young's modulus.

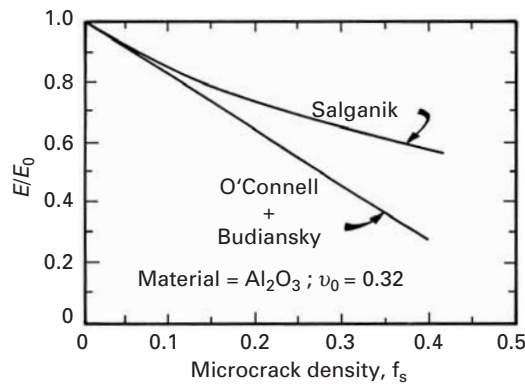
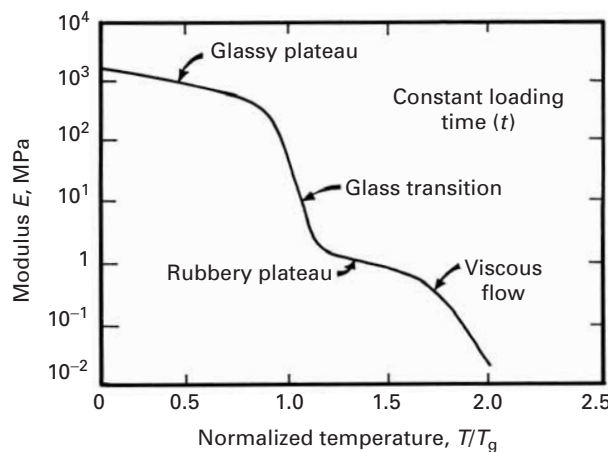


**Fig. 2.16** Schematic variation in the modulus of elasticity of a linear polymer with temperature.



constants to nine. The  $S_{ij}$  matrix for an orthotropic material is:

$$S_{ij} = \begin{bmatrix} S_{11} & S_{12} & S_{13} & 0 & 0 & 0 \\ S_{21} & S_{22} & S_{23} & 0 & 0 & 0 \\ S_{31} & S_{32} & S_{33} & 0 & 0 & 0 \\ 0 & 0 & 0 & S_{44} & 0 & 0 \\ 0 & 0 & 0 & 0 & S_{55} & 0 \\ 0 & 0 & 0 & 0 & 0 & S_{66} \end{bmatrix}$$

The compliance matrix for orthotropic materials in terms of  $E$ ,  $G$ , and  $\nu$  corresponds to:

$$S_{ij} = \begin{bmatrix} 1/E_1 & -\nu_{21}/E_2 & -\nu_{31}/E_3 & 0 & 0 & 0 \\ -\nu_{12}/E_1 & 1/E_2 & -\nu_{32}/E_3 & 0 & 0 & 0 \\ -\nu_{13}/E_1 & -\nu_{23}/E_2 & 1/E_3 & 0 & 0 & 0 \\ 0 & 0 & 0 & 1/G_{23} & 0 & 0 \\ 0 & 0 & 0 & 0 & 1/G_{13} & 0 \\ 0 & 0 & 0 & 0 & 0 & 1/G_{12} \end{bmatrix}$$

**Table 2.9** | Elastic Constants of Some Polymers<sup>a</sup>

Material	$E$ (GPa)
Phenolformaldehyde	8
Melamines	6–7
Polymides	3–5
Polyesters	1.3–4.5
Acrylics	1.6–3.4
Nylon	2–4.5
PMMA	3.4
Polystyrene	3–3.4
Polycarbonate	2.1
Epoxies	2.1–5.5
Polypropylene	1.2–1.7
Polyethylene, high-density	0.15–0.24
Foamed polyurethane	0.01–0.06
Polyethylene, low-density	0.15–0.24
Rubbers	0.01–0.1
PVC (unplasticized)	2.4–3.0
Foamed polymers	0.001–0.01

<sup>a</sup> Adapted from M. F. Ashby and D. R. H. Jones, *Engineering Materials* (Oxford: Pergamon Press, 1986), p. 31, Table 3.1.

Notice that there are three different Young's moduli on three perpendicular planes, three shear moduli, and three Poisson's ratios. Thus, we have nine elastic constants, as in the stiffness matrix.

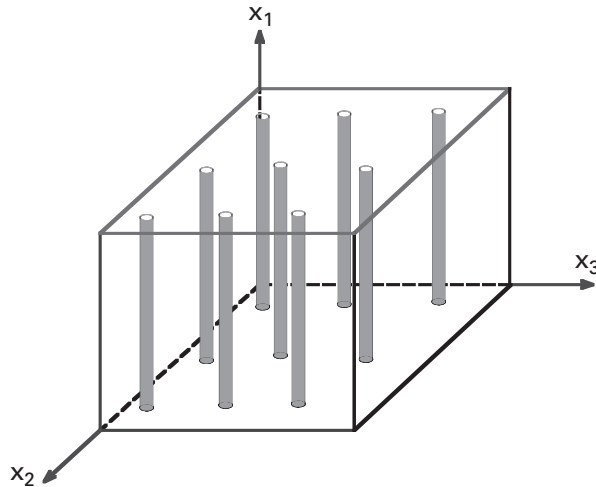
Unidirectionally fiber reinforced composites represent a special case of orthotropy. The plane transverse to the fibers is isotropic, see Figure 2.17. Such a material is called transversely isotropic and has five independent elastic constants. The compliance matrix for such unidirectionally fiber reinforced composite is:

$$S_{ij} = \begin{bmatrix} S_{11} & S_{12} & S_{13} & 0 & 0 & 0 \\ S_{12} & S_{11} & S_{13} & 0 & 0 & 0 \\ S_{13} & S_{13} & S_{33} & 0 & 0 & 0 \\ 0 & 0 & 0 & S_{44} & 0 & 0 \\ 0 & 0 & 0 & 0 & S_{44} & 0 \\ 0 & 0 & 0 & 0 & 0 & 2(S_{11} - S_{12}) \end{bmatrix}$$

In terms of the elastic constants  $E$ ,  $G$ , and  $\nu$ , the elastic compliance matrix for a transversely isotropic material is represented as:

$$S_{ij} = \begin{bmatrix} 1/E_1 & -\nu_{21}/E_1 & -\nu_{31}/E_3 & 0 & 0 & 0 \\ -\nu_{21}/E_1 & 1/E_1 & -\nu_{31}/E_3 & 0 & 0 & 0 \\ -\nu_{31}/E_3 & -\nu_{31}/E_3 & 1/E_3 & 0 & 0 & 0 \\ 0 & 0 & 0 & 1/G_{13} & 0 & 0 \\ 0 & 0 & 0 & 0 & 1/G_{13} & 0 \\ 0 & 0 & 0 & 0 & 0 & \frac{2}{E_1}(1 - \nu_{21}) \end{bmatrix}.$$

**Fig. 2.17** A transversely isotropic fiber composite. The plane transverse to fibers ( $x_2-x_3$  plane) is isotropic.



Notice that there are two Young's moduli, one for any direction in the transverse plane and one for the fiber direction. There are two Poisson's ratios and one shear modulus. Thus, we have five elastic constants.

Another example of a transversely isotropic material is a laminate composite. The elastic properties perpendicular to the plane of the layers are different than in the layer plane.

There are many examples of laminate composites used in everyday life, for example, plywood and cardboard. GLARE is a laminate composed of alternate layers of aluminum and glass fibers in an epoxy matrix. It is used in the aircraft industry, specifically in the Airbus A380 superjumbo jet. The laminate structure gives it excellent fatigue resistance because the cracks are arrested at the interface. Another laminate, ARALL, consists of alternate aluminum and aramid fibers in an epoxy matrix.

Figure 2.18 gives the elastic constants for the titanium (20%)-titanium aluminide (80%) laminate. The Young's moduli  $E_{11}$  ( $= 1/S'_{11}$ ) and  $E_{22}$  ( $= 1/S'_{22}$ ) were transformed according to orientation  $\beta$ . Their variation can be seen in Figure 2.18. Likewise, Poisson's ratios  $\nu_{21}$  and  $\nu_{31}$  vary with orientation.

## 2.12 | Viscoelasticity

Glasses or amorphous materials show the phenomenon of time-dependent strain, called viscoelasticity or anelasticity. The deformation of an amorphous material does not involve atomic displacements on specific crystallographic planes, as is the case in crystalline metals. Rather, a continuous displacement of atoms or molecules takes place with time at a constant load. This flow mechanism of noncrystalline

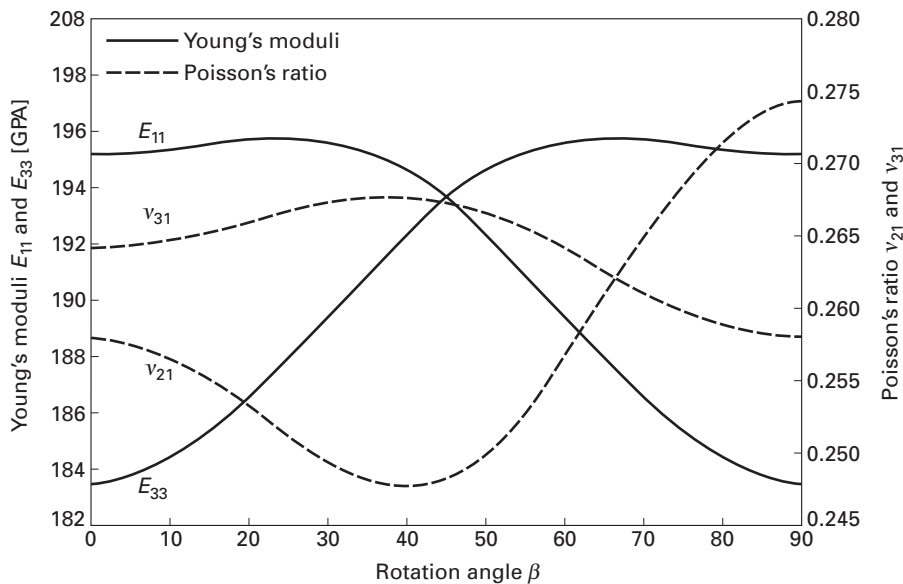


**Fig. 2.18** Elastic constants of 20% Ti–80%  $\text{Al}_3\text{Ti}$  laminate composite as a function of angle  $\beta$  with laminate plane. (Adapted from T. Li, F. Grignon, D. Benson, K. S. Vecchio, E. Olevsky, C. F. Jiang, and M. A. Meyers, *Mater. Sci. Eng.*, A374 (2004) 10.)

materials is associated with the diffusion of atoms or molecules within the material; that is, it is a thermally activated process and is thus described by an Arrhenius-type equation. Of course, at sufficiently high temperatures, where diffusion becomes important, crystalline as well as amorphous materials show a large amount of thermally activated plastic flow. Liquids and even fluids in general show a characteristic resistance to flow called *viscosity*. The viscosity of a fluid results in a frictional energy loss, which appears as heat. The more viscous a fluid, the higher is the frictional energy loss.

Over a range of temperatures, the viscosity  $\eta$  can be described by the Arrhenius-type relationship

$$1/\eta = A \exp(-Q/RT), \quad (2.32)$$

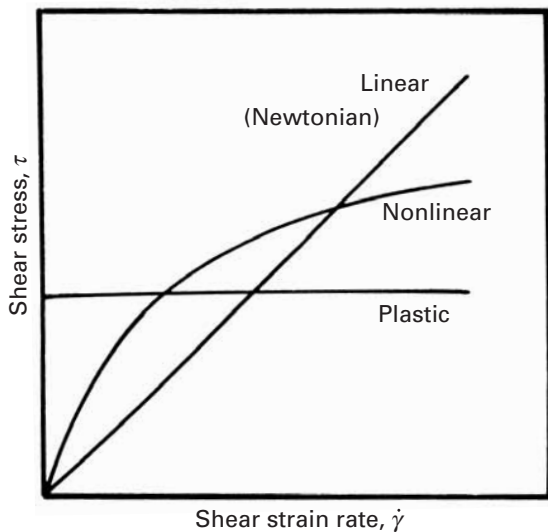
or

$$\boxed{\eta = A \exp(Q/RT),}$$

where  $Q$  represents the activation energy for the atomic or molecular process responsible for the viscosity,  $R$  is the universal gas constant, and  $T$  is the temperature in kelvin. The S. I. units of the viscosity  $\eta$  are  $\text{Nm}^{-2} \text{s}$  or  $\text{Pa} \cdot \text{s}$ . Another common unit of viscosity is poise, P; 1 P = 0.1 Pa · s.

A purely viscous material shows stress proportional to strain rate. Thus, if we apply a shear stress  $\tau$  to a glassy solid above its glass

**Fig. 2.19** Linear or Newtonian response (stress proportional to deformation rate), nonlinear response, and plastic response (stress independent of deformation rate).



transition temperature, then we can write, for the rate of shear deformation,

$$\dot{\gamma} = \frac{d\gamma}{dt} = \frac{\tau}{\eta} = \phi\tau, \quad (2.33)$$

where  $\phi$  is the *fluidity* (the reciprocal of viscosity) of the material.

Equation 2.33 can be written as

$$\boxed{\tau = \eta\dot{\gamma}.} \quad (2.34)$$

If the viscosity of a material does not change with the strain rate (i.e., if the stress is linearly proportional to the strain rate), then we call the viscosity a *Newtonian viscosity* and such a material a *Newtonian material*. Figure 2.19 shows a Newtonian (or linear) response curve. If the stress is not directly proportional to the strain rate, we have a non-Newtonian response, which can be written as

$$\tau = \eta\dot{\gamma}^n. \quad (2.35)$$

This is shown by the curve marked "nonlinear" in the figure. If the stress is independent of the strain rate, we have a plastic material. A special case is that of a material whose viscosity decreases when subjected to high strain rates. Such a material is called a *thixotropic* material, a good example of which is a latex paint. When we apply the paint to a vertical wall, it does not sag, because its viscosity is very high on the wall. However, we can stir and brush the paint easily because its viscosity decreases when subjected to shear stress in the stirring action.

Polymers, polymer solutions and dispersions, metals at very high temperatures, and amorphous materials (organic and inorganic) show viscoelastic behavior – that is, characteristics intermediate between perfectly elastic and perfectly viscous behavior. Commercial

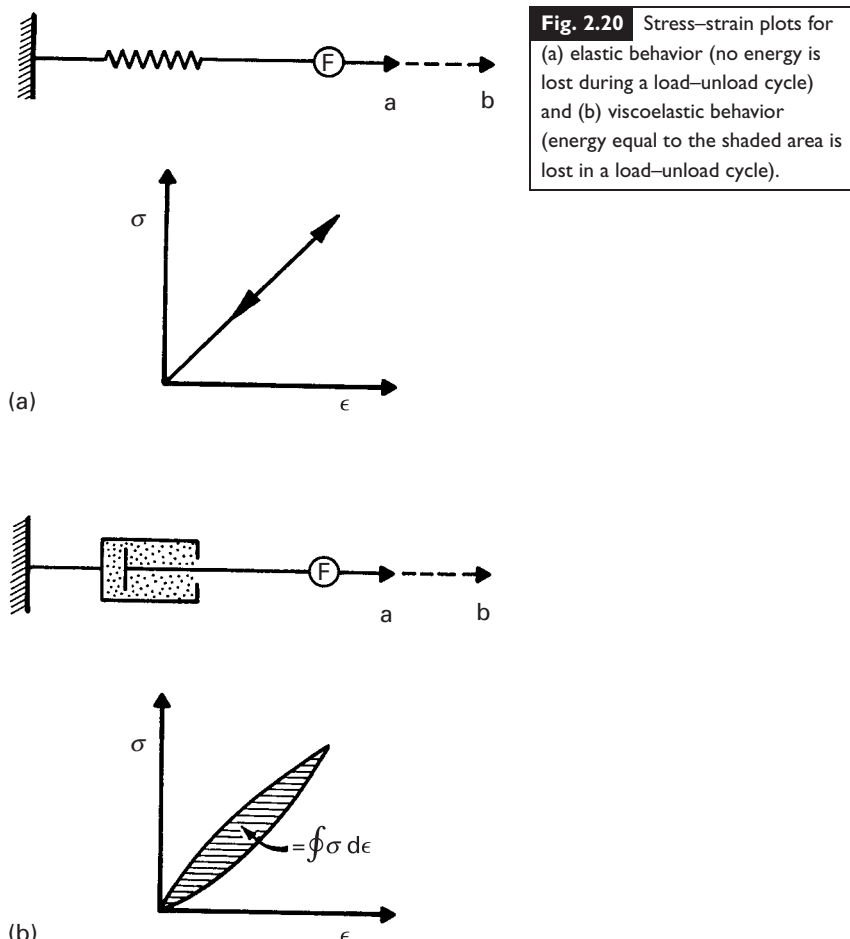


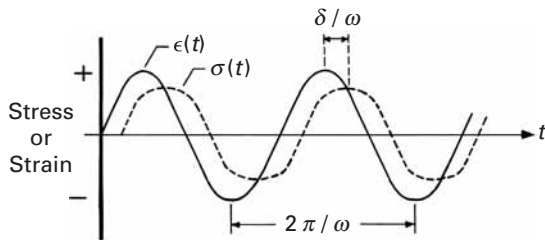
**Fig. 2.20** Stress-strain plots for  
(a) elastic behavior (no energy is  
lost during a load-unload cycle)  
and (b) viscoelastic behavior  
(energy equal to the shaded area is  
lost in a load-unload cycle).

silica-based glasses have a high proportion of additives: about 30% in soda-lime glass and 20% in high-temperature glasses such as Pyrex. The main purpose of the additives is to lower the viscosity by breaking up the silica network, thus making the processing of glass easy.

Conventionally, glasses are formed by melting an appropriate composition and then casting or drawing the melt into a desired form. It is interesting to compare the viscosity values of liquid metals with glasses. Molten metals have about the same viscosity as that of water ( $\sim 10^{-3}$  Pa·s) and transform to a crystalline solid state in a discontinuous manner when cooled. The viscosity of glasses, however, falls slowly and continuously with temperature. The shaping of glass is carried out in the viscosity range of  $10^3$ – $10^6$  Pa·s. Polymers are formed in the range  $10^3$ – $10^5$  Pa·s. Perhaps the most important characteristic of a viscoelastic material is that its rheological properties are dependent on time. This characteristic is manifested very markedly by amorphous or noncrystalline materials such as polymers.

A viscoelastic substance has a viscous and an elastic component. Figure 2.20(a) shows the stress-strain curve of an ideal elastic material. The load and unload curves are the same, and the energy lost as

**Fig. 2.21** Viscoelastic response of material with time lag between stress and strain.



heat per cycle is zero in this case. In practice, there is always present an anelastic (i.e., a time-dependent) component, with the result that the unload curve does not in fact follow the load curve. Energy equal to the shaded area in Figure 2.20(b) is dissipated in each cycle. This phenomenon is exploited in damping out vibrations. Some polymers and soft metals (e.g., lead) have a high damping capacity. In springs and bells, a high damping capacity is undesirable. For such applications, one uses materials such as bronze, spring steel, etc., which have a low damping capacity.

### 2.12.1 Storage and Loss Moduli

In order to characterize the viscoelastic behavior of a material, the material is sinusoidally deformed, and the resulting stress is recorded. For an ideal elastic material, the stress and strain are *in phase*, and the phase shift  $\delta = 0$ . For an ideal viscous material, the stress and strain are  $90^\circ$  *out of phase* (i.e.,  $\delta = 90^\circ$ ). As pointed out before, a viscoelastic behavior – a combination of an ideal elastic response and an ideal viscous response – is more common. Figure 2.21 shows a viscoelastic response with a phase lag between the stress and the strain. Dynamic (commonly sinusoidal) perturbations are used to study the viscoelastic behavior of a material. The material is subjected to an oscillatory strain with frequency  $\omega$ . From the figure, we can write the following expressions for strain and stress:

$$\begin{aligned}\epsilon &= \epsilon_0 \sin \omega t, \\ \sigma &= \sigma_0 \sin (\omega t + \delta).\end{aligned}$$

In the equation for stress,  $\delta$  is the phase angle or phase lag between the stress and strain. From these expressions, we can define two moduli,

$$E' = \left( \frac{\sigma_0}{\epsilon_0} \right) \cos \delta$$

and

$$E'' = \left( \frac{\sigma_0}{\epsilon_0} \right) \sin \delta,$$

where  $E'$  is the tensile storage modulus and  $E''$  is the tensile loss modulus.

Alternatively, we can use complex variables and write

$$\epsilon = \epsilon_0 \exp i(\omega t),$$

$$\begin{aligned}\sigma &= \sigma_0 \exp i(\omega t + \delta), \\ E &= \frac{\sigma}{e} = \frac{\sigma_0}{\epsilon_0} \exp i\delta = \frac{\sigma_0}{\epsilon_0} (\cos \delta + i \sin \delta) \\ &= E' + iE'',\end{aligned}$$

where  $i$  is the imaginary number  $\sqrt{-1}$ .

Figure 2.22 shows graphically the relationship among these quantities. Proceeding in a manner similar to that for deriving the tensile modulus, we can obtain the shear modulus. (Experimentally, this is generally obtained by means of a torsion pendulum.) The complex modulus

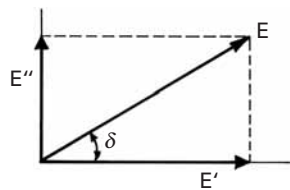


**Fig. 2.22** Relationship between tensile storage and tensile loss modulus.

$$G = G' + iG'',$$

where  $G'$  is the shear storage modulus and  $G''$  is the shear loss modulus. The storage modulus is a measure of the stored energy, i.e., the elastic part. The loss modulus is a measure of the energy lost as heat, i.e., the viscous part. These two modulus components can be written in terms of the phase shift as

$$G'' = G \sin \delta, \quad E'' = E \sin \delta,$$

$$G' = G \cos \delta, \quad E' = E \cos \delta.$$

We can now define a term called the *loss tangent* as follows:

$$\text{Loss tangent} = \tan \delta = \frac{\text{energy loss}}{\text{energy stored}} = \frac{G''}{G'} = \frac{E''}{E'}.$$

Sometimes, a related term called the *logarithmic decrement*  $\Delta$  is used, which is defined as

$$\text{Logarithmic decrement } \Delta = \pi \tan \delta = \frac{\pi E''}{E'}.$$

The logarithmic decrement is the natural logarithm of the amplitude ratio between successive vibrations; that is,

$$\Delta = \frac{\theta_n}{\theta_{n+1}},$$

where  $\theta_n$  and  $\theta_{n+1}$  are the amplitudes of two successive vibrations.

Both the loss tangent and the logarithmic decrement are proportional to the ratio of the maximum energy dissipated per cycle to the maximum energy stored in the cycle.

### Example 2.14

In a free-vibration test, a polymer showed a drop of 50% in two successive amplitudes. Compute the logarithmic decrement for this polymer.

**Solution:** If  $\theta_n$  and  $\theta_{n+1}$  are the successive amplitudes, then the logarithmic decrement,  $\Delta = \ln(\theta_n/\theta_{n+1}) = \ln 2 = 0.69$ .

### Example 2.15

Recall that the stress-strain relationship involving real and imaginary moduli is given by

$$\sigma = (E' + iE'')\varepsilon = E\varepsilon.$$

Derive an expression for the complex modulus  $E$  in terms of  $E'$  and  $\tan \delta$ . Show that for small values of  $\tan \delta$ ,  $E \approx E'$ .

**Solution:** The magnitude of the complex modulus is given by

$$E = \frac{\sigma}{\varepsilon} = (E'^2 + E''^2)^{1/2} = E' [1 + \tan^2 \delta]^{1/2}.$$

For  $\tan \delta < 0.2$ ,  $E$  will be within 2% of  $E'$ .

## 2.13 | Rubber Elasticity

A polymeric molecule is generally not rigid like a straight rod, although there are some special liquid crystal polymers that do have a rigid, rodlike molecule (e.g., the aramid fibers). Barring these special cases, the polymeric molecule is a very long and flexible chain that can change form easily because many independent vibrations and rotations of the individual atoms that compose the molecular chain are possible. Long, flexible polymeric chains can change their configuration and lengths rather easily when a stress is applied. When the number of configurations available is very large and the chains are cross-linked to form a network, we get a special polymer called an *elastomer*. Elastomers characteristically show very high reversible, non-linear extensions (5–700%) in response to an applied stress. The requirement of cross-linking (i.e., the existence of a network) is established to avoid chains slipping past one another in a permanent manner. This process is called ‘vulcanization’ of rubber and is accomplished by adding sulfur. High chain mobility is also required. Glassy and crystalline polymers will not have enough chain mobility, and therefore, the reversible strains are not very large. In crystalline materials such as metals and ceramics, the deformation involves a change in equilibrium interatomic distance, which requires the application of rather large forces. This is why the elastic modulus values of metals and ceramics are very high.

The first law of thermodynamics says that the internal energy of a system is given by

$$dU = dQ + dW, \quad (2.36)$$

where  $dQ$  is the heat absorbed and  $dW$  is the work done on the system by the surroundings. Also, for a reversible process, we can write, from the second law of thermodynamics,

$$dQ = T dS \quad (2.37)$$

and

$$dW = F dl - P dV, \quad (2.38)$$

where  $T$  is the temperature,  $V$  is the volume,  $P$  is the external pressure,  $S$  is the entropy, and  $F$  is the tensile force causing a change in the length  $\ell$ .

From Equations 2.36 and 2.38, we get the following for the internal energy:

$$dU = T dS + F dl - P dV.$$

For conditions of constant temperature and volume, we can write

$$\begin{aligned} F &= \left( \frac{\delta U}{\delta \ell} \right)_{T,V} - T \left( \frac{\delta S}{\delta \ell} \right)_{T,V} \\ &= F_e + F_s, \end{aligned} \quad (2.39)$$

where  $F_e$  is the energy contribution and  $F_s$  is the entropy contribution to the tensile force.

In the case of crystalline metals, the first term in Equation 2.39 is predominant, while the second term is negligible. This is because the crystalline structure of a metal remains essentially unchanged with deformation. Such is not the case with amorphous polymers, especially the polymers that are rubberlike and which show rather large elastic deformations. On deforming these kinds of polymers, the form of the molecular chains can change considerably, and the entropy contribution  $F_s = -T(\delta S/\delta \ell)_{T,V}$  becomes considerably large (see Figure 2.23). In fact, the first term (i.e., the energy term) in Equation 2.39 is equal to zero for an ideal rubbery material. The rubber elasticity thus has its origins in the entropy effects. For such polymers, one can write an expression for the entropy of the form

$$S = k \ln p$$

where  $k$  is Boltzmann's constant and  $p$  is the probability of finding a particular chain configuration for which the entropy effects will be very important.

When an elastomer is stretched, the distance between cross-linked points increases and the number of possible chain configurations decreases. Consider a piece of rubber in the form of a cube. Let the side of the cube be  $\ell_0$ , as shown in Fig. 2.24(a). Then, the volume of rubber before deformation or undeformed volume is equal to  $\ell_0^3$ . Let us now deform the rubber cube in direction 1. The rubber gets elongated in direction 1 and the two transverse directions get shortened to  $\ell_2$  and  $\ell_3$ . The volume of the cube after deformation is equal to  $\ell_1 \ell_2 \ell_3$ . In order to describe the large deformations involved in stretching rubbery materials, we define strain in terms of a parameter called draw ratio,  $\lambda = \text{final length}/\text{original length}$ . Thus, we can write for the draw ratio along direction 1,

$$\lambda_1 = \ell_1 / \ell_0,$$

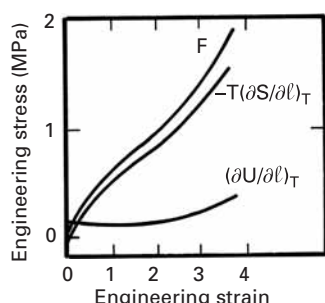
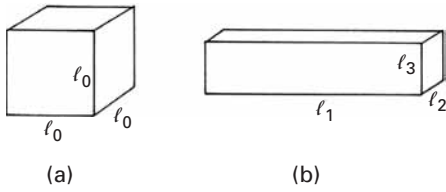


**Fig. 2.23** Changes in internal energy,  $U$ , and entropy,  $S$ , accompanying the extension of rubber.  $F$  is the sum of the two contributions.

**Fig. 2.24** Deformation at constant volume. (a) Unstrained state. (b) Strained state.



or,

$$\ell_1 = \lambda_1 \ell_0.$$

We remind the reader that  $\lambda = 1 + \varepsilon$ .

Elastomeric materials are treated as incompressible materials, i.e., constancy of volume condition holds. Also, taking the strains in the transverse directions to be equal, i.e.,  $\ell_2 = \ell_3$ , we can write

$$\ell_1 \ell_2 \ell_3 = (\lambda_1 \ell_0) \ell_2^2 = \ell_0^3, \quad (2.40)$$

or,

$$\ell_2 = \ell_3 = \ell_0 / \sqrt{\lambda_1} \quad (2.41)$$

Thus, the tensile force applied to the rubber cube in direction 1 leads to draw ratios  $\lambda_1$ ,  $\lambda_2$ , and  $\lambda_3$  along directions 1, 2, and 3, respectively. Rearranging Equation 2.41

$$\lambda_2 = \lambda_3 = 1 / \sqrt{\lambda_1}. \quad (2.42)$$

Flexible polymeric chains are joined by bonds at cross-link points, forming a network. When we stretch a rubber or elastomer, these chains get stretched. The number of configurations available to a stretched polymer is less than the number of configurations available to an unstretched polymer, i.e. *the entropy is reduced on stretching*. We need to use statistics to treat the properties of a single polymeric chain and those of a network of chains. We assume the polymeric chain is freely jointed and has no volume (it is called *volumeless*). One end of the chain is at the origin while the other end is at a distance,  $r$ , from the origin;  $r$  is called the end-to-end distance of the chain. The chain is assumed to be freely jointed and volumeless. The network is treated as a Gaussian network, i.e. a Gaussian distribution function is used to evaluate the probability of finding the other end of the chain in some volume element,  $dV (= dx \cdot dy \cdot dz)$ .

Let the end-to-end distance of a chain be  $r_1$ . We consider a polymer chain with an end fixed at the origin and the other end at the extremity of the vector  $r_1$ , whose magnitude is:

$$r_1 = (x^2 + y^2 + z^2)^{1/2}.$$

Assuming that the polymer chain follows “random walk” statistics, it can be shown that the distribution of lengths,  $r$ , follows a Gaussian distribution. This provides a bell-shaped curve for the distribution of

r. The probability that end-to-end distance is  $r_1$  is given by:

$$P_1(r_1) = \frac{\beta^3}{\pi^{1/2}} \exp(-\beta^2 r_1^2) = \frac{\beta^3}{\pi^{1/2}} \exp(-\beta^2 (x^2 + y^2 + z^2)).$$

The parameter  $\beta$  is related to the number of monomers (units),  $n$ , in the chain and to their length,  $a$ :

$$\beta = \frac{(1.5)^{1/2}}{n^{1/2}a}.$$

This comes from Gaussian statistics, and the intelligent student will readily consult his/her old class notes.

When a cube of rubber is deformed, it becomes a parallelepiped, as shown in Figure 2.24. Internally, the coordinates of the end-to-end vector of a typical flexible chain change from  $x$ ,  $y$ , and  $z$  to  $\lambda_1 x$ ,  $\lambda_2 y$ ,  $\lambda_3 z$ , respectively. The new probability of finding the end of a chain is equal to:

$$P_2(r_2) = \frac{\beta}{\pi^{1/2}} \exp[-\beta^2 (\lambda_1^2 x^2 + \lambda_2^2 y^2 + \lambda_3^2 z^2)].$$

The ratio of probabilities corresponding to the initial and deformed states can be expressed as:

$$\frac{P_2(r_2)}{P_1(r_1)} = \exp\{-\beta^2 [(\lambda_1^2 - 1)x^2 + (\lambda_2^2 - 1)y^2 + (\lambda_3^2 - 1)z^2]\}.$$

We assume that  $x = y = z$ . This leads to a mean value  $r_0$ , equal to:

$$r_0(x^2 + y^2 + z^2)^{1/2} = 3^{1/2} x = 3^{1/2} y = 3^{1/2} z$$

Thus:

$$\frac{P_2(r_2)}{P_1(r_1)} = \exp -\beta^2 (\lambda_1^2 + \lambda_2^2 + \lambda_3^2 - 3) \frac{r_0^2}{3}.$$

The entropy change for one molecular chain associated with the deformation is defined by:

$$\Delta S = k \ln \frac{P_2(r_2)}{P_1(r_1)}.$$

Inserting the expression for the ratio between the probabilities:

$$\Delta S = -k\beta^2 (\lambda_1^2 + \lambda_2^2 + \lambda_3^2 - 3) \frac{r_0^2}{3}.$$

The value of  $r_0 (= n^{1/2}a)$  and that of  $\beta$  can be substituted, yielding:

$$\Delta S = -\frac{k}{2} (\lambda_1^2 + \lambda_2^2 + \lambda_3^2 - 3).$$

The entropy change for  $N$  chains is given by

$$\Delta S = -\frac{1}{2} Nk (\lambda_1^2 + \lambda_2^2 + \lambda_3^2 - 3) \quad (2.43)$$

where  $N$  is the number of chains and  $k$  is the Boltzmann's constant. Substituting Equation 2.42 into Equation 2.43, we can write for the change in entropy as

$$\Delta S = -\frac{1}{2}Nk(\lambda_1^2 + 2\lambda_1^{-1} - 3) \quad (2.44)$$

Recall that Equation 2.39 gives the expression for the tensile force causing a change in length of a rubber or elastomer. It has two components: an energy contribution and an entropic contribution. As explained above, the energy contribution,  $(\delta U/\delta\ell)$  is negligible for rubber for isothermal deformation. So,

$$F = -T(\delta S/\delta\ell)_{T,V}. \quad (2.45)$$

Differentiating Equation 2.44 and substituting into Equation 2.45, we obtain

$$F = \frac{NkT}{\ell_0} (\lambda_1 - \lambda_1^{-2}) \quad (2.46)$$

If we divide the tensile force by the area of cross section, we get the tensile stress. Recall that the volume remains unchanged, i.e.,  $A_1\ell_1 = A_0\ell_0$ . Thus,

$$\sigma = \frac{F}{A_1} = \frac{NkT}{\ell_0} \left( \frac{\ell_1}{A_0\ell_0} \right) (\lambda_1 - \lambda_1^{-2}) \quad (2.47)$$

Let us denote the number of chain segments per unit volume ( $N/A_0\ell_0$ ) by  $n$  and recall that  $\ell_1/\ell_0 = \lambda_1$ ; then we write

$$\boxed{\sigma = nkT (\lambda_1^2 - \lambda_1^{-1})} \quad (2.48)$$

In Equation 2.48, the strength of the rubber is seen to increase with  $n$ , the number of chain segments per unit volume. The more cross-linked the polymer, the greater the number of segments and the smaller the length of molecule from one cross-link to the next. Thus, Equation 2.48 correctly predicts the strengthening of rubber with increasing cross-linking.

Equation 2.48 also shows a linear dependence of stress, at a given strain, on temperature. This follows from the dominance of the entropic elasticity. Any deviation from this linear relationship between stress and temperature of a rubbery or elastomeric materials can be taken as a measure of its deviation from thermodynamic ideal behavior. For an ideal rubbery behavior, the energetic component of force is zero. Also, the stress is not linearly dependent on strain, i.e., the Hooke's law is not obeyed in tension for an elastomer. Up to  $\sim 400\%$  strain, the theoretical stress-strain curve is in quite good accord with experimental values as shown in Figure 2.25. At very large strains, i.e., at strains  $> 400\%$  ( $\lambda = 5$ ) secondary bonds form between the partially aligned chains, i.e., strain induced crystallization occurs. At such large strain values, the chains begin to align

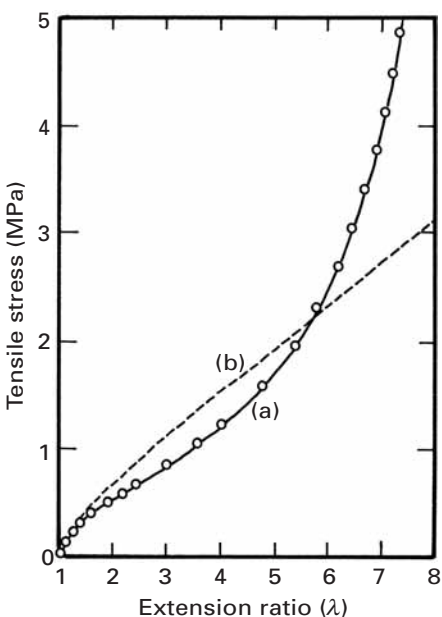


**Fig. 2.25** Force-extension curve for cross-linked rubber. (a) Experimental. (b) Theoretical. (After L. R. G. Treloar, *The Physics of Rubber Elasticity*, 3d ed. (Oxford: Clarendon Press, 1975), p. 87.)

themselves and stretching of the primary bonds in the chain becomes important.

Because the tensile stress-strain curve of rubber is nonlinear, Young's modulus cannot be defined for rubber, as it can be for crystalline metals and ceramics. One can, however, define a secant modulus at a given strain. Another important thing that a perceptive reader may have noticed is that the number of network chains per unit volume and, correspondingly, the modulus of an elastomer increases as the degree of cross-linking increases. This is as expected if we just compare a lightly cross-linked rubber band with a highly cross-linked bowling ball.

For metals, the ordered crystalline structure is retained during elastic deformation. Thus, the entropy, which is a measure of disorder (or randomness) is constant. On the other hand, the internal energy is increased by the work of deformation, which is stored in the metal as elastic energy.

In rubbers, the chains become more aligned with stretching. This decreases the entropy of the system. The internal energy, on the other hand, is constant.

## 2.14 | Mooney–Rivlin Equation

The treatment given above is based on what is called Gaussian network theory. Well before that, in the 1940s, Mooney<sup>10</sup> derived the

<sup>10</sup> M. Mooney, *J. Appl. Phys.*, 11 (1940) 582.

following equation, based on a phenomenological continuum mechanics model of rubber elasticity:

$$\boxed{\sigma = 2 \left( C_1 + \frac{C_2}{\lambda} \right) \left( \lambda - \frac{1}{\lambda^2} \right)'}$$

where  $C_1$  and  $C_2$  are constants (not to be confused with WLF constants discussed in Chapter 13). This equation is referred to as Mooney-Rivlin equation in the literature because of later contributions from Rivlin and Saunders.<sup>11</sup> They formulated the material law as a strain energy function in terms of the first and second principal invariants of the deformation. The formulation is called a strain energy function as the energy is conserved during deformation of these materials under constant temperature. It seems to describe well the deformation of highly elastic bodies which are incompressible (volume is conserved during deformation) and isotropic (the material has the same mechanical properties in all directions at a material point).

The above expression can be rearranged to the following form:

$$\frac{\sigma}{2 \left( \lambda - \frac{1}{\lambda^2} \right)} = \left( C_1 + \frac{C_2}{\lambda} \right).$$

A plot of:

$$\frac{\sigma}{2 \left( \lambda - \frac{1}{\lambda^2} \right)} \text{ against } \left( C_1 + \frac{C_2}{\lambda} \right),$$

called Mooney plot, would give a straight line of slope  $C_2$  and an ordinate of  $(C_1 + C_2)$  at  $1/\lambda$ .

The Mooney-Rivlin equation or its modification by Ogden<sup>12</sup> are commonly used in Finite Element Method codes for elastomeric materials.

### Example 2.16 |

Make a schematic plot of the internal energy and entropy as a function of strain for a crystalline solid (e.g., a metal) and for a rubbery solid (e.g., an elastomer). Make a drawing showing the structure before and after deformation in the two cases.

<sup>11</sup> R. S. Rivlin and D. W. Saunders, *Philosophical Transactions of the Royal Society of London, Series A*, 243 (1951) 251–288.

<sup>12</sup> R. W. Ogden, *Rubber Chemistry and Tech.*, 59 (1986) 386.

*Solution:* Figure E2.16 shows the requested plots.

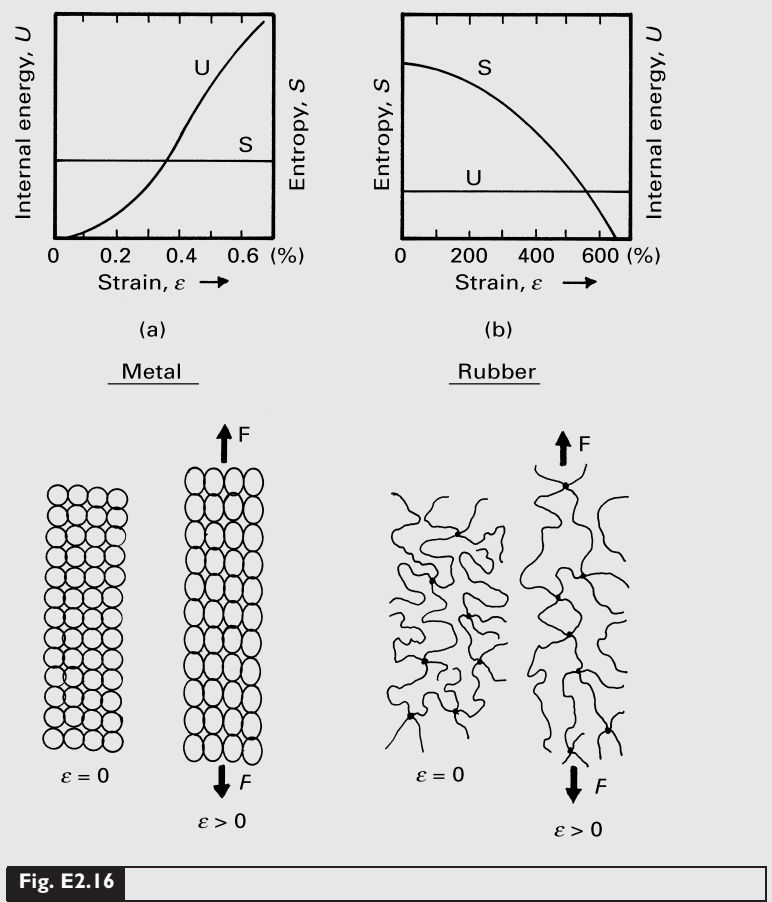


**Fig. E2.16**

### Example 2.17

It is frequently said that elastic deformation on loading and the recovery of strain on unloading involves the stretching of atomic bonds. Would this statement be true of the large elastic deformation that is observed in rubbery, or elastomeric, materials?

*Solution:* No. The large elastic deformation observed in elastomeric materials involves the *uncoiling* of randomly coiled polymeric chains. When we deform an elastomeric material, the end-to-end distance of the chains increases. When the material is unloaded, the chains return to the original random configuration. This uncoiling of chains results in the entropy effects discussed in the text. Such entropy effects are insignificant in metals and other nonelastomeric materials.

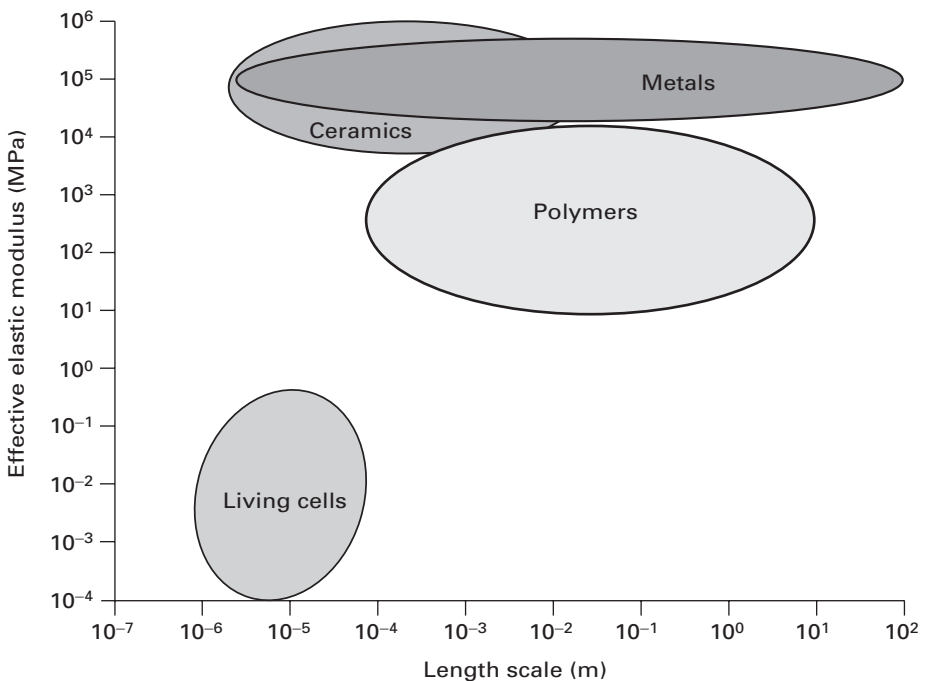


**Fig. 2.26** Range of elastic moduli of biological cells and conventional materials. (After G. Bao and S. Suresh, *Nature Materials*, 2 (2003) 715.)

## 2.15 | Elastic Properties of Biological Materials

Biological materials have complex elastic properties. Soft tissues exhibit nonlinear elasticity. Hard tissues, such as bone, have a linear elastic response conditioned by their density. Figure 2.26 gives an idea of the range of elastic properties of soft biological materials (in this case, living cells) compared to conventional materials. It is interesting to note the elastic moduli of cells are low compared to conventional structural materials by a factor of  $\sim 10^4$ . This is an extreme but illustrates the differences. We give in the following sections two examples of the elastic behavior of materials that occur in our body: blood vessels and cartilage.

### 2.15.1 Blood Vessels

The vascular system provides the transport of nutrients, oxygen, and other chemical signals to the various parts of the body. The vascular system is divided into two subsystems: the pulmonary and the circulatory system. We will not go into any details of the pathology of these two subsystems. We will concentrate on their mechanical properties. Arteries (which carry blood from the heart to the various parts of the body) and veins (that collect blood back to the heart) exhibit some significant differences in structure. Arteries are exposed to higher pressures and fluctuations associated with the diastolic and systolic portions of the cardiac cycle. Figure 2.27 shows the longitudinal and

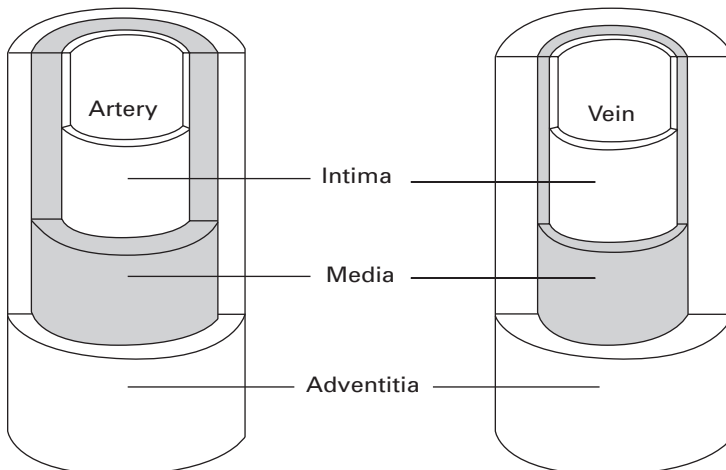


**Fig. 2.27** Cross section of an artery and vein, composed of the endothelium, tunica intima, tunica media, and tunica adventitia.

normal sections of an artery. The structure is layered with three distinct regions: tunica intima (innermost), tunica media (middle), and tunica adventitia (outermost).

Bursting (longitudinal splitting) of blood vessels or aneurysm (tensile instability forming a local bulge) are highly undesirable but all too frequent events in humans. There are two unique aspects of the mechanical response of arteries and veins that are instrumental in minimizing the chance of the aforementioned problems: nonlinear elasticity and residual stresses.

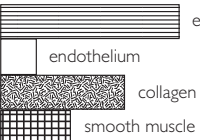
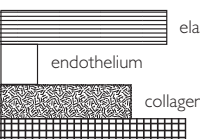
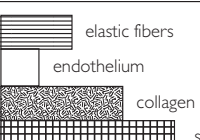
### Nonlinear Elasticity

The three layers comprising blood vessels have different functions and composition. Table 2.10 summarizes the similarities and differences between arteries and veins, including main vessels such as the aorta. The composition of arteries is made up primarily of elastic fibers (elastin), collagen, and smooth muscle. Compared to veins, arteries contain much more elastic material. Thicker arteries, such as the aorta, contain less smooth muscle than both smaller arteries and also veins. These differences account for the ability of arteries to resist large pressure fluctuations during the cardiac cycle.

The mechanical response of blood vessels is shown in Figure 2.28(a). This is the longitudinal stress-strain response of human vena cava. The response is nonlinear elastic. We know that it is elastic because on unloading the artery returns to its original dimension. However, there is a slight hysteresis on loading and unloading, due to viscoelastic processes. We know that it is nonlinear because the slope of the curve increases with strain. This slope approaches infinity as the strain approaches 0.3. This increase in slope is due to the extension of the collagen and elastin fibers. If they are stretched beyond this point, failure takes place. Instead of the strain,  $\varepsilon$ , the stretch ratio ( $\lambda = \varepsilon + 1$ ) is often used.

It is instructive to plot the slope,  $d\sigma/d\varepsilon = E$ , as a function of stress. This is done in Figure 2.28(b) for the aorta of a dog (circumferential strip). The slope first increases by a relationship that can be described

**Table 2.10** Dimensions and composition of blood vessels

Vessel	Dimensions	Composition
Artery	Aorta Vessel diameter, 25 mm Thickness, 2 mm	 <p>elastic fibers endothelium collagen smooth muscle</p>
	Medium-sized artery Vessel diameter, 4 mm Thickness, 1 mm	 <p>elastic fibers endothelium collagen smooth muscle</p>
Vein	Vessel diameter, 20 mm Thickness, 1 mm	 <p>elastic fibers endothelium collagen smooth muscle</p>

by a power function. Then, it reaches a linear range, in which the increase is more gradual. This nonlinear elastic behavior is a characteristic feature of many soft tissues in the human body. It serves as an important function: as the pressure in the blood vessels is increased, the vessels become stiffer.

This response, typical of arteries, has been successfully represented by the Fung equation:

$$\sigma = (\sigma^* + \beta)e^{\alpha(\varepsilon - \varepsilon^*)} - \beta,$$

where  $\alpha$  and  $\beta$  are parameters defined in Figure 2.28(b).  $\alpha$  is the slope of the linear portion and  $\beta$  is related to the intercept.  $\sigma^*$  and  $\varepsilon^*$  correspond to the onset of the linear portion. This equation can also be expressed in terms of  $\lambda$ , the stretch ratio.

### Residual Stresses

Biological materials such as arteries contain residual stress. In the case of a segment of artery that is not under internal blood pressure, the walls of the artery are under strain and therefore have residual stress. Fung<sup>13</sup> has shown that if one makes an axial cut in the wall of an artery, the artery will spontaneously open. This geometry is known as the zero-stress state. The angle by which the artery springs open is defined as the opening angle. As this opening angle increases the stress distribution in the wall becomes more uniform. This makes sense since under normal blood pressure arteries inflate, causing higher strain on the inner wall of the artery (compared to the

<sup>13</sup> Y. C. Fung, *Biomechanics* (New York: Springer, 1993).

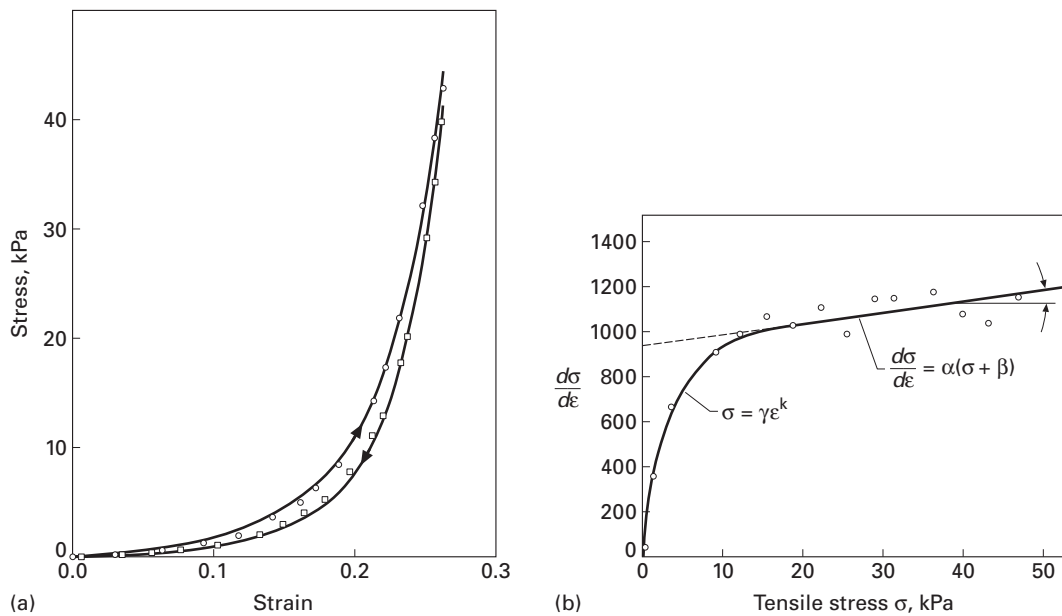


**Fig. 2.28** (a) Stress–strain response of human vena cava: circles – loading; squares – unloading. (Adapted from Y. C. Fung, *Biomechanics* (New York: Springer, 1993), p. 366.)  
(b) Representation of mechanical response in terms of tangent modulus (slope of stress–strain curve) vs. stress. (Adapted from Y. C. Fung, *Biomechanics*, New York: Springer, 1993), p. 329.)

outer wall). In arteries, stress is an exponential function of strain, so the observed increase in strain at the inner wall will be accompanied by an increase in stress at the inner wall. This is shown in Figure 2.29. Four different arteries, with different zero-stress angles, are shown:  $\alpha = 0, 10, 70$ , and  $155^\circ$ . For the same arteries, the wall stresses at two values of the applied internal pressure are shown. For zero pressure, there is a detrimental effect on the stress distribution. However, this is not the critical condition. For 100 mm Hg internal pressure (in the range of pressure of blood inside our body), the artery with the highest value of  $\alpha$  has the lowest stress in the wall. Thus, the residual stress reduces the maximum stress in the artery walls.

### 2.15.2 Articular Cartilage

Articular cartilage, which covers the ends of long bones and bones within synovial joints, is a highly hydrated connective tissue. It consists of two distinct phases: a solid phase made up of collagen, proteoglycans (aggrecan), proteins, and chondrocytes and a liquid phase composed of water and electrolytes. Aggrecan and collagen are primary components of the solid phase, or extracellular matrix, and are responsible for the biomechanical properties (compressive and tensile, respectively) of articular cartilage. Figure 2.30 shows a schematic

**Fig. 2.29** Residual stresses in arteries; the artery is sliced longitudinally and the angle  $\alpha$  is measured. (From Y. C. Fung, *Biomechanics* (New York: Springer, 1993), p. 389.)

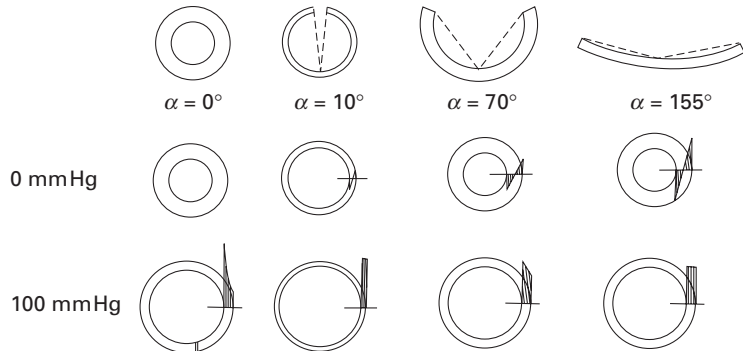
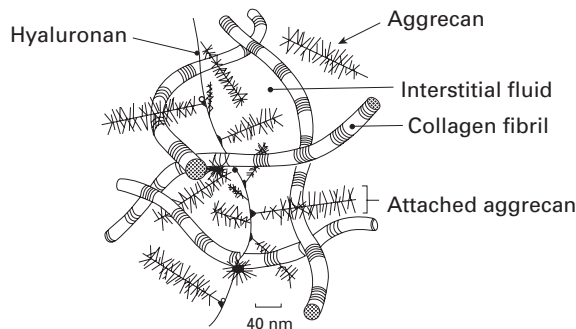


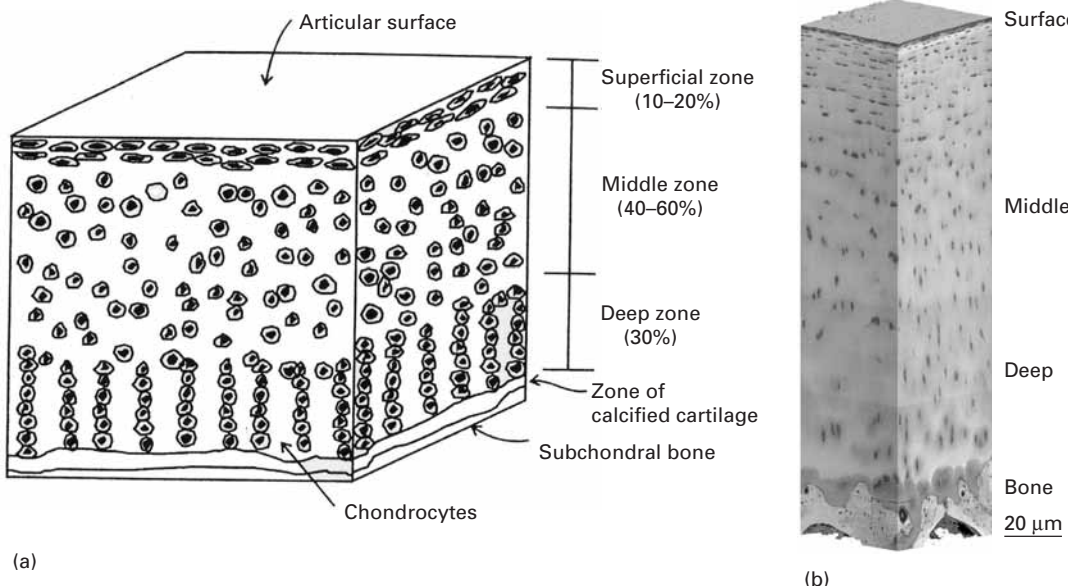
**Fig. 2.30** Schematic of aggrecan–collagen meshwork in cartilage tissue. (After V. C. Mow and A. R. Ratcliffe, Structure and Function of Articular Cartilage and Meniscus, In *Basic Orthopedic Biomechanics*, ed. V. C. Mow and W. C. Hayes (New York: Raven Press, 1997), pp. 113–178.)



of the aggrecan–collagen meshwork in cartilage tissue. The characteristic banded structure of collagen is shown (coral snake-like).

Cartilage is a low friction, weight-bearing, viscoelastic material which distributes stresses generated by translational and rotational motion to the underlying bone. It possesses a stratified architecture made of distinct zones – superficial, middle, and deep. Figure 2.31(a) shows these regions. At the surface, the collagen is arranged parallel to the surface. The chondrocytes are elongated along the surface. In the middle zone, which comprises between 40 and 60% of the cartilage, the chondrocytes are dispersed in a matrix of collagen. The deep zone is composed of spheroidal chondrocytes in columnar arrays. The collagen fibers are of large diameter and are arranged perpendicular to the bone. The last zone and interface with the bone consists of calcified cartilage. The chondrocytes are round and less organized. The cartilage can be considered, from a materials viewpoint, as a gradient material, since the properties and structure vary in a continuous fashion. Figure 2.31(b) shows the mesostructure of human cartilage. The four regions drawn schematically in Figure 2.31(a) are seen in Figure 2.31(b).

The mechanical properties of articular cartilage depend very much on the orientation of the collagen fibrils. At the surface of cartilage, collagen fibrils are oriented parallel to the surface. Therefore, it is not surprising to find that under tension samples from the superficial zone are very strong. This is directly due to collagen content and orientation. Figure 2.32 shows that the cartilage is much stronger



(a)

(b)

**Fig. 2.31** (a) Mesostructure of cartilage (consisting of four zones) showing differences in structure as a function of distance from surface; the bone attachment is at bottom. (From G. L. Lucas, F. W. Cooke, and E. A. Friis, *A Primer on Biomechanics* (New York: Springer, 1999), p. 273.) (b) Cross-section of human cartilage showing regions drawn schematically in (a). (Courtesy of K. D. Jadin and R. I. Sah.)

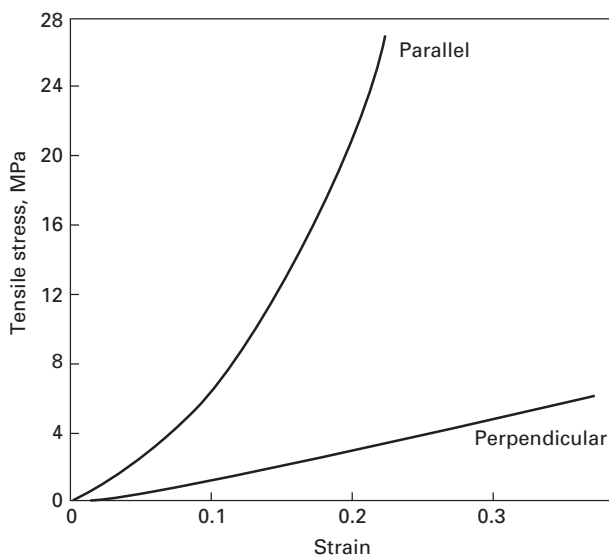


**Fig. 2.32** Stress-strain curve for samples from the superficial zone of articular cartilage. Samples were cut parallel and perpendicular to collagen fiber orientation. (From G. E. Kempson, Mechanical Properties of Articular Cartilage. In *Adult Articular Cartilage*, ed. M. A. R. Freeman (London: Sir Isaac Pitman and Sons Ltd., 1973), pp. 171–228.)

parallel to the surface than perpendicular to it. When cartilage begins to degenerate, due to age and/or excessive exercise (load), defects may form. The stiffness of cartilage is approximately 1/20 of that of subchondral cancellous bone and 1/60 of that of cortical bone. Unfortunately, cartilage does not have capacity to repair itself. For this

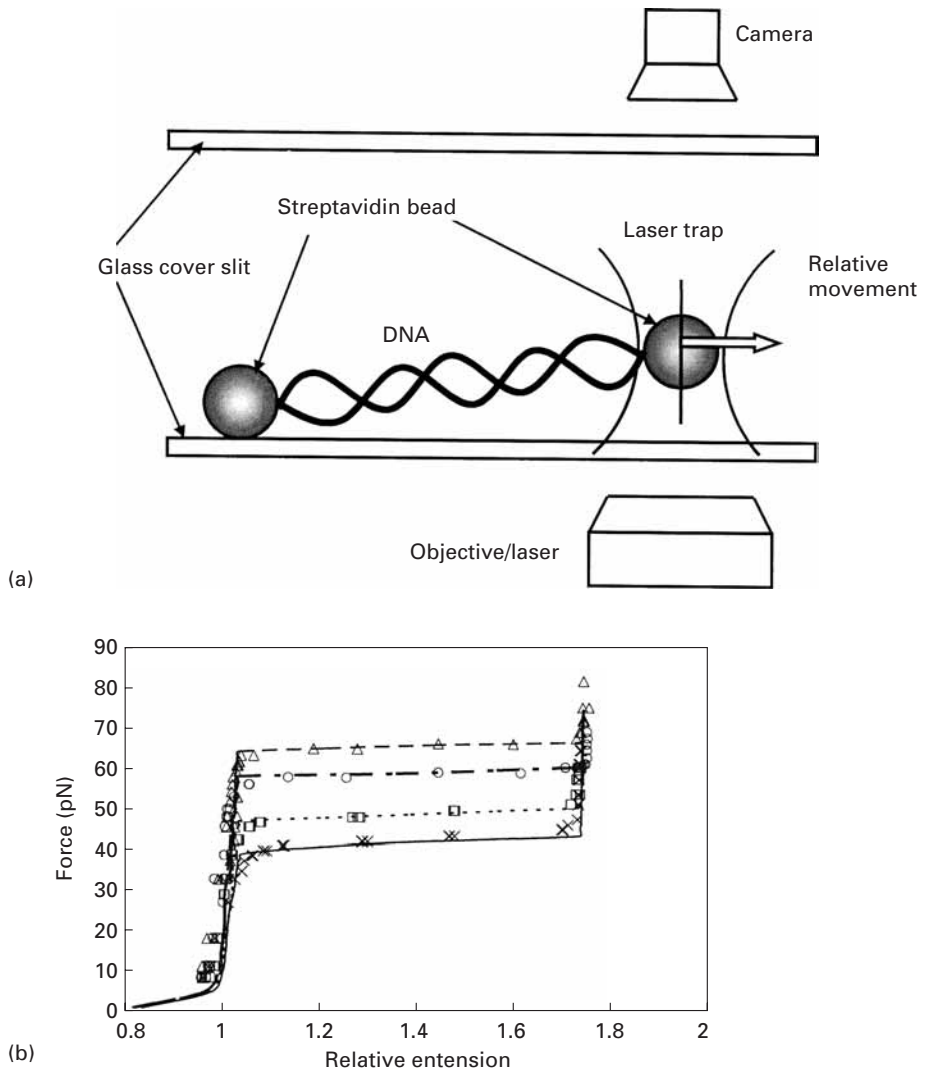


**Fig. 2.33** (a) Schematic of the optical trap setup for the stretching of a double-stranded DNA molecule. (b) Plots of stretching force against relative extension of the single DNA molecule at increasing (from bottom to top curves) concentrations of salt. (Courtesy of C. T. Lim, National Singapore University.)

reason, along with the large numbers of people affected by joint- and arthritis-related ailments, tissue engineering alternatives are explored as an option for repairing cartilage defects.

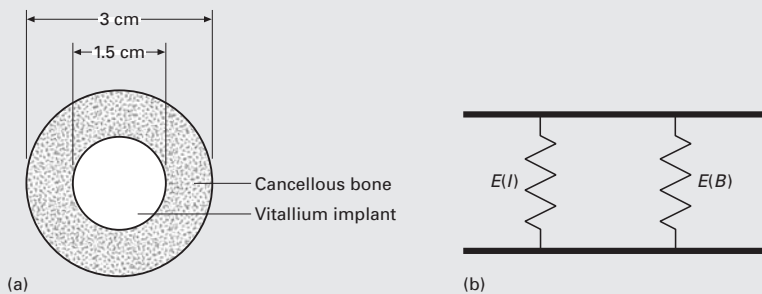
### 2.15.3 Mechanical Properties at the Nanometer Level

Figure 2.33 shows the degree of miniaturization that can be attained with modern methods to establish the mechanical properties of biomaterials. It is possible to stretch single strands of DNA. This is accomplished by using a contraption called optical (laser) tweezer, shown in Fig. 2.33(a). Microsized beads are attached to the DNA strand, one end

is fixed and the other, trapped in the optical tweezer, is pulled. The mechanical response of the DNA is definitely nonlinear, Figure 2.33(b). There is a plateau at a force varying from 40 to 65 pN (depending on the concentration of NaCl). At this plateau, the strand can receive a stretch of up to 1.8. Beyond this value, the DNA stiffness increases considerably. These results show that salinity has a definite effect on DNA mechanical properties.

### Example 2.18 |

Calculate the stress on the femur (a) with and (b) without a total hip replacement prosthesis (see Figure E2.18(a)). Assume that the cross-sectional diameter of the femur is equal to 3 cm and that of the implant is 1.5 cm. (c) What would you do to improve the situation?



**Fig. E2.18**

Given:

$$\text{Weight} = 1000 \text{ N (100 kg)},$$

$$E_I = 210 \text{ GPa},$$

$$E_B = 20 \text{ GPa},$$

where  $E_I$  and  $E_B$  are the moduli of the implant and bone, respectively.

*Solution:*

- (a) In the presence of the implant, we can consider the situation analogous to two springs in parallel, as shown in Figure E2.18(b). For two springs in parallel (the analog for a bone joined to the implant stem), the strains are equal:

$$\varepsilon_I = \varepsilon_B,$$

where  $\varepsilon_I$  and  $\varepsilon_B$  are the strains in the implant and bone, respectively.

The elastic deformation of bone and implant can be expressed as:

$$\frac{\sigma_B}{E_B} = \varepsilon_B$$

and

$$\frac{\sigma_I}{E_I} = \varepsilon_I.$$

The areas are:

$$A_B = \pi \times \left[ \left( \frac{3}{2} \right)^2 - \left( \frac{1.5}{2} \right)^2 \right] \times 10^{-4} = 5.3 \times 10^{-4} \text{ m}^2$$

and

$$A_I = 1.76 \times 10^{-4} \text{ m}^2.$$

The total load is

$$P_T = P_I + P_B = \sigma_I A_I + \sigma_B A_B.$$

But:

$$\frac{\sigma_B}{E_B} = \frac{\sigma_I}{E_I};$$

Thus:

$$\begin{aligned} \sigma_B &= \left( \frac{A_I}{E_B} E_I + A_B \right) = P_T \\ \sigma_B &= \frac{P_T}{\left( \frac{A_I}{E_B} E_I + A_B \right)} = 0.42 \times 10^6 \text{ N/m}^2. \end{aligned}$$

(b) In the absence of implant,

$$\sigma_B = \frac{1000}{\pi \left[ \left( \frac{3}{2} \right)^2 - \left( \frac{1.5}{2} \right)^2 \right] 10^{-4}} = \frac{1000}{5.301 \times 10^{-4}} = 1.89 \times 10^6 \text{ N/m}^2.$$

It can be seen that the stresses in the bone are significantly reduced by the introduction of the implant: they are one-fourth of the original stresses. This has a deleterious effect on the bone growth and leads to weakening of the implant.

(c) One solution would be to develop a metallic foam with a Young's modulus of 20 GPa. This would have the added advantage of enabling bone growth into the implant. However, the strength of this stem would be severely reduced.

### Example 2.19 |

From the curves (Figure E2.19) reporting the force-strain response of human skin along the direction of loading (extension) and perpendicular to it (lateral contraction) determine the in-plane Poisson's ratio at 20, 40, and 60 N.

What can you conclude from the results?

**Solution:** We can see that the behavior of the skin is nonlinear elastic, with the slope increasing with load.

Poisson's ratio is defined as:

$$\nu = -\frac{\varepsilon_{lat}}{\varepsilon_{lon}},$$

where  $\varepsilon_{\text{lat}}$  is the lateral strain and  $\varepsilon_{\text{lon}}$  is the longitudinal strain. The following values are obtained from Figure E2.19:

$$(P = 20 \text{ N})\nu = 0.81,$$

$$(P = 40 \text{ N})\nu = 0.91,$$

$$(P = 70 \text{ N})\nu = 0.95.$$

The values are close to 1. If we assume that the skin volume remains constant during deformation, then we can write for the volume change

$$\varepsilon_{\text{lat}} + \varepsilon_{\text{lon}} + \varepsilon_{\text{th}} = 0,$$

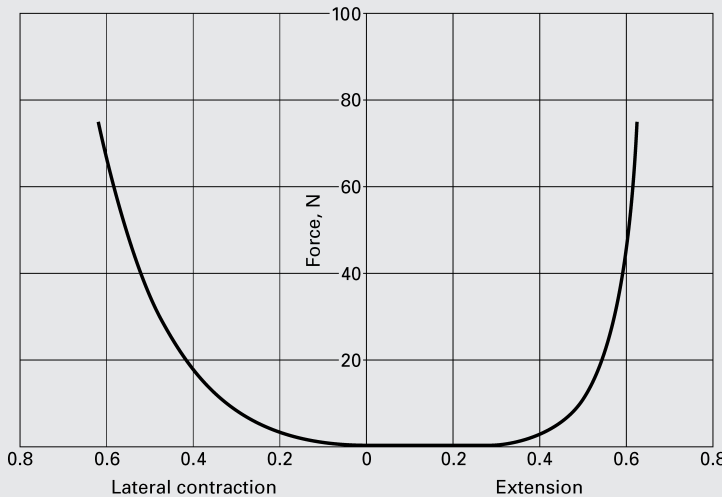


**Fig. E2.19** Force-extension and force-lateral contraction curves for human skin in uniaxial tension. (Adapted from R. M. Kenedi, T. Gibson, J. H. Evans, and J. C. Barbanell, *Phys. Med. Biol.*, 20 (1975) 619.)

where the subscripts lat, long, and th indicate lateral, longitudinal, and thickness directions. Dividing the equation by  $\varepsilon_{\text{lon}}$ :

$$\nu - 1 + \nu_{\text{th}} = 0.$$

Since  $\nu \sim 0.9$ , we have:

$$\nu_{\text{th}} \sim 0.1.$$

The results indicate that the strain in the thickness direction is small in comparison with the in-plane strains. Thus, the thickness of human skin remains approximately constant when it is uniaxially stretched.

## 2.16 | Elastic Properties of Electronic Materials

Microelectronic integrated circuit materials are characteristically composed of a silicon (monocrystalline) substrate and thin film layers (Section 1.3.10). The thickness of the substrate is of the order of

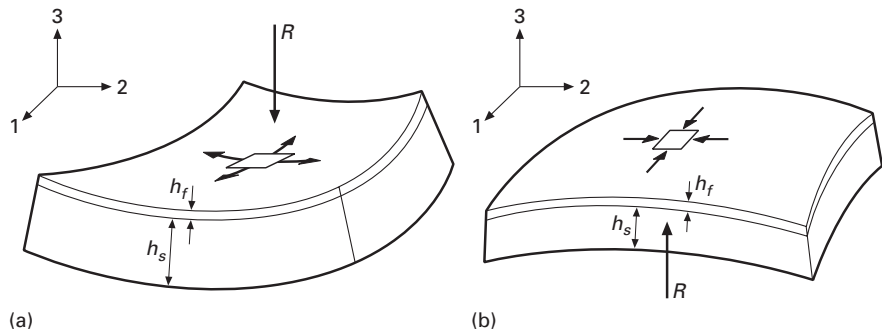


**Fig. 2.34** Effect of stresses acting on thin film on bending of substrate; (a) tensile stresses in thin film; (b) compressive stresses in thin film.

0.5–1 mm, and the thin films are characteristically 1  $\mu\text{m}$  thick. The thin film and substrate have often different coefficients of thermal expansion. Additionally, the substrate density might change as it grows. There are also epitaxial strains, caused by a lattice parameter mismatch between the substrate and film. As a result, the thin film is either under compression or tension. Figure 2.34 shows both situations. If the film is under tension, it will bend the substrate up (Figure 2.34(a)); on the other hand, if the film is under compression, it will bend the substrate down (Figure 2.34(b)). It is possible to estimate the radius of curvature and the stresses. We start with the generalized Hooke's law and set  $\sigma_{33}$  equal to zero in the thin film. We do this because we have a state of plane stress. For isotropic materials, from Equation 2.11:

$$\begin{aligned}\varepsilon_{11} &= \frac{1}{E} [\sigma_{11} - \nu \sigma_{22}], \\ \varepsilon_{22} &= \frac{1}{E} [\sigma_{22} - \nu \sigma_{11}], \\ \varepsilon_{33} &= \frac{1}{E} [-\nu(\sigma_{11} + \sigma_{22})].\end{aligned}$$

Therefore:

$$\varepsilon_{11} = \frac{1-\nu}{E} \sigma_{11}.$$

The term  $E/(1-\nu)$  can be defined as a biaxial modulus. For the substrate:

$$M_s = \frac{E_s}{1-\nu_s}$$

$E_s$  and  $\nu_s$  are the Young's modulus and Poisson's ratio of the substrate, respectively. This is the so-called Stoney equation.

The radius of curvature of the system can be estimated from an equation for plates:

$$R = \frac{E_s h_s^2}{6(1-\nu_s)\sigma_f h_f},$$

where  $h_s$  and  $h_f$ , defined in Figure 2.34, are the thickness of substrate and film, respectively.  $\sigma_f$  is the maximum stress in the film.

For a monocrystalline substrate, one has to compute the biaxial modulus using the elastic stiffness components  $C_{mn}$ .

For instance, the values for Si are:

$$\begin{aligned}C_{11} &= 166 \text{ GPa}, \\C_{12} &= 64 \text{ GPa}, \\C_{44} &= 80 \text{ GPa}.\end{aligned}$$

For the anisotropic case, when the cube plane is parallel to the interface, the following expression can be derived (see Section 2.9):

$$\frac{1}{E_{100}} = S_{11}.$$

For Poisson's ratio, we use the expression:

$$\nu = -\frac{S_{12}}{S_{11}}.$$

Thus:

$$M_{100} = \frac{1/S_{11}}{1 + S_{12}/S_{11}}.$$

We obtain the stiffnesses from the compliances by inverting the matrix (Section 2.9, Example 2.10). The result is:

$$M_s = C_{11} + C_{12} - \frac{2C_{12}^2}{C_{11}} = 180.7 \text{ GPa}.$$

For the (111), we repeat the procedure and obtain:

$$M_{111} = \frac{6C_{44}(C_{11} + 2C_{12})}{C_{11} + 2C_{12} + 4C_{44}}.$$

For the (110) plane, the stiffness depends on direction. For more details, the reader is referred to Nix<sup>14</sup> and Freund and Suresh.<sup>15</sup>

We can also use the isotropic Young's modulus of Si (= 163 GPa) and a Poisson's ratio of 0.2. This would give us close enough results. For  $h_f = 1 \mu\text{m}$  and  $h_s = 500 \mu\text{m}$ , we have, assuming a maximum stress in the film of 500 MPa:

$$R = M_s \frac{h_s^2}{6\sigma_f h_f} = 15 \text{ m}.$$

## 2.17 | Elastic Constants and Bonding

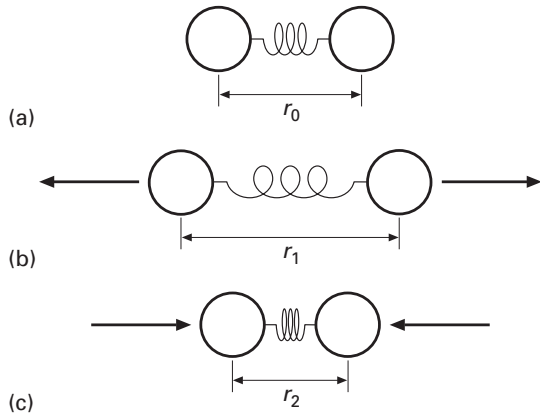
There are four types of bonds between atoms:

- Metallic: metals,
- Ionic: ceramics,
- Covalent: ceramics, backbone of polymers and biological materials,
- van der Waals: polymers and biological materials.

<sup>14</sup> W. D. Nix, *Met. Trans.*, 20A (1989) 2217.

<sup>15</sup> L. B. Freund and S. Suresh, *Thin Film Materials* (Cambridge, U.K.: Cambridge University Press, 2003), Ch. 3.

**Fig. 2.35** Two atoms with an imaginary spring between them; (a) equilibrium position; (b) stretched configuration under tensile force; (c) compressed configuration under compressive force.



The first three are called primary bonds. van der Waals bonds (which include the hydrogen bond) are called secondary bonds. The primary bonds are in general much stronger than secondary bonds. Secondary bonds “melt” between 100 and 500 K.

Many materials have mixed bonds. Intermetallic compounds may be bonded by a mixture of metallic and ionic bonds. Many ceramic and semiconducting compounds have a mix of covalent and ionic bonding. Polymers and biological materials have covalent bonds along the primary chains (C-C, Si-Si, etc.) and van der Waals (often, hydrogen) bonds between segments inside a chain.

The interaction energy between two adjacent atoms is often considered as the sum of an attractive and a repulsive term. The resultant curve gives the potential well. There are many calculations of interatomic potentials, the Condon-Morse and Lennard-Jones being examples.

The linear theory of elasticity makes the assumption that the material is a continuum. The assumption is good when we are dealing with large bodies; the micromechanics of deformation, on the other hand, describes a scale where the continuum breaks down into a periodic array of atoms: the crystalline structure. It is theoretically possible to calculate the elastic constants from the consideration of the interatomic forces. These calculations can be conducted for ionic structures, such as NaCl, considering only electrostatic forces using measured values of the ion sizes. In metals the situation is more complex. Even approximate quantitative determinations require the use of wave mechanics. The effect of temperature on atomic vibrations and/or the lattice parameter is discussed, as well as the attendant changes in elastic properties.

Figure 2.35 shows two atoms, which are at their equilibrium separation  $r_0$ . Tensile forces increase the separation to  $r_1$ ; compressive forces decrease it to  $r_2$ . The variation of the interaction energy with atomic separation is shown in Figure 2.36. At equilibrium, the interaction energy is minimum; the equilibrium separation  $r_0$

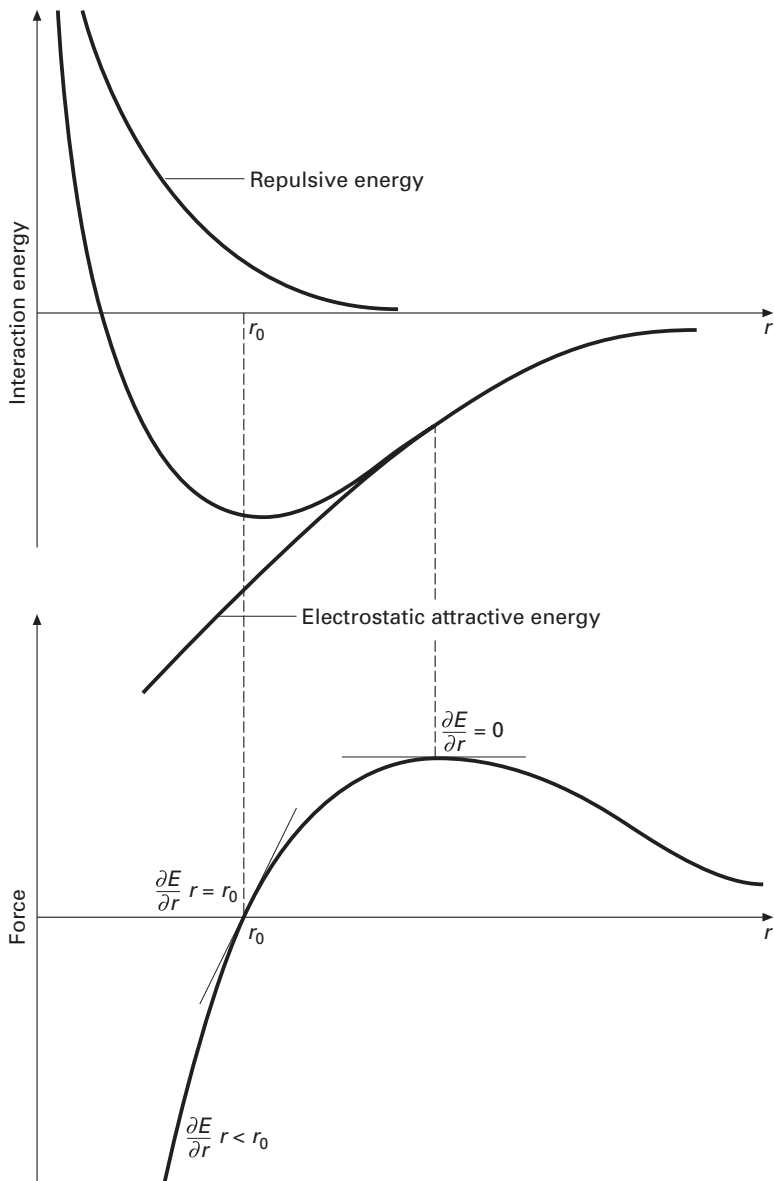


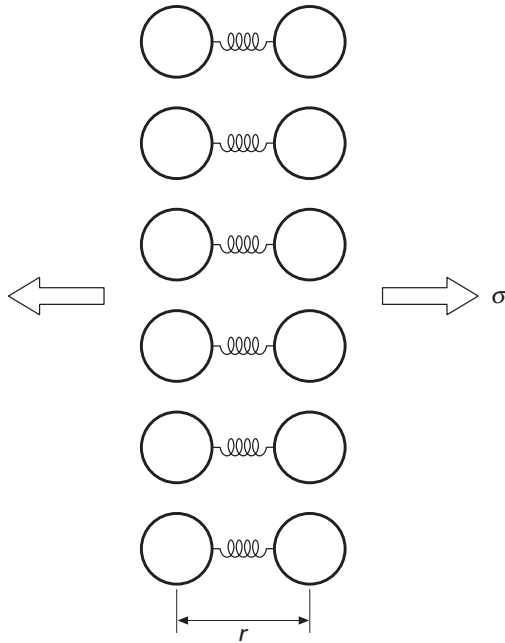
**Fig. 2.36** (a) Interaction energies (attractive and repulsive terms) as a function of separation; (b) Force between two atoms as a function of separation; notice decrease in slope as separation increases.

corresponds to the bottom of the well. One can represent the energy by:

$$U_i = -\frac{A}{r^m} + \frac{B}{r^n}, \quad (2.49)$$

where the first term represents the attraction and the second term the repulsion. The exponent of the repulsive term,  $n$ , is usually much larger than  $m$  because, as the two atoms are brought together, their electronic orbitals superimpose and strong repulsion (due to Pauli's exclusion principle) ensues. This is reflected in Figure 2.36(a), where the repulsive term increases sharply as the separation is decreased

**Fig. 2.37** Array of atoms representing tensile stress applied to crystal.



below  $r_0$ . The repulsive force operates at a close range. The interatomic force is obtained from:

$$F = \frac{\partial U_i}{\partial r}.$$

This force is equal to zero at the bottom (trough) of the interaction energy curve, which corresponds to the equilibrium separation,  $r_0$ . It is possible to estimate the elastic modulus from  $\partial F / \partial r$ . This can be accomplished by expressing stress and strain in terms of atomic positions. Figure 2.37 shows, in a schematic fashion, an array of atoms. We consider only the nearest neighbors aligned with the stress direction. In a more accurate calculation next-nearest and next to next-nearest neighbors have to be included, since they play an important role.

The engineering strain can be expressed as:

$$d\varepsilon = \frac{dr}{r_0},$$

where  $r_0$  is the equilibrium atomic separation and  $dr$  is the change in atomic separation. The stress is equal to:

$$d\sigma = N dF,$$

where  $N$  is the number of atoms per unit area of cross section and  $dF$  is the interatomic force producing a displacement  $dr$ . If we ascribe an area  $r_0 \times r_0$  per atom, we have:

$$d\sigma = \frac{dF}{r_0^2}.$$

The Young's modulus is expressed as:

$$E = \left| \frac{d\sigma}{d\varepsilon} \right|_{\varepsilon=0} = r_0^{-1} \left| \frac{dF}{dr} \right|_{r=r_0} = r_0^{-1} \left| \frac{d^2U_i}{dr^2} \right|_{r=r_0}. \quad (2.50)$$

From Equation 2.49:

$$\frac{dU_i}{dr} = \frac{Am}{r^{m+1}} - \frac{Bn}{r^{n+1}}.$$

At  $r = r_0$ :

$$\frac{Am}{r_0^{m+1}} - \frac{Bn}{r_0^{n+1}} = 0$$

$$Bn = Amr_0^{n-m}.$$

Thus:

$$\begin{aligned} \frac{dU_i}{dr} &= \frac{Am}{r^{m+1}} - \frac{Amr_0^{n-m}}{r^{m+2}} \\ \frac{d^2U_i}{dr^2} &= \frac{dF}{dr} = -\frac{Am(m+1)}{r^{m+2}} + \frac{Am(n+1)r_0^{n-m}}{r^{n+2}}. \end{aligned}$$

At the equilibrium separation,  $r_0$ :

$$\begin{aligned} \left| \frac{dF}{dr} \right|_{r=r_0} &= -\frac{Am(m+1)}{r_0^{m+2}} + \frac{Am(n+1)r_0^{n-m}}{r_0^{n+2}} \\ \left| \frac{dF}{dr} \right|_{r=r_0} &= \frac{Am(n-m)}{r_0^{m+2}} \end{aligned} \quad (2.51)$$

Substituting Equation 2.51 into Equation 2.50:

$$E = \frac{Am(n-m)}{r_0^{m+3}}. \quad (2.52)$$

The attraction forces in ionic solids are of a coulombic nature and the exponent in Equation 2.52 is  $m = 1$ .

Thus:

$$E = \frac{A(n-1)}{r_0^4}.$$

The parameter  $A$  is related to the electrical charges of the ions. For monovalent ions:

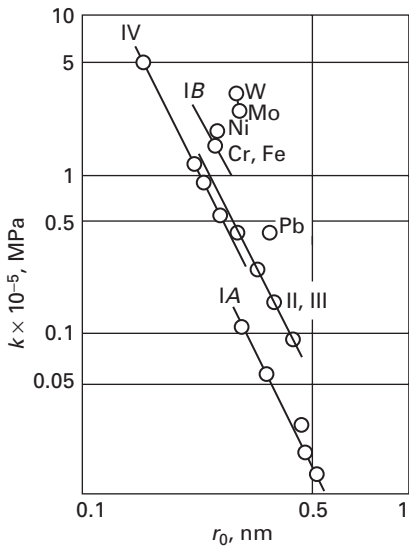
$$A = \frac{e^2}{4\pi\varepsilon_0},$$

where  $e$  is the electric charge of an electron and  $\varepsilon_0$  is the permittivity of vacuum. One can thus estimate the elastic modulus of ionic solids. Thus:

$$E = \frac{ke^2}{r_0^4},$$

where  $k$  comes from the grouping of constants. The  $r_0^{-4}$  dependence of elastic constants is actually much more general.

**Fig. 2.38** Effect of radius of closest approach on bulk modulus for groups I, II, III, IV, and transition elements.



The electrostatic nature of the forces between ionic crystals renders the determination of elastic constants less arduous. The NaCl structure is a simple cubic structure, with Na and Cl occupying alternate positions in the lattice. Each  $\text{Na}^+$  ion is surrounded by six  $\text{Cl}^-$  ions. If we consider one isolated ion (either  $\text{Na}^+$  or  $\text{Cl}^-$ ) and compute all attractive and repulsive forces by neighbors, next-neighbors, and so on, it is possible to determine the resultant electrostatic force.

The force between individual ions is coulombic (i.e. it varies with the square of the distance). Computing all the forces and transforming the resultant force into a stress and the displacement into strain, we showed above that one obtains an equation of the form:

$$E = \frac{ke^2}{r_0^4}, \quad (2.53)$$

where  $r_0$  is the interatomic distance,  $k$  a constant, and  $e$  the charge of an electron. This very simplified calculation shows that Young's modulus should vary with  $r_0^{-4}$ . The same dependence should exist for the bulk modulus  $k$ . Figure 2.38 shows that this type of dependence is actually observed. In the log-log plot, the slope of  $-4$  corresponds to the dependence shown in Equation 2.53. Elements from groups I, II, III, and IV obey that relationship. Elements of the same group were taken together because they have the same valence. Group I elements are monovalent and have the weakest bonding. Hence their line is the lowest in Figure 2.38.

In spite of the fact that bonding is more complex in metals than in ionic crystals, Gilman<sup>16</sup> has shown that an  $r_0^{-4}$  type of relationship can be found for metals. This is shown in Figure 2.39. The alkali

<sup>16</sup> J. J. Gilman, *Electronic Basis of the Strength of Materials* (Cambridge, U.K.: Cambridge University Press, 2003).

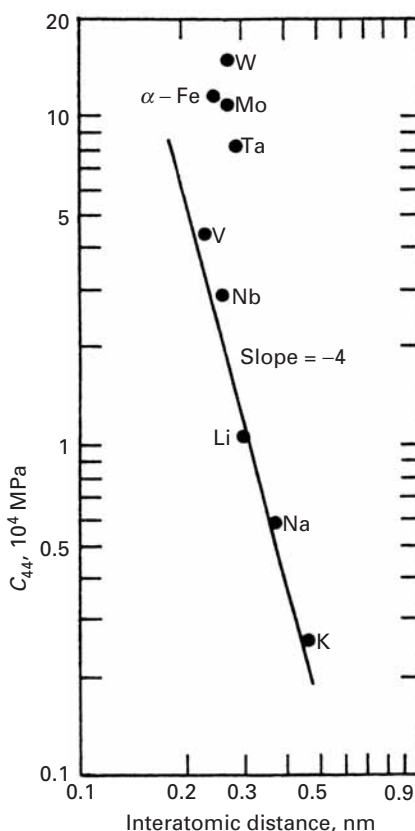


**Fig. 2.39** Variation of elastic constant  $C_{44}$  with  $r_0$  for BCC metals. (Adapted from J. J. Gilman, Mechanical Behavior of Crystalline Solids, NBS Monograph, 59 (1963) 79.)

metals seem to obey the  $r_0^{-4}$  (where  $r_0$  is the interatomic distance) quite well; the transition metals are situated above them. The elastic properties are strongly dependent, obviously, on bonding. Figure 2.40 shows a plot of the bulk modulus versus melting point for a number of transition metals. The melting point is the temperature at which thermal energy is sufficient to disrupt the metallic bonding. Hence, the stronger the bonding, the higher the melting point. This correlation is clearly evident in Figure 2.40. The lines join elements from the same column in the periodic table. Some of the series of three elements fall remarkably well in a straight line: Cr-Mo-W, V-Nb-Ta, Ag-Cu-Au.

A plot that emphasizes the importance of the electronic structure on elastic constants is shown in Figure 2.41. The periodicity in the variation of the Young's moduli (lines represent rows in the periodic table) is indicative of the importance of the electronic structure. Transition metals, which are characterized by strong bonding by electrons from the  $d$  shell, have particularly high Young's moduli. Os, Ru, and Fe have six  $d$  electrons each and are the elements that have the highest melting point for each of the three rows of transition elements in the periodic table. In Figure 2.40, it can be seen that the transition elements have  $C_{44}$  higher than would have been predicted from the  $r_0^{-4}$  relationship. This confirms the indication that the strong  $d$

**Fig. 2.40** Relationship between melting point and bulk modulus for transition elements.

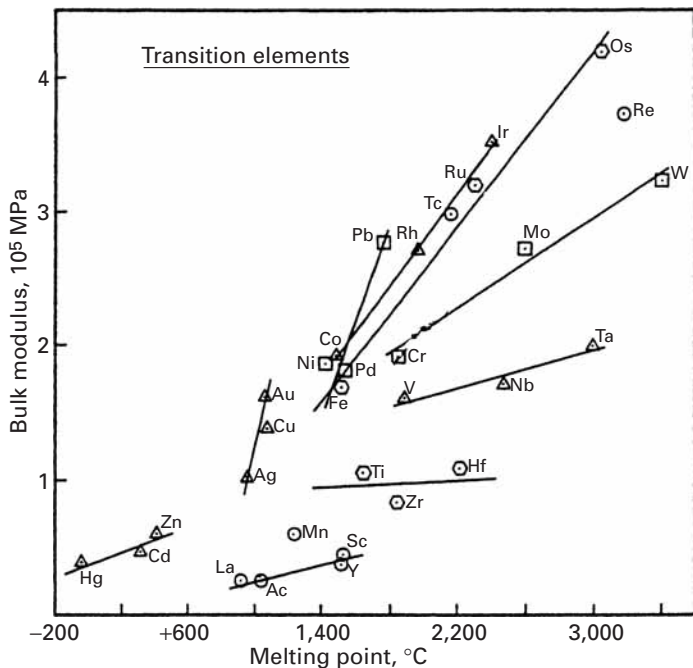
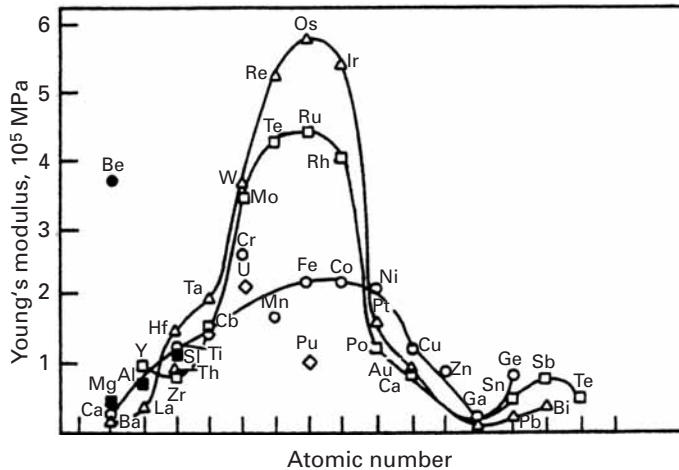


**Fig. 2.41** Periodic variation of Young's modulus of elements. The three lines represent the rows in the periodic table. (Adapted with permission from O. D. Sherby, in *Nature and Properties of Materials*, ed. J. Park (New York: Wiley, 1967), p. 373.)



bonding is responsible for additional stiffness. One element stands out in Figure 2.41: beryllium. Having a relatively small atomic number, it has an extremely high stiffness, comparable with that of tungsten and molybdenum. The ratio between Young's modulus and density is extremely high (six to seven times as high as for titanium and aluminium). It has unique applications in the aerospace industry. Its first use was in spacers for the Minuteman missile, and it is used in space vehicles. A high stiffness is required in large satellites because the lowest natural frequency of vibration must exceed a specified value to avoid resonant coupling with the booster control system during powered flight. The higher the stiffness, the higher the natural

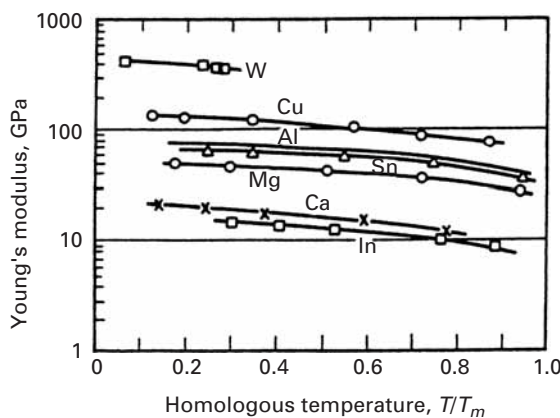


**Fig. 2.42** Effect of temperature on dynamic Young's modulus.  
(Adapted with permission from O. D. Sherby, in *Nature and Properties of Materials*, ed. J. Park (New York: Wiley, 1967), p. 376.)

frequency of vibration. However, the metallurgical problems posed in beryllium production are many, because of its structure (HCP), high chemical reactivity, and high toxicity.

The dependence of elastic properties of a metal on interatomic separation (which can, as a first approximation, be expressed as  $r_0^{-4}$ ) may be applied to rationalize two different phenomena: the temperature dependence of elastic properties and the effect of magnetic fields on elastic properties. They will be discussed below. As the temperature increases, the metals expand; this lattice expansion is treated in detail by Mott and Jones,<sup>17</sup> but is beyond the scope of this book. Suffice to say that as the temperature increases, the amplitude of vibration of the atoms increases. This amplitude increase will accommodate the thermal energy term ( $kT$ ) and the expanded lattice will have a larger  $r_0$ . This, in turn, will produce a decrease in the elastic constants. The change in elastic constants with temperature is much less pronounced than the change of yield stress, tensile strength, and strain to failure. The Young's modulus at the melting point is usually between one-half to two-thirds of the low-temperature value. The temperature dependence of the yield point is much more pronounced because plastic deformation is a thermally activated process. Figure 2.42 illustrates the changes in  $E$  with temperature for some metals.

The effect of magnetic fields can be explained by the same rationale. A magnetic field, due to the magnetostrictive effect, changes the lattice parameter slightly; this, in turn, affects the elastic properties. When the Young's modulus of nickel in the presence and absence of a magnetic field is measured, appreciable differences are found. Actually, between 200 and 360 °C (Curie temperature, where ferromagnetic-paramagnetic transformation takes place) the Young's modulus of nickel increases with temperature.<sup>18</sup> By appropriate alloying it is possible to obtain alloys that have essentially a constant

<sup>17</sup> N. F. Mott and H. Jones, *The Theory of the Properties of Metals and Alloys* (New York: Dover, 1958).

<sup>18</sup> O. D. Sherby, in *Nature and Properties of Materials*, ed. J. Park (New York: Wiley, 1967), pp. 373, 375, 376.

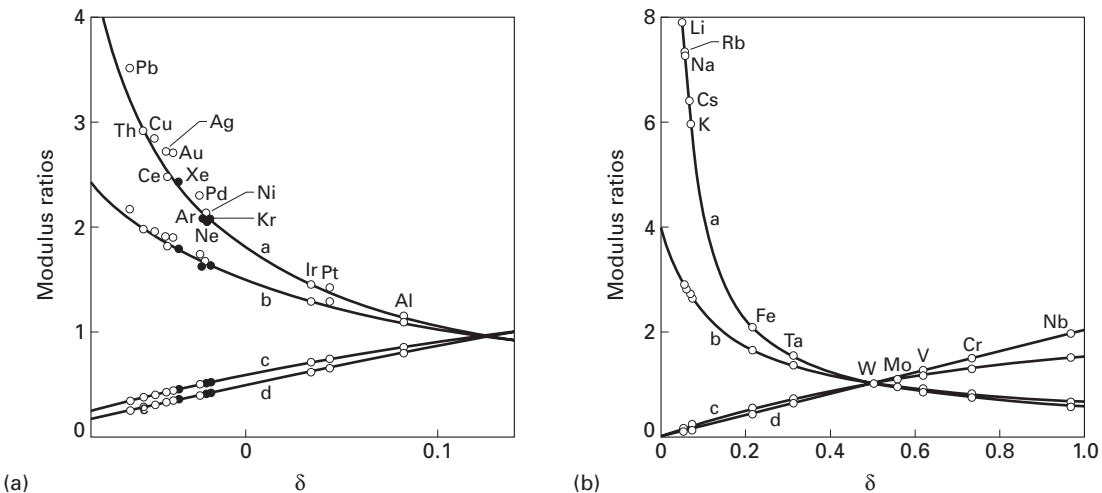


**Fig. 2.43** Young's and shear moduli ratios as a function of  $\delta$ , a parameter that is a measure of the strength of the second neighbour interaction compared to that of the first neighbor interaction. (a) FCC and (b) BCC crystals (data points – experimental; lines – calculated). In each of these figures a, b, c, and d refer to  $E_{111}/E_{100}$ ,  $E_{110}/E_{100}$ ,  $G_{(111)}/G_{(100)}$ , and  $G_{(100)[110]}/G_{(100)}$ , respectively. (From T. Milstein and T. Marschall, *Acta Mater.*, 40 (1992) 1229.)

Young's modulus over a certain temperature range. Such an alloy is Elinvar (36% Ni, 12% Cr, 1 to 2% Si, 0.8% C, balance Fe), and it has an essentially constant  $E$  between 15 and 40 °C; it is ideal for springs in watches and other precision instruments.

The crystal structure has a very marked effect on the elastic anisotropy of crystals. The standard ordering of Young's moduli in FCC and BCC crystals is:

$$E_{111} > E_{110} > E_{100},$$

where the subscripts indicate the cubic axes.

This was clearly seen earlier in Figure 2.9(a), for copper. For simple cubic crystals, the ordering is:

$$E_{100} > E_{110} > E_{111}.$$

This corresponds to the elastic moduli of cubic zirconia, as was seen in Figure 2.9(b). The bonding of atoms along different crystallographic orientations has been correlated with the relative values of Young's moduli.

Milstein and Marschall<sup>19</sup> defined a parameter,  $\delta$ , which is a measure of the strength of the second-neighbor interaction compared with that of the nearest-neighbor interaction. The moduli ratios for FCC and BCC materials as a function of this parameter are shown on Figure 2.43(a) and (b), respectively. We plot ratios  $E_{111}/E_{100}$ ,  $E_{110}/E_{100}$ ,  $G_{(111)}/G_{(100)}$ , and  $G_{(100)[110]}/G_{(100)}$ . Note that among FCC, aluminium has

<sup>19</sup> T. Milstein and T. Marschall, *Acta Mater.*, 40 (1992) 1229.

the least anisotropy; for BCC, W is at the interaction of all curves, corresponding to a ratio of 1, i.e., perfect isotropy. The ratios for Young's moduli values range from 3.2 to 1 for FCC structures and from 8 to 0 for BCC structures. The important conclusion is that second-neighbor interactions are very important in determining these ratios.

The Poisson's ratios ( $\nu$ ) for monocrystals has values that range widely, and can be quite different from the polycrystalline values ( $\sim 0.3$ ). These values vary much more than the bounds calculated earlier for isotropic materials ( $0 < \nu < 0.5$ ).

## Suggested Reading

- Y. C. Fung. *A First Course in Solid Mechanics*, 2nd. ed. Upper Saddle River, NJ: Prentice Hall, 1997.
- H. B. Huntington. *The Elastic Constants of Crystals*. New York, NY: Academic Press, 1958.
- A. Kelly and G. W. Groves. *Crystallography and Crystal Defects*. Reading, MA: Addison-Wesley, 1970.
- J. Lemaître, and J.-L. Chaboche. *Mechanics of Solid Materials*. Cambridge, U.K.: Cambridge University Press, 1990.
- A. E. H. Love. *The Mathematical Theory of Elasticity*. New York, NY: Dover, 1952.
- F. A. McClintock and A. S. Argon, eds. *Mechanical Behavior of Materials*. Reading, MA: Addison-Wesley, 1966.
- J. F. Nye. *Physical Properties of Crystals*. London: Oxford University Press, 1957.
- G. Simmons and H. Wang. *Single Crystal Elastic Constants*. Cambridge, MA: MIT Press, 1971.
- I. S. Sokolnikoff. *Mathematical Theory of Elasticity*, 2nd ed. New York, NY: McGraw-Hill, 1956.
- S. Timoshenko and J. N. Goodier. *Theory of Elasticity*. New York, NY: McGraw-Hill, 1951.
- L. R. G. Treloar. *The Physics of Rubber Elasticity*, 3d ed. Oxford, U.K.: Clarendon Press, 1975.

## Exercises

**2.1** Rubber specimens, having an initial length of 5 cm, are tested, one in compression and one in tension. If the engineering strains are  $-1.5$  and  $+1.5$ , respectively, what will be the final lengths of the specimens? What are the true strains, and why are they numerically different?

**2.2** An aluminum polycrystalline specimen is elastically compressed in plane strain. If the true strain along the compression direction is  $-2 \times 10^{-4}$ , what are the other two longitudinal strains?

**2.3** Determine  $K$ ,  $\lambda$ , and  $G$  for polycrystalline niobium, titanium, and iron, from  $E$  and  $\gamma$ .

**2.4** A state of stress is given by

$$\sigma_{11} = 250 \text{ MPa},$$

$$\sigma_{12} = 70 \text{ MPa},$$

$$\sigma_{22} = 310 \text{ MPa}.$$

Determine the principal stresses and the maximum shear stress, as well as their angle with the system of reference.

**2.5** Calculate the anisotropy ratio for the cubic metals in Table 2.3.

**2.6** Show that a uniaxial compressive stress can be decomposed into a hydrostatic pressure and two states of pure shear. Use sketches if necessary.

**2.7** Determine the principal stresses and the maximum shear stress, as well as their angles with the system of reference given by the following stress state:

$$[\sigma_{ij}] = \begin{pmatrix} 3 & 2 \\ 2 & 0 \end{pmatrix} \text{ MPa.}$$

**2.8** Extensometers attached to the external surface of a steel pressure vessel indicate that  $\varepsilon_t = 0.002$  and  $\varepsilon_f = 0.005$  along the longitudinal and transverse directions, respectively. Determine the corresponding stresses. What would be the error if Poisson's ratio were not considered?

**2.9** Calculate Young's and shear moduli for monocrystalline iron along [100], [110], and [111].

**2.10** From the values obtained in Exercise 2.9, obtain a rough estimate of the Young's modulus of a polycrystalline aggregate, assuming that there are only three orientations for the grains ([100], [110], and [111]) and that they occur proportionally to their multiplicity factors. Compare your result with the predictions of Voigt averages (isostrain) and Reuss averages (isostress).

**2.11** A silver monocrystal is extended along [100]. Obtain the values for the Young's and shear moduli, as well as Poisson's ratio.

**2.12** (a) For Figure 2.25, plot the curve of true stress vs. true strain. (b) Taking the slopes of the curve at various strains, plot the elastic modulus of rubber as a function of strain. (c) Schematically draw polymer chains at different positions in the curve.

**2.13** A steel specimen is subjected to elastic stresses represented by the matrix

$$\sigma_{ij} = \begin{pmatrix} 2 & -3 & 1 \\ -3 & 4 & 5 \\ 1 & 5 & -1 \end{pmatrix} \text{ MPa.}$$

Given that  $E = 200$  GPa,  $\nu = 0.3$ , calculate the corresponding strains.

**2.14** Ultrasonic equipment was used to determine the longitudinal and shear sound velocities of a metallic specimen having a density of  $7.8 \text{ g/cm}^3$ . The values obtained are

$$V_e = 5,300 \text{ m/s},$$

$$V_s = 3,300 \text{ m/s}.$$

Determine the Young's and shear moduli and Poisson's ratio for this material. What is the material?

**2.15** A tubular specimen is being subjected to a torsional moment  $T = 600 \text{ Nm}$ . If the shear modulus of the material (Al) is equal to  $26.1 \text{ GPa}$ , what

is the total angular deflection if the length is 1 m? The tube has a diameter of 5 cm and a wall thickness of 0.5 cm. Assume the process to be elastic.

**2.16** Using the Mohr circle construction, calculate the principal stresses and the maximum shear stresses, as well as their orientation, for the sheet subjected to the stresses shown in Figure Ex2.16.

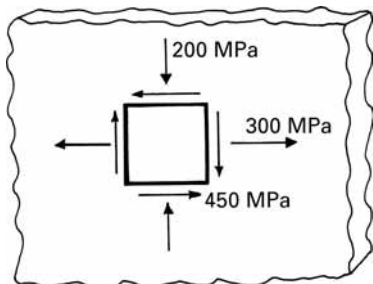


**Fig. Ex2.16**

**2.17** A state of stress is given by

$$\sigma_{11} = -500 \text{ MPa},$$

$$\sigma_{22} = 300 \text{ MPa},$$

$$\sigma_{12} = 150 \text{ MPa}.$$

Determine the principal stresses and the maximum shear stress, as well as their orientation, using the Mohr circle construction.

**2.18** From the elastic stiffnesses for copper (see Table 2.3), determine the elastic compliances.

**2.19** From the elastic compliances  $S_{11}$ ,  $S_{12}$ , and  $S_{14}$  for iron and tungsten, determine the Young's moduli along [111], [110], and [100].

**2.20** Determine the elastic Young's moduli for tungsten and  $\text{ZrO}_2$  along [112], [122], and [123].

**2.21** Determine the polycrystalline Young's modulus for molybdenum using Reuss's and Voigt's averages. Use elastic stiffnesses and compliances from Tables 2.3 and 2.4.

**2.22** Consider a bar made of steel with a cross-sectional area of  $25 \text{ cm}^2$  and length of 20 cm. If we apply a load of 500 N along its length, what is the strain energy density. Take  $E = 210 \text{ GPa}$ .

**2.23** Derive an expression for the strain energy stored in a circular bar of length  $L$  subjected to a torque,  $T$ , along its axis. Recall that the shear stress resulting from the torque  $T$  is given by  $\tau = Tr/J$ , where  $r$  is the distance from the centroid of the cross section and  $J$  is the polar moment of inertia. Use  $G$  as the shear modulus of the material.

**2.24** Plot Young's modulus as a function of porosity for alumina, and show what the value should be for a specimen having 5% porosity ( $E_{\text{Al}_2\text{O}_3} = 378 \text{ GPa}$ ).

**2.25** A specimen of  $\text{Al}_2\text{O}_3$  contains microcracks that are approximately equal to its grain size ( $20 \mu\text{m}$ ). One grain in each 10 grains contains cracks. If the uncracked materials has  $E_0 = 378 \text{ GPa}$ , determine Young's modulus for the

cracked material by use of Budiansky and O'Connell's and Salganik's equations.

**2.26** Young's modulus ( $E$ ) of a cubic single crystal as a function of orientation is given by

$$\frac{1}{E_{hkl}} = \frac{1}{E_{100}} - 3 \left( \frac{1}{E_{100}} - \frac{1}{E_{111}} \right) (\ell_1^2 \ell_2^2 + \ell_2^2 \ell_3^2 + \ell_3^2 \ell_1^2),$$

where  $\ell_1$ ,  $\ell_2$ , and  $\ell_3$  are the direction cosines between the direction  $hkl$  and [100], [010], and [001], respectively. This is another version of the expression given in Example 2.10. For copper,  $E_{111} = 19$  GPa and  $E_{100} = 66$  GPa. Calculate Young's modulus for a copper single crystal in the [110] direction, and check your answer against the one in Example 2.10.

**2.27** A polymer has a viscosity of  $10^{12}$  Pa, at  $150$  °C. If this polymer is subjected to a tensile stress of  $100$  MPa at that temperature, compute the deformation after  $10$  h. Assume the polymer to behave as a Maxwell solid. Take  $E = 5$  GPa, and use the equation

$$\varepsilon_1 = \frac{\sigma}{E} + \frac{1}{3\eta} \sigma t.$$

**2.28** For a given polymer, the activation energy for stress relaxation was measured to be  $10$  kJ/mol. If the stress relaxation time for this polymer at room temperature is  $3,600$  s, what would be the relaxation time at  $100$  °C?

**2.29** For an elastomeric material, we have the constitutive equation

$$\sigma = G \left( \lambda - \frac{1}{\lambda^2} \right) = \frac{E}{3} \left[ \lambda - \frac{1}{\lambda^2} \right],$$

where  $E$  is the elastic modulus at zero elongation. Show that, for very small strains, this equation reduces to  $\sigma = E\varepsilon$ .

**2.30** A cylindrical aluminum specimen (length =  $100$  mm, diameter =  $10$  mm) is subjected to a torque equal to  $40$  Nm. If one end of the specimen is fixed what is the deflection of the other end? Take  $E = 70$  GPa and  $v = 0.3$ .

**2.31** A steel bolt has  $12$  threads per mm. If the nut is tightened by one turn, what stress will be generated in the steel bolt and aluminium sleeve? The bolt diameter is  $10$  mm and the sleeve thickness is  $2$  mm.

**2.32** Calculate Young's modulus for rubber with a density of  $1000$  g/mol and having intercross-link segments with a molecular weight of  $2000$  g/mol.

**2.33** Describe dilation that occurs in the elastic deformation of a solid. Give a mathematical expression in terms of strain components.

**2.34** Consider a solid subjected to hydrostatic pressure,  $p$ , that results in a dilation or volumetric strain given by

$$\Delta V/V = \varepsilon_p.$$

The bulk modulus,  $K$ , is defined by the ratio  $p/\varepsilon_p$ . By use of the generalized Hooke's law, show that

$$K = E/3(1 - 2\nu),$$

where  $E$  is the Young's modulus and  $\nu$  is the Poisson's ratio.

**2.35**

- (a) Compute the Poisson's ratio for a material that is undergoing a uniaxial tensile test with zero dilation.
- (b) A student was given three different unidentified materials to determine their Poisson's ratio. She determined the Poisson's ratios to be 0.5, 0.3, and 0. She needs your help in identifying the class of material for each of these  $\nu$  values.

**2.36** Discuss the advantages and disadvantages of Al, Ti, and Vitalium for use in total hip replacement prostheses.

**2.37** From Table 2.5, estimate the theoretical shear and cleavage strength for nickel and titanium.

**2.38** From Table 2.5, estimate the theoretical shear and cleavage strength for magnesium and niobium.

**2.39** From Table 2.3 find the elastic compliances for nickel.

**2.40** From Table 2.3 find the elastic compliances for aluminum.

**2.41** Plot the stress-strain curve for alumina in tension, knowing that the density of microcracks increases linearly with stress ( $N = k\sigma$ ). The grain size is 30  $\mu\text{m}$  and the failure stress is 1 GPa;  $k = 5.45 \times 10^4 \text{ m}^3/\text{Pa}$ ,  $E_0 = 380 \text{ GPa}$ .

**2.42** The following are given for tantalum:

$$C_{11} = 267 \text{ GPa},$$

$$C_{44} = 82.5 \text{ GPa},$$

$$C_{12} = 161 \text{ GPa. E}$$

Determine the Young's moduli in the directions [100], [110], and [111] after calculating the elastic compliances.

**2.43** The following values are given for niobium:

$$E = 105 \text{ GPa},$$

$$\nu = 0.4.$$

Calculate the values of  $G$ ,  $B$ ,  $K$ , and  $\lambda$ .

**2.44** Plot the engineering stress-engineering strain curve for a rubber at ambient temperature and liquid nitrogen temperature, up to a strain of 10, using the Equation 2.48. The number of chain segments per unit volume ( $\text{m}^3$ ) is  $2 \times 10^{25}$ .

**2.45** From the elastic stiffness for a cubic material, Nb ( $C_{11} = 242 \text{ GPa}$ ,  $C_{12} = 129 \text{ GPa}$ ,  $C_{44} = 286 \text{ GPa}$ ), find the elastic compliances.

**2.46** The potential energy of a  $\text{Na}^+$   $\text{Cl}^-$  ion pair at the distance  $r$  is given by:

$$U = U_i - \frac{q^2}{4\pi\epsilon_0 r} + \frac{B}{r^9},$$

where  $q = 1.6 \times 10^{-19} \text{ C}$  is the electronic charge,  $\epsilon_0 = 8.85 \times 10^{-12} \text{ C}^2/\text{Nm}^2$  is the permittivity of vacuum, and  $U_i = 1.12 \text{ eV}$  is the reference energy of two infinitely separated ions. If the equilibrium distance between the ions is  $r_0 = 0.276 \text{ nm}$ , calculate:

- (a) the value of the constant  $B$ ;
- (b) the total force between ions, and its attractive and repulsive portions, when  $r = 0.25 \text{ nm}$ ;

- (c) the total force between ions, and its attractive and repulsive portions, when  $r=0.3$  nm;
- (d) the potential energy between two ions when they are at a distance  $r=1$  nm.

**2.47** The potential energy of two atoms, a distance  $r$  apart, is

$$U = -\frac{A}{r^m} + \frac{B}{r^n}.$$

Given that the atoms form a stable molecule at a separation  $r=r_0$ , with a binding energy  $U=U_0$ , derive:

- (a) the expressions for the constants  $A$  and  $B$  in terms of  $m$ ,  $n$ ,  $r_0$ , and  $U_0$ ;
- (b) the expressions for the stiffness  $S$  of the bond at arbitrary  $r$  and at  $r_0$ ;
- (c) the expression for the distance  $r^*$  of the maximum tensile force (needed to break the bond between atoms), and the expression for that force ( $F^*$ );
- (d) Given that  $m=2$ ,  $n=10$ , and that the atoms form a stable molecule at a separation  $r_0=0.3$  nm, with a binding energy  $U_0=-4$  eV, evaluate  $A$ ,  $B$ ,  $r^*$ ,  $F^*$ , and the stiffness  $S_0$  of the bond at  $r=r_0$ .

**2.48** Plot the stress-strain curve for SiC in tension, knowing that the density of microcracks increases linearly with stress ( $N=k\sigma$ ). The grain size is 20  $\mu\text{m}$ . The failure stress is 1 GPa; given:  $k=5.45 \times 10^4$   $\text{m}^3/\text{Pa}$ ,  $E_0=420$  GPa.

**2.49** Derive the expression:

$$G = \frac{E}{2(1+\nu)}.$$

The symbols have their usual significance.

**2.50** Describe the microscopic changes that occur during the solidification and cooling process of a partly crystalline thermoplastic as it encounters the glass transition regimen.

**2.51** From the data on elastic stiffness and compliances for HCP zirconium (Tables 2.3 and 2.4), determine the elastic stiffness,  $C_{13}$ , missing in Table 2.3.

**2.52** Using the elastic stiffness of tin (exhibiting a tetragonal structure) given in Table 2.3, find the elastic compliances.

**2.53**

- (a) Describe the internal structure of an artery, and state the importance of its components to the mechanical response.
- (b) Explain how you would go about developing an artificial blood vessel, taking into account materials selection and properties, the harsh environment within the body, and biocompatibility.

---

# Chapter 3

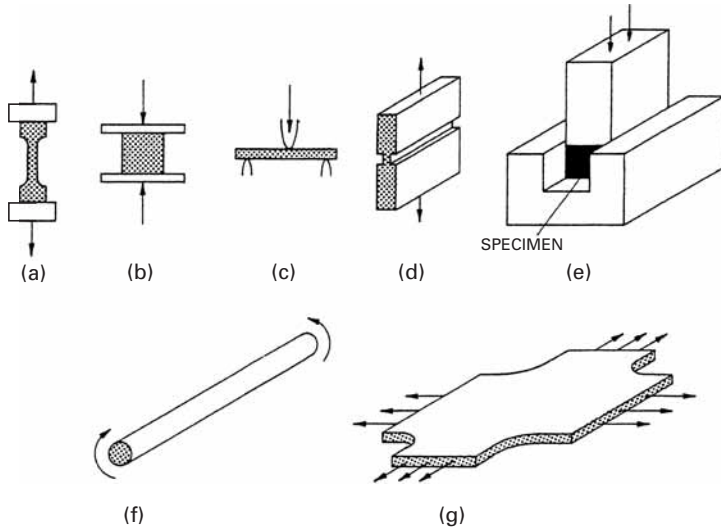
## Plasticity

### 3.1 | Introduction

Upon being mechanically stressed, a material will, in general, exhibit the following sequence of responses: elastic deformation, plastic deformation, and fracture. This chapter addresses the second response: plastic deformation. A sound knowledge of plasticity is of great importance for the following reasons.

- Many projects are executed in which small plastic deformations of the structure are accepted. The “theory of limit design” is used in applications where the weight factor is critical, such as space vehicles and rockets. The rationale for accepting a limited plastic deformation is that the material will work-harden at that region, and plastic deformation will cease once the flow stress (due to work-hardening) reaches the applied stress.
- It is very important to know the stresses and strains involved in deformation processing, such as rolling, forging, extrusion, drawing, and so on. All these processes involve substantial plastic deformation, and the response of the material will depend on its plastic behavior during the processes. The application of plasticity theory to such processes is presented later in this chapter.
- The mechanism of fracture can involve plastic deformation at the tip of a crack. The way in which the high stresses that develop at the crack can be accommodated by the surrounding material is of utmost importance in the propagation of the crack. A material in which plastic deformation can take place at the crack is “tough,” while one in which there is no such deformation is “brittle.”
- The stress at which plastic deformation starts is dependent upon the stress state. A material can have a much greater strength when it is confined – that is, when it is not allowed to flow laterally – than when it is not confined. This will be discussed in detail later. A number of criteria for plastic deformation and fracture will be examined in this chapter.

**Fig. 3.1** Common tests used to determine the monotonic strength of materials. (a) Uniaxial tensile test. (b) Upsetting test. (c) Three-point bending test. (d) Plane-strain tensile test. (e) Plane-strain compression (Ford) test. (f) Torsion test. (g) Biaxial test.



The mechanical strength of a material under a steadily increasing load can be determined in uniaxial tensile tests, compression (upsetting) tests, bend tests, shear tests, plane-strain tensile tests, plane-strain compression (Ford) tests, torsion tests, and biaxial tests. The uniaxial tensile test consists of extending a specimen whose longitudinal dimension is substantially larger than the two lateral dimensions (Figure 3.1(a)). The upsetting test consists of compressing a cylinder between parallel platens; the height/diameter ratio has to be lower than a critical value in order to eliminate the possibility of instability (buckling) (Figure 3.1(b)). After a certain amount of strain, “barreling” takes place, destroying the state of uniaxial compression. The three-point bend test is one of the most common bending tests. A specimen is simply placed between two supports; a wedge advances and bends it through its middle point (Figure 3.1(c)). Plane-strain tests simulate the conditions encountered by a metal in, for instance, rolling. Loading is imparted in such a way as to result in zero strain along one direction. The two most common geometries are shown in Figure 3.1(d) and (e). In the tensile mode, two grooves are made parallel to each other, on opposite sides of a plate. The width of the plate is much greater than its thickness in the region of reduced thickness; hence, flow is restricted in the direction of the width. In the compressive mode (Ford test), a parallelepiped of metal is machined and inserted between the groove-and-punch setup of Figure 3.1(e). As the top punch is lowered, the specimen is plastically deformed. Strain is restricted in one direction. In the torsion test (Figure 3.1(f)), the cylindrical (or tubular) specimen is subjected to a torque and undergoes an attendant angular displacement. One of the problems in the analysis of the torsion test is that the stress varies as the distance from the central axis of the specimen. Accordingly, the biaxial test is usually applied to thin sheets, and one of the configurations is shown



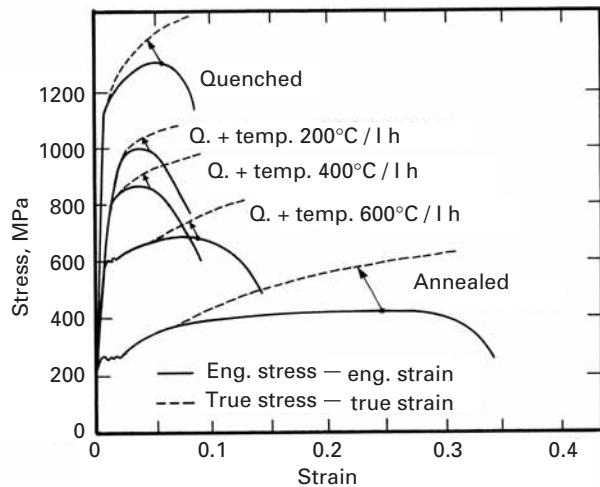
**Fig. 3.2** A servohydraulic universal testing machine linked to a computer. (Courtesy of MTS Systems Corp.)

in Figure 3.1(g). Other configurations involve testing a tubular specimen in tension with an internal pressure and testing a tubular specimen in tension with torsion. The results of the tests just described can be expressed graphically as stress-versus-strain curves. They can be compared directly by using effective stresses and effective strains. A machine commonly used to carry out the tests is the so-called universal testing machine. Both screw-driven (Figure 2.1) and servohydraulic machines are very useful for mechanical testing. Figure 3.2 shows a typical servohydraulic testing machine.

## 3.2 | Plastic Deformation in Tension

Figure 3.3 shows a number of stress-strain curves for the same material: AISI 1040 steel. This might look surprising at first, but it merely reflects the complexity of the microstructural-mechanical behavior interactions. Both engineering and true stress-strain curves are shown. (The definitions of these are given in Chapter 2.) Engineering (or nominal) stress is defined as  $P/A_0$ , while true stress is  $P/A$ , where  $A_0$  and  $A$  are the initial and current cross-sectional areas, respectively. Engineering (or nominal) strain is defined as  $\Delta L/L_0$ , while true strain is  $\ln L/L_0$ , where  $L$  and  $L_0$  are the current and initial lengths,

**Fig. 3.3** Stress-strain curves for AISI 1040 steel subjected to different heat treatments; curves obtained from tensile tests.



respectively. The yield stress varies from 250 to 1,100 MPa, depending on the heat treatment. Conversely, the total strain varies from 0.38 to 0.1. The properties of steel are highly dependent upon heat treatment, and quenching produces a hard, martensitic structure, which is gradually softened by tempering treatments at higher temperatures (200, 400, and 600 °C). The annealed structure is ductile, but has a low yield stress. The ultimate tensile stresses (the maximum engineering stresses) are marked by arrows. After these points, plastic deformation becomes localized (called *necking*), and the engineering stresses drop because of the localized reduction in cross-sectional area. However, the true stress continues to rise because the cross-sectional area decreases and the material work-hardens in the neck region. The true-stress-true-strain curves are obtained by converting the tensile stress and its corresponding strain into true values and extending the curve.

We know that the volume  $V$  is constant in plastic deformation:

$$V = A_0 L_0 = A L .$$

Consequently,

$$A = \frac{A_0 L_0}{L} . \quad (3.1)$$

In what follows, we use the subscripts  $e$  and  $t$  for engineering (nominal) and true stresses and strains, respectively. We have

$$\varepsilon_e = \frac{L - L_0}{L_0} = \frac{A_0}{A} - 1 , \quad (3.2)$$

$$\frac{\sigma_t}{\sigma_e} = \frac{P}{A} \times \frac{A_0}{P} = \frac{A_0}{A} = 1 + \varepsilon_e , \quad (3.3)$$

$$[\sigma_t = (1 + \varepsilon_e)\sigma_e .] \quad (3.4)$$

On the other hand, the incremental longitudinal true strain is defined as

$$d\varepsilon_t = \frac{dL}{L}. \quad (3.5)$$

For extended deformations, integration is required:

$$\varepsilon_t = \int_{L_0}^L \frac{dL}{L} = \ln \frac{L}{L_0}, \quad (3.6)$$

$$\exp(\varepsilon_t) = \frac{L}{L_0}. \quad (3.7)$$

Substituting Equations 3.2 and 3.3 into Equation 3.7, we get

$$\sigma_t = \frac{P}{A_0} \exp(\varepsilon_t). \quad (3.8)$$

Engineering (or nominal) stresses and strains are commonly used in tensile tests, with the double objective of avoiding complications in the computation of  $\sigma$  and  $\varepsilon$  and obtaining values that are more significant from an engineering point of view. Indeed, the load-bearing ability of a beam is better described by the engineering stress, referred to the initial area  $A_0$ . It is possible to correlate engineering and true values.

From Equations 3.4 and 3.8, the following relationship is obtained:

$$\boxed{\varepsilon_t = \ln(1 + \varepsilon_e)} \quad (3.9)$$

All of the preceding curves, as well as other ones, are represented schematically by simple equations in various ways. Figure 3.4 shows four different idealized shapes for stress-strain curves. Note that these are true-stress-true-strain curves. When we have a large amount of plastic deformation, the plastic strain is large with respect to the elastic strain, and the latter can be neglected. If the material does not work-harden, the plastic curve is horizontal, and the idealized behavior is called perfectly plastic. This is shown in Figure 3.4(a). If the plastic deformation is not so large, the elastic portion of the curve cannot be neglected, and one has an ideal elastoplastic material (Figure 3.4(b)). A further approximation to the behavior of real materials is the ideal elastoplastic behavior depicted in Figure 3.4(c); this is a linear curve with two slopes  $E_1$  and  $E_2$  that represent the material's elastic and plastic behavior, respectively. One could represent the behavior of the steels in Figure 3.3 fairly well by this elastoplastic, linear work-hardening behavior. It can be seen that  $E_2 \ll E_1$ . For example, for annealed steel,  $E_2 \approx 70$  MPa, while  $E_1 = 210$  GPa. However, a better representation of the work-hardening behavior is obtained by assuming a gradual decrease in the slope of the curve as plastic deformation proceeds (shown in Figure 3.4(d)). The convex

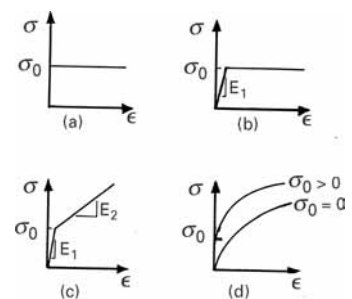


**Fig. 3.4** Idealized shapes of uniaxial stress-strain curve. (a) Perfectly plastic. (b) Ideal elastoplastic. (c) Ideal elastoplastic with linear work-hardening. (d) Parabolic work-hardening ( $\sigma = \sigma_0 + K\varepsilon^n$ ).

shape of the curve is well represented by an equation of the type

$$\sigma = K \varepsilon^n, \quad (3.10)$$

where  $n < 1$ . This response is usually called “parabolic” hardening, and one can translate it upward by assuming a yield stress  $\sigma_0$ , so that Equation 3.10 becomes

$$\boxed{\sigma = \sigma_0 + K \varepsilon^n.} \quad (3.11)$$

The exponent  $n$  is called the work-hardening coefficient.

These equations that describe the stress-strain curve of a polycrystalline metal are known as the Ludwik-Hollomon equations.<sup>1</sup> In them,  $K$  is a constant, and the exponent  $n$  depends on the nature of the material, the temperature at which it is work-hardened, and the strain. The exponent  $n$  generally varies between 0.2 and 0.5, while the value of  $K$  varies between  $G/100$  and  $G/1,000$ ,  $G$  being the shear modulus. In Equation 3.11  $\varepsilon$  is the true plastic strain, while in Equation 3.10  $\varepsilon$  is true total strain. Equations 3.11 and 3.10 describe parabolic behavior. However, such a description is valid only in a narrow stretch of the stress-strain curve. There are two reasons for this. First, the equations predict a slope of infinity for  $\varepsilon = 0$ , which does not conform with the experimental facts. Second, the equations imply that  $\sigma \rightarrow \infty$  when  $\varepsilon \rightarrow \infty$ . But we know that this is not correct and that, experimentally, a saturation of stress occurs at higher strains.

Voce<sup>2</sup> introduced a much different equation,

$$\boxed{\frac{\sigma_s - \sigma}{\sigma_s - \sigma_0} = \exp\left(-\frac{\varepsilon}{\varepsilon_c}\right),} \quad (3.12)$$

where  $\sigma_s$ ,  $\sigma_0$ , and  $\varepsilon_c$  are empirical parameters that depend on the material, the temperature, and the strain rate. This equation says that the stress exponentially reaches an asymptotic value of  $\sigma_s$  at higher strain values. Furthermore, it gives a finite slope to the stress-strain curve at  $\varepsilon = 0$  or  $\sigma = \sigma_0$ .

It should be noted that the parameters in the preceding equations (3.10 to 3.12) depend on the choice of the initial stress and/or strain. For instance, if one prestrained a material, one would affect  $K$  in the Ludwik-Hollomon equation.

The fact that some equations reasonably approximate the stress-strain curves does not imply that they are capable of describing the curves in a physically satisfactory way. There are two reasons for this: (1) In the different positions of stress-strain curves, different microscopic processes predominate. (2) Plastic deformation is a complex

<sup>1</sup> See P. Ludwik, *Elemente der Technologischen Mechanik* (Berlin: Springer, 1909), p. 32; and J. H. Hollomon, *Trans. AIME*, 162 (1945) 268.

<sup>2</sup> E. Voce, *J. Inst. Met.*, 74 (1948) 537.

physical process that depends on the path taken; it is not a thermodynamic state function. That is to say, the accumulated plastic deformation is not uniquely related to the dislocation structure of the material. This being so, it is not very likely that simple expressions could be derived for the stress-strain curves in which the parameters would have definite physical significance.

Some alloys, such as stainless steels, undergo martensitic phase transformations induced by plastic strain. This type of transformation alters the stress-strain curve. (See Chapter 11.) Other alloys undergo mechanical twinning beyond a threshold stress (or strain), which affects the shape of the curve. In these cases, it is necessary to divide the plastic regimen into stages. It is often useful to plot the slope of the stress-strain curve vs. stress (or strain) to reveal changes in mechanism more clearly.

In spite of its limitations, the Ludwik-Hollomon Equation 3.11 is the most common representation of plastic response. When  $n=0$ , it represents ideal plastic behavior (no work-hardening). More general forms of this equation, incorporating both strain rate and thermal effects, are often used to represent the response of metals; in that case they are called *constitutive equations*. As will be shown in Chapter 6, the flow stress of metals increases with increasing strain rate and decreasing temperature, because thermally activated dislocation motion is inhibited.

The Johnson-Cook equation

$$\sigma = (\sigma_0 + K \varepsilon^n) \left( 1 + C \ln \frac{\dot{\varepsilon}}{\dot{\varepsilon}_0} \right) \left[ 1 - \left( \frac{T - T_r}{T_m - T_r} \right)^m \right] \quad (3.13)$$

is widely used in large-scale deformation codes. The three groups of terms in parentheses represent work-hardening, strain rate, and thermal effects, respectively. The constants  $K$ ,  $n$ ,  $C$ , and  $m$  are material parameters, and  $T_r$  is the reference temperature,  $T_m$  the melting point, and  $\dot{\varepsilon}_0$  the reference strain rate. There are additional equations that incorporate the microstructural elements such as grain size and dislocation interactions and dynamics: they are therefore called “physically based.” The most common ones are the Zerilli-Armstrong<sup>3</sup> and the MTS (materials threshold stress, developed at Los Alamos National Laboratory) equations. The basic idea is to develop one equation that represents the mechanical response of a material from 0 K to 0.5  $T_m$  and from very low strain rates ( $\sim 10^{-5}$  s<sup>-1</sup>) to very high strain rates ( $\sim 10^5$  s<sup>-1</sup>). Nevertheless, three factors throw monkey wrenches into these equations: creep (see Chapter 13), fatigue (Chapter 14), and environmental effects (Chapter 16). The effects of these factors are very complex and cannot be simply “plugged into” the equations.

<sup>3</sup> See F. Zerilli and R. W. Armstrong, *J. Appl. Phys.*, 68 (1990) 1580.

### Example 3.1

For the stress-strain curve shown in Figure E3.1.1 (tantalum tested at strain rate of  $10^{-4} \text{ s}^{-1}$ ), obtain the parameters of the Ludwik-Hollomon equation. Estimate the duration of the test in seconds.

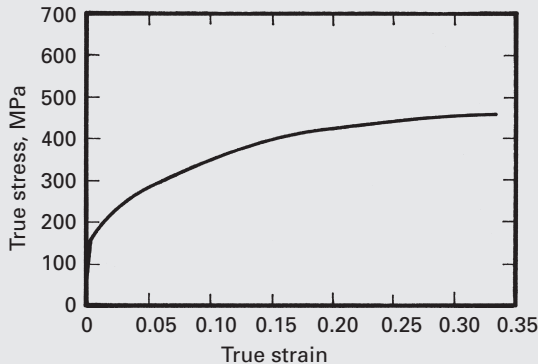


**Fig. E3.1.1**

**Solution:** From the  $\sigma - \varepsilon$  curve, we have

$$\sigma_0 = 160 \text{ MPa}.$$

We use the Ludwik-Hollomon equation

$$\sigma - \sigma_0 = K \varepsilon^n,$$

so that

$$\log(\sigma - \sigma_0) = \log K + n \log \varepsilon,$$

which is a linear equation. We then make a plot of  $\log(\sigma - \sigma_0)$  vs  $\log \varepsilon$  (shown in Figure E3.1.2) from the following table of values.

$\sigma$	$\varepsilon$	$\log(\sigma - \sigma_0)$	$\log \varepsilon$
280	0.05	2.08	-1.3
345	0.1	2.27	-1
385	0.15	2.35	-0.82
415	0.2	2.41	-0.70
435	0.25	2.44	-0.60
455	0.3	2.47	-0.52

From the new plot, we have

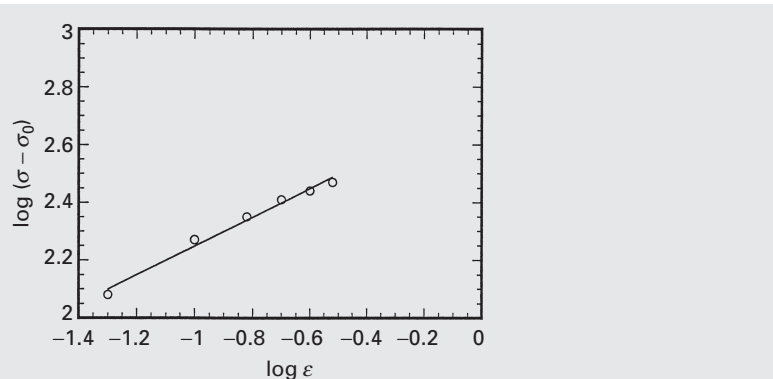
$$\log K = 2.75,$$

$$K = 589,$$

$$n = \text{slope} \approx 0.5.$$

Substituting  $K$  and  $n$  into the Ludwik-Hollomon equation yields

$$\sigma = 160 + 589\varepsilon^{0.5} \text{ (in MPa).}$$

**Fig. E3.1.2**

The duration of the test, given that

$$\begin{aligned}\dot{\varepsilon} &= 10^{-4} \text{ s}^{-1} \\ &= \frac{d\varepsilon}{dt} \approx \frac{\Delta\varepsilon}{\Delta t},\end{aligned}$$

is

$$\begin{aligned}\Delta t &= \frac{\Delta\varepsilon}{\dot{\varepsilon}} \approx \frac{0.33}{10^{-4}} \\ &= 3.3 \times 10^3 \text{ s}.\end{aligned}$$

The volume of a material is assumed to be constant in plastic deformation. It is known that such is not the case in elastic deformation. As was shown in Section 2.5, the constancy in volume implies that

$$\varepsilon_{11} + \varepsilon_{22} + \varepsilon_{33} = 0$$

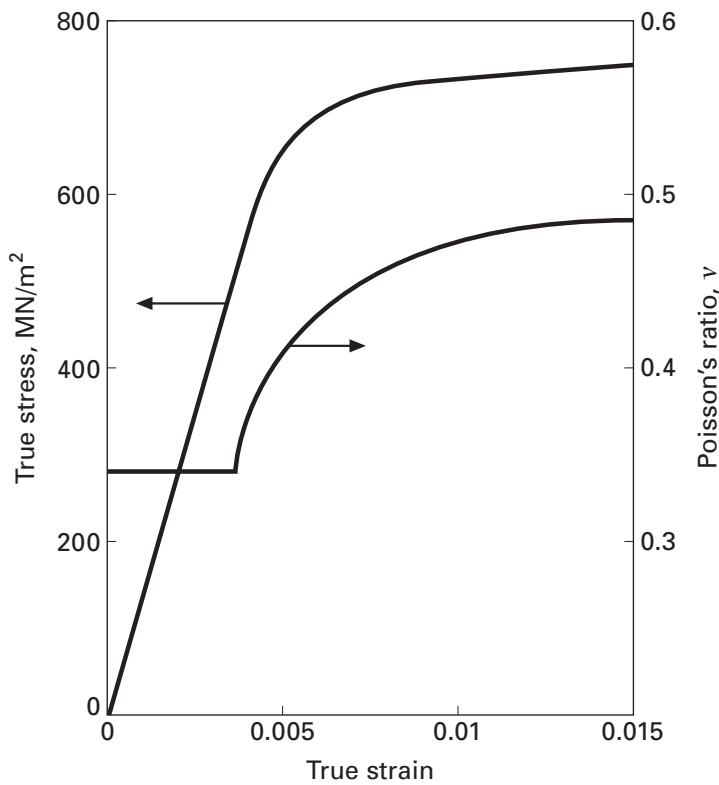
or

$$\varepsilon_1 + \varepsilon_2 + \varepsilon_3 = 0 \quad (3.14)$$

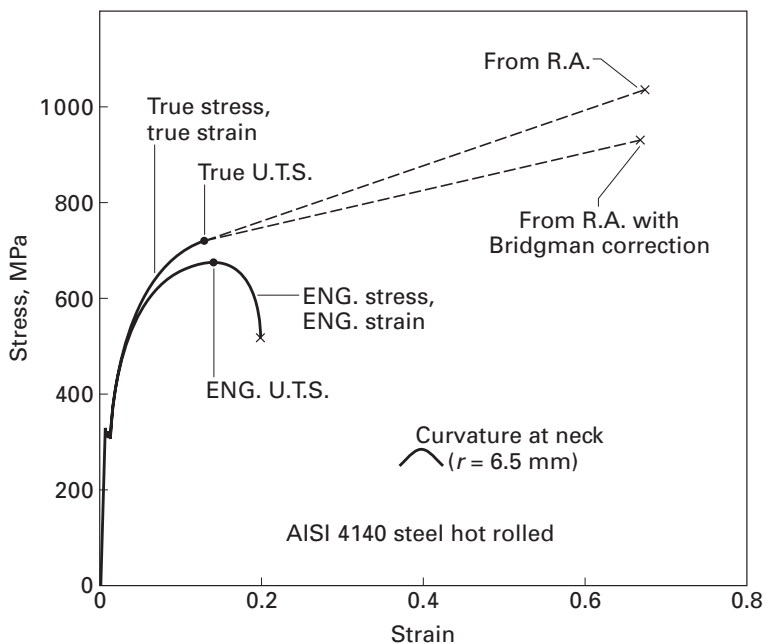
and that Poisson's ratio is 0.5. Figure 3.5 shows that this assumption is reasonable and that  $\nu$  rises from 0.3 to 0.5 as deformation goes from elastic to plastic.

However, prior to delving into the plasticity theories, we have to know, for a complex state of stress, the stress level at which the body starts to flow plastically. The methods developed to determine this are called *flow criteria* (see Section 3.7). Figure 3.6 shows engineering- and true-stress-strain curves for the same hot-rolled AISI 4140 steel. In the elastic regimen the coincidence is exact, because strains are very small ( $\sim 0.5\%$ ). From Equation 3.9, we can see that we would have  $\varepsilon_e \approx \varepsilon_t$ . As plastic deformation increases,  $\varepsilon_t$  and  $\varepsilon_e$  become progressively different. For  $\varepsilon_t = 0.20$  (a common value for metals), we have  $\varepsilon_e = 0.221$ . For this deformation, the true stress is 22.1% higher than the nominal one. It can be seen that these differences become greater with increasing plastic deformation. Another *basic* difference between

**Fig. 3.5** Change in Poisson's ratio as the deformation regimen changes from elastic to plastic.



**Fig. 3.6** True- and engineering-stress-strain curves for AISI 4140 hot-rolled steel. R. A. is reduction in area.



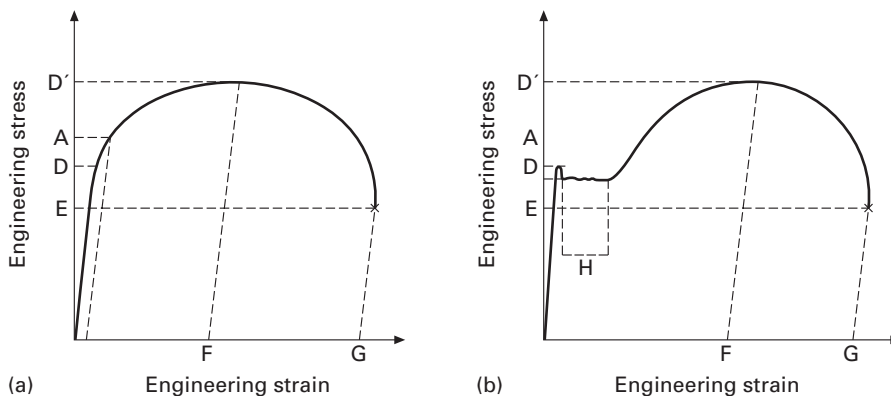


**Fig. 3.7** Engineering- (or nominal-) stress–strain curves (a) without and (b) with a yield point.

the two curves is the decrease in the engineering stress beyond a certain value of strain ( $\sim 0.14$  in Figure 3.6). This phenomenon is described in detail in Section 3.2.2.

### 3.2.1 Tensile Curve Parameters

Figure 3.7 shows two types of engineering stress–strain curves. The first does not exhibit a yield point, while the second does. Many parameters are used to describe the various features of these curves. First, there is the elastic limit. Since it is difficult to determine the maximum stress for which there is no permanent deformation, the 0.2% offset yield stress (point A in the Figure 3.7(a)) is used instead; it corresponds to a permanent strain of 0.2% after unloading. Actually, there is evidence of dislocation activity in a specimen at stress levels as low as 25% of the yield stress. The region between 25 and 100% of the yield stress is called the *microyield* region and has been the object of careful investigations. In case there is a drop in yield, an *upper* (B) and a *lower* (C) *yield point* are defined in Figure 3.7(b). The lower yield point depends on the machine stiffness. A *proportional limit* is also sometimes defined (D); it corresponds to the stress at which the curve deviates from linearity. The maximum engineering stress is called the *ultimate tensile stress* (UTS); it corresponds to point D' in Figure 3.7. Beyond the UTS, the engineering stress drops until the *rupture stress* (E) is reached. The *uniform strain* (F) corresponds to the plastic strain that takes place uniformly in the specimen. Beyond that point, necking occurs. Necking is treated in detail in Section 3.2.2. G is the *strain-to-failure*. Additional parameters can be obtained from the stress–strain curve: (1) The elastic energy absorbed by the specimen (the area under the elastic portion of the curve) is called *resilience*; (2) the total energy absorbed by the specimen during deformation, up to fracture (the area under the whole curve), is called *work of fracture*. The strain rate undergone by the specimen,  $\dot{\varepsilon}_e = d\varepsilon_e/dt$ , is equal to the crosshead velocity, divided by the initial length  $L_0$  of the specimen.

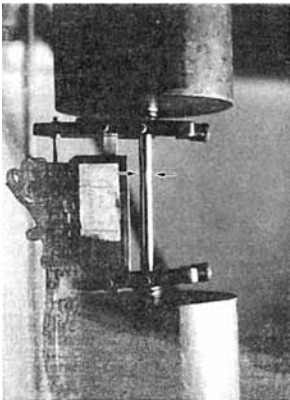


**Fig. 3.8** Tensile specimen being tested; arrows show onset of necking.

The *reduction in area* is defined as

$$q = \frac{A_0 - A_f}{A_0}, \quad (3.15)$$

where  $A_0$  and  $A_f$  are the initial area and cross-sectional area in the fracture region, respectively. The true strain at the fracture is defined as

$$\varepsilon_f = \ln \frac{A_0}{A_f}. \quad (3.16)$$

The true uniform strain is

$$\varepsilon_u = \ln \frac{A_0}{A_u}, \quad (3.17)$$

where  $A_u$  is the cross-sectional area corresponding to the onset of necking (when the stress is equal to the UTS).

### 3.2.2 Necking

Necking corresponds to the part of the tensile test in which instability exists. The neck is a localized region in the reduced section of the specimen in which the greatest portion of strain concentrates. The specimen “necks” down in this region. Figure 3.8 shows the onset of necking in a tensile specimen; arrows show the region where the cross section starts to decrease.

Several criteria for necking have been developed. The oldest one is due to Considère.<sup>4</sup> According to Considère, necking starts at the maximum stress (UTS), when the increase in strength of the material attributed to work-hardening is less than the decrease in the load-bearing ability owing to the decrease in cross-sectional area. In other words, necking starts when the increase in stress due to the reduction in cross-sectional area starts to exceed the increase in load-bearing ability because of work-hardening. We have, at the onset of necking,

$$\frac{d\sigma_e}{d\varepsilon_e} = 0 \quad (3.18)$$

Substituting Equations 3.4 and 3.9 into 3.18 yields

$$\frac{d \left( \frac{\sigma_t}{1+\varepsilon_e} \right)}{d(e^{\varepsilon_t} - 1)} = \frac{d \left( \frac{\sigma_t}{e^{\varepsilon_t}} \right)}{d(e^{\varepsilon_t} - 1)} = 0.$$

Making the transformation of variables

$$e^{\varepsilon_t} - 1 = Z, \quad e^{\varepsilon_t} = Z + 1$$

yields

$$\frac{d \left( \frac{\sigma_t}{Z+1} \right)}{dZ} = \sigma_t \frac{d(Z+1)^{-1}}{dZ} + (Z+1)^{-1} \frac{d\sigma_t}{dZ} = 0,$$

$$-\sigma_t(Z+1)^{-2} + (Z+1)^{-1} \frac{d\sigma_t}{dZ} = 0,$$

<sup>4</sup> A. Considère, *Ann. Ponts. Chaussées*, Ser. 6. (1885) 574.

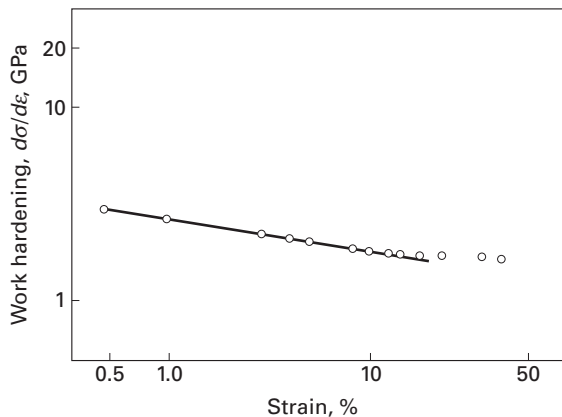


**Fig. 3.9** Log  $d\sigma/d\varepsilon$  versus  $\log \varepsilon$  for stainless steel AISI 302.  
(Adapted with permission from  
A. S. de S. e Silva and S. N.  
Monteiro, *Metalurgia-ABM*, 33  
(1977) 417.)

or

$$-\sigma_t e^{-2\varepsilon_t} + e^{-\varepsilon_t} = \frac{d\sigma_t}{d(e^{\varepsilon_t} - 1)} = 0,$$

$$\frac{d\sigma_t}{d(e^{\varepsilon_t} - 1)} = \sigma_t e^{-\varepsilon_t},$$

$$\frac{d\sigma_t}{\sigma_t} = e^{-\varepsilon_t} d(e^{\varepsilon_t} - 1) = d\varepsilon_t.$$

Using Equation 3.10, we obtain

$$d\sigma_t = nK \varepsilon^{n-1} d\varepsilon_t, \text{ or } \frac{d\sigma}{d\varepsilon_t} = \sigma_t \quad (3.19)$$

and it follows from Equation 3.19 that  $\sigma_t = nK\varepsilon^{n-1}$ . Finally, applying Equation 3.10 again results in  $K\varepsilon^n = nK\varepsilon^{n-1}$ , so that

$$\varepsilon_u = n.$$

This is an important result. The work-hardening coefficient is numerically equal to the true uniform strain and can be easily obtained in this way.

It is sometimes useful to present results of tensile tests in plots of  $d\sigma/d\varepsilon$  versus  $\sigma$  or  $d\sigma/d\varepsilon$  versus  $\varepsilon$ . An example of a plot of  $\log(d\sigma/d\varepsilon)$  versus  $\log \varepsilon$  for AISI 302 stainless steel is given in Figure 3.9. It can be seen that  $d\sigma/d\varepsilon$  decreases with  $\varepsilon$ , indicating that the necking tendency steadily increases. For metals that do not exhibit any work-hardening capability, necking should start immediately at the onset of plastic flow. Under certain conditions (predeformation at very low temperature or very high strain rate) some metals can exhibit this response, called *work-softening*.

The formation of the neck results in an accelerated and localized decrease in the cross-sectional area. Figure 3.6 shows how the true-stress–true-strain curve continues to rise after the onset of necking. It can also be seen that the true strain at fracture is much higher than the “total strain.” The correct plotting of the true-stress–true-strain curve beyond the UTS requires determination of the cross-sectional area in the neck region continuously after necking. This is difficult to do, and the simplest way is to obtain one single point on the

plot, joining it to the point corresponding to the maximum load. For this reason, a dashed line is used in Figure 3.6. The deformation in the neck region is much higher than the one uniformly distributed in the specimen. It can be said that the neck acts as a second tensile specimen. Since its length is smaller than that of the specimen, and the crosshead velocity is constant, the strain rate is necessarily higher.

The onset of necking is accompanied by the establishment of a triaxial state of stress in the neck; the uniaxial stress state is destroyed by the geometrical irregularity. After studying flow criteria (see Section 3.7), we will readily see that the flow stress of a material is strongly dependent on the state of stress. Hence, a correction has to be introduced to convert the triaxial flow stress into a uniaxial one. If we imagine an elemental cube aligned with the tensile axis and situated in the neck region, it can be seen that it is subjected to tensile stresses along three directions. (The external boundaries of the neck generate the tensile components perpendicular to the axis of the specimen.) The magnitude of the transverse tensile stresses depends on the geometry of the neck, the material, the shape of the specimen, the strain-rate sensitivity of the material, the temperature, the pressure, and so on. Bridgman<sup>5</sup> introduced a correction from a stress analysis in the neck. His analysis applies to cylindrical specimens. The equation that expresses the corrected stress is

$$\sigma = \frac{\sigma_{av}}{(1 + 2R/r_n) \ln(1 + r_n/2R)}, \quad (3.20)$$

where  $R$  is the radius of curvature of the neck and  $r_n$  is the radius of the cross section in the thinnest part of the neck. Thus, one has to continuously monitor the changes in  $R$  and  $r_n$  during the test to perform the correction.

Figure 3.10 presents a plot in which the corrections have already been computed as a function of strain beyond necking. There are three curves, for copper, steel, and aluminum. The correction factor can be read directly from the plot shown.  $\varepsilon_u$  is the true uniform strain (the strain at onset of necking). In Figure 3.6, the true-stress–true-strain curve that was corrected for necking by the Bridgman technique lies slightly below the one determined strictly from the reduction in area at fracture and the load at the breaking point. This is consistent with Figure 3.10;  $\sigma$  is always lower than  $\sigma_{av}$ .

Necking is a characteristic of tensile stresses; compressive stresses are not characterized by necking. Barreling is the corresponding deviation from the uniaxial state in compressive tests. Hence, metals will exhibit necking during deformation processing only if the state of stress is conducive to it (tensile). Figure 3.11 shows plainly how the work-hardening capacity of a metal greatly exceeds that in an individual tensile test. Wire was drawn to different strains: drawing the

<sup>5</sup> P. W. Bridgman, *Trans. ASM*, 32 (1974) 553.

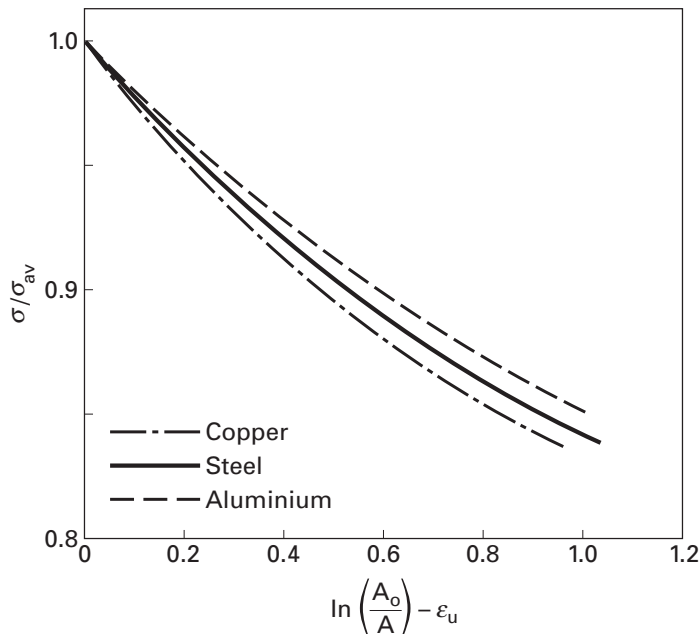


**Fig. 3.10** Correction factor for necking as a function of strain in neck,  $\ln(A_0/A)$ , minus strain at necking,  $\varepsilon_u$ . (Adapted with permission from W. J. McGregor Tegart, *Elements of Mechanical Metallurgy* (New York: MacMillan, 1964), p. 22.)

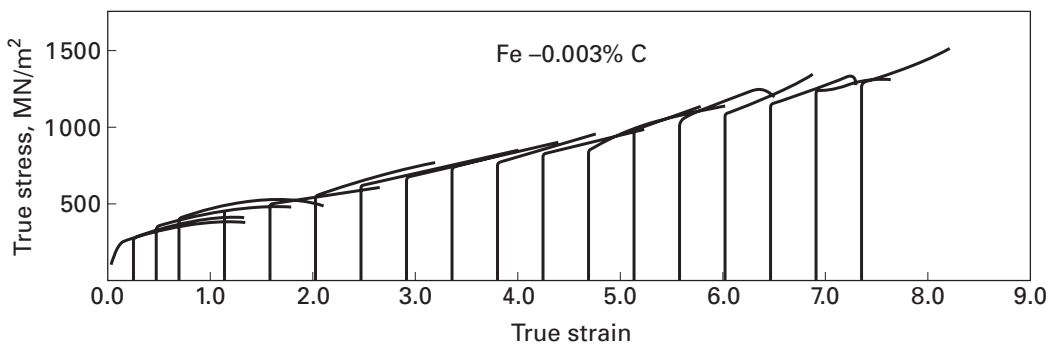


**Fig. 3.11** Stress-strain curves for Fe-0.003% C alloy wire, deformed to increasing strains by drawing; each curve is started at the strain corresponding to the prior wire-drawing reduction. (Courtesy of H. J. Rack.)

wire consists of pulling it through a conical die; at each pass, there is a reduction in cross section. Tensile tests were conducted after different degrees of straining (0 to 7.4) by wire drawing; it can be seen that the wire work-hardens at each step. However, the individual tensile tests are interrupted by necking and fracture. In wire-drawing, necking and fracture are inhibited by the state of stress in the deformation zone (compressive). The individual true-stress-true-strain curves were corrected for necking by Bridgman's technique; in each case, the individual curve fits fairly well into the overall work-hardening curve. It may be concluded that the individual tensile test gives only a very

limited picture of the overall work-hardening response of a metal; for the wire in Figure 3.11 the total strain exceeded 7.4.

### 3.2.3 Strain Rate Effects

For many materials, the stress-strain curves are sensitive to the strain rate  $\dot{\varepsilon}$ . The lowest range of strain rates corresponds to creep and stress-relaxation tests. The tensile tests are usually conducted in the range  $10^{-4} \text{ s}^{-1} < \dot{\varepsilon} < 10^{-2} \text{ s}^{-1}$ . At strain rates on the order of  $10^2 \text{ s}^{-1}$ , inertial and wave-propagation effects start to become important. The highest range of strain rates corresponds to the passage of a shock wave through the material.

More often than not, the flow stress increases with strain rate; the work-hardening rate is also affected by it. A parameter defined to describe these effects

$$m = \left. \frac{\partial \ln \sigma}{\partial \ln \dot{\varepsilon}} \right|_{\varepsilon, T}, \quad (3.21)$$

is known as the *strain rate sensitivity*. Equation 3.21 can also be expressed as

$$\boxed{\sigma = K \dot{\varepsilon}^m.} \quad (3.22)$$

where  $K$  is a constant. Note that this  $K$  is different from the Ludwik-Hollomon parameter.

Materials can be tested over a wide range of strain rates; however, standardized tensile tests require well-characterized strain rates that do not exceed a critical value. High-strain-rate tests are often used to obtain information on the performance of materials under dynamic impact conditions. The cam plastometer is one of the instruments used. In certain industrial applications, metals are also deformed at high strain rates. Rolling mills generate bar velocities of 180 km/h; the attendant strain rates are extremely high. In wire-drawing, the situation is similar.

Figure 3.12(a) shows the effect of different strain rates on the tensile response of AISI 1040 steel. The yield stress and flow stresses at different values of strain increase with strain rate. The work-hardening rate, on the other hand, is not as sensitive to strain rate. This illustrates the importance of correctly specifying the strain rate when giving the yield stress of a metal. Not all metals exhibit a high strain rate sensitivity: Aluminum and some of its alloys have either zero or negative  $m$ . In general,  $m$  varies between 0.02 and 0.2 for homologous temperatures between 0 and 0.9 (90% of the melting point in K). Hence, one would have, at the most, an increase of 15% in the yield stress by doubling the strain rate. It is possible to determine  $m$  from tensile tests by changing the strain rate suddenly and by measuring the instantaneous change in stress. This technique is illustrated in

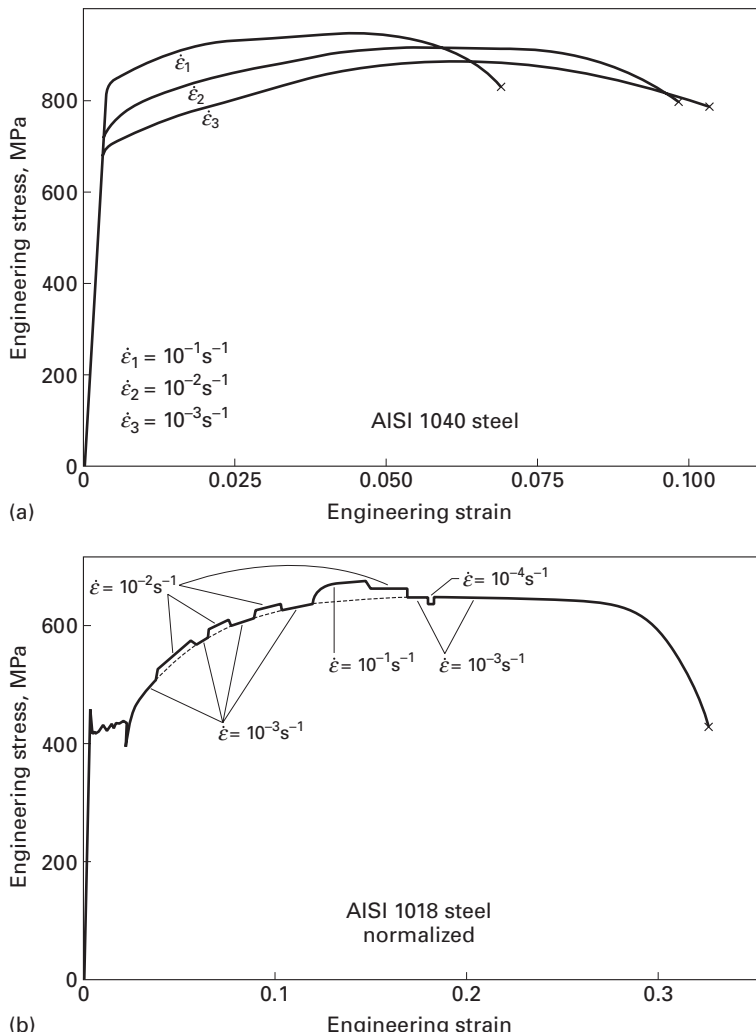


**Fig. 3.12** (a) Effect of strain rate on the stress-strain curves for AISI 1040 steel. (b) Strain-rate changes during tensile test. Four strain rates are shown:  $10^{-1}$ ,  $10^{-2}$ ,  $10^{-3}$ , and  $10^{-4} \text{ s}^{-1}$ .

Figure 3.12(b). Applying Equation 3.22 to two strain rates and eliminating  $K$ , we have

$$m = \frac{\ln(\sigma_2/\sigma_1)}{\ln(\dot{\varepsilon}_2/\dot{\varepsilon}_1)} \quad (3.23)$$

The reader can easily obtain  $m$  from the strain-rate changes in the figure.

Some alloys show a peculiar plastic behavior and are called *superplastic*. When necking starts, the deformation concentrates itself at the neck. Since the velocity of deformation is constant, and the effective length of the specimen is reduced during necking, the strain rate increases ( $\dot{\varepsilon} = v/L$ ). If a material exhibits a positive strain-rate sensitivity, the flow stress in the neck region will increase due to the increased strain rate; hence, necking is inhibited. This topic is treated

in greater detail in Section 15.8 – Superplasticity; it is what takes place in superplastic alloys, which can undergo uniform plastic strains of up to 5,000%.

---

### Example 3.2

Can the necking phenomenon be observed in *any* kind of mechanical test? Point out some of the problems that this phenomenon can cause during tensile testing.

**Solution:** No, necking is an artifact of the tensile test only. A reduction in cross-sectional area at any irregularities along the length of the specimen occurs in the tension mode only, and therefore, the phenomenon of necking occurs in tension only. In compression, the specimen bulges out.

After necking starts, the plastic deformation is concentrated in a very narrow region of the sample. Thus, one must not compare the total deformation corresponding to failure for two specimens that have different gage lengths. In order to avoid such complications, one should only compare the uniform elongation or use the reduction in area, i.e., the true-strain definition of the final strain. Strain gages and clip-on extensometers will not function properly or give accurate results after necking has begun.

---

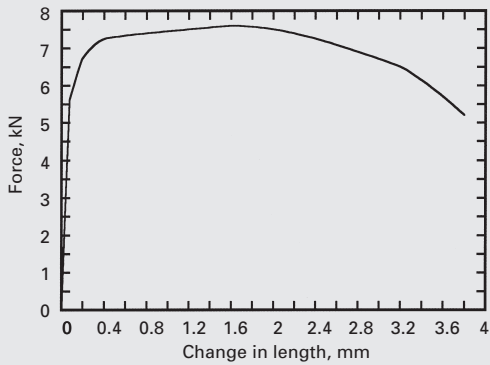
### Example 3.3

Tensile testing of brittle materials such as ceramics is not very common, but is being resorted to in many laboratories. Why? Comment on the problems of doing tensile testing on ceramics.

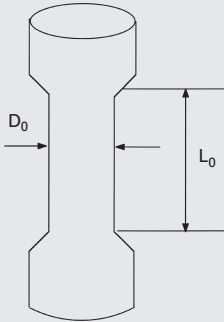
**Solution:** Direct tensile testing of a sample results in a simple stress state over the whole volume of the sample gage length. All the volume and surface flaws in the gage length of the specimen are called into play and lead to a true measure of the material strength. Hence, there is increasing interest in tensile testing of ceramics. One major problem, however, is that of alignment of the sample. Any offcenter application of the load or loading at an angle can result in a combined state of bending and tension in the specimen. Stresses induced in such a state are called *parasitic bending stresses* and can lead to errors in the computed tensile strength values or even fracture the sample while it is being aligned in the machine. Some self-aligning grips have been designed to take care of these problems. This leads to rather long specimens and rather complex machining of the specimen. All of this makes tensile testing of ceramics very expensive!

**Example 3.4**

Determine, for the curve shown in Figure E3.4.1,

**Fig. E3.4.1**

- (a) Young's modulus
- (b) the UTS
- (c) the yield stress (with a 0.2% offset)
- (d) the uniform strain
- (e) the total strain
- (f) the engineering stress-strain curve.

**Fig. E3.4.2**

The dimensions of the specimen, which is depicted in Figure E3.4.2, are:

$$L_0 = 20 \text{ mm},$$

$$D_0 = 4 \text{ mm}.$$

*Solution:*

- (a) The elastic region is the straight line of the stress-strain curve. Taking both ends of this line, we obtain

$$\text{Point 1 : } F_1 = 0 \text{ kN}, \quad \Delta l_1 = 0,$$

$$\text{Point 2 : } F_2 = 5.5 \text{ kN}, \quad \Delta l_2 = 0.175 \text{ mm}.$$

To calculate Young's modulus ( $E = \Delta\sigma/\Delta\varepsilon$ ), we have to change  $F$ ,  $\Delta l$  in terms of  $\sigma$ ,  $\varepsilon$ :

$$\sigma_1 = \frac{F_1}{A_0} = 0,$$

Point 1:  
 $\varepsilon_1 = \frac{\Delta l_1}{L_0} = 0.$

$$\sigma_2 = \frac{F_2}{A_0} = \frac{5.5}{\pi(2)^2} \frac{\text{kN}}{\text{mm}^2} \approx 0.44 \text{ kN/mm}^2 = 440 \text{ MPa},$$

Point 2:  
 $\varepsilon_2 = \frac{\Delta l_2}{L_0} \approx \frac{0.175}{20} \approx 0.009.$

So

$$E = \frac{\Delta\sigma}{\Delta\varepsilon} = \frac{\sigma_2 - \sigma_1}{\varepsilon_2 - \varepsilon_1} \approx \frac{440}{0.009} \approx 49000 \text{ MPa} \approx 49 \text{ GPa}$$

- (b) The UTS is the maximum value of the stress reached just before necking. Therefore, from the stress-strain curve, the UTS is equal to the stress corresponding to  $F \approx 7.5 \text{ kN}$ . So

$$\text{UTS} = \frac{7.5}{\pi(2)^2} \approx 0.6 \text{ kN/mm}^2 \approx 600 \text{ MPa}$$

- (c) The 0.2%-offset yield stress is

$$\varepsilon = \frac{\Delta l}{L_0}, \quad \varepsilon = 0.2\% = 0.002, \quad l_0 = 20 \text{ mm}.$$

Therefore,

$$\Delta l = \varepsilon \cdot l_0 = 0.002 \times 20 = 0.04 \text{ mm}.$$

If you draw a line parallel to the elastic region calculated in part (a), from  $\Delta l = 0.04 \text{ mm}$ , you will find that the point of intersection with the stress-strain curve is at  $F \approx 6 \text{ kN}$ . At that point,

$$\sigma_y = \frac{6}{\pi(2)^2} \approx 0.48 \text{ kN/mm}^2 = 480 \text{ MPa}.$$

- (d) For uniform strain, make a parallel line from the UTS point to the stress axis. You will then find that

$$\Delta l_u \approx 1.5 \text{ mm}.$$

The percent uniform strain is

$$\frac{\Delta l_u}{L_0} \times 100\% = \frac{1.5}{20} \times 100\% = 7.5\%.$$

- (e) To find the total strain, we repeat (d) from the failure point. We have

$$\Delta l_t \approx 3.7 \text{ mm}.$$

The percent total strain is

$$\frac{\Delta l_t}{L_0} \times 100\% = \frac{3.7}{20} \times 100\% = 18.5\%.$$

(f) The engineering stress-strain curve is as shown in Figure E3.4.3.

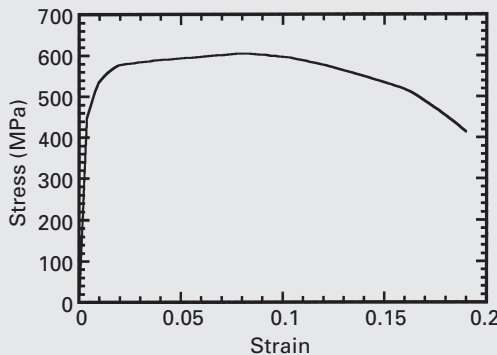


Fig. E3.4.3

### Example 3.5

The load-extension curve of an aluminum alloy, shown in Figure E3.5.1 was taken directly from a testing machine. A strain-gage extensometer was used, so machine stiffness effects can be ignored. From this curve, obtain the true and engineering stress-strain curves. Also, calculate the following parameters:

- (a) Young's modulus
- (b) the UTS
- (c) the 0.2%-offset yield stress
- (d) the uniform strain
- (e) the total strain
- (f) the reduction in area at the fracture.

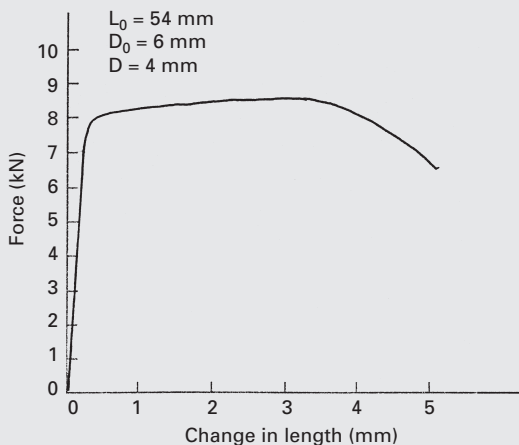


Fig. E3.5.1

**Solution:** We first change the coordinates to stress and strain. For engineering stresses, this is easily done:

$$\sigma_e = \frac{P}{A_0} \quad (A_0 = 28.26 \text{ mm}^2),$$

$$\varepsilon_e = \frac{\Delta L}{L_0} \quad (L_0 = 54 \text{ mm}).$$

The shape of the curve remains the same. For true stresses and true strains, we have to convert the engineering values into true values using the equations

$$\sigma_t = \sigma_e(1 + \varepsilon_e),$$

$$\varepsilon_t = \ln(1 + \varepsilon_e).$$

This is valid up to the onset of necking. Beyond necking (which starts at the UTS), we have only one point: that corresponding to failure. We can establish the true strain in the neck from the equation

$$\varepsilon_f = \ln \frac{A_0}{A_f} = \ln \frac{\pi \times 9}{\pi \times 4} = 0.81.$$

The corresponding true stress is

$$\sigma_t = \frac{P}{A} = \frac{6.5}{\pi \times 4} \frac{\text{kN}}{\text{mm}^2},$$

$$\sigma_t = 515 \text{ MPa.}$$

The other parameters are determined as follows:

(a) Young's modulus:

$$E = \text{slope of elastic part}$$

$$= \frac{\Delta \sigma}{\Delta \varepsilon}$$

$$= \frac{250}{0.004} \text{ MPa}$$

$$\approx 63 \text{ GPa.}$$

(b) UTS  $\approx 300$  MPa ( $\sigma_{\max}$ ).

The corresponding true stress is

$$\sigma_t = 300(1 + 0.056) = 317 \text{ MPa.}$$

(c) 0.2%-offset yield stress:

$$\sigma_{ys} \approx 280 \text{ MPa.}$$

(d) The uniform strain is approximately equal to 0.056.

The corresponding true strain is

$$\varepsilon_t = \ln(1 + 0.056) = 0.054.$$

(e) The total strain is approximately equal to 9%.

(f) Reduction in area at the fracture:

$$q = \frac{A_0 - A_f}{A_0} = \frac{\pi \times 3^2 - \pi \times 2^2}{\pi \times 3^2} = 0.55, \quad \text{or} \quad 55\%.$$

The true and engineering stress-strain curves are shown in Figure E3.5.2(a). The engineering curve is shown blown up in Figure E3.5.2(b).

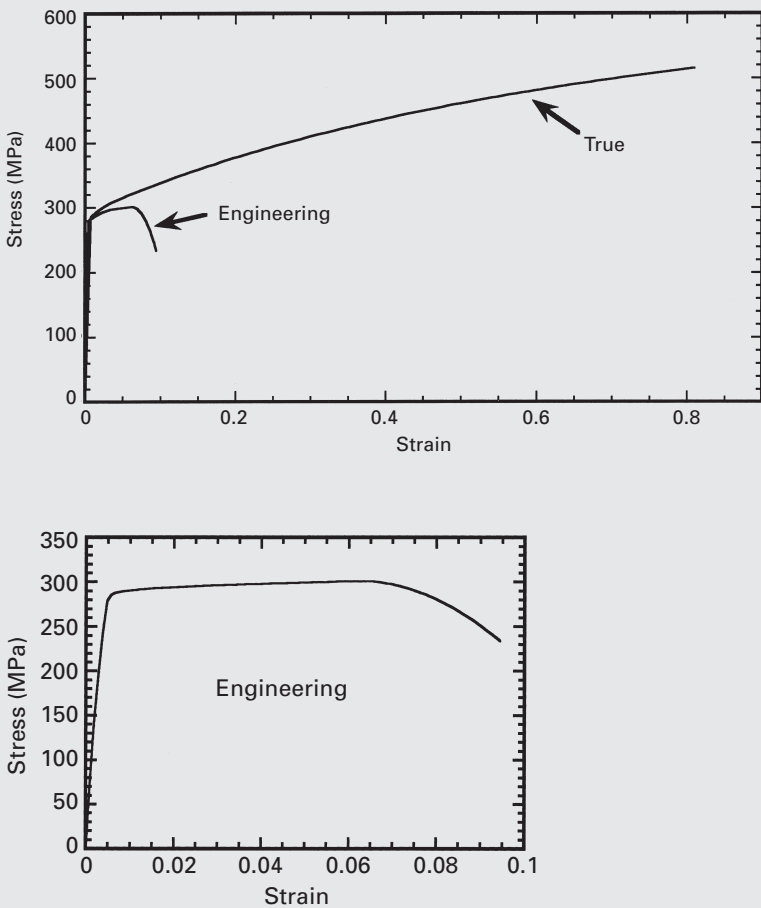
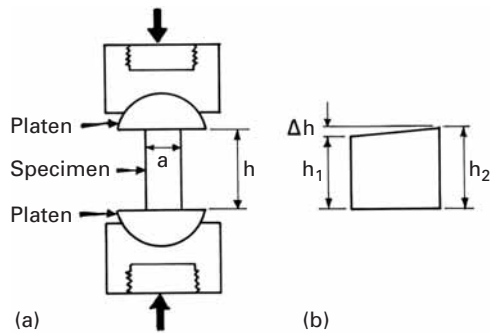


Fig. E3.5.2

### 3.3 | Plastic Deformation in Compression Testing

In compression testing, a cylinder or a parallelepiped cube (with one side – the one parallel to the loading direction – longer than the other two) is subjected to compression between two parallel plates. The plates should have a self-alignment system, and they often ride on one or two hemispherical caps, as shown in Figure 3.13(a). If ceramics are being tested, it is also common to use special ceramic (WC, for instance) inserts between the specimen and the hemispherical caps. This eliminates indentation and plastic deformation of platens. Lubrication between the specimen and the plate is also very desirable, to decrease barreling (nonuniform deformation) of the specimen.

**Fig. 3.13** (a) Compression specimen between parallel platens.  
 (b) Length inhomogeneity in specimen.



(Barreling will be discussed shortly.) The use of a thin Teflon™ coating, molybdenum disulfide, or graphite is recommended. It is also very important to ensure homogeneous loading of the specimen. This is particularly critical for ceramics, which often fail in the elastic range. It is easy to calculate stresses that arise when one of the parallel sides of a specimen is longer than the other. Figure 3.13(b) shows a specimen with a height difference  $\Delta h$ . The right side will experience a stress  $\sigma = E(\Delta h/h_2)$  before the left side is loaded. For a typical ceramic, it is a simple matter to calculate the relationship between  $\Delta\sigma$ , the difference in stress from one side to the other, from  $\Delta h$ . For example, consider alumina, for which  $E = 400$  GPa and  $h = 10$  mm. The compressive strength of alumina can be as high as

$$\sigma_c = 4 \text{ GPa}.$$

Therefore, the failure strain is

$$\varepsilon_f = \frac{\sigma}{E} = 10^{-2}.$$

The corresponding displacement is

$$\Delta h = \varepsilon h = 0.1 \text{ mm}.$$

If the difference in height in the specimen is greater than 0.1 mm, the right side will fail as the left side starts to experience loading. This inhomogeneous loading is eliminated by the hemispherical caps, which can rotate to accommodate differences in height. However, if the surfaces of the specimen are not flat, stress inhomogeneities will arise, which can cause significant differences in the stress-strain response.

In reality, the platens also undergo elastic deformation, and a more uniform stress state is reached. Nevertheless, it is not a good practice to have the stresses on the two sides vary significantly, as this will result in erroneous strength determinations. The use of Teflon or thin metallic shims (stainless steel foil) also helps to alleviate the problem. This example illustrates the care that has to be exercised in choosing the dimensions of the specimen. In the case of ductile materials, it is not so critical, because plastic deformation will “homogenize” stresses.

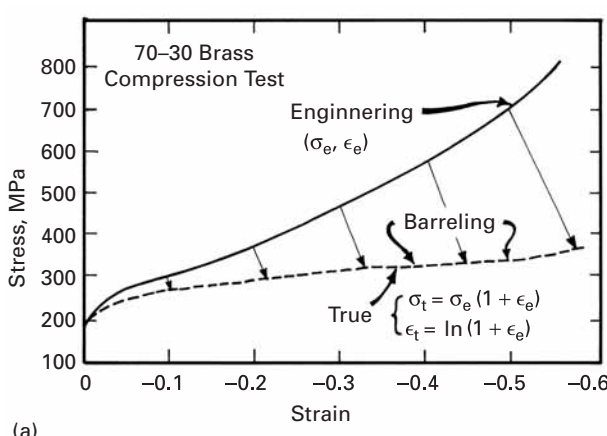


**Fig. 3.14** (a) Stress-strain (engineering and true) curves for 70-30 brass in compression. (b) Change of shape of specimen and barreling.

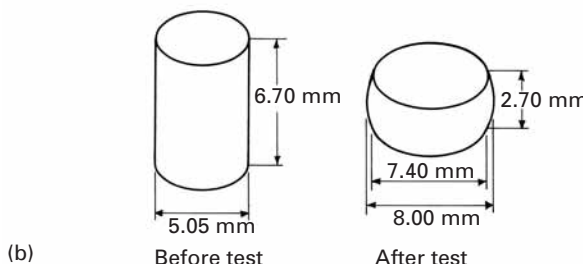
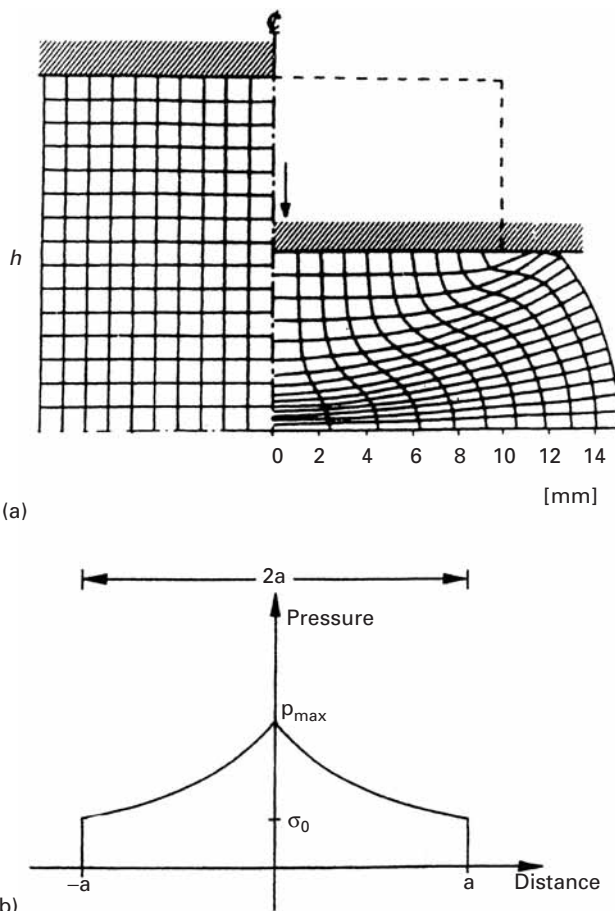


Figure 3.14(a) shows a typical compressive stress-strain curve for a metal (70-30 brass). The engineering-stress-engineering-strain curve ( $\sigma_e, \epsilon_e$ ) is concave, whereas it is convex in a tensile test. (See, for instance, Figure 3.3). The true-stress-true-strain curve is obtained by means of Equations 3.4 and 3.9. (See also Section 2.2). The translation of five points by using these equations is shown in Figure 3.14(a). After conversion to true-stress-true-strain values, the concavity of the curve is, for the most part, lost. In contrast, the true stress-strain curves in tension are displaced to the left (on the strain axis) and up (on the stress axis) from the engineering stress-strain curves. (See Figure 3.6) The phenomenon of necking is absent in compression testing, and much higher strains are reached. However, necking is replaced by barreling, a nonuniform plastic deformation resulting from friction between the specimen and the platen. Figure 3.14(b) shows the barreling of the brass specimen after the test. This barreling is responsible for some concavity in the true stress-strain curve (at a strain greater than -0.4) and limits the range of strain in compression testing of ductile materials to approximately -0.3 to -0.4. It will be shown, through a stress analysis, that frictional effects play an increasing role as the length/diameter ratio is decreased. This can significantly affect the results of a test. The compression of a cylindrical specimen under an engineering strain of -0.5, as simulated by finite elements under sticking conditions (i.e., there is no sliding at the



**Fig. 3.15** (a) Distortion of Finite Element Method (FEM) grid after 50% reduction in height  $h$  of specimen under sticking-friction conditions. (Reprinted with permission from H. Kudo and S. Matsubara, *Metal Forming Plasticity* (Berlin: Springer, 1979), p. 395.) (b) Variation in pressure on surface of cylindrical specimen being compressed.

specimen–platen interface), is shown in Figure 3.15. The distortion of the initially perpendicular grid is visible. This is an extreme case; strain inhomogeneities in the specimen are evident by differences in distortion of the grid. Barreling also can be seen.

The pressure or compressive stress is not uniform over the top and bottom surfaces of the specimen. Pressure differences can be calculated from an equation derived by Meyers and Chawla:<sup>6</sup>

$$p = \sigma_0 e^{2\mu(a-r)/h}.$$

<sup>6</sup> M. A. Meyers and K. K. Chawla, *Mechanical Metallurgy* (Englewood Cliffs, NJ: Prentice-Hall, 1984), p. 122.

This is the equation for the “friction hill.” The compressive stress at the outside ( $r = a$ ) is equal to  $\sigma_0$ , the material flow stress. In the center, it rises to  $p_{\max}$ . The greater the ratio  $a/h$ , the more severe the problem is. The “friction hill” is schematically plotted in Figure 3.15(b). The pressure rises exponentially toward the center of the cylinder. The greater the coefficient of friction, the greater is  $p_{\max}$ . A friction coefficient  $\mu = 0.15$  is a reasonable assumption. It is instructive to calculate the maximum pressure for three  $a/h$  ratios:

$$\begin{aligned} a/h = 2, \quad p_{\max} &= 1.82\sigma_0; \\ a/h = 1, \quad p_{\max} &= 1.34\sigma_0; \\ a/h = 0.5, \quad p_{\max} &= 1.16\sigma_0. \end{aligned}$$

A specimen with an initial length/diameter ratio of 2 would have a maximum pressure of  $1.07\sigma_0$ . However, after a 50% reduction in length, the ratio  $a/h$  is changed to  $1.23\sigma_0$ . The calculation is left as a challenge to the student; remember that the volume is constant. This can cause significant differences between the actual strength values of materials and stress readings. It is therefore recommended that these effects be considered. On the other hand, if  $a/h$  is too small, the specimen will tend to buckle under the load.

### 3.4 | The Bauschinger Effect

In most materials, plastic deformation in one direction will affect subsequent plastic response in another direction. The translation of the von Mises ellipse (kinematic hardening; see Section 3.7.4) is a manifestation of this relationship. The ellipse will move toward the direction in which the material is stressed. In one-dimensional deformation, the phenomenon is known as the *Bauschinger effect*. A material that is pulled in tension, for example, shows a reduction in compressive strength. Figure 3.16 illustrates the effect. A stress-strain curve is drawn, and the sequence 0–1–2 represents the loading direction. The material is first loaded in tension and yields at 1. At 2, the loading direction is reversed. Unloading occurs along the elastic line until the stresses become compressive. If there were no directionality effect, the material would start flowing plastically at a stress equal to  $\sigma_2$ . The idealized reverse curve is also shown in the figure. If the material did not exhibit a dependence on the stress direction, the compressive curve would be symmetrically opposite to the tensile curve. This idealized curve is drawn in dashed lines. The sequence is 0–1R–2R. Thus, compressive plastic flow, after the 0–1–2 tensile sequence, should occur at  $\sigma_3 = \sigma_2R = -\sigma_2$ . If the material exhibits a Bauschinger effect, this stress is decreased from  $\sigma_3$  to  $\sigma_4$ . Hence, the material “softens” upon inversion of the loading direction.

An actual example is shown in Figure 3.17. The 0.2% proof stress (the stress at which 0.2% plastic strain occurs) in compression is divided by the tensile flow stress that preceded it. These values are

**Fig. 3.16** The Bauschinger effect.

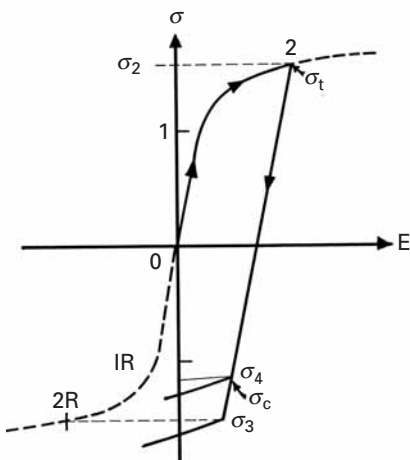
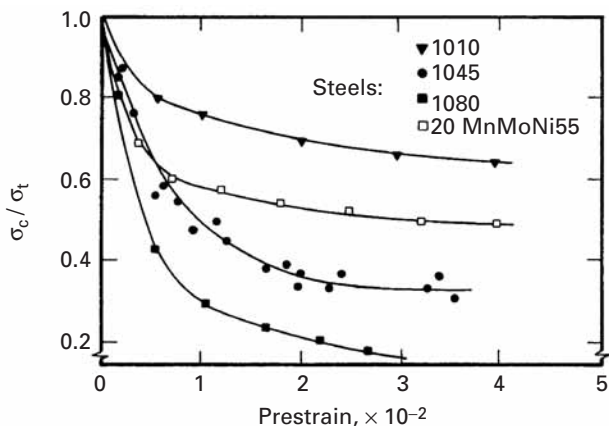


**Fig. 3.17** Ratio of compressive flow stress (0.2% plastic strain) and tensile flow stress at different levels of plastic strain for different steels. (After B. Scholtes, O. Vöhringer, and E. Macherauch, Proc. ICMA6, Vol. I (New York: Pergamon, 1982), p. 255.)



marked in the figure, which shows three plain carbon steels and one alloy steel. The change in flow stress is indeed highly significant and increases with plastic strain in tension. Thus, this factor cannot be ignored in design considerations when a component is to be subjected to compression stresses in service after being plastically deformed in tension.

### 3.5 | Plastic Deformation of Polymers

#### 3.5.1 Stress–Strain Curves

At a microscopic level, deformation in polymers involves stretching and rotating of molecular bonds. More commonly, one distinguishes the deformation mechanisms in polymers as brittle, ductile (with or without necking), and elastomeric. Figure 3.18 shows schematically the curves that correspond to these mechanisms. Clearly, factors such as the strain rate and temperature affect the shape of stress–strain

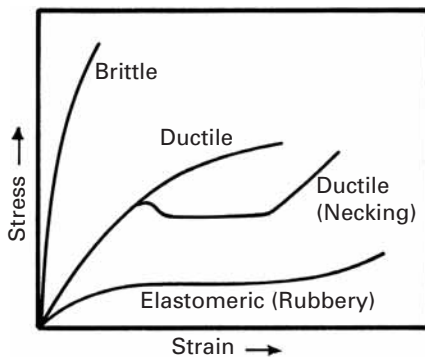


**Fig. 3.18** Schematic of the different types of stress-strain curves in a polymer.

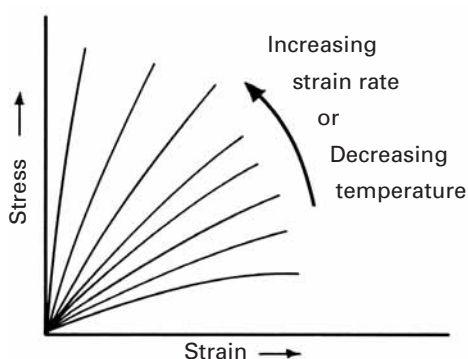


**Fig. 3.19** Effect of strain rate and temperature on stress-strain curves.

curves, much more so in polymers than in ceramics or metals. This is because the polymers are viscoelastic; that is, their stress-strain behavior is dependent on time. Temperature and strain rate have opposite effects. Increasing the strain rate (or decreasing the temperature) will lead to higher stress levels, but lower values of strain. Figure 3.19 shows this schematically.

Polymers (especially, linear, semicrystalline polymers), in a manner superficially similar to metals, can show the phenomena of yielding and necking. The necking condition for polymers can be represented, again in a manner similar to that for metals (see Section 3.2.2, Equation 3.19), by:

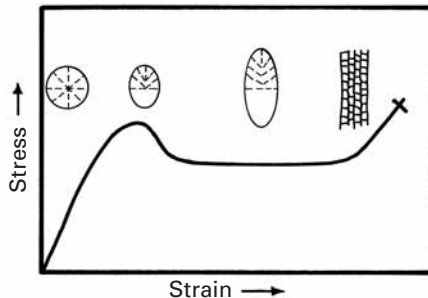
$$\frac{d\sigma_t}{d\varepsilon_t} = \sigma_t. \quad (3.24)$$

This equation says that necking occurs when the work-hardening rate  $d\sigma_t/d\varepsilon_t$  attains a value equal to  $\sigma$ . At that point, the increase in strength due to work-hardening cannot compensate for the loss in strength caused by a decrease in cross-sectional area, and necking ensues.

### 3.5.2 Glassy Polymers

In a manner similar to its occurrence in metals, plastic deformation occurs inhomogeneously in polymers. Two forms of inhomogeneous

**Fig. 3.20** Schematic of necking and drawing in a semicrystalline polymer.

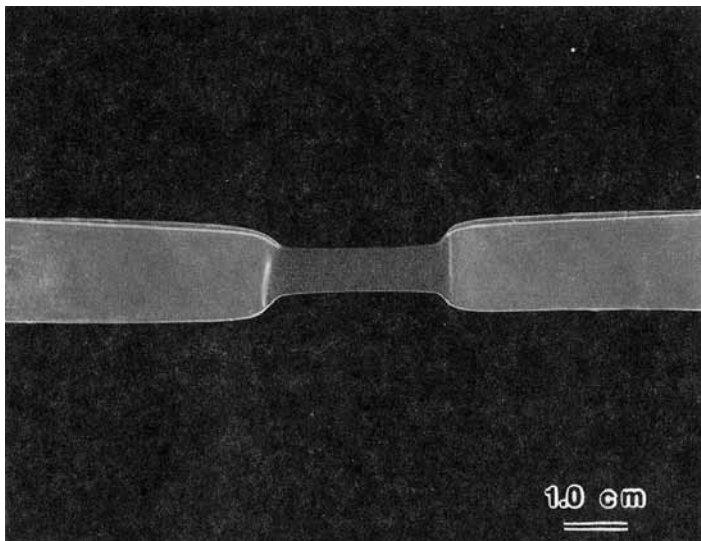


deformation are observed in glassy polymers: shear bands and crazes. Shear bands form at about  $45^\circ$  to the largest principal stress. The polymeric molecular chains become oriented within the shear bands without any accompanying change in volume. The process of shear band formation can contribute to a polymer's toughness because it is an energy-dissipating process. Shear yielding can take two forms: diffuse shear yielding and localized shear band formation. In localized shear, the shear is concentrated in thin planar regions, and the process involves a "cooperative" movement of molecular chains. The bands form at about  $45^\circ$  to the stress axis. Crazes are narrow zones of highly deformed polymer containing voids; the zones are oriented perpendicular to the stress axis. In the crazed zone, the molecular chains are aligned along the stress axis, but they are interspersed with voids. The void content in a craze may be as much as 55%. Unlike shear band formation, craze formation does not require the condition of constancy of volume. Generally, crazing occurs in brittle polymers. It can also occur to some extent in ductile polymers, but the dominant mode of deformation in these polymers is shear yielding. The phenomena of shear yielding and crazing are discussed further in Chapter 8.

Like ceramics, glassy or amorphous polymers show different stress – strain behaviors in tension and compression. The reason for this is that the surface flaws are much more dangerous in tension than in compression.

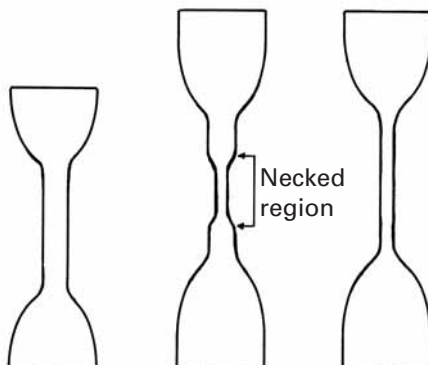
### 3.5.3 Semicrystalline Polymers

Semicrystalline polymers containing spherulites show a highly complex mode of deformation. Characteristically, these materials exhibit a ductile stress-strain curve with necking. Figure 3.20 shows such a stress-strain curve. Also illustrated is the process of transformation of a spherulitic structure to a fibrillar structure under the action of a tensile stress. Such orientation of polymeric chains parallel to the direction of stress increases the strength in that direction. Figure 3.21(a) shows a picture of the neck propagating in a linear polyethylene tensile sample while Figure 3.21(b) shows a schematic of the neck formation and propagation.



(a)

**Fig. 3.21** (a) Neck propagation in a sheet of linear polyethylene.  
 (b) Neck formation and propagation in a specimen, shown in schematic fashion.



(b)

### 3.5.4 Viscous Flow

At high temperatures ( $T \geq T_g$ , the glass transition temperature), polymers undergo a viscous flow. Under these conditions, the stress is related to the strain rate, rather than the strain. Thus,

$$\boxed{\tau = \eta \frac{d\gamma}{dt}}, \quad (3.25)$$

where  $\tau$  is the shear stress,  $\eta$  is the viscosity, and  $t$  is the time. (The derivation of Equation 3.25 is given in Section 3.6.2.)

Viscous flow is a thermally activated process. It occurs by molecular motion, which increases as the temperature increases. The reader can appreciate the fact that such a viscous flow would involve the local breaking and re-forming of the polymeric network structure. The thermal energy for this is available above the glass transition

temperature  $T_g$ . Below  $T_g$ , the thermal energy is too low for breaking and re-forming bonds, and the material does not flow so easily. At very high temperatures, the viscosity  $\eta$  is given by the Arrhenius-type relationship

$$\eta = A \exp\left(\frac{Q}{RT}\right), \quad (3.26)$$

where  $A$  is a constant,  $Q$  is the activation energy,  $R$  is the universal gas constant, and  $T$  is the temperature in kelvin.

### 3.5.5 Adiabatic Heating

There is a unique feature associated with the plastic deformation of polymers. Most of the work done during the plastic deformation of any material is converted into heat. In metals, this is not very important, because metals are good conductors, and except at extremely high rates of deformation, the heat generated is dissipated to the surroundings rather quickly, so that the temperature rise of the metal is insignificant. Polymers are generally poor conductors of heat. Thus, any heat generated in localized regions of a specimen due to plastic deformation can cause local softening. In the case of fatigue, heat may be dissipated rather easily at low strains and at low frequencies, even in polymers. A significant amount of softening, however, can result under conditions of high strain rates and high-frequency cyclic loading. This phenomenon is called *adiabatic heating*.

#### Example 3.6

Polyethylene is a linear-chain thermoplastic; that is, relatively speaking, it is easy to crystallize by stretching or plastic deformation. An extreme case of this is the high degree of crystallization obtained in a gel-spun polyethylene fiber. Describe a simple technique that can be used to verify the crystallization in polyethylene.

**Solution:** An easy way would be to use an X-ray diffraction technique. Unstretched polyethylene will consist mostly of amorphous regions. Such a structure will give diffuse halos. A diffuse halo indicates an irregular atomic arrangement – that is, an amorphous structure. A polyethylene sample that has been subjected to stretching or a gel-spun polyethylene fiber will have highly crystalline regions aligned along the draw axis. There may also be some alignment of chains in the amorphous regions. An X-ray diffraction pattern of such a sample would show regular spots and/or regular rings. The discrete spots indicate regular spacing characteristic of an orderly arrangement in a single crystal. Well-spaced regular rings indicate a polycrystalline region. Regular rings result from overlapping spots due to random crystalline orientations.

**Table 3.1** Mechanical Properties of Some Metallic Glasses<sup>a</sup>

Alloy	$HV$ (GPa)	$\sigma_y$ (GPa)	$H/\sigma_y$	$E_g$ (GPa)	$Eg/\sigma_y$
$Ni_{36}Fe_{32}Cr_{14}P_{12}B_6$ (Metglas 286AA)	6.1	1.9 (tension)	3.16	99.36	52
$Ni_{49}Fe_{29}P_{14}B_6S_2$ (Metglas 286B)	5.5	1.7 (tension)	3.26	91.1	54
$Fe_{80}P_{16}C_2B_1$ (Metglas 2615)	5.8	1.7 (tension)	3.35		
$Pd_{77.5}Cu_6Si_{36.5}$	3.4	1.08 (compression)	3.17	61.9	57
$Pd_{64}Ni_{16}P_{20}$	3.1	1 (compression)	3.17	61.9	57
$Fe_{80}B_{20}$ (Metglas 2605)	7.6	2.55 (tension)	2.97	116.6	45

<sup>a</sup>Adapted with permission from: L. A. Davis in *Rapidly Quenched Metals*, N. J. Grant and B. C. Giessen (eds.) (Cambridge, MA: MIT Press, 1976, p. 401), p. 369, Table 1.

## 3.6 | Plastic Deformation of Glasses

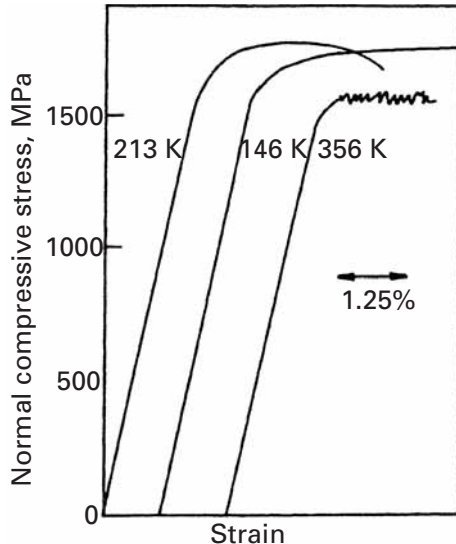
The unique mechanical properties exhibited by metallic glasses are connected to their structure. Table 3.1 lists the hardnesses, yield stresses, and Young's moduli for several metallic glasses. The unique compositions correspond to regions in the phase diagram that have a very low melting point. The low melting points aid in the retention of the "liquid" structure. Metallic glasses are primarily formed by rapid cooling from the molten state, so that the atoms do not have time to form crystals. The Metglas group is commercially produced in wire and ribbon form. Young's modulus for glasses varies between 60 and 70% of the Young's modulus of the equilibrium crystalline structure. Li<sup>7</sup> has proposed a relationship between the shear modulus of the glassy and crystalline states, namely,

$$G_g = \frac{0.947}{1.947 - \nu} G_c \quad (3.27)$$

where  $G_g$  and  $G_c$  are the shear moduli of the glassy and crystalline states, respectively, and  $\nu$  is Poisson's ratio. The crystalline Young's modulus of glasses is recovered when the material is annealed and crystallinity sets in. The yield stresses of metallic glasses are high, as can be seen in Table 3.1. For Fe-B metallic glasses, strength levels over 3.5 GPa were achieved. This is close to the highest yield strengths achieved in polycrystalline metals. (See Section 1.4.) The yield stresses

<sup>7</sup> J. C. M. Li, in *Frontiers in Materials Science – Distinguished Lectures*, L. E. Murr and C. Stein, eds. (New York: Marcel Dekker, 1976), p. 527.

**Fig. 3.22** Compression stress-strain curves for Pd<sub>77.5</sub>Cu<sub>6</sub>Si<sub>16.5</sub>. (Adapted with permission from C. A. Pampillo and H. S. Chen, *Mater. Sci. Eng.*, 13 (1974) 181.)



of the metallic glasses are usually 10 to 30 times higher than the yield stress of the same alloy in the crystalline state.

The micromechanical deformation mechanisms responsible for the unique mechanical properties of metallic glasses are still not very well understood. The absence of crystallinity has a profound effect on the mechanical properties. Grain boundaries, dislocations, mechanical twinning, and other very important components of the deformation of crystalline metals are not directly applicable to metallic glasses. Although the dislocations are not fully described until Chapter 4 (a brief description is given in Section 1.4), the concept is used in this section in an attempt to rationalize the mechanical response of metallic glasses. The lower Young's modulus is probably due to the less efficient packing of atoms, with a consequent larger average interatomic distance. The plastic part of the stress-strain curve also differs from the crystalline one. Here we have to distinguish between the behavior of the metallic glass above and below  $T_g$ , the glass transition temperature. As in silicate glasses, a temperature is defined above which the glass becomes viscous and deformation occurs by a viscous flow that is homogeneous. Only the deformation at temperatures below  $T_g$  will be discussed here. Curves for small cylindrical specimens under compression are shown in Figure 3.22. There is little evidence of work-hardening, and the plastic range is close to horizontal. The surface of the specimens usually exhibits steps produced by shear bands. These shear bands have been found to be 20 nm thick, and the shear offset (step) has been found to be around 200 nm. This shows that deformation is highly inhomogeneous in metallic glasses and that, once shear starts on a certain plane, it tends to continue there. The plane of shear actually becomes softer than the surrounding regions. We can compute

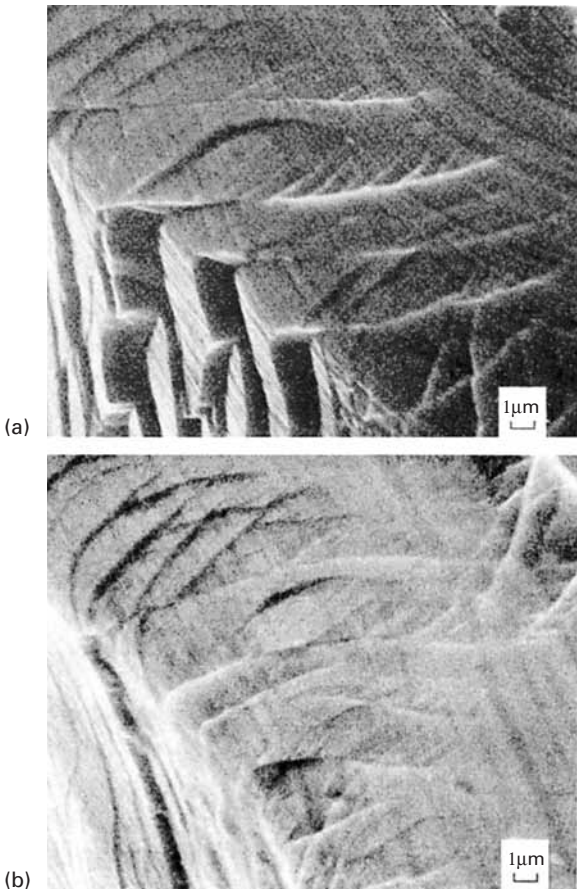


**Fig. 3.23** Shear steps terminating inside material after annealing at  $250^{\circ}\text{C}/\text{h}$ , produced by (a) bending and decreased by (b) unbending Metglas  $\text{Ni}_{82.4}\text{Cr}_7\text{Fe}_3\text{Si}_{4.5}\text{B}_{3.1}$  strip.  
(Courtesy of X. Cao and J. C. M. Li.)

the amount of shear strain in a band by dividing the band offset by the thickness. In the preceding case, it is equal to 10. This behavior is termed work-softening. The curves of Figure 3.22 provide macroscopic support for the absence of work-hardening. The equivalent of a dislocation can exist in a glass. The slip vector of the dislocation would fluctuate in direction and magnitude along the dislocation line, but its mean value would be dictated by some structural parameter.

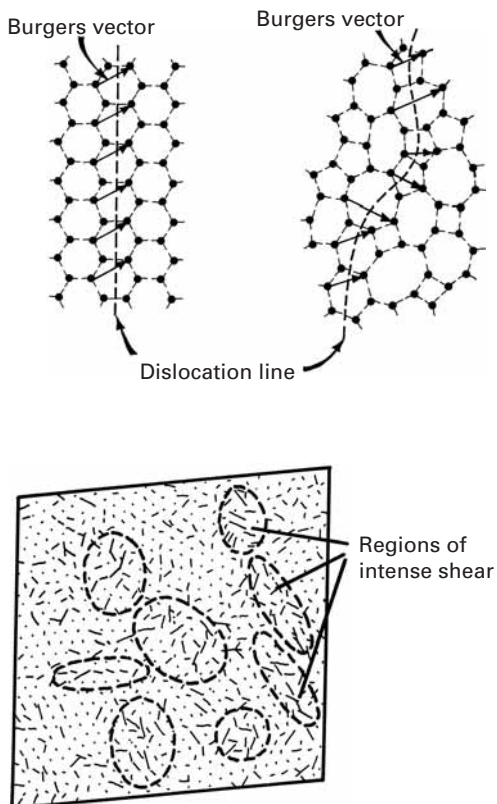
Figure 3.23 shows slip lines and steps produced after bending and after unbending. We can see the slip lines terminating inside the metallic glass. The slips decrease in height on unbending. These observations tend to confirm the relevance of some kind of shear localization in the plastic deformation of metallic glasses.

### 3.6.1 Microscopic Deformation Mechanisms

Of the theories explaining the microscopic aspects of plastic deformation of metallic glasses, the best known are the dislocation theory of Gilman and the strain ellipsoid theory of Argon.

Figure 3.24(a) shows dislocation lines in crystalline and vitreous silica. Dislocations in crystalline solids will be studied in Chapter 4.

**Fig. 3.24** (a) Gilman model of dislocations in crystalline and glassy silica, represented by two-dimensional arrays of polyhedra. (Adapted from J. J. Gilman, *J. Appl. Phys.* 44 (1973) 675) (b) Argon model of displacement fields of atoms (indicated by magnitude and direction of lines) when assemblage of atoms is subjected to shear strain of  $5 \times 10^{-2}$ , in molecular dynamics computation. (Adapted from D. Deng, A. S. Argon, and S. Yip, *Phil. Trans. Roy. Soc. Lond.* A329 (1989) 613.)



The two-dimensional picture in the figure is analogous to the Zachariasen model for silica in Figure 1.18. The dislocation line is shown in the two cases, and we are looking at the dislocation “from the top down;” that is, the extra atomic plane is perpendicular to the surface of the paper. For the regular crystalline structure, all Burgers vectors are parallel and have the same magnitude. For the glassy structure,  $b$  fluctuates both in magnitude and direction. The dislocation line is not forced to remain in a crystallographic plane (there are no such planes in glasses), but can fluctuate. This is the *Gilman* mechanism for plastic deformation of glasses.

Experiments using “bubble rafts” and computational simulations indicate that there are localized regions of approximately ellipsoidal shape that undergo larger distortions than the bulk of the material and that are the main entities responsible for the plastic deformation of glasses. The ellipsoidal regions do not move, but undergo gradual distortion. Figure 3.24(b) shows the result of a computer simulation, including the positions and displacements of individual atoms. The lengths of the lines represent the displacements of the atoms. One can see regions of the material where the displacements of the atoms are larger. The ellipses become distorted, and the entire body deforms. This is the so-called *Argon* model for deformation of glasses, named after a renowned MIT professor (and not after a gas!).

### 3.6.2 Temperature Dependence and Viscosity

The mechanical response of glasses is often represented by their viscosity, which is a property of liquids. The viscosity,  $\eta$  is defined as the velocity gradient that will be generated in a liquid when it is subjected to a specific shear stress, or

$$\tau = \eta \frac{dv}{dy}, \quad (3.28)$$

where  $\tau$  is shear stress,  $v$  is the velocity and  $dv/dy$  is the velocity gradient. For temperature  $T > T_m$ , the viscosity is very low and the glass is a fluid. A characteristic value is  $\eta \cong 10^{-3}$  Pa · s. For  $T \sim T_g$ , (the glass transition temperature), the viscosity is between  $10^{10}$  and  $10^{15}$  Pa · s. A common unit of viscosity is the Poise (P). Note that 1 P = 0.1 Pa · s. For  $T < T_g$ , the viscosity is  $\eta > 10^{15}$  Pa · s. Mechanically speaking, the material is solid. Figure 3.25 shows these different regimens of mechanical response as a function of temperature, for soda-lime-silica glass and for some metallic glasses ( $\text{Au}_{77}\text{Si}_{14}\text{Ge}_{19}$ ,  $\text{Pd}_{77.5}\text{Cu}_6\text{Si}_{16.5}$ ,  $\text{Pd}_{80}\text{Si}_{20}$ , and  $\text{Co}_{75}\text{P}_{25}$ ). The temperature is normalized by dividing it by  $T_g$ . The viscosity decreases at  $T > T_g$ , as

$$\eta = \eta_0 e^{Q/RT}, \quad (3.29)$$

where  $Q$  is the activation energy for viscous flow. This is a classic Arrhenius response. The shear strength of the material can be related to the viscosity by

$$\begin{aligned} v &= \frac{ds}{dt}; \quad \gamma = \frac{ds}{dy} \\ \tau &= \eta \frac{dv}{dy} = \eta \frac{d}{dy} \left( \frac{ds}{dt} \right) = \eta \frac{d}{dt} \left( \frac{ds}{dy} \right) = \eta \frac{d\gamma}{dt} = \eta \dot{\gamma}, \end{aligned}$$

where  $v$  is the velocity of one part of the material with respect to the other. The velocity is the displacement with time,  $ds/dt$ . By changing the order of differentiation, we obtain  $d\gamma = ds/dy$ . The change of strain with time is  $\dot{\gamma} = d\gamma/dt$ . A general relationship between shear stress, shear strain, and shear strain rate is

$$\boxed{\tau = \tau_0 \gamma^n \dot{\gamma}^m,} \quad (3.30)$$

where  $n$  is the work-hardening coefficient and  $m$  is the strain rate sensitivity. Since glasses do not work harden,  $n=1$ . When  $\tau$  is proportional to  $\dot{\gamma}$ , the strain rate sensitivity is equal to unity, and the material will be resistant to necking in tension. This is why glass can be pulled in tension to extremely high strains. Such behavior is discussed in greater detail in Chapter 13. Another class of materials, called *superplastic* materials, also exhibits this response when the grain size of the material is very small.

Viscosity is a very important characteristic of glassy materials. On the viscosity versus temperature curve of a given glassy material, one can identify certain important points. The *strain point* of glass is the temperature at which internal stresses are reduced significantly in a few hours. This corresponds to  $\eta = 10^{13.5}$  Pa · s. The *annealing point* of

**Fig. 3.25** Viscosity of soda-lime-silica glass and of metallic glasses (Au-Si-Ge, Pd-Cu-Si, Pd-Si, C<sub>o</sub>P) as a function of normalized temperature. (Adapted from J. F. Shakelford, *Introduction to Materials Science for Engineers*, 4th ed. (Englewood Cliffs, NJ: Prentice Hall, 1991), p. 331, and F. Spaepen and D. Turnbull in *Metallic Glasses*, ASM.) IP = 0.1 Pa · s.

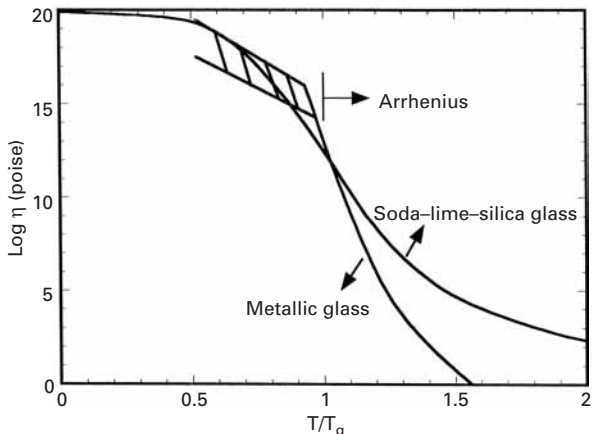
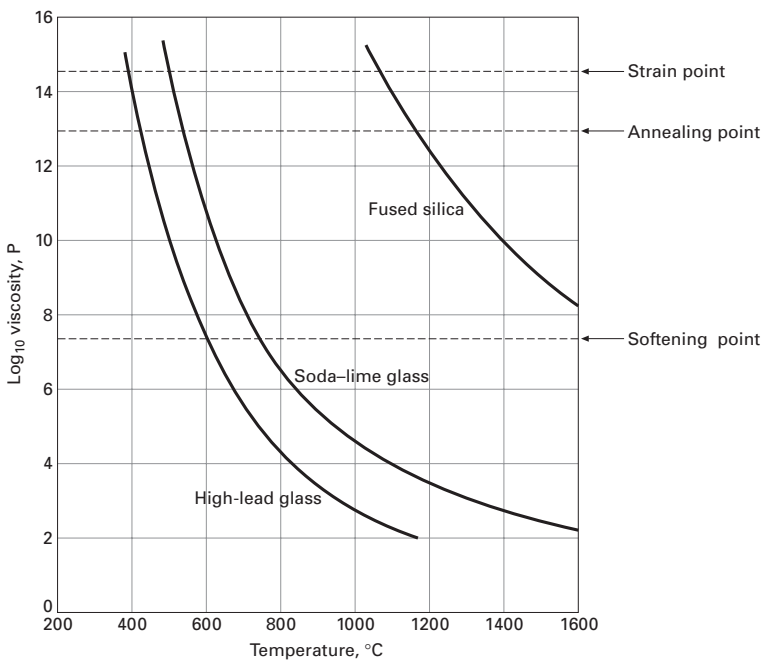


**Fig. 3.26** Viscosity of three glasses as a function of temperature. IP = 0.1 Pa · s.



a glass is the temperature at which the internal stresses are reduced in a few minutes such that  $\eta = 10^{12}$  Pa · s. The *softening point* of a glass corresponds to  $\eta = 10^{6.65}$  Pa · s. At this viscosity, the glass deforms rapidly under its own weight. The *working point* of glass corresponds to  $\eta = 10^3$  Pa · s. At this viscosity, the glass is soft enough to be worked.

The viscosity of glasses is dependent on their composition. Soda-lime-silica and high-lead glasses have lower softening temperatures and are easier to work on. Pure silica, on the other hand, has a significantly higher softening point and requires significantly higher temperatures. On the other hand, it can be used at higher temperatures. Figure 3.26 shows the temperature dependence of viscosity for these three glasses. Note that the ordinate of plot is in P, not Pa · s.

### Example 3.7

Consider a glass with a strain point of 500 °C and a softening point of 800 °C. Using the preceding viscosity values for the strain point and softening point, estimate the activation energy for the deformation of this glass.

**Solution:** We can write the viscosity as a function of temperature as

$$\eta = A \exp[Q/RT].$$

At the softening point,

$$10^{6.65} = A \exp\left[\frac{Q}{8.314 \times 1073}\right],$$

while at the strain point,

$$10^{13.5} = A \exp\left[\frac{Q}{8.314 \times 773}\right].$$

From these two expressions, we obtain, by division

$$10^{6.85} = \exp\left[\left(\frac{Q}{8.314}\right)\left(\frac{1}{773} - \frac{1}{1073}\right)\right],$$

or

$$Q = 362 \text{ kJ/mol.}$$

## 3.7 | Flow, Yield, and Failure Criteria

The terms *flow criterion*, *yield criterion*, and *failure criterion* have different meanings. *Failure criterion* has its historical origin in applications where the onset of plastic deformation indicated failure. However, in deformation-processing operations this is obviously not the case, and plastic flow is desired. *Yield criterion* applies only to materials that are in the annealed condition. It is known that, when a material is previously deformed by, for instance, rolling, its yield stress increases due to work-hardening. (See Chapter 6.) The term *flow stress* is usually reserved for the onset of plastic flow in a previously deformed material. *Failure criterion* is applied to brittle materials, in which the limit of elastic deformation coincides with failure. To be completely general, a flow criterion has to be valid for any stress state. In a uniaxial stress state, plastic flow starts when the stress-strain curve deviates from its initial linear range. Uniaxial stress-strain curves are very easily obtained experimentally, and the deformation response of a material is usually known for this situation. The main function of flow criteria is to predict the onset of plastic deformation in a complex state of stress when one knows the flow stress (under uniaxial tension) of the material. Note that the value of the flow stress is strongly dependent on the state of stress, and if this effect is not considered, it can lead

to potentially dangerous errors in design. We next present some of these criteria.

### 3.7.1 Maximum-Stress Criterion (Rankine)

According to the maximum-stress criterion, plastic flow takes place when the greatest principal stress in a complex state of stress reaches the flow stress in uniaxial tension. Since  $\sigma_1 > \sigma_2 > \sigma_3$ , we have

$$\sigma_0(\text{tension}) < \sigma_1 < \sigma_0 \text{ (compression)},$$

where  $\sigma_0$  is the flow stress of the material. Later (Section 3.7.5) we will see the situation where the compressive strength is greater than the tensile strength. The great weakness of this criterion is that it predicts plastic flow of a material under a hydrostatic state of stress; however, this is impossible, as shown by the following example. It is well known that tiny shrimp can live at very great depths. The hydrostatic pressure due to water is equivalent to 1 atm ( $10^5 \text{ N/m}^2$ ) for every 10 m; at 1,000 m below the surface, the shrimp would be subjected to a hydrostatic stress of  $10^7 \text{ N/m}^2$ . Hence

$$-p = \sigma_1 = \sigma_2 = \sigma_3 = -10^7 \text{ N/m}^2.$$

A quick experiment to determine the yield stress of the shrimp could be conducted by carefully holding it between two fingers and pressing it. By doing the test with a live shrimp, one can define the flow stress as the stress at which the amplitude of the tail wiggling will become less than a critical value. This will certainly occur at a stress of about 0.1 MPa. Hence,

$$\sigma_0 = 0.1 \text{ MPa}.$$

The Rankine criterion would produce shrimp failure at

$$P \equiv -\sigma_0 = -0.1 \text{ MPa}.$$

This corresponds to a depth of only 10 m. Fortunately for all lovers of crustaceans, this is not the case, and hydrostatic stresses do not contribute to plastic flow.

### 3.7.2 Maximum-Shear-Stress Criterion<sup>8</sup> (Tresca)

Plastic flow starts when the maximum shear stress in a complex state of deformation reaches a value equal to the maximum shear stress at the onset of flow in uniaxial tension (or compression). The maximum shear stress is given by (see Section 2.6)

$$\tau_{\max} = \frac{\sigma_1 - \sigma_3}{2}. \quad (3.31)$$

For the uniaxial stress state, we have, at the onset of plastic flow,

$$\sigma_1 = \sigma_0, \quad \sigma_2 = \sigma_3 = 0;$$

so

$$\tau_{\max} = \frac{\sigma_0}{2}.$$

---

<sup>8</sup> H. Tresca, *Compt. Rend. Acad. Sci. Paris*, 59 (1864) 754; 64 (1867) 809.

Therefore,

$$\sigma_0 = \sigma_1 - \sigma_3. \quad (3.32)$$

This criterion corresponds to taking the differences between  $\sigma_1$  and  $\sigma_3$  and making it equal to the flow stress in uniaxial tension (or compression). It can be seen that it does not predict failure under hydrostatic stress, because we would have  $\sigma_1 = \sigma_3 = p$  and no resulting shear stress.

### 3.7.3 Maximum-Distortion-Energy Criterion (von Mises)<sup>9</sup>

This criterion was originally proposed by Huber as "When the expression

$$\frac{\sqrt{2}}{2} [(\sigma_1 - \sigma_2)^2 + (\sigma_2 - \sigma_3)^2 + (\sigma_1 - \sigma_3)^2]^{1/2} > \sigma_0 \quad (3.33)$$

then the material will plastically flow." The left hand side is known as *effective stress*. The criterion was stated by von Mises without a physical interpretation. It is now accepted that it expresses the critical value of the distortion (or shear) component of the deformation energy of a body. Based on this interpretation, a body flows plastically in a complex state of stress when the distortional (or shear) deformation energy is equal to the distortional (or shear) deformation energy in uniaxial stress (tension or compression). This will be shown shortly. This criterion is also called  $J_2$ , which is the second invariant of the stress deviator. Students will learn about this in advanced "Mechanics of Materials" courses.  $J_2$  is given by:

$$J_2 = \frac{1}{G} [(\sigma_1 - \sigma_2)^2 + (\sigma_2 - \sigma_3)^2 + (\sigma_1 - \sigma_3)^2]$$

Hence:  $J_n \geq \frac{\sigma_0^2}{3}$ .

### 3.7.4 Graphical Representation and Experimental Verification of Rankine, Tresca, and von Mises Criteria

There is a convenient way to represent the Rankine, Tresca, and von Mises criteria for a plane state of stress. For this, one makes  $\sigma_3 = 0$  and has  $\sigma_1$  and  $\sigma_2$ . It will be necessary to momentarily forget the convention that  $\sigma_1 > \sigma_2 > \sigma_3$ , because it would not be obeyed for  $\sigma_2 < 0$ ; we have  $\sigma_2 < \sigma_3 = 0$ . Figure 3.27(a) shows a plot of  $\sigma_1$  versus  $\sigma_2$ . According to the Tresca criterion, plastic flow starts when

$$\tau_{\max} = \frac{\sigma_0}{2}.$$

The four quadrants have to be analyzed separately. In the first quadrant, there are two possible situations. For  $\sigma_1$  greater than  $\sigma_2$ ,  $\tau_{\max} = (\sigma_1 - \sigma_3)/2$  and  $\sigma_1 = \sigma_0$ . This is a line passing through  $\sigma_1 = \sigma_0$  and parallel to  $O\sigma_2$ . For  $\sigma_2$  greater than  $\sigma_1$ , we have the converse situation and a line passing through  $\sigma_2 = \sigma_0$  and parallel to  $\sigma_1$ .

<sup>9</sup> R. von Mises, *Göttinger Naehr. Math. Phys. Klasse*, 1913, p. 582.

In the second quadrant,  $\sigma_2 > 0$  and  $\sigma_1 < 0$ . We have

$$\tau_{\max} = \frac{\sigma_1 - \sigma_2}{2} \quad \text{and} \quad \sigma_1 - \sigma_2 = \sigma_0.$$

This equation represents a straight line intersecting the  $0\sigma_1$  axis at  $\sigma_0$  and the  $0\sigma_2$  axis at  $-\sigma_0$ . The flow criteria for quadrants III and IV are found in a similar way.

For the von Mises<sup>10</sup> criterion, we have, from Equation 3.33 and  $\sigma_3 = 0$ ,

$$\begin{aligned}\sigma_0 &= \frac{\sqrt{2}}{2}[(\sigma_1 - \sigma_2)^2 + \sigma_2^2 + \sigma_1^2]^{1/2}, \\ \sigma_1^2 - \sigma_1\sigma_2 + \sigma_2^2 &= \sigma_0^2.\end{aligned}$$

This is the equation of an ellipse whose major and minor axes are rotated  $45^\circ$  from the orthogonal axes  $0\sigma_1$  and  $0\sigma_2$ , respectively. It can be easily shown by applying a rotation of axes to the equation of an ellipse referred to its axes:

$$\left(\frac{\sigma_1}{a}\right)^2 + \left(\frac{\sigma_2}{b}\right)^2 = k^2. \quad (3.34)$$

From Equation 3.34, it can be seen that the Tresca criterion is more conservative than von Mises. The criterion would predict plastic flow for the stress state defined by point  $P_1$ , whereas the von Mises would not. However, both criteria are fairly close. It can be seen from Figure 3.27(a) that plastic flow may require a stress  $\sigma_1$  greater than  $\sigma_0$  for a combined state of stress. (See point  $P_2$ ). However, there are regions (when one stress is tensile and another is compressive) where plastic flow starts when both stresses are within the interval

$$\sigma_0 < \sigma_1, \quad \sigma_2 < \sigma_0.$$

This occurs in the second and fourth quadrants. Point  $P_2$  shows the situation very clearly. The conclusion is that the correct application of a yield criterion is very important for design purposes. For comparison purposes, the maximum-normal stress (Rankine) criterion is also drawn in Figure 3.27(a). It is just a square with sides parallel to the  $0\sigma_1$  and  $0\sigma_2$  axes and intersecting them at  $(\sigma_0, 0)$ ,  $(-\sigma_0, 0)$ ,  $(0, \sigma_0)$ , and  $(0, -\sigma_0)$ . We see that there is a considerable difference between the Rankine criterion, on the one hand, and the Tresca and von Mises criteria, on the other, for quadrants II and IV. This difference is readily explained by the fact that the Rankine criterion applies to brittle solids (including cast irons and steel below the ductile-brittle transition temperature), in which failure (or fracture) is produced by tensile stresses.

Figure 3.27(b) shows the three criteria, together with experimental results for copper, aluminum, steel, and cast iron. While copper and aluminum tend to follow the von Mises criterion (and, in a more conservative way, the Tresca criterion), cast iron clearly obeys the Rankine criterion. This is plainly in line with the low ductility exhibited by

<sup>10</sup> It is also called  $J_2$  criterion; in this case, flow occurs at a critical value of  $J_2 = \frac{1}{6}[(\sigma_1 - \sigma_2)^2 + \sigma_2^2 + \sigma_1^2]$ .

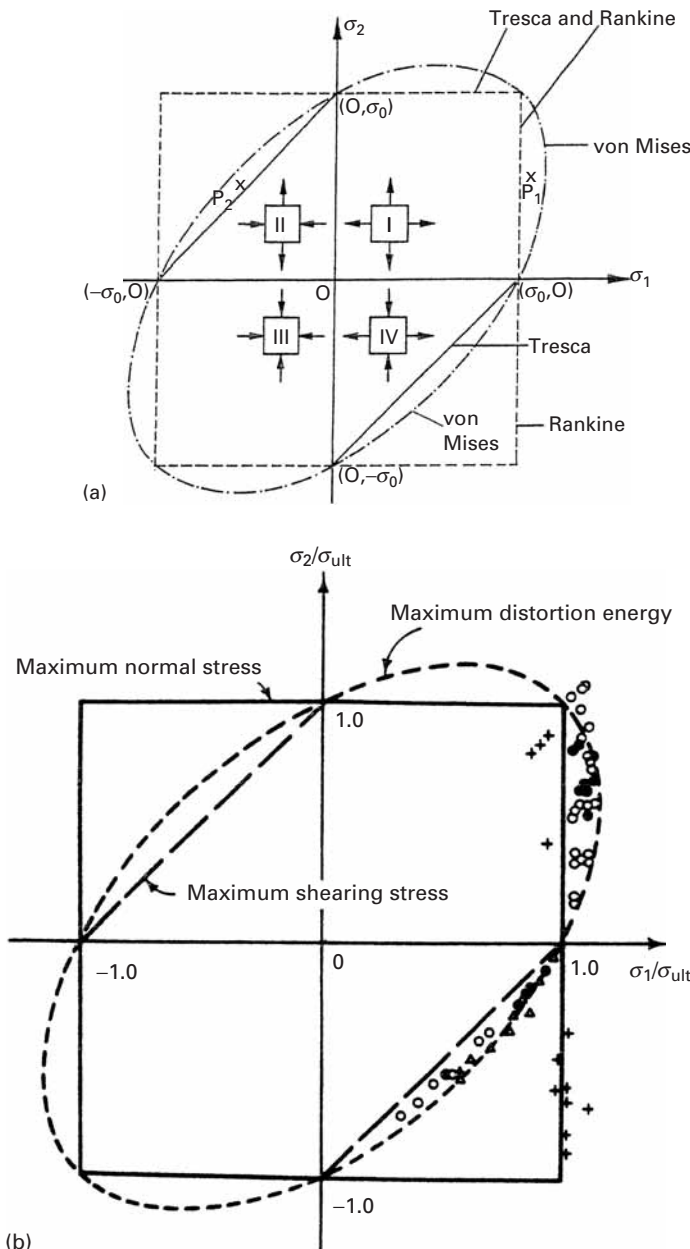
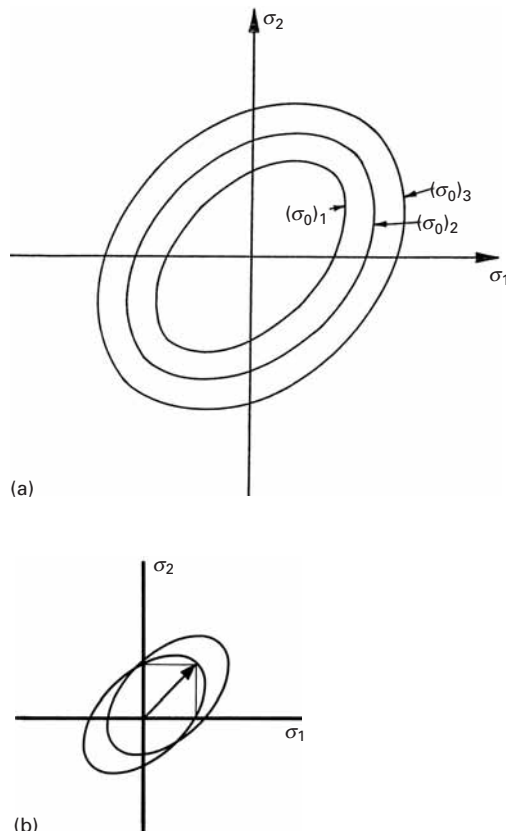


**Fig. 3.27** (a) Comparison of the Rankine, von Mises, and Tresca criteria. (b) Comparison of failure criteria with test. (Reprinted with permission from E. P. Popov, *Mechanics of Materials*, 2nd ed. (Englewood Cliffs, NJ: Prentice-Hall, 1976), and G. Murphy, *Advanced Mechanics of Materials* (New York: McGraw-Hill, 1964), p. 83.)

cast iron. The reader is warned that the ratio  $\sigma/\sigma_{\text{ult}}$ , and not  $\sigma/\sigma_0$ , is used in the figure. Nevertheless, it serves to illustrate the difference in response.

The determination of the flow locus is usually conducted in biaxial testing machines, which operate in a combined tension-torsion or tension-hydrostatic-pressure mode. These two modes use tubular specimens, and one has to use the appropriate calculations to find the principal stresses. As the material is plastically deformed, we have an expansion of the flow locus. For the von Mises criterion, we can

**Fig. 3.28** Displacement of the yield locus as the flow stress of the material due to plastic deformation. (a) Isotropic hardening. (b) Kinematic hardening.



envision concentric ellipses having increasing major and minor axes. This is illustrated in Figure 3.28(a). When the ellipse expands in a symmetric fashion, the hardening is the same in all directions and is called *isotropic*. Often, however, hardening in one direction (the loading direction) causes a change in flow stress in other directions that is different. This is very important in plastic-forming operations (stamping, deep drawing). The extreme case where the ellipse is just translated is shown in Figure 3.28(b). This case is called *kinematic hardening*. (See Section 3.4.)

### Example 3.8

A region on the surface of a 6061-T4 aluminum alloy component has strain gages attached, which indicate the following stresses:

$$\begin{aligned}\sigma_{11} &= 70 \text{ MPa}, \\ \sigma_{22} &= 120 \text{ MPa}, \\ \sigma_{12} &= 60 \text{ MPa}.\end{aligned}$$

Determine the yielding for both the Tresca and von Mises criteria, given that  $\sigma_0 = 150$  MPa (the yield stress).

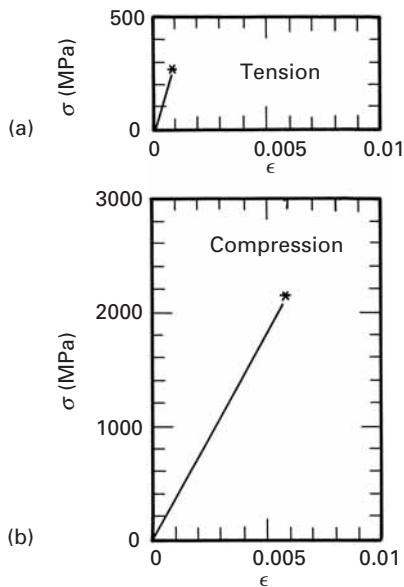


**Fig. 3.29** (a) Tensile strength and (b) compressive strength of  $\text{Al}_2\text{O}_3$ .

**Solution:** We first have to establish the principal stresses. This is easily accomplished by a Mohr circle construction or by its analytical expression (the equation of a circle):

$$\sigma_{1,2} = \frac{\sigma_{11} + \sigma_{22}}{2} \pm \left[ \left( \frac{\sigma_{11} - \sigma_{22}}{2} \right)^2 + \sigma_{12}^2 \right]^{1/2},$$

$$\sigma_1 = 160 \text{ MPa}; \quad \sigma_2 = 30 \text{ MPa}; \quad \sigma_3 = 0.$$

According to Tresca,  $\tau_{\max} = (160 - 0)/2 = 80 \text{ MPa}$ .

The value  $\tau_{\max} = 80 \text{ MPa}$  exceeds the Tresca criterion ( $\sigma_0/2 = 75 \text{ MPa}$ ) and the alloy would be unsafe. The von Mises criterion gives

$$\begin{aligned} J_2 &= \frac{1}{6} [(\sigma_1 - \sigma_2)^2 + (\sigma_1 - \sigma_3)^2 + (\sigma_2 - \sigma_3)^2] \\ &= \frac{1}{6} [130^2 + 160^2 + 30^2] \\ &= 7233 \text{ MPa}^2. \end{aligned}$$

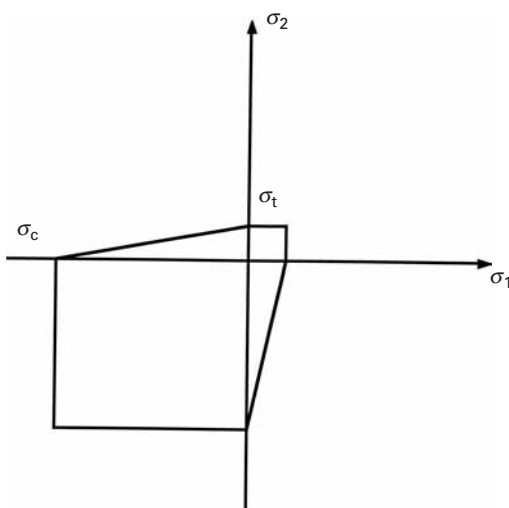
The maximum value of  $J_2^M = (1/3)\sigma_0^2 = (1/3)150^2 = 7500 \text{ MPa}^2$ .

So  $J_2 < J_2^M$ , and the material does not yield. Plainly, the Tresca criterion is more conservative than von Mises.

### 3.7.5 Failure Criteria for Brittle Materials

As shown in Figure 3.29, the tensile strength of  $\text{Al}_2\text{O}_3$  is approximately one-tenth of its compressive strength. Such is also the case for many brittle materials, such as concrete, rock, etc. Therefore, the Rankine, Tresca, and von Mises criteria have to be modified to incorporate this behavior. This will be done in the rest of the section, with the presentation of the Mohr-Coulomb, Griffith, and McClintock-Walsh criteria.

**Fig. 3.30** Schematic two-dimensional representation of Mohr–Coulomb failure criterion.



There are also other criteria (e.g., Babel–Sines), which will *not* be presented here.

#### Mohr–Coulomb Failure Criterion

This is simply the equivalent of the Tresca criterion with different tensile and compressive strengths. Figure 3.30 shows the Mohr–Coulomb criterion in a schematic fashion. The criterion for failure is a maximum shear stress; the compressive strength  $\sigma_c$  is much higher than the tensile strength  $\sigma_t$ .

#### Griffith Failure Criterion<sup>11</sup>

This criterion simply states that failure will occur when the tensile stress tangential to an ellipsoidal cavity and at the cavity surface reaches a critical level  $\sigma_0$ . The criterion is a classic spin-off of Griffith's work of 1919. Griffith recognized that brittle materials contained flaws and that failure would occur at a specific level of stress at the flaw surfaces. He considered an elliptical crack oriented in a general direction with respect to the compression axis and calculated the stresses generated at the surface of the crack. Tensile stresses are generated by compressive loading; this might appear surprising at first sight, but will become clear in Chapter 7. If  $\sigma_0$  is the tensile strength of the material, the following relationship is obtained:

$$\begin{cases} (\sigma_1 - \sigma_2)^2 + 8\sigma_0(\sigma_1 + \sigma_2) = 0 & \text{if } \sigma_1 + 2\sigma_2 > 0, \\ \sigma_2 = \sigma_0 & \text{if } \sigma_1 + 2\sigma_2 < 0. \end{cases} \quad (3.35)$$

The criterion proposed by Griffith is shown in Figure 3.31. The compressive failure stress is eight times the tensile failure stress, as is evident from Equation 3.31. This very important result is consistent with the experimental results observed for brittle materials.

<sup>11</sup> A. A. Griffith, *Proc. 1st Int'l. Congress in Appl. Mech.*, 1925, p. 55.

### McClintock–Walsh Criterion

McClintock and Walsh<sup>12</sup> extended Griffith's criterion by considering a frictional component acting on the flaw faces that had to be overcome in order for the crack to grow. This term is a function of the applied stress. The frictional stress  $f$  was considered equal to the product of the frictional coefficient  $\mu$  and the normal stress  $\sigma_0$  acting on the flaw surface. McClintock and Walsh assumed that there was a stress  $\sigma_c$  at infinity necessary to close the flaw so that the opposite surfaces would touch each other. This approach led to the following expression:

$$\begin{aligned} \sigma_1[(\mu^2 + 1)^{1/2} - \mu] - \sigma_2[(\mu^2 + 1)^{1/2} + \mu] \\ = 4\sigma_0 \left(1 + \frac{\sigma_c}{\sigma_0}\right)^{1/2} - 2\mu\sigma_c. \end{aligned} \quad (3.36)$$

Assuming that  $\sigma_c = 0$ , we get the following simple version of this criterion:

$$\sigma_1[(\mu^2 + 1)^{1/2} - \mu] - \sigma_2[(\mu^2 + 1)^{1/2} + \mu] = 4\sigma_0 \quad (3.37)$$

McClintock and Walsh's criterion is shown in Figure 3.31 for  $\mu = 1$ . Griffith's criterion is more conservative, and the compressive strength is 10 times the tensile strength for McClintock and Walsh. The frictional forces retard failure in compression.

### Example 3.9

Determine the fracture stress for SiC in compression in a complex loading situation in which  $\sigma_1/\sigma_2 = 2$  if  $\sigma_0$  in tension is 400 MN/m<sup>2</sup>. Perform all calculations assuming (a) no friction between crack surfaces and (b) a friction coefficient of 0.5.

**Solution:** Applying Equation 3.35 (with no friction), we have

$$\begin{aligned} \left(\sigma_1 - \frac{\sigma_1}{2}\right)^2 + 8 \times 400 \left(\sigma_1 + \frac{\sigma_1}{2}\right) &= 0, \\ \frac{\sigma_1}{4} + 4,800 &= 0, \\ \sigma_1 &= -19,200 \text{ MPa}, \\ \sigma_1 &= -19.2 \text{ GPa}. \end{aligned}$$

Applying Equation 3.37 (with friction), we obtain

$$\begin{aligned} \sigma_1[(0.5^2 + 1)^{1/2} - 0.5] - 0.5\sigma_1[(0.5^2 + 1)^{1/2} + 0.5] &= 4 \times 400, \\ \sigma_1(0.618) - \sigma_1(0.809) &= 1,600, \\ \sigma_1 &= \frac{-1,600}{0.272}, \\ \sigma_1 &= -5.88 \text{ GPa}. \end{aligned}$$

The very high compressive strengths are due to the confinement. If the ceramic were not confined (i.e., if  $\sigma_2 = 0$ ), the compressive strengths would be -3.2 GPa (Griffith) and -2.5 GPa (McClintock–Walsh).

<sup>12</sup> F. A. McClintock and J. B. Walsh, *Proc. 4th U.S. Nat'l. Cong. of Appl. Mech.* (1962), p. 1015.

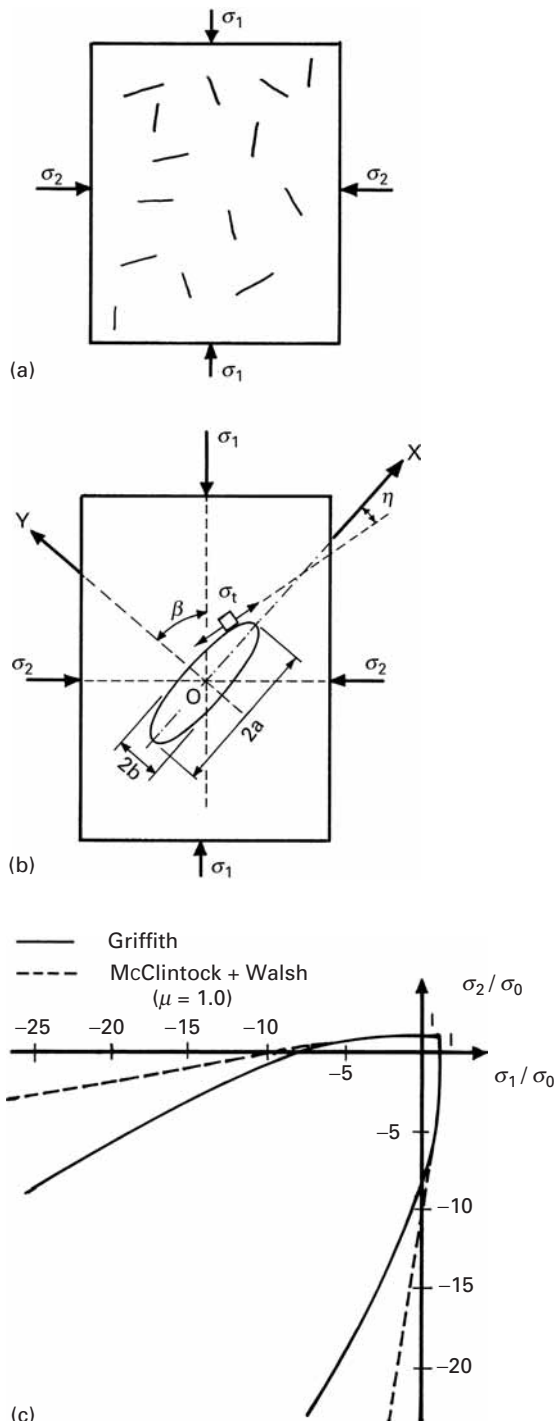


**Fig. 3.31** (a) Simple model for solid with cracks. (b) Elliptical flaw in elastic solid subjected to compression loading. (c) Biaxial fracture criterion for brittle materials initiated from flaws without (Griffith) and with (McClintock and Walsh) crack friction.

### 3.7.6 Yield Criteria for Ductile Polymers

Brittle polymers such as epoxies fail at the end of their linear elastic stage without any significant plastic deformation. Ductile polymers such as thermoplastics undergo plastic deformation. Does this mean that we can use the Tresca or von Mises criteria to describe their yielding? The answer is no, because, unlike the yield strength of metals, that of polymers depends on the hydrostatic component of stress. The Tresca and von Mises criteria, on the other hand, do not show any such dependence. This dependence on hydrostatic stress in polymers stems from the more liquidlike structure of polymers. Specifically, the polymers have some free volume, which makes them highly compressible.

Let us consider the von Mises criterion for isotropic metals. According to this criterion, yielding occurs when the condition

$$(\sigma_1 - \sigma_2)^2(\sigma_2 - \sigma_3)^2 + (\sigma_3 - \sigma_1)^2 \geq 6k^2 = \text{constant}$$

is satisfied, where  $\sigma_1$ ,  $\sigma_2$ , and  $\sigma_3$  are the principal stresses and  $k$  is constant equal to the yield stress in torsion  $\tau_0$ . For metals, we take  $k$  or  $\tau_0$  to be a constant at room temperature, equal to  $\sigma_0/\sqrt{3}$  for uniaxial stress, with  $\sigma_0$  the uniaxial yield stress. This equation also implicitly assumes that the tensile and compressive yield strengths are numerically the same, equal to  $\sqrt{3}k$  or  $\sqrt{3}\tau_0$ . It turns out that for polymers, yield stress in compression is greater than that in tension by 10 to 20%.<sup>13</sup> This stems from the fact that, again unlike yielding in metals, yielding in polymers shows a strong dependence on any superimposed hydrostatic pressure. That is,

$$k = k(\dot{\varepsilon}, T, \sigma_p),$$

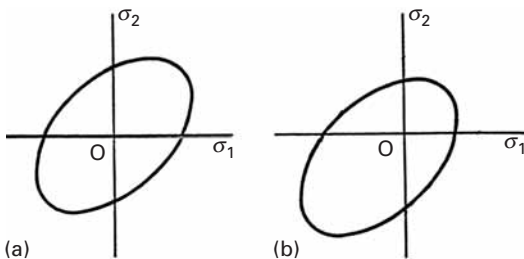
where  $\dot{\varepsilon}$  is the strain rate,  $T$  is the temperature, and  $\sigma_p$  is the hydrostatic pressure. As we mentioned, in molecular terms, this dependence of yield stress on hydrostatic pressure can be traced to the fact that polymers have some *free volume* associated with them, which is diminished by hydrostatic compression. We can modify the yield criterion to take into account this dependence on the hydrostatic compressive stress  $\sigma_p$  by using the expression

$$k = k_0 + A\sigma_p,$$

where  $k_0$  is a constant and  $A$  is another constant that represents the dependence of yield stress on hydrostatic pressure. As  $\sigma_p$  increases, the free volume decreases, and molecular motion becomes more difficult. The presence of a hydrostatic component translates the von Mises ellipse from quadrant I to quadrant III, as shown in Figure 3.32. The yield envelopes for a polymer or metal that does not show yield stress dependence on the hydrostatic component is shown in Figure 3.32(a), while that for a polymer showing yield stress dependence on hydrostatic stress takes the shape shown in Figure 3.32(b). Note that

<sup>13</sup> K. Matsushige, S. V. Radcliffe, and E. Baer, *J. Polymer Sci., Polymer Phys.*, 14 (1976) 703.

**Fig. 3.32** Translation of von Mises ellipse for a polymer due to the presence of hydrostatic stress.  
 (a) No hydrostatic stress, (b) with hydrostatic stress.



crazing occurs only in tension, not in compression. The yield envelope in Figure 3.32(b) has been translated with respect to that in Figure 3.32(a).

Several glassy polymers, such as polystyrene, polycarbonate, and PMMA, show the phenomenon of crazing. (See Section 8.4.2.) Crazing involves the formation of microvoids and stretched chains or fibrils under tension. The fibril formation depends on shear flow and free volume. A yield criterion that takes crazing into account is

$$\sigma_1 - \sigma_2 = A + \frac{B}{(\sigma_1 + \sigma_2)},$$

where  $(\sigma_1 - \sigma_2)$  represents the shear,  $(\sigma_1 + \sigma_2)$  represents the hydrostatic component, and  $A$  and  $B$  are adjustable constants that depend on temperature. Note that as the hydrostatic component  $(\sigma_1 + \sigma_2)$  increases, the shear stress  $(\sigma_1 - \sigma_2)$  required for yielding decreases.

A better and more complete scenario for yielding in polymers is as follows. Under multiaxial stress, glassy polymers can undergo yielding by shear or crazing. Figure 3.33 shows schematically the yield envelope under a biaxial stress condition. The constants  $A$  and  $B$  can be chosen to fit the curve to experimental data. The pure-shear line,  $\sigma_1 = -\sigma_2$ , is the boundary between hydrostatic compression and hydrostatic tension. Below the pure-shear line, crazing (a void-forming process) does not occur because hydrostatic pressure reduces the volume. Above this line, crazing is the main mechanism of failure. The curves for crazing are asymptotic to the pure shear line. The yield envelope shown in the figure also shows the pressure-dependent shear yielding; that is, the envelope has been translated with respect to the conventional von Mises criterion. Note that in the first quadrant the crazing envelope is completely inside the shear yield envelope. This means that for all combinations of biaxial tensile stresses, crazing will precede shear yielding. In the second and fourth quadrants, the two envelopes intersect. The heavy line indicates the overall yielding or failure envelope.

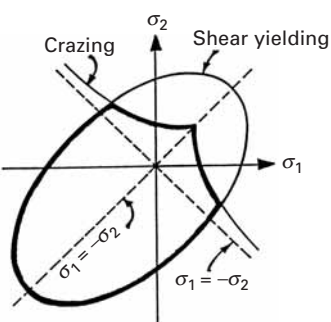


**Fig. 3.33** Envelopes defining shear yielding and crazing for an amorphous polymer under biaxial stress. (After S. S. Sternstein and L. Ongchin, *Am. Chem. Soc., Div. of Polymer Chem., Polymer Preprints*, 10 (1969), 1117.)

A word of caution is in order here. Crazing in air does not occur in pure shear or under conditions of compressive hydrostatic stress. The modified criterion just described requires a dilative component of the applied stress for crazing in air. In the presence of an appropriate environmental agent, crazing can be observed under conditions of simple tension and hydrostatic pressure.

### 3.7.7 Failure Criteria for Composite Materials

Unidirectionally aligned fiber reinforced composites are generally quite anisotropic in elastic constants as well as in strength. This, of course, stems from the fact that fibers generally are a lot stiffer and stronger than the matrix and the fact that the fibers are aligned in the matrix. Quite frequently, the strength in the longitudinal direction is as much as an order of magnitude greater than that in the transverse direction. We shall consider the case of laminated composites made by stacking plies of different orientations in an appropriate sequence. We assume that the fiber reinforced lamina is a homogeneous, orthotropic material. We use a continuum mechanics approach, i.e., we treat the fiber reinforced composite as a homogeneous material, i.e., its properties do not change from point to point. We do, however, consider the fiber reinforced composite to be an orthotropic material, i.e., the anisotropic nature of the composite is taken into account. There are many criteria available in the literature; for a summary, see Chawla<sup>14</sup>. Here, we describe one criterion, called *quadratic interaction criterion*, which is quite general and seems to work quite well for laminated composites made by stacking laminae of fiber reinforced composites in different orientations. The thickness of the individual lamina as well as the laminated composite is much smaller than either the length or width, which allows us to use plane stress condition to analyze the failure criterion. In practical terms, it means that we need to worry about the in-plane stress components, viz, two normal components,  $\sigma_1$  and  $\sigma_2$ , and one in-plane shear component,  $\sigma_{12}$ . In the composite literature, it is customary to use symbol  $\sigma_6$  for  $\sigma_{12}$ . Thus, the reader must keep in mind in what follows that  $\sigma_6$  represents the in-plane shear component.

#### Quadratic Interaction Criterion

This criterion, a combination of linear and quadratic terms, takes into account the stress interactions. Tsai and Wu proposed this, a modification of the Hill theory, for a fiber reinforced composite laminate by adding some additional terms. According to this theory, the failure surface in stress space can be described by a function of the form

$$f(\sigma) = f_i \sigma_i + f_{ij} \sigma_i \sigma_j = 1 \quad i, j = 1, 2, 6 \quad (3.38)$$

where  $f_i$  and  $f_{ij}$  are the strength parameters. For the case of plane stress,  $i, j = 1, 2, 6$  and we can expand Equation (3.38) as follows:

$$\begin{aligned} f_1 + \sigma_1 + f_2 \sigma_2 + f_6 \sigma_6 + f_{11} \sigma_1^2 + f_{22} \sigma_2^2 + f_{66} \sigma_6^2 \\ + 2f_{12} \sigma_1 \sigma_2 + 2f_{16} \sigma_1 \sigma_6 + 2f_{26} \sigma_2 \sigma_6 = 1 \end{aligned} \quad (3.39)$$

For an orthotropic lamina, it is important to distinguish between the signs of normal stresses, i.e., tensile or compressive. The linear stress terms provide for this difference. For the shear stress component, the sign reversal should be immaterial. Thus, terms containing the first degree shear stress must vanish in Equation (3.39). These

<sup>14</sup> K. K. Chawla, *Composite Materials*, 2nd ed. (New York: Springer-Verlag, 1998).

terms are  $f_{66}\sigma_6$ ,  $2f_{16}\sigma_1\sigma_6$ , and  $2f_{26}\sigma_2\sigma_6$ . The stress components in general are not zero. Therefore, for these three terms to vanish we must have

$$f_{16} = f_{26} = f_6 = 0$$

Equation (3.39) is now simplified to

$$f_1\sigma_1 + f_2\sigma_2 + f_{11}\sigma_1^2 + f_{22}\sigma_2^2 + f_{66}\sigma_6^2 + 2f_{12}\sigma_1\sigma_2 = 1 \quad (3.40)$$

There are six strength parameters in Equation (3.40). We can measure five of these by the following simple tests.

#### Longitudinal (Tensile and Compressive) Tests

If  $X_{1t}$  and  $X_{1c}$  are the longitudinal tensile and compressive strengths, respectively, then we can write

$$f_1 X_{1t} + f_{11} X_{1t}^2 = 1$$

and

$$-f_1 X_{1c} + f_{11} X_{1c}^2 = 1.$$

From these two expressions, with two unknowns, we get

$$f_1 = \frac{1}{X_{1t}} - \frac{1}{X_{1c}}$$

and

$$f_{11} = \frac{1}{X_{1t} X_{1c}}.$$

#### Transverse (Tensile and Compressive) Tests

If  $X_{2t}$  and  $X_{2c}$  are the transverse tensile and compressive strengths, respectively, then proceeding as above, we get

$$f_2 = \frac{1}{X_{2t}} - \frac{1}{X_{2c}}$$

and

$$f_{22} = \frac{1}{X_{2t} X_{2c}}.$$

#### Longitudinal Shear Test

If  $X_6$  is the shear strength, we have

$$f_{66} = \frac{1}{X_6^2}.$$

Thus, we can express all the failure strength parameters in Equation 3.40 except  $f_{12}$  in terms of the ultimate intrinsic strength properties of the composite.  $f_{12}$  must be evaluated by means of a biaxial test, which is not easy to do. In the absence of other data, we can take  $f_{12} \approx -0.5(f_{11}f_{22})^{1/2}$ . It turns out, however, that small changes in  $f_{12}$  can significantly affect the predicted strength. Equation 3.40 describes the

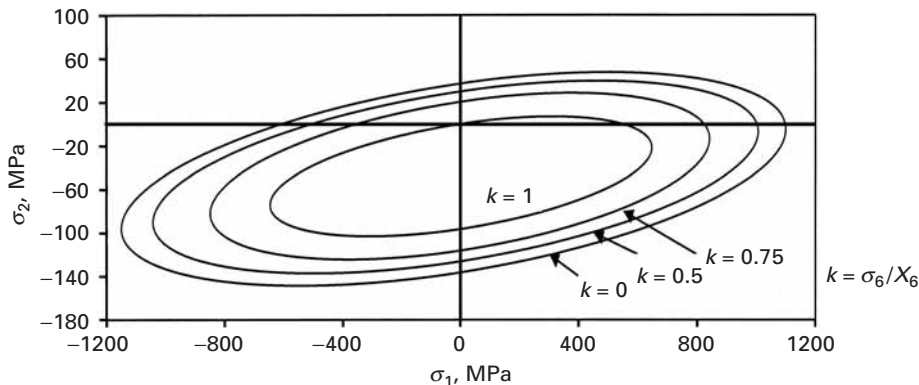


**Fig. 3.34** Failure envelope for unidirectional E-glass/epoxy composite under biaxial loading at different levels of shear stress. (After I. M. Daniel and O. Ishai, *Engineering Mechanics of Composite Materials* (New York: Oxford University Press, 1994), p. 121.)

failure envelope, a three-dimensional ellipsoid, in the  $\sigma_1$ ,  $\sigma_2$ , and  $\sigma_6$  space. For constant values of shear stress,  $\sigma_6 = kX_6$ , we shall have the failure envelope in the form of a two-dimensional ellipse described by the following equation:

$$f_1\sigma_1 + f_2\sigma_2 + f_{11}\sigma_1^2 + f_{22}\sigma_2^2 + f_{66}\sigma_6^2 + 2f_{12}\sigma_1\sigma_2 = 1 - k_2 \quad (3.41)$$

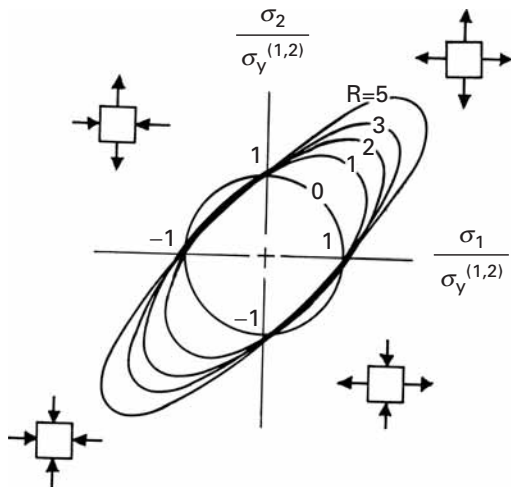
Figure 3.34 shows schematically the failure envelopes under biaxial loading for a unidirectionally reinforced glass fiber/epoxy composite, for different values of  $k$ , where  $k = \sigma_6/X_6$ . Just as the name quadratic interaction indicates, the stress interaction is clear in all quadrants. The reader should note that the quadratic interaction criterion merely predicts the conditions of failure, it does not tell us anything about the mode of failure, i.e., fiber failure, interface failure in shear, etc.

### 3.7.8 Yield and Failure Criteria for Other Anisotropic Materials

Besides fiber reinforced composites, there are other anisotropic materials. The source of anisotropy in these materials can be one of the following.

- A single crystal can have different properties in different directions due to its inherent crystal symmetry.
- A cold-rolled sheet, tube, or wire of a metal or alloy can show a very high degree of preferred orientation of grains. Polymers are also frequently processed by drawing, extrusion, or injection molding techniques. Such techniques impart a high degree of anisotropy to the polymer. Figure 3.35 shows the change in shape of the yield surface as a function of anisotropy, where  $R = \sigma_2/\sigma_1$ . For  $R = 1$ , we have isotropy, and a classical von Mises curve is obtained.

**Fig. 3.35** Plane-stress yield loci for sheets with planar isotropy or textures that are rotationally symmetric about the thickness direction,  $x_3$ . (Values of  $R$  indicate the degree of anisotropy =  $\sigma_2/\sigma_1$ .)



While the most anisotropic crystal would render the plasticity treatment prohibitively complex, there is one type of anisotropy that can be studied without excessive complications. The type of response displayed by wood is a good illustration of this anisotropy. Wood has different yield stresses along the three directions defined by the wood fibers and by the normals to the fibers. Similarly, a rolled sheet or slab of metal will exhibit orthotropic plastic properties; the rolling direction, transverse direction, and thickness direction define the three axes.

### 3.8 | Hardness

The simplest way of determining the resistance of a metal to plastic deformation is through a hardness test. Indentation tests constitute the vast majority of hardness tests. They are essentially divided into three classes, commonly called *nanoindentation*, *microindentation*, and *macroindentation* tests, but improperly referred to as microhardness and macrohardness tests. The division between micro and macro occurs for a load of approximately 200 gf ( $\sim 2$  N). In nanoindentation testing, the load is of the order of mN. The indentation tests in metals measure the resistance to plastic deformation; both the yield stress and the work-hardening characteristics of the metal are important in determining the hardness. In spite of the theoretical studies done on hardness, hardness cannot be considered a fundamental property of a metal. Rather, it represents a quantity measured on an arbitrary scale.<sup>15</sup> Hardness measurements should not be taken

<sup>15</sup> M. C. Shaw, in *The Science of Hardness Testing and its Research Applications*, J. H. Westbrook and H. Conrad, eds. (Metals Park, OH: ASM, 1973), p. 1.

Table 3.2 | Approximate Hardness Conversions for Steels†

Vickers HV	Stand.	HB (Brinell) (10-mm ball, 3,000 kgf)	Rockwell			Rockwell Superficial		Shore Sclero- scope	Approximate Tensile Strength (MPa)
			A (Brinell 60 kgf)	B (1 Brinell 100 kgf)	C (Brinell 150 kgf)	D (Brinell 100 kgf)	15N		
940		85.6	68.0	76.9	93.2	75.4	97		
900		85.0	67.0	76.1	92.9	74.2	95		
860		84.4	65.9	75.3	92.5	73.1	92		
820		73.8	64.7	74.3	92.1	71.8	90		
780		83.0	63.3	73.3	91.5	70.2	87		
740		82.2	61.8	72.1	91.0	68.6	84		
700		65.6	81.3	60.1	70.8	90.3	66.7	81	
660		62.0	80.3	58.3	69.4	89.5	64.7	79	
620		58.2	79.2	56.3	67.9	88.5	62.4	75	206
580		54.5	78.0	54.1	66.2	87.5	59.9	72	192
540		49.6	50.7	76.7	51.7	64.4	86.3	57.0	69
500		46.5	47.1	75.3	49.1	62.2	85.0	53.9	66
460		43.3	43.3	73.6	46.1	60.1	83.6	50.4	62
420		39.7	39.7	71.8	42.7	57.5	81.8	46.4	57
380		36.0	36.0	69.8	38.8	54.4	79.8	41.7	52
340		32.2	32.2	67.6	34.4	51.1	77.4	36.5	47
300		28.4	28.4	65.2	29.8	47.5	74.9	31.1	42
260		24.7	24.7	62.4	24.0	43.1	71.6	24.3	37
220		20.9	20.9	95.0				32	834
200		19.0	19.0	91.5				29	696
180		17.1	17.1	87.1				26	634
160		15.2	15.2	81.7				24	579
140		13.3	13.3	75.0				21	517
120		11.4	11.4	66.7					455
100		9.5	9.5	62.3					
85		8.1	8.1	4.1					

†Tables for other metals and alloys can be found in ASTM 140 (Standard Hardness Conversion Tables for Metals). Adapted with permission from E. R. Petty, in *Techniques of Metals Research*, Vol. 5, Pt. 2, R. F. Bunshah, ed. (New York: Wiley-Interscience, 1971), p. 180.

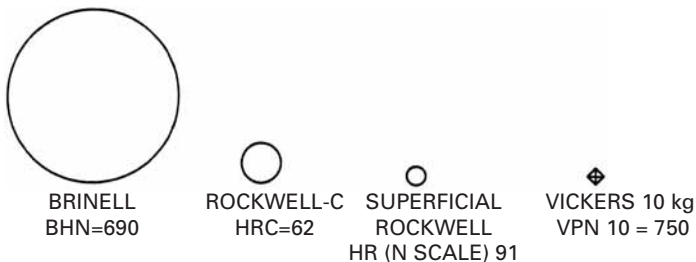


**Fig. 3.36** Comparison of the impression sizes produced by various hardness tests on material of 750 HV. BHN = Brinell hardness number, HRC = Rockwell hardness number on C scale, HRN = Rockwell hardness number on N scale, VPN = Vickers hardness number. (Adapted with permission from E. R. Petty, in *Techniques of Metals Research*, Vol. 5, Pt. 2, R. F. Bunshah, ed. (New York: Wiley-Interscience, 1971), p. 174.)

to mean more than what they are: an empirical, comparative test of the resistance of the metal to plastic deformation. Any correlation with a more fundamental parameter, such as the yield stress, is valid only in the range experimentally determined. Similarly, comparisons between different hardness scales are meaningful only through experimental verification. For steels, Table 3.2 gives a fair conversion of hardness and the tensile strength equivalents.

The most important macro-, micro-, and nanoindentation indentation tests are described in Sections 3.8.1–3.8.3.

### 3.8.1 Macroindentation Tests

The impressions caused by macroindentation tests are shown in Figure 3.36. The Brinell test produces by far the largest indentation. The Vickers test may produce very small indentations, depending on the load used.

#### Brinell Hardness Test

In this test, a steel sphere is pressed against a metal surface for a specified period of time (10 to 15 s, according to the ASTM), and the surface of the indentation is measured. The load (in kgf) divided by the area (in  $\text{mm}^2$ ) of the curved surface gives the hardness HB, or

$$\boxed{\text{HB} = \frac{P}{\pi D \times \text{depth}}} \quad (3.42)$$

$$= \frac{2P}{\pi D(D - \sqrt{D^2 - d^2})}, \quad (3.43)$$

where  $D$  and  $d$  are the diameters of the sphere and impression, respectively. The parameters are indicated in Figure 3.37. Since  $d = D \sin \phi$ , we have

$$\text{HB} = \frac{2P}{\pi D^2(1 - \cos \phi)}. \quad (3.44)$$

Different spheres produce different impressions, and if we want to

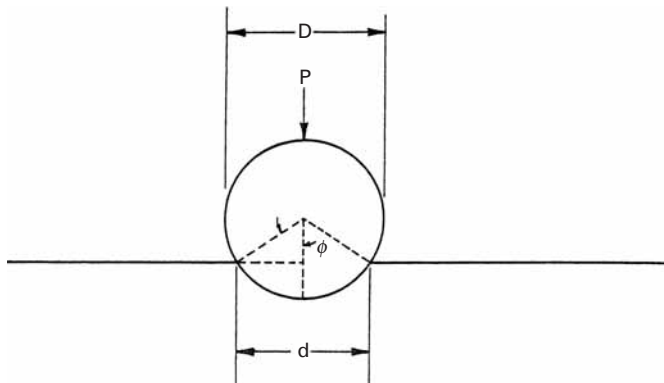


**Fig. 3.37** Impression caused by spherical indenter on metal plate.

maintain the same HB, independent of the size of the sphere, the load has to be varied according to the relationship

$$\frac{P}{D^2} = \text{constant.} \quad (3.45)$$

This assures the same geometrical configuration (the same  $\phi$ ). The diameter of the impressions between  $0.25D$  and  $0.5D$  gives good, reproducible results. The target sought is  $d = 0.375D$ . If the same  $d/D$  ratio is maintained (constant  $\phi$ ), the Brinell test is reliable. Spheres with diameters of 1, 2, 5, and 10 mm have been used, and some of the ratios  $P/D^2$  that provide good  $d/D$  ratios for different metals are: steels and cast irons (30), Cu and Al (5), Cu and Al alloys (10), and Pb and Sn alloys (1). The softer the material, the lower is the  $P/D^2$  ratio required to produce  $d/D = 0.375$ .

One of the problems of the Brinell test is that HB is dependent on the load  $P$  for the same sphere. In general, HB decreases as the load is increased. ASTM standard E10-78 provides details and specifications for Brinell hardness tests. It states that the standard Brinell test is conducted under the following conditions:

Ball diameter: 10 mm

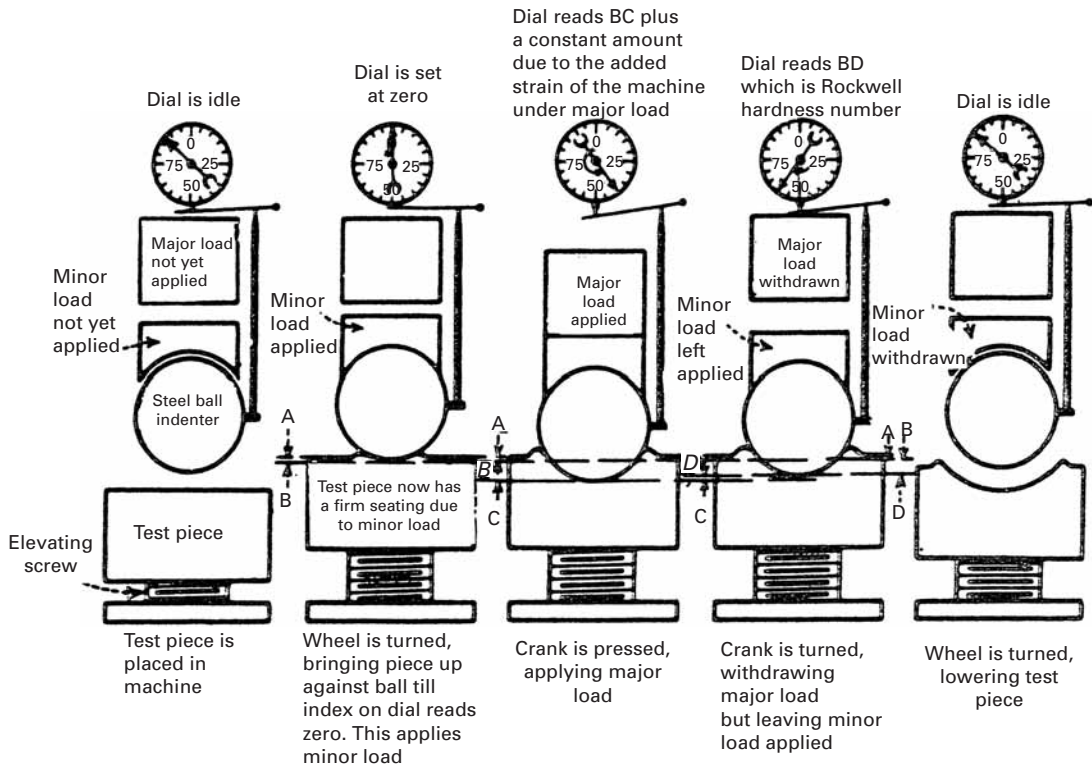
Load: 3000 kgf

Duration of loading: 10 to 15 s

In this case, 360 HB indicates a Brinell hardness of 360 under the foregoing testing conditions. For different conditions, the parameters have to be specified. For example, 63 HB 10/500/30 indicates a Brinell hardness of 63, measured with a ball of 10 mm diameter and a load of 500 kgf applied for 30 s. Brinell tables and additional instructions are provided in ASTM E10-78. Meyer<sup>16</sup> was aware of this problem and proposed a modification of the Brinell formula. He found out that the load divided by the projected area of the indentation ( $\pi d^2/4$ ) was constant. Hence, he proposed, in place of Equation 3.42, the equation

$$\text{Meyer} = \frac{4P}{\pi d^2}, \quad (3.46)$$

<sup>16</sup> E. Meyer, Z. Ver. Dtsch. Ing., 52 (1980) 645, 740, 835.



AB = Depth of hole made by minor load.

AC = Depth of hole made by major load and minor load combined.

DC = Recovery of metal upon withdrawal of major load. This is caused by elastic recovery of the metal under test, and does not enter the hardness reading.

BD = Difference in depth of holes corresponds to Rockwell hardness number.

**Fig. 3.38** Procedure in using Rockwell hardness tester.  
(Reprinted with permission from H. E. Davis, G. E. Troxel, and C. T. Wiscocil, *The Testing and Inspection of Engineering Materials*, (New York: McGraw-Hill, 1941), p. 149.)

where  $P$  is expressed in kilograms force and  $d$  in millimeters. The Meyer hardness never gained wide acceptance, in spite of being more reliable than the Brinell hardness. For work-hardened metals, it seems to be independent of  $P$ .

### Rockwell Hardness Test

The most popular hardness test is also the most convenient, since there is no need to measure the depth or width of the indentation optically. This testing procedure is illustrated in Figure 3.38. A preload is applied prior to the application of the main load. The dial of the machine provides a number that is related to the depth of the indentation produced by the main load. Several Rockwell scales are used, and the numbers refer to arbitrary scales and are not directly related to any fundamental parameter of the material. Two different types of indenters are used. The A, C, D, and N scales use the Brale indenter, which is a diamond cone with a cone angle of  $120^\circ$ . The other scales use either  $1/8$ -in. (3.175-mm) or  $1/16$ -in. (1.587-mm)-diameter steel spheres. The loads also vary, depending on the scale.

**Table 3.3** Details of the More Important Scales Available for the Rockwell Hardness Tester

Scale Designation	Type of Indenter	Major Load (kgf)	Typical Field of Application
A	Brale	60	The only continuous scale from annealed brass to cemented carbide, but is usually used for harder materials
B	1.587 mm-diameter steel ball	100	Medium-hardness range (e.g., annealed steels)
C	Brale	150	Hardened steel > HRB100
D	Brale	100	Case-hardened steels
E	3.175 mm-diameter steel ball	100	Al and Mg alloys
F	1.587 mm-diameter steel ball	60	Annealed Cu and brass
L	6.35 mm-diameter steel ball	60	Pb or plastics
N	N Brale	15, 30, or 45	Superficial Rockwell for thin samples or small impressions

Table 3.3 shows the various loads and typical applications. Usually, the C scale is used for harder steels and the B scale for softer steels; the A scale covers a wider range of hardness. Because of the nature of the measurement, any sagging of the test piece will produce changes in hardness. Therefore, it is of utmost importance to have the sample well supported; specimens embedded in Bakelite cannot be tested. The Brinell and Vickers tests, on the other hand, which are based on optical measurements, are not affected by the support.

For very thin samples, there is a special superficial Rockwell test. The testing procedure is described in detail in the ASTM Standard E18-74, and conversion tables for a number of alloys are given in ASTM Standard E140-78. The symbol used to designate this hardness is, according to the ASTM, HR; 64HRC corresponds to Rockwell hardness number 64 on the C scale.

The following precautions are recommended for reproducible results in Rockwell testing.<sup>17</sup>

1. The indenter and anvil should be clean and well seated.
2. The surface to be tested should be clean, dry, smooth, and free from oxide. A rough-ground surface is usually adequate for the Rockwell test.
3. The surface should be flat and perpendicular to the indenter.
4. Tests on cylindrical surfaces will give low readings, the error depending on the curvature, load, indenter, and hardness of the material. Corrections are given in ASTM E140-78.

<sup>17</sup> G. E. Dieter, *Mechanical Metallurgy*, 2<sup>nd</sup> ed. (New York: McGraw-Hill, 1976), p. 398.

5. The thickness of the specimen should be such that a mark or bulge is not produced on the reverse side of the piece. It is recommended that the thickness be at least 10 times the depth of the indentation. Tests should be made on only a single thickness of material.
6. The spacing between indentations should be three to five times the diameter of the indentation.
7. The speed of application of the load should be standardized. This is done by adjusting the dashpot on the Rockwell tester. Variations in hardness can be appreciable in very soft materials, unless the rate of application of the load is carefully controlled. For such materials, the operating handle of the Rockwell tester should be brought back as soon as the major load has been fully applied.

#### Vickers (or Diamond Pyramid) Hardness Test

This test uses a pyramidal indenter with a square base, made of diamond. The angle between the faces is  $136^\circ$ . The test was introduced because of the problems encountered with the Brinell test. One of the known advantages of the Vickers test is that one indenter covers all the materials, from the softest to the hardest. The load is increased with hardness, and there is a continuity in scale. The angle of  $136^\circ$  was chosen on the basis of results with spherical indenters. For these, the best results were obtained when  $d/D = 0.375$ . If we take the points at which the sphere touches the surface of the specimen and draw perpendiculars to the radii, their intersection will form an angle of  $136^\circ$ . This exercise is left to the student. The description of the procedures used in testing is given in ASTM Standard E92-72. The Vickers hardness (HV) is computed from the equation and is equal to the load divided by the area of the depression

$$\boxed{HV = \frac{2P \sin(\alpha/2)}{d^2} = \frac{1.8544P}{d^2}}, \quad (3.47)$$

where  $P$  is the applied load (in kgf),  $d$  is the average length of the diagonals (in mm), and  $\alpha$  is the angle between the opposite faces of the indenter ( $136^\circ$ ). Conversion to MPa is accomplished by multiplying this value by 9.81. The Vickers test described by ASTM E92-72 uses loads varying from 1 to 120 kgf. For example, 440HV30 represents a Vickers hardness number of 440, measured with a load of 30 kgf. Vickers testing requires a much better preparation of the material's surface than does Rockwell testing; hence, it is more time-consuming. The surface has to be ground and polished, care being taken not to work-harden it. After the indentation, both diagonals of impression are measured, and their average is taken. If the surface is cylindrical or spherical, a correction factor has to be introduced. ASTM Standard E92 (Tables 4 through 6) provide correction factors. As with other hardness tests, the distance between the indentations has to be greater than two-and one-half times the length of the indentation diagonal, to avoid interaction between the work-hardening regions.

The manner in which the material flows and work-hardens (or work-softens) beneath the indenter affects the shape of the impression. The sides of the square impression can be deformed into concave or convex curves, depending on the nature of the deformation process, and this results in reading errors.

### Relationships Between Yield Stress and Hardness

For non-work-hardening materials, one has (this will be derived in Example 3.10):

$$H = 3\sigma_y. \quad (3.48)$$

Since there is a lot of plastic deformation under the indenter, in work-hardening materials we cannot use  $\sigma_y$ . Tabor<sup>18</sup> gives the following equation for the mean plastic strain under the indenter:

$$\varepsilon_p = \frac{d'}{5D},$$

where  $d'$  is the diameter at the top of the pileup and  $D$  is the diameter of the indenter. For  $d'/D = 0.375$ , a reasonable value for indentation, the plastic strain,  $\varepsilon_p = 0.075$ . Hence, for work-hardening metals one should take the flow stress at a plastic strain of 0.375 before multiplying it by 3 for a good correlation with the hardness.

### 3.8.2 Microindentation Tests

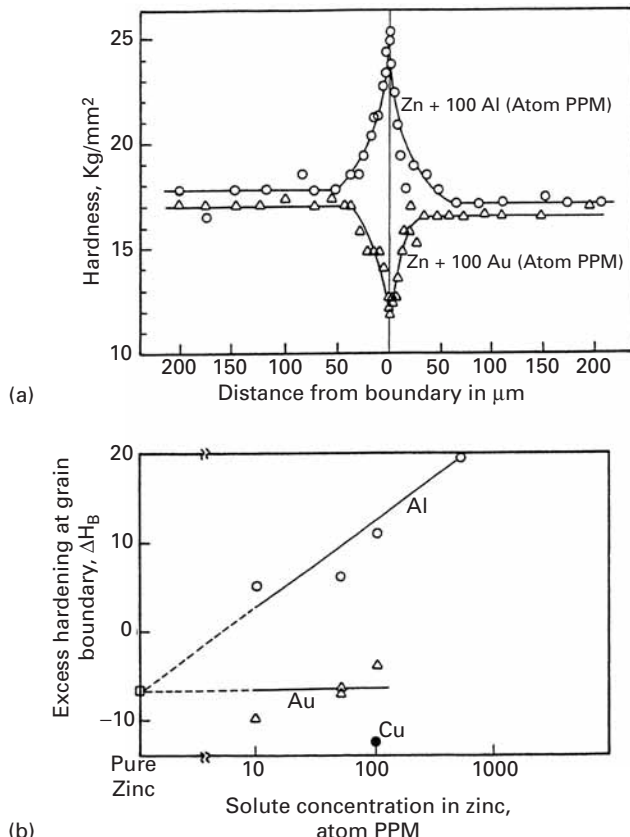
Microindentation hardness tests — or microhardness tests — utilize a load lighter than 200 gf, and very minute impressions are thus formed; a load of 200 gf produces an indentation of about 50  $\mu\text{m}$  for a medium-hardness metal. These tests are ideally suited to investigate changes in hardness at the microscopic scale. One can measure the hardness of a second-phase particle and identify regions within a grain where differences in hardness occur. Microhardness tests are also used to perform routine tests on very small precision components, such as parts of watches.

The results shown in Figure 3.39 illustrate well an application of microindentation testing. When a metal is alloyed, the distribution of the solute is not even throughout the grain, due to the stress fields produced by the solute atom. (See Chapter 7.) The solute atoms often tend to segregate at the grain boundaries. Figure 3.39(a) shows how the addition of aluminum to zinc is reflected by an increase in the hardness in the grain-boundary region, and the addition of gold results in a lowering of the grain-boundary hardness. This effect can be noted at extremely low concentrations of solute (a few parts per million). Figure 3.39(b) shows how this “excess” hardening increases with the concentration of aluminum.

In spite of the attempts made, several problems have arisen in the standardization of microindentation testing and its extrapolation to macroindentation results. There are several reasons for this.

<sup>18</sup> D. Tabor, *The Hardness of Metals*, (Oxford: Oxford University Press, 1951).

**Fig. 3.39** (a) Hardness-distance profiles near a grain boundary in zinc with 100-atom ppm of Al and zinc with 100-atom ppm of Au (1-gf load). (b) Solute concentration dependence of percent excess boundary hardening in zinc containing Al, Au, or Cu (3-gf load). (Adapted with permission from K. T. Aust, R. E. Hanemann, P. Niessen, and J. H. Westbrook, *Acta Met.*, 16 (1968) 291.)



First, almost invariably, the microhardness of any material is higher than its standard macrohardness. Additionally, the microhardness varies with load. Second, there is a tendency for the microhardness to increase (up to a few grams); then the hardness value drops with load. At very low loads, one is essentially measuring the hardness of a single grain; the indenter “sees” a single crystal, and the plastic deformation produced by the indentation is contained in this grain. As the load is increased, plastic deformation of adjoining grains is involved, and a truly polycrystalline deformation regimen is achieved. As we know well (see Chapter 5), the grain size has a marked effect on the yield strength and work-hardening characteristics of metals. Yet another source of error is the work-hardening introduced in the surface by polishing. The effect of crystallographic orientation, when the impression is restricted to a single grain, is of utmost importance. It is well known that both the yield stress and the work-hardening are dependent on the crystallographic orientation of the material. The Schmid law relates the applied stress to the shear stress “seen” by the various slip systems. The Schmid relation is discussed in Section 6.2.2.

The two most common microindentation tests are the Knoop and Vickers tests. The Knoop indenter is an elongated pyramid, shown in

Figure 3.40. The hardness is obtained from the surface area of the impression and is given by

$$KHN = \frac{14.228P}{L^2}, \quad (3.49)$$

where  $P$  is the load of kgf and  $L$  is the length of the major diagonal, in mm. The ratio between the dimensions of the impression is

$$h/W/L = 1 : 4.29 : 30.53.$$

This results in an especially shallow impression, making the technique very helpful for testing brittle materials. Indeed, that was the purpose of introducing the test. The ratio between the major and minor diagonal of the impression is approximately 7:1, resulting in a state of strain in the material that can be considered to be plane strain; the strain in the  $L$  direction may be neglected. This subject is treated in Section 3.3. The very shallow Knoop impression is also helpful in testing thin components, such as electrodeposits or hardened layers. The Vickers microhardness test uses the same  $136^\circ$  pyramid with loads of a few grams. Both Knoop and Vickers indenters require prepollishing of the surface to a microscopic grade.

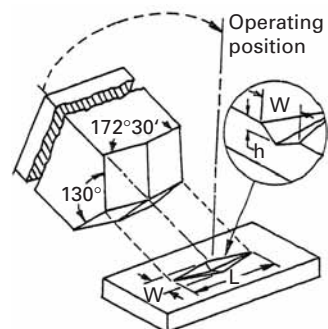


**Fig. 3.40** Some of the details of the Knoop indenter, together with its impression.

### Example 3.10 | (Inspired by M. F. Ashby and D. R. H. Jones)

Obtain, for a simple two-dimensional case, a relationship between the hardness  $H$  and flow stress  $\sigma_0$  of a material.

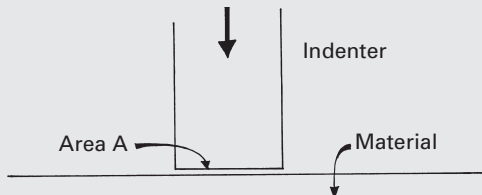


**Fig. E.3.10.1**

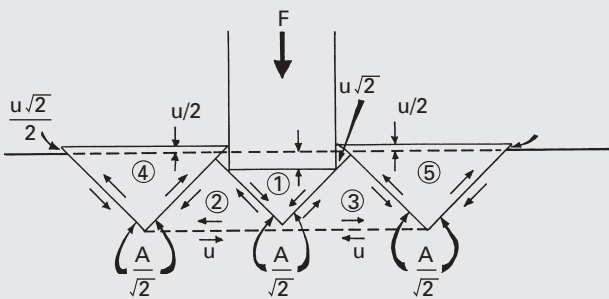


**Fig. E.3.10.2**

**Solution:** We assume a flat indenter and deformation on one plane only, as shown in Figure E.3.10.1. Deformation is assumed to occur by the movement of blocks. We assume a total displacement  $u$  of the punch, shown in Figure E.3.10.2. Block ① moves down by  $u$ . Blocks ② and ③ move sideways by  $u$ . Blocks ④ and ⑤ are pushed upward by  $u/2$  and we compute the forces on two of their surfaces. The shear yield strength is  $\tau_0$ . We set the work done by the punch,  $Fu$ , equal to the energy dissipated at the various interfaces. Student should compute the areas of triangles and assume that the resistance to motion is  $\tau_0$ . The frictional forces between blocks is  $\tau_0$  times the areas ( $A$  or  $A/\sqrt{2}$ ). We have

$$Fu = 2 \times \frac{A\tau_0}{\sqrt{2}} \times u\sqrt{2} + 2 \times A\tau_0 \times u + 4 \times \frac{A\tau_0}{\sqrt{2}} \times \frac{u\sqrt{2}}{2},$$

| ← (block 1) → || ← (blocks 2, 3) → || ← (block 4, 5) → |  
central triangle    two lateral triangles    two end triangles

where  $F$  is the applied force,  $u$  is the displacement of the punch, and  $A$  is the area of the indentation (Figure E.3.10.1).

$$Fu = u6A\tau_0,$$

$$\frac{F}{A} = 6\tau_0.$$

But  $\tau_0 = \sigma_0/2$ ; hence,

$$\boxed{\frac{F}{A} = H = 3\sigma_0.}$$

This is, indeed, Equation 3.48. Thus, the derivation above is a proof for Equation 3.48.

### Example 3.11

Estimate the flow stress of the material shown in Figure E.3.11 if the indentation was done with a load of 1,000 g and the magnification of the photograph is 100×.

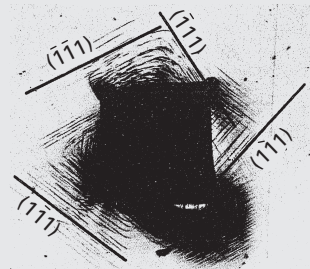


**Fig. E.3.11** Indentation into iron-nickel single crystal; notice  $\{111\}$  traces of slip planes with specimen surface.

**Solution:** This is a Vickers microindentation. We measure the sides of the square, which are more visible (in this case) than the diagonal:

$$a = \frac{26 + 28}{2} = 27 \text{ mm.}$$

The diagonal is  $d = a\sqrt{2} = 38.2 \text{ mm}$ . Dividing this value by the magnification, we obtain  $d' = 0.382 \text{ mm}$ . So

$$H = \frac{1.8544P}{d^2} = \frac{1.8544}{0.145},$$

$$H = 12.80 \text{ kg/mm}^2.$$

We will convert this value to a yield stress, assuming that the material does not work-harden. We have (see Example 3.10)

$$H = 3\sigma_0, \text{ so } \sigma_y = 4.25 \text{ kg/mm}^2.$$

But  $1 \text{ kg/mm}^2 = 9.8 \times 10^6 \text{ Pa}$ ; thus,

$$\sigma_y = 41.8 \text{ MPa.}$$

### 3.8.3 Nanoindentation

An instrumented indentation test, the apparatus for which is sometimes called a *nanoindenter*, was developed in the last quarter of the twentieth century, and is readily available commercially. The instrument is essentially a computer-controlled depth-sensing indentation system that allows extremely small forces and displacements to be measured. Very small volumes of a material can be studied and local characterization of microstructural features such as grain boundary regions, coatings, or reinforcement/matrix interface can be obtained. It can be regarded as a general microstructural investigation technique.

A schematic of a nanoindenter apparatus is shown in Figure 3.41. Commonly, a triangular pyramid or Berkovich indenter is used,

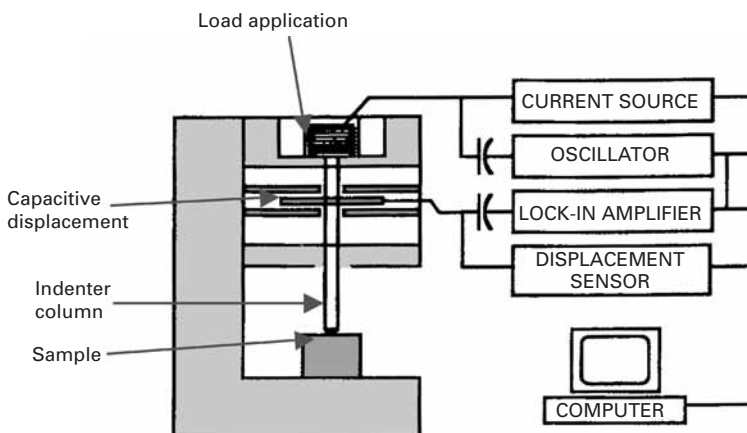
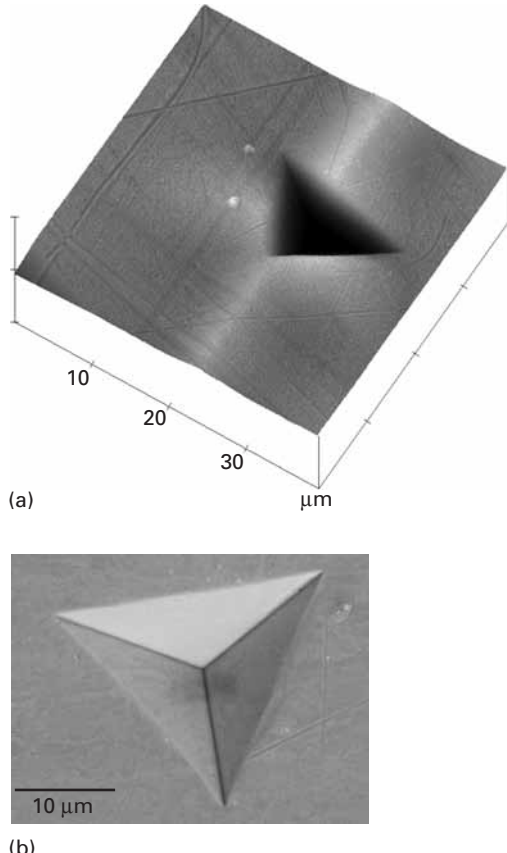


**Fig. 3.41** A schematic of a nanoindenter apparatus.

**Fig. 3.42** An impression made by means of Berkovich indenter in a copper sample. (From X. Deng, M. Koopman, N. Chawla, and K. K. Chawla, *Acta Mater.*, 52 (2004) 4291.) (a) An atomic force micrograph, which shows very nicely the topographic features of the indentation on the sample surface. The scale is the same along the three axes. (b) Berkovich indentation as seen in an SEM.



although other types of indenters can also be used. An impression made by means of Berkovich indenter in a copper sample is shown in Figure 3.42. Figure 3.42(a) is an atomic force micrograph, which shows very nicely the topographic features of the indentation on the sample surface, while Figure 3.42(b) shows a view of the indentation as seen in an SEM micrograph. The penetration of the indenter into the specimen is measured by a very sensitive capacitance gage. The resolution of the applied load may be less than 50 nN while displacement resolutions can be  $<0.02$  nm. Remote position control is done by means of a joystick (motorized in  $x$ -,  $y$ -, and  $z$ - directions).

Generally, a series of load/unload curves is obtained, Figure 3.43. A nanoindenter records the total penetration of an indenter into the sample. The indenter may be moved toward the sample or away from the sample by means of a magnetic coil assembly. One can measure the hardness or elastic modulus of a phase in a material. As the indenter penetrates the specimen, the indentation load and displacement are recorded continuously during a load/unload cycle. The maximum load and the corresponding displacement are calculated from the plastic depth of the indentation. The hardness,  $H$ , is given by

$$H = P_{max}/A,$$

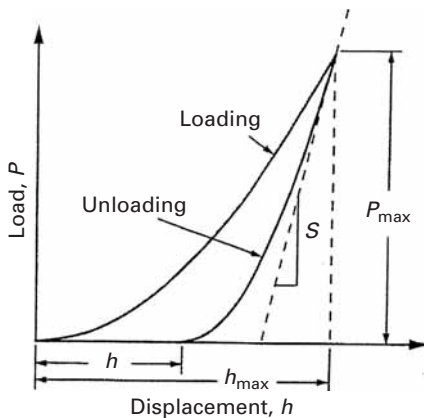


**Fig. 3.43** A schematic representation of load vs. indenter displacement.

where  $P_{\max}$  is the load and  $A$  is the projected area of contact at peak load. The contact area at the peak load is determined by the geometry of the indenter and the depth of contact,  $h_c$ . Assuming that the indenter does not deform significantly, we can write  $A = f(h_c)$ . The form of function  $f$  must be established experimentally. The area  $A$  can be calculated by means of the following expression:

$$A = a + bh_i^{1/2} + ch_i + dh_i^{3/2} + 24.56h_i^2 \quad (3.50)$$

where  $h_i$  is the plastic depth of the indentation and  $a$ ,  $b$ ,  $c$ , and  $d$  are adjustable coefficients. For a perfect tip,  $a = b = c = d = 0$ , and the only coefficient is 24.56.

The stiffness,  $S$ , can be obtained from the load,  $P$  vs. penetration depth,  $h$  by the following expression relating the reduced modulus,  $E_r$ , the contact area  $A$ , and the stiffness,  $S$ :<sup>19,20,21</sup>

$$S = dP/dh = (2/\sqrt{\pi})E_r\sqrt{A}.$$

The reduced modulus  $E_r$  of indenter-sample combination takes into account the fact that elastic deformation under load occurs in the sample as well as in the indenter. The reduced modulus is given by

$$E_r = (1 - \nu_i^2)/E_i + (1 - \nu_s^2)/E_f$$

where  $E_i$  and  $E_s$  are the Young's moduli, and  $\nu_i$  and  $\nu_s$  are the Poisson's ratio of the indenter and sample, respectively. The initial unloading slope gives us the reduced modulus provided one can measure the contact area at the peak load.

Modulus and hardness of a material can be obtained more accurately by measuring contact stiffness throughout the test. This technique is called continuous stiffness measurement (CSM). In this technique, a small harmonic force is superimposed on the primary load,  $P$ . This technique enables the instrument to determine the contact stiffness throughout the experiment. The displacement of the

<sup>19</sup> M. F. Doerner and W. D. Nix, *J. Mater. Res.*, 1 (1986) 601.

<sup>20</sup> W. C. Oliver, *MRS Bull.*, 11 (1985) 15.

<sup>21</sup> W. C. Oliver and G. M. Pharr, *J. Mater. Res.*, 7 (1992) 1564.

indenter at the excitation frequency and the phase angle between force and displacement are measured continuously as a function of depth. The stiffness,  $S$ , is given by the following relationship:

$$S = \left[ \frac{1}{\frac{P_{os}}{h_{(\omega)}} \cos \Phi - (K_s - m\omega^2)} - K_f^{-1} \right]^{-1} \quad (3.51)$$

where  $P_{os}$  is the magnitude of the force oscillation,  $h_{(\omega)}$  is the magnitude of the resulting displacement oscillation,  $\omega$  is the frequency of the oscillation,  $\Phi$  is the phase angle between the force and displacement,  $K_s$  is the spring constant of the leaf springs that support the indenter,  $K_f$  is the stiffness of the indenter frame,  $C_f$  is the compliance of the load frame, and  $m$  is the mass of the indenter.

The nanoindentation technique has been successfully used to measure the interfacial strength in a variety of fiber reinforced composites.<sup>22</sup>

### Example 3.12

A copper specimen was tested in a commercial nanoindentation machine. A Berkovich indenter (pyramid with triangular base) was used. The specimen was loaded to different load levels shown in Figure E.3.12, then unloaded. For each maximum load, determine the hardness. Establish whether the hardness changes with depth of indentation.

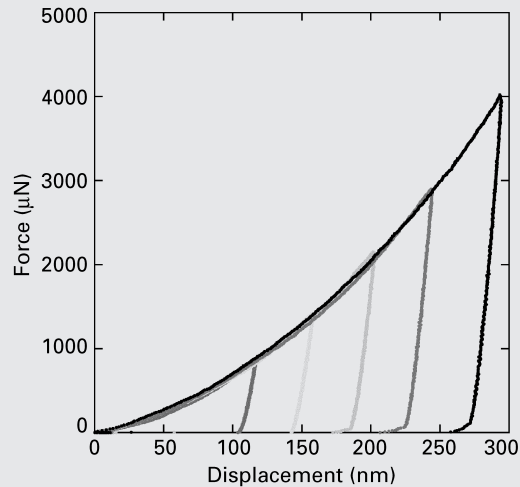


**Fig. E.3.12** Load vs. displacement curves obtained for copper specimen in a Tribolindenter machine. (Courtesy of Andrea Hodge, USC.)

<sup>22</sup> K. K. Chawla, *Ceramic Matrix Composites*, 2nd ed. (Boston: Kluwer Academic Publishers, 2003), p. 176.

**Solution:** The relationship between depth of indentation,  $h_i$ , and area of a perfectly sharp Berkovich tip, is (Equation 3.50):

$$A = 24.56h_i^2$$

We find the forces and displacements at the top of the five loading cycles. We obtain the corresponding displacements (depths of indentation).

Load, $P$ ( $\mu\text{N}$ )	Displacement, $h$ (nm)	Area, $A$ ( $\text{nm}^2$ )	Hardness (GPa)
760	115	324,012	2.34
1350	165	667,012	2.02
2150	205	1,029,612	1.99
2850	243	1,446,700	1.97
3900	295	2,132,112	1.83

There is a slight but consistent decrease in nanoindentation hardness as the load is increased.

## 3.9 | Formability: Important Parameters

Deep drawing and stretching are the two main processes involved in most sheet-metal-forming operations. An excellent introductory overview on sheet-metal forming is provided by Hecker and Ghosh.<sup>23</sup> In a stamping operation, one part of the blank might be subjected to a deformation process similar to deep drawing (thickness increasing with time). In deep drawing the material is required to contract circumferentially, while in stretching the stresses applied on the sheet are tensile in all directions. Sheet-metal forming has evolved from an art into a science, and important material parameters have been identified. These material properties are obtained in special tests and allow a reasonable prediction of the blank in the actual sheet-forming operation.

The work-hardening rate  $n$  is important, because it determines the onset of necking (tensile instability), an undesirable feature. According to Considère's criterion (see Section 3.2.2),  $n$  is equal to  $\varepsilon_u$ , the uniform strain. Hence, the higher  $n$ , the higher  $\varepsilon_u$ . The strain-rate sensitivity  $m$  is an important parameter, too, because it also helps to avoid necking. If  $m$  is positive, the material becomes stronger at incipient necks because the strain rate in the necked region is higher. (See Section 3.2.3.) The parameter  $R$  (the through-thickness plastic anisotropy) is also important; it is equal to the ratio between the strain in the "stretching" direction and the strain in the thickness direction. The greater the resistance to "thinning" in stretching, the better is the formability of the metal. This resistance to thinning corresponds

<sup>23</sup> S. S. Hecker and A. K. Ghosh, *Sci. Am.*, Nov. (1976), p. 100.

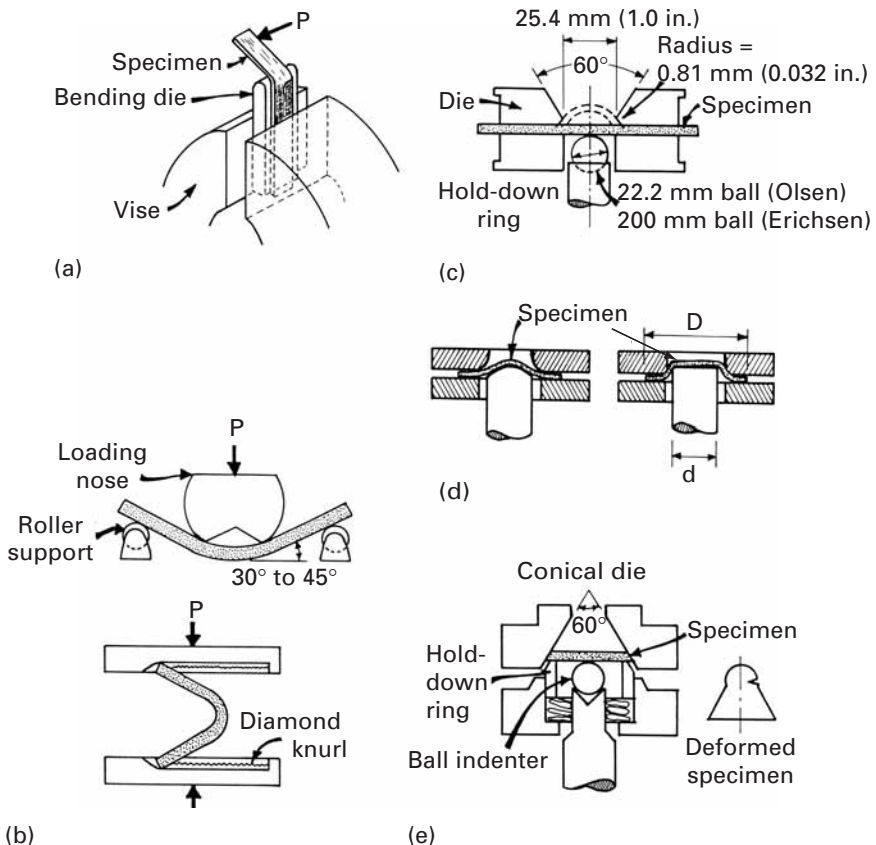


**Fig. 3.44** Simple formability tests for sheets. (a) Simple bending test. (b) Free-bending test. (c) Olsen or Erichsen cup test. (d) Swift cup test. (e) Fukui conical cup test.

to a value of  $R$  larger than 1: the strength in the thickness direction is greater than the strength in the plane of the sheet. The three parameters  $n$ ,  $m$ , and  $R$  are readily obtained in a tensile test. (See Sections 2.2 and 3.2).

Additional important information on the workability of sheets is provided by the yield and flow loci. Section 3.7.8 gives a description of yield criteria and how they are graphically presented in a plane-stress situation. The experimental determination of the yield locus and its expansion as plastic deformation takes place is conducted in biaxial tests. (See Section 3.7.4, Figure 3.28.)

Figure 3.44 shows the most simple formability tests applied to metals. In the simple bending test, the specimen is attached to a die, and one end is clamped in a vise. The other end is bent to a specific radius. Specimens are bent to  $180^\circ$  using bending dies with smaller and smaller bending radii. Observations are made to see whether cracks are formed. In the free-bending test, the specimen is first bent between two rollers until an angle between  $30^\circ$  and  $45^\circ$  is achieved. It is then further bent between two grips, such as a vise.

The Olsen and Erichsen tests are typical stretch tests. A hardened steel sphere (diameter of 22.2 mm for the Olsen test, 20 mm for the Erichsen test) is pushed into the clamped metal, forming a bulge.

The depth of the bulge at the fracture point is measured. The clamp-down pressure is very high (>70 kN), to minimize the drawing of the material.

The Swift and Fukui tests (Figure 3.44(d) and (e)) are drawing tests. The clamp-down pressure in the Swift test allows the sheet to slip inward. The overall diameter of the part is decreased in the process. This test simulates the deep drawing of parts. The drawability is expressed as the limiting draw ratio

$$\text{LDR} = \frac{\text{maximum blank diameter}}{\text{punch diameter}} = \frac{D}{d}$$

There are two geometries for the Swift test, shown in Figure 3.44(d): the round-bottomed cup test and the cup test. The latter test causes stretching of the center of the cup in addition to drawing. The Fukui test (Figure 3.44(e)) is the Japanese (JIS Z 2249) equivalent of the US stretch-drawing Swift test. A sphere 12.5 to 27 mm in diameter is pushed into a disk and advanced until either failure results or necking occurs in the cup. A hold-down ring maintains the specimen in place. The ratio between the diameters of the base of the deformed cup and the original disk provides the Fukui conical cup value. The modern counterpart of these older, but reliable, tests is the forming-limit curve, described in Section 3.9.2. The circle-grid analysis, which consists of applying a circle grid to the blank and measuring the strains in the critical regions of the stamped part, is also described in that section.

### 3.9.1 Plastic Anisotropy

Elastic deformation under anisotropic conditions is described by elastic constants, whose number can vary from 21 for the most anisotropic solid to 3 for one exhibiting cubic symmetry. (For isotropic solids, the number of independent elastic constants is 2.) In a similar way, plasticity increases in complexity as the anisotropy of the solid increases. Sections 3.2–3.3 cover only the isotropic case, and even that in a very superficial way. In polycrystals, anisotropy in plasticity is more the rule than exception. Essentially, there are two sources of anisotropy. First is texture, in which the grains are not randomly oriented, but have one or more preferred orientations. Texturing is often introduced by deformation processing. Well-known and well-characterized textures accompany cold rolling, wire drawing, and extrusion. This type of anisotropy is also called *crystallographic anisotropy*. Second, anisotropy is produced by the alignment of inclusions or second-phase particles along specific directions. When steel is produced, the inclusions existing in the ingot take the shape and orientation of the deformation process (rolling). These inclusions, such as MnS, produce mechanical effects called fiberizing. This type of anisotropy is also known as *mechanical anisotropy*. Whereas crystallographic anisotropy can strongly affect the yield stress, mechanical anisotropy usually manifests itself only in the later stages of deformation, influencing fracture.

**Fig. 3.45** “Ears” formed in deep-drawn cups due to in-plane anisotropy. (Courtesy of Alcoa, Inc.)

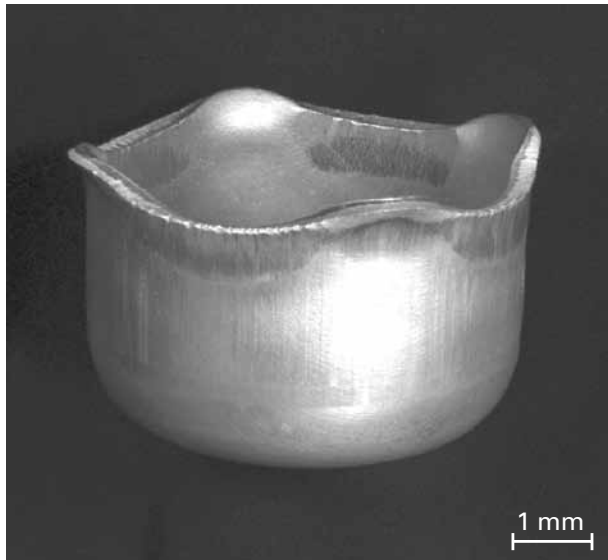


Figure 3.45 shows the effect of texture on a deep-drawn cup. This effect is known as “earing.” Prior to drawing, the sheet exhibited different yield stresses along different directions. The orientation in which the sheet is softer is drawn in faster than the harder direction, resulting in “ears.” The number of ears (four) actually shows the type of texture. Figure 3.46 on the other hand, illustrates the effect of inclusions on the formability of an alloy. Fracture is much more probable if the sheet is bent along the second-phase strings than if it is bent perpendicular to them.

Section 3.7.8 shows the yield locus for anisotropic materials; this equation is an ellipse essentially identical to that described by the von Mises yield criterion in plane stress. (See Section 3.7.4.) The ellipse is distorted, however.

### 3.9.2 Punch–Stretch Tests and Forming-Limit Curves (or Keeler–Goodwin Diagrams)

An ideal test is the one that predicts exactly the performance of a material. The  $m$ ,  $n$ , and  $R$  values are insufficient to predict the formability, and tests more closely resembling the actual plastic-forming operations have been used for a long time. The main parameter that they can provide is the strain to fracture. These tests are called punch–stretch tests, or simply, “cupping” tests.

The punch–stretch test consists of clamping a blank firmly on its edges between two rings or dies; the next step is to force a plunger or punch through the center area of the specimen enclosed by the area of the ring, until the blank fractures. Several punch–stretch tests have been developed over the years, including the Olsen, Erichsen, Guillory, and Wazau tests. These “cupping” tests are routinely used for inspection purposes, since they provide a quick indication of ductility;

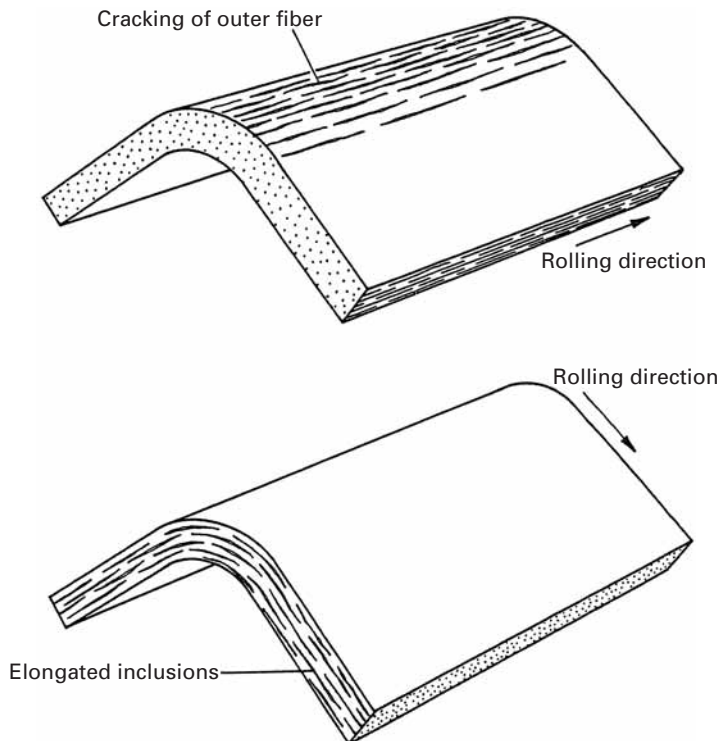
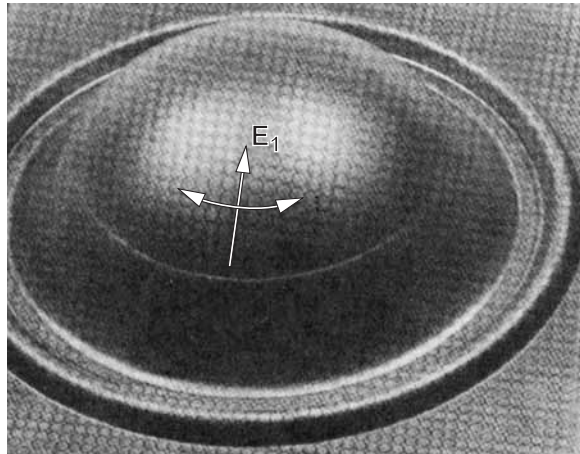


**Fig. 3.46** Effect of “fiberizing” on formability. The bending operation is often an integral part of sheet-metal forming, particularly in making flanges so that the part can be attached to another part. During bending, the fibers of the sheet on the outer side of the bend are under tension, and the inside ones are under compression. Impurities introduced in the metal as it was made become elongated into “stringers” when the metal is rolled into sheet form. During bending, the stringers can cause the sheet to fail by cracking if they are oriented perpendicular to the direction of bending (top). If they are oriented in the direction of the bend (bottom), the ductility of the metal remains normal. (Adapted with permission from S. S. Hecker and A. K. Ghosh, *Sci. Am.*, Nov. (1976), p. 100.)

they also show the change in surface appearance of the sheet upon forming. Two important defects appear in stamping:

1. The orange-peel effect (surface rugosity) is due to the large grain size of the blank. The anisotropy of plastic deformation of the individual grains results in an irregular surface, perfectly visible to the naked eye, when the grain size is large.
2. Stretcher strains are produced when Lüders bands appear in the forming process. The interface between the Lüders band and undeformed materials exhibits a step easily visible to the naked eye. This is an undesirable feature that can be eliminated either by restraining the sheet prior to forming (beyond the Lüders band region) or by alloying the material in such a way as to eliminate the yield drop and plateau from the stress-strain curve. In low-carbon steels, Lüders bands are formed by the interactions of carbon and

**Fig. 3.47** Sheet specimen subjected to punch–stretch test until necking; necking can be seen by the clear line. (Courtesy of S. S. Hecker.)



nitrogen atoms with dislocations. After a process called temper rolling, the susceptibility is eliminated; however, it can return following aging. This problem is easily solved by flexing the sheet by effective roller leveling just prior to forming.<sup>24</sup>

The poor correlation between the common “cupping” test and the actual performance of the metal led investigators to look at some more fundamental parameters. The first breakthrough came in 1963, when Keeler and Backofen<sup>25</sup> found that the localized necking required a critical combination of major and minor strains (along two perpendicular directions in the sheet plane). This concept was extended by Goodwin to the negative strain region, and the resulting diagram is known as the Keeler-Goodwin,<sup>26</sup> or forming-limit, curve (FLC). The FLC is an important addition to the arsenal of techniques for testing formability and is described after the description of Hecker’s testing technique, presented next.<sup>27</sup>

Hecker developed a punch–stretch apparatus and technique well suited for the determination of FLC. The device consists of a punch with a hemispherical head with a 101.6-mm (4-in.) diameter. The die plates are mounted in a servohydraulic testing machine with the punch mounted on the actuator. The hold-down pressure on the die plates (rings) is provided by three hydraulic jacks. (The hold-down load is 133 kN.) The bead-and-groove arrangement in the rings eliminates any possible drawing in. The specimens are all gridded with 2.54-mm circles by a photoprinting technique. The load versus displacement is measured and recorded during the test, and the maximum load is essentially coincident with localized instability and the onset of fracture. A gridded specimen after failure is shown in Figure 3.47. The

<sup>24</sup> H. E. McGannon (ed.), *The Making, Shaping, and Treating of Steel*, 9th ed. (Pittsburgh, PA: US Steel, 1971), pp. 1126, 1260.

<sup>25</sup> S. P. Keeler and W. A. Backofen, *Trans. ASM*, 56 (1963) 25.

<sup>26</sup> G. M. Goodwin, “Application of Strain Analysis to Sheet Metal Forming Problems in the Press Shop,” *SAE Automotive Eng. Congr.*, Detroit, Jan. 1968, SAE Paper No. 680093.

<sup>27</sup> S. S. Hecker, *Metals Eng. Quart.*, 14 (1974) 30.

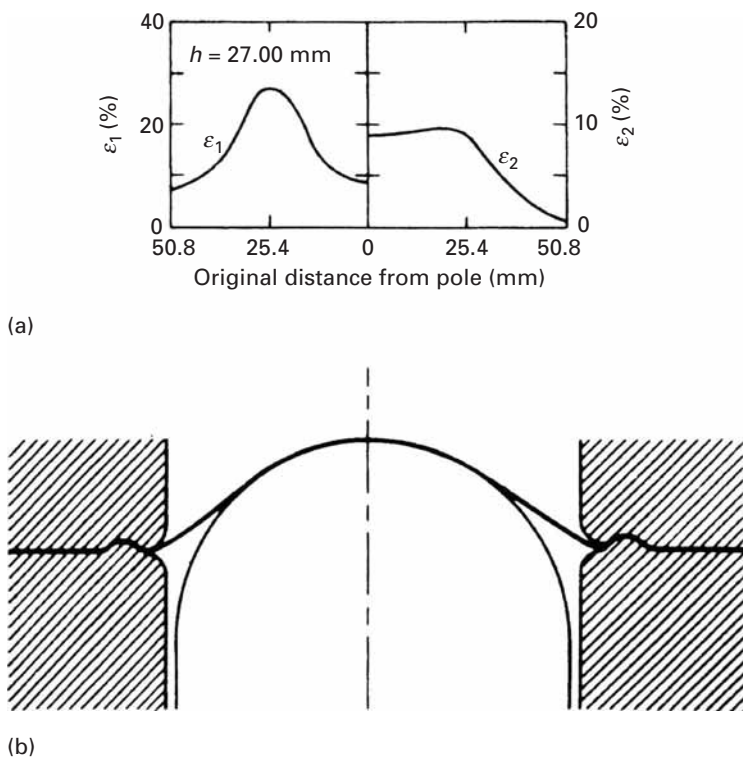


**Fig. 3.48** Schematic of sheet deformed by punch stretching. (a) Representation of strain distribution:  $\varepsilon_1$ , meridional strains;  $\varepsilon_2$ , circumferential strains;  $h$ , cup height. (b) Geometry of deformed sheet.

circles become distorted into ellipses. The clear circumferential mark is due to necking. The strains  $\varepsilon_1$  and  $\varepsilon_2$  are called meridian and circumferential strains, respectively, and are measured at various points when the test is interrupted. Figure 3.48(a) shows how these strains vary with distance from the axis of symmetry of the punch, at the point where the punch has advanced a total distance of  $h = 27 \text{ mm}$ .  $\varepsilon_1$ , the meridional strain, is highest at about 25 mm from the center ( $\varepsilon_1 \approx 0.25$ );  $\varepsilon_2$ , the circumferential strain, shows a definite plateau. By using sheets with different widths and varying lubricants between the sheet and the punch, different strain patterns are obtained. (Figure 3.48(b) shows the geometry of the deformed sheet.) The tests are conducted to obtain different combinations of minor-major strains leading to failure. Figure 3.49 shows how the FLC curve is obtained. The minor strain (circumferential) is plotted on the abscissa, and the major strain (meridional) is plotted on the ordinate axis. Four different specimen geometries are shown. The V-shaped curve (FLC) marks the boundary of the safe-fail zone. The region above the line corresponds to failure; the region below is safe. In order to have both major and minor strains positive, we use a full-sized specimen. By increasing lubrication, the major strain is increased; a polyurethane spacer is used to decrease friction. The drawings on the lower left- and right-hand corners of the figure show the deformation undergone by a circle of the grid. When both strains are positive, there is a net increase in area. Consequently, the thickness of the sheet has to decrease proportionately. On

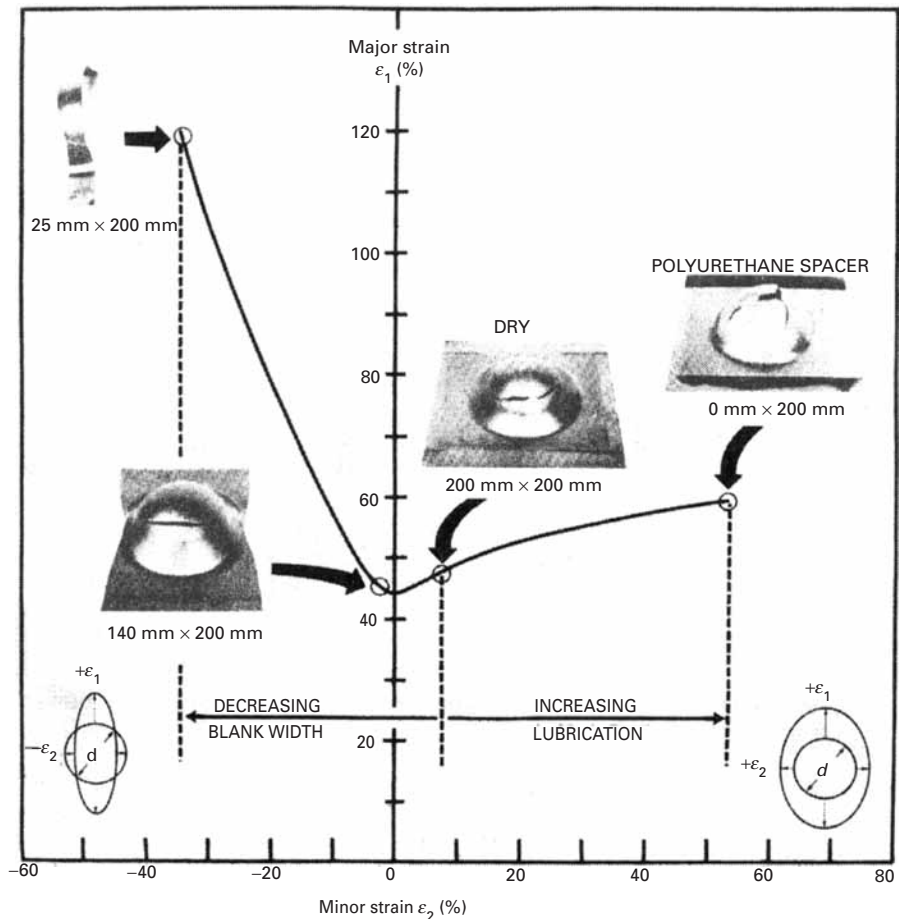


**Fig. 3.49** Construction of a forming-limit curve (or Keeler-Goodwin diagram). (Courtesy of S. S. Hecker.)

the left-hand side of the plot, negative strains are made possible by reducing the lateral dimension of the blank. This allows free contraction in this dimension. The strains in an FLC diagram are obtained by carefully measuring the dimensions of the ellipses adjacent to the neck-failure region. It is interesting to notice that diffuse necking (thinning) starts immediately after deformation, whereas localized necking occurs only after substantial forming. Semiempirical criteria for localized necking that agree well with experimental results have been developed.

FLCs provide helpful guidelines for press-shop formability. Coupled with circle-grid analysis, they can serve as a guide in modifying the shape of stampings. Circle-grid analysis consists of photoprinting a circle pattern on a blank and stamping it, determining the major and minor strains in its critical areas. The strain pattern in the stamping is then compared with the FLC to verify the available safety margin. The strain pattern can be monitored with changes in lubrication, hold-down pressure, and size and shape of drawbeads and the blank; such monitoring can lead to changes in the experimental procedure.

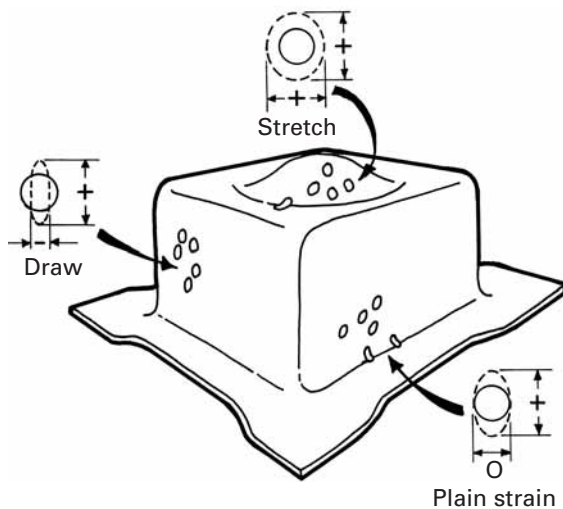


**Fig. 3.50** Different strain patterns in stamped part. (Adapted from W. Brazier, *Closed Loop*, 15, No. 1 (1986) 3.)

Circle-grid analysis also serves, in conjunction with the FLC, to indicate whether a certain alloy might be replaced by another one, possibly cheaper or lighter. During production, the use of occasional circle-grid stampings provides valuable help with respect to wear, faulty lubrication, and changes in hold-down pressure. Hecker and Ghosh<sup>28</sup> claim that the circle-grid analysis has replaced the craftsman's "feel" for the proper flow of the metal.

The strain pattern undergone by a stamped part is shown schematically in Figure 3.50. Different portions exhibit different strains, and this is evident by observing the distortion of circles at different regions.

## 3.10 | Muscle Force

The maximum force that a muscle fiber can generate depends on the velocity at which it is activated. Figure 3.51 shows the stress that can be generated as a function of strain rate for "slow-twitch" and "fast-twitch" muscles. We use slow-twitch muscles for long-range events (e.g., distance running) and fast-twitch muscles for explosive activities, such as sprinting or throwing a punch at our professor. Both muscles show a decreasing ability to generate stress as the strain rate is increased. However, the fast-twitch muscles show a lower decay.

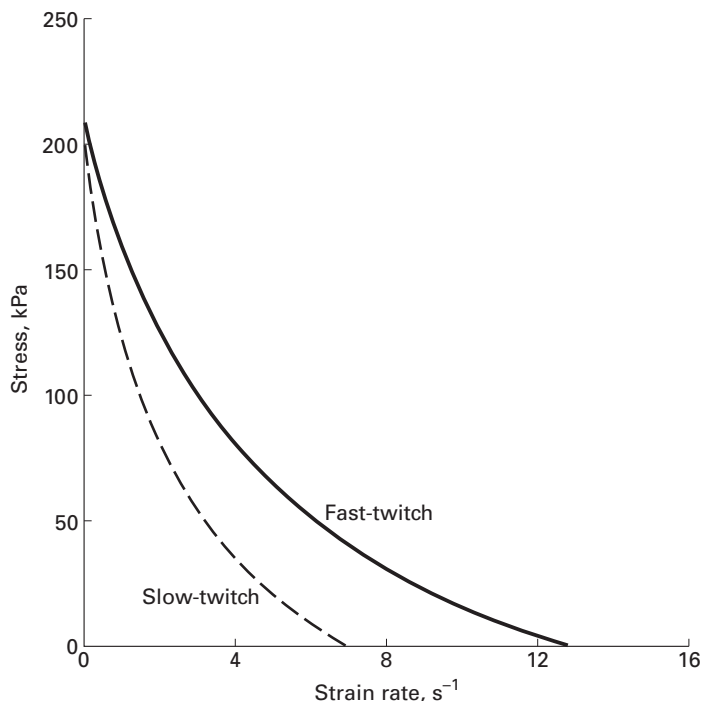
The plot shown in Figure 3.51 is only schematic and represents the rat *soleus* (slow-twitch) and extensor *digitorum longus* (fast-twitch). The equation that describes the response in Figure 3.51 is called the Hill<sup>29</sup> equation. It has the form:

$$(\sigma + a)(\dot{\varepsilon} + b) = (\sigma_0 + a)b,$$

<sup>28</sup> S. S. Hecker and A. K. Ghosh, *Sci. Am.*, Nov. (1976), p. 100.

<sup>29</sup> A. V. Hill, *Proc. Roy. Soc. London*, 126 (1938), 136–195.

**Fig. 3.51** Stress vs. strain rate for slow-twitch and fast-twitch muscles.



where  $\sigma_0$  is the stress at zero velocity (equal to 200 kPa in Figure 3.51). The range of  $\sigma_0$  is usually between 100 and 300 kPa;  $a$  and  $b$  are parameters and  $\dot{\varepsilon}$  is the strain rate (obtained from the velocity).

### Example 3.13

A person is lifting a weight by contracting the biceps muscles. Assuming that each muscle fiber has the capacity to lift 300  $\mu\text{g}$ , and that each muscle fiber has a diameter of 5  $\mu\text{m}$ , what is the required cross section of biceps muscle needed to lift a mass of 20 kg?

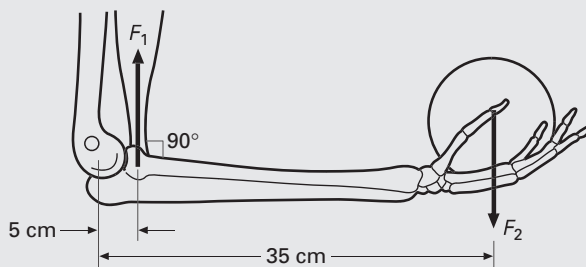


**Fig. E3.13** Forearm and force  $F_2$  exerted by weight and reaction  $F_1$  applied by biceps.

**Solution:** The cross section of each fiber is:

$$A = \frac{\pi}{4} \times 5^2 = 19.625 \mu\text{m}^2.$$

We can see from Figure E3.13 that we need to apply a lever rule to calculate the force that the muscle has to exert. Distances given in Figure E3.13 are typical. Students should check by measuring their arms. Equating the sum of the moments to zero,

$$\begin{aligned}\Sigma M_0 &= 0 \\ F_1 X_1 - F_2 X_2 &= 0.\end{aligned}$$

We have, for typical values:  $X_1 = 5 \text{ cm}$ ;  $X_2 = 35 \text{ cm}$ .

But:

$$F_2 = 20 \times 9.8 = 196 \text{ N.}$$

Thus:

$$F_1 = \frac{196 \times 35}{5} = 1372 \text{ N.}$$

The maximum force that each muscle fiber can lift is:

$$F_f = 300 \times 10^{-6} \times 9.8 \times 10^{-3} = 2940 \times 10^{-9} \text{ N.}$$

The ratio  $F_1/F_f$  gives the number of fibers:

$$N = 4.66 \times 10^8.$$

The total area is equal to:

$$A_t = N \times A = 91.425 \times 10^8 \mu\text{m}^2.$$

This may be converted into  $\text{cm}^2$ :

$$A_t = 91.4 \text{ cm}^2.$$

This is indeed a biceps with a diameter of:

$$D = \left( \frac{4A_t}{\pi} \right)^{1/2} = 10.7 \text{ cm.}$$

This corresponds to Arnold on steroids!

### Example 3.14 |

Determine the safety factor built into the Achilles' tendon of a person weighing 80 kg, assuming a cross-sectional area of  $1.5 \text{ cm}^2$ , if the person can jump up to a height of 1 m, then land with a deceleration time of 0.3 s. Assume that the tensile strength of the tendon is 60 MPa. Dimensions are given in Figure E3.14.

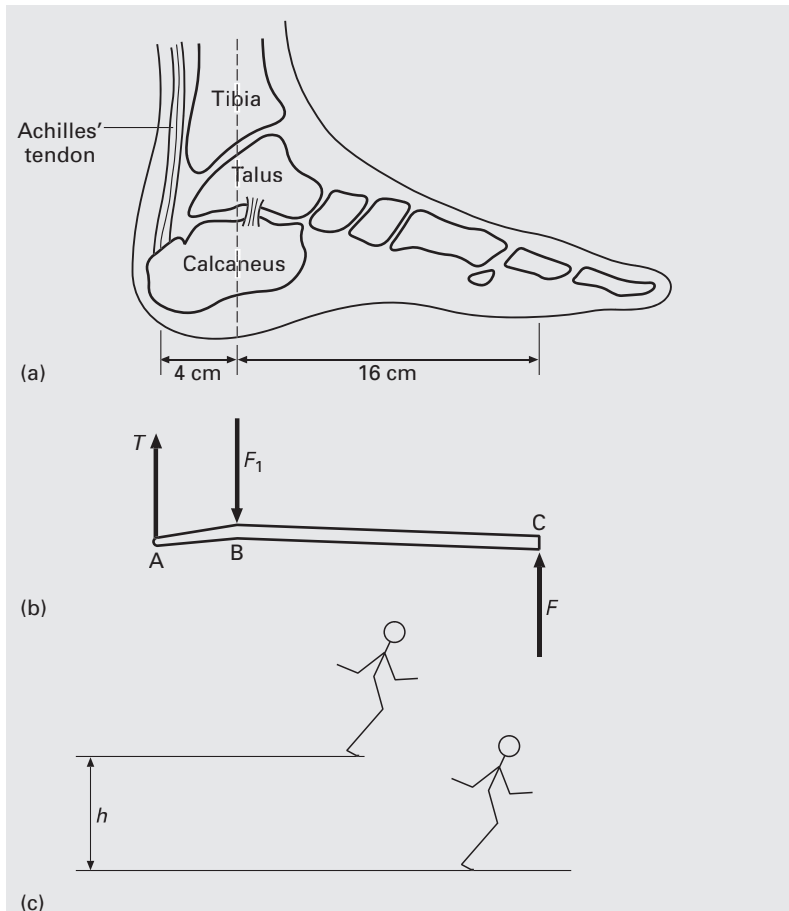


**Fig. E3.14** (a) Structure of foot with Achilles' tendon shown; (b) force  $T$  on tendon; (c) jump from a height  $h$ .

**Solution:** We first calculate the relationship between  $T$ , the tension in the Achilles' tendon, and  $F$ , the force exerted on the ground. We assume that the person is standing on the ball of the foot.

Setting the sum of moments equal to zero,

$$\Sigma M_B = 0,$$

$$BC \times F - AB \times T = 0,$$

$$T = \frac{BC \times F}{AB}.$$

The forces and distances are defined in Figure E3.14(b). We now calculate  $F$  for the static and dynamic cases. For the static case, we simply have:

$$F_s = 80 \times 9.8 = 784 \text{ N.}$$

For the dynamic case, we have to consider the kinetic energy gained by the person, when jumping down from a height of 1 m. The potential

energy is converted into kinetic energy

$$mgh = \frac{1}{2} mv^2,$$

The velocity is:

$$v = (2gh)^{1/2} = 4.43 \text{ m/s.}$$

In order to find the dynamic force,  $F_d$ , we set the impulse equal to the change in momentum:

$$mv - m \times 0 = F_d \times t.$$

The deceleration time is given:  $t = 0.3 \text{ s}$ .

Thus:

$$F_d = 707 \text{ N.}$$

The total force is:

$$F = F_s + F_d = 1492 \text{ N.}$$

From the figure we obtain the values of AB and BC

$$T = 5968 \text{ N.}$$

Assuming a round section, the area of the tendon is:

$$A = \frac{\pi}{4}(1.5 \times 10^{-2})^2 = 1.7 \times 10^{-4} \text{ m}^2.$$

Thus, the stress is:

$$\sigma = \frac{T}{A} = 35.1 \text{ MPa.}$$

The safety factor is:

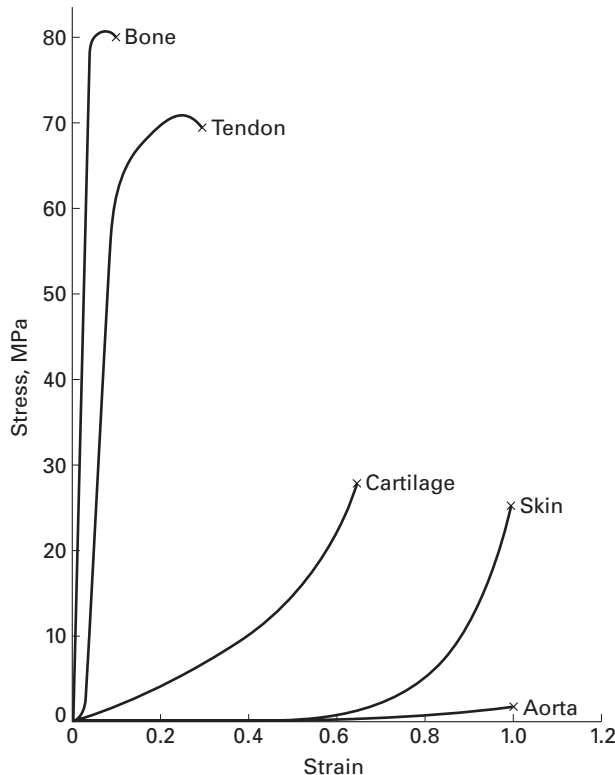
$$SF = \frac{60}{35.5} = 1.7.$$

This is indeed a small number, and a weakened Achilles' tendon could easily rupture. Indeed, this happened to one of the coauthors (MAM) while playing soccer (his last game). The tendon was operated upon and reconnected through stitches. The foot was immobilized in the stretched position for 4 months enabling the tendon to repair itself. Interestingly, the operated tendon now has a cross section twice as large as the other one. Hence, nature somehow remembers the trauma and overcorrects for it. The same thing happens in bones. The healed portion becomes stronger than the original bone.

## 3.11 Mechanical Properties of Some Biological Materials

Figure 3.52 shows the stress-strain response of a number of biological materials. It may be seen that the properties vary widely. As is the case with synthetic materials, the strength increases as the

**Fig. 3.52** Stress-strain response for a number of biological materials.



ductility decreases. The strongest materials in our body are the cortical bone, followed by tendons and ligaments. The wide range in properties is due to differences in structure and constituents, presented in Chapter 1. Table 3.4 provides some important mechanical properties for a number of biological materials.

Elastin, which is described in Chapter 1, is an important component in skin and arteries. As the name implies, it provides elasticity. Figure 3.53 gives the stress-strain response from elastin taken from *ligamentum nuchae* (a long ropelike fiber running along the top of a horse's neck and holding it upright). The material is approximately linearly elastic with a Young's modulus of approximately 0.6 MPa.

Bone is the structural component of our body. It also has other functions, but we will concentrate on the mechanical performance here. There are two principal types of bone: cortical (or compact) and cancellous (or porous). Figure 3.54 shows the structure of a long bone. The surface regions consist of cortical bone; the inside is porous and is cancellous bone. The porosity reduces the strength of the bone, but also reduces its weight. Bones are shaped in such a manner that strength is provided only where it is needed. The porosity of cancellous bone provides interesting mechanical properties, which are quantitatively treated in Chapter 12. The pores also perform other physiological functions and contain the marrow. Thus, bone is a true multifunctional material. Researchers are developing synthetic

**Table 3.4** Mechanical Properties of Some Biological Materials

Material	E (MPa)	Fracture Stress (MPa)	Strain at Fracture
Elastin	0.6		
Resilin	1.8		
Collagen	1,000	70	0.09
Fibroin	10,000		
Cortical bone –			
Longitudinal	$(14-24) \times 10^3$	150	~0.015
Transverse	$(8-18) \times 10^3$	50	
Cancellous (porous) bone	10–200		
Cellulose	80,000	1000	0.024
Tendon	1,300	75	0.09
Keratin	2,500	50	0.02
Alpha (mammalian) Beta (birds)	2,000	20	
Dentine		300	
Spider Silk (radial)		1,500	0.06
Silkworm Silk		500	

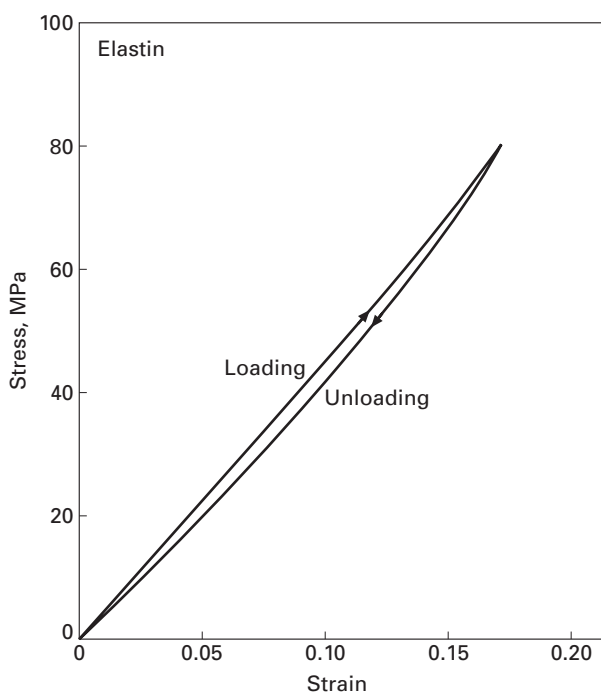


**Fig. 3.53** Stress-strain response for elastin; it is the *ligamentum nuchae* of cattle (Adapted from Y. C. Fung and S. S. Sobin, *J. Biomech. Eng.*, 1103 (1981) 121. Also in Y. C. Fung, *Biomechanics: Mechanics properties of Living Tissues* (New York: Springer, 1993) p. 244.)

multifunctional materials that have more than one function; this particular area of research is based on biological systems and is called “biomimetics” (mimicking nature).

Cortical bone is found in long bones (femur, tibia, fibula, etc.). The longitudinal mechanical properties (strength and stiffness) are higher than the transverse ones. Thus, cortical bone can be

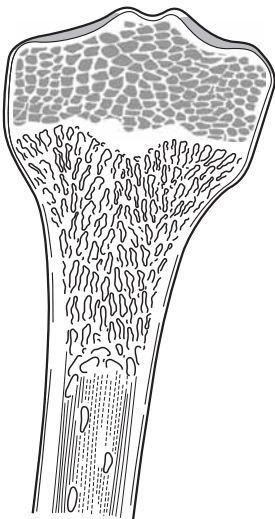


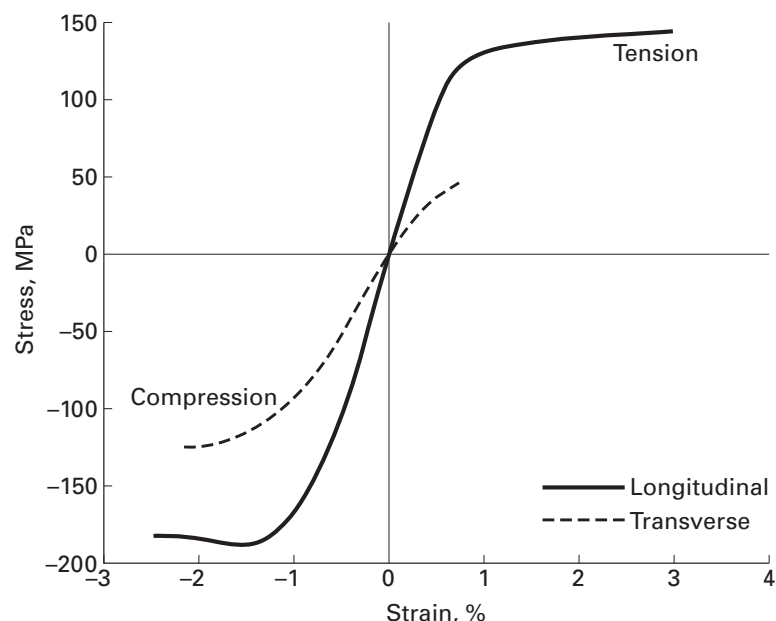
**Fig. 3.54** Longitudinal section of a femur. (From S. Mann, *Biomineratization* (New York: Oxford University Press, 2001).)

considered as transversely isotropic. Figure 3.55 provides the tensile and compressive stress-strain curves for cortical bone in longitudinal and transverse directions. The anisotropy is clearly visible. The bone is stronger in the longitudinal direction.

Bone is a composite of collagen, hydroxyapatite, and water. Hydroxyapatite is a calcium phosphate with the composition:  $3\text{Ca}_3(\text{PO}_4)_2\text{Ca}(\text{OH})_2$ . Water corresponds to 15–25 vol.% of the bone in mammals. The Young's modulus of cortical bone varies from 14 to 24 GPa (see Table 3.4). This is much lower than that of hydroxyapatite, which has a Young's modulus of approximately 130 GPa and a tensile strength of 100 MPa. Although collagen is not linearly elastic, we can define a tangent modulus; it is approximately 1.25 GPa. The strength achieved in bone is therefore higher than both hydroxyapatite (100 MPa) and collagen (50 MPa), demonstrating the synergistic effect of a successful composite. Hydroxyapatite is the major mineral component of bone. The hydroxyapatite content of bone varies from animal to animal, depending on function. For instance, an agile animal like a gazelle has bones that have to be highly elastic. Thus, the hydroxyapatite level is fairly low (around 50% by weight). Collagen provides the elasticity. On the other hand a whale has bones with a much higher mineral content (~80% by weight). We are somewhere in between. A young athletic student has more compliant bones than a sedentary professor!

The mechanical response of bone is also quite strain-rate sensitive. As the velocity of loading increases, both the elastic modulus and the fracture stress increase. Hence, the stiffness increases with strain rate. This is shown in Figure 3.56.

**Fig. 3.55** Tensile and compressive stress-strain curves for cortical bone in longitudinal and transverse directions. (Adapted from G. L. Lucas, F. W. Cooke, and E. A. Friis, *A Primer on Biomechanics* (New York: Springer, 1999).)



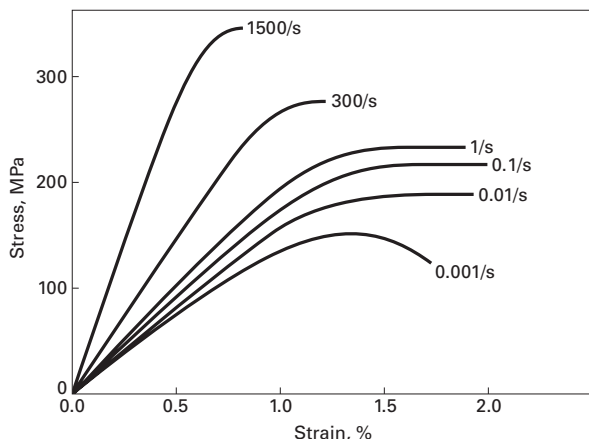


**Fig. 3.56** Strain-rate dependence of tensile response of cortical bone. (Adapted from J. H. McElhaney, *J. Appl. Physiology*, 21(1966) 1231.)

An equation called the the Ramberg–Osgood equation is used to describe this strain-rate dependence of the elastic modulus:

$$E = \frac{\sigma}{\varepsilon} = C(\dot{\varepsilon})^d,$$

where  $\sigma$  is the stress,  $\varepsilon$  is the strain,  $\dot{\varepsilon}$  is the strain rate, and  $C$  and  $d$  are experimental parameters. The following are typical values:

Human cranium:  $C = 15$  GPa;  $d = 0.057$

Bovine cortical bone (longitudinal):  $C = 12$  GPa;  $d = 0.018$ .

## Suggested Reading

### Plasticity

- J. E. Gordon, *The New Science of Strong Materials, or Why You Don't Fall Through the Floor*. Princeton, NJ: Princeton University Press, 1976.
- E. P. Popov, *Engineering Mechanics of Solids*. Englewood Cliffs, NJ: Prentice Hall, 1990.
- D. Roylance, *Mechanics of Materials*. New York, NY: J. Wiley, 1996.
- J. B. Wachtman, *Mechanical Properties of Ceramics*. New York, NY: J. Wiley, 1996.
- R. H. Wagoner and J. L. Chenot, *Fundamentals of Metal Forming*. New York, NY: J. Wiley, 1996.

### Hardness

- H. E. Boyer, ed. *Hardness Testing*. Metals Park, OH: ASM Intl., 1987. *Metals Handbook, Vol. 8: Mechanical Testing*. Metals Park, OH: ASM Int., 1985.
- A. C. Fischer-Cripps, *Nanoindentation*. New York, NY: Springer, 2002.
- M. C. Shaw, *Mechanical Behavior of Materials*. F. A. McClintock and A. S. Argon, eds. Reading, MA: Addison-Wesley, 1966, p. 443.
- D. Tabor, *The Hardness of Metals*. London: Oxford University Press, 1951.
- J. H. Westbrook and H. Conrad, eds., *The Science of Hardness Testing and Its Research Applications*. Metals Park, OH: ASM Intl., 1973.

### Formability

- W. Brazier, *Closed Loop (MTS Journal)*, 15, No. 1 (1986) 3.

- K. S. Chan, *J. Met.*, Feb. (1990) 6.
- S. S. Hecker, in *Constitutive Equations in Viscoplasticity: Computational and Engineering Aspects*. New York, NY: ASME, 1976, p. 1.
- S. S. Hecker and A. K. Ghosh, *Sci. Am.*, Nov. (1976), 100.
- S. S. Hecker, A. K. Ghosh, and H. L. Geigel, eds. *Formability: Analysis, Modeling, and Experimentation*. New York, NY: TMS-AIME, 1978.
- W. F. Hosford and R. M. Caddell, *Metal Forming—Mechanics and Metallurgy*. Englewood Cliffs, NJ: Prentice-Hall, 1983.

## Exercises

**3.1** A polycrystalline metal has a plastic stress-strain curve that obeys Hollomon's equation,

$$\sigma = K \varepsilon^n.$$

Determine  $n$ , knowing that the flow stresses of this material at 2% and 10% plastic deformation (offset) are equal to 175 and 185 MPa, respectively.

**3.2** You are traveling in an airplane. The engineer who designed it is, casually, on your side. He tells you that the wings were designed using the von Mises criterion. Would you feel safer if he had told you that the Tresca criterion had been used? Why?

**3.3** A material is under a state of stress such that  $\sigma_1 = 3\sigma_2 = 2\sigma_3$ . It starts to flow when  $\sigma_2 = 140$  MPa.

- (a) What is the flow stress in uniaxial tension?
- (b) If the material is used under conditions in which  $\sigma_1 = -\sigma_3$  and  $\sigma_2 = 0$ , at which value of  $\sigma_3$  will it flow, according to the Tresca and von Mises criteria?

**3.4** A steel with a yield stress of 300 MPa is tested under a state of stress where  $\sigma_2 = \sigma_1/2$  and  $\sigma_3 = 0$ . What is the stress at which yielding occurs if it is assumed that:

- (a) The maximum-normal-stress criterion holds?
- (b) The maximum-shear-stress criterion holds?
- (c) The distortion-energy criterion holds?

**3.5** Determine the maximum pressure that a cylindrical gas reservoir can withstand, using the three flow criteria. Use the following information:

Material: AISI 304 stainless steel – hot finished and annealed,  $\sigma_0 = 205$  MPa  
Thickness: 25 mm

Diameter: 500 mm

Length: 1 mm

*Hint:* Determine the longitudinal and circumferential (hoop) stresses by the method of sections.

**3.6** Determine the value of Poisson's ratio for an isotropic cube being plastically compressed between two parallel plates.

**3.7** A low-carbon-steel cylinder, having a height of 50 mm and a diameter of 100 mm, is forged (upset) at 1,200°C and a velocity of 1 m/s, until its height is equal to 15 mm. Assuming an efficiency of 60%, and assuming that the flow

stress at the specified strain rate is 80 MPa, determine the power required to forge the specimen.

3.8 Obtain the work-hardening exponent  $n$  using Considère's criterion for the curve of Example 3.4.

3.9 The stress-strain curve of a 70–30 brass is described by the equation

$$\sigma = 600\varepsilon_p^{0.35} \text{ MPa}$$

until the onset of plastic instability.

(a) Find the 0.2% offset yield stress.

(b) Applying Considère's criterion, find the real and engineering stress at the onset of necking.

3.10 The onset of plastic flow in an annealed AISI 1018 steel specimen is marked by a load drop and the formation of a Lüders band. The initial strain rate is  $10^{-4} \text{ s}^{-1}$ , the length of the specimen is 5 cm, and the Lüders plateau extends itself for a strain equal to 0.1. Knowing that each Lüders band is capable of producing a strain of 0.02 after its full motion, determine:

(a) The number of Lüders bands that traverse the specimen.

(b) The velocity of each Lüders band, assuming that only one band exists at each time.

3.11 A tensile test on a steel specimen having a cross-sectional area of  $2 \text{ cm}^2$  and length of 10 cm is conducted in an Instron universal testing machine with stiffness of 20 MN/m. If the initial strain rate is  $10^{-3} \text{ s}^{-1}$ , determine the slope of the load-extension curve in the elastic range ( $E = 210 \text{ GN/m}^2$ ).

3.12 Determine all the parameters that can be obtained from a stress-strain curve from the load-extension curve (for a cylindrical specimen) shown in Figure E.3.12, knowing that the initial cross-sectional area is  $4 \text{ cm}^2$ , the crosshead velocity is 3 mm/s, the gage length is 10 cm, the final cross-sectional area is  $2 \text{ cm}^2$ , and the radius of curvature of the neck is 1 cm.

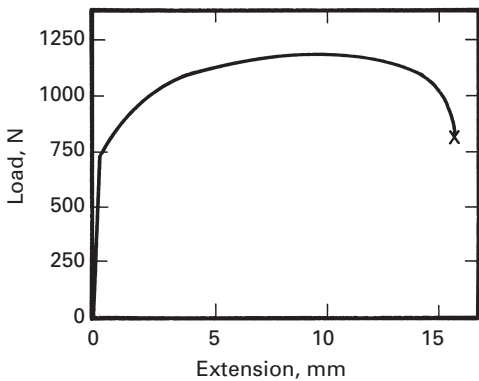


Fig. Ex.3.12

3.13 Draw the engineering-stress-engineering-strain and true-stress-true-strain (with and without Bridgman correction) curves from the curve in Exercise 3.12.

3.14 What is the strain-rate sensitivity of AISI 1040 steel at a strain of 0.02 and a strain rate of 0.05 (Obtain your data from Figure 3.12(a).)

3.15 From the load-extension curve shown in Example 3.4, draw the true-stress–true-strain curve.

3.16 An AISI 1045 steel obeys the following relationship between stress ( $\sigma$ ) and strain ( $e$ ) in tension:

$$\sigma(\text{MPa}) = 300 + 450e^{0.5}.$$

Obtain the compressive stress–strain curve, considering the Bauschinger effect. Use the data from Figure 3.17.

3.17 The PMMA specimens, Figure Ex.3.17, were deformed in uniaxial tension at different temperatures. (a) Plot the total elongation, ultimate tensile stress, and Young's modulus as a function of temperature. (b) Discuss changes in these properties in terms of the internal structure of the specimen.

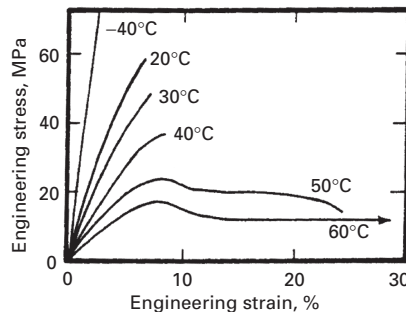


Fig. Ex.3.17

3.18 For the force–displacement curve of Figure Ex.3.18, obtain the engineering and true-stress–strain curves if the specimen were tested in compression.

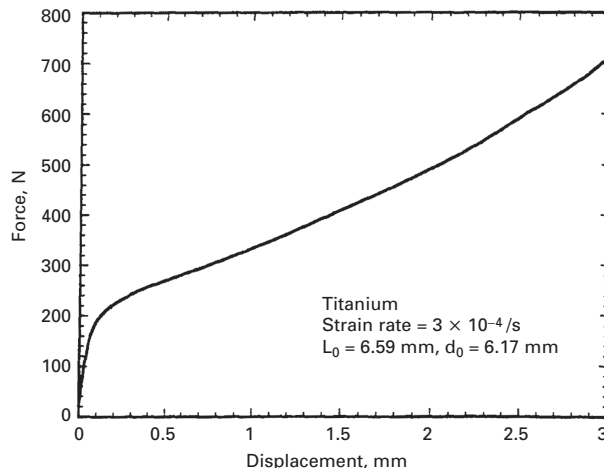


Fig. Ex.3.18

3.19 Calculate the softening temperature for a soda-lime silica glass at which the viscosity is equal to  $10^7 \text{ Pa} \cdot \text{s}$  if the activation energy for viscous flow is  $250 \text{ kJ/mol}$  and the viscosity at  $1,000^\circ\text{C}$  is  $10^3 \text{ Pa} \cdot \text{s}$ .

3.20 The viscosity of a  $\text{SiO}_2$  glass is  $10^{14} \text{ P}$  at  $1,000^\circ\text{C}$  and  $10^{11} \text{ P}$  at  $1,300^\circ\text{C}$ . What is the activation energy for viscous flow in this glass? Note:  $1 \text{ P} = 0.1 \text{ Pa} \cdot \text{s}$ .

3.21 When tested at room temperature, a thermoplastic material showed a yield strength of  $51 \text{ MPa}$  in uniaxial tension and  $55 \text{ MPa}$  in uniaxial compression. Compute the yield strength of this polymer when tested in a pressure chamber with a superimposed hydrostatic pressure of  $300 \text{ MPa}$ .

3.22 From Equation 3.35, obtain Equation 3.34. Then prove that Equation 3.34 represents an ellipse rotated  $45^\circ$  from its principal axis.

3.23 An annealed sheet of AISI 1040 steel ( $0.85 \text{ mm}$  thick and with in-plane isotropy) was tested in uniaxial tension until the onset of necking, to determine its formability. The initial specimen's length and width were  $20$  and  $2 \text{ cm}$ , respectively. At the onset of necking, the length and width were  $25$  and  $1.7 \text{ cm}$ , respectively.

- Determine the ratio between the through-thickness and the in-plane yield stress, assuming that  $R$  does not vary with strain.
- Draw the flow locus of this sheet, assuming that  $\sigma_{y(1,2)} = 180 \text{ MN/m}^2$ .

3.24 Repeat Exercise 3.23 if the final width of the specimen is  $1.9 \text{ cm}$ , and explain the differences. Which case has a better formability?

3.25 Imagine that you want to perform a circle-grid analysis, but you do not have the facilities for photoprinting. Hence, you decide to make a grid of perpendicular and equidistant lines. After plastic deformation of the material, can you still determine the major and minor strains from the distorted grid? (Hint: Use the method for determining principal strains.)

3.26 Determine the activation energy for deformation for the three glasses shown in Figure 3.26. (Hint: plot  $\ln \text{ viscosity vs. } 1/T$ .)

3.27 You are given a  $2.5 \text{ mm}$  diameter cylindrical specimen  $180 \text{ mm}$  long. If the specimen is subjected to a torque of  $50 \text{ N} \cdot \text{m}$ .

- Calculate the deflection of the specimen end, if one end is fixed.
- Will the specimen undergo plastic deformation?

3.28 Calculate the resulting rod diameter for 1040 carbon steel subjected to a  $4000 \text{ N}$  compressive load, with an initial diameter of  $15 \text{ cm}$ .

3.29 You are asked to design a spherical pressure vessel for space application. The weight has to be minimized. Given that  $\sigma = Pr/T$ , among materials below, which one you would select?

Alloy	Density ( $\text{kg/m}^3$ )	Y. S. (MPa)
304 SS	$7.8 \times 10^3$	400
Ti6Al4V	$4.46 \times 10^3$	850
2024 Al	$2.7 \times 10^3$	400

3.30 You have a piece of steel, and you are able to measure its hardness:  $HV = 250 \text{ kg/mm}^2$ . What is its estimated yield stress, in MPa?

3.31 You received a piece of cast iron, and you want to estimate its yield strength. You are able to make a hardness indentation using a 10 mm diameter tungsten carbide sphere. The diameter of the indentation is 4 mm. What is the estimated yield strength?

3.32 Describe the similarities and differences in the phenomena of Lüders band formation in low-carbon steels and tensile drawing of a polymer.

3.33 The shear yield strength of a polymer is 30% higher in compression than in tension. Determine the coefficient  $A$  that represents the dependence of yield stress on hydrostatic pressure.

3.34 Looking at Figure 3.3, give reasons as to why the ultimate tensile stress (UTS) of AISI 1040 steel decreases with increased heat treatment.

### 3.35

- (a) Describe the changes that occur at a microstructural level when a thin semicrystalline polymer begins to neck.
- (b) Why does the strength increase in the load direction? Does the necking region become more or less transparent if the material is made of a semi-transparent material?

3.36 The following stresses were measured on a metal specimen:

$$\sigma_{11} = 94 \text{ MPa}$$

$$\sigma_{22} = 155 \text{ MPa}$$

$$\sigma_{12} = 85 \text{ MPa}.$$

Determine the yielding for both the Tresca and von Mises criteria, given that  $\sigma_0 = 180 \text{ MPa}$  (yield stress). Which criterion is more conservative?

3.37 A flat indenter strikes the surface of an iron block and sinks into the material by 0.4 cm. Assuming that the surface of a piece of iron ( $\tau_0 = 6.6 \text{ GPa}$ ,  $\sigma_0 = 12.6 \text{ GPa}$ ,  $A = 0.5 \text{ cm}^2$ ) can be modeled as triangular blocks as in Figure E2.10.2, determine the force with which the indenter hits the material.

3.38 Determine the hardness of the copper specimen from the nanoindentation SEM image in Figure 3.42(b) knowing that the applied load is 2000  $\mu\text{N}$ .

3.39 Calculate the projected area of an indentation made in keratin, the penetration depth  $h$  is 600 nm. Assume we used the Berkovich tip ( $A = 24.5h^2$ ).

3.40 You are designing a kinetic energy penetrator for the M1 tank. This penetrator is made of depleted (non-radioactive but highly lethal!) uranium-0.75%Ti. Plot the stress-strain curve, from 0 to 1:

- (a) At the following strain rates:  $10^{-3} \text{ s}^{-1}$ ,  $10^3 \text{ s}^{-1}$  (ambient temperature).
- (b) At a strain rate of  $10^{-3} \text{ s}^{-1}$  and the following temperatures: 77 K, 100 K, 300 K.

Given:

$$T_m = 1473 \text{ K}$$

$$\sigma_0 = 1079 \text{ MPa}$$

$$K = 1120 \text{ MPa}$$

$$n = 0.25$$

$$C = 0.007$$

$$m = 1$$

$$\dot{\varepsilon} = 10^{-4} \text{ s}^{-1}$$

---

# Chapter 4

## Imperfections: Point and Line Defects

### 4.1 | Introduction

The mechanical properties of materials are often limited by their imperfections. The theoretical cleavage and shear strengths of materials are given by (see Section 4.2):

$$\sigma_{\text{th}} = \sqrt{\frac{E \gamma}{a}} \approx \frac{E}{\pi} \quad \text{and} \quad \tau_{\text{th}} = \frac{Gb}{2\pi a} \approx \frac{G}{2\pi},$$

where  $E$  and  $G$  are the Young's and shear moduli, respectively;  $a$  is the interatomic spacing, and  $\gamma$  is the surface energy of the material. These equations predict exceedingly high strengths (on the order of GPa), and few materials reach such strengths. (See Chapter 1.) Indeed, this is somehow the Holy Grail of materials science: If materials were perfect, those values could be reached. However, all materials contain imperfections, either by design or inadvertently produced during processing. We review these in this and subsequent chapters. They are classified, according to their dimensions, into four kinds, each discussed in a separate section as follows:

- Point (atomic or electronic) defects (Section 4.3)
- Line (or one-dimensional) defects (Section 4.3)
- Interfacial (or two-dimensional) defects (Chapter 5, Section 5.1)
- Volume (or three-dimensional) defects (Chapter 5, Section 5.2).

Cracks are discussed in chapters 7 and 8, on fracture.

Imperfections determine the mechanical response of materials, and the manner in which the response is used to enhance performance in a material will be analyzed in considerable detail in chapters 5 through 9. Note that the dimensional scale of defects covers a wide spectrum,  $10^{-14}$  m, as shown schematically in Figure 4.1. Electronic point defects do not affect mechanical properties significantly and will therefore not be discussed in this text.

**Fig. 4.1** Dimensional ranges of different classes of defects.

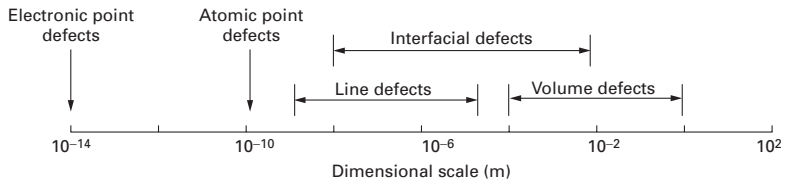
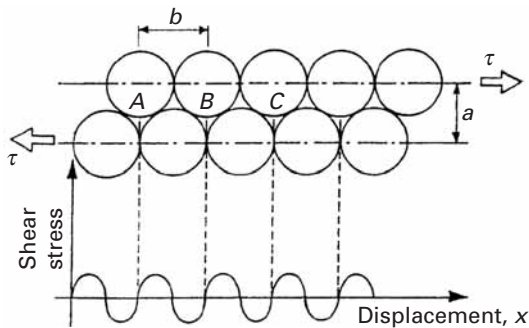


**Fig. 4.2** Stress required to shear a crystal.



## 4.2 | Theoretical Shear Strength

Frenkel<sup>1</sup> performed a simple calculation of the theoretical shear strength of crystals by considering two adjacent and parallel lines of atoms subjected to a shear stress; this configuration is shown in Figure 4.2 where  $a$  is the separation between the adjacent planes and  $b$  is the interatomic distance. Under the action of the stress  $\tau$ , the top line will move in relation to the bottom line; the atoms will pass through successive equilibrium positions  $A$ ,  $B$ ,  $C$ , for which  $\tau$  is zero. When the applied shear stress is enough to overcome these barriers, plastic deformation will occur, and the atoms will move until a shear fracture is produced. The stress is also zero when the atoms are exactly superimposed; in that case, the equilibrium is metastable. Between these values the stress varies cyclically with a period  $b$ . Frenkel assumed a sine function, as one would expect:

$$\tau = k \sin \frac{2\pi x}{b}, \quad (4.1)$$

where  $x$  is the displacement,  $b$  is the Burgers vector, and  $k$  is the constant to be determined (see below).

For small displacements,

$$\tau = k \frac{2\pi x}{b}. \quad (4.2)$$

Since, for small displacements, one can consider the material to deform elastically, we have

$$\tau = G \frac{x}{a}, \quad (4.3)$$

where  $x/a$  is the shear strain and  $G$  is the shear modulus. Substituting Equation 4.3 into Equation 4.2, we have

$$k = \frac{G b}{2\pi a}. \quad (4.4)$$

<sup>1</sup> J. Frenkel, *Z. Phys.*, 37 (1926) 572.

**Table 4.1** | Theoretical Shear Strength<sup>a</sup>

Element	$G$ (GPa)	$\tau_{\max}$ (GPa)	$\tau_{\max}/G$
Iron	60.0	6.6	0.11
Silver	19.7	0.77	0.039
Gold	19.0	0.74	0.039
Copper	30.8	1.2	0.039
Tungsten	150.0	16.5	0.11
Diamond	505.0	121.0	0.24
NaCl	23.7	2.8	0.12

<sup>a</sup> From A. Kelly, *Strong Solids* (Oxford, U.K.: Clarendon Press, 1973), p. 28.

Substituting Equation 4.4 into Equation 4.1 yields

$$\tau = \frac{Gb}{2\pi a} \sin \frac{2\pi x}{b}.$$

The maximum of  $\tau$  occurs for  $x = b/4$ :

$$\boxed{\tau_{\max} = \frac{Gb}{2\pi a}.} \quad (4.5)$$

For FCC materials, the relationship between  $a_0$  (the lattice parameter),  $a$ , and  $b$  can be calculated. Drawing a unit cell, the student will be able to show that  $b = a_0/2$ ; the spacing between adjacent planes is given by (see crystallography textbooks):

$$d_{hkl} = \frac{a_0}{\sqrt{h^2 + k^2 + \ell^2}}.$$

For (111) planes:

$$d_{111} = a_0/\sqrt{3}.$$

This is equal to  $a$  in Figure 4.2.

Substituting  $b$  and  $a$  into Equation 4.5, we obtain

$$\tau_{\max} \approx \frac{G}{5.1}. \quad (4.6)$$

More complex models have been advanced in which the sine function is replaced by more precise curves expressing the interaction energy. The method used by Kelly (Mackenzie's method) is an example. Kelly took into account the distortion of the planes. Table 4.1 shows the stresses calculated by Mackenzie's method. Note that the ratio  $\tau_{\max}/G$  varies between 0.039 and 0.24. Consequently, it is fairly close to Frenkel's ratio (0.18), obtained by the simpler method.

The theoretical strength derived above is on the order of gigapascals; unfortunately, the actual strength of materials is orders of magnitude below that. We derive an expression for theoretical cleavage strength in Chapter 7.

### Example 4.1

Estimate the theoretical shear and cleavage strength for copper and iron. From Table 2.5 in Chapter 2, we have the following data:

Iron	$E = 211.4 \text{ GPa}$	$G = 81.6 \text{ GPa}$
Copper	$E = 129.8 \text{ GPa}$	$G = 43.3 \text{ GPa}$

For the shear strength, we assume, to a first approximation, that  $b = a$ . Thus,

$$\boxed{\tau_{\max} = \frac{G}{2\pi}}$$

and

$$\text{Fe: } \tau_{\max} = 13.0 \text{ GPa}$$

$$\text{Cu: } \tau_{\max} = 7.7 \text{ GPa.}$$

For the cleavage strength,

$$\sigma_{\max} = \sqrt{\frac{E\gamma}{a_0}} \quad \text{and} \quad \gamma \approx \frac{Ea_0}{10};$$

So

$$\sigma_{\max} \approx \sqrt{\frac{E^2}{10}} \approx \boxed{\frac{E}{3.16}}.$$

Therefore, we have

$$\text{Fe: } \sigma_{\max} = 66.9 \text{ GPa}$$

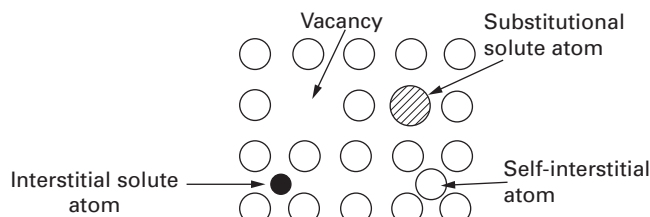
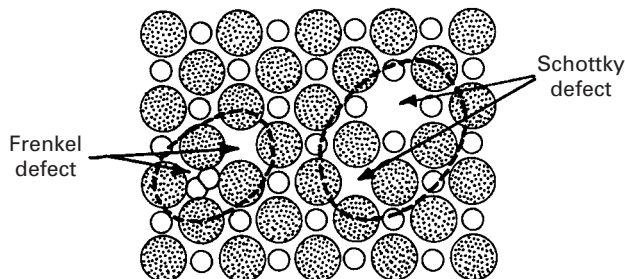
$$\text{Cu: } \sigma_{\max} = 41.1 \text{ GPa.}$$

The actual tensile strength of pure Fe and Cu is on the order of 0.1 GPa. Since these metals fail by shear, the actual shear strength is equal to 0.05 GPa.

## 4.3 | Atomic or Electronic Point Defects

These defects exist on an atomic scale. These defects can have a diameter of approximately  $10^{-10} \text{ m}$ . Although relatively small compared to other imperfections, atomic defects do generate a stress field in the crystal lattice and affect the properties of the material. Figure 4.3 shows the following three types of atomic point defects.

1. *Vacancy*. When an atomic position in the Bravais lattice is vacant.
2. *Interstitial point defect*. When an atom occupies an interstitial position. This interstitial position can be occupied by an atom of the material itself or by a foreign atom; the defect is called a self-interstitial and an interstitial impurity, respectively, for the two cases.

**Fig. 4.3** Atomic point defects.**Fig. 4.4** Two most common point defects in compounds: Schottky and Frenkel defects.

3. **Substitutional point defect.** When a regular atomic position is occupied by a foreign atom.

The vacancy concentration in pure elements is very low at low temperatures. The probability that an atomic site is a vacancy is approximately  $10^{-6}$  at low temperatures, rising to  $10^{-3}$  at the melting point. In spite of their low concentration, vacancies have a very important effect on the properties of a material, because they control the self-diffusion and substitutional diffusion rates. The movement of atoms in the structure is coupled to the movement of vacancies. In Section 4.3.1, the equilibrium concentration of vacancies is calculated.

In compounds (ceramics and intermetallics), defects cannot occur as freely as in metals, because we have additional requirements, such as electrical neutrality. Two types of defects are prominent in compounds and are shown in Figure 4.4: the Schottky defect, which is a pair of vacancies that have opposite sign (one cation and one anion); and the Frenkel defect, which consists of a vacancy–self-interstitial pair.

The self-interstitial and interstitial impurities lodge themselves in the “holes” that the structure has. There is more than one type of hole in the FCC, BCC, and HCP structures, and their diameters and positions will be determined in what follows.

The FCC structure, shown in Figure 4.5 has two types of voids: the larger, called octahedral, and the smaller, called tetrahedral. The names are derived from the nearest neighbor atoms; they form the vertices of the polyhedra shown. If we consider the atoms as rigid spheres, we can calculate the maximum radius of a sphere that would fit into the void without straining the lattice. The reader is encouraged to engage in this exercise; with some luck, he or she will find radii of 55 and 31 pm for octahedral and tetrahedral voids, respectively, in  $\gamma$ -iron. Hence, carbon ( $r = 80$  pm) and nitrogen ( $r = 70$  pm) produce distortions in the lattice when they occupy the voids.

**Fig. 4.5** Interstices in FCC structure. (a) Octahedral void.  
(b) Tetrahedral void.

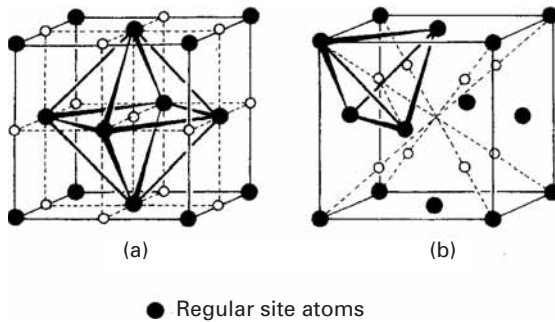


**Fig. 4.6** Interstices in the BCC structure. (a) Octahedral void.  
(b) Tetrahedral void.

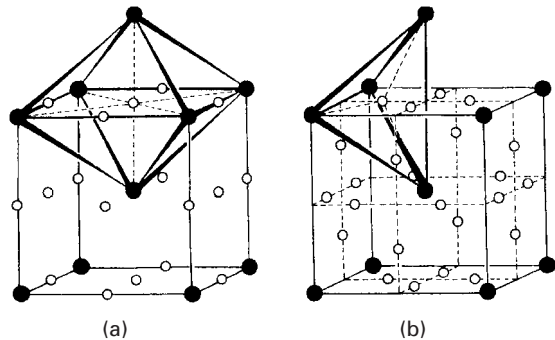
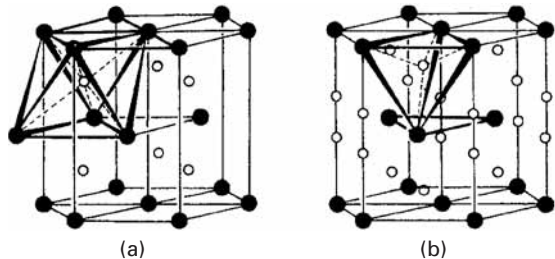


**Fig. 4.7** Interstices in the HCP structure. (a) Octahedral void.  
(b) Tetrahedral void.



In BCC metals there are also octahedral and tetrahedral voids, as shown in Figure 4.6. In this case, however, the larger void is tetrahedral. For rigid spheres in  $\alpha$ -iron, the void radii are 36 and 19 pm for tetrahedral and octahedral interstices, respectively. Hence, a solute atom is accommodated in an easier way in FCC than in BCC iron, in spite of the fact that the FCC structure is more closely packed.

Analogously, the HCP structure presents tetrahedral and octahedral voids, shown in Figure 4.7; the reader is reminded of the similarity between the FCC and HCP structures, which explains the presence of the same voids.

### 4.3.1 Equilibrium Concentration of Point Defects

A very important characteristic of vacancies and self-interstitial atoms, in contrast to line and surface defects, is that they can exist in thermodynamic equilibrium at temperatures above 0 K. The thermodynamic equilibrium in a system of constant mass, at a constant pressure and temperature, and that does not execute any work in addition

to the work against pressure, is reached when the Gibbs free energy is minimum. The formation of point defects in a metal requires a certain quantity of heat  $\delta q$  (as there is no work being executed, except against pressure). Hence, if  $dH = \delta q$ , the enthalpy  $H$  of the system increases. The configurational entropy  $S$  also increases, because there are a certain number of different ways of putting the defects into the system.

The Gibbs free energy is, by definition,

$$G = H - TS. \quad (4.7)$$

One can thus see that the free energy will reach a minimum for a certain value of  $n$  (the number of point defects) different from zero; at 0 K, the entropic term is zero and the equilibrium concentration is zero.

The equilibrium concentration of point defects can be calculated from statistical considerations and is given by

$$\frac{n}{N} = \exp(-G_f/kT) \quad (4.8)$$

where  $n$  and  $N$  are the number of point defects and sites, respectively,  $G_f$  is the free energy of formation of the defects, and  $k$  is Boltzmann's constant. For copper, the formation of vacancies and interstitials are

$$G_v = 83 \text{ kJ/mol}, \quad G_i = 580 \text{ kJ/mol}.$$

We have, approximately, the following ratio:

$$\frac{G_i}{G_v} \approx 7.$$

Therefore, for copper, the free energy of formation of a vacancy is approximately one-seventh that of a self-interstitial defect. Using Equation 4.8, we can obtain the ratio between the vacancy ( $X_v$ ) and interstitial ( $X_i$ ) concentrations:

$$\frac{X_v}{X_i} \approx \exp\left(\frac{G_i - G_v}{kT}\right). \quad (4.9)$$

For copper at 1,000 K (we have to convert molar quantities or use  $R = 8.314 \text{ J/(mol K)}$ ):

$$\frac{X_v}{X_i} \approx 10^{26}.$$

It can be concluded that, at least in close-packed structures, the concentration of interstitials is negligible with respect to that of the vacancies. Using Equation 4.9 for copper at 1,000 K, we obtain

$$X_v \cong 4.5 \times 10^{-5}.$$

Hence, there is only one vacancy for each  $2 \times 10^4$  copper atoms at 1,000 K. This number is very small; in spite of this, it corresponds to approximately  $10^{14}$  vacancies/cm<sup>3</sup>. The low concentration of self-interstitials in close-packed structures is a consequence of the

small diameter of the interstitial voids. (See Figures 4.5 and 4.6.) In more open structures these concentrations can be higher. Even so, high interstitial concentrations are not observed in equilibrium structures.

### Example 4.2

If, at 400 °C, the concentration of vacancies in aluminum is  $2.3 \times 10^{-5}$ , what is the excess concentration of vacancies if the aluminum is quenched from 600 °C to room temperature? What is the number of vacancies in one cubic  $\mu\text{m}$  of quenched aluminum?

We are given:

$$\begin{aligned}G_v &= 0.62 \text{ eV}, \\k &= 86.2 \times 10^{-6} \text{ eV/K}, \\r_{\text{Al}} &= 0.143 \text{ nm}.\end{aligned}$$

**Solution:** We have

$$\frac{n_v}{N} = e^{-Gv/kT}.$$

At 400 °C (= 673 K),

$$2.3 \times 10^{-5} = e^{-0.62/86.2 \times 10^{-6} \times 673},$$

Thus,

$$\frac{n_v}{n} = e^{-0.62/86.2 \times 10^{-6} \times 873} = 2.6 \times 10^{-4}.$$

Aluminum has the FCC structure, with four atoms per unit cell. The lattice parameter  $a$  is related to the unit cell by

$$a = 2\sqrt{2}r = 0.404 \text{ nm}.$$

The corresponding volume is

$$V = a^3 = 0.0662 \text{ nm}^3.$$

In one  $\mu\text{m}^3$ , the number of atoms is

$$\begin{aligned}n &= \frac{4 \times 10^9}{0.0662} = 6.04 \times 10^{10}, \\n_v &= (2.6 \times 10^{-4})n = 1.6 \times 10^7.\end{aligned}$$

Hence, there are about  $1.6 \times 10^7$  vacancies per cubic  $\mu\text{m}$  of the quenched aluminum.

Point defects can group themselves in more complex arrangements (for instance, two vacancies form a divacancy, two interstitials form a diinterstitial, etc.) The energy of formation of divacancies has been determined for several metals. For example, for copper (with  $G_f = 5.63 \times 10^{-19} \text{ J}$ ), it is:  $0.96 \times 10^{-19} \text{ J}$ . The energy of formation of divacancies in noble metals is on the order of  $0.48 \times 10^{-19} \text{ J}$ . It is thought that divacancies are stable, in spite of the fact that their enthalpies of bonding are not very well known.

Diinterstitials also exist, and their energies can be calculated by the same processes as for monointerstitials. Similarly, the vacancies can bind themselves to atoms of impurities when the binding energy is positive.

### 4.3.2 Production of Point Defects

Intrinsic point defects in a metal – either vacancies or self-interstitials – exist in well-established equilibrium concentrations. (See Section 4.3.1.) By appropriate processing, the concentration of these defects can be increased. Quenching, or ultra-high-speed cooling, is one of these methods. The concentration of vacancies in BCC, FCC, and HCP metals is greatly superior to that of interstitials and on the order of  $10^{-3}$  when the metal is at a temperature close to the melting point; it is only  $10^{-6}$  when the metal is at a temperature of about half the melting point. Hence, if a specimen is cooled at a high enough rate, the high-temperature concentration can be retained at low temperatures. For this to occur, the rate of cooling has to be such that the vacancies cannot diffuse to sinks – grain boundaries, dislocations, surface, and so on. Theoretically, gold would have to be cooled from 1,330 K to ambient temperature at a rate of  $10^{11}$  K/s to retain its high-temperature vacancy concentration. The fastest quenching technique to cool thin wires produces cooling rates lower than  $10^5$  K/s; nevertheless, a significant portion of the high-temperature point defects is retained.

Another method of increasing the concentration of point defects is by plastic deformation. The movement of dislocations generates point defects by two mechanisms: the nonconservative motion of jogs, and the annihilation of parallel dislocations of opposite sign, producing a line of vacancies or interstitials. Jogs are created by dislocation intersections; since they cannot glide with dislocations, they have to climb as the dislocation moves. In a screw dislocation, they are small segments having the character of an edge. The slip plane of this segment is not compatible with that of the dislocation. The climb is possible only by continuous emission of vacancies or interstitials. The second mechanism is depicted schematically in Figure 4.8. When the two dislocations cancel each other, they create a row of interstitials or vacancies if their slip planes do not coincide.

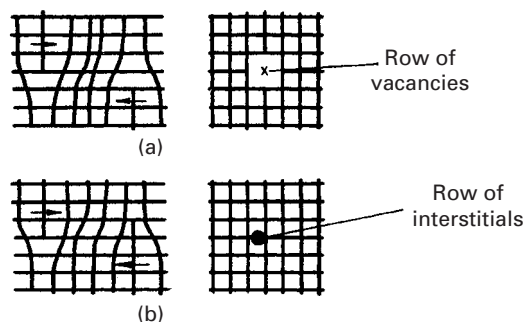


**Fig. 4.8** Formation of point defects by the annihilation of dislocations. (a) Row of vacancies. (b) Row of interstitials.

Quenching produces mostly vacancies and vacancy groups. The concentrations obtained are lower than  $10^{-4}$ . Deformation, on the other hand, can introduce higher concentrations of vacancies and equivalent ones of interstitials; the problem is that it also introduces a number of other substructural changes that complicate the situation. Dislocations are introduced, and they interact strongly with point defects. One method of producing point defects does not present these problems: *Irradiation* of the metal by high-energy particles allows the introduction of a high concentration of point defects. The radiation displaces the electrons, or ionizes, displaces atoms by elastic collisions, and produces fission and thermal spikes. This subject is treated in greater detail in Section 4.3.4. The displacement of atoms is produced by the elastic collision of the bombarding particles with the lattice atoms, transferring the kinetic energy of the particles to the atoms. This may cause the atoms to travel through the lattice. In the majority of cases, an atom travels a few atomic distances and enters an interstitial site. Consequently, a vacancy is produced, together with a self-interstitial. The energy transferred in the collision has to be well above the energy required to form an interstitial-vacancy pair in a reversible thermodynamic process (3 to 6 eV, or  $4.8 \times 10^{-19}$  to  $9.6 \times 10^{-19}$  J). It is believed that the energy transferred to the atom has to be approximately 25 eV ( $40 \times 10^{-19}$  J). Different particles can be used in the bombardment process: neutrons, electrons,  $\gamma$  rays, and  $\alpha$  particles.

#### 4.3.3 Effect of Point Defects on Mechanical Properties

Point defects have a marked effect on the mechanical properties of a material. For this reason, the effect of radiation is of great importance. Maddin and Cottrell<sup>2</sup> used aluminum single crystals with various purity levels, observing that the yield stress increased with quenching. Quenching was accomplished by taking the specimens from 600 °C and throwing them into a water-ice mixture, while annealed material was slowly cooled in the furnace. The yield stress increased from 550 to 5,900 kPa, on average. The effect of impurity atoms could be neglected because the increase in yield stress was consistent throughout the specimens. The effect of possible residual stresses due to quenching was also neglected. With the purpose of obtaining evidence that was still more convincing, a single crystal was tested immediately after quenching, while another was tested after staying a few days at ambient temperature. The yield stress increased from 5.9 MPa to 8.4 MPa in the aged condition. The strengthening by quenching is due to the interaction of dislocations and vacancies or groups thereof. The effect of jogs, formed by the condensation of vacancies on the dislocations, can also be considerable. During aging, the excess concentration of vacancies forms groups and/or annihilates preexisting dislocations.

---

<sup>2</sup> R. Maddin and A. H. Cottrell, *Phil. Mag.*, 46 (1955) 735.

There are also alterations in the plastic portion of the stress-versus-strain curve seen in Figure 4.9. The initial work-hardening rate of the quenched aluminum is lower than that of slowly (furnace) cooled aluminum. At greater strains, however, the two work-hardening rates become fairly similar. Hence, the effect of quenching disappears at higher strains. This is thought to be because the excess concentrations of point defects are eliminated during plastic deformation; at the same time, excess vacancies are generated by dislocation motion, so that the concentrations in the quenched and furnace cooled materials become the same.

The increase in hardness in many quenched metals is negligible, in spite of the obvious changes in the stress-versus-strain curve. This is explained by the fact that the effect of quenching disappears after a certain amount of plastic deformation. Since the indenter deforms the metal plastically (in an extensive way), the effect of quenching is minimal.

#### 4.3.4 Radiation Damage

Irradiation of solids by high-energy particles may produce one or more of the following effects:

1. Displaced electrons (i.e., ionization).
2. Displaced atoms by elastic collision.
3. Fission and thermal spikes.

Ionization has a much more important role in nonmetals than it has in metals. The high electrical conductivity of metals leads to a very quick neutralization of ionization, and there is no observable change in properties due to this phenomenon. Electronic excitations in metals are also eliminated almost instantaneously. Such would not be the case in semiconductors and dielectrics, where electronic excitation configurations are almost permanent. Thus, in the case of metals, only collisions among incident particles and atomic nuclei are of importance. The basic mechanism in all processes of radiation damage is the transfer of energy and motion from the incident particle beams to the atoms of the material. The incident particle beam may consist of positive particles (protons, for example), negative particles (which are invariably electrons), or neutral particles (X-rays,  $\gamma$ -rays, neutrons, etc.). Irradiation by neutrons results in a large spectrum of constant energy until the maximum energy that a particle can transmit to an atom which suffered the impact. A neutron of 1 MeV (0.16 pJ) can transfer about  $10^5$  eV (0.016 pJ) to an atom. High-energy transfers can also be obtained by means of positive particles, but such energy transfers are less common. In the case of electrons, only low-energy transfers are possible. We shall consider here mainly the effects of neutron radiation on metals. The primary collision has the function of transferring energy to the atomic system. The subsequent events that occur are as follows.

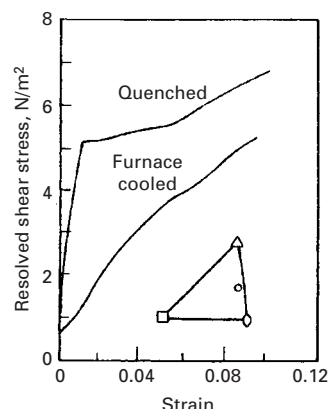


**Fig. 4.9** Stress-versus-strain curves for aluminum single crystals. The crystallographic orientation is shown in the stereographic triangle. (Adapted with permission from A. H. Cottrell, *Phil. Mag.*, 46 (1955) p. 737.)

1. Displacement of an atom from its normal position in the lattice to a position between the normal lattice sites.
2. Creation of defects by displacements and their migrations and interactions.

When an atom is displaced from its normal lattice site, two defects are created: an interstitial atom referred to as autointerstitial or self-interstitial, and a vacant lattice site called a vacancy. More complex configurations can be regarded as having started from this fundamental step. When an atom receives an energy impulse greater than a certain value  $E_e$ , called the *effective displacement energy*, some atom is displaced from its normal position to an interstitial position. In the most simple case, if an atom receives the primary impact of energy  $E_e$ , the atom itself is displaced. This, however, is not inevitable; sometimes another atom, a neighboring one, is displaced. With an increase in the energy imparted to the affected atom, various events can occur. At low energies, but higher than  $E_e$ , only an interstitial and its connected vacancy are possible. At high energies, the affected atom becomes an important particle for creating more damage. This leads to cascade elements.

Near the end of its trajectory, an energetic atom displaces all the atoms that it encounters; this is called a “displacement spike.” Through a cascade effect, damage propagates through the lattice. Many atoms that spread about by displacement spikes will become situated along the atomic packing lines, and thus these lines will be a most efficient manner of transporting energy far away from the spike. The impact transferred along a crystallographic direction is called a *Focuson* (analogous to *photon* and *phonon*). If the energy is not well above the energy required for atomic displacement, it will be transferred into a chain of exchange collisions that makes the atom travel far away from the spike before it comes to a stop as an interstitial. The efficiency of this process is much higher in the close-packed directions (the  $\langle 110 \rangle$  directions in FCC crystals). The atomic configuration in the  $\langle 110 \rangle$  direction in which an interstitial is propagated along a line is called a *dynamic crowdion*. The efficiency of the focusing processes is directly proportional to the interatomic potential, being higher for heavy metals and lower for light metals (such as Al). According to the Seeger model, at zero kelvin, for each initially displaced atom, one would have one or more regions in which a good fraction of atoms (about 30%) disappear. These regions are surrounded by interstitial clouds that extend a few hundreds of atomic distances in noble metals and perhaps a few atomic distances in a metal such as Al. Seeger called the region of lost atoms in the center of a cascade a “depleted zone” and estimated that its typical size would be less than 1 nm. Figure 4.10 shows the Seeger model of damage produced by irradiation.

Vacancies generated during exposure to radiation often condense and form voids inside the material. An illustration of this is provided in Figure 4.11, which shows Ni irradiated by a high dosage of

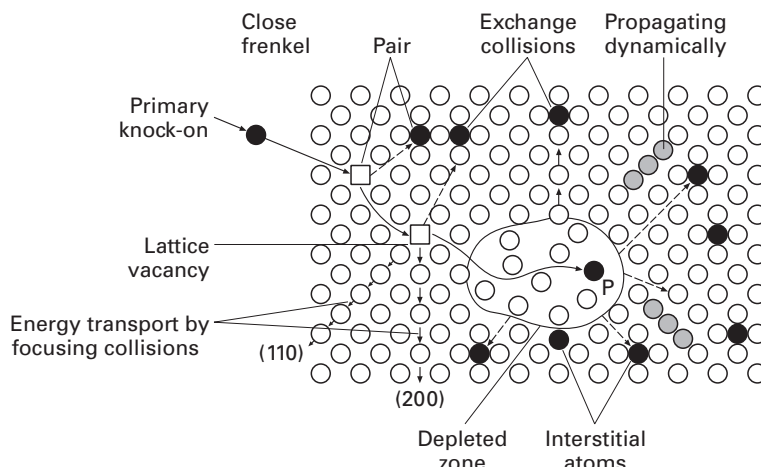


**Fig. 4.10** Seeger model of damage produced by irradiation.  $P$  indicates the position where the first “knock-on” terminates.  
(Reprinted with permission from A. Seeger, in *Proc. Symp. Radiat. Damage Solids React.*, Vol. I, (Vienna, IAEA, 1962) pp. 101, 105.)

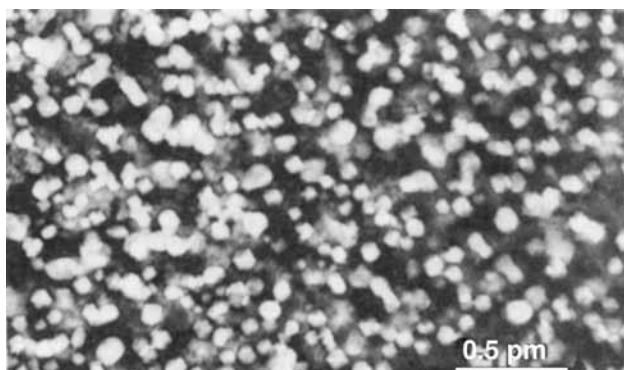


**Fig. 4.11** Voids formed in nickel irradiated using 400 keV  $^{14}\text{N}_2^+$  ions to a dose of 40 dpa at 500 °C; notice the voids with polyhedral shape; dpa = displacements per atom. (Courtesy of L. J. Chen and A. J. Ardell.)

$\text{N}_2^+$  ions. A high concentration of voids is produced. The voids have polyhedral shapes because the surface energy is anisotropic and this shape, rather than a sphere, minimizes the overall surface energy.

In any event, a major portion of radiation damage in common metals caused by neutrons in reactors consists of a large number of interstitials and vacancies produced in a cascade process that follows after a primary knock-on impact. These point defects act as small obstacles to dislocation movement and result in a hardening of the metals. Besides this direct effect on mechanical properties, some indirect effects are possible. These indirect effects, which arise from the fact that irradiation by neutrons changes the rates and mechanisms of atomic interchange, are as follows.

1. Destruction of order of lattice.
2. Fractionating of precipitates.
3. Acceleration of nucleation.
4. Acceleration of diffusion.

These processes have their origin, directly or indirectly, in the kinetic energy exchanges between energetic neutrons and atoms. According to Seeger's model, atoms can be transported long distances by “cooperative” focalization along the more densely packed

directions, and the collision processes create simple defects, such as interstitials and vacancies, and complex defects, such as displacement spikes. If an alloy is ordered, focalization and displacement spikes may destroy the order. If the alloy contains precipitates, a displacement spike may break the precipitates if they are smaller than the spike and thus return the precipitates into solution. In an alloy that can have precipitates, the damaged regions caused by spikes can serve as nucleation sites. The excess vacancies produced by irradiation can accelerate the diffusion rate. All these effects influence significantly the mechanical properties. At ordinary temperatures (i.e., ambient or slightly above) one or both the defects (interstitials and vacancies) are mobile, and thus, the ones that survive the annihilation, due to recombination or loss of identity at sinks such as dislocations or interfaces, group together. It is well established that in a majority of metals, irradiation at low temperatures ( $<0.2T_m$ , where  $T_m$  is the melting point, in kelvins) results in joining of vacancies and interstitials to form groups that are surrounded by dislocations (i.e., loops and tetrahedral packing defects). These groups impede dislocation motion, as well as increase the strength and reduce the ductility of the material. At high temperatures, the vacancies can group together to form voids. The formation of such groups of defects can cause important and undesirable changes in mechanical properties and result in a dimensional instability of the material. Damage accumulated during irradiation by neutrons (and other particles) can cause significant changes in important properties. For example, the yield stress or the flow stress increases, and frequently there is a loss of ductility.

The problem of mechanical and dimensional stability is a very serious one for structural components in fast reactors. In 1967, it was discovered that nuclear fuel cladding consisting of austenitic stainless steel, when exposed to high doses of fast neutrons, showed internal cavities ( $\sim 10$  nm). These cavities, called *voids*, result in an increase in the dimensions of the material. It is estimated that the maximum possible dilation in the structural components is of the order of 10%. However, as neutron flux and the temperature of the sodium coolant are not uniform in the core, the swelling of the component will be nonuniform. This nonuniformity can influence the component's behavior.

Irradiation by neutrons causes marked changes in the properties of the zirconium alloys Zircaloy-2 and Zircaloy-4 (both very much used in light water reactors) and in 304 and 316 stainless steels (used in liquid metal fast-breeder reactors). Figure 4.12 shows the increase in strength (yield strength and ultimate tensile strength) of Zircaloy after neutron radiation. The exact nature of the defects introduced by radiation that are responsible for these changes in Zircaloy are not well characterized. There is a considerable variation in the observed microstructures. One of the few observations about which there exists general agreement is the absence of radiation-induced vacancies in Zircaloy, which is a significant difference compared with, say, the behavior of stainless steels. Stainless steels show swelling due to

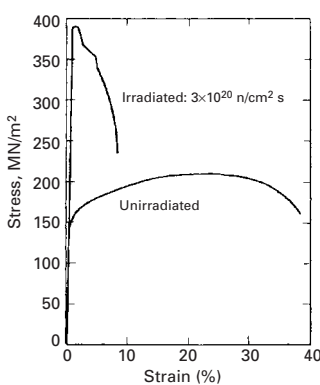


**Fig. 4.12** Stress-strain curves for irradiated and unirradiated Zircaloy. (Adapted with permission from J. T. A. Roberts, IEEE Trans. Nucl. Sci., NS-22, (1975) 2219.)

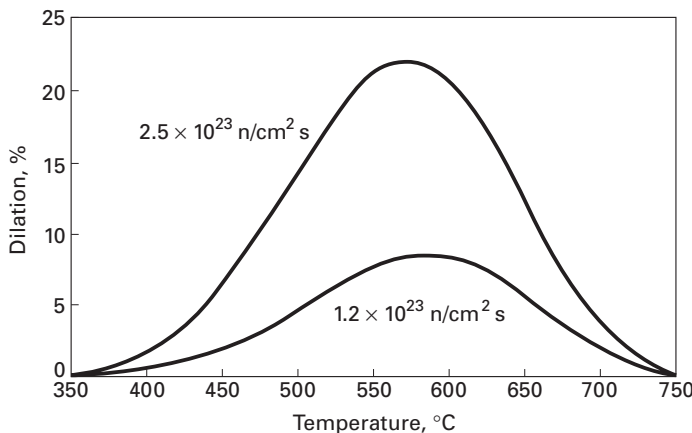


**Fig. 4.13** Stress-free dilation in AISI 316 steel (20% cold-worked). (Adapted with permission from J. T. A. Roberts, *IEEE Trans. Nucl. Sci.*, NS-22, (1975) 2219.)

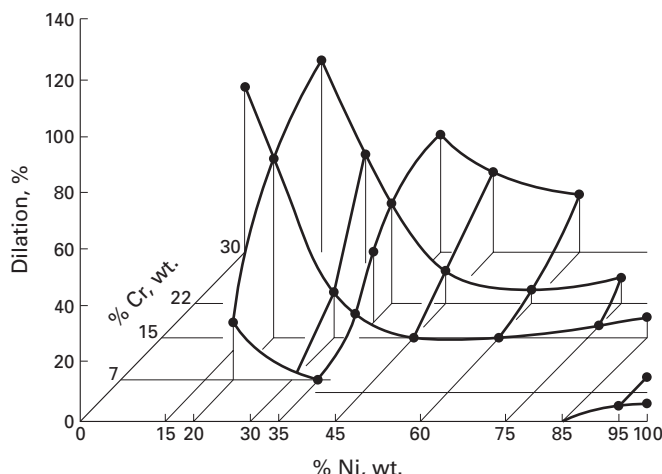


**Fig. 4.14** Dependence of fast neutron-induced dilation in stainless steel (Fe–Cr–Ni) as a function of Ni and Cr amounts. (Adapted with permission from W. B. Hillig, *Science*, 191 (1976) 733.)

neutron irradiation. The dilation induced by neutron irradiation in stainless steel depends on the neutron flux and the temperature, as shown in Figure 4.13. It is believed that the vacancies introduced by irradiation combine to form voids, while the interstitials are preferentially attracted to dislocations. According to Shewmon<sup>3</sup> this dilation of stainless steel does not affect the viability or security of breeder-type reactors, but will have a significant effect on core design and economy of reproduction. It would appear that, in spite of not being able to eliminate the effect completely, cold work, heat treatments, or changes in composition can reduce the swelling by a factor of two or more. Figure 4.14 shows the change in dilation of stainless steel as a function of Cr and Ni content.

#### 4.3.5 Ion Implantation

An interesting technological application using charged particles is called *ion implantation*. Charged ions are accelerated in an electric field (e.g., in a linear accelerator) to very high energies ( $\sim 200$  keV) and

<sup>3</sup> P. G. Shewmon, *Science*, 173 (1971) 987.

allowed to strike the target solid in a moderate vacuum ( $\sim 1$  mPa). It is worth emphasizing that the selected species of ions is *implanted* into, and not deposited on, the target surface. The technique, originally developed for preparing semiconductor devices in a controlled fashion, has been made into a sophisticated tool for altering the composition and structure of surfaces for any number of purposes – for example, modifying the surface chemistry for better corrosion and oxidation resistance, tribological properties, and superconductivity. The reader can well imagine the power of the technique by the fact that it allows one to introduce elements into a surface, which may not be possible in conventional heat treatment because of low diffusivity. Depending on the dose,  $B^+$ ,  $N^+$ , and  $Mo^+$  ions implanted into steel can reduce the wear of a tool by an order of magnitude.

The ion implantation technique of modifying the composition and structure of surfaces has a number of advantages over conventional techniques:

1. The process is essentially a cold one; therefore, there is no loss of surface finish and dimensions (i.e., the process can be applied to finished parts).
2. One can implant a range of metallic and nonmetallic ions, individually or combined.
3. One can implant selected critical areas.

Ion implantation is particularly suited for the selected modification of small, critical parts. Oil burners used for injecting a mixture of fuel oil and air into boilers of oil-fired power plants face rather severe erosion conditions. Ti and B implantation of oil-burner tips improved erosion properties and increased the service life of the boilers.

Another very important aspect of ion implantation has to do with the fact that it is basically a nonequilibrium process. There are thus no thermodynamic constraints, such as solubility limits. In other words, we are able to produce metastable alloys with new and unusual characteristics, amorphous alloys, and so on. Hence, the technique offers a novel way of producing surfaces, in a controlled manner, for scientific studies.

---

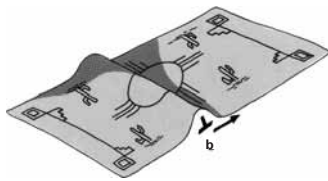
## 4.4 | Line Defects

Bands in the surface of plastically deformed metallic specimens were reported as early as the 19th century. With the discovery of the crystalline nature of metals, these bands were interpreted as being the result of the shear of one part of the specimen with respect to the other. Similar slip bands (or markings) were observed by geologists in rocks. However, calculations of the theoretical strength of crystals based on the simultaneous motion of all atoms along the slip band showed systematic deviations of several orders of magnitude with respect to the experimental values. (See Section 4.2.) This discrepancy led to the concept of line imperfections in crystals called *dislocations*.

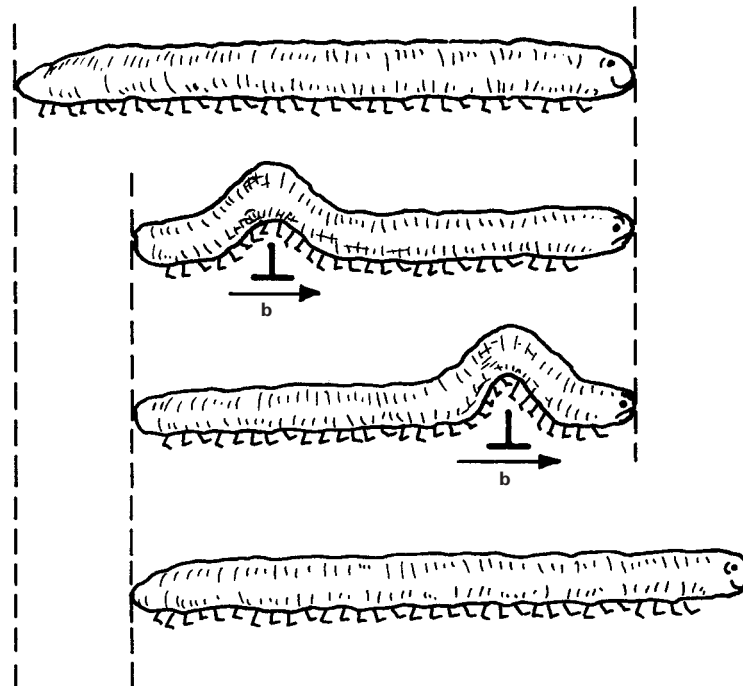
Later, the actual existence of such imperfections was verified by a variety of techniques.

Figures 4.15 and 4.16 present two analogies that help us to visualize dislocations. The displacement of a rug can be accomplished by applying a much lower force if a wave is created in the rug and moved from the back to the front. This displacement,  $b$ , is indicated in Figure 4.15. In a similar manner, caterpillars move by creating a “dislocation” and displacing it from the back to the front. (See Figure 4.16.) Sidewinders use a similar principle: these snakes generate “waves” along their bodies. Having understood this concept, the diligent student can readily comprehend how the movement of a dislocation in a body can produce plastic deformation.

Figure 4.17 shows two distinct types of dislocations encountered in crystalline solids: edge and screw dislocations. The atomic arrangement surrounding these dislocations is distorted from the regular periodicity of the lattice. The edge dislocation (Figure 4.17(a)) may be visualized as an extra half plane of atoms terminating at the dislocation line (perpendicular to the plane of the paper and passing through the symbol “ $\perp$ .”) The screw dislocation can be visualized as a “parking garage:” a car, driving around the dislocation line will go up or down the building. Another analogy is the screw. Figure 4.17(a) shows the atomic arrangement. The distortion of the periodic atomic arrangement is represented by the Burgers vector  $b$ . A circuit is created around the dislocation line, as indicated by ABCDE. AB and CD correspond to  $4a$ , where  $a$  is the interatomic spacing. BC and DE correspond

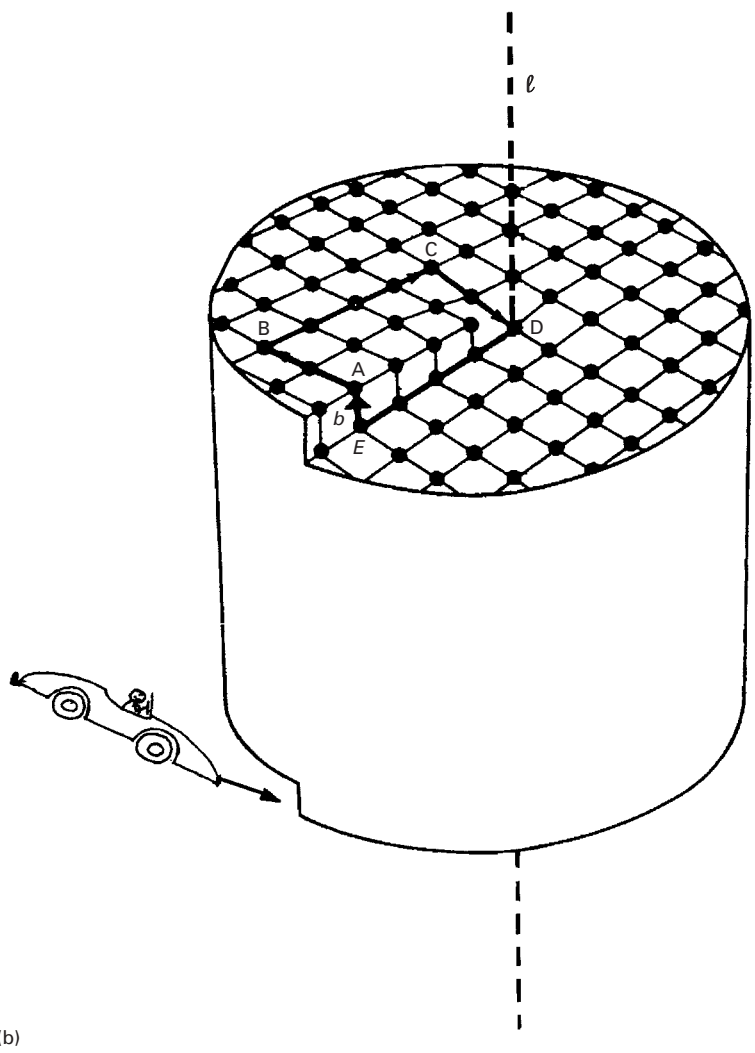
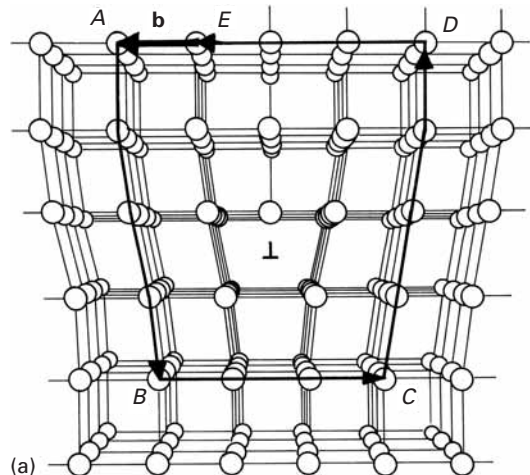


**Fig. 4.15** (a) Rug with a fold.



**Fig. 4.16** Caterpillar with a hump.

**Fig. 4.17** (a) Arrangement of atoms in an edge dislocation and the Burgers vector  $\mathbf{b}$  that produces closure of circuit ABCDE. (b) Arrangement of atoms in screw dislocation with “parking garage” setup. (Notice car entering garage.)



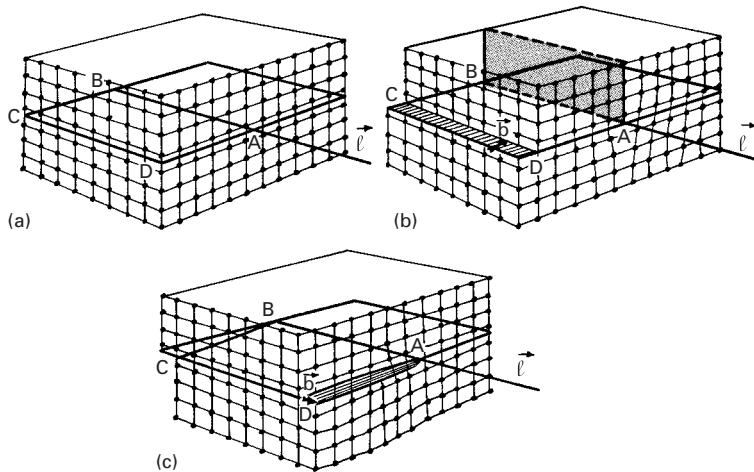


**Fig. 4.18** Geometrical production of dislocations.  
 (a) Perfect crystal. (b) Edge dislocation. (c) Screw dislocation.

to 3a. The failure of the circuit to close represents the vector  $\mathbf{b}$ . A Burgers circuit is also represented around the screw dislocation in Figure 4.17(b). The essential difference between these two types of dislocation is that in the edge dislocation,  $\mathbf{b}$  is perpendicular to dislocation line vector,  $\ell$ , whereas in the screw dislocation,  $\mathbf{b}$  is parallel to  $\ell$ .

Edge dislocations were proposed by Orowan, Polanyi and Taylor, in 1934.<sup>4</sup> Screw dislocations were proposed by Burgers in 1939.<sup>5</sup> Figure 4.18 shows how the shearing of the lattice can generate edge and screw dislocations. Imagine a cut made along ABCD in Figure 4.18(a). If the shearing direction is as marked in Figure 4.18(b), the Burgers vector is perpendicular to line AB or  $\ell$ . The resultant dislocation is of edge character. If the shearing direction, defined by  $\mathbf{b}$ , is parallel to AB, then  $\mathbf{b} \parallel \ell$ , and the resulting dislocation is of screw character. (See Figure 4.18(c).) The movement of an edge dislocation under an applied shear stress  $\tau$  is shown in Figure 4.19. The perfect lattice shown in Figure 4.19(a) is broken and the dislocation is formed as shown in Figure 4.19(b). This edge dislocation ( $\mathbf{b} \perp \ell$ ) moves from left to right, and the final, deformed configuration is shown in Figure 4.19(c). The relationship between the applied shear stress, the direction of movement of dislocation, and the plastic strain generated is quite different for the two types of dislocation. Figure 4.20 shows how a hypothetical crystal subjected to a shear stress  $\tau$  undergoes plastic deformation by means of the propagation of (a) an edge dislocation and (b) a screw dislocation. The direction of motion of the dislocations is always parallel to  $\mathbf{b}$ . The final shear is the same, but the motion of the two dislocations is completely different. There is also a mixed dislocation that possesses both screw and edge character. Figure 4.21 shows such a dislocation, together with the “cut.” It can be seen that the shear direction is neither parallel (screw) nor perpendicular (edge) to the direction of the cut.

<sup>4</sup> E. Orowan, *Z. Phys.*, 89 (1934) 604. M. Polanyi, *Z. Phys.*, 89 (1934) 660. G. I. Taylor, *Proc. Roy. Soc. (London)*, A145 (1934) 362.

<sup>5</sup> J. M. Burgers, *Proc. Kon. Ned. Akad. Wetenschap.*, 42 (1939) 293, 378.

**Fig. 4.19** The plastic deformation of a crystal by the movement of a dislocation along a slip plane.

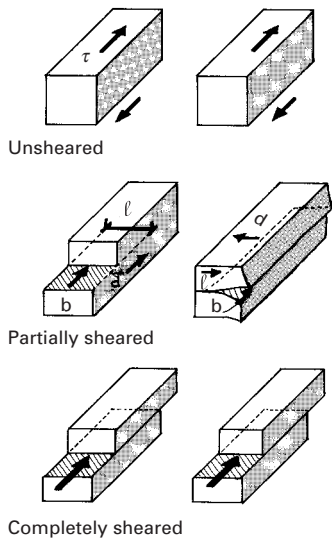
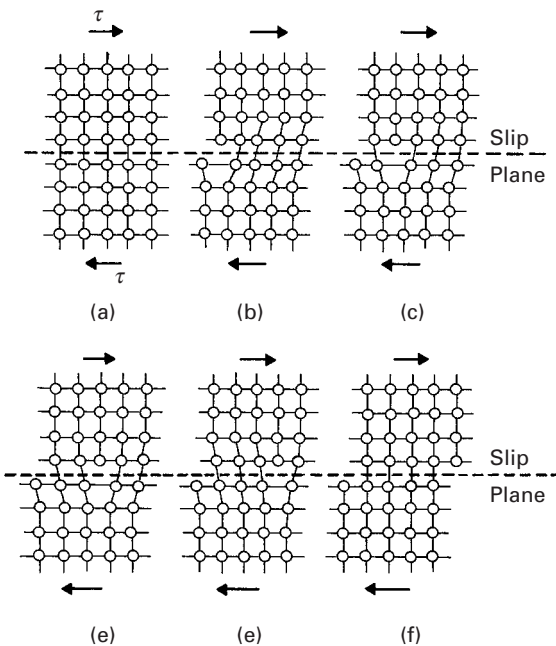


**Fig. 4.20** Plastic deformation (shear) produced by the movement of (a) edge dislocation and (b) screw dislocation. Note  $d$  is the direction of dislocation motion;  $\ell$  is the direction of dislocation line.

Another type of dislocation is called a *helical dislocation*. It forms a large helix and is sometimes observed in crystals that were heat-treated to produce climb. “Climb” is the movement of a dislocation perpendicular to its slip plane. “Glide” is the movement along the slip plane. Climb is described in Chapter 13 (Creep). These dislocations are of mixed character; the reader should not confuse them with screw dislocations.

Dislocations will be studied in detail in this chapter, since they are the building blocks for the understanding of the mechanical response of metals. The treatment, however, still is far from comprehensive. For further details, the reader is referred to the suggested readings at the end of the chapter.

#### 4.4.1 Experimental Observation of Dislocations

It took 20 years to prove, beyond any doubt, the existence of dislocations experimentally, and this period (1935–1955) was surrounded by skepticism and harsh polemics. Nevertheless, the existence of dislocations is nowadays universally recognized, and the “lunatic” theories and models have been proven to be remarkably correct. A number of techniques have allowed the observation of dislocations, including etch pitting, X-ray diffraction (Berg-Barrett topography), and, most importantly, transmission electron microscopy (TEM). The last one is established as the principal method for observing dislocations.

In TEM, the foil has to be thinned to a thickness between 0.1 and 0.3  $\mu\text{m}$ , becoming transparent to electrons when the accelerating voltage is in the 100–300 kV range. Dislocations produce distortions

of the atomic planes. Hence, for certain orientations of the foil with respect to the beam, the region around a dislocation diffracts the beam. The dislocations can then be seen as dark, thin lines under a bright field. TEMs with higher operating voltages (in the megavolt range) are available and allow thicker specimens to be observed. Figure 4.22 shows dislocations in titanium and silicon rendered visible by this technique. The dislocations in titanium (Figure 4.22(a)) appear as sets of parallel segments; the segments are parallel because the dislocations minimize their energy by being along certain crystallographic planes. The same phenomenon is observed in silicon (see Figure 4.22(b)). A hardness indentation (lower right-hand corner) generated a profusion of dislocation loops. These loops are not circular, but consist of segments that are crystallographically aligned because of energy minimization considerations. The dislocation configurations in materials are highly varied and depend on a number of parameters, such as total strain, strain rate, stress state, deformation temperatures, crystallographic structure, etc. Note that the dislocations in silicon (Figure 4.22(b)) appear as white lines, whereas in Figure 4.22(a) they are dark lines. This is because Figure 4.22(b) is a dark-field image, in which the grain diffracts, and the dislocation transmits, the electron beam. The figure is opposite to the normal bright-field transmission images (Figure 4.22(a)).

Dislocations are also present in ceramics, although they are less mobile. They can be produced by plastic deformation at high temperatures, by thermal stresses during cooling, or by applying very high stresses, made possible by, for instance, impacts at several hundred meters per second. Figure 4.23 shows dislocations observed in alumina

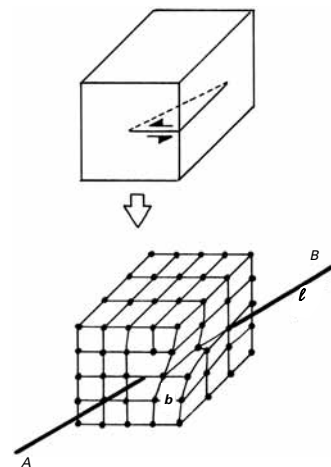
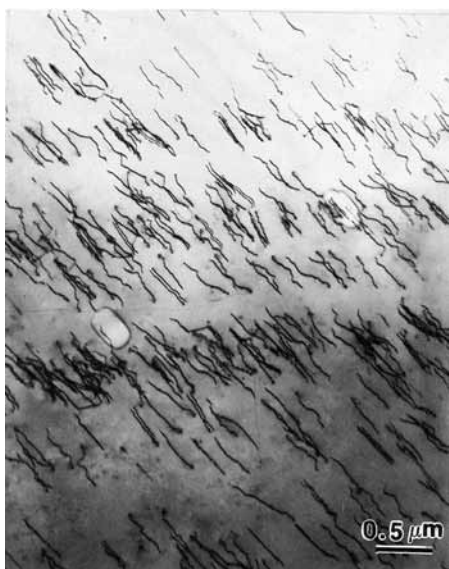
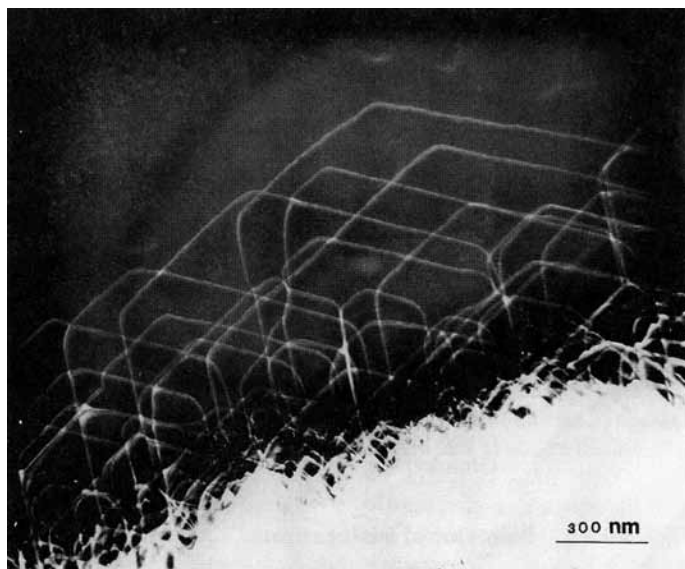


**Fig. 4.21** Mixed dislocation obtained from cut-and-shear operation; notice the angle between  $\mathbf{b}$  and  $\ell$ .



(a)



(b)

**Fig. 4.22** Dislocations in metals. (a) Titanium. (Courtesy of B. K. Kad.) (b) Silicon.

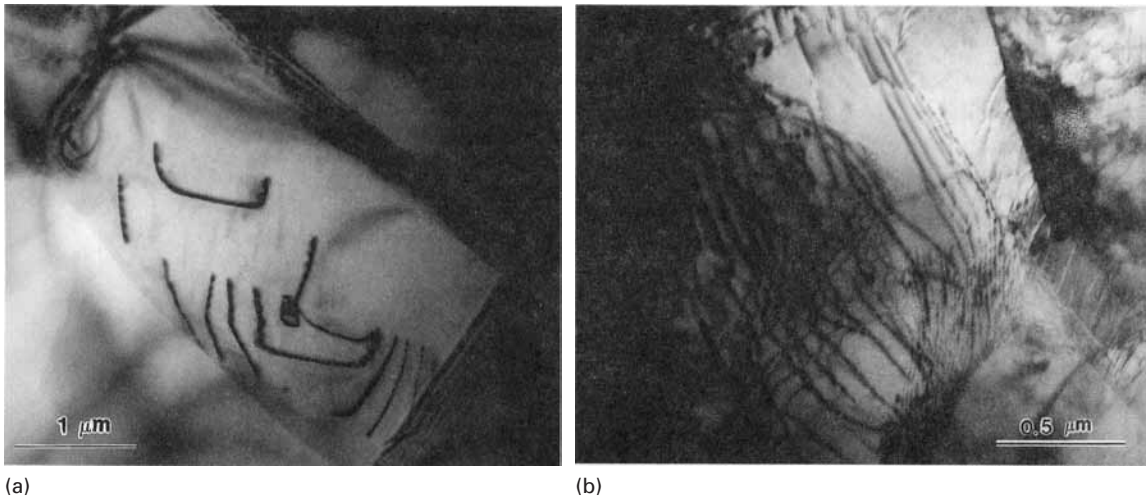


**Fig. 4.23** Dislocations in (a) Al<sub>2</sub>O<sub>3</sub> and (b) TiC. (Courtesy of J. C. LaSalvia.)

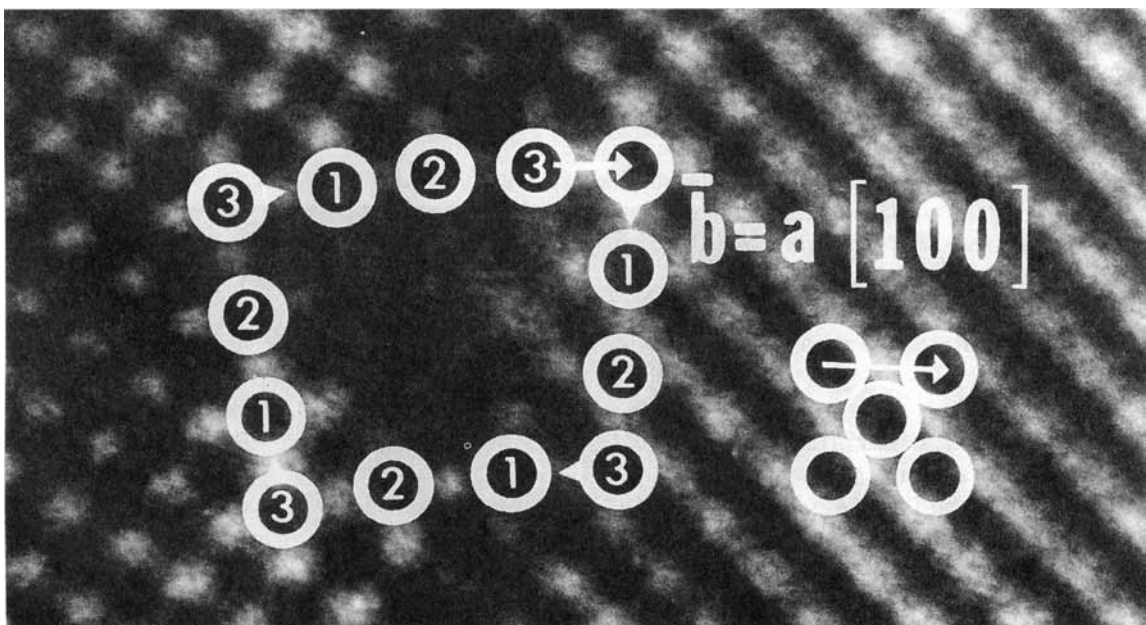


**Fig. 4.24** Atomic resolution transmission electron micrograph of dislocation in molybdenum with a Burgers circuit around it. (Courtesy of R. Gronsky.)

and titanium carbide. The dislocations in the alumina were generated by impact at 600 m/s. The dislocations in the titanium carbide were produced by plastic deformation above the material's ductile-to-brittle transition temperature ( $\sim 2,000^\circ\text{C}$ ). At room temperature, this ceramic would simply undergo brittle fracture.

High-resolution TEM can resolve the individual atoms and identify the lattice distortions around a dislocation. Figure 4.24 shows

molybdenum imaged in such a fashion. The dark spots represent one atom each. Mo has the BCC structure, and the foil plane imaged is (100). The right-hand side of the picture shows a unit cell. A Burgers circuit is drawn around an edge dislocation, which has a line  $\ell$  perpendicular to the plane of the foil. The closure gap represents the Burgers vector of the dislocation. A comparison of the figure with the unit cell establishes the magnitude of the Burgers vector; it is equal to the lattice parameter  $a$ . This is clearly indicated in the figure. The presence of the dislocation can also be felt by noticing the break in the [110] planes, making  $45^\circ$  with the cube axes.

The electron micrographs of Figures 4.22–4.24 illustrate the presence and variety of dislocation configurations observed in crystalline materials.

#### 4.4.2 Behavior of Dislocations

##### *Dislocation Loops*

A dislocation line can form a closed loop, instead of extending until it reaches an interface or the surface of the crystal. This is illustrated in Figure 4.25(a), where a square loop is sketched. Two cuts, along perpendicular sections, were made: AAA and BBB. Figure 4.25(b) and (c) show these sections. It can clearly be seen that the dislocation segments CF and DE (Figure 4.25(b)) are of edge character, while segments CD and FE (Figure 4.25(c)) are of screw character. This is due to the direction of the shear. The loop can be imagined as a cut made in the interior of the crystal (an impossible feat, of course); the edges of the cut form the dislocation line, after shear is applied to the crystal. Dislocations CF and DE are of the same type, with opposite signs; the same applies to CD and FE. The sign convention used for edge dislocations is the following: If the extra semiplane (wedge) is on the top portion, it is positive; if on the bottom, it is negative. Hence, CF is positive and DE is negative. For screw dislocations, a similar convention is used. If the helix turns in accord with a normal screw, it is positive. If not, it is negative. According to this convention, CD is positive and FE is negative.

The actual dislocation loops are not necessarily square. An elliptical shape would be more favorable energetically than a square. For an elliptical or circular shape, the character of the dislocation changes continuously along the line. Figure 4.26(a) shows this situation; the regions that are edge and screw are shown by appropriate symbols. The symbols most commonly used are an inverted T ( $\perp$ ) for a positive edge, and an S for a positive screw dislocation. The negative signs can be described by a correct T and by an inverted S ( $\langle\mathcal{Q}\rangle$ ). In Figure 4.26(a), all the portions of the loop between the short segments of pure screw and edge character are mixed. These loop segments move as shown in the figure. The loop expands and eventually “pops out” of the parallelepiped, creating the shear shown in Figure 4.26(b). Figure 4.26(c) shows a shear loop in copper.

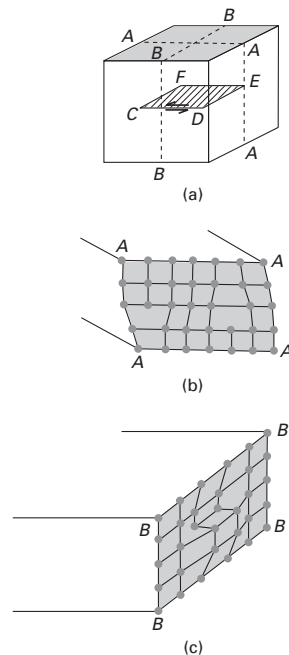


**Fig. 4.25** Square dislocation loop.

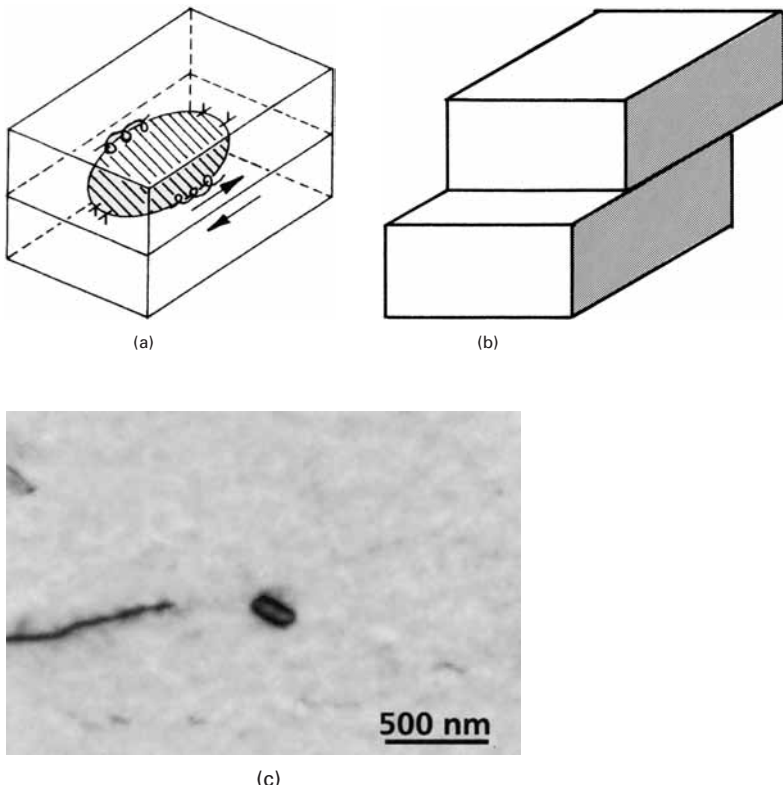


**Fig. 4.26** Elliptic dislocation loop. (a) Intermediate position. (b) Final (sheared) position. (c) TEM of shear loop in copper (Courtesy of F. Gregori and M. S. Schneider.)

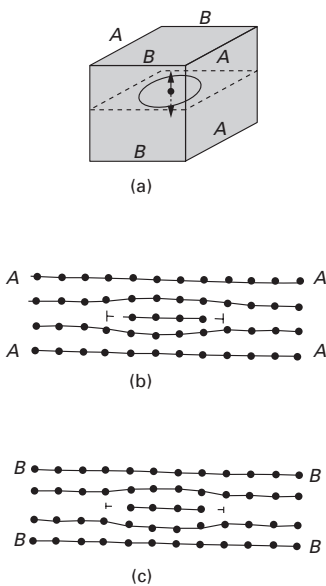


**Fig. 4.27** Prismatic loop produced by the introduction of a disk into metal. (a) Perspective view. (b) Section AAAA. (c) Section BBBB.

### Movement of Dislocations

The plastic deformation of metals is normally accomplished by the movement of dislocations. The elements of dislocation motion are reviewed in this section, together with the resulting deformations. In actual deformation and for elevated strains, complex interactions occur between dislocations. These interactions can be broken down

into simple basic mechanisms that will be described next. Two edge dislocations are shown in Figure 4.28(a). After the passage of one of them, one part of the lattice is displaced in relation to the other part by a distance equal to the Burgers vector. Both a positive and a negative dislocation can generate the same shear; however, they have to move in opposite directions in order to accomplish this. The reader is reminded (see Figure 4.20(a)) that the shear and motion directions are the same for edge dislocation.

Screw dislocations can produce the same lattice shear (Figure 4.28(b)). However, in this case the shear takes place perpendicular to the direction of motion of the dislocations; positive and negative screw dislocations have to move in opposite directions in order to produce the same shear strain.

The plane in which a dislocation moves is called a *slip plane*. The slip plane and the loop plane coincide in Figure 4.29. A loop will eventually be ejected from a crystal upon expanding if there is no barrier to its motion. The expansion of a loop will produce an amount of shear in the crystal equal to the Burgers vector of the dislocation. It is worth noting that the shears of the different dislocations are all compatible; there is no incompatibility of movement.

The prismatic loops, consisting totally of edge dislocations, cannot expand like the normal loops. Thus, because the plane of the dislocation does not coincide with the loop plane, the coupled movement of the edge dislocations will force the loop to move perpendicular to its plane, maintaining the same diameter. Upon being ejected from the crystal, a step will be formed at the surface. Figure 4.30 shows a succession of vacancy loops formed by punching of prismatic dislocations.

#### 4.4.3 Stress Field Around Dislocations

Dislocations are defects; hence, they introduce stresses and strains in the surrounding lattice of a material. The mathematical treatment of these stresses and strains can be substantially simplified if the medium is considered to be isotropic and continuous. Under conditions of isotropy, a dislocation is completely described by the line and Burgers vectors. With this in mind, and considering the simplest possible situation, dislocations are assumed to be straight, infinitely long lines. Figure 4.31 shows hollow cylinders sectioned

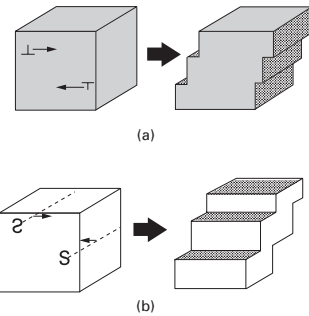


**Fig. 4.28** Slip produced by the movement of dislocation. (a) Positive and negative edge dislocations. (b) Positive and negative screw dislocations.

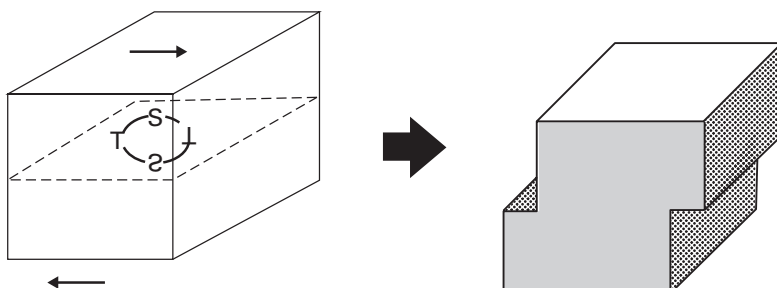


**Fig. 4.29** Expansion of a dislocation loop.

**Fig. 4.30** Nickel heated at 600 °C for 10 min and quenched in liquid nitrogen. Strings of vacancy loops can be clearly seen.  
(Courtesy of L. E. Murr.)

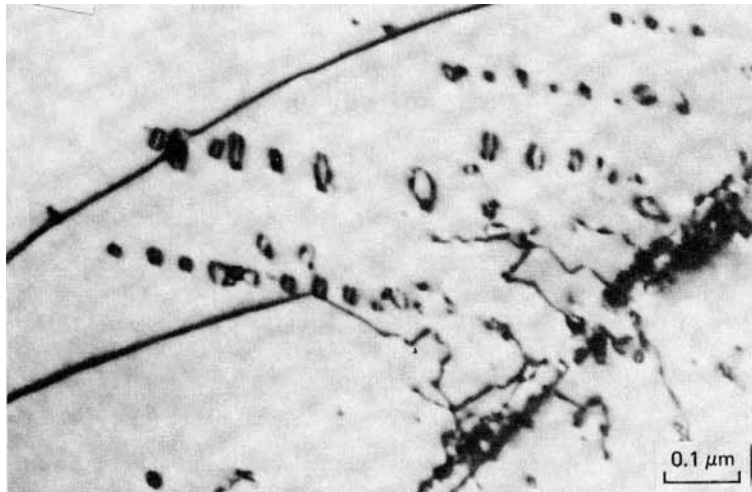
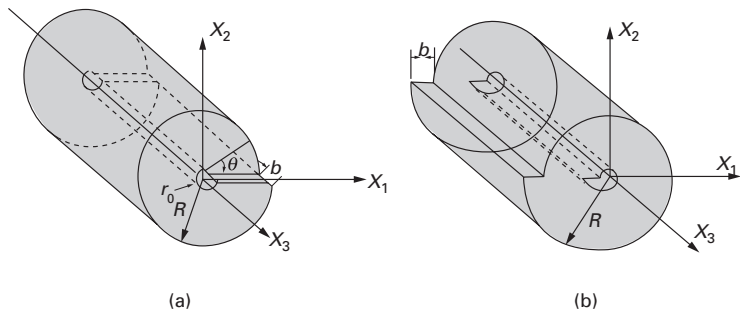


**Fig. 4.31** Simple models for (a) screw and (b) edge dislocations; the deformation fields can be obtained by cutting a slit longitudinally along a thick-walled cylinder and displacing the surface by  $b$  parallel (screw) and perpendicular (edge) to the dislocation line.



along the longitudinal direction. Different deformations are applied in the two cases. The one in Figure 4.31(a) portrays the deformation around a screw dislocation, while Figure 4.31(b) is an idealization of the strains around an edge dislocation. The cylinders, with external radii  $R$ , were longitudinally and transversally displaced by the Burgers vector  $b$ , which is parallel (perpendicular) to the cylinder axis in the representation of a screw (an edge) dislocation. In either case, an internal hole with radius  $r_0$  is made through the center. This is done to simplify the mathematical treatment. In a continuous medium, the stresses on the center would build up and become infinite in the absence of a hole; in real dislocations the crystalline lattice is periodic, and this does not occur. In mechanics terminology, this is called a *singularity*. A “singularity” is a spike, or a single event. For instance, the Kilimanjaro is a singularity in the African plains. Therefore, we “drill out” the central core, which is a way of reconciling the continuous-medium hypothesis with the periodic nature of the structure. To analyze the stresses around a dislocation, we use the formal theory of elasticity. For that, one has to use the relationships between stresses and strains (constitutive relationships), the equilibrium equations, the compatibility equations, and the boundary conditions. Hence, the problem is somewhat elaborate. We present the derivation of these relationships here only for the screw

dislocation; see Kuhlmann-Wilsdorf, and Weertman and Weertman (in the suggested reading) for details.

In Figure 4.31, we have the following displacements, for a screw dislocation, along the axes  $x_1$ ,  $x_2$ , and  $x_3$ :

$$u_1 = 0, \quad u_2 = 0, \quad u_3 \neq 0.$$

The displacement in the direction  $x_3$  can be assumed to be approximately equal to

$$u_3 = f(\theta) = \frac{b}{2\pi}\theta.$$

This is so because the displacement is  $b$  after a rotation of  $2\pi$ . The angle  $\theta$  is given by  $\tan \theta = x_1/x_2$ , thus

$$u_3 = \frac{b}{2\pi} \arctan \frac{x_2}{x_1}. \quad (4.10a)$$

The strain components in indicial notation are:

$$\varepsilon_{ij} = \frac{1}{2} \left( \frac{\partial u_i}{\partial x_j} + \frac{\partial u_j}{\partial x_i} \right) \quad i, j = 1, 2, 3$$

$$\varepsilon_{11} = 0, \quad \varepsilon_{22} = 0,$$

$$\varepsilon_{12} = 0, \quad \varepsilon_{23} = \frac{1}{2} \frac{\partial u_3}{\partial x_2},$$

$$\varepsilon_{13} = \frac{1}{2} \frac{\partial u_3}{\partial x_1}, \quad \varepsilon_{33} = \frac{\partial u_3}{\partial x_3} = 0.$$

Substituting Equation 4.10a into the equations above, we obtain

$$\varepsilon_{13} = \frac{-bx_2}{4\pi(x_1^2 + x_2^2)}, \quad (4.10b)$$

$$\varepsilon_{23} = \frac{bx_1}{4\pi(x_1^2 + x_2^2)}, \quad (4.10c)$$

$$\sigma_{33} = 0.$$

Now, using the generalized Hooke's law, we have

$$\sigma_{13} = 2G\varepsilon_{13},$$

$$\sigma_{23} = 2G\varepsilon_{23}.$$

$$\sigma_{13} = \sigma_{31} = -\frac{Gb x_2}{2\pi(x_1^2 + x_2^2)}, \quad (4.11a)$$

$$\sigma_{23} = \sigma_{32} = \frac{Gb x_1}{2\pi(x_1^2 + x_2^2)}. \quad (4.11b)$$

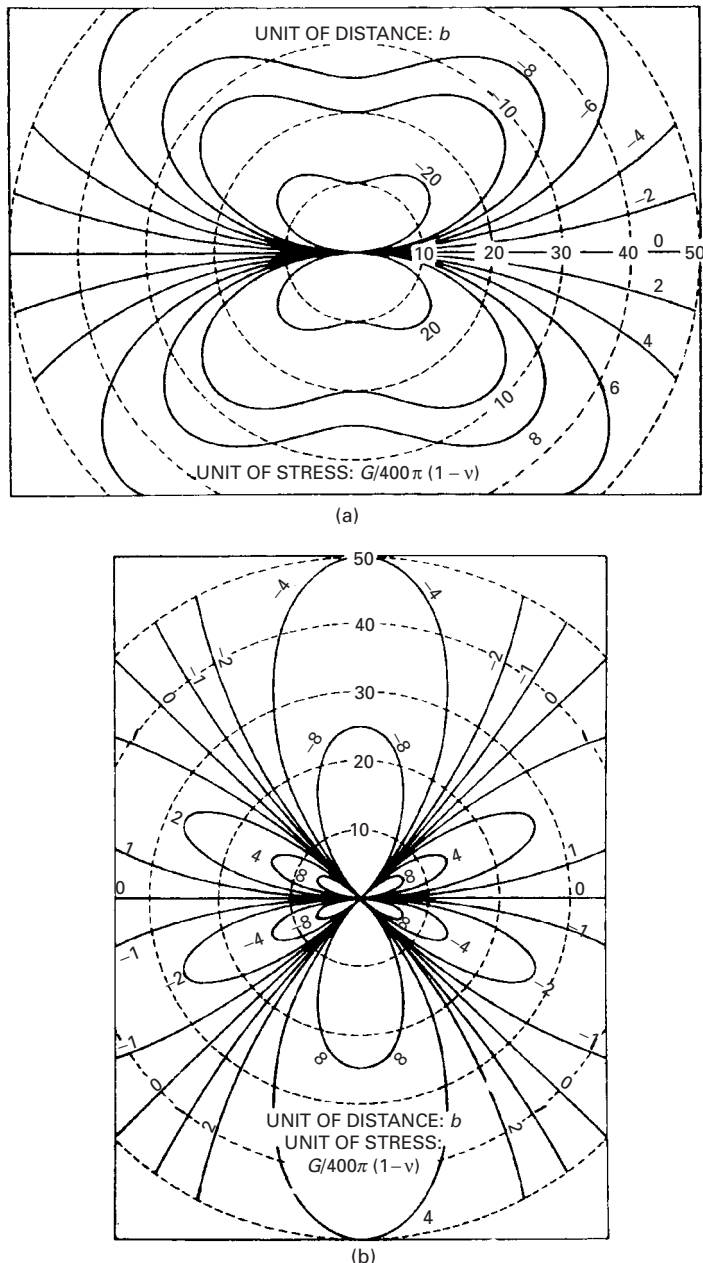
The stresses around an edge dislocation are (given without derivation):

$$\sigma_{11} = -\frac{Gb x_2(3x_1^2 + x_2^2)}{2\pi(1-\nu)(x_1^2 + x_2^2)^2}, \quad (4.12a)$$

$$\sigma_{12} = \frac{Gb x_1(x_1^2 - x_2^2)}{2\pi(1-\nu)(x_1^2 + x_2^2)^2}, \quad (4.12b)$$

$$\sigma_{22} = \frac{Gb x_2(x_1^2 - x_2^2)}{2\pi(1-\nu)(x_1^2 + x_2^2)^2}. \quad (4.12c)$$

**Fig. 4.32** Stress fields around an edge dislocation. (The dislocation line is  $Ox_3$ ): (a)  $\sigma_{11}$ ; (b)  $\sigma_{22}$ ; (c)  $\sigma_{33}$ ; (d)  $\sigma_{12}$ . (Adapted with permission from J. C. M. Li, in *Electron Microscopy and Strength of Crystals*, eds. G. Thomas and J. Washburn (New York: Interscience Publishers, 1963).)



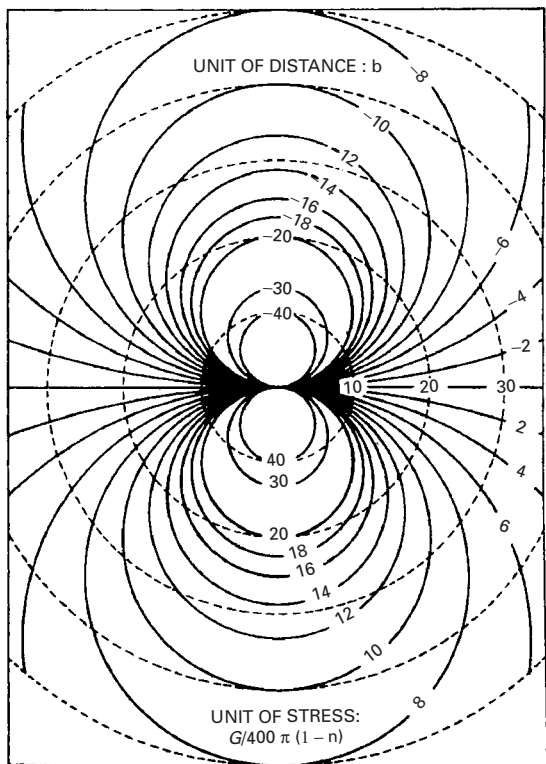
It then follows that

$$\sigma_{33} = \nu(\sigma_{11} + \sigma_{22}) = -\frac{G b v x_2}{\pi(1-\nu)(x_1^2 + x_2^2)}. \quad (4.12d)$$

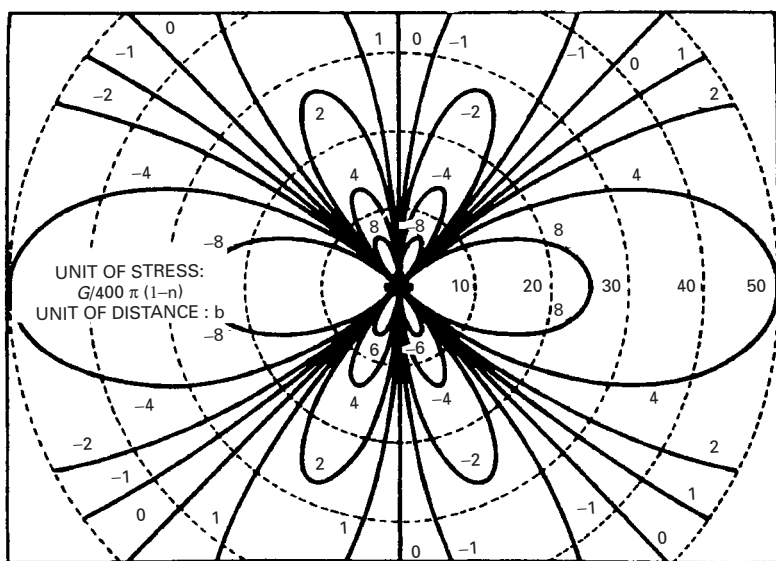
These stresses are shown in Figure 4.32 through isostress lines.

#### 4.4.4 Energy of Dislocations

The elastic deformation energy of a dislocation can be found by integrating the elastic deformation energy over the whole volume of the



(c)



(d)

**Fig. 4.32** (continued)

deformed crystal. The deformation energy is given by

$$U = \frac{1}{2} \sigma_{ij} \epsilon_{ij}. \quad (4.13)$$

For an isotropic material, converting the strains to stresses, we have

$$\begin{aligned} U = \frac{1}{2G} & \left[ \frac{1}{2(1+\nu)} (\sigma_{11}^2 + \sigma_{22}^2 + \sigma_{33}^2) + (\sigma_{12}^2 + \sigma_{13}^2 + \sigma_{23}^2) \right. \\ & \left. - \frac{\nu}{(1+\nu)} (\sigma_{11}\sigma_{33} + \sigma_{11}\sigma_{22} + \sigma_{22}\sigma_{33}) \right]. \end{aligned} \quad (4.13a)$$

Using Equations 4.10a and 4.10b we have, for a screw dislocation,

$$\begin{aligned} U_s &= \frac{1}{2G} \left[ \frac{G^2 b^2 x_2^2}{4\pi^2(x_1^2 + x_2^2)^2} + \frac{G^2 b^2 x_1^2}{4\pi^2(x_1^2 + x_2^2)^2} \right] \\ &= \frac{Gb^2}{8\pi^2(x_1^2 + x_2^2)}. \end{aligned} \quad (4.14)$$

Substituting  $(x_1^2 + x_2^2)$  by  $r^2$  (see Figure 4.31), we find that

$$U_s = \frac{Gb^2}{8\pi^2 r^2}. \quad (4.15)$$

Integrating Equation 4.15 between  $r_0$  and  $R$ , we get

$$U_s = \int_{r_0}^R \frac{Gb^2}{8\pi^2 r^2} 2\pi r dr = \frac{Gb^2}{4\pi} \ln \frac{R}{r_0}. \quad (4.16)$$

In a similar way, the energy of a straight edge dislocation per unit length is equal to

$$U_\perp = \frac{Gb^2}{4\pi(1-\nu)} \ln \frac{R}{r_0}. \quad (4.17)$$

It should be observed that the factor  $(1 - \nu)$  is approximately equal to  $2/3$ . Hence, the energy of an edge dislocation is about  $3/2$  of that of a screw dislocation.

The schematic drawing of Figure 4.31 removes the core of the dislocation so as to avoid the infinite stresses along the dislocation line. Several methods have been used to estimate  $r_0$ . In this book,  $r_0$  will be assumed to be equal to  $5b$ . Note that the energy given by the foregoing equations become infinite for infinite  $R$ ; hence, one has to establish an approximate value for  $R$ . Dislocations in a metal never occur in a completely isolated manner; they form irregular arrays with mean density  $\rho$ . This density is given as the total length of dislocation line per unit volume. The spaghetti analogy can be used here. Imagine a pot with water and spaghetti. The density of the spaghetti would be obtained by measuring the total length of the spaghetti and dividing it by the volume of the pot. The stress fields of the various dislocations interact, as will be seen in subsequent sections; we generally assume a value of  $R$  equal to the average distance between the

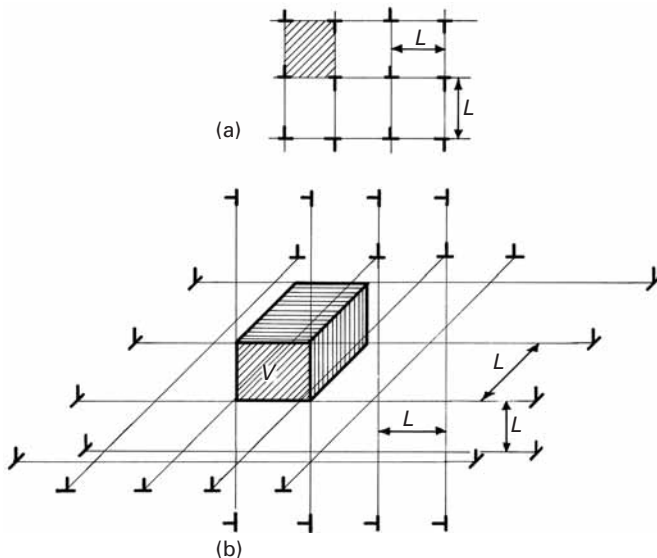


**Fig. 4.33** Schematic representation of an idealized dislocation array (a) in two dimensions and (b) in three dimensions; note that dislocations on three perpendicular atomic planes define a volume  $V$ .

dislocations. It can be shown, by means of a simplified array, that the average distance or mean free path of dislocations is approximately equal to  $\rho^{-1/2}$ .

It is possible to calculate the radius of influence of each dislocation line,  $R$ , from the dislocation density  $\rho$ . This radius of influence is equal to  $L/2$ , in Figure 4.33(a). Figure 4.33(a) shows a two-dimensional array of dislocations; all dislocation lines “poke out” of the plane of the page. The mean spacing is  $L$ , and the hatched area is  $L^2$ . This area is bounded by four dislocations, and each dislocation is shared by four areas. Thus,

$$\begin{aligned} L^2 \text{ area} &\rightarrow 1 \text{ dislocation,} \\ \text{unit area} &\rightarrow \rho \text{ dislocations.} \end{aligned}$$

As a result,

$$\boxed{\rho = L^{-2}.} \quad (4.18)$$

The tridimensional calculation is slightly more complicated. Figure 4.33(b) shows a tridimensional array of dislocations. The hatched volume is  $V = L^3$ . This volume is composed of dislocations that lie along the edges. The total dislocation length can be taken to be  $12L$ . However, each dislocation is shared by four adjacent cubes. Hence,

$$\rho = \frac{12L/4}{L^3} = 3L^{-2}. \quad (4.19)$$

But

$$R = \frac{L}{2},$$

so that

$$\rho = 3(2R)^{-2}$$

and

$$R = \frac{1}{2} \left( \frac{\rho}{3} \right)^{-1/2} = 0.86\rho^{-1/2}.$$

The average dislocation radius is often taken to be

$$R \approx \rho^{-1/2}.$$

We now add the energy of the dislocation core. This energy is taken to be  $Gb^2/10$  for metals. Hence, the total energy of a dislocation is

$$U_r = U_{\text{nucleus}} + U_{\text{periphery}}.$$

Equation 4.17 can then be generalized to:

$$U_r = \frac{Gb^2}{10} + \frac{Gb^2}{4\pi(1-v)}(1-v\cos^2\alpha)\ln\frac{\rho^{-1/2}}{5b}, \quad (4.20)$$

where  $\alpha$  is a parameter that describes the nature of the dislocation (edge  $\alpha = \pi/2$ , screw  $\alpha = 0$ ), which can be mixed.

The energy of dislocations is often taken to be approximately

$$U_r = \frac{Gb^2}{2}. \quad (4.21)$$

For typical metals,  $U_r$  is equal to a few electron volts per atomic plane. The energy of the nucleus is 10% of this total. The energy of a dislocation per atomic plane is high in comparison with that of a vacancy: approximately 3 eV ( $4.8 \times 10^{-19}$  J) versus about 1 eV ( $1.6 \times 10^{-19}$  J).

### Example 4.3

Annealed materials have a dislocation density of approximately  $10^8 \text{ cm}^{-2}$  or  $10^{12} \text{ m}^{-2}$ . Calculate the total strain energy for copper.

**Solution:** For copper, the Burgers vector is  $b = 0.25 \text{ nm}$ . Inserting these values into Equation 4.14 and using  $\alpha = 0$  (for a screw dislocation), we obtain

$$U = 0.1Gb^2 + \frac{Gb^2}{4\pi} \ln \frac{10^{-6}}{5 \times 0.25 \times 10^{-9}} = 0.63Gb^2 = \frac{Gb^2}{1.587} \cong \frac{Gb^2}{2}.$$

For this example, the energy per unit length is equal to  $1.5 \times 10^{-9} \text{ J/m}$  ( $G = 48.3 \text{ GPa}$ ). The total strain energy is  $1.5 \text{ kJ/m}^3$ .

#### 4.4.5 Force Required to Bow a Dislocation

Two additional equations will be derived next: the force required to curve a dislocation to a radius  $R$  and the Peach-Koehler equation. The analogy of a string helps to explain the energy of a dislocation. In the absence of an external stress field, a dislocation will tend to be straight, minimizing its length and overall energy. The same occurs for a string under tension. If the string is pushed by a force, it will exert a force back. Thus, a curved dislocation is said to possess a “line tension,” which can be calculated. The energy of a curved dislocation

with radius  $R$  can be calculated (see Weertman and Weertman, p. 50, in the suggested reading) and is equal to

$$U = \frac{Gb^2}{4\pi} \ln \frac{R}{5b}. \quad (4.22a)$$

It is possible to calculate the force  $F$  required to bend a dislocation into a radius  $R$ . Figure 4.34 shows a curved dislocation with radius  $R$ . The line tension  $T$  is defined as the self-energy per unit length of dislocation. In the figure, the segment of the dislocation  $ds$  is “sectioned off,” and the remaining dislocation is replaced by two tensions  $T$  acting tangentially to the line at the section points. The line tension is always tangential to the dislocation line. The (downward) vertical force exerted by the line tension on the segment  $ds$  is

$$F_1 = 2T \sin(d\theta/2).$$

This is balanced by the force  $F_2$  (per unit length) exerted on the dislocation, multiplied by its length:

$$F_2 ds = 2T \sin(d\theta/2).$$

Since  $d\theta/2$  is a small quantity,

$$F_2 ds = T d\theta.$$

But

$$R d\theta = ds,$$

$$F_2 R d\theta = T d\theta,$$

$$F_2 = T/R$$

Assuming, to a first approximation, that the line tension of a curved dislocation is equal to the energy of a straight dislocation (Eqn. 4.21), we have

$$F = G b^2 / 2R. \quad (4.22b)$$

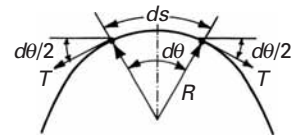


**Fig. 4.34** Curved dislocation.

### Peach-Koehler equation

The Peach-Koehler equation relates the force applied to a dislocation to a stress.  $F$  is the force per unit length of dislocation, and  $\tau$  is the shear stress acting on the slip plane along the slip direction. This relation can be demonstrated by considering a parallelepiped with dimensions  $dx_1, dx_2, dx_3$ . If a dislocation, with length  $dx_1$ , on which a force per unit length is  $F$ , moves through the parallelepiped, the work done is

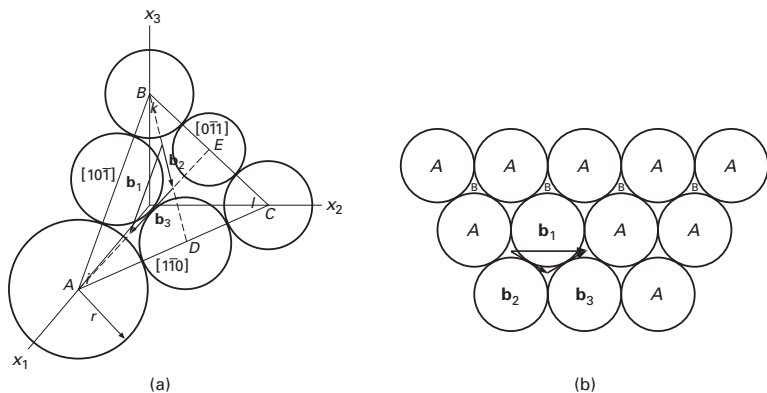
$$W = (F dx_1) dx_2.$$

The change in strain energy of the cube is equal to  $1/2 > \gamma$  in elasticity and  $= \zeta \gamma$  in plasticity.

For volume  $dx_1 dx_2 dx_3$ :

$$U = (\tau \gamma) dx_1 dx_2 dx_3,$$

**Fig. 4.35** Decomposition of dislocation in an FCC crystal.



where  $dx_1 dx_2 dx_3$  is the volume of the parallelepiped. The shear strain produced by one dislocation is

$$\gamma = b/dx_3.$$

Since  $W = U$ ,

$$(F dx_1) dx_2 = (\tau b/dx_3) dx_1 dx_2 dx_3$$

and

$$F = \tau b. \quad (4.22c)$$

By applying the Peach–Koehler equation to Equation 4.2b, we get the stress required to bow a dislocation to radius  $R$ :

$$\tau = G b/2R. \quad (4.22d)$$

#### 4.4.6 Dislocations in Various Structures

##### *Dislocations in Face-Centered Cubic Crystals*

In Section 1.3.2, we saw that, among the 80 or so metals, 55 are FCC. The FCC structure is the closest packed one, together with the HCP structure. Thus, it is natural that dislocations be more carefully studied for the FCC structure.

When we visualize a dislocation, we generally think of a defect that, upon passing, recomposes the original structure of the crystal. Hence, in a simple cubic structure, the Burgers vector would have the direction [100] and magnitude  $a$  (lattice parameter). However, there are cases in which the original structure is not recomposed. This type of dislocation is called *imperfect* or *partial*.

In FCC crystals, the closest packed planes are (111). These planes are usually termed  $A$ ,  $B$ , and  $C$ , depending on their order in the stacking sequence. Figure 4.35 shows an atomic plane  $A$ . The glide movement of the atoms of the plane  $A$  that would recompose the same lattice would be indicated by the Burgers vector  $b_1$ . This vector has the direction  $[10\bar{1}]$ . Its magnitude is (it can be also seen in Figure 4.35 that it is equal to the atomic size, and half the side  $AB$ ):

$$b_1 = \frac{|\overrightarrow{BA}|}{2} = 2r \quad (4.23)$$

Vector  $\mathbf{b}_1$  is expressed with respect to unit vectors  $i$ ,  $j$ , and  $k$  of the coordinate system  $Ox_1x_2x_3$  as

$$\overrightarrow{BA} = a(\mathbf{i} + 0\mathbf{j} - \mathbf{k}) \quad \mathbf{b}_1 = \frac{a}{2}\mathbf{i} + 0\mathbf{j} - \frac{a}{2}\mathbf{k} = \frac{a}{2}(\mathbf{i} - \mathbf{k}). \quad (4.24)$$

It can be seen that the magnitude is

$$|\mathbf{b}_1| = \frac{a}{\sqrt{2}}.$$

This vector is, logically, the same as that of Equation 4.23. The simplified notation used for Burgers vectors is

$$\mathbf{b}_1 = \frac{a}{2}[10\bar{1}] \quad \text{or} \quad \mathbf{b}_1 = \frac{1}{2}[10\bar{1}].$$

Hence, the term in brackets gives the direction of the vector, while the term that precedes it is the same fraction as that used in the definition of the unit vectors  $i$ ,  $j$ , and  $k$  (see Equation 4.24). There is also a graphic method to determine this fraction. First, one draws the vector  $\mathbf{b}$  connecting point  $(0, 0, 0)$  to point  $(1, 0, -1)$ . Then one draws  $\mathbf{b}_1$ , which will be a fraction of  $b$  (in this case, half). The fraction is the term that precedes the bracketed term.

One possibility of decomposition for the dislocation is shown in Figure 4.35, where  $\mathbf{b}_2$  and  $\mathbf{b}_3$  add up to  $\mathbf{b}_1$ .  $\mathbf{b}_2$  is obtained from  $BD$  and  $\mathbf{b}_3$  from  $EA$ .

$$\overrightarrow{BD} = \frac{a}{2}\mathbf{i} + \frac{a}{2}\mathbf{j} - a\mathbf{k}$$

$$\overrightarrow{EA} = a\mathbf{i} - \frac{a}{2}\mathbf{j} - \frac{a}{2}\mathbf{k}.$$

It can be shown that  $\mathbf{b}_2 = BD/3$  and that  $\mathbf{b}_3 = EA/3$ . Both  $\mathbf{b}_2$  and  $\mathbf{b}_3$  define partial dislocations, because they change the stacking sequence  $ABC$ . But, acting together (or sequentially), they would have the same effect as  $\mathbf{b}_1$  and maintain the correct stacking sequence.  $\mathbf{b}_2$  and  $\mathbf{b}_3$  are:

$$\mathbf{b}_2 = \frac{a}{6}(\mathbf{i} + \mathbf{j} - 2\mathbf{k})$$

$$\mathbf{b}_3 = \frac{a}{6}(2\mathbf{i} - \mathbf{j} - \mathbf{k})$$

and

$$\mathbf{b}_1 = \mathbf{b}_2 + \mathbf{b}_3.$$

It is easy to establish whether  $\mathbf{b}_1$ ,  $\mathbf{b}_2$ , and  $\mathbf{b}_3$  belong to  $(111)$ : the scalar product should be zero, because  $[111]$ , which is perpendicular to  $(111)$ , should also be perpendicular to  $\mathbf{b}_1$ ,  $\mathbf{b}_2$ , and  $\mathbf{b}_3$ . The magnitude of  $\mathbf{b}_2$  is given by:

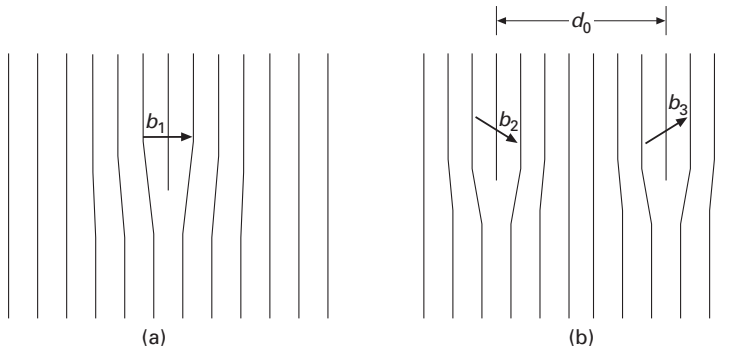
$$|\mathbf{b}_2| = \left[ \frac{a^2}{36}(1 + 1 + 4) \right]^{1/2}$$

$$= \frac{a}{\sqrt{6}}.$$

Hence, we have the following possible reaction:

$$\frac{a}{2}[10\bar{1}] \rightarrow \frac{a}{6}[11\bar{2}] + \frac{a}{6}[2\bar{1}\bar{1}].$$

**Fig. 4.36** Decomposition of a dislocation  $b_1$  into two partial dislocations  $b_2$  and  $b_3$ , separated by a distance  $d_0$ .



From Equation 4.21, the energy is  $Gb^2/2$ . Therefore, we need to check whether

$$\frac{Gb_1^2}{2} \Rightarrow \frac{Gb_2^2}{2} + \frac{Gb_3^2}{2},$$

or  $b_1^2 = b_2^2 + b_3^2$ . Taking the square of the magnitude of the Burgers vectors yields

$$\frac{a^2}{2} > \frac{a^2}{6} + \frac{a^2}{6},$$

and we can see that the total energy decreases with decomposition.

When a perfect dislocation decomposes itself into partials, a region of faulty stacking is created between the partials. This decomposition is shown in Figure 4.36. The dislocations generate a region in which the stacking is ABC AC ABC. Hence, we have four planes in which the stacking is CACA. This is exactly the stacking sequence of the HCP structure. This structure has a higher Gibbs free energy than the equilibrium FCC structure, because it is not thermodynamically stable under the imposed conditions. This specific array of planes is called the *stacking fault*, and the energy associated with it determines the separation between the two partial dislocations: The repulsive force between the two partials is balanced by the attraction trying to minimize the region with the stacking fault. The following equations from [Murr<sup>6</sup> and Kelly and Groves, (see the suggested reading) respectively], allow the calculation of the equilibrium separation between the partial dislocations  $d$ :

$$\gamma_{SF} = \frac{G |b_p|^2}{8\pi d} \left[ \frac{2-v}{1-v} \left( 1 - \frac{2v \cos 2\theta}{2-v} \right) \right],$$

$$\gamma_{SF} = \frac{Gb_1b_2}{2\pi d} \left( \cos \theta_1 \cos \theta_2 + \frac{\sin \theta_1 \sin \theta_2}{2-v} \right),$$

or, in simplified form:

$$\boxed{\gamma_{SF} = \frac{Gb^2}{2\pi d}} \quad (4.25)$$

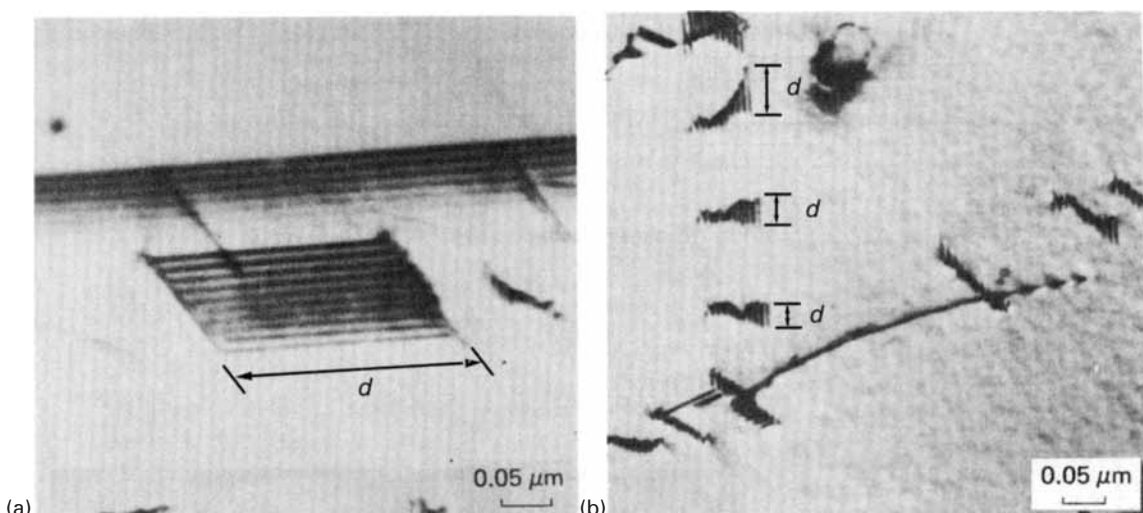
Here,  $\gamma$  is the stacking-fault free energy (SFE) per unit area (free energy of HCP minus free energy of FCC),  $b_p$  is the Burgers vector of

<sup>6</sup> L. E. Murr, *Interfacial Phenomena in Metals and Alloys* (Reading, MA: Addison-Wesley, 1975), p. 142.

**Table 4.2** | Stacking Fault Free Energies and Separation between Shockley Partials for Metals ( $\theta = 30^\circ$ )<sup>a</sup>

Metal	$\gamma$ (mJ/m <sup>2</sup> )	$a_0$ (nm)	$b$ (nm)	$G$ (GPa)	$d$ (nm)
Aluminum	166	0.41	0.286	26.1	1
Copper	78	0.367	0.255	48.3	3.2
Gold	45	0.408	0.288	27.0	
Nickel	128	0.352	0.249	76.0	2.9
Silver	22	0.409	0.289	30.3	9

<sup>a</sup> Adapted from L. E. Murr, *Interfacial Phenomena in Metals and Alloys* (Reading, MA: Addison-Wesley, 1975).



the partial dislocation, and  $\theta$  is the angle of the Burgers vector with the dislocation line. Table 4.2 presents the SFEs for some materials. From the preceding equations, it can be seen that  $d$  is inversely proportional to  $\gamma$ . The effect of alloying elements is generally to decrease the SFE. The addition of aluminum to copper has a drastic effect on the latter's SFE, dropping it from 78 to 6 mJ/m<sup>2</sup>. Aluminum, which has a high SFE (166 mJ/m<sup>2</sup>), does exhibit a very small separation between partials: 1 nm. On the other hand, in certain alloy systems, the distance can go up to 10 nm or more.

The stacking-fault energy is very sensitive to composition. Usually, alloying has the effect of decreasing the SFE. Hence, brasses have an SFE lower than that of copper, and Al alloys have an SFE lower than that of Al.

Figure 4.37 shows some stacking faults in AISI 304 stainless steels viewed by transmission electron microscopy. The region corresponding to the stacking fault can be clearly seen by the characteristic fringe (||||) pattern. The extremities of the fringes are bound by the partial dislocations. In Figure 4.37(a), the stacking fault lies parallel to a coherent twin boundary, which is much longer than the stacking fault. The fault can be distinguished from the coherent twin

**Fig. 4.37** (a) Short segment of stacking fault in AISI 304 stainless steel overlapping with coherent twin boundary. (a) Differences in the nature of these defects are illustrated by fringe contrast differences. (b) Dislocations in AISI 304 stainless steel splitting into partials bounded by short stacking-fault region. Partial spacing marked as  $d$ . (Courtesy of L. E. Murr.)

boundary by the differences in fringe contrast. While all the fringes of the stacking fault are dark, the ones in the twin are dark at the top and become successively lighter. Figure 4.37(b) shows a number of dislocations (probably emitted from the same source) whose segments are trapped on the foil. These segments have decomposed into partials, and one can clearly distinguish the stacking-fault regions by the characteristic fringe contrast.

The effect of the stacking-fault energy on the deformation substructure can be seen in Figure 4.38. This figure shows (a) a copper and (b) Cu-Al alloy after deformation by shock loading under identical conditions (40 GPa peak pressure, 3 ns pulse duration). The Cu-Al alloy has a significantly lower stacking-fault energy ( $\gamma_{SF} = 39 \text{ mJ/m}^2$ ) than does pure copper ( $\gamma_{SF} = 78 \text{ mJ/m}^2$ ), and the resultant deformation substructures seem to be strongly affected by this difference. Low-SFE metals tend to exhibit a deformation substructure characterized by banded, linear arrays of dislocations, whereas high-SFE metals tend to exhibit dislocations arranged in tangles or cells. Cross-slip is more difficult in low-SFE alloys because the dislocations have to constrict in order to change slip planes. (See Chapter 6.) Therefore, the dislocations arrange themselves into parallel bands. The SFE also affects the work-hardening of alloys.

Another type of dislocation in FCC structures is called a *sessile* or *Frank dislocation*, which is immobile. Sessile or Frank dislocations appear under two specific conditions, shown in Figure 4.39. In Figure 4.39(a), a disk was removed in plane (111); in Figure 4.39(b), a disk was added. It can be seen that in both cases the stacking sequence was changed, to ABCBCA and ABCBABC for Figure 4.39(a) and (b), respectively. The Burgers vector is given by:

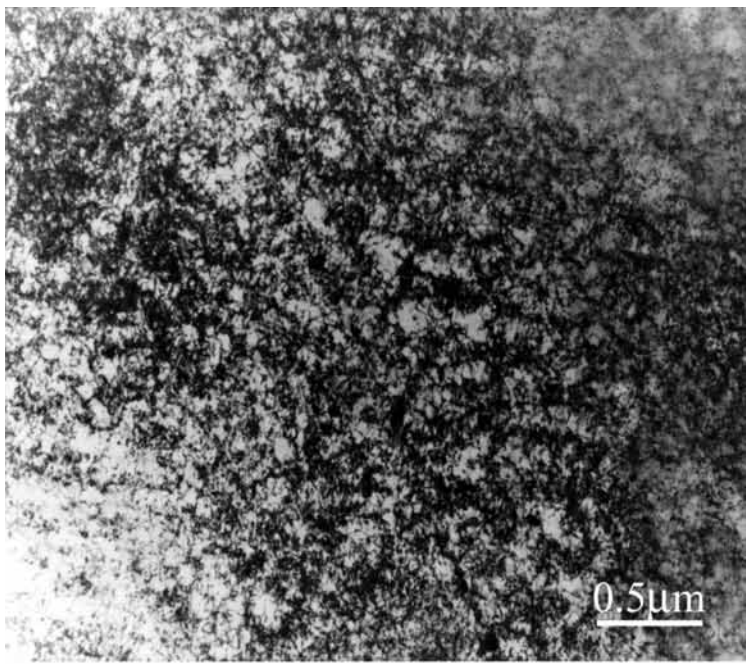
$$\mathbf{b} = \frac{a}{3}[111].$$

We have a sample of an *intrinsic* stacking fault in Figure 4.39(a) and an *extrinsic*, or double-stacking fault in Figure 4.39(b). Since the Burgers vector is not in the slip plane, the two faults are immobile. Another type of immobile dislocation that can occur in FCC metals is the Lomer-Cottrell lock. Let us consider two (111) and (11̄1) planes. The three perfect dislocations on (111) are

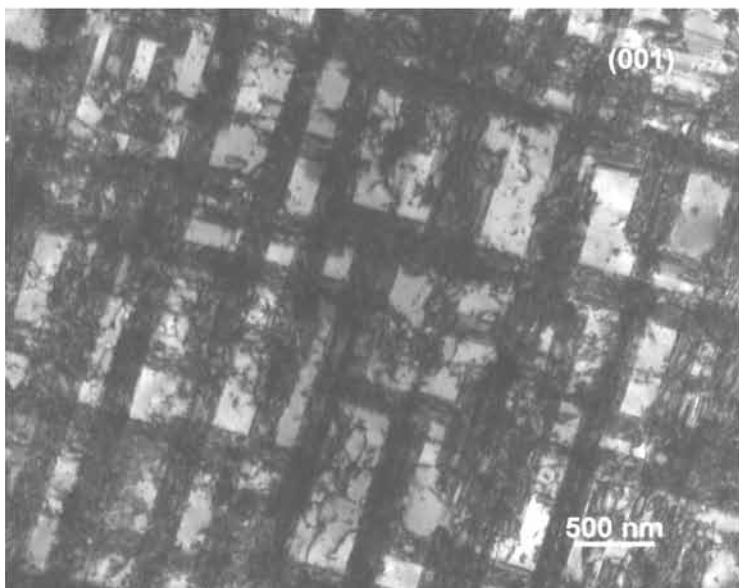
$$\begin{aligned}\mathbf{b}_1 &= \frac{a}{2}[1\bar{1}0], \\ \mathbf{b}_2 &= \frac{a}{2}[\bar{1}01], \\ \mathbf{b}_3 &= \frac{a}{2}[01\bar{1}],\end{aligned}$$

For plane (11̄1), we have

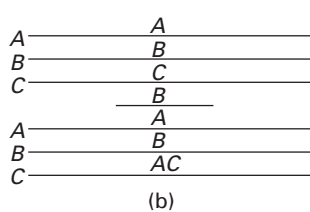
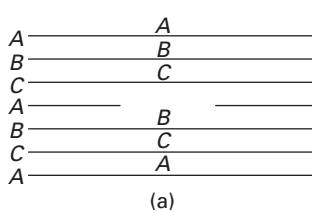
$$\begin{aligned}\mathbf{b}_4 &= \frac{a}{2}[\bar{1}10], \\ \mathbf{b}_5 &= \frac{a}{2}[101], \\ \mathbf{b}_6 &= \frac{a}{2}[011].\end{aligned}$$



(a)

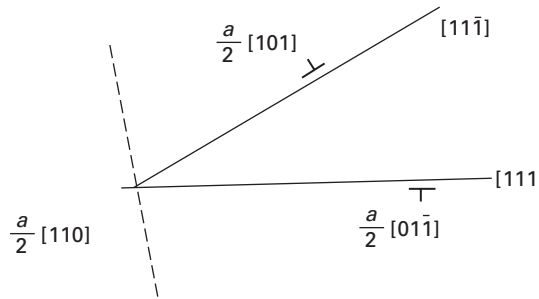
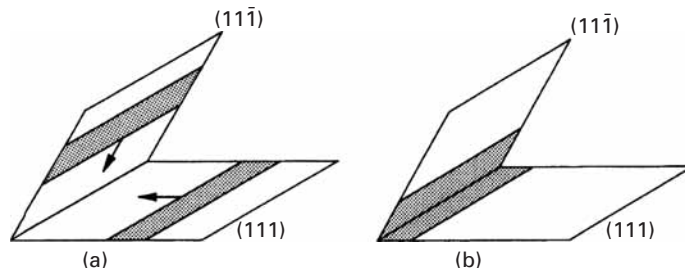


(b)



**Fig. 4.38** Effect of stacking-fault energy on dislocation substructure. (a) High-stacking-fault-energy material (pure copper); (b) lower-stacking-fault-energy material (copper-2 wt% aluminium). Both materials were laser-shock compressed with an initial pressure of 40 GPa and pulse duration of 3 ns. (Courtesy of M. S. Schneider.)

**Fig. 4.39** Frank or Sessile dislocations. (a) Intrinsic. (b) Extrinsic.

**Fig. 4.40** Cottrell-Lomer lock.**Fig. 4.41** Stairway dislocation.

One good rule to determine whether a direction belongs to a plane is that the scalar product between the direction  $\mathbf{b}$  and the normal to the plane must be zero (in a cubic structure). This rule comes from vector calculus. Vectors  $\mathbf{b}_1$  and  $\mathbf{b}_4$  have the same direction and opposite senses; the common direction is also that of the intersection of the two planes. Hence, both dislocations will cancel when they encounter each other. The combination of  $\mathbf{b}_2$  and  $\mathbf{b}_5$  would result in

$$\mathbf{b}_2 + \mathbf{b}_5 = \frac{a}{2}[\bar{1}01] + \frac{a}{2}[101] = \frac{a}{2}[002] = a[001].$$

The energy of these dislocations is

$$\frac{a^2}{2} + \frac{a^2}{2} = a^2$$

Therefore, this reaction will not occur, because it will not result in a reduction of the energy. The only combinations that would result in a decrease in the overall energy would be of the type

$$\begin{aligned}\mathbf{b}_3 + \mathbf{b}_5 &= \frac{a}{2}[01\bar{1}] + \frac{a}{2}[101] \\ &= \frac{a}{2}[110].\end{aligned}$$

This reaction, which is energetically favorable, is shown in Figure 4.40. The dislocation is not mobile in either the (111) or (11̄̄) plane; hence, it acts as a barrier for any additional dislocation moving in these planes. Since it impedes slip, it is called a Lomer-Cottrell "lock."

The resultant configuration is shown in Figure 4.41; it resembles a "stair-rod" or "stairway" dislocation. The

leading partials react and immobilize the partials coupled to them (the trailing partials). The bands of stacking faults form a configuration resembling steps on a stairway. These steps are barriers to further slip on the atomic planes involved, as well as in the adjacent planes.

### Dislocations in Hexagonal Close-Packed Crystals

In HCP crystals, the stacking sequence of the most densely packed planes is *ABAB*. These planes are known as basal planes. Figure 4.42 shows the main planes in the HCP structure. Perfect dislocations moving in the basal plane can decompose into Shockley partials, just as in the FCC structure. Stacking faults are also formed (only *intrinsic* stacking faults). This analogy can be easily understood if one realizes the similarity between the two structures. The (111) planes in the FCC structure are the equivalent of the basal planes in the HCP structures. A perfect dislocation in the basal plane has the Burgers vector

$$b = \frac{a}{3}[2\bar{1}\bar{1}0].$$

In an ideal hexagonal crystal, the  $c/a$  ratio is 1.633. However, in real hexagonal crystals this never happens. It has been experimentally observed that, for crystals with  $c/a > 1.633$ , slip occurs mainly on the basal plane, while the pyramidal and prism planes are “preferred” in crystals with  $c/a < 1.633$ . This is due to the dependence of the distance between the atoms upon  $c/a$ ; it is well known that the dislocations tend to move in the highest packed planes. A detailed treatment of dislocations in HCP metals is given by Teutonico.<sup>7</sup>

### Dislocations in Body-Centered Cubic Crystals

In BCC crystals, the atoms are closest to each other along the  $\langle 111 \rangle$  direction. Any plane in the BCC crystal that contains this direction is a suitable slip plane. Slip has been experimentally observed in (110), (112), and (123) planes. The slip markings in BCC metals are usually wavy and ill-defined. The following reaction has been suggested for a perfect dislocation having its Burgers vector along  $\langle 111 \rangle$ :

$$\frac{a}{2}[\bar{1}\bar{1}1] \rightarrow \frac{a}{8}[\bar{1}\bar{1}0] + \frac{a}{4}[\bar{1}\bar{1}2] + \frac{a}{8}[\bar{1}\bar{1}0].$$

This corresponds to the equivalent of Shockley partials. Apparently, the stacking-fault energy is very high, because the faults cannot be observed by transmission electron microscopy. The waviness of the slip markings is also indicative of the high stacking-fault energy. If the partials were well separated, slip would be limited to one plane. Cross-slip, which will be treated in Chapter 6, is much easier when the stacking-fault energy is high. If one adds up all the slip systems for BCC, one obtains a number of 48. This is much higher than the number for FCC.

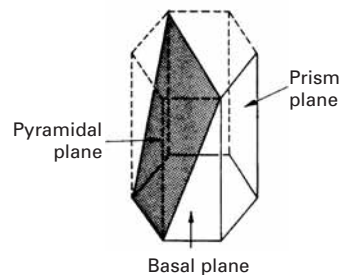
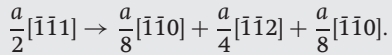


**Fig. 4.42** Basal, pyramidal, and prism plane in HCP structure.

<sup>7</sup> L. J. Teutonico, *Mater. Sci & Eng.*, 6 (1970) 27.

### Example 4.4 |

Consider the following body-centered cubic dislocation reaction:



- a. Prove that this reaction will occur.
- b. What kind of dislocations are the  $(a/8)\langle 110 \rangle$  and  $(a/4)\langle 112 \rangle$ ?
- c. What kind of crystal imperfection results from this dislocation reaction?
- d. What determines the distance of separation of the  $(a/8)[\bar{1}\bar{1}0]$  and the  $(a/4)[\bar{1}\bar{1}2]$  dislocations?

*Solution:* (a)  $U \propto b^2$ :

$$\frac{a}{2}[\bar{1}\bar{1}1] \rightarrow \frac{a}{8}[\bar{1}\bar{1}0] + \frac{a}{4}[\bar{1}\bar{1}2] + \frac{a}{8}[\bar{1}\bar{1}0].$$

On the left-hand side:

$$b^2 = \left(\frac{-a}{2}\right)^2 + \left(\frac{-a}{2}\right)^2 + \left(\frac{a}{2}\right)^2 = \frac{3}{4}a^2.$$

On the right-hand side:

$$\begin{aligned} b_1^2 + b_2^2 + b_3^2 &= \left[\left(\frac{-a}{8}\right)^2 + \left(\frac{-a}{8}\right)^2 + 0^2\right] + \left[\left(\frac{-a}{4}\right)^2 + \left(\frac{-a}{4}\right)^2 + \left(\frac{2a}{4}\right)^2\right] \\ &\quad + \left[\left(\frac{-a}{8}\right)^2 + \left(\frac{-a}{8}\right)^2 + 0^2\right] \\ &= \frac{a^2}{32} + \frac{3a^2}{8} + \frac{a^2}{32} = \frac{7a^2}{16}. \end{aligned}$$

Since

$$\frac{3}{4}a^2 > \frac{7a^2}{16},$$

the energy is lower after the reaction, and therefore, the reaction will occur.

- (b) Partial dislocations.
- (c) Stacking fault.
- (d) Stacking-fault energy,  $\gamma_{SF}$ .

$$\gamma_{SF} \propto \frac{b_1 b_2}{d},$$

with  $b_1$ ,  $b_2$  known from (a),

$$\begin{aligned} \Rightarrow \gamma_{SF} &\propto \frac{1}{d} \\ \Rightarrow d &\propto \frac{1}{\gamma_{SF}}. \end{aligned}$$

That is, if  $\gamma_{SF}$  increases, the distance between the dislocations decreases.

### Example 4.5

Make a table with all the 48 slip systems for the BCC structure.

**Solution:** For each slip system, we have to satisfy the condition  $\mathbf{u} \cdot \mathbf{v} = 0$ . For  $(110)[\bar{1}\bar{1}1]$ ,  $1 \times 1 + 1 \times (-1) + 0 \times 1 = 0$ .

The table of 48 slip systems for the BCC structure is as follows.

Slip Plane $\{1\bar{1}0\}$	Slip Plane $\{\bar{1}12\}$	Slip Plane $\{\bar{1}23\}$
$(110)$	$[\bar{1}\bar{1}1]$	$(123)$
$(110)$	$[\bar{1}\bar{1}\bar{1}]$	$(132)$
$(\bar{1}\bar{1}0)$	$[\bar{1}\bar{1}1]$	$(312)$
$(110)$	$[\bar{1}\bar{1}1]$	$(321)$
$(10\bar{1})$	$[\bar{1}\bar{1}1]$	$(213)$
$(10\bar{1})$	$[\bar{1}\bar{1}1]$	$(231)$
$(101)$	$[\bar{1}\bar{1}1]$	$(123)$
$(101)$	$[\bar{1}\bar{1}\bar{1}]$	$(\bar{1}23)$
$(101)$	$[\bar{1}\bar{1}\bar{1}]$	$(\bar{1}32)$
$(011)$	$[\bar{1}\bar{1}1]$	$(312)$
$(011)$	$[\bar{1}\bar{1}1]$	$(321)$
$(011)$	$[\bar{1}\bar{1}1]$	$(213)$
$(0\bar{1}1)$	$[\bar{1}\bar{1}1]$	$(231)$

#### 4.4.7 Dislocations in Ceramics

Transmission electron microscopy has revealed dislocations in most nonmetals. Dislocations in semiconductors, minerals, oxide ceramics, and carbides, nitrides, and borides have been described and characterized. Many nonmetals tend to exhibit brittle behavior, in which dislocations play a minor role. However, if the temperature or lateral confinement of the material is sufficiently high, ductile behavior can be observed; in this case, dislocations play an important role. The role of confinement, or externally applied traction on planes parallel to the principal direction of external loading, is described in Chapter 7. The principal effect is to eliminate tensile stresses at the tips of internal flaws, thereby enabling the nonmetal to deform plastically. The temperature provides thermal activation that assists the overcoming of short-range obstacles by dislocations.

Table 4.3 lists the minimum temperatures at which ductile behavior is observed in ceramics. Most ceramics have high ductile-to-brittle transition temperature, and this has rendered the study of dislocations difficult. These high temperatures also affect the mechanisms of dislocation motion, since diffusion plays an important role at temperatures greater than or equal to  $0.4T_m$  where  $T_m$  is the melting point in K. The climb of dislocations is an effective mechanism for overcoming obstacles.

**Table 4.3** Approximate Temperature for Macroscopic Plasticity in Some Ceramics

Ceramic	Melting point, $T_m$ (K)	Softening point, $0.4T_m$ (K)
B <sub>4</sub> C	2,725	1,090
TiC	3,400	1,360
HfC	4,425	1,770
WC	3,000	1,200
SiC	2,970	1,188
MgO	3,100	1,240
ZrO <sub>2</sub>	3,100	1,240
Al <sub>2</sub> O <sub>3</sub>	2,325	930
TiO <sub>2</sub>	2,100	844
SiO <sub>2</sub> (cristobalite)	1,990	796
S <sub>3</sub> N <sub>4</sub>	2,715	1,086
MoSi <sub>2</sub>	2,300	920

**Table 4.4** Crystal Structures, Slip Systems, and Burgers Vectors for Ceramics (Courtesy of T. E. Mitchell)

Oxide	Slip system	Burgers vector	Other slip systems
MgO	{110} {1̄10}	$\frac{1}{2} \langle 1\bar{1}0 \rangle = d_0$	{001} {1̄10}, {111} {1̄10}
MgAl <sub>2</sub> O <sub>4</sub>	{111} {1̄10}	$\frac{1}{2} \langle 1\bar{1}0 \rangle = 2d_0$	{110} {1̄10}
Al <sub>2</sub> O <sub>3</sub>	(0001) {11̄20}	$\frac{1}{3} \langle 11\bar{2}0 \rangle = \sqrt{3}d_0$	{1120} {10̄10}, {1̄102} {11̄20}
TiO <sub>2</sub>	{001} {0̄11}	$\langle 0\bar{1}1 \rangle \simeq 2d_0$	{110} [001]
Mg <sub>2</sub> SiO <sub>4</sub>	(100), {110} [001]	[011] = 2d <sub>0</sub>	(100) [010], {0k/l} [100]
BeO	(0001) {11̄20}	$\frac{1}{3} \langle 11\bar{2}0 \rangle = d_0$	{1100} {11̄20}, [0001] {10̄10}
UO <sub>2</sub>	{001} {1̄10}	$\frac{1}{2} \langle 1\bar{1}0 \rangle = \sqrt{2}d_0$	{110}, {111} {1̄10}
SiO <sub>2</sub> (quartz)	(0001) {11̄20}	$\frac{1}{3} \langle 11\bar{2}0 \rangle$	{1120}, {1010} [0001]

The structures of a number of ceramics are given in Chapter 1. (See Figure 1.17.) In general, ceramics tend to slip along directions that are closest packed. Since ceramics possess ordered structures, and a perfect dislocation must recompose the original atomic arrangement, the Burgers vectors tend to be large.

Table 4.4 lists slip systems and Burgers vectors for a number of ceramics. For the oxide ceramics, the oxygen atoms (anions) tend to arrange themselves in close-packed structures (FCC or HCP), and this determines the slip systems. For instance, Al<sub>2</sub>O<sub>3</sub> (HCP) has basal slip, where the slip lane is (0001) and the slip directions are <11̄20>. Prismatic or pyramidal slip are also possible. (See Table 4.4.) The Burgers vector is given by

$$b = \frac{1}{3} \langle 11\bar{2}0 \rangle = \sqrt{3}d_0,$$

where  $d_0$  is the nearest distance between oxygen atoms. Recall that the oxygen atoms form an HCP structure. The arrangement of atoms in the basal plane is shown in Figure 4.43. The large circles are the

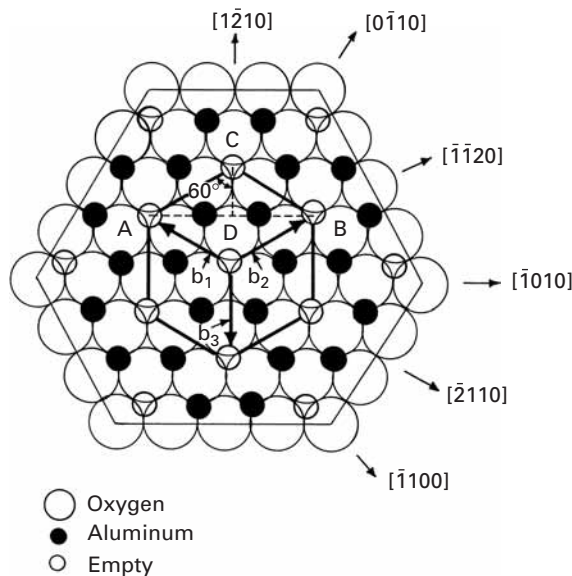


**Fig. 4.43** Basal plane in  $\text{Al}_2\text{O}_3$ .

oxygen anions, forming a closed-packed hexagonal array. The full circles are the aluminum cations, which stack in the *ABC* sequence (similar to the FCC structure). The empty circles are normally empty octahedral interstices. The vectors  $\mathbf{b}_1$ ,  $\mathbf{b}_2$ , and  $\mathbf{b}_3$  are the Burgers vectors. They translate interstitial sites in such a manner that they become superposed. The magnitude of the Burgers vectors is equal to  $\sqrt{3}$ . This can be shown from the triangle  $ABC$ , where  $BC = \sqrt{3}d_0$  and the angle  $BCA$  is equal to  $120^\circ$ .

For  $\text{MgO}$ , the anions form an FCC structure, and the Burgers vector has the direction  $<1\bar{1}0>$  and a magnitude equal to  $d_0$ , the smallest oxygen spacing. Thus,

$$b = \frac{1}{2} <1\bar{1}0> = d_0.$$

The dislocations in ceramics generally have a high energy, due to the large shear modulus and Burgers vector ( $U \sim Gb^2/2$ ). Table 4.5 gives Burgers vectors and self-energies for dislocations in a number of intermetallics and ceramics. For purposes of comparison, the dislocation energy of aluminum is shown. The differences can be dramatic. The Peierls–Nabarro stress (see Section 4.4.12) is very high, in general, because of the directionality of bonding in ionic and covalent structures. For instance, the bond angles of  $109^\circ$  for the carbon atom need very high forces to be distorted. The movement of a dislocation requires the breaking and remaking of bonds, and distortions are produced around the dislocations. Therefore, the movement of dislocations in ceramics is, in general, difficult. There are exceptions, however, such as  $\text{MgO}$ , which can exhibit significant plasticity at close to ambient temperature.

Dislocation interactions and reactions occur in a manner similar to that in metals and intermetallics. An example is given in Figure 4.44. Dislocation dipoles are often observed in the deformation

Table 4.5 | Elastic Energy for Dislocations in Ceramics and Intermetallics (Courtesy of Veyssiére)

	Oxygen Sublattice	<b>b</b>	b(nm)	G(GPa)	$Gb^2/2$
Al		$\frac{1}{2} <110>$	0.286	27	1.2
$\text{Ni}_3\text{Al}$		$<110>$	0.356	100	6.4
MgO	FCC	$\frac{1}{2} <110>$	0.298	125	5.1
CoO	FCC	$\frac{1}{2} <110>$	0.301	70	3.2
NiO	FCC	$\frac{1}{2} <110>$	0.296	135	5.9
$\text{MgAl}_2\text{O}_4$	FCC	$\frac{1}{2} <110>$	0.57	120	19.5
BeO	HCP	$\frac{1}{3} <11\bar{2}0>$	0.27	160	5.9
$\text{Al}_2\text{O}_3 - \alpha$	HCP	$\frac{1}{3} <11\bar{2}0>$	0.476	200	22.6
$\text{TiO}_2$	distorted	$<001>$	0.296	100	4.4
	HCP	$<101>$	0.546		14.9
$\text{CuO}_2$	BCC	$<001>$	0.427	10	0.9
		$<011>$	0.604		1.8
$\text{UO}_2$	cubic	$\frac{1}{2} <110>$	0.386	94	7.0
$\text{Y}_2\text{O}_3$	vacancy — containing cubic	$\frac{1}{2} <111>$	0.918	65	27.4
$\text{Y}_3\text{Fe}_5\text{O}_{12}$	highly distorted	$<100>$	1.06		31.5
		$\frac{1}{2} <111>$	1.072	78	44.8
		$<100>$	1.038		42.0

of sapphire and are shown in Figure 4.44(a). These dipoles are parallel edge dislocations of opposite sign that are attracted together into a position of approximately  $45^\circ$  ( $55^\circ$  if there is anisotropy) in order to minimize the elastic fields. This is shown in Figure 4.44(b). In Figure 4.32(d), the elastic (shear stress) fields of edge distortions are shown. The shear stresses  $\sigma_{12}$  are minimized if they place themselves at  $45^\circ$ . These dipoles break down and form loops, as indicated in Figure 4.44(a). The stress fields of one dislocation are canceled by those of the other dislocation, at  $45^\circ$ , as shown in Figure 4.44(b). Dislocation dissociations and reactions are also observed and can be predicted from energetics. A hexagonal dislocation network is shown in Figure 4.45. The total Burgers vector at the nodes has to be equal to zero under equilibrium. This is called *Frank's rule*. For basal dislocations in a hexagonal structure, we have, at the nodes,

$$\frac{1}{3}[11\bar{2}0] + \frac{1}{3}[1\bar{2}10] + \frac{1}{3}[\bar{2}110] = 0.$$

And for the FCC structure,

$$\frac{1}{2}[1\bar{1}0] + \frac{1}{2}[01\bar{1}] + \frac{1}{2}[\bar{1}01] = 0.$$

These structures are often produced during recovery.

The dissociation of a perfect dislocation into partial dislocations is treated in a manner similar to that in metals. The criterion of energy

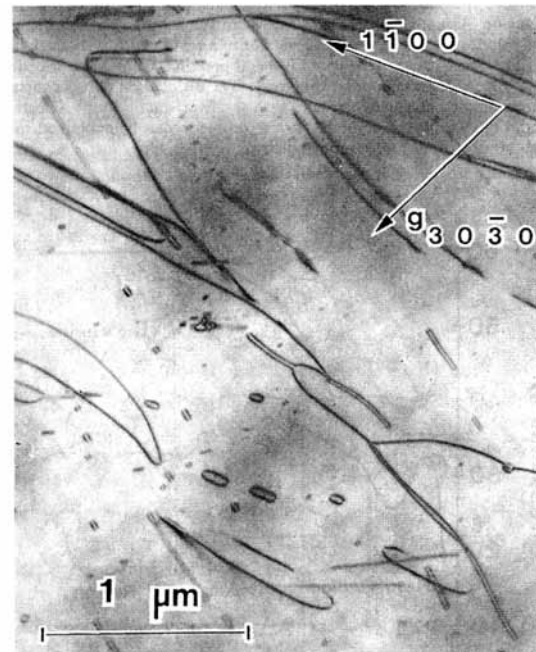
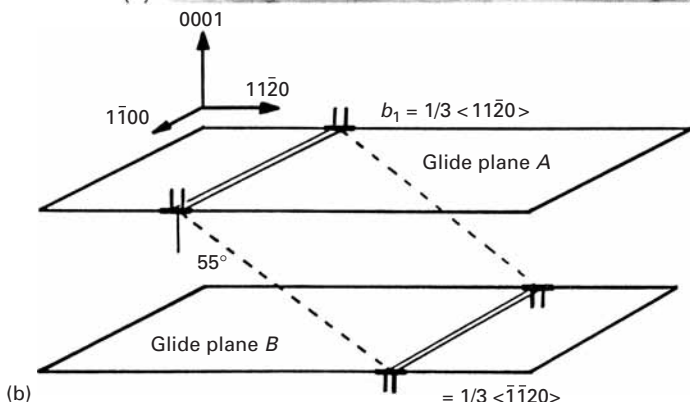


**Fig. 4.44** (a) Dislocations, dipoles, and loops in sapphire. (b) Interaction between dislocations in sapphire. (From K. P. D. Lagerdorf, B. J. Pletka, T. E. Mitchell, and A. H. Heuer, *Radiation Effects*, 74 (1983) 87.)



decrease ( $U \approx Gb^2/2$ ) is applied, and dissociation is stable if  $b^2 > b_1^2 + b_2^2$ .

A few dislocation dissociations have been observed in ceramics. In the spinel structure, the dissociation

$$\frac{1}{2}[1\bar{1}0] \rightarrow \frac{1}{4}[1\bar{1}0] + \frac{1}{4}[1\bar{1}0]$$

was observed, and the following dissociation was suggested to occur in  $\text{Al}_2\text{O}_3$ :

$$\frac{1}{3}[1\bar{1}20] \rightarrow \frac{1}{3}[10\bar{1}0] + \frac{1}{3}[01\bar{1}0].$$

This dissociation has been observed to occur only by climb.

As an illustration of the occurrence of stacking faults in ceramics, Figure 4.46 shows a TEM of gallium phosphide. The large concentration of these faults is evident. They are a common occurrence in thin

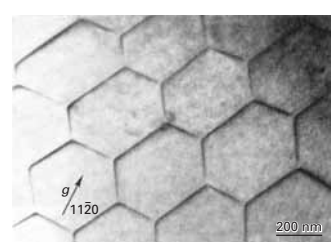
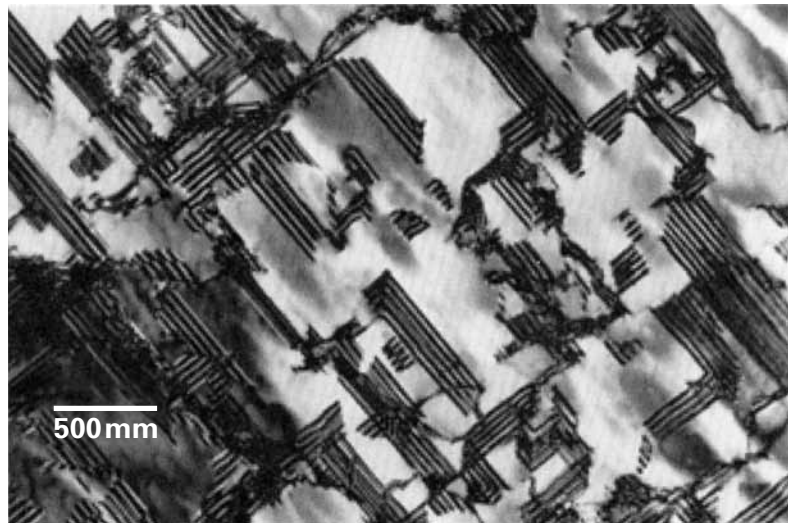


**Fig. 4.45** Hexagonal array of dislocations in titanium diboride. (Courtesy of D. A. Hoke and G. T. Gray)

**Fig. 4.46** Stacking faults in GaP.  
(Courtesy of P. Pirouz.)



films deposited on Si substrates by molecular beam epitaxy (MBE), chemical vapor deposition (CVD), or metal-organic CVD (MOCVD). Section 4.4.14 describes the stresses generated in epitaxial growth on a substrate. These mismatch stresses, as well as thermal stresses and growth faults, are responsible for the high concentration of stacking faults, which decreases with distance from the interface. Profuse stacking faults bounded by Shockley partial dislocations and stair-rod dislocations have been observed to occur in SiC grown on Si wafers. The configuration of stacking faults observed in SiC is analogous to that for GaP shown in Figure 4.46.

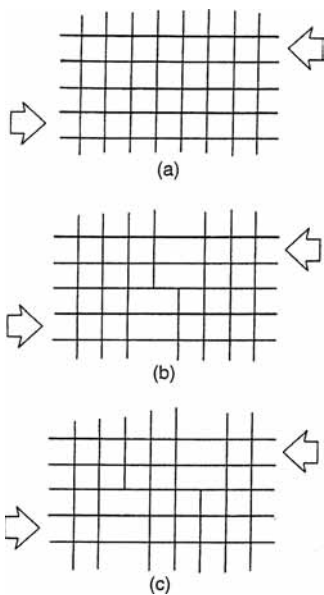


**Fig. 4.47** Homogeneous nucleation of dislocation in conventional deformation.

#### 4.4.8 Sources of Dislocations

It is experimentally observed that the dislocation density increases with plastic deformation; specifically, the relationship  $\tau \propto \rho^{1/2}$  (see Chapter 6 Section 6.3) has been found to be closely obeyed. While the dislocation density of an annealed polycrystalline specimen is typically  $10^7 \text{ cm}^{-2}$ , a plastic strain of 10% raises this density to  $10^{10} \text{ cm}^{-2}$  or more, an increase of three orders of magnitude. This is an apparent paradox, because one would think that the existing dislocations would be ejected out of the crystalline structure by the applied stress. If one calculates the strain that the existing dislocations in an annealed metal would be able to produce by their motion until they would leave the crystal, one would arrive at very small numbers. Consequently, the density of dislocations has to increase with plastic deformation, and internal sources have to be activated. Some possible dislocation-generation mechanisms are discussed in the next few paragraphs.

The homogeneous nucleation of a dislocation occurs by the rupture of the atomic bonds of a material along a certain line. Figure 4.47 shows schematically the sequence of steps leading to the formation of a pair of edge dislocations (one negative, one positive). In

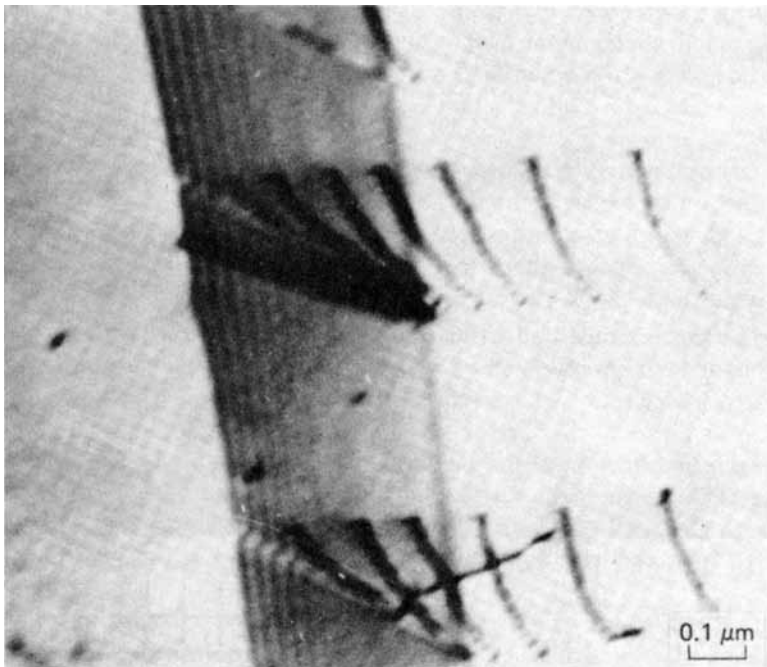


**Fig. 4.48** Emission of dislocations from ledges in grain boundary, as observed in transmission electron microscopy during heating by electron beam. (Courtesy of L. E. Murr.)

Figure 4.47(a) the lattice is elastically stressed, until, in Figure 4.47(b), an atomic plane is sheared; this generates two dislocations that move in opposite senses. Such a mechanism allows the formation of dislocations from an initially perfect lattice. It can be seen intuitively that the stress required would be extremely high. Calculations were done by Hirth and Lothe (see the suggested reading), and for copper, this stress is on the order of

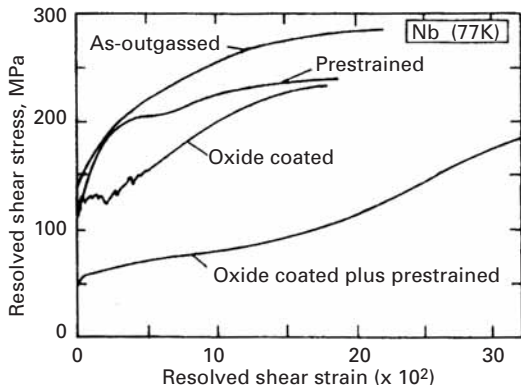
$$\frac{\tau_{\text{hom}}}{G} = 7.4 \times 10^{-2}.$$

Comparing this with the theoretical strength of crystals, one can see that the difference is not very large. Hence, such values would be obtained only if the applied stresses were very high or there were internal regions of high stress concentration. In conventional deformation, other dislocation-generation mechanisms should become operational at much lower stresses, rendering homogeneous nucleation highly unlikely.

Grain boundaries can serve as sources of dislocation. Irregularities at the boundaries (steps or ledges) could be responsible for the emission of dislocations into the grains. Figure 4.48 shows the emission of dislocations from a grain-boundary source; dislocations are seen as they are generated at the ledge. The stress due to heating produced by the electron beam produces the force on the dislocations. It is thought that dislocation emission from grain boundaries can be an important source of dislocations in the first stages of plastic deformation of a polycrystal.

In monocrystals, the surfaces can act as sources of dislocation. Small steps at the surfaces act as stress concentration sites; hence,

**Fig. 4.49** Effect of oxide layer on the tensile properties of niobium.  
(Reprinted with permission from V. K. Sethi and R. Gibala, *Scripta Met.* 9 (1975) 527.)



the stress can be several times higher than the average stress. At these regions, dislocations can be generated and “pumped” into the monocrystals. The majority of dislocations in monocrystals deformed in tension are generated at the surface. Pangborn *et al.*<sup>8</sup> investigated the bulk and surface dislocation mechanism in monocrystals. The dislocation density close to the surface was up to six times greater than that in the bulk. The dislocation surface layer (with higher dislocation density) extended for approximately 200  $\mu\text{m}$  into the material at the surface. The surface sources cannot have a significant effect on polycrystal deformation, because the majority of the grains would not be in contact with the free surface. Since dislocation activity is restricted to the grains, the surface sources would not be able to affect the internal grains. Incoherent interfaces between the matrix and precipitates, dispersed phases, or reinforcing fibers (in composites) are also sources of dislocations.

The importance of interfaces in the production of dislocations is seen in the results shown in Figure 4.49. The low-temperature tensile response of BCC metals was dramatically affected by the presence of an oxide layer. The figure exemplifies this response for niobium. The flow stress of monocrystalline niobium at 77 K is highly dependent on the state of the surface. The oxide softens the material. Two effects are responsible for the lowering of the flow stress by the introduction of an oxide layer:

1. The oxide puts the surface layers under tensile stresses, because the introduction of oxygen into the lattice expands it. On the other hand, the oxide is under compression. The resultant resolved shear stress at the surface is much higher (in the presence of the oxide layer) than that due exclusively to the externally applied load.
2. The predeformed and oxide-coated specimen (the lowest curve in the figure) has an even lower flow stress because the predeformation introduces surface steps, which act as stress-concentration sites.

<sup>8</sup> P. N. Pangborn, S. Weissman, and I. R. Kramer, *Met. Trans.* 12A (1981) 109.

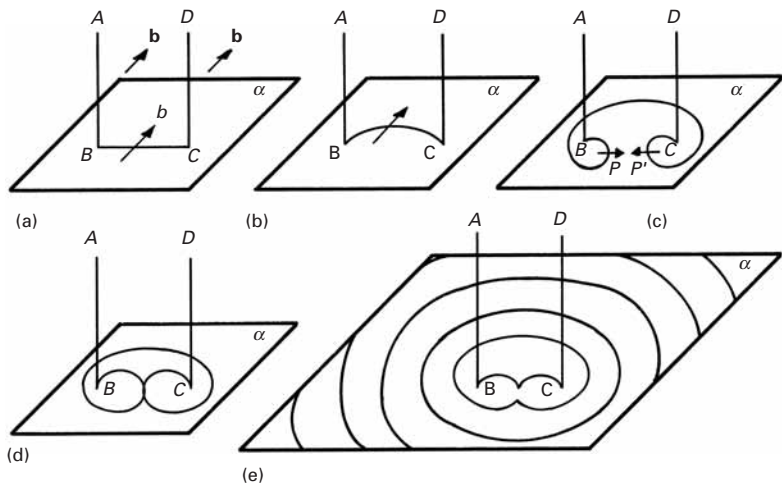


**Fig. 4.50** Sequence of the formation of dislocation loop by the Frank-Read mechanism.

Hence, the joint action of the internal stresses generated by the oxide and the surface steps activates the dislocation sources at the surface.

The classic mechanism for dislocation multiplication is called the *Frank-Read source*. In Figure 4.50(a), there is a dislocation ABCD with Burgers vector  $b$ . Only the segment BC is mobile in the slip plane  $\alpha$ . Segments AB and CD do not move under the imposed stress. The applied stress will generate a force per unit length on segment BC equal to (Section 4.45)

$$F = \frac{T ds}{R}.$$

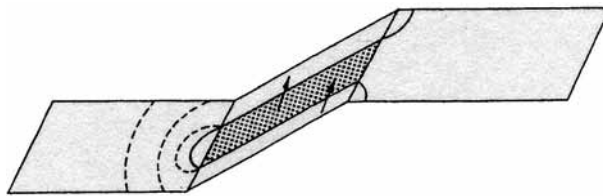
The radius of curvature of the dislocation segment decreases until it reaches its minimum, equal to  $BC/2$ . At this point, the force is maximum (and so is the stress). Hence, the dislocation reaches a condition of instability beyond that point. The critical position is shown in Figure 4.50(c). When  $P$  approaches  $P'$ , the dislocation segments have opposite signs; accordingly, they attract each other, forming a complete loop when they touch, and are then pinched off. The stress required to activate a Frank-Read source is equal to that needed to curve the segment BC into a semicircle with radius  $BC/2$ ; beyond this point, the stress decreases. Thus from Equation 4.22d:

$$\tau = \frac{Gb}{BC} = \frac{Gb}{2R}.$$

However, as loops are formed, they establish a back stress, so that the stress required to generate successive loops increases steadily. If the loops are expelled from the material, they cease to exert a back stress.

Only a few Frank-Read sources have been observed in metals. However, in a tridimensional array of dislocations, nodes define segments. These segments can bow and effectively act as Frank-Read sources. Another possibility is that the source forms when a screw dislocation cross-slips and returns to a plane parallel to the original slip

**Fig. 4.51** Frank–Read source formed by cross-slip.



plane. (See Figure 4.51.) Incidentally, edge dislocations cannot cross-slip because their Burgers vector could not be contained in the cross-slip plane. The Burgers vector of a screw dislocation, on the other hand, is parallel to its line and will be in the cross-slip plane if the intersection of the two dislocations is parallel to it. After the segment in the cross-slip plane advances a certain extent, the stress system applied might force it into a plane parallel to the original slip plane. At this point, a Frank–Read source is formed. Although it is thought that the original formulation of the Frank–Read source is not common, its modifications just cited – the node and the cross-slip case – might be the important mechanism of dislocation generation, after the first few percent of plastic strain.

Crystals formed by growth over a substrate (a technique commonly employed in the production of thin films) show dislocations whose formation can be easily explained. The substrate never has exactly the same lattice parameter as the crystal overgrowth. Figure 4.52 shows the sequence of formation of dislocations as the crystal grows over the substrate. If  $a_s$  and  $a_0$  are the lattice parameters of the substrate and overgrowth, respectively, the separation between the dislocations is

$$d = \frac{a_s^2}{|a_s - a_0|}.$$

Often, the impurity content of a crystal varies cyclically due to solidification; this is called *segregation*. The periodic change in composition is associated with changes in the lattice parameter, which can be accommodated by dislocation arrays.

Vacancies can condense and form disks as well as prismatic loops if they are present in a “supersaturated” concentration. In FCC crystals, these disks and loops occur on  $\{111\}$  planes. As seen in Figure 4.39, the dislocations that form the edges of these features are called *Frank dislocations*. Kuhlmann–Wilsdorf (see suggested reading) proposed, that they can act as Frank–Read sources, and this was later confirmed experimentally.

#### 4.4.9 Dislocation Pileups

All dislocations generated by a Frank–Read source are in the same slip plane if they do not cross-slip. In metals with low stacking-fault energy, the large separation between the partials renders cross-slip more difficult. In case one of the dislocations encounters an obstacle (a grain boundary, a precipitate, etc.), its motion will be hampered.

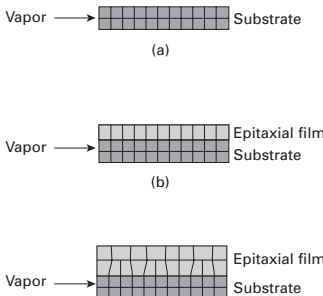


**Fig. 4.52** Epitaxial growth of thin film. (a) Substrate. (b) Start of epitaxial growth. (c) Formation of dislocations.

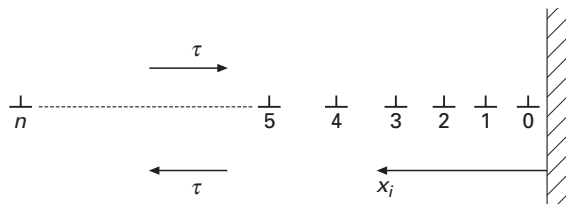


**Fig. 4.53** Pileup of dislocations against a barrier.

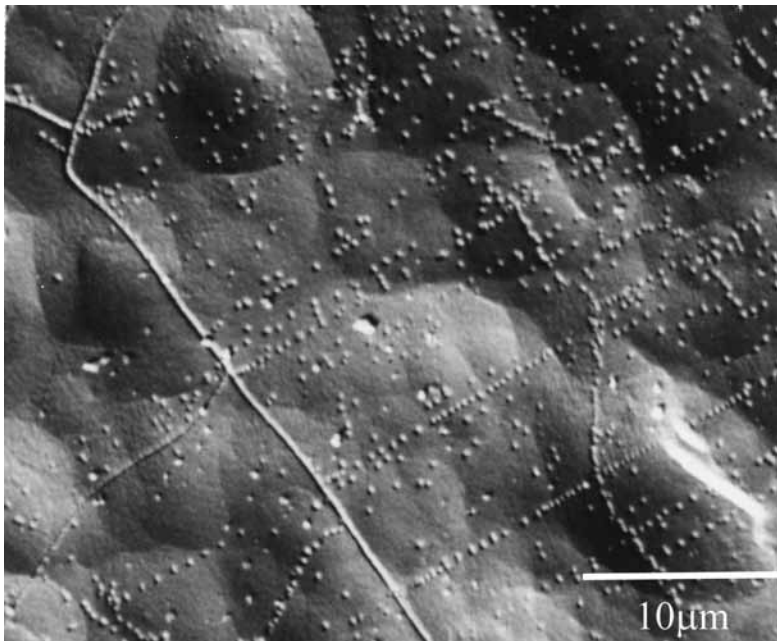


**Fig. 4.54** Pileup of dislocations against grain boundaries (or dislocations being emitted from grain-boundary sources?) in copper observed by etch pitting.

The subsequent dislocations will “pileup” behind the leading dislocation, after being produced by the Frank–Read source. Figure 4.53 is a schematic diagram of a pileup. The distance between the dislocations increases as their distance from the obstacle increases. On the other hand, if the metal has a very high stacking-fault energy, cross-slip will easily occur, and the planar array will be destroyed; edge dislocations cannot, obviously, cross-slip because of their Burgers vector.

Figure 4.54 shows an example of a pileup, obtained by etch pitting in copper. Observe that the dislocation configurations for a pileup and a grain-boundary source are similar and that many grain-boundary sources have in the past been mistaken for pileups. Figure 4.48 shows a grain-boundary source.

Each dislocation in a pileup is in equilibrium under the effect of the applied stress and of the stresses due to the other dislocations (in the pileup). Assuming that the dislocations are of edge character and parallel, the resulting force acting on the  $i$ th dislocation is obtained

by applying the equation that gives the forces between dislocations:

$$\tau b - \sum_{\substack{j=0 \\ i \neq j}}^n \frac{Gb^2}{2\pi(1-\nu)(x_i - x_j)} = 0. \quad (4.25)$$

$n$  is the number of dislocations in the pileup.

Solving the  $n$  equations with  $n$  unknowns ( $x_i - x_j$ ) for the dislocations behind the lead dislocation, we obtain the positions of the dislocations. This derivation was introduced by Eshelby *et al.*<sup>9</sup> and we present the results without derivation.

The stress acting on the lead dislocation due to the presence of the other dislocations and due to the applied stress is found to be

$$\boxed{\tau^* = n\tau.} \quad (4.26)$$

So the effect of the  $n$  dislocations in the pileup is to create a stress at the lead dislocation  $n$  times greater than the applied stress. For this reason, the dislocation pileup is sometimes treated as a superdislocation with a Burgers vector  $nb$ . The foregoing calculations can also be applied to screw dislocations by removing the term  $(1 - \nu)$ . The length of the pileup under an applied shear stress  $\tau$  is given by

$$L = \frac{nGb}{\pi\tau}. \quad (4.26a)$$

#### 4.4.10 Intersection of Dislocations

A dislocation, when moving in its slip plane, encounters other dislocations, moving along other slip planes. If we imagine the first dislocation moving in a horizontal plane, it will “see” the other dislocations as “trees” in a “forest.” The latter name designates dislocations in other slip planes. When the dislocation intersects another dislocation, since it shears the material equally (by a quantity  $b$ ) on the two sides of the slip plane, it will form one or more steps. These steps are of two types: *jogs* if the “tree” dislocation was transferred to another slip plane, and *kink* if the “tree” dislocation remains in the same slip system. Various possible outcomes from dislocation intersections are shown in Figure 4.55. Figure 4.55(a) shows an edge dislocation traversing a “forest” composed of two edge and one screw dislocation. A good rule to determine the direction of jogs and kinks is the following: The direction of the segment is the same as the Burgers vector of the dislocation that is traversing the “forest;” on the other hand, the Burgers vector of the jog or kink is the Burgers vector of the dislocation in which it is located, because the Burgers vector is always the same along the length of a dislocation. Figure 4.55(b) shows a screw dislocation after traversing a “forest.” The reader is asked to verify the directions of dislocation segments and Burgers vector; he or she should also verify whether they are jogs or kinks.

The ability of these segments to slip with a dislocation is of great importance in determining the work-hardening of metal. It should

---

<sup>9</sup> J. D. Eshelby, F. C. Frank, and F. R. N. Nabarro, *Phil. Mag.*, 42 (1951) 351.

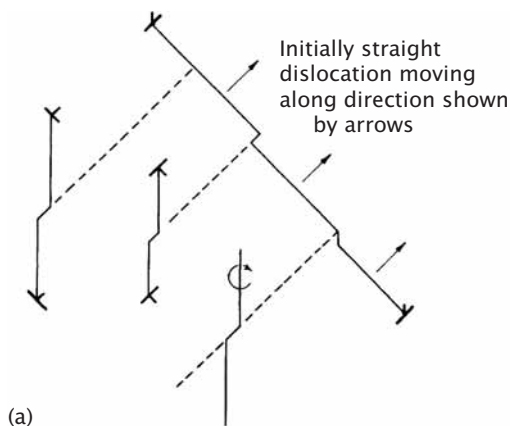
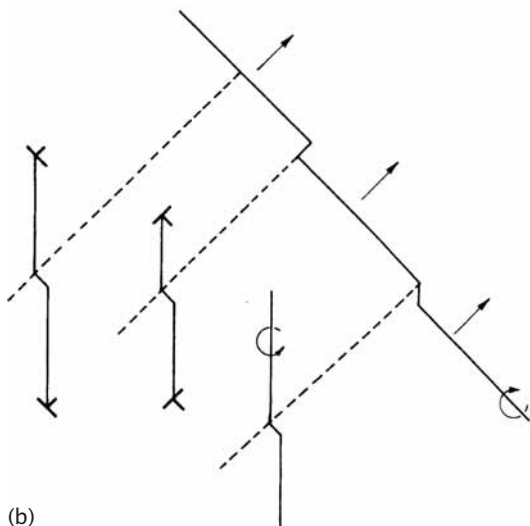


**Fig. 4.55** (a) Edge dislocation traversing “forest” dislocations.  
 (b) Screw dislocation traversing “forest” dislocations.



be noted that some authors use the name “jog” for both types of segments. Jogs and kinks can have either a screw or an edge character. From Figure 4.56(a), it can be seen that segments on an edge dislocation cannot impede the motion of jogs or kinks, because the segments can slip with the dislocation. On the other hand, in screw dislocations, there are segments that can slip with the dislocations and segments that cannot. When the segment can move with the dislocation, the motion is called *conservative*. When the segment cannot move by slip, the motion is called *nonconservative*. Figure 4.56(b) shows some interactions. At the left there is a conservative motion by slip, and at the right a nonconservative motion. The nonconservative motion of a jog is, in essence, a climb process and requires thermal activation. Vacancies or interstitials are produced as the segment moves. If the temperature is not high enough to provide sufficient thermal activation, the jog does not move, and loops are formed as the dislocation advances; this is shown in Figure 4.57. The

**Fig. 4.56** (a) Kink and jog in edge dislocation. (b) Kink and jog in screw dislocation.

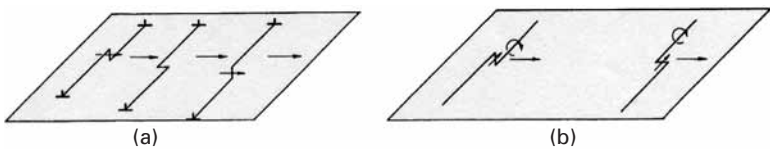


**Fig. 4.57** Loop being pinched out when jog is left behind by dislocation motion.

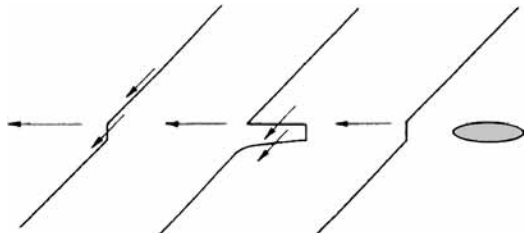
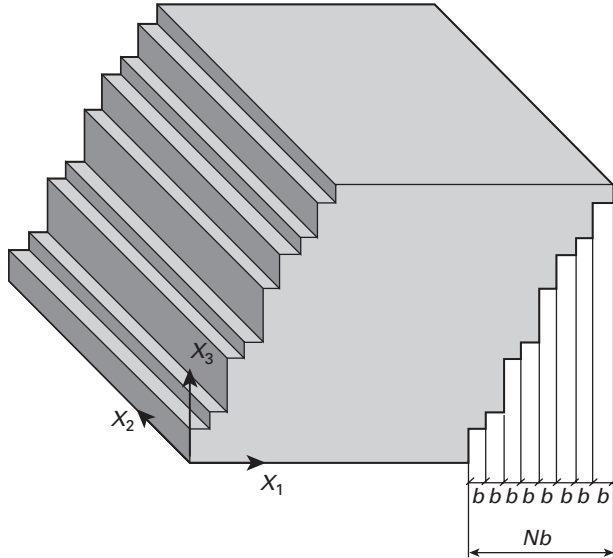


**Fig. 4.58** Shear produced by the passage of parallel dislocations.



dislocation forms a dipole upon advancing, because the jog stays back. At a certain point, the dipole will be pinched out, producing a loop.

#### 4.4.11 Deformation Produced by Motion of Dislocations (Orowan's Equation)

Upon moving, a dislocation produces a certain deformation in a material. This deformation is inhomogeneous. Figure 4.58 shows the steps generated by the passage of dislocations. If we consider a large number of dislocations acting on different systems, we can posit the association of a large number of small steps as creating a homogeneous state of deformation. The deformation is related to both the number of dislocations that move and the distance traveled by them. This equation is known as *Orowan's* or *Taylor-Orowan's equation* and is derived in this section. Figure 4.58 shows a cube dimensions  $dx_1$ ,  $dx_2$ , and  $dx_3$  that was sheared by the passage of  $N$  dislocations moving

along the plane  $Ox_1x_2$ . The plastic shear strain can be expressed as

$$d\gamma_{13} = \frac{Nb}{dx_3}. \quad (4.27)$$

This is so because all dislocations are of edge character and have the same sign, with identical Burgers vector  $b$ . The density of dislocations,  $\rho$ , is the total length  $N dx_2$  in the volume  $dx_1 dx_2 dx_3$ . Therefore,

$$\rho = \frac{N dx_2}{dx_1 dx_2 dx_3} \quad \text{and} \quad N = \rho dx_1 dx_3. \quad (4.28)$$

Substituting Equation 4.28 into Equation 4.27 yields

$$d\gamma_{13} = \rho b dx_1.$$

A cube isolated in space, in which dislocations are generated on one face and pop out of the opposite face is an idealization. In real situations, dislocations remain within the material, and the deformation generated by each dislocation is related to the distance traveled by it. Assuming that dislocations travel an average distance,  $\bar{l}$ , we have

$$\boxed{\gamma_{13} = \rho b \bar{l}.}$$

But in a general case of deformation, five independent slip systems are activated. The deformation is not perfectly aligned with the movement of dislocations, and it is necessary to introduce a correction parameter  $k$  that takes this into account:

$$\gamma_p = k\rho b \bar{l}. \quad (4.29)$$

This is the Orowan equation. If one assumes that the density of mobile dislocations is not affected by the rate of deformation (strain rate), one would have, taking the time derivative of both sides of Equation 4.29,

$$\frac{d\gamma_p}{dt} = k\rho b \frac{d\bar{l}}{dt} + k\bar{l}b \frac{d\rho}{d\bar{l}}. \quad (4.30)$$

If we assume that  $\rho$  does not vary with time,

$$\boxed{\gamma_p = k\rho b \bar{v}},$$

where  $\bar{v}$  is the mean velocity of the dislocations. We can also use the longitudinal strain  $\varepsilon_{11}$  if we are applying the situation to a tensile test. It can be shown that  $\gamma = 2\varepsilon$  (see Section 6.2.3) for an ideal orientation for slip.

As an illustration, if iron ( $b \approx 0.25$  nm) is being deformed at  $10^{-3}$  s $^{-1}$ , and the density of mobile dislocations is around  $10^{10}$  cm $^{-2}$ , their approximate velocity will be  $4 \times 10^{-6}$  cm/s.

Attention should be called to the fact that the density of mobile dislocations is lower than the total density of dislocations in the material. As the dislocation density increases in a deformed material, a greater and greater number of dislocations is locked by various types of barriers, such as grain boundaries, cell walls, or the action

of a great number of jogs. The actual density of mobile dislocations is only a fraction of the total dislocation density.

### Example 4.6 |

Titanium is deformed by basal slip with edge dislocations. If a cube with one of its sides parallel to the  $c$ -axis is being deformed by shear through the passage of dislocations on every fifth (0001) plane, what shear strain  $\gamma$  is the cube undergoing? Take the radius of Ti atom

$$r_{Ti} = 0.147 \text{ nm.}$$

*Solution:* We first determine

$$a = 2r = 0.294 \text{ nm.}$$

We assume an ideal  $c/a$  ratio equal to 1.633. Thus,  $c = 0.48 \text{ nm}$ . The Burgers vector for basal slip is equal to  $a$ .

Every fifth atomic plane corresponds to a distance  $d = 5c = 2.4 \text{ nm}$ . The shear strain is thus equal to

$$\gamma = \frac{b}{d} = \frac{0.294}{2.4} = 0.1225.$$

### Example 4.7 |

An FCC monocrystal of nickel is sheared by  $\gamma_{12} = 0.1$ . Assuming that the dislocation density is equal to  $10^8 \text{ cm}^{-2}$  and that it remains constant, what is the average distance each dislocation will have to move? If the shear strain rate is  $10^{-4} \text{ s}^{-1}$ , what is the mean velocity of the dislocation?

*Solution:*

$$r_{Ni} = 0.125 \text{ nm}$$

For FCC,  $b = 2r_{Ni} = 0.250 \text{ nm}$ . Using Orowan's equation, taking  $k = 1$ ,  $\gamma = \rho b \bar{l}$ , we obtain the following:

$$\begin{aligned} \text{(i)} \quad \bar{l} &= \frac{\gamma}{\rho b} \\ &= \frac{0.1}{10^8 \text{ cm}^{-2} \times 0.25 \text{ nm}} \\ &= \frac{0.1}{10^8 \times (10^4 \text{ m}^{-2}) \times 0.25 (10^{-9} \text{ m})} = 4 \times 10^{-4} \text{ m} \end{aligned}$$

$$\text{(ii)} \quad \dot{\gamma} = \rho b \bar{v},$$

so

$$\begin{aligned} \bar{v} &= \frac{\dot{\gamma}}{\rho b} \\ &= \frac{10^{-4} \text{ s}^{-1}}{10^8 \text{ cm}^{-2} \times 0.25 \text{ nm}} = 4 \times 10^7 \text{ m/s.} \end{aligned}$$

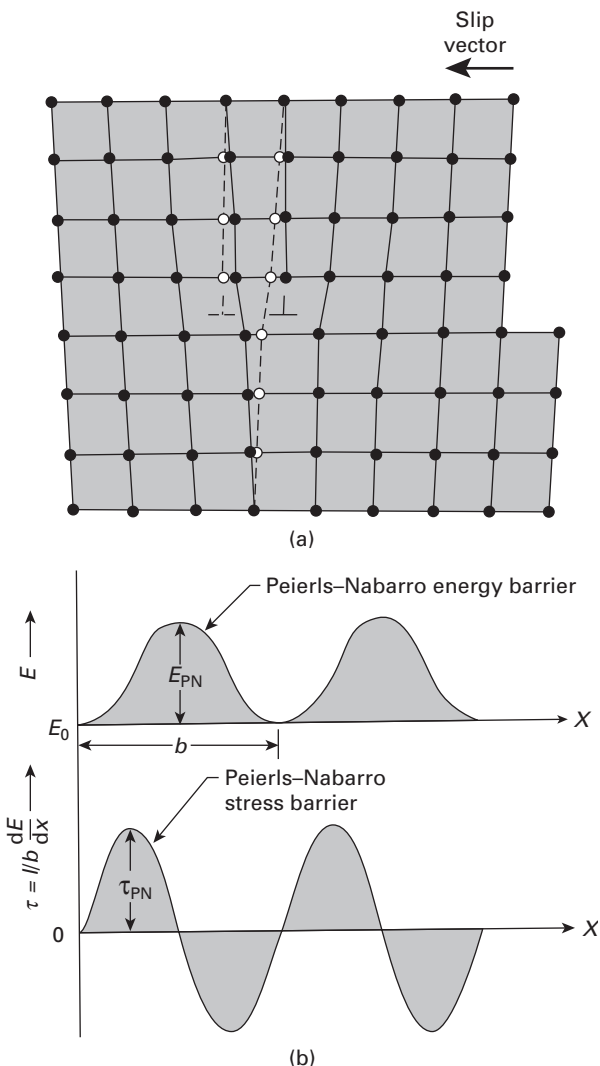
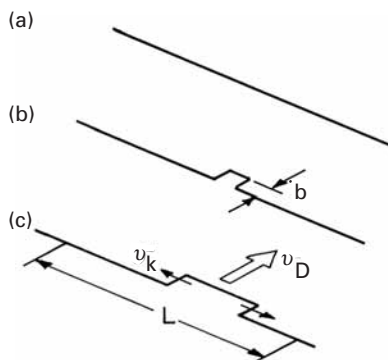


**Fig. 4.59** (a) Movement of dislocation away from its equilibrium position. (b) Variation of Peierls–Nabarro stress with distance. (Reprinted with permission from H. Conrad, *J. Metals*, 16 (1964) 583.)

#### 4.4.12 The Peierls–Nabarro Stress

The Peierls–Nabarro stress represents the resistance that the crystalline lattice offers to the movement of a dislocation. Figure 4.59 shows the stress that one has to apply to a dislocation to make it move a distance  $b$ . When the extra plane is moved away from its equilibrium position (either to the right or to the left), one has to overcome a barrier. The difference in energy between the equilibrium (saddle point) and the most unstable position is called the *Peierls–Nabarro energy*, and the stress required to overcome this energy barrier is the *Peierls–Nabarro (P–N) stress*. The dislocation does not advance simultaneously over its entire length. (See Figure 4.60(a).) Rather, a small hump, or kink pair is formed, as shown in Figure 4.60(b), via what is known as a Seeger mechanism. This kink pair then moves along the dislocation (the parts of the pair move in opposite directions), and when it has covered the entire front, the dislocation has advanced by

**Fig. 4.60** Overcoming of Peierls barrier by Seeger kink pair mechanism. (a) Original straight dislocation. (b) Dislocation with two kinks. (c) Kinks moving apart at velocity  $v_k$ .



$b$ , the Burgers vector. In Figure 4.60(c) the velocity of movement of a dislocation is  $v_D$ , related to the kink velocity  $v_k$  by

$$v_D = v_k \frac{b}{L}. \quad (4.31)$$

The stress required to overcome the obstacle is known as the Peierls–Nabarro stress. Calculations of this stress are fairly inaccurate because the continuum treatment breaks down for distances on the order of the atomic spacings. The energy of the dislocation is given by  $U(x)$  as it moves through the barrier. The applied force required to bring this dislocation to the top of the energy barrier is

$$F = -\frac{dU}{dx}. \quad (4.32)$$

But from the Peach–Koehler equation ( $F = \tau b$ ), we have

$$\tau = -\frac{1}{b} \frac{dU}{dx}. \quad (4.33)$$

A sinusoidal form for  $U(x)$  was assumed by Peierls and Nabarro, leading to the expression

$$\tau_{PN} = \alpha \frac{Gb}{2c} e^{-\pi a/c} \sin \frac{2\pi x}{c}, \quad (4.34)$$

where  $c$  is the spacing of atoms in the  $x$  direction,  $a$  is the lattice parameter, and  $\alpha$  is a parameter that depends on the nature of the barrier; for  $\alpha = 1$ , the barrier is sinusoidal.

#### 4.4.13 The Movement of Dislocations: Temperature and Strain Rate Effects

The resistance of crystals to plastic deformation is determined by the resolved shear stress that is required to make the dislocations glide in their slip planes. If no obstacles were present, the dislocations would move under infinitesimally small stresses. However, in real metals, the nature and distribution of obstacles determines their mechanical response. Becker<sup>10</sup> was the first to point out the importance of thermal energy in helping the applied stress overcome existing obstacles.

<sup>10</sup> R. Becker, Z. Phys. 26 (1925) 919.

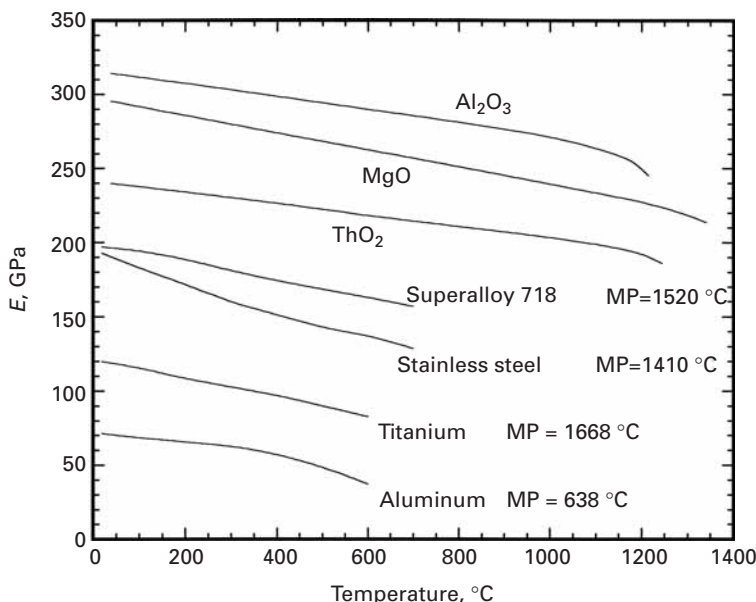


**Fig. 4.61** Effect of temperature on Young's modulus. (Adapted from J. B. Wachtman Jr., W. E. Tefft, D. G. Lam, Jr., and C. S. Apstein, *J. Res. Natl. Bur. Stand.*, 64A (1960) 213; and J. Lemarre and J. L. Chaboche, *Mechanics of Solid Materials*, Cambridge: Cambridge University Press, 1990, p. 143.)

The stress required for deformation,  $\tau$ , can be divided into two parts:  $\tau^*$ , which is dependent on the strain rate and temperature of the material, and  $\sigma_G$ , in which the temperature dependence is equal to that of the shear modulus. Thus,

$$\tau = \tau^* + \sigma_G, \quad (4.35)$$

or, in terms of the normal stresses,

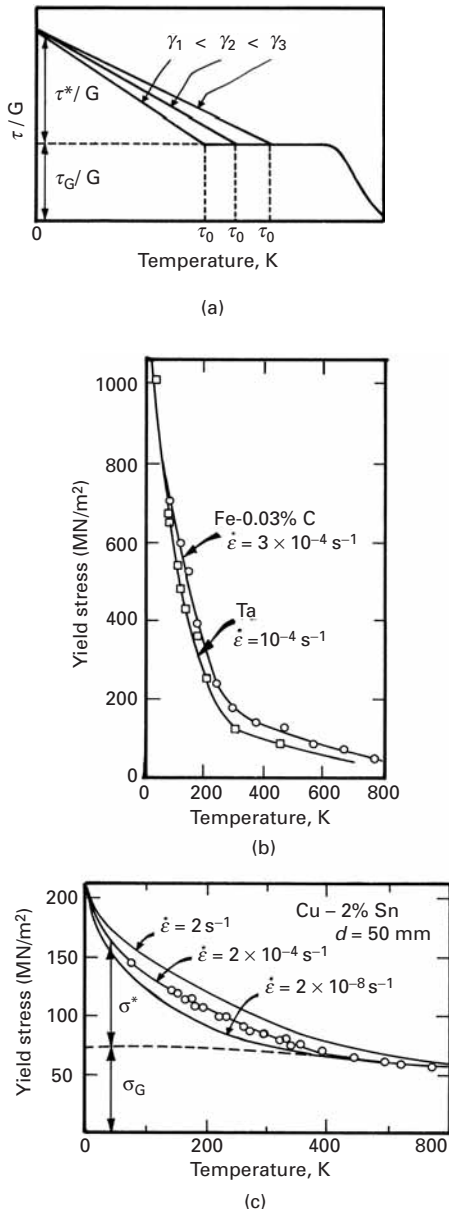
$$\sigma = \sigma^* + \sigma_G. \quad (4.36)$$

The functional dependence can be expressed as

$$\sigma = \sigma^*(T, \dot{\varepsilon}) + \sigma_G(G). \quad (4.37)$$

We know that the elastic properties ( $E$ ,  $G$ ,  $v$ ) are only slightly dependent on temperature. Figure 4.61 shows the temperature dependence of Young's modulus for a number of materials. As the temperature increases, the amplitude of vibration of the atoms increases (but the frequency remains constant at approximately  $10^{13} \text{ s}^{-1}$ ). This results in thermal dilation, which separates the atoms somewhat and changes their equilibrium positions and interatomic forces. The flow stress of metals, on the other hand, is much more sensitive to temperature and strain rate. Figure 4.62 shows the dependence of the yield stress on temperature for typical BCC and FCC structures. BCC metals (Fe, Cr, Ta, W, etc.) exhibit a greater temperature and strain rate sensitivity. It can be seen that the athermal component of stress is  $\sigma_G \approx 50 \text{ MPa}$ , whereas the thermal component exceeds 1,000 MPa at 0 K. The increase in flow stress with decrease in temperature is much more gradual for FCC metals, as shown in Figure 4.62(c). The differences in temperature and strain rate sensitivity are due to different mechanisms controlling the rate of dislocation motion. In BCC metals,

**Fig. 4.62** Flow stress as a function of temperature for (a) an idealized material, (b) BCC metals, and (c) FCC metals. Notice the greater temperature dependence for Ta and Fe (BCC).



Peierls–Nabarro stresses are the major obstacles at low temperatures, and thermal energy can effectively aid the dislocations to overcome these stresses, which constitute a short-range barrier. For FCC metals, dislocations intersecting dislocations (“forest” dislocations) are the main barriers to the motion of dislocations. Thermal energy is less effective in helping dislocations to overcome these barriers.

At temperatures higher than 800 K, there is an additional drop in the flow stress, not shown in Figure 4.62. This drop occurs at  $T \approx 0.5 T_m$ , where  $T_m$  is the melting point of the metal (or alloy). The drop is due to creep, which often involves dislocation climb. Creep is treated separately in Chapter 13.

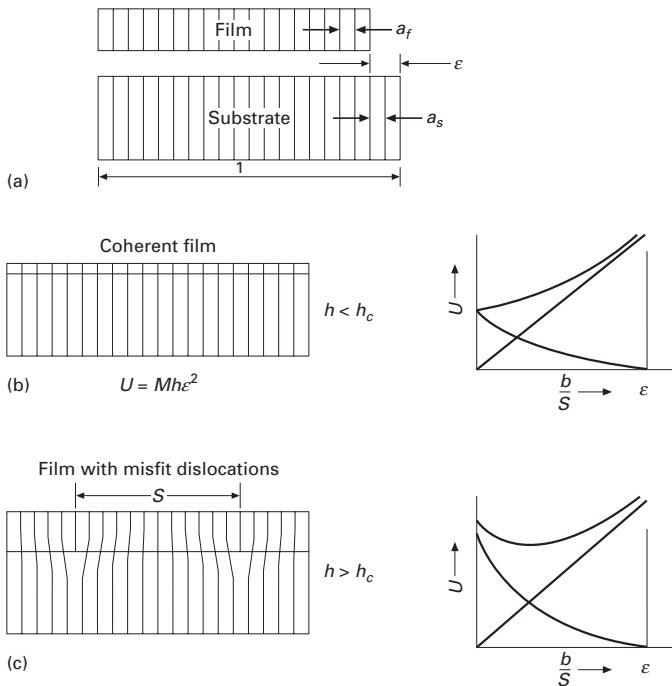


**Fig. 4.63** Stresses and dislocations generated at film–substrate interface: (a) film and substrate with different lattice parameters; (b) elastic (coherent) accommodation of strains by film; (c) elastic + dislocation (semi-coherent) accommodation of strains at a film thickness greater than  $h_c$ . (Adapted from W. D. Nix, *Met. Trans.*, 20A (1989) 2217.)

Johnston and Gilman<sup>11</sup> were the first to measure the velocities of dislocations as a function of applied stress. They used LiF crystals for their measurements and observed, as expected, that the distance a dislocation moves increases with the magnitude and duration of the stress pulse. The distance also increases, at a constant stress, with increasing temperature. This relationship is known as the Johnston-Gilman equation and has the form

$$v = A\tau^m e^{-Q/RT}, \quad (4.38)$$

where  $v$  is the dislocation velocity, exponent  $m$  is a stress dependency that is dependent on  $v$ ,  $Q$  is an activation energy, and  $A$  is a pre-exponential term that depends on the material and the nature of the dislocation (edge or screw). Although this equation predicts an infinite dislocation velocity when the stress is high, it is generally accepted that the limiting dislocation velocity is the velocity of elastic shear waves. Thus, the equation breaks down at velocities close to the shear wave velocity (e.g., ~3,000 m/s for iron).

#### 4.4.14 Dislocations in Electronic Materials

Producing dislocation-free substrates and epitaxial films is an important technological consideration. The presence of dislocations creates a barrier for electric fields and alters electronic properties of thin films. It is therefore undesirable. In order for epitaxial thin films to be stress free, they must have the same lattice parameter as the substrate. Figure 4.63(a) shows a film and substrate, with lattice parameters  $a_f$  and  $a_s$ , respectively. They are shown separately. If they

<sup>11</sup> W. G. Johnston and J. J. Gilman, *J. Appl. Phys.* 33 (1959) 129.

are connected, stresses will arise. The substrate is usually much thicker than the film. Thus, the elastic accommodation is assumed to occur entirely in the substrate. The epitaxial strain is:

$$\varepsilon = \frac{\Delta a}{a} \approx \frac{a_s - a_f}{a_s}.$$

We present below the van der Merwe<sup>12</sup>–Matthews<sup>13</sup> theory for the prediction of thin film configurations. The strain energy, in the case where the substrate is completely coherent with the film, is:

$$U_h = \frac{E}{1-\nu} h \varepsilon^2. \quad (4.39)$$

where  $h$  is the thickness of the thin film; the term  $E/(1-\nu)$  is the biaxial modulus (see Section 2.16). It can be obtained from the generalized Hooke's law assuming a biaxial stress state. As the thickness of the film increases, the strain energy increases, due to the factor  $h$  in Equation 4.39. At first, the film is coherent with the substrate. This is shown in Fig. 4.63(b). When the strain energy reaches a critical level, misfit dislocations are created, decreasing the overall strain. Figure 4.63(c) shows a film with dislocations having a spacing  $S$ . The homogeneous strain is decreased from  $\varepsilon$  to  $(\varepsilon - b/S)$  due to the insertion of dislocations, spacing  $S$ , with displacement (Burgers vector)  $b$ . However, the dislocations created have an energy  $U_d$  that has to be factored in. For misfit edge dislocations with a spacing  $S$ :

$$U_d = \frac{G b^2}{4\pi(1-\nu) S} \frac{2}{S} \ln\left(\frac{h}{b}\right). \quad (4.40)$$

The misfit dislocations form a two-dimensional network. The term  $2/S = 1/S + 1/S$  represents the length of misfit dislocations per unit area (square grid). The total strain energy  $U_t$  is obtained by adding Equations 4.39 (after subtracting the  $b/S$  term) and 4.40:

$$U_t = \frac{E}{1-\nu} h \left( \varepsilon - \frac{b}{S} \right)^2 + \frac{G b^2}{4\pi(1-\nu) S} \frac{2}{S} \ln\left(\frac{h}{b}\right). \quad (4.41)$$

In Figure 4.63, the two plots on the right side represent the energy in the case of coherent and semicoherent interface. In the coherent case, the energy is minimum for an infinite spacing of dislocations ( $b/S = 0$ ). However, as the thickness  $h$  of the film is increased, the second term (logarithmic in  $h$ ) increases in importance. The energy reaches a minimum when critical thickness  $h_c$  is reached. This corresponds to the thickness at which dislocations are created at the interface. This is represented by the plot in Figure 4.63(c).

We can calculate the critical film thickness,  $h_c$  by taking the derivative of Equation 4.41 with respect to  $1/S$ :

$$\frac{\partial U_t}{\partial (1/S)} = -2 \frac{E}{1-\nu} \left( \varepsilon - \frac{b}{S} \right) + \frac{G b^2}{2\pi(1-\nu)} \ln\left(\frac{h}{b}\right) = 0. \quad (4.42)$$

<sup>12</sup> J. H. van der Merwe and N. G. van der Berg, *Surface Science*, 32 (1972) 1.

<sup>13</sup> J. W. Matthews and A. E. Blakeslee, *Journal of Crystal Growth*, 27 (1974) 118; 29 (1975) 273.

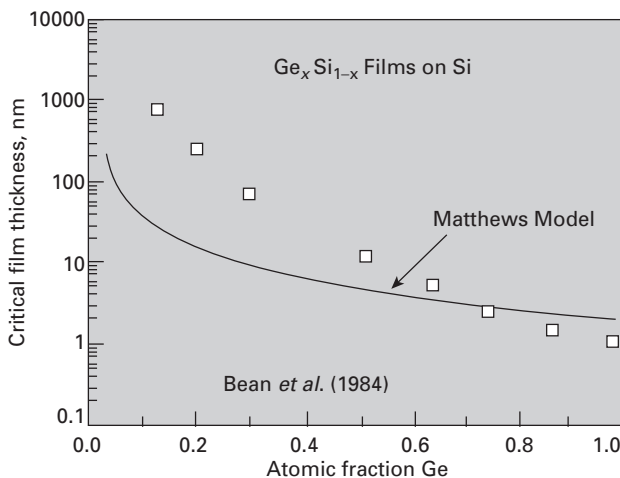
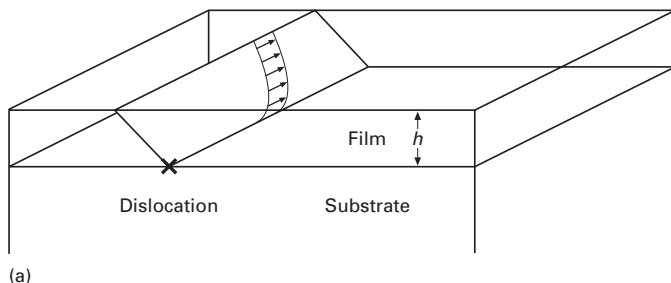
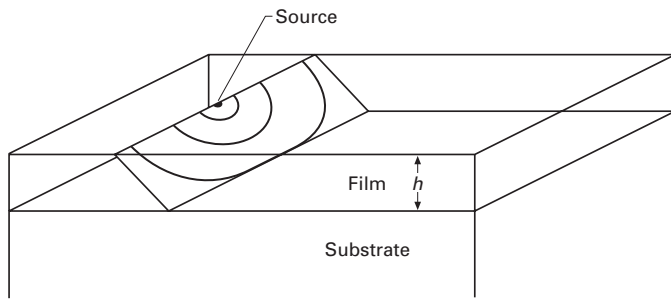


**Fig. 4.64** Critical film thickness as a function of misfit strain for  $\text{Ge}_x\text{Si}_{1-x}$  film grown on Si substrate; the greater the fraction  $\text{Ge}_x$ , the greater the misfit stain and the smaller  $h_c$ . Predictions from van der Merwe-Matthews theory; measurements from J. C. Bean, L. C. Feldman, A. T. Fiory, S. Nakahara, and I. K. Robinson, *J. Vac. Sci. Technol. A*, 2 (1984) 436. (Adapted from W. D. Nix, *Met. Trans.*, 20A (1989) 2216.)



(a)



(b)

**Fig. 4.65** Mechanisms of misfit dislocation generation; (a) Freund mechanism in which a “threading” dislocation preexisting in substrate lays over interface creating misfit dislocation; (b) Nix mechanism, by which surface source creates half-loops that move toward interface.

By setting  $1/S = 0$ , i.e., an infinite dislocation spacing, we obtain the Matthews-Blakeslee equation:

$$\frac{h_c}{\ln\left(\frac{h_c}{v_0}\right)} = \frac{Gb}{4\pi E\varepsilon} = \frac{b}{8\pi(1+\nu)E} \quad (4.43)$$

Figure 4.64 shows the critical film thickness for  $\text{Ge}_x\text{Si}_{1-x}$  growth on a Si substrate. The higher the fraction  $x$  of Ge, the larger the strain in the film,  $\varepsilon$ . Consequently, the smaller will be  $h_c$ . The predictions of Equation 4.43 are compared with experimental results in Figure 4.64. The agreement is only qualitatively satisfactory. For small strains, the predicted thickness is orders of magnitude lower than the observed value.

One of the reasons for the difference is that dislocations cannot appear spontaneously at the interface, once a critical thickness is reached. They have to nucleate somewhere and move to the interface. This requires additional energy. Two possible mechanisms are shown in Figure 4.65. The Freund mechanism requires an existing dislocation that “threads” through substrate and film. This threading dislocation, moving along the interface as shown in Figure 4.65(a), creates the interface dislocation. The Nix mechanism requires a dislocation to be formed at the free surface and move to the interface. A source, operating at the surface, is shown in Figure 4.65(b). It produces half-loops, which expand and reach the interface.

## Suggested Reading

### Point Defects

- C. S. Barrett and T. B. Massalski. *Structure of Metals*, 3rd ed. New York, NY: McGraw-Hill, 1966.
- J. H. Crawford Jr. and L. M. Slifkin, eds. *Point Defects in Solids*. New York, NY: Plenum Press, 1972.
- A. C. Damask and G. J. Dienes. *Point Defects in Metals*. New York, NY: Gordon and Breach, 1963.
- C. P. Flynn. *Point Defects and Diffusion*. Oxford: Clarendon Press, 1972.
- H. Kimura and R. Maddin. *Quench Hardening in Metals*, in the series “Defects in Crystalline Solids,” S. Amelincx, R. Gevers, and J. Nihoul, eds. Amsterdam: North-Holland, 1971.
- A. S. Nowick and B. S. Berry. *Anelastic Relaxation in Crystalline Solids*. New York, NY: Academic Press, 1972.
- H. G. Van Bueren. *Imperfections in Crystals*. Amsterdam: North-Holland, 1961.

### Line Defects

- A. H. Cottrell. *Dislocations and Plastic Flow in Crystals*. Oxford: Clarendon Press, 1953.
- J. C. Fisher, W. G. Johnston, R. Thomson, and T. Vreeland, Jr., eds. *Dislocations and Mechanical Properties of Crystals*. New York, NY: Wiley, 1957.
- J. Friedel. *Dislocations*. Elmsford, NY: Pergamon Press, 1967.
- J. P. Hirth and J. Lothe. *Theory of Dislocations*, 2nd ed. New York, NY: J. Wiley, 1981.
- D. Hull and D. J. Bacon. *Introduction to Dislocations*. New York, NY: Oxford University Press, 1989.
- A. Kelly and G. W. Groves. *Crystallography and Crystal Defects*. Reading, MA: Addison-Wesley, 1974.
- I. Kovacs and L. Zsoldos. *Dislocations and Plastic Deformation*. Elmsford, NY: Pergamon Press, 1973.
- D. Kuhlmann-Wilsdorf, in *Physical Metallurgy*, 3rd ed., R. W. Cahn and P. Haasen, eds. Amsterdam: North Holland, 1990, 1983.
- J. P. Hirth and F. R. N. Nabarro, ed. *Dislocations in Solids*, (15 vols.). New York, NY: Elsevier/North-Holland, 1979–2008.
- W. T. Read, Jr. *Dislocations in Crystals*. New York, NY: McGraw-Hill, 1953.
- J. Weertman and J. R. Weertman. *Elementary Dislocation Theory*. New York, NY: Oxford University Press, 1992.

## Exercises

**4.1** Calculate the radii of the tetrahedral and octahedral holes in BCC and FCC iron; assume lattice parameters of 0.286 and 0.357 nm, respectively.

**4.2** Calculate the concentration of monovacancies in gold at 1,000 K, knowing that  $H_f = 1.4 \times 10^{-19}$  J. If the gold is suddenly quenched to ambient temperature, what will be the excess vacancy concentration?

**4.3** How many vacancies per cubic centimeter are there in gold, at ambient temperature, assuming a lattice parameter of 0.408 nm?

**4.4** What is the effect of vacancies on electrical conductivity?

**4.5** What is the effect of vacancies on the amplitude of vibration of the neighboring atoms?

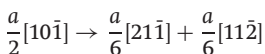
**4.6** What stress is required to render operational a Frank-Read source in iron, knowing that the distance between points *B* and *C* is 20 (Figure 4.50) nm and that the Goldschmidt radius of the iron atoms is 0.14 nm?

**4.7** Make all possible reactions between (perfect) dislocations in  $(1\bar{1}\bar{1})$  and  $(1\bar{1}\bar{1})$  in an FCC crystal. Among them, which ones are Lomer locks?

**4.8** Consider all possible reactions between partial Shockley dislocations (only the front dislocation, from the pair) in  $(111)$  and  $(11\bar{1})$  in an FCC crystal. Among them, which ones will form a stair-rod dislocation?

**4.9**

(a) Show that the reaction



is either vectorially correct or incorrect?

(b) Is the reaction energetically favorable?

**4.10**  $10^7$  and  $10^{11}$  cm $^{-2}$  are typical values for the dislocation density of annealed and deformed nickel, respectively. Calculate the average space among dislocation lines (assuming a random dislocation distribution), as well as the line energy for edge and screw dislocations, in both cases. In nickel,  $E = 210$  GPa,  $v = 0.3$ , and the lowest distance between atom centers is 0.25 nm.

**4.11** Calculate the dislocation density for Figure 4.22b; assume a foil thickness of 0.3  $\mu\text{m}$ .

**4.12** The concentration of vacancies in aluminum at 600 °C is  $9.4 \times 10^{-4}$ ; by quenching, this concentration is maintained at ambient temperature. The vacancies tend to form disks, with Frank partials at the edges. Determine the loop concentration and dislocation density, assuming that:

(a) Disks with a 5-nm radius are formed.

(b) Disks with a 50-nm radius are formed.

For aluminum, assume that the radius of the atoms is 0.143 nm. (*Hint:* The length of the Frank dislocation corresponding to a disk is equal to the circumference of the circle.)

4.13 The flow stress of monocrystals is on the order of  $10^{-4}$  G. Using the concept of Frank-Read sources, determine the length of segments required for this stress level. If the length of the segments is determined by dislocations on a second slip plane (“tree” dislocations), obtain an estimate for the dislocation density in annealed monocrystals. Assume that the dislocations are equally distributed on the slip planes of an FCC crystal.

4.14 On what planes of a BCC structure can the  $a/2$  [111] move?

4.15 Upon encountering an obstacle, an edge dislocation stops. A second edge dislocation, with identical Burgers vector and moving in the same plane, approaches the first dislocation, driven by a stress equal to 140 MPa.

(a) What will be the equilibrium separation between the two dislocations?

Assume that the metal is nickel ( $E = 210$  GPa,  $\nu = 0.3$ ,  $r = 0.249$  nm).

(b) What would be the equilibrium separation if the dislocations were both screw dislocations?

4.16 LiF is an ionic crystal with a NaCl-type structure (cubic). The Li atoms occupy the vertices and the centers of the faces of the unit cell, while the F atoms occupy the edges, and one F atom is in the body-centered position. There are eight atoms per unit cell. Knowing that the slip plane for LiF is [110], determine the Burgers vector of a perfect dislocation. Remember that one has an ionic crystal and that there is a strong repulsion between ions of the same sign. Explain your results.

4.17 Draw a unit cell for an HCP crystal. Show the perfect dislocations in the base plane. Can they decompose into partials? If so, represent them by the special notation for dislocations.

4.18 Nickel sheet is being rolled at ambient temperature in a rolling mill (roll diameter 50 cm, velocity 200 rpm). See Figure 6.1 for sketch of rolling mill. The initial thickness is 20 mm and the final thickness is 10 mm (one pass).

(a) Calculate the average strain rate.

(b) Calculate the energy that will be stored in the material, assuming that the final dislocation density is  $10^{11}$  cm $^{-2}$ .

(c) Determine the total energy expenditure per unit volume, assuming a flow stress equal to 300 MPa.

(d) Assuming that all energy not stored as dislocations is converted into heat, calculate the temperature rise if the process is adiabatic ( $C_p = 0.49$  J/g °C).

(e) Why does the energy stored represent only a fraction of the energy expended?

4.19 Calculate the largest atom that would fit interstitially into (a) nickel (FCC; atomic radius = 0.125 nm) and (b) molybdenum (BCC; atomic radius = 0.136 nm).

4.20 Calculate, for tungsten (BCC; atomic radius = 0.1369 nm), the radii of the largest atoms that can fit into (a) a tetrahedral interstitial site (at 0, 1/4, 1/2) and (b) an octahedral interstitial site (at 0, 1/2, 1/2).

4.21 If the enthalpy of formation for a vacancy is equal to 80 kJ/mol, what is the fraction of vacant sites at 1,500 K.

4.22 The lattice parameter of a BCC crystal was measured at ambient temperature and at 1,000 °C. The parameter showed an increase of 0.5% due to

thermal expansion. In the same interval of temperature, the density, measured by a separate method, showed a decrease of 2%.

- (a) Assuming that, at room temperature, there is one vacancy per 1,000 atoms, what is the vacancy concentration at 1,000 °C?  
(b) Calculate the activation energy necessary for the production of vacancies.

4.23 The Burgers vector of a dislocation is 0.25 nm in a crystal. The shear modulus  $G = 40$  GPa. Estimate the dislocation energy per unit length in this crystal.

4.24 A dislocation is anchored between two points 10 μm distant. For a metal with  $b = 0.35$  nm and  $G = 30$  GPa, compute the shear stress necessary to bow the dislocation into a semicircle.

4.25 Consider an aluminum polycrystal with a grain size of 10 μm. If a dislocation source at the center of a grain emits dislocations under an applied shear stress of 50 MPa that pile up at the grain boundaries, what is the stress experienced by a grain boundary? Take  $G = 26$  GPa and  $b = 0.3$  nm.

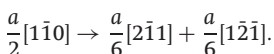
4.26

- (a) Iron ( $r = 0.124$  nm,  $G = 70$  GPa) is being deformed to a shear strain of 0.3. Assuming a constant dislocation density equal to  $10^{10}$  cm<sup>-2</sup>, what is the average distance each dislocation has to move?  
(b) Assuming that the strain rate is  $10^{-2}$  s<sup>-1</sup>, what is the average dislocation velocity?

4.27 Aluminum ( $r = 0.15$  nm,  $G = 26$  GPa) is deformed to a shear strain of 0.5. A dislocation density equal to  $10^{10}$  cm<sup>-2</sup> results.

- (a) What is the average distance each dislocation had to move?  
(b) If the strain rate were  $10^{-2}$  s<sup>-1</sup>, what would be the average dislocation velocity?

4.28 Consider the following dislocation reaction in a face-centered cubic material:



Is it energetically favorable?

4.29 Consider dislocations blocked in gold. If the flow stress is controlled by the stress necessary to operate a Frank–Read source, compute the dislocation density  $\rho$  in the crystal when it is deformed to a point where the resolved shear stress on the slip plane is 45 MPa. Take  $G = 27$  GPa.

4.30 Plot the stresses around a screw dislocation, in terms of isostress fields. Do a plot equivalent to the one in Figure 4.32 (edge dislocations).

4.31 Plot the energy of a single edge dislocation in copper as a function of dislocation density (in units of  $\text{Gb}^2$ ). Start at a density of  $10^6$  cm<sup>-2</sup>, characteristic of well-annealed material, and finish at  $10^{11}$  cm<sup>-2</sup>, characteristic of work-hardened material.

4.32 A dislocation segment is pinned by two obstacles at a distance of 10 μm. Calculate the stress required to bow this segment into a semicircle (this is equal to the stress required to activate a Frank–Read source).  $b = 0.25$  nm;  $G = 40$  GPa.

4.33 A tantalum polycrystal (grain size equal to 50 μm) is deformed to a total shear strain of 0.5 at a strain rate of 10 s<sup>-1</sup>. Assume that dislocations cannot

cross grain boundaries. Given that  $G = 10 \text{ GPa}$ ,  $b = 0.2 \text{ nm}$ , and assuming  $k = 1$ , calculate:

- (a) The dislocation density required.
- (b) The velocity at which each dislocation will move.

**4.34** On eight cubes that have a common vertex, corresponding to the origin of axes, draw the family of  $\{111\}$  planes. Show that they form an octahedron and indicate all  $<110>$  directions.

**4.35** How many vacancies per cubic centimeter are there in gold, at ambient temperature, assuming a lattice parameter of  $0.408 \text{ nm}$ ?  $G_v = 1.4 \times 10^{-19}$ .

**4.36** Burgers vector of a crystal generally lies in a close-packed direction. Why?

**4.37** What is the ideal strength of a crystalline solid? What crystal imperfection allows the material to deform at much lower strength and why?

**4.38** Do you think the addition of dislocations in a crystal changes its density? Explain your answer.

**4.39** Describe in detail the effects of quenching in comparison to furnace cooling. Which process creates higher yield stresses and why?

**4.40** In copper  $G = 48.3 \text{ GPa}$  and  $b$ , the Burgers vector, is taken to be  $0.25 \text{ nm}$ . Find (a) the force required to bend a dislocation into a radius  $R = 10 \mu\text{m}$ ; (b) the energy of this curved dislocation.

**4.41** What is the effect of misfit dislocations on film-substrate interfaces? What happens as the thickness of the film increases?

---

# Chapter 5

## Imperfections: Interfacial and Volumetric Defects

---

### 5.1 | Introduction

In Chapter 4, we dealt with point and line defects. There is another class of defects called *interfacial*, or *planar*, defects. These imperfections, as the name signifies, occupy an area or surface and so are two-dimensional, as well as being of great importance. Examples of such defects are free surfaces of a material, grain boundaries, twin boundaries, domain boundaries, and antiphase boundaries. Of all these, grain boundaries are the most important from the point of view of the mechanical properties of the material. In what follows, we consider in detail the structure of grain and twin boundaries and their importance in various deformation processes, and, very briefly, the structure of other interfacial defects. Details regarding the strengthening of a material by grain boundaries are given in Section 5.3. Volumetric defects, such as voids, also play a major role in the mechanical properties of materials, affecting the strength and elastic properties of the material significantly. Volumetric defects are briefly described in Section 5.7. In Section 5.8, we present the defects occurring in polymers.

---

### 5.2 | Grain Boundaries

Crystalline solids generally consist of a large number of grains separated by boundaries. Most industrial metals and ceramics are polycrystalline aggregates, and the mechanical properties of these polycrystals can be radically different from those of the monocrystals that form the individual grains. Figure 5.1 illustrates a polycrystalline aggregate, in which each grain has a distinct crystallographic orientation. The sizes of these individual grains vary from submicrometer (for nanocrystalline and microcrystalline structures) to millimeters and even centimeters (for materials especially processed for high-temperature creep resistance). Figure 5.2 shows typical equiaxed grain configurations for polycrystalline tantalum and titanium

**Fig. 5.1** Grains in a metal or ceramic; the cube depicted in each grain indicates the crystallographic orientation of the grain in a schematic fashion.

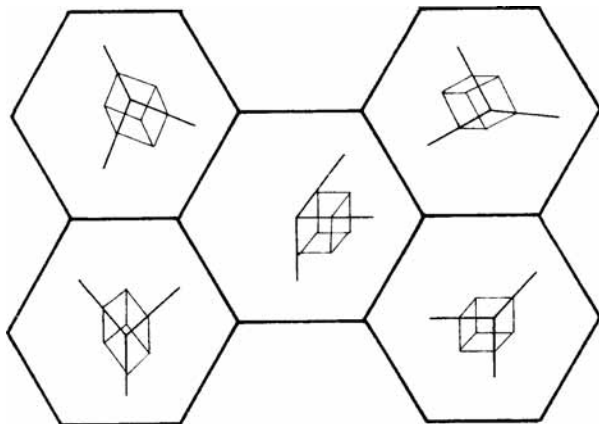
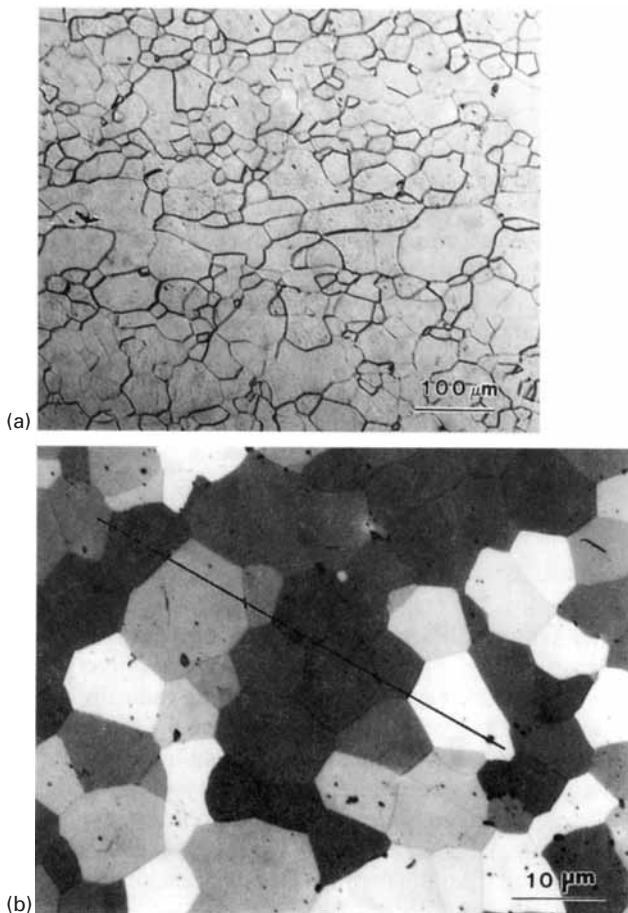


**Fig. 5.2** Micrographs showing polycrystalline (a) tantalum and (b) TiC.



carbide. Grains often are elongated through plastic deformation. Each grain (or subgrain) is a single crystal, and the grain boundaries are thus transition regions between neighboring crystals. These regions may consist of various kinds of dislocations. When the misorientation between two grains is small, the grain boundary can be described

by a relatively simple configuration of dislocations (e.g., an edge dislocation wall) and is, fittingly, called a *low-angle boundary*. When the misorientation is large (called, again appropriately, a *high-angle boundary*), more complicated structures are involved (as in a configuration of soap bubbles simulating the atomic planes in crystal lattices). A general grain boundary has five degrees of freedom. Three degrees specify the orientation of one grain with respect to the other, and two degrees specify the orientation of the boundary with respect to one of the grains.

Grain structure is usually specified by giving the average diameter or using a procedure attributed to the American Society for Testing and Materials (ASTM) according to which the grain size is specified by the number  $n$  in the expression  $N = 2^{n-1}$ , where  $N$  is the number of grains per square inch when the sample is examined at 100 power.

The ASTM procedure is common in engineering applications. In research, it is often preferred to measure the grain size by the lineal intercept technique. In this technique, lines are drawn in the photomicrograph, and the number of grain-boundary intercepts,  $N_\ell$ , along a line is counted. The mean lineal intercept is then

$$\bar{\ell} = \frac{L}{N_\ell M}, \quad (5.1)$$

where  $L$  is the length of line and  $M$  is the magnification in the photomicrograph of the material. In Figure 5.2(b), a line is drawn for purposes of illustration. The length of the line is 6.5 cm. The number of intersections,  $N_\ell$ , is equal to 7, and the magnification (obtained by using the marker of 10  $\mu\text{m}$ )  $M = 1,300$ . Thus,

$$\bar{\ell} = \frac{65 \times 10^{-3}}{7 \times 1300} = 7.1 \mu\text{m}.$$

Several lines should be drawn to obtain a statistically significant result. The mean lineal intercept  $\bar{\ell}$  does not really provide the grain size, but is related to a fundamental size parameter, the grain-boundary area per unit volume,  $S_v$ , by the equation

$$\bar{\ell} = \frac{2}{S_v}. \quad (5.2)$$

The proof of this formula is beyond the scope of this book, but is given by deHoff and Rhines.<sup>1</sup> If we assume, to a first approximation, that the grains are spherical, we have the following relationship between the grain-boundary area and volume:

$$\begin{aligned} S_v &= \frac{1}{2} \frac{4\pi r^2}{\frac{4}{3}\pi r^3} \\ &= \frac{3}{2r} = \frac{3}{D}. \end{aligned} \quad (5.3)$$

<sup>1</sup> R. T. deHoff and F. N. Rhines (eds.), *Quantitative Microscopy* (New York: McGraw-Hill, 1968).

Here,  $D$  is the average grain diameter, and the factor  $1/2$  was introduced because each surface is shared between two grains. From Equations 5.2 and 5.3, we get

$$D = \frac{3}{2}\bar{\ell},$$

which is the most correct way to express the grain size from lineal intercept measurements.

### Example 5.1

The American Society for Testing and Materials (ASTM) has a simple index, called the ASTM grain size number,  $n$ , defined as

$$N = 2^{n-1}$$

where  $N$  is the number of grains in an area of  $1 \text{ in}^2 (= 64.5 \text{ mm}^2)$  in a 100-power micrograph. In one such grain size measurement of an aluminum sample, it was found that there were 56 full grains in the area, and 48 grains were cut by the circumference of the circle of area  $1 \text{ in}^2$ . (a) Calculate ASTM grain size number  $n$  for this sample. (b) Calculate the mean lineal intercept.

**Solution:** The grains cut by the circumference of the circle are taken as one-half the number. Thus,

$$\begin{aligned} N &= 56 + 48/2 \\ &= 56 + 24 = 80 = 2^{n-1} \\ n &= \ln N / \ln 2 + 1 \\ &= \ln 80 / \ln 2 + 1 \\ &= 4.38 / 0.69 + 1 = 7.35. \end{aligned}$$

(b) For the mean lineal intercept, we use the circle:

$$\begin{aligned} \pi r^2 &= 1 \text{ in}^2, \\ r &= 0.56 \text{ in}, \\ \bar{\ell} &= \frac{2\pi r}{N_t M} = \frac{2\pi \times 0.56 \times 25.4}{48 \times 100} \\ &= 0.0186 \text{ mm} = 18.6 \mu\text{m}. \end{aligned}$$

### Example 5.2

Determine the grain size for the microstructure shown in Figure E5.2, using both the lineal intercept method and the ASTM method. The straight marks traversing the grains are annealing twins and should be

counted in the computation. From the mean lineal intercept, obtain the grain diameter.

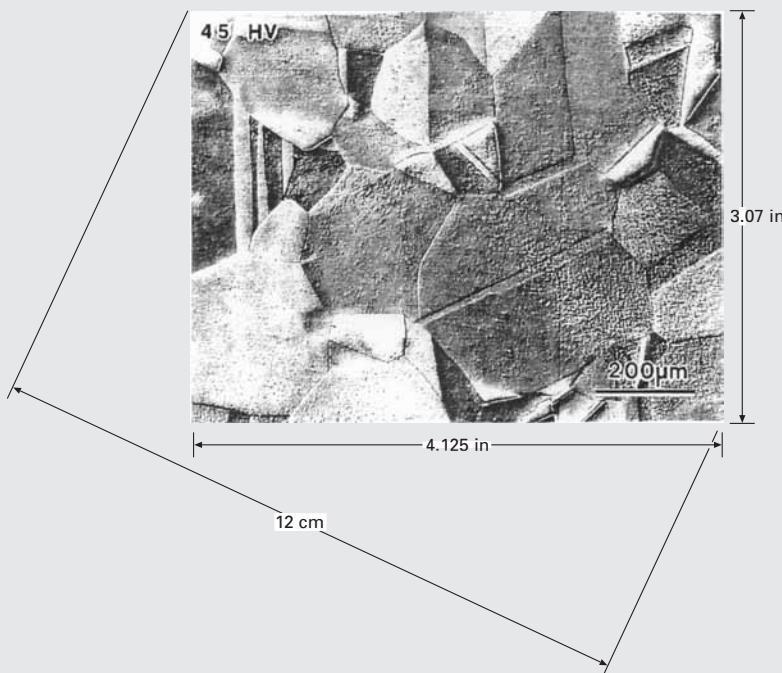


**Fig. E5.2**

**Solution:** From the ASTM method,  $N = 2^{n-1}$ , where  $N$  is the number of grains per unit area ( $\text{in}^2$ ) and  $n$  is the grain size number.

The number of grains counted is approximately 60, and the area of the picture is  $3.07 \times 4.20 = 12.90 \text{ in}^2$ . So we have

$$N = \frac{60}{12.9} = 4.65.$$

We rewrite  $N$  as  $2^{n-1}$ , and taking logarithms, we get

$$\begin{aligned}\ln N &= \ln 2^{n-1} \\ &= (n-1) \ln 2.\end{aligned}$$

So we have

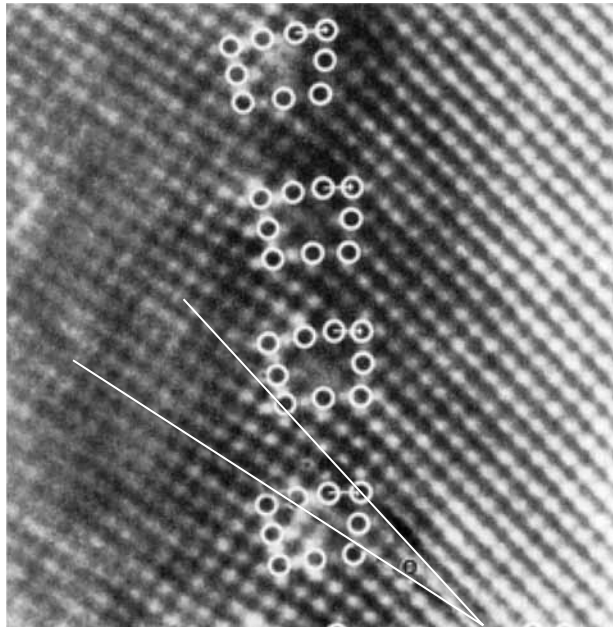
$$1.53 = (n-1) \ln 2,$$

$$n-1 = 2.24,$$

$$n \approx 3.$$

By the lineal intercept method,  $\bar{l} = L / (MN)$ , where  $M = 2 \text{ cm}/200 \mu\text{m} = 100$  is the magnification,  $L = 12 \text{ cm}$  is the straight line drawn, and

**Fig. 5.3** Low-angle grain-boundary observed by high-resolution transmission electron microscopy. Positions of individual dislocations are marked by Burgers circuits. (Courtesy of R. Gronsky.)



$N \approx 9$  is the number of intercepts (with grains). Thus, we have

$$\bar{\ell} = \frac{12}{100 \times 9} = 0.013\text{cm}$$

$$= 130 \mu\text{m}.$$

### 5.2.1 Tilt and Twist Boundaries

The simplest grain boundary consists of a configuration of edge dislocations between two grains. The misfit in the orientation of the two grains (one on each side of the boundary) is accommodated by a perturbation of the regular arrangement of atoms in the boundary region. This is very clearly seen in the high-resolution transmission electron micrograph of Figure 5.3. A low-angle grain-boundary with a misorientation  $\theta = 10^\circ$  between equivalent (100) planes is shown, and the dislocations are highlighted by circles marking their Burgers vector.

Figure 5.4 shows some vertical atomic planes terminating in a boundary, and each termination is represented by an edge dislocation. The misorientation at the boundary is related to the spacing between dislocations,  $D$ , by the relation (see triangle with dimensions)

$$D = \frac{b/2}{\sin(\theta/2)} \cong \frac{B}{\theta} \quad (\text{for very small } \theta), \quad (5.4)$$

where  $b$  is the Burgers vector.

It is instructive to calculate the spacing between dislocations in Figure 5.3 and to compare it with the measured value from the electron micrograph. We will express all values in terms of the lattice spacing along [100] directions. Let us call this value  $a$ , so that

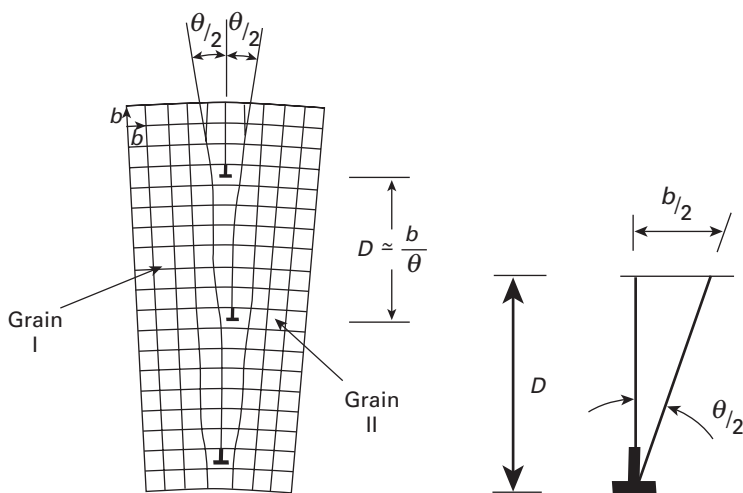


Fig. 5.4 Low-angle tilt boundary.

$$b = 1.3a.$$

The calculated dislocation spacing (from the measured angle  $\theta = 10^\circ \approx (1/6) \text{ rad}$ ) is

$$D = \frac{1.3a}{\theta} \approx 7.8a.$$

The measured dislocation spacing in Figure 5.3 is

$$D = 8a.$$

Thus, the agreement with Equation 5.4 and Figure 5.3 is excellent.

As the misorientation  $\theta$  increases, the spacing between dislocations is reduced, until, at large angles, the description of the boundary in terms of simple dislocation arrangements does not make sense. Theta becomes so large, that the dislocations are separated by one or two atomic spacings; for such small separations, the dislocation core energy becomes important and the linear elasticity does not hold. In these cases, the grain boundary is a region of severe localized disorder.

Boundaries consisting entirely of edge dislocations are called *tilt boundaries*, because the misorientations, as can be seen in Figure 5.4, can be described in terms of a rotation about an axis normal to the plane of the paper and contained in the plane of dislocations. The example shown in that figure is called a *symmetrical tilt wall*, as the two grains are symmetrically located with respect to the boundary. A boundary consisting entirely of screw dislocations is called a *twist boundary*, because the misorientation can be described by a relative rotation of two grains about an axis. Figure 5.5 shows a twist boundary consisting of two groups of screw dislocations.

It is possible to produce misorientations between grains by combined tilt and twist boundaries. In such a case, the grain boundary structure will consist of a network of edge and screw dislocations.

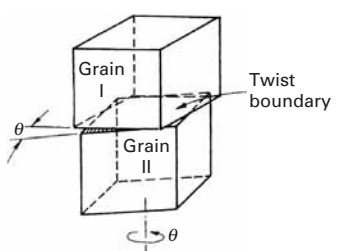


Fig. 5.5 Low-angle twist boundary.

### 5.2.2 Energy of a Grain Boundary

The dislocation model of a grain boundary can be used to compute the energy of low-angle boundaries ( $\theta \leq 10^\circ$ ). For such boundaries, the distance between dislocations in the boundary is more than a few interatomic spaces. We have

$$\frac{b}{D} \cong \theta \leq 10^\circ \cong \frac{1}{6} \text{ rad} \quad \text{or} \quad D \approx 6b,$$

and the energy of the boundary is equal to the total energy of all dislocations per unit length

$$E = E_{\perp} \left( \frac{1}{D} \right) = E_{\perp} \left( \frac{\theta}{b} \right) = \frac{\theta}{b} \left[ \frac{Gb^2}{4\pi(1-v)} \ln \frac{D}{r_0} + E_{\text{core}} \right], \quad (5.5)$$

where  $E_{\perp}$  is the strain energy per dislocation in the grain boundary. Thus, the energy of a tilt boundary is given by<sup>2</sup>

$$E = \theta \frac{Gb}{4\pi(1-v)} (-\ln \theta + A) = E = E_0 \theta (A - \ln \theta), \quad (5.6)$$

where  $A$  is a parameter that emerges in the derivation and

$$E_0 = \frac{Gb}{4\pi(1-v)}. \quad (5.7)$$

#### Example 5.3

In a low-angle tilt boundary in an aluminum sample, the misorientation is  $5^\circ$ . Estimate the spacing between dislocations in this boundary, given that  $b_{\text{Al}} = 0.29 \text{ nm}$ .

**Solution:** We have

$$b = 0.29 \text{ nm}, \theta = 5^\circ = 5/57.3 = 0.087 \text{ rad}.$$

The dislocation spacing is

$$D = b/\theta = 0.29 \text{ nm}/0.087 = 3.33 \text{ nm}.$$

#### Example 5.4

Calculate the energy of a low-angle tilt boundary in nickel as a function of the misorientation  $\theta$ , for  $0 < \theta < 10$ . For Ni,  $r = 0.125 \text{ nm}$ ,  $G = 76 \text{ GPa}$ , and  $v = 0.31$ .

**Solution:** We have

$$E = \frac{Gb}{4\pi(1-v)} \theta (A - \ln \theta).$$

<sup>2</sup> M. A. Meyers and K. K. Chawla, *Mechanical Metallurgy* (Englewood Cliffs, Prentice Hall, 1984), pp. 273-275.

We first calculate  $b$ ; we use  $a = 2r\sqrt{2}$ , and the magnitude of [100] Burgers vectors is

$$d_{[110]} = \frac{a}{\sqrt{h^2 + k^2 + l^2}} = \frac{a}{\sqrt{2}}.$$

Thus,

$$b = \frac{a}{\sqrt{2}} = 2r = 0.250 \text{ nm}$$

and

$$E = \frac{47 \times 10^9 \times 0.25 \times 10^{-9}}{4\pi(1 - 0.31)} \theta(A - \ln \theta).$$

We can assume that the dislocation energy is equal to the core energy when the separation between them is equal to  $10b$ . This is twice the core radius used by many scientists. From that value, we obtain the value of the constant of integration,  $A$ . The sequence of equations is

$$\begin{aligned} U &= \frac{Gb^2}{10} \quad \text{for } D = 10b = \frac{b}{\theta}, \\ E &= \frac{Gb^2}{10D} = \frac{Gb^2}{100b} = \frac{Gb}{100} \quad (\theta = 0.1), \\ \frac{Gb}{100} &= \frac{Gb \times 0.1}{4\pi(1 - v)}(A - \ln 0.1), \\ A &= \frac{4\pi(1 - v)}{10} + \ln 0.1 = 0.866 - 2.30, \\ &= -1.436. \end{aligned}$$

So

$$E = 2.2\theta(-1.436 - \ln \theta).$$

### Example 5.5

Calculate the dislocation spacing and energy of a low-angle tilt boundary in copper crystal if  $\theta = 0.5^\circ$ ,  $G = 48.3$  GPa,  $v = 0.343$ , and  $r_{\text{Cu}} = 0.157$  nm.

*Solution:* The spacing is

$$D = \frac{b}{\theta}.$$

For FCC copper,

$$\begin{aligned} b &= \frac{a}{\sqrt{2}}, \quad 4r_{\text{cu}} = \sqrt{2}a, \\ b &= \frac{(4/\sqrt{2})r_{\text{cu}}}{\sqrt{2}} = 2r_{\text{cu}} = 0.314 \text{ nm}, \\ \theta &= 0.5^\circ = \frac{0.5}{180}\pi = 0.0009 \text{ rad}, \\ D &= \frac{b}{\theta} = \frac{0.314}{0.0009} = 34.9 \text{ nm}. \end{aligned}$$

We next assume that  $D = 10b$ , so

$$\begin{aligned} D &= \frac{b}{\theta} = 10b \\ \theta &= 0.1. \end{aligned}$$

We thus have

$$E = E_{\perp} \left( \frac{1}{D} \right) = \frac{Gb^2}{10} \left( \frac{1}{D} \right) = \frac{Gb}{100}, \quad \theta = 0.1.$$

Also,

$$E = \frac{Gb}{4\pi(1-\nu)} \theta(A - \ln \theta).$$

Hence, setting the two equations for  $E$  equal to each other, we obtain

$$\frac{Gb}{100} = \frac{Gb}{4\pi(1-\nu)} \theta(A - \ln \theta)$$

and it follows that

$$\begin{aligned} A &= \frac{4\pi(1-\nu)}{100\theta} + \ln \theta \\ &= \frac{4\pi(1-0.343)}{100 \times 0.1} + \ln 0.1 \\ &= -1.477. \end{aligned}$$

Substituting this value of  $A$  into the second equation for  $E$  yields

$$E = \frac{Gb}{4\pi(1-\nu)} \theta(-1.477 - \ln \theta).$$

Now, given that  $G = 48.3$  GPa,  $\nu = 0.343$ , and  $\theta = 0.009$  rad, we obtain

$$\begin{aligned} E &= \frac{48.3 \times 10^9 \times 0.314 \times 10^{-9}}{4\pi(1-0.343)} \times 0.009 \times (-1.477 - \ln 0.009) \\ &= 0.053 J/m^2. \end{aligned}$$

### 5.2.3 Variation of Grain-Boundary Energy with Misorientation

Consider Equation 5.6. Because of the  $(-\ln \theta)$  term, a merger of two low-angle boundaries, forming a high-angle boundary, always results in a net decrease in the total energy of the interface. Thus, low-angle boundaries have a tendency to combine and form boundaries of large misorientation.

A plot of  $E$  versus  $\theta$  gives a curve with a maximum at  $\theta_{\max} \approx 0.5$  rad ( $\approx 30^\circ$ ). However, the dislocation model of grain boundaries loses validity at much smaller orientations ( $\theta \leq 10^\circ$ ). Some recent studies, using field-ion microscopy, have shown that the high-angle grain boundaries consist of rather large regions of atomic fit separated by regions of misfit, to which are associated the grain-boundary ledges. The boundary thickness is not more than two to three atomic diameters. Low-angle grain boundaries have a dislocation density that increases proportionally to the misorientation angle (see Equations 5.4 and 5.6), and, consequently, the energy of a low-angle boundary

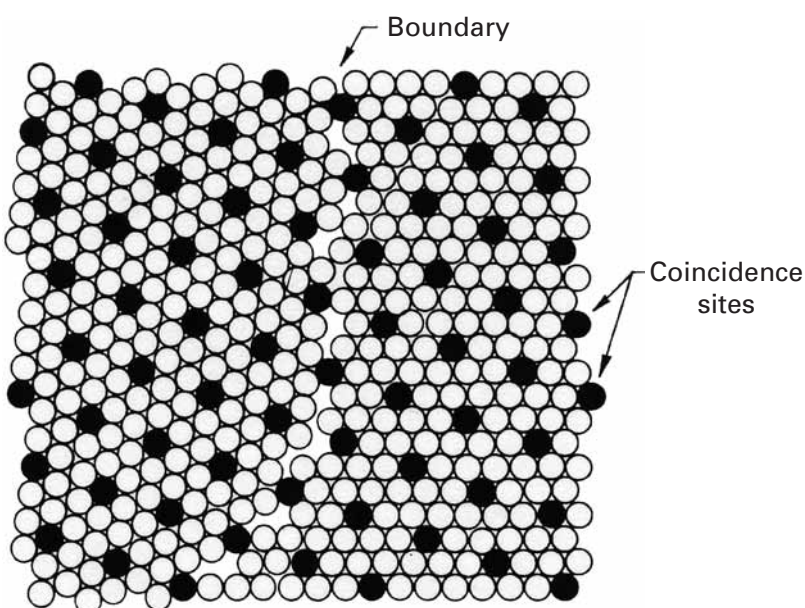
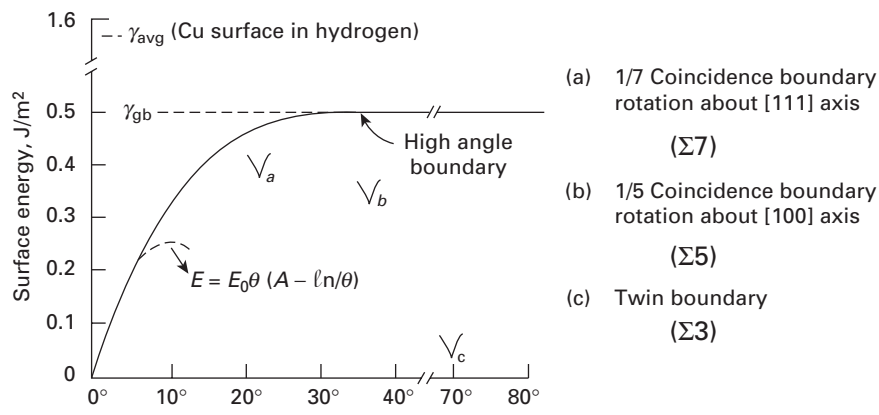


**Fig. 5.6** Variation of grain-boundary energy  $\gamma_{gb}$  with misorientation  $\theta$ . (Adapted with permission from A. G. Guy, *Introduction to Materials Science* (New York: McGraw-Hill, 1972), p. 212.)

increases linearly with  $\theta$  near  $0^\circ$ . After this, the energy increases slowly as the stress fields of adjacent dislocations interact more strongly. This behavior is shown in Figure 5.6. A surface tension,  $\gamma_{gb}$ , can be associated with an ordinary (high-angle) grain boundary, which consists of a mixture of various types of dislocations. Because the value of  $\gamma_{gb}$  is relatively high, it is instructive to determine the stable forms assumed by the grains of a given material. As it happens, there are certain special boundaries for which a particular high angle between two adjacent crystals produces a low value of  $\gamma$ . These special boundaries can be divided into two categories: coincidence boundaries and coherent twin boundaries. A coincidence boundary (Figure 5.7) is incoherent, as is an ordinary grain boundary; that is, a majority of the atoms of one crystal in the boundary do not correspond to the lattice sites of the other crystal. On an average, however, this noncorrespondence in a coincidence boundary is less as the density of coincidence sites increases. For example, in the figure, one

**Fig. 5.7** Coincidence lattice made by every seventh atom in the two grains, misoriented  $22^\circ$  by a rotation around the  $\langle 111 \rangle$  axis. (Adapted from M. L. Kronberg and H. F. Wilson, *Trans. AIME*, 85 (1949), 501.)

**Table 5.1** Some Coincidence Site Boundaries in FCC Crystals<sup>a</sup>

Rotation Axis	Rotation Angle (deg)	Density of Coincidence Sites
(111)	38	1 in 7
	22	1 in 7
	32	1 in 13
	47	1 in 19
(110)	39	1 in 9
	50.5	1 in 11
	26.5	1 in 19
(100)	37	1 in 15

<sup>a</sup> Reprinted with permission from J. W. Christian, *The Theory of Transformation in Metals and Alloys* (Elmsford, NY: Pergamon Press, 1965), p. 326.

atom in seven in the boundary is in a lattice position for both the crystals. We call this boundary a *one-seventh coincidence boundary*, and the atomic sites (the black atoms in the figure) in question form a coincidence lattice for the two grains. Coincidence lattices occur in all common crystalline structures and have a density of sites varying from  $\frac{1}{3}$  to  $\frac{1}{9}$  and less.

A twin boundary is frequently a kind of coincidence boundary, but it is convenient to treat it separately. The energy of a twin boundary,  $\gamma_{\text{twin}}$ , is generally about 0.1  $\gamma_{\text{gb}}$  (see Figure 5.6), whereas the energy of a coincidence boundary is only slightly less than  $\gamma_{\text{gb}}$ . The two most common twin orientations are (1) rotation twins (coincidence), produced by a rotation about a direction  $[hkl]$  called the twinning axis, and (2) reflection twins, in which the two lattices maintain a mirror symmetry with respect to a plane  $[hkl]$  called the twinning plane.

Some of the orientations that give the highest density of coincidence lattice sites in crystals are shown in Table 5.1. These boundaries have lower energies than those of random high-angle boundaries. Contrary to the great majority of low-energy boundaries, coincidence site boundaries have greater mobility than that of random boundaries. Twin boundaries, even with low energies, have lower mobility because they are coherent.

The interfaces between different phases (interphase interfaces) are more complex, since the accommodation of the atoms has to be more drastic. Nevertheless, strong interfaces can be formed, even between different ceramic phases. An illustration of this is provided in Figure 5.8, which shows the interface between alumina (hexagonal) and the spinel structure ( $\text{NiAl}_2\text{O}_4$ ). In ceramics, the requirement of electrical charges puts additional restrictions on the boundaries. Nevertheless, the boundary shown in Figure 5.8(a) and the atomic positions clearly marked in Figure 5.8(b) are of high coherence.

### 5.2.4 Coincidence Site Lattice (CSL) Boundaries

It is instructive to consider some other important aspects of coincidence site lattice (CSL) boundaries. As described earlier, we get a CSL

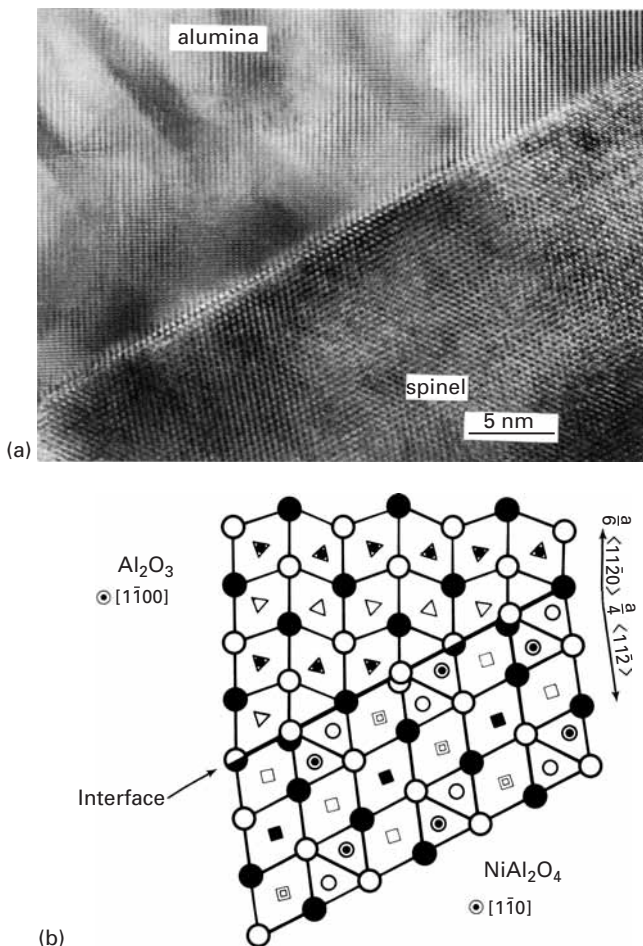
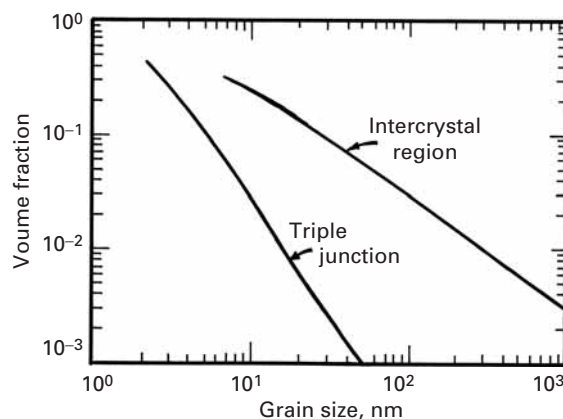


**Fig. 5.8** Interface between alumina and  $\text{NiAl}_2\text{O}_4$  (spinel). (a) High-resolution TEM. (b) Representation of individual atomic positions. (Courtesy of C. B. Carter.)

boundary when a certain rotation of one grain relative to another grain results in a three-dimensional atomic pattern in which a certain fraction of lattice points coincide in the two grains. The volume of the CSL primitive cell is a small multiple of the volume of the lattice primitive cell. Such a CSL boundary is characterized by a parameter  $\Sigma$ , the reciprocal of the fraction of lattice sites that coincide (in Table 5.1,  $\Sigma = 7, 9, 13, 15, 19$ ). Equivalently,  $\Sigma$  is the ratio of the volume of the CSL primitive cell to that of the lattice primitive cell. A coherent twin boundary is  $\Sigma 3$ . It has been observed that CSL grain boundaries with relatively low values of  $\Sigma$  can have a significant influence on the mechanical behavior of a polycrystalline material. CSL boundaries with small values of  $\Sigma$  result in short-period ordered structures in the grain boundary. CSL boundaries with  $\Sigma$  less than 29 show the following advantages over random grain boundaries or boundaries with higher  $\Sigma$  values:

- lower grain boundary energy in pure metals
- lower diffusivity
- lower electrical resistivity
- lower susceptibility to solute segregation

**Fig. 5.9** The effect of grain size on calculated volume fractions of intercrystal regions and triple junctions, assuming a grain boundary thickness of 1 nm. (Adapted from B. Palumbo, S. J. Thorpe, and K. T. Aust, *Scripta Met.*, 24 (1990) 1347.)



- greater resistance to grain boundary sliding, fracture, and cavitation
- greater resistance to initiation of localized corrosion
- greater boundary mobility with specific solutes in a specific concentration range.

It would thus appear that control of the character and density of low- $\Sigma$  boundaries can be a means of producing a superior polycrystalline material.

### 5.2.5 Grain-Boundary Triple Junctions

Grain-boundary triple junctions are sites where four grains or three grain boundaries meet. Such boundaries are commonly observed in crystalline materials. The number of triple junctions can have a great influence on the mechanical properties of the material. The number of triple junctions in a polycrystalline material will depend on the grain size and crystal geometry of the material. Palumbo *et al.*<sup>3</sup> considered a three-dimensional distribution of tetrakaidecahedral grains and obtained the volume fractions of intercrystalline region (grain-boundary) and triple-boundary junctions. Figure 5.9 shows the effect of grain size on calculated volume fractions of these entities. Note the highly pronounced effect for grain sizes less than 20 nm, i.e., in the nanometer range.

### 5.2.6 Grain-Boundary Dislocations and Ledges

Various experimental observations of the structure of grain boundaries have demonstrated the existence of grain-boundary dislocations (GBDs) when the orientation relations deviate from the ideal coincidence lattice site orientations. A grain-boundary dislocation belongs to the grain boundary and is not a common lattice dislocation.

Grain-boundary dislocations can acquire the geometry of a grain-boundary ledge by grouping together. This agglomeration, which leads to the formation of a step, is shown in Figure 5.10. Figure 5.10(a)

<sup>3</sup> B. Palumbo, S. J. Thorpe, and K. T. Aust, *Scripta Met.*, 24 (1990) 1347.

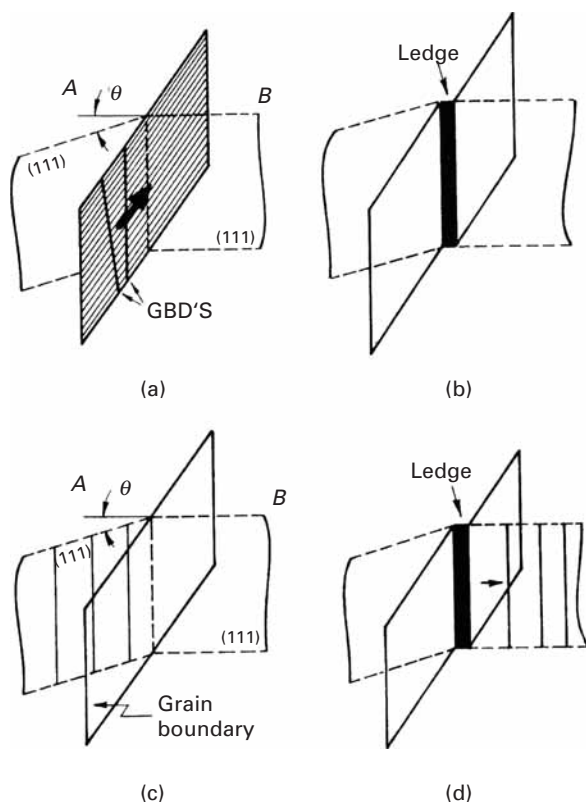


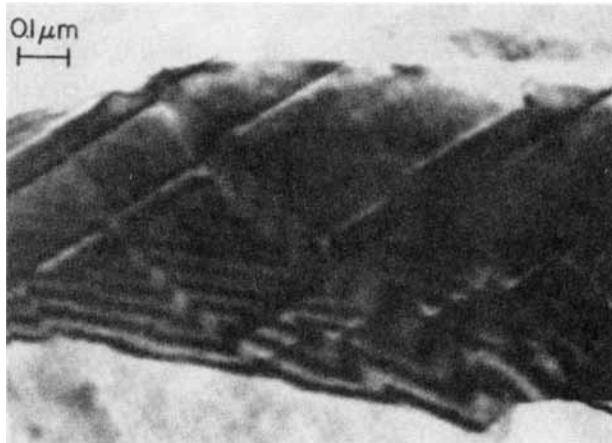
**Fig. 5.10** Models of ledge formation in a grain boundary.  
 (Reprinted with permission from L. E. Murr, *Interfacial Phenomena in Metals and Alloys* (Reading, MA: Addison Wesley, 1975), p. 255.)

shows the movement of GBDs along the grain-boundary plane in the direction indicated by the arrow. Figure 5.10(b) shows the coalescence of GBDs to make a grain-boundary ledge. Another way of ledge formation is shown in Figures 5.10(c) and (d). Under the applied tension, lattice dislocations can move from grain A through the boundary plane to grain B (Figure 5.10(c)). The passage through the boundary results in heterogeneous shear of the boundary, forming a ledge.

The distinction between a ledge and an intrinsic GBD is one of height; the smallest ledge corresponds to a GBD. Detailed analyses showing how slip can transfer from one grain to another via the formation of intrinsic GBDs have been carried out. Figure 5.11 shows a TEM that reveals ledges and GBDs. The larger steps can be considered ledges, whereas the lines could be GBDs.

In the simplified situation shown in Figure 5.10, the (111) planes of the neighboring grains intersect along the boundaries. Ledges in the grain boundaries constitute an important structural characteristic of the high-angle boundaries. It has been observed that the density of ledges increases with an increase in the boundary misorientation. One of the important aspects of this structure of boundaries is that the ledges can function as effective sources of dislocations, a fact that has important implications for the mechanical properties of polycrystals.

**Fig. 5.11** Grain boundary ledges observed by TEM. (Courtesy of L. E. Murr.)



### 5.2.7 Grain Boundaries as a Packing of Polyhedral Units

The grain-boundary structure can also be described in terms of a packing of polyhedral units. If equal spheres are packed to form a shell such that all spheres touch their neighbors, then the centers of the spheres are at the vertices of a “deltahedron,” a polyhedron with equilateral triangles as faces. Ashby *et al.*<sup>4</sup> regard a crystal as a regular packing of polyhedral holes. The FCC structure, for example, consists of a regular packing of tetrahedra and octahedra. The main advantage of such a description of the structure is that it remains valid even when the structure becomes completely disordered (i.e., amorphous). Any grain boundary between metallic crystals can be described in terms of this scheme as a packing of eight basic deltahedra. Ashby *et al.*’s model is able to describe a number of properties associated with grain boundaries – for example, the segregation of certain elements to the boundaries, the characteristically high diffusion rates in the boundaries, and grain-boundary faceting in the presence of impurities. Figure 5.12(a) shows an image-enhanced transmission electron micrograph of a symmetric tilt boundary in gold. The angle  $\theta$  between the [110] directions in the two grains is approximately  $32^\circ$ . The boundary can be represented (as shown in Figure 5.12(b)) as an array of polyhedra. The figure represents the atomic positions along two planes (“+” and “●”) of the TEM of Figure 5.12(a).

---

## 5.3 | Twinning and Twin Boundaries

There are two types of twin boundaries: deformation twins and annealing twins. A brief description of deformation twins follows.

---

<sup>4</sup> M. F. Ashby, F. Spaepen, and S. Williams, *Acta Met.*, 26 (1978) 1053.

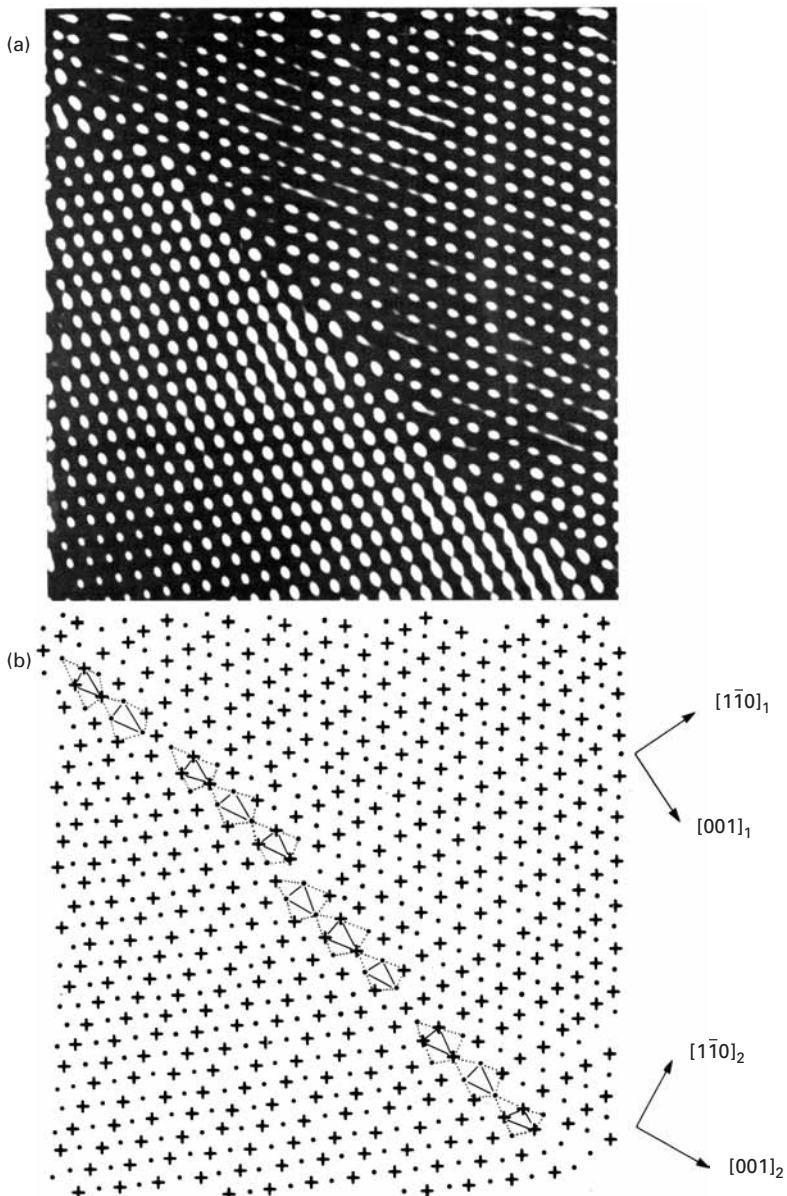


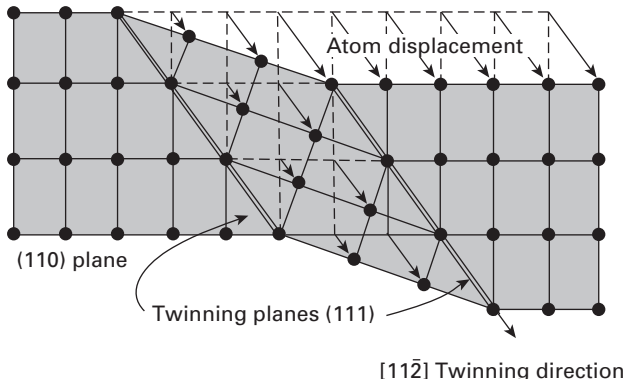
**Fig. 5.12** Image and atomic position model of an approximately  $32^\circ$   $[1\bar{1}0]$  tilt boundary in gold; note the arrangement of polygons, which represents the boundary. (From W. Krakow and D. A. Smith, *J. Mater. Res.* 22 (1986) 54.)

### 5.3.1 Crystallography and Morphology

Deformation or mechanical twinning is the second most important mechanism of plastic deformation after slip, although it is not nearly as common as slip. The crystallographic nature of deformation twins is shown in Figure 5.13. When a crystal deforms plastically by twinning, atomic displacements occur, as shown in the figure, which give rise to crystal bands within the grain that are twin oriented. Hexagonal metals, such as Zn and Mg, behave in this way when they are deformed at ambient temperatures, while BCC metals, such as

**Table 5.2** Twinning Planes, Directions, and Shears

Structure	Twin Plane and Direction	Shear Strain, $\gamma$
FCC	(111)[11̄2]	0.707
BCC	(11̄2)[111]	0.707
HCP	(10̄12) [10̄1̄1]	{ Cd: 0.171 Zn: 0.139 Mg: 0.129 Ti: 0.139 Be: 0.199}

**Fig. 5.13** Schematic of twinning in FCC metals.

iron, show this behavior when they are deformed at subambient temperatures. This mechanism is not of great importance in the deformation of FCC metals. The twin planes, twin vectors, and the shear produced by them are given in Table 5.2 for FCC, BCC, and HCP crystals.

Figures 5.14(a) and (b) show deformation twins in Fe-Si and tungsten, respectively. It is clear that twins are crystallographically oriented along specific planes. Figure 5.14(b) shows several grains, as well as the twins that extend, at most, from grain boundary to grain boundary. A few of them are marked by arrows and number 2. They cannot propagate through grain boundaries because of the crystallographic requirements. The sagacious reader will note that there is a mixture of microcracks and deformation twins in the figure, but this issue will not be discussed.

Figure 5.15 illustrates the formation of deformation twins in ceramics. A grain of silicon nitride subjected to compressive loading is imaged in Figure 5.15(a). The diffraction pattern (the spots in Figure 5.15(c)) reveals more than one crystallographic orientation. It is possible, by focusing on only one family of reflections, to image one family of twins. This is shown in Figure 5.15(b). All the bright twins in this dark-field image have the same orientation.

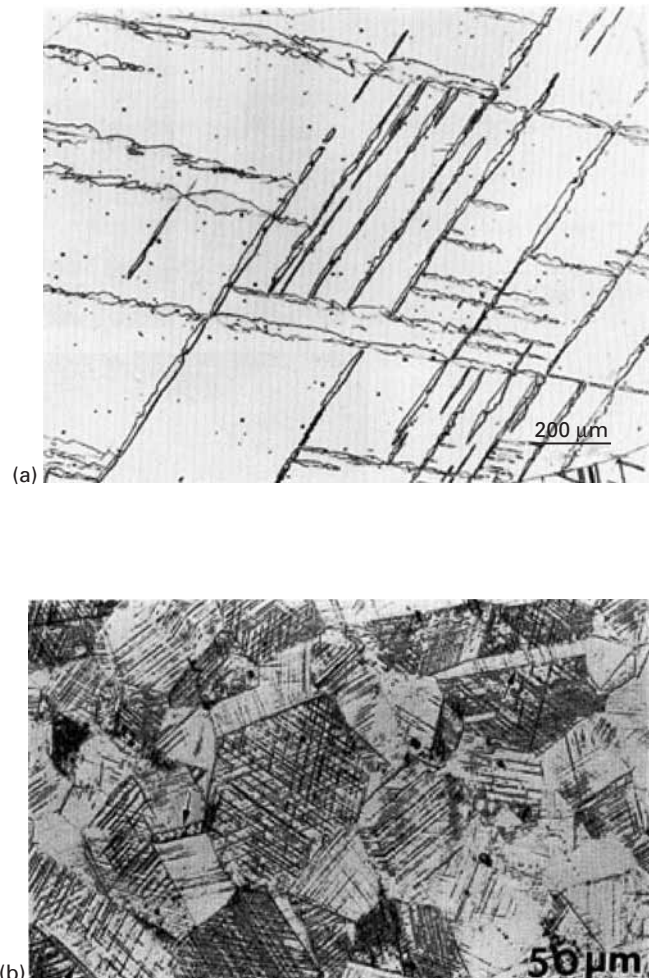


**Fig. 5.14** Deformation twins in (a) iron–silicon (courtesy of O. Vöhringer) and (b) tungsten.

The mechanism of plastic deformation by twinning is very different from that of slip. First, the twinned region of a grain is a mirror image of the original lattice, while the slipped region has the same orientation as that of the original, unslipped grain. Second, slip consists of a shear displacement of an entire block of crystal, while twinning consists of uniform shear strain. Third, the slip direction can be positive or negative (i.e., in tension or compression), while the twinning direction is always polar. Twinning results in a change of shape of a definite type and magnitude, as determined by the crystallographic nature of the twinning elements.

The stress necessary to form twins is, generally, greater, but less sensitive to temperature, than that necessary for slip. This stress required to initiate twinning is much larger than the stress necessary for its propagation. Deformation twinning occurs when the

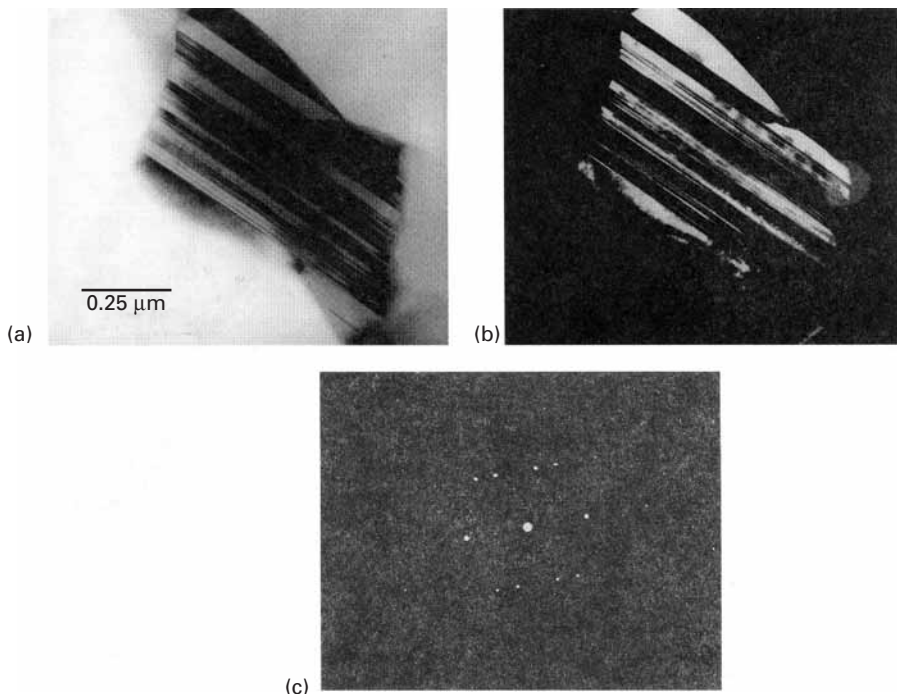


**Fig. 5.15** Deformation twins in silicon nitride observed by TEM. (a) Bright field. (b) Dark field. (c) Electron diffraction pattern showing spots from two twin variants, A and B. (Courtesy of K. S. Vecchio.)

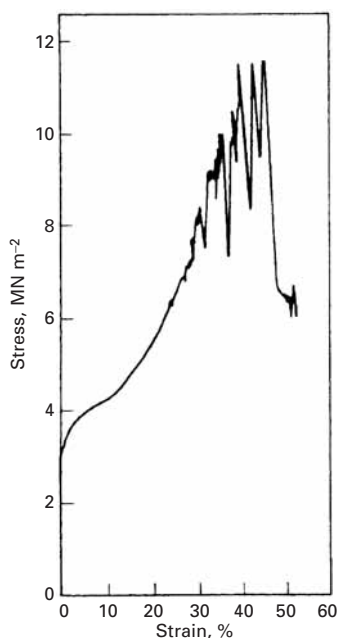


**Fig. 5.16** Serrated stress-strain curve due to twinning in a Cd single crystal. (Adapted with permission from W. Boas and E. Schmid, *Z. Phys.*, 54 (1929) 16.)

applied stress is high due to work-hardening, low temperatures, or, in the case of HCP metals, when the resolved shear stress on the basal plane is low. Copper and other FCC metals can be made to deform by twinning at very low temperatures or at very high strain rates. Deformation twins, however, play an important role in the straining of HCP metals. The “cry” heard when a polycrystalline sample of tin is bent plastically is caused by the sudden formation of deformation twins. The bursting of twins during straining can lead to a serrated form of stress-strain curve (Figure 5.16). In many HCP metals, the slip is restricted to basal planes. Thus, twinning can contribute to plastic deformation by the shear that it produces, but this is generally small. (See Table 5.2.) More importantly, the twinning process serves to reorient the crystal lattice to favor further basal slip. In HCP metals, the common twinning elements are the  $(10\bar{1}2)$  plane and  $[10\bar{1}\bar{1}]$  direction (see Figure 5.17). Twinning results in a compression or elongation along the  $c$ -axis, depending on the ratio  $c/a$ . For  $c/a > \sqrt{3}$  (the case of Zn and Cd), twinning occurs on  $(10\bar{1}\bar{2})$   $[10\bar{1}\bar{1}]$  when the metal is compressed along the  $c$ -axis. When  $c/a > \sqrt{3}$ , the twinning shear is zero. For  $c/a < \sqrt{3}$  (the case of Mg and Be), twinning occurs under tension along the  $c$ -axis. Figure 5.17 shows this dependence on the ratio  $c/a$ .

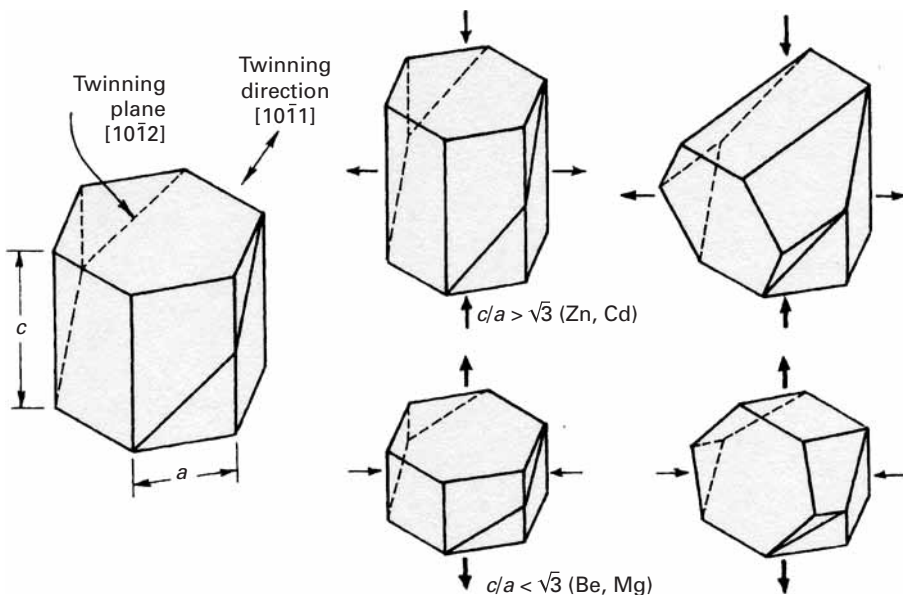


**Fig. 5.17** Twinning in HCP metals with  $c/a$  ratio more or less than  $\sqrt{3}$ .

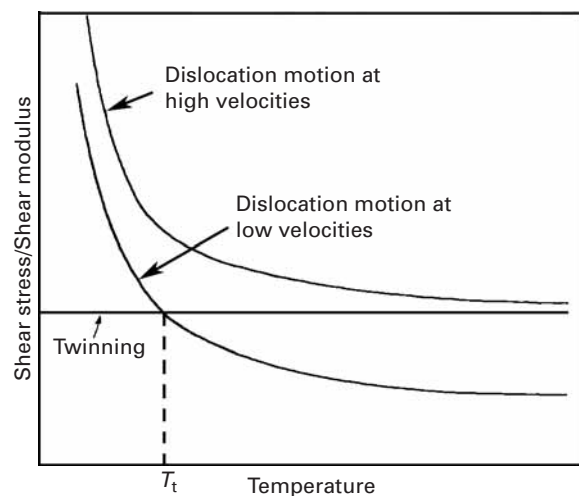
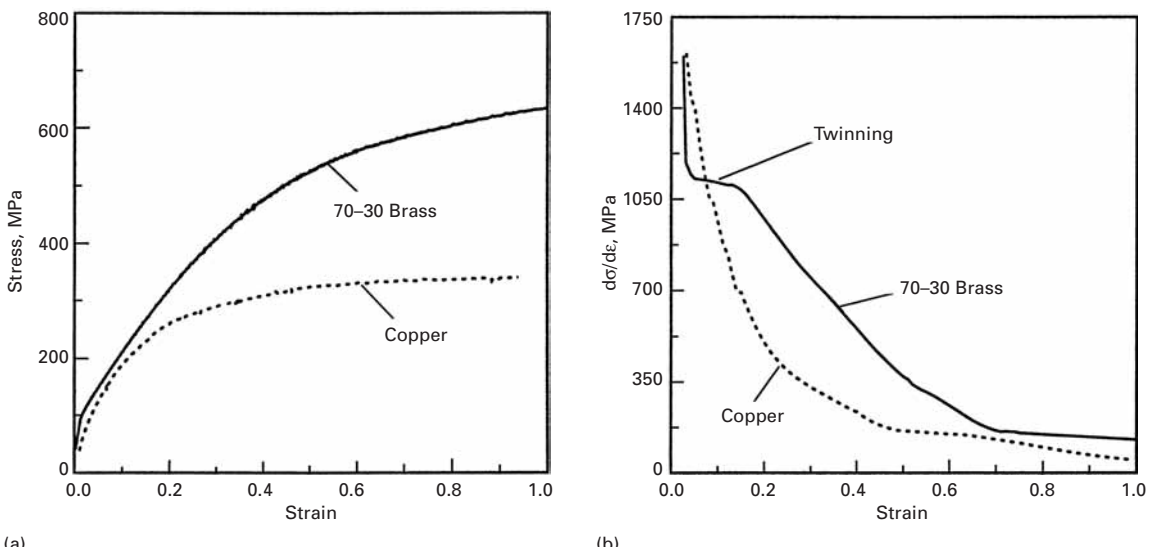


**Fig. 5.18** Effect of temperature on the stress required for twinning and slip (at low and high strain rates). (Courtesy of G. Thomas.)

### 5.3.2 Mechanical Effects

One may regard slip and twinning as competing mechanisms; experimentally, it has been found that either an increase in strain rate or a decrease in temperature tends to favor twinning over slip. In this context, the graphical scheme proposed by G. Thomas and presented in Figure 5.18 is helpful. The low temperature dependence of the stress required to initiate twinning is a strong indication that it is not a thermally activated mechanism. Hence,  $\tau/G$  for twinning is not temperature dependent. On the other hand, the thermally activated dislocation motion becomes very difficult at low temperatures;  $T_t$  is



(a)

(b)

**Fig. 5.19** (a) Stress–strain curves for copper (which deforms by slip) and 70% Cu–30% Zn brass (which deforms by slip and twinning). (b) Work-hardening slope  $d\sigma/d\varepsilon$  as a function of plastic strain; a plateau occurs for brass at the onset of twinning. (After S. Asgari, E. El-Danaf, S. R. Kalidindi, and R. D. Doherty, *Met. and Mater. Trans.*, 28A (1997) 1781.)

the temperature below which the material will yield by twinning in conventional deformation. However, at high strain rates, dislocation generation and dynamics are such that the whole curve is translated upward, while the twinning curve is stationary, for reasons that will be given later. As a consequence, the intersection of the two curves takes place at a higher temperature.

As the stacking-fault energy of an alloy is decreased, the propensity for twinning increases. The addition of zinc to copper decreases the stacking-fault energy dramatically, from 78 mJ/m<sup>2</sup> (for pure Cu) to 7 mJ/m<sup>2</sup> (for 75–25 brass). This leads to a much greater planarity of slip, which eventually results in twinning. Twinning generates internal barriers to slip and breaks down a material's microstructure into progressively smaller domains. The result is an increase in work-hardening; that is, the movement of dislocations is hampered. Figure 5.19(a) illustrates this effect. The work-hardening rate of copper decreases with plastic strain, in the expected fashion, while brass, in which twinning is prevalent, shows an almost constant work-hardening, over a significant plastic strain range. The onset of twinning is clearly seen in the plateau of the work-hardening rate, in Fig 5.19(b).

As shown in Figure 5.18, the twinning stress seems to be quite insensitive to the temperature. Figure 5.20 shows the twinning stress for a number of metals. The stress required for slip, on the other hand, is quite sensitive to temperature; see Figure 5.18.

Mechanical twinning is, in FCC metals, quite sensitive to the stacking-fault energy. The stress required for twinning increases as the stacking-fault energy is increased. Figure 5.21 shows the twinning stress for a number of copper alloys. The following relationship is obeyed between the twinning stress,  $\sigma_T$ , and the stacking-fault energy,  $\gamma_{SF}$ :

$$\sigma_T = K \left( \frac{\gamma_{SF}}{Gb} \right)^{1/2},$$

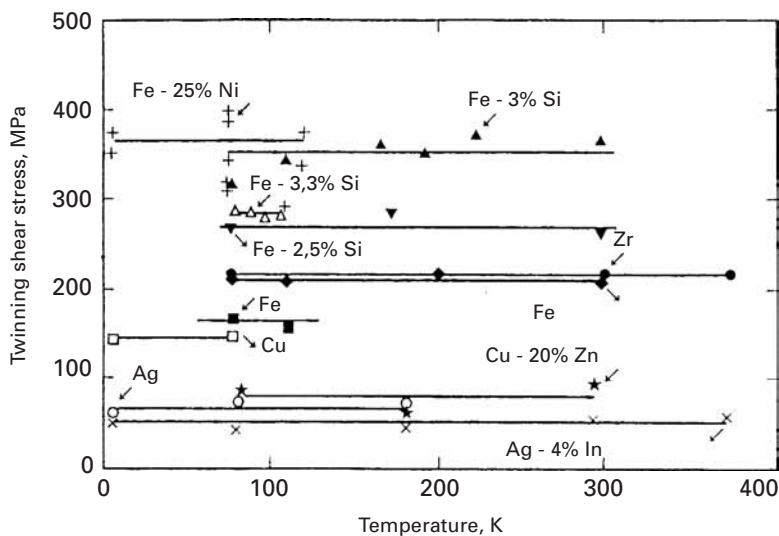


**Fig. 5.20** Effect of temperature on twinning stress for a number of metals. (From M. A. Meyers, O. Voehringer, and V. A. Lubarda, *Acta Mater.*, 49 (2001) 4025.)

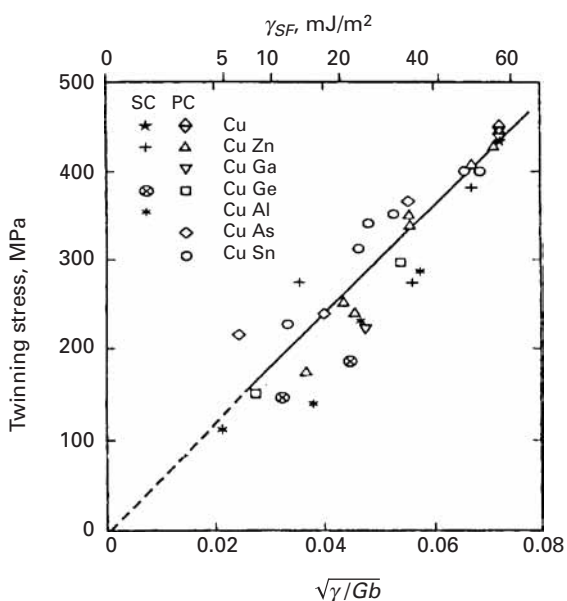


**Fig. 5.21** Effect of stacking-fault energy on the twinning stress for several copper alloys. (From M. A. Meyers, O. Voehringer, and V. A. Lubarda, *Acta Mater.*, 49 (2001) 4025.)

where  $G$  is the shear modulus,  $b$  is the Burgers vector, and  $K$  is a constant.

By setting the twinning stress equal to the slip stress, one can obtain the domains in which twinning and slip are prevalent as a function of grain size, stacking-fault energy, etc. For the strain rate, temperature, and grain size dependence of the slip stress, we use constitutive equations such as the Johnson-Cook equation (Section 3.2). One sets the slip stress,  $\sigma_s$ , equal to the twinning stress:

$$\sigma_T = \sigma_s.$$

The application of this equation for titanium with different grain sizes provides the plot shown in Figure 5.22(a). The lines in the

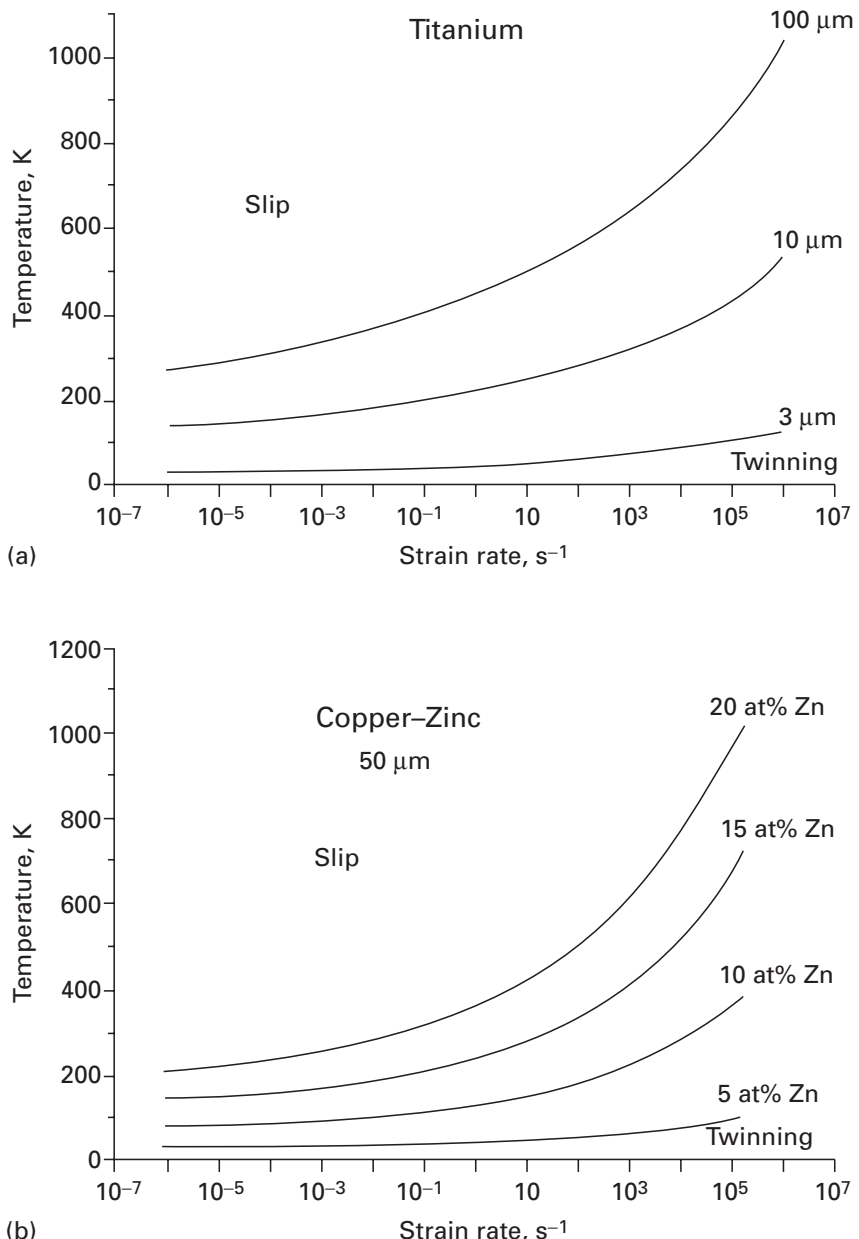


**Fig. 5.22** Temperature-strain rate plots with slip and twinning domains; (a) effect of grain size in titanium; (b) effect of stacking-fault energy in copper-zinc alloys. (From M. A. Meyers, O. Voehringer, and V. A. Lubarda, *Acta Mater.*, 49 (2001) 4025.)

plot separate the twinning and slip domains. As the strain rate is increased, the maximum temperature for twinning is increased. The same plot shows the effect of grain size (different lines). As the grain size is decreased, the twinning domain decreases. Figure 5.22(b) shows the effect of stacking-fault energy on the domains. This is done for a monocrystalline copper-zinc alloy. The stacking-fault energy decreases with increasing zinc content. Whereas the Cu-20 at% Zn alloy twins at ambient temperature and low strain rate, it is necessary to apply a very high strain rate at a low temperature to trigger twinning in a Cu-5 at% Zn alloy.

## 5.4 Grain Boundaries in Plastic Deformation (Grain-Size Strengthening)

Grain boundaries have a very important role in the plastic deformation of polycrystalline materials. The following are among the more important aspects of this role.

1. At low temperatures ( $T < 0.5T_m$ , where  $T_m$  is the melting point in K), the grain boundaries act as strong obstacles to dislocation motion. Mobile dislocations can pile up against the boundaries and thus give rise to stress concentrations that can be relaxed by initiating locally multiple slip.
2. There exists a condition of compatibility among the neighboring grains during the deformation of polycrystals that is, if the development of voids or cracks is not permitted, the deformation in each grain must be accommodated by its neighbors.<sup>5</sup> This accommodation is realized by multiple slip in the vicinity of the boundaries, which leads to a high strain-hardening rate. It can be shown, following von Mises, that for each grain to stay in contiguity with others during deformation, at least five independent slip systems must be operating. (See Section 6.2.5.) This condition of strain compatibility leads a polycrystalline sample to have multiple slip in the vicinity of grain boundaries. The smaller the grain size, the larger will be the total boundary surface area per unit volume. In other words, for a given deformation in the beginning of the stress-strain curve, the total volume occupied by the work-hardened material increases with decreasing grain size. This implies a greater hardening due to dislocation interactions induced by multiple slip.
3. At high temperatures, the grain boundaries function as sites of weakness. Grain boundary sliding may occur, leading to plastic flow or opening up voids along the boundaries. (See Chapter 13.)
4. Grain boundaries can act as sources and sinks for vacancies at high temperatures, leading to diffusion currents, as, for example, in the Nabarro-Herring creep mechanism. (See Chapter 13.)
5. In polycrystalline materials, the individual grains usually have a random orientation with respect to one another. Frequently, however, the grains of a material may be preferentially oriented. For example, an Fe-3% Si solid-solution alloy, used for electrical transformer sheets because of its excellent magnetic properties, has grains with their {110} planes nearly parallel and their <100> direction along the rolling direction of the sheet. This material is said to have a *texture* or *preferred orientation*. A preferred orientation of grains is also frequently observed in drawn wires.

<sup>5</sup> J. P. Hirth, *Met. Trans.* 3 (1972) 3047.

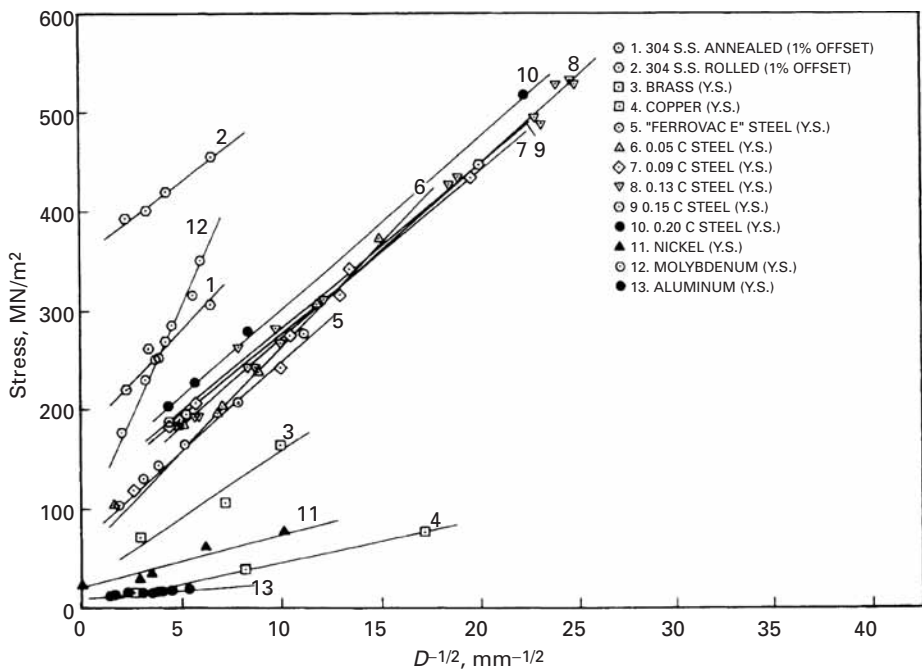


**Fig. 5.23** Hall-Petch plot for a number of metals and alloys. Y. S. indicates yield strength.

Ever since Hall and Petch<sup>6</sup> introduced their well-known relationship between the lower yield point of low-carbon steels and grain size, a great deal of effort has been devoted to explaining that relationship from a fundamental point of view and applying it to the yield and flow stress of different metals and alloy systems. The Hall-Petch (H-P) equation has the form

$$\sigma_y = \sigma_0 + kD^{-1/2}, \quad (5.8)$$

where  $\sigma_y$  is the yield stress,  $\sigma_0$  is a frictional stress required to move dislocations,  $k$  is the H-P slope, and  $D$  is the grain size. This equation has been applied to many systems, with varying degrees of success. It seems to be a satisfactory description of the dependence of yield stress on grain size when a somewhat limited range of grain sizes is being investigated. Figure 5.23 illustrates the Hall-Petch equation for several metals. BCC and FCC metals exhibiting smooth elastic-plastic transitions and yield points are represented. Table 5.3 presents the parameters for a number of metals.

Figure 5.24 shows the yield strength of iron over a much wider range than that presented in Figure 5.23. The plot is of the Hall-Petch line (full line) and the upper bound (theoretical strength, assumed to be  $E/30$ ), as well as the lower bound (single crystal). Substantial deviations from a single Hall-Petch curve that has approximately the slope for ferrovac E steel and 0.05C steel are observed. The very broad range of grain sizes is the reason for the deviation. Thus, the Hall-Petch

<sup>6</sup> E. O. Hall, Proc. Roy. Soc. (London) B64 (1951) 474; N. J. Petch, J. Iron Steel Inst. 174 (1953) 25.

**Table 5.3** Tabulation of  $\sigma_0$  and  $k$  Values for BCC, FCC, and HCP Structures<sup>a</sup>

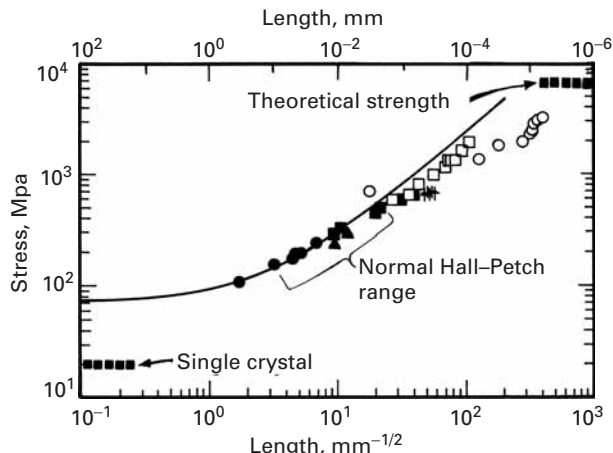
Material Specification <sup>b</sup>	$\sigma_0$ (MPa)	$k$ (MN/m <sup>3/2</sup> )
Body-Centered Cubic		
Mild steel, y.p.	70.60	0.74
Mild steel, $\varepsilon = 0.10$	294.18	0.39
Swedish iron, y.p.	47.07	0.71
Swedish iron, no y.p.	36.28	0.20
Fe-3% Si, y.p., -196 °C	505.99	1.54
Fe-3% Si, twinning, -196 °C	284.37	3.32
Fe-18% Ni, $\varepsilon = 0.002$	650.14	0.22
Fe-18% Ni, twinning, -196 °C	843.32	1.30
FeCo, ordered, $\varepsilon = 0.004$	50.01	0.90
FeCo, disordered, $\varepsilon = 0.004$	319.68	0.33
Chromium, y.p.	178.47	0.90
Chromium, twinning, -196 °C	592.52	4.37
Molybdenum, y.p.	107.87	1.77
Molybdenum, $\varepsilon = 0.10$	392.24	0.53
Tungsten, y.p.	640.33	0.79
Vanadium, y.p.	318.70	0.30
Niobium, y.p.	68.64	0.04
Tantalum, with O <sub>2</sub> , y.p. 0 °C	186.31	0.64
Face-Centered Cubic		
Copper, $\varepsilon = 0.005$	25.50	0.11
Cu-3.2% Sn, y.p.	111.79	0.19
Cu-30% Zn, y.p.	45.11	0.31
Aluminum, $\varepsilon = 0.005$	15.69	0.07
Aluminum, fracture, 4K	539.33	1.67
Al-3.5% Mg, y.p.	49.03	0.26
Silver, $\varepsilon = 0.005$	37.26	0.07
Silver, $\varepsilon = 0.002$	23.53	0.17
Silver, $\varepsilon = 0.20$	150.03	0.16
Hexagonal Close- Packed		
Cadmium, $\varepsilon = 0.001$ , -196 °C	17.65	0.35
Zinc, $\varepsilon = 0.005$ , 0 °C	32.36	0.22
Zinc, $\varepsilon = 0.175$ , 0 °C	71.58	0.36
Magnesium, $\varepsilon = 0.002$	6.86	0.28
Magnesium, $\varepsilon = 0.002$ , -196 °C	14.71	0.47
Titanium, y.p.	78.45	0.40
Zirconium, $\varepsilon = 0.002$	29.42	0.25
Beryllium, y.p.	21.57	0.41

<sup>a</sup> Adapted with permission from R. W. Armstrong, in *Advances in Materials Research*, Vol. 5, R. F. Bunshah, ed. (New York: Wiley-Interscience, 1971),

p. 101.

<sup>b</sup> y.p. = yield point.

**Fig. 5.24** Hall-Petch plot for iron and low-carbon steel extending from monocrystal to nanocrystal; notice the change in slope. (After T. R. Smith, R. W. Armstrong, P. M. Hazzledine, R. A. Masumura, and C. S. Pande, *Matls. Res. Soc. Symp. Proc.*, 362 (1995) 31.)



behavior should be considered not a universal law, but an approximation over a limited range of grain sizes. Since most engineering alloys have grain sizes in the range 10–100  $\mu\text{m}$ , the Hall-Petch equation is indeed very useful.

The principal theories advanced to explain the Hall-Petch relationship are presented next. The first two theories have lost a lot of their credibility, because dislocation pileups are not thought to be as important as they used to be, especially in high-stacking-fault energy materials.

#### 5.4.1 Hall-Petch Theory

The basic idea behind the separate propositions of Hall and Petch is that a dislocation pileup can “burst” through a grain boundary due to stress concentration at the head of the pileup. If  $\tau_a$  is the resolved shear stress applied on the slip plane, then the stress acting at the head of a pileup containing  $n$  dislocations is  $n\tau_a$  (Equation 4.26). The number of dislocations in a pileup depends on the length of the pileup, which, in turn, is proportional to the grain diameter  $D$ . According to Eshelby *et al.*<sup>7</sup> (see Equation 4.26(a)):

$$L = \frac{\alpha n G b}{\pi \tau_a}. \quad (5.9)$$

In this equation we have added a geometrical constant  $\alpha$  which is equal to unity for screw dislocations and equal to  $1(1 - \nu)$  for edge dislocations. If the source of the dislocation pileup is located at the centre of the grain, then  $L = D/2$ .

If  $\tau_c$  is the critical stress required to overcome the grain-boundary obstacles, then the dislocations of the pileup will be able to traverse the grain boundary if

$$n\tau_a \geq \tau_c. \quad (5.10)$$

<sup>7</sup> J. D. Eshelby, F. C. Frank, and F. R. N. Nabarro, *Phil. Mag.* 42 (1951) 351.

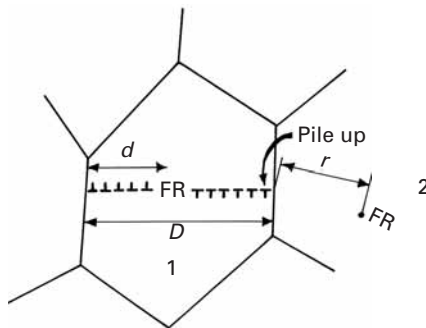


**Fig. 5.25** Frank-Read source operating in center of grain 1 and producing two pileups at grain boundaries; the Frank-Read source in grain 2 is activated by stress concentration.

From Equation 5.9

$$\frac{\alpha D \tau_a}{2G b / \pi} \tau_a \geq \tau_c, \quad \text{or} \quad \frac{\alpha \pi D \tau_a^2}{2G b} \geq \tau_c.$$

In order to take into account the friction stress  $\tau_0$  needed to move the dislocations in the absence of any obstacle, we have to add the term  $\tau_0$ . Thus,

$$\tau_a \geq \tau_0 + k D^{-1/2}. \quad (5.11)$$

Equation 5.11 is essentially identical to Equation 5.8, once the shear stresses are converted into normal stresses. Note that Eshelby's equation is valid only for a large number of dislocations; hence, the equation is not applicable to grain sizes below a few micrometers.

### 5.4.2 Cottrell's Theory

Cottrell<sup>8</sup> used a somewhat similar approach to that of Hall and Petch; however, he recognized that it is virtually impossible for dislocations to "burst" through boundaries. Instead, he assumed that the stress concentration produced by a pileup in one grain activated dislocation sources in the adjacent grain. Figure 5.25 shows how a Frank-Read source at a distance  $r$  from the boundary is activated by the pileup produced by a Frank-Read source in the adjacent grain. The slip band blocked in the boundary was treated by Cottrell as a shear crack. The maximum shear stress at a distance  $r$  ahead of a shear crack is given by

$$\tau = (\tau_a - \tau_0) \left( \frac{D}{4r} \right)^{1/2},$$

where  $\tau_0$  is the frictional stress required to move dislocations and  $r < D/2$ . The stress required to activate the Frank-Read source in the neighboring grain is given by

$$\tau_c = (\tau_a - \tau_0) \left( \frac{D}{4r} \right)^{1/2},$$

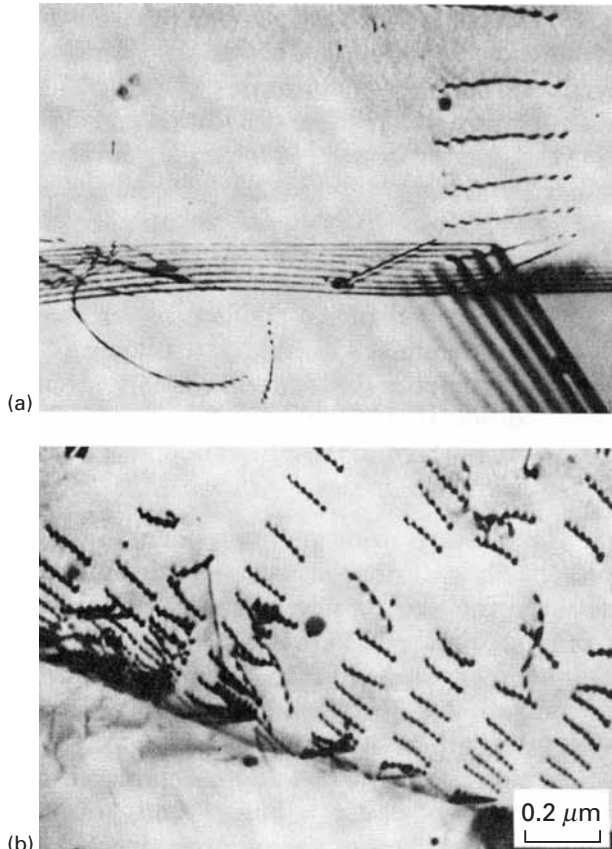
or

$$\tau_a = \tau_0 + 2\tau_c r^{1/2} D^{-1/2}.$$

This equation is of a Hall-Petch form.

<sup>8</sup> A. H. Cottrell, *Trans. TMS-AIME*, 212 (1958) 192.

**Fig. 5.26** Dislocation activity at grain boundaries in AISI 304 stainless steel ( $\dot{\epsilon} = 10^{-3} \text{ s}^{-1}$ ). (a) Typical dislocation profiles after a strain of 0.15%. (b) Same after a strain of 1.5%. (Courtesy of L. E. Murr.)



### 5.4.3 Li's Theory

Li<sup>9</sup> used a different approach to obtain a relationship between the yield stress and grain size. Instead of using pileups, he considered the grain boundary to be a source of dislocations. The concept of grain-boundary dislocation sources is discussed in Section 4.4.8, and it is thought that the onset of yielding in polycrystals is associated with the activation of these sources. Li suggested that the grain-boundary ledges generated dislocations, "pumping" them into the grain. Figure 5.26 shows dislocation activity in stainless steel in the grain-boundary regions. These patterns can be interpreted as being due to dislocation pileups or dislocation emission from grain-boundary ledges. Such dislocations act as Taylor (Section 4.4.10) "forests" in regions close to the boundary. The yield stress is, according to Li, the stress required to move dislocations through these "forests." For many metals, the flow stress is related, under most conditions, to the dislocation density by the relationship (Section 6.3)

$$\tau = \tau_0 + \alpha G b \sqrt{\rho}, \quad (5.12)$$

<sup>9</sup> J. C. M. Li, *Trans. TMS-AIME*, 227 (1963) 239.

where  $\tau_0$  is the friction stress,  $\alpha$  is a numerical constant, and  $\rho$  is the dislocation density. At this point, use was made of the experimental observation:  $\rho$  was taken to be inversely proportional to the grain diameter  $D$ . Li rationalized this as follows: The ledges “pump” dislocations into the grains. The number of dislocations generated per unit deformation is proportional to the number of ledges, or to the grain-boundary surface per unit volume, assuming the same ledge density per unit area for different grain sizes. That is,

$$\rho \propto S_v. \quad (5.13)$$

Equation 5.3 shows that the grain boundary surface per unit volume,  $S_v$ , is inversely proportional to  $D$ . Thus:

$$\rho \propto \frac{1}{D}. \quad (5.14)$$

Substituting Equation 5.14 into Equation 5.12, we obtain

$$\tau = \tau_0 + G b D^{-1/2}.$$

Again, this is a Hall-Petch equation.

#### 5.4.4 Meyers–Ashworth Theory

There have been other proposals, including one by Meyers and Ashworth,<sup>10</sup> who analyzed elastic and plastic incompatibility stress between neighboring grains. Stress concentrations occur at grain boundaries during elastic loading because the strains have to be compatible. For metals having anisotropy ratios different from unity (see Chapter 2, Equation 2.17), the Young's moduli in different directions are different. For example, for nickel,

$$\begin{aligned} E[100] &= 137 \text{ GPa}, \\ E[110] &= 233 \text{ GPa}, \\ E[111] &= 303 \text{ GPa}. \end{aligned}$$

The incompatibility stresses were calculated by Meyers and Ashworth by finite element analysis and found to be

$$\tau_I = 1.37\sigma_{AP},$$

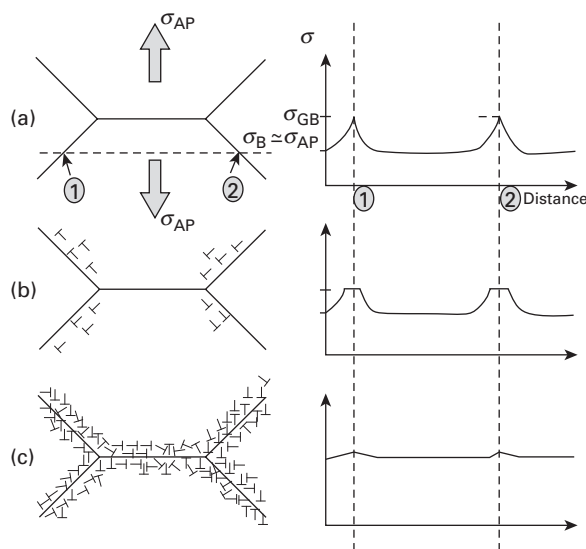
where  $\sigma_{AP}$  is the normal stress applied to the specimen. Hence, the interfacial shear stress due to the incompatibility is almost three times higher than the resolved shear stress homogeneously applied on the grain ( $\tau_H = \sigma_{AP}/2$ ). This means that dislocation activity at the grain boundary starts before dislocation activity at the center of the grains.

When the stress reaches the critical level required for emission, localized plastic deformation will start (Figure 5.27(b)). These dislocations do not propagate throughout the grain, for two reasons:

---

<sup>10</sup> M. A. Meyers and E. Ashworth, *Phil. Mag.*, 46 (1982) 737.

**Fig. 5.27** Sequence of stages in (a) polycrystalline deformation, starting with (b) localized plastic flow in the grain-boundary regions (microyielding), forming (c) a work-hardened grain-boundary layer that effectively reinforces the microstructure.



1. The stress decreases rapidly with distance from the grain boundary.
2. The center of the grains is under homogeneous shear stress control, which is maximum at  $45^\circ$  to the tensile axis. On the other hand, the interfacial and homogeneous shear stresses have different orientations. Figure 5.27 shows how the dislocations emitted from the grain boundaries will undergo cross-slip. Extensive cross-slip and the generation of dislocation locks will result in a localized layer with high dislocation density.

The plastic flow of the grain-boundary region attenuates the stress concentration; geometrically necessary dislocations accommodate these stresses (Figures 5.27(b) and (c)). This marks the onset of microyielding. The dislocations do not propagate throughout the whole grain, because of cross-slip induced by the difference in orientation between the maximum shear stress (due to the applied load) and the stress concentration due to elastic incompatibility. The work-hardened grain-boundary layer has a flow stress  $\sigma_{GB}$ , while the bulk has a flow stress  $\sigma_B$  ( $\sigma_{GB} > \sigma_B$ ). The material behaves, at increasing applied loads, as a composite made out of a continuous network of grain-boundary film with flow stress  $\sigma_{GB}$  and of discontinuous “islands” of bulk material with flow stress  $\sigma_B$ . The increasing applied stress  $\sigma_{AP}$  does not produce plastic flow in the bulk in spite of the fact that  $\sigma_{AP} > \sigma_B$ , because the continuous grain-boundary network provides rigidity to the structure. The total strain in the continuous grain-boundary network does not exceed 0.005, since it is elastic; hence, plastic deformation in the bulk is inhibited. This situation can be termed “plastic incompatibility.”

When the applied load is such that the stress in the grain-boundary region becomes equal to  $\sigma_{GB}$ , plastic deformation re-establishes itself in this region. The plastic deformation of the continuous matrix results in increases in stress in the bulk with plastic

flow (Figure 5.27(c)). This marks the onset of *macroyielding*. After a certain amount of plastic flow, dislocation densities in the bulk and grain-boundary regions become the same; then, since both regions have the same flow stress, plastic incompatibility disappears, and we have  $\sigma_{AP} = \sigma_{GB} = \sigma_B$ .

One arrives at a relationship

$$\sigma_y = \sigma_B + 8k(\sigma_{GB} - \sigma_B)D^{-1/2} - 16k^2(\sigma_{GB} - \sigma_B)D^{-1}. \quad (5.15)$$

The last term becomes important at small grain sizes and decreases the slope.

### Example 5.6

If you could produce AISI 1020 steel with a grain size of 50 nm, what would be the expected yield stress, assuming a Hall-Petch response? (Use data from Figure 5.23.)

**Solution:** The Hall-Petch equation for this problem is  $\sigma_y = \sigma_0 + kD^{-1/2}$ . From Figure 5.23

$$\sigma_0 = 120 \text{ MPa},$$

$$k = 18 \text{ MPa/mm}^{1/2} = 0.56 \text{ MN/m}^{3/2}.$$

Therefore,

$$\begin{aligned} \sigma &= (120 \times 10^6) + (0.56 \times 10^6) \times (50 \times 10^{-9})^{-1/2} \\ &= 2.65 \times 10^9 \text{ Pa} \\ &= 2.65 \text{ GPa}. \end{aligned}$$

## 5.5 | Other Internal Obstacles

There are other internal obstacles to the motion of dislocations that may have an effect analogous to grain boundaries. Examples are cell walls and deformation twins. These barriers were studied by several investigators, and their effect on flow stress may be represented by the general equation

$$\sigma_f = \sigma_0 + K \Delta^{-m}, \quad (5.16a)$$

where the coefficient  $m$  has been found to vary between  $\frac{1}{2}$  and 1. If we want to include the effects of both grain size and substructure refinement due to the internal barriers, we can use the following overall equation, which describes the response of the material reasonably well:

$$\sigma_f = \sigma_0 + K_1 D^{-1/2} + K_2 \Delta^{-m}. \quad (5.16b)$$

**Fig. 5.28** Deformation twins in shock-loaded nickel (45 GPa peak pressure; 2  $\mu$ s pulse duration). Plane of foil (100); twinning planes (111) making 90°. (Courtesy of L. E. Murr.)

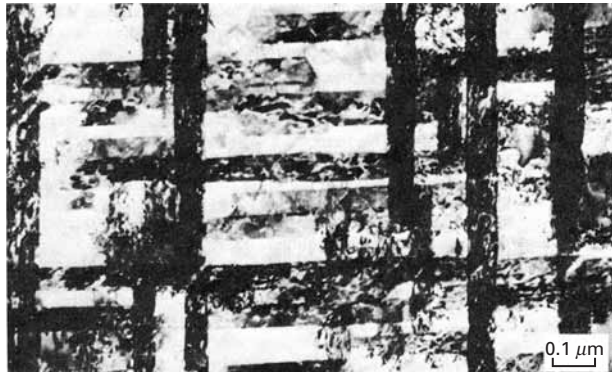


**Fig. 5.29** Strength of wire-drawn and recovered Fe-0.003% C as a function of transverse lineal-intercept cell size. Recovery temperatures (in °C) as indicated. (Adapted with permission from H. J. Rack and M. Cohen, in *Frontiers in Materials Science: Distinguished Lectures*, L. E. Murr, ed. (New York: M. Dekker, 1976), p. 365.)

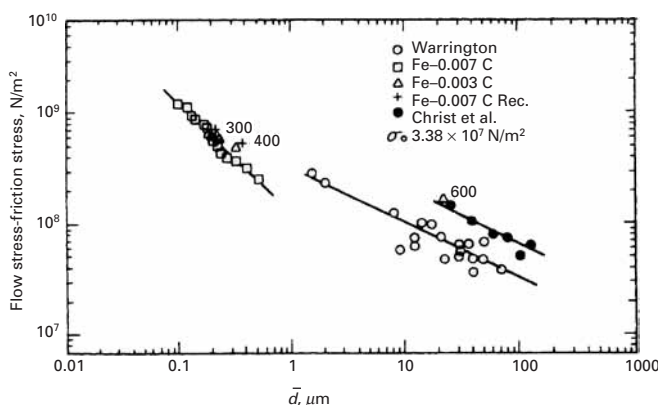


Figure 5.28 shows an example of substructural refinement in nickel. The twins were induced by shock loading at 45 GPa and 2  $\mu$ s. It is easy to understand why these obstacles strengthen the metal. Dislocation movement occurring in subsequent deformation by, say, tensile testing is severely hampered by all such planar obstacles. Internal cells are also very effective barriers.

The effect of the dislocation cell size on the flow stress of highly cold-worked low-carbon steel wire is shown in Figure 5.29. The straining to high levels was accomplished by wire drawing, and the material was recovered and showed thin cell walls and virtually dislocation-free cell interiors. The slope in the log-log plot is  $-1$ , and we have, consequently,

$$\log(\sigma_f - \sigma_0) - \log(\sigma_1 - \sigma_0) = -1(\log \bar{d} - \log \bar{d}_1), \quad (5.17)$$

where this equation expresses the straight line passing through  $(\sigma_f - \sigma_0, \bar{d})$  and  $(\sigma_1 - \sigma_0, \bar{d}_1)$ . Notice that the ordinate in Figure 5.26 is  $\sigma - \sigma_0$ . Manipulation of Equation 5.17 will yield

$$\log \frac{(\sigma_f - \sigma_0)}{(\sigma_f - \sigma_0)} = \log \left( \frac{\bar{d}}{\bar{d}_1} \right)^{-1}.$$

Hence,

$$\sigma_f - \sigma_0 = \frac{\sigma_1 - \sigma_0}{\bar{d}_1^{-1}} \bar{d}^{-1} = K \bar{d}^{-1}.$$

$$\sigma_f = \sigma_0 + K \bar{d}^{-1}.$$

On the other hand, when the annealings were done at 600 °C and above, recrystallization took place, and the group of points on the right side of the plot were found. The slope was decreased to  $-\frac{1}{2}$ , leading to a regular Hall-Petch relationship.

In low-carbon steels, the yield stress is strongly dependent on grain size; a steel with a grain size of 0.5 mm and  $\sigma_y$  of 104 MN/m<sup>2</sup> has its yield stress increased to approximately 402 MN/m<sup>2</sup> when the grain size is reduced to 0.005 mm. As the carbon content is increased and the steel tends more and more toward eutectoid, other effects, such as the ferrite–pearlite ratio, the spacing of cementite layers in the pearlite, and the size of the pearlite colonies, become important parameters. Gladman, McIvor, and Pickering<sup>11</sup> developed an expression for pearlite–ferrite mixtures, namely,

$$\sigma_y(\text{ksi}) = f_\alpha^{1/3}[2.3 + 3.81(\% \text{ Mn}) + 1.13D^{-1/2}] + (1 - f_\alpha^{1/3})[11.6 + 0.25S_0^{-1/2}] + 4.1(\% \text{ Si}) + 27.6(\sqrt{\% \text{ N}}),$$

where  $f_\alpha$  is the ferrite fraction,  $D$  is the ferrite grain size (in mm),  $S$  is the interlamellar spacing in pearlite (in mm), and % Mn, Si, and N are the weight percentages of manganese, silicon, and nitrogen, respectively.

Hyzak and Bernstein<sup>12</sup> proposed the following equation for fully pearlitic steels:

$$\sigma_y(\text{MPa}) = 2.18 S^{-1/2} - 0.40 P^{-1/2} - 2.88 D^{-1/2} + 52.30.$$

Here,  $S$  is the pearlite interlamellar spacing,  $P$  is the pearlite colony size, and  $D$  is the austenite grain size. (The units of  $S$ ,  $P$ , and  $D$  are not given by Hyzak and Bernstein, but should be cm.)

## 5.6 | Nanocrystalline Materials

Since 1985, a great deal of research has been devoted to materials containing grain sizes in the nanometer range. These materials possess mechanical, magnetic, and electronic properties that are quite different from those of conventional crystalline materials ( $10 \mu\text{m} \leq d \leq 300 \mu\text{m}$ ). It is clear that high strength levels can be achieved through reductions in grain size. Another beneficial effect is an enhanced deformability of ceramics, due to the large grain-boundary interface. A strength level of 4,000 MPa was obtained in a drawn steel that had a grain size of 10 nm (0.01 μm).

<sup>11</sup> T. Gladman, I. D. McIvor, and R. E. Pickering, *J. Iron Steel Inst.*, 210 (1972) 916.

<sup>12</sup> J. M. Hyzak and I. M. Bernstein, *Met. Trans.*, 7A (1976) 1217.

**Fig. 5.30** Gleiter representation of atomic structure of a nanocrystalline material; white circles indicate grain-boundary regions. (Courtesy of H. Gleiter.)

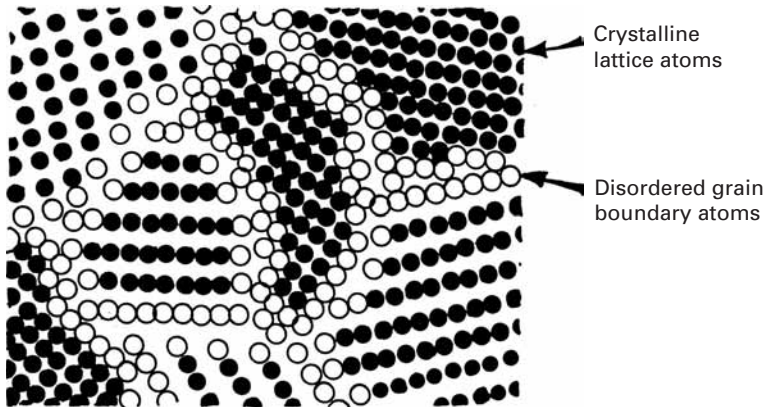


Figure 5.30 shows the schematic atomic structure of a nanocrystalline material. The atoms in the centers of the crystals (black circles) have a crystalline periodic arrangement. The configuration was developed by Gleiter, based on a Morse potential fitted to gold. At the boundaries, the spacings are altered. Thus, nanocrystalline materials can be considered a new class of disordered materials created by having a sizeable fraction of the atoms at disordered sites. The boundary region is characterized by a lower atomic density, and this is indeed a characteristic of nanocrystalline materials (between 75 and 90% of the crystalline density). The densities of nanocrystalline materials vary from 83–96% for Pd and 72–97% for Cu. In conjunction with the lower density, the Young's modulus of nanocrystalline materials is also lowered. For Cu and Pd (with theoretical values of Young's modulus  $E$  of 120–130 GPa), the reported  $E$  value in the nanocrystalline state is 21–66 GPa.

Two principal methods are used to produce these nanocrystalline materials:

1. Evaporation of metal from melt and condensation on to a “cold finger;” this nanosized powder is subsequently densified by pressing.
2. Extreme mechanical deformation of powders in, for instance, a ball-milling machine. Hard spheres impinge upon powders numerous times until a saturation of defects occurs, causing recrystallization.

There are also other techniques: molecular beam epitaxy, rapid solidification from melt, reactive sputtering, sol-gel, electrochemical deposition, and spark erosion.

The mechanical properties of nanocrystalline materials are quite distinct from those of conventional polycrystalline materials. A simple extrapolation using the Hall-Petch equation would predict extraordinarily high values of the yield stress. For example, copper with a grain size of 25 nm should have a yield stress of 720 MPa (data extrapolated from Table 5.3). Indeed, experimental results, shown in Figure 5.31, show a very high yield stress ( $\sim 185$  MPa). However, a

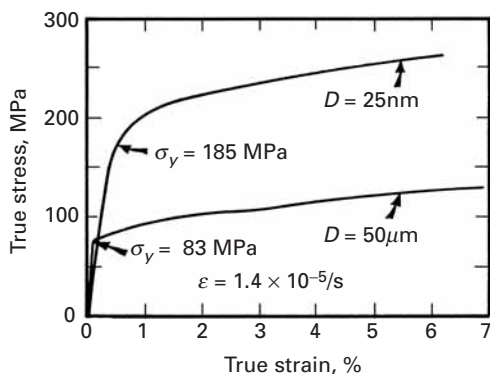


**Fig. 5.31** Stress-strain curves for conventional ( $D = 50 \mu\text{m}$ ) and nanocrystalline ( $D = 25 \mu\text{m}$ ) copper. (Adapted from G. W. Nieman, J. R. Weertman, and R. W. Siegel, *Nanostructured Materials*, I (1992) 185.)

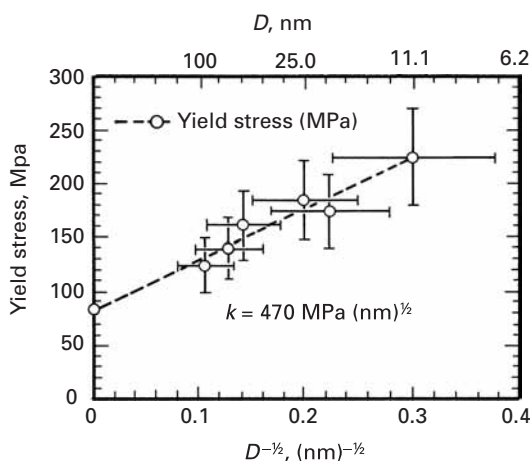


**Fig. 5.32** Hall-Petch relationship for nanocrystalline copper. (After G. W. Nieman, J. R. Weertman, and R. W. Siegel, *Nanostructured Matls.*, I (1992) 185.)

simple extrapolation using the Hall-Petch equation does not predict quantitatively correct results. The Hall-Petch slope decreases as the grain size is decreased. Figure 5.32 shows the Hall-Petch relationship obtained in the nanocrystalline regimen (grain sizes between 10 and 100 nm). The slope  $k$  is equal to  $470 \text{ MPa} \sqrt{\text{nm}}$ . This can be converted into  $0.014 \text{ MN/m}^{3/2}$ . There has been considerable discussion as to the nature of the strength of nanocrystals. Some of the ideas<sup>13,14,15</sup> that have been bandied about are briefly presented in the following list.

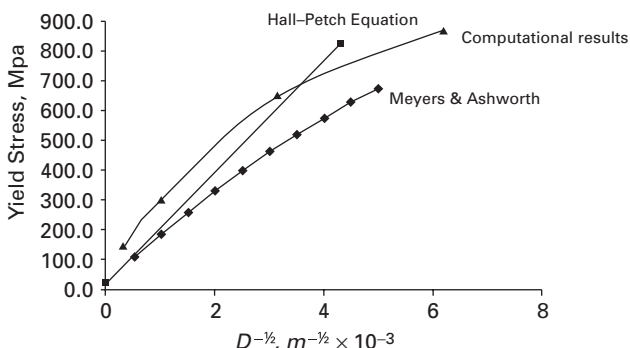
1. *Dislocation pileups.* There is a minimum number of dislocations below which the equation for the stress concentration is no longer operative.
2. *Dislocation network models.* Models such as Li's or Meyers and Ashworth's use dislocation networks within the grain-boundary regions as the parameters determining the effects of grain size. Chang and Koch<sup>13</sup> and Scattergood and Koch<sup>14</sup> addressed these

<sup>13</sup> J. S. C. Chang and C. C. Koch, *Scripta Met. Mat.*, 24 (1990) 1599.

<sup>14</sup> R. O. Scattergood and C. C. Koch, *Scripta Met. Mat.*, 27 (1992) 1195.

<sup>15</sup> M. A. Meyers, A. Mishra, and D. J. Benson, *Prog. Mater. Sci.*, 51 (2006) 427.

**Fig. 5.33** Classical Hall-Petch slope compared with Meyers and Ashworth equation and computations assuming a grain-boundary region and grain interior with different work-hardening curves. As grain size is decreased, grain-boundary region gradually dominates the deformation process. (From H.-H. Fu, D. J. Benson, and M. A. Meyers, *Acta Mater.*, 49 (2001) 2567.)



phenomena and proposed that, below a critical grain size  $D_c$ , a dislocation-network mechanism controlled the flow stress. Meyers and Ashworth's formulation predicted a decrease in the Hall-Petch slope for smaller grain sizes, in line with experimental observations. Their theory is based on the formation of a hardened region along the grain boundaries (Section 5.4.4).

3. *Grain-boundary sliding.* In the nanocrystalline domain, sliding along grain boundaries becomes a significant component of plastic deformation for  $D < 10$  nm.

The incorporation of the  $D^{-1}$  term into the Hall-Petch equation that was carried by Meyers and Ashworth, and is described in Section 5.4.4, leads to results that are shown in Figure 5.33. The  $D^{-1}$  term in Equation 5.15 is negative and produces a gradual decrease in the slope of the Hall-Petch curve. This is evident from the plot in Figure 5.33, made by the application of Equation 5.15.

The same curvature was obtained by means of computational modeling carried out by Fu *et al.*<sup>16</sup> These calculations were made for grains as small as 26 nm. Figure 5.33 also shows the classical Hall-Petch slope for the micrometer-sized grains. It is a straight line. The slopes predicted from Equation 5.15 and from the computational prediction decrease with decreasing grain size and the yield stress approaches a saturation value as the grain size is reduced.

When the grain size is smaller than 10 nm, other processes start operating; grain-boundary sliding becomes important, as pointed out above, and some researchers have even reported a negative Hall-Petch slope.

## 5.7 | Volumetric or Tridimensional Defects

Voids and inclusions are among the principal tridimensional defects in materials. Inclusions are often produced in metals by the accidental incorporation of slag or pieces of refractory bricks into the melt or

<sup>16</sup> H.-H. Fu, D. J. Benson, and M. A. Meyers, *Acta Mater.*, 49 (2001) 2567.

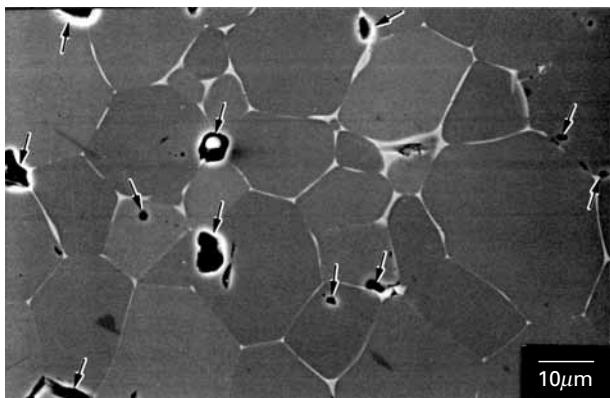
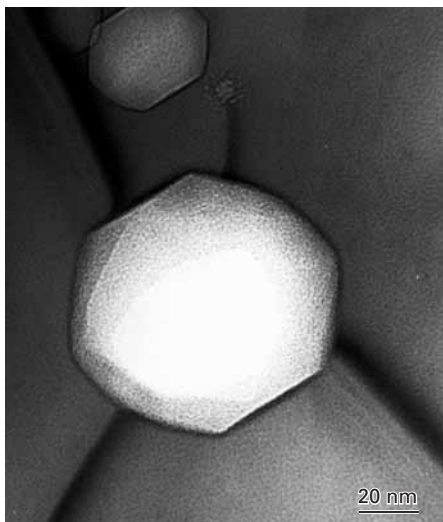


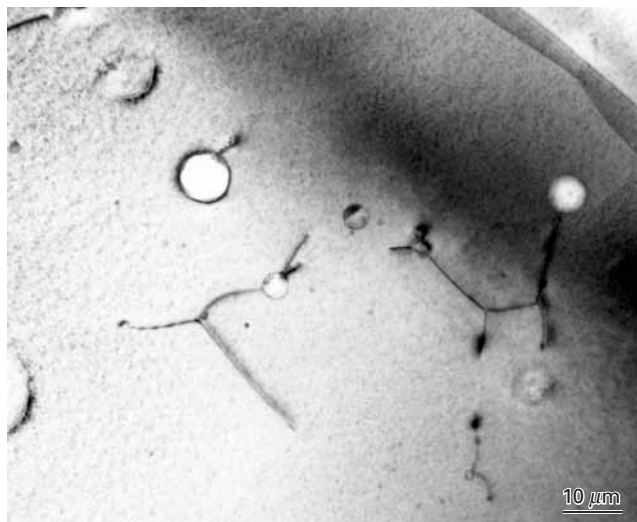
**Fig. 5.34** Voids (dark spots marked by arrows) in titanium carbide. The intergranular phase (light) is nickel, which was added to increase the toughness of the TiC.

in powder metallurgy processes, from extraneous matter. Inclusions are also often the result of impurities, such as sulfur and phosphorous in steel. Vacuum arc remelting and other refining processes lead to alloys in which the inclusion content is minimized. Ceramics and brittle metals and intermetallics are especially sensitive to inclusions and voids. As will be seen in Chapter 8, these are easy sites for the initiation of fracture. Spherical and elongated flaws are the principal failure initiation sites in brittle materials. Such flaws are activated both in tension and compression, and are responsible for the great differences between compressive and tensile strength (a factor of 5–10).

Ceramics are often produced by sintering or hot pressing of powders. This often leaves a residual porosity, which is a major source of concern. Figure 5.34 shows the microstructure of titanium carbide produced by hot pressing of powders. Residual porosity can be seen, and the voids are indicated by arrows. These voids have diameters of 1–4  $\mu\text{m}$ . It is difficult to completely eliminate porosity in ceramics. Small, intragranular pores that are only visible by TEM, such as the ones in  $\text{Al}_2\text{O}_3$  in Figure 5.35(a), are very difficult to remove, because bulk diffusion is orders of magnitude slower than grain-boundary diffusion. If the voids were at the confluence of grain boundaries, it would be easier to eliminate them by high-temperature sintering. The voids seen in Figure 5.27(a) are faceted because this shape minimizes the overall surface energy; the surface energy is anisotropic, and the surfaces with the least number of broken bonds per unit area have the least energy. This is evident from the hexagonal voids shown in Figure 5.35(a), which all have parallel faces. The TEM of Figure 5.35(b) also shows dislocations, which are produced during hot pressing of titanium carbide. The difficulty of hot pressing or sintering pure, high-temperature ceramics without voids is often bypassed by using sintering aids, or materials with a lower melting point. These materials — usually glasses — become viscous at high temperatures and fill the existing voids. They also act as a high-temperature lubricant between the ceramic particles and help to densify the ceramic, by capillary action. An illustration of the use of sintering aids to help



(a)



(b)

**Fig. 5.35** (a) Transmission electron micrograph illustrating faceted grain-interior voids within alumina and (b) voids in titanium carbide; dislocations are pinned by voids.

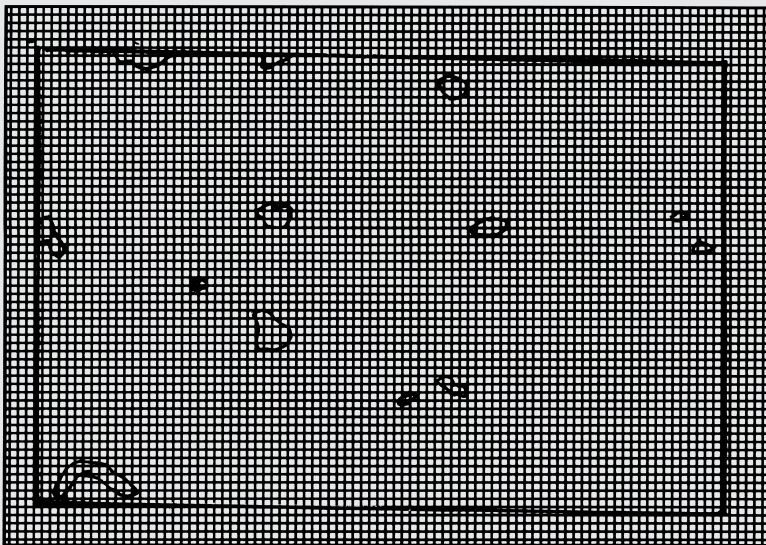


**Fig. 5.36** Glassy phase at triple point in silicon nitride; notice the individual crystallographic planes in  $\text{Si}_3\text{N}_4$ . (Courtesy of K. S. Vecchio.)

the consolidation is given in Figure 5.36. Three silicon nitride grains are imaged by the TEM; the interplanar spacing, 0.65 nm, is shown. The three grains surround a glassy material, marked G. If no sintering aid were used, a central void would be formed. Nevertheless, the glassy phase is a volumetric defect and results in a weaker material than a fully dense, pure  $\text{Si}_3\text{N}_4$ .

**Example 5.7**

- Calculate the volume fraction of voids in the micrograph in Figure 5.34.
- If Young's modulus for fully dense TiC is 440 GPa, what is Young's modulus for the porous TiC?

**Fig. E5.7**

*Solution:*

- We overlay a grid on the micrograph and count the intersections of lines falling within the voids. (See Figure E5.7.)

Total numbers of intersections in grid =  $72 \times 47 = 3,384$ ;

Total numbers of intersections inside voids  $\approx 66$ .

Therefore, the porosity is approximately  $66/3,384 = 2\%$ .

- From Chapter 2, we obtain the equation for Young's modulus (Equation 2.25):

$$\begin{aligned}E &= E_0(1 - 1.9p) \\&= 440 \times (1 - 1.9 \times 0.02) \\&= 423 \text{ GPa.}\end{aligned}$$

## 5.8 | Imperfections in Polymers

Let us consider again the basic “cooked spaghetti” structure of a polymer. In an amorphous polymer, there is no apparent order among

the molecules, and the polymeric chains are arranged randomly. As we pointed out in Chapter 1, macromolecules can be made to crystallize. However, unlike metals or ceramics, long-chain polymers or macromolecules (synthetic or natural) do *not* form exact, periodic structures having long-range order in three dimensions. This is because such a highly ordered structure in a polymer, in general, will not be in equilibrium. It is, however, possible to obtain a variety of metastable chain conformations, depending on the route taken to reach a particular state. In any of these metastable states, order may be locally present; that is, we can have crystalline regions interspersed with amorphous regions. Polymers can thus be amorphous or partially crystalline, a 100% crystalline polymer being difficult to obtain in practice. In a partially crystalline or semicrystalline polymer, depending on its type, molecular weight, and crystallization temperature, the amount of crystallinity can vary from 30 to 90%. The inability to attain a fully crystalline structure is due mainly to the long chain structure of polymers: Some twisted and entangled segments of chains that get trapped between crystalline regions never undergo the conformational reorganization necessary to achieve a fully crystalline state. Molecular architecture also has an important bearing on the polymer crystallization behavior: Linear molecules with small or no side groups crystallize easily; branched chain molecules with bulky side groups do not. For example, linear, high-density polyethylene can be crystallized to more than 90%, whereas branched polyethylene can be crystallized only to about 65%.

Amorphous polymers can be considered to be fairly homogeneous on a supramolecular scale. Semicrystalline polymers, consisting of tiny crystalline regions randomly distributed in an amorphous material, are heterogeneous, multiphasic, or even *composite* in nature. Lamellar crystals can form when a crystallizable polymer such as a linear polymer is cooled very slowly from its melting point. Small, platelike lamellar single crystals can also be obtained by the precipitation of a polymer from a dilute solution. The long molecular chains in the lamellae are folded in a regular manner. In a lamellar-polymer single crystal, the thickness of a lamella is typically about 10 nm, while the length of the chain is about 100 to 1,000 nm. The extremely long chain is conformed into a narrow lamella by the process of chain folding during crystallization. Figure 1.26c shows this phenomenon of chain folding. Many such lamellar crystallites group together and form spherulites. (See Chapter 1.)

Crystalline defects such as those described for metals and ceramics are not at all ubiquitous in polymers. One may define defects in polymers in simple chemical and physical terms. Chemical defects include defects such as a linear polymer branching off into two branches that grow at different rates to give branches of different lengths. One can also have syndiotactic defects, which are stereochemical in nature. For example, an isotactic polymer chain can have syndiotactic defects embedded in it. Physical aspects of defects involve conformational defects in chain coiling. It is easy to see that kinetic and energetic

factors will be very important in these type of defects, because such defects involve chain movement. Variables such as temperature, pressure, concentration, molecular weight, chain polarity, etc., are important, and statistical mechanics needs to be used. Thus, point defects in polymers are chain-conformational kinks, jogs, and inclusions. Point defects also include an interstitial or substitutional molecule. For example, if a macromolecular chain consisting of species A has a monomer B trapped inside the polymer crystal, that would be an interstitial point defect. If there is a break in the length of the molecular chain we will have a chain end and a vacancy or a row of vacancies.

As we have seen, in metals dislocations are very important because they are mobile, while in ceramics they are immobile under most conditions. Although dislocations can exist in polymeric crystals also, they do not play such a major role in the deformation of polymers. Direct observations of dislocations have been made in some semicrystalline polymers by transmission electron microscopy, which has been instrumental in elucidating the structural imperfections in metals and ceramics. One of the great limitations to the use of electron microscopy in the study of polymers is the radiation damage produced in the polymers by the electron beam. Images produced by electron diffraction contrast, as well as electron diffraction patterns, depend on the crystallinity of the specimen. A large dose of electrons will tend to destroy the long-range crystalline order, more so in polymers than in metals or ceramics, because nonpolymeric crystalline materials such as metals and ceramics are more resistant to electron irradiation. Thus, only a limited number of scattered electrons can be used to obtain crystallographic information from the sample under study before the diffraction pattern changes from crystalline reflections to broad, amorphous haloes. Radiation damage can establish cross-links and cause strain in the lattice at first. Continued exposure to an electron beam can make the diffraction contrast weaker and eventually disappear. It is therefore necessary to take special precautions before examining the structure of polymers in an electron microscope. Perhaps the most widely studied polymer in this regard is polyethylene, although it is difficult to take high-resolution images of polyethylene at room temperature by TEM because of the sensitivity of the polymer to radiation. By comparison, thermoplastics such as PPS, PEEK, and PEK are fairly resistant to electron irradiation. Experimentally, giant screw dislocations showing growth spirals have been observed in these thermoplastics. Terminating moiré fringes have been used to show the existence of dislocations in a polyethylene crystal. A lattice-imaging technique has been used on poly (para phenylene terephthalamide) PPTA and poly (paraphenylene benzobis thiazole) PBT fibers. In these fibrous materials, one has, relative to polyethylene, rather high radiation stability for electron microscopic observations because of the electronic conjugation of the backbone chain.

In crystalline metals and ceramics, two-dimensional defects such as grain boundaries are thin regions where two grains meet. In polymeric crystals, grain boundaries can be very complex, again because

of the chain connectivity. Besides, the electron beam sensitivity of polymers makes TEM observations and their interpretation quite difficult. Planar defects such as stacking faults and twins have been observed in samples of poly (diacetylene) crystals.

## Suggested Reading

### Interfacial Defects

- H. Gleiter. "On the Structure of Grain Boundaries in Metals." *Mater. Sci. Eng.*, 52 (1982) 91.
- H. Gleiter and B. Chalmers. "High-Angle Grain Boundaries," *Progress in Materials Science*, vol. 16, B. Chalmers, J. W. Christian, and T. B. Massalski, eds. Elmsford, NY: Pergamon Press, 1972.
- L. E. Murr. *Interfacial Phenomena in Metals and Alloys*. Reading, MA: Addison-Wesley, 1975.
- A. P. Sutton and R. W. Balluffi. *Interfaces in Crystalline Materials*. New York, NY: Oxford University Press, 1994.

### Twining

- R. E. Reed-Hill, J. P. Hirth, and H. C. Rogers, eds., *Deformation Twinning*. TMS-AIME Conf. Proc. New York, NY: Gordon and Breach, 1965.
- J. W. Christian and S. Mahajan. *Deformation Twinning*. New York, NY: Oxford University Press, 1995.

### Grain-Size Effects

- R. W. Armstrong. "The Influence of Polycrystal Grain Size on Mechanical Properties" in *Advances in Materials Research*, vol. 4, H. Herman, ed. New York, NY: Wiley Interscience, 1971, p. 101.
- R. W. Armstrong, in *Yield, Flow, and Fracture of Polycrystals*, T. N. Baker, ed. London: Appl. Sci. Publ., 1983, p. 1.
- H. Gleiter, "Nanocrystalline Materials," *Progress in Materials Science*, 33 (1989) 223.

## Exercises

**5.1** Calculate the dislocation spacing in a symmetrical tilt boundary ( $\theta = 0.5^\circ$ ) in a copper crystal.

**5.2** Starting from the equation  $E = E_0\theta(A - \ln \theta)$  for a low-angle boundary, show how one can obtain graphically the values of  $E_0$  and  $A$ .

**5.3** Taking  $A = 0.3$ , compute the value of  $\theta_{\max}$ .

**5.4** Show that, for a low-angle boundary, we have

$$\frac{E}{E_{\max}} = \frac{\theta}{\theta_{\max}} \left( 1 - \ln \frac{\theta}{\theta_{\max}} \right),$$

where  $E_{\max}$  and  $\theta_{\max}$  correspond to the maximum in the  $E$ -versus- $\theta$  curve.

**5.5** Consider two parallel tilt boundaries with misorientations  $\theta_1$  and  $\theta_2$ . Show that, thermodynamically, we would expect the two boundaries to join and form one boundary with misorientation  $\theta_1 + \theta_2$ .

**5.6** Can you suggest a quick technique to check whether lines observed in an optical microscope on the surface of a polished sample after deformation are slip lines or twin markings?

**5.7** A twin boundary separates two crystals of different orientations; however, we do not necessarily need dislocations to form a twin. Why?

**5.8** Let  $m$  be the total length of dislocations per unit area of a grain boundary. Assume that at yield, all the dislocations in the grain interiors ( $\rho$ ) are the ones emitted by the boundaries. Assume also that the grains are spherical (with diameter  $D$ ). Derive the Hall-Petch relation ( $\sigma = \sigma_0 + kD^{-1/2}$ ) for this case, and give the expression for  $k$ .

**5.9** Consider a piano wire that has a 100% pearlitic structure. When this wire undergoes a reduction in diameter from  $D_0$  to  $D_\varepsilon$ , the pearlite interlamellar spacing normal to the wire axis is reduced from  $d_0$  to  $d_\varepsilon$ , that is,

$$\frac{d_0}{d_\varepsilon} = \frac{D_0}{D_\varepsilon},$$

where the subscript 0 refers to the original dimensions, while the subscript  $\varepsilon$  refers to the dimensions after a true plastic strain of  $\varepsilon$ . If the wire obeys a Hall-Petch type of relationship between the flow stress and the pearlite interlamellar spacing, show that the flow stress of the piano wire can be expressed as

$$\sigma = \sigma_i + \frac{k'}{\sqrt{d_0}} \exp\left(\frac{\varepsilon}{4}\right).$$

#### 5.10

- (a) Determine the mean lineal intercept, the surface area per unit volume, and the estimated grain diameter for the specimen shown in Figure Ex5.10.
- (b) Estimate the yield stress of the specimen (AISI 304 stainless steel).
- (c) Estimate the parameters of part (a), excluding the annealing twins. By what percentage is the yield stress going to differ?

**5.11** Professor M. I. Dum conducted a study on the effect of grain size on the yield stress of a number of metals using thin foil specimens (thickness 0.1 mm and width 6.25 mm). He investigated grain sizes of 5, 25, 45, and 100  $\mu\text{m}$ . Which specimens can be considered truly polycrystalline?

**5.12** Thompson<sup>17</sup> obtained the following results for the yield stress of nickel:



Fig. Ex5.10

Grain Size ( $\mu\text{m}$ )	Yield Stress ( $\text{MN/m}^2$ )
0.96	251
2	185
10	86
20	95
95	33
130	25

<sup>17</sup> A. W. Thompson, *Acta Met.*, 25 (1977) 83.

- (a) Find the parameters in the Hall-Petch equation. Plot the yield stress versus  $D^{-1}$ ,  $D^{-1/2}$ , and  $D^{-1/3}$ . Which plot shows the best linearity?
- (b) Show how you can determine the correct exponent by another plot (not by trial and error).

5.13 If the grain size of a metal is doubled by an appropriate annealing, by what percentage is the surface area per unit volume of the metal changed?

5.14 Nilles and Owen<sup>18</sup> found a strong grain-size dependence of the stress required for twinning when deforming an Fe-25 at.% Ni alloy at 4 K. From what you learned in the text, is this behavior expected? Compare the ratio of the Hall-Petch slopes of the twinning and yield stresses for Fe-25% Ni with the ratio found for chromium and Fe-Si.

5.15 Most polycrystalline materials, when etched, form grooves at grain boundaries. When annealed, ceramics form thermal grooves at grain boundaries. A schematic of such a groove is shown in Figure Ex5.15. If the surface energy per unit area of the material is  $\gamma_s$ , derive an expression for the energy per unit area of the grain boundary between grains 1 and 2.

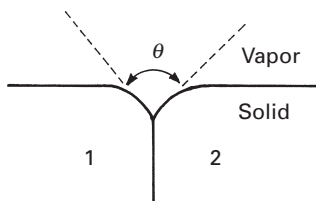


**Fig. Ex5.15**

5.16 Estimate the average grain diameter and the grain-boundary area per unit volume for a material that has isotropic grains (the same dimension in all directions) and ASTM grain size 6.

5.17 How many grains in an area of  $5 \times 5$  cm would be counted, in a photomicrograph taken at a magnification of  $500\times$ , for a metal with ASTM grain size 3?

5.18 A graduate student (undergraduates are much brighter!) measured the grain size of a metallic specimen and found that it was equal to ASTM #2. However, he had the wrong magnification in his picture ( $400\times$  instead of  $100\times$ ). (a) What is the correct ASTM grain size? (b) What is the approximate grain diameter?

5.19 Nanophase materials show many different characteristics vis-à-vis conventional materials. Discuss the sintering behavior of a nanophase powder in relation to that of a conventional powder.

5.20 Calculate the volume fraction of voids in the TiC specimen shown in Figure 5.35(b).

5.21 Examine Figure Ex5.21.

- (a) Using the lineal intercept method, determine the mean lineal intercept and the grain size if the material is TiC.
- (b) Determine the grain size using the ASTM method.

5.22

- (a) Using the mean lineal intercept, calculate the grain diameter for tantalum, given the micrograph in Figure 5.29(a).
- (b) Calculate the ASTM grain size.
- (c) Estimate the yield stress for this specimen of tantalum, using values from Table 5.3.

<sup>18</sup> J. L. Nilles and W. S. Owen, *Met. Trans.*, 3 (1972) 1877.

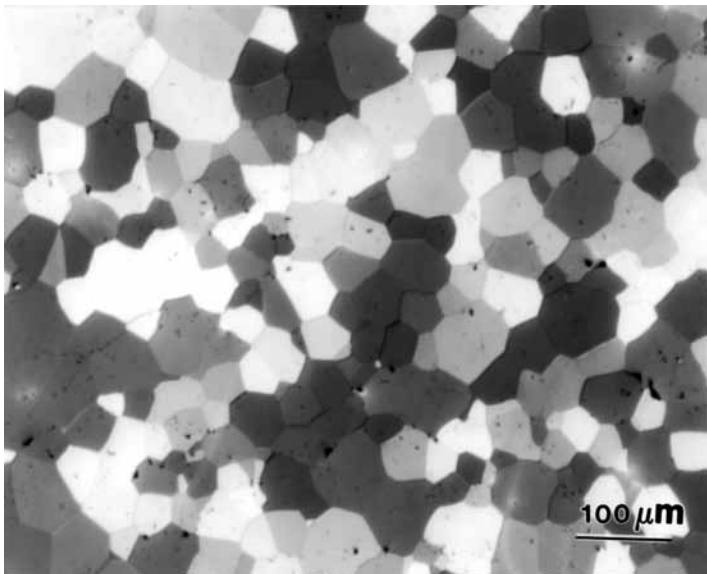


Fig. Ex5.21

5.23 A polycrystalline sample has 16 grains per square inch in a photomicrograph taken at magnification  $100\times$ . What is the ASTM grain size number?

5.24 A 20-cm line gave seven intersections in a  $100\times$  micrograph. Using the lineal intercept method, determine the mean lineal intercept and the grain size.

5.25 How many grains in an area of  $5 \times 5$  cm would be counted in a photomicrograph taken at a magnification of  $500\times$  for a metal with an ASTM grain size 3.

5.26 The yield stress of AISI 1020 steel with a grain size of  $200 \mu\text{m}$  is 200 MPa. Estimate the yield stress for a grain size of  $10 \mu\text{m}$  if the Hall-Petch constant  $k = 0.8 \text{ MN/m}^{3/2}$ .

5.27 A small-angle tilt boundary has a misorientation of  $0.1^\circ$ . What is the spacing between the dislocations in this boundary if the Burgers vector of the dislocation is  $0.33 \text{ nm}$ ?

5.28 Calculate the dislocation spacing of a low-angle tilt boundary in aluminum for  $\theta = 0.5^\circ$ . Take  $G = 26.1 \text{ GPa}$ ,  $v = 0.345$ , and  $r_{\text{Al}} = 0.143 \text{ nm}$ .

5.29

- Determine the grain size for the microstructure of zirconium shown in Figure Ex5.29, using the lineal intercept method. Use the scale given at the bottom.
- Use the Hall-Petch equation to determine the yield stress of this material, given  $\sigma_0 = 29 \text{ MPa}$ ,  $k = 0.25 \text{ MPa m}^{1/2}$ .

5.30 From Figure 5.2 (a, b) find the grain diameter of samples using the lineal intercept ASTM method,  $N = 2^{n-1}$ .

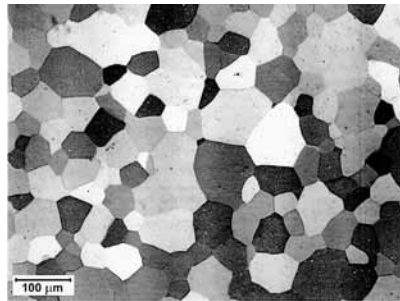


**Fig. Ex5.29** Microstructure of zirconium. (Courtesy of S. Barabas and M. E. Kissner.)

5.31 Calculate the dislocation spacing and energy of a low-angle tilt boundary in Ni if  $\theta = 0.5^\circ$ ,  $G = 76 \text{ GPa}$ ,  $r = 0.125 \text{ nm}$ ,  $v = 0.31$ .

5.32 If a sample of copper had a grain size of 75 mm, what would be the expected yield stress, assuming a Hall-Petch response? (Use the data from Figure 5.23.)

5.33 Describe the difference between deformation twins and annealing twins. Describe the differences in twinning in HCP, BCC, and FCC crystals.

---

## Chapter 6

# Geometry of Deformation and Work-Hardening

### 6.1 | Introduction

The relaxation times for the molecular processes in gases and in a majority of liquids are so short, that molecules/atoms are almost always in a well-defined state of complete equilibrium. Consequently, the structure of a gas or liquid does not depend on its past history. In contrast, the relaxation times for some of the significant atomic processes in crystals are so long, that a state of equilibrium is rarely, if ever, achieved. It is for this reason that metals in general (and ceramics and polymers, under special conditions) show the usually desirable characteristic of work-hardening with straining, or strain-hardening. In other words, plastic deformation distorts the atoms from their equilibrium positions, and this manifests itself subsequently in hardening.

In fact, hardening by plastic deformation (rolling, drawing, etc.) is one of the most important methods of strengthening metals, in general. Figure 6.1 shows a few deformation-processing techniques in which metals are work-hardened. These industrial processes are used in the fabrication of parts and enable the shape of metals to be changed. The figure is self-explanatory. Rolling is used to produce flat products such as plates, sheets, and also more complicated shapes (with special rolling cylinders). In forging, the top hammer comes down, and the part is pushed into a die (closed-die forging) or is simply compressed. Extrusion uses a principle similar to that in the use of a tube of toothpaste. The material is squeezed through a die, and its diameter is reduced. In stamping, first the ends of a blank are held, and then the upper die comes down, punching the blank into the lower die.

If deformation is carried out at low and moderate temperatures, the metal workhardens. However, if the temperature is sufficiently high, the dislocations generated in work-hardening are annealed out, and the final metal is in the annealed condition. *Hot working* designates all work done on a metal or alloy above its recrystallization temperature, while *cold working* indicates work done below the

**Fig. 6.1** Common metalworking methods. (a) Rolling. (b) Forging (open and closed die). (c) Extrusion (direct and indirect). (d) Wire drawing. (e) Stamping.

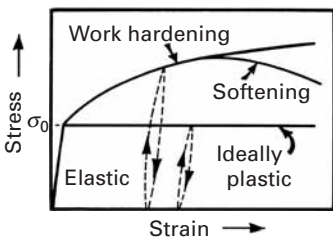
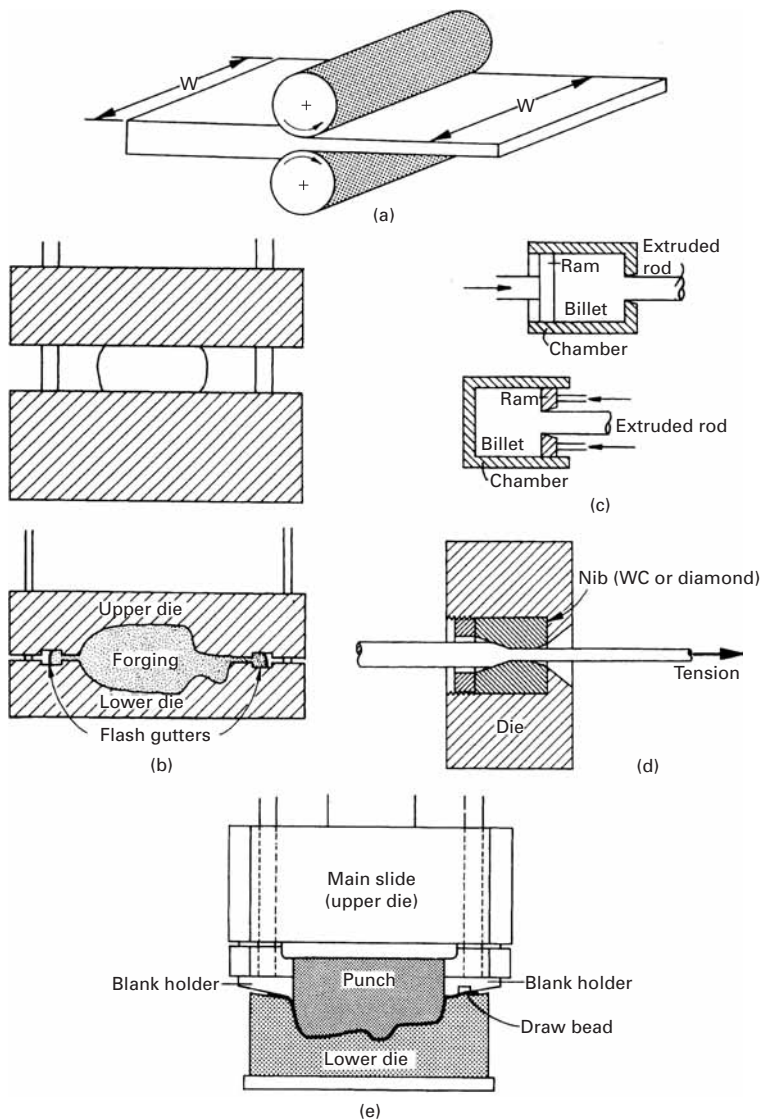
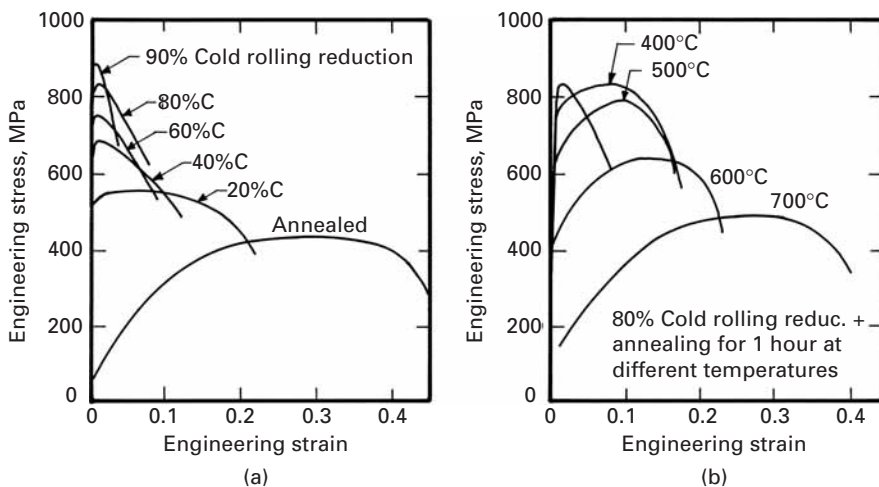


**Fig. 6.2** Stress-strain curves (schematic) for an elastic, ideally plastic; a work-hardening; and a work-softening material.

recrystallization temperature of the metal or alloy. Certain metals, in particular (e.g., copper), do not have many precipitation hardening systems, but are ductile and can be appreciably hardened by cold working. If the relaxation times were short, the structure would return almost immediately to its state of equilibrium, and a constant stress for plastic deformation would result, independent of the extent of deformation. This is shown in Figure 6.2 as the elastic, ideally plastic solid. However, when a real crystalline solid is deformed plastically, it turns more resistant to deformation, and a greater stress is required for additional deformation. The phenomenon is called *work-hardening*. If the stress is interrupted, and the material is unloaded after a certain plastic strain, the unloading slope is equal to the Young's modulus. Upon loading, the stress returns to its original



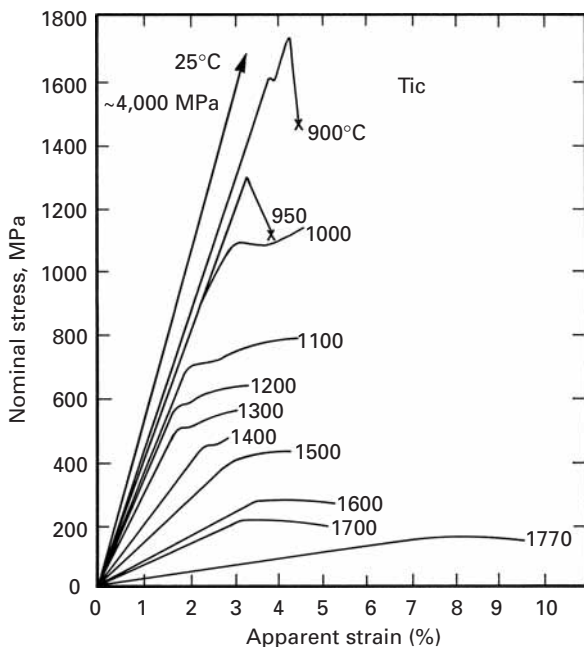
value. Thus, for a work-hardening material, the flow stress is increased above  $\sigma_0$ , whereas for an ideally plastic material, the flow stress is constant at  $\sigma_0$ . Under certain conditions, the material can also soften. This is also shown in Figure 6.2 and is discussed in greater detail in Section 6.4.

In Chapter 4, we discussed the various kinds of defects in materials. Of these defects, the primary carriers of plastic deformation in metals and ceramics are dislocations and twins. From the simple motion of dislocations along specific planes, we derived the Orowan Equation 4.29, which relates the global plastic strain to the individual dislocation motion and density. Basically, the hardening in a crystalline structure occurs because these materials deform plastically by the movement of dislocations, which interact directly among themselves and with other imperfections, or indirectly with the internal stress field (short range or long range) of various imperfections and obstacles. All these interactions lead to a reduction in the mean mobility of dislocations, which then require a greater stress for accomplishing further movement (i.e., with continuing plastic deformation, we need to apply an ever greater stress for further plastic deformation); hence the phenomenon of work-hardening.

Figure 6.3 illustrates how a metal (in this case, nickel) work-hardens by cold rolling. As the nickel plate is reduced in thickness (and increased in length), its stress-strain response changes. In the figure, we plot engineering stress versus engineering strain, and all the curves show a softening after hardening. This softening is due not to an inherent structural “softening,” but to a localized reduction in cross section, called *necking*. (See Chapter 3.) The yield stress increases from less than 100 MPa (in the annealed condition) to approximately 850 MPa (after 90% reduction in thickness by cold rolling). Concomitantly, the ductility decreases. The sample that received 80% reduction was subjected to one-hour annealings at various temperatures; the resulting mechanical response is shown in Figure 6.3(b). After a 700°C annealing, the curve is almost coincident with the original

**Fig. 6.3** Engineering-stress–engineering-strain curves for nickel. (a) Nickel subjected to 0, 20, 40, 60, 80, and 90% cold-rolling reduction. (b) Nickel cold rolled to 80%, followed by annealing at different temperatures. (From D. Jaramillo, V. S. Kuriyama, and M. A. Meyers, *Acta Met.* 34 (1986) 313.)

**Fig. 6.4** Stress-strain curves for annealed polycrystalline TiC deformed in compression at the temperatures indicated ( $\varepsilon = 1.7 \times 10^{-4} \text{ s}^{-1}$ ). (Adapted from G. Das, K. S. Mazdiyasni, and H. A. Lipsitt, *J. Am. Cer. Soc.*, 65 (1982) 104.)



annealed curve, showing that the effects of cold rolling have been eliminated. This occurs because the dislocations produced by plastic deformation have been eliminated by the annealing. The nickel specimens were polycrystalline, with a grain size of  $40 \mu\text{m}$ .

In Chapter 4, we dealt exclusively with monocrystals; we will see, in this chapter, how the plastic deformation in one single crystallographic direction is related to the overall deformation of a crystal and how different crystals in a polycrystal deform in a “cooperative” manner.

In ceramics, plastic deformation is not so common. At room temperatures many ceramics are brittle, and it was seen in Chapter 4 that the Peierls–Nabarro stress opposing dislocations is much higher and that the mobility of dislocations is much more restricted than for metals. This is illustrated in Figure 6.4 which shows results of compression tests on TiC specimens carried out at different temperatures. Note that the elastic portion of the curves shows a slope that is considerably lower than the prediction from the Young’s modulus, because no extensometer was used to measure strain. Thus, the abscissa records both the strain in the specimen and the deflection in the machine; for this reason, the term “apparent strain” is used. The ambient-temperature compressive strength of TiC is approximately 4,000 MPa. As the temperature is increased beyond  $950^\circ\text{C}$ , plastic deformation gradually sets in. This is called the *ductile–brittle transition*. As the temperature is increased, the flow stress decreases. In this temperature regimen, the material exhibits plasticity. In monocrystalline  $\text{Al}_2\text{O}_3$  deformed at high temperatures, significant plastic deformation is also observed. Figure 6.5 shows the

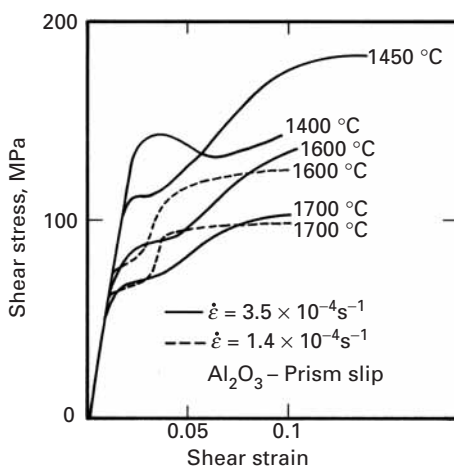


**Fig. 6.5** Shear stress  $\tau$  vs. shear strain  $\gamma$  for prism plane slip in  $\text{Al}_2\text{O}_3$  at various temperatures;  $\dot{\epsilon} = 3.5 \times 10^{-4} \text{ s}^{-1}$  for the solid curves,  $\dot{\epsilon} = 1.4 \times 10^{-4} \text{ s}^{-1}$  for the dashed curves. (Courtesy of T. E. Mitchell.)

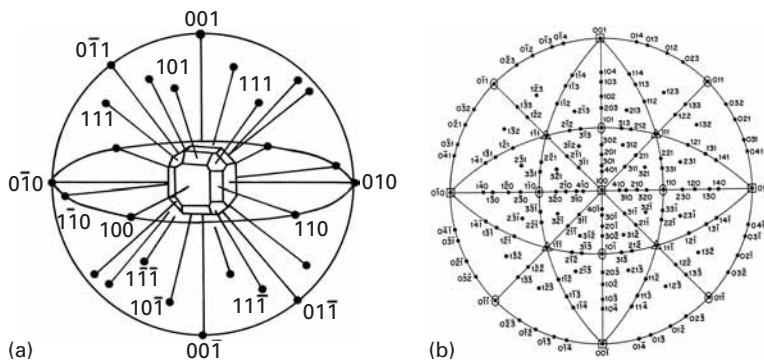


**Fig. 6.6** (a) Representation of crystallographic directions and poles (normals to planes) for cubic structure. (b) Standard [100] stereographic projection.  
(Reprinted with permission from C. S. Barrett and T. B. Massalski, *The Structure of Metals*, 3d ed. (New York: McGraw-Hill, 1966), p. 39.)

shear-stress-shear-strain response for  $\text{Al}_2\text{O}_3$  oriented for prismatic slip. (See Section 4.4.7.)

## 6.2 | Geometry of Deformation

### 6.2.1 Stereographic Projections

The mechanical properties of crystals are anisotropic, and slip occurs only on certain planes, along certain directions. For this reason, it is important to define the *orientation* of a crystal. The most common technique for doing so is the stereographic projection, which will be presented here in an abbreviated way; greater details are given in Barrett and Massalski. (See suggested reading.) The stereographic projection is a geometric representation of the directions and planes of a crystal. From stereographic projections, one can determine the angles between planes, planes and directions, and directions. The stereographic projection is the projection of a sphere on a plane. We imagine a unit cell of a certain crystalline structure at the center of the sphere. (See Figure 6.6(a).) The directions and plane poles (normals to the planes passing through the origins) intercept a sphere at points; these points are projected onto a plane. Figure 6.6(b) shows a standard

cubic projection. This projection is known as a [100] standard projection because the  $<001>$  direction corresponds to the center. There are other standard projections: [110], [111], [112], and so on. Theoretically, the angles between directions and/or plane poles are measured on the sphere; in practice, however, these angles are measured on the standard projection, making use of a special chart called the Wulff net. This chart is the projection of a plane of a sphere in which all the meridians and parallels are marked at regular degree intervals. The sphere has the same diameter as the standard projection. By inserting a tack at the center and rotating the standard projection around it, we can easily find all desired angles.

An analogy can be made with maps. Imagine that we look at the earth from the “top;” that is, we view the northern hemisphere with the north pole at the center. If we now draw a map on a circle, we have a situation analogous to a stereographic projection. The meridians of the map correspond to great circles on the stereographic projection – that is, circles whose center is coincident with the center of the sphere. The four great circles that are perpendicular to the plane of the paper are projected as straight lines.

In a stereographic projection, the crystalline symmetry can be clearly seen. For instance, the  $<100>$  directions form a cross in Figure 6.6, with the crystalline symmetry indicated in Figure 6.6(b); two-, three-, four-, and six-fold symmetry axes are shown. (The symmetries have been introduced in Section 2.8, and the reader is referred to Table 2.1.) For the  $<111>$ ,  $<110>$ , and  $<100>$  directions, the symmetry is four-, two-, and threefold, respectively, in the cubic system. Two-, three-, and fourfold symmetries are indicated by lens, triangle, and square, respectively. As a consequence, the standard projection can be divided, by means of great circles, into 24 spherical triangles that are crystallographically equivalent. The vertices of these triangles are  $<100>$ ,  $<110>$ , and  $<111>$ , as can be seen in Figure 6.7. Comparing this figure with Figure 6.6(b), we can see that the directions on the sides and within the spherical triangles are also equivalent. Consequently, one single triangle is sufficient to specify any crystallographic orientation in the cubic system; the [100], [110], [111] triangle is used most commonly. The reader is warned, however, that this simplification is not applicable to the other crystal systems.

### 6.2.2 Stress Required for Slip

The flow stresses of crystals are highly anisotropic. For instance, the yield stress of zinc under uniaxial tension can vary by as much as a factor of 6, depending on the orientation. Consequently, it is very important to specify the orientation of the load with respect to that of the crystal. In shear or torsion tests, the shear plane and directions are precisely known. Because dislocations can glide only under the effect of shear stresses, these shear stresses have to be determined. In uniaxial tensile and compressive tests (the most common tests), one has to determine mathematically the shear component of the applied stress acting on the plane in which slip is taking place.

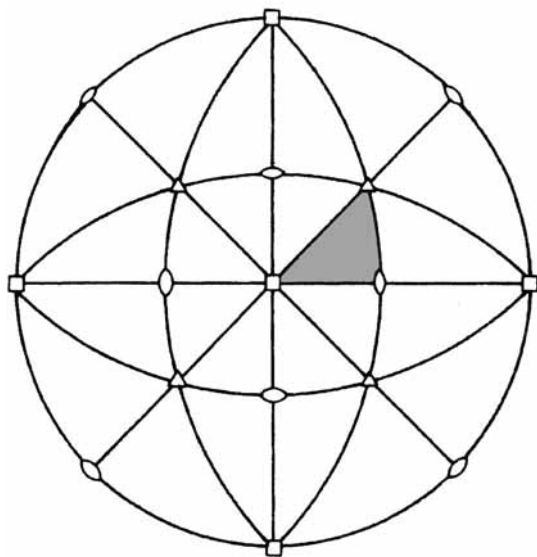


**Fig. 6.7** Standard [001]  
stereographic projection divided  
into 24 triangles.

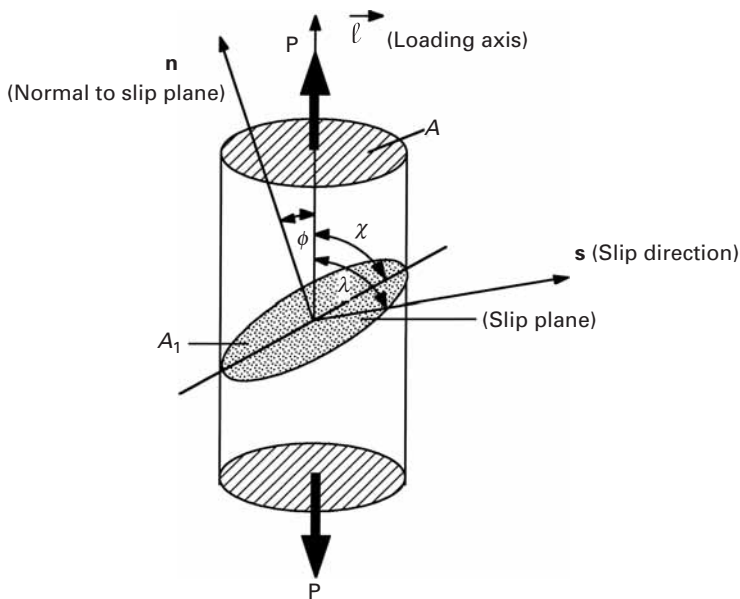


**Fig. 6.8** Relationship between  
loading axis and slip plane and  
direction.

Figure 6.8 shows a crystal with a normal cross-sectional area  $A$  upon which a tensile load  $P$  acts, generating a uniaxial stress  $P/A$ . The slip plane and direction are indicated, respectively, by the angles  $\phi$  and  $\lambda$  that they make with the tensile axis. The normal  $n$  of the slip plane, cross-sectional area  $A_1$ , that makes an angle  $\phi$  with the loading direction  $\ell$ .

The areas  $A_1$  and  $A$  are related by the angle  $\phi$ . Area  $A$  is the projection of  $A_1$  onto the horizontal plane; thus, we can write

$$A = A_1 \cos \phi.$$

The shear stress  $\tau$  acting on the slip plane and along the slip direction  $s$  is obtained by dividing the resolved load along the slip direction ( $P \cos \lambda$ ) by  $A_1$ :

$$\tau = \frac{P \cos \lambda}{A_1} = \frac{P}{A} \cos \phi \cos \lambda.$$

But  $P/A = \sigma$  is the normal stress applied to the specimen. Hence,

$$\tau = \sigma \cos \phi \cos \lambda.$$

Note that  $\cos \phi = \sin \chi$ .

This equation shows that  $\tau$  will be zero when either  $\lambda$  or  $\phi$  is equal to  $90^\circ$ . On the other hand, the shear component is maximum when both  $\phi$  and  $\lambda$  are equal to  $45^\circ$ . We have, in this case,

$$\tau_{\max} = \sigma \cos 45^\circ \cos 45^\circ = \frac{\sigma}{2}.$$

The angle between any two directions  $\mathbf{a}$  and  $\mathbf{b}$  can be obtained from the scalar product of these vectors:

$$\mathbf{a} \cdot \mathbf{b} = |\mathbf{a}| |\mathbf{b}| \cos \theta$$

or

$$\cos \theta = \frac{\mathbf{a} \cdot \mathbf{b}}{|\mathbf{a}| |\mathbf{b}|}.$$

For cubic crystals, planes and directions with the same indices are perpendicular, and the angle is determined from the coefficients,  $h$ ,  $k$ , and  $l$ . For two vectors

$$\mathbf{a} = h_1 \mathbf{i} + k_1 \mathbf{j} + l_1 \mathbf{k}$$

and

$$\mathbf{b} = h_2 \mathbf{i} + k_2 \mathbf{j} + l_2 \mathbf{k},$$

the angle  $\theta$  is given by

$$\cos \theta = \frac{h_1 h_2 + k_1 k_2 + l_1 l_2}{(h_1^2 + k_1^2 + l_1^2)^{1/2} (h_2^2 + k_2^2 + l_2^2)^{1/2}}.$$

(6.1)

If two directions are perpendicular, their dot product is zero; and the same is true for a direction that is contained in a plane. From Equation 6.1, it is possible to obtain the  $\cos \phi$  and  $\cos \lambda$  terms for all desired crystallographic directions of a crystal. For instance, if the loading direction is [123] for an FCC crystal, then the Schmid factors (see below) of the various slip systems are found by obtaining the angles of [123] with  $\langle 111 \rangle$  (perpendicular to slip planes) and  $\langle 110 \rangle$  (slip directions). Note that each slip plane contains three slip directions and that 12 values ( $4 \times 3$ ) have to be obtained.

Schmid and coworkers<sup>1</sup> used the variation in the resolved shear stress to explain the great differences in the yield stresses of monocrystals of certain metals. They proposed the following rationalization, known as the Schmid law: Metal flows plastically when the resolved shear stress acting in the plane and along the direction of slip reaches the critical value

$$\tau_c = \sigma_0 \sin \chi \cos \lambda = M \sigma_0, \quad (6.2)$$

$$M = \sin \chi \cos \lambda = \cos \phi \cos \lambda, \quad (6.3)$$

where the factor  $M$  is usually known as the *Schmid factor*.

Schmid's law has found experimental confirmation principally in hexagonal crystals. Figure 6.9 shows the experimental results, compared with Schmid's prediction for high-purity zinc. The full line shows the hyperbola obtained by the use of Equation 6.3, assuming a critical resolved shear stress of 184 kPa. It is worth noting that the yield stress is minimum for  $M = 0.5$ .

For cubic crystals, the correspondence between Schmid's law and experiments is not as good. This is mainly due to the great number of slip systems in these structures. For nickel, the critical resolved shear stress is practically orientation independent. On the other hand, for copper, the critical resolved shear stress is dependent on orientation, being constant in the center of the stereographic triangle and assuming higher values close to the sides. Figure 6.10 shows the inverse of Schmid's factor in the stereographic triangle based on a  $\{111\} <110>$  slip: This is the situation for FCC crystals. The orientation for which FCC crystals are softest is  $M = 0.5$ , or  $M^{-1} = 2$ , which occurs approximately at the center of the triangle. The dependence of  $\tau_c$  on the orientation for cubic systems is thought to be because the components of compressive stresses acting normal to the slip planes are different for different orientations at the same applied stress level. These compressive stresses should have an effect on  $\tau_c$ . Easy glide in FCC crystals is greatest in the center of the stereographic projection, in the region closer to (but not coinciding with) the  $<110>$  corner. It is affected by a number of parameters, the most notable being the following.

- Specimen size.* Specimens with a smaller cross-sectional area tend to have a more extended easy-glide region.
- Temperature.* Easy glide is more pronounced at lower temperatures and may vanish completely at high temperatures.
- Stacking-fault energy.* FCC metals with low stacking-fault energy tend to have a more pronounced easy-glide region. Why?
- Solute atoms.* If solute atoms pin the dislocations, they will shorten their mean free path and the extent of easy glide. If solute atoms contribute primarily to the lowering of the stacking-fault energy or to ordering, they will increase the easy glide range.

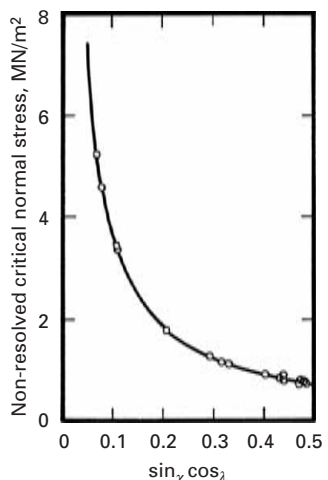


**Fig. 6.9** Comparison of Schmid law prediction with experimental results for zinc. (Adapted with permission from D. C. Jillson, *Trans. AIME*, 188 (1950) 1120.)

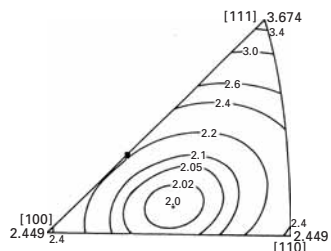


**Fig. 6.10** Effect of orientation on the inverse of Schmid's factor ( $1/M$ ) for FCC metals. (Adapted with permission from G. Y. Chin, "Inhomogeneities of Plastic Deformation," in *The Role of Preferred Orientation in Plastic Deformation* (Metals Park, OH: ASM, 1973), pp. 83, 85.)

<sup>1</sup> E. Schmid and W. Boas, *Kristalplastizitat (Plasticity of Crystals)* (Berlin and London: Springer and Hughes, 1950).

### Example 6.1

A single crystal of copper is deformed in tension. The loading axis is [112].

- Calculate the Schmid factors for the different slip systems.
- If the critical resolved shear stress is 50 MPa, what is the tensile stress at which the material will start to deform plastically?

*Solution:*

- Copper is FCC, which has 12 slip systems of the type  $\{111\} <110>$ ; thus, we have

$$\cos \phi = \frac{\mathbf{n} \cdot \ell}{|\mathbf{n}| \cdot |\ell|},$$

$$\cos \lambda = \frac{\mathbf{s} \cdot \ell}{|\mathbf{s}| \cdot |\ell|},$$

and the following table:

Slip plane ( $\mathbf{n}$ )	Slip direction ( $\mathbf{s}$ )	$\cos \phi$	$\cos \lambda$	Schmid factor ( $\cos \phi \cos \lambda$ )	$\sigma$ (MPa)
(111)	[ $\bar{1}10$ ]	$2\sqrt{2}/3$	0	0	Not deformed
	[ $\bar{1}01$ ]	$2\sqrt{2}/3$	$\sqrt{3}/6$	$\sqrt{6}/9$	184
	[ $0\bar{1}1$ ]	$2\sqrt{2}/3$	$\sqrt{3}/6$	$\sqrt{6}/9$	184
( $\bar{1}\bar{1}1$ )	[ $1\bar{1}0$ ]	$\sqrt{2}/3$	$\sqrt{3}/3$	$\sqrt{6}/9$	184
	[ $10\bar{1}$ ]	$\sqrt{2}/3$	$\sqrt{3}/2$	$\sqrt{6}/6$	122
	[ $0\bar{1}\bar{1}$ ]	$\sqrt{2}/3$	$\sqrt{3}/6$	$\sqrt{6}/18$	367
( $1\bar{1}\bar{1}$ )	[ $1\bar{1}0$ ]	$\sqrt{2}/3$	$\sqrt{3}/3$	$\sqrt{6}/9$	184
	[ $10\bar{1}$ ]	$\sqrt{2}/3$	$\sqrt{3}/6$	$\sqrt{6}/18$	367
	[ $011$ ]	$\sqrt{2}/3$	$\sqrt{3}/2$	$\sqrt{6}/6$	122
(11 $\bar{1}$ )	[ $\bar{1}10$ ]	0	0	0	Not deformed
	[ $\bar{1}01$ ]	0	$\sqrt{3}/2$	0	Not deformed
	[ $011$ ]	0	$\sqrt{3}/2$	0	Not deformed

A diagram showing the loading axis [112] is given in Figure E6.1.

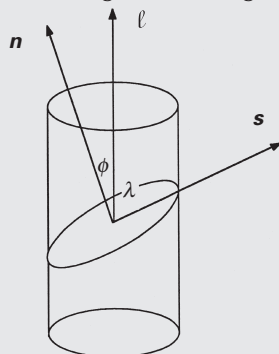


Fig. E6.1

$$(b) \tau_{\text{crss}} = \sigma \cos \phi \cos \lambda,$$

$$\sigma = \frac{\tau_{\text{crss}}}{\cos \phi \cos \lambda} = \frac{50}{\cos \phi \cos \lambda}.$$

Results are shown in the foregoing table.

### Example 6.2

Calculate the total energy due to dislocations in iron in the annealed condition, after 20% plastic deformation and 100% plastic deformation. Use both the exact (Equation 4.20) and the approximate equation (Equation 4.21) ( $U = Gb^2/2$ ). Assume that the core has a radius equal to  $5b$  and that dislocations are evenly distributed between edge and screw types. Given the following information:

$$G = 81.6 \text{ GPa},$$

$$v = 0.293,$$

$$r = 0.124 \text{ nm}.$$

The relationship between the stress and dislocation density is (see Section 6.3):

$$\tau = 40 \times 10^6 + 16.67\sqrt{\rho} \quad (\text{in Pa}).$$

The stress-strain relationship is:

$$\tau = \tau_0 + k\gamma^n,$$

where  $\tau_0 = 50 \times 10^6$ ,  $k = 100 \times 10^6$ , and  $n = 1/2$ .

**Solution:** The stress levels for  $\gamma = 0$ , 0.4, and 2 ( $\gamma = 2\varepsilon$ ) are

$$\tau = 50,113, \text{ and } 191.4 \times 10^6 \text{ Pa}.$$

The dislocation density is:

$$\rho = (\tau - 40 \times 10^6)^2 \times \frac{1}{16.67^2} = 3.5 \times 10^{-3}(\tau - 40 \times 10^6)^2.$$

Hence, for

$$\varepsilon = 0, \quad \rho = 3.5 \times 10^9 \text{ m}^{-2},$$

$$\varepsilon = 0.2, \quad \rho = 3.71 \times 10^{13} \text{ m}^{-2},$$

$$\varepsilon = 1, \quad \rho = 1.15 \times 10^{14} \text{ m}^{-2}.$$

We now obtain the dislocation spacing. It is known that

$$\ell = \frac{1}{\rho^{1/2}}.$$

So, for

$$\varepsilon = 0, \quad l \approx 1.69 \times 10^{-5} \text{ m},$$

$$\varepsilon = 0.2, \quad l \approx 1.64 \times 10^{-7} \text{ m},$$

$$\varepsilon = 1, \quad l \approx 0.93 \times 10^{-7} \text{ m},$$

and we have

$$U_T = \frac{Gb^2}{10} + \frac{Gb^2}{4\pi(1-\nu)}(1-\nu \cos^2 \alpha) \frac{\rho^{-1/2}}{5b}.$$

For 50% edge and 50% screw dislocations, we make  $\alpha = 45^\circ$ . The Burgers vector can then be calculated from the radius of the atoms. If the lattice parameter is  $a$ , the Burgers vector is, along [111]

$$\begin{aligned} |\mathbf{b}| &= a\sqrt{1^2 + 1^2 + 1^2} = 4r \\ &= 0.496 \text{ nm}. \end{aligned}$$

Thus, for

$$\begin{aligned} \varepsilon = 0, \quad U_T &= (0.1 + 0.847)G b^2 = 0.947 Gb^2, \\ \varepsilon = 0.2, \quad U_T &= (0.1 + 0.402)G b^2 = 0.502 Gb^2, \\ \varepsilon = 1, \quad U_T &= (0.1 + 0.34)G b^2 = 0.44 Gb^2. \end{aligned}$$

The approximate expression for the dislocation self-energy ( $U_T = Gb^2/2$ ) becomes gradually better as the density is increased. The total energy of dislocations per unit volume is

$$U = U_T \rho,$$

and for

$$\begin{aligned} \varepsilon = 0, \quad U &= 696.3 \text{ J/m}^3, \\ \varepsilon = 0.2, \quad U &= 74.2 \times 10^4 \text{ J/m}^3, \\ \varepsilon = 1, \quad U &= 2.3 \times 10^5 \text{ J/m}^3. \end{aligned}$$

### 6.2.3 Shear Deformation

Just as a tensile test does not directly provide the shear stress in the slip plane and along the slip direction, it does not directly provide the corresponding deformation. Accordingly, one must determine shear by taking into account the relative orientations of the tensile axis and the slip system. If a tensile specimen is attached to the grips of a tensile-testing machine by means of universal joints, it can be seen that the slip plane will rotate with respect to the tensile axis as deformation proceeds. Therefore, it is important to know the deformation and, consequently, the change in orientation, along with the attendant alteration in Schmid's factor. In a similar way, it can be shown that the shear strain  $d\gamma$  in the slip system is related to the longitudinal strain  $d\varepsilon$  by

$$d\lambda = \frac{d\varepsilon}{\sin \chi \cos \lambda} = \frac{d\varepsilon}{M}. \quad (6.4)$$

Therefore, when  $M = 0.5$ , we have  $\tau = 0.5\sigma$  and  $\gamma = 2\varepsilon$ . (Notice that  $\tau = \sigma/2!$ ).

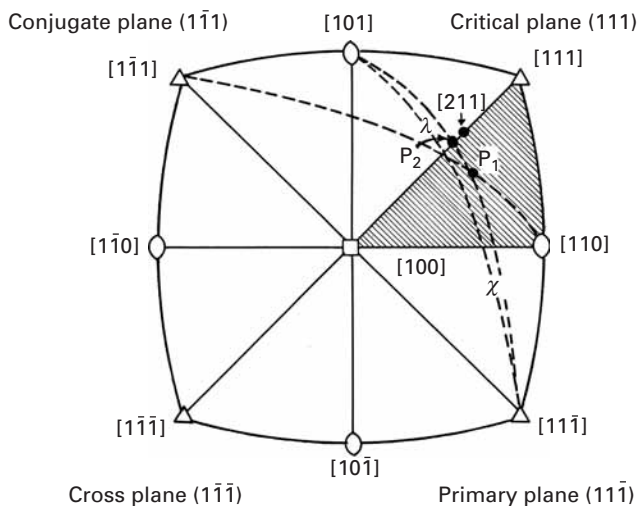


**Fig. 6.11** Stereographic projection showing the rotation of slip plane during deformation. Direction  $P_1$ , inside stereographic triangle moves toward  $P_2$  on boundary  $[100]-[1\bar{1}\bar{1}]$ . Then,  $P_2$  moves toward  $[211]$ .

#### 6.2.4 Slip in Systems and Work-Hardening

Equations 6.3 and 6.4 establish the stress and strain in the plane and in the direction of shear and are therefore important from the point of view of dislocation motion. In HCP structures, the slip is more easily maintained in one plane. However, in BCC and FCC structures, other slip systems are easily activated. The rotation and direction of the slip plane will easily put other systems in a favorable position. This situation is shown in the stereographic projection of Figure 6.11. A certain crystal has its tensile axis within the crosshatched stereographic triangle. The first slip system to be activated will be the one with the highest Schmid factor. (See Equations 6.2 and 6.3). There are eight slip systems around axis  $P_1$  in the figure. There are other ones in the total stereographic projection. By using great circles, the reader can check whether the following systems of directions really belong to the planes:

- (11̄1)[101], (11̄1)[1̄10],
- (111)[1̄10], (111)[10̄1],
- (1̄1̄1)[10̄1], (1̄1̄1)[110],
- (1̄1̄1)[110], (1̄1̄1)[101].

The maximum value of Schmid's factor,  $M = 0.5$ , is obtained for  $\chi = \lambda = 45^\circ$ . The angles between  $P_1$  and the  $<100>$  directions are determined by means of a Wulff net, passing a great circle through the two poles. Among the preceding eight systems, the slip system having the highest Schmid factor is (11̄1) [101]; slip will initially take place in this system. Plane (11̄1) is therefore called the *primary slip plane*. As deformation proceeds,  $\chi$  and  $\lambda$  will rotate. In the stereographic projection, this is indicated by rotation of the axis  $P_1$ . Actually, the specimen rotates with respect to the axis.  $P_1$  will tend to align itself with direction [101], decreasing  $\lambda$  in the process; this is shown in

**Fig. 6.12** Shear-stress vs. shear-strain curves for Nb(BCC) monocrystals at different crystallographic orientations; arrows indicate calculated strain at which conjugate slip is initiated. (From T. E. Mitchell, *Prog. App. Matls. Res.* 6 (1964) 117.)

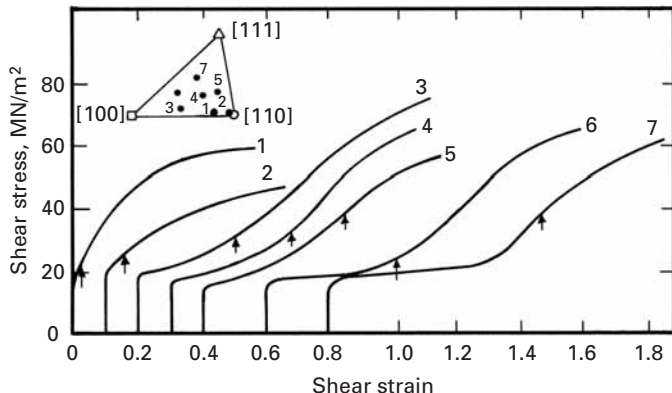


Figure 6.11. However, when the great circle passing through [100] and [111] is reached, the primary system and the *conjugate slip system* ( $\bar{1}\bar{1}1$ ) [ $\bar{1}\bar{1}0$ ] will have the same Schmid factor. The typical behavior in this case is double slip in both systems: The axis  $P_1$  will tend toward the direction [211], as shown in the figure. In reality, there are deviations from this behavior, and there is a tendency to “overshoot” and subsequent correction. The two other slip systems are called the *cross system* and the *critical system*. This nomenclature, however, is not universal: Often, the term “cross-slip” is used to describe a different situation – small slip segments in a secondary slip system joining slip lines in a primary slip system.

As a conclusion to the foregoing discussion, it can be said that a cubic crystal will initially undergo slip in one system if  $P_1$  is within the stereographic triangle. If  $P_1$  is on the sides of the triangle, two systems have the same Schmid factor. On the other hand, if  $P_1$  coincides with one of the edges, the situation is more complicated: Eight systems will have the same Schmid factor if  $P_1$  coincides with [100], four if it coincides with [110], and six if it coincides with [111]. The term “polyslip” refers to a crystal oriented in such a way that more than one system is activated.

When a cubic monocrystal with an orientation inside the stereographic triangle is deformed, one single slip system is often activated. Such orientations in the center of the stereographic triangle are considered “soft” orientations, and Figure 6.12 illustrates the different stress-strain curves obtained for niobium. Orientations 1 and 2 are close to polyslip, and the stress-strain curves have the characteristic parabolic hardening shape. Several slip systems are activated at the onset of yielding. For orientations 3 through 7, inside the stereographic triangle, one single slip system is activated first. The onset of conjugate slip requires rotation of the crystal toward an orientation along the sides of the triangle; this occurs only at a certain amount of strain, which depends on the orientation. Single slip is characterized by a very low work-hardening rate; once the conjugate slip becomes operative, the work-hardening rate increases significantly.

Figure 6.13 shows generic shear-stress-shear-strain curves for FCC single crystals. Any such curve can be divided, conveniently, into three regions: I, II, and III;  $\theta_I$ ,  $\theta_{II}$ , and  $\theta_{III}$  are the respective work-hardening slopes ( $d\tau/d\gamma$ ) of the regions. In what follows, we describe the salient points of the various stages.

Stage I starts after elastic deformation at the critical stress  $\tau_0$ . This stage, called “easy glide,” is a linear region of low strain-hardening rate.  $\theta_I$  is approximately  $G/3000$ . Stage I is characterized by long slip lines (100 to 1,000  $\mu\text{m}$ ), straight and uniformly spaced (10 to 100 nm apart). We adopt the nomenclature used by A. Seeger.<sup>2</sup> Slip lines are the “elementary structure” of slip and can be observed only via the electron microscope. With the optical microscope, one observes slip bands; they occur at the higher strains and are made up of clusters of slip lines. On the other hand, slip markings are observed as steps at the surface of the specimen. Stage I does not exist in polycrystals or in monocrystals oriented for polyslip. The extent of this stage depends strongly on the crystal orientation. The strain at the end of stage I ( $\gamma_2$ ) has a maximum value when the crystal orientation is located in the center of the standard stereographic triangle. The end of stage I is considered to be the start of secondary slip (when, in Figure 6.11, point  $P_1$  has moved to  $P_2$ ).

Stage II, or the linear hardening stage, has the following important characteristics.

1. A linear hardening regimen with a high  $\theta_{II}$ .
2.  $\theta_{II}/G \approx 1/300$ . This parameter is relatively constant for a great majority of metals. (The maximum variation is a factor of about 2).

$\theta_{II}$  is approximately equal to  $10\theta_I$  and is relatively independent of temperature, although temperature has a significant effect on the extent of stage II.

Stage III is characterized by cross-slip. Stage III is difficult to occur at a low level of stresses, and its operation is aided by high temperatures. Thus, one expects that the stress necessary at the start of stage III,  $\tau_3$ , would depend on temperature, and such, indeed, is the case in practice:  $\tau_3$  increases with a decrease in temperature.

The start of Stage III is also markedly dependent on the stacking-fault energy of the metal. Metals with relatively low stacking-fault energies – for example, brasses, bronzes, and austenitic steels – have a rather wide stacking-fault ribbon and, consequently, need a higher activation energy for cross-slip to occur. (See Figure 6.14.) This is so because, for cross-slip to occur in these metals, it is necessary to form a constriction over a wide ribbon of the stacking fault, in order to have a certain length of perfect dislocation. Thus, in metals and alloys with low stacking-fault energies, cross-slip will be difficult to bring about at normal stress levels. This, in turn, makes it difficult for the screw dislocations to change their slip plane. The dislocation density is high,

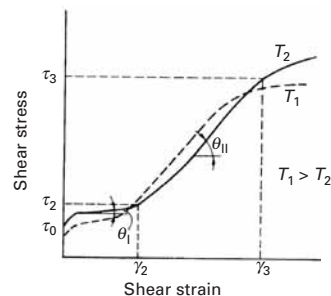
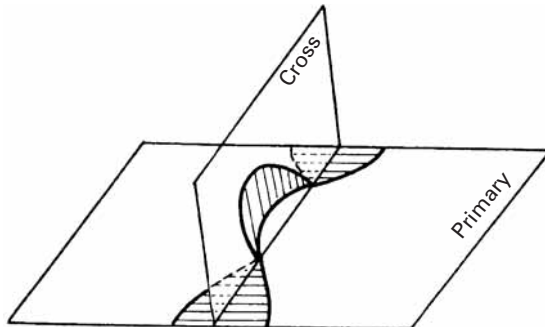


**Fig. 6.13** Generic shear-stress-shear-strain curves for FCC single crystals for two different temperatures.

<sup>2</sup> A. Seeger, in J. C. Fischer, W. G. Johnston, and T. Vreeland (eds.), *Dislocations and Mechanical Properties of Crystals* (New York: John Wiley, 1957), p. 243.

**Fig. 6.14** Model of cross-slip.



and the transition from stage II to stage III is retarded. Aluminum, on the other hand, has a higher stacking-fault energy. Thus, the stress necessary for cross-slip to occur in aluminum, at a given temperature, is much lower than in, say, copper or brass.

### 6.2.5 Independent Slip Systems in Polycrystals

For any FCC crystal whose tensile axis is near the center of the stereographic triangle, deformation should start on the primary system. However, if the crystal is surrounded by other crystals with different crystallographic orientations – as is likely in a polycrystalline aggregate – all the crystals (grains) are not likely to start deforming in the same manner. The strain taking place in the first grain must be compatible with the neighboring grains. In other words, it is not possible to form discontinuities along the grain boundaries; deformation has to propagate from one grain to another if continuity at the boundary is to be maintained. Five independent slip systems are required to produce a general homogeneous strain in a crystal by slip.

The slip along several parallel systems produces, macroscopically, a translation of one part of the crystal with respect to the other and, consequently, a certain shear. Since the plastic flow generally occurs without any appreciable change in volume, we have  $\varepsilon_{11} + \varepsilon_{22} + \varepsilon_{33} = 0$ . This relationship reduces the components of strain from six ( $\varepsilon_{11}$ ,  $\varepsilon_{22}$ ,  $\varepsilon_{33}$ ,  $\varepsilon_{12}$ ,  $\varepsilon_{13}$ ,  $\varepsilon_{23}$ ) to five; the operation of one slip system produces only one independent component of the strain tensor. Therefore, one may conclude that five independent slip systems are required for the deformation of one grain in a polycrystalline aggregate. Consequently, polycrystals do not exhibit stage I (easy glide) of work-hardening.

## 6.3 | Work-Hardening in Polycrystals

In the preceding sections, work-hardening in single crystals was attributed to the interaction of dislocations with other dislocations and barriers that impede the motion of dislocations through the crystal lattice. In polycrystals, too, this basic idea remains valid.

However, due to the mutual interference of neighboring grains and the problem of compatible deformations among adjacent grains, multiple slip occurs rather easily, and, consequently, there is an appreciable work-hardening right at the beginning of straining.

In a manner similar to that in single crystals, primary dislocations interact with secondary dislocations, giving rise to dislocation dipoles and loops which result in local dislocation tangles and, eventually, a three-dimensional network of subboundaries. Generally, the size of these cells decreases with increasing strain. The structural differences between one metal and another are mainly in the sharpness of these cell boundaries. In BCC metals and in FCC metals with high stacking-fault energy, such as Al, the dislocation tangles rearrange into a well-defined cell structure, while in metals or alloys with low stacking-fault energy (e.g., brasses, bronzes, austenitic steels, etc.), where the cross-slip is rather difficult and the dislocations are extended, the sharp subboundaries do not form even at very large strains.

The plastic deformation and the consequent work-hardening results in an increase in the dislocation density. An annealed metal, for example, will have about  $10^6$  to  $10^8$  dislocations per  $\text{cm}^2$ , while a plastically cold-worked metal may contain up to  $10^{12}$  dislocations per  $\text{cm}^2$ . The relationship between the flow stress and the dislocation density is the same as that observed for single crystals – that is,

$$\tau = \tau_0 + \alpha G b \sqrt{\rho}, \quad (6.5)$$

where  $\alpha$  is a constant with a value between 0.3 and 0.6. This relationship has been observed to be valid for a majority of the cases.  $\tau_0$  is the stress necessary to move a dislocation in the absence of other dislocations. Figure 6.15 shows that Equation 6.5 is obeyed for copper monocrystals (with one, two, and six slip systems operating), as well as polycrystals. The relationship is very important and serves as a basis for work-hardening theories. In ceramics, only limited observations of such kind have been made. Nevertheless, they show the same trend. Measurements of dislocation densities in sapphire (single-crystal  $\alpha$ -alumina) subjected to plastic deformation at high temperatures (1,400–1,720 °C), above the ductile-to-brittle transition, are shown in Figure 6.16. These dislocation densities were measured at strains  $\gamma < 0.23$ , and it was observed that the dislocation density showed a stress dependence analogous to Equation 6.5, with  $\tau_0 = 0$ . The proportionality coefficient was dependent on temperature and varied in the range 0.2–0.5, which is very similar to the corresponding range for metals.

Many theories have been advanced to explain the phenomenon of work-hardening. The most important and difficult part in the attempt to predict work-hardening behavior is to determine how the density and distribution of dislocations vary with the plastic strain. The problem is that stress is a state function in the thermodynamic sense

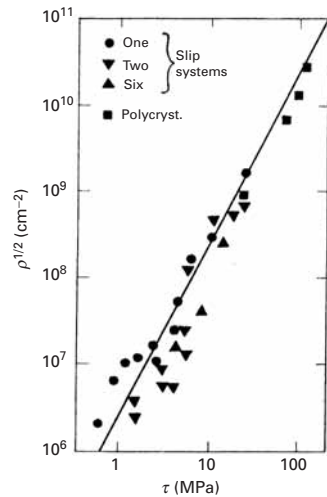
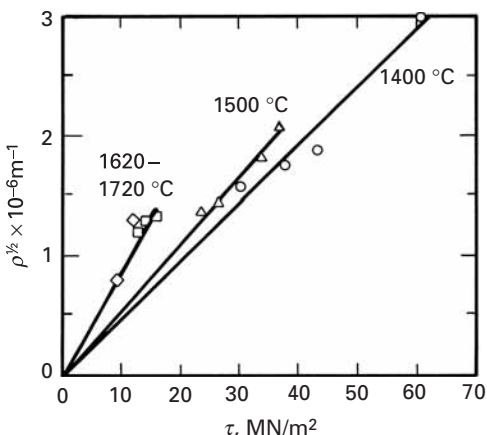


**Fig. 6.15** Average dislocation density  $\rho$  as a function of the resolved shear stress  $\tau$  for copper. (Adapted with permission from H. Wiedersich, *J. Metals*, 16 (1964) p. 425, 427.)

**Fig. 6.16** Relationship between flow shear stress and dislocation density for monocrystalline sapphire ( $\text{Al}_2\text{O}_3$ ) deformed at different temperatures. (Adapted from B. J. Pletka, A. H. Heuer, and T. E. Mitchell, *Acta Met.*, 25 (1977) 25.)



(i.e., it depends only on its position or value, not on how that particular value of stress was attained.) Plastic strain, on the other hand, is a path function of its position (i.e., it depends on the actual path traversed in reaching a certain strain value.) In other words, plastic strain is dependent on its history. Thus, the presence or absence of dislocations and their distributions can tell us nothing about how a certain amount of strain was accumulated in the crystal, because we do not know the path that dislocations traversed to accumulate that strain. Hence, one constructs models that recreate the processes by means of which the various dislocation configurations emerge; one then tries to correlate the models with the configurations observed experimentally. Both the density and the distribution of dislocations are very sensitive functions of the crystal structure, stacking-fault energy, temperature, and rate of deformation. In view of all this, it is not surprising that a unique theory of work-hardening which would explain all of its aspects does not exist.

In what follows, we briefly review three of the best-known theories of workhardening – those of Taylor, Seeger, and Kuhlmann–Wilsdorf.

### 6.3.1 Taylor's Theory

Taylor's theory<sup>3</sup> is one of the oldest theories of work-hardening. At the time the theory was postulated (1934), the stress-strain curve for metallic crystals such as aluminum was considered to be parabolic. (The single-crystal stress-strain curve consisting of three stages was unknown; see Figure 6.13.) This being so, Taylor proposed a model that would predict the parabolic curve. The principal idea, which, incidentally, is still used in one form or another by modern theories, was that the dislocations, on moving, elastically interact with other dislocations in the crystal and become trapped. These trapped dislocations give rise to internal stresses that increase the stress necessary for deformation (i.e., the flow stress).

<sup>3</sup> G. I. Taylor, *Proc. Roy. Soc. (London)*, A145 (1934) 362.

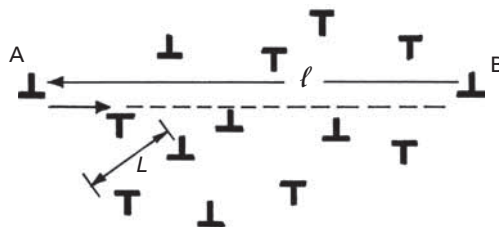


**Fig. 6.17** Taylor model of interaction among dislocations in a crystal.

Let  $\ell$  be the average distance that a dislocation moves before it is stopped. The initial and final positions  $A$  and  $B$  are marked in Figure 6.17. Let  $\rho$  be the dislocation density after a certain strain. Then the shear strain is given by (see Equation 4.29)

$$\gamma = k\rho b\ell, \quad (6.6)$$

where  $k$  is an orientation-dependent factor and  $b$  is the Burgers vector.

Taylor considered only edge dislocations and assumed that the dislocation distribution was uniform; thus, the separation between dislocations,  $L$ , will be equal to  $\rho^{-1/2}$ . (See Figure 6.17.) The effective internal stress  $\tau$ , caused by these interactions among dislocations, is the stress necessary to force two dislocations past each other. The interactions among dislocations are complex, involving attraction, repulsion, reactions, etc. Taylor considered only a very simple case: As the dislocation moves from  $A$  to  $B$ , it will approach the other dislocations, with the minimum distance being  $L/2$ . Taking into account just the repulsion from the dislocations, we can assume that, for an edge dislocation, the shear stress fields given in Chapter 4 are (Equation 4.12)

$$\sigma_{12} = \frac{Gb}{2\pi(1-\nu)} \frac{x_1(x_1^2 - x_2^2)}{(x_1^2 + x_2^2)}.$$

Supposing that  $x_2 = L/2$  and  $x_1 = 0$ , we arrive at

$$\sigma_{12} = \frac{Gb}{\pi(1-\nu)L} = \frac{K G b}{L},$$

where  $K$  is a constant. In order for the moving dislocation to overcome this stress field, a shear stress

$$\tau = \frac{K G b}{L}$$

has to be applied. Or, recalling that  $L = \rho^{-1/2}$ , we obtain

$$\tau = K G b \sqrt{\rho}. \quad (6.7)$$

From Equations 6.6 and 6.7, we get

$$\tau = K G b \sqrt{\frac{\gamma}{kb\ell}} = k' G \sqrt{\frac{\gamma}{\ell}}. \quad (6.8)$$

We could add a frictional term  $\tau_0$  that is required to move the dislocation in the absence of other dislocations, and arrive at:

$$\tau = \tau_0 + k''\gamma^{1/2}$$

Equation 6.8 is a parabolic relation between the stress  $\tau$  and the strain  $\gamma$ . It describes, approximately, the behavior of many materials at large deformations. Among the criticisms of the Taylor theory, one may include the following.

1. Such regular configurations of dislocations are rarely observed in cold-worked crystals.
2. Screw dislocations are not involved, and thus, the cross-slip is excluded; edge dislocations cannot cross-slip.
3. Two dislocations on neighboring planes may be trapped in each other's stress fields and may thus become incapable of moving independently of each other. But the pair of dislocations may be pushed by a third dislocation.
4. We know now that stress-strain curves for hexagonal crystals, as well as those for stage II of cubic crystals, are linear. Taylor's theory does not explain this linear hardening.
5. Taylor's parabolic relation derives from the supposition that there is a uniform distribution of deformed regions inside the crystal. In reality, the distribution is not uniform, and experimentally, we observe slip bands, cells, and other nonuniform arrangements.

### 6.3.2 Seeger's Theory

Seeger's theory, (see the suggested reading for details) addresses the three stages of work-hardening of a monocrystal (easy glide, linear hardening, and parabolic hardening) and proposes specific mechanisms for each stage. The values of the slopes for the three stages are obtained from dislocation considerations. In stage I, long-range interactions between well-spaced dislocations are considered. The dislocation loops are blocked by unspecified obstacles, all on the primary system. Slip activity on secondary slip systems begins in stage II of hardening. The secondary activity furnishes barriers such as Lomer-Cottrell barriers. The dislocations pile up against such barriers in Stage II and give rise to long-range internal stresses that control the flow stress. Without going into complex details, we can say that the long-range theory of Seeger *et al.* does predict that  $\theta_{II}/G \approx 1/300$  for FCC metals.

### 6.3.3 Kuhlmann–Wilsdorf's Theory

The substructures developed during metal deformation processes resemble the idealized models only in the initial stages. As the imposed deformation increases, dislocation cells start to form in alloys with medium and high stacking-fault energies. With increasing deformation, the cell diameters decrease, and the cells become elongated in the general direction of the deformation. The cell walls

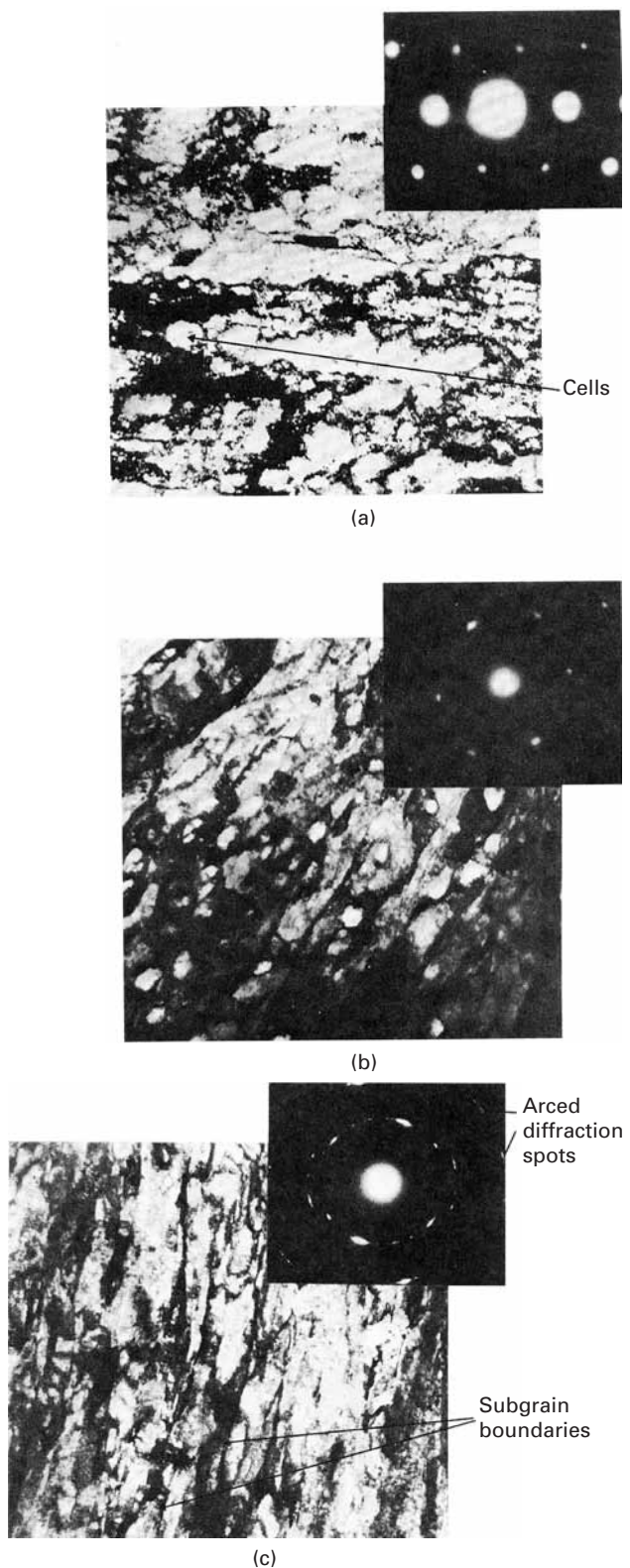


**Fig. 6.18** Development of substructure of Nickel-200 as a function of plastic deformation by cold rolling. (a) 20% reduction. (b) 40% reduction. (c) 80% reduction.

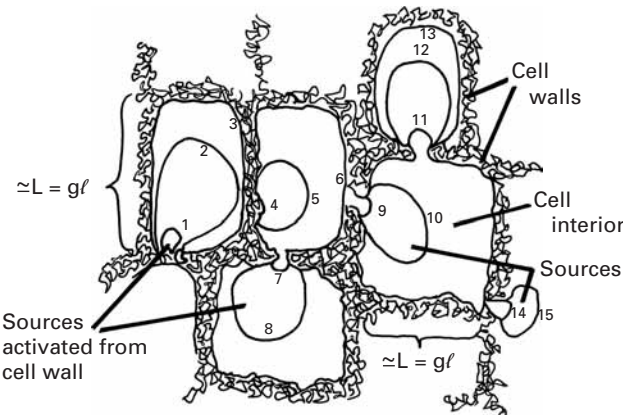
tend to become progressively sharper as the misorientation between two adjacent cells increases. A cell wall is essentially a low-angle grain boundary, but when the misorientation between adjacent cell walls reaches a certain critical value, we can no longer refer to the boundary in these terms. The boundary between two cells becomes free of dislocations, and subgrains are formed in a process called *polygonization*. This transition from cells to subgrains occurs at different effective strains for different materials: 0.80 for 99.97% pure Al and 1 to 1.20 for copper. A detailed treatment of the work-hardening and formation of texture at large imposed plastic strains is given by Gil Sevillano *et al.*<sup>4</sup> For metals with low stacking-fault energies, the development of a fine lamellar substructure consisting of microtwins, twin bundles, shear bands, and stacking faults is the characteristic feature of high-strain deformation.

Figure 6.18 shows the changes in substructure observed in nickel rolled at room temperature. At reductions up to 40%, we clearly have a cellular structure. We can see that at 40% (Figure 6.18(b)) we already have a large dislocation density. At 80% reduction, we can clearly see that many of the cell walls have disappeared and are replaced by well-defined boundaries. The observation is made more difficult because of the large density of dislocations. The electron diffraction patterns (right-hand corner of photomicrographs) show the effect very well. Up to 40% reductions, the diffraction spots are fairly clear, with little asterism (elliptical distortion). At 80% (Figure 6.18(c)), the asterism is very pronounced, and elongated spots break down into smaller spots, indicating that a distorted grain has broken down into subgrains, which have relatively little distortion. Based on observations of dislocation cells in plastically deformed metals with medium and high stacking-fault energies, Kuhlmann-Wilsdorf<sup>5</sup> proposed the so-called mesh-length theory, which is based on the stress necessary for dislocation bowing. In stage I, the dislocations multiply into certain restricted regions and penetrate into regions as yet substantially free of mobile dislocations, until a quasiuniform distribution of dislocations is obtained. The only resistance to deformation is the dislocation line tension. Thus, hardening occurs because free segments of dislocations become ever smaller. Stage II starts when there are no more "virgin" areas left for penetration by new dislocations. The stress required to bow segments of dislocation is responsible for a great part of stage II hardening: Dislocation segments can bow out inside the cells. Figure 6.19 shows, in a schematic manner, dislocation cells of size  $L$  in which the cell walls occupy a fraction  $f$  of the total crystal. Dislocation sources with mean width  $\ell$  are activated and form loops, as shown in the figure. As these loops are formed, the dislocation density increases and the cell size decreases. Kuhlmann-Wilsdorf was able to explain, in quantitative manner, the three stages of work-hardening.

---

<sup>4</sup> J. Gil Sevillano, P. van Houtte, and E. Aernoudt, *Prog. Mater. Sci.*, 25 (1981) 69.

<sup>5</sup> D. Kuhlmann-Wilsdorf, *Met. Trans.* 11A (1985) 2091.



**Fig. 6.19** Schematic representation of dislocation cells of size  $L$ , with activation of dislocation sources from the cell walls and bowing out of loops into the cell interior. (Courtesy of D. Kuhlmann-Wilsdorf.)

### Example 6.3

Consider dislocations blocked in a copper crystal. If the flow stress is controlled by the stress necessary to operate a Frank-Read source, compute the dislocation density  $\rho$  in this crystal when it is deformed to a point where the resolved shear stress in the slip plane is 42 MPa. Take  $G = 50$  GPa.

**Solution:** The dislocation line length is related to the dislocation density by

$$\ell = \rho^{-1/2}.$$

The flow stress is the shear stress necessary to operate a Frank-Read source. Hence (from Equation 4.22d),

$$\tau = G b / \ell = G b \sqrt{\rho}.$$

For copper,  $b = 3.6 \times 10^{-10}(\sqrt{2}/2) \text{ m} = 2.55 \times 10^{-10} \text{ m}$ , where  $3.6 \times 10^{-10} \text{ m}$  is the Cu lattice parameter. Rearranging the preceding expression, we obtain the dislocation density

$$\rho = \tau^2 / G^2 b^2 = (42 \times 10^6)^2 / (50 \times 10^9)^2 \times (2.55 \times 10^{-1})^2,$$

or

$$\rho = 1.09 \times 10^{13} \text{ m}^{-2}.$$

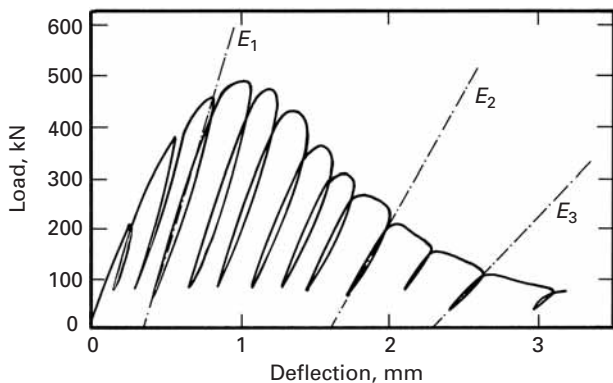
### Example 6.4

For the single crystal of an FCC metal, the work-hardening rate in shear is  $d\tau/d\gamma = 0.3$  GPa. Compute the work-hardening rate in tension,  $d\sigma/d\varepsilon$ , for a polycrystal of this metal. Take the Schmid factor  $M_p$  to be 1/3.1.

**Solution:** The tensile stress is related to the shear stress by the Schmid factor

$$\sigma = M_p^{-1} \tau.$$

**Fig. 6.20** Typical load deformation curve for concrete under uniaxial compression; the specimen was unloaded and reloaded at different stages of deformation. (From G. A. Hegemier and H. E. Reed, *Mech. Mater.*, 4 (1985) 215; data originally from A. Anvar.)



Thus,

$$d\sigma = M_p^{-1} d\tau. \quad (1)$$

Also, the tensile strain  $\varepsilon$  is related to the shear strain  $\gamma$  by

$$\varepsilon = M_p y.$$

Thus,

$$d\varepsilon = M_p^{-1} d\tau. \quad (2)$$

Dividing Equation 1 by Equation 2, we have

$$d\sigma/d\varepsilon = M_p^{-2} (d\tau/d\gamma) = (d\tau/d\gamma)(3.1)^2,$$

or

$$d\sigma/d\varepsilon = 9.61(d\tau/d\gamma) = 9.61 \times 0.3 = 2.88 \text{ GPa.}$$

## 6.4 | Softening Mechanisms

Under special circumstances, materials can undergo softening during plastic deformation. This degradation of a material's strength can be caused by a number of mechanisms. *Damage accumulation* is the most common mechanism in ceramics and composites. Damage can be of many types: microcracks forming in the material, a breakup of the matrix/reinforcement interface, cracking of second phase, etc. Figure 6.20 shows softening observed in concrete. The compression was halted at several points, and the specimen was unloaded and subsequently reloaded. The damage consists of microcracks, which results in the reduction in the Young's modulus of concrete as the compression evolves ( $E_1 > E_2 > E_3$ ). In Chapter 2, we saw how microcracks affect the Young's modulus of brittle materials. A discussion of damage accumulation in composites is given in Chapter 15.

*Softening of radiation-hardened materials* occurs when the sweeping of radiation induced defects (point defects) by dislocations leads to the formation of “soft” channels.

In *geometric softening*, during plastic deformation, individual grains rotate toward crystallographic orientations for which the Schmid factor is increased. This rotation can lead to global softening of the material in spite of the hardening along the individual slip systems.

We describe the last of the major softening mechanisms, *thermal softening*, in detail. The plastic deformation of a metal is an irreversible process, and most of the work of deformation is converted into heat. At most, only 10% of plastic deformation is stored as defects (primarily dislocations) as shown in the example below.

### Example 6.5

Calculate the stored energy in a copper crystal with a dislocation density of  $\sim 10^{11} \text{ cm}^{-2}$ , typical of a highly deformed metal.

*Solution:* We first find the total energy in the crystal which is equal to

$$U = \rho \frac{Gb^2}{2}.$$

For copper,  $G = 48.3 \text{ GPa}$  and  $b = 0.25 \text{ nm}$ . Thus, the total deformation energy is ( $\rho = 10^{11} \text{ cm}^{-2} = 10^{15} \text{ m}^{-2}$ ):

$$\begin{aligned} U &= \frac{1}{2} \times 10^{15} \times 48.3 \times 10^9 \times 0.0625 \times 10^{-18} \\ &= 1.5 \times 10^6 \text{ J/m}^3. \end{aligned}$$

Assuming that this sample of copper exhibits work-hardening and that the constitutive equation is (see Equation 3.11)

$$\sigma = \sigma_0 + K \varepsilon^n,$$

where

$$\sigma_0 = 50 \text{ MPa},$$

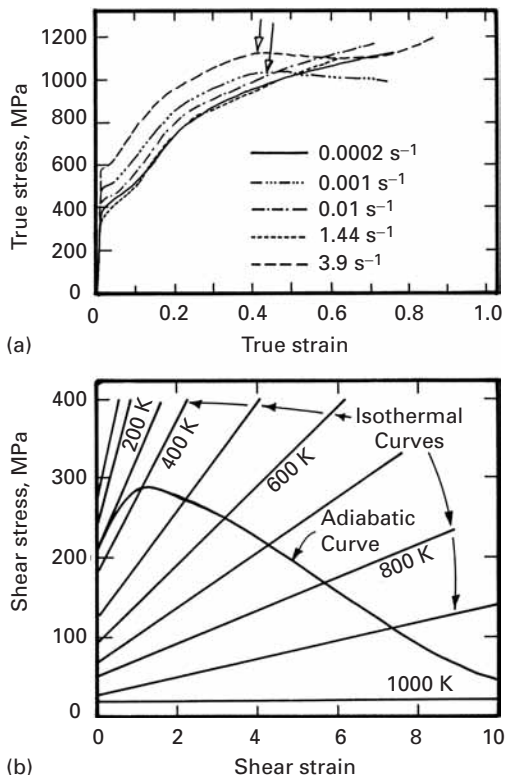
$$n = 0.5,$$

$$K = 500 \text{ MPa}.$$

We can calculate the total deformation energy per unit volume at a strain of 0.5:

$$\begin{aligned} U &= \int_0^\varepsilon \sigma d\varepsilon = \int_0^{\varepsilon_1} (\sigma_0 + K \varepsilon^n) d\varepsilon \\ &= \sigma_0 \varepsilon_1 + K \frac{\varepsilon_1^{n+1}}{n+1} = 50 \times 10^6 \times 0.5 + 500 \times 10^6 \times \frac{0.35}{1.5} \\ &= (25 + 116) \times 10^6 \\ &= 1.41 \times 10^8 \text{ J/m}^3. \end{aligned}$$

**Fig. 6.21** (a) Compressive true-stress–true-strain curves for titanium at different strain rates; notice the onset of softening at the arrows. (Adapted from M. A. Meyers, G. Subhash, B. K. Kad, and L. Prasad, *Mech. Mater.*, 17 (1994) 175.) (b) Schematic linear shear-stress–shear-strain curves for titanium at different temperatures, with superimposed adiabatic curve constructed from isothermal curves by incrementally converting deformation work into heat (and a consequent rise in temperature.) (Adapted from M. A. Meyers and H.-R. Pak, *Acta Met.*, 34 (1986) 2493.)



Thus, the dislocation energy represents 1.4% of the total work of deformation. The work of deformation leads to a rise in the temperature of the specimen.

If there is insufficient time for the heat to escape from the specimen during deformation, the material cannot be considered isothermal any longer, and the loss of strength caused by the increase in temperature will, at a certain point, exceed the increase in strength due to work-hardening. At this point, the stress-strain curve starts to go down, and thermal softening sets in. This is shown in Figure 6.21(a). At lower strain rates ( $2 \times 10^{-4} \text{ s}^{-1}$ ,  $10^{-3} \text{ s}^{-1}$ , and  $10^{-2} \text{ s}^{-1}$ ), the curves show the normal work-hardening behavior up to high strains. However, for the strain rates of  $1.44 \text{ s}^{-1}$  and  $3.9 \text{ s}^{-1}$ , the stress-strain curves show maxima beyond which softening sets in. It is easy to understand and to predict this softening. Figure 6.21(b) shows shear-stress–shear-strain curves for titanium at different temperatures. For simplicity, linear work-hardening was assumed. These curves are all isothermal. We now compute the temperature elevation produced by plastic deformation, by applying the following equation:

$$dT = \frac{\beta}{\sigma C_p} \sigma d\varepsilon,$$

where  $\beta$  is the conversion factor for mechanical energy into heat,  $C_p$  is the heat capacity and  $\rho$  the density of the material. By taking small increments of strain, we obtain

$$\Delta T = \frac{\beta}{\rho C_p} \sigma \Delta \varepsilon.$$

In Figure 6.21(b), an adiabatic curve was built in such a fashion. The work-to-heat conversion factor  $\beta$  is usually taken to be in the range 0.9–1.0. (Most of the work is converted to heat.) The adiabatic curve shows a maximum at  $\gamma$  approximately equal to 1; this marks the shear strain at which softening starts.

The softening of the material will lead to the phenomenon of adiabatic shear localization. Adiabatic shear bands are narrow regions where softening occurs and where concentrated plastic deformation takes place. Steels, titanium alloys, and aluminum alloys are quite prone to shear-band formation, which occurs in machining and which is responsible for the breakup of the machining chips. Shear-band formation also occurs in high-strain-rate operations, such as forging and shearing, as well as in ballistic impact.

Shear bands formed during forging operations are highly undesirable, because they can lead to subsequent fracture of the specimen. The microstructure within shear bands is quite different from that of the surrounding material. The shear bands often undergo dynamic recrystallization, due to the high local temperature.

In the ballistic impact of projectiles against armor, shear bands play a major role both in the defeat of the armor and in the breakup of the projectiles. Since recrystallization occurs very rapidly, the resultant grain size is very small, typically 0.1  $\mu\text{m}$ . Figure 6.22(a) shows a shear band in titanium with a width of approximately 10  $\mu\text{m}$ . The fine microcrystalline structure inside of the shear band is seen in the photomicrograph of Figure 6.22(b); the initial grain size of the material was 50  $\mu\text{m}$ .

## 6.5 | Texture Strengthening

A single crystal rotates when it deforms plastically in a particular slip system. (See Section 6.2.4.) When a polycrystal is deformed in rolling, forging, drawing, and so on, the randomly oriented grains will slip on their appropriate glide systems and rotate from their initial conditions, but this time under a constraint from the neighboring grains. Consequently, a strong preferred orientation or texture develops after large strains; that is, certain slip planes tend to align parallel to the rolling plane, while certain slip directions tend to align in the direction of rolling or wire drawing. In metals, annealing can also result in a texture generally different from that obtained by mechanical working, but still dependent on the history of the mechanical working. As an illustration, Figure 6.23 shows the microstructures along three perpendicular planes for nickel cold-rolled to a reduction in

**Fig. 6.22** Shear bands in titanium. (a) Optical micrograph, showing band. (b) Transmission electron micrograph, showing microcrystalline structure, with grain size approximately equal to  $0.2 \mu\text{m}$ . The original grain size of the specimen was  $50 \mu\text{m}$ .

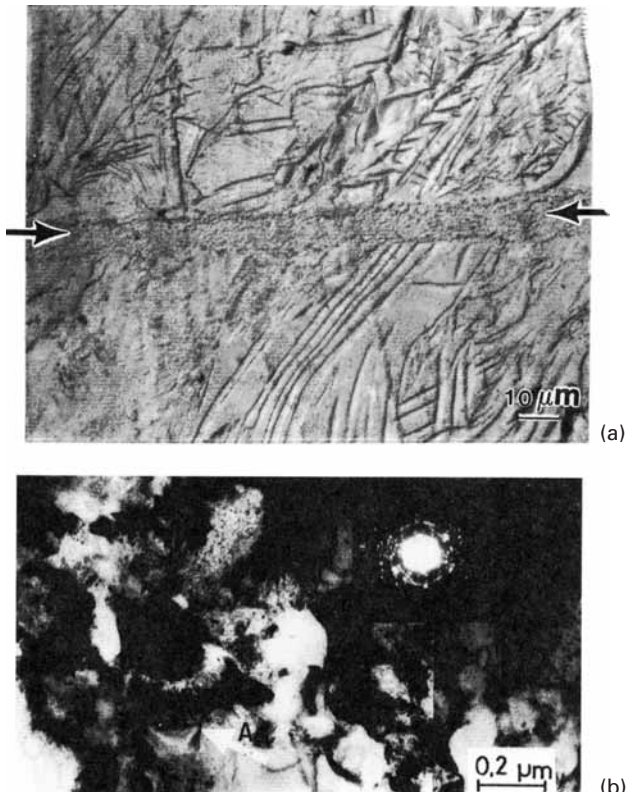
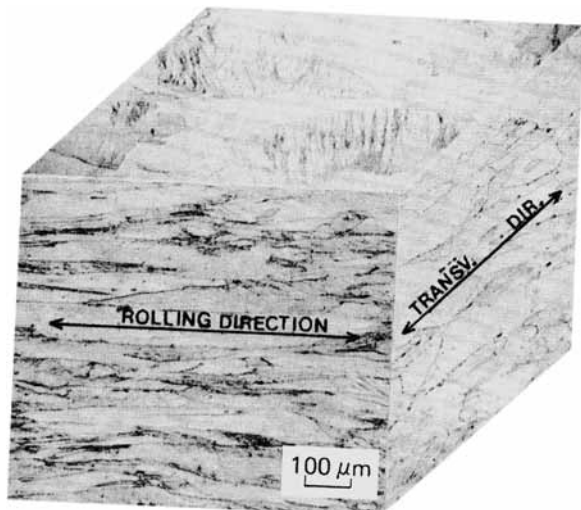
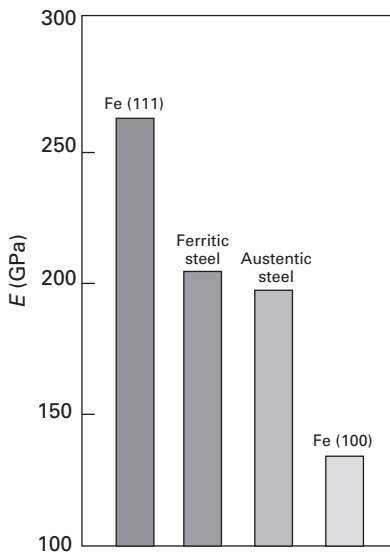


**Fig. 6.23** Perspective view of microstructure of Nickel-200 cold-rolled to a reduction in thickness of 60%.

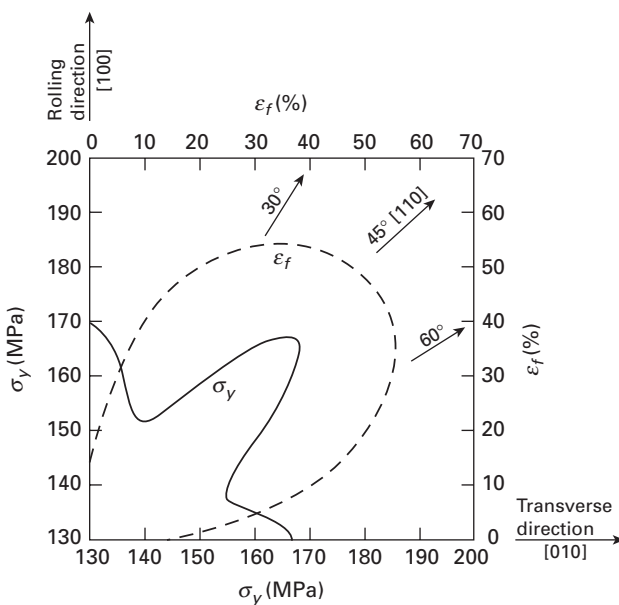


thickness of 60%. The highly elongated grains along the rolling direction are readily seen.

A strongly textured material can exhibit highly anisotropic properties. This is not intrinsically bad; in fact, controlled anisotropy in sheet metals can be exploited to obtain an improved final product. The



**Fig. 6.24** Theoretical bounds on the Young's modulus  $E$  of steel.

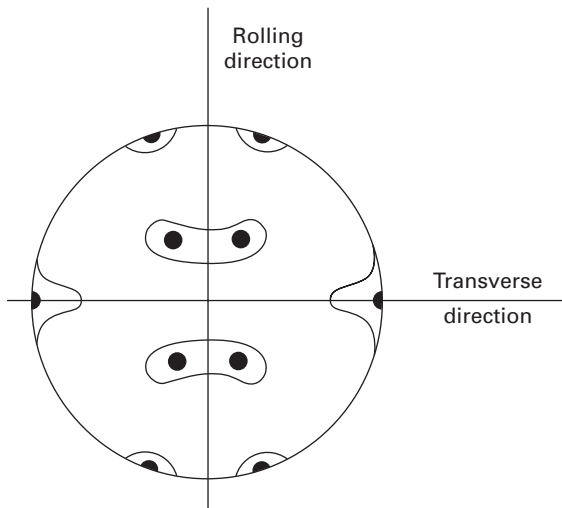


**Fig. 6.25** Orientation dependence of yield strength  $\sigma_y$  and strain to fracture,  $\varepsilon_f$ , of a rolled copper sheet.

Young's modulus  $E$  of steel can, theoretically, have a value between the extreme values of the iron monocrystal (i.e., between Fe[111] and Fe[100]), as shown in Figure 6.24. The Young's modulus cannot be changed much by alloying, but texture can – again, theoretically – have some influence. We caution the reader that the effect on  $E$ , for all practical purposes, is rather small. This is not the case, however, for many other properties. For example, Figure 6.25 shows the rather marked orientation dependence of the yield strength  $\sigma_y$  and the strain to fracture,  $\varepsilon_f$ , of a rolled copper sheet. Clearly, cups made out of this material by deep drawing would show “earing” at 90° intervals due to this texture (see Figure 3.45 for illustration of

**Table 6.1** Some Common Wire and Sheet Textures

	Wire (Fiber Texture)	Sheet (Rolling Texture)
FCC	$[1\bar{1}\bar{1}] + [100]$	$(110)[1\bar{1}2] + (112)[1\bar{1}\bar{1}]$
BCC	$1\bar{1}0$	$(100)[011]$
HCP	$[10\bar{1}0]$	$(0001)[1\bar{1}\bar{2}0]$

**Fig. 6.26**  $[111]$  pole figure of a rolled-brass sheet.

“earing”). Use is made of such texture development in Fe–3% Si. Sheets of this material are used to make transformer cores, wherein thermo-mechanical treatments are given to develop a desirable magnetic anisotropy that improves electrical performance.

Crystallographic texture is commonly represented in the form of normal-pole or inverse-pole figures. A normal-pole figure is a stereographic projection showing the intensity of normals to a specific plane in all directions, while an inverse-pole figure is a stereographic projection showing the intensities of all planes in a specific direction. The experimental procedure involves measuring relative intensities of X-ray reflections from the polycrystalline material at different angular settings. Details of the experimental determination of pole figures can be found in standard texts on the subject.

Figure 6.26 shows the  $[111]$  pole figure of a heavily deformed  $\alpha$ -brass (70% Cu–30% Zn) sheet. This texture, called brass-type texture, is a  $(110)[1\bar{1}2]$  texture, i.e., with  $(110)$  planes parallel to the rolling plane and  $[1\bar{1}2]$  directions parallel to the rolling direction. The double texture indicated for FCC structures in Table 6.1 is not obtained in  $\alpha$ -brass, but single  $(110)[1\bar{1}2]$  texture develops, owing to the material’s low stacking-fault energy or (probably) to mechanical twinning.

## Suggested Reading

### Geometry of Deformation

- J. GilSevillano, P. van Houtte, and E. Aernoudt, "Large Strain Work Hardening and Textures", in *Progress in Materials Science*, vol. 25, J. W. Christian, P. Haasen, and T. B. Massalski, eds., Elmsford, NY: Pergamon Press, 1981, p. 69.
- R. W. K. Honeycombe and H. K. D. H. Bhadeshia. *The Plastic Deformation of Metals*. New York, NY: St. Martin's Press, 1995.
- W. F. Hosford, *The Mechanics of Crystals and Textured Polycrystals*. New York, NY: Oxford University Press, 1993.

### Work-Hardening

- L. M. Clarebrough and M. E. Hargreaves. "Work Hardening of Metals," in *Progress in Metal Physics*, Vol. 8, B. Chalmers and W. Hume-Rothery, eds. New York, NY: Pergamon Press, 1959, p. 1.
- A. H. Cottrell. *Dislocations and Plastic Flow in Crystals*. Oxford: Clarendon Press, 1953.
- P. B. Hirsch, ed. *The Physics of Metals*, Vol. 2: Defects. Cambridge, U.K.: Cambridge University Press, 1975.
- J. P. Hirth and J. Lothe. *Theory of Dislocations*, 2nd. ed. New York, NY: J. Wiley, 1982.
- D. Kuhlmann-Wilsdorf, *Met. Trans.* 11A (1985) 2091.
- A. Seeger, in *Work Hardening*, TMS-AIME Conf., Vol. 46, 1966, p. 27.
- A. W. Thompson, ed. *Work Hardening in Tension and Fatigue*. New York, NY: TMS-AIME, 1977.

## Exercises

**6.1** Discuss the merits and demerits of the use of transmission electron microscopy techniques to study the dislocation behavior in crystalline materials.

**6.2** Explain why a metal like lead does not work-harden when deformed at room temperature, whereas a metal such as iron does.

**6.3** What is the effect of cold work and annealing on the Young's modulus of a metal?

**6.4** If we strain an FCC and an HCP single crystal, which of the two will have a larger amount of easy glide, and why?

**6.5** In a cold-worked metal, a dislocation density of  $1 \times 10^{16} \text{ m}^{-2}$  was measured after a shear strain of 10%. Assuming that the dislocations are uniformly distributed, estimate the flow stress of this metal. Take  $G = 25 \text{ GPa}$ .

**6.6** Consider dislocations blocked with an average spacing of  $\ell$  in a copper crystal. If the flow stress is controlled by the stress necessary to operate a Frank-Read source, compute the dislocation density  $\rho$  in this crystal when it is deformed to a point where the resolved shear stress in the slip plane is 42 MPa. Take  $G = 50 \text{ GPa}$ .

**6.7** Make a schematic plot showing the variation in the following parameters with percent cold work:

- (a) ultimate tensile strength,
- (b) yield strength in tension,
- (c) strain to failure,
- (d) reduction in area.

**6.8** The stress axis in an FCC crystal makes angles of  $31^\circ$  and  $62^\circ$  with the normal to the slip plane and with the slip direction, respectively. The applied stress is  $10 \text{ MN/m}^2$ .

- (a) Determine the resolved stress in the shear plane.
- (b) Is the resolved stress larger when the angles are  $45^\circ$  and  $32^\circ$ , respectively?
- (c) Using a stereographic projection, determine the resolved stresses on the other slip systems.

**6.9** Magnesium oxide is cubic (having the same structure as NaCl). The slip planes and directions are [110] and  $<110>$ , respectively. Along which directions, if any, can a tensile (or compressive) stress be applied without producing slip?

**6.10** A Cu monocrystal (FCC) of 10 cm length is pulled in tension. The stress axis is [123].

- (a) Which is the stress system with the highest resolved shear stress?
- (b) If the extension of the crystal continues until a second slip system becomes operational, what will this system be?
- (c) What rotation will be required to activate the second system?
- (d) How much longitudinal strain is required to activate the second system?

**6.11** Flow stress varies with strain rate; one equation that has been used to express this dependence is

$$\sigma = c\dot{\varepsilon}^{m'} f(\varepsilon, T),$$

where  $m'$  is the strain-rate sensitivity, which is generally less than 0.1. Some metals, called superplastic, can undergo elongations of up to 1,000% in uniaxial tension. Assuming that these tests are performed at a uniform velocity of the crosshead, will the metals have a very high or a very low value of  $m'$ ? Explain, in terms of the formation and inhibition of the neck.

**6.12** Johnston and Gilman<sup>6</sup> experimentally determined the relationship between dislocation velocity and applied stress

$$v = A\sigma^m,$$

where  $A$  is the constant of proportionality. Assuming that the mobile dislocation density does not depend on the velocity of the dislocations, obtain a relationship between  $m$  and  $m'$  (from Exercise 6.11).

**6.13** The following results were obtained in an ambient-temperature tensile test, for an aluminum monocrystal having a cross-sectional area of  $9 \text{ mm}^2$  and a stress axis making angles of  $27^\circ$  with [100],  $24.5^\circ$  with [110], and  $29.5^\circ$  with [111]:

---

<sup>6</sup> W. G. Johnston and J. J. Gilman, *J. Appl. Phys.*, 30 (1959) 129.

Load (N)	Length (cm)
0	10.000
12.40	10.005
14.30	10.040
16.34	10.100
18.15	10.150
21.10	10.180
23.60	10.200
26.65	10.220

- (a) Plot the results in terms of true stress versus true strain.  
 (b) Determine the resolved shear stress on the system that will slip first.  
 (c) Determine the longitudinal strain at the end of the easy-glide stage (when a second slip system becomes operative).

**6.14** Take a stereographic triangle for a cubic metal. If the FCC slip systems are operative, indicate the number of slip systems having the same Schmid factor if the stress axis is:

- (a) [111],  
 (b) [110],  
 (c) [100],  
 (d) [123].

Use the stereographic projections to show your results.

**6.15** A copper bicrystal is composed of two monocrystals separated by a coherent twin boundary (111). The bicrystal is being compressed in a homogeneous upset test in such a way that the twin boundary is perpendicular to machine plates. The compression direction is the same for both crystals, namely, [134].

- (a) Is this crystal isoaxial?  
 (b) Is deformation in the two crystals compatible or incompatible?

**6.16** The flow stress  $\sigma$  is related to the dislocation density  $\rho$  by the relationship

$$\sigma_1 = \sigma_i + \alpha G b \sqrt{\rho},$$

where the symbols have their usual significance. If the dislocation density is inversely related to the grain size  $d$ , show that a Hall-Petch type of dependence of flow stress on grain size is obtained.

**6.17** For an FCC polycrystalline metal, TEM analysis showed that the dislocation density after cold working was  $5 \times 10^{10} \text{ m}^{-2}$ . If the friction stress is 100 MPa,  $G = 40 \text{ GPa}$ , and  $b = 0.3 \text{ nm}$ , compute the flow stress of this metal.

**6.18** The stress-strain curve of a polycrystalline aluminum sample can be represented by

$$\sigma = 25 + 200\epsilon^{0.5}.$$

Calculate the energy of deformation per unit volume corresponding to uniform strain (i.e., just prior to the onset of necking) in this material.

**6.19** An FCC crystal is pulled in tension along the [100] direction.

- Determine the Schmid factor for all slip systems.
- Identify the slip system(s) that will be activated first.
- What is the tensile stress at which this crystal will flow plastically? ( $\tau = 50 \text{ MPa}$ .)

**6.20** Calculate the total energy due to dislocations for copper that underwent 20% plastic deformation, resulting in a dislocation density of  $10^{14} \text{ m}^{-2}$ . Assume that  $b = 0.3 \text{ nm}$ .

**6.21** Using data from Figure Ex6.21 for (Ni-22%Cr-12%Co-9%Mo), obtain appropriate parameters for the Johnson-Cook equation (see Chapter 3). Assume  $\dot{\varepsilon}_0 = 3 \times 10^{-4} \text{ s}^{-1}$  and  $T_m = 1,600 \text{ K}$ .

- Using the Johnson-Cook equation, plot stress-strain curves for temperatures of 77, 173, 473, and 1,473 K.
- If  $C = 0.02$ , plot the stress strain curves for a strain rate of  $3 \times 10^4 \text{ s}^{-1}$ .

**6.22** A monocrystal (diameter 4 mm, length 100 mm) is being pulled in tension.

- What is the elongation undergone by the specimen if 1,000 dislocations on slip planes making  $45^\circ$  with the tension axis cross the specimen completely? Take  $b = 0.25 \text{ nm}$ .
- What would the elongation be if all dislocations existing in the crystal ( $10^6 \text{ cm}^{-2}$ ) were ejected by the applied stress? Assume a homogeneous distribution of dislocations. Assume that the crystal is FCC and all the dislocations are in the same slip system.

**6.23** A long crystal with a square cross section ( $1 \times 1 \text{ cm}$ ) is bent to form a semicircle with radius  $R = 25 \text{ cm}$ .

- Determine the total number of dislocations generated if all bending is accommodated by edge dislocations.
- Determine the dislocation density ( $b = 0.3 \text{ nm}$ ).

**6.24** The response of copper to plastic deformation can be described by Holomon's equation  $\sigma = K \varepsilon^{0.7}$ .

It is known that for  $\varepsilon = 0.25$ ,  $\sigma = 120 \text{ MPa}$ . The dislocation density varies with flow stress according to the well-known relationship

$$\sigma = K' \rho^{1/2}.$$

- If the dislocation density at a plastic strain of 0.4 is equal to  $10^{11} \text{ cm}^{-2}$ , plot the dislocation density versus strain.
- Calculate the work performed to deform the specimen.
- Calculate the total energy stored in the metal as dislocations after a plastic deformation of 0.4, and compare this value with the one obtained in part (d).
- Explain the difference.

**6.25** A single crystal of silver is pulled in tension along the [100] direction. Determine the Schmid factor for all slip systems. What is the tensile stress at which this crystal will flow plastically? ( $\tau = 100 \text{ MPa}$ .)

**6.26** Determine the area of the slip plane in Ni deformed parallel to [100] and under a load  $P = 150 \times 10^3 \text{ N}$ . The shear stress is 600 MPa.

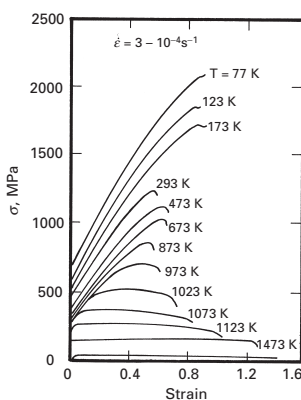


**Fig. Ex6.21** (After D. Viereck, G. Merckling, K. H. Lang, D. Eifler, and D. Löhe, in *Festigkeit und Verformung bei Höherer Temperatur*, K. Schneider, ed. (Oberursel: Informationsgesellschaft, pp. 102–208.)

6.27 Compute the dislocation density in tungsten if the flow stress is controlled by the stress necessary to operate a Frank–Read source. The shear stress in the slip plane is 50 MPa. Take  $G = 166$  GPa.

6.28 List all the slip systems in single crystal copper. Calculate the Schmid factors for them with loading axis as [221]. Which system will be activated first when we apply the load?

6.29 Obtain the parameters for the relationship between the flow stress and the dislocation density for copper with one, two, and six slip systems from the data in Figure 6.15. Use the equation:

$$\tau = \tau_0 + \alpha G b \sqrt{\rho}.$$

6.30 What is the dislocation density in iron with a shear strain of 0.4?

Given:

- (a)  $\tau = \tau_0 + K \gamma^n$ ,  $\tau_0 = 50 \times 10^6$  MPa,  $K = 10^8$  MPa,  $n = 0.5$ ,
- (b)  $\tau = \tau_0 + \alpha G b \sqrt{\rho}$ ,  $G = 81.6$  GPa,  $b = 0.25$  nm,  $\alpha = 0.5$ .

6.31 The flow stress for an alloy is 100 MPa when its dislocation density is  $10^6$  cm $^{-2}$ , and 150 MPa when its dislocation density is  $10^8$  cm $^{-2}$ . When the flow stress is 190 MPa, what is the dislocation density?

6.32 A copper sample exhibits work-hardening described by:

$$\sigma = \sigma_0 + K \varepsilon^n,$$

where  $\sigma_0 = 50$  MPa,  $n = 0.5$ ,  $K = 500$  MPa.

Calculate the temperature rise when the sample is deformed up to a strain of 0.2. Assume that the conversion factor is 1.0, and given: density = 8.9 g/cm $^3$ ; heat capacity = 360 J/kg K.

---

## Chapter 7

# Fracture: Macroscopic Aspects

---

### 7.1 | Introduction

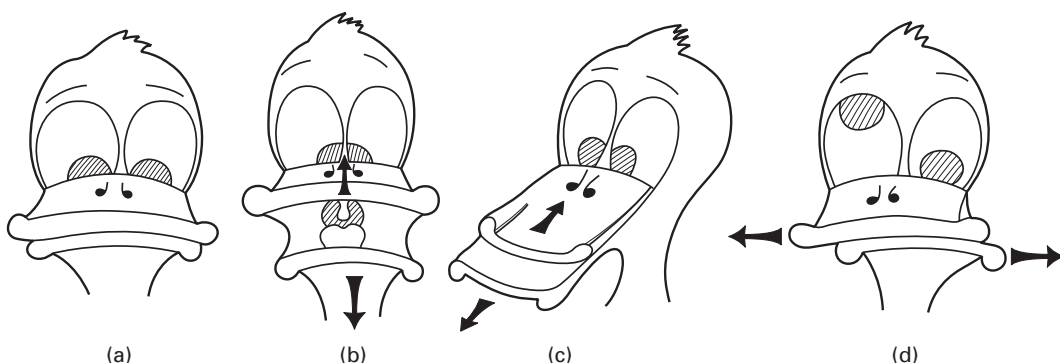
The separation or fragmentation of a solid body into two or more parts, under the action of stresses, is called *fracture*. The subject of fracture is vast and involves disciplines as diverse as solid-state physics, materials science, and continuum mechanics. Fracture of a material by cracking can occur in many ways, principally the following:

1. Slow application of external loads.
2. Rapid application of external loads (impact).
3. Cyclic or repeated loading (fatigue).
4. Time-dependent deformation (creep).
5. Internal stresses, such as thermal stresses caused by anisotropy of the thermal expansion coefficient or temperature differences in a body.
6. Environmental effects (stress corrosion cracking, hydrogen embrittlement, liquid metal embrittlement, etc.)

The process of fracture can, in most cases, be subdivided into the following categories:

1. Damage accumulation.
2. Nucleation of one or more cracks or voids.
3. Growth of cracks or voids. (This may involve a coalescence of the cracks or voids.)

Damage accumulation is associated with the properties of a material, such as its atomic structure, crystal lattice, grain boundaries, and prior loading history. When the local strength or ductility is exceeded, a crack (two free surfaces) is formed. On continued loading, the crack propagates through the section until complete rupture occurs. Linear elastic fracture mechanics (LEFM) applies the theory of linear elasticity to the phenomenon of fracture – mainly, the propagation of cracks. If we define the fracture toughness of a material as its resistance to crack propagation, then we can use LEFM to



provide us with a quantitative measure of fracture toughness. Various standardization bodies, such as the American Society for Testing and Materials (ASTM), British Standards Institution (BSI), and Japan Institute of Standards (JIS), have standards for fracture toughness tests.

In this chapter, we will develop a quantitative understanding of cracks. It is very important to calculate the stresses at the tip (or in the vicinity of the tip) of a crack, because these calculations help us answer a very important practical question: At what value of the external load will a crack start to grow?

Figure 7.1 shows a simple analog that will assist the student in the visualization of different types of crack. In Figure 7.1(a), “goofy duck” has its beak initially closed. Let us consider the spacing between the upper and lower beaks as a crack. Depending on how the goofy duck moves its beak, different modes of crack loading are generated:

- The opening mode, shown in Figure 7.1(b) is caused by loading that is perpendicular to the crack plane.
- The sliding mode, shown in Figure 7.1(c) is produced by forces parallel to the crack plane and perpendicular to the crack “line” (crack extremity).
- The tearing mode (Figure 7.1d) is produced by forces parallel to the crack surface and to the crack “line.”

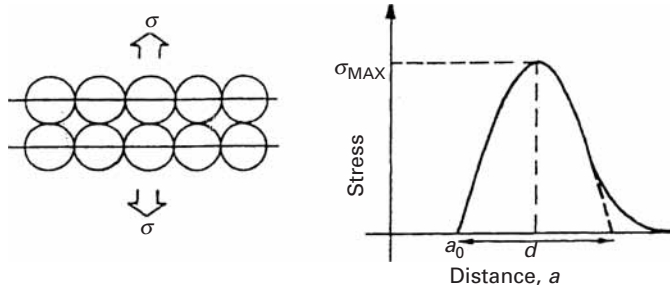
Among the parameters and tests that have been developed, mostly during the last quarter of the twentieth century, to describe the resistance to fracture of a material in a quantitative and reproducible manner, is the *plane strain fracture toughness*, defined as the critical stress intensity factor under plane strain conditions and mode I loading. This is the stress intensity factor at which a crack of a given size starts to grow in an unstable manner. The fracture toughness is related to the applied stress by an equation of the following form:

$$K_{Ic} = Y \sigma \sqrt{\pi a},$$

where  $K_{Ic}$  is the fracture toughness in mode I loading,  $a$  is the characteristic dimension (semilength) of the crack and  $Y$  is a

**Fig. 7.1** “Goofy duck” analog for three modes of crack loading. (a) Crack/beak closed. (b) Opening mode. (c) Sliding mode. (d) Tearing mode. (Courtesy of M. H. Meyers.)

**Fig. 7.2** Stress required to separate two atomic layers.



factor that depends on the geometry of the specimen, the location of the crack, and the loading configuration. One can see that the stress which can be safely applied decreases with the square root of the size of the crack. Also, note that  $K_{lc}$  is a parameter of the material in the same manner as are hardness and yield strength. We will explain this in detail in Section 7.5. First we derive an expression for the theoretical tensile strength of a crystal.

## 7.2 | Theoretical Tensile Strength

A material is said to *cleave* when it breaks under normal stress and the fracture path is perpendicular to the applied stress. The process involves the separation of the atoms along the direction of the applied stress. Orowan developed a simple method for obtaining the theoretical tensile strength of a crystal.<sup>1</sup> With his method, no stress concentrations at the tip of the crack are assumed; instead, it is assumed that all atoms separate simultaneously once their separation reaches a critical value. Figure 7.2 shows how the stress required to separate two planes will vary as a function of the distance between planes. The distance is initially equal to  $a_0$ . Naturally,  $\sigma$  for  $a = a_0$ ;  $\sigma$  will also be zero when the separation is infinite. The exact form of the curve of  $\sigma$  versus  $a$  depends on the nature of the interatomic forces. In Orowan's model, the curve is simply assumed to be a sine function – hence the generality of the model. The area under the curve is the work required to cleave the crystal. This work of deformation – and here there is a certain similarity with Griffith's crack propagation theory to be presented in Section 7.4 – cannot be lower than the energy of the two new surfaces created by the cleavage. If the surface energy per unit area is  $\gamma$  and the cross-sectional area of the specimen is  $A$ , the total energy is  $2\gamma A$  (two surfaces formed). The stress dependence on plane separation is then given by the following equations, admitting a sine function and assuming a periodicity of  $2d$ :

$$\sigma = K \sin \frac{2\pi}{2d} (a - a_0). \quad (7.1)$$

<sup>1</sup> E. Orowan, "Fracture and Strength of Solids," *Rep. Prog. Phys.*, 12 (1949) 185.

$K$  is a constant that can be determined by the following artifice: When  $a$  is close to  $a_0$ , the material responds linearly to the applied loads (Hookean behavior). Assuming that the elastic deformation is restricted to the two planes shown in Figure 7.2 and that the material is isotropic, the fractional change in the distance between the planes,  $da/a_0$ , is defined as the incremental strain  $d\varepsilon$ .

$$\frac{da}{a_0} = d\varepsilon$$

$$\frac{d\sigma}{d\varepsilon} = \frac{d\sigma}{da/a_0} = E, \quad (7.2)$$

where  $E$  is Young's modulus, which is defined as  $d\sigma/d\varepsilon$  in the elastic region. Thus,

$$a_0 \frac{d\sigma}{da} = E.$$

Taking the derivative of Equation 7.1 and substituting into Equation 7.2 for  $a = a_0$ ,

$$a_0 \frac{d\sigma}{da} = K \frac{\pi}{d} a_0 \cos \frac{\pi}{d} (a - a_0) = E,$$

$$K = \frac{E}{\pi} \frac{d}{a_0}. \quad (7.3)$$

However,  $d$  is not known; to determine  $d$ , the area under the curve has to be equated to the energy of the two surfaces created:

$$\int_{a_0}^{a_0+d} \sigma da = 2\gamma. \quad (7.4)$$

Substituting Equation 7.1 into 7.4, we get

$$\int_{a_0}^{a_0+d} K \sin \frac{2\pi}{2d} (a - a_0) da = 2\gamma. \quad (7.5)$$

From a standard mathematics text, the preceding integral can be evaluated:

$$\int \sin ax dx = \frac{1}{a} \cos ax. \quad (7.6)$$

A substitution of variables is required to solve Equation 7.5; applying the standard Equation 7.6, we have  $a - a_0 = y$ ; therefore,  $da = dy$ , and

$$K \int_0^d \sin \frac{\pi}{d} y dy = 2\gamma,$$

$$K \frac{d}{\pi} = \gamma,$$

and

$$d = \frac{\pi\gamma}{K}. \quad (7.7)$$

The maximum value of  $\sigma$  is equal to the theoretical cleavage stress. From Equation 7.1, and making the sine equal to 1, we have,

**Table 7.1** Theoretical Cleavage Stresses According to Orowan's Theory\*

Element	Direction	Young's Modulus (GPa)	Surface Energy (mJ/m <sup>2</sup> )	$\sigma_{\max}$ (GPa)	$\sigma_{\max}/E$
$\alpha$ -Iron	<100>	132	2	30	0.23
	<111>	260	2	46	0.18
Silver	<111>	121	1.13	24	0.20
Gold	<111>	110	1.35	27	0.25
Copper	<111>	192	1.65	39	0.20
	<100>	67	1.65	25	0.38
Tungsten	<100>	390	3.00	86	0.22
Diamond	<111>	1,210	5.4	205	0.17

\* Adapted with permission from A. Kelly, *Strong Solids*, 2nd ed. (Oxford, U.K.: Clarendon Press, 1973), p. 73.

from Equation 7.3,

$$\sigma_{\max} = K = \frac{E}{\pi} \frac{d}{a_0}. \quad (7.8)$$

Substituting Equation 7.7 into Equation 7.8 yields

$$K = \sigma_{\max} = \frac{E \gamma}{a_0 K},$$

and

$$K^2 = (\sigma_{\max})^2 = \frac{E \gamma}{a_0},$$

or

$$\sigma_{\max} = \sqrt{\frac{E \gamma}{a_0}}. \quad (7.9)$$

According to Orowan's model, the surface energy is given by

$$\gamma = \frac{Kd}{\pi} = \frac{E}{a_0} \left( \frac{d}{\pi} \right)^2 \quad (7.10)$$

$$\gamma = \frac{Ea_0}{10} \quad \text{and} \quad \boxed{\sigma_{\max} \cong \frac{E}{\pi}} \quad (7.11)$$

We can conclude from Equation 7.9 that, in order to have a high theoretical cleavage strength, a material must have a high Young's modulus and surface energy and a small distance  $a_0$  between atomic planes. Table 7.1 presents the theoretical cleavage strengths for a number of metals. The greatest source of error is  $\gamma$ : it is not easy to determine  $\gamma$  with great precision in solids, and the values used in the table come from different sources and were not necessarily determined at the same temperature.

## 7.3 Stress Concentration and Griffith Criterion of Fracture

The most fundamental requisite for the propagation of a crack is that the stress at the tip of the crack must exceed the theoretical cohesive strength of the material. This is indeed the fundamental criterion, but it is not very useful, because it is almost impossible to measure the stress at the tip of the crack. An equivalent criterion, called the Griffith criterion, is more useful and predicts the force that must be applied to a body containing a crack for the propagation of the crack. The Griffith criterion is based on an energy balance and is described in Section 7.4. Let us first grasp the basic idea of stress concentration in a solid.

### 7.3.1 Stress Concentrations

The failure of a material is associated with the presence of high local stresses and strains in the vicinity of defects. Thus, it is important to know the magnitude and distribution of these stresses and strains around cracklike defects.

Consider a plate having a through-the-thickness notch and subjected to a uniform tensile stress away from the notch (Figure 7.3). We can imagine the applied external force being transmitted from one end of the plate to the other by means of lines of force (similar to the well-known magnetic lines of force). At the ends of the plate, which is being uniformly stretched, the spacing between the lines is uniform. The lines of force in the central region of the plate are severely distorted by the presence of the notch (i.e., the stress field is perturbed). The lines of force, acting as elastic strings, tend to minimize their lengths and thus group together near the ends of the elliptic hole. This grouping together of lines causes a decrease in the line spacing locally and, consequently, an increase in the local stress (a stress concentration), there being more lines of force in the same area.

### 7.3.2 Stress Concentration Factor

The theoretical fracture stress of a solid is on the order  $E/10$  (see Section 7.2), but the strength of solids (crystalline or otherwise) in practice is orders of magnitude less than this value. The first attempt

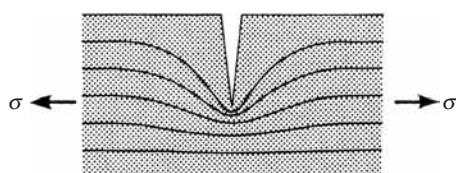


**Fig. 7.3** “Lines of force” in a bar with a side notch. The direction and density of the lines indicate the direction and magnitude of stress in the bar under a uniform stress  $\sigma$  away from the notch. There is a concentration of the lines of force at the tip of the notch.

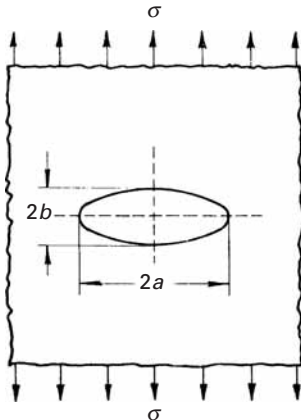


**Fig. 7.4** Griffith model of a crack.

at giving a rational explanation of this discrepancy was attributed to Griffith. His analytical model was based on the elastic solution of a cavity elongated in the form of an ellipse.

Figure 7.4 shows an elliptical cavity in a plate under a uniform stress  $\sigma$  away from the cavity. The maximum stress occurs at the ends of the major axis of the cavity and is given by Inglis's formula,<sup>2</sup>

$$\sigma_{\max} = \sigma \left( 1 + 2 \frac{a}{b} \right). \quad (7.12)$$

where  $2a$  and  $2b$  are the major and minor axes of the ellipse, respectively.<sup>3</sup> The value of the stress at the leading edge of the cavity becomes extremely large as the ellipse is flattened. In the case of an extremely flat ellipse or a very narrow crack of length  $2a$  and having a radius of curvature  $\rho = b^2/a$ , Equation 7.12 can be written as

$$\sigma_{\max} = \sigma \left( 1 + 2 \sqrt{\frac{a}{\rho}} \right) \cong 2\sigma \sqrt{\frac{a}{\rho}} \quad \text{for } \rho \ll a. \quad (7.13)$$

We note that as  $\rho$  becomes very small,  $\sigma_{\max}$  becomes very large, and in the limit, as  $\rho \rightarrow 0$ ,  $\sigma_{\max} \rightarrow \infty$ . We define the term  $2\sqrt{a/\rho}$  as the stress concentration factor  $K_t$  (i.e.,  $K_t = \sigma_{\max}/\sigma$ ).  $K_t$  simply describes the geometric effect of the crack on the local stress (i.e., at the tip of the crack). Note that  $K_t$  depends more on the form of the cavity than on its size. A number of texts and handbooks give a compilation of stress concentration factors  $K_t$  for components containing cracks or notches of various configurations.

As an example of the importance of stress concentration, we point out the use of square windows in the COMET commercial jet aircraft. Fatigue cracks, initiated at the corners of the windows, caused catastrophic failures of several of these aircraft.

In addition to producing a stress concentration, a notch produces a local situation of biaxial or triaxial stress. For example, in the case of a plate containing a circular hole and subject to an axial force, there exist radial as well as tangential stresses. The stresses in a large plate containing a circular hole (with diameter  $2a$ ) and axially loaded (Figure 7.5(a)) can be expressed as<sup>4</sup>

$$\begin{aligned} \sigma_{rr} &= \frac{\sigma}{2} \left( 1 - \frac{a^2}{r^2} \right) + \frac{\sigma}{2} \left( 1 + 3 \frac{a^4}{r^4} - 4 \frac{a^2}{r^2} \right) \cos 2\theta, \\ \sigma_{\theta\theta} &= \frac{\sigma}{2} \left( 1 + \frac{a^2}{r^2} \right) - \frac{\sigma}{2} \left( 1 + 3 \frac{a^4}{r^4} \right) \cos 2\theta, \\ \sigma_{r\theta} &= -\frac{\sigma}{2} \left( 1 - \frac{3a^4}{r^4} + \frac{2a^2}{r^2} \right) \sin 2\theta. \end{aligned} \quad (7.14)$$

<sup>2</sup> C. E. Inglis, *Proc. Inst. Naval Arch.*, 55 (1913) 163, 219.

<sup>3</sup> The derivation of this equation, which can be found in more advanced texts [e.g., J. F. Knott, *Fundamentals of Fracture Mechanics*, (London: Butterworths, 1973), p. 51], involves the solution of the biharmonic equation, the choice of an appropriate Airy stress function, and complex variables.

<sup>4</sup> See, for example, S. Timoshenko and J. N. Goodier, *Theory of Elasticity*, 2nd ed. (New York: McGraw-Hill, 1951), p. 78.

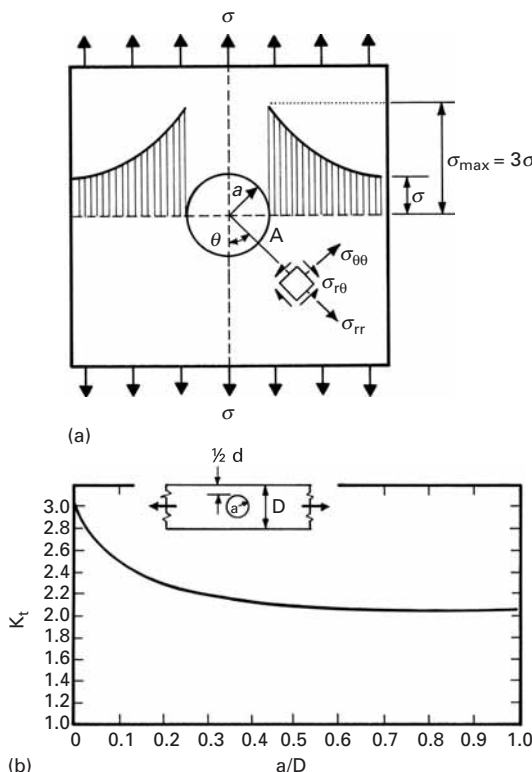


**Fig. 7.5** (a) Stress distribution in a large plate containing a circular hole. (b) Stress concentration factor  $K_t$  as a function of the radius of a circular hole in a large plate in tension.

The maximum stress occurs at point  $A$  in Figure 7.5(a), where  $\theta = \pi/2$  and  $r = a$ . In this case,

$$\sigma_{\theta\theta} = 3\sigma = \sigma_{\max},$$

where  $\sigma$  is the uniform stress applied at the ends of the plate. The stress concentration  $K_t = \sigma_{\max}/\sigma = 3$ . Figure 7.5(b) shows the stress concentration for a circular hole in a plate of finite lateral dimensions. When  $D$ , the lateral dimension, decreases, or the radius of the hole increases, the stress concentration  $K_t$  drops from 3 to 2.2.

Goodier<sup>5</sup> calculated the stresses around spherical voids in perfectly elastic materials. Although his solution was obtained when the applied stress was tensile, it can be extended to compressive stress by changing the signs. The stresses given by Timoshenko and Goodier can be determined from the methods of elasticity theory. At the equatorial plane ( $\theta = \pi/2$ ), the tangential stress  $\sigma_{\theta\theta}$  is equal to

$$\sigma_{\theta\theta} = \left[ 1 + \frac{4 - 5\nu}{2(7 - 5\nu)} \frac{a^3}{r^3} + \frac{9}{2(7 - 5\nu)} \frac{a^5}{r^5} \right] \sigma, \quad (7.15)$$

where  $a$  is the radius of the hole,  $r$  is the radial coordinate, and  $\nu$  is the Poisson's ratio. For  $r = a$ ,  $\nu = 0.3$ , and we have

$$(\sigma_{\theta\theta})_{\max} = \frac{45}{22} \sigma \approx 2\sigma.$$

<sup>5</sup> J. N. Goodier, *App. Mech.* 1 (1933) 39; see also Timoshenko and Goodier, *op. cit.*

Thus, as expected, the stress concentration for a spherical void is approximately 2. The stress  $\sigma_{\theta\theta}$  decays quite rapidly with  $r$ , as can be seen from Equation 7.15; the decay is given by  $r^{-3}$ . For  $r = 2a$ , we have  $\sigma_{\theta\theta} = 1.054$ . This decay is faster than for the circular hole, where it goes with  $r^{-2}$  (Equation 7.14). For  $\theta = 0$  (north and south poles), Timoshenko and Goodier have the equation

$$(\sigma_{rr})_\theta = (\sigma_{\theta\theta})_{\theta=0} = -\frac{3 + 15\nu}{2(7 - 5\nu)}\sigma.$$

Hence, a compressive stress generates a tensile stress at  $\theta = 0$ . This result is very important and shows that compressive stress can generate cracks at spherical flaws such as voids. Taking  $\nu = 0.2\text{--}0.3$  (typical of ceramics), one arrives at the following values:

$$\frac{1}{2} \leq (\sigma_{\theta\theta})_{\theta=0} \leq \frac{7.5}{11}.$$

Thus, the tensile stress is 50–80% of the applied compressive stress. If failure is determined by cracking at spherical voids, cracking should start at a compressive stress level equal to  $-4\sigma_t$  (depending on  $\nu$ ; in this case, for  $\nu = 0.2$ ), where  $\sigma_t$  is the tensile strength of the material. This value represents, to a first approximation, the marked differences between the tensile and compressive strengths of cast irons, intermetallic compounds, and ceramics. The result is fairly close to the stress generated around a circular hole, given in Equation 7.14. In that case, for  $r = a$ , we find that

$$\sigma_{\theta\theta} = -\sigma.$$

In tensile loading, the stress  $\sigma_{\theta\theta} = 3\sigma$ , which would predict a three-fold difference in tensile and compressive strengths. More general (elliptical) flaws can be assumed, and their response under compressive loading provides a better understanding of the compressive strength of brittle materials. The generation and growth of cracks from these flaws also needs to be analyzed, for more realistic predictions. This will be carried out in Section 8.3.4.

Stress concentration caused by an elliptical hole is shown in Figure 7.6. In this figure,  $\sigma_L$  is the longitudinal stress applied along  $x_2$ . It is also referred to as the far-field stress. Locally at the crack tip we have a biaxial or triaxial stress situation. In particular, for an elliptical hole, with  $a = 3b$ , Figure 7.6 shows that  $\sigma_{22}$  falls from its maximum value at the crack tip and attains  $\sigma_L$  asymptotically. The stress component,  $\sigma_{11}$ , however is zero at the crack tip, increases to a peak value and then falls to zero with the same tendency as  $\sigma_{22}$ . The general result is that a major perturbation in the applied stress state occurs over a distance approximately equal to  $a$  from the boundaries of the cavity, with the major stress gradients being confined to a region of dimensions roughly equal to  $\rho$  surrounding the maximum concentration position.

Although the exact formulas vary according to the form of the crack, in all cases  $K_t$  increases with an increase in the crack length  $a$  and a decrease in the root radius at the crack tip,  $\rho$ .

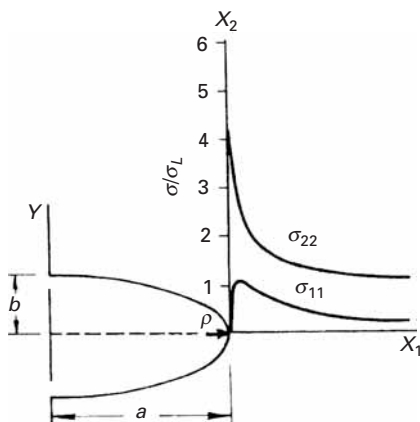


**Fig. 7.6** Stress concentration at an elliptical hole for  $a = 3b$ .

Despite the fact that the analysis of Inglis represented a great advance, the fundamental nature of the fracture mechanism remained obscure. If the Inglis analysis was applicable to a body containing a crack, how does one explain that, in practice, larger cracks propagate more easily than smaller cracks? What is the physical significance of the root radius at the tip of the crack?

### Example 7.1

Although the elastic modulus of silica-based glass is rather low ( $E = 70$  GPa), the theoretical strength of a defect-free glass can be as high as 3 GPa. Generally, such high strength values are not measured in practice. Why?

**Solution:** Extremely minute crack-like defects form rather easily on the glass surface. Such imperfections can lead to a drastic reduction in the strength of glass. This is the reason that, in the making of a glass fiber, a protective coating called a size is applied to the fiber immediately as it comes out of the spinneret. Just to get an estimate of the reduction in strength caused by a tiny imperfection – say, a 1-μm-long, atomically sharp scratch – we can use the Inglis expression (Equation 7.13),

$$\sigma_{th} = 2\sigma(a/\rho)^{0.5}, \quad \text{or} \quad \sigma = 0.5 \sigma_{th}(\rho/a)^{0.5},$$

where  $\sigma_{th}$  is the theoretical strength (3 GPa),  $a$  is the crack length (1 μm), and  $\rho$  is the root radius at the crack tip, which, since the tip is atomically sharp, can be taken to be 0.25 nm. Plugging these values into the preceding expression, we find that the real strength of such a glass is only 24 MPa! Note that in this problem we made an estimate of the notch root radius. In practice, this is very difficult to measure. That is why the concept of stress intensity factor, involving the far-field stress and the square root of the crack length, is much more convenient to deal with in fracture toughness problems, as we shall see later in this chapter (Section 7.6).

### Example 7.2 |

Determine the stresses at distances equal to 0,  $a/2$ ,  $a$ ,  $3a/2$ , and  $2a$  from the surface of a spherical hole and for  $\theta = 0$  and  $\pi/2$ .

**Solution:** We use Equation 7.14. By setting  $\theta = 0$ , we have

$$\begin{aligned}\sigma_{rr} &= \frac{\sigma}{2} \left( 2 - \frac{5a^2}{r^2} + \frac{3a^4}{r^4} \right), \\ \sigma_{\theta\theta} &= \frac{\sigma}{2} \left( \frac{a^2}{r^2} - \frac{3a^2}{r^4} \right), \\ \tau_{r\theta} &= 0.\end{aligned}$$

For  $\theta = \pi/2$ ,

$$\begin{aligned}\sigma_{rr} &= \frac{\sigma}{2} \left( \frac{3a^2}{r^2} - \frac{3a^4}{r^4} \right), \\ \sigma_{\theta\theta} &= \frac{\sigma}{2} \left( 2 + \frac{a^2}{r^2} + \frac{3a^4}{r^4} \right), \\ \tau_{r\theta} &= 0.\end{aligned}$$

We calculate the stresses for  $r = 0, a, 3a/2$ , and  $2a$  and plot them as shown in Figure E7.2 in terms of a dimensionless parameter  $r/a$ .

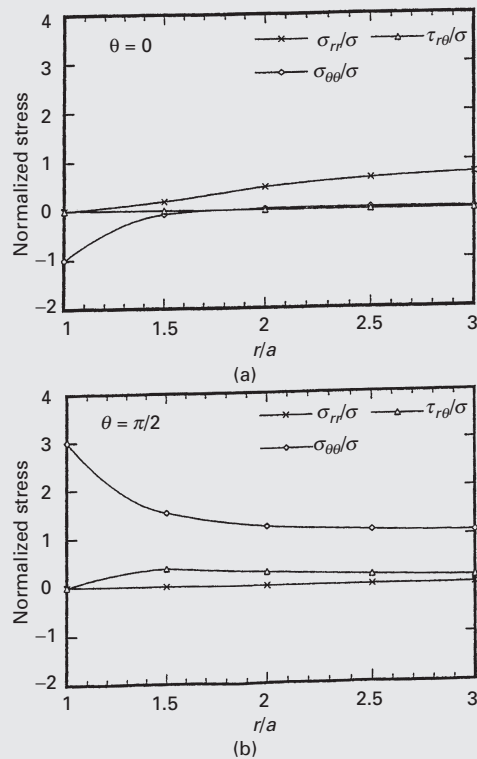


Fig. E7.2

### Example 7.3

Two flat plates are being pulled in tension. (See Figure E7.3.) The flow stress of the materials is 150 MPa.

- Calculate the maximum stresses in the plate.
- Will the material flow plastically?
- For which configuration is the stress higher?

*Solution:*

- Normal stress:

$$\sigma = \frac{P}{A} = \frac{100 \text{ kN}}{10 \text{ cm} \times 1 \text{ cm}}$$

$$= 100 \text{ MPa},$$

$$\sigma_{\max} = \sigma \left(1 + 2 \frac{a}{b}\right).$$

Circular hole:

$$a = b = 3/2 \text{ cm} = 1.5 \text{ cm},$$

$$\sigma_{\max} = 100 \times \left(1 + 2 \times \frac{1.5}{1.5}\right) = 300 \text{ MPa}.$$

Elliptical hole:

$$a = 3/2 \text{ cm} = 1.5 \text{ cm}, b = 1/2 \text{ cm} = 0.5 \text{ cm},$$

$$\sigma_{\max} = 100 \times \left(1 + 2 \times \frac{1.5}{0.5}\right) = 700 \text{ MPa}.$$

- Yes, because in both cases, the stress is greater than the flow stress (150 MPa).
- The elliptical hole has higher stress than the circular one.

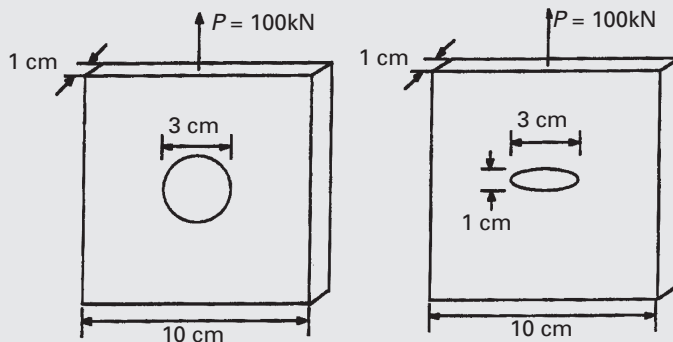
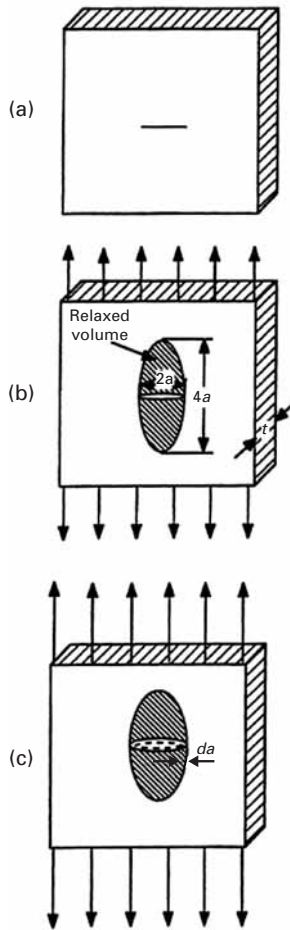


Fig. E7.3



**Fig. 7.7** A plate of thickness  $t$  containing a crack of length  $2a$ . (a) Unloaded condition. (b) and (c) Loaded condition.

## 7.4 | Griffith Criterion

Griffith proposed a criterion based on a thermodynamic energy balance. He pointed out that two things happen when a crack propagates: Elastic strain energy is released in a volume of material, and two new crack surfaces are created, which represent a surface-energy term. Thus, according to Griffith, an existing crack will propagate if the elastic strain energy released by doing so is greater than the surface energy created by the two new crack surfaces. Figure 7.7(a) shows an infinite plate of thickness  $t$  that contains a crack of length  $2a$  under plane stress. As the stress is applied, the crack opens up. The shaded region denotes the approximate volume of material in which the stored elastic strain energy is released (Figure 7.7(b)). When the crack extends a distance  $da$  on the extremities, the volume over which elastic energy is released increases, as shown in Figure 7.7(c). The elastic energy per unit volume in a solid under stress is given by  $\sigma^2/2E$ . (See Chapter 2.) To get the total strain energy released, we need to multiply this quantity by the volume of the material in which this energy is released. In the present case, this volume is the area of the ellipse times the plate thickness. The area of the shaded ellipse is  $\pi(2a)a = 2\pi a^2$ ; therefore, the volume in which the strain energy is relaxed is  $2\pi a^2 t$ . The total strain energy released is thus

$$\left(\frac{\sigma^2}{2E}\right)(2\pi a^2 t) = \frac{\pi \sigma^2 a^2 t}{E},$$

or, in terms of the per-unit thickness of the plate under plane stress, the energy released is

$$U_e = \pi \sigma^2 a^2 / E.$$

The decrease in strain energy,  $U_e$ , when a crack propagates is balanced by an increase in the surface energy,  $U_s$ , produced by the creation of the two new crack surfaces. The increase in surface energy equals:

$$U_s = (2at)(2\gamma_s),$$

here  $\gamma_s$  is the specific surface energy, i.e., the energy per unit area. In terms of the per-unit thickness of the plate, the increase in surface energy is  $4a\gamma_s$ . Now, when an elliptical crack is introduced into the plate, we can write, for the change in potential energy of the plate,

$$\begin{aligned} \Delta U &= U_s - U_e, \\ \Delta U &= 4a\gamma_s - \frac{\pi \sigma^2 a^2 t}{E}, \end{aligned}$$

where  $\Delta U$  is the change in the potential energy per unit thickness of the plate in the presence of the crack,  $\sigma$  is the applied stress,  $a$  is half the crack length,  $E$  is the modulus of elasticity of the plate, and  $\gamma_s$  is the specific surface energy (i.e., the surface energy per unit area) of the plate.

As the crack grows, strain energy is released, but additional surfaces are created. The crack becomes stable when these energy components balance each other. If they are not in balance, we have an unstable crack (i.e., the crack will grow). We can obtain the equilibrium condition by equating to zero the first derivative of the potential energy  $\Delta U$  with respect to the crack length. Thus,

$$\frac{\Delta U}{\partial a} = 4\gamma_s - \frac{2\pi\sigma^2 a}{E} = 0, \quad (7.16a)$$

or

$$2\gamma_s = \frac{\pi\sigma^2 a}{E}. \quad (7.16b)$$

The reader can check the nature of this equilibrium further by taking the second derivative of  $U$  with respect to  $a$ . A negative second derivative would imply that Equation 7.16a represents an unstable equilibrium condition and that the crack will advance.

Rearranging Equation 7.16b, we may write, for the critical stress required for the crack to propagate in the plane-stress situation,

$$\sigma_c = \sqrt{\frac{2E\gamma_s}{\pi a}} \quad (\text{plane stress}). \quad (7.17a)$$

We can rearrange Equation 7.17a to get the following expression:

$$\sigma\sqrt{\pi a} = \sqrt{2E\gamma_s}.$$

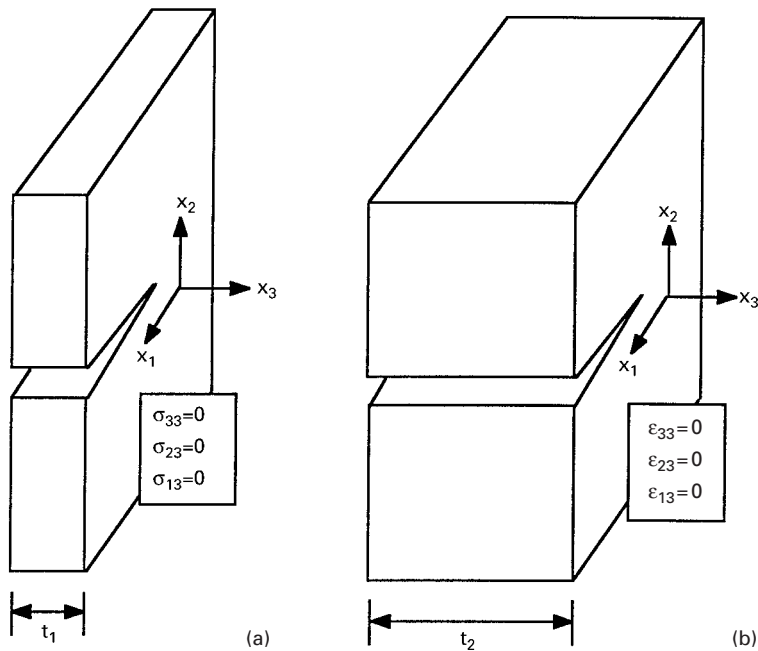
The reader should note that the left-hand side of this expression involves critical stress for crack propagation and square root of crack length. This product is called fracture toughness. Note that the right-hand side of the expression consists only of material parameters:  $E$  and  $\gamma_s$ , i.e., the above expression represents a material property, viz., fracture toughness.

For the plane-strain situation, we will have the factor  $(1 - \nu^2)$  in the denominator because of the confinement in the direction of thickness. The expression for the critical stress for crack propagation then becomes

$$\sigma_c = \sqrt{\frac{2E\gamma_s}{\pi a(1 - \nu^2)}} \quad (\text{plane strain}). \quad (7.17b)$$

The distinction between plane stress and plane strain is shown in Figure 7.8. Normal and shear stresses at free surfaces are zero; hence, for a thin plate,  $\sigma_{33} = \sigma_{23} = \sigma_{13} = 0$ . This is the plane-stress state (Figure 7.8(a)). In very thick plates ( $t_2 > t_1$ ), the flow of material in the  $x_3$  direction is restricted. Therefore,  $\varepsilon_{33} = 0$ , and so are,  $\varepsilon_{23} = \varepsilon_{13} = 0$ . This is the plane-strain condition (Figure 7.8(b)). Note that the factor  $(1 - \nu^2)$  is less than unity and is in the denominator. Therefore, the critical stress corresponding to fracture in the plane-strain situation will be higher than that in the plane-stress state. This is as expected,

**Fig. 7.8** Crack in (a) thin ( $t_1$ ) and (b) thick ( $t_2$ ) plates. Note the plane-stress state in (a) and the plane-strain state in (b).



because of the confinement in the direction of thickness in the case of plane strain. For many metals,  $\nu \approx 0.3$ , and  $(1 - \nu^2) \approx 0.91$ . Thus, the difference is not very large for most metals.

The importance of the length of the crack is implicit in Griffith's analysis. In modern fracture mechanics, as we shall see later, the crack length enters as a square-root term in the product  $\sigma\sqrt{a}$ . According to Griffith's thermodynamic analysis, a necessary condition for crack propagation is

$$-\frac{\partial U_e}{\partial a} \geq \frac{\partial U_s}{\partial a},$$

where  $U_e$  is the elastic energy of the system (i.e., the machine plus the test piece) and  $U_s$  is the surface energy of the two crack faces. This is a necessary condition for fracture by rapid crack propagation. But it may not always be sufficient: if the local stress at the crack tip is not sufficiently large to break the atomic bonds, the energy criterion of Griffith will be inadequate.

Let us consider Equation 7.17a or 7.17b again. Note that the fracture stress, or critical stress required for crack propagation,  $\sigma_c$ , is inversely proportional to  $\sqrt{a}$ . More importantly, the quantity  $\sigma_c\sqrt{a}$  depends only on material constants. It is instructive, then, to examine the Inglis result, Equation 7.13, and the Griffith result, Equation 7.17a or 7.17b in the form

$$\sigma_c\sqrt{a} = \frac{1}{2}(\sigma_{\max})_c \sqrt{\rho} = \text{constant.}$$

Here,  $\sigma_c$  is the critical far-field or uniform stress (i.e., the stress at fracture),  $a$  is the crack length corresponding to  $\sigma_c$ ,  $(\sigma_{\max})_c$  is the

stress at the crack tip at fracture, and  $\rho$  is the root radius at the tip of the crack.

Both analyses, Inglis's and Griffith's lead to the same result, viz., that a crack will propagate when an appropriate quantity with dimensions of stress times the square root of length reaches a critical value, a material constant. It is easy to see that the parameters in the Inglis analysis,  $(\sigma_{\max})_c$  and  $\rho$ , are local parameters and very difficult to measure, while the Griffith analysis allows us to use the far-field applied stress and crack length, which are easy to measure. It is this quantity,  $\sigma_c\sqrt{a}$ , that is called the fracture toughness and is denoted by  $K_{lc}$ . We treat fracture toughness in detail in Section 7.6.

### Example 7.4

Consider a brittle material with  $\gamma_s = 1 \text{ J/m}^2$  and  $E = 100 \text{ GPa}$ . (a) What is the breaking strength of this material if it contains crack-like defects as long as 1 mm? (b) Should it be possible to increase  $\gamma_s$  to  $3,000 \text{ J/m}^2$ , what would be the breaking strength for a 1-mm-long crack?

#### *Solution*

(a) We have

$$\gamma_s = 1 \text{ J/m}^2 \quad \text{and} \quad E = 100 \text{ GPa},$$

and

$$2a = 1 \text{ mm} \quad \text{and} \quad a = 0.5 \text{ mm}.$$

Thus,

$$\begin{aligned} \sigma_c &= \sqrt{\frac{2E\gamma_s}{\pi a}} = \sqrt{\frac{2 \times 100 \times 10^9 \times 1}{\pi \times (0.5 \times 10^{-3})}} \\ &= 11.3 \text{ MPa}. \end{aligned}$$

(b) If  $\gamma_s$  increases to  $3,000 \text{ J/m}^2$ ,

$$2a = 1 \text{ mm} \quad \text{and} \quad a = 0.5 \text{ mm},$$

so that

$$\begin{aligned} \sigma_c &= \sqrt{\frac{2E\gamma_s}{\pi a}} = \sqrt{\frac{2 \times 100 \times 10^9 \times 3,000}{\pi \times (0.5 \times 10^{-3})}} \\ &= 618 \text{ MPa}. \end{aligned}$$

## 7.5 | Crack Propagation with Plasticity

If the material in which a crack is propagating can deform plastically, the form of the crack tip changes because of plastic strain. A sharp crack tip will be blunted. Another important factor is time: because



**Fig. 7.9** Dislocations emitted from a crack tip in copper. (Courtesy of S. M. Ohr.)

plastic deformation requires time, the amount of plastic deformation that can occur at the crack tip will depend on how fast the crack is moving. Figure 7.9, a TEM micrograph, shows dislocations that were generated at a crack tip and that propagated along crystallographic planes. The crack is at the left-hand side, and the plane of the copper foil is (123). In a great majority of materials, localized plastic deformation at and around the crack tip is produced because of the stress concentrations there. In such a case, a certain amount of plastic work is done during crack propagation, in addition to the elastic work done in the creation of two fracture surfaces. The mechanics of fracture will, then, depend on the magnitude of  $\gamma_p$ , the plastic work done, which in its turn depends on the crack speed, temperature, and the nature of the material. For an inherently brittle material, at low temperatures and at high crack velocities  $\gamma_p$  is relatively small ( $\gamma_p < 0.1\gamma_s$ ). In such a case, the crack propagation would be continuous and elastic. These cases are usefully treated by means of linear elastic fracture mechanics, which is dealt with in Section 7.6. In any event, in the case of plastic deformation, the work done in the propagation of a crack per unit area of the fracture surface is increased from  $\gamma_s$  to  $(\gamma_s + \gamma_p)$ . Consequently, the Griffith criterion (Equation 7.17a or 7.17b) is modified to

$$\sigma_c = \sqrt{\frac{2E}{\pi a}(\gamma_s + \gamma_p)} \quad (\text{plane stress}) \quad (7.18a)$$

and

$$\sigma_c = \sqrt{\frac{2E}{\pi a(1 - \nu^2)}(\gamma_s + \gamma_p)} \quad (\text{plane strain}). \quad (7.18b)$$

Rearranging Equation 7.18a, we get

$$\sigma_c = \sqrt{\frac{2E \gamma_s}{\pi a} \left(1 + \frac{\gamma_p}{\gamma_s}\right)}.$$

For  $\gamma_p/\gamma_s \gg 1$ ,

$$\sigma_c \approx \sqrt{\frac{2E \gamma_p}{\pi a}}.$$

Thus, the plastic deformation around the crack tip makes it blunt and serves to relax the stress concentration by increasing the radius of curvature of the crack at its tip. Localized plastic deformation at the crack tip therefore improves the fracture toughness of the material.

This is the conventional treatment of the plastic work contribution to the fracture process, wherein  $\gamma_p$  is considered to be a constant. However, the reader should be warned that this is not strictly true. As a matter of fact, the value of  $\gamma_p$  increases with the stress intensity factor  $K (=Y\sigma\sqrt{a})$ . Consider Equation 7.18a. As was pointed out, in the conventional approach  $\gamma_p$  will be very much larger than  $\gamma_s$  for a ductile material such as polycrystalline copper. Thus, according to this conventional treatment, the fracture stress  $\sigma_c$  should be relatively insensitive to changes in  $\gamma_s$ . However, in the embrittlement of copper with beryllium, all we change is the  $\gamma_s$  part of Equation 7.18a (along the grain boundaries where the fracture proceeds). The  $\gamma_p$  part in that equation (i.e., the plastic behavior of copper) does not change appreciably by the addition of beryllium to copper.

As pointed out earlier, equations of the type 7.17a or 7.18 are difficult to use in practice. It is not a trivial matter to measure quantities such as surface energy and the energy of plastic deformation. In a manner similar to that of Griffith, Irwin made a fundamental contribution to the mechanics of fracture when he proposed that fracture occurs at a stress that corresponds to a critical value of the crack extension force

$$G = \frac{1}{2} \frac{\partial U_e}{\partial a} = \text{rate of change of energy with crack length.}$$

$G$  is sometimes called the *strain energy release rate*.

Now,  $U_e = \pi a^2 \sigma^2 / E$ , the energy released by the advancing crack per unit of plate thickness. This is for plane stress. For plane strain, a factor of  $(1 - \nu^2)$  is introduced in the denominator. Thus,

$$G = \frac{\pi a \sigma^2}{E}.$$

At fracture,  $G = G_c$ , and

$$\sigma_c = \sqrt{\frac{EG_c}{\pi a}} \quad (\text{plane stress}) \quad (7.19a)$$

or

$$\sigma_c = \sqrt{\frac{EG_c}{\pi a(1 - \nu^2)}} \quad (\text{plane strain}). \quad (7.19b)$$

From Equations 7.18 and 7.19, we see that

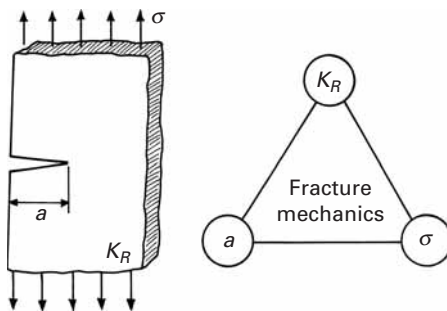
$$G_c = 2(\gamma_s + \gamma_p).$$

We shall come back to this idea of crack extension force later in the chapter.

## 7.6 | Linear Elastic Fracture Mechanics

A nonductile material has a very low capacity to deform plastically; that is, it is not capable of relaxing peak stresses at crack-like defects.

**Fig. 7.10** Inherent material resistance to crack growth and its relationship to the applied stress  $\sigma$  and crack size  $a$ .



In such a material, a crack will propagate very rapidly with little plastic deformation around the crack tip, resulting in what is called a brittle fracture. Typically, such a fracture is also characterized by a crack propagation that is sudden, rapid, and unstable. In practical terms, this definition of brittleness, which refers to the onset of instability under an applied stress smaller than the stress corresponding to plastic yielding of the material, is very useful. Numerous brittle fractures have occurred in service, and there are abundant examples of them in a great variety of structural and mechanical engineering fields involving ships, bridges, pressure vessels, oil ducts, turbines, and so on. In view of the great importance of brittle fracture in real life, a discipline called linear elastic fracture mechanics (LEFM) has emerged, enabling us to obtain a quantitative measure of the resistance of a brittle material to unstable or catastrophic crack propagation. Extension of these efforts into nonlinear elastic and plastic regimens has led to the development of elasto-plastic fracture mechanics (EPFM), also called post-yield fracture mechanics (see Section 7.9).

### 7.6.1 Fracture Toughness

Fracture mechanics gives us a quantitative handle on the process of fracture in materials. Its approach is based on the concept that the relevant material property, fracture toughness, is the force necessary to extend a crack through a structural member. Under certain circumstances, this crack extension force (or an equivalent parameter) becomes independent of the dimensions of the specimen. The parameter can then be used as a quantitative measure of the fracture toughness of the material.

Fracture mechanics adopts an entirely new approach to designing against fracture. Admittedly defects will always be present in a structural component. But consider a structure or a component with a crack-like defect. We can simulate this with single edge notch of length  $a$  in a plate. (See Figure 7.10.) Alternatively, we can say that we are increasing the applied stress intensity factor  $K$  at the crack tip. The material at the tip, however, presents resistance to crack growth. We denote this inherent material resistance by  $K_R$  (sometimes the symbol  $R$  alone is used in place of  $K_R$ .) The discipline of fracture mechanics

can then be represented by a triangle as shown in Figure 7.10; that is, we have an interplay among the following three quantities:

1. The far-field stress,  $\sigma$ .
2. The characteristic crack length,  $a$ .
3. The inherent material resistance to cracking,  $K_R$ .

Various parameters are used to represent  $K_R$ . We discuss their equivalence in Section 7.7.5. Here we wish to clarify one common point of confusion. The symbol  $K$  is used to designate the stress intensity factor at the crack tip corresponding to a given applied stress and crack length. The symbol  $K_R$  (or one of its equivalents) represents fracture toughness. In this regard, the following analogy is helpful. The stress intensity factor,  $K$ , is to stress as fracture toughness,  $K_R$ , is to strength. Stress and stress intensity factor vary with the external loading conditions; strength and toughness are material parameters, independent of loading and specimen size considerations.

We now seek an answer to the question: Given a certain applied stress, what is the largest size defect (crack) that can be tolerated without the failure of the member? Once we know the answer to this question, it remains only to use appropriate inspection techniques to select/repair/replace a material so that defects larger than the critical size for the given design stress are not present.

### 7.6.2 Hypotheses of LEFM

The basic hypotheses of LEFM are as follows:

1. Cracks are inherently present in a material, because there is a limit to the sensibility or resolution of any crack-detecting equipment.
2. A crack is a free, internal, plane surface in a linear elastic stress field. With this hypothesis, linear elasticity furnishes us stresses near the crack tip as

$$\sigma_{r\theta} = \frac{K}{\sqrt{2\pi r}} f(\theta), \quad (7.20)$$

where  $r$  and  $\theta$  are polar coordinates and  $K$  is a constant called the *stress intensity factor* (SIF).

3. The growth of the crack leading to the failure of the structural member is then predicted in terms of the tensile stress acting at the crack tip. In other words, the stress situation at the crack tip is characterized by the value of  $K$ . It can be shown by elasticity theory that  $K = Y\sigma\sqrt{\pi a}$ , where  $\sigma$  is the applied stress,  $a$  is half the crack length, and  $Y$  is a constant that depends on the crack opening mode and the geometry of the specimen.

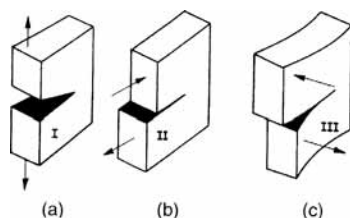


**Fig. 7.11** The three modes of fracture. (a) Mode I: opening mode. (b) Mode II: sliding mode. (c) Mode III: tearing mode (see also Figure 7.1).

### 7.6.3 Crack-Tip Separation Modes

The three modes of fracture are shown in Figure 7.11. Mode I (Figure 7.11(a)), called the opening mode, has tensile stress normal to the crack faces. Mode II (Figure 7.10(b)) is called the sliding mode or the forward shear mode. In this mode, the shear stress is normal

to the advancing crack front. Mode III (Figure 7.11(c)) is called the tearing mode or transverse shear mode, with the shear stress parallel to the advancing crack front. The “goofy duck” analog of Figure 7.1 shows this in a more illustrative fashion.

#### 7.6.4 Stress Field in an Isotropic Material in the Vicinity of a Crack Tip

The stress components for the three fracture modes in an isotropic material are given next. In the case of anisotropic materials, these relations must be modified to permit the asymmetry of stress at the crack tip.  $K_I$ ,  $K_{II}$ , and  $K_{III}$  represent stress intensity factors in modes I, II, and III, respectively. We have (the derivation of these expressions is attributed to Westergaard<sup>6</sup>):

Mode I:

$$\begin{bmatrix} \sigma_{11} \\ \sigma_{22} \\ \sigma_{12} \end{bmatrix} = \frac{K_I}{\sqrt{2\pi r}} \cos \frac{\theta}{2} \begin{bmatrix} 1 - \sin \frac{\theta}{2} & \sin \frac{3\theta}{2} \\ 1 + \sin \frac{\theta}{2} & \sin \frac{3\theta}{2} \\ \sin \frac{\theta}{2} & \cos \frac{3\theta}{2} \end{bmatrix},$$

$$\sigma_{13} = \sigma_{23} = 0,$$

$$\sigma_{33} = 0, \quad (\text{plane stress}),$$

$$\sigma_{33} = \nu(\sigma_{11} + \sigma_{22}), \quad (\text{plane strain}). \quad (7.21)$$

Mode II:

$$\begin{bmatrix} \sigma_{11} \\ \sigma_{22} \\ \sigma_{12} \end{bmatrix} = \frac{K_{II}}{\sqrt{2\pi r}} \begin{bmatrix} -\sin \frac{\theta}{2} & \left(2 \cos \frac{\theta}{2} \cos \frac{3\theta}{2}\right) \\ \sin \frac{\theta}{2} & \cos \frac{\theta}{2} \cos \frac{3\theta}{2} \\ \cos \frac{\theta}{2} & \left(1 - \sin \frac{\theta}{2} \sin \frac{3\theta}{2}\right) \end{bmatrix},$$

$$\sigma_{13} = \sigma_{23} = 0,$$

$$\sigma_{33} = 0, \quad (\text{plane stress}),$$

$$\sigma_{33} = \nu(\sigma_{11} + \sigma_{22}) \quad (\text{plane strain}). \quad (7.22)$$

Mode III:

$$\begin{bmatrix} \sigma_{13} \\ \sigma_{23} \end{bmatrix} = \frac{K_{III}}{2\pi r} \begin{bmatrix} -\sin \frac{\theta}{2} \\ \cos \frac{\theta}{2} \end{bmatrix}$$

$$\sigma_{11} = \sigma_{22} = \sigma_{33} = \sigma_{12} = 0. \quad (7.23)$$

The derivation of this expression for Mode III is given in the Appendix at the end of this chapter

---

<sup>6</sup> H. M. Westergaard, *J. Appl. Mech.*, 5A (1939) 49.

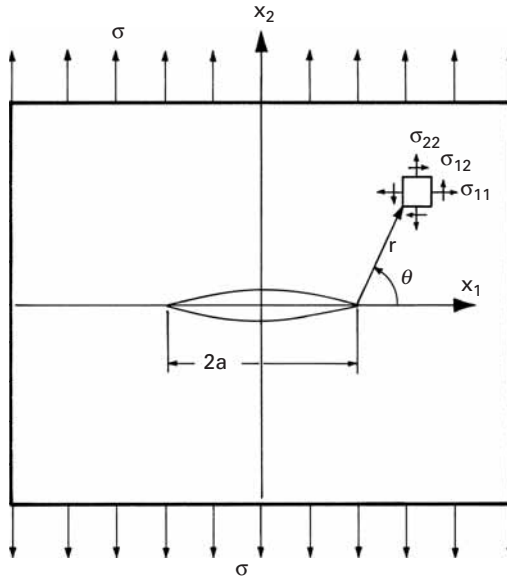


**Fig. 7.12** Infinite, homogeneous, elastic plate containing a through-the-thickness central crack of length  $2a$ , subjected to a tensile stress  $\sigma$ .

### 7.6.5 Details of the Crack-Tip Stress Field in Mode I

Consider an infinite, homogeneous, elastic plate containing a crack of length  $2a$  (Figure 7.12). The plate is subjected to a tensile stress  $\sigma$  far away from and normal to the crack. The stresses at a point  $(r, \theta)$  near the tip of the crack are given by Equation 7.21. Ignoring the subscript of  $K$ , we may write the stress components in expanded form as:

$$\begin{aligned}\sigma_{11} &= \frac{K}{\sqrt{2\pi r}} \cos \frac{\theta}{2} \left( 1 - \sin \frac{\theta}{2} \sin \frac{3\theta}{2} \right), \\ \sigma_{22} &= \frac{K}{\sqrt{2\pi r}} \cos \frac{\theta}{2} \left( 1 + \sin \frac{\theta}{2} \sin \frac{3\theta}{2} \right), \\ \sigma_{12} &= \frac{K}{\sqrt{2\pi r}} \cos \frac{\theta}{2} \sin \frac{\theta}{2} \cos \frac{3\theta}{2}, \\ \sigma_{13} &= \sigma_{13} = 0, \\ \sigma_{33} &= 0 \quad (\text{plane stress}), \\ \sigma_{33} &= v(\sigma_{11} + \sigma_{22}) \quad (\text{plane strain}),\end{aligned}\tag{7.24}$$

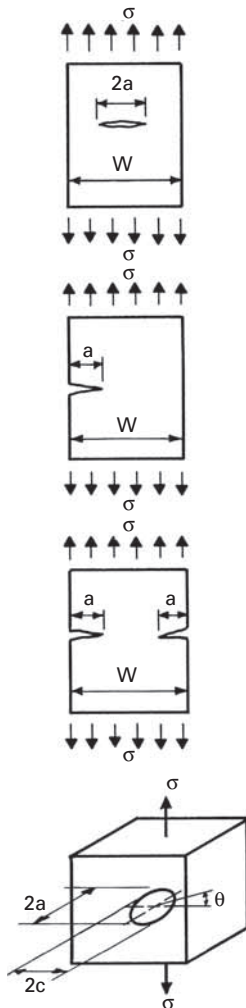
where

$$K = \sigma \sqrt{\pi a}\tag{7.25}$$

is the stress intensity factor for the plate and has the units ( $\text{N/m}^2$ )  $\sqrt{\text{m}}$ , or  $\text{Pa}\sqrt{\text{m}}$ , or  $\text{Nm}^{-3/2}$ . Note that Equation 7.25 is applicable in the region  $r \ll a$  (i.e., in the vicinity of the crack tip). For larger  $r$ , higher order terms must be included.

For a thin plate, one has plane-stress conditions, and  $\sigma_{33} = \sigma_{13} = \sigma_{23} = 0$ . For a thick plate (infinite in the direction of thickness), there exist plane-strain conditions (i.e.,  $\sigma_{33}=v(\sigma_{11} + \sigma_{22})$  and  $\sigma_{13} = \sigma_{23} = 0$ ).

Consider again Equation 7.24. The right-hand side has three quantities:  $K$ ,  $r$ , and  $f(\theta)$ , here designating the group of terms containing the angle  $\theta$  in Equation 7.24. The terms  $r$  and  $f(\theta)$  describe



Center crack:  $K_1 = Y\sigma\sqrt{\pi a}$

$$Y = 1 + 0.256 \left( \frac{a}{W} \right) - 1.152 \left( \frac{a}{W} \right)^2 + 12.200 \left( \frac{a}{W} \right)^3$$

$$\text{or } Y = \sqrt{\sec \left( \frac{\pi a}{W} \right)}$$

$$\text{or } Y = \frac{1}{\sqrt{1 - \left( \frac{2a}{W} \right)^2}}$$

Single edge notch:  $K_1 = Y\sigma\sqrt{\pi a}$

$Y = 1.12$  for small cracks

$$\text{or } Y = 1.12 - 0.231 \left( \frac{a}{W} \right) + 10.55 \left( \frac{a}{W} \right)^2 - 21.72 \left( \frac{a}{W} \right)^3 + 30.39 \left( \frac{a}{W} \right)^4$$

up to  $a/W = 0.6$

Double edge notch:  $K_1 = Y\sigma\sqrt{\pi a}$

$Y = 1.12$  for small cracks

$$\text{or } Y = \frac{1.222 - 0.561 \left( \frac{a}{W} \right) - 0.205 \left( \frac{a}{W} \right)^2 + 0.471 \left( \frac{a}{W} \right)^3 - 0.190 \left( \frac{a}{W} \right)^4}{\sqrt{1 - \frac{a}{W}}}$$

#### Embedded Cracks

Elliptical crack:  $K_1 = Y\sigma\sqrt{\pi a}$

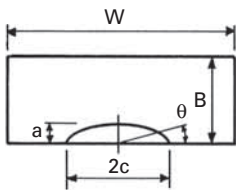
$$Y = \left( \sin^2 \theta + \frac{a^2}{c^2} \cos^2 \theta \right)^{1/4} / \left( \frac{3\pi}{8} + \frac{\pi}{8} \frac{a^2}{c^2} \right)$$

Circular crack:  $K_1 = Y\sigma\sqrt{\pi a}$

$$Y = \frac{2}{\pi}$$

**Fig. 7.13** Some common load and crack configurations and the corresponding expressions for the stress intensity factor,  $K$ .

the stress distribution around the crack tip. These two characteristics (i.e., dependence on  $\sqrt{r}$  and  $f(\theta)$ ) are identical for all cracks in two- or three-dimensional elastic solids. The stress intensity factor  $K$  includes the influence of the applied stress  $\sigma$  and the appropriate crack dimensions, in this case half the crack length  $a$ . Thus,  $K$  will characterize the external conditions (i.e., the nominal applied stress  $\sigma$  and half the crack length  $a$ ) that correspond to fracture when stresses and strains at the crack tip reach a critical value. This critical value of  $K$  is designated as  $K_c$ . It turns out, as we shall see later, that  $K_c$  depends on the dimensions of the specimen. In the case of a thin sample (plane-stress conditions),  $K_c$  depends on the thickness of the sample, whereas in the case of a sufficiently thick sample (plane-strain conditions),  $K$  is independent of the thickness of the specimen and is designated as  $K_{lc}$ .



Semi-elliptical surface flaw in tension:

$$K_1 = Y \frac{\sigma \sqrt{\pi a}}{\frac{3\pi}{8} + \frac{\pi}{8} \frac{a^2}{c^2}} \left( \sin^2 \theta + \frac{a^2}{c^2} \cos^2 \theta \right)^{1/4}$$

$$Y = 1.12 \text{ (for } W, B \text{ Large)}$$

$$Y = \left( \frac{a}{B}, \frac{a}{c}, \frac{c}{W}, \theta \right)$$

$$Y = \left[ Y_1 + Y_2 \left( \frac{a}{B} \right)^2 + Y_3 \left( \frac{a}{B} \right)^4 \right] Y_4 g(\theta) g(W)$$

$$Y_1 = 1.13 - 0.09 \left( \frac{a}{c} \right)$$

$$Y_2 = -0.54 + \frac{0.89}{0.2 + \left( \frac{a}{c} \right)}$$

$$Y_3 = 0.5 - \frac{1.0}{0.65 + \left( \frac{a}{c} \right)} + 14 \left( 1.0 - \frac{a}{c} \right)^{24}$$

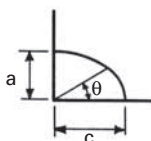
$$Y_4 = 1 + \left[ 0.1 + 0.35 \left( \frac{a}{B} \right)^2 \right] (1 - \sin \theta)^2$$

$$g(\theta) = \left[ \sin^2 \theta + \left( \frac{a}{c} \right)^2 \cos^2 \theta \right]^{1/8}$$

$$g(W) = \left[ \sec \frac{\pi c}{W} \sqrt{\frac{a}{B}} \right]^{1/2}$$

$$\text{for: } 0 < \frac{a}{c} < 1 \quad 0 < \frac{a}{B} < 1$$

$$0 < \frac{c}{B} < 0.5 \quad 0 < \theta < \pi$$



Quarter elliptical corner crack in tension:

$$K_1 = Y \frac{\sigma \sqrt{\pi a}}{\frac{3\pi}{8} + \frac{\pi}{8} \frac{a^2}{c^2}} \left( \sin^2 \theta + \frac{a^2}{c^2} \cos^2 \theta \right)^{1/4}$$

$$Y = 1.2$$

**Fig. 7.13** (cont.)

The stress intensity factor  $K$  measures the amplitude of the stress field around the crack tip and should not be confused with the stress concentration factor  $K_t$  discussed in Section 7.3.2. It is also important to distinguish between  $K$  and  $K_c$  or  $K_{lc}$ . The stress intensity factor  $K$  is a quantity, determined analytically or not, that varies as a function of configuration (i.e., the geometry of the crack and the manner of application of the external load). Thus, the analytical expression for  $K$  varies from one system to another. However, once  $K$  attains its critical value,  $K_{lc}$ , in plane strain for a given system and material, it is essentially a constant for all the systems made of this material. The difference between  $K_c$  and  $K_{lc}$  is that  $K_c$  depends on the thickness of the specimen, whereas  $K_{lc}$  is independent of the thickness. The forms of  $K$  for various load and crack configurations have been calculated and are available in various handbooks. Some of the more common configurations and the corresponding expressions for  $K$  are presented in Figure 7.13.

For samples of finite dimensions, the general practice is to consider the solution for an infinite plate and modify it by an algebraic or trigonometric function that would make the surface tractions vanish. Thus, for a central through-the-thickness crack of length  $2a$ , in a plate of width  $W$ , we have

$$K = \sigma \left( W \tan \frac{\pi a}{W} \right)^{1/2}. \quad (7.26)$$

For the same crack in an infinite plate, we have

$$K = \sigma \sqrt{\pi a}.$$

If we expand  $\tan \pi a/W$  in a series (Equation 7.26), we get

$$\begin{aligned} K &= \sigma W^{1/2} \left( \frac{\pi a}{W} + \frac{\pi^3 a^3}{3W^3} + \dots \right)^{1/2} \\ &= \sigma \sqrt{\pi a} \left( 1 + \frac{\pi^3 a^3}{3W^3} + \dots \right)^{1/2}. \end{aligned}$$

Thus, for an infinite solid,  $a/W = 0$ , and we have  $K = \sigma \sqrt{\pi a}$ , as expected. For an edge crack in a semi-infinite plate, we have  $K = 1.12 \sigma \sqrt{\pi a}$ . The factor 1.12 here takes care of the fact that stresses normal to the free surface must be zero.

At this point, it is appropriate to make some comments on the limitations of LEFM. It was pointed out earlier that the expressions for stress components (Equations 7.21–7.23) are valid only in the neighborhood of the crack tip. The reader will have noticed that these stress components tend to infinity as we approach the tip (i.e., as  $r$  goes to zero). Now, there does not exist a material in real life that can resist an infinite stress. The material in the neighborhood of the crack tip, in fact, would inevitably deform plastically. Thus, these expressions for stress components based on linear elasticity theory are not valid in the plastic zone at the crack tip. The deformation process in a plastic zone, as is well known, will be a sensitive function of the microstructure, among other things. However, in spite of ignorance of the exact nature of the plastic zone, the LEFM treatment is valid for low-enough stresses such that the size of the plastic zone at the crack tip is small with respect to the crack length and the dimensions of the sample. We shall see in the next section how to incorporate a correction term for the presence of a plastic zone at the crack tip.

### 7.6.6 Plastic-Zone Size Correction

Equations 7.21–7.23 show a  $\sqrt{r}$  singularity; that is,  $\sigma_{11}$ ,  $\sigma_{22}$ , and  $\sigma_{12}$  go to infinity when  $\sqrt{r}$  goes to zero. For a great majority of materials, local yielding will occur at the crack tip, which would relax the peak stresses. As we shall see shortly, the utility of the elastic stress field equations is not affected by the presence of this plastic zone as long as the nominal stress in the material is below the general yielding stress of the material.

When yielding occurs at the crack tip, it becomes blunted; that is, the crack surfaces separate without any crack extension. (See

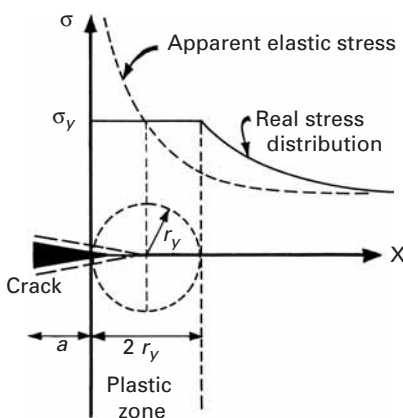


**Fig. 7.14** Plastic-zone correction. The effective crack length is  $(a + r_y)$ .

Figure 7.14.) The plastic zone (radius  $r_y$ ) will then be embedded in an elastic stress field. Outside and far away from the plastic zone, the elastic stress field “sees” the crack and the perturbation due to the plastic zone, as if there were present a crack in an elastic material with the leading edge of the crack situated inside the plastic zone. A crack of length  $2(a + r_y)$  in an ideal elastic material produces stresses almost identical to elastic stresses in a locally yielded member outside the plastic zone. If the stress applied is too large, the plastic zone increases in size in relation to the crack length, and the elastic stress field equations lose precision. When the whole of the reduced section yields, the plastic zone spreads to the edges of the sample, and  $K$  does not have any validity as a parameter defining the stress field.

When the plastic zone is small in relation to the crack length, it can be visualized as a cylinder (Figure 7.14) of radius  $r_y$  at the crack tip. From Equation 7.24, for  $\theta = 0$ ,  $r = r_y$ , and  $\sigma_{22} = \sigma_y$ , the yield stress, we can write

$$\sigma_y = \frac{K}{\sqrt{2\pi r_y}},$$

and, to a first approximation, the plastic-zone radius will be

$$r_y = \frac{1}{2\pi} \left( \frac{K}{\sigma_y} \right)^2. \quad (7.27)$$

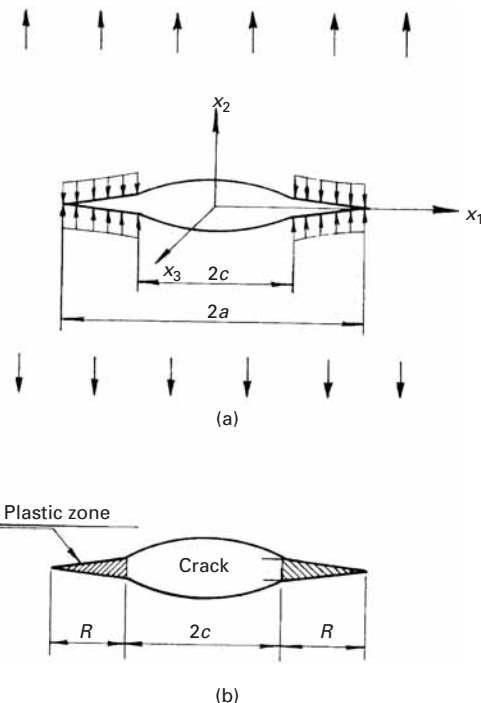
In fact, the plastic-zone radius is a little bigger than  $(1/2\pi)(K/\sigma_y)^2$ , due to redistribution of load in the vicinity of the crack tip. Irwin,<sup>7</sup> taking into account the plastic constraint factor in the case of plane strain, gave the following expressions for the size of the plastic zone:

$$r_y \approx \frac{1}{2\pi} \left( \frac{K}{\sigma_y} \right)^2 \quad (\text{plane stress}),$$

$$r_y \approx \frac{1}{6\pi} \left( \frac{K}{\sigma_y} \right)^2 \quad (\text{plane strain}).$$

<sup>7</sup> G. R. Irwin, in *Encyclopaedia of Physics*, Vol. VI (Heidelberg: Springer-Verlag, 1958); see also *J. Basic Eng., Trans. ASME*, 82 (1960) 417.

**Fig. 7.15** Dugdale–Bilby–Cottrell–Swinden (BCS) model of a crack.



Thus, the center of perturbation, the apparent crack tip, is located a distance  $r_y$  from the real crack tip. The effective crack length is, then,

$$(2a)_{\text{eff}} = 2(a + r_y).$$

Substituting  $(a + r_y)$  for  $a$  in the elastic stress field equations gives an adequate adjustment for the crack-tip plasticity under conditions of small-scale yielding. With this adjustment, the stress intensity factor  $K$  is useful for characterization of the fracture conditions.

There is another model for the plastic zone at the crack tip for the plane-stress case, called the Dugdale–BCS model.<sup>8</sup> In this model, the plasticity spreads out at the two ends of a crack in the form of narrow strips of length  $R$  (Figure 7.15). These narrow plastic strips in front of the actual crack tips are under the yield stress  $\sigma_y$  that tends to close the crack. Mathematically, the internal crack of length  $2c$  is allowed to extend elastically a distance  $2a$ , and then internal stress is applied to reclose the crack in this region. Combining the internal stress field surrounding the plastic enclaves with the external stress field associated with the applied stress  $\sigma$  acting on the crack, Dugdale showed that

$$\frac{c}{a} = \cos \frac{\pi \sigma}{2\sigma_y}.$$

<sup>8</sup> B. A. Bilby, A. H. Cottrell, and K. H. Swinden, Proc. Roy. Soc., A272 (1963) 304; D. S. Dugdale, J. Mech. Phys. Solids, 8 (1960) 100.

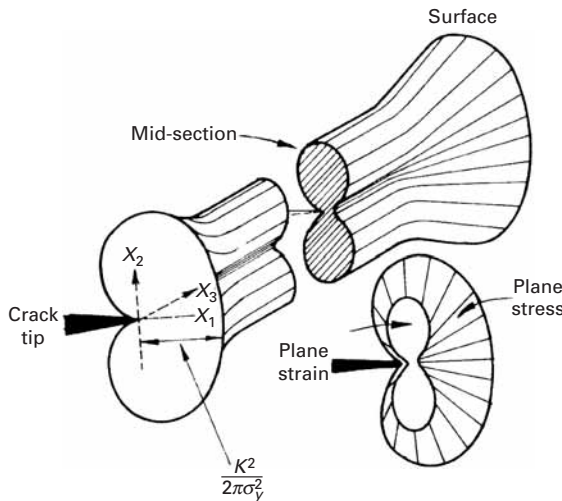


**Fig. 7.16** Formal representation of the plastic zone at the crack tip for a through-the-thickness crack in a plate.

From this relation, one notes that as  $\sigma \rightarrow \sigma_y$ ,  $c/a \rightarrow 0$ ,  $a \rightarrow \infty$  (i.e., general yielding occurs). On the other hand, as  $\sigma/\sigma_y$  decreases, we can write (using the series expansion for cosine),

$$\frac{c}{a} = 1 - \frac{\pi^2 \sigma^2}{8\sigma_y^2} + \dots$$

Noting that  $a = c + R$  and using the binomial expansion, we have

$$\frac{c}{a} = \frac{c}{c+R} = \left(1 + \frac{R}{c}\right)^{-1} = 1 - \frac{R}{c} + \dots$$

Thus, for  $\sigma \ll \sigma_y$ ,

$$\frac{R}{c} \approx \frac{\pi^2}{8} \left(\frac{\sigma}{\sigma_y}\right)^2,$$

or

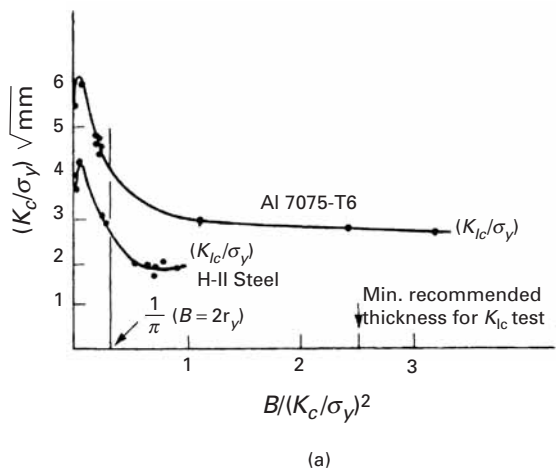
$$R \approx \frac{\pi}{8} \left(\frac{K}{\sigma_y}\right)^2. \quad (7.28)$$

Comparing Equation 7.28 with Equation 7.27, we see that there is good agreement between the two ( $\pi/8 \approx 1/\pi$ ). In fact, the size of the plastic zone varies with  $\theta$  also. A formal representation of the plastic zone at the crack front through the plate thickness is shown in Figure 7.16.

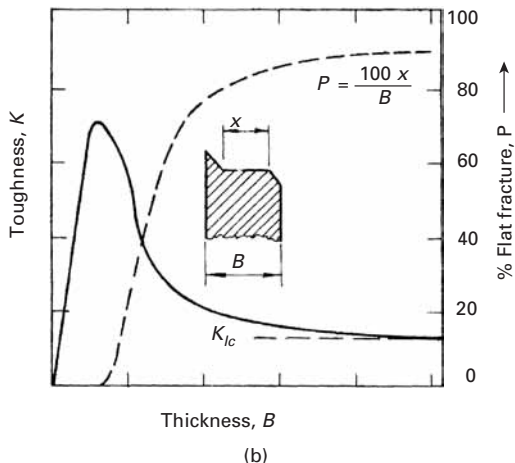
### 7.6.7 Variation in Fracture Toughness with Thickness

The elastic stress state is markedly influenced by the plate thickness, as indicated by Equation 7.24. The material in the plastic zone deforms in such a way that its volume is kept constant. Thus, the large deformations in the  $x_1$  and  $x_2$  directions tend to induce a contraction in the  $x_3$  direction (parallel to the direction of the crack front or the plate thickness), which is resisted by the surrounding elastic material. We next perform a dimensional analysis. Since the elastic material

**Fig. 7.17** (a) Variation in fracture toughness ( $K_c$ ) with plate thickness ( $B$ ) for Al 7075-T6 and H-11 Steel. (Reprinted with permission from J. E. Srawley and W. F. Brown, ASTM STP 381 (Philadelphia: ASTM, 1965), p 133, and G. R. Irwin, in *Encyclopaedia of Physics*, Vol. VI (Heidelberg: Springer Verlag, 1958); see also *J. Basic Eng., Trans. ASME*, 82 (1960) 417.) (b) Schematic variation of fracture toughness  $K_c$  and percentage of flat fracture  $P$  with the plate thickness  $B$ .



(a)



(b)

surrounding the plastic zone is the primary source of constraint, the size of the plastic zone,  $2r_y$ , should be compared with the plate thickness  $B$ . The ratio of the plate thickness  $B$  to the size of the plastic zone,  $2r_y$ , is given by

$$\frac{B}{2r_y} = \pi \frac{B}{(K_c/\sigma_y)^2},$$

and this would be a convenient parameter to characterize the variation of fracture toughness,  $K_c$ , with thickness. Data for Al 7075-T6 and H-11 steel are plotted in Figure 7.17(a) in the form<sup>9</sup> of  $K_c/\sigma_y$  versus  $B/(K_c/\sigma_y)^2$ . Observe that when  $B/(K_c/\sigma_y)^2$  is greater than  $1/\pi$  (i.e.,  $B \gg 2r_y$ ), the fracture toughness value  $K_c$  does not change with  $B$ . Apparently, beyond a thickness  $B \gg 2r_y$ , the constraint in the thickness direction ( $x_3$ ) is completely effective, and additional plate thickness

<sup>9</sup> J. E. Srawley and W. F. Brown, American Society for Testing and Materials, Special Technical Publication (ASTM STP) 381 (Philadelphia: ASTM, 1965), p. 133; W. F. Brown and J. E. Srawley, ASTM STP 410 (Philadelphia: ASTM, 1966), p. 1.

does not change  $K_c$ . This particular value of  $K_c$  that is independent of the thickness of the specimen is labeled the fracture toughness of the material, and the symbol  $K_{lc}$  is used to denote it.

On the other extreme, when the ratio  $B/(K_c/\sigma_y)^2$  is much smaller than  $1/\pi$  (i.e.,  $B \ll 2r_y$ ), we expect the fracture toughness to increase linearly with the plate thickness. In the region of  $B/(K_c/\sigma_y)^2 = 1/\pi$  corresponding to  $B = 2r_y$ , the data for both materials show a rapid fall to a constant level of  $K_{lc}$ . This decrease in the peak value of  $K_c$  (Figure 7.17(b)) to the  $K_{lc}$  level represents a change in the fracture mode from a plane-stress type to a plane-strain condition. The fracture in a relatively thin plate (plane stress) usually consists of a certain fraction of slant fracture (high energy) and another fraction of flat fracture (low energy). In general, with increasing thickness of the specimen, the percentage of slant fracture decreases, and the energy necessary for crack propagation also decreases – hence the fall in the  $K_c$  value. At a certain critical thickness, the crack propagates under plane-strain conditions, and the stress intensity factor reaches the minimum value designated as  $K_{lc}$ . Figure 7.17(b) shows schematically the variation of  $K_c$  and the percentage of flat fracture  $P$  with the plate thickness  $B$ .  $K_{lc}$  is especially relevant in the evaluation of the material, as it is a constant that is essentially independent of the dimensions of the specimen.

### Example 7.5

Establish the maximum load that the component shown in Figure E7.5, made of Ti-6Al-4V alloy, can withstand ( $\sigma_y = 900$  MPa,  $K_{lc} = 100$  MPa  $m^{1/2}$ ).

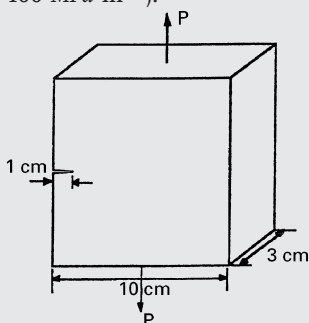


Fig. E7.5

*Solution:*

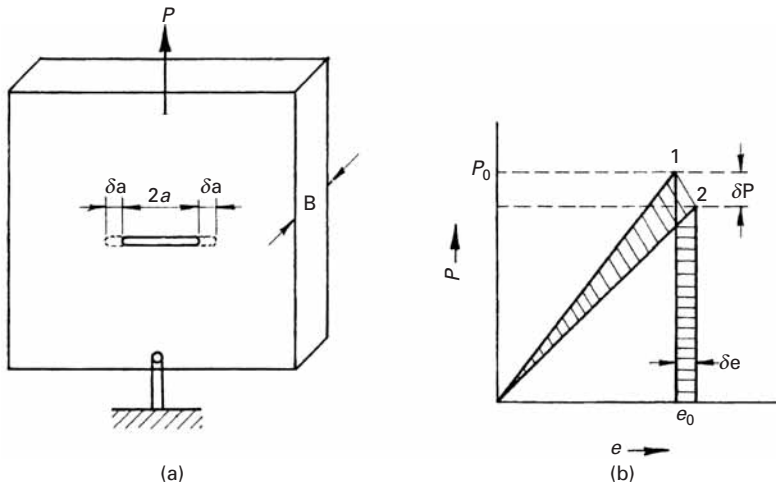
$$a = 1 \text{ cm},$$

$$W = 1 \text{ cm}.$$

$$K_{lc} = Y\sigma\sqrt{\pi a}, \quad (1)$$

$$\begin{aligned} Y &= 1.12 - 0.231 \left( \frac{a}{W} \right) + 10.55 \left( \frac{a}{W} \right)^2 \\ &= 1.12 - 0.231 \left( \frac{1}{10} \right) + 10.55 \left( \frac{1}{10} \right)^2 \\ &= 1.20. \end{aligned}$$

**Fig. 7.18** (a) Elastic body containing a crack of length  $2a$  under load  $P$ . (b) Diagram of load  $P$  versus displacement  $e$ .



We rewrite Equation 1 as

$$\sigma = \frac{K_{Ic}}{Y\sqrt{\pi a}}$$

to get

$$\sigma = \frac{100}{1.20\sqrt{\pi} \times 10^{-2}} = 470 \text{ MPa} < \sigma_y.$$

Therefore,

$$\begin{aligned} \frac{P}{A} &= \sigma \quad \text{and} \quad P = \sigma A = (470 \times 10^6) \times (10 \times 10^{-2} \times 3 \times 10^{-2}) \\ &= 1,410 \text{ kN}. \end{aligned}$$

Hence, the existing flaw, and not the yield stress, limits the maximum load.

## 7.7 | Fracture Toughness Parameters

In this section, we describe the variety of fracture toughness parameters that have come into being.

### 7.7.1 Crack Extension Force $G$

The concept of the crack extension force  $G$ , attributed to Irwin, can be interpreted as a generalized force. One can say that fracture mechanics is the study of the response of a crack (measured in terms of its velocity) to the application of various magnitudes of the crack extension force. Let us consider an elastic body of uniform thickness  $B$ , containing a through-the-thickness crack of length  $2a$ . Let the body be loaded as shown in Figure 7.18(a). With increasing load  $P$ , the displacement  $e$  of the loading point increases. The load-displacement diagram is shown in Figure 7.18(b). At point 1, we have the load as  $P_0$  and displacement as  $e_0$ . Now let us consider a “gedanken” experiment in which the crack extends by a small increment,  $\delta a$ . Due to this

small increment in crack extension, the loading point is displaced by  $\delta e$ , while the load falls by  $\delta P$ . Now, before the crack extension, the potential energy stored in body was

$$U_1 = \frac{1}{2}Pe,$$

represented by the area of the triangle through point 1 in the figure. After the crack extension, the potential energy stored in the body is

$$U_2 = \frac{1}{2}(P - \delta P)(e + \delta e),$$

represented by the area of the triangle passing through point 2 in the figure. In this process of crack extension, the change in potential energy,  $U_2 - U_1$  is given by the difference in the areas of the two crosshatched regions in the figure. Considering the small increment  $\delta a$  in crack length, we can write an equation for  $G$ , the crack extension force per unit length, as

$$GB \delta a = U_2 - U_1 = \delta U.$$

The change in elastic strain energy with respect to the crack area, in the limit of the area going to zero, equals the crack extension force; that is,

$$G = \lim_{\delta A \rightarrow 0} \frac{\delta U}{\delta A},$$

where  $\delta A = B \delta a$ .

It is convenient to evaluate  $G$  in terms of the compliance  $c$  of the sample, defined as

$$e = cP. \quad (7.29)$$

Now,

$$\delta U = U_2 - U_1 = \frac{1}{2}(p - \delta P)(e + \delta e) - \frac{1}{2}Pe,$$

or

$$\delta U = \frac{1}{2}P \delta e - \frac{1}{2}e \delta P - \frac{1}{2}\delta P \delta e. \quad (7.30)$$

Differentiating Equation 7.29, we have

$$\delta e = c \delta P + P \delta c. \quad (7.31)$$

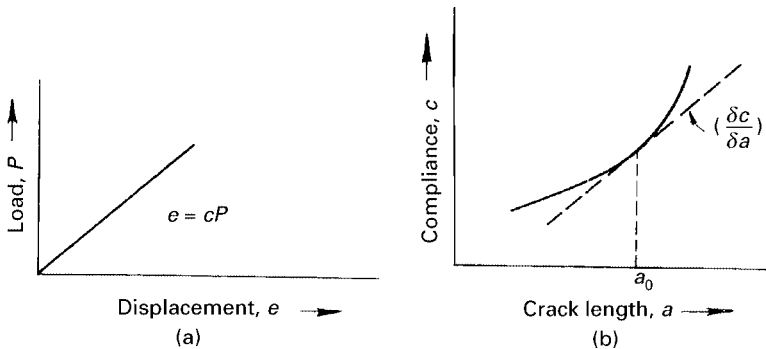
Substituting Equation 7.31 in Equation 7.30, we obtain

$$\delta U = \frac{1}{2}Pc \delta P + \frac{1}{2}P^2 \delta c - \frac{1}{2}e \delta P - \frac{1}{2}e(\delta P)^2 - \frac{1}{2}P \delta P \delta c. \quad (7.32)$$

Remembering that  $e = cP$  and ignoring the higher order product terms, we can write

$$\delta U = \frac{1}{2}Pc \delta P + \frac{1}{2}P^2 \delta c - \frac{1}{2}Pc \delta P,$$

**Fig. 7.19** (a) Load  $P$  versus displacement  $e$ . Compliance  $c$  is the inverse of the slope of this curve. (b) Compliance  $c$  versus crack length  $a$ .  $a_0$  is the initial crack length.



or

$$\delta U = \frac{1}{2} P^2 \delta c. \quad (7.33)$$

Then

$$G = \lim_{\delta A \rightarrow 0} \frac{\delta U}{\delta A} = \lim_{\delta A \rightarrow 0} \frac{\frac{1}{2} P^2 \delta c}{\delta A},$$

or

$$G = \frac{1}{2} \frac{P^2}{B} \frac{\delta c}{\delta a}. \quad (7.34)$$

From Equation 7.34, we see that  $G$  is independent of the rigidity of the surrounding structure and the test machine. In fact,  $G$  depends only on the change in compliance of the cracked member due to crack extension. Thus, to obtain  $G$  for a specimen, all we need to do is to determine the compliance of the specimen as a function of crack length and measure the gradient of the resultant curve,  $\delta c/\delta a$ , at the appropriate initial crack length (Figure 7.19).

This method is more useful for relatively small test samples, on which exact measurements can be made in the laboratory. One of the important uses of Equation 7.34 is that it provides a value of  $G$  (or  $K$ ) for complex structures that have not been (or cannot be) treated analytically. An experimental determination of  $G_c$ , the critical crack extension force, using this equation requires the value of fracture load (measured experimentally) and the value of  $\delta c/\delta a$ . The compliance can be measured by calibrating a series of samples with different crack lengths. We obtain a diagram of  $c$  versus  $a$ , and  $\delta c/\delta a$  is evaluated as the slope at the appropriate initial crack length.

### Example 7.6

A titanium alloy (Ti-6% Al-4% V) is used for aircraft applications. The NDE methods used cannot detect flaws whose size is smaller than 1 mm. You are asked, as the design engineer, to specify the maximum tensile stress that the part can bear in plane-stress and plane-strain

situations. The yield stress of the alloy is 1,450 MPa.

$$E = 115 \text{ GPa},$$

$$\nu = 0.312,$$

$$G_c = 23.6 \text{ kN/m}.$$

*Solution:* We have

$$2a = 1 \text{ mm},$$

so that

$$a = 0.5 \times 10^{-3} \text{ m.}$$

The critical stress in plane stress is

$$\begin{aligned}\sigma_c &= \sqrt{\frac{EG_c}{\pi a}} \\ &= \left( \frac{115 \times 10^9 \times 23.6 \times 10^3}{\pi \times 0.5 \times 10^{-3}} \right)^{1/2} \\ &= 1.31 \times 10^9 \text{ Pa.}\end{aligned}$$

The critical stress in plane strain is

$$\begin{aligned}\sigma_c &= \sqrt{\frac{EG_c}{\pi a(1 - \nu^2)}} \\ &= 1.385 \times 10^9 \text{ Pa.}\end{aligned}$$

Thus, the maximum stresses are 1.31 GPa (plane stress) and 1.385 GPa (plane strain).

From consideration of fracture toughness, the maximum stress is lower than the yield stress; hence, the former is the limiting stress.

### 7.7.2 Crack Opening Displacement

The development of a plastic zone at the tip of the crack results in a displacement of the faces without crack extension. This relative displacement of opposite crack edges is called the crack opening displacement (COD) (Figure 7.20). Wells<sup>10</sup> suggested that when this displacement at the crack tip reaches a critical value  $\delta_c$ , fracture would ensue.

LEFM is applicable only when the plastic zone is small in relation to the crack length (i.e., well below the yield stress and in plane strain). Consider a small crack in a brittle material. We have

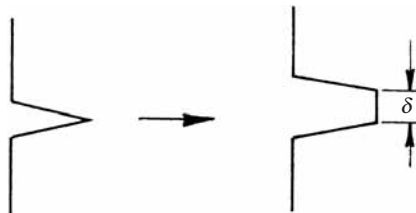
$$\sigma_c = K_{Ic}(\sqrt{\pi a})^{-1}, \quad \text{as } a \rightarrow 0, \quad \sigma_c \rightarrow \infty.$$

But this, as we very well know, does not occur. Instead, a plastic zone develops and may extend through the section such that

$$\sigma_{\text{net}} = \sigma \frac{W}{W - a} \geq \sigma_y,$$

<sup>10</sup> A. A. Wells, *Brit. Weld. J.*, 13 (1965) 2.

**Fig. 7.20** Crack opening displacement.



where  $W$  is the width of sample and  $\sigma_y$  is the yield stress. In practice,  $\sigma_c \leq 0.66\sigma_y$  for the  $K_{Ic}$  validity.

In more ductile materials, the critical stress predicted by LEFM will be higher than  $\sigma_y$ . One can use the concept of COD in such cases. In the elastic case (Figure 7.20),

$$COD = \Delta = \frac{4\sigma}{E} \sqrt{(a^2 - x^2)}. \quad (7.35)$$

At the center of the crack ( $x = 0$ ), the maximum opening is

$$\Delta_{\max} = \frac{4\sigma a}{E}.$$

Applying the plastic zone correction, we have, from Equation 7.35,

$$\Delta = \frac{4\sigma}{E} \sqrt{(a + r_y)^2 - x^2},$$

where  $(a + r_y)$  is the effective crack length.

The crack-tip opening displacement (CTOD),  $\delta$ , is given for  $x = a$  and  $r_y \ll a$  as

$$\delta = \frac{4\sigma}{E} \sqrt{2ar_y}. \quad (7.36)$$

A displacement of the origin to the crack tip gives a general expression for the crack opening:

$$\Delta = \frac{4\sigma}{E} \sqrt{2a_{\text{eff}}r_y}.$$

Substituting  $r_y = \sigma^2 a / 2\sigma_y^2$  (see Equation 7.27) in Equation 7.36 gives

$$\delta = \frac{4}{\pi} \frac{K_I^2}{E\sigma_y}. \quad (7.37)$$

Equation 7.37 is valid in the LEFM regime, and fracture occurs when  $K_I = K_{Ic}$ , which corresponds to  $\delta = \delta_{lc}$ , a material constant.

The use of the COD criterion demands the measurement of  $\delta_c$ . Direct measurement of  $\delta_c$  is not easy. An indirect way is the following. We have

$$\begin{aligned} \Delta &= \frac{4\sigma}{E} \sqrt{(a + r_y)^2 - x^2} \\ &= \frac{4\sigma}{E} \sqrt{a + 2ar_y + r_y^2 - x^2}. \end{aligned}$$

Ignoring the  $r_y^2$  term and using the relationship of Equation 7.36, we can write

$$\Delta = \frac{4\sigma}{E} \left( a^2 - x^2 + \frac{E^2}{16\sigma^2} \delta^2 \right)^{1/2}. \quad (7.38)$$

According to this equation,  $\delta$  can be measured indirectly from a COD measurement (e.g., at  $x = 0$ , at the center of the crack) without making any simplifications about the plastic-zone size correction.  $\Delta$  can be measured by means of a clip gage.

Another way of obtaining  $\delta$  is to use the equations of Dugdale-BCS model of the crack. (See Section 7.6.6.) According to Dugdale-BCS model (Bilby, Cotrell, Swinden, op. cit.; Dugdale, op. cit.)

$$\delta = \frac{8\sigma_y a}{\pi E} \log \sec \frac{\pi\sigma}{2\sigma_y}.$$

Expanding the log sec function in series, we get

$$\delta = \frac{8\sigma_y a}{\pi E} \left[ \frac{1}{2} \left( \frac{\pi\sigma^2}{2\sigma_y} \right)^2 + \frac{1}{12} \left( \frac{\pi\sigma}{2\sigma_y} \right)^4 + \dots \right].$$

For  $\sigma \ll \sigma_y$ , we can write (neglecting fourth- and higher-order terms)

$$\delta = \frac{\pi\sigma^2}{E\sigma_y} = \frac{G_I}{\sigma_y}. \quad (7.39)$$

Comparing Equation 7.39 with Equation 7.37, we note that the difference is in the factor  $4/\pi$ , which comes from the plastic-zone correction. In general,

$$\delta = \frac{G_I}{\lambda\sigma_y} = \frac{K_I^2(1-\nu^2)}{E\lambda\sigma_y} \quad (\text{for plane strain}). \quad (7.40)$$

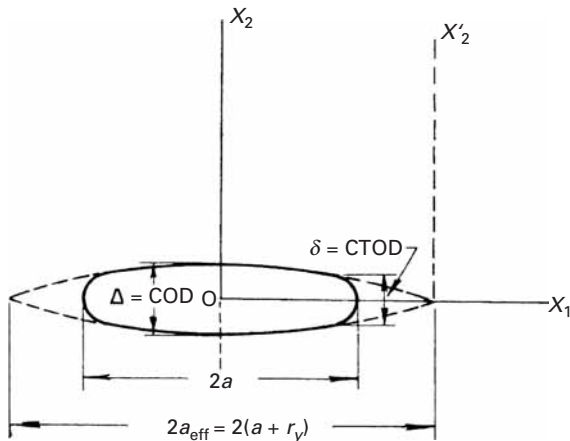
The factor  $(1 - \nu^2)$  should be ignored in the case of plane stress.

In the literature, we encounter various values of  $\lambda$ . These depend on the exact location where CTOD is determined (i.e., the exact location of the crack tip). Wells<sup>11</sup> suggested that, experimentally,  $\lambda \approx 2.1$  for compatibility with LEFM (i.e., limited plasticity). For cases involving extensive plasticity, the engineering design application approach is to take  $\lambda \approx 1$ .

Thus, at unstable fracture,  $G_{lc} = \lambda\sigma_y \delta_c$ . The important point about COD is that, theoretically,  $\delta_c$  can be computed for both elastic and plastic materials, whereas  $G_{lc}$  is restricted only to the elastic regimen. The COD thus allows one treat fracture under plastic conditions. A word of caution is in order, however. Figure 7.21 presents a comparison between COD and CTOD. We should realize that the strain fields and crack opening displacements associated with a crack tip will be different for different specimen configurations. Thus, we cannot define a single critical COD value for a given material in a manner

<sup>11</sup> A. A. Wells, Eng. Fract. Mech., 1 (1970) 399.

**Fig. 7.21** Relationship between crack opening displacement (COD,  $\Delta$ ), crack-tip opening displacement (CTOD,  $\delta$ ), crack length ( $2a$ ), and size of plastic zone ( $r_y$ ).



equivalent to that of  $K_{lc}$ , as the COD value will be affected by the geometry of the test specimen.

### Example 7.7

If the toughness of a thermoplastic polymer  $G_c = 103 \text{ J m}^{-2}$ , what would be the critical crack length under an applied stress of 200 MPa? Take Young's modulus of the polymer to be 10 GPa.

**Solution:** We have

$$G_c = 10^3 \text{ J m}^{-2}, \quad E = 10 \text{ GPa}, \quad \sigma = 200 \text{ MPa.}$$

Thus, the critical crack length  $a_c = EG_c/\pi\sigma^2 = 10 \times 10^9 \times 10^3/\pi (200 \times 10^6)^2 = 0.08 \text{ mm.}$

### 7.7.3 *J* Integral

*J* integral is another variant for fracture toughness analysis. It provides a value of energy required to propagate a crack in an elastic-plastic material. The mathematical foundation for the *J* integral was laid by Eshelby,<sup>12</sup> who applied it to dislocations. Cherepanov<sup>13</sup> and Rice<sup>14</sup> applied it, independently, to cracks. Figure 7.22 shows a closed contour  $\Gamma$  in a two-dimensional body. When such a body is subjected to external forces, internal stresses arise in it. On the basis of the theory of conservation of energy, Eshelby showed that the integral *J* is equal to zero for a closed contour; that is,

$$J = \int_{\Gamma} \left( W dx_2 - T \frac{\partial u}{\partial x_1} ds \right) = 0, \quad (7.41)$$

<sup>12</sup> J. D. Eshelby, *Phil. Trans. Roy. Soc London*, A244 (1951) 87.

<sup>13</sup> G. P. Cherepanov, *Appl. Math. Mech. (Prinl. Mat. Mekh.)*, 31, no. 3 (1967) 503.

<sup>14</sup> J. R. Rice, *J. Appl. Mech.*, 35 (1968) 379.

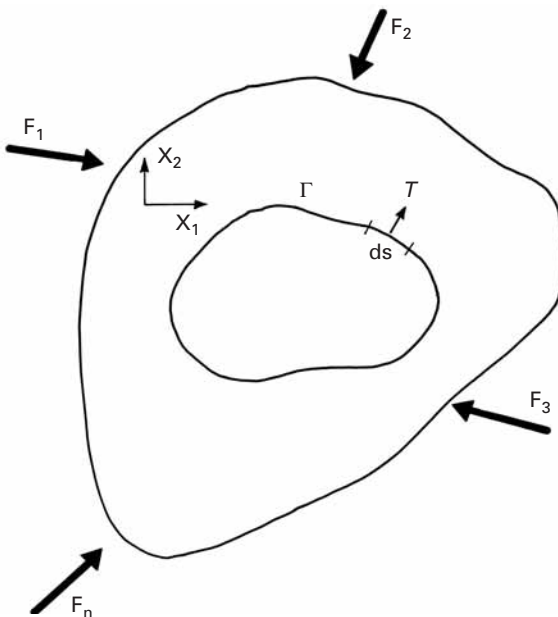


**Fig. 7.22** A body subjected to external forces  $F_1, F_2, \dots, F_n$  and with a closed contour  $\Gamma$ .

where

$$W = \int_0^{\Sigma_{ij}} \sigma_{ij} d\varepsilon_{ij}$$

is the strain energy per unit volume (see Chapter 2),  $T$  is the tension vector (traction) perpendicular to  $\Gamma$  and pointing to the outside of the contour,  $ds$  is an element of length along the contour, and  $u$  is the displacement in the  $x_1$  direction. The  $J$  integral is an energy related quantity; similar to the crack extension force  $G$ ,  $J$  has the units of energy per unit area ( $J/m^2$ ) or force per unit length ( $N/m$ ).

Figure 7.23 shows a crack, around which a contour  $ABCDEF$ A is made. The total  $J$  must be zero, i.e.,

$$J = J_{\Gamma_1 + \Gamma_2} = 0.$$

Along  $AF$  and  $CD$  (crack surfaces), the tractions  $T$  are equal to zero. The same is true for the normal and shear stresses. Thus,  $J_{AF} = J_{CD} = 0$ . It can therefore be concluded that

$$J_{\Gamma_1 + \Gamma_2} = J_{\Gamma_1} + J_{\Gamma_2} + J_{AF} + J_{CD} = 0, \quad J_{\Gamma_1} = -J_{\Gamma_2}.$$

Hence, the  $J$  integral along two different paths around a crack has the same value. That is, in general, the  $J$  integral around a crack is path independent.

From a physical point of view, the  $J$  integral represents the difference in the potential energies of identical bodies containing cracks of length  $a$  and  $a + da$ ; in other words, the  $J$  integral around a crack is equal to the change in potential energy for a crack extension  $da$ . For a body of thickness  $B$ , this can be written as

$$J = \frac{1}{B} \frac{\delta U}{\delta a}, \quad (7.42)$$

**Fig. 7.23** Eshelby contours around cracks.

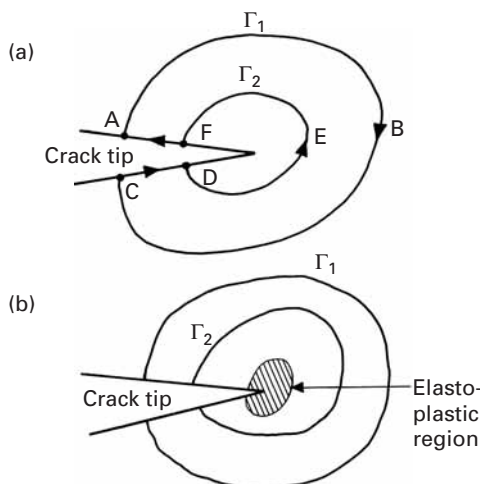
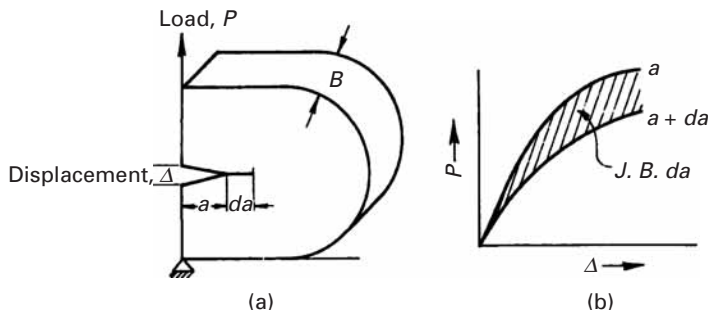


**Fig. 7.24** Physical interpretation of the  $J$  integral. The  $J$  integral represents the difference in potential energy (shaded area) of identical bodies containing cracks of length  $a$  and  $a + da$ .



where  $U$  is the potential energy,  $a$  the crack length, and  $B$  the plate thickness.  $U$  is equal to the area under the curve of load versus displacement. Figure 7.24 shows this interpretation, where the shaded area is  $\delta U = JB \delta a$ . Like  $G_{lc}$ ,  $J_{lc}$  measures the critical energy associated with the initiation of crack growth, but in this case accompanied by substantial plastic deformation. In fact, Begley and Landes<sup>15</sup> showed the formal equivalence of  $J_{lc}$  and  $G_{lc}$  by measuring the  $J_{lc}$  from small fully plastic specimens and the  $G_{lc}$  from large elastic specimens satisfying the plane-strain conditions for the LEFM test.

The path independence of the  $J$  integral, together with this interpretation in terms of energy, makes it a powerful analytical tool. The  $J$  integral is path independent in the case of either linear or nonlinear materials behaving elastically. When extensive plastic deformation occurs, the practice is to assume that the plastic yielding can be described by the deformation theory of plasticity. According to this theory, stresses and strains are functions only of the point of measurement and not of the path taken to get to that point. As in the case of slow, stable crack growth, there will be a relaxation of stresses at the crack tip, so there will be a violation of this postulate.

<sup>15</sup> J. A. Begley and J. D. Landes, ASTM STP 514, (Philadelphia: ASTM, 1972), p. 1.

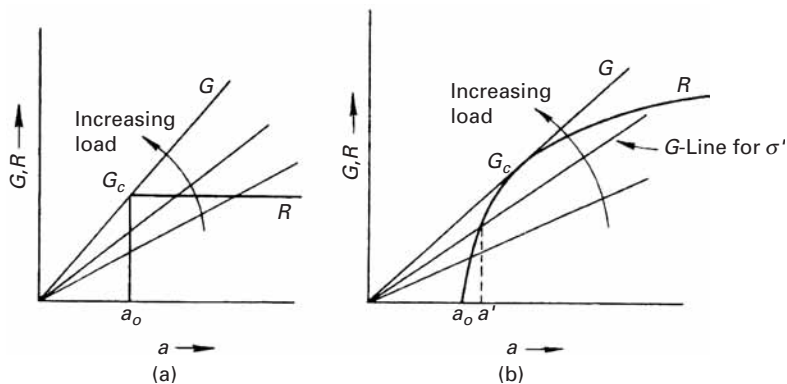


**Fig. 7.25** *R* curves for (a) brittle material and (b) ductile material.

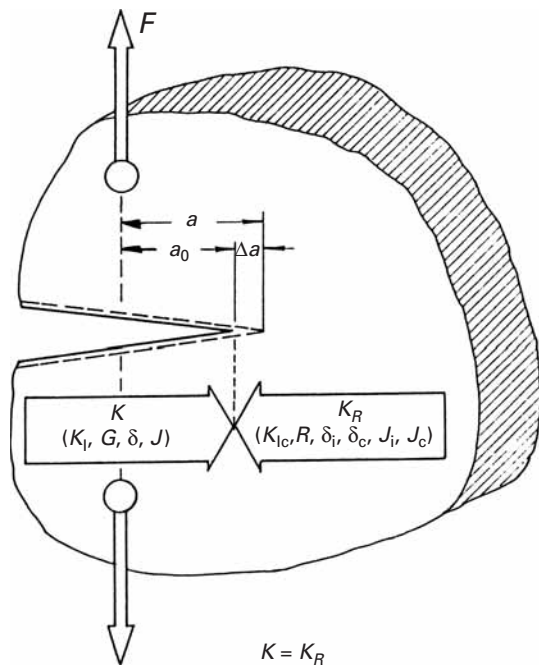
Thus, the use of the  $J$  integral should be limited to the initiation of crack propagation, by stable or unstable processes. Studies using incremental plasticity or flow theories with finite elements indicate the path independence of the  $J$  integral.

#### 7.7.4 *R* Curve

The *R* curve characterizes the resistance of a material to fracture during slow and stable propagation of a crack. An *R* curve graphically represents this resistance to crack propagation of the material as a function of crack growth. With increasing load in a cracked structure, the crack extension force  $G$  at the crack tip also increases. (See Equation 7.34.) However, the material at the tip presents a resistance  $R$  (sometimes, the symbol  $K_R$  is used) to crack growth. According to Irwin, failure will occur when the rate of change of the crack extension force ( $\partial G/\partial a$ ) equals the rate of change of this resistance to crack growth in the material ( $\partial R/\partial a$ ). The resistance of the material to crack growth,  $R$ , increases with an increase in the size of the plastic zone. Since the plastic zone size increases nonlinearly with  $a$ ,  $R$  will also be expected to increase nonlinearly with  $a$ .  $G$  increases linearly with  $a$ . Figure 7.25 shows the instability criterion: the point of tangency between the curves of  $G$  versus  $a$  and  $R$  versus  $a$ . Figure 7.25(a) shows the *R* curve for a brittle material, and Figure 7.25(b) shows the *R* curve for a ductile material. Crack extension occurs for  $G > R$ . Consider the  $G$  line for a stress  $\sigma'$ , shown in Figure 7.25(b). At the stress  $\sigma'$ , the crack in the material will grow only from  $a_0$  to  $a'$ , since  $G > R$  for  $a < a'$ ,  $G < R$  for  $a > a'$ , and the crack does not extend beyond  $a'$ . As the load is increased, the position of the  $G$  line changes, as indicated in the figure. When  $G$  becomes tangent to  $R$ , unstable fracture ensues. The *R* curve for a brittle material (Figure 7.25(a)) is a "square" curve, and the crack does not extend at all until the contact is reached, at which point  $G = G_c$  and the unstable fracture follows.

The *R*-curve method is another version of the Griffith energy balance. One can conveniently make this kind of analysis if an analytical expression for the *R* curve is available. Experimental determination of *R* curves, however, is complicated and time consuming.

**Fig. 7.26** Different parameters describing the growth of a crack.



### 7.7.5 Relationships among Different Fracture Toughness Parameters

So far, we have seen that, in our effort to develop a quantitative description of fracture toughness, various parameters, such as  $K$ ,  $G$ ,  $J$ ,  $\delta$ ,  $R$ , etc., have been developed. Since all these parameters define the same physical quantity, it is not unexpected that they are interrelated. And we have mentioned in different sections the relationships among the parameters. Figure 7.26 summarizes these relationships. It would, however, be helpful to the reader to recapitulate these relationships, even at the risk of repeating. That is what we will do in this section.

If we take into account the stress distribution around the tip of a crack, we get the stress-intensity-factor ( $K$ ) approach. The magnitude or the intensity of the local stresses is determined by  $K$ , because the form of the local crack-tip stress field is the same for all situations involving a remote stress  $\sigma$ . Thus,  $K$ , and not  $\sigma$ , is the local characterizing parameter. The fracture then occurs when the applied  $K$  attains the critical value  $K_c$ . In particular, when the specimen's dimensions satisfy the plane-strain condition, we call this value the plane-strain fracture toughness and denote it by  $K_{lc}$ . The stress and the crack length corresponding to  $K_{lc}$  are the fracture stress  $\sigma_c$  and the fracture crack length  $a_c$ . Note that the elastic constants of the material are not involved. The energy-release-rate approach gives us the crack extension force  $G$ , which is related to the parameters  $K$  by the equation

$$K^2 = E'G,$$

where  $E' = E$ , Young's modulus, in the case of plane stress and  $E' = E/(1 - \nu^2)$  in the case of plane strain. Note that, in characterizing the fracture behavior in terms of  $G$ , we need to know the elastic constants of the material. Because in the case of polymers  $E$  is time dependent and very precise modulus data are not available, there is some advantage to using the  $K$  approach.

The critical crack opening displacement  $\delta_c$  is another useful parameter. It is related to  $K$  by the equation

$$\delta_c = K_{Ic}^2 / \lambda E \sigma_y,$$

where  $\lambda$  is a dimensionless constant that depends on the geometry of the specimen, its state of stress, and the work-hardening capacity of the material.  $\lambda$  has a value between 1 and 2. In particular, for the strip-yielding model of Dugdale-BCS,  $\lambda = 1$ .

The  $J$  integral provides yet another measure of fracture toughness. And, for small-scale yielding, we have

$$J = \lambda \delta \sigma_y.$$

In short, for small-scale yielding, we can sum up the relationships among the different fracture toughness parameters as

$$J = G = K^2/E' = \lambda \sigma_y \delta,$$

where the symbols have the usual meaning.

## 7.8 | Importance of $K_{Ic}$ in Practice

$K_{Ic}$  is the critical stress intensity factor under conditions of plane strain ( $\varepsilon_{33} = 0$ ), which is characterized by small-scale plasticity at the crack tip. The material is fully constrained in the direction of thickness. When determined under these rigorous conditions,  $K_{Ic}$  will be a material constant. Thus, when one needs to characterize materials by their toughness (in the same way that one characterizes materials by their ultimate tensile strength or tensile yield strength), only valid  $K_{Ic}$  data should be considered. This will be explained in Chapter 8.

$K_c$  is the critical stress intensity factor under conditions of plane stress ( $\sigma_{33} = 0$ ), which is characterized by large plasticity at the crack tip. In this case, the through-thickness constraint is negligible.  $K_c$  values can be up to two times greater than the  $K_{Ic}$  values of the same material.  $K_{Ic}$  depends on the temperature  $T$ , on the strain rate  $\dot{\varepsilon}$ , and on microstructural variables.

In general,  $K_c$  or  $K_{Ic}$  decreases as the (yield or ultimate) strength of a material increases. This inverse relationship between fracture toughness and strength is shown schematically in Figure 7.27. With concurrent improvement in the material's strength and toughness, this curve shifts in the direction of the arrow. The dependence of  $K_{Ic}$  on tensile strength and on sulfur level in a steel is shown in Figure 7.28. As expected,  $K_{Ic}$  decreases monotonically with increases in tensile

**Fig. 7.27** Relationship between fracture toughness and yield stress.

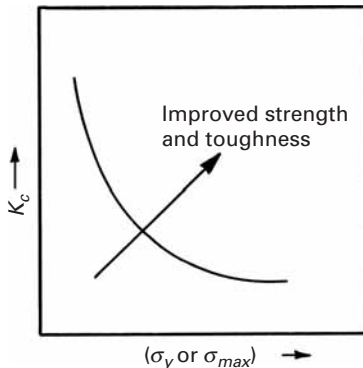
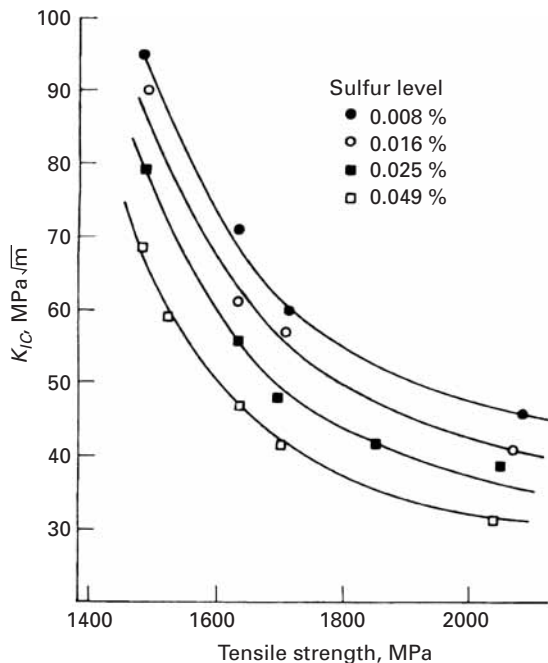


**Fig. 7.28** Variation of fracture toughness  $K_{Ic}$  with tensile strength and sulfur content in a steel.  
(Adapted from A. J. Birkle, R. P. Wei, and G. E. Pellissier, *Trans. ASM*, 59 (1966) 981.)



strength or sulfur content. (Sulfur is well known to embrittle steels.) Figure 7.29 shows that the same holds for  $K_{Ic}$  as a function of the yield strength.  $K_c$  also depends on these variables.

Table 7.2 shows representative fracture toughnesses for selected materials. Metals have the highest toughness. For most ceramics,  $K_{Ic}$  does not exceed  $5 \text{ MPa} \sqrt{\text{m}}$ . The addition of partially stabilized zirconia to alumina increases  $K_{Ic}$  to  $10 \text{ MPa} \sqrt{\text{m}}$  and even higher. The reason for this is a martensitic transformation that is described in greater detail in Chapter 11. Plastics have low  $K_{Ic}$ ; however, we should remember that their density is only a small fraction of that of metals.

**Table 7.2** Plane-Strain Fracture Toughnesses for Representative Materials

	Material	$K_{Ic}$ (MPa m <sup>1/2</sup> )
(a)	<i>Metals</i>	
	300M steel 300 °C temper	65
	300M steel 650 °C temper	152
	18-Ni maraging steel, vacuum melted	176
	18-Ni maraging steel, air melted	123
	AISI 4130 steel	110
	2024-T651 aluminum	24
	2024-T351 aluminum	34
	6061-T651 aluminum	34
	7075-T651 aluminum	29
	Ti-6Al-4V, mill annealed	106–123
	Ti-6Al-4V, recrystallized, annealed	77–116
(b)	<i>Ceramics</i>	
	Cement/concrete	0.2
	Soda-lime glass	0.7–0.9
	MgO	3
	Al <sub>2</sub> O <sub>3</sub>	3–5
	Al <sub>2</sub> O <sub>3</sub> + 15% ZrO <sub>2</sub>	10
	SiC	3–4
	Si <sub>3</sub> N <sub>4</sub>	4–5
(c)	<i>Polymers</i>	
	Epoxy	0.3–0.6
	Polyethylene, high-density	2
	Polyethylene, low-density	1
	Polypropylene	3
	ABS	3–4
	Polycarbonate	1–2.6
	PVC	2.4
	PVC (rubber modified)	3.4
	PMMA	1.8

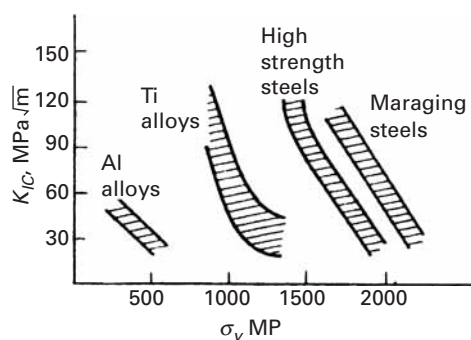
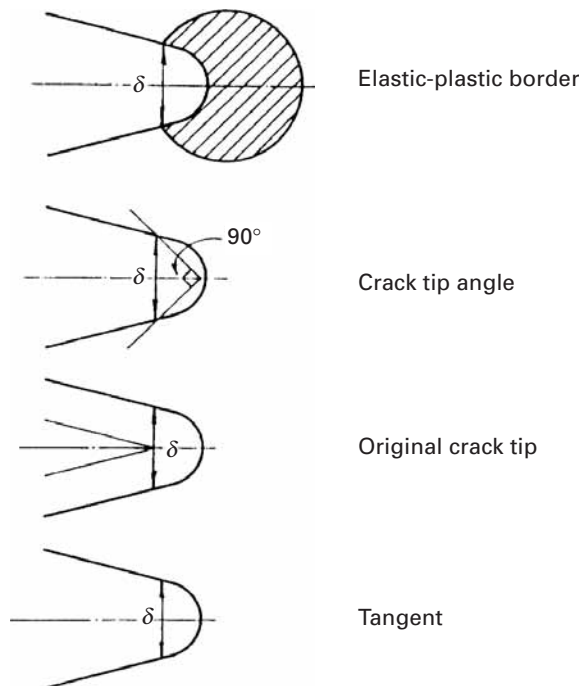


**Fig. 7.29** Variation of fracture toughness  $K_{Ic}$  with yield strength  $\sigma_y$  for a series of alloys. (Adapted from D. Broek, *Elementary Engineering Fracture Mechanics*, 3rd ed. (Amsterdam: Martinus Nijhoff, 1978), p. 270.)

**Fig. 7.30** Different measures of crack-tip opening displacement.



## 7.9 | Post-Yield Fracture Mechanics

The concepts of crack opening displacement and the  $J$  integral are complementary. The crack tip opening displacement (CTOD),  $\delta$ , is the parameter that controls crack extension. But the notion of CTOD is not problem free. For example, there exists a considerable amount of diversity in its very definition. Figure 7.30 shows some ways of measuring  $\delta$ . The experimental determination of  $\delta$  and the calculation of the relevant value for a cracked structure also involve uncertainties. We can split the CTOD value into an elastic and a plastic component, to wit:

$$\delta_t = \delta_{el} + \delta_{pl}.$$

The elastic portion is, of course, related to  $K$  or  $G$ , as indicated earlier. In particular,  $K_{lc}$  and  $G_{lc}$  correspond to  $\delta_{lc}$ , the CTOD value at the initiation of unstable fracture. The plastic portion is not strictly a material property, in as much as it depends on the specimen's dimensions, constraints, etc.

The  $J$  integral is, mathematically, a path-independent integral. From a practical engineering point of view, the  $J$  integral represents, similarly to  $G$ , a strain energy release rate and is related to the area under the curve load,  $P$ , and the *load line displacement*.

Just as we did for the concept of COD, we can write, for  $J$ ,

$$J_{\text{total}} = J_{el} + J_{pl},$$

where  $J_{el}$  is the elastic portion, equal to  $K_I^2/E'$ . Here again,  $E'$  equals  $E$  for plane stress and  $E/(1 - \nu^2)$  for plane strain.  $J_{pl}$  is a function of the geometry of the component and the crack load corresponding to extensive plastic deformation, and the material characteristics such as the yield strength, ultimate tensile strength, etc.

This division of the crack driving force into elastic and plastic parts is conceptually very convenient. Tests for the  $J$  integral, as well as for COD, are based on the fact that a ductile structure containing a crack is characterized by three successive stages:

1. Crack blunting and the initiation of propagation.
2. Slow and stable crack growth under increasing load.
3. Unstable crack growth, i.e., the instability.

A curve showing these stages is called a *resistance curve* ( $\delta$ -R or  $J$ -R). It describes the material resistance as a function of stable crack growth  $a$ .

## 7.10 | Statistical Analysis of Failure Strength

As we have repeatedly pointed out, materials in real life are never perfect. No matter how carefully processed a material is, it will always contain a distributions of flaws. The presence of flaws in ductile metals is not very serious, because these metals have the ability to deform plastically and thus attenuate, at least to some extent, the insidious effect of flaws on strength. The same cannot be said of brittle materials. Such preexisting flaws are responsible for the phenomenon of catastrophic fracture in these materials. In general, flaws vary in size, shape, and orientation; consequently, the strength of a material will vary from specimen to specimen. When we test a brittle material, one or several of the larger flaws propagate. In the case of a ductile material such as aluminum, most of the flaws get blunted because of plastic deformation, and only after considerable plastic deformation do microvoids form and coalesce, leading to an eventual fracture. (See Chapter 8.) If we were to test a large number of identical samples and plot the strength distribution of a brittle and a ductile solid, we would get the curves shown in Figure 7.31. The strength distribution curve for the ductile solid is very narrow and close to a Gaussian or normal distribution, while that for the brittle solid is very broad with a large tail on the high-strength side – that is, a non-Gaussian distribution. It turns out that the strength distribution of a brittle solid can be explained by a statistical distribution called the *Weibull distribution*, named after the Swedish engineer who first proposed it.<sup>16</sup> We next describe this distribution and its application to the analysis of the strength of brittle solids.

The basic assumption in Weibull distribution is that a body of material with volume  $V$  has a statistical distribution of noninteracting

<sup>16</sup> W. Weibull, *J. App. Mech.*, 18 (1951), 293.

**Fig. 7.31** Strength distribution of a brittle and a ductile solid.

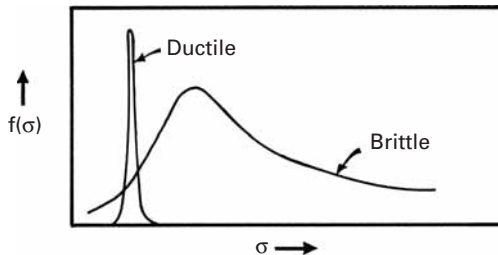
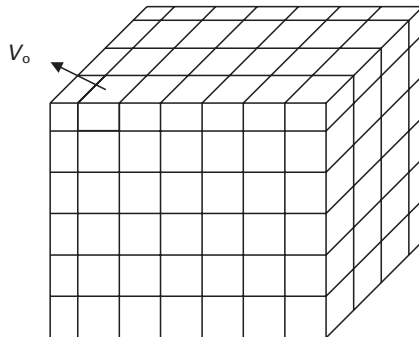


**Fig. 7.32** Solid body with volume  $V$  composed of  $n$  cubes with volume  $V_0$  each.



flaws. Thus, the body of volume  $V$  can be considered to be made up of  $n$  volume elements, each of unit volume  $V_0$  and having the same flaw distribution. (See Figure 7.32.) Now, if we subject such a solid to an applied stress  $\sigma$ , the probability that the solid will survive can be written as

$$P(V) = P(V_0)P(V_0) \dots P(V_0) = P(V_0)^n, \quad (7.43)$$

where  $V_0$  is the volume of an element and  $n$  is the number of volume elements. Taking logarithms, we have

$$\ln P(V) = n \ln P(V_0),$$

or

$$P(V) = \exp[n \ln P(V_0)]. \quad (7.44)$$

Weibull defined a risk-of-rupture parameter

$$R = -[\ln P(V_0)], \quad (7.45)$$

or, alternatively,

$$P(V_0) = \exp(-R). \quad (7.46)$$

He then postulated that this parameter is given by

$$R = [(\sigma - \sigma_u)/\sigma_0]^m, \quad (7.47)$$

where  $\sigma$  is the applied stress and  $m$ ,  $\sigma_0$ , and  $\sigma_u$  are material constants for a constant-flaw population, i.e., the flaw population does

**Table 7.3** | Typical Values of the Weibull Modulus  $m$  for Some Materials

Material	$m$
<i>Traditional Ceramics:</i>	
Brick, Pottery, Chalk	<3
<i>Engineered Ceramics:</i>	
SiC, Al <sub>2</sub> O <sub>3</sub> , Si <sub>3</sub> N <sub>4</sub>	5–10
<i>Metals:</i>	
Aluminum, Steel	90–100

not change from element to element.  $\sigma_u$  is the stress below which the probability of failure is zero. If we assume that any tensile stress will cause failure in a brittle solid, then we can take  $\sigma_u$  to be zero. For such a material,  $\sigma_0$  is a characteristic strength – often taken to be approximately the mean strength – of the material, and  $m$ , called the *Weibull modulus*, is a measure of the variability of the strength of the material; the higher the value of  $m$ , the less is the material's variability in strength.  $m$  can have any value between 0 and  $\infty$ , i.e.,  $0 < m < \infty$ . As  $m \rightarrow 0$ ,  $R \rightarrow 1$ , and the material will fail at any stress. Also, when  $m \rightarrow \infty$ , the material will not fracture at any stress below  $\sigma_0$ . Table 7.3 gives some typical values of  $m$  for some materials.

From Equations (7.46) and (7.47), we can write, for the survival probability of a brittle material

$$P(V_0) = \exp \left[ - \left( \frac{\sigma - \sigma_u}{\sigma_0} \right)^m \right]. \quad (7.48)$$

We can write the failure probability as

$$F(V_0) = 1 - P(V_0) = 1 - \exp \left[ - \left( \frac{\sigma - \sigma_u}{\sigma_0} \right)^m \right]. \quad (7.49)$$

As explained in the preceding paragraph, we can take  $\sigma_u = 0$  for a brittle material. This will make Equation 7.48 become

$$P(V_0) = \exp \left[ - \left( \frac{\sigma}{\sigma_0} \right)^m \right]. \quad (7.50)$$

Equation 7.50 says that when the applied stress  $\sigma = 0$ , the survival probability  $P(V_0) = 1$ , and all samples of the material tested survive. As the applied stress increases, more samples fail, and the survival probability decreases. Eventually, as  $\sigma \rightarrow \infty$ ,  $P(V_0) \rightarrow 0$ ; that is, all samples fail at very high stresses. We can arrive at a value of  $\sigma_0$  by noting that, when  $\sigma = \sigma_0$ ,

$$P(V_0) = \frac{1}{e} = 0.37.$$

Thus,  $\sigma_0$  is the stress corresponding to a survival probability of 37%. Taking logarithms of Equation 7.50, we get

$$\ln \left[ \frac{1}{P(V_0)} \right] = \left( \frac{\sigma}{\sigma_0} \right)^m. \quad (7.51)$$

Thus, a double-logarithmic plot of Equation 7.51 will give a straight line with slope  $m$ . This yields a convenient way of obtaining a Weibull analysis of the strength of a given material. If  $N$  samples are tested, we rank their strengths in ascending order and obtain the probability of survival for the  $i$ th strength value as

$$P_i(V_0) = (N + 1 - i)/(N + 1).$$

Note that there will be  $N + 1$  strength intervals for  $N$  tests. Alternatively, we can use the failure probability:

$$F_i(V_0) = 1 - P_i(V_0) = i/(N + 1).$$

We can incorporate a volume dependence into Equation 7.50. Let  $V_0$  be a reference volume of a material with a survival probability of  $P(V_0)$ , i.e., fraction of samples, each of volume  $V_0$ , that survive when loaded to a stress,  $\sigma$ . Now consider a volume  $V$  of this material such that  $V = nV_0$ . Then, from Equation 7.43, we can write

$$P(V) = P(V_0)^n = [P(V_0)]^{V/V_0}.$$

Taking logarithms, we get

$$\ln P(V) = \frac{V}{V_0} \ln P(V_0),$$

or

$$P(V) = \exp \left[ \frac{V}{V_0} \ln P(V_0) \right]. \quad (7.52)$$

From Equations 7.50 and 7.52, we have

$$\boxed{P(V) = \exp \left[ -\frac{V}{V_0} \left( \frac{\sigma}{\sigma_0} \right)^m \right]}, \quad (7.53)$$

or

$$\ln P(V) = -\frac{V}{V_0} \left( \frac{\sigma}{\sigma_0} \right)^m. \quad (7.54)$$

We can convert Equation 7.54 to the following form by taking logarithms again.

$$\ln \ln \left[ \frac{1}{P(V)} \right] = \ln \frac{V}{V_0} + m \ln \frac{\sigma}{\sigma_0}.$$

Equation 7.54 tells us that, for a given probability of survival and for two volumes  $V_1$  and  $V_2$  of a material,

$$\ln P(V) = -\frac{V_1}{V_0} \left[ \frac{\sigma_1}{\sigma_0} \right]^m = -\frac{V_2}{V_0} \left[ \frac{\sigma_2}{\sigma_0} \right]^m,$$

where  $\sigma_1$  and  $\sigma_2$  are the strengths of the material in volumes  $V_1$  and  $V_2$ , respectively.

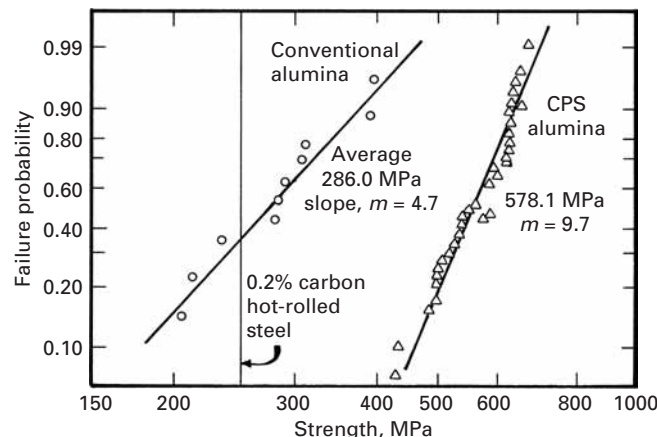


**Fig. 7.33** A Weibull plot for a steel, a conventional alumina, and a controlled-particle-size (CPS) alumina. Note that the slope (Weibull modulus  $m$ )  $\rightarrow \infty$  for steel. For CPS alumina,  $m$  is double that of conventional alumina. (After E. J. Kubel, *Adv. Mater. Proc.*, Aug (1988) 25.)

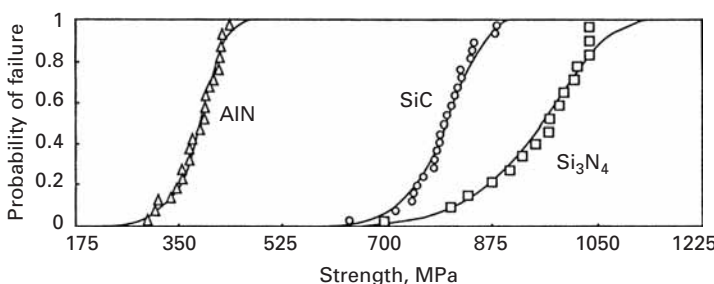


**Fig. 7.34** Cummulative probability of flexural strengths (four-point bend test with inner and outer spans 20 and 40 mm, respectively, and cross section of 3  $\times$  4 mm) for three ceramics. (Courtesy of C. J. Shih.)

Hence,

$$V_1\sigma_1^m = V_2\sigma_2^m,$$

or

$$\frac{\sigma_1}{\sigma_2} = \left( \frac{V_2}{V_1} \right)^{1/m}. \quad (7.55)$$

Thus we see that, for an equal probability of survival, the larger the volume ( $V_2 > V_1$ ), the smaller must be the fracture strength ( $\sigma_1 < \sigma_2$ ).

An interesting application of the Weibull distribution is illustrated in Figure 7.33, which shows a double-logarithmic plot as per Equation 7.51. Note that the failure probability  $F(V) = 1 - P(V)$ , rather than the survival probability  $P(V)$  is plotted. The figure shows the following items:

1. The Weibull modulus  $m$  of steel  $\rightarrow \infty$ . (Note the vertical line.)
2. The Weibull modulus  $m$  of conventionally processed alumina is 4.7.
3. If we process alumina carefully – say, by using a controlled particle size (CPS in Figure 7.33) – the value of  $m$  is doubled, to 9.7. By a controlled particle size, we mean a monosize powder that enhances packing, less use of a binder material (which produces flaws after sintering), more uniform shrinkage, etc.

Figure 7.34 shows the cummulative probability of failure as a function of stress for three important engineering ceramics: AlN, SiC, and

$\text{Si}_3\text{N}_4$ . As the Weibull modulus increases, the slope of the curve becomes steeper. When we plot the curves on logarithmic abscissa and ordinate axes, a straight line is obtained that can be used to obtain  $m$  as shown in Figure 7.33.

Some words of caution regarding the use of Weibull probability plots are in order. The tail of the distribution (see Figure 7.31) must be included in the analysis. In practical terms, this means that the statistical sample size should be sufficiently large. Typically, for an allowable failure rate  $P = 0.01$ , the sample size would be greater than 100. Also, the preceding analysis assumes a “well-behaved flaw population.” Bimodal flaw populations can result in two linear parts on the Weibull plot, indicating two values of the Weibull modulus.

### Example 7.8

The data obtained in four-point bend (or flexure) tests on SiC specimens processed in three different ways are reported in Table E7.8.1. Calculate the Weibull modulus  $m$  and the characteristic strength  $\sigma_0$ , and make the Weibull plot, for each specimen. Each specimen had outer and inner spans of 40 and 20 mm, respectively. The height and width of the specimens are 3 mm and 4 mm, respectively.

Table E7.8.1 | Fracture Load (N) of Three Hot-Pressed SiC Specimens

Test No.	SiC-A	SiC-B	SiC-N
1	497	421	466
2	291	690	618
3	493	556	529
4	605	573	627
5	511	618	564
6	524	609	564
7	327	690	573
8	484	654	394
9	394	618	618
10	448	645	493
11	511	591	511
12	497	739	475
13	426	739	618
14	345	703	493
15	358	569	591
16	287	685	627
17	412	708	618
18	466	573	600
19	493	717	645
20	591	676	614

**Solution:** We first obtain the stresses from the loads in Table E7.8.1. The moment is

$$M = \frac{P}{2} \times \frac{L}{4}.$$

(See Figure E7.8.1.) The maximum tensile stress is

$$\sigma = \frac{Mc}{I},$$

where  $h$  is the height,  $b$  is the breadth,  $I$  is the moment of inertia of the beam, and

$$c = \frac{h}{2},$$

$$I = \frac{bh^3}{12}.$$

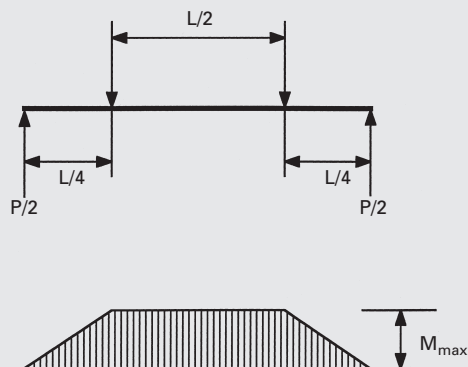


Fig. E7.8.1

The calculated stresses are shown in Figure E7.8.2. Hence,

$$\sigma = \frac{pLh \times 12}{8 \times bh^3} = \frac{3}{4} \frac{PL}{bh^2}.$$

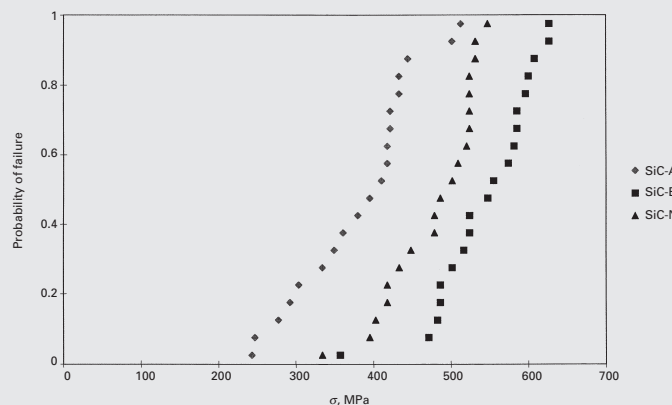


Fig. E7.8.2

To obtain the Weibull parameters, we use Equation 7.50:

$$P(V) = \exp \left[ - \left( \frac{\sigma}{\sigma_0} \right)^m \right],$$

or

$$1 - F(V) = \exp \left[ - \left( \frac{\sigma}{\sigma_0} \right)^m \right].$$

Taking logarithms yields

$$\ln[1 - F(V)] = - \left( \frac{\sigma}{\sigma_0} \right)^m.$$

Taking logarithms again results in

$$\ln \ln[1 - F(V)] = -m(\ln \sigma - \ln \sigma_0),$$

or

$$\ln \ln \left[ \frac{1}{1 - F(V)} \right] = m(\ln \sigma - \ln \sigma_0).$$

To obtain  $F(V)$  for each point, we use the following equation:

$$1 - P_i(V) = F_i(V) = \frac{i}{N + 1},$$

where  $N$  is the total number of specimens tested.

In the present case,  $N = 20$ . Hence,  $F_1(V) = 1/21$ ,  $F_2(V) = 2/21$ ,  $F_3(V) = 3/21$ . . . . These results are plotted in Figure E7.8.3. We use a double logarithm for  $1/[1 - F(V)]$  and the logarithm for  $\sigma$ . The slope of this plot provides  $m$ . The horizontal line passing through zero gives the values of the characteristic strengths. We summarize our results in Table E7.8.2. Figure E7.8.4 shows the Weibull curves with the preceding parameters superimposed on the data points of Figure E7.8.3.

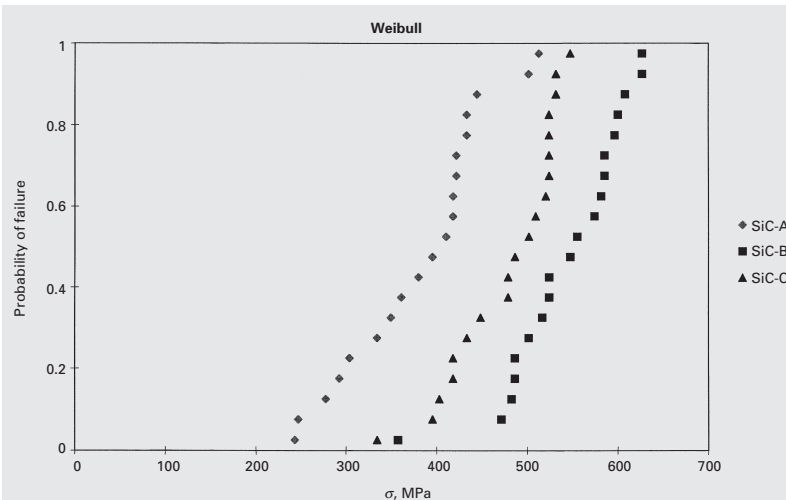


Fig. E7.8.3

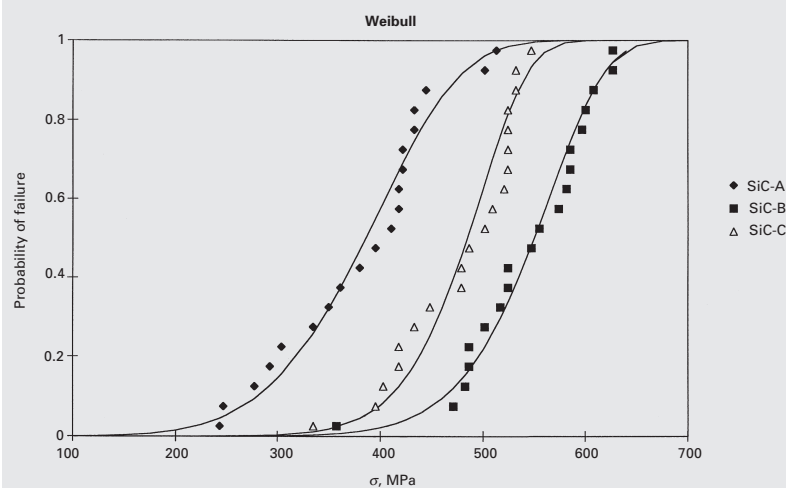


Fig. E7.8.4

Table E7.8.2

Specimen	$m$	$\sigma_0$ (MPa)	Average Stress ± S.D. (MPa)
SiC-A	5.61	411.3	$380.7 \pm 63.1$
SiC-B	9.10	572.1	$542.0 \pm 52.6$
SiC-N	9.22	502.9	$476.8 \pm 48.7$

S.D. = Standard deviation.

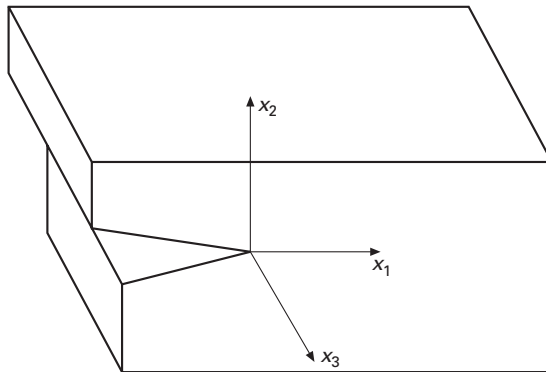


Fig. A1

## Appendix: Stress Singularity at Crack Tip

It is relatively simple to obtain the stress singularity close to a crack in Mode III. (See Figure A1.) For Modes I and II, other more complex solutions exist.

The displacements are, for the three directions ( $X_1$ ,  $X_2$ , and  $X_3$ ):

$$u = 0,$$

$$v = 0,$$

$$w = 0.$$

The strains are:

$$\gamma_{31} = \gamma_{13} = \frac{\partial w}{\partial x_1},$$

$$\gamma_{32} = \gamma_{23} = \frac{\partial w}{\partial x_2}.$$

All the other components are zero.

The stresses are given by

$$\sigma_{13} = G \gamma_{13},$$

$$\sigma_{23} = G \gamma_{23}.$$

The equilibrium equation is

$$\frac{\partial \sigma_{ij}}{\partial x_j} = \rho \ddot{u}_i.$$

In our case, since the acceleration is zero

$$\frac{\partial \sigma_{ij}}{\partial x_j} = 0.$$

In the extended notation we can write:

$$\frac{\partial \sigma_{13}}{\partial x_1} + \frac{\partial \sigma_{23}}{\partial x_2} = 0,$$

$$G \frac{\partial^2 w}{\partial x_1^2} + G \frac{\partial^2 w}{\partial x_2^2} = 0,$$

$$\nabla^2 w = 0.$$

We now change to radial coordinates. (See Figure A2.)

The form of Laplacian operator in radial coordinates is:

$$\nabla^2 = \frac{\partial^2}{\partial x_1^2} + \frac{\partial^2}{\partial x_2^2} = \frac{\partial^2}{\partial r^2} + \frac{1}{r} \frac{\partial}{\partial r} + \frac{1}{r^2} \frac{\partial^2}{\partial \theta^2}.$$

The solution to this equation is given in differential equation books.<sup>17</sup>

$$w = r^\lambda f(\theta),$$

$$\nabla^2 w = \lambda(\lambda - 1)r^{\lambda-2}f(\theta) + \frac{1}{r}\lambda r^{\lambda-1}f'(\theta) + \frac{1}{r^2}r^\lambda f''(\theta),$$

$$r^{\lambda-2}(\lambda(\lambda - 1)f(\theta) + \lambda f'(\theta) + f''(\theta)) = 0.$$

Apply for all  $r$ ,

$$\lambda^2 f(\theta) + f''(\theta) = 0,$$

$$f(\theta) = A \sin \lambda \theta + B \cos \lambda \theta,$$

$$w = r^\lambda (A \sin \lambda \theta + B \cos \lambda \theta).$$

The boundary conditions are:

$$w(r, \theta) = -w(r, -\theta),$$

$$w(r, \theta) = r^\lambda (A \sin \lambda \theta + B \cos \lambda \theta),$$

$$w(r, -\theta) = r^\lambda (-A \sin \lambda \theta + B \cos \lambda \theta),$$

$$B = 0,$$

$$w(r, \theta) = r^\lambda A \sin \lambda \theta.$$

For  $\theta = \pm\pi$ ,  $\sigma_{r\theta} = 0$ .

$$\sigma_{z\theta} = G \frac{1}{r} \frac{\partial w}{\partial \theta} = 0,$$

$$\frac{\partial w}{\partial \theta} = r^\lambda A \lambda \cos \lambda \theta \quad \text{at} \quad \theta = \pi,$$

$$\lambda = \pm \frac{1}{2}, \pm \frac{3}{2}, \pm \frac{5}{2}, \quad \lambda = \frac{2n-1}{2}.$$

In a general way, one can write:

$$w(r, \theta) = \sum_{n=1}^N \left( r^{\frac{2n-1}{2}} A \sin \frac{2n-1}{2} \theta \right).$$

We will only use  $A > 0$ , then the first terms becomes:

$$w(r, \theta) = A_1 r^{\frac{1}{2}} \sin \frac{1}{2} \theta,$$

$$\sigma_{z\theta} = G \frac{1}{r} \frac{\partial w}{\partial \theta} = \frac{A_1}{r} G r^{\frac{1}{2}} \frac{1}{2} \cos \frac{\theta}{2},$$

$$\sigma_{z\theta} = \frac{A_1 G}{2r^{\frac{1}{2}}} \cos \frac{\theta}{2}.$$

where  $G$  is the shear modulus.

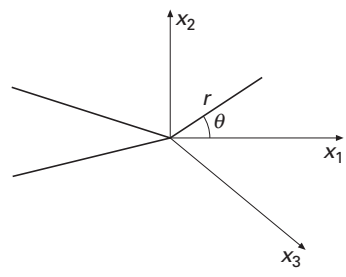


**Fig. A2**

<sup>17</sup> See, for example, R. Haberman, *Elementary Applied Partial Differential Equations* (Upper Saddle River, NJ: Prentice Hall, 1998).

We use the term  $K_{III}$  to group the constants:

$$\sigma_{z\theta} = \frac{K_{III}}{\sqrt{2\pi r}} \cos \frac{\theta}{2},$$

$$\sigma_{r\theta} = G \frac{\partial w}{\partial r} = \frac{A_1 G}{2r^{\frac{1}{2}}} \sin \frac{\theta}{2},$$

or,

$$\sigma_{r\theta} = \frac{K_{III}}{\sqrt{2\pi r}} \sin \frac{\theta}{2}.$$

These expressions are equivalent to Equation 7.23 and demonstrate the square root singularity of the stresses at the tip of the crack.

## Suggested Reading

- T. L. Anderson. *Fracture Mechanics*, 2nd ed. Boca Raton, FL: CRC Press, 1995.
- J. M. Barsom and S. T. Roffe. *Fracture and Fatigue Control in Structures*, 2nd ed. Englewood Cliffs, NJ: Prentice Hall, 1987.
- D. Broek. *Elementary Engineering Fracture Mechanics*, 3rd ed. The Hague: Sijhoff and Noordhoff, 1978.
- H. L. Ewalds and R. J. H. Wanhill. *Fracture Mechanics*. London: Arnold, 1984.
- M. F. Kanninen and C. H. Popelar. *Advanced Fracture Mechanics*. New York, NY: Oxford University Press, 1985.
- J. F. Knott. *Fundamentals of Fracture Mechanics*, 3rd ed. London: Butterworths, 1993.
- R. J. Sanford, *Principles of Fracture Mechanics*. Upper Saddle River, NJ: Prentice Hall, 2003.
- H. Tada, P. C. Paris, and G. R. Irwin, *The Stress Analysis of Cracks Handbook*, 3rd ed., New York, NY: ASME, 2000.

## Exercises

- 7.1** In a polyvinyl chloride (PVC) plate, there is an elliptical, through-the-thickness cavity. The dimensions of the cavity are:

major axis = 1 mm,  
minor axis = 0.1 mm.

Compute the stress concentration factor  $K_t$  at the extremities of the cavity.

- 7.2** Calculate the maximum tensile stress at the surfaces of a circular hole (in the case of a thin sheet) and of a spherical hole (in the case of a thick specimen) subjected to a tensile stress of 200 MPa. The material is  $\text{Al}_2\text{O}_3$  with  $\nu = 0.2$ .

- 7.3** Calculate the maximum tensile stress if the applied stress is compressive for a circular hole for which  $\sigma_c = 200$  MPa and  $\nu = 0.2$ .

- 7.4** The strength of alumina is approximately  $E/15$ , where  $E$  is the Young's modulus of alumina, equal to 380 GPa. Use the Griffith equation in the plane-strain form to estimate the critical size of defect corresponding to fracture of alumina.

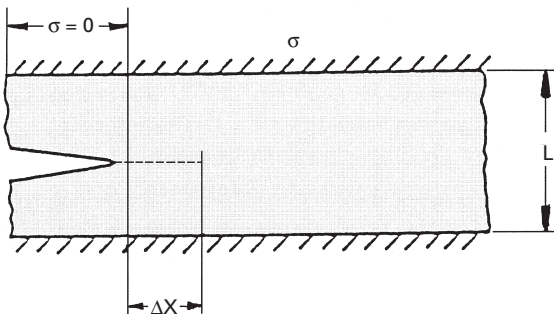


**Fig. Ex7.7**

**7.5** Compute the ratio of stress required to propagate a crack in a brittle material under plane-stress and plane-strain conditions. Take Poisson's ratio  $\nu$  of the material to be 0.3.

**7.6** An  $\text{Al}_2\text{O}_3$  specimen is being pulled in tension. The specimen contains flaws having a size of 100  $\mu\text{m}$ . If the surface energy of  $\text{Al}_2\text{O}_3$  is 0.8  $\text{J/m}^2$ , what is the fracture stress? Use Griffith's criterion.  $E = 380 \text{ GPa}$ .

**7.7** A thin plate is rigidly fixed at its edges (see Figure Ex7.7). The plate has a height  $L$  and thickness  $t$  (normal to the plane of the figure). A crack moves from left to right through the plate. Every time the crack moves a distance  $\Delta x$ , two things happen:

1. Two new surfaces (with specific surface energy) are created.
2. The stress falls to zero behind the advancing crack front in a certain volume of the material.

Obtain an expression for the critical stress necessary for crack propagation in this case. Explain the physical significance of this expression. Assume the stress,  $\sigma$ , ahead of the crack is uniform.

**7.8** A central through-the-thickness crack, 50 mm long, propagates in a thermoset polymer in an unstable manner at an applied stress of 5 MPa. Find  $K_c$ .

**7.9** Machining of SiC produced surface flaws of a semielliptical geometry. The flaws that were generated have dimensions  $a = 1 \text{ mm}$ , width  $w = 100 \text{ mm}$ , and  $c = 5 \text{ mm}$ , and the thickness of the specimen is  $B = 20 \text{ mm}$ . Calculate the maximum stress that the specimen can withstand in tension.  $K_{lc} = 4 \text{ MPa m}^{1/2}$ .

**7.10** (a) An AISI 4340 steel plate has a width  $W$  of 30 cm and has a central crack  $2a$  of 3 mm. The plate is under a uniform stress  $\sigma$ . This steel has a  $K_{lc}$  value of  $50 \text{ MPa m}^{1/2}$ . Find the maximum stress for this crack length. (b) If the operating stress is 1,500 MPa, compute the maximum crack size that the steel may have without failure.

**7.11** A microalloyed steel, quenched and tempered at  $250^\circ\text{C}$ , has a yield strength ( $\sigma_y$ ) of 1,750 MPa and a plane-strain fracture toughness  $K_{lc}$  of  $43.50 \text{ MPa m}^{1/2}$ . What is the largest disk-type inclusion, oriented most unfavorably, that can be tolerated in this steel at an applied stress of  $0.5\sigma_y$ ?

**7.12** A 25-mm<sup>2</sup> bar of cast iron contains a crack 5 mm long and normal to one face. What is the load required to break this bar if it is subjected to three-point bending with the crack toward the tensile side and the supports 250 mm apart?

**7.13** Consider a maraging steel plate of thickness ( $B$ ) 3 mm. Two specimens of width ( $W$ ) equal to 50 mm and 5 mm were taken out of this plate. What is the largest through-the-thickness crack that can be tolerated in the two cases at an applied stress of  $\sigma = 0.6\sigma_y$ , where  $\sigma_y$  (yield stress) = 2.5 GPa? The plane-strain fracture toughness  $K_{lc}$  of the steel is 70 MPa m<sup>1/2</sup>. What are the critical dimensions in the case of a single-edge notch specimen?

**7.14** An infinitely large plate containing a central crack of length  $2a = 50/\pi$  mm is subjected to a nominal stress of 300 MPa. The material yields at 500 MPa. Compute:

- (a) The stress intensity factor at the crack tip.
- (b) The size of the plastic zone at the crack tip.

Comment on the validity of Irwin's correction for the size of the plastic zone in this case.

**7.15** A steel plate containing a through-the-thickness central crack of length 15 mm is subjected to a stress of 350 MPa normal to the crack plane. The yield stress of the steel is 1,500 MPa. Compute the size of the plastic zone and the effective stress intensity factor.

**7.16** The size of the plastic zone at the crack tip in the general plane-stress case is given by

$$r_y = \frac{K_l^2}{2\pi\sigma_y^2} \cos^2 \frac{\theta}{2} \left( 4 - 3 \cos^2 \frac{\theta}{2} \right).$$

- (a) Determine the radius of the plastic zone in the direction of the crack.
- (b) Determine the angle  $\theta$  at which the plastic zone is the largest.

**7.17** For the plane-strain case, the expression for the size of the plastic zone is

$$r_y = \frac{K_l^2}{2\pi\sigma_y^2} \cos^2 \frac{\theta}{2} \left\{ 4[1 - \nu(1 - \nu)] - 3 \cos^2 \frac{\theta}{2} \right\}.$$

- (a) Show that this expression reduces to the one for plane stress.
- (b) Make plots of the size of the plastic zone as a function of  $\theta$  for  $\nu = 0$ ,  $\nu = \frac{1}{3}$ , and  $\nu = \frac{1}{2}$ . Comment on the size and form of the zone in the three cases.

**7.18** A sheet of polystyrene has a thin central crack with  $2a = 50$  mm. The crack propagates catastrophically at an applied stress of 10 MPa. The Young's modulus polystyrene is 3.8 GPa, and the Poisson's ratio is 0.4. Find  $G_{lc}$ .

**7.19** Compute the approximate size of the plastic zone,  $r_v$ , for an alloy that has a Young's modulus  $E = 70$  GPa, yield strength  $\sigma_v = 500$  MPa, and toughness  $G_c = 20$  kJ/m<sup>2</sup>.

**7.20** 300-M steel, commonly used for airplane landing gears, has a  $G_c$  value of 10 kN/m. A nondestructive examination technique capable of detecting cracks that are 1 mm long is available. Compute the stress level that the landing gear can support without failure.

7.21 A thermoplastic material has a yield stress of 75 MPa and a  $G_{lc}$  value of 300 J/m<sup>2</sup>. What would be the corresponding critical crack opening displacement? Take  $\lambda = 1$ . Also, compute  $J_{lc}$ .

7.22 A pipe line with overall diameter of 1 m and 25-mm thickness is constructed from a microalloyed steel ( $K_{lc} = 60 \text{ MPa m}^{1/2}$ ;  $\sigma_y = 600 \text{ MPa}$ ). Calculate the maximum pressure for which the leak-before-break criterion will be obeyed. The leak-before-break criterion states that a through-the-thickness crack ( $a = t$ ) will not propagate catastrophically.

7.23  $\text{Al}_2\text{O}_3$  has a fracture toughness of approximately 3 MPa m<sup>1/2</sup>. Suppose you carried out a characterization of the surface of the specimen and detected surface flaws with a radius  $a = 50 \mu\text{m}$ . Estimate the tensile and compressive strengths of this specimen; show by sketches, how flaws will be activated in compression and tension.

7.24 Using the Weibull equation, establish the tensile strength, with a 50% survival probability, of specimens with a length of 60 mm and a diameter of 5 mm. Uniaxial tensile tests carried out on specimens with a length of 20 mm and the same diameter yielded the following results in MPa (10 tests were carried out): 321, 389, 411, 423, 438, 454, 475, 489, 497, 501.

7.25 An engineering ceramic has a flexure strength that obeys Weibull statistics with  $m = 10$ . If the flexure strength is equal to 200 MPa at 50% survival probability, what is the flexure strength level at which the survival probability is 90%?

7.26 What would be the flexure strength, at 90% survival probability, if the ceramic in the preceding problem is subjected to a hot isostatic processing (HIP) treatment that greatly reduces the population of flaws and increases  $m$  to 60. Assume that the flexure strength at 50% survival probability is unchanged.

7.27 Ten rectangular bars of  $\text{Al}_2\text{O}_3$  (10 mm wide and 5 mm in height) were tested in three-point bending, the span being 50 mm. The failure loads were 1,040, 1,092, 1,120, 1,210, 1,320, 1,381, 1,410, 1,470, 1,490, and 1,540 N. Determine the characteristic flexure strength and Weibull's modulus for the specimens. (See Section 9.6.1 for the flexure formula.)

7.28 Verify the values of  $m$  in Figure 7.34, and obtain the characteristic strengths  $\sigma_0$  for the three materials. If the fracture toughness of SiC,  $\text{Si}_3\text{N}_4$ , and AlN are equal to 5.2, 5.7, and 2.4 MNm<sup>3/2</sup>, respectively, what are the largest flaws that can be tolerated in these specimens?

7.29 Aluminum has a surface energy of 0.5 Jm<sup>-2</sup> and a Young's modulus of 70 GPa. Compute the stress at the crack tip for two different crack lengths: 1 mm and 1 cm.

7.30 Determine the stress required for crack propagation under plane strain for a crack of length equal to 2 mm in aluminum. Take the surface energy equal to 0.048 J/m<sup>2</sup>, Poisson's ratio to 0.345, and the modulus of  $E = 70.3$  GPa.

7.31 Calculate the maximum load that a 2024-T851 aluminum alloy (10 cm × 2 cm) with a central through-the-thickness crack (length 0.1 mm) can withstand without yielding. Given:  $\sigma_y = 500 \text{ MPa}$  and  $K_{lc} = 30 \text{ MPa m}^{1/2}$ .

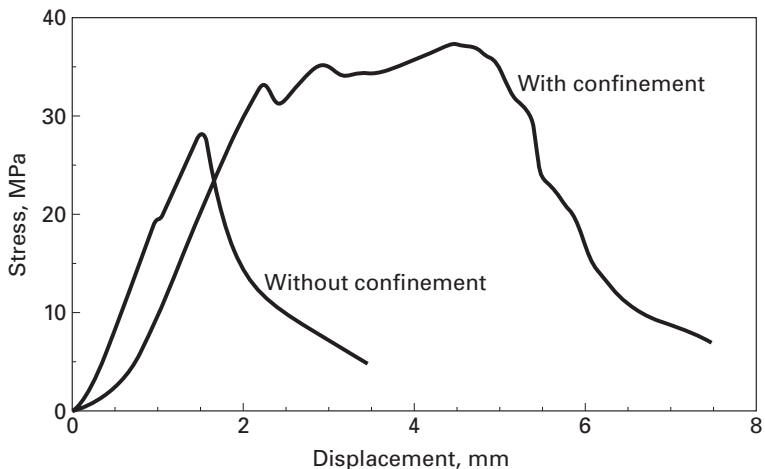


Fig. Ex7.34

7.32 An infinitely large sheet is subjected to a far-field stress of 300 MPa. The material has a yield strength of 600 MPa, and there is a central crack  $7/\pi$  cm long.

- (a) Calculate the stress intensity factor at the tip of the crack.
- (b) Estimate the size of the plastic zone size at the tip of the crack.

7.33 What is the maximum allowable crack size for a material that has  $K_{Ic} = 55 \text{ MPa m}^{1/2}$  and  $\sigma_y = 1,380 \text{ MPa}$ ? Assume a plane-strain condition and a central crack.

7.34 Two specimens of concrete were tested in compression. One was wrapped with a very strong composite tape. They exhibited substantial differences in strength, shown in Figure Ex7.34. Explain, in terms of microstructural behavior, the reason for the difference in response. Use sketches.

7.35 An  $\text{Al}_2\text{O}_3$  specimen is being pulled in tension. The specimen contains flaws having a size of 100  $\mu\text{m}$ .

- (a) If the surface energy of  $\text{Al}_2\text{O}_3$  is  $0.8 \text{ J/m}^2$ , what is the fracture stress? Use the Griffith criterion.  $E = 380 \text{ GPa}$ .
- (b) Using your vast fracture mechanics knowledge and advanced equations, estimate the fracture stress if the fracture toughness is  $4 \text{ MPa m}^{1/2}$ . Assume two positions for flaw: in the center of an infinite body and at the edge.

7.36 A structural steel component has a surface crack of 2 mm. This steel has a fracture toughness of  $75 \text{ MPa m}^{1/2}$ . By how much can this crack grow before catastrophic failure?

7.37 A titanium alloy (Ti-6Al-4V) has a yield strength of 1280 MPa and a fracture toughness of  $77 \text{ MPa m}^{1/2}$ . If we apply a stress of  $0.3\sigma_y$ , what will be the size of the surface crack that will lead to catastrophic failure?

7.38 An AISI steel plate has a crack with the size of 2 mm in the center. If the plate is under a uniform stress, and the width of the plate is 24 cm:

- (a) Find the maximum value of the stress if  $K_{lc} = 45 \text{ MPa m}^{1/2}$ .  
(b) Find the maximum crack size that the plate can have, if it has to operate at a stress of 1,250 MPa.

**7.39** In an Al alloy 7178-T651 (thick plate), find the critical crack length if it is under a stress of 500 MPa. Given:  $K_{lc} = 28 \text{ MPa m}^{1/2}$ .

**7.40** What is the largest flaw size of a ceramic material that can support a strength of 280 MPa and  $K_{lc} = 2.2 \text{ MPa m}^{1/2}$ , assuming  $Y = 1$ ?

**7.41** Determine the tensile strength of an alumina specimen having a grain size of  $1 \mu\text{m}$ , if the tensile strength of the same material with a grain size of  $50 \mu\text{m}$  is 1 GPa. Assume that the flaw size is equal to one half the grain size.

**7.42** A brittle material (Sialon) is used as a support plate. Sialon has a fracture toughness of  $9 \text{ MPa m}^{1/2}$ . The plate has to withstand a tensile load of 200kN. We have three non-destructive inspection techniques at our disposal: X-ray radiography (can detect flaws greater than 0.5 mm); gamma-ray radiography (flaws greater than 0.20 mm) and ultrasonic inspection (flaws greater than 0.125 mm). Calculate the cross-sectional area of the plate for the different NDE testing methods.

**7.43**

- (a) An AISI steel plate has width  $W = 30 \text{ cm}$  and a central crack with size of 3 mm. The plate is under a uniform stress. Find the maximum value of the stress is  $K_{lc} = 50 \text{ MPa m}^{1/2}$ .  
(b) If the part has to operate at a stress of 1,500 MPa, compute the maximum crack size that the plate can have.

**7.44** A polymer contains internal flaws (penny shaped) with a diameter of 2 mm and fails, in tension, at an applied stress of 30 MPa. What is the fracture toughness of this polymer?

**7.45** Rank the estimated strength of three ceramic parts, made of  $\text{Al}_2\text{O}_3$ , with three different volumes:  $V = 10 \text{ cm}^3$ ;  $V = 100 \text{ cm}^3$ ;  $V = 1 \text{ m}^3$ .

**7.46** Establish the maximum tensile load that a block with a cross-section of  $10 \times 10 \text{ cm}$  can take, if its fracture toughness is equal to  $90 \text{ MPa m}^{1/2}$  and its yield stress is 1,000 MPa. This part contains an embedded crack with a radius of 10 mm.

**7.47** Engineers are designing a ceramic component for a jet engine. The ceramic has a fracture toughness of  $8 \text{ MPa m}^{1/2}$ . The ceramic is subjected to a maximum tensile stress of 500 MPa. Calculate the maximum size of surface flaws that the part can have.

**7.48** A cylindrical pressure vessel (length of 10 m; diameter of 1 m) is made from a high strength steel with  $K_{lc} = 100 \text{ MPa m}^{1/2}$  and a yield strength of 1,600 MPa. The thickness of the vessel is 25 mm. NDE has revealed a longitudinal crack penetrating 7 mm into the cylinder wall.

- (a) What maximum pressure can the cylinder be loaded to?  
(b) What is the percentage reduction in maximum pressure due to the presence of flaw?

---

## Chapter 8

# Fracture: Microscopic Aspects

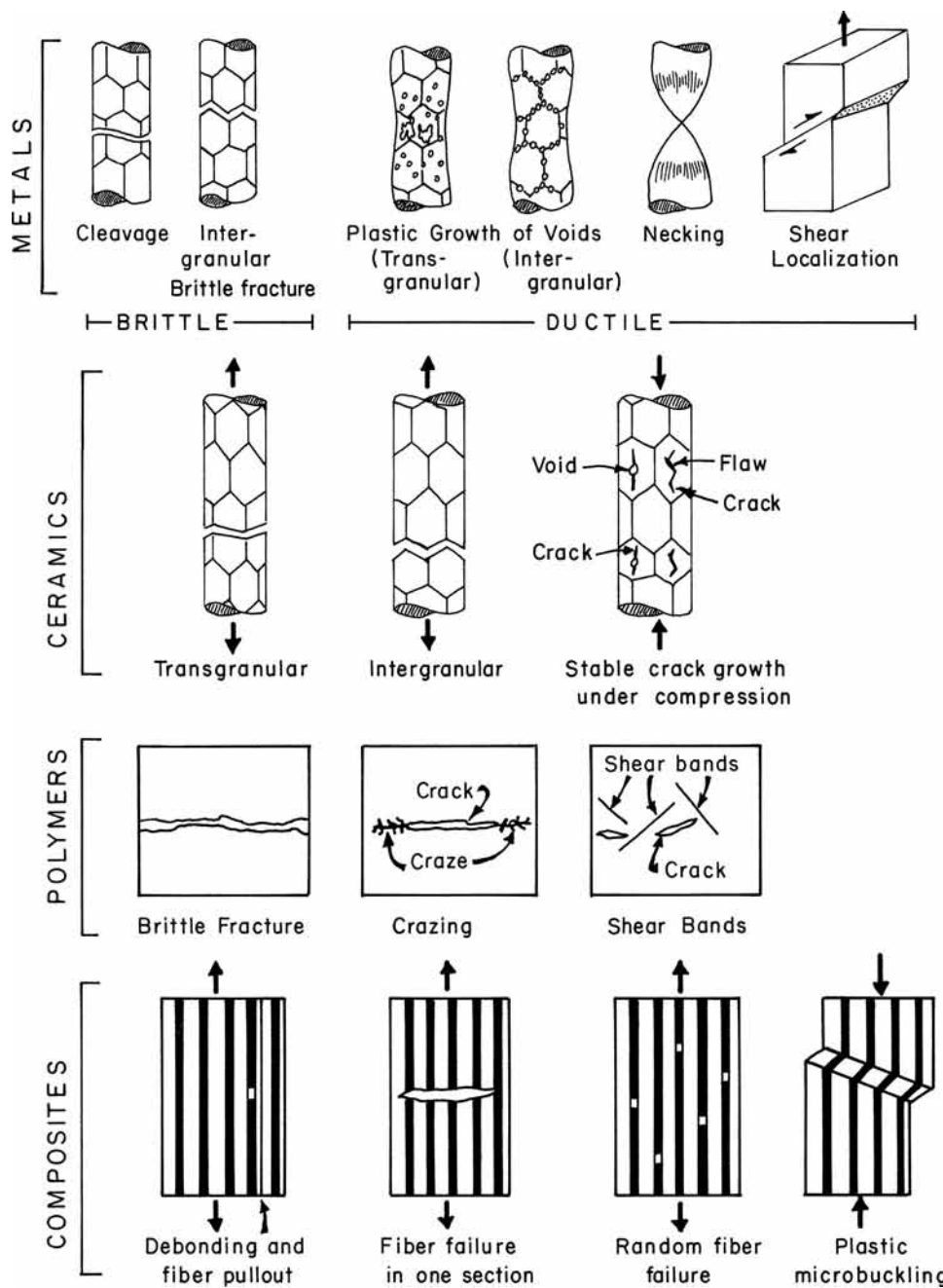
---

### 8.1 | Introduction

In Chapter 7, we described the macroscopic aspects of the fracture behavior of materials. As with other characteristics, the microstructure of a material has a great influence on its fracture behavior. In what follows, we present a brief description of the microstructural aspects of crack nucleation and propagation, as well as the effect of the environment on the fracture behavior of different materials. Figure 8.1 shows, schematically, some important fracture modes in a variety of materials. These different modes will be analyzed in some detail in this chapter. Metals fail by two broad classes of mechanisms: *ductile* and *brittle* failure.

Ductile failure occurs by (a) the nucleation, growth, and coalescence of voids, (b) continuous reduction in the metal's cross-sectional area until it is equal to zero, or (c) shearing along a plane of maximum shear. Ductile failure by void nucleation and growth usually starts at second-phase particles. If these particles are spread throughout the interiors of the grains, the fracture will be transgranular (or transcrystalline). If these voids are located preferentially at grain boundaries, fracture will occur in an intergranular (or intercrystalline) mode. The appearance of a ductile fracture, at high magnification ( $500\times$  or higher) is of a surface with indentations, as if marked by an ice-cream scooper. This surface morphology is appropriately called *dimpled*. Rupture by total necking is very rare, because most metals contain second-phase particles that act as initiation sites for voids. However, high-purity metals, such as copper, nickel, gold, and other very ductile materials, fail with very high reductions in their areas.

Brittle fracture is characterized by the propagation of one or more cracks through the structure. While totally elastic fracture describes the behavior of most ceramics fairly well, metals and some polymers undergo irreversible deformation at the tip of the crack, which affects its propagation. Figure 8.1 shows the variety of morphologies and processes occurring during fracturing of materials. For metals and ceramics, two modes of crack propagation: transgranular



fracture (or cleavage) and intergranular fracture are observed. For energy-related reasons, a crack will tend to take the path of least resistance. If this path lies along the grain boundaries, the fracture will be intergranular.

Often, a crack also tends to run along specific crystallographic planes, as is the case for brittle fracture in steel. Upon observation at high magnification, transgranular brittle fracture is characterized by

**Fig. 8.1** Schematic classification of fracture morphologies and processes. (After M. F. Ashby.)

clear, smooth facets that have the size of the grains. In steel, brittle fracture has the typical shiny appearance, while ductile fracture has a dull, grayish aspect. In addition to brittle fracture, polymers undergo a mode of fracture involving *crazing*, in which the polymer chains ahead of a crack align themselves along the tensile axis, so that the stress concentration is released.

Another mode of deformation that is a precursor to fracture is the phenomenon of *shear banding* in a polymer. If one stretches the polymer material, one observes the formation of a band of material with a much higher flow stress than exists in the unstretched state. Shear banding (or localization) is also prevalent in metals.

Composites – especially fibrous ones – can exhibit a range of failure modes that is dependent on the components of the material (matrix and reinforcement) and on bonding. If the bond strength is higher than the strength of the matrix and reinforcement, the fracture will propagate through the latter (Figure 8.1). If the bonding is weak, one has debonding and fiber pullout. In compression, composites can fail by a kinking mechanism, also shown in the figure; the fibers break, and the entire structure rotates along a band, resulting in a shortening of the composite. This mechanism is known as *plastic microbuckling*.

---

## 8.2 | Fracture in Metals

Metals are characterized by a highly mobile dislocation density, and they generally show a ductile fracture. In this section, we discuss the various aspects of void and crack nucleation and propagation in metals.

### 8.2.1 Crack Nucleation

Nucleation of a crack in a perfect crystal essentially involves the rupture of interatomic bonds. The stress necessary to do this is the theoretical cohesive stress, which was dealt with in Chapter 7, starting from an expression for interatomic forces. From this expression, we see that ordinary materials break at much lower stresses than do perfect crystals – on the order of  $E/10^4$ , where  $E$  is Young's modulus of the material. The explanation of this behavior lies in the existence of surface and internal defects that act as preexisting cracks and in the plastic deformation that precedes fracture. When both plastic deformation and fracture are eliminated – for example, in “whiskers” – stresses on the order of the theoretical cohesive stresses are obtained.

Crack nucleation mechanisms vary according to the type of material: brittle, semibrittle, or ductile. The brittleness of a material has to do with the behavior of dislocations in the region of crack nucleation. In highly brittle materials the dislocations are practically immobile, in semibrittle materials dislocations are mobile, but

**Table 8.1** Materials of Various Degrees of Brittleness<sup>a</sup>

Type	Principal Factors	Materials
Brittle	Bond rupture	Structures of type diamond, ZnS, silicates, alumina, mica, boron, carbides, and nitrides
Semibrittle	Bond rupture, dislocation mobility	Structures of type NaCl, ionic crystals, hexagonal close-packed metals, majority of body-centered cubic metals, glassy polymers
Ductile	Dislocation mobility	Face-centered cubic metals, some body-centered cubic metals, semicrystalline polymers

<sup>a</sup> Adapted with permission from B. R. Lawn and T. R. Wilshaw, *Fracture of Brittle Solids* (Cambridge, U.K.: Cambridge University Press, 1975), p. 17.

only on a restricted number of slip planes, and in ductile materials there are no restrictions on the movement of dislocations other than those inherent in the crystalline structure of the material. Table 8.1 presents various materials classified according to this criterion regarding the mobility of dislocations.

The exposed surface of a brittle material can suffer damage by mechanical contact with even microscopic dust particles. If a glass fiber without surface treatment were rolled over a tabletop, it would be seriously damaged mechanically.

Any heterogeneity in a material that produces a stress concentration can nucleate cracks. For example, steps, striations, depressions, holes, and so on act as stress raisers on apparently perfect surfaces. In the interior of the material, there can exist voids, air bubbles, second-phase particles, etc. Crack nucleation will occur at the weakest of these defects, where the conditions would be most favorable. We generally assume that the sizes as well as the locations of defects are distributed in the material according to some function of standard distribution whose parameters are adjusted to conform to experimental data. In this assumption, there is no explicit consideration of the nature or origin of the defects.

In semibrittle materials, there is a tendency for slip initially, followed by fracture on well-defined crystallographic planes. That is, there exists a certain inflexibility in the deformation process, and the material, not being able to accommodate localized plastic strains, initiates a crack to relax stresses.

Various models are based on the idea of crack nucleation at an obstruction site. For example, the intersection of a slip band with a grain boundary, another slip band, and so on, would be an obstruction site.

### 8.2.2 Ductile Fracture

In ductile materials, the role of plastic deformation is very important. The important feature is the flexibility of slip. Dislocations can move

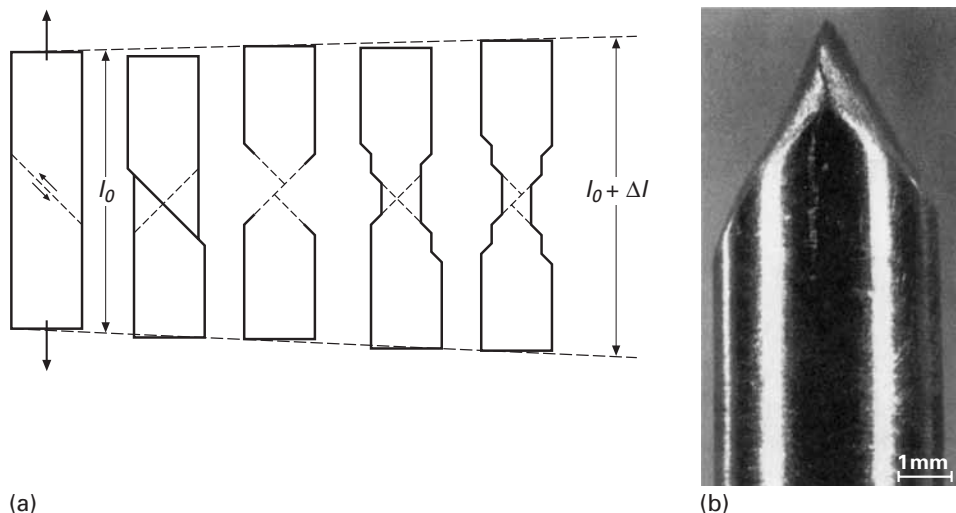


**Fig. 8.2** (a) Failure by shear (glide) in a pure metal. (Reprinted with permission from D. Broek, *Elementary Engineering Fracture Mechanics*, 3rd ed. (The Hague, Netherlands: Martinus Nijhoff, 1982), p. 33.) (b) A point fracture in a soft single-crystal sample of copper. (Courtesy of J. D. Embury.)

on a large number of slip systems and even cross from one plane to another (in cross-slip). Consider the deformation of a single crystal of copper, a ductile metal, under uniaxial tension. The single crystal undergoes slip throughout its section. There is no nucleation of cracks, and the crystal deforms plastically until the start of plastic instability, called necking. From this point onward, the deformation is concentrated in the region of plastic instability until the crystal separates along a line or a point. (See Figure 8.2(a).) In the case of a cylindrical sample, a soft single crystal of a metal such as copper will reduce to a point fracture. Figure 8.2(b) shows an example of such a fracture in a single crystal of copper. However, if, in a ductile material, there are microstructural elements such as particles of a second phase, internal interfaces, and so on, then microcavities may be nucleated in regions of high stress concentration in a manner similar to that of semibrittle materials, except that, due to the ductile material's large plasticity, cracks generally do not propagate from these cavities. The regions between the cavities, though, behave as small test samples that elongate and break by plastic instability, as described for the single crystal.

In crystalline solids, cracks can be nucleated by the grouping of dislocations piled up against a barrier. Such cracks are called Zener-Stroh cracks.<sup>1</sup> High stresses at the head of a pileup are relaxed by crack nucleation, as shown in Figure 8.3, but this would occur only in the case where there is no relaxation of stresses by the movement of dislocations on the other side of the barrier. Depending on the

<sup>1</sup> C. Zener, *The Fracturing of Metals* (Metals Park, OH: ASM, 1948).

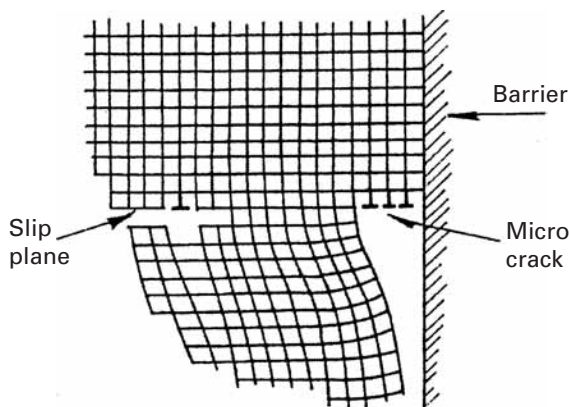


**Fig. 8.3** Grouping of dislocations piled up at a barrier and leading to the formation of a microcrack (Zener-Stroh crack).

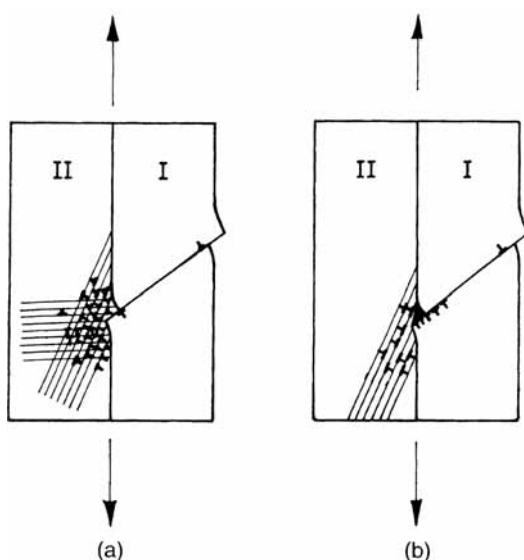


**Fig. 8.4** Bicrystal with a slip band in grain I. (a) The stress concentration at the boundary of the barrier due to slip band is fully relaxed by multiple slip. (b) The stress concentration is only partially relaxed, resulting in a crack at the boundary.

slip geometry in the two parts and the kinetics of the motion and multiplication of dislocations, such a combination of events could occur. (See Table 8.1.) Figure 8.4(a) shows a bicrystal that has a slip band in grain I. The stress concentration at the barrier due to the slip band is completely relaxed by slip on two systems in grain II. Figure 8.4(b) shows the case of only a partial relaxation and the resulting appearance of a crack at the barrier. Lattice rotation associated with the bend planes and deformation twins can also nucleate cracks. Figure 8.5 shows crack nucleation in zinc as per the model shown in Figure 8.5(a). Cracks can also begin at the intersections of various boundaries in a metal, which represent sites at which there is a concentration of stress. Figure 8.6 presents examples of crack nucleation at the intersection of twin boundaries and at the intersection of twin steps and boundaries.

Fracture at high temperature can occur by a variety of other modes as well. For example, grain-boundary sliding occurs rather easily at high temperatures. Grain-boundary sliding can lead to the

**Fig. 8.5** Crack nucleation by (a) lattice rotation due to bend planes and (b) deformation twins. (c) Crack nucleation in zinc due to lattice rotation associated with bend planes. (Reprinted with permission from J. J. Gilman, *Physical Nature of Plastic Flow and Fracture*, General Electric Report No. 60-RL-2410M, April, 1960, p. 83.)

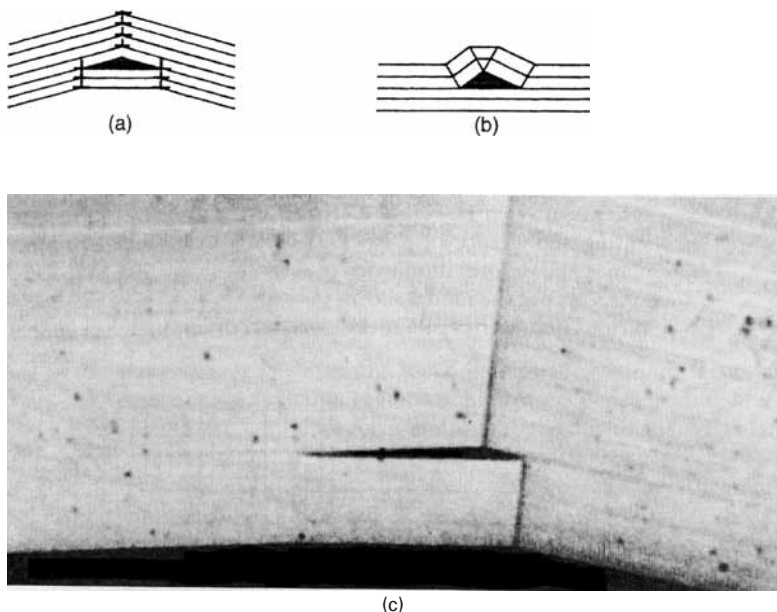


**Fig. 8.6** Initiation of failure by microcrack formation in tungsten deformed at approximately  $10^4 \text{ s}^{-1}$  at room temperature. (a) Twin steps. (b) Twin steps and twin-twin intersection. (From T. Dümmen, J. C. LaSalvia, M. A. Meyers, and G. Ravichandran, *Acta Mater.*, 46 (1998) 959.)

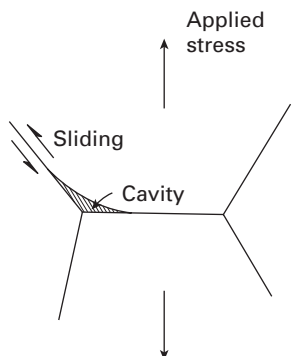
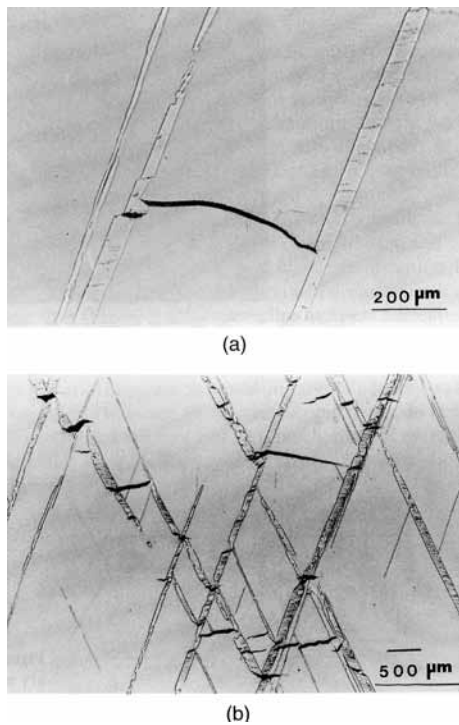


**Fig. 8.7** w-type cavitation at a grain-boundary triple point.

development of stress concentrations at grain-boundary triple points (where three grain boundaries meet). Cracks nucleate at such triple points as shown schematically in Figure 8.7. Figure 8.8 shows a micrograph of copper in which such a crack nucleation has occurred. This type of crack is called *w-type cavitation* or *w-type cracking*. Yet

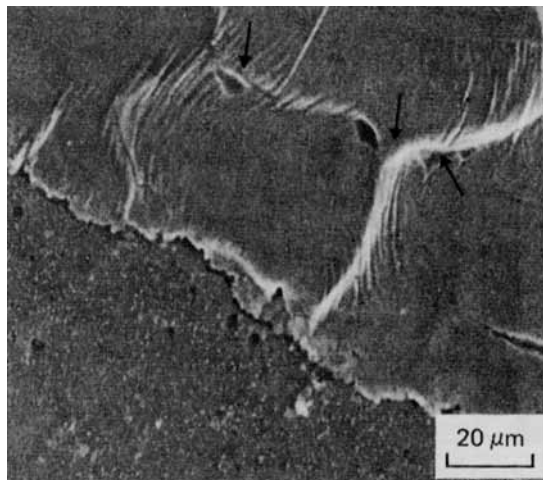


**Fig. 8.8** w-type cavities nucleated at grain boundaries in copper; SEM.

another type of cracking occurs, characteristically, under conditions of low stresses and high temperature. Small cavities form at grain boundaries that are predominantly at approximately  $90^\circ$  to the stress axis, as shown in Figure 8.9. This is called *r-type cavitation* or *r-type cracking*. Figure 8.10 shows such intergranular voids in copper.

The most familiar example of ductile fracture is that in uniaxial tension, giving the classic “cup and cone” fracture. When the maximum load is reached, the plastic deformation in a cylindrical tensile test piece becomes macroscopically heterogeneous and is concentrated in a small region. This phenomenon is called necking (see Section 3.2). The final fracture occurs in this necked region and has the characteristic appearance of a conical region on the periphery resulting from shear and a central flat region resulting from the voids created there. In extremely pure metal single crystals (e.g., those free of inclusions, etc.), plastic deformation continues until the sample section is reduced to a point, a geometric consequence of slip, as shown in Figure 8.2.

In practice, materials generally contain a large quantity of dispersed phases. These can be very small particles (1 to 20 nm) such as carbides of alloy elements, particles of intermediate size (50 to 500 nm) such as alloy element compounds (carbides, nitrides,

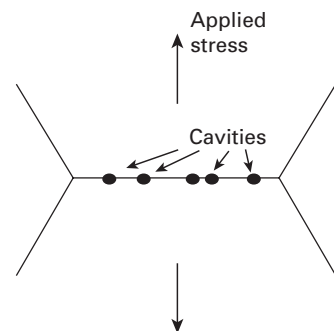


**Fig. 8.9** r-type cavitation at a grain boundary normal to the stress axis.

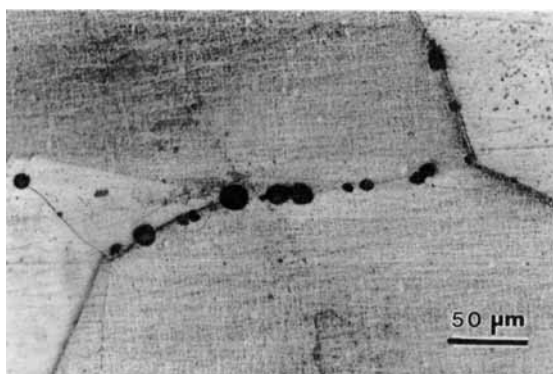
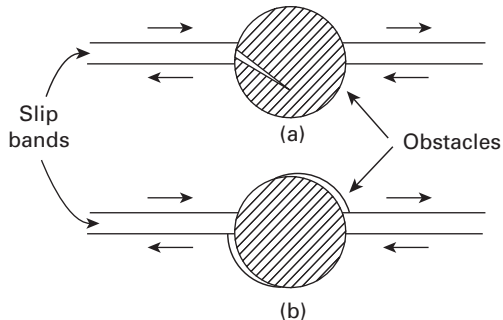


**Fig. 8.10** r-type cavities nucleated at grain boundaries in copper, seen through an optical microscope.

**Fig. 8.11** Nucleation of a cavity at a second-phase particle in a ductile material. (Adapted with permission from B. R. Lawn and T. R. Wilshaw, *Fracture of Brittle Solids* (Cambridge: Cambridge University Press, 1975), p. 40.)

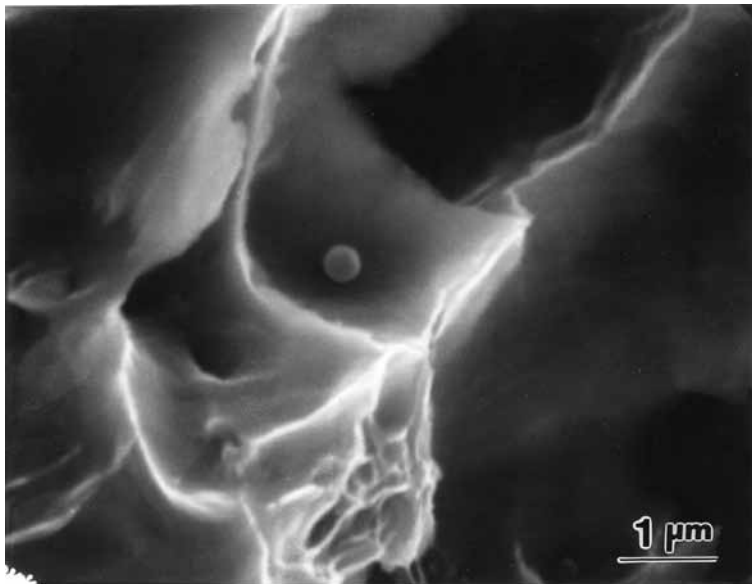


carbonitrides) in steels, or dispersions such as  $\text{Al}_2\text{O}_3$  in aluminum and  $\text{ThO}_2$  in nickel. Precipitate particles obtained by appropriate heat treatment also form part of this class (e.g., an Al-Cu-Mg system), as do inclusions of large size (on the order of millimeters) – for example, oxides and sulfides.

If the second-phase particles are brittle and the matrix is ductile, the former will not be able to accommodate the large plastic strains of the matrix, and consequently, these brittle particles will break in the very beginning of plastic deformation. In case the particle/matrix interface is very weak, interfacial separation will occur. In both cases, microcavities are nucleated at these sites (Figure 8.11). Generally, the voids nucleate after a few percent of plastic deformation, while the final separation may occur around 25%. The microcavities grow with slip, and the material between the cavities can be visualized as a small tensile test piece. The material between the voids undergoes necking on a microscopic scale, and the voids join together. However, these microscopic necks do not contribute significantly to the total elongation of the material. This mechanism of initiation, growth, and coalescence of microcavities gives the fracture surface a characteristic appearance. When viewed in the scanning electron microscope, such a fracture appears to consist of small dimples, which represent the microcavities after coalescence. In many of these dimples, one can see the inclusions that were responsible for the void nucleation. (See Figure 8.12.) At times, due to unequal triaxial stresses, these voids are elongated in one or the other direction. We describe the process of fracture by void nucleation, growth, and coalescence in some detail because of its great importance in metals.

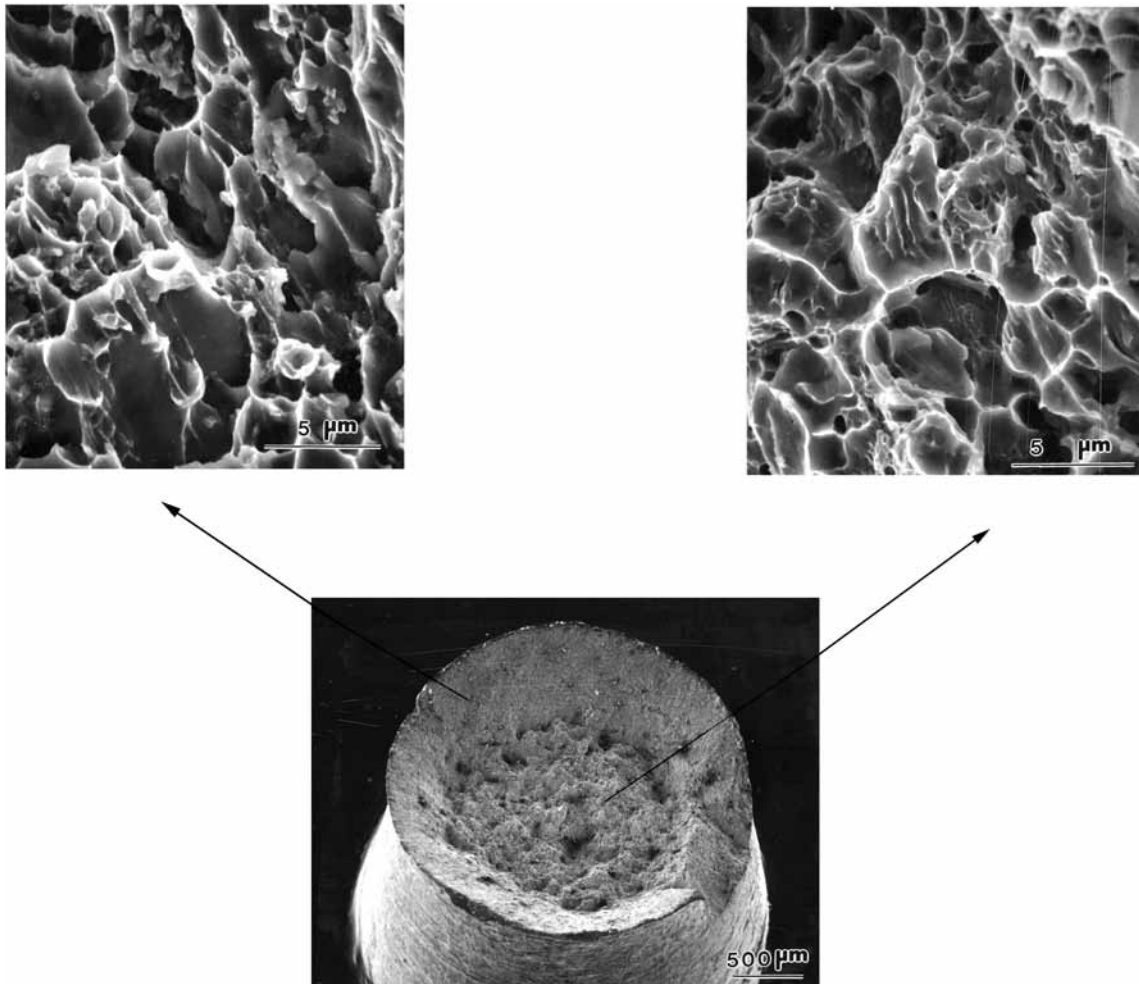
#### Fracture by Void Nucleation, Growth, and Coalescence

Figure 8.13 shows the classic cup-and-cone fracture observed in many tensile specimens with a cylindrical cross section. The configuration is typical of ductile fracture, and upon observation at a higher magnification ( $1,000\times$  or higher, best done in a scanning electron microscope), one sees the typical “dimple” features. The dimples are equiaxial in the central portion of the fracture and tend to be inclined in the sidewalls of the “cup.” The top two pictures show scanning electron micrographs of these two areas. In the central region fracture is



**Fig. 8.12** Scanning electron micrograph of dimple fracture resulting from the nucleation, growth, and coalescence of microcavities. The micrograph shows an inclusion, which served as the microcavity nucleation site.

essentially tensile, with the surface perpendicular to the tensile axis. On the sides, the fracture has a strong shear character, and the dimples show the typical “inclined” morphology, i.e., they appear to be elliptical with one side missing. Figure 8.14 shows, in a very schematic fashion, what is thought to occur in the specimen that leads to failure. Voids nucleate and grow in the interior of the specimen when the overall plastic strain reaches a critical level. The voids grow until they coalesce. Initially equiaxial, their shape changes in accordance with the overall stress field. As the voids coalesce, they expand into adjoining areas, due to the stress concentration effect. When the center of the specimen is essentially separated, this failure will grow toward the outside. Since the elastic-plastic constraints change, the plane of maximum shear (approximately  $45^\circ$  to the tensile axis) is favored, and further growth will take place along these planes, which form the sides of the cup. Although it is easy to describe this process in a qualitative way, an analytical derivation is very complex and involves plasticity theory, which is beyond the scope of the text. Figure 8.15 shows the sequence of ductile fracture propagation, with the formation of dimples. The dimples are produced by voids nucleating ahead of the principal crack (Figures 8.15(a) and (b)), which has a blunted tip because of the plasticity of the material. The void ahead of the crack grows (Figure 8.15(c)) and eventually coalesces with the main crack (Figure 8.15(d)). New voids nucleate ahead of the growing crack, and the process repeats itself. Figure 8.16 shows the propagation of ductile fracture in a specimen of AISI 304 stainless steel undergoing extension, as seen in a high-voltage transmission electron microscope. A referential fixed to the material was added to help visualize the progression of the crack. Figure 8.16(a) shows the growth of a void ahead of the tip of the crack, while Figure 8.16(b) shows new voids



**Fig. 8.13** Scanning electron micrographs at low magnification (center) and high magnification (right and left) of AISI 1008 steel specimen ruptured in tension. Notice the equiaxial dimples in the central region and elongated dimples on the shear walls, the sides of the cup.

being nucleated. In Figure 8.16(c), the crack has advanced by joining with these growing voids. New voids have nucleated.

The nucleation and growth of voids is of great importance in determining the fracture characteristics of ductile materials. Many researchers have identified second-phase particles and inclusions as the main sources of voids.<sup>2</sup> Indeed, Figure 8.12 shows dimples, at the bottoms of which second-phase particles can be seen. The size, separation, and interfacial bonding of these particles determine the overall propagation characteristics of ductile cracks and, therefore, the ductility of the material. The role of second-phase particles is illustrated in Figure 8.17. Copper-based alloys with different amounts of second-phase particles (fractions from 0 to 0.24) were tested in tension, and

<sup>2</sup> See, for example, H. C. Rogers, in *Ductility* (Metals Park, OH: ASM, 1967), p. 31; and L. M. Brown and J. D. Embury, in *Microstructure in Design of Alloys*, Vol. 1 (London: Institute of Metals/Iron and Steel Institute, 1973), p. 164.

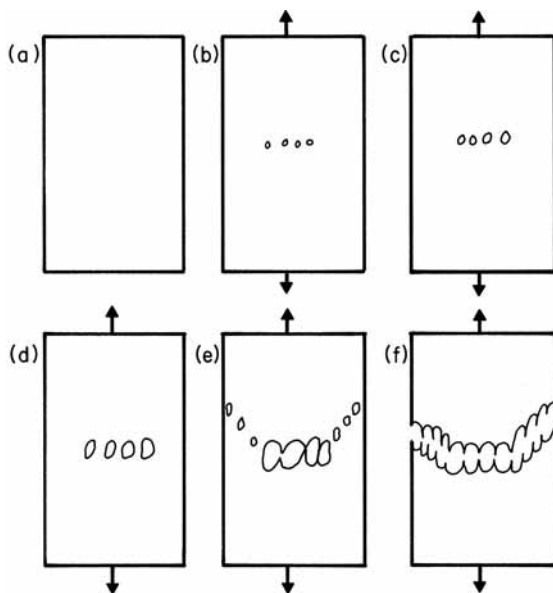


**Fig. 8.14** Schematic sequence of events leading to the formation of a cup-and-cone fracture.

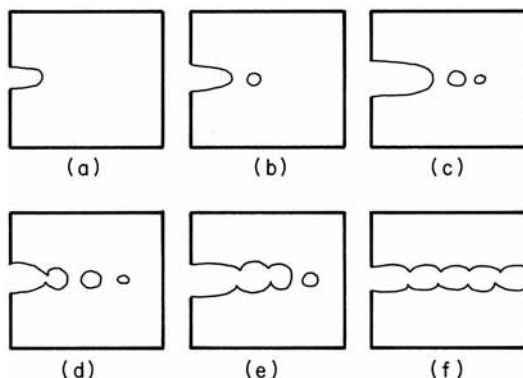


**Fig. 8.15** Sequence of events in the propagation of ductile fracture by nucleation, growth, and coalescence of voids.

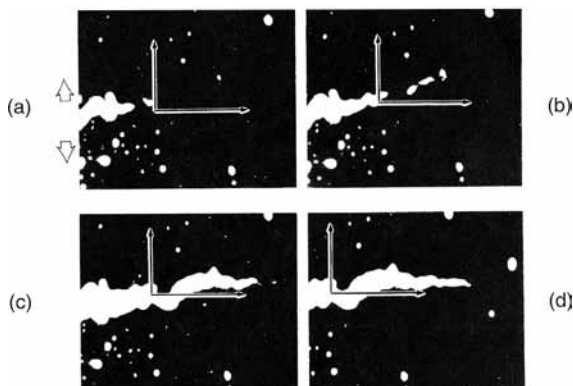
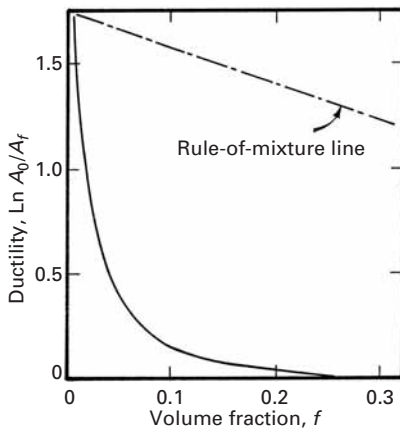


**Fig. 8.16** Observation of progression of ductile fracture while specimen is stressed in high-voltage transmission electron microscope. Referential is fixed to material. (Courtesy of L. E. Murr.)

**Fig. 8.17** Combined plot of ductility vs. volume fraction of second phase,  $f$ , for copper specimens containing various second phases and for notched copper specimens. The dashed line represents the prediction from the law of mixtures, assuming zero ductility for the second-phase particles. (From B. I. Edelson and W. J. Baldwin, Jr., *Trans. ASM*, 55 (1962) 230.)



the ductility of the material was measured. The ductility is given by the reduction in area of the specimens at the fracture point ( $\ln A_0/A_f$ , where  $A_0$  and  $A_f$  are the initial and final cross-sectional areas, respectively). By a simple rule of mixtures, assuming that the second-phase particles have zero ductility, one obtains the straight line shown in the figure. However, the effect of second-phase particles is much more drastic, and ductility is reduced to zero at  $f = 0.24$ . This is a clear indication that second-phase particles play a key role in the propagation of ductile fracture.

Various models have been proposed for void growth. When the growth rate is very low, or the temperature is high (such as in creep) vacancies flow into the void and make it grow. However, at low temperatures and higher strain rates the migration of vacancies cannot account for void growth. A mechanism involving dislocations needs to be considered. In Chapter 4 (Figure 4.26) we studied prismatic loops. These loops consist of a disk of atoms. We assume, for simplicity, a two-dimensional situation shown in Figure 8.18(a). If a prismatic loop moves by glide of the dislocations, the extra disk of matter is carried away and the void diameter increases by  $b$ , equal to the Burgers vector. Figure 8.18(a) shows four prismatic loops originating at the void surface and moving out.

It can be shown that the shear stresses at  $45^\circ$  to the surface of a void are maximum. Assuming elastic stresses and if the remote stresses are hydrostatic, the tangential stress at the void surface is:

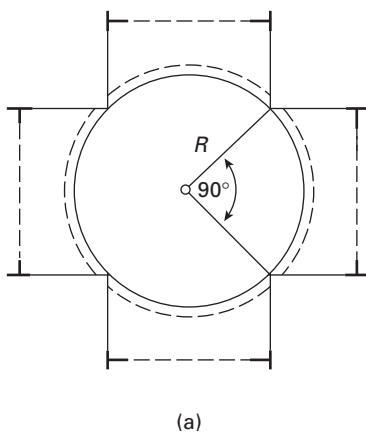
$$\sigma_\theta = 3\sigma.$$

The radial stress is equal to zero, since normal stresses at a free surface are equal to the external tractions:

$$\sigma_r = 0.$$

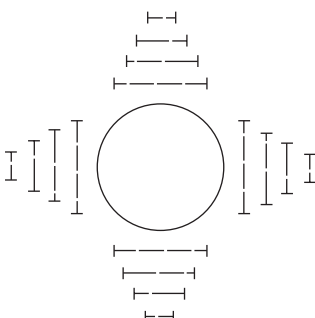
The maximum shear stress bisects these two stresses and is therefore at  $45^\circ$ . Its magnitude is:

$$\tau_{\max} = \frac{\sigma_\theta - \sigma_r}{2} = 1.5\sigma.$$

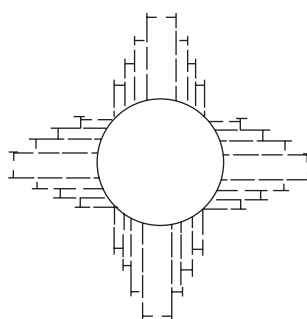


(a)

**Fig. 8.18** (a) Schematic showing how the emission of four loops starting at  $45^\circ$  to void surface increases void diameter by Burgers vector  $b$ . Network of (b) prismatic loops and (c) shear loops (dislocation loops) were sequentially emitted from the surface of the growing void and move into the material. (From V. A. Lubarda, M. S. Schneider, D. H. Kalantar, B. R. Remington, and M. A. Meyers, *Acta Mater.* 52 (2004) 1397.)



(b)

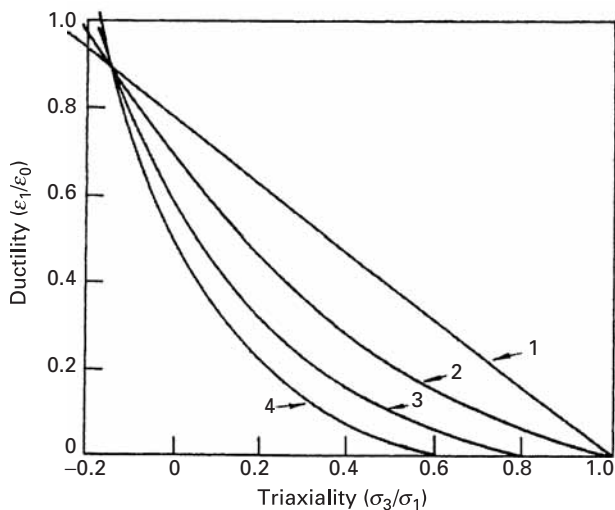


(c)

When this shear stress reaches a critical level, a dislocation can be emitted from the void. Two mechanisms accounting for the generation of the geometrically-necessary dislocations required for void growth are shown in Figure 8.18(b) and (c). Figure 8.18(b) shows successive prismatic loops emitted from a growing void. As the void grows, so does the diameter of the loops. This is a two-dimensional representation, and a full three-dimensional picture would be more complex. Figure 8.18(c) shows shear loops, that can also accomplish the same goal of removing matter from the void surface and extending it. The actual growth of voids is more complex, since the loops interact with each other and their outward motion is therefore impeded. Nevertheless, the net result is that a large density of dislocations is generated around a growing void. Indeed, transmission electron microscopy reveals that voids are surrounded by a highly work-hardened layer.

Before we close this section, it is worth pointing out here that the term “ductility” signifies a material’s capacity to undergo plastic deformation. Ductility is not a fundamental property of the material, because the plastic strain before fracture is a function of the state of stress, strain rate, temperature, environment, and prior history of the material. The state of stress is defined by the three-dimensional

**Fig. 8.19** Variation of maximum plastic strain (ductility) with the degree of triaxiality, according to (1) theory of maximum tensile stress failure, (2) plane-strain conditions, (3) von Mises criterion, and (4) power law of plastic strain. (Adapted with permission from M. J. Manjoine, in *Fracture: An Advanced Treatise*, Vol. 3, H. Liebowitz, ed. (New York: Academic Press, 1971), p. 265.)



distribution of normal and shear stresses at a point or by the three principal stresses at a point. (See Chapter 2.) The multiaxial stresses may be obtained by external multiaxial loading, by geometry of the structure or microstructure under load, by thermal stresses, or by volumetric microstructural changes. One can define a simple “triaxiality” factor by the ratio  $\sigma_3/\sigma_1$ , where  $\sigma_1 > \sigma_2 > \sigma_3$  are the principal stresses. If  $\epsilon_0$  is the plastic strain at fracture in uniaxial tension and  $\epsilon_1$  is the maximum principal plastic strain, one can define a ductility ratio as  $\epsilon_1/\epsilon_0$ . This ductility ratio shows, theoretically, a decrease with increasing triaxiality; that is,  $\epsilon_1/\epsilon_0$  goes to zero as  $\sigma_3/\sigma_1$  goes to unity (Figure 8.19). Thus, an increase in the degree of stress triaxiality results in a decrease in the ductility of the material.

The temperature and the strain rate have contrary effects. A high temperature (or a low strain rate) leads to high ductility, whereas a low temperature (or a high strain rate) leads to low ductility.

### 8.2.3 Brittle, or Cleavage, Fracture

The most brittle form of fracture is cleavage fracture. The tendency for a cleavage fracture increases with an increase in the strain rate or a decrease in the test temperature of a material. This is shown, typically, by a ductile-brittle transition in steel in a Charpy impact test (Figure 8.20). The ductile-brittle transition temperature (DBTT) increases with an increase in the strain rate. Above the DBTT the steel shows a ductile fracture, while below the DBTT it shows a brittle fracture. The ductile fracture needs a lot more energy than the brittle fracture. We deal with these aspects of DBTT in more detail in Chapter 9.

Cleavage occurs by direct separation along specific crystallographic planes by means of a simple rupturing of atomic bonds (Figure 8.21(a)). Iron, for example, undergoes cleavage along its cubic planes (100). This gives the characteristic flat surface appearance

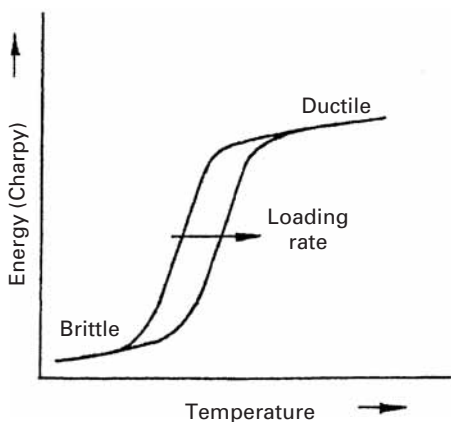


**Fig. 8.20** Ductile–brittle transition in steel and the effect of loading rate (schematic).

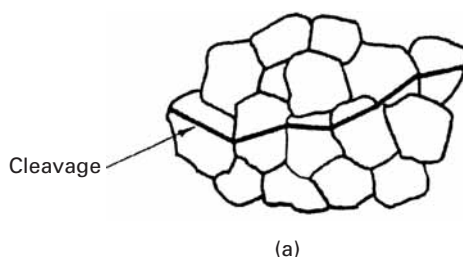
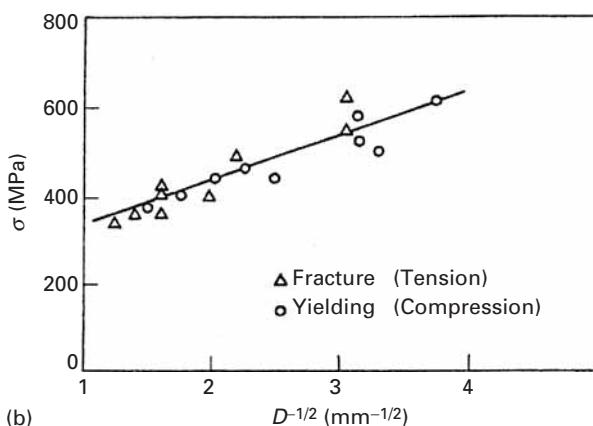
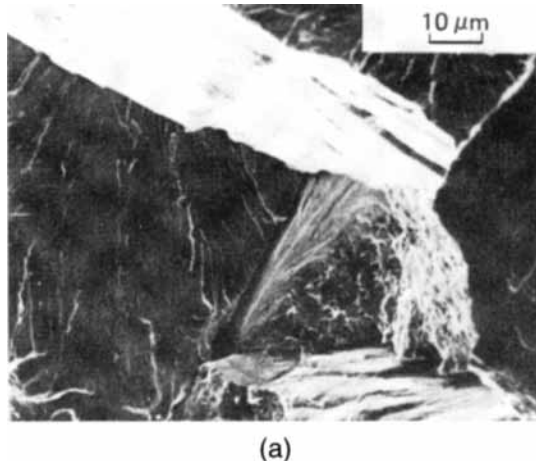


**Fig. 8.21** (a) Propagation of transgranular cleavage. (b) Effect of grain size on fracture and yield stress of a carbon steel at 77 K.  
(Adapted from J. R. Low, in *Madrid Colloquium on Deformation and Flow of Solids* (Berlin: Springer-Verlag, 1956), p. 60.)

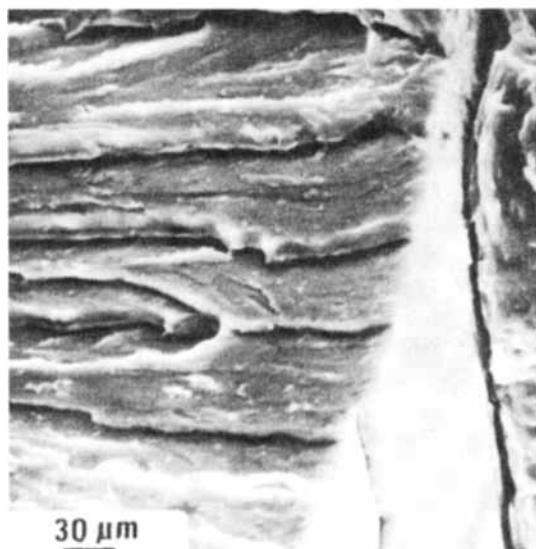


within a grain on the fracture surface. There is evidence that some kind of plastic yielding and dislocation interaction is responsible for cleavage fracture. Low studied the fracture behavior of a low-carbon steel at 77 K, comparing the yield stress in compression (in which case fracture does not occur) with the stress for cleavage in tension. He did this for a number of samples with different grain sizes and obtained the plot shown in Figure 8.21(b). The variation in grain size in both cases followed a Hall-Petch type of relationship, which showed that the controlling mechanism in yielding was also the controlling mechanism for initiating fractures. At 77 K, yielding is closely associated with mechanical twinning. (See Section 5.3.)

**Fig. 8.22** (a) Cleavage facets in 300-M steel (scanning electron micrograph). (b) River markings on a cleavage facet in 300-M steel (scanning electron micrograph).



(a)



(b)

Earlier, we mentioned that cleavage occurs along specific crystallographic planes. As in a polycrystalline material, the adjacent grains have different orientations; the cleavage crack changes direction at the grain boundary in order to continue along the given crystallographic planes. The cleavage facets seen through the grains have a high reflectivity, which gives the fracture surface a shiny appearance (Figure 8.22(a)). Sometimes the cleavage fracture surface shows some small irregularities – for example, the river markings in Figure 8.22(b). What happens is that, within a grain, cracks may grow simultaneously on two parallel crystallographic planes (Figure 8.23(a)). The two parallel cracks can then join together, by secondary cleavage or by shear, to form a step. Cleavage steps can be initiated by the passage of a screw dislocation, as shown in Figure 8.23(b). In general, the

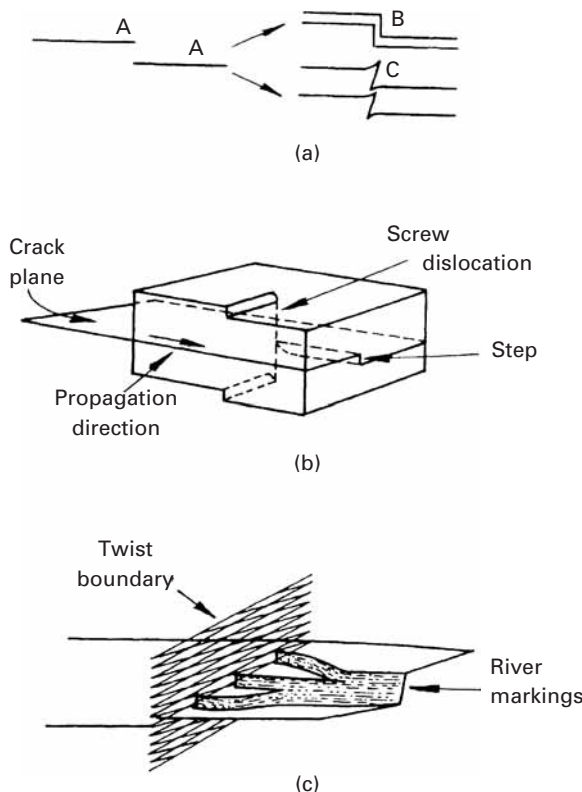
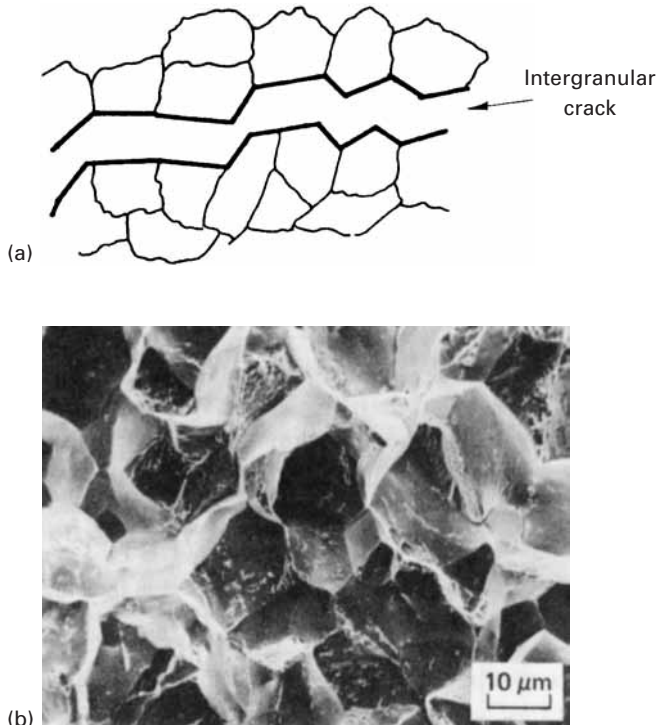


**Fig. 8.23** Formation of cleavage steps. (a) Parallel cracks (A, A) join together by cleavage (B) or shear (C). (b) Cleavage step initiation by the passage of a screw dislocation. (c) Formation of river markings after the passage of a grain boundary. (Adapted from D. Broek, *Elementary Engineering Fracture Mechanics*, 3rd ed. (The Hague, Netherlands: Martinus Nijhoff, 1982), p. 33.)

cleavage step will be parallel to the crack's direction of propagation and perpendicular to the plane containing the crack, as this configuration would minimize the energy for the step formation by creating a minimum of additional surface. A large number of cleavage steps can join and form a multiple step. On the other hand, steps of opposite signs can join and disappear. The junction of cleavage steps results in a figure of a river and its tributaries. River markings can appear by the passage of a grain boundary, as shown in Figure 8.23(c). We know that cleavage crack tends to propagate along a specific crystallographic plane. This being so, when a crack passes through a grain boundary, it has to propagate in a grain with a different orientation. Figure 8.23(c) shows the encounter of a cleavage crack with a grain boundary. After they meet, the crack should propagate on a cleavage plane that is oriented in a different manner. The crack can do this at various points and spread into the new grain. Such a process gives rise to the formation of a number of steps that can group together, generating a river marking (Figure 8.23(c)). The convergence of tributaries is always in the direction of flow of the river (i.e., "downstream"). This fact furnishes the possibility of determining the local direction of propagation of crack in a micrograph.

Under normal circumstances, face-centered cubic (FCC) metals do not show cleavage. In these metals, a large amount of plastic

**Fig. 8.24** (a) An intergranular fracture (schematic). (b) Intergranular fracture in steel (scanning electron micrograph).



deformation will occur before the stress necessary for cleavage is reached. Cleavage is common in body-centered cubic (BCC) and hexagonal close-packed (HCP) structures, particularly in iron and low-carbon steels (BCC). Tungsten, molybdenum, and chromium (all BCC) and zinc, beryllium, and magnesium (all HCP) are other examples of metals that commonly show cleavage.

*Quasi cleavage* is a type of fracture that is formed when cleavage occurs on a very fine scale and on cleavage planes that are not very well defined. Typically, one sees this type of fracture in quenched and tempered steels. These steels contain tempered martensite and a network of carbide particles whose size and distribution can lead to a poor definition of cleavage planes in the austenite grain. Thus, the real cleavage planes are exchanged for small and ill-defined cleavage facets that initiate at the carbide particles. Such small facets can give the appearance of a much more ductile fracture than that of normal cleavage, and generally, river markings are not observed.

*Intergranular fracture* is a low-energy fracture mode. The crack follows the grain boundaries, as shown schematically in Figure 8.24(a), giving the fracture a bright and reflective appearance on a macroscopic scale. On a microscopic scale, the crack may deviate around a particle and make some microcavities locally. Figure 8.24(b) shows an example of this deviation in a micrograph of an intergranular fracture in steel. Intergranular fractures tend to occur when the grain boundaries are more brittle than the crystal lattice. This occurs, for example, in stainless steel when it is accidentally sensitized. This

accident in the heat treatment produces a film of brittle carbides along the grain boundaries. The film is then the preferred trajectory of the crack tip. The segregation of phosphorus or sulfur to grain boundaries can also lead to intergranular fracture. In many cases, fracture at high temperatures and in creep tends to be intergranular.

The ductile-brittle transition temperature of steels and other BCC metals and alloys is significantly affected by grain size. Failure by cleavage (or quasi-brittle crack propagation) and by ductile means are competing mechanisms. When cleavage cracks form and propagate at a greater rate than plastic deformation, the material fails in a brittle manner. It is well known that a reduction in grain size causes a reduction in the ductile-to-brittle transition temperature in steels. Indeed, a reduction in grain size is a very effective means of producing steels that are ductile at low temperature. The explanation of this effect is known as the Armstrong criterion<sup>3</sup> and is discussed briefly next.

The yield stress is well represented by the Hall-Petch Equation (see Section 5.4), namely,

$$\sigma_y = \sigma_0 + k_y D^{-1/2}.$$

The temperature effect can be expressed by

$$\sigma_0 = B \exp(-\beta T),$$

where  $B$  and  $\beta$  are thermal softening parameters. As  $T$  increases,  $\sigma_0$  decreases. The cleavage stress, on the other hand, is also represented by a Hall-Petch relationship:

$$\sigma_c = \sigma_{0c} + k_c D^{-1/2}.$$

Note that  $\sigma_c$  is not dependent on temperature. Note also that  $k_c > k_y$ .<sup>4</sup> By setting  $\sigma_c$  equal to  $\sigma_y$ , we can obtain the ductile-to-brittle transition temperature:

$$\begin{aligned} \sigma_y &= \sigma_c, \\ T_c &= \frac{1}{\beta} [\ln B - \ln\{(k_c - k_y) + \sigma_{0c} D^{1/2}\} - \ln D^{-1/2}]. \end{aligned}$$

Figure 8.25 shows, in a schematic fashion, how the yield stress of a steel with two grain sizes ( $D_1 < D_2$ ) varies with temperature. The ductile-brittle transition temperatures (DBTT) for the two grain sizes are also marked in the figure. The Armstrong criterion applied to the two grain sizes leads to the prediction:

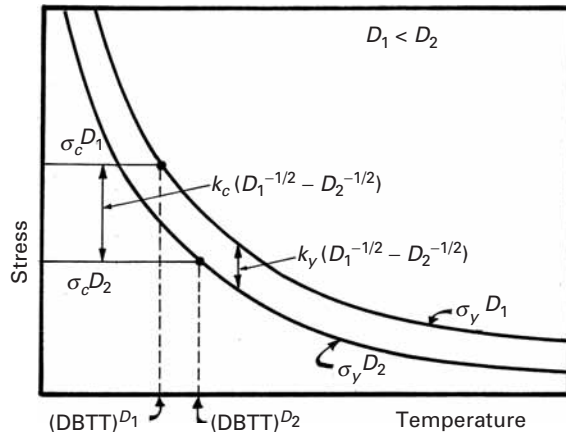
$$(DBTT)_2^D > (DBTT)_1^D.$$

Thus, the steel with the smaller grain size ( $D_1$ ) has the lower DBTT. One can see that grain-size reduction is important in increasing both

<sup>3</sup> R. W. Armstrong, *Phil. Mag.*, 9 (1964) 1063.

<sup>4</sup> In Figure 8.21 yielding (by twinning) and fracture (by cleavage) have the same  $k$ . This is because the Hall-Petch slope for twinning is much higher than the one for slip.

**Fig. 8.25** Armstrong criterion showing effect of grain size on ductile-to-brittle transition temperature.



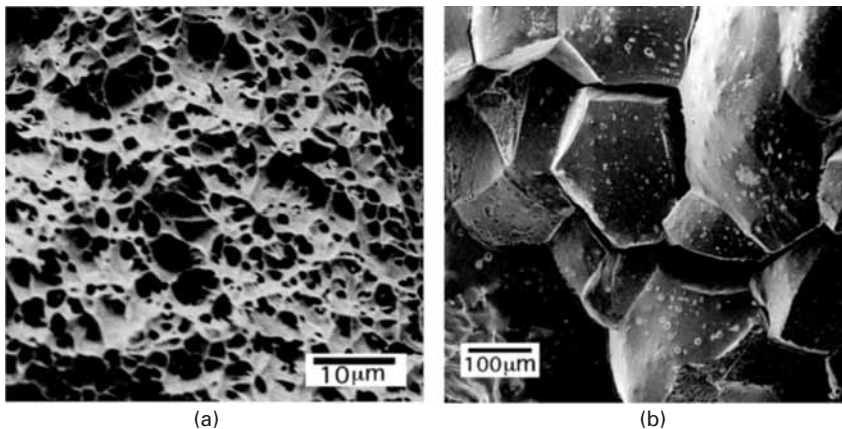
the strength and the range of temperatures over which it is ductile and tough.

Brittle failure of materials is a serious problem. The record of catastrophic brittle failure studies keeps increasing and has encompassed classic examples such as the *Titanic* and the World War II Liberty Ships. In the *Titanic*, rivets containing high levels of sulfur and phosphorus had a high ductile-to-brittle transition temperature and fractured in a brittle fashion, so that entire plates broke loose upon impact of the ship with the iceberg. The Liberty Ships built hurriedly during World War II were made by welding plates. The poor quality of the welds led to brittle failure in cold oceans. This led to the loss of approximately 25% of the 5,000 ships built. The problem of brittle failure is as current today as it was in past centuries, when British soldiers discovered that their cartridges were cracked during monsoon season (a classical example of environmental-assisted cracking). In 2001, the space shuttle fleet was grounded twice; first by the discovery of cracking in the liquid hydrogen flow liners and second by bearing cracks in the crawlers that transport the shuttles to the launch site.<sup>5</sup>

Brittle failure takes many forms, e.g. hydrogen embrittlement, temper embrittlement, stress-corrosion cracking, fatigue failure, irradiation-induced embrittlement, and liquid-metal embrittlement. Some of these will be discussed separately in Chapter 14 (Fatigue) and Chapter 16 (Environmental Effects).

The grain boundary and segregation of undesirable elements to the boundary play a role in many brittle fractures. Minute amounts of additions can completely change the fracture mechanism and morphology. The impurities often segregate to the grain boundaries, changing their strength. A few parts per million (ppm) of impurities are sufficient to decrease the grain boundary cohesion. This is

<sup>5</sup> D. B. Williams, M. Watanabe, C. Li, and V. J. Keast, in *Nano and Microstructural Design of Advanced Materials*, eds. M. A. Meyers, R. O. Ritchie, and M. Sarikaya (Oxford, U.K.: Elsevier, 2003).



illustrated in Figure 8.26. Figure 8.26(a) shows a ductile fracture in copper, characterized by dimples and void nucleation and growth. Figure 8.26(b) shows a fracture surface in copper to which 20 ppm Bi was added. The two morphologies are completely different. The fracture mode in Figure 8.26(b) is intergranular and the material has been dramatically embrittled.

**Fig. 8.26** SEM images of the fracture surface of (a) pure Cu and (b) Cu doped with 20 ppm Bi. (From D. B. Williams, M. Watanabe, C. Li, and V. J. Keast, in *Nano and Microstructural Design of Advanced Materials*, (Elsevier, Oxford, 2003).)

## 8.3 | Fracture in Ceramics

### 8.3.1 Microstructural Aspects

Ceramics are characterized by high strength and very low ductility. Among the approaches developed to enhance the ductility (and, consequently, the fracture toughness) of ceramics are:

1. The addition of fibers to the ceramic to form a composite, making crack propagation more difficult because of crack bridging, crack deflection, fiber pullout, etc.
2. The addition of a second phase that transforms at the crack tip with a shear and dilatational component, thus reducing the stress concentration at the tip of the crack.
3. The production of microcracks ahead of the crack, causing crack branching and distributing the strain energy over a larger area.
4. Careful processing in such a manner that all flaws of a size greater than the grain size are eliminated.

Figure 8.27 shows three toughening mechanisms for ceramics. The addition of fibers renders the propagation of a crack more difficult by one or more of the mechanisms to be explained in Chapter 15, on composites. The addition of a phase that undergoes a transformation is an ingenious strengthening method with great potential. It is described in detail in Chapter 11. Partially stabilized zirconia (zirconia with small additions of yttria) is the phase most commonly added. This phase has a tetragonal structure. At the crack tip, the stress field is such that the transformation from a tetragonal to a monoclinic structure takes place. This transformation produces a volume

**Fig. 8.27** Some toughening mechanisms in ceramics.

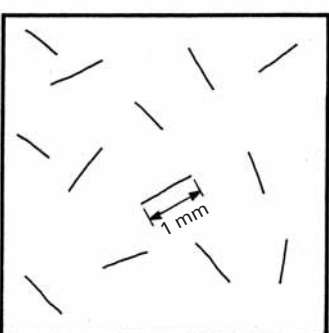
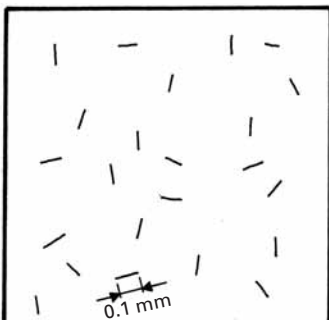
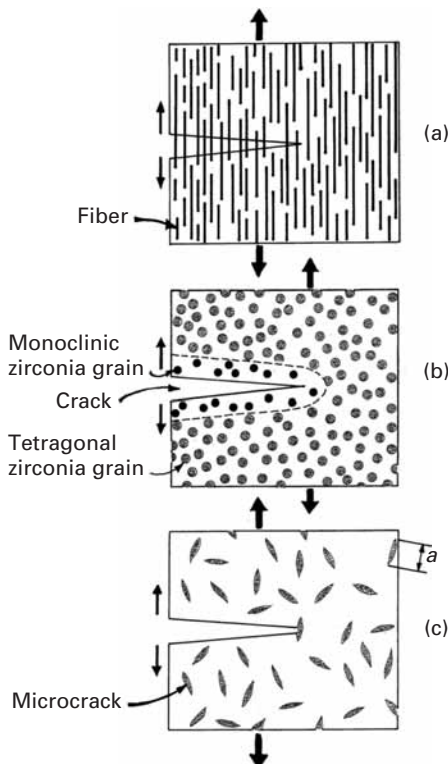


**Fig. 8.28** Ceramic with two flaw-size distributions.

expansion and a shear. The dilation (volumetric strain) is approximately 4%, and the shear strain is approximately 0.16. The regions ahead of the crack tip (Figure 8.27(b)) that have the right stress state will undergo the transformation, which has the effect of adding a compressive stress at the crack tip that will tend to close it. Thus, further progression of crack is more difficult. The fracture toughness of alumina with partially stabilized zirconia can be much higher than that of alumina alone. Also, if microcracks are generated around the second-phase particles, they will decrease the stress concentration ahead of the crack tip.

A third mechanism for toughening ceramics is to form microcracks ahead of the main crack. This is shown in Figure 8.27(c). The microcracks have the effect of decreasing the stress intensity factor at the root of the principal crack. An additional effect is that they can lead to crack branching. One single crack branches into several cracks, and the stress required to drive a number of cracks is higher than that required to drive a single crack.

A fourth mechanism for strengthening ceramics is careful processing so as to eliminate, as much as possible, flaws in the material. Figure 8.28 shows identical materials with two flaw-size distributions. Application of the simple equation from fracture mechanics,  $K_{Ic} = \sigma \sqrt{\pi a}$ , tells us that, for a common ceramic having a fracture toughness of 4 MPa m<sup>1/2</sup> a reduction in flaw size from 1 to 0.1 mm has the

**Table 8.2** Compressive, Tensile, and Flexural Strengths of Ceramics<sup>a</sup>

		Compressive Strength, MPa	Tensile Strength, MPa	Flexural Strength, MPa
Alumina (different purities)	85	1,620	120	290
	90	2,415	140	320
	95	2,411	190	340
	99	2,583	210	340
Aluminosilicate		275	17	62
ZrO <sub>2</sub> –Al <sub>2</sub> O <sub>3</sub>		2,411		
3% Y <sub>2</sub> O <sub>3</sub> PSZ <sup>b</sup>		2,962		1,170
Transformation Toughened Zirconia		1,757	350	630
9% MgO Partially Stabilized Zirconia <sup>b</sup>		1,860		690
Reaction-bonded SiC		689	140	255
Pressureless sintered SiC		3,858	170	550
Sintered SiC with free silicon		1,030	165	320
Sintered SiC with graphite		410	35	55
Reaction-bonded Si <sub>3</sub> N <sub>4</sub>		770		210
Hot-pressed Si <sub>3</sub> N <sub>4</sub>		3,445		860

<sup>a</sup> Adapted with permission from *Guide to Engineered Materials* (Metals Park, OH: ASM International, 1985), p. 16.

<sup>b</sup> Data are from a variety of commercial sources.

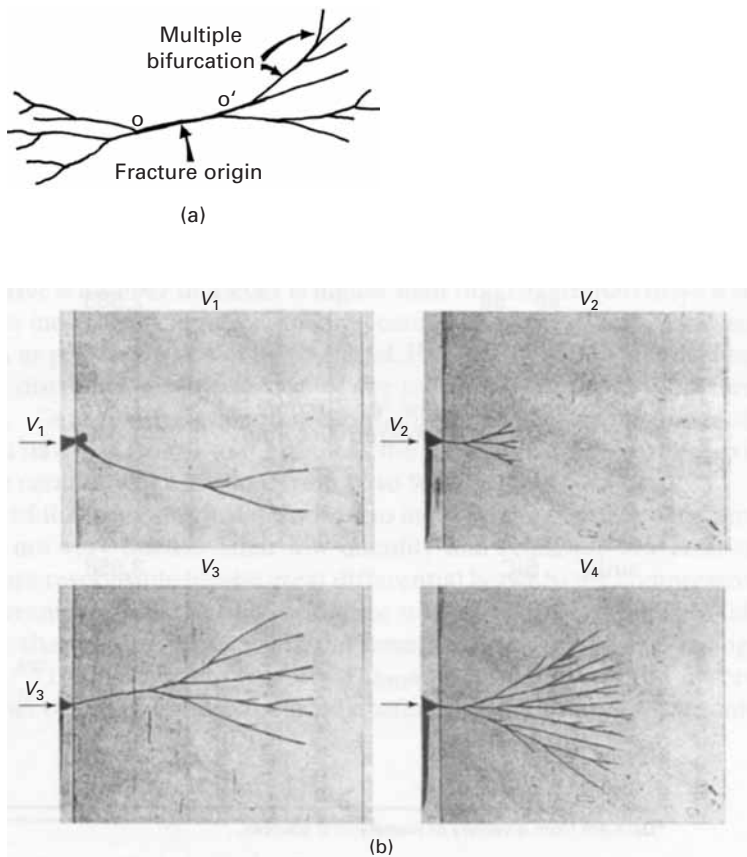
effect of increasing the maximum tensile stress that the ceramic will withstand from 16 to 56 MPa.

In spite of the processes just described to increase the ductility of ceramics, as a rule, ceramics are not very ductile. Their low ductility and relatively low resistance to crack propagation are responsible for the great differential between the compressive and tensile strength of ceramics. In metals, the difference is relatively small, because failure is often initiated only after considerable plastic deformation. The compressive strength of ceramics is close to ten times their tensile stress. This same proportion is also observed in rocks. Table 8.2 shows the compressive and tensile strengths of a number of ceramics.

It is the *inability* of ceramics to undergo plastic deformation that is responsible for the drastic difference in mechanical performance between metals and ceramics. This inability renders ceramics much stronger, but their ability to resist the propagation of cracks is decreased drastically.

The surface morphology of fractures in ceramics tends to present some markedly different features from those appearing in metals. Usually, failure begins at a flaw and propagates slowly. As it accelerates, its energy release rate increases, and there is a tendency for branching; Figure 8.29(a) shows a crack schematically. The origin of the crack is shown by the leftmost arrow. At O and O' in a brittle material, branching starts, and the crack becomes a multitude of cracks. This is seen most clearly in glass, but is also observed in crystalline

**Fig. 8.29** (a) Schematic illustrating a typical crack morphology in the vicinity of the origin, and (b) crack bifurcation in glass from an edge initiated failure, caused by sharp instrument blow on left-hand side; blow velocity  $V_1 < V_2 < V_3 < V_4$ . (Adapted from H. Schardin, in *Fracture*, eds. B. L. Averbach, D. K. Felbeck, G. T. Hahn, and D. A. Thomas (Cambridge, MA: MIT Press, 1959), p. 297.)



ceramics. Figure 8.29(b) shows a sequence of photographs of crack branching (or bifurcation) in glass. A sharp hammer impacted the left-hand side of the glass at different velocities in Figure 8.29(b). As the velocity (and force) of the blow increase, the extent of bifurcation of the cracks increases. Hence, we can understand how shattering of brittle materials occurs. The student is well aware that a glass or a coffee mug (a ceramic!) will break into more parts if the fall is from a greater height. In Figure 8.29(b), the blow velocities are  $V_4 > V_3 > V_2 > V_1$ . If one looks at the fracture surface, one can often identify the origin of the failure by a smooth area, called the *mirror* region. At the center of this smooth area, the vestiges of the initial flaw can be seen. This mirror area becomes more irregular as the crack propagates from the initial flaw. This is called the *mist* region. As branching becomes prevalent, the flat, smooth surface becomes markedly irregular, and this region is called the *hackle* region. (These are similar to the ones observed in polymers and shown later on in Figure 8.42.)

When crack branching (bifurcation) starts, the fracture surface becomes increasingly irregular, because, on separation, different fracture planes become interconnected. In ceramics, the flaws are extremely important, and their concentration and size determine the strength of the ceramic. These flaws can be classified into three groups: flaws produced during processing, flaws induced by improper

**Table 8.3** Sources of Flaws in Ceramics

Processing	Thermal stresses Machining Large pores Isolated large grains Cracked grains Inclusions
Design	Laminations during pressing Stress concentrations due to sharp corners, holes, improper design, etc.
Service	Impact Environmental degradation

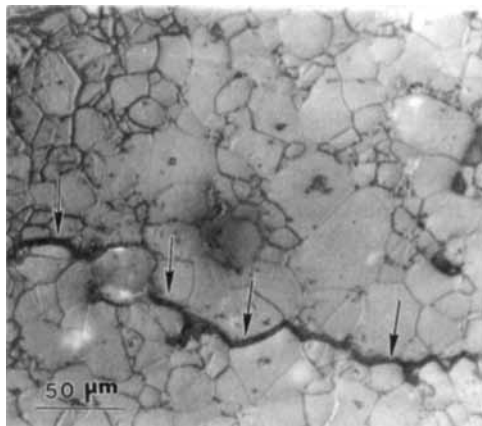


**Fig. 8.30** Intergranular crack produced by thermal shock (rapid cooling) of alumina. (See arrows.)

design, and flaws introduced during service. Table 8.3 gives examples of the various flaws. Since the strength of ceramics is determined by the basic equation of fracture mechanics, that is,

$$K_{Ic} = \sigma \sqrt{\pi a},$$

it is essential to take care to eliminate flaws (or reduce their number as much as possible).

Flaws induced during processing can be of various kinds. Thermal stresses are an important source of cracks. Thermal stresses are caused by the anisotropy of thermal expansion coefficients in non-cubic ceramics. If the ceramic is rapidly cooled, intense internal stresses are set up, leading to microcracks and even total fragmentation of the object. Figure 8.30 shows an intergranular crack produced by thermal shock in alumina. This piece of alumina was cooled fairly rapidly by quenching it in water, from 1,000 °C. The intergranular crack can be clearly seen. Figure 8.31(a) shows voids in AD85 alumina (85% Al<sub>2</sub>O<sub>3</sub>, plus a glassy phase). These voids account for approximately 12% of the volume of the material and are a commonly encountered feature of crystalline ceramics. The voids are larger than the individual grains of the material; the micrograph in Figure 8.31(b) reveals the inside of a void, which clearly shows

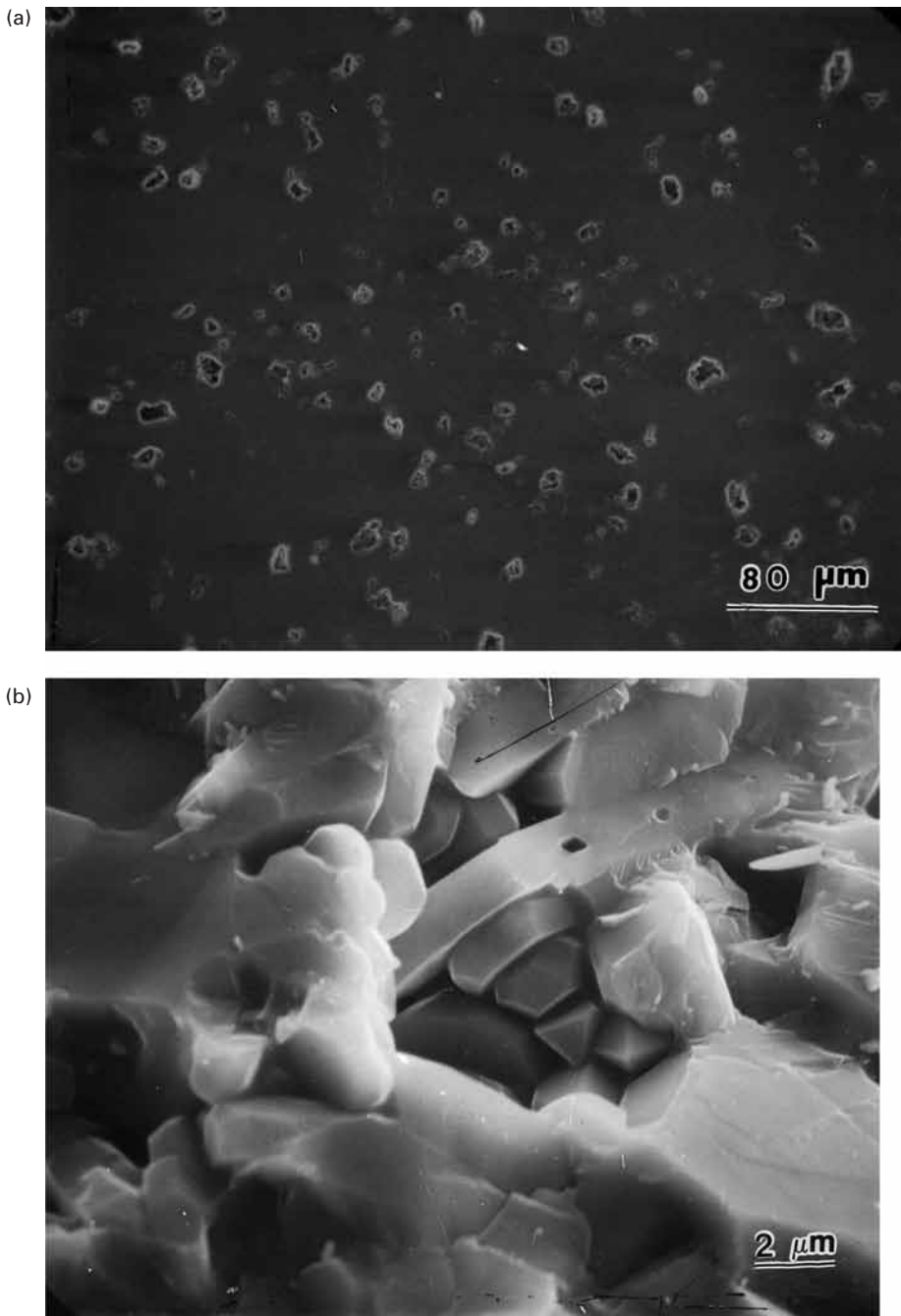


**Fig. 8.31** Voids in AD85 alumina. (a) Scanning electron micrograph of sectioned surface at low magnification. (b) Enlarged view of one void. These voids are larger than the grains.

the individual grains. Defects introduced by machining are also elusive, but dangerous, flaws. These flaws are close to the surface. Isolated large grains, cracked grains, and inclusions are other sources of flaws. Inclusions are often the result of contamination during processing. During pressing or subsequent drying, laminations are often formed. During drying, the laminations can become separated from each other.

**Table 8.4** | Toughness Values for Ceramics<sup>a</sup> (Adapted with permission from *Guide to Engineered Materials* (Metals Park, OH: ASM International), p. 16)

Material	Comments	Toughness, $K_c$ (MPa m <sup>1/2</sup> ) <sup>b</sup>
NaCl	Monocrystal	0.4
Soda-lime glass <sup>b</sup>	Amorphous	0.74 DCB
Aluminosilicate glass	Amorphous	0.91 DCB
WC/Co	Composite	13.0
ZnS	Vapor deposited	1.0
Si <sub>3</sub> N <sub>4</sub>	Hot pressed	5.0
Al <sub>2</sub> O <sub>3</sub>	MgO doped	4.0
Al <sub>2</sub> O <sub>3</sub> (sapphire)	Monocrystal	2.1
SiC	Hot pressed	4.0
SiC-ZrO <sub>2</sub> <sup>c</sup>	Hot pressed	5.0
MgF	Hot pressed	0.9
MgO <sup>2</sup>	Hot pressed	1.2
B <sub>4</sub> C	Hot pressed	6.0
Si	Monocrystal	0.6
ZrO <sub>2</sub>	Ca stabilized	7.6 DCB

<sup>a</sup> Obtained by double torsion measurement technique, except where double cantilever beam test (DCB) is indicated.

<sup>b</sup> Commercial sheet glass.

<sup>c</sup> 20% ZrO<sub>2</sub> 14% mullite by weight. ZrO<sub>2</sub> present in monoclinic form; no transformation toughening.

The second category of sources of flaws listed in Table 8.3 consists of flaws introduced during the design of the material. Ceramic components have to be designed in such a manner as to avoid sharp corners that are stress raisers. Rather large stress concentrations can be generated by notches, holes, etc. (See Chapter 7.) Regions of components under tension should be minimized because of the great differences between the compressive and tensile strength of ceramics. Design should maximize compression for this reason. It is also known that a component under compression and having a hole will be subjected to some tension (see Section 7.3.2).

The last category of sources of flaws given in Table 8.3 involves those flaws introduced during service of the material, as a product. The classic example of the flaw introduced by a rock hitting the glass windshield of an automobile is the most common. The small flaw thus created will eventually generate a crack, which, in most cases, will make the windshield unusable after a certain time. Ceramics are subjected to similar effects, by impact or other sources. Another source of flaws in ceramics is the environment, coupled with stresses. Environmentally assisted cracking in ceramics has many similarities with that in metals.

The fracture of ceramics under tensile loading is essentially dictated by linear elastic fracture mechanics. Thus, the concepts  $K_{lc}$ ,  $J_{lc}$ , and R curve are all applicable to ceramics. Table 8.4 presents fracture

toughness values for a number of ceramics; they are much lower than those of metals, shown in Table 7.1. The second-highest toughness listed in the table is that for zirconia, approximately  $8 \text{ MPa m}^{1/2}$ . The highest listed is that of WC/Co, which has a small amount of cobalt as a matrix, i.e. a metal matrix composite; this is the reason for the high value of  $13 \text{ MPa m}^{1/2}$ . Zirconia undergoes a tetragonal monoclinic transformation at the tip of the crack, decreasing the stress concentration there. Ceramics with tetragonal zirconia particles can benefit from this transformation. (See Chapter 11.)

### Example 8.1

Consider polycrystalline alumina samples with two grain sizes: 0.5 and  $50 \mu\text{m}$ . During cooling, the thermal expansion mismatch produces cracks that have approximate dimensions equal to the grain-boundary facets. If  $K_{lc} = 4 \text{ MN m}^{1/2}$ , determine the tensile strength of each sample.

*Solution:* We assume that the flaw size, i.e.,  $2a$ , is equal to the grain size. Then

$$a_1 = \frac{0.5}{2} \times 10^{-6} \text{ m},$$

$$a_2 = 25 \times 10^{-6} \text{ m},$$

$$K_{lc} = Y\sigma\sqrt{\pi a}.$$

We take the geometric factor  $Y$  to be 1.12:

$$\sigma_1 = \frac{K_{lc}}{Y\sqrt{\pi a}} = \frac{4 \times 10^6}{9.9 \times 10^{-4}} \approx 4 \text{ GPa},$$

$$\sigma_2 = \frac{4 \times 10^6}{9.9 \times 10^{-3}} = 400 \text{ MPa}.$$

### 8.3.2 Effect of Grain Size on Strength of Ceramics

Mechanical properties of ceramics are affected by grain size in several ways. The most important effect is the reduction in the sizes of inherent flaws, as the grain size is reduced. One often finds flaws in a ceramic, caused by processing, that have a characteristic size of the same order of the grain size. The fracture toughness  $K_{lc}$  of a ceramic being an intrinsic property, the tensile stress at which a flaw will be activated is dictated by the equation

$$\sigma = K_{lc}/\sqrt{\pi a}. \quad (8.1)$$

Since the flaw size is often established by the grain size ( $2a = D$ ), one has

$$\sigma = \frac{\sqrt{K_{lc}}}{\sqrt{\pi D/2}}. \quad (8.2)$$

This factor is important in the tensile strength of ceramics.

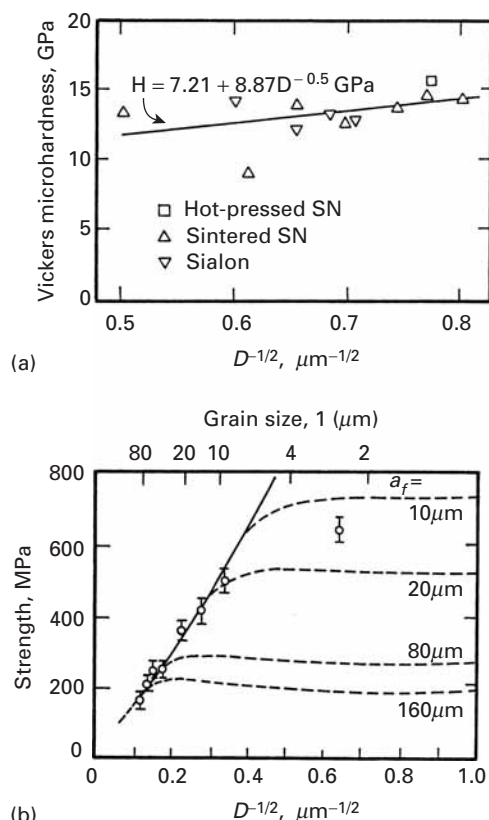


**Fig. 8.32** (a) Effect of grain size on microhardness of hot-pressed and sintered  $\text{Si}_3\text{N}_4$  and sialon. (From A. K. Mukhopadhyay, S. K. Datta, and D. Chakraborty, *J. European Cer. Soc.*, 6 (1990) 303.) (b) Strength as function of grain size for alumina;  $a_f$  is the flaw size. The solid curve refers to flaws having size  $a_f = 0.5D$  (facet flaws) and the dashed lines to flaws of fixed size. (Adapted from P. Chantikul, S. J. Bennison, and B. R. Lawn, *J. Am Cer. Soc.* 73 (1990) 2419.)

The microindentation hardness of ceramics has also been found to be somewhat sensitive to grain size. Figure 8.32(a) shows microhardnesses for hot pressed and sintered silicon nitride, as well as for sialon (a silicon-aluminum-oxygen-nitrogen compound). The hardness increases with a decrease in grain size ( $D$ ), and the results are plotted in a Hall-Petch fashion i.e., hardness vs.  $D^{-1/2}$ . However, this effect is not as important as in metals.

Figure 8.32(b) shows the effect of grain size of the strength of alumina. The solid line represents the application of Equation 8.2. For smaller grain sizes, there are deviations (dashed lines), and other factors enter into consideration as well. Nanocrystalline ceramics possess a property of considerable technological significance: superplasticity. This property enables ceramics to undergo plastic deformation in tension and compression. Tensile elongations as high as 800% have been obtained at moderate temperatures (half the melting point of the material). Nanocrystalline  $\text{TiO}_2$  deforms superplastically at temperatures as low as 600 °C, around 300 °C lower than the submicrometer-size oxide. Nanocrystalline zirconia has been shown to exhibit superplastic strain rates 34 times faster than 0.3- $\mu\text{m}$  zirconia. These results can be rationalized in terms of the decreasing distance between the grain boundaries, helping plastic deformation by both Coble (grain-boundary sliding) or Nabarro-Herring creep, each of

which is described in detail in Chapter 5. Nabarro-Herring creep predicts a strain rate that is a function of  $D^{-3}$ , whereas grain-boundary creep predicts a strain rate that varies with  $D^{-2}$ . Clearly, the strain rate in creep is a strong function of the grain size  $D$ .

### 8.3.3 Fracture of Ceramics in Tension

Most often, tensile stresses produce mode I fracture in ceramics. Such tensile stresses can be generated by actual tensile testing or by flexural testing. Flexural testing produces a tensile stress in the outer layers of the specimen. The crack propagation path is the one that requires the least energy, and intergranular fracture is often observed in ceramics. Figure 8.33(a) shows an intergranular fracture in alumina produced by bending. The fracture follows, for the most part, the grain boundaries, although transgranular fracture is also observed in some places. Figure 8.33(b) shows a primarily intergranular fracture in  $\text{TiB}_2$ .

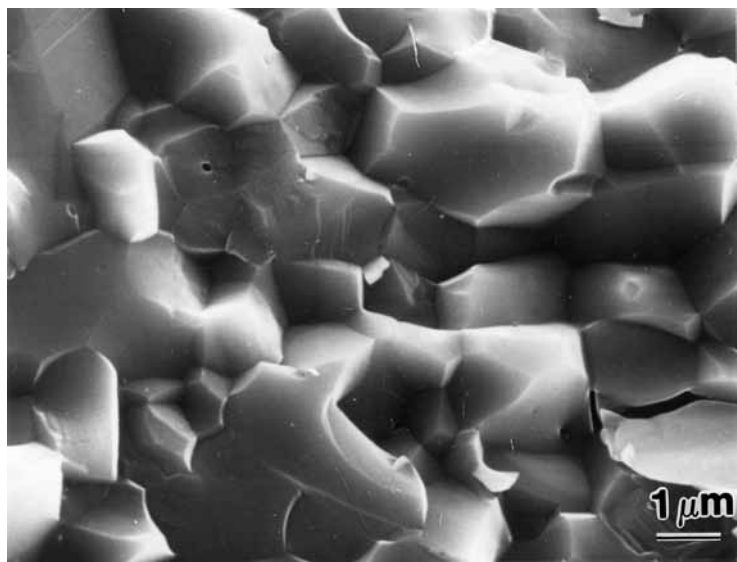
In single-crystal alumina (sapphire), there are no grain boundaries; therefore, the fracture cannot be intergranular, but will instead propagate through the crystal. In such a monocrystal, different crystallographic planes have different surface energies, and fracture will occur on those planes with the least energy. For polycrystalline alumina, the tensile strength is approximately 0.20 GPa, while the tensile strength of single-crystal alumina is 7–15 GPa. This is fairly close to the theoretical strength. The fracture of sapphire usually does not occur along the basal plane, because the surface energy of the (0001) plane is very high. Separation along this plane is difficult, as it is not electrostatically neutral. The basal plane can be visualized as consisting of oxygen atoms. (See Figure 4.43.) Thus, basal plane (0001) fracture would necessitate the separation of oppositely charged ions between planes and would require great energy. Table 8.5 shows the surface energies for sapphire along different planes. From these values, one can see that the {1010} and {1012} planes would be the preferred fracture planes. These high values of surface energy also explain why fracture in polycrystals tends to be intergranular. Another reason is that, in anisotropic materials (materials that are anisotropic in their elastic constants or thermal expansion coefficients), the grain boundaries are regions of stress concentration in which the initiation of a fracture is more likely to occur than in other regions. Figure 8.34 shows a scanning electron micrograph of a fracture surface in a single crystal of sapphire. The flat surfaces are the planes where the surface energy is the lowest.

According to fracture mechanics, internal flaws intensify the externally applied forces; furthermore, this intensification factor depends on the size of the flaw. Thus, specimens with different flaw size distributions will have different strengths. It is well known that the tensile strength of ceramics shows a much greater variability than that of metals. While the yield stress of most metals shows a standard deviation of 5% or less, the tensile strength of ceramics often shows a standard deviation of 25%. The great variation in results from test to test necessitates the use of statistics. In this regard, Weibull's

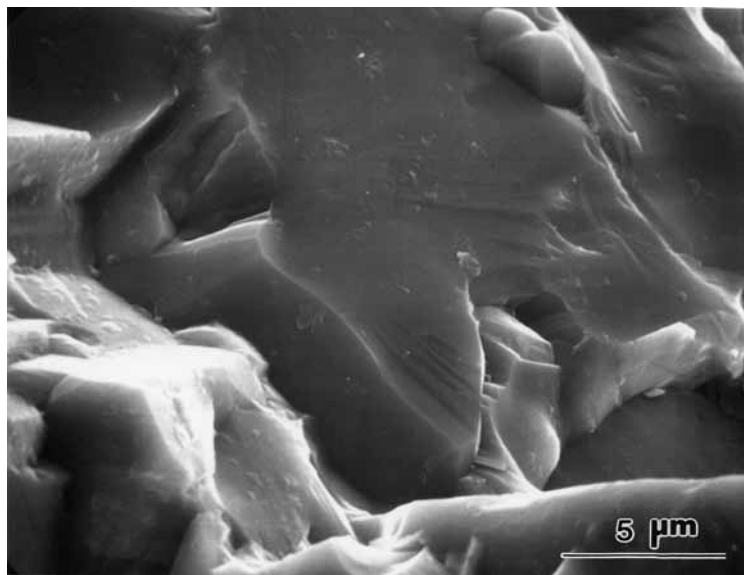
**Table 8.5** | Fracture Surface Energy of Sapphire at Room Temperature<sup>a</sup>

Fracture Plane	Fracture Surface Energy (J/m <sup>2</sup> )
{0001}	>40
{1010}	7.3
{1012}	6
{1126}	24.4

<sup>a</sup> From S. M. Wiederhorn, *J. Am. Cer. Soc.* 50 (1967) 407, Table I, p. 486.



(a)



(b)

**Fig. 8.33** (a) Scanning electron micrograph of fracture surface in 99.4% pure alumina. Fracture is primarily intergranular. (b) Scanning electron micrograph of tensile fracture surface in TiB<sub>2</sub>. Fracture is primarily transgranular.

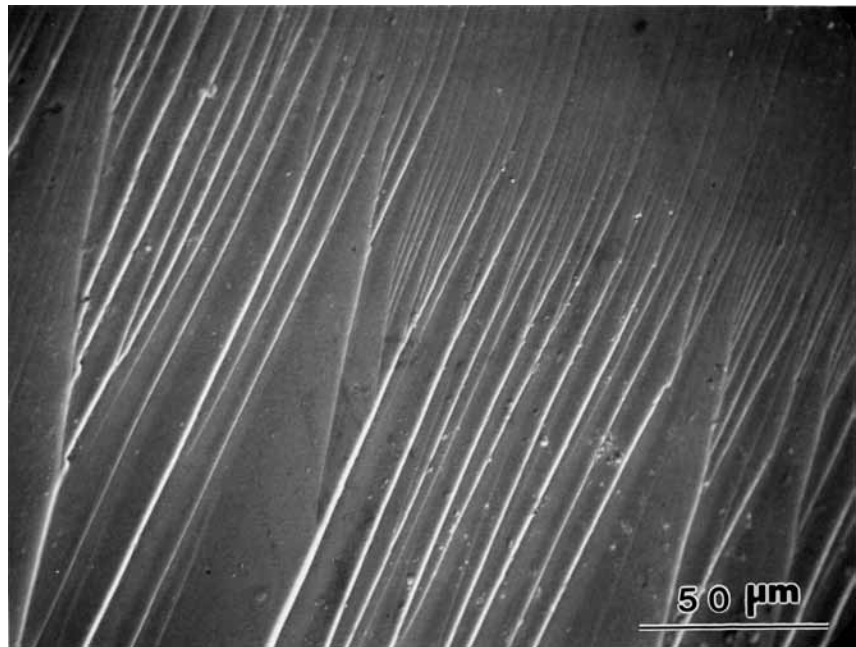


**Fig. 8.34** Scanning electron micrograph of fracture surface in sapphire (monocrystalline alumina).

contribution is universally recognized.<sup>6</sup> The Weibull analysis is described in Chapter 7; it is sufficient here to give the basic equation for the probability that a specimen of volume  $V$  will not fail at an applied tensile stress  $\sigma$ . This equation is (see Equations 7.49 and 7.53)

$$P(V) = \exp \left[ -\frac{V}{V_0} \left( \frac{\sigma - \sigma_u}{\sigma_0} \right)^m \right]$$

where  $\sigma_0$  and  $V_0$  are normalizing parameters,  $\sigma_u$  is the stress below which fracture is assumed to have zero probability, and  $m$  is called the *Weibull modulus*, a measure of the variability of the strength of the material: The greater  $m$ , the less variation there is in the strength. The Weibull modulus for ceramics is usually between 5 and 20. The equation also shows that the strength of a ceramic decreases as its volume increases. This is due to a greater probability of finding large flaws in a large specimen than in a small one. The important conclusion that can be drawn is that *it is the largest flaw that determines failure*.

The fracture toughness of monolithic ceramics varies between 1 and 5 MPa m<sup>1/2</sup>. This toughness is dictated by the strength of the material's interatomic bonds, since little plastic deformation is involved in propagating a crack. Many methods can be used to enhance fracture toughness. However, ceramics retain sharp cracks and low ductility. Note that, although one idealizes the propagation

<sup>6</sup> W. Weibull, *J. Appl. Mech.*, 18 (1951) 293.

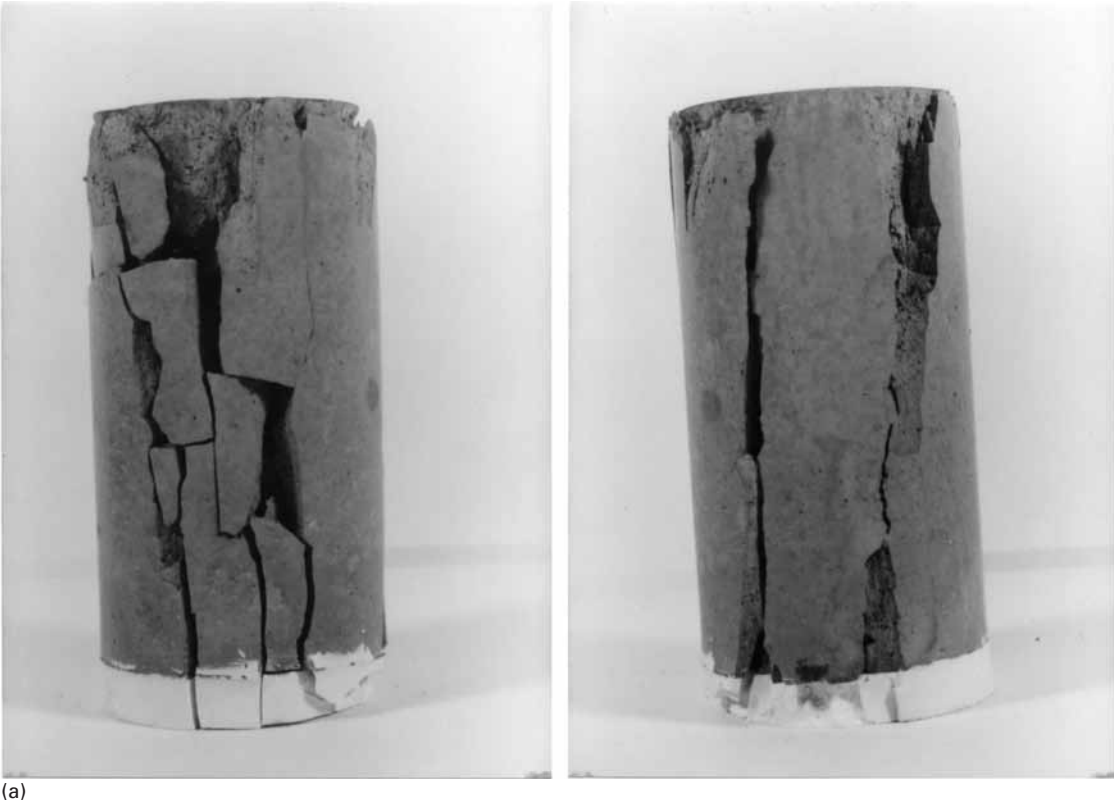
of a crack as an isolated event in a perfectly elastic material, it has been found that the stresses set up at the tip of the crack tend to generate microcracks. These microcracks change the stress field ahead of the major crack, altering its response to the applied load.

### 8.3.4 Fracture in Ceramics Under Compression

Fracture under tension is easy to understand, since it involves the formation of cracks (mainly at imperfections in the material) and their propagation. When a brittle metal, an intermetallic compound, or a ceramic is subjected to compression, it will eventually fail, although at stresses much higher than the tensile strength. How does it fail, since we know that cracks propagate (in mode I) under tension only? Several mechanisms have been proposed, and they all involve the formation of localized regions of tension in the material, caused by the interaction of the externally applied compressive stresses with microstructural defects. Figure 8.35(a) shows a specimen of grout (cement and sand) that failed in compression. The cracks are aligned primarily with the compression axis. The student can reproduce this type of failure by taking a piece of chalk and compressing it in a clamp or vise. The same pattern of cracks will form. This failure mode is called *axial splitting* and is very prominent for unconfined brittle materials. The sequence of events leading from the activation of existing flaws to the growth of cracks, their coalescence, and the formation of slender columns under compression is shown in Figure 8.35(b). The columns become unstable and buckle under the applied compressive loads, ejecting fragments, increasing the load on the remaining specimen, and leading to complete failure.

Griffith was the first to propose a mechanism for the compressive fracture of brittle materials.<sup>7</sup> The mechanism is shown in Figure 8.36. It is based on a pre-existing crack of length  $2a$  oriented at an angle  $\psi$  to the highest compressive stress ( $\sigma_c$ ). This compressive stress will cause a shear stress acting on the opposite faces of the pre-existing flaw. Thus, sliding of the two surfaces will take place. At the ends of the flaw, this sliding is prevented. This will lead to a localized tensile stress ahead of flaw (marked by a plus sign in Figure 8.36(a)) that will, eventually, nucleate two cracks (Figure 8.36(b)). Initially, the cracks will grow at an angle of  $70^\circ$  to the face of the flaw and will then align themselves with the direction of the maximum compressive stress (Figure 8.36(b)). The equations developed by Griffith, called the Griffith criterion, are given in Section 3.7.5. They predict a compressive strength for brittle material eight times larger than the tensile strength. The mathematical analysis of the stresses created at the end of the flaw is based on the scheme shown in Figure 8.36(c). Normal and shear stresses  $\sigma'_{22}$  and  $\sigma'_{12}$  are determined in the plane of the flaw. A frictional resistance  $\mu$  can be assumed at the flaw surfaces. The wing cracks have length  $\ell$  in Figure 8.36(c). A simpler situation

<sup>7</sup> A. A. Griffith, Proc. First Int. Cong. App. Mech., 1 (1924) 55.



(a)

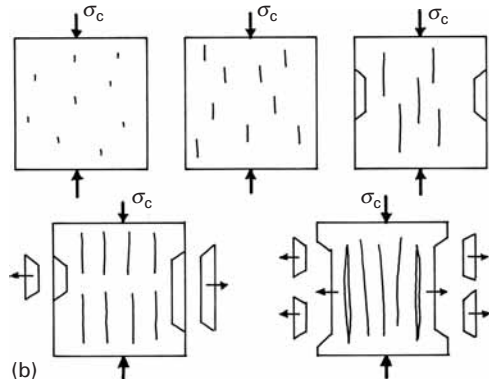
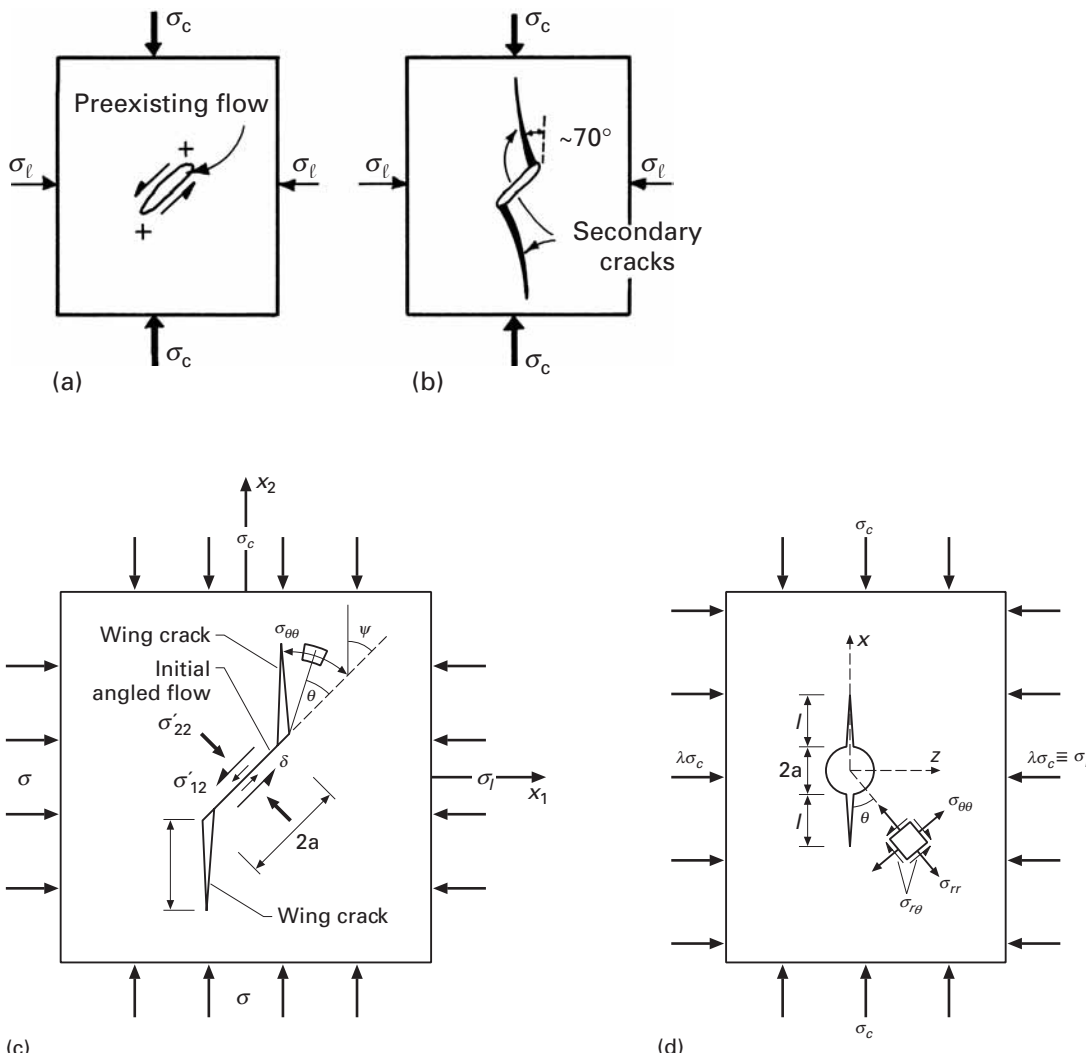


**Fig. 8.35** (a) Compressive failure of brittle material by axial splitting. (b) Schematic representation of growth of critical cracks, producing axial splitting and spalling of fragments; separate columns under compression will collapse.

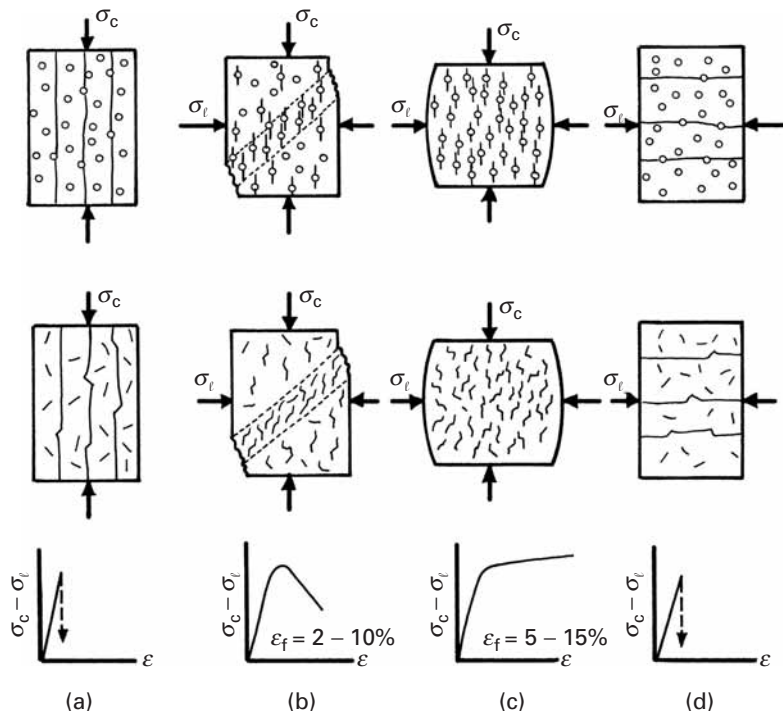
is when the flaw is spherical. In this case, (tangential) tensile stresses generated at the north and south pole of the flaw can generate cracks. (See Figure 8.36(d).) The introduction of lateral stresses  $\sigma_\ell$  (also called lateral confinement) alters the propagation of wing cracks and their interaction and has a profound effect on final failure.



Failure of brittle materials under compression is activated by existing flaws. Brittle metals (cast iron, intermetallics), ceramics, ceramic composites, concrete, and rock are subjected to these mechanisms. Spherical voids and sharp (crack-like) flaws are often produced during the processing of brittle materials. For example, spherical voids are generated during sintering and hot pressing of ceramic powders and are the remnants of the material's initial porosity. Microcracks are created by thermal expansion mismatch (especially in noncubic materials). Frequently, the scale of the microcracks is that of the grain size; they tend to extend from boundary to boundary. The compressive failure of brittle materials is strongly affected by lateral confinement (stresses transverse to the loading direction). Figure 8.37 shows how cracks aligned with the principal direction of loading are generated at spherical and sharp flaws and how they lead to failure. The stress-strain curves and the interactions between the cracks

**Fig. 8.36** (a) Schematic representation of elliptical flaw subjected to compressive stress  $\sigma_c$ ;  $\sigma_l$  is lateral stress. (b) Formation of "wing" cracks from ends of flaw. (c) Stresses generated by flaw of orientation  $\psi$  with compressive axis. (Adapted from M. F. Ashby and S. D. Hallam, *Acta Met.*, 34 (1986) 497.) (d) Circular flaw generating crack. (Adapted from C. G. Sammis and M. F. Ashby, *Acta Met.*, 34 (1986) 511.)

**Fig. 8.37** Failure modes in compression for brittle materials containing spherical and flat flaws, as a function of increasing confinement ( $\sigma_\ell/\sigma_c$ ). (a) Simple compression, giving failure by “axial splitting,” or “slabbing.” (b) Small confining stress, resulting in shear failure. (c) Large confining stresses  $\sigma_\ell$ , providing homogeneous microcracking and a “pseudoplastic” response. (d)  $\sigma_c$  becomes equal to zero; the situation is identical to (a), but rotated by  $90^\circ$ . (Adapted from C. G. Sammis and M. F. Ashby, *Acta Met.*, 34 (1986) 511; and M. F. Ashby and S. D. Hallam, *Acta Met.*, 34 (1986) 497.)



are dependent on the lateral confinement of the material, which is increased from left to right. In the absence of confinement ( $\sigma_\ell = 0$ ), the cracks generated at flaws can grow indefinitely under increasing compressive stress  $\sigma_c$ . They split the specimen vertically, and the segments become unstable and crumble – for instance, from Euler instability. As confinement is increased, the growth of cracks is hindered, and failure occurs along a band of shear localization, where a larger number of cracks is formed. At a still larger confinement (Figure 8.37(c)) the brittle material exhibits a “pseudoplastic” response, with numerous flaws activating cracks. Finally, in Figure 8.37(d), axial splitting (also called “slabbing”) occurs at  $90^\circ$  to the first case (Figure 8.37(a)).

Calculations analogous to those of Griffith were carried out for elliptical flaws by Ashby and Hallam<sup>8</sup> and Horii and Nemat-Nasser.<sup>9</sup> The Ashby-Hallam equations are given here.

When the friction coefficient  $\mu$  is zero, the angle  $\psi$  for which  $K_I$  is maximum is, as expected,  $45^\circ$ . By making  $\sigma_\ell/\sigma_c = \lambda$ , the following equation is obtained:

$$K_I = -\frac{\sigma_c \sqrt{\pi a}}{\sqrt{3}} [(1 - \lambda)(1 + \mu^2)^{1/2} - (1 + \lambda)\mu].$$

<sup>8</sup> M. E. Ashby and S. D. Hallam, *Acta Met.*, 34 (1986), 497.

<sup>9</sup> H. Horii and S. Nemat-Nasser, *J. Geophys. Res.*, 90 (1985) 3105; and *Phil. Trans. Roy Soc. (London)*, 319 (1986) 337.

The critical value of the stress intensity factor,  $K_{Ic}$ , is reached at the stress level at which wing crack growth starts. For a crack making an angle  $\psi = (1/2)\tan^{-1}(1/\mu)$  with the principal loading axis, we have

$$\frac{\sigma_c \sqrt{\pi a}}{K_{Ic}} = \frac{-\sqrt{3}}{[(1-\lambda)(1+\mu^2)^{1/2} - (1+\lambda)\mu]}.$$

Ashby and Hallam also obtained an expression for the increase in length of the winged cracks,  $\ell/a = L$ , as a function of normalized stress:

$$\frac{\sigma_c \sqrt{\pi a}}{K_{Ic}} = \frac{-(1+L)^{3/2}}{[1-\lambda-\mu(1+\lambda)-4.3\lambda L]\left[0.23L + \frac{1}{\sqrt{3}(1+L)^{1/2}}\right]}.$$

For spherical and circular flaws, the equations given in Section 7.3 can be applied. This results in the following expression:

$$\frac{\sigma_c \sqrt{\pi a}}{K_{Ic}} = -\frac{1}{L^{1/2}\left[\frac{1.1(1-2.1\lambda)}{(1+L)^{3.3}} - \lambda\right]}.$$

Under simple compression ( $\lambda = 0$ ,  $\sigma_\ell = 0$ ), the crack grows in a stable fashion from an initial value of normalized stress equal to 4. In an initial stage, from  $L = 0$  to  $L = 0.2$ , the stress actually drops with increasing length. This corresponds to the initial “pop-in” stage of crack formation. Since  $K_{Ic}$  is a material constant, the compressive stress at which a crack grows decreases with increasing void size. Hence, *larger voids are more effective crack starters*. For lateral tension ( $\lambda < 0$ ), the crack grows in a stable fashion to a certain size and then grows unstably (in the region where  $\sigma_c$  decreases with increasing  $L$ ). The equations also show the total suppression of crack growth when  $\lambda \geq \frac{1}{3}$ .

Additional mechanisms involving dislocations, anisotropy of the elastic properties of adjacent grains, and dislocation-grain-boundary interactions were proposed by Lankford,<sup>10</sup> who studied the behavior of alumina under compression and found localized plasticity (caused by either twinning or dislocations) at stresses below the compressive failure stress. The interaction of deformation bands with grain boundaries caused microcracks to begin forming. Figure 8.38 shows a schematic indicating how microstructural anisotropy can lead to stress concentrations at the grain boundaries. If two adjacent grains have different elastic moduli along the axis of compression (because of differences in crystallographic orientation), they will tend to deform differently. This will impose additional stresses on the grain boundaries because of compatibility requirements (Figure 8.38(a)). In a similar way, deformation bands (whether they be dislocations or twins) will create stress concentrations at the grain boundaries (Figure 8.38(b)). Figure 8.38(c) shows examples of a crack produced by different interactions with a grain boundary. Thus, failure of a ceramic under compression is a gradual process, although the actual fracture

<sup>10</sup> J. Lankford, *J. Mater. Sci.*, 12 (1977) 791.

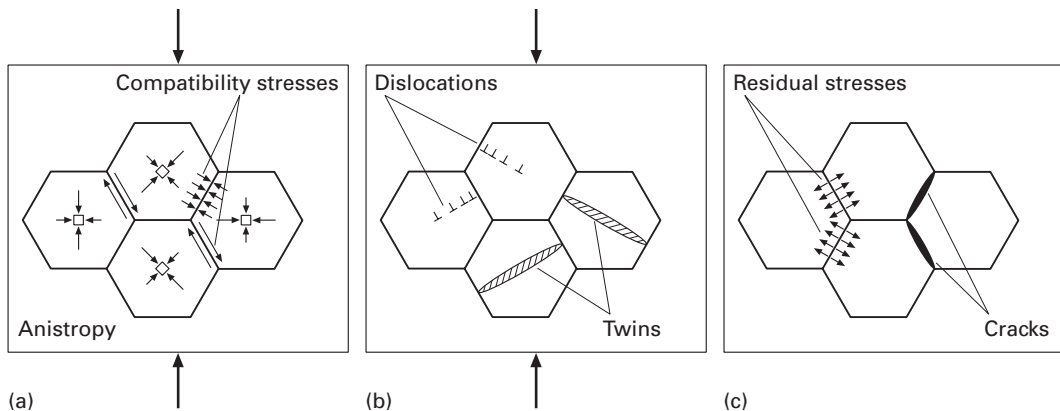


**Fig. 8.38** Schematic showing how (a) anisotropy of elastic properties and (b) localized plastic deformation can lead to stress concentrations and (c) cracking at grain boundaries during unloading. (After M. A. Meyers, *Dynamic Behavior of Materials* (New York: J. Wiley, 1994), p. 559.)

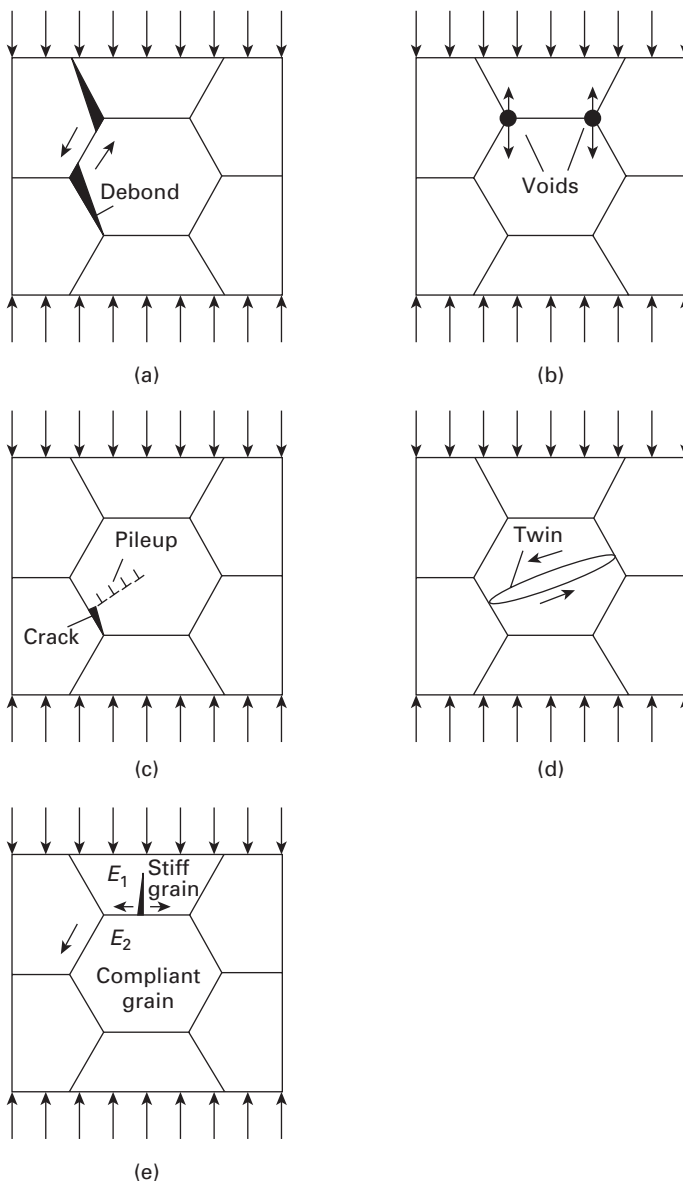
often occurs in an “explosive” manner, as the ceramic fragments into many pieces due to the coalescence of microcracks.

Figure 8.39 shows several mechanisms that were identified as leading to cracking in SiC. Some of these mechanisms have been presented in Figure 8.38. Others, such as grain-boundary debonding, are specific to ceramics where the grain boundaries have a lower strength than the grain interiors. Such is often the case when ceramics are sintered and sintering agents (glasses) are used. They form a thin film at the grain boundaries. Voids are also significant initiators of cracking. Dislocation pileups create stress concentrations which eventually cause debonding (Figure 8.3) and formation of Zener-Stroh-type cracks.

### 8.3.5 Thermally Induced Fracture in Ceramics

Thermal stresses induced during cooling can have a profound effect on the mechanical strength of the ceramics. This can be explained in a qualitative manner by Figure 8.40. The polycrystalline aggregate is schematically represented by an array of hexagons. When the temperature is reduced from  $T_2$  to  $T_1$ , the hexagonal grains contract. The noncubic structure of alumina and many other ceramics results in different contractions along different crystallographic orientations. The same effect manifests itself in noncubic metals. In some metals, substantial plastic deformation is observed after thermal cycling (numerous heating and cooling cycles). The problem is especially crucial in composites, where the different components often have quite different thermal expansion coefficients. The thermal expansion coefficient along the  $c$ -axis of  $\text{Al}_2\text{O}_3$  is about 10% higher than perpendicular to it. The stresses set up by these differences in thermal expansion are sufficient to introduce microcracks into the material after cooling. In Figure 8.40, we would have  $\Delta L_1 \neq \Delta L_2$  if the grains were free. However, each grain is constrained by its neighbors, and stresses therefore arise. These stresses are given by

$$\sigma = \frac{2}{3(1-\nu)} \int_{T_1}^{T_2} E(\alpha_c - \alpha_a) dT,$$



**Fig. 8.39** Schematic overview of principal damage initiation mechanisms in SiC: (a) grain boundary debonding; (b) foreign particles, such as inclusions and voids at the grain boundaries; (c) dislocation pileups, leading to Zener–Stroh cracks; (d) twins and stacking faults; (e) dilatant crack produced by elastic anisotropy. (From C. J. Shih, M. A. Meyers, V. F. Nesterenko and S. J. Chen, *Acta Mater.*, 40 (2000) 2399.)

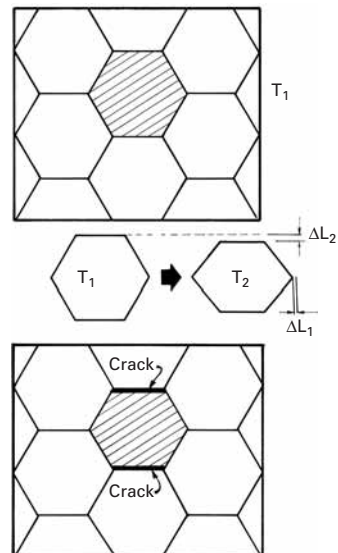


**Fig. 8.40** Thermally induced cracks created when grains contract in an anisotropic fashion during cooling from  $T_1$  to  $T_2$ .

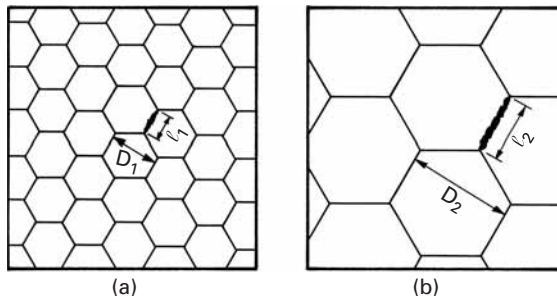
where  $T_1$  and  $T_2$  are the extreme temperatures of the thermal cycle, and  $\alpha_a$  and  $\alpha_c$  are the thermal expansion coefficients perpendicular and parallel to the  $c$ -axis, respectively. For constant expansion coefficients, and assuming a constant  $E$ , we get

$$\sigma = \frac{2E}{3(1-\nu)} \Delta\alpha \Delta T.$$

Cooling a polycrystalline alumina sample from 1,020 °C to 20 °C would generate stresses on the order of

$$\sigma = \frac{2 \times 400}{3(1-0.31)} (0.7 \times 10^{-6}) \times 1,000 = 0.27 \text{ GPa} = 270 \text{ MPa}$$

**Fig. 8.41** Thermally induced microcracks in ceramic specimens with two grain sizes.



between two grains of orientations *a* and *c*. This is approximately  $1\frac{1}{2}$  times the tensile strength of alumina, as can be seen from Table 8.2. Thus, microcracks can be generated by anisotropy of an expansion coefficient. Even in the case where no microcracks are generated, internal stresses remain within the grains. When a ceramic is subjected to external loading, the internal stresses due to thermal differences interact with the externally applied loads and can considerably reduce the stresses required for fracture.

The anisotropic effect of expansion on microcracking affects the strength of ceramics in a manner that is dependent on grain size. This effect, is illustrated in Figure 8.41. Here we assume that microcracks are generated by thermal anisotropy in the two specimens. The microcracks will extend over one grain face. The sizes of the two microcracks are  $\ell_1$  and  $\ell_2$  for the small and large grain-sized specimens, respectively. If the grain sizes are  $D_1$  and  $D_2$ , we can say that

$$\frac{\ell_1}{D_1} = \frac{\ell_2}{D_2}.$$

The fracture mechanics equation

$$K_{Ic} = \sigma \sqrt{\pi a}$$

can then be applied to determine the tensile strength of the ceramics.

Thus, the tensile strength can be written as

$$\sigma = \frac{K_{Ic}}{\sqrt{\pi a}} = \frac{K_{Ic}}{\sqrt{\frac{\pi \ell}{2}}}.$$

By substituting  $D$  for  $\ell$  and combining all constants into one, we obtain

$$\sigma = K_{Ic} k D^{-1/2}.$$

$k$  is a parameter. This simple equation expresses the experimentally observed fact that thermal anisotropy is much more effective in weakening specimens with a large grain size than specimens with a small grain size.

Another serious problem of a thermal nature affecting ceramics is cracking, because of temperature differentials within one component. We all know that china will fracture if rapidly cooled. Ceramics

are subject to very intense stress concentrations if temperature differentials are set up within them. This is so because plastic deformation, which serves to accommodate stresses due to severe temperature gradients in metals, is mostly absent in ceramics. Thus, there are limits to the rates at which components can be cooled or heated. If these rates are exceeded, the components fail. A simple example is a furnace tube that is heated to a high temperature. If the resistance wire that heats the furnace touches the ceramic, a significant temperature gradient is established over a small distance. This temperature gradient creates stresses that lead to fracture if the tensile strength of the ceramic is exceeded. It is very common for ceramic bricks (refractory bricks) to break during cooling. In ceramics thermal shock or rapid cooling can have catastrophic effects, and the superb high-temperature properties of ceramics are of no advantage if the ceramic fails during cooling. When ceramics are used in conjunction with metals in machines, the difference between the thermal expansion coefficient of the metal and that of the ceramic can lead to failure. These aspects must be considered in the design of ceramic components, and heat transfer equations should be used to estimate the temperature differentials and the associated stresses within the ceramic.

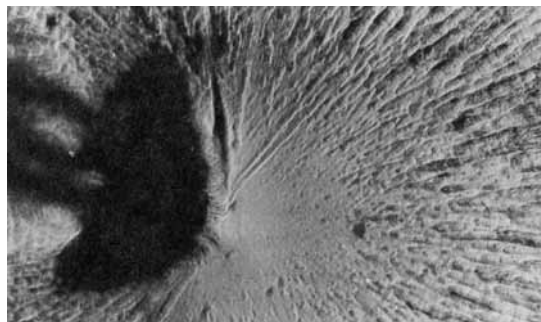
## 8.4 | Fracture in Polymers

The fracture process in polymers involves the breaking of inter- and intramolecular bonds. Recall that amorphous or glassy polymers have a glass transition temperature  $T_g$ , but no melting point  $T_m$ . These glassy polymers are rigid below  $T_g$  and less viscous above that temperature. Semicrystalline polymers have both a melting point and a glass transition temperature, the former referring to the crystalline phase, the latter to the amorphous phase surrounding the crystalline phase. More information about the structure of polymers is given in Chapter 1.

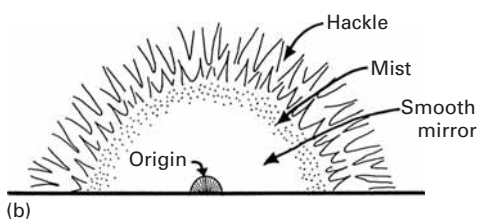
### 8.4.1 Brittle Fracture

Many polymers fracture in a brittle manner below their glass transition temperature. This is particularly true of polymers having large, bulky side groups or a high density of cross-links. Under either of these circumstances, the molecular chain structure of the polymer becomes so rigid, that chain disentanglement and/or slipping becomes very difficult. Examples of such polymers are thermosets, such as epoxy, polyester, and polystyrene. The stress-strain curve of these polymers is quite linear to fracture, and the strain to failure is typically less than 1%. Figure 8.42(a), a scanning electron micrograph, shows an example of a brittle fracture surface in a cross-linked polyester; Figure 8.42(b) shows schematically the different regions that compose such a surface. There are three regions:

**Fig. 8.42** (a) Brittle fracture in a highly cross-linked thermoset (polyester). (b) The three different regions that compose the brittle fracture surface in (a).



(a)



(b)

1. A mirrorlike, or specular, region adjoining the crack nucleation site, indicating slow crack growth.
2. A coarse and flat region indicative of fast crack growth; sometimes this region is called the region of *hackle*, and one can see that the crack has propagated on different levels over small areas. When hackle is elongated in the direction of crack propagation, the pattern is called “river markings.”
3. A transitional region between the preceding two that has a *misty* appearance and no resolvable features.

Similar brittle fracture surface features are observed in ceramics. (See Figure 8.29.) In highly cross-linked thermosets, such as epoxies and polyesters, the plastic deformation before fracture is negligible. Consequently, manifestations of plastic deformation, such as crazing and shear yielding, are generally not observed.

#### 8.4.2 Crazing and Shear Yielding

Frequently, the phenomena of crazing and shear yielding precede actual fracture in a polymer. Both these phenomena involve a localization of the plastic deformation in the material. The major difference between the two is that crazing occurs with an increase in volume, whereas shear yielding occurs at constant volume.

In glassy polymers, one can regard crazing and shear yielding as competing processes. In brittle glassy polymers, such as polymethyl methacrylate (PMMA) or polystyrene (PS), crazing precedes the final brittle fracture. In comparatively more ductile polymers (for example, polycarbonate or oriented polyethylene), which have flexible main-chain linkages, shear yielding is the dominant mode of deformation,

and the final fracture is ductile. In particular, if an oriented high-density polyethylene sheet is deformed in a direction oblique to the initial draw direction, it will show a shear deformation band in which highly localized plastic deformation occurs.

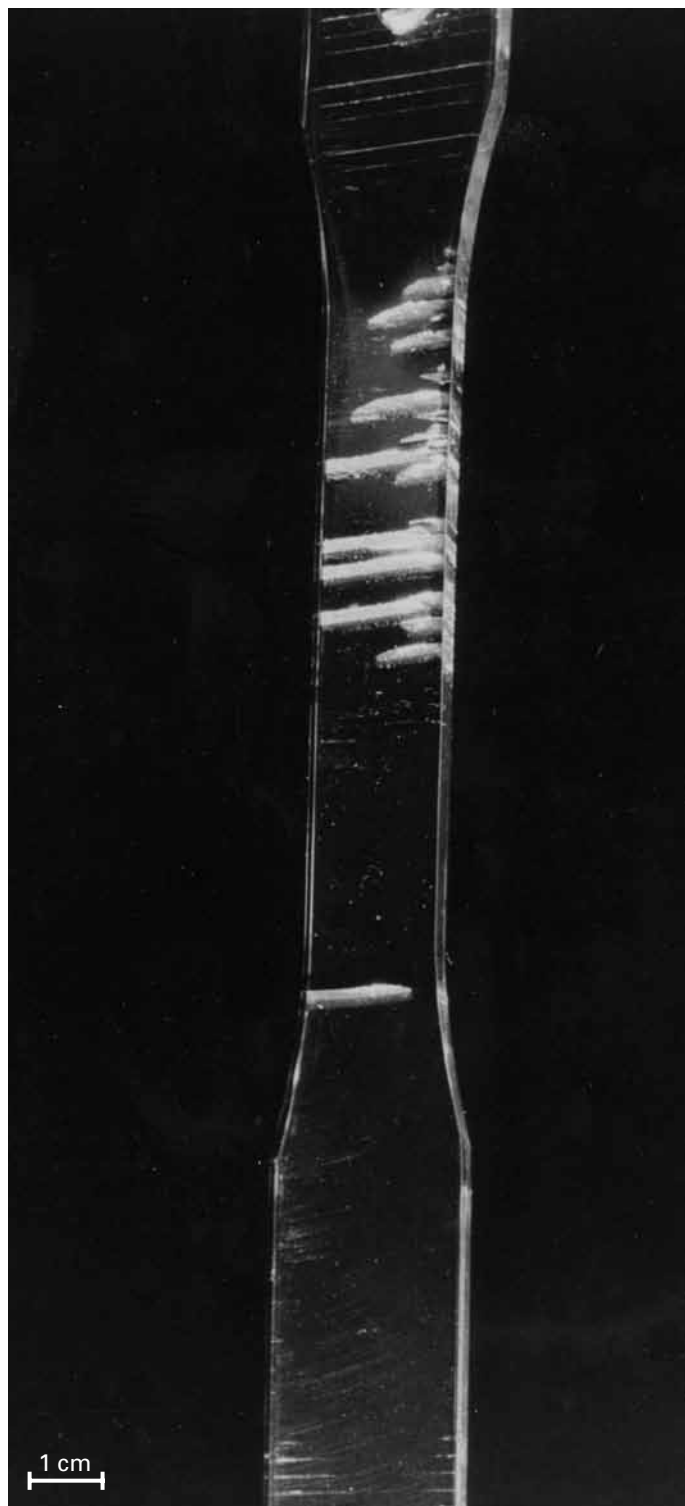
It is thought that molecular entanglements control the geometry of crazes and shear yield zones. A craze is a region of a polymer in which the normal “cooked-spaghetti-like” chain arrangement characteristic of the amorphous state has been transformed into drawn-out molecular chains interspersed by voids. The crazed region is a very small percentage of the total region of the polymer (a few nanometers to a few micrometers). Because of the presence of voids in a craze, the plastic deformation of the small volume of material in the craze occurs without an accompanying lateral contraction; that is, the constancy-of-volume condition which holds in the regular bulk polymer does not hold in the crazed material.

A craze is neither a void nor a crack. Detailed optical- and electron-microscopic observations of crazed regions show that crazes are not voids and that they are capable of transmitting load. The refractive index of a craze in a polymer such as polycarbonate, in the dry state and after immersion in ethanol, would be different. From such measurements, it was concluded that crazes contain about 50–55% by volume of free space; that is, the density of the material in the crazed region is lower than that of bulk polymer. The lower density of the crazed region reduces the refractive index of the region and causes its characteristic reflectivity. Figure 8.43 shows a series of crazes reproduced in a tensile specimen of polycarbonate. Note that several crazes have run through the entire cross section without failure of the specimen, indicating the load-bearing nature of the crazes. The volume fraction of the polymer in the craze is inversely proportional to  $\lambda$ , the draw ratio (final length  $\div$  original length) of the craze.

Although crazes are not cracks, cracks leading to final fracture may indeed start at a craze. The polymeric chains in the crazed region get highly oriented in the direction of the applied stress. The void content, as previously mentioned, can be as high as 50 to 60%. Molecular chain entanglements play an important role in controlling craze geometry. Figure 8.44 shows, schematically, craze formation at a crack tip. Crazes are usually nucleated either at surface flaws (scratches, gouge marks, and cracks) or at internal flaws (dust particles and pores). In polymers, microvoids, which are an integral part of crazes, can form at various inhomogeneities in the microstructure, such as random density fluctuations in amorphous polymers, ordered regions in semicrystalline polymers, and particulate matter or inclusions such as fillers, flame retardants, or stabilizers in either kind of polymer. Craze formation is a process of dilation and is aided by hydrostatic tension and retarded by hydrostatic compression.

Atomic force microscopy (AFM) is a powerful addition to the arsenal of characterization and mechanical testing methods. The atomic force microscope enables observation of the surface at the nanometer scale. It can also be used to determine forces at the surface and the

**Fig. 8.43** A series of crazes produced in a tensile specimen of polycarbonate. (Used with permission from R. P. Kambour, *Polymer*, 4 (1963) 143.)



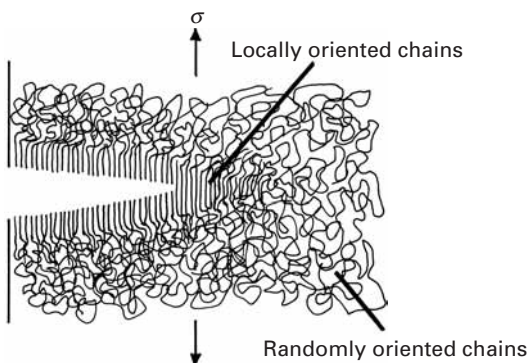


**Fig. 8.44** Schematic of craze formation at a crack tip.

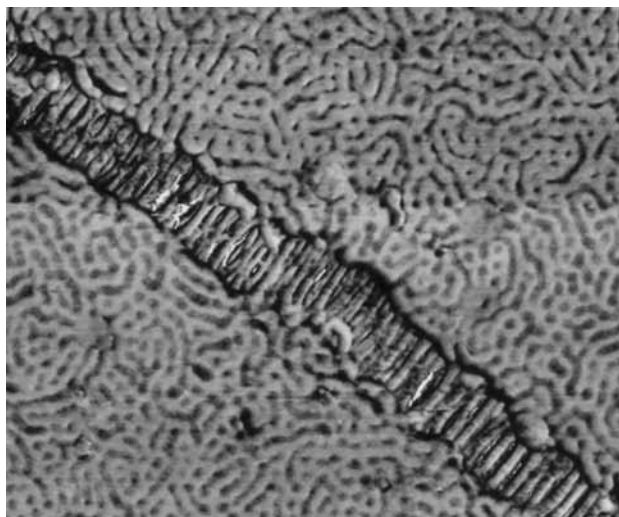


**Fig. 8.45** An incipient craze in polymer; note extended polymer chains in craze; Atomic force microscope (AFM) picture. (Courtesy of J. E. Kramer.)

mechanical properties of macromolecules, such as proteins. The tip of the AFM can be used as an indenter. The force is given through the stiffness of the cantilever beam. Figure 8.45 shows an AFM of a polymer containing a craze. The individual polymer molecules are imaged. They are random; thus, the polymer is glassy. An incipient craze runs diagonally through the micrograph. The polymer chains inside the craze are aligned.

The competition between shear yielding and crazing and the importance of the microstructure are shown in Figure 8.46. Polystyrene and polyphenylene oxide (PPO) are completely miscible at all concentrations. Atactic polystyrene (APS) shows the phenomenon of crazing preceding brittle fracture. By mixing the APS and PPO, we can suppress this embrittling tendency. In fact, near 50–50 concentration, crazing in APS is completely suppressed. Instead, extensive shear yielding occurs. The figure shows this phenomenon of transition between shear yielding and crazing in 300-nm films made of blends of APS and PPO and deformed 10% at room temperature. The lower left-hand corners show the weight percentages of APS in the mixture. The letters C, D, and S indicate crazing,

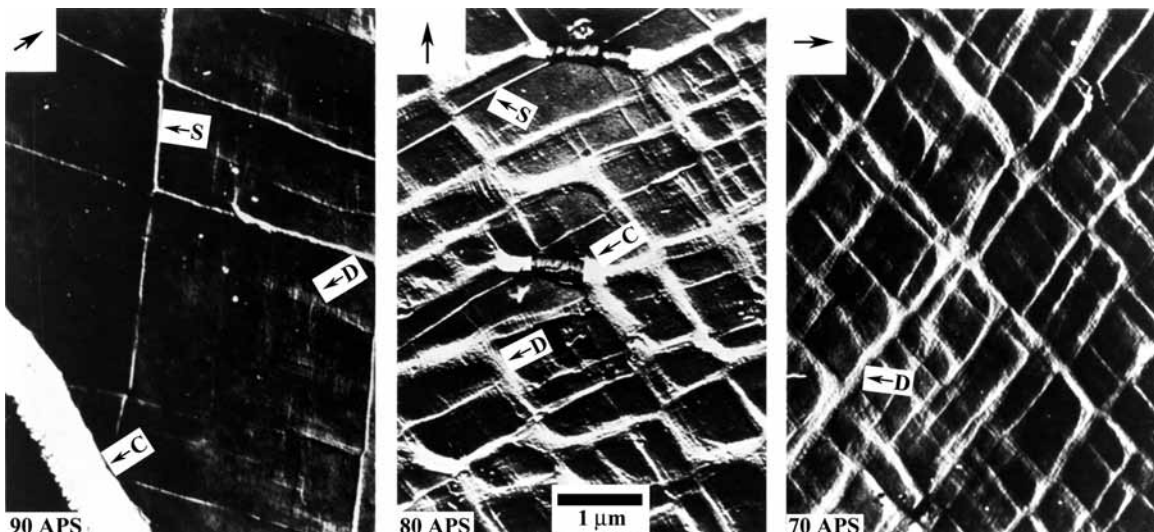


**Fig. 8.46** A transition between shear yielding and crazing in film blends of polypropylene oxide (PPO) and atactic polystyrene (APS) deformed 10% at room temperature (Used with permission from E. Baer, A. Hiltner, and H. D. Keith, *Science*, 235 (1987) 1015.). The APS weight percentages are shown in the lower left-hand corners. C, D, and S indicate crazing, diffuse shear, and sharp shear banding, respectively. The arrows indicate the direction of deformation.

diffuse shear banding, and sharp shear banding, respectively. The upper left-hand corners indicate the direction of deformation. Note that, as the amount of PPO increases, more and more crazes are blunted by shear bands. At 70% APS (or 30% PPO), only diffuse shear bands appear.

### 8.4.3 Fracture in Semicrystalline and Crystalline Polymers

The crystalline regions in a semicrystalline polymer have a folded chain structure; that is, the molecular chains fold back upon themselves to form thin platelets called lamellae. (See Chapter 1.) Amorphous material, containing chain ends, tie molecules, and other material that is difficult to crystallize, separates the different lamellae. The properties of such semicrystalline polymers can be highly anisotropic – very strong and stiff in the main chain direction and weak in the transverse direction. Parameters such as the degree of crystallinity, molecular weight, orientation of the crystals, etc., affect the mechanical behavior in general and the fracture behavior in particular. Because the polymers show a significant amount of viscoelastic behavior at their service temperature, the strain rate has a profound effect on their fracture behavior. Figure 8.47 shows schematically the effect of strain rate on the fracture path through a spherulitic polypropylene. At low strain rates the fracture follows an interspherulitic path, while at high strain rates the fracture becomes transsspherulitic.

As described in Chapter 1, polymers are generally amorphous or semicrystalline; it is almost impossible to get a 100% crystalline polymer. Invariably, there is some amorphous material in between crystalline regions, because defects such as chain ends, loops, chain folds, and entanglement are almost impossible to eliminate completely. Single crystals of monomeric polymers are prepared from dilute solutions

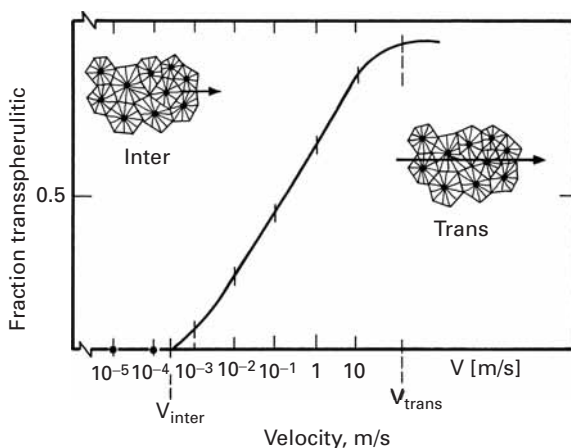


**Fig. 8.47** Effect of strain rate on the fracture path through polypropylene. At low strain rates the fracture is interspherulitic, while at high strain rates it is transsspherulitic. (After J. M. Schultz, *Polym. Sci. & Eng.*, 24 (1984) 770.)

or vapor phase deposition. These are transformed into polymers by means of a solid-state reaction. The technique has been successful with only certain substituted diacetylenes, and that, too, in an essentially one-dimensional form, i.e., short fibers. Nevertheless, these can be used to study the behavior of single-crystal polymers. Specifically, in terms of their fracture behavior, it has been observed that single-crystal polymers cleave parallel to the chain direction because of rather weak van der Waals bonding normal to the chain and strong covalent bonding in the direction of the chain. In polydiacetylene single-crystal fibers, the fracture strength  $\sigma_f$  shows the following dependence on fiber diameter<sup>11</sup>,  $d$ :  $\sigma \propto d^{-1/2}$ . This is similar to the size effect seen in other fibers; that is, preexisting defects lead to fracture, and the size of these defects is inversely proportional to the square root fiber diameter.

#### 8.4.4 Toughness of Polymers

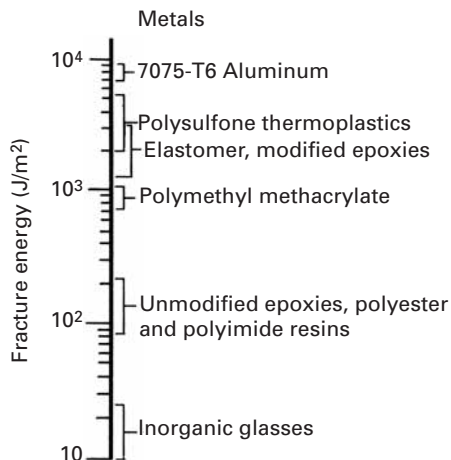
Thermosetting polymers such as polyesters, epoxies, and polyimides are highly cross-linked and provide adequate modulus, strength, and creep resistance. But the same cross-linking of molecular chains causes extreme brittleness, i.e., very low fracture toughness. Table 8.6 gives the plane-strain fracture toughness values of some common polymers at room temperature and in air. Figure 8.48 compares some common materials in terms of their fracture toughness, as measured by the fracture energy ( $G_{lc}$ ) in  $J/m^2$ . Note that thermosetting resins have values only slightly higher than those of inorganic glasses. Thermoplastic resins, such as polymethyl methacrylate, have fracture energies of about  $1\text{ kJ/m}^2$ , while polysulfone thermoplastics have fracture energies of several  $\text{kJ/m}^2$ , almost approaching those of the 7075-T6 aluminum alloy.

<sup>11</sup> R. J. Young, in *Developments in Oriented Polymers*, Vol. 2, ed. I. M. Ward (Essex, U.K.: Elsevier Applied Science, 1987), p. 1.

**Table 8.6** Plane-Strain Fracture Toughness ( $K_{Ic}$ ) of Some Polymers in Air at 20 °C

Polymer	$K_{Ic}$ (MPa m <sup>1/2</sup> )
Epoxy, unsaturated polyester	0.6
Polycarbonate	2.2
Polystyrene	1.0
Polymethylmethacrylate (PMMA)	1.7
Polyethylene	
High-density	2.1
Medium-density	5.0
Nylon	2.8
Polyvinyl chloride (PVC)	2.5

**Fig. 8.48** Fracture energy ( $G_{Ic}$ ) of some common materials. (After R. Y. Ting, in *The Role of Polymeric Matrix in the Processing and Structural Properties of Composites* (New York: Plenum Press, 1983), p. 171.)



Many approaches have been used to improve the toughness of polymers. Alloying or blending a given polymer with a polymer of higher toughness improves the toughness of the polymer. Among the well-known modified thermoplastics are acrylonitrile–butadiene–styrene (ABS) copolymer, high-impact polystyrene (HIPS), and nylon containing a polyolefin. Copolymerization can also lead to improved toughness levels. Generally, thermoplastics are tougher than thermosets, but there are ways to raise the toughness level of thermosets to that of thermoplastics or even higher. One such approach involves the addition of rubbery, soft particles to a brittle thermoset. For example, a class of thermosetting resins that comes close to polysulfones, insofar as toughness is concerned, is the elastomer-modified epoxies. Elastomer- or rubber-modified thermosetting epoxies make multiphase systems, i.e., a kind of composite. Small (a few micrometers or less), soft, rubbery inclusions distributed in a hard, brittle epoxy enhance its toughness by several orders of magnitude. The methods of incorporation of elastomeric particles can be

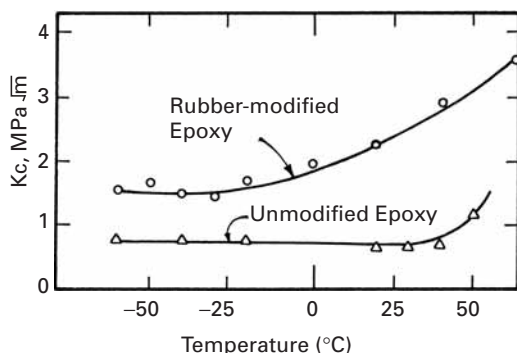


**Fig. 8.49** Fracture toughness as a function of temperature of unmodified epoxy and rubber-modified epoxy. (After J. N. Sultan and F. J. McGarry, *Polymer Eng. Sci.*, 13 (1973) 29.)

simple mechanical blending of the soft, rubbery particles and the resin or copolymerization of a mixture of the two. Mechanical blending allows only a small amount (less than 10%) of rubber to be added, whereas larger amounts can be added during polymerization. Figure 8.49 shows toughness as a function of temperature for an unmodified epoxy and a rubber-modified epoxy. Note the higher toughness and enhanced temperature dependence of the rubber-modified epoxy. Epoxy and polyester resins can also be modified by introducing carboxyl-terminated butadiene-acrylonitrile copolymers (CTBNs). Figure 8.50 shows the increase in fracture surface energy of an epoxy as a function of the percent weight of CTBN elastomer. Toughening of glassy polymers by elastomeric additions involves different mechanisms in different polymers. Among the proposed mechanisms for this enhanced toughness are triaxial dilation of the rubber particles at the crack tip, particle elongation, craze initiation, and shear yielding of the polymer.

Like the fracture toughness of a metal or a ceramic, the fracture toughness of a polymer is a sensitive function of its microstructure and test temperature. Most polymers, however, are viscoelastic, and this time-dependent property can influence their fracture toughness as well. The data in Table 8.6 were obtained at ambient temperature, and we see that the toughness range for polymers is 1–5 MPa  $m^{1/2}$  compared to 10–100 MPa  $m^{1/2}$  for metals and 1–10 MPa  $m^{1/2}$  for ceramics. In an elastic or time-independent material, fracture toughness is independent of the crack velocity; in a viscoelastic or time-dependent material, steady-state crack growth can occur at an applied stress intensity that is less than the critical value. Figure 8.51(a) shows this schematically, while Figure 8.51(b) shows an actual curve of stress intensity versus crack velocity for PMMA. Note that the data are plotted on a log-log scale. A semilog plot of the same curve for PMMA to much higher crack velocities is shown in Figure 8.52. The same trend is observed in metals, where the yield stress increases with strain rate.<sup>12</sup>

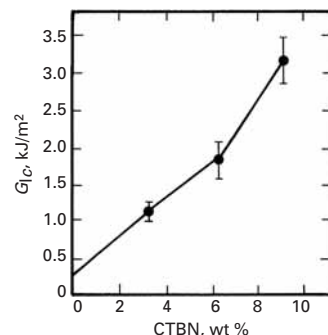


**Fig. 8.50** Increase in fracture energy as a function of percent weight of carboxyl-terminated butadiene-acrylonitrile. (After A. K. St. Clair and T. L. St. Clair, *Int. J. Adhesion and Adhesives*, 1 (1981) 249.)

<sup>12</sup> M. A. Meyers, *Dynamic Behavior of Materials* (New York: J. Wiley, 1994).

**Fig. 8.51** (a) Variation of stress intensity ( $\ln K$ ) as a function of crack velocity ( $\ln \dot{a}$ ) for an elastic and viscoelastic material. (b) Stress intensity ( $K$ ) vs. crack velocity ( $\ln \dot{a}$ ) for PMMA.  $K_{lc}$  corresponds to a crack velocity of several hundred  $\text{m s}^{-1}$ . (After G. P. Marshall, L. H. Coutts, and J. G. Williams, *J. Mater. Sci.*, 9 (1974) 1409.)

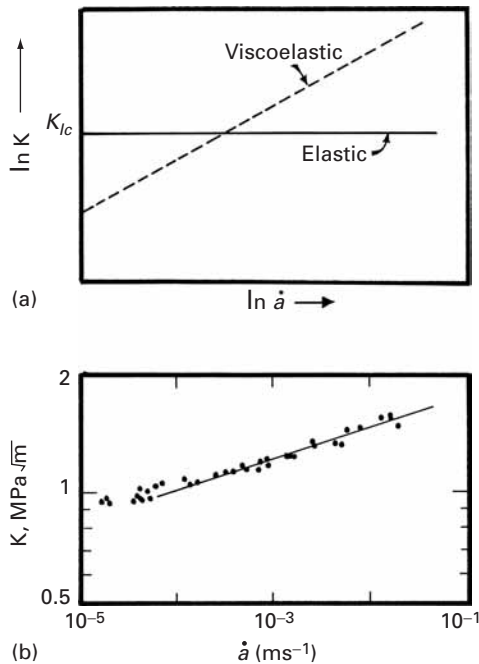
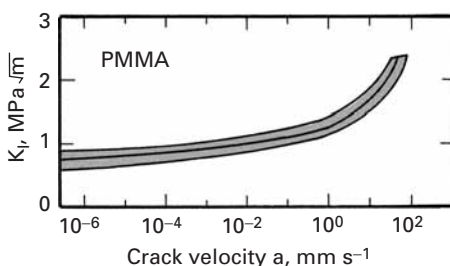


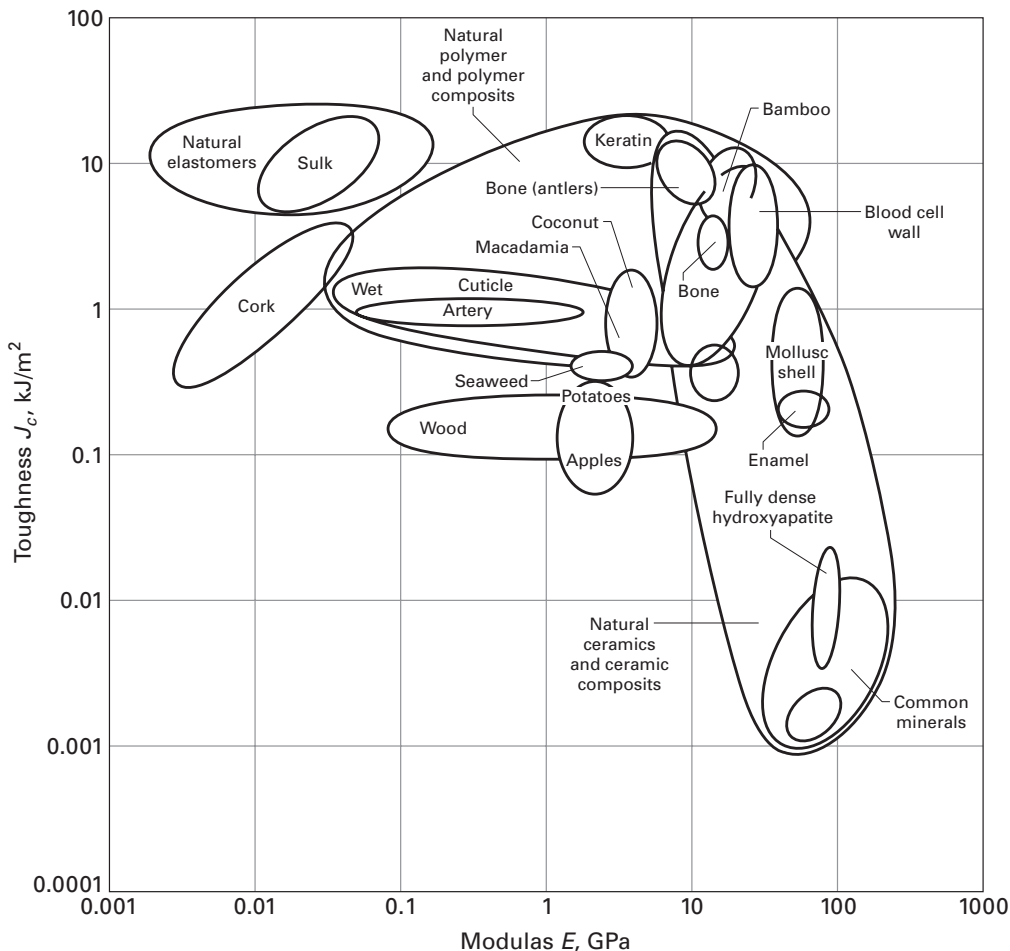
**Fig. 8.52** Variation of stress intensity factor with crack velocity in PMMA. (After W. Döll, *Advances in Polymer Science* (Berlin: Springer-Verlag, 1983), p. 119.)



### Example 8.2 |

Describe how the phenomenon of crazing can be exploited to improve the toughness of a polymer.

**Answer:** Craze formation requires energy. Thus, if we increase the number of crazes nucleated, but do not allow them to grow to fracture, we can improve the toughness of a polymer. Such a mechanism is made use of in acrylonitrile butadiene styrene (ABS), which has a much higher toughness than polystyrene (PS). The acrylonitrile and styrene form a single-phase copolymer. Butadiene is dispersed in this copolymer matrix as elastomeric particles. These particles have a layer of styrene-acrylonitrile grafted onto them. Thus, ABS has a two-phase structure. When ABS is stressed, crazes nucleate at rather low strains at the elastomer-styrene interface. However, the high extensibility of



elastomeric particles inhibits the growth of these crazes. A small and uniform particle size aids in producing a high density and an even distribution of crazes in ABS. The reader can easily verify this phenomenon by bending a thin strip of ABS. It will become white, called *stress whitening*, due to the formation of a large number of crazes.

**Fig. 8.53** Toughness of biological materials as a function of strength; fracture toughness  $K_c = (EJ_c)^{1/2}$ . (Courtesy of M. F. Ashby.)

## 8.5 Fracture and Toughness of Biological Materials

Figure 8.53 provides the fracture toughness ( $J_c$ ) for a number of biological materials as a function of elastic modulus. The square of fracture toughness ( $K_c$ ) can be obtained by multiplying  $J_c$  by the Young modulus. (See Section 7.7.5.) Figure 8.53 provides a valuable insight into the toughness of biological materials. For instance, shells have a toughness much superior to calcite, although the composition is similar. This is because shells are a composite of calcium carbonate and a thin organic glue layer.

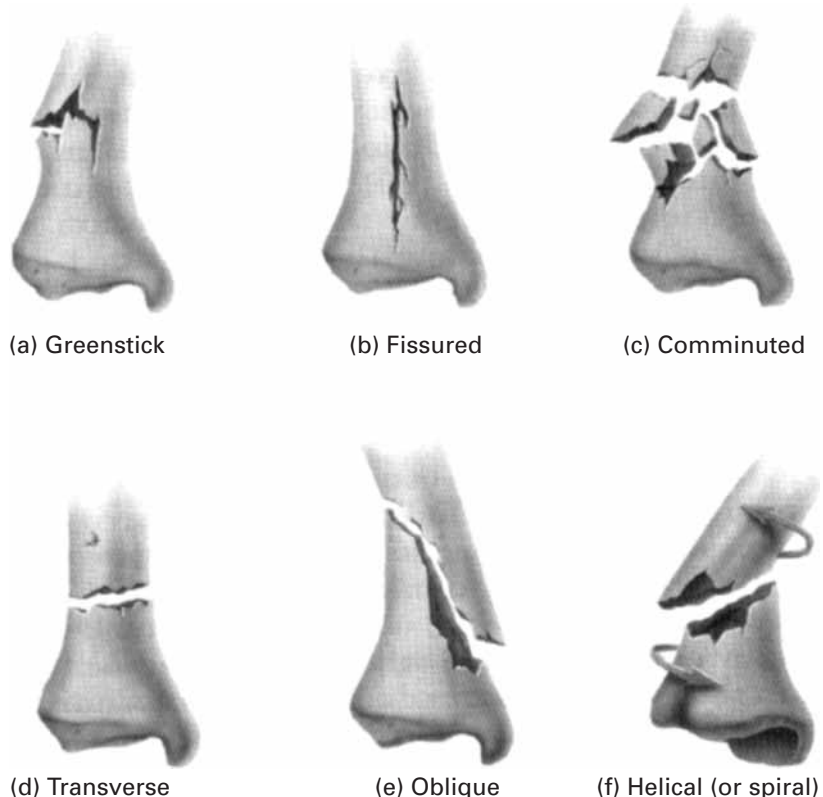


**Fig. 8.54** Six modes of fracture in bone. (Adapted from S. J. Hall, *Basic Biomechanics*, 4th ed. (Boston: McGraw Hill, 2003), p. 102.)

Of extreme importance is the fracture and fracture prevention in bone. We know that bone strength decreases as porosity increases. This is one of the changes undergone by bone with aging. There are many fracture morphologies in bone, depending on the loading stresses, rate of loading, and condition of bone. Figure 8.54 presents some of these modalities.

- (a) **Greenstick fracture:** This occurs in young bone, that has a large volume fraction of collagen, and can break as a green twig. This zig-zag fracture indicates a high toughness.
- (b) **Fissured fracture:** This corresponds to a longitudinal crack in bone.
- (c) **Comminuted fracture:** In this many fragments are formed. This is typical of a fracture caused by impact at high velocities. Two factors play a key role. As the velocity of projectile is increased, its kinetic energy increases. This energy is transferred to the bone. The second factor is that at high rates, many cracks are produced simultaneously; they can grow independently until their surfaces intersect. This is the reason why a glass, when thrown on the ground violently, shatters into many small fragments. An additional reason is that the bone becomes stiffer and more brittle as the strain rate is increased.

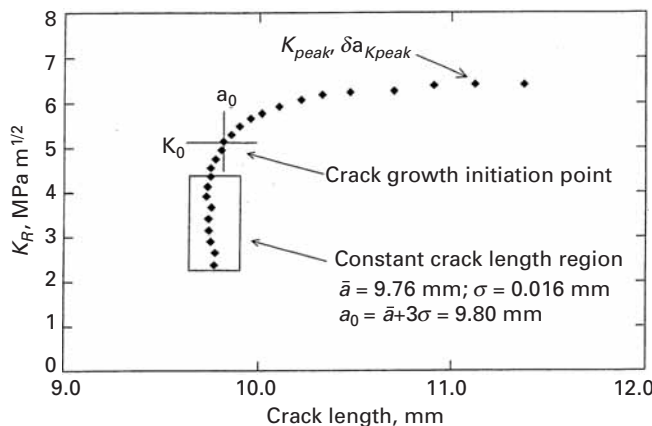


**Fig. 8.55** Crack resistance curve as a function of length for horse bone. (From C. L. Malik, J. C. Gibeling, R. B. Martin, and S. M. Stover, “R-Curve Fracture Mechanics of Equine Cortical Bone,” *J. Biomech.*, 36 (2003) 191.)

- (d) **Transverse fracture:** This is a complete fracture approximately normal to the axis of the bone.
- (e) **Oblique fracture:** This is a complete fracture oblique to the bone axis.
- (f) **Helical fracture:** This fracture, which is also called spiral, is caused by torsional stresses.

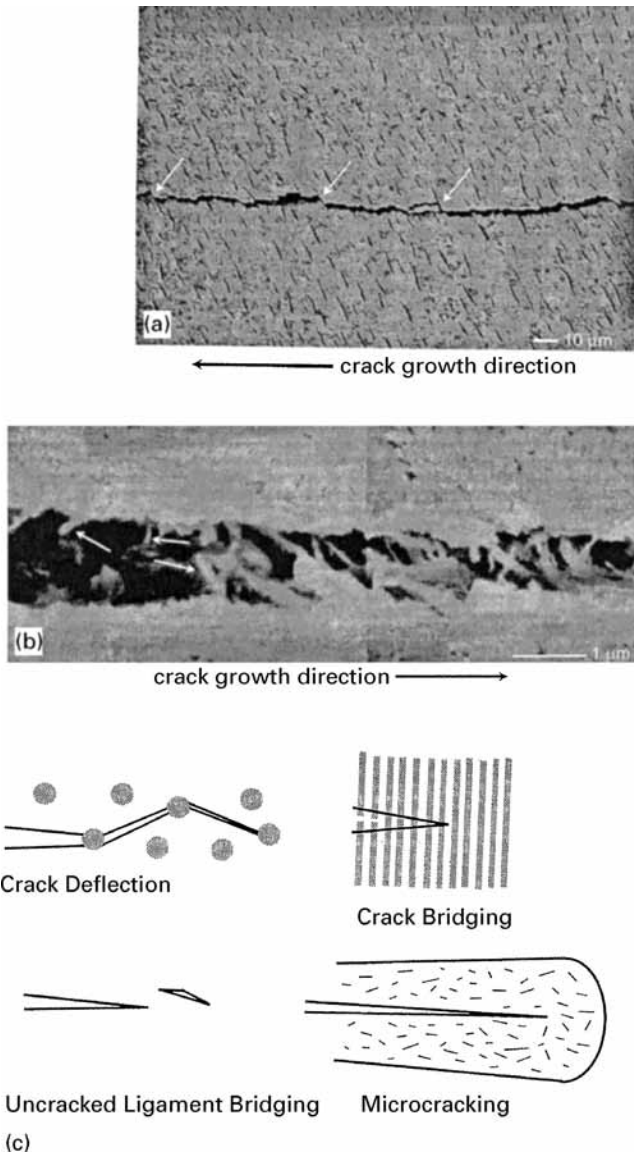
The curious student should take a piece of chalk and twist it with her hands. A beautiful helical fracture will result. This type of fracture is known, in the medical community, as spiral. However, this name is not correct, and a helix describes the crack trajectory better than a spiral. Chapter 2 (Example 2.6) provides more information.

Biological materials such as bones and teeth also can be characterized by means of fracture mechanics parameters. For instance, Malik and coworkers<sup>13</sup> studied the fracture toughness of the leg bones (third metacarpal bone) in horses and found that fracture toughness increased with crack length. This behavior is similar to ceramic matrix composites. This increase in fracture toughness with crack growth in ceramic matrix composites is indicative of mechanisms of toughening in the material that are due to the existence of the reinforcing and matrix component. Microcracks in the ceramic phase can produce a decrease in overall stress concentration.

When the fracture toughness is dependent on crack size, linear elastic fracture mechanics cannot be applied and one has to apply other testing methods, such as R curve. In the case of horse leg bone, it was found that there was debonding along macroscopic lamellar structures ahead of the crack, leading to crack deflection, crack energy absorption, and toughening as the crack grew. Figure 8.55 shows the increase in  $K_R$  with crack length. For an initial crack length of 9.76 mm, the initial value of the toughness is 5  $\text{MPa m}^{1/2}$ . The toughness increases to  $>6 \text{ MPa m}^{1/2}$  with increasing crack length.

<sup>13</sup> C. L. Malik, J. C. Gibeling, R. B. Martin, and S. M. Stover, *J. Biomech.*, 36 (2003) 191.

**Fig. 8.56** (a) Microcracks in wake of crack and deflection of crack plane by microcracks; (b) bridging behind crack by collagen ligaments; (c) schematic showing four mechanisms contributing to toughening in dentin. (From R. K. Nalla, J. H. Kinney, and R. O. Ritchie, *Biomaterials*, 24 (2003) 3955.)



Several mechanisms of toughening can be identified in dentin, the major component of teeth. Dentin is a composite consisting of nanosized apatite crystals and collagen. The structure is characterized by tubules, which are hollow tubes with a diameter of approximately 1 μm (in elephant tusk). In human teeth, the tubules are similar but have a circular, not elliptical, cross section.

The crack propagation is affected by microcracks produced during loading. Figure 8.56(a) shows microcracks forming a regular pattern and contributing to an irregular crack path. The areas where the crack front was affected by existing microcracks is marked by arrows. These microcracks form ahead of the crack tip and would, at first sight, be considered a weakening mechanism. However, they toughen brittle

materials by delocalizing the stresses. Another toughening mechanism that was identified was the bridging of the crack by collagen fibers. This is shown in Figure 8.56(b). Figure 8.56(c) shows a schematic of the four toughening mechanisms thought to operate in dentin.

## 8.6 | Fracture Mechanism Maps

Data presented in the form of mechanism maps can be very useful, in as much as such maps organize information that is widely scattered in a variety of sources. The idea of mechanism maps is just an extension of the concept of phase diagrams in alloy chemistry, in which different phases coexisting in multicomponent systems are represented as a function of composition and temperature.

Fracture mechanism maps provide information about mechanical properties in a compact form. With these maps, one can plot normalized tensile strength  $\sigma/E$  against the homologous temperature  $T/T_m$ . Regions of different types of fracture are classified on the basis of fractography, or fracture-time or fracture-strain studies. Figure 8.57 shows examples of fracture mechanism maps. Such maps can be developed for metals (see Figure 8.57(a) for nickel), ceramics (see Figure 8.57(b) for alumina), and polymers. One can also plot stress intensity factor against temperature and obtain information about crack growth during the fracture process.

## Suggested Reading

M. F. Ashby, *Materials Selection in Mechanical Design*, 2nd ed. Oxford: Elsevier, 1999.

## Exercises

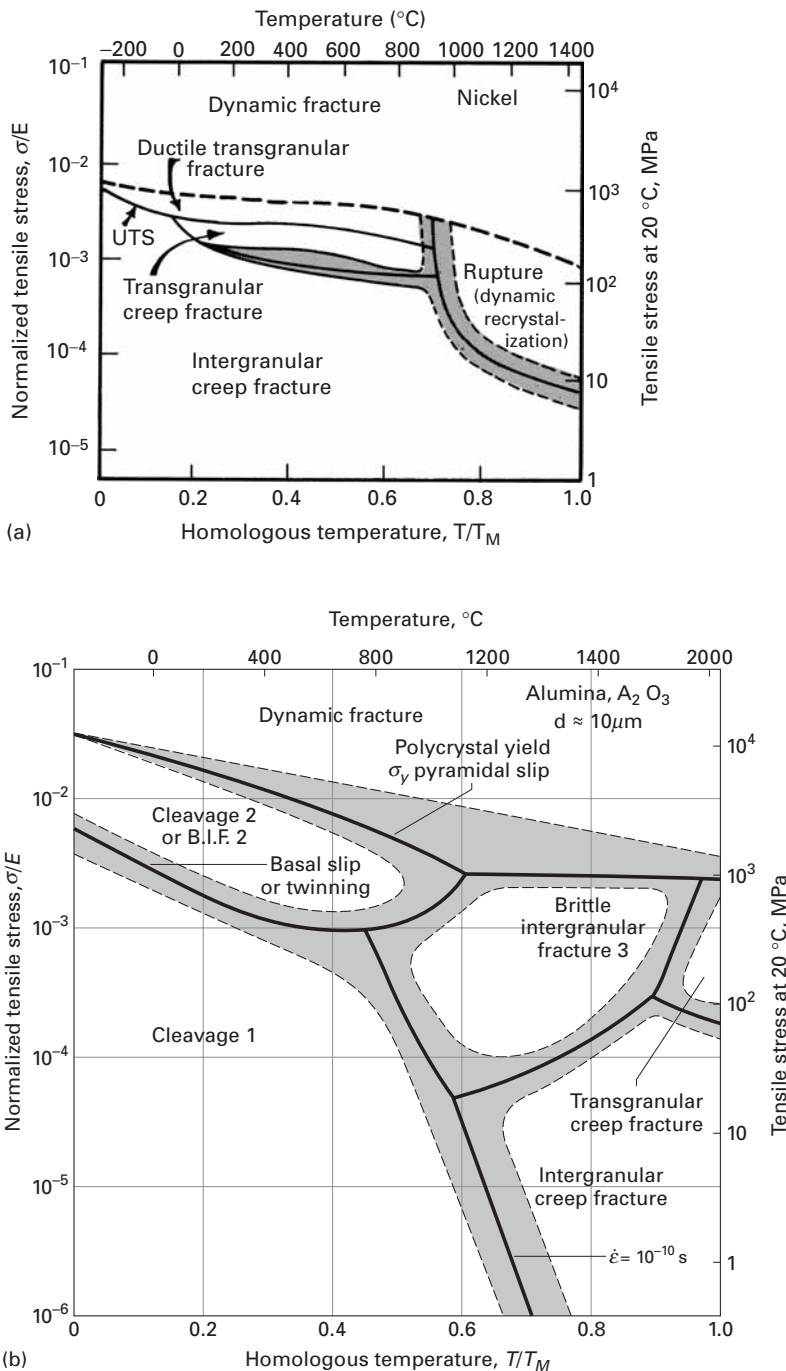
**8.1** In Figure 8.6, mechanical twinning has generated microcracks that, in subsequent tensile tests, weakened the specimen. The ultimate tensile strength of tungsten is 1.2 GPa, and its fracture toughness is approximately  $70 \text{ MPa m}^{1/2}$ . By how much is the fracture stress decreased due to the presence of the microcracks?

**8.2** Explain why FCC metals show a ductile fracture even at low temperatures, while BCC metals do not.

**8.3** Show, by a sequence of sketches, how the neck in pure copper and in copper with 15% volume fraction of a second phase will develop. Using values from Figure 8.17, show the approximate configuration of the final neck.

**8.4** Alumina specimens contain flaws introduced during processing; these flaws are, approximately, equal to the grain size. Plot the fracture stress vs. grain size (for grains below 200  $\mu\text{m}$ ), knowing that the fracture toughness for alumina is equal to  $4 \text{ MPa m}^{1/2}$ . Assume  $Y = 1$ .

**Fig. 8.57** (a) Fracture mechanism map for nickel tested in tension; shading indicates a mixed mode of fracture. (Adapted from M. F. Ashby, C. Gandhi, and D. M. R. Taplin, *Acta Met.*, 27 (1979), 699.) (b) Fracture mechanism map for alumina with grain size of  $10 \mu\text{m}$ . (Adapted from C. Gandhi and M. F. Ashby, *Acta Met.*, 27 (1979), 1565.)



8.5 Calculate the theoretical cleavage stress for sapphire (monocrystalline  $\text{Al}_2\text{O}_3$ ) along its four crystallographic orientations. (See Table 8.5.)

#### 8.6

- (a) Calculate the compressive strength for a ceramic containing crack of size  $100 \mu\text{m}$ . Let  $\mu$  be the coefficient of friction between the flaw walls and  $\ell$

be the length of the cracks generated at the ends of an existing flaw. (See Figure 8.36.) Assume that the onset of failure corresponds to a value of  $\ell = 2a$  and that  $\mu = 1$ , and that  $K_{Ic} = 4 \text{ MN m}^{1/2}$ .

- (b) Compare the tensile strength with the compressive strength that you obtained in part (a).

**8.7** A ceramic with  $K_{Ic} = 4 \text{ MPa m}^{1/2}$  contains pores with radius  $a = 5 \mu\text{m}$  due to incomplete sintering. These pores lead to a decrease in the failure stress of the material in both tension and compression. One in every ten grain-boundary junctions contains a void; the grain size of the ceramic is  $50 \mu\text{m}$ . The ceramic fails in compression when the length  $\ell$  of each crack generated at the voids equals one-half of the spacing between the voids.

- (a) Determine the compression strength of the ceramic, using the equation from Sammis and Ashby.  
(b) Determine the tensile strength of the ceramic, assuming flaws with size  $a$ .

**8.8** Using the micrographs of Figure 8.31, establish, for  $\text{Al}_2\text{O}_3$  ( $K_{Ic} = 2.5 \text{ MPa m}^{1/2}$ ), (a) the strength in compression, using the Sammis–Ashby equation from the previous problem, and (b) the tensile strength.

**8.9** Tempering is the treatment given to flat glass (e.g., the glass window in the oven in your kitchen) by quenching the glass in a suitable liquid. Draw schematically the stress distribution in such a glass as a function of the thickness of a glass sheet. Discuss the significance of the stress distribution obtained in tempered glass.

**8.10** Estimate the internal thermal stress generated in a polycrystalline sample of titanium dioxide for  $\Delta T = 1,000^\circ\text{C}$ . Young's modulus for  $\text{TiO}_2 = 290 \text{ GPa}$ , and the expansion coefficients along the direction  $a$  and  $c$  are:

$$\alpha_a = 6.8 \times 10^{-6} \text{ K}^{-1},$$

$$\alpha_c = 8.3 \times 10^{-6} \text{ K}^{-1}.$$

Assume  $K_c = \sigma \sqrt{\pi a}$ .

**8.11**  $\text{Si}_3\text{N}_4$  has a surface energy equal to  $30 \text{ J/m}^2$  and an atomic spacing  $a_0 \approx 0.2 \text{ nm}$ . Calculate the theoretical strength of this material (see Chapter 7), and compare the value you get with the one experimentally observed in tension testing ( $\sigma = 550 \text{ MPa}$ ). Calculate the flaw size that would cause this failure stress.

**8.12** The theoretical density of a polymer is  $1.21 \text{ g cm}^{-3}$ . By an optical technique, it was determined that the crazed region in this polymer had 40% porosity. What is the density of the crazed region? Can you estimate the elastic modulus of the crazed region as a percentage of the modulus of the normal polymer?

**8.13** A polycarbonate sample showed a craze growth length and time relationship of

$$\ell = k \log(t/t_0),$$

where  $\ell$  is the craze length at time  $t$ ,  $t_0$  is the time crazing is initiated after the application of the load, and  $k$  is a constant. For a given temperature and

stress, find the rate of craze growth. Comment on the implications of the relationship that you obtain.

**8.14** Craze formation is a plastic deformation mechanism that occurs without lateral contraction. What can you say about the Poisson ratio of the crazed material?

**8.15** The *Titanic* sank on April 14–15, 1912 after hitting an iceberg. Ironically, this ship had been dubbed the “Unsinkable.” This was a tremendous shock. In 1985, the wreck was discovered and explored. Why did the 46,000-ton ship sink in less than three hours?

Hint: Entire hull steel plates littered the bottom of the sea. Metallurgical examinations carried out at NIST revealed that the wrought iron in the rivets that joined the plates contained three times today's allowable amount of slag (the glassy residue left behind after the smelting of ore).

**8.16** The famous accident of the NASA *Challenger* space shuttle that occurred on a cold night was caused by a faulty O-ring. Explain the accident.

**8.17** Describe the microscopic processes that take place during ductile and brittle fracture. What are the differences in appearance of these fractures?

**8.18** Figure 8.10 shows *r*-type cavities nucleated at grain boundaries in copper. Assuming that the applied stress is in the vertical direction, make a sketch of the consecutive events that would occur along the grain boundaries.

**8.19** At a homologous temperature ( $T/T_m$ ) of 0.6, describe the fracture mechanism changes that alumina would undergo as the normalized stress is increased from  $10^{-5}$  to  $10^{-3}$ . Use the fracture mechanism map for alumina (Figure 8.57(b)) to answer this question.

---

# Chapter 9

## Fracture Testing

---

### 9.1 | Introduction

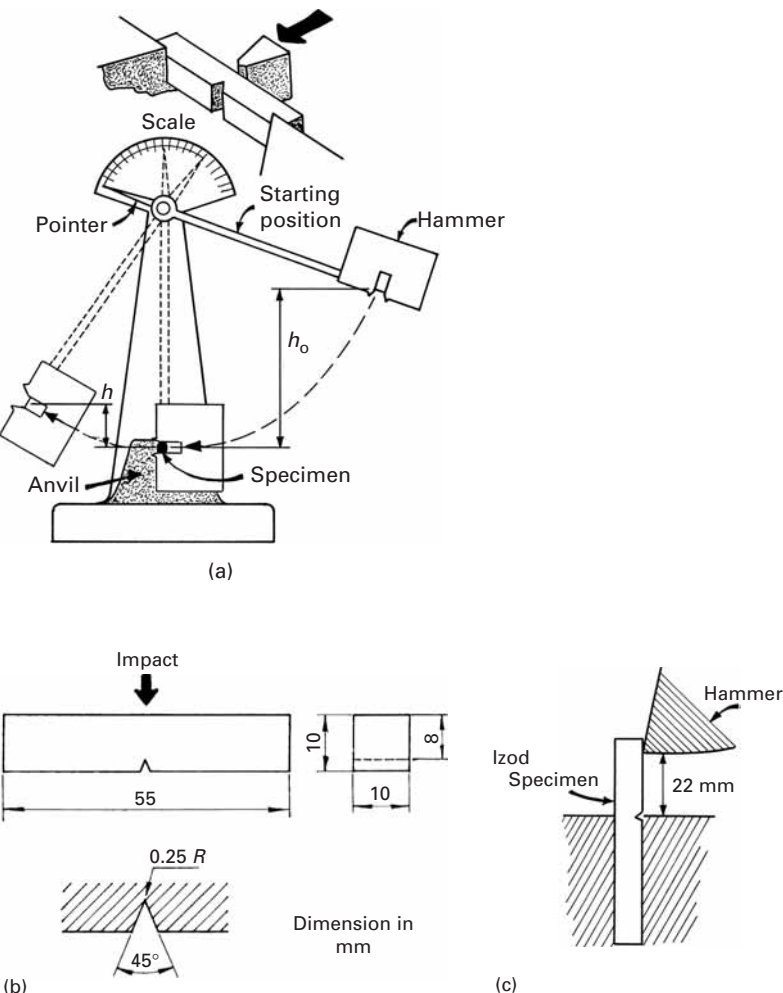
Fracture of any material (be it a recently acquired child's toy or a nuclear pressure vessel) is generally an undesirable happening, resulting in economic loss, an interruption in the availability of a desired service, and, possibly, damage to human beings. Besides, one has good, technical reasons to do fracture testing: to compare and select the toughest (and most economical material) for given service conditions; to compare a particular material's fracture characteristics against a specified standard; to predict the effects of service conditions (e.g., corrosion, fatigue, stress corrosion) on the material toughness; and to study the effects of microstructural changes on material toughness. One or more of these reasons for fracture testing may apply during the design, selection, construction, and/or operation of material structures. There are two broad categories of fracture tests; qualitative and quantitative. The Charpy impact test exemplifies the former, and the plane-strain fracture toughness ( $K_{Ic}$ ) test illustrates the latter. We describe briefly important tests in both of these categories.

---

### 9.2 | Impact Testing

We saw in Chapter 7 that stress concentrations, like cracks and notches, are sites where failure of a material starts. It has been long appreciated that the failure of a given material in the presence of a notch is controlled by the material's fracture toughness. Many tests have been developed and standardized to measure this "notch toughness" of a material. Almost all are qualitative and comparative in nature. As pointed out in Chapter 7, a triaxial stress state, high strain rate, and low temperature all contribute to a brittle failure of the material. Thus, in order to simulate most severe service conditions, almost all of these tests involve a notched sample, to be broken by impact over a range of temperatures.

**Fig. 9.1** (a) Charpy impact testing machine. (b) Charpy impact test specimen. (c) Izod impact test specimen.



### 9.2.1 Charpy Impact Test

The Charpy V-notch impact test is an ASTM standard. The notch is located in the center of the test specimen, which is supported horizontally at two points. The specimen receives an impact from a pendulum of a specific weight on the side opposite that of the notch (Figure 9.1). The specimen fails in flexure under impact.

The energy absorbed by the specimen when it receives the impact from the hammer is equal to the difference between the potential energies of the hammer before and after impact. If the hammer has mass  $m$ , then

$$E_f = mg(h_0 - h_1),$$

where  $E_f$  is the sum of the energy of plastic deformation, the energy of the new surfaces generated, and the vibrational energy of the entire system;  $h_0$  is the initial height of the hammer;  $h_1$  is the hammer's final height; and  $g$  is the acceleration due to gravity. Of these, the

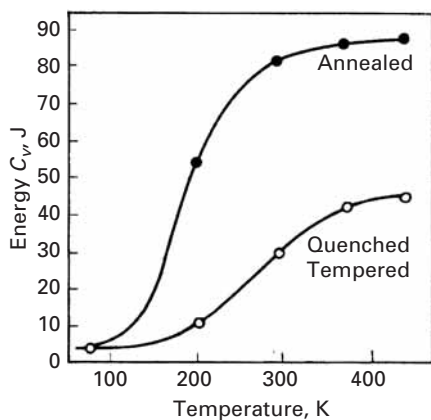


**Fig. 9.2** Energy absorbed versus temperature for a steel in annealed and in quenched and tempered states. (Adapted with permission from J. C. Miguez Suarez and K. K. Chawla, *Metalurgia-ABM*, 34 (1978) 825.)

first is the most significant term, and it may be assumed that the Charpy energy is

$$CV \approx mg(h_0 - h_1). \quad (9.1)$$

At impact with the specimen, the hammer has a velocity (the student should consult his or her physics textbook)

$$v = (2gh_0)^{1/2}.$$

For a difference in height of 1 m,

$$v = 4.5 \text{ m/s.}$$

If we assume that the average length over which plastic deformation takes place is 5 mm, we have

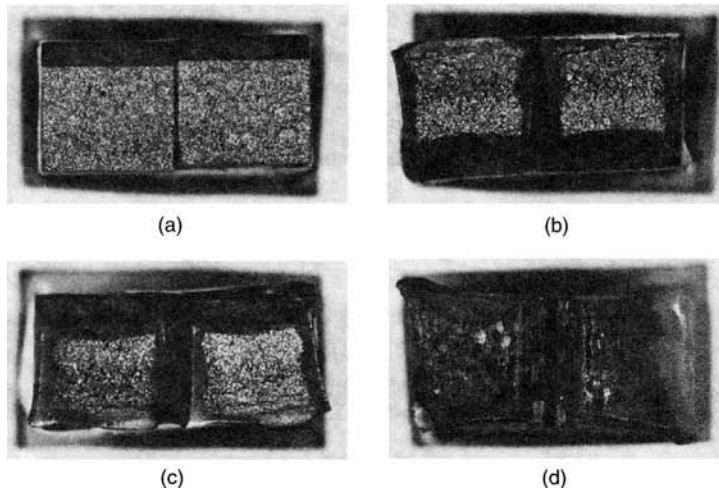
$$\dot{\varepsilon} = \frac{v}{L} \approx 10^3 \text{s}^{-1}.$$

We see, then, that the strain rate in a Charpy test is very high.

In the region around the notch in the test piece, there exists a triaxial stress state due to a plastic yielding constraint there. This triaxial stress state and the high strain rates enhance the tendency toward brittle failure. Generally, we present the results of a Charpy test as the energy absorbed in fracturing the test piece. An indication of the tenacity of the material can be obtained by an examination of the fracture surface. Ductile materials show a fibrous aspect, whereas brittle materials show a flat fracture.

A Charpy test at only one temperature is not sufficient, however, because the energy absorbed in fracture drops with decreasing test temperature. Figure 9.2 shows this variation in the energy absorbed as a function of temperature for a steel in the annealed and in the quenched and tempered states. The temperature at which a change occurs from a high-energy fracture to a low-energy one is called the *ductile-brittle transition temperature* (DBTT). However, since, in practice, there occurs not a sharp change in energy, but instead, a transition zone, it becomes difficult to obtain this DBTT with precision. Figure 9.3 shows how the morphology of the fracture surface changes

**Fig. 9.3** Effect of temperature on the morphology of fracture surface of Charpy steel specimen. Test temperatures  $T_a < T_b < T_c < T_d$ . (a) Fully brittle fracture. (b, c) Mixed-mode fractures. (d) Fully ductile (fibrous) fracture. Each side of the specimen is 10 mm.



in the transition region. The greater the fraction of fibrous fracture, the greater is the energy absorbed by the specimen. A brittle fracture has a typical cleavage appearance and does not require as much energy as a fibrous fracture. BCC and HCP metals or alloys show a ductile-brittle transition, whereas FCC structures do not. Thus, generally a series of tests at different temperatures is conducted that permits us to determine a transition temperature. This temperature, however arbitrary, is an important parameter in the selection of materials, from the point of view of tenacity, or the tendency of occurrence of brittle fracture. Because the transition temperature is, generally, not very well defined, there exist a number of empirical ways of determining it, based on a certain absorbed energy (e.g., 15 J), change in aspect of the fracture (e.g., the temperature corresponding to 50% fibrous fracture), lateral contraction (e.g., 1%) that occurs at the notch root, or lateral expansion of the specimen. The transition temperature depends on the chemical composition, heat treatment, processing, and microstructure of the material. Among these variables, grain refinement is the only method that results in both an increase in strength of the material in accordance with the Hall-Petch relation and, at the same time, a reduction in the transition temperature (see Section 8.2.2). Heslop and Petch<sup>1</sup> showed that the transition temperature  $T_c$  depended on the grain size  $D$  according to the formula

$$\frac{dT_c}{d \ln D^{1/2}} = -\frac{1}{\beta},$$

where  $\beta$  is a constant. This is explained by the Armstrong criterion (Section 8.2.3). Thus, a graph of  $T_c$  against  $\ln D^{1/2}$  will be a straight line with slope  $-1/\beta$ .

In Figure 9.4, the fraction of the fracture area that is cleavage and the lateral expansion of the Charpy specimen are plotted, in

<sup>1</sup> J. Heslop and N. J. Petch, *Phil. Mag.*, 3 (1958) 1128.

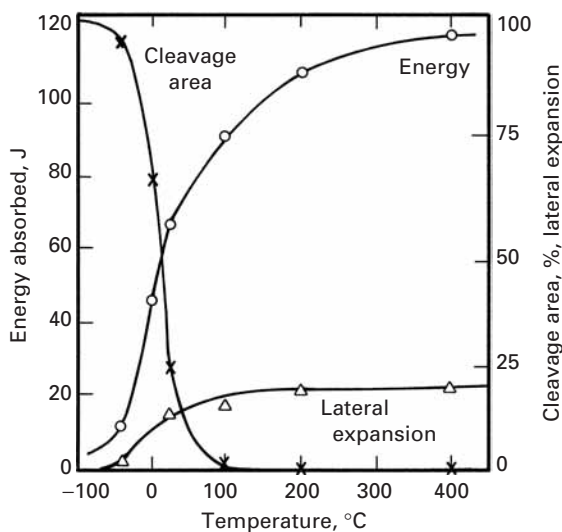


**Fig. 9.4** Results of Charpy tests for AISI 1018 steel (cold-drawn).

addition to the energy absorbed by the hammer. The excellent correlation among the three curves is plain, and this test simulates the dynamic response of a metal.

Figure 9.1(c) shows a second specimen geometry also commonly used (especially for plastics) in the same experimental configuration as the Charpy test. It is called the “Izod” specimen. The cross section ( $10 \times 10$  mm) and V-notch geometry of the specimen are identical, but one of the sides is longer. The specimen is held up vertically, and the notch is, in this case, on the same side as the impact.

There is a good “engineering” correlation between Charpy V-notch energy (CVN) and the fracture toughness of some steels in the upper shelf (above the ductile–brittle transition temperature):

$$\left(\frac{K_{Ic}}{\sigma_{ys}}\right)^2 = \frac{5}{\sigma_{ys}} \left( CVN - \frac{\sigma_{ys}}{20} \right).$$

Like many “engineering” correlations, it is unit dependent. In the equation above, the following units should be used:  $K_{Ic} \rightarrow \text{ksi.in}^{1/2}$  and  $\sigma_{ys} \rightarrow \text{ksi}$ , where  $\sigma_{ys}$  is the yield strength. This equation enables us to estimate the fracture toughness (a complicated test) from the Charpy V-notch energy (a simple test).

### 9.2.2 Drop-Weight Test

The drop-weight test is used to determine a reproducible and well-defined ductile–brittle transition in steels. The specimen consists of a steel plate containing a brittle weld on one surface. A cut is made in the weld with a saw to localize the fracture (Figure 9.5). The specimen is treated as a “simple edge-supported beam” with a stop placed below the center to limit the deformation to a small amount (3%) and prevent general yielding in different steels. The load is applied by means of a freely falling weight striking the side of the specimen opposite to the crack starter. Tests are conducted at 5-K intervals,

**Fig. 9.5** Drop-weight test specimen.

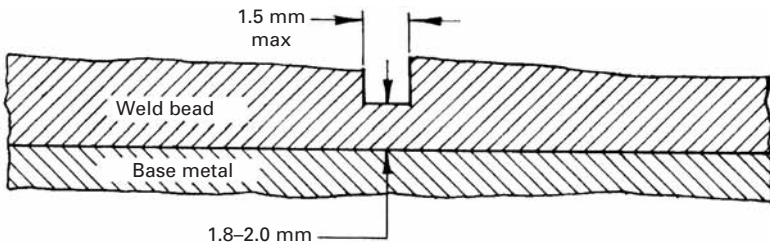
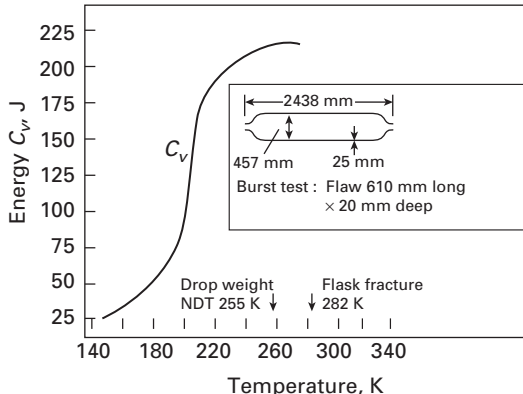


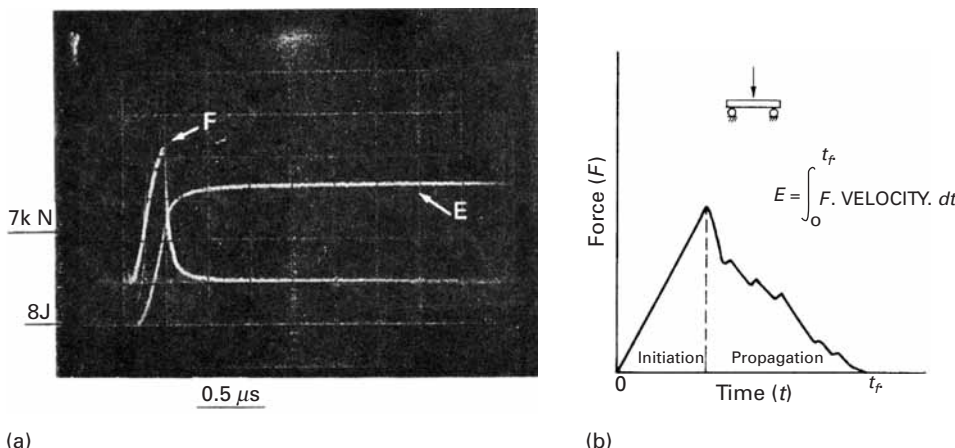
**Fig. 9.6** Charpy V-notch curve for a pressure-vessel steel. Note that the NDT temperature determined by the drop-weight test corresponds to the high-toughness region of the Charpy curve. Pneumatic pressurization; material: 2.25 Cr-1 Mo steel, yield stress 590 MPa. (After W. J. Langford, *Can. Met. Quart.*, 19 (1980) 13.)



and a break/no-break temperature, called the *nil ductility transition (NDT) temperature*, is determined. The NDT temperature is thus the temperature below which a fast, unstable fracture (i.e., brittle fracture) is highly probable. Above that temperature, the toughness of the steel increases rapidly with temperature. This transition temperature is more precise than the Charpy-based transition temperature. The drop-weight test uses a sharp crack that moves rapidly from a notch in a brittle weld material, and thus, the NDT temperature correlates well with the information from a  $K_{Ic}$  test, described in Section 9.3. The drop-weight test provides a useful link between the qualitative “transition temperature” approach and the quantitative “ $K_{Ic}$ ” approach to fracture.

The test affords a simple means of quality control through the NDT temperature, which can be used to group and classify various steels. For some steels, identification of the NDT temperature indicates safe minimum operating temperatures for a given stress. That the drop-weight NDT test is more reliable than a Charpy V-notch value of the transition temperature is illustrated in Figure 9.6 for a pressure-vessel steel. The vessel fractured in an almost brittle manner near its NDT temperature, although, according to the Charpy curve, it was still very tough.

The drop-weight test is applicable primarily to steels in the thickness range 18 to 50 mm. The NDT temperature is unaffected by section sizes above about 12 mm; because of the small notch and the limited



(a)

(b)

deformation due to brittle weld bead material, sufficient notch-tip restraint is ensured.

**Fig. 9.7** (a) Typical oscilloscope record of an instrumented Charpy impact test. (b) Schematic representation of (a).

### 9.2.3 Instrumented Charpy Impact Test

The Charpy impact test described in Section 9.2.1 is one of the most common tests for characterizing the mechanical behavior of materials. The principal advantages of the test are the ease of preparation of the specimen, the execution of the test proper, speed, and low cost. However, one must recognize that the common Charpy test basically furnishes information of only a comparative character. The transition temperature, for example, depends on the thickness of the specimen (hence, the need to use standard samples); that is, this transition temperature can be used to compare, say, two steels, but it is not an absolute material property. Besides, the common Charpy test measures the total energy absorbed ( $E_T$ ), which is the sum of the energies spent in initiation ( $E_i$ ) and in propagation ( $E_p$ ) of the crack (i.e.,  $E_T = E_i + E_p$ ). In view of this problem, a test called the *instrumented Charpy impact test* has been developed. This test furnishes, besides the absorbed energy, the variation in the applied load with time. The instrumentation involves the recording of the signal from a load cell on the pendulum by means of an oscilloscope in the form of a load-time curve of the test sample. Figure 9.7(a) shows a typical oscilloscope record, and Figure 9.7(b) shows a schematic representation of that record. This type of curve can provide information about the load at general yield, maximum load, load at fracture, and so on. The energy spent in impact can also be obtained by integration of the load-time curve. From this curve, one can obtain the energy of fracture if the velocity of the pendulum is known. Assuming this velocity to be constant during the test, we can write the energy of fracture as

$$E' = V_0 \int_0^t P dt, \quad (9.2)$$

where  $E'$  is the total fracture energy, based on the constant velocity of the pendulum,  $V_0$  is the initial velocity of the pendulum,  $P$  is the instantaneous load, and  $t$  is the time.

In fact, the assumption that the velocity of the pendulum is constant is not valid. According to Augland,<sup>2</sup>

$$E_t = E' (1 - \alpha), \quad (9.3)$$

where  $E_t$  is the total fracture energy,  $E' = V_0 \int_0^t P dt$ ,  $\alpha = E'/4E_0$ , and  $E_0$  is the initial energy of the pendulum. The values of total energy absorbed in fracture computed this way from the load-time curves show a one-to-one correspondence with the values determined in a conventional Charpy test. Based on this correspondence, we can use Equation 9.3 for computing the initiation and propagation energies at a given temperature. This information, together with the load at yielding, maximum load, and load at fracture, can allow us to identify the various stages of the fracture process.

It is well known (see Section 9.3) that the plane-strain fracture toughness ( $K_{Ic}$ ) test gives a much better and precise idea of a material's tenacity than the instrumented Charpy test does. Also,  $K_{Ic}$  is a material property. However, as will be seen shortly, the  $K_{Ic}$  test possesses certain disadvantages: The preparation of equipment and the specimen is rather expensive, the test is relatively slow and not simple to execute, and so on. Consequently, there have been attempts at developing empirical correlations between the energy absorbed in a conventional Charpy test (CV) and the plane-strain fracture toughness ( $K_{Ic}$ ). The reader is warned that such correlations are completely empirical and are valid only for the specific metals tested. The instrumented Charpy test, with samples precracked and containing side grooves in order to assure a plane-strain condition, can be used to determine the dynamic fracture toughness  $K_{ID}$ . For ultra high-strength metals ( $\sigma_y$  very large),  $K_{ID} \approx K_{Ic}$ . Thus, we may use the instrumented Charpy test to determine  $K_{Ic}$  or  $K_{ID}$  for very high-strength steels. But we must check the results obtained with those obtained from a standard ASTM  $K_{Ic}$  test, as described in the next section.

### 9.3 | Plane-Strain Fracture Toughness Test

The fracture toughness  $K_{Ic}$  of a material may be determined by means of a number of standards, e.g., ASTM 399 or BS 544 for metals. For plastic materials, ASTM D5045-91 gives standard test methods for plane-strain fracture toughness and strain energy release rate. There are different standards for ceramic materials (see Section 9.7). The essential steps in fracture toughness tests involve the measurement of crack extension and load at the sudden failure of the sample. Because it is difficult to measure crack extension directly, one measures the

<sup>2</sup> B. Augland, *Brit. Weld.*, 9 (1962) 434.

relative displacement of two points on opposite sides of the crack plane. This displacement can be calibrated and related to the real crack front extension.

The typical test samples used in fracture toughness tests carried out in accordance with the ASTM standard are shown in Figure 9.8. Figure 9.8(c) shows the size of the specimens. (Tensile and Charpy specimens are also shown for comparison.) The relation between the applied load and the crack opening displacement depends on the size of the crack and the thickness of the sample in relation to the extent of the plastic zones. When the crack length and the sample thickness are very large in relation to the quantity  $(K_{lc}/\sigma_y)^2$ , the load-displacement curve is of the type shown in Figure 9.9(a). The load at the brittle fracture that corresponds to  $K_{lc}$  is then well defined. When the specimen is of reduced thickness, a step called "pop-in" occurs in the curve, indicating an increase in the crack opening displacement without an increase in the load (Figure 9.9(b)). This phenomenon is attributed to the fact that the crack front advances only in the center of the plate thickness, where the material is constrained under plane-strain condition. However, near the free surface, plastic deformation is much more pronounced than at the center, and it approaches the conditions of plane stress. Consequently, the plane-strain crack advances much more in the central portion of the plate thickness, and in regions of material near the surfaces of the specimen, the failure eventually is by shear.

When the test piece becomes even thinner, the plane-stress condition prevails, and the load-displacement curve becomes as shown in Figure 9.9(c). To make valid fracture toughness measurements in plane strain, the influence of the free surface, which relaxes the constraint, must be maintained small. This enables the plastic zone to be constrained completely by elastic material. The crack length must also be maintained greater than a certain lower limit.

Figure 9.10 shows the plastic zone at the crack front in a plate of finite thickness. At the edges of the plate ( $x_3 \rightarrow \pm B/2$ ), the stress state approaches that of plane stress. At the center of a sufficiently thick plate, the stress state approaches that of plane strain. This is so because the  $\varepsilon_{33}$  component of strain is equal to zero at the center, as the material there in that direction is constrained, whereas near the edges the material can yield in the  $x_3$  direction, so  $\varepsilon_{33}$  is different from zero.

Up to this point, the sample size and the crack length have been discussed in a qualitative way. The lower limits on width, thickness, and crack length all depend on the extent of plastic deformation through the  $(K_{lc}/\sigma_y)^2$  factor. In view of the lack of knowledge about the exact size of the plastic zone for the crack in mode I (the crack opening mode), it is very difficult to determine the lower limits of dimension of the test piece theoretically. These lower limits above which  $K_{lc}$  remains constant are determined by means of trial tests. Samples of dimensions smaller than those limits tend to overestimate the  $K_{lc}$  limit.

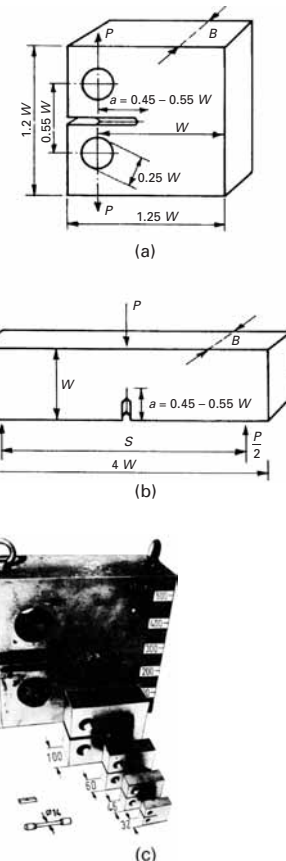


**Fig. 9.8** Typical ASTM standard plane-strain fracture toughness test specimens. (a) Compact tension. (b) Bending. (c) Photograph of specimens of various sizes. Charpy and tensile specimens are also shown, for comparison purposes. (Courtesy of MPA, Stuttgart.)

**Fig. 9.9** Schematic of typical load-displacement curves in a  $K_{Ic}$  test.

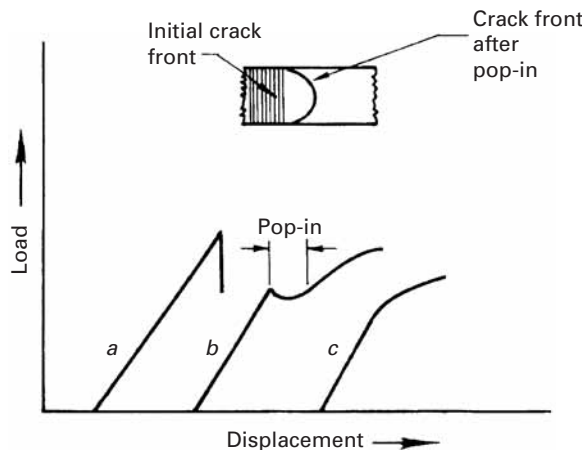
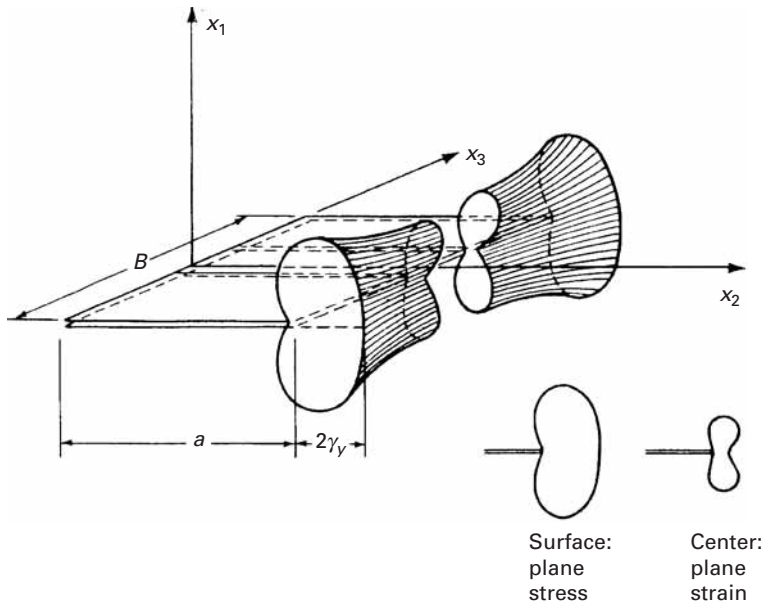


**Fig. 9.10** Plastic zone at the crack tip in a plate of finite thickness.



Preferably, in fracture toughness tests, the crack is introduced by fatigue from a starter notch in the sample. The fatigue crack length should be long enough to avoid interference in the crack-tip stress field by the shape of the notch. Under an applied load, the crack opening displacement can be measured between two points on the notch surfaces by various types of transducers. Figure 9.11 shows an assembly for measuring displacement in a notched specimen. Electrical resistance measurements have also been used to detect crack propagation. Calibration curves are utilized for converting displacement measurements and resistance measurements into crack extension.

The load-displacement curves generally show a gradual deviation from linearity, and the "pop-in" step is very small (Figure 9.12). The

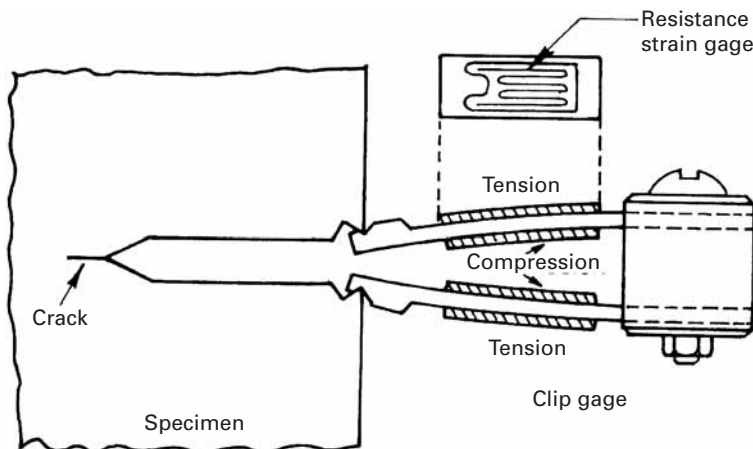


**Fig. 9.11** Assembly for measuring displacement in a notched specimen.

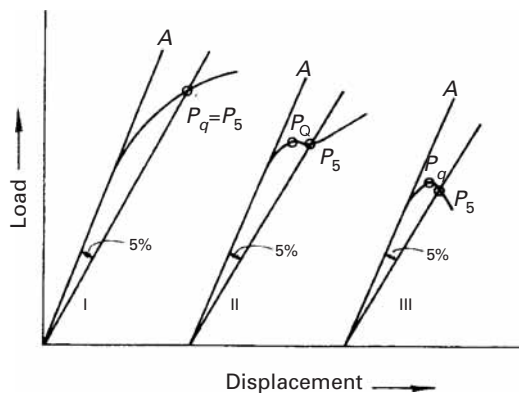


**Fig. 9.12** Procedure used for measuring the conditional value  $K_Q$ .

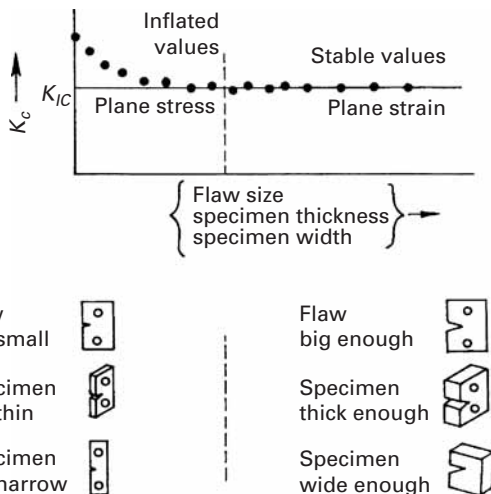
procedure used in the analysis of load-displacement records of this type can be explained by means of the figure. Let us designate the linear-slope part as  $OA$ . A secant line,  $OP_5$ , is drawn at a slope 5% less than that of line  $OA$ . The point of intersection of the secant with the load-displacement record is called  $P_5$ . We define the load  $P_Q$ , for computing a conditional value of  $K_{lc}$ , called  $K_Q$ , as follows: If the load on every point of curve before  $P_5$  is less than  $P_5$ , then  $P_5 = P_Q$  (case I in the figure). If there is a load more than  $P_5$  and before  $P_5$ , this load is considered to be  $P_Q$  (cases II and III in the figure). In these cases, if  $P_{max}/P_Q > 1.1$ , the test is not valid;  $K_Q$  does not represent the  $K_{lc}$  value, and a new test needs to be done. After determining the point  $P_Q$ , we calculate the value of  $K_Q$  according to the known equation for the geometry of the test piece used. A checklist of points is given in Table 9.1 and Figure 9.13 shows schematically the variation of  $K_c$ , with the flaw size, specimen thickness, and specimen width. The stress intensity factor is calculated by using the equation

$$K_1 = f \left( \frac{a}{W} \right) \frac{P}{B\sqrt{W}} \quad (9.4)$$

**Table 9.1** Checklist for the  $K_{Ic}$  Test

1. Dimensions of test piece
  - a. Thickness,  $B \geq 2.5 (K_{Ic}/\sigma_y)^2$
  - b. Crack length,  $a \geq 2.5 (K_{Ic}/\sigma_y)^2$
2. Fatigue precracking
  - a.  $K_{max}/K_{Ic} \leq 0.6$
  - b. Crack front curvature  $\leq 5\%$  of crack length
  - c. Inclination  $\leq 10^\circ$
  - d. Length between 0.45  $W$  and 0.55  $W$ , where  $W$  is the width of the test sample
3. Characteristics of load–displacement curve. This is effectively to limit the plasticity during the test and determines whether the gradual curvature in the load–displacement curve is due to plastic deformation or crack growth.
  - a.  $P_{max}/P_Q \leq 1.1$

**Fig. 9.13** Variation in  $K_c$  with flaw size, specimen thickness, and specimen width.



The function  $f(a/W)$  has a different form for each specimen geometry. For the compact specimen (Figure 9.8(a)),

$$f\left(\frac{a}{W}\right) = \frac{2 + \frac{a}{W}}{\left(1 - \frac{a}{W}\right)^{3/2}} \left[ 0.886 + 4.64\left(\frac{a}{W}\right) - 13.32\left(\frac{a}{W}\right)^2 + 14.72\left(\frac{a}{W}\right)^3 - 5.60\left(\frac{a}{W}\right)^4 \right]. \quad (9.5)$$

For the single-edge notched-bend specimen loaded in three-point bending (Figure 9.8(b)),

$$f\left(\frac{a}{W}\right) = \frac{3\frac{S}{W}\sqrt{\frac{a}{W}}}{2\left(1 + 2\frac{a}{W}\right)\left(1 - \frac{a}{W}\right)^{3/2}} \left[ 1.99 - \frac{a}{W}\left(1 - \frac{a}{W}\right) \times \left\{ 2.15 - 3.93\left(\frac{a}{W}\right) + 2.7\left(\frac{a}{W}\right)^2 \right\} \right]. \quad (9.6)$$

The preceding expressions are polynomial fits to functions.

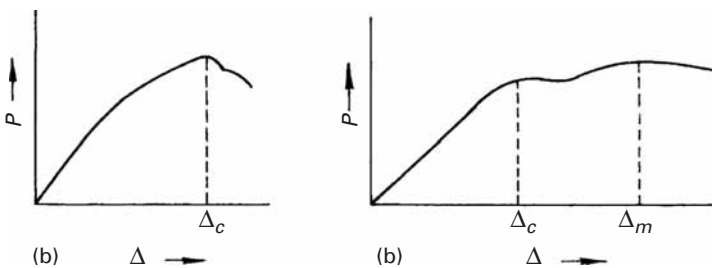


**Fig. 9.14** Schematics of load  $P$  versus crack opening displacement  $\Delta$ .

### Example 9.1

Estimate the minimum specimen thickness for a valid plane-strain fracture toughness test for material having the following properties:

Yield stress  $\sigma_y = 400 \text{ MPa}$ ,

Fracture toughness  $K_{Ic} = 100 \text{ MPa m}^{1/2}$ .

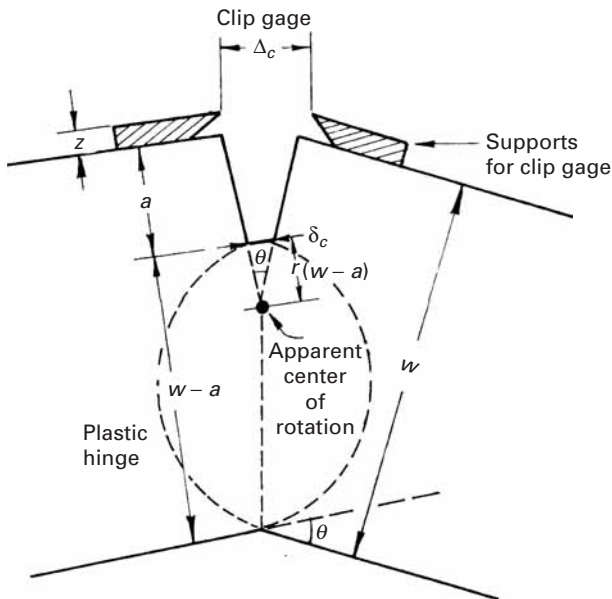
**Solution:** The minimum thickness of the specimen is  $2.5 (K_{Ic}/\sigma_y)^2 = 2.5 (1/4)^2 = 0.156 \text{ m} = 156 \text{ mm}$ .

## 9.4 | Crack Opening Displacement Testing

For crack opening displacement (COD) testing, the test sample for determining  $\delta_c$  is a slow-bend test specimen similar to the one used for  $K_{Ic}$  testing. A clip gage is used to obtain the crack opening displacement. During the test, one obtains a continuous record of the load  $P$  versus the opening displacement  $\Delta$  (Figure 9.14). In the case of a smooth  $P$ - $\Delta$  curve, the critical value,  $\Delta_c$ , is the total value (elastic + plastic) corresponding to the maximum load (Figure 9.14(a)). In case the  $P$ - $\Delta$  curve shows a region of increase in displacement at a constant or decreasing load, followed by an increase in load before fracture, one needs to make auxiliary measurements to determine that this behavior is associated with crack propagation. Should this be so,  $\Delta_c$  will correspond to the first instability in the curve. If the  $P$ - $\Delta$  curve shows a maximum, and  $\Delta$  increases with a reduction in  $P$ , then either a stable crack propagation is occurring or a “plastic hinge” is being formed. The “ $\Delta_c$ ” in this case (Figure 9.14(b)) is the value corresponding to the point at which a certain specified crack growth has started. If it is not possible to determine this point, one cannot measure the COD at the start of crack propagation. However, we can measure, for comparative purposes, an opening displacement  $\delta_m$ , computed from the clip gage output  $\Delta_m$ , corresponding to the first load maximum. The results in this case will depend on the geometry of the specimen.

Experimentally, we obtain  $\Delta_c$ , the critical displacement of the clip gage. We need to obtain  $\delta_c$ , the critical CTOD. Various methods are

**Fig. 9.15** “Plastic hinge” mechanism of deformation.



available, all based on the hypothesis that the deformation occurs by a “hinge” mechanism around a center of rotation at a depth of  $r(w - a)$  below the crack tip, (Figure 9.15), where  $w$  is the width, and  $a$  is the length. Experimental calibrations of the crack using specimens of up to 50 mm in thickness, have shown that, for COD in the range 0.0625 to 0.625 mm,  $\delta_c$  can be obtained to a very good approximation from the relation

$$\delta_c = \frac{(w - a) \Delta_c}{w + 2a + 3z}.$$

This relation is derived on the basis of the assumption that the deformation occurs by a hinge mechanism about a center of rotation at a depth of  $(w - a)/3$  below the crack tip (i.e.,  $r = \frac{1}{3}$ ). However,  $r$  can be smaller for smaller values of  $\Delta_c$ . Note that  $r \approx 0$  in the elastic case (very limited plastic deformation at the crack tip), and  $r \approx \frac{1}{3}$  for a totally plastic ligament.

## 9.5 | J-Integral Testing

$J_{lc}$  defines the onset of crack propagation in a material in which large-scale plastic yielding makes direct measurement almost impossible. Thus, one can use  $J$ -integral testing to find the value of  $K_{lc}$  for a very ductile material from a specimen of dimensions too small to satisfy the requirements of a proper  $K_{lc}$  test.

ASTM standard E819-89 provides a procedure for determining  $J_c$ , the critical value of  $J$ . As pointed out in Chapter 7, the physical interpretation of the  $J$ -integral is related to the area under the

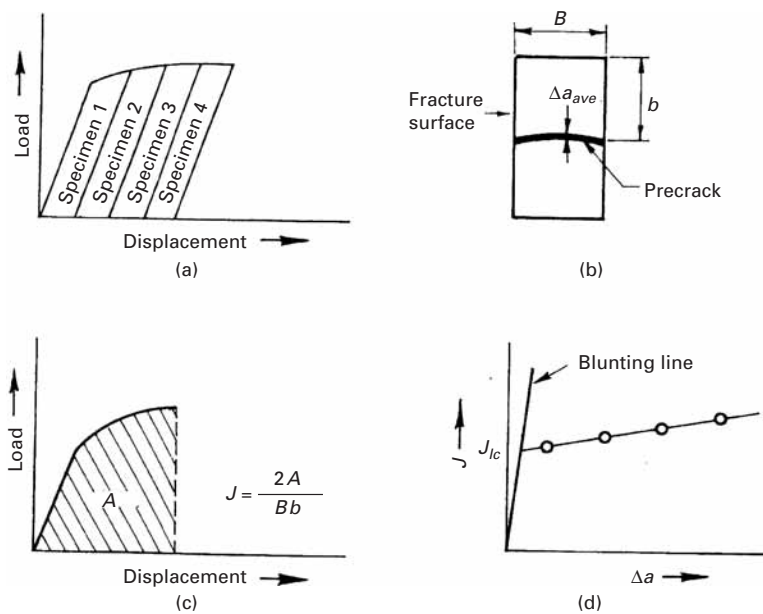


**Fig. 9.16** Method for determining  $J_{lc}$ . (a) Load identical specimens to different displacements. (b) Measure the average crack extension by heat tinting. (c) Calculate  $J$  for each specimen. (d) Plot  $J$  versus  $\Delta a$  to find  $J_{lc}$ .

curve of the load versus the load-point displacement for a cracked sample. Both compact tension and bend specimens can be used. The ASTM standard requires at least four specimens to be tested. Each specimen is loaded to different amounts of crack extensions (Figure 9.16). One calculates the value of  $J$  for each specimen from the expression

$$J = \frac{2A}{Bb},$$

where  $A$  is the area under load versus the load-point displacement curve,  $B$  is the specimen thickness, and  $b$  is the uncracked ligament. The value of  $J$  so derived is plotted against  $\Delta a$ , the crack extension of each specimen. One way of obtaining  $\Delta a$  is to heat-tint the specimen after testing and then break it open. When the specimen is heated, the crack surfaces oxidize. Next, a “best line” through the  $J$  points and a “blunting line” from the origin are drawn. This blunting line (indicating the onset of crack blunting due to plastic deformation) is obtained from the equation

$$J = 2\sigma_{flow}\Delta a, \quad (9.7)$$

where  $\sigma_{flow} = (\sigma_y + \sigma_{UTS})/2$ , in which  $\sigma_y$  is the yield stress and  $\sigma_{UTS}$  is the ultimate tensile stress.

The intercept of the  $J$  line and the blunting line gives  $J_{lc}$ .  $J_{lc}$  is related to  $K$  by

$$J_{lc} = \frac{K_{Jc}^2}{E}. \quad (9.8)$$

## 9.6 | Flexure Test

The flexure or bend test is one of the easiest tests to do and is very commonly resorted to, especially with brittle materials that behave in a linear elastic manner. A very small amount of material is required, and preparation of the sample is relatively easy. The following assumptions are made in analyzing the flexure behavior of materials. We assume that the Euler-Bernoulli theory is applicable to a freely supported beam. (The beam is not clamped at any point.) That the Euler-Bernoulli theory is applicable means that plane sections remain plane, deformations are small, stress varies linearly with thickness, and there is no Poisson's contraction or expansion. The condition of small deformation comes from the Euler-Bernoulli assumption that the specimen beam is bent into a circular arc. The condition of a small deformation can be easily violated if the material is deformed in a nonlinear, viscoelastic, or plastic manner. Then stress gradients across the vertical section of the beam will not be linear.<sup>3</sup>

The two basic governing equations for a simple beam elastically stressed in bending are

$$\frac{M}{I} = \frac{E}{R} \quad (9.9)$$

and

$$\frac{M}{I} = \frac{\sigma}{y}, \quad (9.10)$$

where  $M$  is the applied bending moment,  $I$  is the second moment of area of the beam section about the neutral plane,  $E$  is Young's modulus of elasticity of the material,  $R$  is the radius of curvature of the bent beam, and  $\sigma$  is the tensile or compressive stress on a plane distant  $y$  from the neutral plane.

For a uniform circular section of beam,

$$I = \frac{\pi d^4}{64}, \quad (9.11)$$

where  $d$  is the diameter of the section.

For a uniform, rectangular section of beam,

$$I = \frac{bh^3}{12} \quad (9.12)$$

where  $b$  is the width of the beam and  $h$  is the height of the beam.

Bending takes place in the direction of the depth; that is,  $h$  and  $y$  are measured in the same direction. Also, for a beam with a symmetrical section with respect to the neutral plane, replacing  $h/2$  (or  $d/2$ ) for  $y$  in Equation (9.10) gives the stress at the beam surface.

---

<sup>3</sup> The student should recall discussions on beam deflections in courses on mechanics of materials.

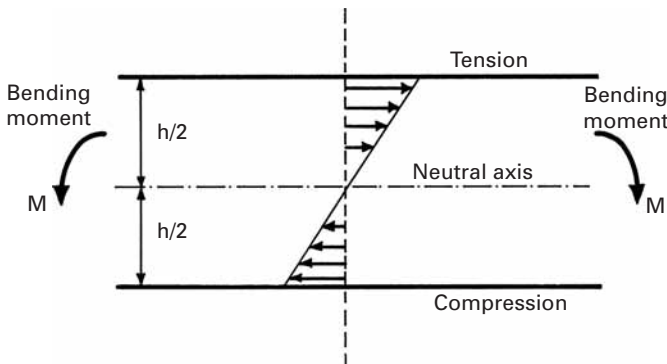


**Fig. 9.17** Normal stresses along a section of beam for linearly elastic material.

In the elastic regimen, stress and strain are related by Hooke's law,

$$\sigma = E \varepsilon. \quad (9.13)$$

From Equations (9.9), (9.10), and (9.13), we obtain the following simple relation, valid in the elastic regimen:

$$\varepsilon = \frac{y}{R}. \quad (9.14)$$

Figure 9.17 shows the elastic normal stress distribution through the thickness when a beam is bent. The stress and strain vary linearly with the thickness  $y$  across the section, with the neutral plane ( $y = 0$ ) representing the zero level. The material on the outside or above the neutral plane of the bent beam is stressed in tension, while that on the inside or below the neutral plane is stressed in compression. Thus, the elastic strain  $\varepsilon$  in a beam bent to a radius of curvature  $R$  varies linearly with distance  $y$  from the neutral plane across the beam thickness.

Two main types of flexure tests are three-point and four-point bend tests. Another variant of flexure tests is the so-called interlaminar shear stress (ILSS) that is used in fiber reinforced composites. We describe these briefly.

### 9.6.1 Three-Point Bend Test

In the three-point bend test, the load is applied at the center point of the beam, and the bending moment  $M$  increases from the two extremities to a maximum at the center point. (See Figure 9.18(a).) In this case,

$$M = (P/2)(S/2) = PS/4,$$

while the moment of inertia, for a beam of a rectangular section, is

$$I = bh^3/12.$$

Using Equation 9.10, we can obtain the maximum stress in the outermost layer ( $y = h/2$ ) as

$$\sigma_{\max} = 3PS/2bh^2. \quad (9.15)$$

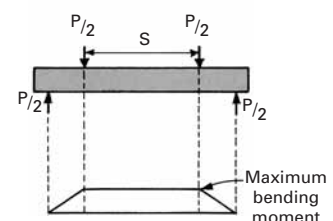
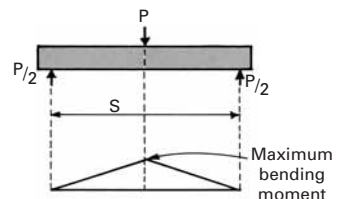


**Fig. 9.18** Application of loads and bending moment diagrams for (a) three-point bending and (b) four-point bending tests.

### 9.6.2 Four-Point Bending

Four-point bending is also called pure bending, since there are no transverse shear stresses on the cross-sections of the beam in the inner span. For an elastic beam bent at four points, the bending moment is constant in the inner span (see Figure 9.18(b)) and is given by

$$M = \frac{\sigma_{\max} I}{h/2} = \frac{P}{2} \cdot \frac{S}{4} \quad (9.16)$$

where  $I$  is the moment of inertia,  $h/2$  is the distance from the neutral axis to the outer surface, and  $\sigma_{\max}$  is the normal stress on a transverse section of the same outer fiber. The maximum stress in a rectangular beam undergoing a four-point bending is

$$\boxed{\sigma_{\max} = 3PS/4bh^2}, \quad (9.17)$$

where  $S$  is the outer span and  $b$  is the breadth of the beam.

The three- and four-point bending tests are extremely helpful in determining the strength of brittle materials, and especially of ceramics. If brittle materials are tested in tension the alignment of the grips is very critical. Slight misalignments cause major stress inhomogeneities which significantly affect the strength. Flexure tests, on the other hand, are simple and reliable. The four-point bending test presents the following advantage over the three-point bending test: the entire span length is subjected to a constant stress. In a three-point bend, the maximum stress occurs only at the mid-section (see Example 9.2). The resultant strength is called bend strength, flexural strength or, commonly but erroneously, MOR (modulus of rupture).

Examples:

$\text{Al}_2\text{O}_3$ (99.5% dense)	400 MPa
SiC (hot-pressed)	600 MPa
Soda-lime glass	65 MPa

A systematic comparison of 1,500 sintered alumina specimens (AD-999) with varying dimensions ( $3 \times 4 \times 50$  mm and other sizes) revealed that the Weibull modulus was equal to 10 and the characteristic strength of the bend bar was equal to 466 MPa in three-point bending. The four-point bending results were  $m = 9.8$  (Weibull modulus) and  $\sigma_0 = 374$  MPa. The value of  $\sigma_0$  corresponds to the 63.2% probability of failure,  $(1 - 1/e)$ . The four-point bend test results show a lower  $\sigma_0$  because of a larger surface (and thus a greater probability of flaws  $\geq a_c$ , the critical length) is subjected to the maximum stress.

A miniaturized bend test was developed for use in small specimens with 3 mm diameter.<sup>4</sup> In this setup, a disk instead of a bar is used. The deflection of specimen is measured with an LVDT (linear variable differential transducer) as it is deformed by a punch. The setup is shown in Figure 9.19.

The maximum stress in the specimen is given by:

$$\sigma = \frac{3P}{2\pi t^2} \left[ 1 + (1 + \nu) \ln \frac{R}{r'} \right],$$

<sup>4</sup> H. Li, F. C. Chen, and A. J. Ardell, *Met. Trans A*, 22 (1991) 2061.

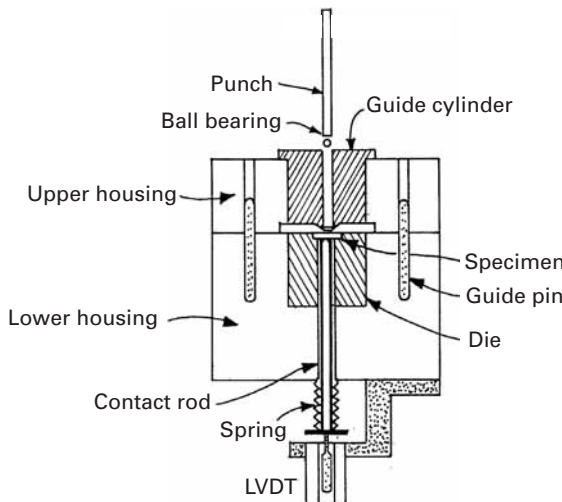


**Fig. 9.19** Cematic drawing of the miniaturized disk-bend test. (Adapted from H. Li, F. C. Chen, and A. J. Ardell, *Met. Trans A*, 22 (1991) 2061.)

where  $P$  is the load,  $t$  is the specimen thickness,  $R$  is the radius of the lower supporting die (smaller than 3 mm),  $r$  is the radius of the contact area between the ball at the tip of the punch and the specimen, and  $r'$  has one of the values:

$$r' = (1.6r^2 + t^2) - 0.675t \quad \text{if } r \leq t/2$$

and

$$r' = r \quad \text{if } r > t/2.$$

This miniaturized bend test can be used on ductile or brittle materials and is well suited when material is available in small sizes.

### 9.6.3 Interlaminar Shear Strength Test

The interlaminar shear strength test is also known as the short-beam shear test. It is commonly used with fiber reinforced composites, with the fiber length parallel to the length of a three-point bend bar. In such a test, the maximum shear stress occurs at the midplane and is given by

$$\boxed{\tau_{\max} = \frac{3P}{4bh}}. \quad (9.18)$$

The maximum tensile stress occurs at the outermost surface and is given by Equation 9.15. Dividing Equation 9.18 by Equation 9.15, we get

$$\boxed{\frac{\tau_{\max}}{\sigma_{\max}} = \frac{h}{2S}}. \quad (9.19)$$

Equation 9.19 says that if we make the load span  $S$  very small, we can maximize the shear stress  $\tau$  so that the specimen fails under shear with a crack running along the midplane. Thus, if we deliberately make the span very small (hence the name, “short beam”), then it is likely that failure will occur under shear. A word of caution is in order about the interpretation of this test: The test becomes invalid

if the fibers fail in tension before shear induced failure occurs. The test will also be invalid if shear and tensile failure occur simultaneously. It is advisable to examine the fracture surface after the test, to make sure that the crack is along the interface and not through the matrix.

### Example 9.2

In a three-point bend test (see Figure E9.2), the specimen has a span of 50 mm and a load  $P$  of 50 N. The width and height are 5 mm each. Draw the moment and shear force diagrams. Find the maximum moment and maximum stress.

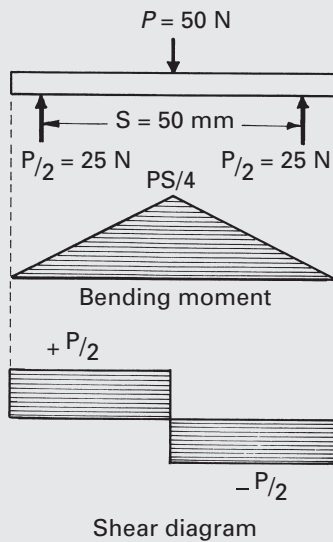


**Fig. E9.2**

**Solution:** We have

$$\text{Load, } P = 50 \text{ N}, \quad \text{Span, } S = 50 \text{ mm} = 50 \times 10^{-3} \text{ m.}$$

In three-point bending, the maximum bending moment occurs at the midpoint of the beam and is given by

$$\frac{P}{2} \times \frac{S}{2} = \frac{PS}{4} = \frac{50 \text{ N} \times 50 \times 10^{-3} \text{ m}}{4} = 625 \times 10^{-3} \text{ N} \cdot \text{m.}$$

Note that the maximum stress also occurs along the centerline of the specimen; that is, the whole of the specimen is not subjected to a uniform stress, as would be the case in a tensile test. We have

$$\begin{aligned} \text{Maximum stress (Equation 9.15)} &= \frac{3 \cdot PS}{bh^2} = \frac{3 \cdot 50 \times (50 \times 10^{-3})}{5 \times 10^{-3} (5 \times 10^{-3})^2} \\ &= 60 \text{ MPa.} \end{aligned}$$

### Example 9.3

It is generally known that a given material will show a higher strength in a three-point bend test than in an axial tension test. Consider a rod of a square cross section and side  $a$ . If the span in the bend test is  $S$ , show that the ratio of the bend strength to the tensile strength is

$$\sigma_{\text{bend}}/\sigma_{\text{ten}} = 3S/2a.$$

**Solution:** For uniaxial tension:

$$\text{Force} = P,$$

$$\text{Cross-sectional area} = a^2,$$

$$\text{Tensile strength } \sigma_{\text{ten}} = P/a^2.$$

For three-point bending:

The maximum stress in three-point bending is  $\sigma_{\text{bend}} = \sigma_{\text{max}} = M_{\text{max}}y_{\text{max}}/I$ , where

$$I = bh^3/12 = a^4/12,$$

$$M = PS/4,$$

$$y_{\text{max}} = a/2.$$

Hence,

$$\frac{\sigma_{\text{bend}}}{\sigma_{\text{ten}}} = \frac{P S}{4} \times \frac{a}{2} \times \frac{12}{a^4}, \frac{a^2}{P} = \frac{3S}{2a}.$$

Thus, the maximum stress in bending is  $3S/2a$  times the tensile stress. Generally,  $S \gg a$ , so the difference can be very large indeed!

## 9.7 Fracture Toughness Testing of Brittle Materials

In brittle materials – especially ceramics – the strength is largely determined by the size and sharpness of flaws and by the resistance of cracks to propagation. Since plasticity is very limited in such materials, the size of the specimen can be reduced much more than in metals. Recall that the thickness  $B$  of the test specimen should exceed  $2.5(K_{Ic}/\sigma_y)^2$ . This ensures a plastic zone size that is small with respect to  $B$ , and therefore, the state of plane strain can be assumed. We will estimate the minimum acceptable specimen thickness for a typical ceramic, alumina, for which

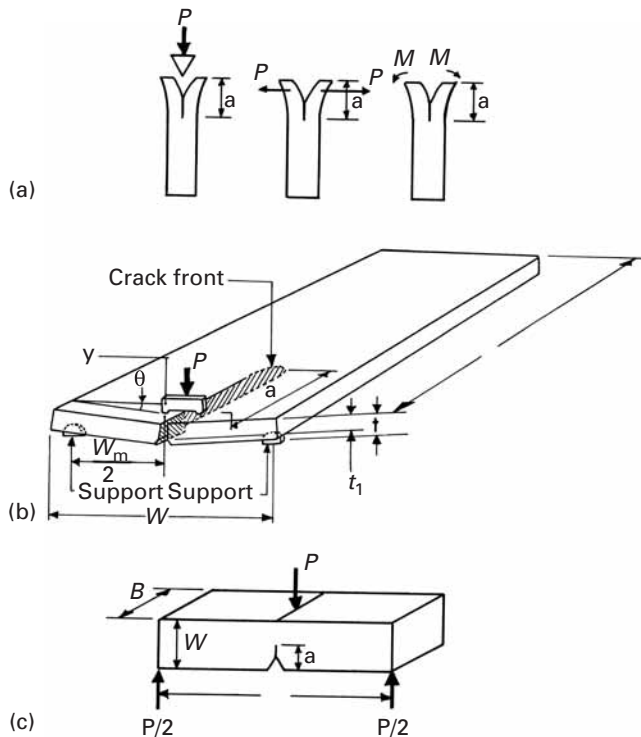
$$K_{Ic} \approx 4 \text{ MPa m}^{1/2},$$

$$\sigma \approx 400 \text{ MPa.}$$

For this specimen,

$$B \geq 2.5 \times 10^{-4} \text{ m.}$$

**Fig. 9.20** Fracture-testing methods for brittle materials. (a) Double-cantilever beam (DCB). (b) Double torsion. (c) Notch flexure.



Therefore, the minimum thickness is very small, and microstructural inhomogeneities limit the size of the specimen. We next discuss the most common methods of testing brittle materials (Figure 9.20).

A double-cantilever specimen (DCB) with a precrack of size  $a$  is illustrated in Figure 9.20(a). Three possible loading configurations are shown: wedge loading, applied load  $P$ , and applied moment  $M$ . A groove is machined into the specimen to guide the propagation of the crack. The three loading methods provide essentially three relationships between  $K_I$ , the stress intensity factor and the crack length.

A double-torsion specimen is very convenient for determining the fracture toughness of ceramics at high temperatures. It requires only the application of a compressive load  $P$  (Figure 9.20(b)). The stress intensity  $K_I$  does not depend on the length of the crack for  $0.25 L < a < 0.75 L$ . The fracture toughness is given by

$$K_I = P W_m \left[ \frac{3}{W t^3 t_1 (1 - v) \xi} \right]^{1/2}, \quad (9.20)$$

where  $\xi$  is a geometrical factor that depends on the thickness of the specimen,  $t_1$ .

The notch bend test (Figure 9.20(c)) is analogous to the same test applied to metals. A notch is cut into the brittle material. A crack

“pops in” during loading and then grows with  $P$ . This technique requires only small specimens.

### 9.7.1 Chevron Notch Test

The main advantage of the chevron notch test is that the critical stress intensity factor can be determined from the maximum load without resorting to precracking and crack length measurement. The test requires that the specimen undergo stable crack growth before reaching the maximum load, as indicated by the load-displacement curve deviating slightly from the initial linear part before final fracture.

The notches in the samples can be conveniently made with a low-speed diamond saw. The dimensions of the specimen should obey the following guidelines, as recommended in various references:<sup>5</sup>

$$S/W = 4, \quad W/B = 1.5, \quad \alpha_0 = a_0/W \geq 0.3, \quad \text{and} \quad \theta = 60^\circ.$$

Here,  $S$  is the span,  $W$  is the height of the specimen,  $B$  is the width of the specimen, and  $\theta$  is the included angle. Figure 9.21(a) shows a schematic of the test arrangement and the details of the notch plane. The test can be performed in a universal testing machine at a constant crosshead speed. The chevron tip length,  $a_0$ , can be measured from optical micrographs of broken specimens, as shown in Figure 9.21(b). The critical stress intensity factor can be obtained from the relationship

$$K_{Ic} = \frac{P_{\max}}{B\sqrt{W}} Y_c(\alpha_0),$$

where  $P_{\max}$  is the maximum load,  $B$  is the width of the specimen,  $W$  is the height of the specimen, and  $Y_c$  is a dimensionless coefficient<sup>6</sup> given by

$$Y_c(\alpha_0) = 5.639 + 27.44\alpha_0 + 18.93\alpha_0^3 - 43.42\alpha_0^3 + 338.9\alpha_0^4$$

for the geometry of the specimen in this study (i.e.,  $\theta = 60^\circ$  and  $W/B = 1.5$ ).

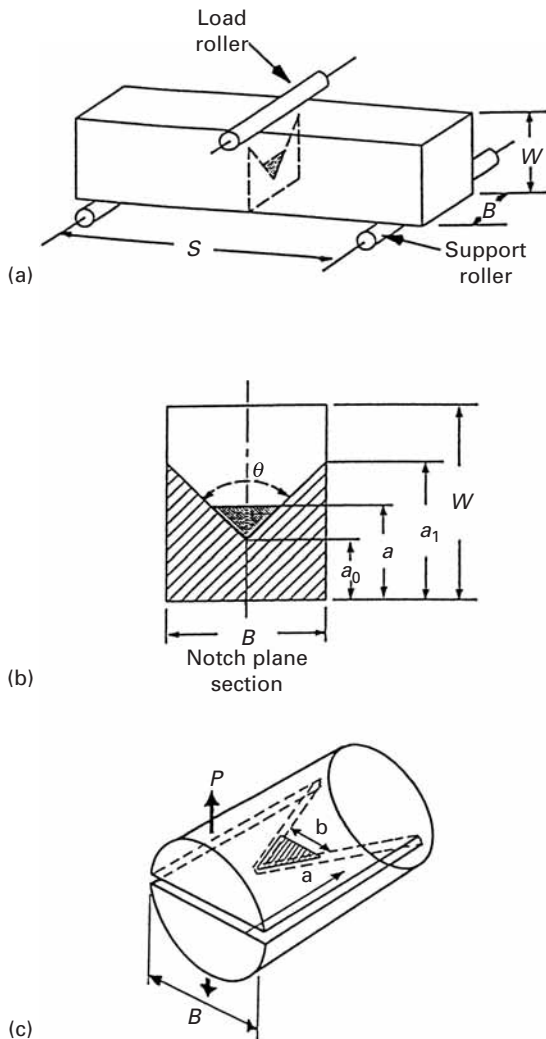
In another variant of the chevron test, the chevron-notched short-rod specimen shown in Figure 9.21(c) which has been standardized by ASTM (E1304-89), has a wedge inserted into a slit that is cut in it, leaving a thin layer of ceramic with a V-shape. A crack is initiated at the tip of the wedge; the width of the crack increases as the crack moves forward. The wedge also guides the crack as it grows. The load

<sup>5</sup> S.-X. Wu, *Eng. Fracture Mech.*, 19 (1984) 221.

<sup>6</sup> S.-X. Wu, *Chevron-Notched Specimens: Testing and Stress Analysis*, eds. J. H. Underwood, S. W. Freiman, and F. I. Baratta (Philadelphia: ASTM, 1984), p. 176.

**Fig. 9.21** Chevron notch test.

(a) Schematic of the test arrangement and the details of the notch plane. (b) The chevron tip length,  $a_0$ , can be measured from optical micrographs of broken specimens. (c) Chevron short-rod specimen.



that opens the crack can be supplied by applying tension to the two sides or by an ingenious bladder mechanism. In this mechanism, a bag containing a fluid is inserted into the slit. The fluid is then pressurized, creating a crack opening force  $P$ . The fracture toughness of the specimen is determined from

$$K_{Ic} \approx 22P_c B^{-3/2},$$

where  $P_c$  is the maximum load for crack propagation and  $B$  is the diameter of the short rod. This technique has also been extended to metals (with a different equation). This geometry of the specimen does not require any fatigue precracking; this is a considerable advantage, because fatigue precracking can be complicated and “tricky,” especially in ceramics.

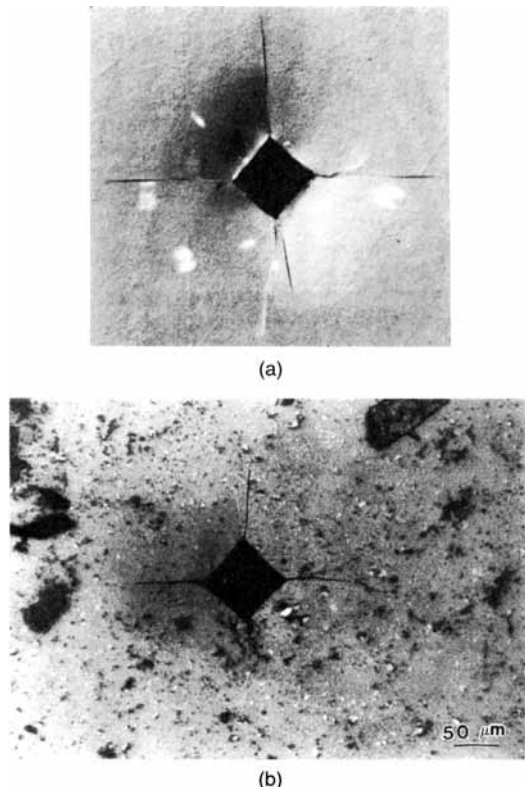


**Fig. 9.22** Fractures produced by hardness indentations in (a)  $\text{AsS}_3$  glass (courtesy of B. R. Lawn and B. J. Hockey) and (b)  $\text{Al}_2\text{O}_3$ .

### 9.7.2 Indentation Methods for Determining Toughness

Hardness indentations can generate cracks in brittle materials; two such examples are shown in Figure 9.22. Tensile stresses are generated under conical and pyramidal indentations. These tensile stresses can generate cracks, and the length of the cracks can be used to calculate a fracture toughness. A second use of such cracks is as initiation sites for fracture in the conventional bending test. The very attractive feature of these microhardness-induced cracks is that they are very small and on the same scale as cracks naturally occurring in ceramics (<1 mm).

Palmqvist was the first to recognize that indentation cracks could be used to obtain quantitative estimates of the fracture toughness of brittle materials.<sup>7</sup> Later, detailed studies by Lawn, Wilshaw, Evans, and coworkers laid the foundation for indentation fracture toughness tests.<sup>8</sup> A simple dimensional analysis shows that the hardness of a material (i.e., the material's resistance to plastic deformation) is given by

$$H = \frac{P}{\alpha c^2},$$

<sup>7</sup> S. Palmqvist, *Jernkontorets Ann.*, 141 (1957) 300; *Arch. Eisenhuttenwes.*, 33 (1962) 629.

<sup>8</sup> B. R. Lawn and T. R. Wilshaw, *J. Mater. Sci.*, 10 (1975) 1049; A. G. Evans and T. R. Wilshaw, *Acta Met.*, 24 (1976) 939; A. G. Evans and E. A. Charles, *J. Am. Cer. Soc.*, 59 (1976) 371.

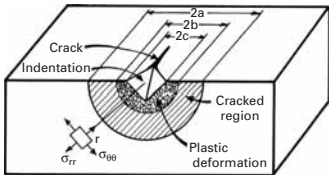


**Fig. 9.23** Schematic representation of indentation generating a plastic deformation region and a semicircular crack.

where  $c$  is the diagonal of the impression and  $P$  is the load. The area of the impression is  $0.5c^2$ , setting the value of the parameter  $\alpha$  to  $(1/1.854)$  for Vickers indentation. (See Section 3.8.1.) In a similar way, the toughness of the material is related to the load and crack size by

$$K_c = \frac{P}{\beta a^{3/2}}.$$

This gives the correct units for  $K_c$ :  $\text{Nm}^{-3/2}$  or  $\text{Pa m}^{1/2}$ . The factor  $\beta$  incorporates a complex elasto-plastic interaction that will not be discussed here. It is important to emphasize that the crack is not always produced during the indentation period, but can be generated during unloading. There are elastic stresses caused by the indentation, producing compressive tangential components of stress; there is also plastic deformation, creating residual stresses on unloading. It is these residual stresses, with a tensile tangential component, that drive the crack. The problem can be analyzed as an internal cavity pressurized in an infinite body. This generates compressive radial stresses  $\sigma_{rr}$  and tensile tangential stresses  $\sigma_{θθ}$ . The tangential stresses decay with  $1/r^2$ . On the other hand, a crack with length  $2a$  forms, under ideal circumstances, a semicircle under the indentation, as shown in Figure 9.23. The residual stress intensity factor, in its turn, is given by

$$K_r = Y \sigma_{θθ} \sqrt{\pi a}.$$

Since

$$\sigma_{θθ} = \frac{kP}{a^2},$$

it follows that

$$K_r = \frac{kY\pi^{1/2}P}{a^{3/2}} = \frac{k'P}{a^{3/2}},$$

where  $k'$  is a parameter. It has been shown that the size of the indentation depends on the hardness of the material and on the Young's modulus  $E$ . The following functional relationship has been found:

$$k' = \delta \left( \frac{E}{H} \right)^{1/2},$$

where  $\delta$  is a geometrical factor that depends on the indentation. Thus,

$$K_r = \delta \left( \frac{E}{H} \right)^{1/2} \frac{P}{a^{3/2}}$$

Anstis *et al.*<sup>9</sup> take  $\delta = 0.016 \pm 0.004$  (for a Vickers indentation). The fracture toughness of the material is the residual stress intensity factor at which the crack stops growing. Hence,

$$K_{Ic} = \delta \left( \frac{E}{H} \right)^{1/2} \frac{P}{a^{3/2}}.$$

<sup>9</sup> G. R. Anstis, P. Chantikul, B. R. Lawn, and D. B. Marshall, *J. Am. Cer. Soc.*, 64 (1981) 533.

Sometimes, equilibrium conditions are not established until after the load is removed. Slow growth of the cracks can then take place, and the measurement of  $a$  depends on the time interval involved. Sometimes, no well-defined radial cracks are formed. In that case, the load  $P$  should be adjusted so that well-developed cracks are generated – that is, cracks for which  $a > 2c$ . Figure 9.24 compares conventional and indentation fracture toughnesses for a number of ceramics. The error bars show the variability of the measurements. It can be seen that the results agree within 30%. The great advantage of indentation fracture toughness tests over conventional tests is that comparative tests with various materials can be carried out readily, providing relative values.

A second manner in which indentation is used is to generate a “starter” crack for the three-point bending test. A Knoop indenter is preferred, and a sharp crack is generated at the center of the specimen and in the side opposite the one where  $P$  (the center load) is applied.

### Example 9.4

Estimate the fracture toughness of the alumina specimen shown in Figure 9.22(b). The indentation was caused by a load of 10 kgf using a Vickers diamond indenter attached to a uniaxial testing machine. The alumina specification is AD 95.

**Solution:** We measure

$$2c = 14 \text{ mm},$$

$$2a = 36.5 \text{ mm}.$$

From the magnification marker, we establish the magnification:  $160\times$ . Thus,

$$2c = 0.087 \text{ mm},$$

$$2a = 0.228 \text{ mm},$$

$$P = 10 \text{ kgf} = 102 \text{ N},$$

and we have

$$K_r = 0.016 \left( \frac{E}{H} \right)^{1/2} \frac{P}{a^{3/2}}.$$

From Table 2.8,

$$E = 365 \text{ GPa}.$$

$H$  is the hardness in  $\text{N}/\text{m}^2$ . We have

$$\begin{aligned} H &= \frac{10 \times 1.85}{7.6 \times 10^{-3}} = 2,434 \text{ kg}/\text{mm}^2 \\ &= 23.85 \text{ GPa}. \end{aligned}$$

Also,

$$\begin{aligned} K_r &= 0.016 \left( \frac{365}{23.85} \right)^{1/2} \frac{10^2}{(0.114 \times 10^{-3})^{3/2}} \\ &= 5.13 \text{ MPa m}^{1/2}. \end{aligned}$$

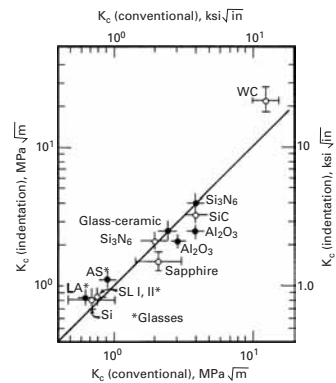


**Fig. 9.24** Comparison between conventional and indentation fracture toughness determinations for glasses and ceramics. (From G. R. Anstis, P. Chankitul, B. R. Lawn, and D. B. Marshall, *J. Am. Cer. Soc.*, 64 (1981) 533.)

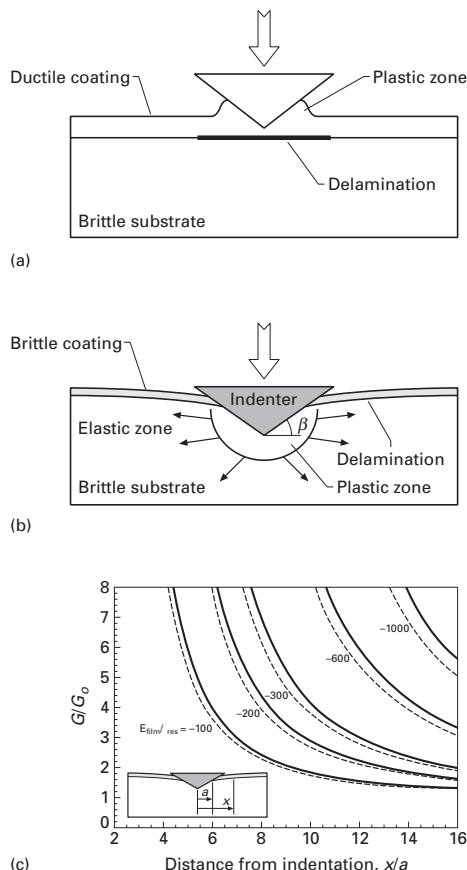
## 9.8 | Adhesion of Thin Films to Substrates

The reliability of many electronic components is dependent on the adherence of the thin film to the substrate. There are methods to determine the toughness of this adherence. The most common is the scratch test, in which an indenter is drawn over the thin films to different depths and the load is recorded. There is a depth at which the film detaches itself from the substrate. This is recognized by the load record, which shows a drop.

The indentation test is another alternative, providing quantitative estimates of the energy required to “peel off” the thin film from the substrate. There are two situations: (a) ductile film on brittle substrate; (b) brittle film on ductile substrate. The techniques used are slightly different. We describe the two methods below.

(a) Ductile film on brittle substrate. An indentation is made, typically with a micro or nanoindenter, in such a manner that it only penetrates the ductile thin film, pushing it aside as shown in Figure 9.25(a). The residual stresses caused by the deformed thin film cause delamination, once the indenter is removed, and if the deformation is sufficiently large. The diameter of the delam-

**Fig. 9.25** Indentation tests for the determination of toughness of bond between substrate and thin film; (a) method used for ductile coating on brittle substrate (typical of electronic components); (b) method used for brittle coatings on ductile substrate; (c) calculated normalized energy release rate as a function of normalized crack diameter. (Adapted from J. J. Vlassak, M. D. Drory, and W. D. Nix, *J. Mater. Res.*, 12 (1997) 100.)



inated region can be related directly to the energy release rate for delamination.

- (b) Brittle film on ductile substrate. This is the opposite situation. In this case, the analysis is quite different. We follow here the approach of Vlassak, Drory, and Nix.<sup>10</sup> Figure 9.25(b) shows the configuration used by them. The indenter is made to penetrate through the thin film, into the substrate, deforming it plastically. A crack of size  $x$  is formed along the interface. It is possible to determine the critical energy release rate by using the Vlassak-Drory-Nix analysis. Figure 9.25(c) shows the relationship between  $G/G_0$  and the normalized crack diameter,  $x/a$ , for different values of  $E_{\text{film}}/\sigma_{\text{res}}$ .  $E_{\text{film}}$  is the Young's modulus of film and  $\sigma_{\text{res}}$  is the residual stress.  $G_0$  is the energy release rate due to just the residual stress. It is given by:

$$G_0 = \frac{(1 - \nu_{\text{film}}^2)}{2E_{\text{film}}} \sigma_{\text{res}}^2 t,$$

where  $t$  is the film thickness, and  $\nu_{\text{film}}$  is Poisson's ratio of the film.  $\sigma_{\text{res}}$  has to be separately calculated or measured. This simple technique enables the determination of the toughness of the bond between substrate and film. An example is the toughness of the titanium-diamond interface. Vlassak, Drory, and Nix obtained a value of  $51 \text{ J/m}^2$ . Diamond coatings are used in many applications where a hard, wear-resistant surface is required.

## Suggested Reading

- T. L. Andersen. *Fracture Mechanics*, 2nd ed. Boca Raton, FL: CRC, 1995.  
 R. W. Hertzberg. *Deformation and Fracture Mechanics of Engineering Materials*, 4th ed. New York, NY: John Wiley, 1996.  
 B. Lawn. *Fracture of Brittle Solids*, 2nd ed. Cambridge, U.K.: Cambridge University Press, 1993.  
 S. T. Rolfe and J. M. Barsom. *Fracture and Fatigue Control in Structures*. Englewood Cliffs, NJ: Prentice-Hall, 1977.

## Exercises

- 9.1** A Charpy machine with a hammer weighing 200 N has a 1-m-long arm. The initial height  $h_0$  is equal to 1.2 m. The Charpy specimen, (see Figure 9.2), absorbs 80 J of energy in the fracturing process. Determine:

- (a) The velocity of the hammer upon impact with the specimen.
- (b) The velocity of the hammer after breaking the specimen.
- (c) The average strain rate in the specimen.
- (d) The final height attained by the hammer.

- 9.2** Estimate the fraction of cleavage area in the four specimens shown in Figure 9.3.

<sup>10</sup> J. J. Vlassak, M. D. Drory, and W. D. Nix, *J. Mater. Res.*, 12 (1997) 1900.

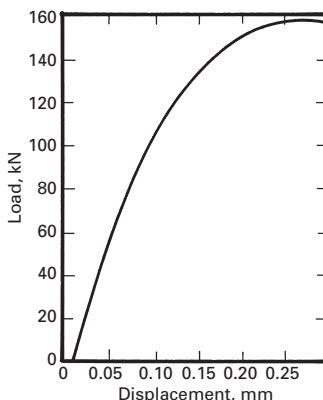


Fig. Ex9.5

9.3 Schematically show how the Charpy energy vs. temperature curve would be translated if the tests were carried at a low strain rate (approximately  $10^{-2} \text{ s}^{-1}$ ).

9.4 If, instead of Charpy specimens with standard thickness equal to 10 mm, you were to test specimens with reduced thickness (e.g., 5 mm) and increased thickness (e.g., 30 mm) what changes would you expect in the Charpy energy value, normalized to the thickness of the specimen.

9.5 The load-displacement curve, obtained from a fracture toughness test on metal sample is shown in Figure Ex9.5. The dimensions etc. are as follows:

Crack length  $a = 10 \text{ mm}$ ,  
Specimen thickness  $B = 15 \text{ mm}$ ,  
Specimen width  $W = 25 \text{ mm}$ ,  
Span  $S = 50 \text{ mm}$ ,  
Yield stress,  $\sigma_y = 300 \text{ MPa}$ .

Use the recommended procedure to determine the  $K_{Ic}$  from this curve. Check whether this is a valid  $K_{Ic}$  test.

9.6 A thermoplastic polymer has a plane-strain fracture toughness  $K_{Ic} = 15 \text{ MPa m}^{1/2}$  and a yield stress  $\sigma_y = 80 \text{ MPa}$ . Estimate the requirements for dimensions of a fracture toughness specimen for this material.

9.7 Two samples of 0.45% C steel, one quenched and the other normalized, were tested for fracture toughness in a three-point bend test. The dimensions of the sample and the load-deflection curves for the two are shown in Figure Ex9.7 Determine  $K_{Ic}$  for the two samples, and establish whether the tests are valid. Verify whether the plane-strain conditions are met. Which steel would you expect to show a higher toughness? Does the result match your expectation?

Given:

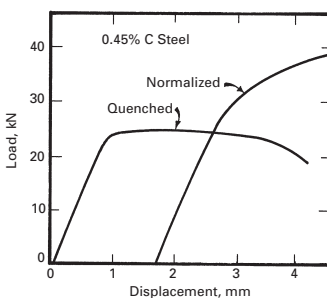
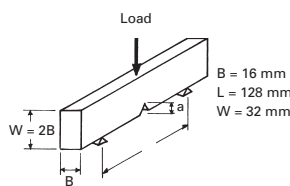


Fig. Ex9.7

	QUENCHED	NORMALIZED
$\sigma_y$	$1,050 \text{ MN/m}^2$	$620 \text{ MN/m}^2$
$a_1$	13.7 mm	9.3 mm
Precrack lengths:	$a_2 = 11.6 \text{ mm}$ $a_3 = 9.6 \text{ mm}$	$a_2 = 8.9 \text{ mm}$ $a_3 = 9.4 \text{ mm}$

9.8 A notched polymer specimen was tested for fracture toughness in a three-point bend test. The relevant dimensions of the specimen are:

Thickness  $B = 5 \text{ mm}$ ,  
Width  $W = 15 \text{ mm}$ ,  
Crack length  $a = 1 \text{ mm}$ ,  
 $S = 3.5W$

The load-deflection curve was linear until fracture occurred at 150 N. Compute  $K_{Ic}$  for this material.

9.9 A compact tension specimen of a polymer with the following dimensions was used in a fracture toughness test:

Thickness  $B = 5 \text{ mm}$ ,  
Width  $W = 50 \text{ mm}$ ,  
Crack length  $a = 20 \text{ mm}$ .

Assuming a linear displacement curve to failure at a load of 200 N, compute  $K_{Ic}$  for this polymer.

**9.10** A rectangular bar of ceramic 3 mm thick, 4 mm wide, and 60 mm long fractures in a four-point bend test at a load of 310 N. If the span of fixture is 50 mm, what is the flexure strength of the bar?

**9.11** Norton NC-132 hot pressed  $\text{Si}_3\text{N}_4$  has the following strengths for the given tests:

Three-point bending: 930 MPa,

Four-point bending: 720 MPa,

Uniaxial tension: 550 MPa.

Comment on the flaw sizes necessary to produce these failure stresses.

**9.12** Calculate the tensile stresses generated by a load of 200 N acting on a specimen of SiC (a rectangular section of 5 mm height and 10 mm width) subjected to (a) three-point and (b) four-point bending. The span width is 50 mm and, for the four-point bending setup, the inner span is 25 mm. If the specimens are prenotched, with a notch depth of 1 mm, what are the stress intensity factors?

**9.13** A cylindrical structural component with diameter 100 mm is subjected to a force of 100 kN at a distance of 500 mm from the clamp. The material used for the cylinder has a yield stress of 600 MPa. Will it yield plastically under the loading configuration shown in Figure Ex9.13? Use  $I = \pi r^4/4$  for the moment of inertia of a cylindrical shaft.

**9.14** In a sample of  $\text{MoSi}_2$ , an indentation made by a Vickers indenter gave the impression shown in Figure Ex9.14 under a load of 1 kN. Compute the hardness  $H$  of  $\text{MoSi}_2$ . Taking  $E$  for  $\text{MoSi}_2$  to be 300 GPa, compute the fracture toughness of the sample.

**9.15** Estimate the fracture toughness for  $\text{AsS}_3$  glass shown in Figure 9.22a, knowing that the indentation was made with load  $P = 10$  N. Young's modulus for this glass is  $E = 75$  GPa. Assume same magnification for the two micrographs.

**9.16** A chevron short-rod specimen with a diameter of 5 cm ( $\text{Al}_2\text{O}_3$ ) was tested, and the critical load  $P_c$  was equal to 2,000 N. Determine the fracture toughness of the specimen.

**9.17** Polymer specimens (PMMA (polymethyl methacrylate), PC (polycarbonate), and PP (polypropylene)) with the geometry shown in Figure Ex9.17 were tested.

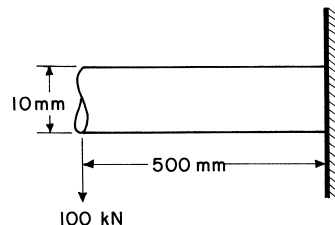


Fig. Ex9.13

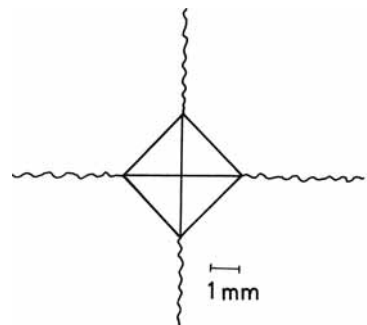


Fig. Ex9.14

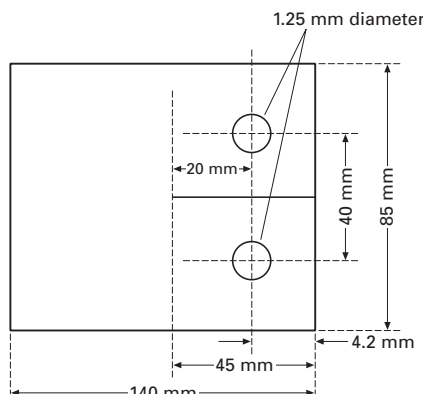
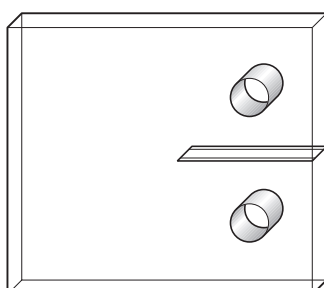


Fig. Ex9.17

The dimensions of specimens, crack, and load fracture for a number of tests are:

Test	Material	Crack Length, $a$ (mm)	Width, $W$ (mm)	Specimen thickness, $B$ (mm)	Load, $P$ (N)
1	PMMA	24.60	76.34	3.7	220.08
2	PMMA	24.80	75.88	5.92	421.00
3	PMMA	24.90	76.14	9.32	995.01
4	PMMA	23.88	76.24	11.54	1002.68
5	PMMA	13.52	76.18	11.38	1422.20
6	PMMA	19.72	76.14	11.63	1136.16
7	PMMA	37.86	76.24	11.58	621.80
8	PMMA	26.10	76.10	5.30	1184.15
9	PMMA	27.24	76.18	5.18	692.64
10	PMMA	27.72	76.20	5.32	1838.86
11	PMMA	28.68	76.16	5.84	1380.00
12	PC	25.04	76.10	5.82	2980.00
13	PP	24.28	76.14	6.36	1417.86

Calculate the fracture toughness for the specimens. Use the following equations:

$$K = \frac{P}{BW^{1/2}} f(a/W)$$

$$f(a/W) = \frac{[2 + (a/W)]}{[1 - (a/W)]^{3/2}} [0.886 + 4.64(a/W) - 13.32(a/W)^2 + 14.72(a/W)^3 - 5.6(A/W)^4].$$

**9.18** A compact tension specimen is used for the determination of fracture toughness. When it is loaded, the crack ( $a = 45$  mm) starts to propagate at an applied force of  $10^5$  N. The specimen thickness is  $B = 60$  mm. The dimension  $W$  is equal to 90 mm. Is this test valid? In other words, do we have a state of plane strain? The yield stress of the material is 500 MPa.

**9.19** After Charpy testing, what is the correlation between the energy absorbed and the appearance of the fracture surface? How does this relate to ductile and brittle materials?

**9.20** List the advantages and disadvantages of the Charpy test, drop-weight test, instrumented Charpy impact test, and plane-strain fracture toughness test.

**9.21** Estimate the minimum specimen thickness for a valid plane-strain fracture toughness test for a material having the following properties: yield stress,  $\sigma_y = 600$  MPa; fracture toughness,  $K_{Ic} = 150$  MPa m $^{1/2}$ .

**9.22** A structural aluminum plate (7075-T561,  $K_{Ic} = 29$  MPa m $^{1/2}$ ), part of an engineering design, has to support 200 MPa under tension. Determine the largest crack size that this plate can sustain.

**9.23** A test sample undergoes a crack opening displacement (COD) test. The thickness of the specimen is 7 mm, and the clip gage thickness is 0.6 mm.

The critical displacement,  $\Delta_c$ , of the clip gage is experimentally determined to be 1.5 mm, and the crack length is 1.4 mm. Compute the opening displacement,  $\delta_c$ .

**9.24** In a four-point bend test, the specimen has a span of 70 mm and a load,  $P$ , of 80 N. The width and height are 6 mm each. Draw the moment and shear diagrams. Find the maximum moment and maximum stress.

**9.25** A number of Charpy impact tests were conducted on steels containing different levels of Ni. The energy levels (in  $J/m^2$ ) are given in the table below:

Test Temperature (°C)	0% Ni	2% Ni	5% Ni	8% Ni
-200	2	2	5	28
-150	3	5	30	35
-100	6	15	55	37
-50	15	55	70	47
0	60	80	75	60
50	75	85	80	65
100	75	85	85	67

- (a) Plot the curves for the different alloys.
- (b) Find the DBTT for each alloy.
- (c) What can you conclude from your analysis?

---

## Chapter 10

# Solid Solution, Precipitation, and Dispersion Strengthening

## 10.1 | Introduction

A *solution* can be defined as a homogeneous mixture of two or more substances. Generally, one thinks of a solution as liquid, but gaseous or solid forms are possible as well. Indeed, we can have solutions of gases in a gas, gases in a liquid, liquids in a liquid, solids in a liquid, and solids in a solid. A solution can have one or more solutes dissolved in a solvent. The *solute* is the substance that is dissolved; the *solvent* is the substance in which the solute is dissolved. In a solution, there is always less solute than solvent. There are two kinds of solid solutions: substitutional and interstitial. Figure 10.1 shows examples of each in a schematic manner. Figure 10.1(a) is of brass, which is a substitutional solid solution of zinc (the solute) in copper (the solvent). We call such an alloy substitutional because the solute atoms merely substitute for the solvent atoms in their normal positions. In a substitutional solution, the atomic sizes of the solute and solvent atoms are fairly close. The maximum size difference is approximately 15%. When the atomic sizes of the solute and solvent are very different, as in the case of carbon or nitrogen in iron, we get an interstitial solid solution. Figure 10.1(b) shows such a solid solution of carbon in iron. We call these solutions interstitial solid solutions because the solute atoms occupy interstitial positions in the solvent lattice.

In this chapter, we first focus our attention on the phenomenon of *solid solution* and the *strengthening* that can be obtained by this process. Simply put, the phenomenon can be regarded as one form of restricting dislocation motion in crystalline materials, especially metals. We then extend this idea to precipitation and dispersion strengthening. Precipitates can be formed in certain alloys in the solid state. One starts with a solid solution at a high temperature, quenches it to a low temperature, and then ages it at an intermediate temperature to obtain a finely distributed precipitate. During aging, precipitates appear in a variety of sequences, depending on the alloy system under consideration. *Precipitation strengthening* has to do with the interaction of dislocations with precipitates, rather than with single atoms

of solutes. A logical extension of this idea is to artificially disperse hard ceramic phases in a soft metallic matrix, instead of obtaining them via a precipitation process. The mobility of dislocations is then restricted by these hard particles, and the alloy is strengthened. This process is called *dispersion strengthening*.

## 10.2 | Solid-Solution Strengthening

Dislocations are quite mobile in pure metals, and plastic deformation occurs by means of dislocation motion (i.e., by shear). A very versatile method of obtaining high strength levels in metals would be to restrict this rather easy motion of dislocations. We saw earlier that grain boundaries (Chapter 5) and stress fields of other dislocations (Chapter 6) can play this restrictive role at low temperatures and increase the strength of the material. When the dislocation mobility in a solid is restricted by the introduction of solute atoms, the resultant strengthening is called *solid-solution-hardening*, and the alloy is called a *solid solution*. An example of the strengthening that can be achieved by solid solution is shown in Figure 10.2(a), in which we plot the increase in yield stress of steel as a function of the content of the solute. Note that solutes such as carbon and nitrogen, which go into interstitial positions of the iron lattice, have much larger strengthening effects than substitutional atoms such as manganese. We shall explain this shortly. In order to analyze the phenomenon of hardening due to the presence of solute atoms, we must consider the increase in the stress necessary to move a dislocation in its slip plane in the presence of discrete barriers to the motion of dislocations. Conceptually, it is useful and easier to think in terms of an energy of interaction between the dislocation and the barrier (e.g., a solute atom or a precipitate). In the case of substitutional solutions, for a stationary dislocation, the interaction energy is the change in energy of the system consisting of a crystal and a dislocation when a solvent atom is removed and substituted with a solute atom. Knowing the interaction energy  $U$ , we can calculate the force  $dU/dx$  necessary to move a dislocation a distance  $dx$  normal to its length. In ceramics, solutes can also exercise a strengthening effect, as demonstrated by Figure 10.2(b) for monocrystalline alumina with additions of chromium. This increase manifests itself at high temperatures, where the ceramics become relatively ductile.

A dislocation has a stress field associated with it. (See Chapter 4.) Solute atoms, especially when their sizes are too large or too small in relation to the size of the host atom, are also centers of elastic strain. A solute atom is said to be a *point source* of dilation. A vacancy (i.e., a vacant lattice site) can also be considered a point source of (negative) dilation. Consequently, the stress fields from these sources (dislocations and point defects) can interact and mutually exert forces. Such an interaction due to size difference is called the *elastic misfit interaction* or *dilatational misfit interaction*. Other types of interactions,

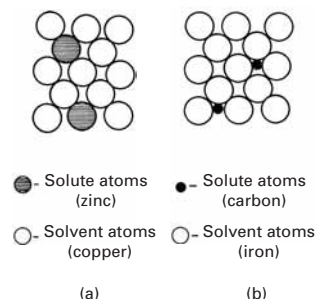


**Fig. 10.1** The two basic forms of solid solutions. (a) Substitutional solid solution of zinc in copper to form brass. (b) Interstitial solid solution of carbon in iron to form steel. The interstitial solid-solution carbon atoms are shown in the face-centered cubic form of iron.

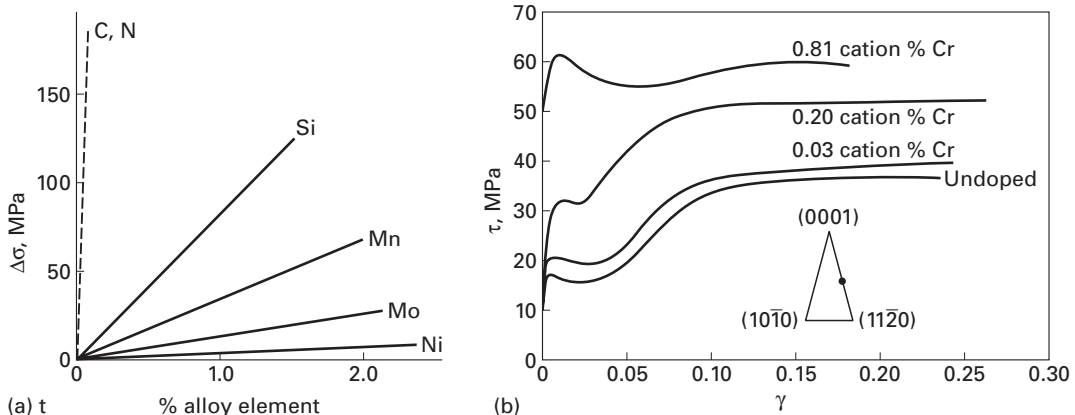
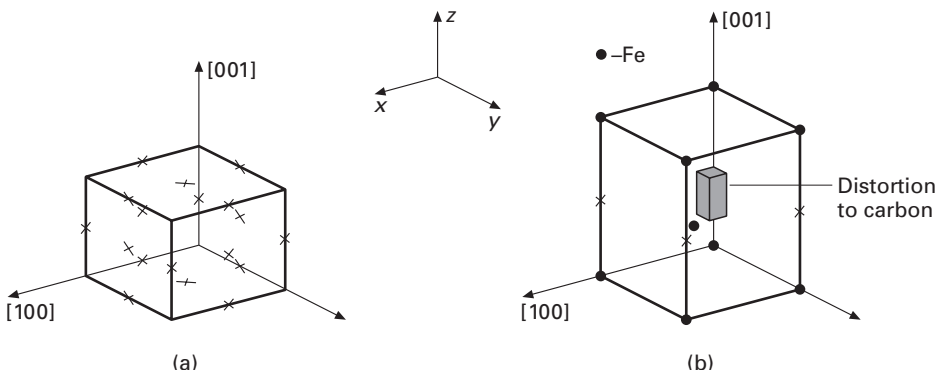


**Fig. 10.2** (a) Increase in strength,  $\Delta\sigma$ , of steel as a function of content of solute. The solid lines represent substitutional solute additions, while the dashed line represents interstitial solute additions. (After F. B. Pickering and T. Gladman, ISI Special Report 81, Iron and Steel Inst., (London: 1963), p. 10). (b) Increase in strength of sapphire (monocrystalline alumina) with small additions of chromium at 1400 °C (Adapted from K. P. D. Lagerlof, B. J. Pletka, T. E. Mitchell, and A. H. Heuer, *Radiation Effects*, 74 (1983) 87.)

such as electrical and chemical elastic modulus mismatch, are also possible. Each of these interactions represents an energy barrier to dislocation motion.

### 10.2.1 Elastic Interaction

In the case of a positive edge dislocation, there is an extra half plane above the slip plane. Hence, there will be a compressive stress above the slip plane and a tensile stress under it (Chapter 4). Because a solute atom placed randomly in a crystal has a stress field around it, this stress field would be minimized if the solute atom were to move to the dislocation. For the case of an interstitial atom of carbon in iron, the minimum-energy position at an edge dislocation is the dilated region near the core. A substitutional atom that is smaller than the solvent atom will tend to move to the compressive side. On the other hand, if a solute atom is larger than the solvent atom, it will be expected to move to the tensile side. Substitutional atoms such as Zn in Cu give rise to a completely symmetrical spherical distortion in the lattice, which corresponds to the elastic misfit problem associated with inserting a ball in a bigger or smaller hole; that is, the substitutional solute atom acts as a point source of dilation of spherical symmetry. It is important to note that such spherically symmetric stress fields caused by substitutional impurity atoms can interact only with defects that have a hydrostatic component in their stress fields, as happens to be the case with an edge dislocation (see Equations 4.12a–c). Screw dislocations, by contrast, have a stress field of a pure shear character; that is, the hydrostatic component of a screw dislocation is zero (see Equations 4.11a and b). Therefore, to a first approximation, there is no interaction between screw dislocations and substitutional atoms, such as Zn in Cu or Mn in Fe. Interstitial atoms such as carbon or nitrogen in  $\alpha$ -iron, however, not only produce a dilational misfit (in volume), but also induce a tetragonal distortion. Both carbon and nitrogen occupy interstitial positions at the face centers and/or the midpoints of the edges of the body-centered cubic structure (Figure 10.3). Carbon atoms occupy the midpoints of  $\langle 001 \rangle$  edges. In Figure 10.3(a), we indicate the positions of the carbon atoms



by crosses. Figure 10.3(b) depicts the tetragonal distortion produced when a carbon atom moves to one of the cube edges of iron. The cubic shape changes to tetragonal, producing a tetragonal distortion along that particular  $\langle 001 \rangle$  axis. Note that the figure shows the tetragonal distortion produced by a carbon atom in the iron cube; the carbon atom does not have an elongated form! The strain field attributed to this tetragonal distortion will interact with hydrostatic as well as shear stress fields. The important effect of the tetragonal distortion is that the interstitial atoms such as C and N in iron will interact and form atmospheres at both edge and screw dislocations and will lead to a more effective impediment to the movement of dislocations than in the case of substitutional atoms. (See Figure 10.2.)

We now derive an expression for the energy of interaction between an edge dislocation and a point source of expansion, such as an oversized (or undersized) solute atom. This was first done by Cottrell<sup>1</sup> and Bilby.<sup>2</sup> Let  $\sigma_\rho$  be the hydrostatic component of the stress field of a dislocation, and let  $\Delta V$  be the change in volume induced by the introduction of a solute atom of radius  $r_0(1 + \varepsilon)$  in a cavity of radius  $r_0$ , where  $\varepsilon$  is positive. Then, for  $\varepsilon$  very small, we can write the change in volume as

$$\Delta V = \left(\frac{4}{3}\right)\pi r_0^3(1 + \varepsilon)^3 - \frac{4}{3}\pi r_0^3 = \frac{4}{3}\pi r_0^3[(1 + \varepsilon)^3 - 1],$$

so that

$$\Delta V \approx \frac{4}{3}\pi r_0^3 3\varepsilon,$$

or

$$\Delta V \approx 4\pi r_0^3 \varepsilon. \quad (10.1)$$

The stress field of an edge dislocation is given in rectangular coordinates in Chapter 4 (Equations 12a–c). In cylindrical coordinates, we

**Fig. 10.3** (a) Positions of interstitial atoms in the cube. (b) Carbon atom shown as a producer of a tetragonal distortion.

<sup>1</sup> A. H. Cottrell, in Proceedings of Conference on Strength of Solids, Physical Society, London, 1968, p. 30.

<sup>2</sup> B. A. Bilby, Proc. Phys. Soc., A63 (1950) 191.

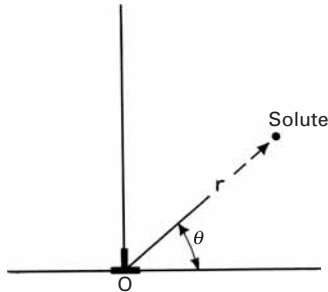


**Fig. 10.4**  $(r, \theta)$ -coordinates of a solute atom in the strain field of an edge dislocation.

have (the student can do this as an exercise):

$$\begin{aligned}\sigma_{rr} = \sigma_{\theta\theta} &= -\frac{Gb}{2\pi(1-v)} \frac{\sin \theta}{r}, \\ \sigma_{zz} &= -\frac{vGb}{\pi(1-v)} \frac{\sin \theta}{r}, \\ \sigma_{r\theta} &= -\frac{Gb}{2\pi(1-v)} \frac{\cos \theta}{r}, \\ \sigma_{\theta z} = \sigma_{zr} &= 0.\end{aligned}$$

The hydrostatic pressure  $\sigma_p$  is, by definition, equal to  $-1/3(\sigma_{rr} + \sigma_{\theta\theta} + \sigma_{zz})$ . Thus, the hydrostatic stress associated with an edge dislocation, obtained from the preceding stress field, is

$$\sigma_p = \frac{1+v}{1-v} \frac{Gb}{3\pi} \frac{\sin \theta}{r}. \quad (10.2)$$

If we wish to convert this expression into rectangular coordinates, we need only use the relationship  $r = (x^2 + y^2)^{1/2}$  and  $\sin \theta = y/(x^2 + y^2)^{1/2}$ .

The interaction energy ( $U_{\text{int}}$ ) was defined by Eshelby<sup>3</sup> for a general ellipsoid of volume  $V$  in which both deviatoric and hydrostatic components of strain are generated and a general external stress field  $\sigma_{ij}$  as

$$U_{\text{int}} = V \sigma_{ij} (\varepsilon_{ij})_T,$$

where  $(\varepsilon_{ij})_T$  is the strain tensor due to the transformation. For the simplified case of the solute atom, the stress is  $\sigma_p$  and the strain is  $\Delta V$  per unit volume. We can calculate  $U_{\text{int}}$  in the following manner. Figure 10.4 shows the coordinates of a solute atom in the strain field of a dislocation. The elastic interaction energy due to misfit,  $U_{\text{misfit}}$ , for a solute atom at  $(r, \theta)$  and at the dislocation origin  $(0, 0)$  can be obtained from Equations 10.1 and 10.2 as

$$U_{\text{misfit}} = \sigma_p \Delta V = \frac{1+v}{1-v} \frac{Gb}{3\pi} \frac{\sin \theta}{r} 4\pi \varepsilon r_0^3 = A \frac{\sin \theta}{r}, \quad (10.3a)$$

where

$$A = \frac{4}{3} \frac{1+v}{1-v} G b \varepsilon r_0^3.$$

The force exerted by the solute on the dislocation is

$$F = -\partial U_{\text{misfit}} / \partial r = A \sin \theta / r^2. \quad (10.3b)$$

Hence, solute atoms are attracted to dislocations and form what is called a “Cottrell atmosphere” around them, pinning them. This is especially true for interstitials, which tend to have a high mobility. Calculations similar to the foregoing can be carried out for interstitials that cause nonspherical distortions. Equation 10.3a is derived on the basis of linear elasticity theory; thus, it will not be valid at

<sup>3</sup> J. D. Eshelby, Proc. Roy. Soc., A241 (1957) 376; A252 (1959) 561.

the dislocation core region, where linear elasticity does not apply. This is a great omission, as the binding energy will be a maximum precisely at the dislocation core. Therefore, the reader is forewarned that the interaction energy just determined is only an estimate. Consider again Equation 10.3a and Figure 10.4. The interaction energy  $U$  is positive in the region above the slip plane ( $0 < \theta < \pi$ ) and is negative below the slip plane ( $\pi < \theta < 2\pi$ ) for large solute atoms. This means that a solute atom larger in size than the matrix atom (i.e.,  $\Delta V$  positive) will be repelled by the compressive side of the edge dislocation and will be attracted by the tensile side, as the interaction energy will be negative there. For a solute atom of smaller size than the matrix atom (i.e.,  $\Delta V$  negative), the interaction energy will be negative in the upper part ( $0 < \theta < \pi$ ) of the dislocation, and the solute will be attracted there. In both cases, solute atoms will migrate to the dislocation, which will result in a reduction in the free energy of the system.

It is possible to estimate the increase in stress required to move a dislocation from the number of solute atoms surrounding it. Let the maximum force  $F_{\max}$  between a dislocation and a solute atom be given by Equation 10.3b. When  $r$  reaches a sufficiently low value, we have (from Peach-Koehler's equation, Equation 4.22c, Chapter 4)

$$\Delta\tau = F_{\max}/bL = A \sin \theta / r^2 b L,$$

where  $L$  is the spacing of solute atoms that "pin" a dislocation. A number of assumptions can be made to establish  $F_{\max}$  and  $L$ . We shall make the very simple assumption that all solute atoms move to certain distance  $b$  from the dislocation. If  $C$  is the concentration of solute atoms per unit volume and  $\rho$  is the dislocation density (equal to the dislocation length per unit volume), then the spacing between solute atoms along a dislocation is

$$L = \rho/C.$$

Thus,

$$\Delta\tau = A \sin \theta C / r^2 b \rho.$$

If  $r \approx b$  and  $\sin \theta \approx 1$ , we get

$$\Delta\tau = A C / b^3 \rho.$$

Figure 10.2 shows such dependence of change in yield stress on solute content. On the other hand, if the solute atoms form a rigid network in the lattice, the average spacing between solute atoms is

$$L' \approx C^{-1/3}.$$

The spacing  $L$  of solute atoms along the plane of a moving dislocation is determined by several factors, including the angle of bowing out of the dislocation between obstacles. The misfit interaction energy in such a case may be calculated by use of statistics.

The misfit energy for screw dislocations is given by

$$U_{\text{misfit}} = \varepsilon_{ij} \sigma_{ij}^{\text{screw}} \Omega,$$

where  $\sigma_{ij}^{\text{screw}}$  represents the stress field associated with a screw dislocation and  $\Omega$  is the specific volume given by  $\Delta V = 3\Omega\varepsilon$ , in which  $\varepsilon$  is the misfit parameter. The resultant force exerted by the interstitial atom on the dislocation has an equation similar to that in the case of a substitutional solute atom, but with the misfit parameter replaced by  $(\varepsilon_{11} - \varepsilon_{22})/3$ . A substitutional solute atom produces an isotropic strain field, i.e.,  $\varepsilon_{11} = \varepsilon_{22} = \varepsilon_{33}$ , and it does not interact with a screw dislocation. However, for C in  $\alpha$ -Fe, one has the extensional strain in the [100] direction,  $\varepsilon_{11} = 0.38$ , while the contractional strain along each of the two orthogonal directions, [010] and [001], is  $-0.026$ . Therefore, C in  $\alpha$ -Fe hinders both edge and screw dislocations. It turns out that interstitial atoms with  $(\varepsilon_{11} - \varepsilon_{22})$  as much as unity can show solubility in BCC metals. The reason for this is that metals can accommodate a greater uniaxial distortion than isotropic distortion by solute atoms, since the electron energy depends mainly on the specific volume.

### 10.2.2 Other Interactions

Besides the dilation and elastic misfit interactions there are other sources of dislocation-solute interactions: interactions due to a difference in modulus between the solute and the solvent, electrical interaction, chemical interaction, and local-order interaction due to the fact that a random atomic arrangement may not be the minimum-energy state in a solid solution. All these interactions will further hinder dislocation motion in a solid solution. Generally, however, their contributions are less important than the size effect described earlier.

## 10.3 Mechanical Effects Associated with Solid Solutions

Many important mechanical effects are associated with the phenomenon of solid solution. In the case of steels, solute-dislocation interaction leads to a migration of interstitial solute atoms to a dislocation, where they form an atmosphere around it. This solute atmosphere, called the *Cottrell atmosphere*, has the effect of locking-in the dislocation, making it necessary to apply more force to free the dislocation from the atmosphere. This results in the well-known phenomenon of a pronounced yield drop in annealed low-carbon steels. A word of caution is in order here. Temperature is an important variable in the migration of solute atoms to a dislocation. If the temperature is too low, the solute may not be able to diffuse to allow a redistribution of solute atoms to dislocations. Such a redistribution may be thermodynamically expected, but if the temperature is too low, it will not occur in a reasonable length of time. At very high

temperatures ( $>0.5T_m$ , where  $T_m$  is the melting point in kelvin), the mobility of foreign atoms will be much higher than that of dislocations, with the result that they will not restrict dislocation motion. In the range of temperatures where solute atoms and dislocations are about equally mobile, strong interactions with dislocations occur. The serrated stress-strain curve (or the Portevin-Le Chatelier effect) is another manifestation of this. We next describe some technologically important effects of solid-solution hardening.

### Example 10.1 |

Why are substitutional solid solutions more common than interstitial solid solutions?

**Solution:** Substitutional solid solutions are more common than interstitial ones mainly because of the atomic size limitations. Substitutional solid solubility can be quite appreciable – up to a difference of 14% in the atomic diameters of two metals can be accommodated. Copper (atomic radius = 0.128 nm), for example, can dissolve up to about 35% of zinc (atomic radius = 0.1331 nm) atoms in a substitutional manner. Cu and Ni (atomic radius = 0.1246 nm) have complete miscibility, from 0 to 100%. In the case of interstitial solid solutions, a small atom (C, N, or H, for instance) has to lodge itself in the interstices of the solvent metal atoms. C in  $\gamma$ -Fe (FCC) has available larger sized interstices than it does in  $\alpha$ -Fe (BCC), although there are more interstices available in the latter. This is the reason that C has a comparatively greater solubility in  $\gamma$ -Fe than in  $\alpha$ -Fe. In general, however, the range of interstitial hole sizes available is not very large – hence, the less common occurrence of interstitial solid solutions.

#### 10.3.1 Well-Defined Yield Point in the Stress–Strain Curves

A schematic stress–strain curve exhibiting a well-defined yield point is shown in Figure 10.5(a). Characteristically, annealed low-carbon steels show such stress–strain behavior. According to the theory of Cottrell and Bilby, the dislocations in annealed steels ( $\rho \sim 10^7 \text{ cm}^{-2}$ ) are locked-in by the interstitial solute atoms (carbon). When stress is applied to such a steel in a tensile test, it must exceed a certain critical value to unlock the dislocations. The stress necessary to move the dislocations is less than the stress required to unlock them – hence the phenomenon of a sharp yield drop and the appearance of an upper and lower yield point in the tensile stress–strain curve. Figure 10.5(b) shows how a steel containing 0.008% C reacts to one-hour aging treatments. The progressive formation of a yield point with a subsequent plateau is clearly seen. After the dislocations have freed themselves from the Cottrell atmosphere, all the tensile curves in Figure 10.5(b) become identical. The solute atoms

**Fig. 10.5** (a) Schematic stress-strain curve of an annealed low-carbon steel showing the yield-point phenomenon. (b) Low-carbon steel in a temper-rolled condition and annealed for one hour between 100 °C and 343 °C. (Courtesy of R. Foley.)

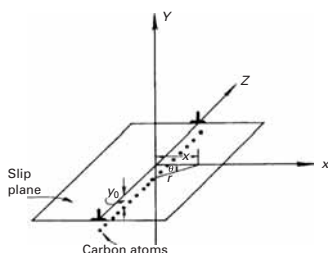
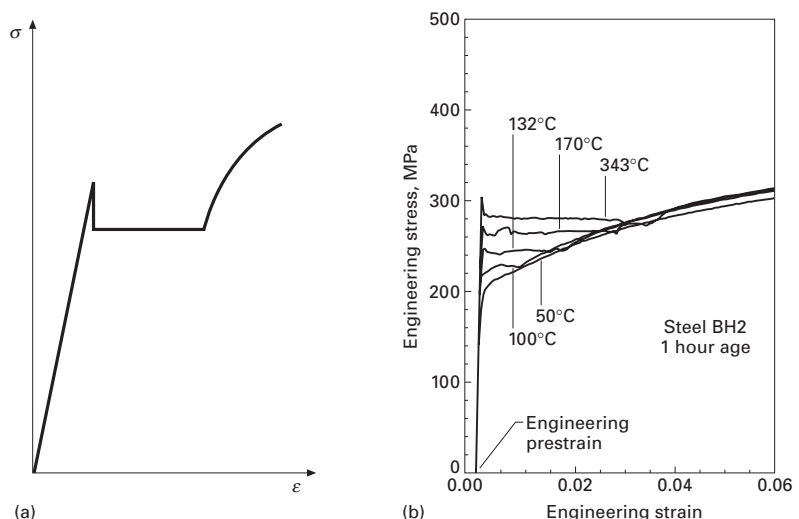


**Fig. 10.6** Cottrell atmosphere in iron consisting of an edge dislocation and a row of carbon atoms.

segregate to the dislocations because this results in a decrease in the free energy. Given proper conditions for atomic diffusion, one would expect complete segregation of solute atoms to dislocations. Figure 10.6 shows schematically a Cottrell atmosphere of C atoms at a dislocation core in iron. In iron, atoms of carbon and nitrogen diffuse easily at ambient temperatures, but in many substitutional alloys one has to resort to treatments at higher temperatures.

### 10.3.2 Plateau in the Stress–Strain Curve and Lüders Band

After the load drop corresponding to the upper yield point, there follows a plateau region in which the stress fluctuates around a certain value. The elongation that occurs in this plateau is called the *yield-point elongation*. (See Figure 10.5.) It corresponds to a region of nonhomogeneous deformation. In a portion of the tensile sample where there is a stress concentration, a deformation band appears such as that indicated in Figure 10.7(a). As the material is deformed, this band propagates through the test sample. An intermediate position is indicated in Figure 10.7(b). The deformation is restricted to the interface. This deformation band is known as the *Lüders band*. In the plateau region of the stress–strain curve, there could be two or more such bands. Sometimes Lüders bands are visible to the naked eye. After the formation of the last band, the stress–strain curve resumes its normal trajectory of strain-hardening. Knowing the cross-sectional areas  $A_1$  and  $A_2$  in Figure 10.7(b), one can determine the number of Lüders bands from the yield-point elongation. One can also determine, from the strain rate of the sample, the speed of propagation of these bands. An aspect of great technological importance is the formation of Lüders bands during the stamping of low-carbon steels, with the consequent irregularities in the final thickness of the sheet (see Section 3.9.2). This problem is tackled, in practice, in two ways:

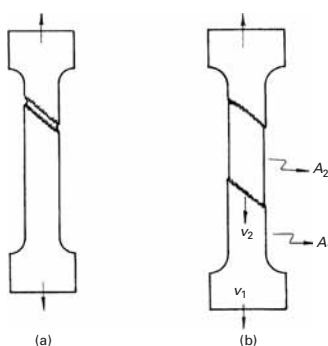


**Fig. 10.7** Propagation of Lüders band in a tensile sample.  $v_1$  and  $v_2$  are the velocities of deformation of the specimen and the Lüders band, respectively.

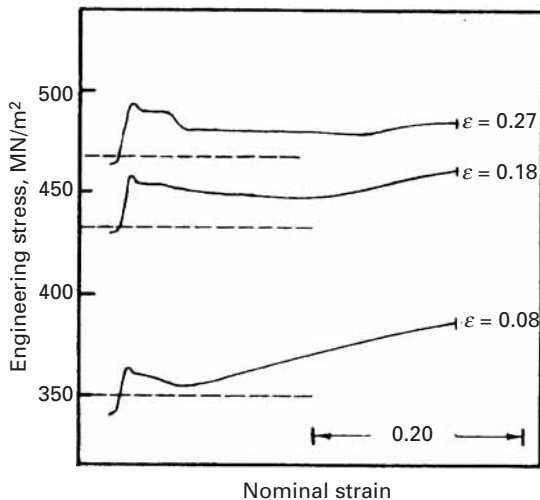


**Fig. 10.8** Reloading curves after stopping a test for three hours at nominal strains of 0.08, 0.18, and 0.27. The dashed lines indicate the stresses at which the test was stopped. Note the formation of a well-defined yield point in the three cases (Reprinted with permission from M. A. Meyers and J. R. C. Guimarães, *Metalurgia – ABM*, 34 (1978) 707.)

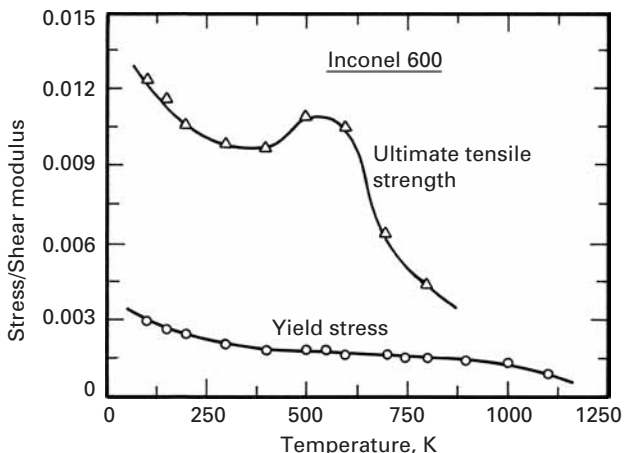
1. By changing the composition of the alloy to eliminate the yield point. The addition of aluminum, vanadium, titanium, niobium, or boron to steel leads to the formation of carbides and nitrides as precipitates, which serve to remove the interstitial atoms from the solid solution.
2. By prestraining the sheet to a strain greater than the yield point strain such that the strains during the stamping operations occur in the strain-hardening region.

The explanation for the formation of Lüders bands is intimately related to the cause of the appearance of the well-defined yield point. The unlocking of dislocations that occurs at the upper yield point is, initially, a localized phenomenon. The unlocked dislocations move at a very high speed, because the stress required to unlock them is much higher than the stress required to move them, until they are stopped at grain boundaries. The stress concentration due to the dislocations that accumulate at grain boundaries unlocks the dislocations in the neighboring grains.

### 10.3.3 Strain Aging

As pointed out in the preceding sections, prestraining the steel to a strain greater than the yield strain will result in the removal of the yield point. However, if we let the sample rest before retesting, the yield point will return. This phenomenon is known as *strain aging*. Figure 10.8 shows the result of experiments done with an annealed austenitic alloy of composition Fe – 31% Ni – 0.1% C. The tensile test was stopped three times, each time for 3 hours, after three different strains:  $\epsilon = 0.08$ ,  $0.18$ , and  $0.27$ . The test was stopped simply by turning off the machine. Initially, the sample did not show a well-defined yield point. However, on reloading after the three-hour rest, the stress-strain curve showed clearly the appearance of a yield point followed by a plateau – i.e., a horizontal load-drop region – and, finally, a return to the original trajectory. The dashed lines indicate the

**Fig. 10.9** Dependence of yield stress and ultimate tensile stress on temperature for Inconel 600, a nickel-based superalloy. The hump in the curve due to dynamic strain aging is usually evident only at large strains. (After R. A. Mulford and U. F. Kocks, *Acta Met.*, 27 (1979) 1125.)



values of stress at which the test was stopped. Note that, on reloading, the yield stress of the alloy increased for the three strains. The term “aging” is normally used when a precipitate forms. (See Section 10.4.) However, this is not the case in the example at hand. As the test was alternately carried out and interrupted at ambient temperature, interstitial atoms would migrate to dislocations during the interruptions, locking the dislocations. On reloading, the dislocations were unlocked, and a well-defined yield point appeared. The experiments were carried out under identical conditions, but keeping the test sample unloaded for three hours. The well-defined yield point reappeared, but it was less marked. The above experiment indicates that the applied stress has an accelerating effect on the strain-aging process. Generally, low-carbon steels show strain aging.

Another commonly observed effect due to strain aging is an enhancement of the work-hardening rate, leading to an increase in the ultimate tensile strength of the material. This effect is sometimes referred to as *dynamic strain aging*, because it occurs concurrently with plastic deformation. In some cases, the plot of flow stress vs. temperature shows a hump. The hump in the curve of ultimate tensile strength (UTS) vs. temperature for a nickel-based superalloy, Inconel 600, is shown in Figure 10.9. This hump is caused by solute atoms that have a mobility higher than the dislocations and that, therefore, can continue to “drag” them, leading to increased work-hardening. This enhanced work-hardening leads to a higher UTS. Note that the yield stress does not show such a hump.

#### 10.3.4 Serrated Stress–Strain Curve

Under certain conditions, some metallic alloys show irregularities in their stress-strain curves that can be caused by the interaction of solute atoms with dislocations, by mechanical twinning, or by stress-assisted (“burst”-type) martensitic transformations. The first type (i.e., due to solute–dislocation interaction) has been called the *Portevin–Le Chatelier* effect. It generally occurs within a specific range of

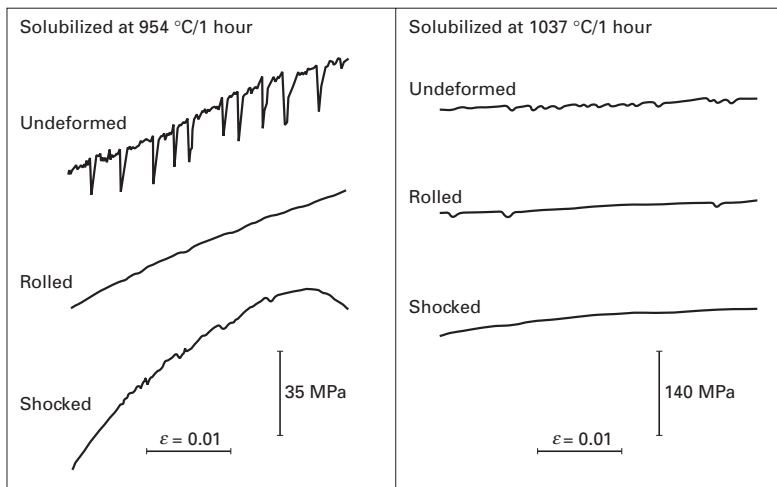


**Fig. 10.10** Serrated flow observed in tensile test performed at 650 °C in Inconel 718 (a nickel–iron-based superalloy) solubilized at two temperatures. The undeformed, cold-rolled (19.1% reduction) and shock-loaded (51 GPa peak pressure) conditions are shown. (From M. A. Meyers, Ph.D. dissertation, 1974.)

temperatures and strain rates. The solute atoms, being able to diffuse through the test sample at a speed greater than the displacement speed of the dislocations (imposed by the applied strain rate), “chase” the dislocations, eventually locking them. With increasing load, the unlocking of dislocations causes a load drop with the formation of small irregularities in the stress–strain curve.

Irregularities in the stress–strain curves of a nickel–iron-based superalloy, Inconel 718, tested in tension at 650 °C after different processing schedules, are shown in Figure 10.10. Interactions between the solute atoms are more intense in the metal’s undeformed condition. The stabilization treatment of 554 °C for one hour produced more pronounced load drops. The Portevin–Le Chatelier effect is dependent on the density of dislocations, strain rate, concentration and mobility of solute atoms, and other factors. The effect occurs in a region where there is inverse strain-rate sensitivity (i.e., if the strain is increased, the flow stress decreases). This relationship is attributed to the interplay between solute atoms and dislocations. Under normal conditions – that is, in the absence of solute – the flow stress increases with strain rate. In the Portevin–Le Chatelier regimen, an increase in strain rate frees the dislocations from the solute atoms.

### 10.3.5 Snoek Effect

Interstitial solute atoms such as carbon and nitrogen can, under the action of an applied stress, migrate in the  $\alpha$ -Fe lattice. Such short-range migrations of C or N can result in an anelastic or internal friction effect, called the Snoek effect after the person who discovered it. As mentioned earlier, carbon or nitrogen atoms occupy the octahedral interstices located at the midpoints of the cube edges and at the centers of the cube faces. If we apply a stress along the  $z$ , or [001], direction, the octahedral interstices along the  $x$ - and  $y$ -axes will contract, while the ones in the  $z$ -direction will expand. Given the right time and temperature, the interstitial atoms will move to sites

along the  $z$ -axis. Such a change of site leads to a reduction in strain energy. On the other hand, a stress applied in the [111] direction will not result in a change of site, because all three of the cube's directions will be equally stressed and, on average, equally occupied by the carbon atoms. Such a movement of interstitials, when stress is applied along a cube direction and at levels less than the yield stress, can cause strain to lag behind stress; that is, the material will show the phenomenon of *internal friction*. The effect of this internal friction is commonly measured by a torsional pendulum. The angle of lag is called  $\delta$ , and  $\tan \delta$  is taken as a measure of the internal friction. Mathematically,

$$\tan \delta = \frac{\text{log decrement}}{\pi} = Q^{-1},$$

where the logarithmic decrement is the ratio of successive amplitudes of the swing of the pendulum. If the amplitude decays to  $1/n$  of its original value in time  $t$ , then

$$\tan \delta = Q^{-1} = \frac{\ln(1/n)}{\pi v t},$$

where  $v$  is the vibrational frequency of the pendulum.

Only the interstitials that occupy the normal sites in an undistorted lattice will contribute to internal friction. Interstitials in the strain fields of a dislocation or a substitutional solute atom, or those at a grain boundary, will have their behavior altered. Thus, the Snoek effect can be used to measure C or N concentration in *high-purity* ferrite, i.e., BCC  $\alpha$ -Fe. Would you expect to observe the Snoek effect in  $\gamma$ -Fe?

### 10.3.6 Blue Brittleness

Carbon steels heated in the temperature range of 230 and 370 °C show a notable reduction in elongation. This phenomenon is due to the interaction of dislocations in motion with the solute atoms (carbon or nitrogen) and is intimately connected with the Portevin-Le Chatelier effect. We classify it separately because of its distinct importance. When the temperature and the strain rate are such that the speed of the interstitial atoms is more than that of the dislocations, the dislocations are continually captured by the interstitials. This results in a very high strain-hardening rate and strength with a reduction in elongation. With increasing strain rates, the effect occurs at higher temperatures, as diffusivity increases with temperature. Called *blue brittleness*, this effect refers to the coloration that the steel acquires due to the oxide layer formed in the given temperature range. In the range of temperature and strain rate in which the material is subjected to dynamic aging, the strain-rate sensitivity is also affected, tending to increase linearly with temperature. However, in the presence of dynamic aging, the strain-rate sensitivity becomes very small, and the yield stress becomes practically independent of the strain rate.

## 10.4 | Precipitation- and Dispersion-Hardening

Precipitation-hardening, or age-hardening, is a very versatile method of strengthening certain metallic alloys. Two important alloy systems that exploit this strengthening technique are aluminum alloys and nickel-based superalloys. Figure 10.11 shows examples of precipitates in some systems. Figure 10.11 (a) shows a typical example of an Al–Cu alloy, with  $\theta$  ( $\text{CuAl}_2$ ) precipitates at the grain boundaries and  $\theta'$  ( $\text{Cu}_2\text{Al}$ ) precipitates in the grain interiors, Figure 10.11(b) shows  $\text{Al}_3\text{Li}$  precipitates in an Al–Li alloy, and Figure 10.11(c) shows  $\gamma'$  ( $\text{Ni}_3\text{Al}$ )

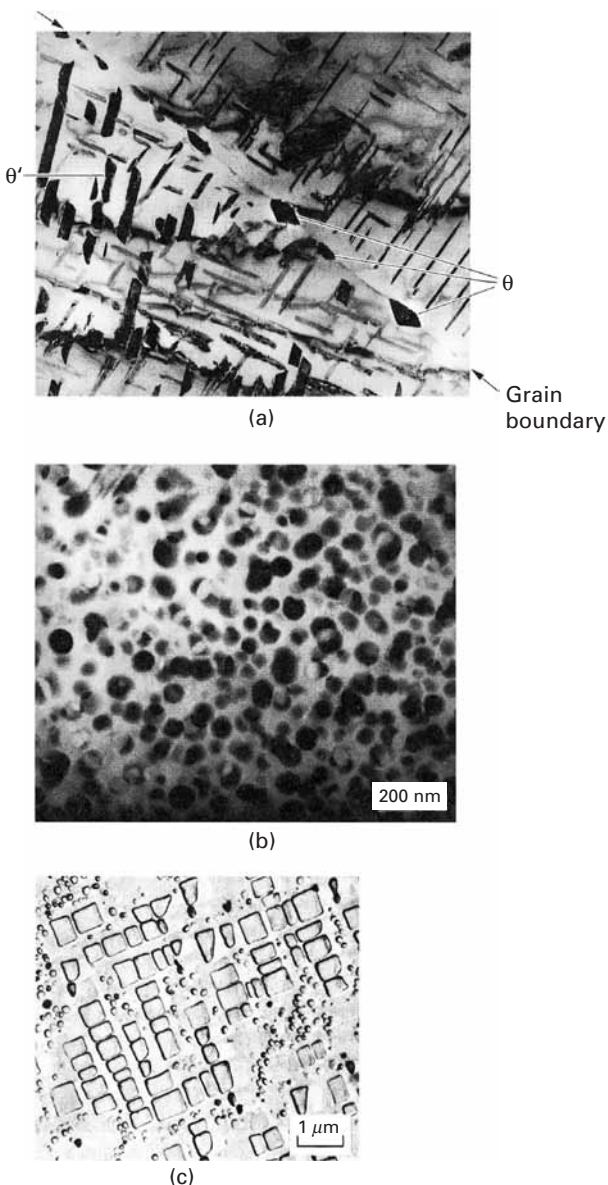
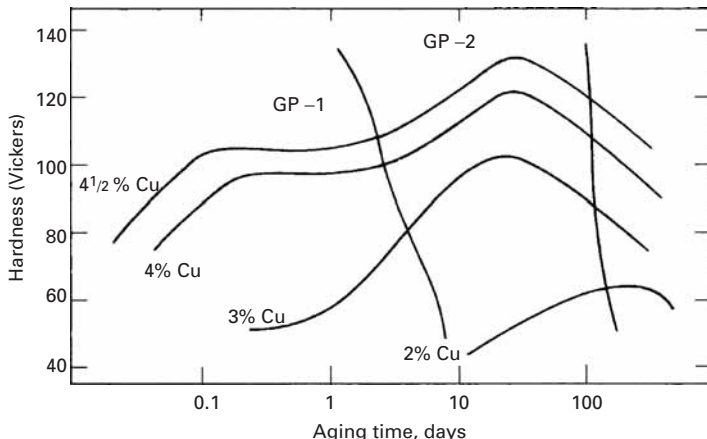


**Fig. 10.11** (a)  $\theta$  precipitates (at grain boundaries) and  $\theta'$  precipitates (in grain interior) in Al–Cu alloy. (Courtesy of K. S. Vecchio.) (b)  $\text{Al}_3\text{Li}$  precipitates in Al–Li alloy (TEM, dark field). (Courtesy of K. S. Vecchio.) (c)  $\gamma'$  precipitates and aged carbides in a superalloy. (Courtesy of R. N. Orava.)

**Fig. 10.12** Change in hardness with time of various Al–Cu alloys aged at 130 °C. (Adapted with permission from H. K. Hardy and T. J. Heal, *Prog. Metal Phys.*, 5 (1954) 195.)



precipitates and aged carbides in a nickel-based superalloy. The aging treatment involves the precipitation of a series of metastable and stable precipitates out of a homogeneous, supersaturated solid solution. Various metastable structures offer different levels of resistance to dislocation motion. Figure 10.12 shows the variation in hardness with aging time in the aluminum–copper system. Also shown are the different types of precipitate that occur during the aging treatment. Peak hardness or strength corresponds to a critical distribution of coherent or semicoherent precipitates.

In dispersion-hardening, we incorporate hard, insoluble second phases in a soft metallic matrix. Here, it is important to distinguish dispersion-strengthened metals from particle-reinforced metallic composites. The volume fraction of dispersoids in dispersion-strengthened metals is generally low, 3–4% maximum. The idea is to use these small, but hard, particles as obstacles to dislocation motion in the metal and thus strengthen the metal or alloy without affecting its stiffness in any significant way. In the case of metallic particulate composites, the objective is to make use of the high stiffness of particles such as alumina to produce a composite that is stiffer than the metal alone. Improvements in strength, especially at high temperatures, also result, but at the expense of ductility and toughness. Examples of dispersion-strengthened systems include  $\text{Al}_2\text{O}_3$  in Al or Cu,  $\text{ThO}_2$  in Ni, and more. TD Nickel is the name of an oxide-dispersion-strengthened nickel. Very small spherical particles (20–30 nm in diameter) of thorium dioxide ( $\text{ThO}_2$ ) are dispersed in nickel matrix by powder metallurgical processing. Dispersion-strengthened copper is made by an internal oxidation technique. An alloy of copper and a small amount of aluminum is melted and atomized into a fine powder. Heating the powder under oxidizing conditions leads to an *in situ* conversion of aluminum into alumina. Any excess oxygen in the copper is removed by heating the powder in a reducing atmosphere. The powder is then consolidated, followed by conventional metalworking. We give some examples of dispersion-hardened systems later in this chapter. Suffice it here merely to point out

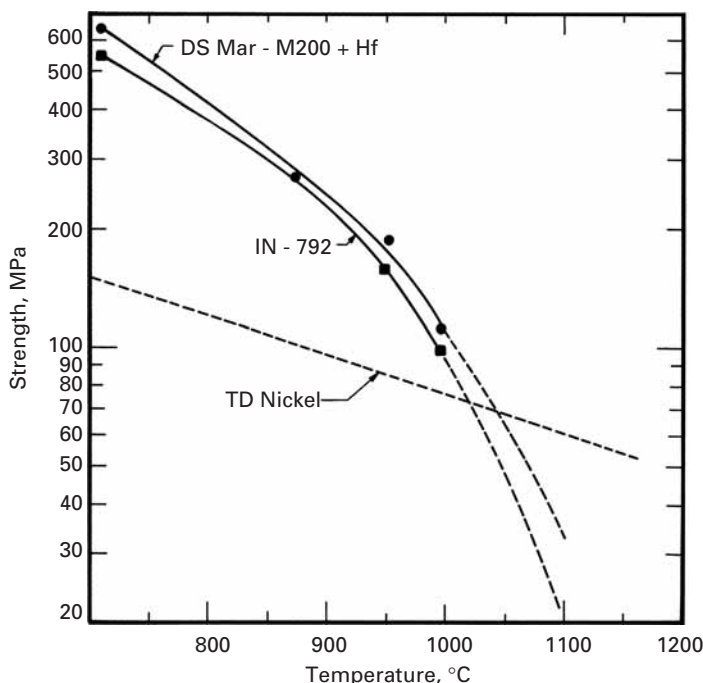


**Fig. 10.13** Comparison of yield strength of dispersion-hardened thoria-dispersed (TD) nickel with two nickel-based superalloys strengthened by precipitates (IN-792) and directionally solidified (DS) MAR M 200.

that dispersion-hardened systems have one great advantage over those hardened by precipitation, viz., the stability of the dispersoids. Thus, dispersion-hardened systems maintain high strength at high temperatures, at which precipitates tend to dissolve in the matrix. Figure 10.13 illustrates the differences between strengthening by precipitation and by dispersion-hardening. Nickel-based superalloys IN792 and MAR M-200 are precipitation-hardened by  $\gamma''$  or  $\gamma'$  precipitates having compositions of  $\text{Ni}_3\text{Nb}$  and  $\text{Ni}_3\text{Al}$ , respectively. The TD nickel, on the other hand, contains a fine dispersion of  $\text{ThO}_2$ , a high-melting-point oxide that is insoluble in the matrix. At lower temperatures (up to 1,000 °C), precipitation hardening is more effective; however, at approximately 1,100 °C, the precipitates dissolve in the matrix and the strength is drastically reduced. The dispersoids continue to be effective strengtheners at still higher temperatures.

The strengthening in these systems, hardened by either precipitates or dispersoids, has its origin in the interaction of dislocations with the particles. In general, the interaction depends on the dimensions, strength, spacing, and amount of the precipitate. The detailed behavior, of course, differs from system to system. Let us first describe the phenomenon of precipitation-, or age-, hardening. The supersaturated solid solution is obtained by sudden cooling from a sufficiently high temperature at which the alloy has a single phase. The heat treatment that causes precipitation of the solute is called aging. The process may be applied to a number of alloy systems. Although the specific behavior varies with the alloy, the alloy must, at least:

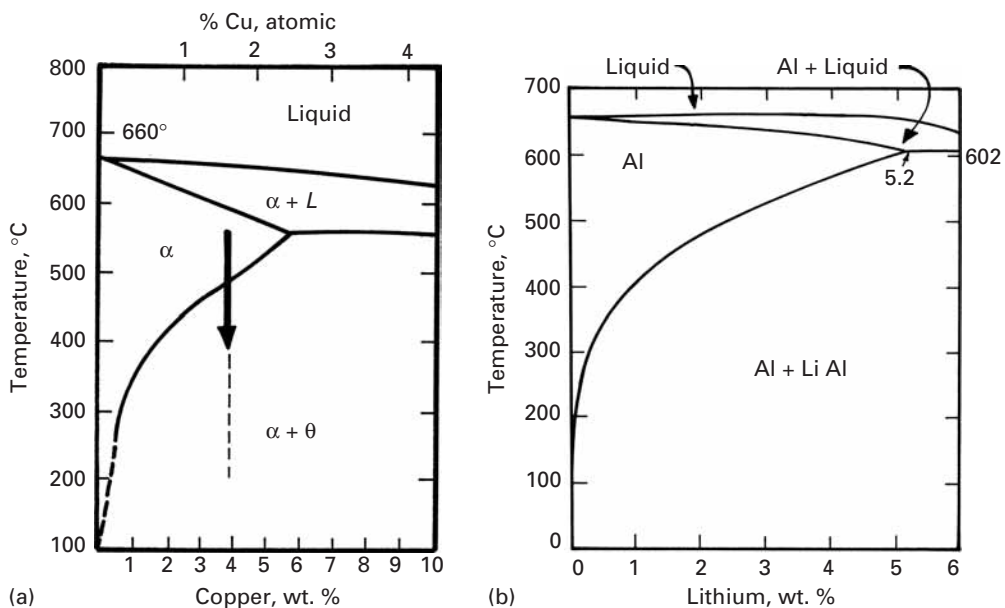


**Fig. 10.14** (a) Phase diagram of the Al-rich end of the Al–Cu system. (b) Phase diagram of the Al-rich end of Al–Li system.

1. Form a monophase solid solution at high temperatures.
2. Reject a finely dispersed precipitate during aging, i.e., the phase diagram must show a declining solvus line.<sup>4</sup>

Figure 10.14(a) shows a part of the phase diagram of the Al–Cu system in which precipitation-hardening can occur, while Figure 10.14(b) shows the phase diagram of the Al–Li system. Lithium is interesting in that its addition to aluminum results in a lowering of the density, as well as a substantial increase in the modulus of the alloy. Both of the systems shown in Figure 10.14 fulfill the prerequisites for precipitation-hardening to occur. The precipitation treatment consists of the following steps:

1. **Solubilization.** This involves heating the alloy to the monophase region and maintaining it there for a sufficiently long time to dissolve any soluble precipitates.
2. **Quenching.** This involves cooling the single-phase alloy very rapidly to room temperature or lower so that the formation of stable precipitates is avoided. Thus, one obtains a supersaturated solid solution.
3. **Aging.** This treatment consists of leaving the supersaturated solid solution at room temperature or at a slightly higher temperature. It results in the appearance of fine-scale precipitates.

Table 10.1 presents some precipitation-hardening systems, with the precipitation sequence and the equilibrium precipitates. Although the behavior of different systems varies in detail, one may write the

<sup>4</sup> The solvus line is the locus of points representing the limit of solid solubility as a function of temperature.

**Table 10.1** Some Precipitation-Hardening Systems

Base Metal	Alloy	Sequence of Precipitates
Al	Al–Ag	Zones (spheres) — $\gamma'$ (plates) — $\gamma$ (Ag <sub>3</sub> Al)
	Al–Cu	Zones (disks) — $\theta''$ (disks) — $\theta'$ — $\theta$ (CuAl <sub>2</sub> )
	Al–Zn–Mg	Zones (spheres) — M' (plates) — (MgZn <sub>2</sub> )
	Al–Mg–Si	Zones (rods) — $\beta'$ — (Mg <sub>2</sub> Si)
	Al–Mg–Cu	Zones (rods or spheres) — S' — S(Al <sub>2</sub> CuMg)
	Al–Li–Cu	Zones — $\theta''$ —> $\theta'$ —> $\theta$ (CuAl <sub>2</sub> ) Ti(CuAl <sub>2</sub> Li) $\delta'$ —> $\delta$ (AlLi)
Cu	Cu–Be	Zones (disks) — $\gamma'$ — $\gamma$ (CuBe)
	Cu–Co	Zones (spheres) — $\beta$
Fe	Fe–C	$\varepsilon$ -Carbide (disks) — Fe <sub>3</sub> C("laths")
	Fe–N	$\alpha''$ (disks) — Fe <sub>4</sub> N
Ni	Ni–Cr–Ti–Al	$\gamma'$ (cubes) — $\gamma$ (Ni <sub>2</sub> Ti)

general aging sequence as follows:

supersaturated solid solution → transition structures  
→ aged phase.

In the initial stages of the aging treatment, zones that are coherent with the matrix appear. These zones are nothing but clusters of solute atoms on certain crystallographic planes of the matrix. In the case of aluminum–copper, the zones are a clustering of copper atoms on [100] planes of aluminum. The zones are transition structuring and are referred to as *Guinier-Preston zones*, or *GP zones*, in honor of the two researchers who first discovered them. We call them zones rather than precipitates in order to emphasize the fact the zones represent a small clustering of solute atoms that has not yet taken the form of precipitate particles. The GP zones are very small and have a very small lattice mismatch with the aluminum matrix. Thus, they are coherent with the matrix; that is, the lattice planes cross the interface in a continuous manner. Such coherent interfaces have very low energies, but there are small elastic coherency strains in the matrix. As these coherency strains grow, the elastic energy associated with them is reduced by the formation of semicoherent zones where dislocations form at the interface to take up the misfit strain. Further growth of the semicoherent zones, or precipitates, results in a complete loss of coherency: An incoherent interface forms between the precipitate and the matrix.

The nature of precipitate/matrix interface produced during the aging treatment can be coherent, semicoherent, or incoherent (Figure 10.15). Coherency signifies that there exists a one-to-one correspondence between the precipitate lattice and that of the matrix.

**Fig. 10.15** Different crystallographic relationships between matrix and second phase.  
 (a) Complete coherency.  
 (b) Coherency with strained, but continuous, lattice planes across the boundary.  
 (c) Semicoherent, partial continuity of lattice planes across the interface.  
 (d) Incoherent equilibrium precipitate,  $\theta$ ; no continuity of lattice planes across the interface.

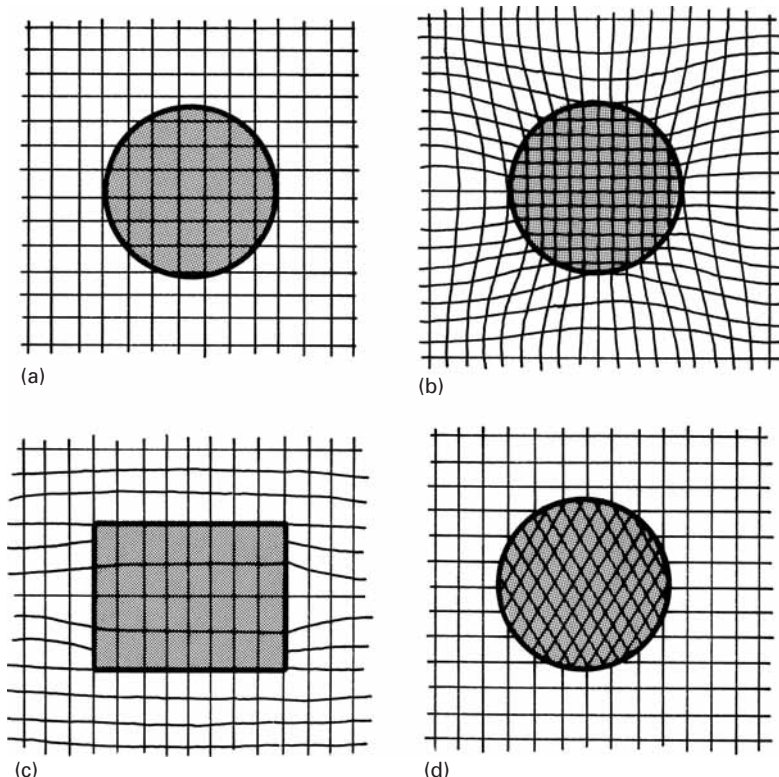


**Fig. 10.16** Interfacial dislocations formed in a semicoherent precipitate. (From G. C. Weatherly and R. B. Nicholson, *Phil. Mag.*, 17 (1968), 801.)



(See Figure 10.15(a) and (b)). A semicoherent precipitate signifies that there is only a partial correspondence between the two sets of lattice planes. The lattice mismatch is accommodated by the introduction of dislocations at the noncorrespondence sites, as shown in Figure 10.15(c). Figure 10.16 shows such interfacial dislocations at semicoherent interfaces. An incoherent interface, shown in Figure 10.15(d), implies that there is no correspondence between the two lattices. Such an interface is also present in dispersion-hardened systems.

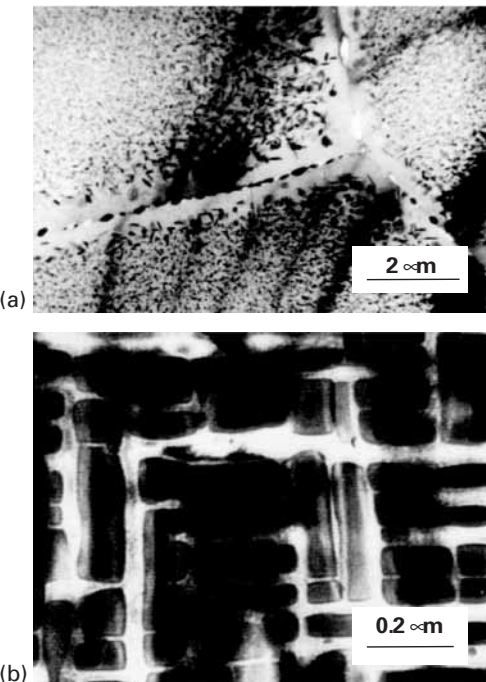


**Fig. 10.17** (a) Al–Zn–Mg alloy showing precipitate-free zone along grain boundaries. (b) Spinodally decomposed Cu–Ni–Fe alloy resulting from aging within the ternary miscibility gap. The light phase is Cu rich, the dark phase, Ni–Fe rich. (Courtesy of G. Thomas.)

The shape of the aging curve (see Figure 10.12) can be explained as follows. Immediately after quenching, only solid-solution-hardening is present. As GP zones form, hardness or strength increases because extra stress is needed to make dislocations shear the coherent zones. The hardness increases as the size of the GP zones increases, making it ever more difficult for the dislocations to shear the zones. As time goes on, incoherent equilibrium precipitates start appearing, and the mechanism of Orowan bowing (see Section 10.5) of dislocations around the particles becomes operative. The peak hardness or strength is associated with a critical dispersion of coherent or semi-coherent precipitates. Further aging results in an increase in the interparticle distance, and a lower strength results as dislocation bowing becomes easier.

Under certain conditions, precipitation may occur in a non-uniform manner, and often grain boundaries are favored sites. This may result in a region close to the grain boundary in which precipitation is virtually absent because the solute was used up in the formation of precipitates along the boundary. The aluminium-zinc-magnesium alloy shown in Figure 10.17(a) was used in the Comet aircraft. This TEM micrograph clearly shows the “precipitate-free zones” along both sides of the boundary, forming a rosary. The younger students might not remember this, but the British De Havilland company built the first commercial jet aircraft in 1952. Alas, after four accidents confidence in the new plane was destroyed and so was British supremacy in commercial aircraft. This costly mistake was attributed to two reasons:

- (a) The plane used square windows, at whose corners fatigue cracks started to propagate. Square corners produce a high stress concentration. Interestingly, the U.S. Civil Aeronautics Administration (predecessor to the Federal Aviation Administration, FAA) had doubts about the wisdom of using square windows and had refused to grant the Comet an air-worthiness certificate.
- (b) The alloy and heat treatment used in the aircraft exhibited the microstructure shown in Figure 10.17(a).

Thomas and Nutting<sup>5</sup> showed quite clearly, using TEM, the occurrence of precipitate-free zone (PFZ) adjacent to grain boundaries, and a coarser precipitate distribution adjacent to the PFZ, when compared to the surrounding matrix. This leads to intergranular corrosion and accelerates fatigue failure. One needs TEM to characterize such PFZs.

There is another mechanism of forming a second phase that does not involve nucleation and growth. It is called spinodal decomposition. It starts with fluctuations in composition that become gradually (with time) more pronounced. This eventually leads to phase separation. Spinodal decomposition is not as common as precipitation. Figure 10.17(b) shows the microstructure produced in a Cu-Ni-Fe alloy by spinodal decomposition.

### Example 10.2

Dispersion-hardened materials have a stable microstructure at high temperatures, compared to precipitation-hardened materials. Is there any advantage, then, to strengthening by precipitation over that by dispersion of strong, inert particles?

**Solution:** In general a dispersion-hardened material, because it is very hard, can be very difficult to machine or work. A precipitation-hardened material, on the other hand, can be machined or worked before it is given the aging treatment, i.e., when it is soft. After machining, one can give the material the appropriate aging treatment to get the maximum strength and hardness.

### Example 10.3

Figure E10.3 shows the Al-Mg phase diagram. For an alloy with 5% Mg by weight, calculate the  $\text{Al}_2\text{Mg}$  ( $\beta$ ) equilibrium volume fraction of precipitate if the densities of Al and  $\text{Al}_2\text{Mg}$  are 2.7 and  $2.3 \text{ g/cm}^3$ , respectively.

**Solution:** Basically, we have to calculate the volume fraction of  $\text{Al}_2\text{Mg}$  at room temperature ( $25^\circ\text{C}$ ). However, in this phase diagram, the data

<sup>5</sup> G. Thomas and J. Nutting, *J. Inst. Metals*, 88 (1959–60) 81; R. B. Nicholson, G. Thomas, and J. Nutting, *Acta Met.*, 8 (1960) 172.

are given to 100 °C. We assume that there is not much change between 100 °C and 25 °C. Applying the lever rule,<sup>6</sup> we find that the fraction of  $\beta$  ( $\text{Al}_2\text{Mg}$ ) by weight is

$$\frac{5 - 1}{35 - 1} = 0.12.$$

Changing this into the volume fraction (divide the respective mass fraction by the density of each component) we have

$$f = \frac{0.12/2.3}{0.88/2.7 + 0.12/2.3} \left( = \frac{V_{\text{Al}_2\text{Mg}}}{V_{\text{Al}} + V_{\text{Al}_2\text{Mg}}} \right)$$

$$= 0.14 \text{ or } 14\%.$$

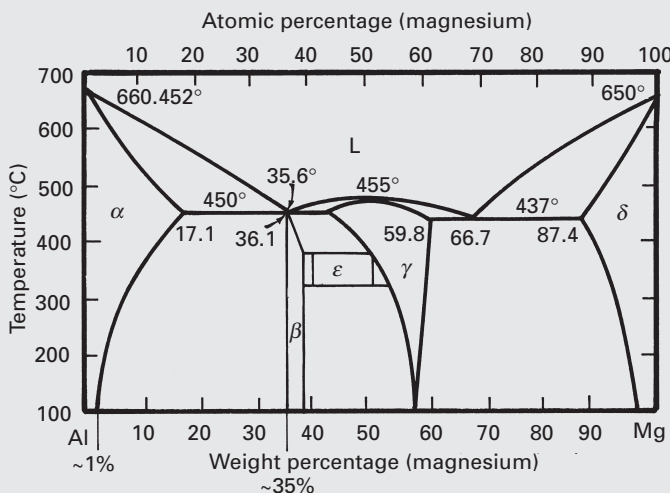


**Fig. E10.3**

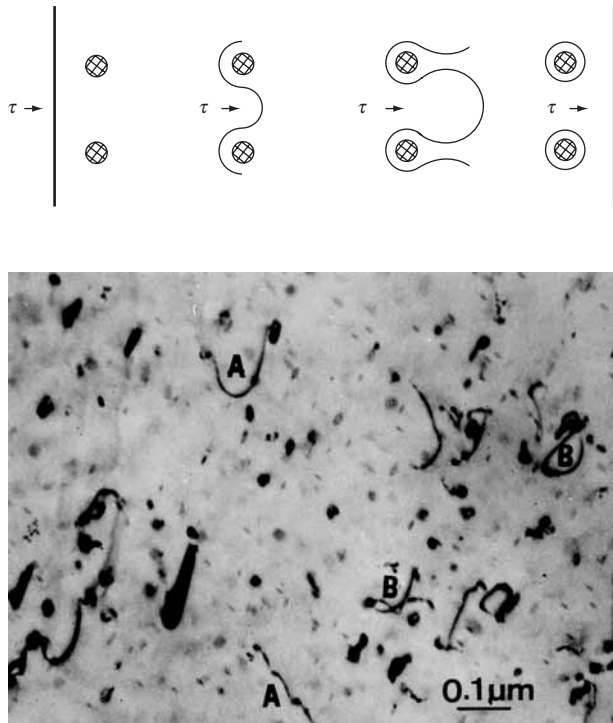
## 10.5 Dislocation–Precipitate Interaction

Finely distributed precipitates present an effective barrier to the motion of dislocations. Two of the important models that explain the strengthening due to precipitates respectively involving (1) dislocations cutting through the particles in the slip plane and (2) dislocations circumnavigating around the particles in the slip plane. Depending on both the nature of the precipitate and the crystallographic relationship between the precipitate and the matrix, we can have two limiting cases:

1. *The precipitate particles are impenetrable to the dislocations.* Orowan pointed out that if a ductile matrix has second-phase particles interpenetrating the slip plane of dislocations, an additional stress

<sup>6</sup> The lever rule allows us to compute the relative phase amounts in a two-phase alloy. The student should consult any introductory book on materials engineering.

**Fig. 10.18** (a) The Orowan model. (After E. Orowan, in *Internal Stresses in Metals and Alloys* (London: Institute of Metals, 1948), p. 451.) (b) Obstruction of dislocation motion by uniformly distributed nonshearing particles in an aluminum alloy (transmission electron microscope) (Courtesy of M. V. Heimendahl.)



will be necessary to make a dislocation expand between the particles. The applied stress should be sufficiently high to bend the dislocations in a roughly semicircular form between the particles. If so, the dislocations will extrude between the particles, leaving dislocation loops around them, as per the mechanism shown schematically in Figure 10.18(a). Under an applied shear stress  $\tau$ , the dislocation bows in between the precipitate particles until segments of dislocation with opposite Burgers vector cancel each other out, leaving behind dislocation loops around the particle. An example of Orowan bowing is shown in a TEM in Figure 10.18(b). The material is an Al-0.2% Au alloy, solution annealed, followed by 60 hours at 200 °C and 5% plastic deformation. At points marked A in this figure, one can see dislocations pinned by the precipitates and Orowan bowing of dislocation segments. At point B, the dislocations have left the slip plane and formed prismatic dislocation loops. The dislocations in the micrograph are characteristically very short and have been severely impeded in their movement.

Now, the stress necessary to bend a dislocation to a radius  $r$  is given roughly by (see Section 4.4.5, Equation 4.22d)

$$\tau \approx Gb/2r \quad (10.4)$$

Let  $x$  be the average separation between two particles in the slip lane. Then a dislocation, under a shear stress  $\tau$ , must be bent to a radius on the order of  $x/2$  for it to be extruded between the particles instead

of cutting them. The shear stress to do this is given by making  $r = x/2$  in Equation 10.4; that is,

$$\tau \approx \frac{Gb}{2r} = Gb/x. \quad (10.5)$$

Should the stress necessary to cause the particle shear be greater than  $Gb/x$  (rigorously speaking,  $2T/bx$ , where  $T$  is the dislocation line tension), the dislocation will bow between the particles rather than shear them. This, in essence, is the Orowan model of strengthening due to dispersion or incoherent precipitates. The increase in the yield stress because of the presence of particles is given by Equation 10.5, so that, as long as there is no particle shear, the total yield stress for an alloy strengthened by a dispersed phase or an incoherent precipitate is given by

$$\tau_y = \tau_m + Gb/x, \quad (10.6)$$

where  $\tau_m$  is the critical shear stress for matrix yielding in the absence of a precipitate. Note that more precise formulations of the Orowan stress have been made, involving more accurate expressions for the dislocation line tension  $T$  and taking into account the effect of the finite particle size on the average interparticle spacing.

Ashby<sup>7</sup> improved on the original Orowan equation and proposed the following form, incorporating the radius of the precipitate,  $r_0$ :

$$\tau_y = \tau_m + \left[ \frac{Gb}{2.38\pi(1-\nu)^{1/2}} \ln \left( \frac{r_0}{b} \right) \right] / x.$$

The above equation predicts results that are about one-half of the Orowan equation, for  $x = 10$  nm,  $b = 0.3$  nm, and  $\nu = 0.3$ .

The comparison of the predicted Orowan–Ashby equation and experimental values for a Cu–0.74% Ni–0.14% P alloy is shown in Figure 10.19. The experimental precipitation strengthening is qualitatively similar to the Orowan equation. The strengthening decreases with precipitate size, because this corresponds to an increase in the spacing (at a constant volume fraction of 0.009). However, the actual increase in strength is only about half of the predicted value. This was attributed to microstructural effects. It is very seldom that theoretical predictions are quantitatively obeyed in materials and therefore the calculations are considered satisfactory.

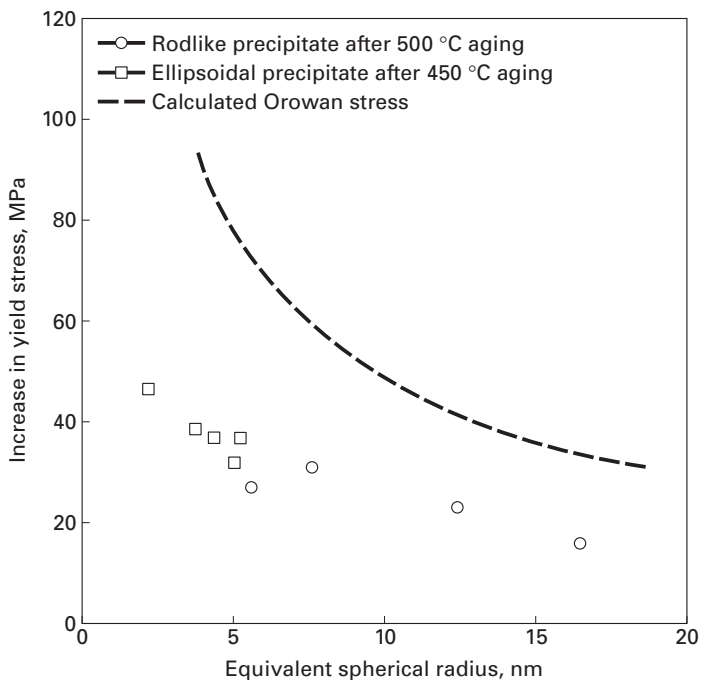
2. *The precipitate particles are penetrable to dislocations;* that is, the particles are sheared by dislocations in their slip planes. If the extra stress (in addition to  $\tau_m$ ) necessary for particle shear is less than that for bending the dislocation between the particles ( $= Gb/x$ ), the particles will be sheared by dislocations during yielding, and we can write

$$\tau_y < \tau_m + Gb/x.$$

---

<sup>7</sup> M. F. Ashby, in *Oxide Dispersion Strengthening*, G. S. Ansell, ed. (New York: Gordon and Breach, 1968) p. 431.

**Fig. 10.19** Comparison of Orowan–Ashby calculated increase in strength in aluminium alloy with experimental results, for different particle diameters (and spacings) at a constant volume fraction  $f$ . (Adapted from J. Miyake and M. E. Fine, *Acta Met.*, 40 (1992) 733.)



Thus, we see that the strength of the particle and the crystallographic nature of the particle/matrix interface will determine whether dislocations will cut the particles. In internally oxidized alloys (e.g., Cu + SiO<sub>2</sub>), where the obstacles to dislocation motion are small, very hard ceramic particles with a very high shear modulus and an incoherent interface, the initial flow stress is controlled by the stress necessary to extrude the dislocations between the hard and impenetrable particles, as per the Orowan mechanism. Since the shear strength of the obstacles is generally very much higher than that of the matrix, very large stresses will be required for particle shear to occur. The initial yield stress is then controlled by the interparticle spacing. Such behavior is also shown by precipitation-hardened alloys when the equilibrium precipitate is an intermetallic compound (e.g., CuAl<sub>2</sub> in the system Al–Cu). However, in the initial stages of aging, the small precipitates or zones are coherent with the matrix and thus can be sheared by dislocations. A vivid example of particle (Ni<sub>3</sub>Al) shear by dislocation is illustrated in Figure 10.20: a Ni-19% Cr-69% Al alloy aged at 750 °C for 540 hours and strained 2%.

Consider the encounter of a dislocation such as that at A in Figure 10.21(a) with spherical particles (radius  $r_0$  in the slip plane) that are interpenetrating the slip planes. Let  $x$  be the separation between particles in the slip plane. If the interface is coherent and the particles are not strong enough to support the Orowan stress, the dislocation will cut the particles (of radius  $r_0$ ) in moving from position A to position B, as shown in Figure 10.21(a). The passage of a matrix dislocation, which generally will not be a slip dislocation for the precipitate,

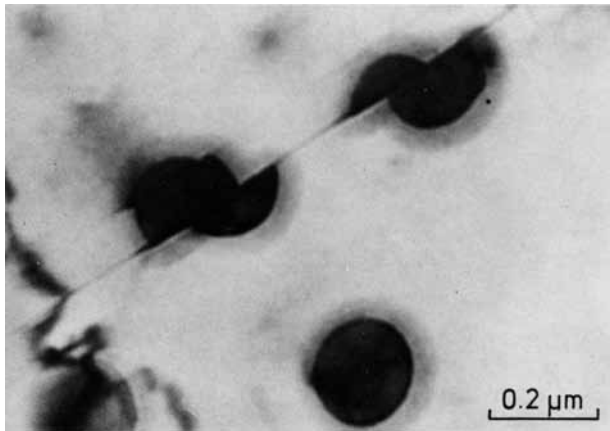


**Fig. 10.20**  $\gamma'$ -precipitate particles sheared by dislocations in a Ni–19% Cr–69% Al alloy aged at 750 °C for 540 hours and strained 2%. The arrows indicate the two slip-plane traces (transmission electron microscopy) (Courtesy of H. Gleiter.)

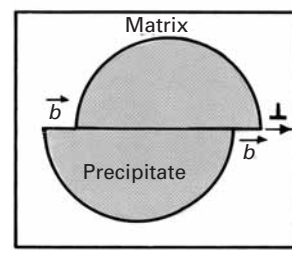
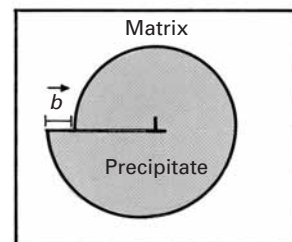
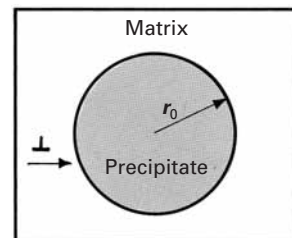
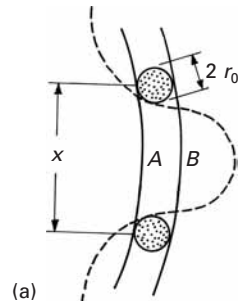


**Fig. 10.21** (a) Dislocation at two successive positions A and B. (b) Dislocation shearing precipitate.

will result in a faulted plane or an interface, say, of specific energy  $\gamma$ . Figure 10.21(b) shows schematically the formation of such an interface. The increase in the energy of the particle is  $\pi r_0^2 \gamma$ . Then, in the absence of any thermally activated process, the stress  $\tau_{\text{shear}}$  necessary to move a dislocation of length  $x$  from A to B by particle shear can be obtained as follows. A dislocation under an applied stress  $\tau_{\text{shear}}$  has a force per unit length of  $\tau_{\text{shear}} b$  on it; therefore, the dislocation of length  $x$  will have a force of  $\tau_{\text{shear}} bx$  on it. When the dislocation moves through a distance equal to the particle diameter ( $2r_0$ ), the work done by this force is  $\tau_{\text{shear}} bx 2r_0$ . This work must equal the surface energy of the interface created by cutting of the particle, viz.,  $\pi r_0^2 \gamma$ . Thus, we can write

$$\tau_{\text{shear}} bx 2r_0 = \pi r_0^2 \gamma,$$

or

$$\tau_{\text{shear}} = \pi r_0 \gamma / 2bx. \quad (10.7a)$$

We can make an estimate of interparticle spacing as follows. The particle spacing  $x$  is shown in Figure 10.22: a simplified array of precipitates in a cubic arrangement. It is possible to express the volume fraction of precipitate as

$$f = \left( \frac{4}{3} \pi r_0^3 \right) / x^3. \quad (10.7b)$$

It is assumed that each corner precipitate contributes one-eighth to the total volume; the eight corner precipitates together count as one. Expressing Equation 10.7b in terms of  $r_0/x$ , we have

$$r_0/x = [(3/4\pi)f]^{1/3}. \quad (10.7c)$$

Inserting equation 10.7c into 10.7a yields

$$\tau_{\text{shear}} = \text{constant } f^{1/3}.$$

Hence, the stress required to shear precipitates is a function only of the volume fraction of the particle that has been transformed. However, in the early stages of precipitation, the volume fraction

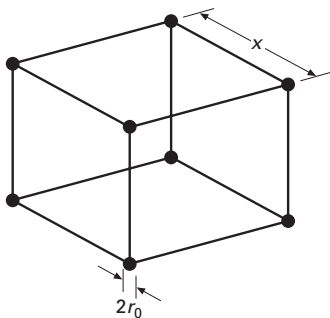


**Fig. 10.22** An array of precipitates (diameter =  $2r_0$ ) in a cubic arrangement with the cube side =  $x$ .

transformed increases with time until it reaches the equilibrium value, which is determined from the phase diagram.

We discuss next the transition between the particle shear and Orowan bowing mechanisms. In the initial stages, as precipitation or aging continues, the precipitate particles increase in size and volume. As the size and amount of particles increase, more work needs to be done by the dislocation in shearing the particles. It turns out<sup>8</sup> that the shear strength  $\tau$  of the alloy depends on the particle radius  $r$  and the particle volume fraction  $f$  according to the proportionality

$$\tau \propto \sqrt{rf}.$$

With aging of the precipitates, both  $r$  and  $f$  increase. Soon, however, a stage is reached in which the precipitate volume fraction does not increase any more. Actually, the maximum precipitate volume fraction is dictated by the alloy phase diagram. The precipitate size, however, continues to increase on further aging, because larger particles tend to grow at the expense of smaller particles. This growth is called *precipitate coarsening*. In nickel-based superalloys, the term *Ostwald ripening* is also used for this phenomenon. The thermodynamic driving force for precipitate coarsening is the decrease in surface area, and thus, surface energy of the precipitate with increasing size. In the initial stages of aging, both  $r$  and  $f$  increase, and the strength of the alloy increases. This, however, does not go on indefinitely, because, as precipitate coarsening occurs, the interparticle distance  $x$  increases. In fact,  $x$  becomes so large, that an alternative deformation process begins, viz., dislocation bowing or looping around the particles via the Orowan mechanism. This happens because the shear stress required to bow the dislocation between the particles is less than that required to shear them.

The stress necessary to bend a dislocation in between the particles,  $\tau_{\text{Orowan}}$ , is given by Equation 10.5. If  $\tau_{\text{shear}} > \tau_{\text{Orowan}}$ , the dislocation will expand between the precipitate particles, and if  $\tau_{\text{shear}} < \tau_{\text{Orowan}}$ , the particles will be cut. Whether or not the particles will be sheared depends on  $r_0$ , the particle size, and on  $\gamma$ , the specific interface energy. For coherent precipitates – for example, the GP zones in Al alloys – the values of  $\gamma$  are expected to be on the order of the magnitude of antiphase domain boundaries, with a maximum value of about 100 mJ/m<sup>2</sup>. Thus, from such values of  $\gamma$ , we can estimate that only very small particles ( $2r_0 < 50$  nm) will be cut. With aging, the second-phase particles grow in size, so that the average spacing between them also increases (for a given precipitate volume fraction), and  $\tau_{\text{Orowan}}$ , representing the stress necessary to bend a dislocation between particles, decreases monotonically (Figure 10.23). By contrast, the stress necessary to cut the particles increases with the particle size or aging time, because the fraction transformed increases until it reaches saturation. The figure shows the curves for dislocation bowing

<sup>8</sup> V. Gerold and H. Haberkorn, *Phys. Stat. Solidi*, 16 (1966) 67.

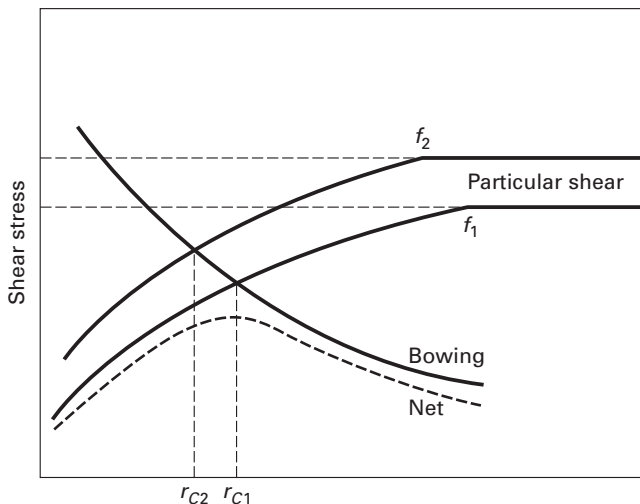


**Fig. 10.23** Competition between particle shear and dislocation bowing mechanisms.  $f_1$  and  $f_2$  represent two volume fractions of precipitates ( $f_2 > f_1$ ); the different volume fractions can be obtained by using different alloy compositions.

in between the particles and particle shear for two different equilibrium volume fractions,  $f_2 > f_1$ . These different volume fractions are obtained by changing the composition of the alloy. For instance, by increasing the Cu content of an Al-Cu alloy, we increase  $f$ . The corresponding transitions between the cutting and bowing mechanisms occur at  $r_{c1}$  and  $r_{c2}$ , respectively. The yield stress of the alloy as a function of aging time will then follow the dashed curve, a resultant of the two mechanisms. The transition between the shearing of the particle and bowing between the particles will occur at a critical radius,  $r_c$ , given by Equation 10.1, with  $r_c$  substituting for  $r_o$ .

## 10.6 Precipitation in Microalloyed Steels

Steels form one of the most important groups of engineering materials. Over the years, the physical and process metallurgy of steels has continually evolved to meet newer demands and challenges. The development of microalloyed steels in the second half of the twentieth century may be regarded as one of the greatest metallurgical achievements ever. This success can be attributed, in a large measure, to a clearer understanding of structure–property relations in low-carbon steels. Of course, the final product resulted from a fruitful combination of physical, mechanical, and process metallurgy. Microalloyed steels<sup>9</sup> have largely substituted the mild steel<sup>10</sup> as the basic structural material. A microalloyed steel is a low-carbon steel (0.05 to 0.2% C, 0.6 to 1.6% Mn) that contains about 0.1% of elements such as Nb,

<sup>9</sup> There is some confusion about the terminology in the literature. Earlier, the commonly accepted term was “high-strength low-alloy (HSLA) steels”; later the term “microalloyed steels” gained wider acceptance.

<sup>10</sup> Mild steel is the term used to denote a carbon steel with a carbon content between 0.1 and 0.3%.

**Table 10.2** Important Precipitates in High-Strength Low-Alloy (HSLA) Steels

Principal Element(s)	Main Precipitates
Niobium	Nb(C,N), Nb <sub>4</sub> C <sub>3</sub>
Vanadium	V (C,N), V <sub>4</sub> C <sub>3</sub>
Niobium + molybdenum	(Nb,Mo)C
Vanadium	VN
Copper + niobium	Cu,Nb(C,N)
Titanium	Ti(C,N), TiC
Aluminum	AlN

V, or Ti. Some other elements (e.g., Cu, Ni, Cr, and Mo) may also be present in small proportions (up to about 0.1%). Elements such as Al, B, O, and N have significant effects as well. Table 10.2 lists some important second phases generally encountered in high-strength low-alloy (HSLA) steels. Microalloyed steels are usually subjected to what is called a *controlled-rolling* treatment. Controlled rolling is nothing but a sequence of deformations by hot rolling at certain specific temperatures, followed by controlled cooling. The main objective of this treatment is to obtain a fine ferritic grain size. The ferritic grain size obtained after austenitization and cooling depends on the initial austenitic grain size, because ferrite nucleates preferentially at the austenite grain boundaries. The ferrite grain size also depends on the transformation temperature of the reaction austenite ( $\gamma$ )  $\rightarrow$  ferrite ( $\alpha$ ). Lower transformation temperatures favor the nucleation rate that results in a large number of ferritic grains and, consequently, in a very small ferritic grain size (5 to 10  $\mu\text{m}$ ). Thus, to obtain a maximum of grain refinement, the controlled-rolling procedure modifies the hot-rolling process with a view toward exploiting the capacity of the microalloying elements so as to retard the recrystallization of the deformed austenite grains. The microalloyed additions result in the precipitation of second-phase particles during the austenitization treatment, and these particles impede the growth of the austenite grains. Hence, precipitates of, say, carbides or carbonitrides of Nb, V, or Ti can inhibit or retard the growth of these grains, resulting in a posterior ferrite grain refinement. The Hall-Petch relationship between the yield stress and the ferrite grain size (see Section 5.3) indicates the strengthening that is possible through grain size refinement. Besides grain size strengthening, some strengthening occurs due to carbide precipitation. In summary, then, during hot rolling, the fine carbide particles form in austenite and control its recrystallization. The result is a fine ferritic grain size. Secondly, carbides of Nb, V, or Ti precipitate during and soon after the  $\gamma \rightarrow \alpha$  transformation and lead to a precipitation strengthening of the ferrite. Together, these two strengthening methods lead to steels with yield strengths in the range 400 to 600 MPa and with good toughness.

We saw earlier in this chapter that, in general, when the precipitates are dispersed through the matrix with very small interparticle spacing ( $\leq 10$  nm), the stress required to extrude the dislocations in between the particles will be very high, and dislocations will shear the particles. However, there is little evidence of such shear of precipitates in steels. The carbides, nitrides, and carbonitrides are very hard (Diamond Pyramid Hardness 2,500 to 3,000), and the presence of such hard particles in a matrix means that dislocations will be able to cut them only when they are extremely small. The critical particle size, which corresponds to a transition between the Orowan mechanism and the particle shear mechanism, decreases with an increase in the particle hardness, as shown schematically in Figure 10.24.

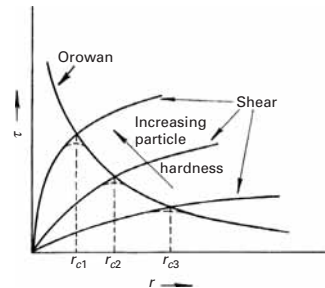


**Fig. 10.24** Change in shear stress  $\tau$  with increasing particle radius and hardness.

### Example 10.4

Make a schematic of the precipitate volume fraction  $f$  as a function of time. Explain your diagram in terms of nucleation and growth of precipitate from a supersaturated solid solution.

**Solution:** The precipitates nucleate in the matrix after an initial incubation period,  $t_0$ , the time required to form stable nuclei. Following nucleation, the precipitate particles grow in size over time. Such nucleation and growth processes generally show very fast kinetics at first and then finish slowly because of the depletion of solute in the matrix. Figure E10.4 shows the desired schematic. Note the logarithmic time scale.

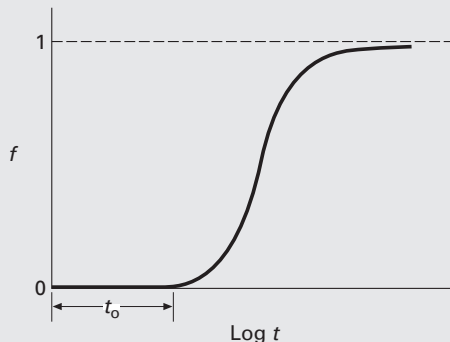


**Fig. E10.4**

### Example 10.5

Consider a precipitation-strengthened aluminum alloy. After an appropriate heat treatment, the microstructure of the alloy consists of precipitates with a mean spacing of  $0.2 \mu\text{m}$ . Compute the shear stress required for Orowan bowing of dislocations in this material.

For aluminum, we have the following data:

Lattice parameter  $a_0 = 0.4$  nm,  
Shear modulus = 30 GPa.

**Solution:** The shear stress for Orowan bowing is given by

$$\tau \approx \frac{Gb}{l} = \frac{Gb}{2r}.$$

The Burgers vector for aluminum (FCC) is

$$b = \frac{\sqrt{2}}{2}a = \frac{\sqrt{2}}{2}0.4 \text{ nm} = 0.29 \text{ nm}.$$

We can assume that a dislocation bowing around the precipitates becomes unstable when it becomes a semicircle – that is, when its radius is equal to half the interparticle spacing. Thus,

$$\begin{aligned} r &= \frac{l}{2} = 0.1 \mu\text{m}, \\ \tau &= \frac{30 \times 10^9 \times 0.28 \times 10^9}{2 \times 0.1 \times 10^{-6}} = 42.42 \text{ MPa}. \end{aligned}$$

### Example 10.6

Consider a dispersion-strengthened alloy with average interparticle spacing of  $\lambda$ . If  $N_v$  is the number of particles per unit volume,  $d$  is the mean particle diameter, and  $f$  is the volume fraction of particles, then show that

$$\lambda \approx d[(1/2f)^{1/3} - 1].$$

**Solution:** Let  $r$  be the mean radius of the particle, i.e.,  $2r = d$ . Then the number of particles per unit volume,  $N_v = f/(4\pi r^3/3)$ , or  $1/N_v = 4\pi r^3/3f$ .

Taking the cube root of both sides, we obtain

$$1/(N_v)^{1/3} = (4\pi r^3/3f)^{1/3} = r(4\pi/3f)^{1/3} = 2r(\pi/6f)^{1/3} = d/(\pi/6f)^3.$$

Now, the interparticle spacing  $\lambda$  is the average center-to-center spacing between two particles, less a particle diameter, i.e.,

$$\lambda = 1/(N_v)^{1/3} - d.$$

Hence,

$$\lambda = d(\pi/6f)^{1/3} - d \approx d[(1/2f)^{1/3} - 1].$$

### Example 10.7

For an alloy containing  $\text{Al}_2\text{Mg}$  precipitates, calculate the critical spacing of precipitates at which the mechanism of hardening changes from

particle shear to particle bypass. Take

$$\gamma_{\text{Al}_2\text{Mg}} = 1,400 \text{ mJ m}^{-2},$$

$$\text{Atomic radius (A1)} = 0.143 \text{ nm},$$

$$G_{\text{Al}} = 26.1 \text{ GPa.}$$

**Solution:** Assume that the precipitates are arrayed as SC (simple cubic). Therefore, the spacing  $x$  of precipitates is equal to the edge length, and for  $\text{Al}_2\text{Mg}$  in a cubic arrangement,

$$V_{\text{Al}_2\text{Mg}} = 4/3 \pi r_{\text{Al}_2\text{Mg}}^3.$$

From Equation 10.7b, we calculate the volume fraction for precipitates:

$$f = 4/3(\pi r_{\text{Al}_2\text{Mg}}^3)/x^3.$$

Thus,

$$r_{\text{Al}_2\text{Mg}} = (3f/4\pi)^{1/3}x = 0.323x.$$

For particle shear,

$$\tau_{\text{shear}} = (\pi r_{\text{Al}_2\text{Mg}} \gamma_{\text{Al}_2\text{Mg}})/2bx.$$

For bypass,

$$\tau_{\text{Orowan}} = G b/x.$$

The critical condition is obtained by setting  $\tau_{\text{shear}} = \tau_{\text{Orowan}}$ . Hence,

$$(\pi r_{\text{Al}_2\text{Mg}} \gamma_{\text{Al}_2\text{Mg}})/2bx = G b/x.$$

Now,  $r_{\text{Al}_2\text{Mg}} = 0.323x$  and  $b = 2r_{\text{Al}}$  because Al is FCC. Substituting these values into the preceding equation, we get

$$(0.323\pi \gamma_{\text{Al}_2\text{Mg}} x)/4r_{\text{Al}}x = 2G r_{\text{Al}}/x,$$

or

$$\begin{aligned} x &= (8G r_{\text{Al}}^2)/0.323\pi \gamma_{\text{Al}_2\text{Mg}} \\ &= (8 \times 26.1 \times 10^9 \times 0.143 \times 10^{-9})/(0.323\pi 1,400 \times 10^{-7}/10^{-4}) \\ &= 3.0 \times 10^{-9} \text{ m} \\ &= 3.0 \text{ nm}. \end{aligned}$$

### Example 10.8 |

Steel is one of the most important engineering materials. Consider the different strengthening mechanisms discussed in this and earlier chapters, and make a list of different contributions to the strength of low-carbon steel.

**Solution:** Here is a list of the various possible contributions to the strength of steel:

1. Lattice friction stress, or the Peierls–Nabarro stress,  $\sigma_i$ .
2. Solid-solution strengthening,  $k\sqrt{C}$ , where  $k$  is a constant and  $C$  is the solute concentration.
3. Dislocation or strain hardening,  $\alpha G b \sqrt{\rho}$ , where  $\alpha$  is a constant approximately equal to 0.5,  $G$  is the shear modulus,  $b$  is the Burgers vector, and  $\rho$  is the dislocation density. (This contribution is discussed in Chapter 6.)
4. Grain-size strengthening,  $k_y D^{-0.5}$ , where  $k_y$  is the Hall–Petch constant and  $D$  is the grain size. (This contribution is discussed in Chapter 5.)
5. A precipitation-hardening contribution if there are any precipitates present, such as carbides of iron, niobium, titanium, or vanadium.

## 10.7 | Dual-Phase Steels

Dual-phase steels have a microstructure consisting of 5 to 20 vol.% of hard martensitic islands in a ductile ferritic matrix. The term dual-phase is a misnomer but that is the prevalent usage. Ferritic-martensitic steels would be a better name. As one would expect of such a particulate composite, the yield and ultimate tensile strength of dual-phase steels is a function of the volume fraction of martensite, the carbon content of martensite, cooling rate, etc. Frequently, depending on the cooling conditions used, there may be some retained austenite, bainite, pearlite, and new ferrite in these steels.

These steels are produced by an intercritical treatment; this involves quenching from a suitable temperature in the intercritical range between  $A_1$  and  $A_3$  in the Fe-C phase diagram (not shown here). In this intercritical treatment the austenite phase transforms to martensite giving us a ferrite–martensite structure instead of the conventional ferrite–pearlite microstructure. These steels are characterized by low yield strength, an absence of discontinuous yielding, and a very high strain hardening rate. These characteristics lead to a high strength component in the as-formed state. They also have excellent stretch-formability, which is exploited in automotive applications. Dual-phase steels, for a similar strength to conventional HSLA steels, offer better formability and enhanced crashworthiness. Typical composition for cold-rolled dual-phase steels (wt.%) is 0.08–0.18% C, 1.6–2.2% Mn, 0.4% (Cr + Mo). A hot-rolled dual-phase steel would be 0.05% C, 1% Si, 1.5% Mn, 0.6% Cr, and 0.4% Mo.

## Suggested Reading

- V. Gerold, in *Dislocations in Solids*, vol. 4, F. R. N. Nabarro, ed. New York, NY: Elsevier/North Holland, 1979, p. 219.
- A. Kelly and R. B. Nicholson, eds. *Strengthening Methods in Crystals*. Amsterdam: Elsevier, 1971.
- D. T. Llewellyn. *Steels: Metallurgy and Applications*, 2nd ed. Oxford: Butterworth-Heinemann, 1992.

- J. W. Martin *Precipitation Hardening*. Oxford: Pergamon Press, 1968.
- E. Nembach and D. G. Neite. *Precipitation Hardening of Superalloys by Ordered  $\gamma'$ -Particles*, Progress in Materials Science Series, vol. 29. Oxford: Pergamon Press, 1985, p. 177.
- A. K. Vasudevan and R. D. Doherty, eds., *Aluminum Alloys: Contemporary Research and Applications*. Boston, MA: Academic Press, 1989.

## Exercises

**10.1** Compute the hydrostatic stress, in terms of an  $(r, \theta)$  coordinate, associated with an edge and a screw dislocation in an aluminum lattice. Take  $G = 26$  GPa and  $b = 0.3$  nm. For a given  $r$ , what is the maximum value of this stress?

**10.2** Consider the copper–zinc system that is used to make a series of brasses. The radius of solute zinc atom is 0.133 nm, while that of solvent copper atom is 0.128 nm. Calculate the dilatational misfit  $\Delta V$  for this alloy. Compute the hydrostatic stress  $\sigma_p$  for an edge and a screw dislocation in the system. Use the two quantities  $\sigma_p$  and  $\Delta V$  to obtain the dilatational misfit energy for the alloy. Also, compute the force exerted by a solute atom of zinc on a dislocation in copper.

**10.3** The interaction energy between an edge dislocation (at the origin) and a solute atom (at  $r, \theta$ ) is given by

$$U = \frac{A}{r} \sin \theta,$$

where  $A$  is a constant. Transforming into Cartesian coordinates, plot lines of constant energy of interaction for different values (positive and negative) of  $A/2U$ . On the same graph, plot the curves for the interaction force. Indicate by arrows the direction in which the solute atoms, with  $\Delta V$  positive, will migrate.

**10.4** Consider a metal with shear modulus  $G = 40$  GPa and atomic radius  $r_0 = 0.15$  nm. Suppose the metal has a solute that results in a misfit of  $\varepsilon = (R - r_0)/r_0 = 0.14$ . Compute the elastic misfit energy per mole of solute.

**10.5** Estimate the amount of solute (atomic percent) necessary to put one solute atom at each site along all the dislocations in iron. Assume that 1 mm<sup>3</sup> of iron contains about  $10^6$  nm of dislocation lines.

**10.6** Compute the condensation temperature  $T_c$  for the following cases:

- (a) Carbon in iron with  $C_0$  (average concentration) = 0.01% and  $U_i$  (interaction energy) = 0.08 aJ (0.5 eV); note prefix “a” stands for “atto” =  $10^{-18}$ .
- (b) Zinc in copper with  $C_0 = 0.01\%$  and  $U_i = 0.019$  aJ (0.12 eV).

**10.7** One of the Hume-Rothery rules for solid solutions<sup>11</sup> is that the solubility of solute  $B$  in solvent  $A$  becomes negligible when the atomic radii of  $A$  and  $B$  differ by more than 15%. Plot the maximum solubility (atomic percent) of

<sup>11</sup> W. Hume-Rothery and G. V. Raynor, *The Structure of Metals and Alloys* (London: Institute of Metals, 1956), p. 97.

Ni, Pt, Au, Al, Ag, and Pb as a function of the ratio of solute and solvent (Cu) radii, and verify that the solid solubility in Cu drops precipitously at a size ratio of about 1.15. Use the following data:

$$r_{\text{Ni}} = 0.1246 \text{ nm} \quad r_{\text{Al}} = 0.143 \text{ nm}$$

$$r_{\text{Ag}} = 0.1444 \text{ nm}$$

$$r_{\text{Pt}} = 0.139 \text{ nm} \quad r_{\text{Pb}} = 0.1750 \text{ nm}$$

$$r_{\text{Cu}} = 0.1278 \text{ nm} \quad r_{\text{Au}} = 0.1441 \text{ nm}$$

**10.8** A steel specimen is being tested at a strain rate of  $3 \times 10^{-3} \text{ s}^{-1}$ . The cross-sectional length is 0.1 m. A Lüders band forms at the section, with an instantaneous strain of 0.2. What is the velocity of propagation of the two Lüders fronts?

**10.9** An overaged, precipitation-hardenable alloy has a yield strength of 500 MPa. Estimate the interparticle spacing in the alloy, given that  $G = 30 \text{ GPa}$  and  $b = 0.25 \text{ nm}$ .

**10.10** Consider a unit cube of a matrix containing uniform spherical particles (with radius  $r$ ) of a dispersed second phase. Compute the average distance between the particles for a volume fraction  $f$  of particles equal to 0.001 and  $r = 10^{-6} \text{ cm}$ .

**10.11** For a precipitation-hardenable alloy, estimate the maximum precipitate size that can undergo shear by dislocations under plastic strain. Take matrix shear modulus = 35 GPa, Burgers vector = 0.3 nm, and specific energy of precipitate-interface created by shear = 100 mJ/m<sup>2</sup>.

**10.12** An aluminum alloy contains 2% volume fraction of a precipitate that results in  $\varepsilon = 5 \times 10^{-3}$ . Determine the average spacing  $l$  between precipitates above which there will be a significant contribution to strength due to the difference in atomic volume of the matrix and the precipitate. Below this critical value of  $l$ , what will be the mechanism controlling yielding?

**10.13** Calculate the critical radius of precipitates for which an Al-Mg alloy containing 10% Mg will be strengthened by Orowan looping instead of particle shear. Use the following data:

$$\gamma_{\text{Al}_2\text{Mg}} = 1.4 \text{ J/m}^2,$$

$$G_{\text{Al}} = 26.1 \text{ GPa},$$

$$r_{\text{Al}} = 0.143 \text{ nm}.$$

**10.14** An Al-Cu alloy with 4% weight Cu is aged to form  $\theta$  precipitates ( $\text{CuAl}_2$ ).

(a) Using Figure 10.14(a), determine the volume fraction of  $\text{CuAl}_2$ . Take  $\rho_{\text{Al}} = 2.7 \times 10^3 \text{ kg/m}^3$  and  $\rho_{\text{Cu}} = 8.9 \times 10^3 \text{ kg/m}^3$ .

(b) Establish the stresses required for precipitate shearing and bypass by dislocations as a function of precipitate radius, given that  $\gamma_{\text{CuAl}_2} = 2.7 \text{ J/m}^2$ ,  $G_{\text{Al}} = 26.1 \text{ GPa}$ , and  $r_{\text{Al}} = 0.143 \text{ nm}$ .

**10.15** Figure E10.3 shows the Al-Mg phase diagram. For an alloy with 10% Mg by weight, calculate the  $\text{Al}_2\text{Mg}$  equilibrium volume fraction of precipitates if the densities of Al and  $\text{Al}_2\text{Mg}$  are 2.7 and 2.3 g/cm<sup>3</sup>, respectively.

10.16 An aluminum alloy is strengthened by dispersed alumina particles. These particles are spherical and have a diameter of 15  $\mu\text{m}$ . The weight percentage of alumina in aluminium is 3%. Estimate the dispersion strengthening.

Given:

$$G_{\text{Al}} = 28 \text{ GPa},$$

$$\text{Density (Al)} = 2.70 \text{ g/cm}^3,$$

$$\text{Density (Al}_2\text{O}_3\text{)} = 3.96 \text{ g/cm}^3.$$

---

## Chapter 11

# Martensitic Transformation

---

### 11.1 | Introduction

In this chapter, we discuss one important means of altering the mechanical response of metals and ceramics: martensitic transformation. Martensitic transformation is a highly effective means of increasing the strength of steel. An annealed medium-carbon steel (such as AISI 1040) has a strength of approximately 100 MPa. By quenching (and producing martensite), the strength may be made to reach about 1 GPa, a tenfold increase. The ductility of the steel is, alas, decreased.

A quite different effect is observed in ceramics. Martensitic transformation can be exploited to enhance the toughness of some ceramics. If a ceramic undergoes a martensitic transformation during the application of a mechanical load, the propagation of cracks is inhibited. For example, partially stabilized zirconia has a fracture toughness of approximately  $7 \text{ MPa m}^{1/2}$ . An equivalent ceramic not undergoing martensitic transformation would have a toughness less than or equal to  $3 \text{ MPa m}^{1/2}$ .

An additional, and very important, effect associated with martensitic transformations is the “shape-memory effect.” Alloys undergoing this effect “remember” their shape prior to deformation. The three effects just described have important technological applications.

---

### 11.2 | Structures and Morphologies of Martensite

Quenching has been known for over 3,000 years and is, up to this day, the single most effective mechanism known for strengthening steel. However, it is only fairly recently that the underlying mechanism has been studied in a scientific manner and understood. Initially attributed to a beta phase supposedly existing in the Fe–C system, the strengthening effect is now known to be due to a metastable phase: *martensite*. The term martensite was used in honor of a German scientist Martens. The investigations leading to the understanding of

**Table 11.1** Systems in which Martensitic or Quasi-Martensitic Transformation Occurs<sup>a</sup>

Alloy	Structure Change
Co, Fe–Mn, Fe–Cr–Ni	FCC→HCP
Fe–Ni	FCC→BCC
Fe–C, Fe–Ni–C, Fe–Cr–C, Fe–Mn–C	FCC→BCT
In–Tl, Mn–Cu	FCC→FCT
Li, Zr, Ti, Ti–Mo, Ti–Mn	BCC→HCP
Cu–Zn, Cu–Sn	BCC→FCT
Cu–Al	BCC→distorted HCP
Au–Cd	BCC→orthorhombic
ZrO <sub>2</sub>	tetragonal→monoclinic

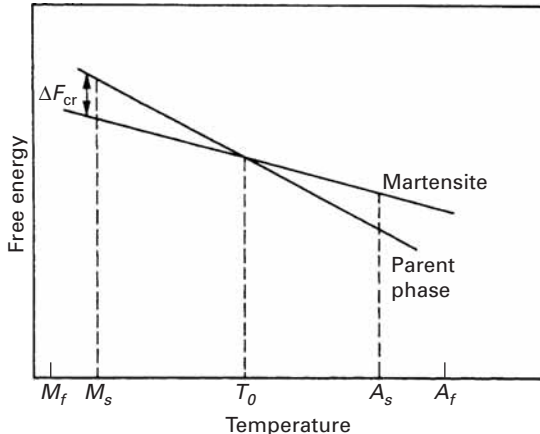
<sup>a</sup> Adapted with permission from V. F. Zackay, M. W. Justusson, and D. J. Schmatz, *Strengthening Mechanisms in Solids*, (Metals Park, OH: ASM, 1962), p. 179.

the mechanisms governing, and factors affecting, martensitic transformations have posed a great challenge to researchers over the second half of the twentieth century. Out of a confusing maze of apparently contradictory phenomena, order has appeared. Martensitic-like transformations have been identified in a great number of systems, including pure metals, solid solutions, intermetallic compounds, and ceramics. In order to assess the mechanical behavior of martensite and take advantage of its unique responses in technological applications, one has to understand the fundamental aspects of the transformation. Table 11.1 presents a number of systems in which martensitic-like transformations have been observed.

The original use of the martensitic transformation was exclusively to harden steel. Other developments have led to its use in different contexts. In transformation-induced plasticity (TRIP) steels, the martensitic transformation occurs during deformation and strengthens the regions ahead of a crack or near the neck in a tensile specimen, the ductility of the material is enhanced, while the strength level remains high. This results in great toughness. Ceramics (zirconia) are toughened through the same principle; the fracture toughness of partially stabilized zirconia can be as high as three times that of conventional ceramics.

Another manifestation of the martensitic transformation is the shape-memory effect. Upon being plastically deformed, the material undergoes internal changes in the configuration of the martensite plates. Heating the material recomposes the initial shape. This effect

**Fig. 11.1** Free energy versus temperature for austenitic and martensitic phases.  $M_s$ ,  $M_f$ ,  $A_s$ , and  $A_f$  marked on abscissa.



is discussed in detail in Section 11.5. More complex processing procedures involving the martensitic transformation, such as ausforming and maraging, have been developed for steels.

A martensitic transformation is a lattice-distortional, virtually diffusionless structural change having a dominant deviatoric component and an associated change in shape so that strain energy dominates the kinetics and morphology of the transformation. The requirement that there be no diffusion stems from thermodynamics: The driving energy required for martensitic transformation is much higher (in the case of irreversible martensites, especially) than that needed for diffusional decomposition (such as precipitation or spinodal decomposition). Hence, as the alloy is cooled, the diffusional transformations would take place at a higher temperature, where the free-energy difference between the two phases is not very large. Figure 11.1 shows the free energies of the parent and martensitic phase as a function of temperature. At  $T_0$ , the equilibrium temperature, the two phases have the same free energy.  $M_s$  is the highest temperature at which martensite starts to form spontaneously. The critical free energy required for the martensitic transformation is  $\Delta F_{cr}$  and is around 1,200 kJ/mol for Fe-Ni and Fe-C alloys. Hence, if a diffusion-induced transformation competes with the martensitic transformation, the cooling in the region where  $T_0 \rightarrow M_s$  has to be fast enough to avoid the diffusional transformation. On the other hand, if  $T_0$  is low enough, there is essentially no diffusion, and slow cooling will produce martensite. Upon heating above austenite start temperature  $A_s$ , the martensite reverts to austenite. For irreversible martensites, the gap between  $M_s$  and  $A_s$  is a few hundred kelvins; for reversible martensite, the gap is of a few tens of kelvin.

The martensite phase can exhibit a variety of morphologies, depending on the composition of the alloy, the conditions in which it is formed, and its crystalline structure. The three most common morphologies are the lenticular (lens-shaped), the lath (a large number of blocks juxtaposed in a shinglelike arrangement), and the acicular (needle-shaped). These are shown in Figures 11.2 through 11.5. Lenticular martensite occurs in Fe-Ni and Fe-Ni-C alloys with

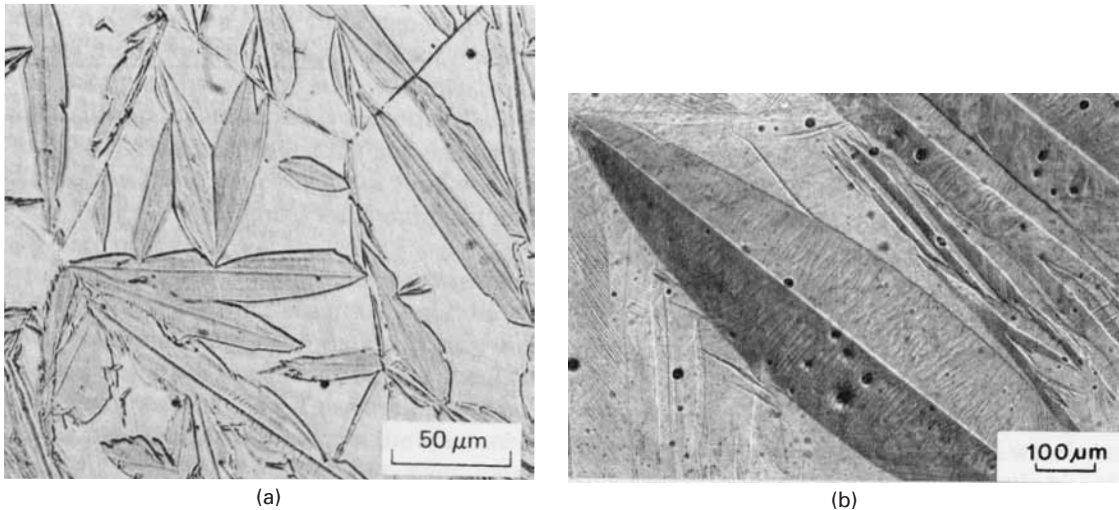


**Fig. 11.2** (a) Lenticular martensite in an Fe-30% Ni alloy.  
(Courtesy of J. R. C. Guimarães.)  
(b) Lenticular (thermoelastic) martensite in Cu-Al-Ni alloy.  
(Courtesy of R. J. Salzbrenner.)

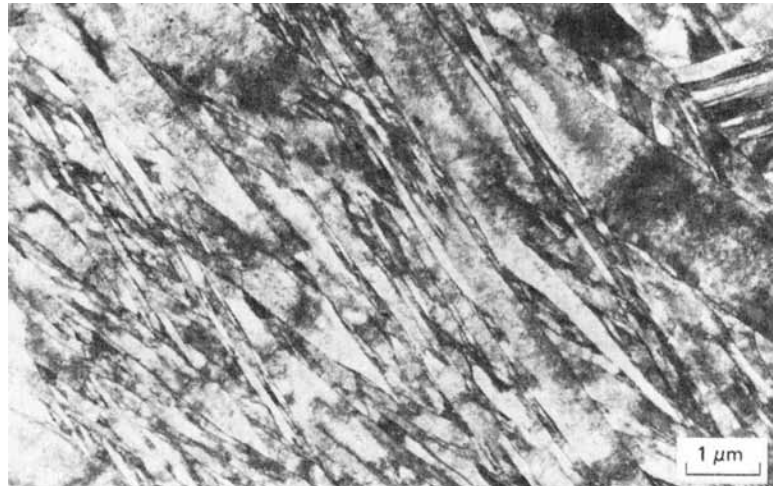
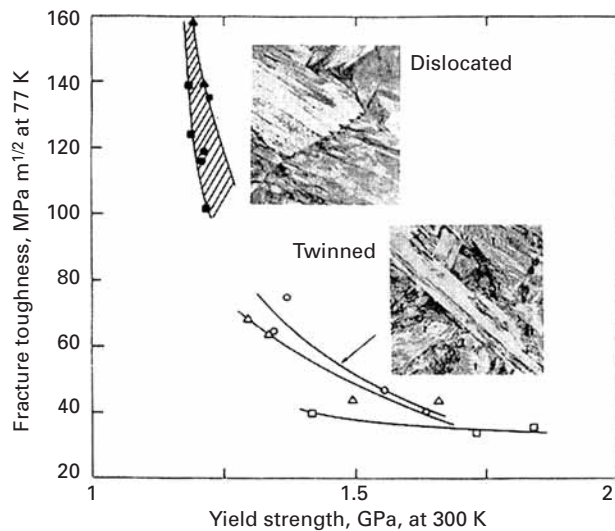
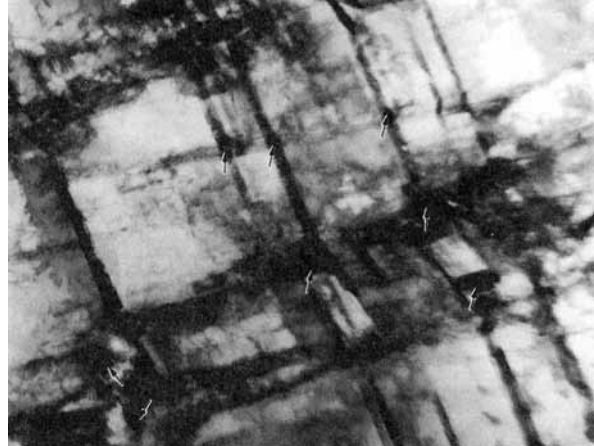
approximately 30% Ni and in Fe-C alloys with over 0.6% C. The central region is called the *midrib* and etches preferentially. The substructure is characterized by twins, dislocations, or both. In the particular case of Figure 11.2(a), the region adjacent to the midrib is twinned, and the external parts are dislocated. Figure 11.2(b) shows lenticular martensite in a Cu-Al-Ni alloy. This material exhibits the shape-memory effect. Lath martensite, on the other hand, is quite different, consisting of small, juxtaposed blocks that are arranged in packets separated by low-angle grain boundaries. Each packet is composed of blocks with a thickness varying between a few micrometers and a few tens of micrometers; the blocks make specific angles with their neighbors. There is a repetitive pattern in each packet, leading to a 360° rotation and a resultant periodicity. Low-carbon steels and Fe-Ni alloys with less than about 30% nickel exhibit this morphology, shown in Figure 11.3.

In steels, there is a significant difference in the mechanical properties of twinned and dislocated martensites. Figure 11.4 shows a medium-carbon steel (0.3% C) that can exhibit both lath (dislocated) and lenticular (twinned) martensites. It can be seen that twinned martensite gives poor toughness, which is consistent with what we learned about twinning in Chapter 5. Mechanical twinning can give rise to microcracks, which are initiation sites for failure of the material (see Figure 8.6). The example of Figure 11.4 is a wonderful illustration of how the microstructure (in this case, inside the martensite lenses and laths) can have a dramatic effect on mechanical properties. This fact is often overlooked by engineers.

Acicular martensite is shown in Figure 11.5. This form occurs in austenitic stainless steel (Fe-Cr-Ni alloys) after deformation. Needles form at the intersection of the slip bands (either dislocations, stacking faults, twins,  $\varepsilon$ -martensite, or a combination thereof). Since the intersection of these bands is a thin “tube,” the martensite forming in it has this specific shape (marked by arrows in the figure). Acicular martensite has the BCC or BCT structure and has a marked

**Fig. 11.3** Lath martensite.

(Reprinted with permission from C. A. Apple, R. N. Caron, and G. Krauss, *Met. Trans.*, 5 (1974) 593.)

**Fig. 11.4** Comparison of mechanical properties between twinned and dislocated martensite in medium-carbon (0.3% C) steel. (Courtesy of G. Thomas.)**Fig. 11.5** Acicular martensite in stainless steel forming at intersection of slip bands (Courtesy of G. A. Stone.)

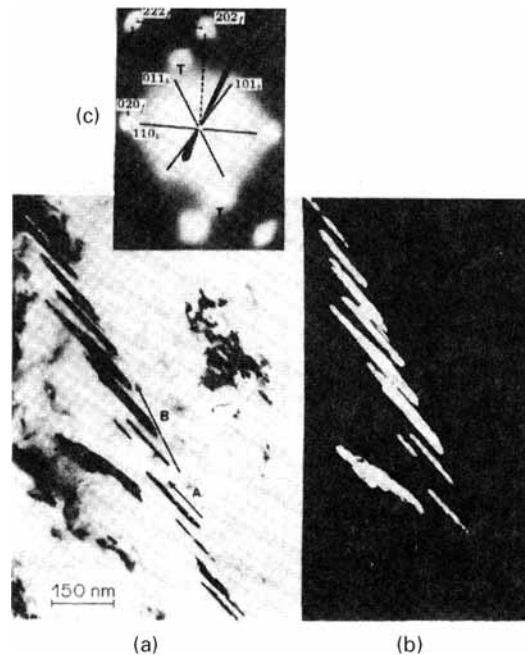


**Fig. 11.6** (a) Transmission electron micrograph showing a group of twins inside martensite transformed at  $-140^{\circ}\text{C}$  and 2 GPa. (b) Dark-field image of twins on  $(112)_b$  plane; (c) Stereographic analysis for habit (in FCC) and twin (in BCC) planes. (From S. N. Chang and M. A. Meyers, *Acta Met.*, 36 (1988) 1085.)

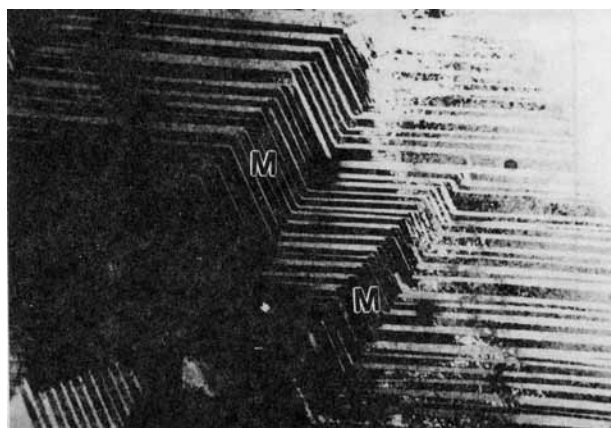


**Fig. 11.7** Martensite lenses (M) being transversed by twins, which produce self-accommodation. (Courtesy of A. R. Romig.)

effect on the strength and work-hardening ability of the alloy. Other martensite morphologies have been observed also.  $\varepsilon$ -martensite is HCP and forms in plates. It can be produced in steel by subjecting the metal to a high pressure ( $>13$  GPa) or in austenitic stainless steels by deformation. After substantial plastic deformation, sheaves of fine parallel laths were observed to form along the austenite slip bands in austenitic Fe–Ni–C alloys. Yet another morphology is the butterfly martensite, so called because two lenses form in a coupled manner; the resultant microstructure resembles a number of butterflies. The plastic deformation accompanying the martensite, constrained by the surrounding matrix, can occur by either slip or twinning. Examples of twinned martensite are shown in Figure 11.6 (for an Fe alloy with 22.5 wt.% Ni and 4 wt.% Mn) and Figure 11.7 (for a U–Re alloy). The transmission electron micrograph (Figure 11.6(a)) and dark-field

picture (Figure 11.6(b)) show the group of twins inside a martensite lens. Crystallographic analysis of the electron diffraction pattern of Figure 11.6(c) reveals the habit and twinning planes. In the case of the U-Re system (Figure 11.7), the twins propagate from the lenses into the matrix; the two martensite lenses are indicated by  $M$ .

In spite of these differences in morphology, some unique features are common to all martensites. The most important is the existence of an *undistorted and unrotated plane*. The crystallographic orientation relationship between parent and martensite phases is such that there *always* is a plane that has the same indices in the two structures. This undistorted and unrotated plane is called the *habit plane*; it is usually a plane with irrational indices. For a steel with 1.4% carbon, Kurdjumov and Sachs found the following relationships for habit plane (225):<sup>1</sup>

$$(111)_A \parallel (011)_M \\ [10\bar{1}]_A \parallel [01\bar{1}]_M.$$

Steels with less than 1.4% carbon exhibit the same relationship. This specific martensite is known as (225). Nishiyama investigated the Fe-Ni-C alloys and steels with carbon content greater than 1.4% and obtained the following relationship for habit plane (259):<sup>2</sup>

$$(111)_A \parallel (011)_M \\ [11\bar{2}]_A \parallel [01\bar{1}]_M.$$

### 11.3 | Strength of Martensite

The martensitic transformation has the ability to confer a great degree of strength on steels; other alloys do not seem to have such strong martensites. The strength of martensite in steel is dependent on a number of factors, the most important being the carbon content of the steel. While the Rockwell C hardness of iron increases from 5 to 10 when it is transformed to martensite, it increases from 15 to 65 when the carbon content is 0.80% (eutectoid steel). The origin of the high hardness of martensite has been the object of great controversy in the past. It is now fairly well established that there is no single, unique mechanism responsible for it. Rather, a number of strengthening mechanisms operate, most of which we have described in chapters 5, 6, and 10. Nevertheless, the relative importance of these strengthening mechanisms and their interactions are still the object of controversy. It seems that interstitial solution-hardening and substructure strengthening (work-hardening) are the most important ones.

Most metals exhibit a dependence of yield stress on grain size; the martensite lenses divide and subdivide the grain when they

<sup>1</sup> G. Kurdjumov and G. Sachs, *Z. Phys.*, 64 (1930) 325.

<sup>2</sup> Z. Nishiyama, *Sci Rep. Tohoku Univ.*, 2B (1934) 627.

form. Hence, a small-grained alloy produces small martensitic plates, whereas a large-grained alloy produces a distribution of sizes whose mean is much larger. This is shown in Figure 11.8. Three commercial steels (AISI 4310, 4340, and 8650) exhibit a dependence of yield stress on prior austenitic grain size. The slope of the Hall-Petch plot seems to be the same for the three. However, for the range of grain sizes usually encountered, the contribution of grain size is not very important: The grain sizes are equal to 0.1 mm or more. Only in steels that have undergone thermomechanical processing to reduce the austenitic grain size is this strengthening mechanism of significance.

The contribution of substitutional solid-solution elements to the strength of ferrous martensites is relatively unimportant; additionally, it is difficult to separate it from other indirect effects, such as the change in  $M_s$ , and stacking-fault energy due to the addition of these elements.

On the other hand, interstitial solutes (carbon and nitrogen, for instance) can play an important effect. If we regard martensite as a supersaturated solution of carbon in ferrite, a great portion of its strength could be ascribed to solution-hardening. Foreman and Makin developed an equation of the following form to express the effect of the solute concentration  $C$  on the shear yield stress of the alloy if only the interaction between dislocations and single-atom obstacles is considered:<sup>3</sup>

$$\tau_0 = \left(1 - \frac{\phi'}{5\pi}\right) G \left(\frac{F_{\max}}{2T}\right)^{3/2} (3C)^{1/2}. \quad (11.1)$$

Here,  $F_{\max}$  is the maximum force exerted by the obstacle on the dislocation,  $T$  is the line tension of the dislocation line,  $G$  is the shear modulus, and  $\phi'$  is the angle turned through by the dislocation immediately before it frees itself from the obstacle. The interesting aspect of this equation is that the yield stress should increase with the square root of the solute concentration. And indeed, results obtained by Roberts and Owen confirm Equation 11.1, as can be seen in Figure 11.9. These researchers used alloys with very low  $M_s$  (below 77 K), to avoid any secondary effect of the carbon atoms, such as precipitation-hardening or the formation of a Cottrell atmosphere. The fact that the room-temperature tests exhibit the same slope as the ones conducted at 77 K shows that even at room temperature, solid-solution-hardening is operating and effectively strengthening martensite.

Snoek ordering consists of the reorientation of a system of point defects of tetragonal or lower symmetry that are randomly distributed in the stress field of a dislocation (see Section 10.3.5). Single jumps of carbon atoms can organize the atoms in such a way as to minimize their energy. Snoek ordering can take place in a much shorter time interval than does the formation of a Cottrell atmosphere, because no long-range diffusion is required.

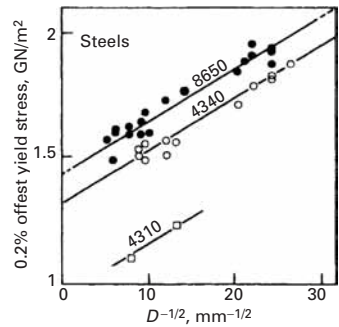
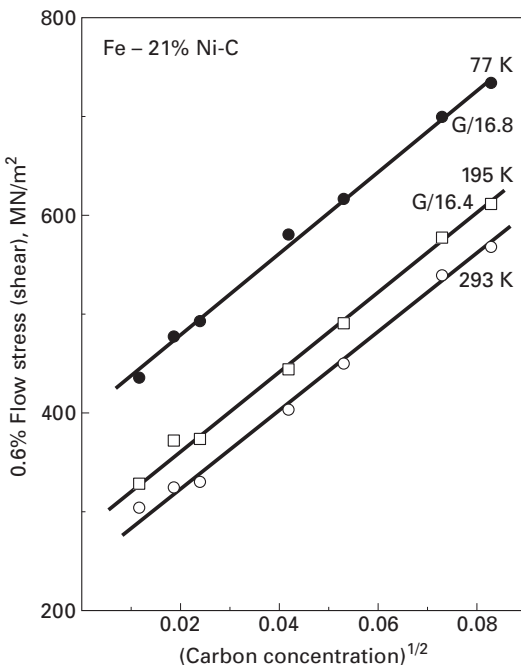


**Fig. 11.8** Effect of prior austenite grain size on the yield stress of three commercial martensitic steels. (Adapted with permission from R. A. Grange, *Trans. ASM*, 59 (1966) 26.)

<sup>3</sup> A. J. E. Foreman and M. J. Makin, *Phil Mag.*, 14 (1966) 191.

**Fig. II.9** Plot of 0.6% proof stress (one-half of tensile stress) versus  $C^{1/2}$  for Fe–Ni–C lath martensite at various temperatures. The slopes are shown as fractions of the shear modulus, which is denoted by  $G$ . (Adapted with permission from M. J. Roberts and W. J. Owen, *J. Iron Steel Inst.*, 206 (1968) 37.)



The formation of a Cottrell atmosphere, on the other hand, requires that the atoms diffuse toward regions in the dislocation in which their strain energy will be minimized. Carbon atoms produce tetragonal distortions and shear stresses; hence, they seek regions around both edge and screw dislocations in which the shear strains cancel each other. Cottrell atmospheres produce both static and dynamic aging. A manifestation of the latter is the serrated flow (the Portevin–Le Chatelier effect: see also Section 10.3.4).

Carbon atoms have also been shown to exhibit a clustering behavior. Carbon-rich regions have been identified by transmission electron microscopy in steels that had been exposed to temperatures no higher than ambient temperature. These clusters do not change the crystalline structure of the martensite, but produce periodic strain fields, resulting in a “modulated” structure. In this sense, the clustering is closer to a spinodal decomposition than to a precipitation reaction. If the martensite is aged at higher temperatures, cementite and other metal carbides are precipitated. The latter process is called *tempering*.

Frequently, precipitation is observed in martensite. Quenched carbon steels with  $M_s$  above room temperature may contain precipitates that form during cooling. In certain low-carbon steels these precipitates have been identified as cementite. It seems that carbon is a more efficient strengthener as a precipitate than in solid solution. The contribution of precipitates in ferrous martensites exceeds that of a solid solution. A very important contribution is that of strain hardening. In twinned martensite, a very fine array of twins 5 to 9 nm thick presents a very effective barrier for additional deformation. These fine twins are the most important factor in the strength of martensite. When

martensite is dislocated, the density of dislocations is typically  $10^{10}$  to  $10^{11} \text{ cm}^{-2}$ ; the substructure resembles that of BCC steel that has been heavily deformed by conventional means.

The contributions to the strength of the martensite in a 0.4% carbon steel can be distributed as follows.<sup>4</sup>

Boundary strengthening	620 MPa
Dislocation density	270 MPa
Solid solution of carbon	400 MPa
Rearrangement of carbon in quench (Cottrell atmosphere)	
Snoek effect, clustering, precipitation)	750 MPa
Other effects	<u>200 MPa</u>
Total	2,240 MPa

Williams and Thompson<sup>4</sup> point out that these effects are not necessarily additive; however, this simplified scheme shows the various contributions.

Yet another source of strengthening is the intrinsic resistance of the lattice to dislocation motion (Peierls-Nabarro stress). This type of resistance accounts for the temperature dependence of yield stress in martensite. Iron exhibits a strong temperature dependence of yield stress at low temperatures, as do other BCC metals. This same behavior is observed in martensite, independent of the existence of precipitates and solutes.

## 11.4 Mechanical Effects

A martensite lens introduces macroscopic strains in the lattice surrounding it. This is best seen by making fiducial<sup>5</sup> marks on the surface and transforming the material. The fiducial marks will be distorted by the strains. The strains introduced by a martensite lens can be decomposed into a dilational and a shear strain. The dilational strain is perpendicular to the midrib plane, and the shear strain is parallel to the midrib plane. In ferrous alloys, the dilation is approximately 0.05 and the shear strain  $\gamma$  is about 0.02. Figure 11.10 shows a fiducial mark made on the surface of a hypothetical alloy. The shear direction is such that the plane is not distorted. Hence,  $\tan \theta = \gamma$ , and  $\theta$  is equal to  $11^\circ$ . The strain matrix can be expressed as

$$\begin{pmatrix} \varepsilon_{11} & \varepsilon_{12} & \varepsilon_{13} \\ \varepsilon_{12} & \varepsilon_{22} & \varepsilon_{23} \\ \varepsilon_{13} & \varepsilon_{23} & \varepsilon_{33} \end{pmatrix} = \begin{pmatrix} 0 & 0 & 0 \\ 0 & 0 & 0.10 \\ 0 & 0.10 & 0.05 \end{pmatrix}. \quad (11.2)$$

Recall that  $\varepsilon_{23} = \gamma_{23}/2$ . These strains are well beyond the elastic limit of the matrix, and there is plastic deformation in the region

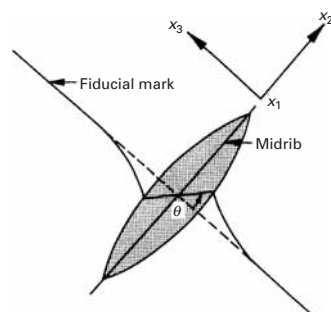
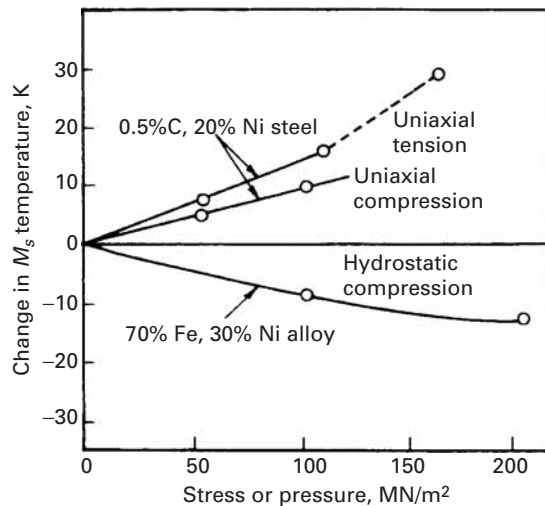


Fig. 11.10 Distortion produced by martensite lens on fiducial mark on surface of specimen.

<sup>4</sup> J. C. Williams and A. W. Thompson, in *Metallurgical Treatises*, J. K. Tien and J. F. Elliott, eds. (Warrendale, PA: TMS-AIME, 1981), p. 487.

<sup>5</sup> A fiducial linear marking is a straight line, imaginary or real, drawn before the transformation.

**Fig. 11.11** Change in  $M_s$  temperature as a function of loading condition. (Adapted with permission from J. R. Patel and M. Cohen, *Acta Met.*, 1 (1953) 531.)



surrounding the martensitic lens. This is reflected in Figure 11.10 by the distortion of the fiducial line.

The dilational and shear stresses and strains imposed by the martensitic transformation interact with externally applied stresses, and very special responses ensue. The effects of externally applied tensile, compressive, and hydrostatic stresses are shown in Figure 11.11. The uniaxial tension and compression increase  $M_s$ , whereas hydrostatic compression lowers it. The explanation is that, under the effect of the applied stress, the mechanical work done by the transformation, which can be decomposed into the dilational and shear components,  $\sigma\varepsilon$  and  $\tau\gamma$ , is either increased or decreased:

$$W = \sigma\varepsilon + \tau\gamma. \quad (11.3)$$

The hydrostatic stress counters the lattice expansion produced by martensite, but does not affect the shear stress. Hence, a greater amount of free energy is required to trigger the transformation. Referring to Figure 11.1 we can see that a greater  $\Delta F$  will require a lowering of  $M_s$ . For the tensile test, the applied stress can be decomposed into a normal (positive) stress and a shear stress, both of which aid the transformation. The shear stress aids the martensite variants aligned with the direction of maximum shear ( $45^\circ$  to the tensile axis). These variants will form preferentially; hence, the free-energy requirement is decreased and  $M_s$  is increased. In the compressive test, the normal portion of the stress is negative and counters the dilational stress of the transformation, whereas the shear stress favors it. (There are always favorably oriented variants.) Since the shear stress term dominates the expression (because of the greater shear strain  $\gamma$ ), the tensile stress should be more effective in increasing  $M_s$  than the compressive stress is. This is exactly what is shown in Figure 11.11.

Another experimental procedure consists of conducting tensile tests at temperatures above  $M_s$ . When the stress level reaches the value at which martensite forms at the test temperature, a significant

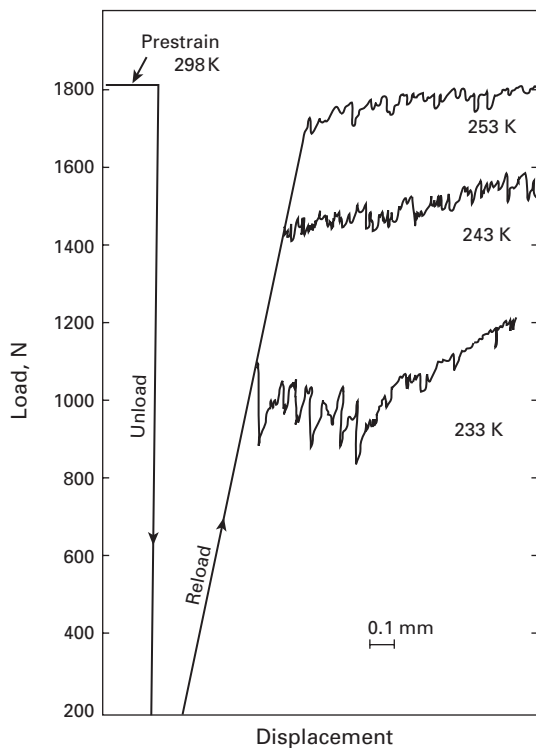


**Fig. 11.12** Tensile curves for Fe-Ni-C alloy above  $M_s$ , showing martensite forming in elastic range (stress assisted). (Courtesy of J. R. C. Guimarães.)

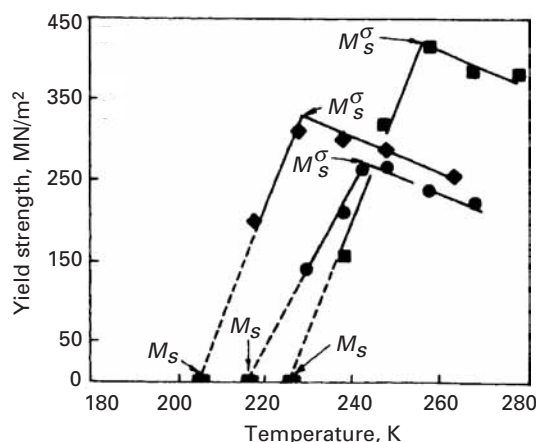


**Fig. 11.13** Temperature dependence of the yield strength of Fe-31% Ni-0.1% C. ■, predeformed by shocking; ●, larger grain size; ◆, smaller grain size. (Adapted with permission from J. R. C. Guimarães, J. C. Gomes, and M. A. Meyers, *Suppl. Trans. Japan Inst. of Metals*, 17 (1976) 41.)

load drop is observed. Figure 11.12 shows this effect. The load drop is attributed to the shear strain of the martensite, which produces an instantaneous increase in strain of the martensite, which produces an instantaneous increase in length of the specimen. As the difference between the test temperature and  $M_s$  increases, the stress at which martensite starts forming increases; this can be directly inferred from Figure 11.12. In Figure 11.13 the yield strength is plotted as a function of temperature; when martensite forms in the elastic line, the stress at which it forms is equal to the yield strength (as in Figure 11.12, for instance). The temperature dependence of the stress for martensite transformation is clearly shown by the three straight lines in

**Fig. 11.14** Volume fraction transformed (right-hand side),  $f$ , and stress (left-hand side) as a function of plastic strain for an austenitic (metastable) steel deformed at  $-50^{\circ}\text{C}$ ; experimental and idealized stress-strain curves for austenite, martensite, and mixture. (After R. G. Stringfellow, D. M. Parks, and G. B. Olson, *Acta Met.*, 40 (1992) 1703.)

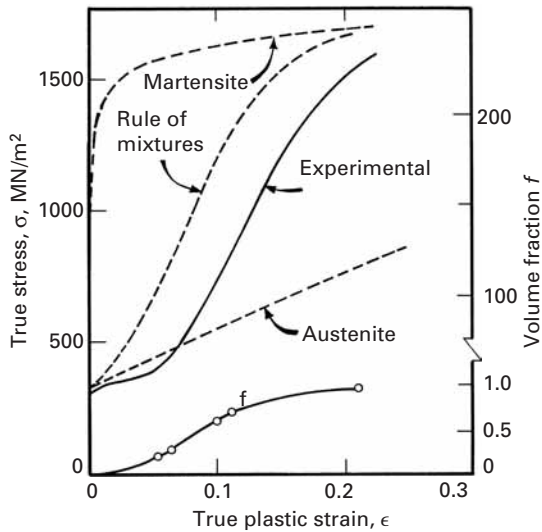
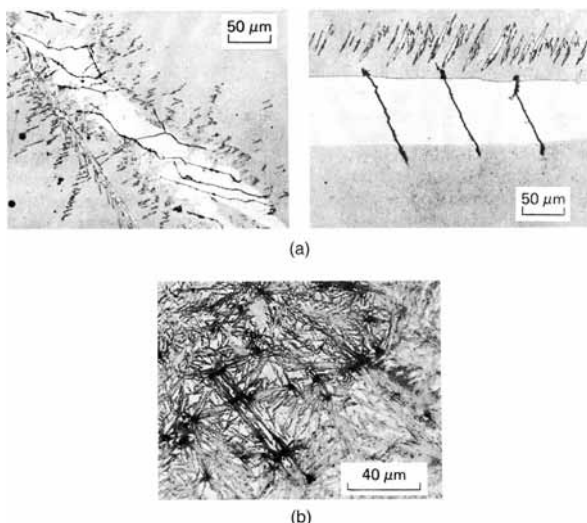


Figure 11.13. At  $M_s$ , as expected, martensite forms spontaneously, without any stress. The plots of yield strength versus temperature for three different conditions have inverted-V shapes. At the point marked  $M_s^\sigma$ , the slope of the curve changes, and above this temperature, the yield stress is produced by conventional dislocation motion; hence, it shows the regular increase with decreasing temperature. Between  $M_s$  and  $M_s^\sigma$ , on the other hand, we have stress-assisted martensite establishing yield, and the temperature dependence is inverted, leading to a yield stress of zero at  $M_s$ . It is worth noting that the three alloys in Figure 11.13 have the same composition, but different processing histories.  $M_s$  temperature is affected by grain size.  $M_s$  increases with increasing grain size and predeformation; in the case shown in the figure, predeformation was accomplished by shock loading.

The formation of strain-induced martensite occurs in the temperature range above  $M_s^\sigma$  in Figure 11.13. Substantial plastic deformation, in which the substructure has to be sensitized, is required before the first martensite forms. This kind of martensite is called *strain induced*, to differentiate it from *stress-assisted* martensite. Figure 11.14 illustrates the effect of strain-induced martensite on the stress-strain curve of an austenitic stainless steel at  $-50^{\circ}\text{C}$ . The austenite has a low yield stress and work-hardening rate; the transformation to martensite is also shown (right-hand axis). The experimentally obtained curve reflects the fact that an increase in martensite volume fraction is accompanied by plastic strain; the simple rule-of-mixtures curve is higher than the experimental curve because there are complex synergistic processes between the two phases ( $\alpha$  and  $\gamma$ ).

Strain-induced martensite is responsible for a very beneficial effect: the transformation-induced plasticity (TRIP). Remarkable combinations of high strength and toughness have been obtained in TRIP steels. The high strength is due to work-hardening, carbide precipitation, and dislocation pinning by solutes during thermomechanical



**Fig. 11.15** Microcracks generated by martensite.  
 (a) Fe-8% Cr-1% C (225 martensite sectioned parallel to habit plane). (Courtesy of J. S. Bowles, University of South Wales.)  
 (b) Carburized steel. (Reprinted with permission from C. A. Apple and G. Krauss, *Met. Trans.*, 4 (1973) 1195.)

treatment. The high toughness comes from a combination of high strength and high ductility. The ductility is a direct consequence of the strain-induced martensite transformation. If a certain region in the metal is severely deformed plastically, strain-induced transformation takes place, increasing the local work-hardening rate and inhibiting an incipient neck from further growth. On the other hand, if a crack has already formed, martensitic transformation at the crack tip will render its propagation more and more difficult. In Section 11.6, the toughening of a ceramic ( $\text{ZrO}_2$ ) by stress-assisted martensite will be described.

Another mechanical aspect of importance is the fracture of martensite. Fracture is usually initiated in a martensitic alloy along the martensite-austenite or martensite-martensite boundaries. Indeed, upon investigating the fracture surfaces of Fe-31% Ni-0.1% C alloy, Chawla *et al.*<sup>6</sup> found that the density of dimples increased as a function of the amount of martensite in the cross section; the same result was obtained by decreasing the grain size. Hence, the dimple size was tied to the density of interfaces. In carbon-free or low-carbon steels, martensite is fairly soft, and the fracture is, consequently, ductile. In high-carbon steels, on the other hand, martensite is hard and brittle, and the fracture surface takes a cleavage appearance, with the fracture path traversing the plates (or laths). Of great importance in the initiation of fracture is the existence of microcracks in the structure. Marder *et al.*<sup>7</sup> found a great number of microcracks in Fe-C martensites; when the grain size was decreased, the incidence of microcracks decreased. The microcracks were formed when one lens impinged on another. Figure 11.15 shows how these cracks occur. The microcracks act as stress-concentration sites when the specimen is loaded; they are initiation sites for macrocracks.

<sup>6</sup> K. K. Chawla, J. R. C. Guimarães, and M. A. Meyers, *Metallography*, 10 (1977) 201.

<sup>7</sup> A. R. Marder, A. D. Benscoter, and G. Krauss, *Met. Trans.*, 1 (1970) 1545.

Tempering of martensite<sup>8</sup> in steels is performed to improve toughness. However, the tempering process might induce embrittlement. Temper martensite embrittlement (TME) results from the segregation of impurities to the previous austenitic grain boundaries, providing a brittle path for propagation of the fracture. The fracture takes on the intergranular morphology. Temper embrittlement (TE) is caused by the impurities such as antimony, phosphorus, tin, and arsenic (less than 100 ppm required) or larger amounts of silicon and manganese. TME and TE occur in different ranges of temperatures; TME is a much more rapid process.

---

## 11.5 | Shape-Memory Effect

The *shape-memory effect* (SME) is the unique property that some alloys possess according to which, after being deformed at one temperature, they recover their original shape upon being heated to a second temperature. The built-in memory is produced by the martensitic transformation. The effect was first discussed by the Russian metallurgist Kurdjumov. In 1951, Chang and Read<sup>9</sup> reported its occurrence in an In-Ti alloy. However, wide exposure of this property came only after the development of the nickel-titanium alloy by the Naval Ordnance Laboratory (NiTiNOL) in 1968.<sup>10</sup> Since then, research activity in this field has been intense, and a number of  $\beta$ -phase SME alloys have been investigated, including AgCd, AgZn, AuCd, CuAl, CuZn, FeBe, FePt, NbTi, NiAl, and ternary alloys. The Nitinol family of alloys has found wide technological applications, and adjustments in composition can be made to produce  $M_s$  temperatures between  $-273$  and  $100$  °C. This is an extremely helpful feature, and alloys are tailored for specific applications. In the majority of SME alloys the high-temperature phase is a disordered  $\beta$ -phase (body-centered cubic), while the martensitic phase is an ordered BCC structure with a superlattice or orthorhombic structure. Two separate mechanical effects characterize the response of SME alloys: *pseudoelasticity* and *strain-memory effect*. We describe these next, in connection with tensile and compressive tests.

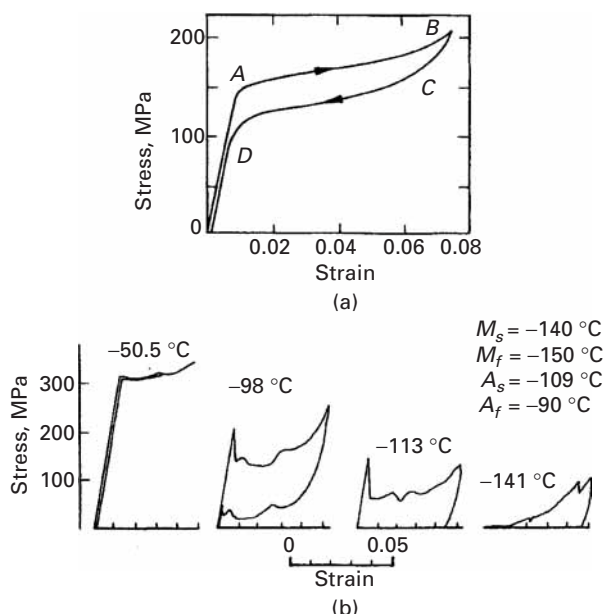
*Pseudoelasticity*, or superelasticity, is the result of stress-induced martensitic transformation in a tensile test in which martensite reverts to the parent phase upon unloading. The individual martensite plates do not grow explosively, as in the ferrous martensites, and little irreversible damage is done to the lattice. The shear strain of one plate is accommodated by neighboring plates. The complex motion of the interfaces between the martensite plates along the various variants and within the same martensite plate takes place by the displacement of the interfaces between the different twins.

---

<sup>8</sup> Tempering consists of heating the martensitic structure to an intermediate temperature.

<sup>9</sup> L. C. Chang and T. A. Read, *Trans. Met. Soc. AIME*, 191 (1951) 49.

<sup>10</sup> W. J. Buehler and F. E. Wang, *Ocean Eng.*, 1 (1968) 150.



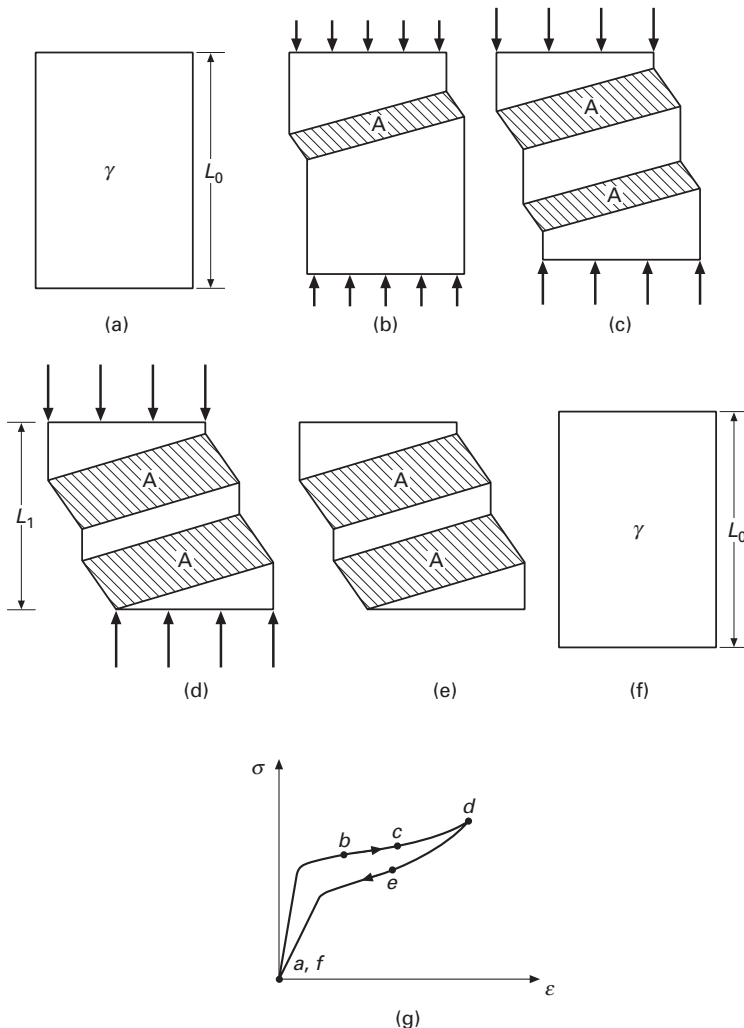
**Fig. 11.16** (a) Pseudoelastic stress-strain curve for a single-crystal Cu-Al-Ni alloy at 24 °C (72 °C above  $M_s$ ).  
 (b) Dependence on temperature of stress-strain characteristics along the characteristic transformation temperatures.  
 Strain rate:  $2.5 \times 10^{-3} \text{ min}^{-1}$ .  
 (Reprinted with permission from C. Rodriguez and L. C. Brown, in *Shape Memory Effects*, (New York: Plenum Press, 1975), p. 29.)

Figure 11.16(a) shows the pseudoelastic effect for a Cu-Al-Ni alloy with  $M_s = -48^\circ\text{C}$ . The test was conducted at  $24^\circ\text{C}$  ( $72^\circ\text{C}$  above  $M_s$ ). At A, stress-induced martensite starts to form. At B, the martensitic transformation has been completed, and any straining beyond that point will produce irreversible plastic deformation or fracture. Upon unloading, the martensite reverts to the parent phase between C and D. Further unloading results in the return to the original length of the specimen. The pseudoelastic strain exceeds 6%. The magnitude of the pseudoelastic strain can be calculated from a knowledge of the habit plane of the martensite (and its orientation with respect to the tensile axis) and the magnitude of the shear strain for the transformation. Since the habit plane of martensite is irrational, it has a multiplicity of 24, and there is always a habit plane oriented very close to the plane of maximum shear.

The pseudoelastic (or superelastic) effect is illustrated in a very simplified fashion in Figure 11.17. A specimen with initial length  $L_0$  is compressed. Stress-induced martensitic transformation takes place, and the austenite-martensite interfaces are glissile; that is, they can move under the applied stress. In Figure 11.17(c), two martensite lenses are shown. They continue to grow in Figure 11.17(d). When the stress is decreased, they shrink in the same order as the initial growth. When the stress is reduced to zero, all martensite has disappeared, and the specimen has returned to the original length  $L_0$ . Figure 11.17(g) shows the corresponding stages on a stress-strain curve, similar to the stress-strain curve in Figure 11.16(a). The stress-strain curve returns to the origin after the load is removed.

It is not sufficient for the temperature at which testing is conducted to be above  $M_s$  to obtain the pseudoelastic effect, as shown in Figure 11.16(b). These tests were conducted on a Cu-Al-Ni alloy. The

**Fig. 11.17** Schematic representation of pseudoelastic (or superelastic) effect. (a) Initial specimen with length  $L_0$ . (b, c, d) Formation of martensite and growth by glissile motion of interfaces under increasing compressive loading. (e) Unloading of specimen with decrease in martensite. (f) Final unloaded configuration with length  $L_0$ . (g) Corresponding stress-strain curve with different stages indicated.



temperatures  $A_s$  and  $A_f$  (austenite start and finish, respectively) are also important. If the testing temperature is below  $A_s$ , the martensite will not revert to austenite upon unloading; the tests conducted at  $-141^\circ\text{C}$  and  $-113^\circ\text{C}$  show this irreversibility. For the test conducted at  $-50.5^\circ\text{C}$  and  $-98^\circ\text{C}$ , total reversibility is obtained, since this temperature is above  $A_f$  ( $-90^\circ\text{C}$ ). Another observation that can be made in Figure 11.16(b) is that the stress at which martensite forms increases with increasing temperature.

When the deformation is irreversible (at  $-113^\circ\text{C}$  and  $-141^\circ\text{C}$  in Figure 11.16), the effect receives the name *strain-memory effect*. Additional heating is required to return the martensite to its original shape, since the deformation temperature is below  $A_s$ . Upon heating, the original dimensions will be regained, as the martensite interfaces move back to retransform the lattice. The sequences in which the plates form and in which they disappear are inverted: the first plate to form is the last to disappear.

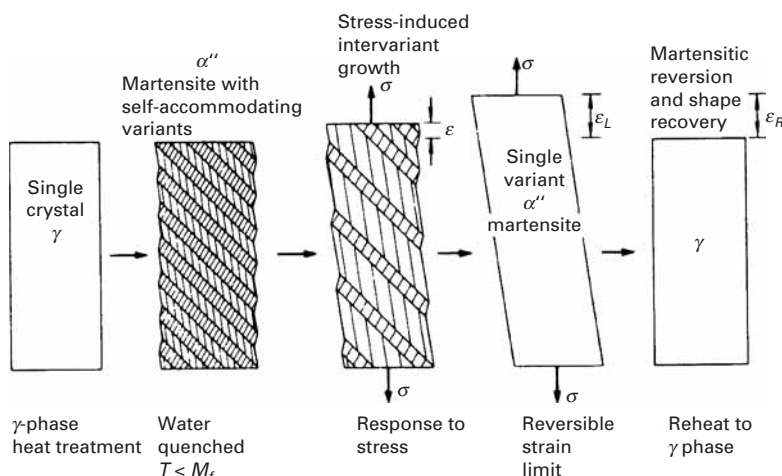


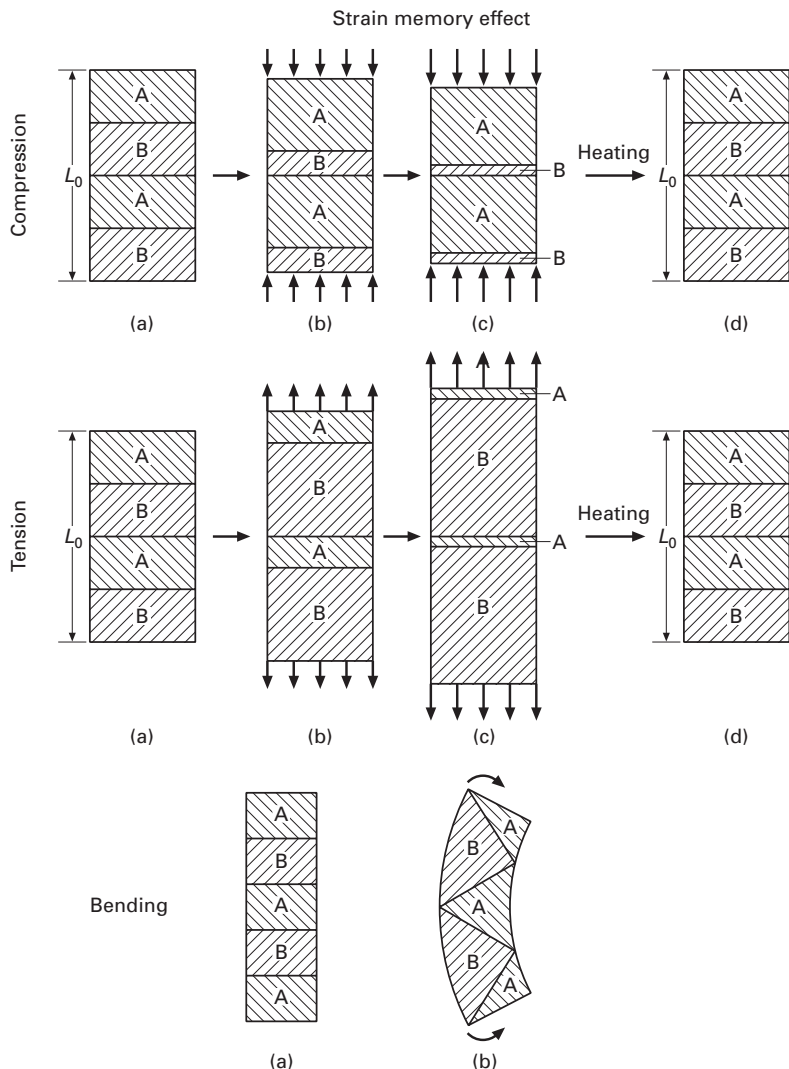
**Fig. 11.18** Sequence showing how growth of one martensite variant and shrinkage of others results in strain  $\varepsilon_L$ . (Courtesy of R. Vandermeer.)

The strain-memory effect is also obtained when deformation is imparted at temperatures below  $M_s$ . This is actually the procedure used in most technological applications. In this case, the structure consists of thermally induced martensite; it is present in such a way that all variants occur. When the external stress is applied, the variants that have shear strains aligned with the applied shear strain tend to grow, and the unfavorably oriented variants shrink. Figure 11.18 shows schematically how this takes place. Only two variants are shown, for simplicity. The variant that favors the applied tensile strain grows at the expense of the unfavorably oriented one. Hence, all unfavorable variants disappear, and the favorable variant takes over the structure. On heating, the structure reverts to the original one, composed of equal distribution of the two variants, giving the strain recovery.

Figure 11.19 shows the strain-memory effect for compressive, tensile, and flexure loading. Only two martensite variants are shown: A and B. In this drawing, variant B favors tensile strains, whereas variant A produces compression in the direction of loading. Under compressive stresses, variant A grows at the expense of B. Under tensile loading, the opposite is true. And under bending, variant B grows on the outside, while variant A grows on the inside. The situation in a real material is much more complex, and polycrystalline effects come into play. Nevertheless, the simple scheme of Figure 11.19 shows the essential features of the strain-memory effect. Upon heating, the three specimens return to the original shape by the reverse motion of the martensite interfaces. Further heating would make the martensite revert to austenite.

When the strain-memory effect is obtained above  $M_s$ , a fully austenitic structure gradually becomes martensitic under stress. This is shown in the schematic representation of Figure 11.20. Only one variant of martensite is depicted. The loading stage is similar to that for the superelastic effect. However, upon unloading, the martensite remains in the material, and heating is required to return the

**Fig. III.19** Schematic representation of strain-memory effect in compression, tension, and bending. Variant A favors a decrease in dimension in the direction of its length, whereas variant B favors an increase in dimension.



martensite to its original dimensions. The reverse transformation occurs in the same order as the martensite transformation, and the specimen “remembers” its original slope.

Other potential benefits of the shape-memory effect involve the increased damping capacity of the material, which can become very large because of the work required to form the martensite. Circuit breakers, pseudoelastic wires for support in brassieres, overheat protection systems, sensors in heating and ventilation, components in the Hubble telescope, pseudoelastic dental arch wires, a pseudoelastic scoliosis correction system (a biomedical application), and porous pseudoelastic tissue are additional examples of applications of the pseudoelastic and strain-memory effects.

Structures containing their own sensors, actuators, and computational or control capabilities are called “smart,” “adaptive,” or

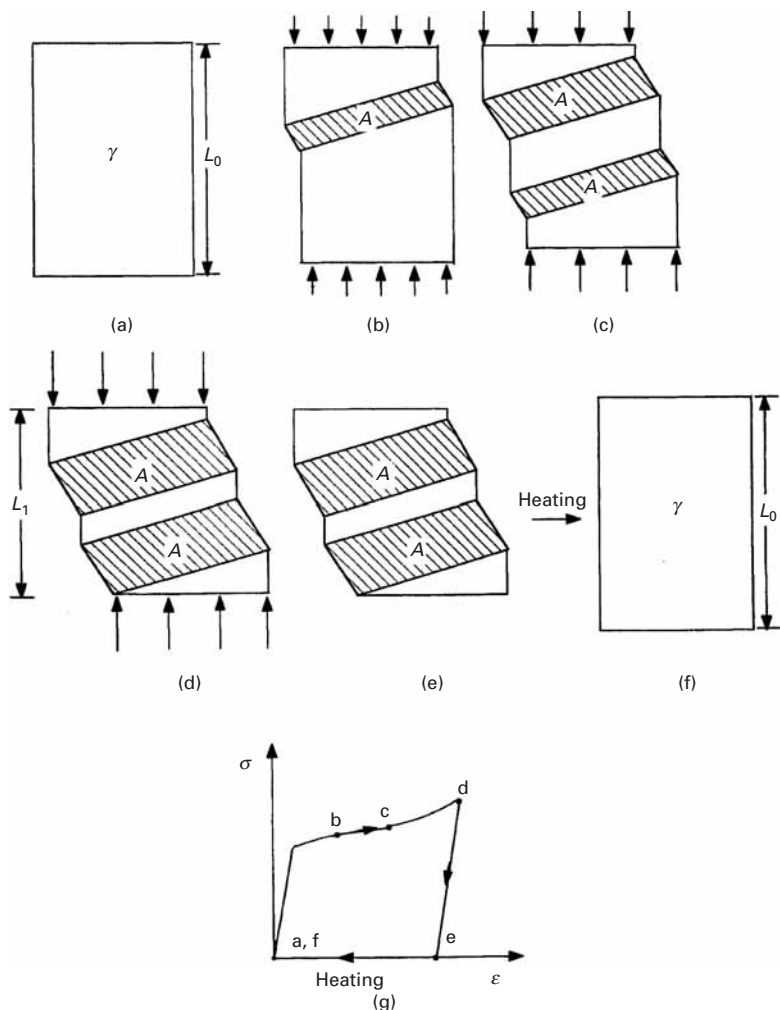


**Fig. 11.20** Schematic representation of strain-memory effect. (a) Initial specimen with length  $L_0$ . (b, c, d) Formation of martensite and growth by glissile motion of interfaces under increasing compressive stresses. (e) Unloading of specimen. (f) Heating of specimen with reverse transformation. (g) Corresponding stress-strain curve with different stages indicated.

“intelligent” structures. Alloys with good strain-memory effects play an important role in the design of these structures, and novel uses are being continually introduced. Indeed, the shape-memory effect has found some unique uses. One is as a tight coupling for pneumatic and hydraulic lines. The F-14 jet fighter tube couplings are made of Nitinol that is fabricated at room temperature with a diameter 4% less than that of the tubes which will be joined. Then, the couplings are cooled below  $M_s$  ( $-120^{\circ}\text{C}$ ) and expanded mechanically until their diameter is 4% larger than those of the tubes. They are held at this temperature until they are placed over the tube ends. Allowed to warm, they shrink to their initial diameter; impeded by the tube, they provide a tight fit. Electrical connectors that are opened and closed by changes in temperature are another application. Orthopedic and orthodontic aids have also been made of SME alloys, and Nitinol seems to react well in the body fluid environment. The pen-drive mechanism in recorders is a very successful application of the SME; many such drives are in service.

### 11.5.1 Shape-Memory Effect in Polymers

Some polymers can show a shape-memory effect, wherein they change their shape after we increase their temperature. In metallic alloys, the shape-memory effect has origin in a martensitic phase transformation. The story is a bit different in polymers. In polymers, we need two components at the molecular level to induce a shape-memory effect: cross-links that control the permanent shape and switching segments that allow us to fix the temporary shape. Above a critical temperature,  $T_c$ , we can deform the polymer. When we cool it below  $T_c$  and release the external stress, we get the temporary shape. When we heat the polymer to a temperature  $T > T_c$ , it regains its permanent shape. Lendlein *et al.*<sup>11,12</sup> showed this phenomenon in phase-segregated, multiblock copolymers wherein molecular parameters can be used to tailor macroscopic properties. One component, oligo( $\epsilon$ -caprolactone) dimethacrylate, furnishes the crystallizable “switching” segment that determines both the temporary and permanent shape of the polymer. By varying the amount of the comonomer, *n*-butyl acrylate, in the polymer network, the cross-link density can be adjusted. In this way, the characteristics of a polymer network can be exploited to tailor the mechanical strength and transition temperature over a wide range. It should be mentioned that homopolymers of both monomers are known to be biocompatible, which is of great importance for biomedical applications. The external stimulus, e.g. an increase in temperature, can be obtained by means of electrical current or light. This ability of polymers to take predetermined temporary shapes and then recover their original shape at ambient temperature by exposure to light could be useful in biomedical applications. Among the potential medical uses of these shape-memory polymers are: stents, used to keep blood vessels open, and catheters and sutures with more “give” than those currently available.

---

## 11.6 | Martensitic Transformation in Ceramics

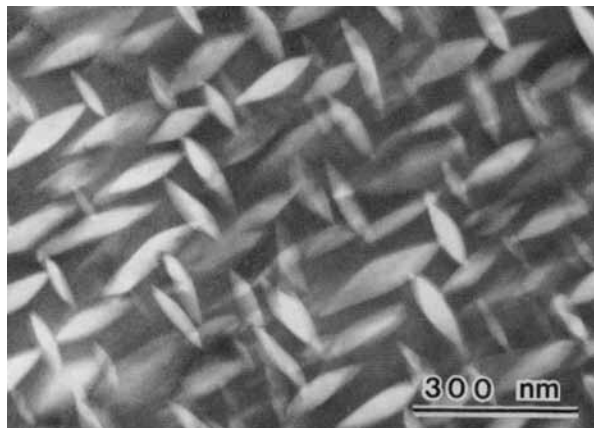
By far the most important, but not the only, martensitic transformation in a ceramic is the tetragonal-to-monoclinic transformation exhibited by zirconia ( $ZrO_2$ ). This transformation leads to a significant enhancement in the toughness of ceramics if  $ZrO_2$  is used either alone or as a distributed phase in other ceramics, such as alumina. Garvie *et al.* reported a very significant increase in tensile strength (from 250 to 650 MPa) and work of fracture (a measure of toughness) for tetragonal zirconia, in comparison with monoclinic zirconia.<sup>13</sup> They attributed this increase in strength to a martensitic transformation occurring during deformation, in a manner analogous to the TRIP

---

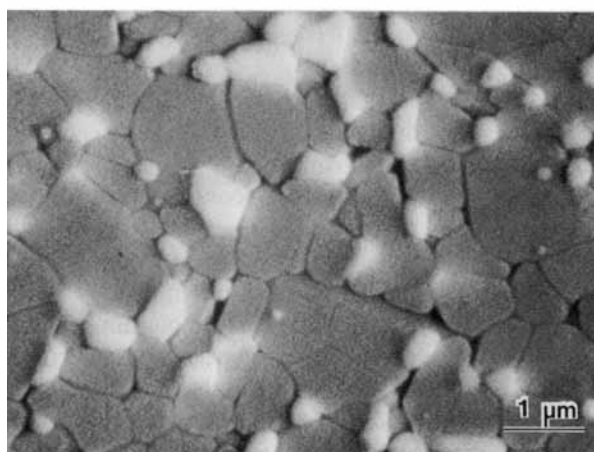
<sup>11</sup> A. Lendlein, H. Jiang, O Jünger, and R. Langer, *Nature*, 434 (2005) 879.

<sup>12</sup> A. Lendlein and R. Langer, *Science*, 296 (2002) 1673.

<sup>13</sup> R. C. Garvie, R. H. Hannink, and R. T. Pascal, *Nature*, 258 (1975) 703.



(a)



(b)

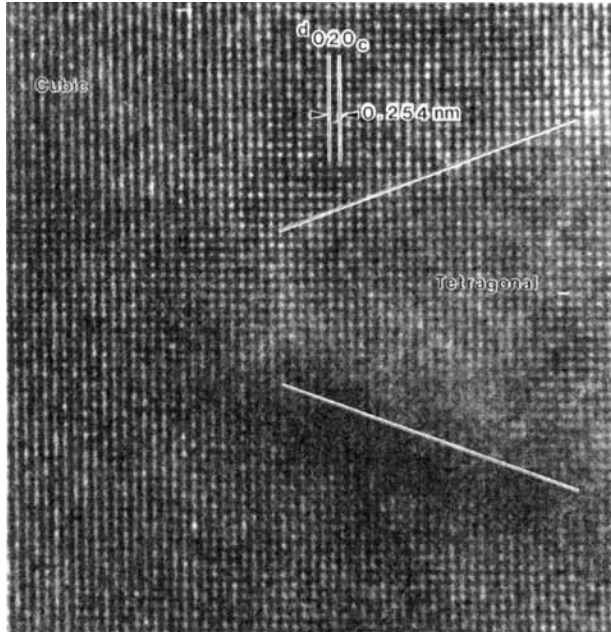
**Fig. 11.21** (a) Lenticular tetragonal zirconia precipitates in cubic zirconia (PSZ). (b) Equiaxial  $ZrO_2$  particles (bright) dispersed in alumina (ZTA). (Courtesy of A. H. Heuer.)

effect. The three most common ways in which this transformation is used are as follows:

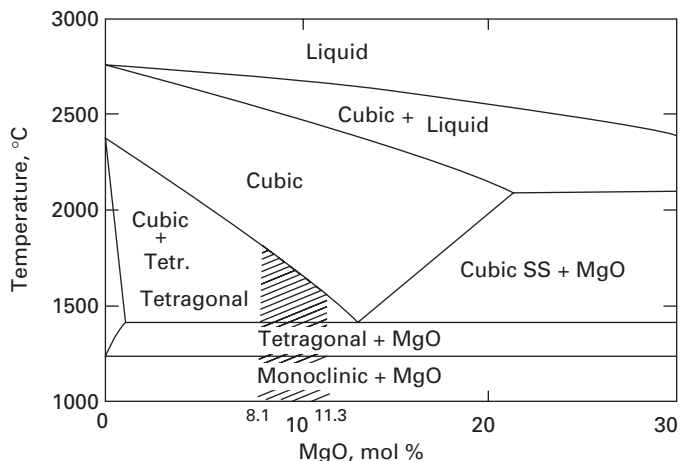
1. Tetragonal zirconia polycrystals (TZPs), which are nearly single-phase polycrystalline ceramics. TZPs are fabricated from fine-grained zirconia powders by sintering.
2. Partially stabilized zirconia (PSZ), in which tetragonal- $ZrO_2$  is a precipitate phase and the matrix is cubic zirconia. The highest toughnesses reported in PSZ are around  $18 \text{ MPa m}^{1/2}$ .
3. Zirconia-toughened alumina (ZTA), in which zirconia is a dispersed phase in the alumina matrix. ZTA materials are fabricated by co-sintering  $Al_2O_3$  and  $ZrO_2$  powders. ZTA materials are relatively tough ( $K_{Ic}$  up to approximately  $14 \text{ MPa m}^{1/2}$ ) and have high strength (1–2 GPa). This represents a significant enhancement in comparison with pure  $Al_2O_3$  ( $K_{Ic}$  about  $3 \text{ MPa m}^{1/2}$ ).

Figure 11.21(a) shows lenticular PSZ precipitates in cubic zirconia. The lens plane corresponds to the {100} planes of the cubic phase; thus,

**Fig. 11.22** Atomic-resolution transmission electron micrograph showing extremity of tetragonal lens in cubic zirconia; notice the coherency of boundary. (Courtesy of A. H. Heuer).



**Fig. 11.23** ZrO<sub>2</sub>-rich portion of ZrO<sub>2</sub>-MgO phase diagram. Notice the three crystal structures of ZrO<sub>2</sub>: cubic, monoclinic, and tetragonal.



there are three possible variants for the precipitates. The tetragonal lens is coherent with the cubic matrix, and the atomic-resolution TEM of Figure 11.22 shows the correspondence between the planes; the (100) of the tetragonal and cubic phases are parallel. The lenses are shaped approximately as oblate spheroids with an aspect ratio of 5. Figure 11.21(b) shows ZrO<sub>2</sub> particles (bright) in an alumina ceramic.

Zirconia has three allotropic forms: cubic, tetragonal, and monoclinic. Figure 11.23 shows the ZrO<sub>2</sub>-MgO phase diagram. In pure zirconia, only very small particles (approximately 60 nm across) can be retained at room temperature in the tetragonal structure. By using a stabilizing compound such as magnesia (MgO), calcia (CaO), yttria



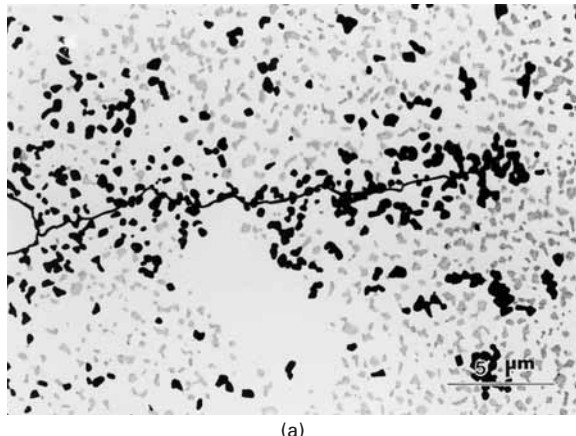
**Fig. 11.24** TEM of martensitic monoclinic lenses in ZrO<sub>2</sub> stabilized with 4 wt% Y<sub>2</sub>O<sub>3</sub> and rapidly solidified; the zigzag pattern of lenses is due to autocatalysis. (Courtesy of B. A. Bender and R. P. Ingel.)

(Y<sub>2</sub>O<sub>3</sub>), or ceria (CeO<sub>2</sub>), it is possible to retain the tetragonal phase, generally stable only between 1,240 and 1,400 °C, at room temperature. The range of MgO additions for which this occurs is shown in the phase diagram by hatching. The tetragonal-to-monoclinic transformation, which takes place martensitically under applied stress, has a dilatational (about 4–6%) and a shear (approximately 14%) component. The martensitic nature of the transformation is evident in the transmission electron micrograph of Figure 11.24. The martensite lenses form a zigzag pattern between two larger lenses; this is a typical autocatalytic nucleation sequence, in which one lens, impinging on a boundary, generates the defects that nucleate the subsequent lens. The process continues, leading to the characteristic pattern. The martensite shown in the figure was generated through rapid solidification.

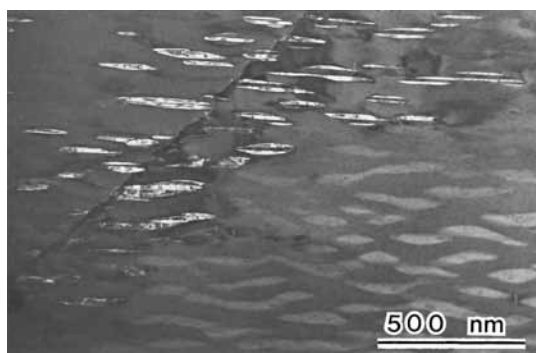
The increase in toughness due to the martensitic tetragonal-to-monoclinic transformation can be qualitatively explained as follows. In the regions surrounding a propagating crack, the stresses induce the transformation, which has dilatational and shear strain components. These strains work against the stress field generated by the crack, decreasing the overall stress intensity factor and, thereby, increasing the toughness. Figure 11.25(a) illustrates this behavior in ZTA; Figure 11.25(b) shows the effect in PSZ. The gray grains indicate tetragonal ZrO<sub>2</sub>, whereas the black grains are transformed to the monoclinic phase. The crack, advancing from left to right, triggers the transformation; more black dots surround the crack, leading to its arrest. In Figure 11.25(b), the lenticular tetragonal ZrO<sub>2</sub> precipitates in the cubic matrix are transformed to monoclinic in the region surrounding the crack. They appear as brighter lenses in the TEM because of favorable transmission conditions.

**Fig. 11.25**

- (a) Zirconia-toughened alumina (ZTA) traversed by a crack. The black regions represent monoclinic (transformed) zirconia, the gray regions tetragonal (untransformed) zirconia.  
 (Courtesy of A. H. Heuer.)  
 (b) Partially stabilized zirconia (PSZ) lenticular precipitates transformed from tetragonal to monoclinic in the vicinity of a crack. Notice the brighter transformed precipitates.  
 (Courtesy of A. H. Heuer.)



(a)



(b)

## Suggested Reading

- J. W. Christian. "The Strength of Martensite," in *Strengthening Methods in Crystals*, A. Kelly and R. B. Nicholson, eds. Amsterdam: Elsevier, 1971, p. 261.
- J. W. Christian. *The Theory of Transformations in Metals and Alloys*, 2nd ed. Elmsford, NY: Pergamon Press, 1981.
- D. J. Green, R. H. J. Hannink, and M. V. Swain. *Transformation Toughening of Ceramics*. Boca Raton, FL: CRC, 1989.
- A. H. Heuer. "Fracture-Tough Ceramics," in *Frontiers in Materials Technologies*, M. A. Meyers and O. T. Inal, eds. Amsterdam: Elsevier, 1985, p. 265.
- A. H. Heuer, F. F. Lange, M. V. Swain, and A. G. Evans. "Transformation Toughening: An Overview." *J. Am. Cer. Soc.*, 69 (1986) i-iv.
- G. Krauss. *Principles of Heat Treatment of Steel*. Metals Park, OH: ASM, 1980.
- Z. Nishiyama. *Martensitic Transformation*. New York, NY: Academic Press, 1978.
- G. B. Olson and M. Cohen. "Principles of Martensitic Transformations," in *Frontiers in Materials Technologies*, M. A. Meyers and O. T. Inal, eds. Amsterdam: Elsevier, 1985, p. 43.
- G. B. Olson and W. S. Owen, eds., *Martensite*. Metals Park, OH: ASM, 1992.
- J. Perkins, ed. *Shape Memory Effects in Alloys*. New York, NY: Plenum Press, 1975.
- G. Thomas. "The Physical Metallurgy and Alloy Design of Dual Phase Steel," in *Frontiers in Materials Technologies*, M. A. Meyers and O. T. Inal, eds. Amsterdam: Elsevier, 1985, p. 89.

## Exercises

**11.1** Martensitic transformation involves the Bain transformation, shown schematically in Figure Ex11.1. The FCC structure is transformed into the BCC structure. Assuming that there is a 5% expansion in volume during the FCC-to-BCC transformation, (a) calculate the lattice parameter of the BCC structure in terms of  $a_0$ , and (b) determine the strains in the three orthogonal directions.

**11.2** Plot hydrostatic strain versus carbon content for the martensitic transformation in steel from the plot shown in Ex11.2.

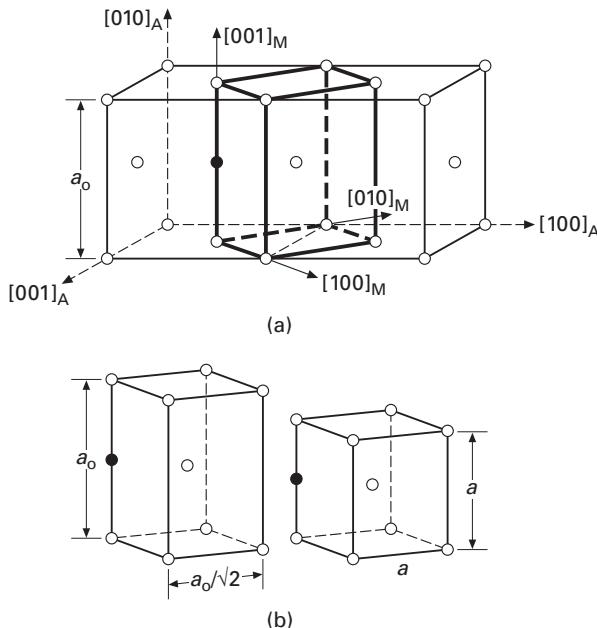


**Fig. Ex11.1** Lattice correspondence for the formation of martensite in steels.  
 (a) Body-centered tetragonal cell of axial ratio 2 outlined in austenite structure of cell size  $a_0$ .  
 (b) Deformation carrying this structure into martensite cell with parameter  $a$ . Open circles are iron atoms; filled circles are one possible carbon site.

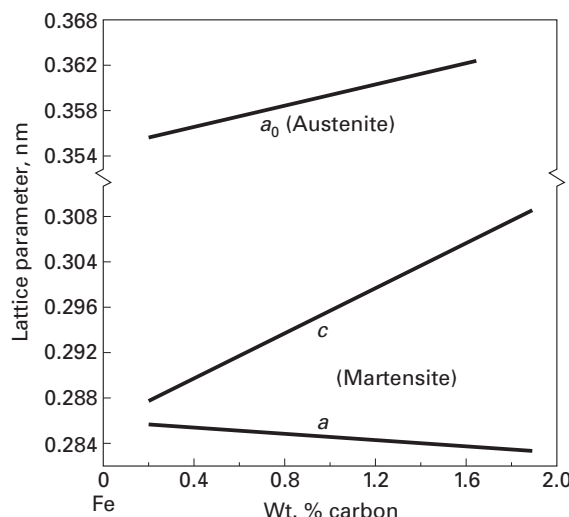


**Fig. Ex11.2**

**11.3** From the data of Figure 11.12, estimate the  $M_s$  temperature of the alloy at zero stress.

**11.4** The steel shown in Figure 11.15(b) has a plane strain fracture toughness of 110 MPa  $\text{m}^{1/2}$  and a yield stress of 320 MPa. Will the cracks shown in the figure have a catastrophic effect if a specimen is stressed to 180 MPa?

**11.5** Write down all the possible martensite variants for the Kurdjumov–Sachs orientation.

**11.6** In addition to the commercial applications of shape-memory alloys described in the text, new developments are continuously taking place. Briefly describe three additional applications. (You may use L. M. Shetky, in *Intermetallic Compounds*, Vol. 2, J. L. Westbrook and R. L. Fleischer, eds. (New York: J. Wiley, 1994).)

**11.7** Using Cu–Zn–Al, design a pen-drive system for an X–Y recorder. Based on the plot presented by L. M. Shetky (*Sci. Am.*, 241 (Nov., 1979) 74), what composition would you choose for the alloy?

**11.8** Calculate the total strain energy associated with a martensite lens having a volume of  $10 \mu\text{m}^3$ , assuming that all the energy is elastically stored. Specify the assumptions made; include both shear and longitudinal strain components from Equation 11.2.

**11.9** Plot the stress required to form martensite as a function of temperature in Figure 11.16b.

**11.10** (a) To what radius can a wire with diameter of 1 mm be curved using the superelastic effect if the maximum strain is approximately 0.05? (b) If the wire were made of a high-strength piano wire steel ( $\sigma_y \sim 2\text{GPa}$ ), what would be the minimum radius to which it could be curved? Take  $E = 210 \text{ GPa}$ . (c) Discuss the differences obtained in (a) and (b).

**11.11** What is the volume change associated with the tetragonal-to-monoclinic transformation in zirconia?

Given:

Monoclinic zirconia Tetragonal zirconia

$$a = 0.5156 \text{ nm} \quad a = 0.5094 \text{ nm}$$

$$b = 0.5191 \text{ nm} \quad b = 0.5304 \text{ nm}$$

$$c = 0.5304 \text{ nm}$$

$$\beta = 98.9^\circ$$

**11.12** Give three technological applications (at least one of which is a bioengineering application) for shape-memory alloys.

---

## Chapter 12

# Special Materials: Intermetallics and Foams

---

### 12.1 | Introduction

An intermetallic is a compound phase of two or more normal metals (ordered or disordered). Interest in intermetallics waned in the 1960s and 1970s. However, the demand for materials that are strong, stiff, and ductile at high temperatures has led to a resurgence of interest in intermetallics, especially silicides and ordered intermetallics such as aluminides. A testimony to this resurgence was the appearance in 1994 on the subject of a two-volume set by J. H. Westbrook and R. L. Fleischer, *Intermetallic Compounds: Principles and Practice* (New York: John Wiley). Intermetallic aluminides and silicides can be very oxidation and corrosion resistant, because they form strongly adherent surface oxide films. Also, intermetallics span a wide range of unusual properties. An important example outside the field of high-temperature materials involves the exploitation of martensitic transformations, exotic colors, and the phenomenon of shape memory in gold-based intermetallics in jewelry making. In what follows, we first describe the silicides, then the ordered intermetallics, and finally the basic structure and properties of foams.

---

### 12.2 | Silicides

About 300 intermetallic compounds melt at temperatures above 1,500 °C. A survey of some silicide intermetallics for high-temperature applications showed that, based on criteria such as availability, phase changes in the temperature range of interest, and oxidation resistance,  $Ti_5S_3$  and  $MoSi_2$  seem to be the most promising materials:  $Ti_5Si_3$  has the lowest density of all intermetallics, and  $MoSi_2$  has a superior oxidation resistance. For service at temperature up to 1,600 °C, one needs characteristics such as high strength, creep resistance, fracture toughness, oxidation resistance, and microstructural stability. Figure 12.1 shows a plot of melting point vs. density for

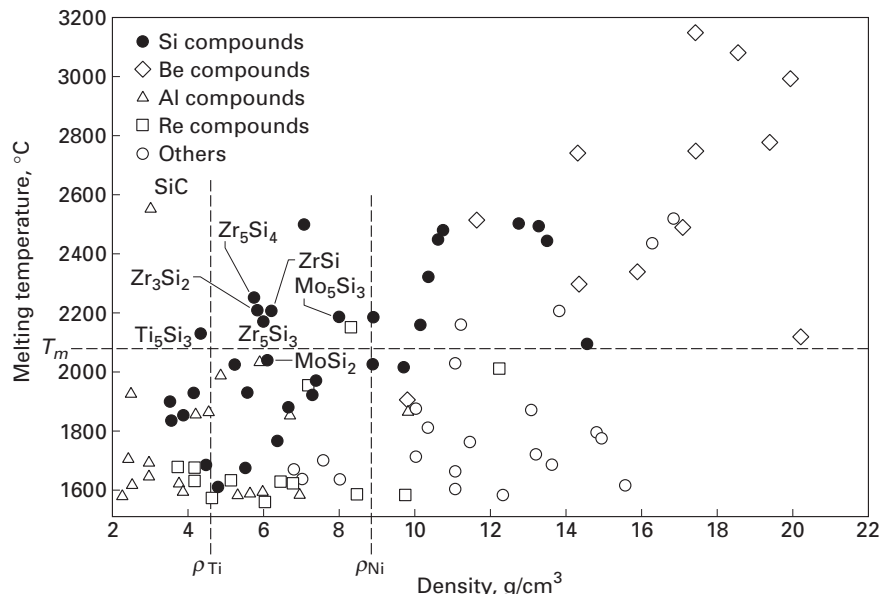


**Fig. 12.1** A plot of melting point vs. density for intermetallics having  $0.8T_m = 1,600$  °C. (After P. J. Meschter and D. S. Schwartz, *J. Minerals, Metals Materials Soc.*, 41 (Nov. 1989), 52.)

intermetallics having  $0.8T_m = 1,600$  °C. Here we are assuming that intermetallics retain their strength up to temperatures of 80%  $T_m$ , the melting point of the material in K. This puts a lower limit on  $T_m$  equal to 2,067 °C for a service temperature of 1,600 °C. Also selected in the plot is an upper limit on density, viz., the density of nickel.

Molybdenum disilicide is a very promising intermetallic because of several of its characteristics.  $\text{MoSi}_2$  has a tetragonal crystal structures, a high melting point, a relatively moderate density ( $6.31 \text{ g cm}^{-3}$ ), an excellent oxidation resistance, and a brittle-to-ductile transition at around 1,000 °C, which can result in high toughness at the service temperature. Among the problems associated with  $\text{MoSi}_2$  are its rather low low-temperature toughness and low high-temperature strength.  $\text{MoSi}_2$  shows a catastrophic oxidation behavior around 500 °C. In the literature, this problem has been termed pesting and is described as the retention of  $\text{MoO}_3$  as an oxidation product at the grain boundaries. The expansion in volume accompanying the formation of  $\text{MoO}_3$  results in severe microcracking. Among the efforts to ameliorate these problems, perhaps the most promising one is to use the approach of making a composite with  $\text{MoSi}_2$  as a matrix. Table 12.1 summarizes the advantages and limitations of  $\text{MoSi}_2$ .

### 12.3 | Ordered Intermetallics

In the simple description of crystal structure of metals given in Chapter 1, we tacitly assumed a *random* atomic arrangement of A and

**Table 12.1** Advantages and Limitations of Monolithic MoSi<sub>2</sub>*Advantages*

Moderate density: 6.24 g/cm<sup>3</sup>  
 High melting point: 2,020 °C  
 Outstanding oxidation resistance at <1,700 °C  
 Potential upper temperature limit: 1,600 °C  
 Deforms plastically above 1,000–1,200 °C  
 Amenable to electrodischarge machining (EDM)

*Limitations*

Low room-temperature fracture toughness (3.0 MPa m<sup>1/2</sup>)  
 Low strength and creep resistance at elevated temperatures (e.g.,  
 140 MPa at 1,200°C)

**Table 12.2** Physical and Mechanical Properties of Important Intermetallic Compounds

	Density (g/cm <sup>3</sup> )	Crystal Structure (Ordered)	Young's Modulus (GPa)	Coefficient of thermal expansion (10 <sup>-6</sup> /°C)	Tensile yield stress (MPa)	Melting point (°C)
Al <sub>3</sub> Ti	3.4–4.0	DO <sub>22</sub> (tetr.)	215	12–15	120–425	1350
TiAl	3.8–4.0	L1 <sub>0</sub> (tetr)	160–175	11.7	400–775	1480
Ti <sub>3</sub> Al	4.1–4.7	DO <sub>19</sub> (HCP)	120	12	700–900	1680
MoSi <sub>2</sub>	6.1	Tetragonal	380–440	8.1–8.5	200–400	2020
Ni <sub>3</sub> Al	7.4–7.7	L1 <sub>2</sub> (FCC)	180–200	14–16	200–900	1397
NiAl	5.9	B2(FCC)	177–190	14–16	175–300	1638
Ni <sub>5</sub> Si <sub>3</sub>	7.2		340	N/A	550	N/A
Fe <sub>3</sub> Al	6.7	DO <sub>3</sub>	140–170	19	600–1350	1540
FeAl	5.6–5.8	B2	160–250	21.5	500–700	N/A

B atoms in a unit cell of a metallic alloy consisting of atoms of species A and B. When A and B are arranged in a random manner, we have a *disordered alloy*. In such an alloy, equivalent crystallographic planes are statistically identical. Truly random – that is, completely disordered – alloys are not common, but there are many alloy systems that come close to having a random or disordered distribution of species A and B. It turns out that in a vast number of alloy systems, it is energetically favorable for atoms A and B to segregate to preferred lattice sites. Generally, such an ordered arrangement of atoms is obtained below a critical temperature  $T_c$  and in certain well-defined atomic proportions, i.e., stoichiometric compounds such as AB<sub>3</sub>, AB, etc. Among examples of these systems, one may cite CuAu, Cu<sub>3</sub>Au, Mg<sub>3</sub>Cd, FeCo, FeAl, and aluminides of Ni and Ti. When the bonding is not totally metallic, but is partly ionic in nature, such an alloy is called an *intermetallic compound*. Table 12.2 gives a summary of important characteristics of

some intermetallics. In what follows, we examine (1) the differences in the dislocation behavior in ordered alloys vis-à-vis disordered, or ordinary, alloys, (2) the effect of ordering on mechanical behavior, and (3) efforts to enhance the low-temperature ductility of ordered alloys, with a special emphasis on nickel aluminide ( $\text{Ni}_3\text{Al}$ ), which has some very unusual properties.

---

### Example 12.1

---

Molybdenum disilicide shows a phenomenon called *pesting*. Describe this phenomenon and indicate some means of overcoming it.

**Solution:** It has been observed that at about 500 °C,  $\text{MoSi}_2$  shows an accelerated oxidation. A product of this oxidation is  $\text{MoO}_3$ , which is accompanied by a rather large change in volume. This catastrophic oxidation can result in severe microcracking. Among some of the proposed remedies to overcome pesting are the following:

- Preoxidize the  $\text{MoSi}_2$ , to form a continuous  $\text{SiO}_2$  surface film.
- Minimize porosity, to minimize the formation of  $\text{MoO}_3$  at the pore surfaces.
- Use alloying to alter the oxidation characteristics of  $\text{MoSi}_2$ .
- Use metal coatings.

---

### Example 12.2

---

There is some interest in the use of gold-based intermetallic alloys in the jewelry industry. Can you describe some other possibilities in this area?

**Solution:** Platinum-based intermetallic alloys represent a possibility. Platinum is a soft metal like gold, but has a silver-like color. Thus, platinum alloys based on a  $\text{PtAl}_2$  intermetallic may be of interest because they show a higher hardness than Pt and they can range in color from orange through pink to the yellow of pure gold.<sup>1</sup>

#### 12.3.1 Dislocation Structures in Ordered Intermetallics

There are some very important differences between the dislocation structures observed in common metals and those in ordered intermetallics. In FCC metals, dislocations split into partials, and the partials are separated by a stacking-fault ribbon. (See Chapter 4.) The partials, however, are confined to a single slip plane and do not have

---

<sup>1</sup> J. Hurly and P. T. Wedepohl, *J. Mater. Sci.*, 28 (1993) 5648.

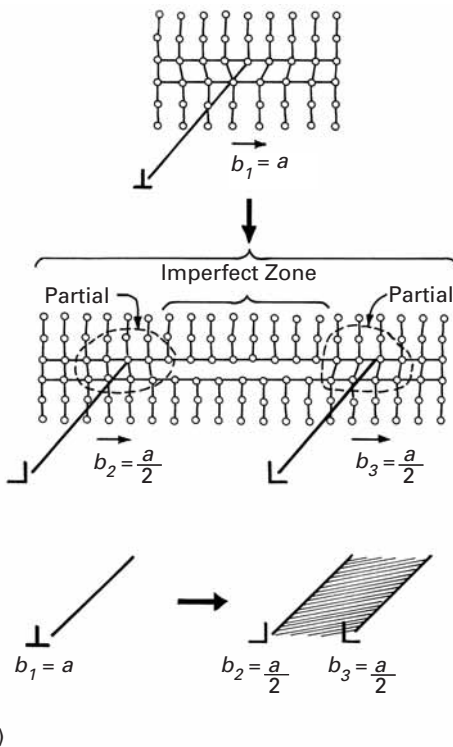
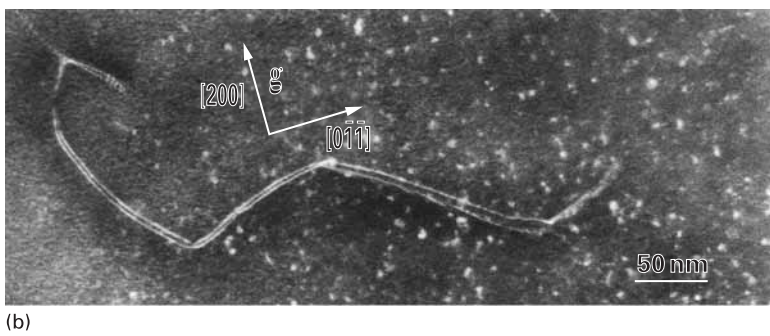


**Fig. 12.2** The characteristic dislocation structure in an ordered alloy consists of two superpartial dislocations, separated by a faulted region or an antiphase boundary (APB). (b) Superpartial dislocations separated by approximately 5 nm in Ni<sub>3</sub>Al deformed at 800 °C;  $b = [1\bar{1}0]$  and superpartials  $b_1 = b_2 = \frac{1}{2} [1\bar{1}0]$ . (Courtesy of R. P. Veyssiére.)



parallel Burgers vectors. As illustrated in Figure 12.2, the characteristic dislocation structure in an ordered alloy consists of two partial dislocations separated by a faulted region or what is also called an *antiphase boundary* (APB). Figure 12.2(b) shows an example of partial dislocations separated by a faulted region of 5 nm width in Ni<sub>3</sub>Al deformed at 800 °C.

An ordered structure results in some interesting characteristics. The ordered state in A<sub>3</sub>B-type alloys is a low-energy state, so the movement of dislocations and vacancies results in a destruction of the local order; that is, a higher energy state is produced. Thus, activities such as dislocation motion and vacancy migration are subject to some restrictions. For example, in ordered structures, the dislocations

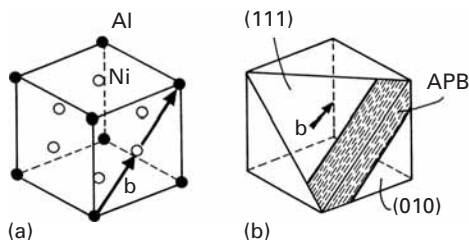


**Fig. 12.3** (a) The  $\text{L}1_2$  crystal structure of  $\text{Ni}_3\text{Al}$ . The aluminum atoms are located at the corners of a cube, while the Ni atoms are at the centers of the faces. (b) A (111) slip plane and the slip direction  $<010>$ , consisting of two  $\frac{1}{2}<110>$  vectors, in  $\text{Ni}_3\text{Al}$ . Note that the APB in between the two superpartials lies partly on the (111) and partly on the (010) face.

must travel in pairs – a leading dislocation and a trailing dislocation. The passage of a leading dislocation destroys the order, while the passage of a trailing dislocation restores it. Also, thermally activated phenomena, such as diffusion via vacancies, suffer retardation.

Let us consider the ordered  $\text{Ni}_3\text{Al}$  intermetallic. The  $\text{L}1_2$  crystal structure of  $\text{Ni}_3\text{Al}$  is shown in Figure 12.3(a). The aluminum atoms are located at corners of cubes, while the Ni atoms are at the centers of the faces of the cube. Figure 12.3(b) shows a (111) slip plane and the slip direction  $<010>$ , consisting of two  $\frac{1}{2}<010>$  vectors, in  $\text{Ni}_3\text{Al}$ . Note that the APB in between the two partials lies partly on the (111) and partly on the (010) face. Interestingly, the partials in this case have the same Burgers vectors (along the screw direction). These partials can extend to any slip plane that contains the dislocation line or Burgers vector. The APB can be transferred from one plane to the other by cross-slip of the partial screws. This situation allows the partials to reduce the energy of the intermetallic by extending to the plane with a minimum APB energy, because the configurational energy decreases with decreasing APB energy. When a pair of screw partials is fully transferred from the (111) plane to the cross-slip plane (010), we get what is called *Kear-Wilsdorf lock*.<sup>2</sup> We can estimate the energy change associated with this lock in the following way. The APB, a kind of stacking fault, results in an energy increase that is proportional to the quantity  $(E_{AA} + E_{BB} - 2E_{AB})$ , where  $E_{AA}$ ,  $E_{BB}$ , and  $E_{AB}$  are the bonding energies of AA, BB, and AB pairs, respectively. The superpartials of a pair repel each other elastically, but are held together by the APB. If  $r$  is the separation between two superpartials, the interaction energy is given by  $-K \ln r$ , where  $K$  is a constant involving elastic constants of materials and the character of the dislocation. If  $\gamma$  is the surface energy of the APB, then the energy of an APB of width  $r$  is  $\gamma r$ . Thus, the energy of a pair of superpartials with an APB of width  $r$  can be

<sup>2</sup> B. H. Kear and H. G. F. Wilsdorf, *Trans. AIME*, 224 (1962) 382.

written as

$$E(r) = \gamma r - K \ln r. \quad (12.1)$$

At the equilibrium separation  $r_0$ , the two components of the energy balance, and we can write

$$dE/dr = 0 = \gamma - K/r_0, \quad (12.2)$$

or

$$\gamma = K/r_0.$$

From Equations 12.1 and 12.2, we get, at  $r = r_0$ , the equilibrium energy

$$E(r_0) = (K/r_0)r_0 - K \ln(K/\gamma).$$

or

$$E(r_0) = K[1 + \ln(\gamma/K)]. \quad (12.3)$$

Applying Equation 12.3 to the primary and cross-slip planes, we can write:

For primary slip

$$E_p(r_0) = K[1 + \ln(\gamma_p/K)].$$

For cross-slip

$$E_c(r_0) = K[1 + \ln(\gamma_c/K)].$$

Hence

$$\Delta E(r_0) = E_c(r_0) - E_p(r_0) = K[\ln(\gamma_c/K) - \ln(\gamma_p/K)].$$

Thus, the energy associated with the Kear-Wilsdorf lock may be written as

$$\Delta E = K \ln \lambda,$$

where  $\lambda = \gamma_c/\gamma_p$ , in which the subscripts  $c$  and  $p$  represent the cross-slip and primary planes, respectively. Kear-Wilsdorf locks harden the intermetallic because they inhibit slip; as  $\lambda$  decreases, the tendency to form these locks increases.

There are some other differences between intermetallics and common alloys. Generally, common disordered alloys show an isotropic behavior, whereas most intermetallic compounds have anisotropic elastic properties. This can result in excessive elastic strain on certain planes; in particular, it can introduce shear stresses perpendicular to screw dislocation lines. These dislocations not only will repel each

other along the radial directions, but also will exert a torque on each other.<sup>3</sup>

### 12.3.2 Effect of Ordering on Mechanical Properties

Mechanical properties of an alloy are altered when it has an ordered structure. We define the degree of long-range order (LRO) by means of a parameter

$$S = \frac{r - f_A}{1 - f_A}, \quad (12.4)$$

where  $r$  is the fraction of  $A$  sites occupied by  $A$  atoms and  $f_A$  is the fraction of  $A$  atoms in the alloy. Thus,  $S$  goes from 0 (completely disordered) to 1 (perfectly ordered). Different dislocation morphologies observed in ordered alloy.

A superdislocation (i.e., closely spaced pairs of unit dislocations bound together by an antiphase boundary) in a perfectly ordered crystal and a single dislocation in a completely disordered crystal will both experience less friction stress than either of them will experience at an intermediate degree of order  $S$ . Thus, qualitatively, one would expect a yield stress maximum at an intermediate degree of order (i.e., the change in yield stress is not directly related to the degree of ordering). For example,  $\text{Cu}_3\text{Au}$  crystals show a lower yield stress when fully ordered than when only partially ordered. Experiments showed that this results from the fact that the maximum in strength is associated with a critical domain size. Short-range order (SRO) results in a distribution of neighboring atoms that is not random. Thus, the passage of a dislocation will destroy the SRO between the atoms across the slip plane. The stress required to do this is large. A crystal of  $\text{Cu}_3\text{Au}$  in the quenched state (SRO) has nearly double the yield stress of that in the annealed (LRO). The maximum in strength is exhibited by a partially ordered alloy with a critical domain size of about 6 nm. The transition from deformation by unit dislocations in the disordered state to deformation by superdislocations in the ordered state gives rise to a peak in the curve of flow stress versus degree of order.

The presence of atomic order leads to a marked change in the flow curve of the alloy. Figure 12.4 shows the flow curves of a fully ordered FeCo alloy at low temperatures, where the order is not affected. Stage I is associated with a well-defined yield point. This is followed by a high linear work-hardening stage, II. Finally, there occurs stage III, with nearly zero work-hardening. The stress-strain curves of the same alloy in the disordered state are shown in Figure 12.5. The curves in Figure 12.4 (ordered) are markedly different from the ones in Figure 12.5 (disordered). The sharp yield point and stage II are absent in the disordered alloy, which goes straight into stage III after gradual yielding. Fully ordered alloys deform by means of the movement of superlattice dislocations at rather low stresses. However, the superdislocations

---

<sup>3</sup> M. H. Yoo, *Acta Met.*, 35 (1987) 1559.

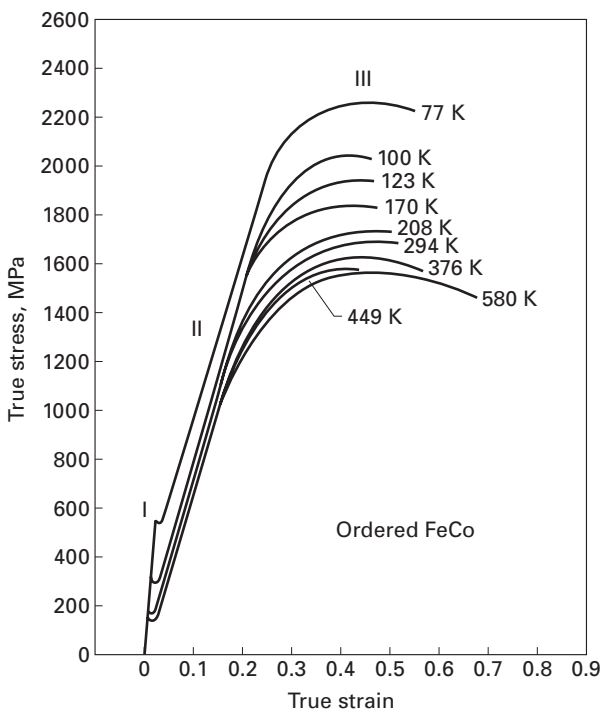


**Fig. 12.4** Stress-strain curves of ordered FeCo alloys at different temperatures. (Adapted with permission from S. T. Fong, K. Sadananda, and M. J. Marcinkowski, *TransAIIME*, 233 (1965) 29.)

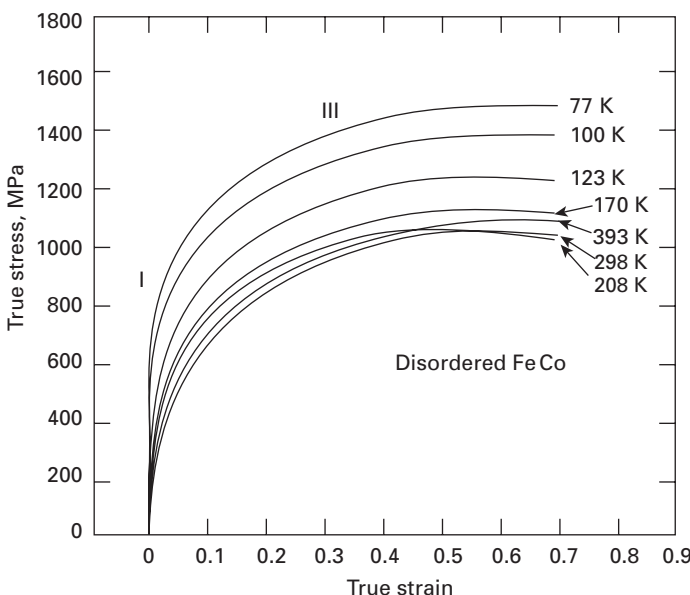
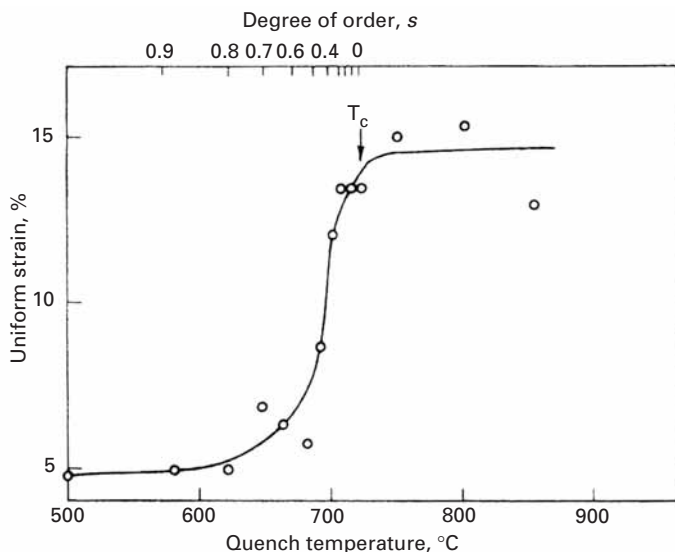


**Fig. 12.5** Stress-strain curves of fully disordered FeCo alloys at different temperatures. (Adapted with permission from S. T. Fong, K. Sadananda, and M. J. Marcinkowski, *TransAIIME*, 233 (1965) 29.)

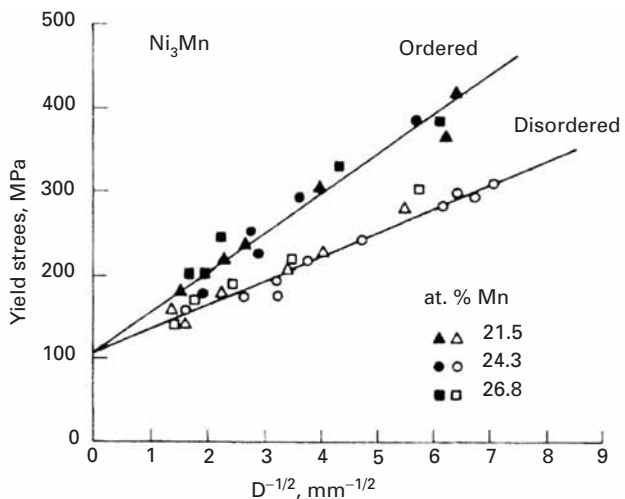
must move as a group in order to maintain the ordered arrangement of atoms. This makes cross-slip difficult. Long-range order thus leads to high strain-hardening rates and frequently, to brittle fracture.

Figure 12.6 shows this effect of ordering on uniform elongation of FeCo-2% V at room temperature. The ductility of the alloy decreases with increasing LRO.  $Mg_3Cd$  is the only known exception to this

**Fig. 12.6** Effect of atomic order on uniform strain (ductility) of Fe–Co–2% V at 25 °C. (Adapted with permission from N. S. Stoloff and R. G. Davies, *Acta Met.*, 12 (1964) 473.)



**Fig. 12.7** Hall–Petch relationship for ordered and disordered alloys. (Adapted with permission from T. L. Johnston, R. G. Davies, and N. S. Stoloff, *Phil Mag.*, 12 (1965) 305.)



tendency toward brittleness, because of a restricted number of slip systems or less easy cross-slip.

Ordered alloys such as FeCo and Ni<sub>3</sub>M obey the Hall–Petch relationship between flow stress and grain size; viz., (see Chapter 5)

$$\sigma = \sigma_0 + kD^{-1/2},$$

where  $\sigma$  is the flow stress at a given strain,  $\sigma_0$  and  $k$  are constants for that strain, and  $D$  is the grain diameter. In these alloys, long-range order increases  $k$ , as shown in Figure 12.7 for Ni<sub>3</sub>Mn. This increase in  $k$  with long-range order can be explained by the change in the number of slip systems with order, since the ease of spreading of slip across boundaries is controlled by the degree of order.

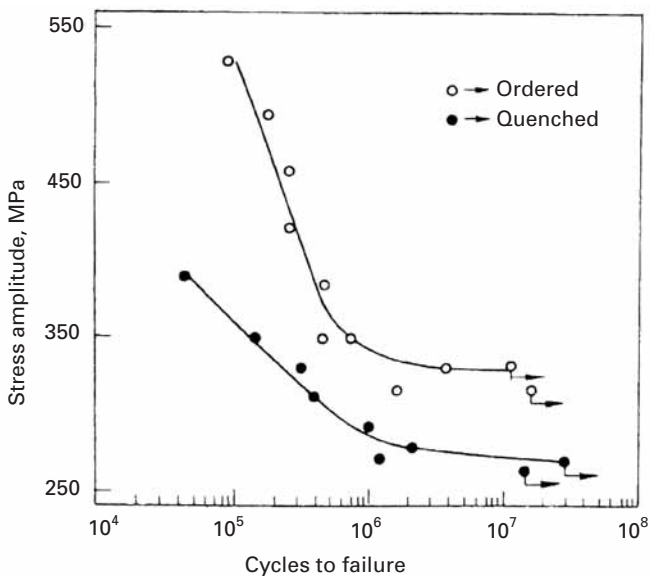


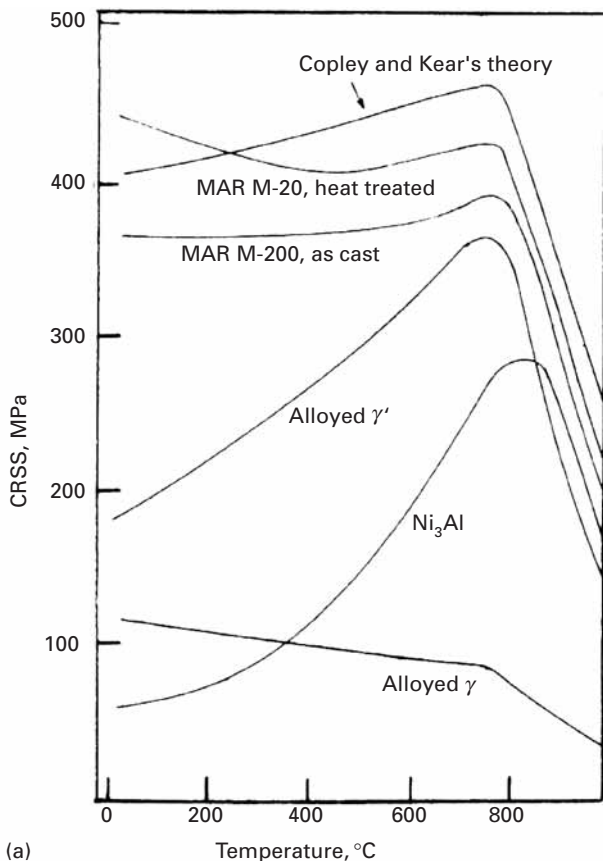
**Fig. 12.8** Effect of atomic order on fatigue behavior of  $\text{Ni}_3\text{Mn}$ . (Adapted with permission from R. C. Boettner, N. S. Stoloff, and R. G. Davies, *Trans. AIME*, 236 (1968) 131.)

The effect of atomic ordering on fatigue behavior is shown in Figure 12.8 in the form of stress ( $S$ ) vs. cycles to failure ( $N$ ) (see Chapter 14 for S-N curves) for ordered and disordered  $\text{Ni}_3\text{Mn}$ . The improved fatigue performance in the ordered state is explained by difficulty of cross-slip and a decrease in slip-band formation in that state. Slip bands lead to the formation of extrusions and intrusions on the sample surface, which in turn lead to fatigue crack nucleation. (See Chapter 14.)

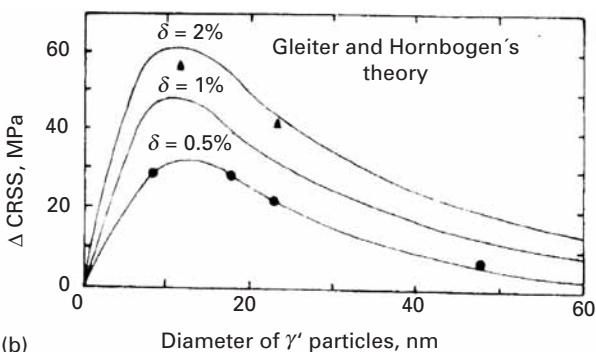
Gamma-prime-strengthened superalloys are an example of the effect of ordering on strength. The  $\text{Ni}_3\text{Al}$  precipitate produces very low coherency stresses and is coherent with the austenitic matrix. The strengthening effect is clearly evident in Figure 12.9(a), which shows the strength of the austenitic matrix and  $\text{Ni}_3\text{Al}$  separately, and the strength of MAR M-200, composed of 65 to 85% gamma prime (the ordered  $\text{Ni}_3\text{Al}$ ). In ordered structures, it is energetically favorable for dislocations to move in groups, forming antiphase boundaries between them as seen in Section 12.3. The equilibrium distance between the pairs, as well as their form, was found to depend on the particle size, particle distribution, energy of the antiphase boundary, elastic constants, and external shear stress. The preceding parameters are part of the equations derived by Gleiter and Hornbogen<sup>4</sup> for the increase in the critical resolved shear stress,  $\Delta\tau$  or  $\Delta\text{CRSS}$ . The results of calculations are compared with observed results for a Ni–Cr–Al alloy in Fig. 12.9(b), where  $\delta$  is the atomic percent aluminum. The experimental results are marked by dots and triangles; they refer to 0.5 and 1.8% aluminum, respectively. The correlation is good, and maximum strengthening is obtained for particles having a diameter of 10 nm.

<sup>4</sup> H. Gleiter and E. Hornbogen, *Phys. Status Solids*, 12 (1965), 235, 251.

**Fig. 12.9** (a) Effect of temperature on CRSS for  $\text{Ni}_3\text{Al}$ ,  $\gamma$ , and Mar M-200 superalloy ( $\gamma + \gamma'$ ). (Adapted with permission from S. M. Copley and B. H. Kear, *Trans. TMS-AIME*, 239 (1967) 987.) (b) Calculated and observed increase in the critical resolved shear stress (CRSS) in an Ni–Cr–Al alloy as a function of the diameter of the precipitate; full lines represent calculations ( $\bullet$ ,  $\delta = 0.5\% \text{ Al}$ ;  $\blacktriangle$ ,  $\delta = 1.8\% \text{ Al}$ );  $\delta$  is atomic percent aluminum. (Adapted with permission from H. Gleiter and H. Hornbogen, *Phys. Status Solidi*, 12 (1965) 235.

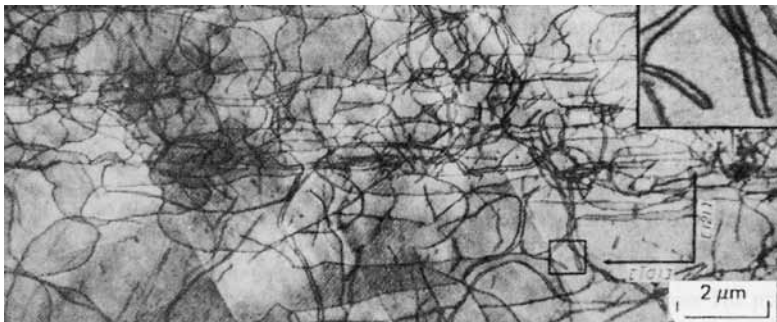


(a)

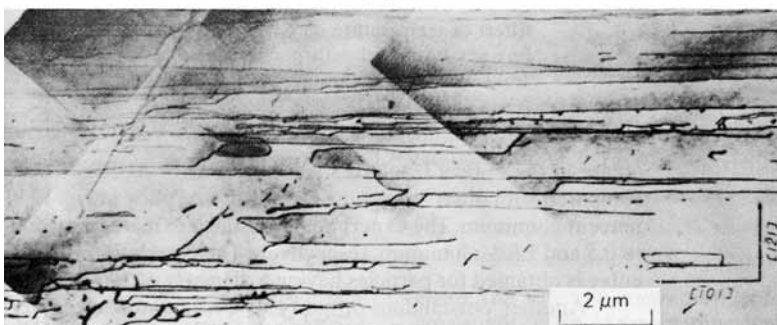


(b)

Another outstanding property of  $\text{Ni}_3\text{Al}$  and some other intermetallics is the increase in yield stress with temperature. As is seen from Figure 12.9(a), the yield stress increases by a factor of 5 when the temperature is raised from ambient temperature to 800 °C. This temperature dependence is unique and contrary to what would be expected on the basis of thermally activated motion of dislocations. (We discuss this and other aspects of ordered intermetallics in Section 12.3.3.) Thus, in spite of the normal temperature dependence



(a)



(b)

**Fig. 12.10** Effect of deformation temperature on the dislocation arrangement in the {111} primary slip plane of ordered Ni<sub>3</sub>Ge.  
 (a)  $T = -196\text{ }^{\circ}\text{C}$ ,  $\varepsilon_p = 2.4\%$ .  
 (b)  $T = 27\text{ }^{\circ}\text{C}$ ,  $\varepsilon_p = 1.8\%$ .  
 (Courtesy of H.-R. Pak.)

of the austenite (also shown in Figure 12.9(a)), the alloy Mar M-200 exhibits a constant yield stress up to 800 °C; the decrease in the flow stress of  $\gamma$  is compensated for by the increase of  $\gamma'$  (Ni<sub>3</sub>Al). It is interesting to note that other ordered alloys, such as Cu<sub>3</sub>Au and Ir<sub>3</sub>Cr, do not exhibit this unique behavior, while Ni<sub>3</sub>Ge, Ni<sub>3</sub>Si, Co<sub>3</sub>Ti, and Ni<sub>3</sub>Ga do. High voltage TEM work on Ni<sub>3</sub>Ge has shown dramatic changes in dislocation configuration. For Ni<sub>3</sub>Ge, it was found that the substructure at -196 °C consisted roughly of an equal number of edge and screw dislocations, while at 27 °C it consisted mostly of screw dislocations aligned along [101]. (See Figure 12.10.) Thus, the decreased mobility of screw dislocations with increasing temperature was responsible for the strengthening effect. At temperatures above the one providing maximum strength, the change in slip plane from {111} to {100} would be responsible for the decrease in strength. This explanation is different from the one previously provided.

It is this very unusual behavior – the increase in flow stress with temperature – that makes nickel aluminides very attractive for high-temperature applications. Ni<sub>3</sub>Al remains ordered up to its melting point (1,400 °C) and also shows an increasing yield strength with temperature. A decrease in yield strength occurs at very high temperatures due to the start of thermally activated slip on {100} planes, and not because of disorder.

Long-range ordered alloys of the Ni<sub>3</sub>Al type show some important and unique features alluded to earlier, such as an increasing yield stress with increasing temperature. The problem with these alloys,

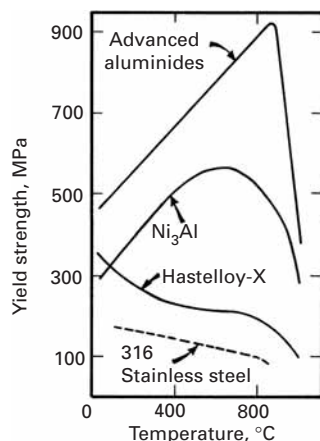


**Fig. 12.11** Yield stress as a function of test temperatures for Ni<sub>3</sub>Al-based aluminide alloys, Hastelloy-X, and type 316 stainless steel. (Adapted from C. T. Liu and J. O. Stiegler, *Science*, 226 (1984) 636.)

however, is their lack of ambient temperature ductility. Figure 12.11 shows yield strength as a function of temperature for Ni<sub>3</sub>Al-based alloys, Hastelloy-X, and type 316 stainless steel. It is not surprising that L<sub>1</sub><sub>2</sub>-type intermetallics are major candidates for use at elevated temperatures, about 900–1000 °C.

The anomalous yield behavior of Ni<sub>3</sub>Al has been the subject of a number of investigations. At temperatures  $T < T_p$ , slip occurs mainly on the octahedral {111} planes, while at temperatures  $T > T_p$ , slip becomes dominant on cubic {100} planes.  $T_p$  is the temperature corresponding to the maximum in strength ≈800 °C. Sun and Hazzledine used weak-beam TEM to identify dislocation structures with low mobilities in Ni<sub>3</sub>Al-type ordered intermetallics.<sup>5</sup> They observed that in the region of yield stress anomaly, a kink mechanism unlocks the Kear-Wilsdorf locks described earlier. This mechanism leads to the formation of special kink configurations with switched superpartials, as well as the formation of what are called APB tubes. In summary, the increase in yield strength below  $T_p$  is related to the formation of K-W locks (lowering of  $\lambda$ ) while the decrease in yield strength above  $T_p$  is attributed to the change of slip from {111} <110> to {100} <110>. (See Figure 12.3.)

### 12.3.3 Ductility of Intermetallics

As we have seen, many alloy systems of the general composition A<sub>3</sub>B have an ordered structure formed by regular stacking of close-packed layers. The stacking sequence, however, can range from the more common cubic or hexagonal to less common and more complex transition structures with unit cells extending over 15 layers. Such intermetallics are generally quite brittle at low temperatures, which makes their processing very difficult. There are two common causes of brittleness in intermetallics:

1. The crystal structure is of low symmetry; that is, not enough slip systems are available for general plastic deformation to occur. As is well known, one needs at least five independent systems for an arbitrary change in shape to occur.
2. Enough slip systems are available, but there are crack propagation paths along the grain boundaries that are easy to take and that will cause embrittlement.

Generally, ordered hexagonal alloys have very limited ductility and ability to process while ordered cubic alloys have good ductility. Various researchers have tried to make ordered intermetallics more ductile by different approaches. Baker and Munroe<sup>6</sup> classify these attempts into four categories: microalloying, macroalloying, processing-induced microstructure control, and fiber reinforcement. We summarize these efforts next.

<sup>5</sup> Y. Q. Sun and P. M. Hazzledine, in *High Temperature Ordered Intermetallic Alloys* (Dordrecht, The Netherlands, Kluwer, 1992), p. 177.

<sup>6</sup> I. Baker and P. R. Munroe, *Journal of Metals*, 40 (Feb. 1988) 28.

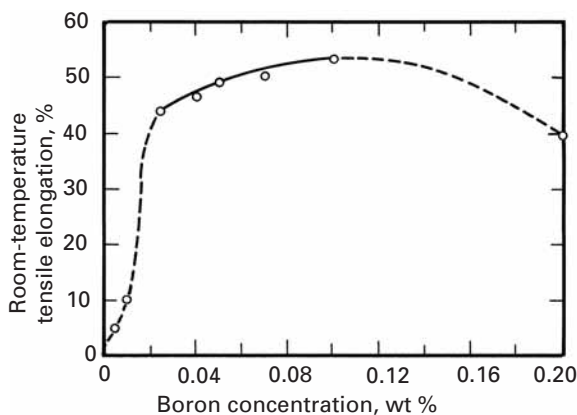


**Fig. 12.12** Restoration of room-temperature ductility in  $\text{Ni}_3\text{Al}$  as a function of boron content. (After K. Aoki and O. Izumi, *Nippon Kinzoku Takkashishi*, 43 (1979) 1190.)

### Microalloying

An examination of the Ni-Al phase diagram shows four intermetallics:  $\text{NiAl}_3$ ,  $\text{Ni}_2\text{Al}_3$ ,  $\text{NiAl}$ , and  $\text{Ni}_3\text{Al}$ .  $\text{Ni}_3\text{Al}$  is nothing but  $\gamma'$ , the strengthening phase in many Ni-based superalloys meant for high-temperature use as described earlier.  $\text{Ni}_3\text{Al}$  has an  $\text{L}1_2$  crystal structure with Al atoms at the cube corners and Ni atoms at the face-centered positions. (See Figure 12.3a.) Single-crystal  $\text{Ni}_3\text{Al}$  is very ductile at and below room temperature. Its ductility decreases with temperature until the peak in yield strength occurs. In polycrystalline form, nickel aluminide has practically no ductility at room temperature.  $\text{Ni}_3\text{Al}$  does possess five independent slip systems of the type  $\langle 111 \rangle \{110\}$ , which is the condition for generalized plastic flow, as per von Mises criterion. Instead of high ductility, polycrystalline  $\text{Ni}_3\text{Al}$  shows intrinsic grain-boundary weakness, as evidenced by its tendency toward brittle, intergranular fracture at room temperature. It turns out that boron is a very effective dopant for restoration of ductility in  $\text{Ni}_3\text{Al}$ . Boron-free polycrystals fracture without any plastic yielding, and very small additions of boron can lead to dramatic results. As little as 0.05% wt.% B can improve the strain to failure from nearly 0 to 50% and can alter the fracture mode from intergranular to transgranular. Figure 12.12 shows this restoration of room-temperature ductility in  $\text{Ni}_3\text{Al}$  as a function of boron content. Note the very small amount of boron required to do the job. As the figure reveals, boron-doped  $\text{Ni}_3\text{Al}$  shows a broad maximum in strength. The poor ductility of intermetallics and the effect of boron are generally explained in terms of environmental effects, especially moisture. (See the end of this section.)

Intergranular failure at room temperature also has been attributed to the segregation of impurities such as sulfur to grain boundaries. In one experiment, a decrease in ductility was measured as the sulfur content of the  $\text{Ni}_3\text{Al}$  increased from 32 to 176 ppm by weight. Auger electron spectroscopy showed that sulfur did indeed segregate to grain boundaries. Attempts at purifying  $\text{Ni}_3\text{Al}$  to restore its ductility have not worked in practice.

### Macroalloying

Macroalloying additions (less than 1 at.%) have been used to introduce modifications in intermetallics that lead to enhanced ductility. Such modifications include changing the crystal structure to one of higher symmetry, promoting the operation of additional or different slip systems, and other changes.

Alloys of the  $(\text{Ni}, \text{Co}, \text{Fe})_3\text{V}$  system can have ordered structure (cubic, hexagonal, or more complex transitional). The ordered hexagonal structure is too brittle for processing. Macroalloying can be used to create a window in the composition space in the  $(\text{Ni}, \text{Co}, \text{Fe})_3\text{V}$  system that has an intrinsically ductile, ordered cubic structure. An important parameter in the characterization of intermetallics is the electron concentration ( $e/a$ ), which is the number of valence electrons per atom. Ordered structures of the type  $A_3B$  are built by stacking close-packed layers. The stacking sequence is influenced by the atomic radius ratio ( $R_a/R_0$ ) and the electron concentration. In the  $(\text{Ni}, \text{Co}, \text{Fe})_3\text{V}$  system, nickel, cobalt, and iron have about the same atomic size. Thus, these elements influence the crystal structure through their electronic effects. If a portion of Co in  $(\text{Fe}, \text{Co})_3\text{V}$  is replaced by an equal number of Ni and Fe atoms, then we shall have altered the composition of the compound, but not the  $e/a$  ratio. In  $\text{Co}_3\text{V}$ , a six-layer stacking sequence occurs, with one-third of the layers having a hexagonal character (ABABAB . . .) and two-thirds of the layers having a cubic character (ABCABC . . .). Replacing Co by Ni gives a higher  $e/a$  ratio and a predominantly hexagonal stacking first, followed by fully hexagonal stacking. A reduction in the  $e/a$  ratio to 7.89 or less gives an cubic ordered structure ( $\text{L}1_2$ ). Thus, one can choose a suitable combination of Ni, Co, and Fe to obtain the desirable cubic ordered structure (the same as that of  $\text{Cu}_3\text{Au}$ ).

Titanium-based alloys are lighter than Co-based and Ni-based superalloys. However, the service temperature of Ti-based alloys is less than 500 °C.  $\text{TiAl}$  and  $\text{Ti}_3\text{Al}$ , the aluminides of titanium, have lower densities, higher stiffness, and higher use temperatures than nickel aluminides. Titanium aluminides show good oxidation resistance up to 900 °C, but have poor ductility and strength at low temperatures. Additions of  $\beta$ -stabilizing elements such as Nb, Mo, and W can result in some improvement in ductility in  $\text{Ti}_3\text{Al}$ . However, such macroalloying additions of heavier elements are accompanied by a penalty on density.

### Processing-induced microstructural control

Polycrystalline nickel aluminides are brittle at room temperature. Single-crystal nickel aluminides, however, are ductile. One very straightforward approach would be to use single crystals of these materials. Another approach is to combine grain refinement with another ductility-enhancing feature, such as a martensitic transformation. A fine grain size would result in slip homogenization, eliminate grain boundary segregation, and allow enough deformation for

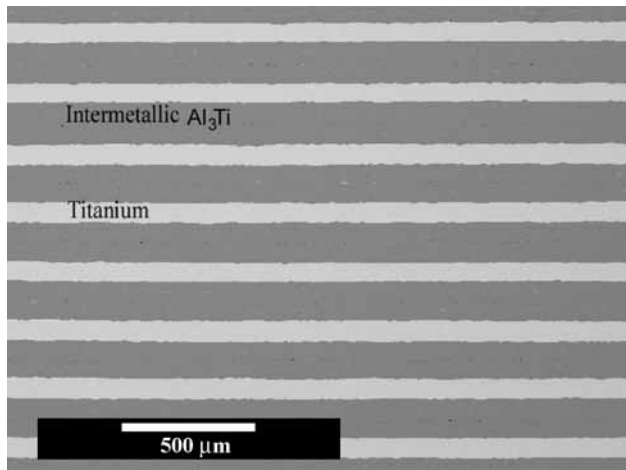


**Fig. 12.13** Al<sub>3</sub>Ti–Ti laminate composite. (Courtesy of K. S. Vecchio.)

the martensitic transformation to be induced. In principle, such a technique should work for any intermetallic. In practice, though, the grain size required for ductility may be too small (perhaps less than 1  $\mu\text{m}$ ) and thus difficult to achieve. An example of the beneficial effect of fine grain size is the use of rapid solidification technology to produce very fine grains in Ti<sub>3</sub>Al. The reader should be cautioned, however, that although a grain refinement can lead to improvement in low-temperature properties, it can result in rather poor creep properties at high temperature because of the grain-boundary-related creep processes. (See Chapter 13.)

Ordered iron aluminides based on Fe<sub>3</sub>Al also offer oxidation resistance and low material cost, but have limited ductility at ambient temperatures. In addition, the strength drops drastically above 600 °C. Sikka used thermomechanical processing to improve room-temperature ductility in iron aluminides.<sup>7</sup> A suitable combination of melting practice, processing, heat treatments, and test conditions resulted in 15–20% room-temperature elongation values. The recipe involves an alloy lean in alloying elements, vacuum melting, an unrecrystallized or only slightly recrystallized microstructure, oil quenching after heat treatment, higher-than-normal strain rates, and a moisture-free environment.

### Composite route

This approach involves the use of fibers or layers to toughen the intermetallics. The idea is the same as that in ceramic matrix composites – viz., provide a weak interface ahead of a propagating crack, and thus bring into play a variety of energy-dissipating processes such as crack deflection, fiber pullout, etc. (See Chapter 15.)

Figure 12.13 shows a laminate composite in which the intermetallic compound Al<sub>3</sub>Ti is the hard phase and titanium is the ductile

<sup>7</sup> V. K. Sikka, *Sampe Quarterly*, 22 (July 1991) 2.

component. The insertion of the metallic component increases the toughness of  $\text{Al}_3\text{Ti}$  dramatically. The propagation of cracks is hindered by the ductile component, which arrests them. An important problem to be considered with care when designing intermetallic-based composites is the mismatch in thermal expansion coefficient. When the composite is cooled down from the processing temperature to ambient temperature, the mismatch in thermal expansion coefficient can generate large internal stresses. One should design the composite in such a manner that the intermetallic matrix is not in tension. Putting the intermetallic in tension is not a desirable situation because intermetallics tend to be stronger in compression than in tension. This can generate tensile cracks within the intermetallic.

#### Environmental effects in intermetallics

There is evidence that the poor ambient ductility encountered in ordered intermetallics is due mainly to environmental effects.<sup>8</sup> Both moisture and hydrogen, at levels found in ambient air, are thought to be responsible for inducing embrittlement in ordered intermetallics. In the case of water vapor, the phenomenon involves the reaction of reactive elements in the intermetallics with the ambient water vapor, to form an oxide (or hydroxide) and generate atomic hydrogen, which leads to a loss of ductility accompanied by a change in fracture mode from transgranular to intergranular. In the case of  $\text{H}_2$ , atomic hydrogen is produced by dissociation of physisorbed hydrogen molecules on intermetallic surfaces. It would thus appear that the main reason for the efficacy of boron in rendering  $\text{Ni}_3\text{Al}$  more ductile is that boron suppresses the environmental embrittlement, possibly by slowing diffusion of hydrogen.

Iron aluminides based on  $\text{Fe}_3\text{Al}$  are also sensitive to environmental effects. A major problem again is the ever-present moisture in the air. The water vapor reacts with aluminum to produce hydrogen at the surface of the metal. This hydrogen is adsorbed in the aluminide during plastic deformation, leading to low ambient ductility.

---

#### Example 12.3

What is the source of the excellent high-temperature oxidation resistance shown by aluminides of nickel, cobalt, and iron?

**Solution:** Although the aluminides are quite brittle, they readily form a layer of alumina at high temperatures. The alumina layer provides the excellent oxidation resistance up to 1,000 °C. Such aluminides are used as coatings on gas turbine components. Kanthal alloys used for heating elements are also based on iron aluminides.

---

<sup>8</sup> E. P. George, C. T. Liu, H. Lin, and D. P. Pope, *Mater. Sci. & Eng.*, A192 (1995) 277; E. P. George, C. T. Liu, and D. P. Pope, *Acta Met.*, 44 (1996) 1757.

## 12.4 | Cellular Materials

### 12.4.1 Structure

Many naturally occurring materials are not fully dense, i.e., they possess internal voids. This type of design is intentional, since it reduces the density. Examples are cork, bones, wood, sponge, and plant stalks and they are shown in Figure 12.14. Figure 1.32 shows also synthetic aluminum sponge as well as the cellular core in a toucan's beak. This form has been adopted in modern synthetic materials, and we have metallic, ceramic, and polymeric foams. Some are of common and every day usage, such as Styrofoam. Others are quite esoteric, such as the space shuttle tiles, which have a density of  $0.141 \text{ g/cm}^3$  and can withstand a maximum temperature of  $1260^\circ\text{C}$ . These tiles, made from silica fiber, prevent the shuttle from burning up during the reentry phase of space travel. The intense heat generated from friction with the atmosphere, at high velocities, would otherwise be fatal. This was demonstrated by the *Columbia* tragedy, in which a few tiles were knocked out during takeoff. Each space shuttle has 70% of its external surface protected by tiles (24,000 tiles per orbiter). Aluminum foam is commercially fabricated in relative densities (defined as the density of the cellular material/density of solid) varying between 0.033 and 0.1; the pore sizes can be varied independently. The aluminum foam shown in Figure 1.33 has a relative density of 0.07.

An example of a biological cellular material is bone. Bone is designed to have a variable density. Regions subjected to higher stress are denser. The outside surface is made of high density material and is called compact bone. The inside of bone tends to have a lower density and is termed cancellous bone. Figure 12.15 shows the cross section of a tibia and a glassy foam.

The mechanical properties of cancellous bone (and, for that matter of all cellular materials) are very sensitive to the relative density. Some marked effects shown by their stress-strain curves, are (see Figure 12.16):

- a. Young's modulus increases with increasing relative density.
- b. Plastic collapse plateau increases with relative density.
- c. Densification stage.

There are numerous other examples of synthetic cellular materials. These cellular materials are used either by themselves or as a core in sandwich arrangements. Sandwich structures range from common cardboard used in packaging to important uses in the aircraft industry. The basic idea is to have a dense skin and a light-weight interior. They are briefly described in Section 1.3.8.

### 12.4.2 Modeling of the Mechanical Response

The compressive stress-strain curves of cellular materials have three characteristic regions: (a) an elastic region, (b) a collapse plateau, and

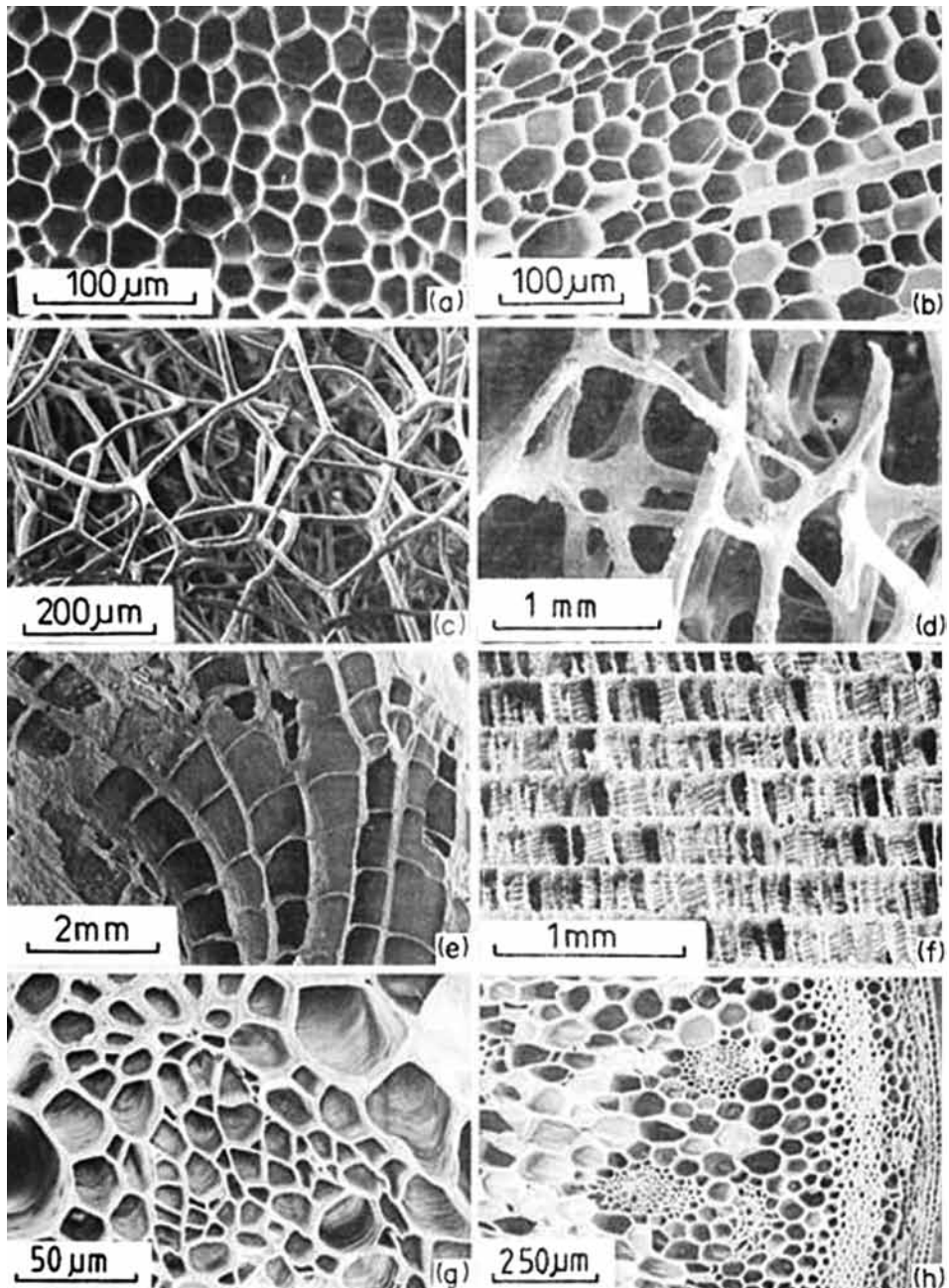


**Fig. 12.14** Examples of cellular materials: (a) cork; (b) balsa; (c) sponge; (d) cancellous bone; (e) coral; (f) cuttlefish bone; (g) iris leaf; (h) stalk of plant. (From L. Gibson and M. F. Ashby, *Cellular Materials* (Cambridge, U.K.: Cambridge University Press, 1988).)

(c) a densification region. These are shown in Figure 12.17. The higher the initial density, expressed in Figure 12.17 by  $\rho^*/\rho_s$ , the smaller the collapse plateau region. It also occurs at a higher stress.

Following Gibson and Ashby we develop expressions that predict this behavior. They are developed for an open cell geometry that represents well cellular materials with a low relative density. Figure 12.18 represents this open-cell structure. It consists of straight beams with a square cross-section. The model is very simple but captures the

essential physics. There are two characteristic dimensions; the cell size,  $\ell$ , and the beam thickness,  $t$ .

In order to characterize the elastic region of an isotropic foam, we can define three elastic constants:

### Elastic Region

Three elastic constants are defined for an isotropic foam:  $E^*$ ,  $G^*$ , and  $v^*$ . The density of the cellular material is  $\rho^*$ , and that of the solid material is  $\rho$ . From Figure 12.18 we can obtain an expression for the density in terms of  $\ell$  and  $t$ :

$$\frac{\rho^*}{\rho_s} = C_1 \left( \frac{t}{\ell} \right)^2, \quad (12.5)$$

where  $C_1$  is a proportionality constant. When the cell is subjected to compressive loading, it will deflect as shown in Figure 12.19. The vertical columns push on the horizontal beams and cause them to bend. A force  $F$  on each column produces a deflection  $\delta$  in the beam. The moment of inertia of a beam with a rectangular section (sides of  $b$  and  $h$ ) is:

$$I = \frac{bh^3}{12}. \quad (12.6)$$

The student should consult a mechanics of materials text for the derivation of the above expression.

For a beam with a square cross section with side  $t$ :

$$I = \frac{t^4}{12}. \quad (12.7)$$

Beam theory states that the deflection,  $\delta$ , is given by:

$$\delta = C_2 \frac{F\ell^3}{E_s I}, \quad (12.8)$$



(a)



(b)

**Fig. 12.15** (a) Cross section of tibia. (From L. Gibson and M. F. Ashby, *Cellular Materials* (Cambridge, UK: Cambridge University Press, 1988).); (b) Glassy  $\text{SiO}_2$  foam for space shuttle tiles.

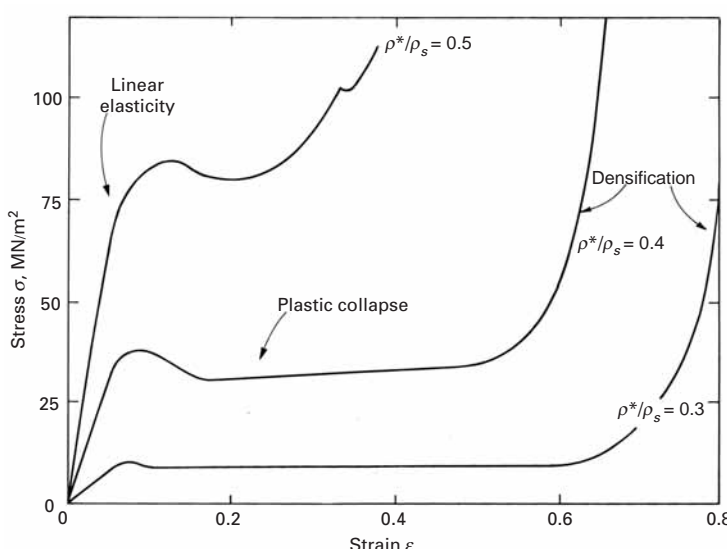


**Fig. 12.16** Stress-strain curves for cancellous bone at three different relative densities,  $\rho^*/\rho_s$ : 0.3, 0.4, and 0.5. (From L. Gibson and M. F. Ashby, *Cellular Materials* (Cambridge, UK: Cambridge University Press, 1988).)

**Fig. 12.17** Compressive stress-strain curves of elastomeric foams showing the three characteristic regions: (a) elastic region, (b) collapse plateau, (c) densification region.

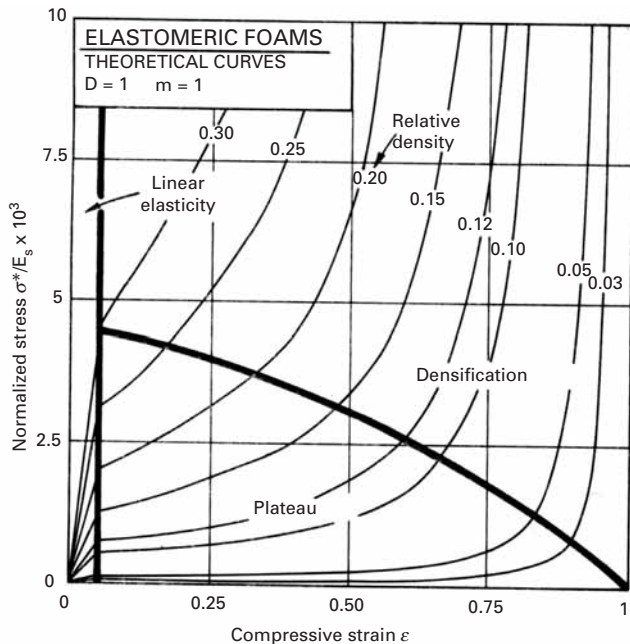
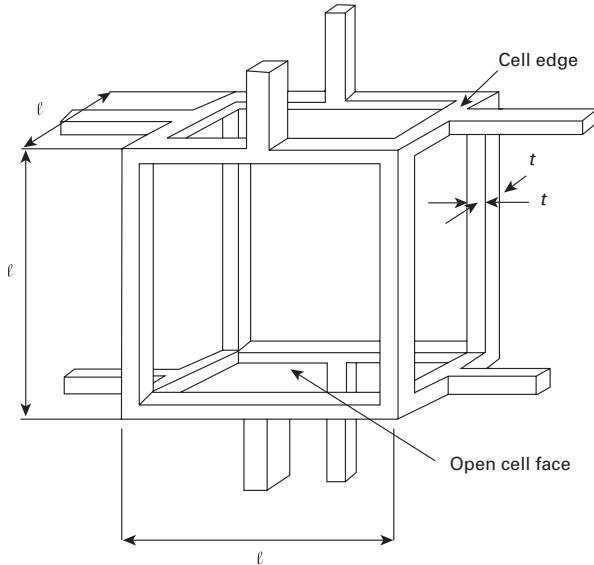


**Fig. 12.18** Open-cell structure for cellular materials with low relative density. This is the structure upon which the Gibson–Ashby equations are based.



where  $C_2$  is a constant,  $E_s$  is the Young's modulus of the solid. The stress acting on the cell is related to the force,  $F$ , by (each force  $F$  is shared by two neighboring cells):

$$\sigma = \frac{F}{\ell^2}.$$

The strain,  $\varepsilon$ , is related to the deflection by:

$$\varepsilon = \frac{2\delta}{\ell}.$$

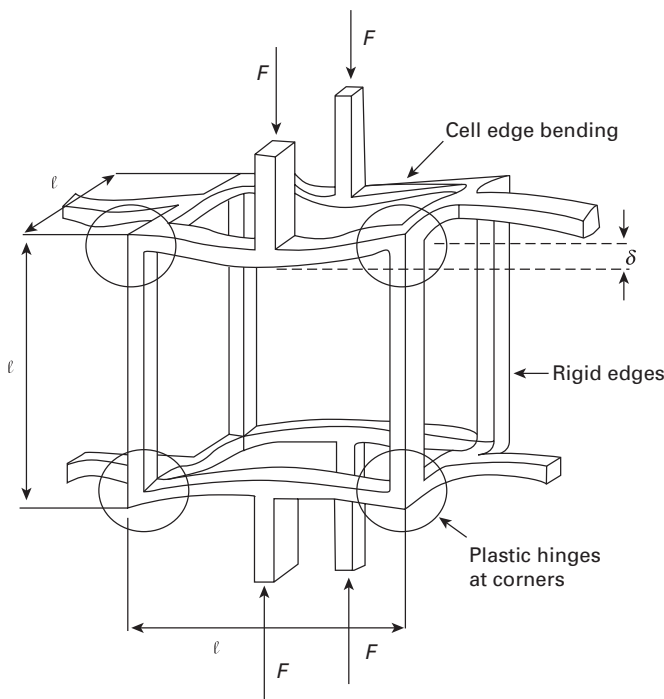


**Fig. 12.19** Open-cell configuration under compressive loading. Note the deflection,  $\delta$ .

Thus, the Young's modulus,  $E^*$ , is given by:

$$E^* = \frac{E_s I}{2C_2 \ell^4} = \frac{E_s t^4}{24C_2 \ell^4}.$$

This can be expressed as a function of density (Equation 12.5):

$$\frac{E^*}{E_s} = \frac{C_1}{24C_2} \left( \frac{\rho^*}{\rho_s} \right)^2. \quad (12.9)$$

Experimental measurements indicate that  $C_1/24C_2$  should be approximately equal to one. Thus:

$$\frac{E^*}{E_s} \sim \left( \frac{\rho^*}{\rho_s} \right)^2. \quad (12.10)$$

Similarly, an expression for the shear modulus can be obtained:

$$\frac{G}{E_s} = \frac{3}{8} \left( \frac{\rho^*}{\rho_s} \right)^2. \quad (12.11)$$

### Plastic Plateau

At a certain level of deformation, elastic behavior gives way to plastic deformation. The Gibson–Ashby equations are based on the formation of plastic hinges at the regions where the beams terminate. One of these plastic hinges is circled in Figure 12.19.

The student should recall the classic equation from mechanics of materials:

$$\sigma = \frac{Mc}{I}, \quad (12.12)$$

where  $M$  is the bending moment of a beam,  $I$  its moment of inertia,  $c$  the distance from neutral axis to external fiber, and  $\sigma$  is the maximum stress. For our case, we have, in the case of plastic deformation ( $\sigma = \sigma_y$ ), the stresses acting on the cross section are uniform and tensile above the neutral axis and uniform and compressive below the neutral axis. Figure 12.19 shows the configuration.

The plastic moment,  $M_p$ , about the neutral axis is:

$$M_p = F \frac{t}{2}. \quad (12.13)$$

The yield stress is related to  $F$  by:

$$\sigma_y = \frac{F}{t \frac{t}{2}}. \quad (12.14)$$

Thus, substituting Equation 12.13 into 12.14:

$$M_p = \frac{1}{4} \sigma_y. \quad (12.15)$$

But, taking the beam with length  $\ell/2$  and considering the force  $F/2$  applied to each of the two hinges:

$$M_p = \frac{F}{2} \frac{\ell}{2} = \frac{1}{4} F \ell. \quad (12.16)$$

The global stress acting on the foam is the force  $F$  divided by the area upon which it acts,  $\ell^2$ .

$$\sigma_p^* = \frac{F}{\ell^2} \quad (12.17)$$

From Equations 12.15, 12.16, and 12.17 we get:

$$\frac{\sigma_p^*}{\sigma_y} = \left( \frac{t}{\ell} \right)^3. \quad (12.18)$$

Substituting Equation 12.5 into Equation 12.18:

$$\frac{\sigma_p^*}{\sigma_y} = C_1^{-3/2} \left( \frac{\rho_*}{\rho_s} \right)^{3/2}. \quad (12.19)$$

### Densification

Densification starts when the plastic plateau comes to an end. This region is characterized by a complex deformation pattern. The stress required for the densification rises rapidly as the open spaces between the collapsed cell structure close up. The analytical treatment for the collapse of pores and voids will not be presented here. There are theories that address this problem. One of the best known, the Carroll-Holt theory, assumes a spherical hole inside a solid sphere. By applying an external pressure it is possible to collapse the internal hole. The smaller the hole, the higher the stress. The Gurson model addresses the same problem. This is discussed in Section 12.4.5.

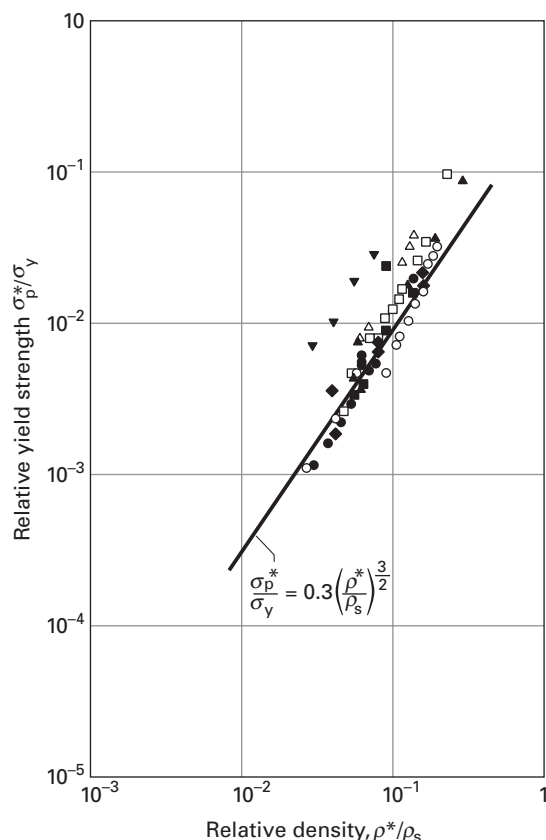


**Fig. 12.20** Yield strength of foams as a function of relative density. Experimental results are for a number of materials: polyurethane, aluminum, polystyrene, polymethyl methacrylate, polyvinyl chloride. (Adapted from L. Gibson and M. F. Ashby, *Cellular Materials*, Cambridge University Press, 1988.)

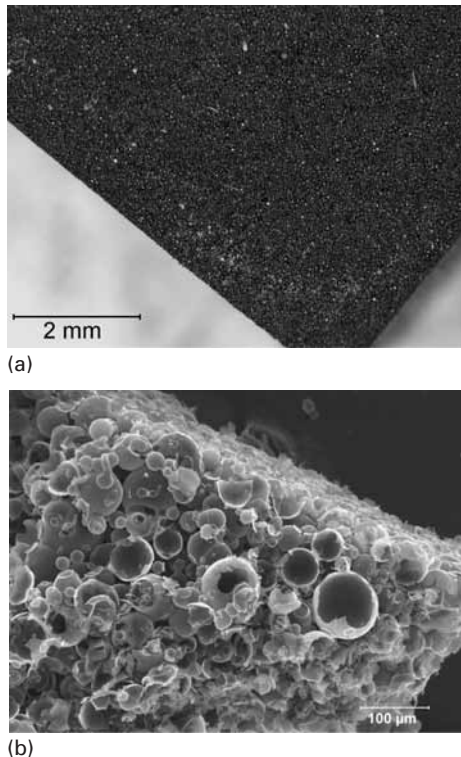
### 12.4.3 Comparison of Predictions and Experimental Results

Figure 12.20 shows experimental results for a number of foams undergoing plastic collapse after a stage of elastic deformation. These foams are made from aluminum, aluminum-7% magnesium, polyurethane, polyvinyl chloride, polystyrene, and polymethyl methacrylate. The  $3/2$  dependence on relative density is clearly seen in the figure. The best fit of Equation 12.19 with experimental results is obtained using a value of 0.3 for  $C_1^{-3/2}$ . The match between Equation 12.19 and the experimental results for a number of materials is considered excellent.

### 12.4.4 Syntactic Foam

The micrographs in Figure 12.21 show another type of cellular material called syntactic foam. The word *syntactic* comes from Greek meaning to arrange parts together in a unit. Syntactic foams are made by mixing hollow spheres or microballoons (glass, aluminum, or carbon) in a very small amount of resin. Microspheres, also called microballoons, can range in size from hundreds of nanometers to a few millimeters. Typically, the resin matrix phase in syntactic foam has a large amount of open voids. Strictly speaking, the matrix can be a polymer, metal, or ceramic. The polymer matrix can be epoxy,

**Fig. 12.21** (a) A low magnification optical picture of syntactic foam made of carbon microballoons dispersed in small amount of resin. (b) A higher magnification scanning electron micrograph of the foam in (a) showing the carbon microballoons. (From K. Carlisle, K. K. Chawla, G. Gouadec, M. Koopman, and G. M. Gladysz, in *Proceedings of the 14<sup>th</sup> International Conference on Composite Materials, ICCM-14, San Diego, CA, 2003.*)



phenolic, ester cyanate, etc. Figure 12.21(a) shows a carbon microballoon foam at low magnification while Figure 12.21(b) shows a higher magnification picture where the individual carbon microballoons can be seen. Such foams generally have over 90% voids; they show very high specific compressive strength and excellent insulating properties. They find extensive use in deep-sea applications where buoyancy effects become very important.

#### 12.4.5 Plastic Behavior of Porous Materials

Porous materials are gaining in technological importance. Metals and ceramics frequently involve powders that most often have to be pressed. Metallic foams, cellular materials (such as wood) are examples of low-density materials used in structural applications.

We will discuss here briefly the plastic response of powders subjected to compressive loads. Figure 12.22 shows experimentally obtained pressure vs. green density for iron, copper, and nickel powders. The behavior is mostly linear, when the pressure is plotted against  $\ln(1 - D)$ , where  $D$  is the relative density of powder,  $D = \rho/\rho_s$ . At full consolidation, the cellular density is equal to the solid density and  $D = 1$ . This behavior can be represented by:

$$P = \frac{1}{k} \left[ \ln \frac{1}{1 - D} + B \right],$$

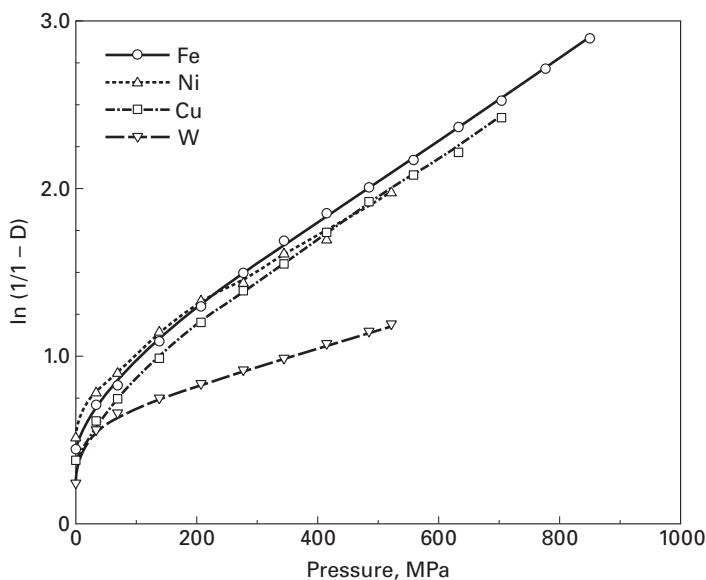


**Fig. 12.22** Relationship between pressure and relative green density for several powders. (Adapted from R. M. German, *Powder Metallurgy Science* (Princeton, NJ: Powder Industries Federation), 1984.)

where  $k$  and  $B$  are experimental parameters. This is an empirical relationship, in which the strength of the powder is not incorporated. Except at low pressures, this equation is obeyed. The constant  $B$  is the intercept and  $k$  is the slope of the curve. Figure 12.23(a) shows a powder (spherical particles) prior to and during plastic deformation. The particles undergo deformation at the contact points as the external pressure is increased.

The model developed by Fischmeister and Arzt<sup>9</sup> and applied by Helle<sup>10</sup> et al. to sintering is presented here. It represents very well the densification of powders from the initial density (approximately, in many cases, from 0.5 to 0.65 of the theoretical density) to 0.9 of the theoretical density. This is the range in which the individual particles are recognizable. Beyond 0.9 the model proposed by Torre<sup>11</sup> and generalized by Carroll and Holt<sup>12</sup> is more realistic, since it describes the collapse of individual pores (voids) under hydrostatic pressure. Schematic representations of both models are shown in Figure 12.23.

We develop equations for both models. Fischmeister and Arzt assumed that each particle (assumed to be initially spherical) had  $Z$  neighbors, and that the number of neighbors increased with density. Again, the relative density  $D = \rho/\rho_s$ . For the solid, this coordination number is taken as 12. This is equal to the coordination number for atoms in the FCC and HCP structures. Thus:

$$Z = 12D.$$

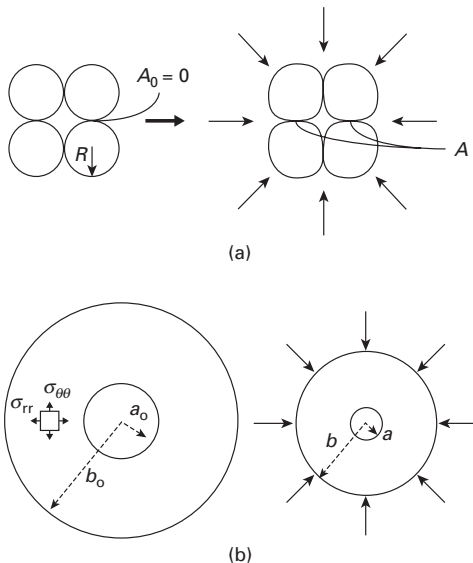
<sup>9</sup> H. Fischmeister and E. Arzt, *Powder Met.*, 26 (1982) 82.

<sup>10</sup> A. S. Helle, K. E. Easterling, and M. F. Ashby, *Acta Met.*, 33 (1985) 2163.

<sup>11</sup> C. Torre, *Huttenmonats. Hochschule Leoben*, 93 (1948) 62.

<sup>12</sup> M. Carroll and A. C. Holt, *J. Appl. Phys.*, 43 (1972) 759.

**Fig. 12.23** (a) Particle flattening (Fischmeister–Arzt) densification mechanism; (b) Hollow sphere model (Torre and Carroll–Holt).



At  $D_0$  (initial value of  $D$ ) = 0.64,  $Z = 7.7$ ; for  $D = 1$ ,  $Z = 12$ . The average area of contact between neighbors,  $A$ , is shown in Figure 12.23(a).  $A$  increases from  $A_0 = 0$  to one-twelfth ( $1/12$ ) of the particle surface area,  $4\pi r^2$ , since, as the contact points are flattened, their surface area increases. The maximum area is equal to the total sphere surface divided by the number of neighbors. A simple expression for  $A$  is:

$$A = \frac{\pi(D - D_0)}{3(1 - D_0)} R^2.$$

When  $D = D_0$ ,  $A = 0$ ; when  $D = 1$ ,  $A = 4\pi R^2/12 = (\pi/3)R^2$ .  $R$  is the radius of particles (Figure 2.23(a)).

The force applied to each contact region,  $F$ , is related to the external pressure by:

$$F = \frac{4\pi R^2}{ZD} P.$$

This force, divided by the contact area  $A$ , gives the average pressure on the particle at contact region,  $P_p$ :

$$P_p = \frac{F}{A} = \frac{4\pi R^2}{AZD} P. \quad (12.20)$$

It is shown in Chapter 3 (hardness testing) that the stress required to make an indentation on a surface is equal to  $\approx 3\sigma_y$ , where  $\sigma_y$  is the yield stress of the material. Thus:

$$3\sigma_y = \frac{4\pi R^2}{AZD} P; \quad (12.21)$$

and, substituting Equation 12.21 Into Equation 12.20:

$$P = Z\sigma_0 \frac{D(D - D_0)}{4(1 - D_0)}. \quad (12.22)$$

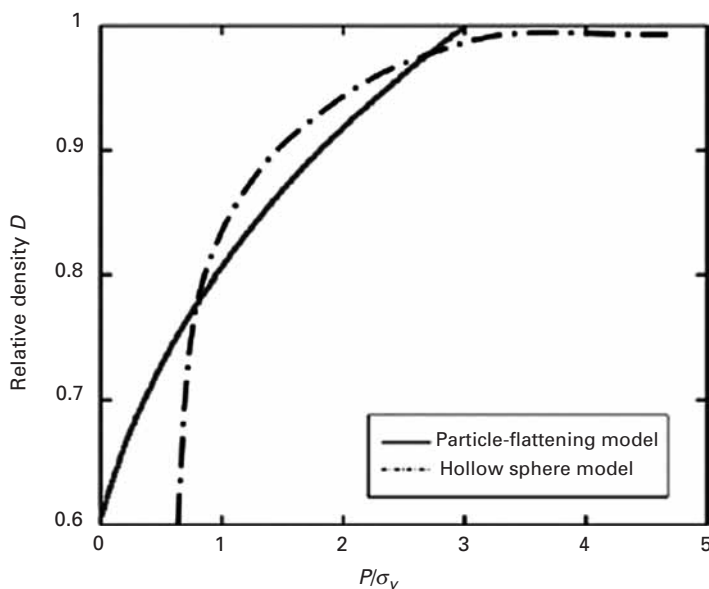


**Fig. 12.24** Comparison of particle-flattening and hollow-sphere models for densification under hydrostatic stress.

Equation 14.22 gives a relationship between pressure and the relative density. It is plotted in Figure 12.24 from an initial relative density of 0.6.

The Torre–Carroll–Holt equation is obtained by the application of an analytical treatment to the configuration shown in Figure 12.23(b). The hollow sphere can be used to define a relative density:

$$D = \frac{b^3 - a^3}{b^3},$$

where  $b$  is the outer radius and  $a$  is the inner radius. In spherical coordinates, the equilibrium equation of stresses acting on an element (shown in Figure 12.23(b)) is:

$$\frac{d\sigma_r}{dr} + \frac{2}{r}(\sigma_r - \sigma_\theta) = 0, \quad (12.23)$$

where  $\sigma_r$  and  $\sigma_\theta$  are the radial and circumferential stress components, respectively, and  $r$  is the radius. The boundary conditions are:

$$\begin{aligned} \sigma_r &= -P & \text{at } r = b; \\ \sigma_r &= 0 & \text{at } r = a. \end{aligned}$$

We assume that Tresca's yield criterion holds, i.e., plastic flow occurs when:

$$\sigma_r - \sigma_\theta = \sigma_0,$$

where  $\sigma_0$  is the flow stress. By integrating Equation 12.23 From  $a$  to  $b$ , we have:

$$\begin{aligned} \int_a^b d\sigma_r &= -2\sigma_0 \int_a^b \frac{dr}{r}, \\ -P &= -2\sigma_0 \ln \frac{b}{a} = -\frac{2}{3}\sigma_0 \ln \frac{b^3}{a^3}. \end{aligned}$$

But

$$\frac{b^3}{a^3} = \frac{1}{1 - D}.$$

Hence

$$P = \frac{2}{3} \sigma_0 \ln \frac{1}{1 - D}.$$

This equation is plotted in Figure 12.24 and compared with the particle flattening model. The pore collapse model predicts much higher pressures to achieve full densification ( $P/\sigma_y > 5$ ). In this context, it is more realistic for high relative densities ( $D > 0.9$ ). It should be noted that when powders are pressed in cylinders, additional frictional effects at the walls have to be considered. Another complication is that the state of stress deviates from hydrostatic. Thus, a flow criterion has to be incorporated into analysis. In summary, everything becomes increasingly complicated if all effects are incorporated.

## Suggested Reading

- E. P. George, M. Yamaguchi, K. S. Kumar, and C. T. Liu. *Ann. Rev. Mater. Sci.*, 24 (1994) 409.
- C. T. Liu, R. W. Cahn, and G. Sauthoff, eds. *High-temperature Ordered Intermetallic Alloys – Physical Metallurgy/Mechanical Behavior*. Boston and Dordrecht: Kluwer, 1992.
- A. K. Vasudevan and J. J. Petrovic, eds. *High Temperature Structural Silicides*. Amsterdam: Elsevier, 1992.
- J. H. Westbrook and R. L. Fleischer, eds. *Intermetallic Compounds: Principles and Practice*. New York, NY: John Wiley, 1994.

## Exercises

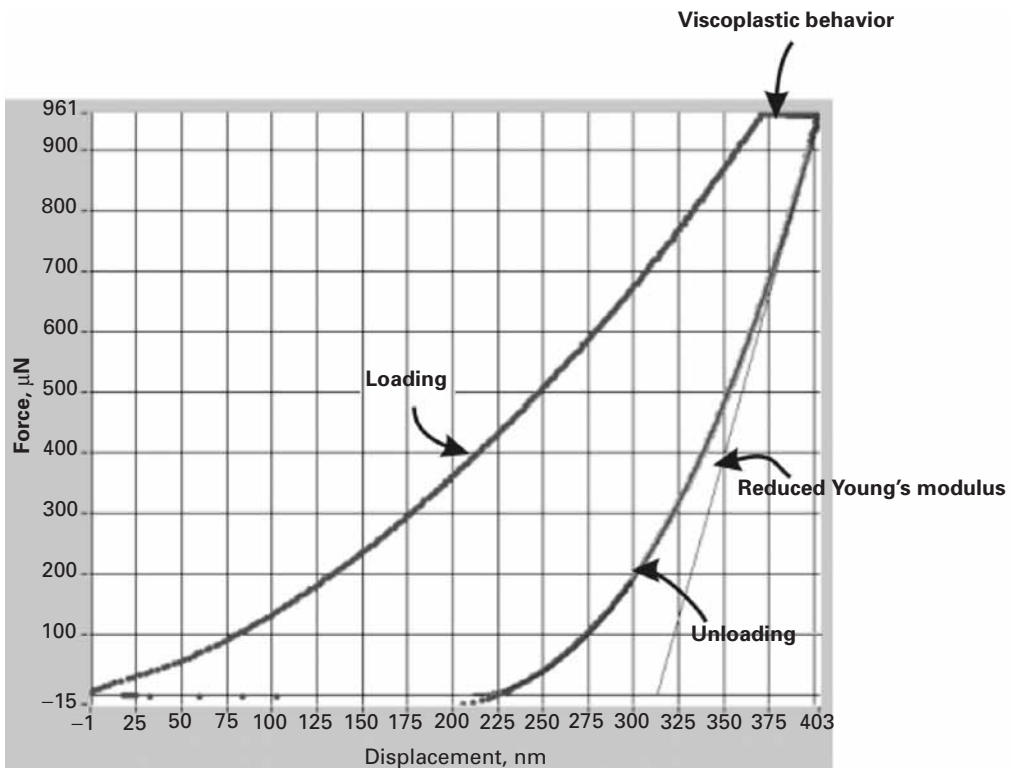
**12.1** High-temperature applications of intermetallics in air would require oxidation resistance. Comment on some possible sources of such oxidation resistance in intermetallics.

**12.2** The formation of a silica film at grain boundaries in  $\text{MoSi}_2$  can lead to embrittlement. Suggest some means of avoiding this phenomenon.

**12.3** Order and disorder transitions are commonly associated with metals, not with polymers. Why?

**12.4** An intermetallic compound of Al and Mg has a stable range of 52Mg–48Al to 56Mg–44Al (on a weight basis). What atomic ratios do these compositions correspond to? The atomic weight of Al is 27, and that of Mg is 24.31.

**12.5** A metallic laminate consists of FeAl as matrix and Ti as reinforcement. If the temperature rises from 300 K to 325 K, estimate the expansion of



laminated composite. What kinds of problems do you think will be caused by this? Expalin.

12.6 Find the relationship between pressure and relative density of powder from the data shown in Figure 12.22 for Fe, Ni, Cu, and W.

12.7 Plot the strength of the cancellous bone as a function of porosity, assuming that the strength of the fully dense bone is equal to 300 MPa (assume  $C_1 = 3$ ).

12.8 Calculate  $C_1$  in the equation:

$$\frac{\rho^*}{\rho_s} = C_1 \left( \frac{t}{\ell} \right)^2.$$

*Hint:* Assume fully dense material.

12.9 Determine the pressure required to densify a copper powder ( $\sigma_0 = 100$  MPa) to 90% of the theoretical density using:

- (a) The Fischmeister and Arzt equation:
- (b) The Carroll-Holt-Torre equation.

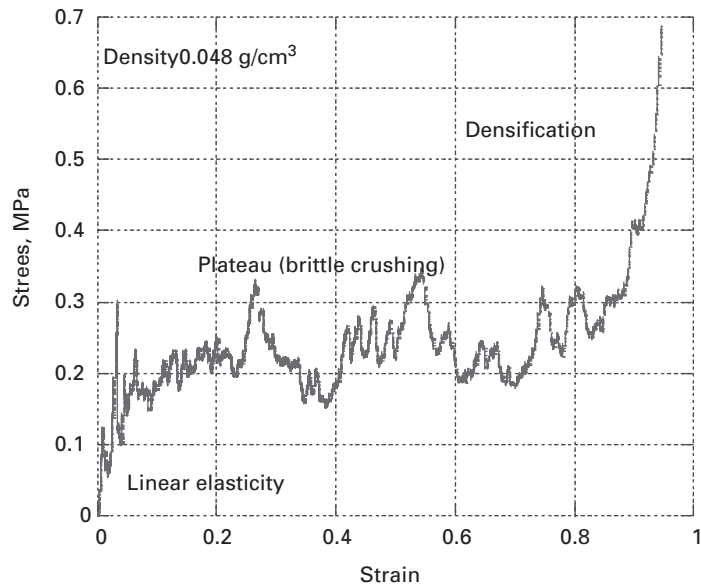
12.10 From load vs. displacement for keratin shown in Figure Ex12.10, calculate hardness of keratin. Hardness is given by:

$$H = \frac{P}{A},$$

where  $P$  = load,  $A$  = projected area. Assume Berkovich tip was used.

**Fig. Ex12.10** Load vs. displacement from nanoindentation on keratin by use of Berkovich tip.

**Fig. Ex12.12** Compressive stress-strain curve for foams (toucan beak).



**12.11** Figure Ex12.12 shows the compressive stress-strain curve from the foam of a toucan beak. Calculate the densification strain, Young's modulus, shear modulus, and plastic collapse stress of this foam. Assume this foam is open celled.

Densification strain is given by:

$$\varepsilon_d = 1 - 1.4 \left( \frac{\rho^*}{\rho_s} \right).$$

Density of the foam  $\rho^* = 0.04 \text{ g/cm}^3$ ;

Density of the cell wall  $\rho_s = 0.5 \text{ g/cm}^3$ ;

Young's modulus of the cell wall  $E_s = 12.7 \text{ GPa}$ ;

Yield stress of the cell wall  $\sigma_y = 90 \text{ MPa}$ .

---

## Chapter 13

# Creep and Superplasticity

### 13.1 | Introduction

The technological developments wrought since the early twentieth century have required materials that resist higher and higher temperatures. Applications of these developments lie mainly in the following areas:

1. Gas turbines (stationary and on aircraft), whose blades operate at temperatures of 800–950 K. The burner and afterburner sections operate at even higher temperatures, viz. 1,300–1,400 K.
2. Nuclear reactors, where pressure vessels and piping operate at 650–750 K. Reactor skirts operate at 850–950 K.
3. Chemical and petrochemical industries.

All of these temperatures are in the range  $(0.4\text{--}0.65) T_m$ , where  $T_m$  is the melting point of the material in kelvin.

The degradation undergone by materials in these extreme conditions can be classified into two groups:

1. *Mechanical degradation.* In spite of initially resisting the applied loads, the material undergoes anelastic deformation; its dimensions change with time.
2. *Chemical degradation.* This is due to the reaction of the material with the chemical environment and to the diffusion of external elements into the materials. Chlorination (which affects the properties of superalloys used in jet turbines) and internal oxidation are examples of chemical degradation.

This chapter deals exclusively with mechanical degradation. The time-dependent deformation of a material is known as *creep*. A great number of high-temperature failures can be attributed either to creep or to a combination of creep and fatigue. Creep is characterized by a slow flow of the material, which behaves as if it were viscous. If a mechanical component of a structure is subjected to a constant tensile load, the decrease in cross-sectional area (due to the increase in length resulting from creep) generates an increase in stress; when the stress

reaches the value at which failure occurs statically (ultimate tensile stress), failure occurs. The temperature regime, in kelvins, for which creep is important in metals and ceramics is  $0.5T_m < T < T_m$ , the melting of the material. This is the temperature range in which diffusion is a significant factor. A thermally activated process, diffusion shows an exponential dependence on temperature. Below  $0.5T_m$ , the diffusion coefficient is so low, that any deformation mode exclusively dependent on it can effectively be neglected.

In glasses and polymers, creep becomes important at temperatures above  $T_g$ , the glass transition temperature. At  $T > T_g$ , these materials turn rubbery or leathery, and viscoelastic and viscoplastic effects become important. Section 13.3 presents the various mechanisms responsible for creep. The critical temperature for creep varies from material to material; lead creeps at ambient temperature, whereas in iron creep becomes important above 600 °C. In general, the phenomenon of creep is important at high temperatures. Some nickel-based superalloys can withstand temperatures as high as 1,500 K, and ceramics have temperature capabilities that are considerably higher (up to 2,000 K). Ice, on the other hand, also undergoes creep, which is responsible for the slow flow of glaciers.<sup>1</sup> Even the earth's mantle is subjected to creep, giving it an effective viscosity.

Creep in rocks has been at the center of controversy concerning the nature of geological processes on the planet Venus. The maximum height of mountains on Venus has been calculated on the basis of rock creep, assuming a certain temperature and period of time. (The mountains are subjected to compressive stresses due to their own weight.) This maximum calculated height has been compared with actual topographic observations from the space probe *Galileo*. It happens that dry rock has a creep rate orders of magnitude lower than that of hydrated rock. Weertman has performed calculations for both dry and wet rock, each resulting in a value of  $10^9$  years for the period of active creep in the mountains. Based on this figure, the maximum height of mountains made of quartzite would be 0.12 km (wet) and 7.6 km (dry). The calculations were done for  $T = 750$  K, the surface temperature on Venus. They help to elucidate the mechanisms involved in the formation of the planetary surface.

In spite of the fact that creep has been known since 1834, when Vicat conducted the first experiments assessing the phenomenon, it is only in the twentieth century that systematic investigations have been conducted. The creep test is rather simple and consists of subjecting a specimen to a constant load (or stress) and measuring its length as a function of time, at a constant temperature. Figure 13.1 shows the characteristic curve; the ordinate shows the strain and the abscissa shows time. Three tests are represented in the figure; three constant loads corresponding to three engineering stresses,  $\sigma_a$ ,  $\sigma_b$ , and  $\sigma_c$ , were used. The creep curves are usually divided into three stages: I, primary or transient; II, secondary, constant rate, or quasi viscous;

---

<sup>1</sup> J. Weertman, *Ann. Rev. Earth Plan. Sci.*, 11 (1983) 215.

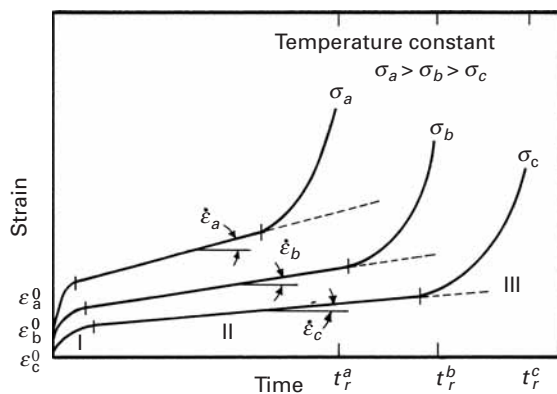


**Fig. 13.1** Creep strain vs. time at different constant stress levels and temperature.

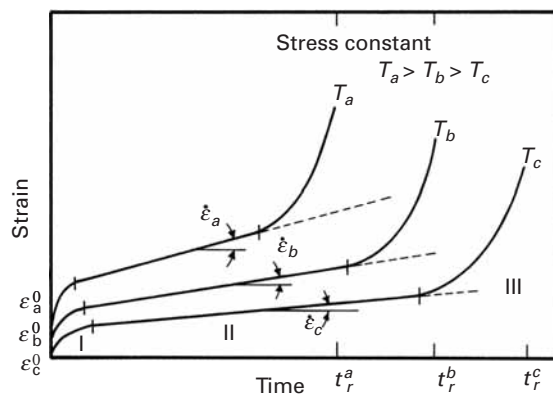


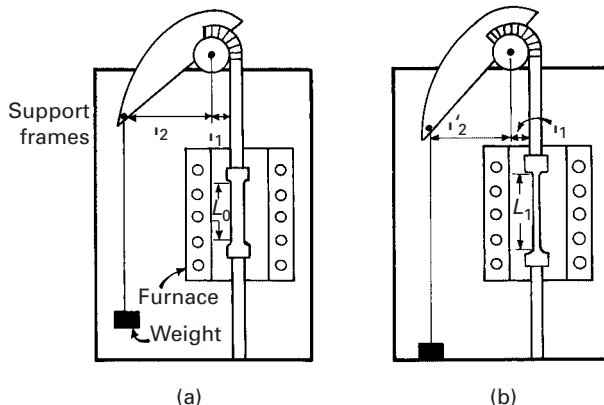
**Fig. 13.2** Creep strain vs. time at a constant engineering stress and different temperatures.

and III, tertiary. This division into stages was made by Andrade, one of the pioneers in the study of creep. Stage II, in which the creep rate  $\dot{\varepsilon}$  is constant, is the most important. It can be seen that  $\dot{\varepsilon}_a > \dot{\varepsilon}_b > \dot{\varepsilon}_c$  as a consequence of the relationship  $\sigma_a > \sigma_b > \sigma_c$ . This creep rate is also known as the *minimum creep rate*, because it corresponds to the inflection point of the curve. (See Figure 13.1.) In stage III there is an acceleration in the creep rate, leading to eventual rupture of the specimen.

In Figure 13.1, the rupture times  $t_r^a$ ,  $t_r^b$ , and  $t_r^c$  increase with decreasing stress. The strains  $\varepsilon^0$  are called *instantaneous strains* and correspond to the strains at the instant of loading. In Figure 13.2, the engineering stress was kept constant and the temperature was varied. Since the tests are conducted in tension, the stress rises as the length of the specimen increases, because of the reduction in area. The dashed lines in Figures 13.1 and 13.2 represent the constant stress curves. Initially they are identical, because  $\varepsilon_e$ , the elastic strain, = 0. As the specimen increases in length, the stress increases and so does the creep rate, at a constant load. The failure times under constant stress and constant load can be drastically different. The curves shown in Figure 13.2 have been expressed mathematically as

$$\varepsilon_t = \varepsilon^0 + \varepsilon[1 - \exp(-mt)] + \dot{\varepsilon}_s t \quad (13.1)$$

**Fig. 13.3** Creep machine with variable lever arms to ensure constant stress on specimen; note that  $l_2$  decreases as the length of the specimen increases. (a) Initial position. (b) Length of specimen has increased from  $L_0$  to  $L_1$ .



where  $\varepsilon^0$  is the instantaneous strain (the strain at the instant of application of load),  $\dot{\varepsilon}_s t$  is a linear function of time, depicting stage II, and the term  $\varepsilon[1 - \exp(-mt)]$  represents stage I in which  $m$  is the exponential time parameter and  $\varepsilon$  is the limiting transient creep strain (strain at end of that stage minus  $\varepsilon^0$ ).

From a fundamental point of view, there are significant differences between the constant-load and constant-stress creep tests. Andrade realized this important difference and built a constant true-stress creep machine that used a weight which dropped gradually into a fluid as the specimen extended.<sup>2</sup> Thus, by Archimedes' principle, the force exerted by the weight decreased with displacement. The shape of the weight was such that a constant stress on the specimen was ensured. For this type of machine, the load should decrease with an increase in length in such a way that the true stress remains constant.

Another important difference between the two tests is that the onset of stage III is greatly retarded at constant stress. The dashed lines in Figure 13.2 show the trajectory that a constant true-stress test would follow.

From an engineering point of view, the creep test at constant load is more important than the one at constant stress because it is the load, not the stress, that is maintained constant in engineering applications. On the other hand, fundamental studies should be conducted at constant stress, with the objective of elucidating the underlying mechanisms. The reason for this is that the study of the evolution of the substructure of an alloy under increasing stress would be excessively complex.

The essential components and principles of operation of a constant-stress creep-testing machine are shown in Figure 13.3. This system contains a variable lever arm, which is a curved line that acts as a cam in such a manner that the force acting on the specimen is a function of its length. Two positions are shown in the figure. If

<sup>2</sup> E. N. da L. Andrade, Proc. Roy Soc. (London), A84 (1911) 1.

the initial and current cross-sections of the specimen are  $A_0$  and  $A_1$ , respectively, then

$$\sigma_0 A_0 \ell_1 = P \ell_2 \quad (13.2)$$

and

$$\sigma_1 A_1 \ell_1 = P \ell'_2$$

where  $P$  is the load and  $\ell_1$ ,  $\ell_2$ , and  $\ell'_2$  are lever arms defined in the figure. At constant stress,  $\sigma_0 = \sigma_1$ ; since the volume of the specimen is constant (for stages I and II of creep),

$$A_0 L_0 = A_1 L_1,$$

where  $L_0$  and  $L_1$  are the initial and current lengths of the specimen, respectively. Thus,

$$\frac{L_1}{L_0} = \frac{\ell_2}{\ell'_2}. \quad (13.3)$$

The exact shape of the lever arm can be established in such a manner that Equation 13.3 is obeyed. The astute student will certainly be able to obtain the mathematical description for this curved surface.

It is important to recognize that, even at a constant stress, the creep curve will deviate from linearity at a certain point. This can be due to several causes, the most important being the formation of internal flaws such as cavities (known as creep cavitation) and necking of the specimen. The minimum creep rate, or slope of stage II of creep, is a very important parameter. This stage, also known as steady-state creep, is usually represented by the equation

$$\dot{\varepsilon}_s = \frac{AGb}{kT} D_0 \exp(-Q_c/RT) \left( \frac{b}{d} \right)^p \left( \frac{\sigma}{G} \right)^n, \quad (13.4)$$

where  $A$  is a dimensionless constant,  $D_0$  is a frequency factor,  $G$  is the shear modulus,  $b$  is the Burgers vector,  $k$  is Boltzmann's constant,  $T$  is the absolute temperature,  $\sigma$  is the applied stress,  $d$  is the grain size,  $p$  is the inverse grain-size exponent,  $n$  is the stress exponent,  $Q_c$  is the appropriate activation energy, and  $R$  is the gas constant. This equation is known as the Mukherjee–Bird–Dorn equation.<sup>3</sup> It will be shown in Section 13.3 that the activation energy for diffusion is often equal to the activation energy for creep ( $Q_c = Q_D$ ). The diffusion coefficient is

$$D = D_0 \exp\left(-\frac{Q_D}{RT}\right)$$

and

$$\dot{\varepsilon}_s = \frac{AGbD}{kT} \left( \frac{b}{d} \right)^p \left( \frac{\sigma}{G} \right)^n. \quad (13.5)$$

Essentially, Equations 13.4 and 13.5 express the steady-state creep rate as a function of the applied stress, temperature, and grain size. In

---

<sup>3</sup> A. K. Mukherjee, J. E. Bird, and J. E. Dorn, *Trans. ASM*, 62 (1964) 155.

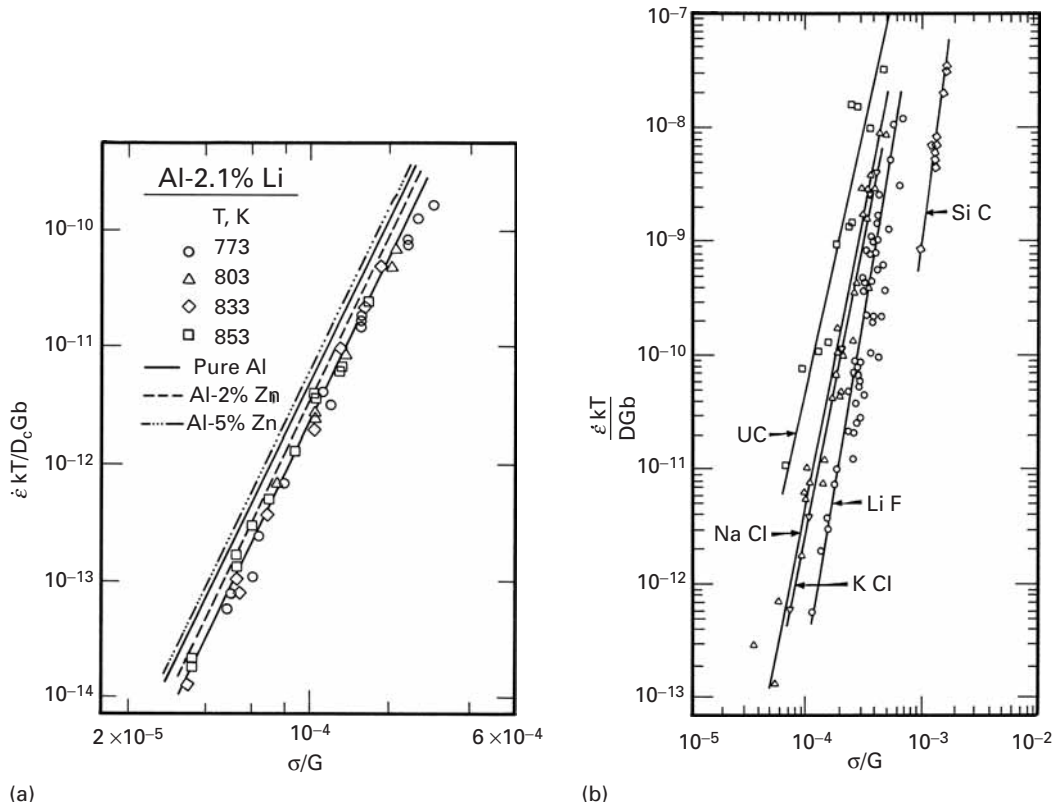


**Fig. 13.4** Normalized creep rate vs. normalized stress (according to Mukherjee–Bird–Dorn equation) for (a) aluminum, Al–Zn, and Al–Li solid solutions. (Adapted from K.-T. Park, E. J. Lavernia, and F. A. Mohamed, *Acta Met. Mat.*, 38 (1990) 1837.) (b) Various ceramics. (From A. H. Chokshi and T. G. Langdon, *Mater. Sci. Techn.*, 7 (1991) 577.)

In this chapter we will use  $d$  to designate the grain size, to differentiate it from  $D$ , the diffusion coefficient. Equation 13.4 is also a fundamental equation in superplasticity. Figure 13.4 illustrates the application of the Mukherjee–Bird–Dorn equation to metals (aluminum and aluminum alloys) and ceramics. This is usually done by plotting a normalized strain rate ( $\dot{\varepsilon} kT / D G b$ ) vs. a normalized stress ( $\sigma/G$ ). The agreement with the equation is excellent, and the slope of these plots enables the exponent  $n$  to be determined. For both cases, it is approximately equal to 5. The exponent, in its turn, can provide information on the fundamental mechanism of creep. This will be discussed at length in Sections 13.3–13.7. In ceramics,  $n$  is observed to be in two ranges: 1–3 or 5–7. The significance of these results will be discussed later.

Equation 13.4 is important because it enables strain to be predicted in a specimen under creep conditions, once the various parameters that describe its creep response are established. The creep rate is dependent on stress, temperature, grain size, and other material parameters.

Another test, commonly used in place of the creep test, is the stress-rupture (or creep-rupture) test. This consists of an accelerated creep test that leads to rupture. It is usually carried out at a constant load, for the sake of simplicity. The important parameter obtained from the

test is the time to rupture, whereas in the regular creep test, the minimum creep rate is the experimental parameter sought.

The sections that follow deal with several important aspects of creep. Section 13.2 describes the extrapolation methods used to obtain the response to creep at very large times after conducting more accelerated tests. Theories of creep are described in Sections 13.3–13.7. The very helpful deformation-mechanism maps called Weertman–Ashby maps are presented in Section 13.8. And some important heat-resisting alloys are described in Section 13.9. Section 13.10 treats polymers and Section 13.11 discusses superplasticity.

## 13.2 Correlation and Extrapolation Methods

The central theme of materials science and engineering is the structure–property–performance triangle. In creep, the correlation between properties and performance is very critical, because in certain applications we want to know the performance during an extended period (20 or more years), while the properties (secondary creep rate or stress-rupture life) are known for a shorter period. In general, industrial equipment operating at a high temperature is designed to have a certain lifetime. For jet turbines, 10,000 hours (about 1 year) is a reasonable value. For stationary turbines, the weight of the components is not so critical, and a life of 100,000 hours (about 11 years) is the goal. For nuclear reactions, for obvious reasons, we use the criterion of 350,000 hours (40 years). A great number of advanced alloys are used in these projects, and the engineer does not have on hand the results of lengthy tests. Hence, several extrapolation methods have been developed that seek to predict the performance of alloys based on tests conducted over a shorter period. The number of parametric methods developed exceeds 30; the three most common are the Larson–Miller, Manson–Haferd, and Sherby–Dorn methods.

In 1952, Larson and Miller proposed a method that correlates the temperature  $T$  (in kelvins) with the time to failure  $t_r$ , at a *constant* engineering stress  $\sigma$ .<sup>4</sup> The Larson–Miller equation has the form

$$T(\log t_r + C) = m, \quad (13.6)$$

where  $C$  is a constant that depends on the alloy,  $m$  is a parameter that depends on stress, and rupture time. Hence, if  $C$  is known for a particular alloy, one can find  $m$  in a single test. From this result, one can then find the rupture times at any temperature, *as long as the same engineering stress is applied*. Thus, the following procedure is adopted. If we want to know the rupture time at a certain stress level  $\sigma_a$  and temperature  $T_a$ , we conduct the test at  $T_b > T_a$  and stress level  $\sigma_a$ . Substituting these values into Equation 13.6, we find  $m$ . The latter

<sup>4</sup> F. R. Larson and J. Miller, *Trans. ASME*, 74 (1952) 765.

**Fig. 13.5** Relationship between time to rupture and temperature at three levels of engineering stress,  $\sigma_a$ ,  $\sigma_b$ , and  $\sigma_c$ , using Larson–Miller equation ( $\sigma_a > \sigma_b > \sigma_c$ ).

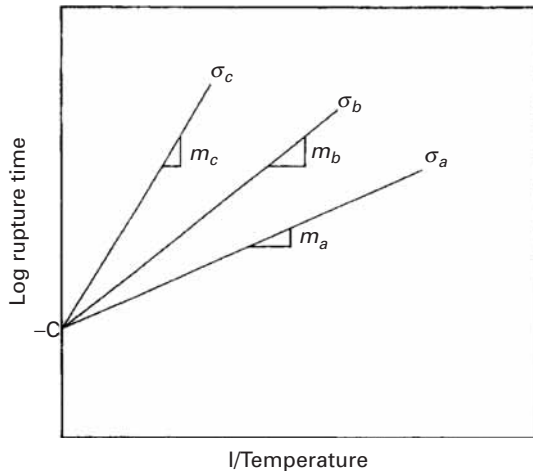
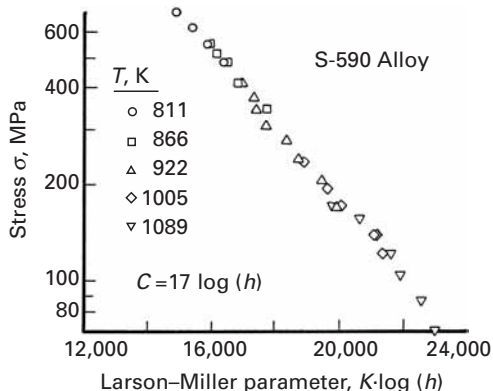


**Fig. 13.6** Master plot for Larson–Miller parameter for S-590 alloy (an Fe-based alloy) ( $C = 17$ ). (From R. M. Goldhoff, *Mater. Design Eng.*, 49 (1959) 93.)



test has a short duration, because the time to rupture decreases with temperature at a constant stress. Figure 13.5 shows schematically the family of lines for different levels of stress. This figure is the graphic representation of Equation 13.6. It can be seen that  $C$  does not depend on the stress; it is the intersection of the various lines. On the other hand, each line has a different slope  $m$ , which is dependent on the stress.

The value of  $C$  is unaltered by the units, as long as the unit of time is hours. However,  $m$  is dependent on units. In the older literature, use is made of English units (Rankine), and a conversion has to be made. At a certain stress level, we need only two data points to establish  $C$  and  $m$ . Since the value of  $C$  is constant for an alloy, we can build a “master plot” that represents the creep rupture response of an alloy over a range of temperatures and stresses. As an example, Figure 13.6 shows the master plot for the ferrous alloy S-590. The data were obtained between 811 and 1,089 K and fall on one single line, due to the correct choice of  $C: 17 \log (\text{hours})$ . From this plot, we can obtain the time to rupture at any temperature and stress.

Soon after Larson and Miller proposed their parameter, Manson and Haferd presented the results of their experiments, which disagreed with Equation 13.6 on the following points:<sup>5</sup>

1. The family of lines intersects not on the ordinate axis ( $1/T = 0$ ), but at a specific point ( $t_a, T_a$ ).
2. A better linearization is obtained if the results are plotted as  $\log t_r$  versus  $T$  instead of  $\log t_r$  versus  $1/T$ .

This led Manson and Haferd to propose the following equation:

$$\frac{\log t_r - \log t_a}{T - T_a} = m. \quad (13.7)$$

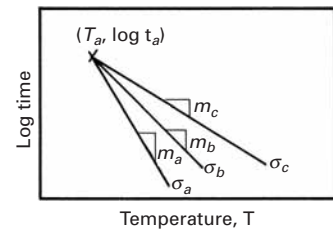


**Fig. 13.7** Relationship between time to rupture and temperature at three levels of stress,  $\sigma_a$ ,  $\sigma_b$ , and  $\sigma_c$ , using Manson-Haferd parameter ( $\sigma_a > \sigma_b > \sigma_c$ ).

Equation 13.7 is represented graphically in Figure 13.7. We use the same extrapolation procedure as that of Larson and Miller to obtain rupture times at different times and temperatures.  $T_a$ ,  $t_r$ , and  $m$  are parameters to be established for a given material.  $T_a$  and  $t_r$  are constant, and  $m$  depends on the stress. In Figure 13.7, three stresses are shown, leading to three lines with different slopes  $m_c > m_b > m_a$ . The times  $t_r$  and  $t_a$  are usually expressed in hours. As with the Larson-Miller parameter, the early literature (up to 1980) usually reports value for the Manson-Haferd parameter in the English system, whereas the more recent literature uses SI units.

Another method that has found considerable success is the Orr-Sherby-Dorn method,<sup>6</sup> based on fundamental studies conducted by Sherby, Dorn, and coworkers with the objective of understanding creep better. The method is based on the fundamental result found by them these researchers, viz.,

$$\ln t_r - \frac{Q}{kT} = m, \quad (13.8)$$

where  $Q$  is the activation energy of diffusion (or creep),  $m$  is the Sherby-Dorn parameter, and  $t_r$  is the time to rupture. Figure 13.8 shows the graphical representation of this parameter. It differs from the Larson-Miller parameter in that the isostress lines are parallel. Equation 13.8 has a certain fundamental justification. Monkman and Grant<sup>7</sup> and others observed that, for a great number of alloys, the minimum creep rate  $\dot{\varepsilon}_s$  was inversely proportional to the rupture time  $t_r$ , or

$$\dot{\varepsilon}_s t_r = k'. \quad (13.9)$$

Applying Equation 13.4, which states that creep is a thermally activated mechanism and that the minimum creep rate increases exponentially with temperature at the same value of stress, and combining

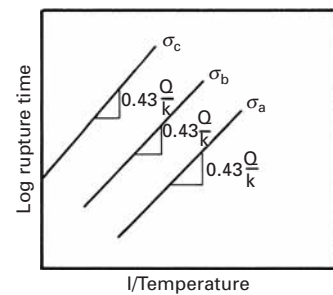


**Fig. 13.8** Relationship between time to rupture and temperature at three levels of stress,  $\sigma_a > \sigma_b > \sigma_c$ , using Sherby-Dorn parameter.

<sup>5</sup> S. S. Manson and A. M. Haferd, NACA TN, 2890, March 1958.

<sup>6</sup> R. L. Orr, O. D. Sherby, and J. E. Dorn, Trans. ASM, 46 (1954) 113.

<sup>7</sup> F. C. Monkman and N. J. Grant, Proc. ASTM, 56 (1956) 593.

**Table 13.1** Some Values of Constants for Time-Temperature Parameters<sup>a</sup>

Material	Sherby-Dorn $Q$ , kJ/mol	Larson-Miller $C$	$T_{a'}$ , K	Manson-Haford $\log t_a$
Various steels and stainless steels	≈400	≈20	—	—
Pure aluminum and dilute alloys	≈150	—	—	—
S-590 alloy (Fe based)	350	17	172	20
A-286 stainless steel	380	20	367	16
Nimonic 81A (Ni-based)	380	18	311	16
1% Cr-1% Mo-0.25%V steel	460	22	311	18

<sup>a</sup> Adapted from N. E. Dowling, *Mechanical Behavior of Materials* (Englewood Cliffs, NJ: Prentice Hall, 1993), p. 699, Table 15.1.

the preexponential terms, we have

$$\dot{\epsilon}_s = A' \exp(-Q_c/kT). \quad (13.10)$$

Substituting Equation 13.9 into Equation 13.10 yields

$$t_r = \frac{k'}{A'} \exp(Q_c/kT).$$

or, taking the logarithm of both sides,

$$\ln t_r - \ln \frac{k'}{A'} = \frac{Q_c}{kT}.$$

Converting to logarithms to the base 10 and setting  $\log k'/A' = m$ , we get

$$2.3 \left( \log t_r - \log \frac{k'}{A'} \right) = \frac{Q_c}{kT}$$

$$\log t_r - m = 0.43 \frac{Q_c}{kT}.$$

The slope of the lines in Figure 13.8 is  $0.43Q_c/k$ , which is equal to  $0.43Q_D/k$ . If we know the activation energy for diffusion and one point on the line, we have all the other points. The activation energy for self-diffusion can be obtained from the diffusion coefficients at two different temperatures. A thermally activated process, the diffusion obeys the equation

$$D = D_0 \exp(-Q_D/kT), \quad (13.11)$$

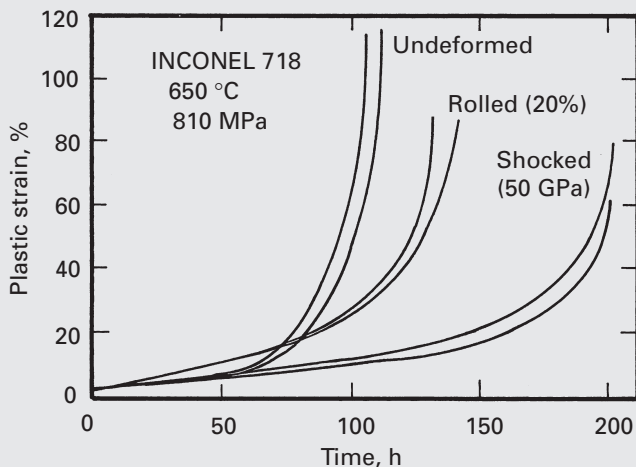
where  $D$  is the diffusion coefficient at  $T$ .

In this and the previous section,  $Q$ , the activation energy, is expressed as energy (joules per atom). If  $Q$  is expressed per mole, or atom gram, then  $R$  (the gas constant) should be used instead of  $k$  (Boltzmann's constant). The value of  $R$  is 8.314 J/(mol K). In Figure 13.8, the slope would be  $(0.43Q)/8.314$ , or  $Q/19.3$  (when  $Q$  is expressed in J/mol).

Table 13.1 presents estimated values for the parameters of the three equations for a number of engineering alloys.

**Example 13.1**

The alloy INCONEL 718 was diligently tested by graduate student M. A. Meyers at 820 MPa and a temperature of 650 °C. Three conditions of the alloy were tested: undeformed, cold-rolled, and shock-hardened (by explosives). After days of patient data collecting (this was in the 1970s prior to automated data recording), he obtained the curves shown in Figure E13.1. Using the Larsen-Miller parameter, determine the times to rupture if this alloy will be used at (a) 550 °C and the same stress and (b) 650 °C and 600 MPa. Take  $C = 18$ .

**Fig. E13.1**

*Solution:*

(a) We use the equation

$$T(\log t_r + C) = m$$

with  $t_r \approx 110$  hours for the undeformed condition,  $t_r \approx 130$  hours for the rolled condition, and  $t_r \approx 200$  hours for the shocked condition. We have

$$T = 650 + 273 = 923 \text{ K}$$

$$923 (\log 110 + 18) = 17,575,$$

$$923 (\log 130 + 18) = 17,642,$$

$$923 (\log 200 + 18) = 17,814.$$

At 550 °C,  $T = 823 \text{ K}$ , and  $t_r = 22.6 \times 10^4$  hours for the undeformed condition,  $t_r = 27.3 \times 10^3$  hours for the rolled condition, and  $t_r = 44.2 \times 10^3$  hours for the shocked condition.

(b) No result can be obtained in this case because the stress has to be constant, for the application of the Larsen-Miller equation to two conditions.

### Example 13.2

Calculate the predicted time to rupture for the undeformed INCONEL 718 superalloy, using the Sherby–Dorn correlation method.

**Solution:** From Table 13.1, (for the Ni-based alloy Nimonic, fairly similar to INCONEL 718):

$$Q \approx 380 \text{ kJ/mol.}$$

We obtain the Sherby–Dorn parameter  $m$ :

$$\log t_r - m = 0.43 \frac{Q_c}{kT},$$

$$m = \log t_r - 0.43 \frac{Q_c}{kT}.$$

Since the activation energy is expressed in J per mol, we have to use  $R$  ( $=8.314 \text{ J/mol K}$ ) instead of  $k$  (Boltzmann's constant). Thus,

$$\begin{aligned} m &= \log 110 - 0.43 \times \frac{380 \times 10^3}{8.314 \times 923} \\ &= 2.04 - 21.29 = -19.25. \end{aligned}$$

Applying Sherby–Dorn's equation to  $550^\circ\text{C}$  ( $823 \text{ K}$ ) yields

$$\log t_r = m + 0.43 \frac{Q_c}{kT} = -19.25 + \frac{0.43 \times 380 \times 10^3}{8.314 \times 823},$$

or

$$t_r = 42.7 \times 10^3 \text{ hours.}$$

### Example 13.3

Calculate the time to rupture at  $650^\circ\text{C}$  and  $100 \text{ MPa}$  stress for a 1% Cr-1% Mo-0.25% V steel, according to the Larson–Miller, Sherby–Dorn, and Manson–Haferd methods, if this alloy underwent rupture in 20 hours when tested in tension at the same stress level at a temperature of  $750^\circ\text{C}$ .

**Solution:** The Larson–Miller equation is  $T(\log t_r + C) = m$ . From Table 13.1,  $C = 22$ . Thus, at  $750^\circ\text{C}$ ,  $T = 750 + 273 = 1,023 \text{ K}$  and  $t_r = 20$  hours. Therefore,

$$m = 1023 \times (\log 20 + 22) \approx 2.4 \times 10^4$$

At  $650^\circ\text{C}$ ,  $T = 650 + 273 = 923 \text{ K}$ , and we have

$$923(\log t_r + 22) = 2.4 \times 10^4,$$

so that

$$\log t_r = \frac{2.4 \times 10^4}{923} - 22$$

and

$$t_r = 6.7 \times 10^3 \text{ hours.}$$

The Sherby-Dorn equation is  $\log t_r - Q/(kT) = m$ . From Table 13.1,  $Q = 460 \text{ kJ/mol}$ . Because  $Q$  here involves moles, we must use  $R$  instead of  $k$ . At  $750^\circ\text{C}$ ,  $T = 1,023 \text{ K}$  and  $t_r = 20 \text{ hours}$ . Thus,

$$m = \log 20 - \frac{460 \times 10^3}{8.314 \times 1023}.$$

At  $650^\circ\text{C}$ ,  $T = 923 \text{ K}$ , and we obtain

$$\log t_r = m + 0.43 \frac{Q}{kT},$$

so that

$$t_r = 6 \times 10^3 \text{ hours.}$$

The Manson-Haferd equation is  $(\log t_r - \log t_a)/(T - T_a) = m$ . From Table 13.1,  $T_a = 311 \text{ K}$ , so that  $\log t_a = 18$ . At  $750^\circ\text{C}$ ,  $T = 1,023 \text{ K}$ , and it follows that  $t_r = 20 \text{ hours}$ . Therefore,

$$m = \frac{\log 20 - 18}{1,023 - 311} = -0.023.$$

At  $650^\circ\text{C}$ ,  $T = 923 \text{ K}$ , and we have

$$\begin{aligned} \frac{\log t_r - \log t_a}{T - T_a} &= m, \\ \frac{\log t_r - 18}{923 - 311} &= -0.023, \\ \log t_r &= 3.924, \\ t_r &= 8.4 \times 10^3 \text{ hours.} \end{aligned}$$

This answer is very sensitive to  $m$ . For  $m = -0.02345$ , we get  $t_r = 4.4 \times 10^3 \text{ hours}$ .

### 13.3 Fundamental Mechanisms Responsible for Creep

The history of progress in our understanding of creep can be divided into two periods: before and after 1954. In that year, Orr et al. introduced the concept that the activation energy for creep and diffusion are the same for an appreciable number of metals (more than 25).<sup>8</sup> Figure 13.9 shows this graphically. The activation energy for diffusion is connected to the diffusion coefficient by Equation 13.11. Note that several mechanisms can be responsible for creep; the rate-controlling mechanism depends both on the stress level and on the temperature, as will be seen in Sections 13.4–13.7. For temperatures below  $0.5T_m$ , half the melting point of the material, in kelvins, the activation

<sup>8</sup> R. L. Orr, O. D. Sherby, and J. E. Dorn, *op. cit.*, 113.

**Fig. 13.9** Activation energies for creep (stage II) and self-diffusion for a number of metals. (Adapted with permission from O. D. Sherby and A. K. Miller, *J. Eng. Mater. Technol.*, 101 (1979) 387.)

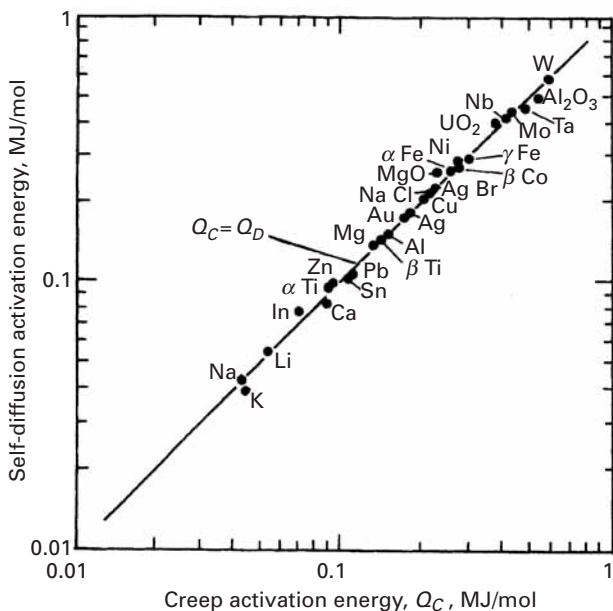
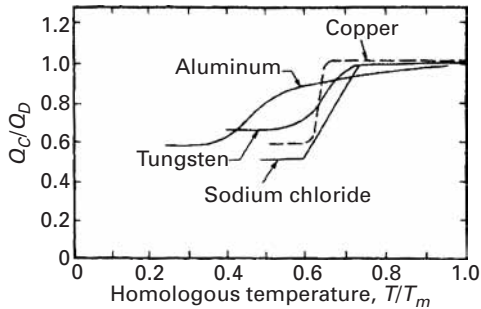


**Fig. 13.10** Ratio between activation energy for secondary creep and activation energy for bulk diffusion as a function of temperature. (Adapted with permission from O. D. Sherby and A. K. Miller, *J. Eng. Mater. Technol.*, 101 (1979) 387.)



energy for creep tends to be lower than that for self-diffusion, because diffusion takes place preferentially along dislocations (pipe diffusion), instead of in bulk. Figure 13.10 shows the variation in  $Q_C/Q_D$  for some metals and ceramics. The activation energy for diffusion through dislocations is considerably lower than that for bulk diffusion.

For the temperature range  $T > 0.5 T_m$ , the mechanisms responsible for creep can be conveniently described as a function of the applied stress. The creep mechanisms can be divided into two major groups: boundary mechanisms, in which grain boundaries and, therefore, grain size, play a major role; and lattice mechanisms, which occur independently of grain boundaries. In Equation 13.4, the exponent  $p = 0$  for lattice mechanisms, and  $p \geq 1$  for boundary mechanisms.

### 13.4 | Diffusion Creep ( $\sigma/G < 10^{-4}$ )

Diffusion creep tends to occur for  $\sigma/G \leq 10^{-4}$ . (This value depends, to a certain extent, on the metal.) Two mechanisms are considered

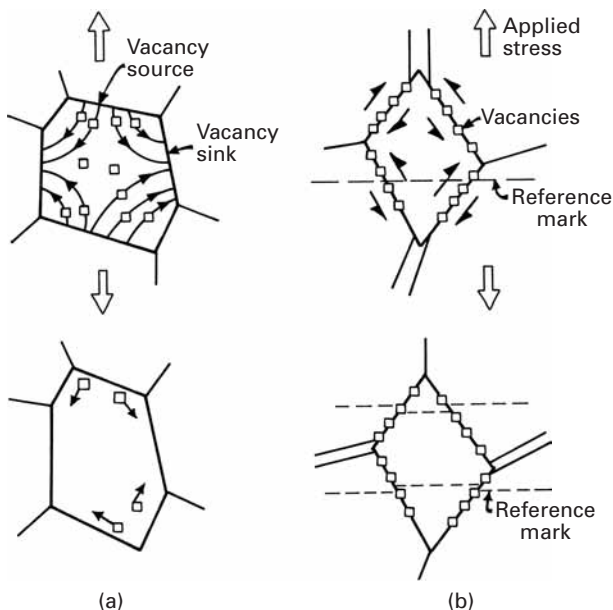


**Fig. 13.11** Flow of vacancies according to (a) Nabarro–Herring and (b) Coble mechanisms, resulting in an increase in the length of the specimen.

important in the region of diffusion creep. Nabarro and Herring proposed the mechanism shown schematically in Figure 13.11(a).<sup>9</sup> It involves the flux of vacancies inside the grain. The vacancies move in such a way as to produce an increase in length of the grain along the direction of applied (tensile) stress. Hence, the vacancies move from the top and bottom region in the figure to the lateral regions of the grain. The boundaries perpendicular (or close to perpendicular) to the loading direction are distended and are sources of vacancies. The boundaries close to parallel to the loading direction act as sinks.

Nabarro and Herring developed a mathematical expression connecting the vacancy flux to the strain rate. They started by supposing that the “source” boundaries had a concentration of vacancies equal to  $C_0 + \Delta C$  and the sink boundaries a concentration  $C_0$ . They assumed that

$$\Delta C = \frac{C_0\sigma}{kT},$$

where  $\sigma$  was the applied stress and  $C_0$  the equilibrium vacancy concentration. The flux of vacancies is therefore given by

$$J = k'D_\ell \left( \frac{\Delta C}{x} \right) = k''D_\ell \left( \frac{\Delta C}{d} \right),$$

where  $x$  is the diffusion distance, which is a direct function of the grain size (approximately equal to  $d/2$ ),  $D_\ell$ , is the lattice diffusion coefficient,  $d$  is the grain diameter, and  $k'$  and  $k''$  are proportionality constants ( $k'' = 2k'$ ). The strain rate is related to the increase in grain

<sup>9</sup> F. R. Nabarro, *Report of a Conference on Strength of Solids*, Physical Society, London, 1948, p. 75; and C. Herring, *J. Appl. Phys.*, 21 (1950), 437.

size  $d$  in the direction of the applied stress:

$$\dot{\varepsilon} = \frac{1}{d} \frac{dd}{dt}.$$

The change in grain length,  $dd/dt$ , can be obtained from the flux of vacancies, each having a volume  $\Omega$ :

$$\frac{dd}{dt} = J\Omega.$$

Thus, the following equation can be obtained for the creep rate:

$$\dot{\varepsilon}_{\text{NH}} = k'' \frac{\Omega D_\ell C_0 \sigma}{d^2 k T}.$$

(“NH,” of course, denotes Nabarro–Herring.) Expressing this equation in the format of Equation 13.5 (making  $\Omega = 0.7b^3$ ), we have:

$$\dot{\varepsilon}_{\text{NH}} = A_{\text{NH}} \frac{D_\ell G b}{kT} \left( \frac{b}{d} \right)^2 \left( \frac{\sigma}{G} \right).$$

(13.12)

$A_{\text{NH}}$  is typically equal to 10–15.

Coble proposed the second mechanism explaining diffusion creep.<sup>10</sup> It is based on diffusion in the grain boundaries instead of in the bulk. This diffusion results in sliding of the grain boundaries. Hence, if a fiducial scratch is made on the surface of the specimen prior to creep testing, the scratch will show a series of discontinuities (at the grain boundaries) after testing if Coble creep is operative.

Figure 13.11(b) shows, in a schematic manner, how the flow of vacancies along a boundary generates shear. Notice that there is also additional accommodational diffusion necessary. Coble creep leads to the relationship

$$\dot{\varepsilon}_c = A_c D_{\text{gb}} \frac{G b}{kT} \left( \frac{\delta}{b} \right) \left( \frac{b}{d} \right)^3 \left( \frac{\sigma}{G} \right), \quad (13.13)$$

where  $A_c$  is typically equal to 30–50,  $\delta$  is the effective width of the grain boundary for diffusion, and  $D_{\text{gb}}$  is the grain-boundary diffusion coefficient.

Note that in Equations 13.12 and 13.13, the strain rate is proportional to the stress – that is,  $n = 1$ . Also, the strain rate goes as  $d^{-2}$  for Nabarro–Herring creep and as  $d^{-3}$  for Coble creep. This enables researchers to differentiate between the two mechanisms: they establish the creep rates for specimens with different grain sizes and find the exponent on the grain size. A practical way of having an alloy with high resistance to Nabarro–Herring or Coble creep is to increase the size of the grains. This method is used in superalloys; a fabricating technique called *directional solidification* has been developed to eliminate virtually all grain boundaries perpendicular and inclined to the tensile axis.

---

<sup>10</sup> R. L. Coble, *J. Appl. Phys.*, 34 (1963) 1679.

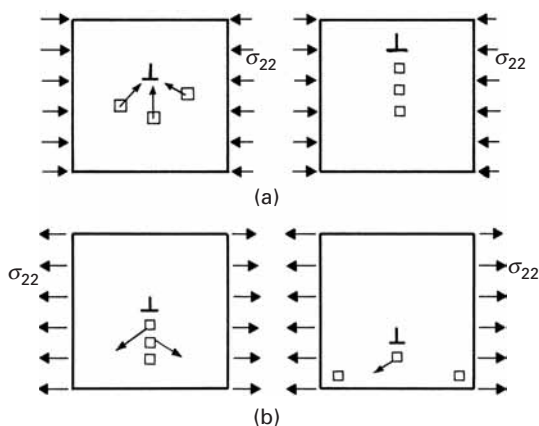


**Fig. 13.12** Dislocation climb (a) upward, under compressive  $\sigma_{22}$  stresses, and (b) downward, under tensile  $\sigma_{22}$  stresses.

Harper and Dorn observed another type of diffusional creep in aluminum.<sup>11</sup> This occurred at high temperatures and low stresses, and the creep rates were over 1,000 times greater than those predicted by Nabarro-Herring. (Also, little Coble creep was observed.) The two researchers concluded that creep occurred exclusively by dislocation climb.

Dislocation climb is shown schematically in Figure 13.12. Under compressive loads, vacancies are attracted to the dislocation line (Figure 13.12(a)). Once a row of vacancies has joined the dislocation line, the line is effectively translated upward. Thus, the dislocation moves perpendicular to the Burgers vector during climb. In tension (Figure 13.12(b)), the opposite occurs: Vacancies move away from the dislocation line, and the dislocation effectively moves down.

Harper-Dorn creep is governed by an equation of the form

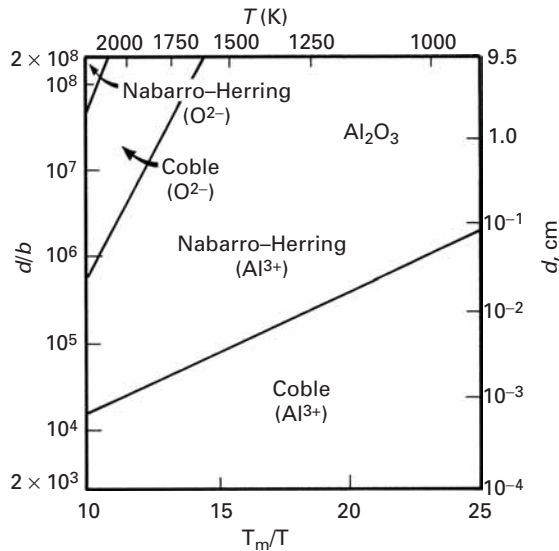
$$\dot{\varepsilon}_{\text{HD}} = A_{\text{HD}} \frac{D_\ell G b}{kT} \left( \frac{\sigma}{G} \right). \quad (13.14)$$

The parameter  $A_{\text{HD}}$  is typically equal to  $10^{-11}$ . Since no grain boundaries are involved in this creep, the grain size does not appear in the equation. For Harper-Dorn creep to make a significant contribution, the grain size of the material has to be large ( $>400 \mu\text{m}$ ); otherwise, Nabarro-Herring and Coble creep dominate.

In metals, Harper-Dorn creep has been observed in a number of systems. In ceramics, there is little evidence for this type of diffusion creep mechanism. Ceramics in general have small grain sizes, which favor other creep mechanisms. The stable, small grain size and the limited number of slip systems, as well as high Peierls-Nabarro stress, lead to the prominence of Nabarro-Herring and Coble creep. Diffusion in ceramics is more complex than in metals, because either one or two ionic species might participate, and in the case of multi-component ceramics, more than one cation or ion might be involved. Figure 13.13 shows the different domains of creep in alumina as a

<sup>11</sup> J. Harper and J. E. Dorn, *Acta Met.*, 5 (1957) 654.

**Fig. 13.13** Different regimens for diffusion creep in alumina; notice that cations ( $\text{Al}^{3+}$ ) and anions ( $\text{O}^{2-}$ ) have different diffusion coefficients, leading to different regimes of dominance. (From A. H. Chokshi and T. G. Langdon, *Defect and Diffusion Forum*, 66–69 (1989) 1205.)



function of grain size and temperature; the main ion is shown for each domain.

### 13.5 Dislocation (or Power Law) Creep ( $10^{-4} < \sigma/G < 10^{-2}$ )

In the stress range  $10^{-4} < \sigma/G < 10^{-2}$ , creep tends to occur by dislocation glide aided by vacancy diffusion (when an obstacle is to be overcome); this is called dislocation creep. This mechanism should not be confused with Harper-Dorn creep, which relies exclusively on dislocation climb. Orowan proposed that creep is a balance between work-hardening (due to plastic strain) and recovery (caused by exposure to high temperatures). Hence, at a constant temperature, the increase in stress is

$$d\sigma = \left( \frac{\partial \sigma}{\partial \varepsilon} \right) d\varepsilon + \left( \frac{\partial \sigma}{\partial t} \right) dt, \quad (13.15)$$

where  $(\partial \sigma/\partial \varepsilon)$  is the rate of hardening, and  $(\partial \sigma/\partial t)$  is the rate of recovery, of the material. The strain rate  $\dot{\varepsilon}$  can be expressed as a ratio between the rate of recovery and the rate of hardening.

In the mid-1950s, Weertman developed a pair of theories of the minimum creep rate based on dislocation climb as the rate-controlling step.<sup>12</sup> In his first theory, Weertman presented Cottrell-Lomer locks as barriers to plastic deformation; his second theory applies to HCP metals, in which these barriers do not exist. Hence, he assumed different barriers, depending on the material. Figure 13.14 shows schematically how the mechanism based on Cottrell-Lomer locks operates. Dislocations are pinned by obstacles, but overcome

<sup>12</sup> J. Weertman, *J. Appl. Phys.*, 26 (1955) 1213; 28 (1957) 362.

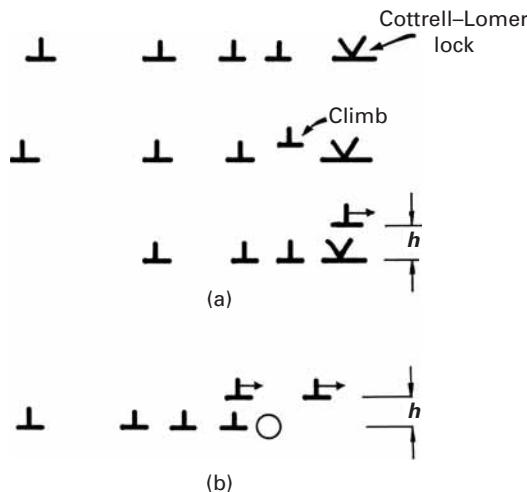


**Fig. 13.14** Dislocation overcoming obstacles by climb, according to Weertman theory.  
(a) Overcoming Cottrell-Lomer locks. (b) Overcoming an obstacle.

them by climb, aided by either interstitial or vacancy generation or destruction. The obstacles are assumed to be Cottrell-Lomer locks, which are formed by dislocations that intersect and react. (See Section 4.4.6.) Figure 13.14(a) shows dislocations pinned between the locks and climbing over them. Note that dislocations are continuously generated by the Frank-Read source in the horizontal plane, and the ones overcoming the obstacle are replaced by others. To calculate the creep rate, we have to find the rate of escape of the dislocations from the locks. The height  $h$  a dislocation has to climb in order to pass through a lock is the position at which the applied stress on the dislocation, owing to the other dislocations in the pileup, is equal to the repulsive force due to the stress field of the lock. Other obstacles (shown in Figure 13.14(b)) can have the same effect.

The stress exerted by a dislocation due to the pileup effect is given in Section 4.4.9 and is (Equation 4.26a):<sup>13</sup>

$$\sigma^* = \tilde{n}\sigma, \quad (13.16)$$

where  $\tilde{n}$  is the number of dislocations in the pileup (we use  $\tilde{n}$  here to avoid confusion with  $n$ , the exponent in power-law creep) and  $\sigma$  is the stress applied on one dislocation. Now, taking the stress field around a dislocation as a function of distance (Section 4.4.3) and equating it to Equation 13.16, Weertman arrives at (this is slightly different from Equation 4.12)

$$h = \frac{Gb}{\tilde{n}\sigma 6\pi(1-v)}. \quad (13.17)$$

The rate of climb is determined by the rate at which the vacancies arrive at or leave the dislocation. (Weertman did the derivation for vacancies and not interstitials.) For the concentration gradient of vacancies, Weertman obtained a rate of climb

$$r = \frac{N_0 D_\ell \tilde{n} \sigma b^5}{kT}, \quad (13.18)$$

<sup>13</sup> Shear stresses were converted into normal stresses.

when  $(\tilde{n}\sigma b^3)/kT < 1$ .  $N_0$  is the equilibrium concentration of vacancies and  $D_\ell$  is the diffusion coefficient at the test temperature  $T$ . With a known climb height and rate of climb, it is possible to calculate the rate of creep. If  $M$  is the number of active Frank-Read sources per unit volume,  $L$  is the distance the edge portion of a dislocation loop moves after breaking away from a barrier, and  $L'$  is the portion the screw moves, then the creep rate is given by

$$\dot{\varepsilon} = \frac{r}{h} LL'M = \frac{6\pi(1-v)\tilde{n}^2b^4N_0LL'MD_\ell\sigma^2}{kGT}. \quad (13.19)$$

If we assume, to a first approximation, that  $\tilde{n}$ , the number of dislocations in a pileup, and  $M$ , the number of Frank-Read sources per unit volume, are proportional to  $\sigma$ , we can recast Equation 13.19 in the Mukherjee-Bird-Dorn format as

$$\dot{\varepsilon} = A \left( \frac{D_\ell G b}{kT} \right) \left( \frac{\sigma}{G} \right)^5.$$

The stress exponent 5 is characteristic of this regimen. The term  $A$  incorporates the various parameters and proportionality coefficients. Power law creep with  $n \approx 5$  has been observed at high stress levels in a number of ceramics, including KBr, KCl, LiF, NaCl, NiO, SiC, ThO<sub>2</sub>, UC, and UO<sub>2</sub>. (See Figure 13.4(b).) As in the case of metals, the substructure is characterized by subgrains with misorientations of approximately 2°.

Creep behavior with a stress exponent  $n \approx 3$  is observed in a number of ceramics, such as Al<sub>2</sub>O<sub>3</sub>, BeO, Fe<sub>2</sub>O<sub>3</sub>, MgO, and ZrO<sub>2</sub> (+ 10% Y<sub>2</sub>O<sub>3</sub>). In this case, few or no solutes are present, and those that are do not play a role.

Dispersion-strengthened alloys are characterized by an exponent higher than 7 and by a high activation energy for creep. Dispersoids (see Chapter 10) are stable up to very high temperatures. Small particles, such as Y<sub>2</sub>O<sub>3</sub> and ErO<sub>2</sub>, are added to the alloy as dispersoids; this increases the high-temperature capability of these materials substantially, and the dispersoids act as effective barriers to dislocation motion.

Particle-reinforced composites (such as SiC and aluminum reinforced with aluminum oxide) exhibit the same effects: The stress exponent  $n$  and activation energy for creep are very high. This is illustrated in Figure 13.15, for an Al-30% SiC composite. The slope in Figure 13.15 is given by

$$n = \frac{\partial \ln \dot{\varepsilon}}{\partial \ln \tau} = \frac{\partial \ln 2\dot{\varepsilon}}{\partial \ln \sigma/2} = \frac{\partial \ln \dot{\varepsilon}}{\partial \ln \sigma}.$$

Taking logarithms and derivatives of both sides, we have (at constant T)

$$\begin{aligned} \dot{\varepsilon} &= A' \left( \frac{\sigma}{G} \right)^n = A'' \sigma^n, \\ \ln \dot{\varepsilon}_s &= \ln A'' + n \ln \sigma, \\ \partial \ln \dot{\varepsilon}_s &= n \partial \ln \sigma, \\ n &= \frac{\partial \ln \dot{\varepsilon}_s}{\partial \ln \sigma}. \end{aligned}$$

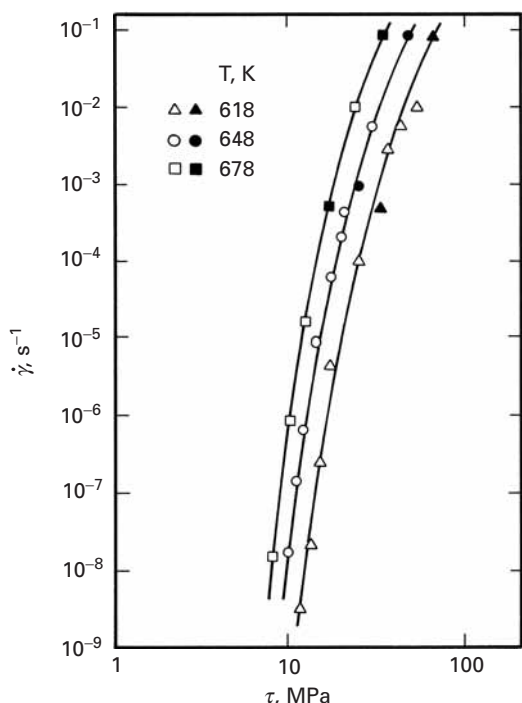


**Fig. 13.15** Shear stress vs. shear strain rate in an aluminum (6061) with 30 vol.% SiC particulate composite in creep. (From K.-T. Park, E. J. Lavernia, and F. A. Mohamed, *Acta Met. Mater.*, 38 (1990) 2149.)

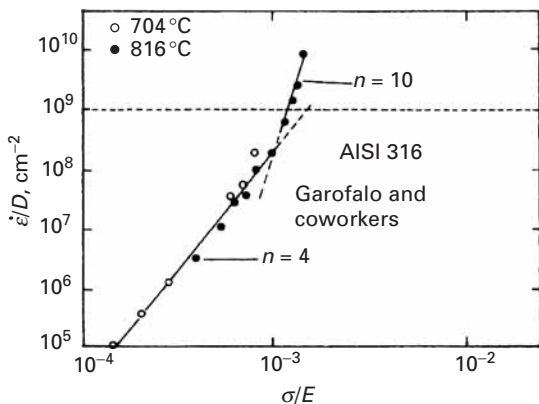


**Fig. 13.16** Power relationship between  $\dot{\epsilon}$  and  $\sigma$  for AISI 316 stainless steel. (Adapted with permission from S. N. Monteiro and T. L. da Silveira, *Metalurgia-ABM*, 35 (1979) 327.)

Thus, the slope is equal to the stress exponent. In Figure 13.15, the slope  $n$  varies from 14.7 to 7.4 as the stress is increased. The activation energy for creep for this aluminum composite has a value of 270–500 kJ/mol; this is significantly higher than the activation energy for aluminum self-diffusion.

### 13.6 | Dislocation Glide ( $\sigma/G > 10^{-2}$ )

Dislocation glide occurs for  $\sigma/G > 10^{-2}$ . At a certain stress level, the power law breaks down. Figure 13.16 presents the region in which the law ( $n = 4$ ) breaks down, and  $n$  increases to 10; this occurs for  $\dot{\epsilon}_s/D > 10^9$ . An analysis of the deformation substructure by transmission electron microscopy and showed that, at high stresses, dislocation

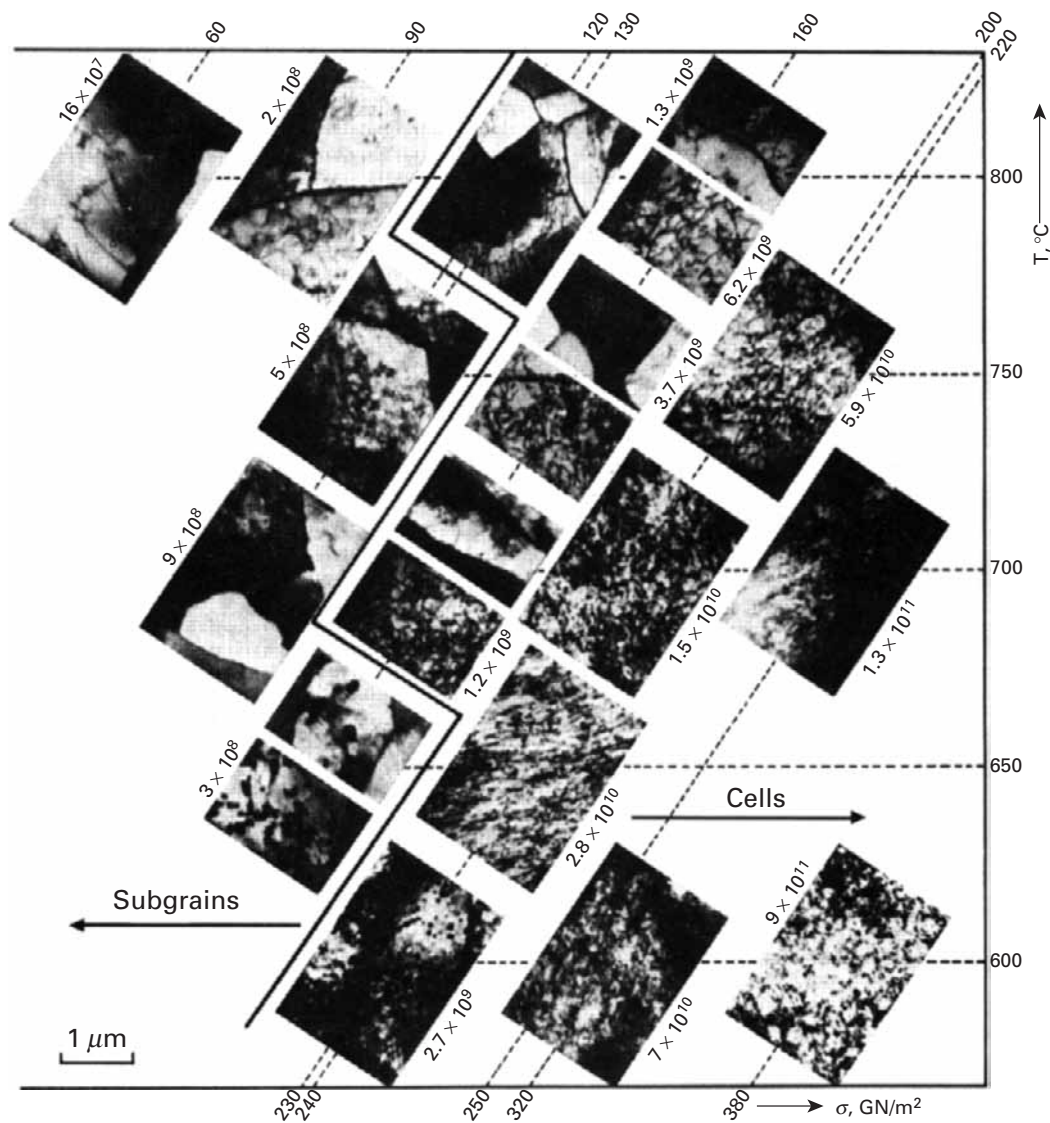


**Fig. 13.17** Effect of stress and temperature on deformation substructure developed in AISI 316 stainless steel in middle of stage II. (Reprinted with permission from H.-J. Kestenbach, W. Krause, and T. L. da Silveira, *Acta Met.*, 26 (1978) 661.)

climb was replaced by dislocation glide, which does not depend on diffusion.<sup>14</sup> Hence, when  $\dot{\varepsilon}_s/D > 10^9$ , thermally activated dislocation glide is the rate-controlling step; this is the same deformation mode as the one in conventional deformation at ambient temperature. Kestenbach et al. observed that the substructure changed from equiaxial subgrains to dislocation tangles and elongated subgrains when the stress reached a critical level. A similar effect is observed when the temperature is decreased and the stress is maintained constant. Figure 13.17 shows the substructures at various values of stress and temperatures for secondary creep.

<sup>14</sup> H.-J. Kestenbach, W. Krause, and T. L. da Silveira, *Acta Met.* 26 (1978) 661.

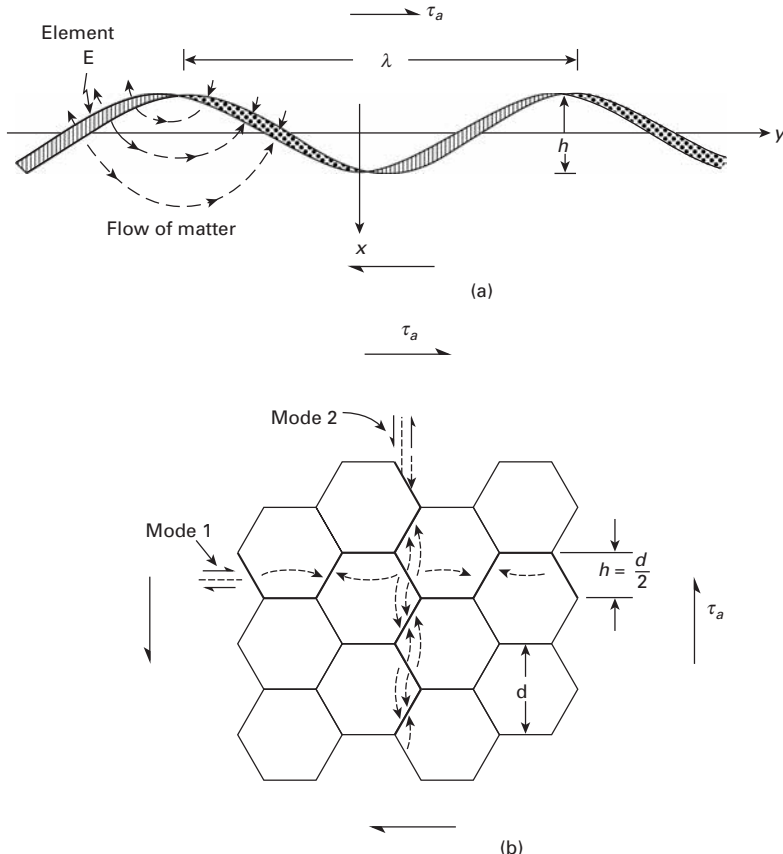


**Fig. 13.18** (a) Steady-state grain-boundary sliding with diffusional accommodations. (b) Same process as in (a), in an idealized polycrystal; the dashed lines show the flow of vacancies. (Reprinted with permission from R. Raj and M. F. Ashby, *Met. Trans.*, 2A (1971) 1113.)

## 13.7 | Grain-Boundary Sliding

Grain-boundary sliding usually does not play an important role during primary or secondary creep. However, in tertiary creep it does contribute to the initiation and propagation of intercrystalline cracks. Another deformation process to which it contributes significantly is superplasticity; it is thought that most of the deformation in superplastic forming takes place by grain-boundary sliding.

The grain-boundary sliding rate is controlled by the accommodating processes where the sliding surface deviates from a perfect plane. One can readily see that we cannot have a perfect plane defined by the boundaries between different grains; we cannot look separately at the sliding between two grains having a common interface. The requirements of strain compatibility are such that we have to model the interface as sinusoidal, as is depicted in Figure 13.18. The applied stress  $\tau_a$  can produce sliding only if it is coupled with diffusional flow that transports material (or vacancies) over a maximum distance of  $\lambda$ , the wavelength of the irregularities. Figure 13.18(b) shows the same effect in a polycrystalline aggregate. The individual grain boundaries

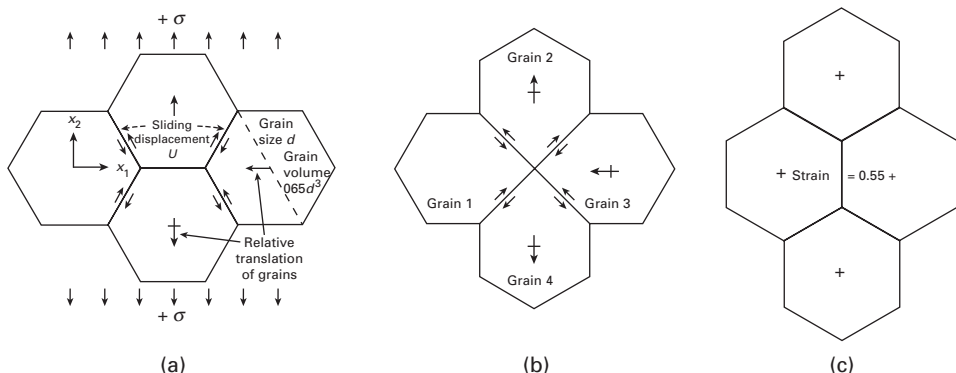


**Fig. 13.19** Grain-boundary sliding assisted by diffusion in Ashby–Verrall’s model. (Reprinted with permission from M. F. Ashby and R. A. Verrall, *Acta Met.*, 21 (1973) 149.)

are translated by a combination of sliding and diffusional flow under the influence of the applied stress.

The manner in which the individual grains move and change their relative positions by sliding and diffusional accommodation is shown in Figure 13.19. The sliding of grains under the influence of  $\sigma$ , coupled with minor changes in shape, makes possible the sequence (a)–(b)–(c), which results in a strain of 0.55; the unique feature of this mechanism is that the sequence is accomplished with relatively little strain *within* the grains.

### 13.8 Deformation-Mechanism (Weertman–Ashby) Maps

Deformation-mechanism maps, so named after two people who first introduced them, are a graphical description of creep, representing the ranges in which the various deformation modes are rate-controlling steps in the stress-versus-temperature space. Weertman–Ashby plots assume, for simplicity, that there are some independent and distinguishable ways by which a polycrystal can be deformed, but still retain its crystallinity:

1. Above the theoretical shear strength, plastic flow of the material can take place without dislocations, by simple glide of one atomic plane over another.
2. Movement of dislocations by glide.
3. Dislocation creep, including glide and climb, both being controlled by diffusion.
4. Nabarro–Herring creep.
5. Coble creep.

The theories developed for these different modes of deformation without loss of crystallinity propose constitutive equations that are used in the establishment of the ranges involved. Figure 13.20 shows a typical map for silver. The theoretical shear stress is approximately equal to  $G/20$  and is practically independent of temperature. A small dependence on temperature is exhibited by  $G$  and is built into the ordinate of

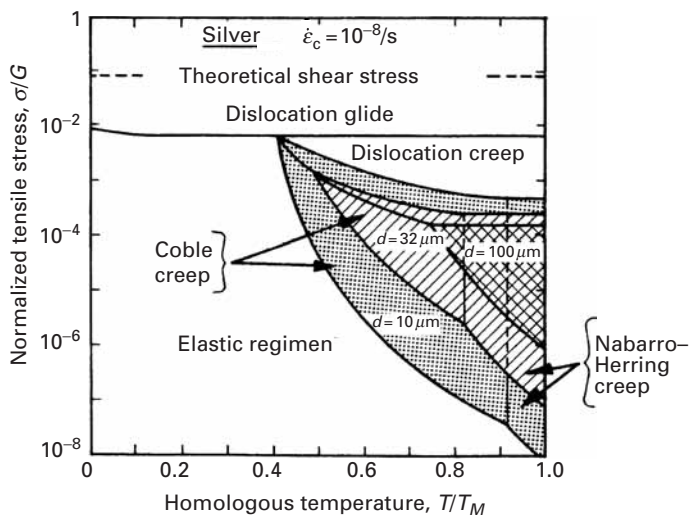


**Fig. 13.20** Weertman-Ashby map for pure silver, established for a critical strain rate of  $10^{-8} \text{ s}^{-1}$ ; it may be seen how the deformation-mechanism fields are affected by the grain size. (Adapted with permission from M. F. Ashby, *Acta Met.*, 20 (1972) 887.)

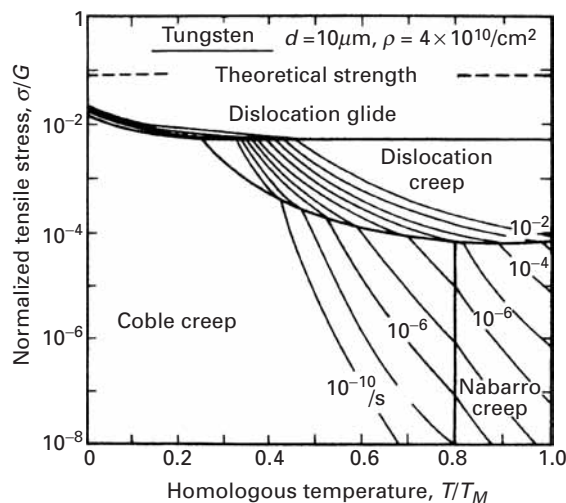
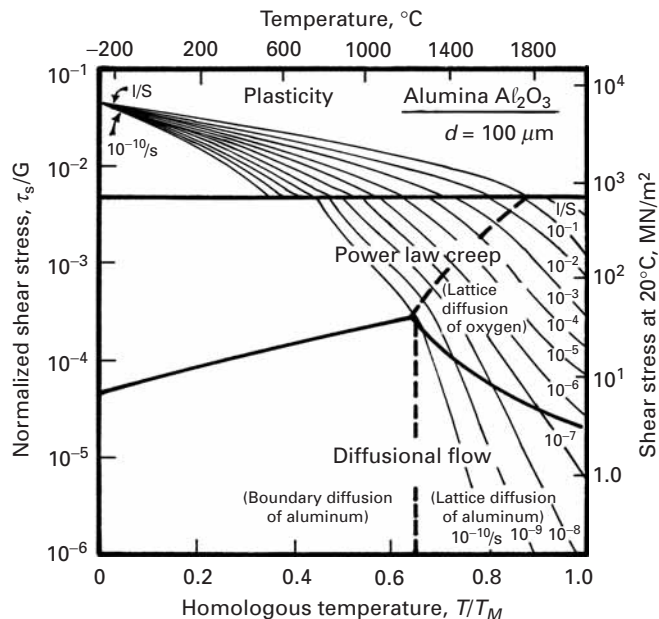


**Fig. 13.21** Weertman-Ashby map for tungsten, showing constant strain-rate contours. (Reprinted with permission from M. F. Ashby, *Acta Met.*, 20 (1972) 887.)

the figure. For values of  $\sigma/G$  between  $10^{-1}$  and  $10^{-2}$ , slip by dislocation movement is the controlling mode at all temperatures. It can be seen that the grain size affects the extent of the fields. Three grain sizes are represented: 10, 32, and 100  $\mu\text{m}$ . The fields also depend on the strain rate. The map shown in Figure 13.21 was made for a strain rate of  $10^{-8} \text{ s}^{-1}$ . The Coble and Nabarro-Herring mechanisms, especially, are affected by the grain size, because of their nature.

Deformation-mechanism maps have technological applications. Consider, for example, a turbine blade operated in a temperature and stress range that is known. The specific stress-temperature profile can be plotted on a deformation-mechanism map in the form of a line. Different parts of the blade undergo different deformation modes. These modes, the rate of creep of each portion, and the respective constitutive equation can be read from the map. Multiaxial stress states can be resolved by calculating the maximum shear stress

**Fig. 13.22** Weertman–Ashby map for  $\text{Al}_2\text{O}_3$  with a grain size of  $100 \mu\text{m}$ . (Adapted from H. J. Frost and M. F. Ashby, *Deformation-Mechanism Maps*, (New York: Pergamon Press, 1982), p. 100.)



or the effective stress. A strengthening mechanism is helpful only if it retards the creep rate in the correct portion of the map. For instance, dispersion-hardening is effective in controlling dislocation glide and climb, but cannot effectively stop Nabarro–Herring or Coble creep.

From the deformation-mechanism map, we can, in addition to determining the dominant mechanism for a certain combination of stress and temperature, find the strain rate (creep rate) that will result. For this, we have to apply the appropriate constitutive equations and plot the constant strain-rate contours. This is shown in Figure 13.21 for tungsten. The lines allow ready identification of the creep rate. The region in Figure 13.20 consisting of the elastic regimen is occupied by Coble creep in Figure 13.21. The reason for this is that Figure 13.20 applies to one constant strain rate ( $10^{-8} \text{ s}^{-1}$ ), whereas Figure 13.21 is built for a whole range of strain rates. Hence, at a strain rate of  $10^{-8} \text{ s}^{-1}$ , the metal might respond elastically, whereas at a strain rate orders of magnitude lower, Coble creep becomes significant.

Similar maps can be built for ceramics, and a representative map is shown in Figure 13.22. The different domains, as well as the curves for constant strain rates (from  $10^{-10}/\text{s}$  to  $1/\text{s}$ ), are illustrated in the plot. Note that the different diffusing ions ( $\text{Al}^{3+}$  and  $\text{O}^{2-}$ ) have to be considered.

### 13.9 | Creep-Induced Fracture

Figure 13.23 shows fracture by nucleation and growth of voids at the grain boundaries. Whereas at low and moderate temperatures metals usually fail by transgranular void or crack formation, at high

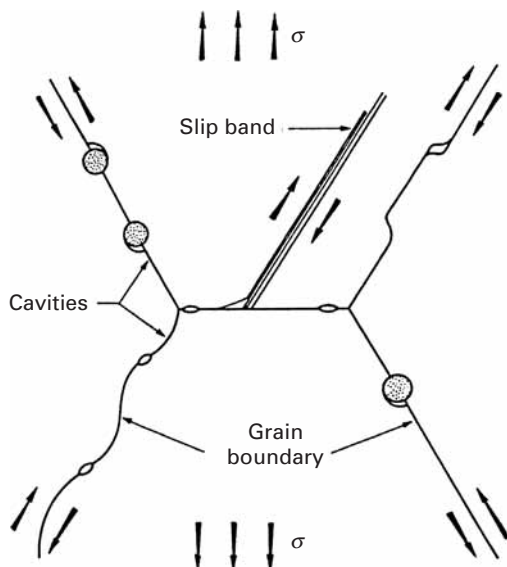


**Fig. 13.23** Mechanisms of intergranular nucleation. (From W. D. Nix and J. C. Gibeling, in *Flow and Fracture at Elevated Temperatures*, ed, R. Raj (Metals Park, OH: ASM, 1985).)

temperatures, and especially after creep and superplastic forming, intergranular cavities start forming; they subsequently grow and coalesce, leading to a fracture morphology which is readily distinguishable: observation by scanning electron microscope reveals entire grains on the fracture surface. There are several reasons why cavities (voids and cracks) form at the grain boundaries.

- Impurity segregation at grain boundaries leads to a weakening of these regions. Since the boundary has a different composition from the matrix, under these conditions, we may have:

$$(T_m)_{gb} < (T_m)_\ell ,$$

where  $T_m$  is the melting point and  $gb$  and  $\ell$  refer to the grain boundary and lattice, respectively. This leads to a selective weakening of the boundaries, at high temperatures.

- Interaction of grain-boundary sliding with geometrical (compatibility) constraints. We saw in Section 13.7 that grain-boundary sliding needs to be coupled with plastic deformation of cavities at grain boundaries due to interaction with grain-boundary inclusion. This is due to a step in the grain boundary, and to waviness of the boundary.
- Slip band-boundary interaction. At higher stresses dislocation glide is important in creep, and the intersection of slip bands with boundaries leads to stress concentrations, which may result in opening up of wedges.
- Enhanced grain-boundary diffusion. The combined effect of stress concentrations and higher grain-boundary diffusion coefficients (can be several orders of magnitude higher than lattice diffusion) leads to void growth at the grain boundaries, which is much faster than in the grain interiors.

As a result of the nucleation and growth of cavities, the creep rate is accelerated even under constant stress testing, and the creep curve starts deviating from stage II. (See Figure 13.1; this marks the onset of stage III, or tertiary creep.)

Creep failure is governed by maximum creep strain in many cases. This is the basis for the Monkman–Grant equation (Equation 13.9, Section 13.2):

$$\dot{\varepsilon}_s t_r = k,$$

where  $\dot{\varepsilon}_s$  is the creep rate in the steady state,  $t_r$  is the time-to-rupture, and  $k$  is a constant. The above expression is obtained from:

$$\int_0^{t_r} \dot{\varepsilon}_s dt = \dot{\varepsilon}_s t_r = \varepsilon_r.$$

We assume that  $\varepsilon_r$ , the ruptuse strain, is a constant for a material. For nickel, the rupture strain, is equal to  $4 \times 10^{-2}$ .

Raj and Ashby<sup>15</sup> developed a model to predict the time-to-rupture time,  $t_r$ , as a function of a number of material parameters. Their expression has the form:

$$t_r = \frac{3\pi^{1/2}}{32} \frac{kT}{\Omega \delta D_{gb}} \frac{\lambda^3}{\sigma} \frac{f_v(\alpha)}{f_b(\alpha)} \int_{A_{min}}^{A_{max}} \frac{dA}{f(A)},$$

where the symbols have the following meanings:  $A$  = areal fraction of grain boundaries occupied by cavities;  $\delta$  = grain-boundary thickness;  $\Omega$  = atomic volume;  $D_{gb}$  = grain-boundary diffusion coefficient;  $\lambda$  = spacing between cavities;  $T$  = temperature in K;  $k$  = Boltzmann's constant.

The function  $f(A)$  in the integral is equal to:

$$f(A) = \frac{\left[1 - \left(\frac{A}{A}\right)^{1/2}\right](1 - A)}{A^{1/2} \left[\frac{1}{2} \ln\left(\frac{1}{A}\right) - \frac{3}{4} + A \left(1 - \frac{A}{4}\right)\right]}.$$

Rupture occurs when  $A$  reaches a maximum value  $A_{max}$ . The functions  $f_v(\alpha)$ ,  $f_b(\alpha)$  represent the dihedral angle (voids at grain boundaries are lens-shaped and not spherical) and the geometry of voids, respectively. When  $A$  reaches a value equal to  $A_{max}$ , the specimen fails.

It may be seen that the Raj–Ashby equation is consistent with the Monkman–Grant equation when the stress exponent in creep is equal to one. This occurs for Nabarro–Herring, Coble, and Harper–Dorn creep (Equations 13.12, 13.13, and 13.14). For instance, substituting the Coble creep equation into the Raj–Ashby equation, we obtain:

$$\dot{\varepsilon}_s t_r = \frac{3\pi^{1/2}}{32} \frac{A_c b^3 \lambda^3}{\Omega d^3} \frac{f_v(\alpha)}{f_b(\alpha)} \int_{A_{min}}^{A_{max}} \frac{dA}{f(A)}.$$

The right-hand side of this equation consists of a number of material parameters. Thus, the product  $\dot{\varepsilon}_s t_r$  should be a constant, which should, in theory, be equal to the rupture strain,  $\varepsilon_r$ .

<sup>15</sup> R. Raj and M. F. Ashby, *Acta Mater.*, 23 (1975) 653.

### Example 13.4

From Figure E13.4 for Zircaloy under two conditions determine the Monkman–Grant rupture strain at three different strain rates. The failure strain is 0.1. Is the Monkman–Grant equation obeyed?

**Solution:** We take the three strain rates:

$$\dot{\varepsilon}_1 = 5 \times 10^{-5},$$

$$\dot{\varepsilon}_2 = 5 \times 10^{-4},$$

$$\dot{\varepsilon}_3 = 5 \times 10^{-3}.$$

The following rupture times are obtained from the plot:

$$t_{r1} = 2,000\text{s},$$

$$t_{r2} = 200\text{s},$$

$$t_{r3} = 20\text{s}.$$

The products are:

$$\dot{\varepsilon}_1 t_{r1} = \dot{\varepsilon}_2 t_{r2} = \dot{\varepsilon}_3 t_{r3} = 10^{-1}$$

This is equal to the rupture strain. The Monkman–Grant equation is obeyed.

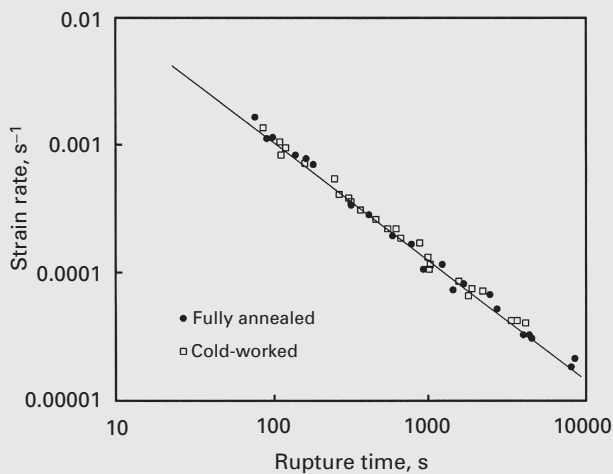


**Fig. E13.4** Monkman–Grant plot for Zircaloy. (Courtesy of M. E. Kassner and T. Haynes.)

## 13.10 Heat-Resistant Materials

High-temperature materials can be classified into two groups: metals and ceramics. High-temperature alloys are, in their turn, classified into superalloys and refractory alloys. The latter are alloys of elements with high melting points, such as tantalum, molybdenum, and tungsten. The superalloys are usually alloys developed for elevated

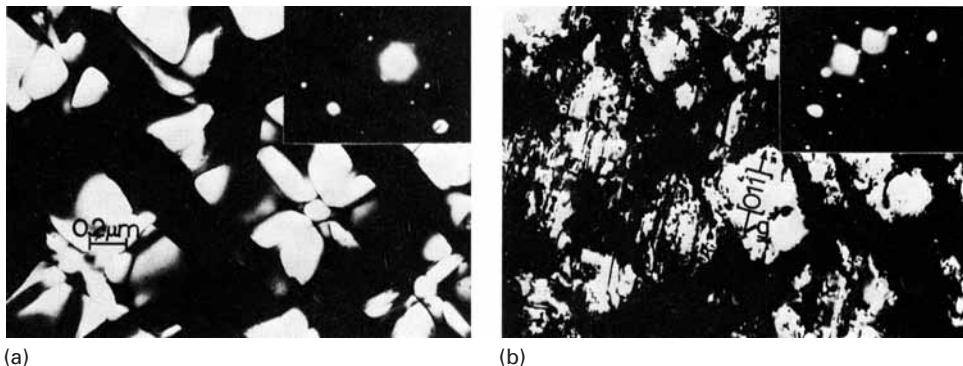


**Fig. 13.24** Transmission electron micrograph of Mar M-200; notice the cuboidal  $\gamma'$  precipitates.  
(Courtesy of L. E. Murr.)

temperature service, usually based on group VIIIa elements, where relatively severe mechanical stressing is encountered and where high surface stability is frequently required.

The development of superalloys was initiated in the 1930s, and their first use was in turbo superchargers of reciprocating aircraft engines. The introduction of the turbine in the 1940s was a strong motivator for subsequent developments. Superalloys encompass the nickel, iron, cobalt, and iron-nickel systems. The majority of authors do not include chromium-based alloys in this group. The maximum service temperature (temperature capability) has increased continuously in the past; it can be around 1,200 °C. The life of turbines has increased from 5,000 to over 20,000 hours. The combined effects of high stresses, high temperatures, and long lifetimes have required improvements in the following properties:

- *Short-term mechanical properties*: yield stress, ductility.
- *Long-term mechanical properties*: low- and high-cycle fatigue, creep, creep-fatigue.
- *Hot corrosion resistance*: the principal deterioration processes are oxidation, chlorination, sulfidation, and carburization.

Nickel-based superalloys are the most important group; most commercial nickel-based alloys have more than ten constituent elements and over ten trace elements. These can be divided into the following categories, depending on the function and position of the element in the periodic chart:

- Elements that form substitutional solid solutions in the austenitic matrix: cobalt, iron, chromium, vanadium, molybdenum, tungsten.
- Elements that form precipitates: aluminum, titanium, niobium, tantalum. Figure 13.24 shows the cuboidally shaped  $\gamma'$  precipitates  $\text{Ni}_3\text{Al}$ ,  $\text{Ni}_3\text{Ti}$ , and  $\text{Ni}_3(\text{Al}, \text{Ti})$  that are aligned along specific planes of the austenitic matrix.
- Carbide-forming elements: chromium, molybdenum, tungsten, vanadium, niobium, tantalum, titanium.
- Elements that segregate along the grain boundaries: magnesium, boron, carbon, zirconium.

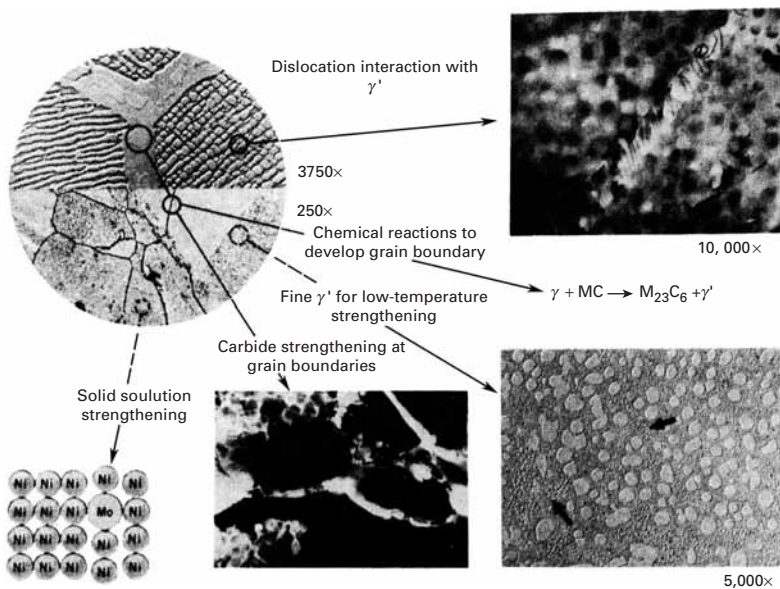


**Fig. 13.25** Major microstructural strengthening mechanisms in nickel-based superalloys. (Reprinted with permission from C. T. Sims and W. C. Hagel, eds., *The Superalloys* (New York: Wiley, 1972), p. 33.)

- Elements forming protective and adherent oxides: chromium, aluminum.
- Rare-earth elements.

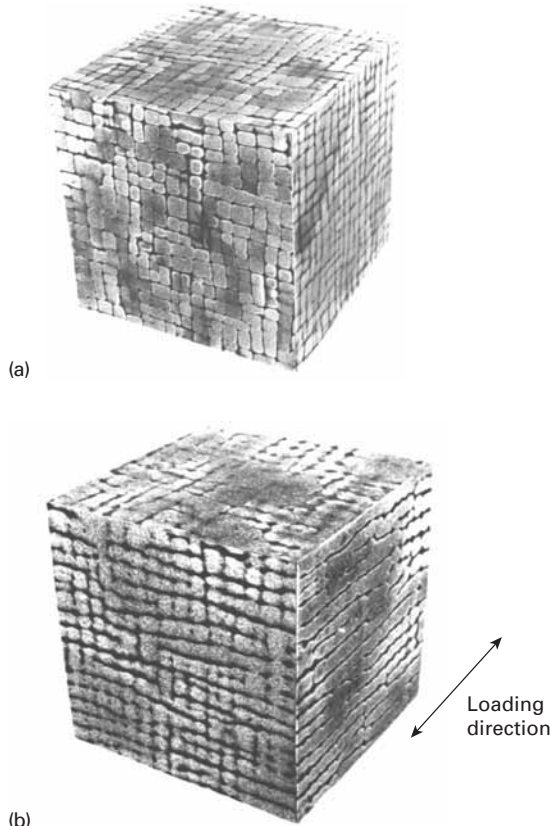
The microstructure of superalloys reflects the concern of using all possible strengthening mechanisms to retard creep. Figure 13.25 is a composite of these features. One has to retard the movement of dislocations. This is achieved by substitutional solid solution atoms and by a great volume percentage of the  $Ni_3(Ti,Al)$  phase  $\gamma'$ . The grain boundaries are strengthened by precipitation of  $M_{23}C_6$  carbides on them. Secondary  $\gamma'$ , very fine, is precipitated in the space between neighboring primary  $\gamma'$ , which is larger. One also wants to carefully avoid the topologically close-packed (TCP) phases  $R$  and  $\sigma$ , that occur accidentally and after long exposure to high temperatures, embrittling the alloy.

An interesting phenomenon occurs when  $\gamma'$  strengthened superalloys are stressed at high temperatures. This phenomenon is called “rafting” and consists of the preferential growth of the gamma prime precipitates in a certain orientation. Figure 13.26(a) shows the initial configuration of the precipitates, aligned with the {100} axes of the cubic matrix. In gamma prime strengthened superalloys, the precipitates are actually the major phase (~70%), with the matrix the minor phase. After the MarM-200 alloy shown in Figure 13.26(a) was creep deformed at 1253 K for 28 hours along the [010] direction (stress = 350 MPa), the precipitates coarsened along that loading direction; this is shown in Figure 13.26(b). They are seen to connect with each other and form continuous sheets.

Figure 13.27 shows the stress-rupture properties of a number of nickel-based superalloys. The stress required for rupture in 1,000 hours is plotted against the temperature. The load-bearing ability in

**Fig. 13.26** Rafting in MAR

M-200 monocrystalline superalloy;  
 (a) original configuration of gamma prime precipitates aligned with three orthogonal cube axes; (b) creep deformed at 1253 K for 28 hours along the [010] direction, leading to coarsening of precipitates along loading direction. (From U. Glatzel, "Microstructure and Internal Strains of Undeformed and Creep Deformed Samples of a Nickel-Based Superalloy," Habilitation Dissertation, Technische Universität, Berlin, 1994.)



the upper range of the use of these superalloys is only a fraction of the one at lower temperatures. The range 800 to 1,000 °C is a very critical one.

Figure 13.28 shows a cross-section of a gas turbine. The temperature of combustion gases is on the order of 1500 °C. The rotational speed of the turbine can be as high as 30,000 rpm, creating centrifugal stresses of the order of 200 MPa. Polycrystalline superalloys have been succeeded by directionally solidified superalloys having most grain boundaries aligned with the blade direction. This minimizes creep by grain-boundary sliding. A further development is the single crystal blade, which has no grain boundary. Figure 13.29 shows such a blade. Notice (arrow) that it has holes. Indeed, internal cooling channels are introduced into modern blades to allow air to circulate inside and create, upon exiting the blade, a protective layer at a lower temperature than the exhaust gases. Turbines with ceramic coatings called thermal barrier coatings (TBC) are used; they shield the metallic turbine from the excessively high temperatures. This poses an enormous challenge, because the metallic and ceramic components have different coefficients of thermal expansion, creating stresses that crack the coating. This problem is alleviated by the introduction of an intermediate layer. Figure 13.29(b) shows the significant increase (>100 °C) that can be accomplished using TBCs.

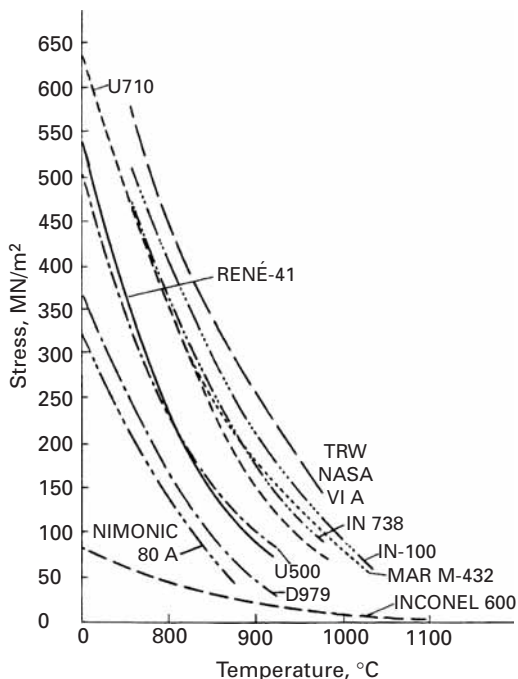


**Fig. 13.27** Stress versus temperatures curves for rupture in 1,000 hours for selected nickel-based superalloys.  
(Reprinted with permission from C. T. Sims and W. C. Hagel, eds., *The Superalloys* (New York: Wiley, 1972), p. vii.)

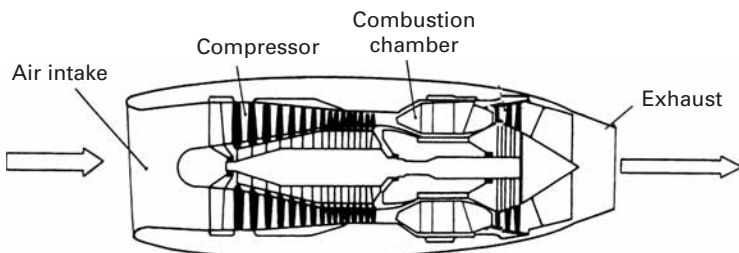


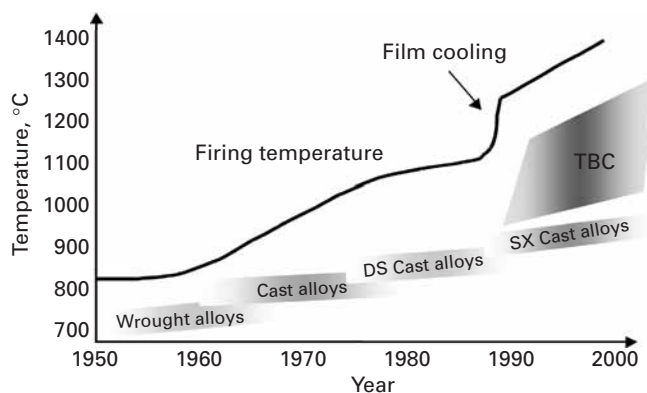
**Fig. 13.28** Cross-section of a gas turbine showing different parts. The temperature of gases in combustion chamber reaches 1500 °C.

The use of single-crystal turbine blades represents a significant technological development: Grain-boundary sliding is eliminated by this technique, and an increase in temperature capability of approximately 50 °C over that of polycrystalline superalloys is achieved. The method of producing single-crystal turbine blades involves investment casting in a controlled thermal environment. An added advantage is that the composition of the alloy is simpler than in polycrystalline superalloys.

High-performance ceramics are prime candidates for structural components in advanced automotive gas turbine engines. Operating conditions for such components involve high mechanical and thermal stresses at elevated temperatures; hence, the creep resistance of these materials is of great importance. Excessive creep deformation can affect the dimensional stability of the component, ultimately leading to a loss of function. Generally, there is a high resistance to slip and diffusional mechanisms in high-performance ceramics such as SiC and  $\text{Si}_3\text{N}_4$ . Damage mechanisms such as cavitation, solution of silicon nitride into the glassy phase at the grain



**Fig. 13.29** (a) Single crystal turbine blade developed for stationary turbine. (Courtesy of U. Glatzel.) (b) Evolution of maximum temperature in gas turbines; notice the significant improvement made possible by the introduction of thermal barrier coatings (TBCs). (Courtesy of V. Thien, Siemens.)



boundary, and grain-boundary sliding are associated with creep in these ceramics. As mentioned earlier in this chapter, different creep mechanisms give different creep activation energies. Cavitation can result in a reduction in the strength of the material and lead to time-dependent failure (i.e., creep rupture). Viscous flow in any glassy grain-boundary phase can lead to excessive creep deformation. Silicon nitride is a good example of a high-performance ceramic material to use for illustrating some of the unusual problems that must be faced

before their full potential can be realized. Silicon nitride has excellent short-term strength and fracture toughness. Generally, hot, isostatically pressed silicon nitride shows superior properties to silicon nitride processed by pressureless sintering or uniaxial hot pressing. The amount and nature of any densification aids can significantly affect creep behavior. Yttria is a common densification aid used in silicon nitride. Another important variable is the testing method (compression, bending, or tensile testing) used for creep. Although tensile testing of ceramics is not very common, it has been used to study the high-performance ceramics.

Studies aimed at evaluating the long-term mechanical performance of silicon nitride (trade designation NT 154) have shown that cavitation along two-grain junctions controls both creep deformation and creep rupture strength.<sup>16</sup> Silicon nitride is available with different purity levels. Ferber et al. observed that the creep and creep rupture behavior of silicon nitride (NT 164) were significantly improved, compared to that of the commercial material (NT 154), if one could ensure the absence of cavitation along two-grain junctions.<sup>17</sup> These authors attributed the growth of cavities to the following processes, which occur in a sequence: (1) solution of silicon nitride into the intergranular phase at the cavity boundary; (2) transport of the dissolved species along the grain boundary; and (3) precipitation of the species at low-stress sites remote from the cavity. Yet another factor in the high-temperature behavior of nonoxide ceramics such as SiC and  $\text{Si}_3\text{N}_4$  is their oxidation resistance in air. Oxidation of silicon nitride, rather than creep, was observed to initiate a stress-oxidation damage zone in the material. Finally, we reiterate the importance of the testing method. Wiederhorn et al. found asymmetric behavior of  $\text{Si}_3\text{N}_4$  in creep.<sup>18</sup> A linear response was obtained in compression, but a power-law response held in tension, with the creep exponent  $n$  in the range  $2 < n < 5$ . These researchers observed minimal cavitation in compression; in tension, however, cavities formed at multigrain junctions, and the creep strain was proportional to the volume fraction of cavities. Thus, cavitation is responsible for creep strain in tension, but not in compression. This discussion should bring home to the reader some important differences between creep mechanisms in metals and in nitrogen ceramics. In metals, a lot of creep strain can occur, but not much of it is due to cavitation. Also, the tertiary creep of metals is absent in silicon nitride.

Ceramics and ceramic composites possess a higher temperature capability than metals. Whereas ceramics tend to be brittle, the addition of reinforcing fibers adds toughness to them. Temperatures

<sup>16</sup> D. C. Cranmer, B. J. Hockey, S. M. Wiederhorn, and R. Yeckley, *Ceram. Eng. Sci. Proc.*, 12 (1991) 1862.

<sup>17</sup> M. K. Ferber and M. G. Jenkins, *J. Am. Ceram. Soc.*, 75 (1992) 2453; and M. K. Ferber, M. G. Jenkins, and T. A. Nolan, *J. Am. Ceram. Soc.*, 77 (1994) 657.

<sup>18</sup> S. M. Wiederhorn, B. J. Hockey, W. E. Luecke, R. Krause, and J. French, unpublished results.

approaching 2,000 °C can be reached with acceptable creep rates. As mentioned earlier, chemical degradation becomes very important at these temperatures, especially for nonoxide ceramics. (Oxides are, obviously, immune to oxidation.) A high-temperature material of some promise is  $\text{MoSi}_2$ , especially as a matrix for high-temperature structural composites (see Chapter 12).

### 13.11 | Creep in Polymers

As mentioned in the preceding sections, creep is a thermally activated process and thus becomes important at high temperatures. The term *high temperature* is a relative one; it is more convenient to use the term *homologous temperature*,  $T_H = T/T_m$ , where  $T$  is the temperature of interest and  $T_m$  is the melting of the material (both in kelvins). Typically, creep becomes a significant deformation mode for metals at a homologous temperature greater than 0.4 and for ceramics at a homologous temperature greater than 0.5. (In the case of amorphous polymers, one uses the glass transition temperature  $T_g$  rather than the melting point  $T_m$ .) At low temperatures, most metals and ceramics show time-independent deformation. In general, polymers show a much larger dependence on time and temperature than metals and ceramics do; that is, polymers show creep effects at much lower stresses and temperatures. This stems from their weak van der Waals interchain forces. In polymers, time-dependent deformation becomes important even at room temperature. Two terms are used to describe the time-dependent behavior of polymers: *creep* and *stress relaxation*. In creep, one applies a constant stress, and the strain response is measured as a function of time. In stress relaxation, one applies a constant strain, and the response is measured in terms of a decrease in stress as a function of time. We have discussed some aspects of these two phenomena in Chapter 2 in connection with viscoelasticity.

For a glassy, viscoelastic polymer subjected to a constant stress  $\sigma_0$ , there is an initial elastic strain recovery, followed by a slow, time-dependent recovery. This viscoelastic response may be modeled as a spring and a dashpot in series (also called the Maxwell model), as shown in Figure 13.30. An application of stress to this system results in a strain  $\epsilon$  in the system. This strain is the sum of two contributions, and we can write

$$\epsilon = \epsilon_1 + \epsilon_2, \quad (13.20)$$

where  $\epsilon_1$  is the strain in the spring and  $\epsilon_2$  is the strain in the dashpot. The stresses in the spring and the dashpot are identical, because the two are in series, i.e.,

$$\sigma = \sigma_1 = \sigma_2. \quad (13.21)$$

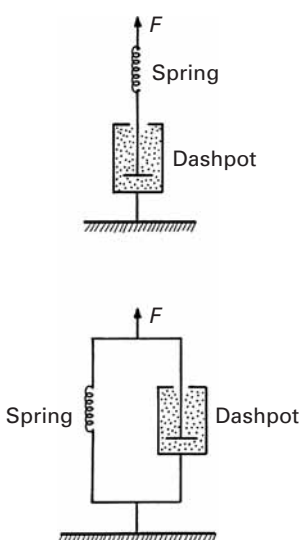


**Fig. 13.30** Spring-dashpot analogs (a) in series and (b) in parallel.

Then, we can write the following relationships for the elastic (Young's modulus,  $E$ ) and the viscous case (viscosity,  $\eta$ ),

$$\frac{d\sigma}{dt} = E \frac{d\varepsilon_1}{dt}, \quad \sigma = \eta \frac{d\varepsilon_2}{dt}. \quad (13.22)$$

From Equations 13.20 and 13.21, we get

$$\frac{d\varepsilon}{dt} = \frac{d\varepsilon_1}{dt} + \frac{d\varepsilon_2}{dt} = \frac{1}{E} \frac{d\sigma}{dt} + \frac{\sigma}{\eta}. \quad (13.23)$$

Note that the series, or Maxwell, model does not correctly predict the behavior of a viscoelastic material under constant stress or creep conditions (i.e.,  $\sigma = \sigma_0$ ), because, in this case,

$$\frac{d\varepsilon}{dt} = \frac{\sigma_0}{\eta}. \quad (13.24)$$

That is, the Maxwell model for creep or constant-stress conditions predicts that the strain increases linearly with time. (See Figure 13.31(a).) Most polymers, however, show  $d\varepsilon/dt$  increasing with time. The Maxwell model is more realistic in the case of a stress relaxation test, during which we impose a constant strain  $\varepsilon = \varepsilon_0$  and  $d\varepsilon/dt = 0$ . Under these conditions, Equation 13.23 can be written as

$$0 = \frac{1}{E} \frac{d\sigma}{dt} + \frac{\sigma}{\eta},$$

or

$$\frac{d\sigma}{\sigma} = -\left(\frac{E}{\eta}\right) dt.$$

We can integrate this expression to get

$$\sigma = \sigma_0 \exp\left(-\frac{Et}{\eta}\right). \quad (13.25)$$

The quantity  $\eta/E$  is referred to as the *relaxation time*  $\tau$ , and we can rewrite Equation 13.25 as

$$\sigma = \sigma_0 \exp(-t/\tau). \quad (13.26)$$

Equation 13.26 says that the stress decays exponentially with time, as shown in Figure 13.31(b) (Maxwell). This is quite reasonable for many polymers; however, the process of stress relaxation does not go on indefinitely in real materials.

In another model, called the Voigt model, the spring and the dashpot are arranged in parallel (Figure 13.30(b)). This means that the strains in the two components are identical, i.e.,

$$\varepsilon = \varepsilon_1 + \varepsilon_2, \quad (13.27)$$

and the stresses in the two components add, to give the stress on the system, i.e.,

$$\sigma = \sigma_1 + \sigma_2. \quad (13.28)$$

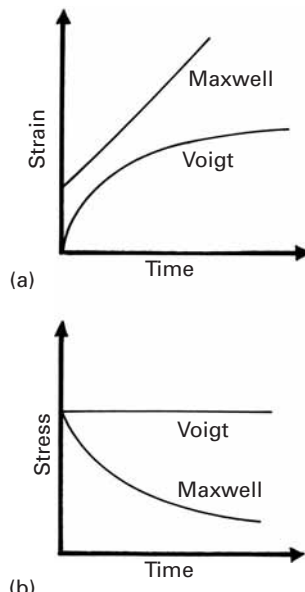


**Fig. 13.31** (a) Strain–time and (b) stress–time predictions for Maxwell and Voigt models.

It may be shown from Equations 13.27 and 13.28 that

$$\frac{d\varepsilon}{dt} = \frac{\sigma_0}{\eta} - E \frac{\varepsilon}{\eta}. \quad (13.29)$$

Let us now examine the predictions of the Voigt model for creep, or constant stress loading, and for stress relaxation. For the constant-stress situation,  $\sigma = \sigma_0$ , Equation 13.29 becomes

$$\frac{d\varepsilon}{dt} + E \frac{\varepsilon}{\eta} = \frac{\sigma_0}{\eta}.$$

This differential equation has the solution

$$\varepsilon = \left(\frac{\sigma_0}{E}\right) \left[1 - \exp\left(\frac{-Et}{\eta}\right)\right]. \quad (13.30)$$

Remembering that the quantity  $\eta/E$  is the relaxation time  $\tau$ , we find that the variation in strain with time at a constant stress (creep) is given by

$$\varepsilon = \left(\frac{\sigma_0}{E}\right) \left[1 - \exp\left(\frac{-t}{\tau}\right)\right]. \quad (13.31)$$

This relationship is shown in Figure 13.31(a); the prediction of the Voigt model is quite realistic, because  $\varepsilon \rightarrow \sigma_0/E$  as  $t \rightarrow \infty$ .

For the stress relaxation case, we have an imposed constant strain  $\varepsilon = \varepsilon_0$ , and therefore,  $d\varepsilon/dt = 0$ . The Voigt model predicts that

$$\frac{\sigma}{\eta} = \frac{E\varepsilon_0}{\eta},$$

or

$$\sigma = E\varepsilon_0.$$

This linear elastic response, however, shown in Figure 13.31(b), does not conform to reality.

The molecular weight of a polymer can affect its creep behavior. The strain response of a polymer as a function of time,  $\varepsilon(t)$ , is shown in Figure 13.32. Also shown is the effect of molecular weight. The effect of increasing the degree of cross-linking is in the same direction as that of increasing the molecular weight. Both tend to promote secondary bonding between chains and thus make the polymer more creep resistant. Compared to glassy polymers, semicrystalline polymers tend to be more creep resistant. Polymers containing aromatic rings in the chain are even more creep resistant. Both increased crystallinity and the incorporation of rigid rings add to the thermal stability, and thus to the creep resistance, of a polymer.

In a constant-stress test of the kind just described, a parameter of interest is the *creep compliance*  $J$ . This is the ratio of strain to stress. Since the strain will be a function of time, the compliance will also be a function of time. Thus,

$$J(t) = \varepsilon(t)/\sigma_0. \quad (13.32)$$

From Equation 13.32 and 13.31, we can write the creep compliance as

$$J(t) = \varepsilon(t)/\sigma_0 = (1/E)[1 - \exp(-t/\tau)]. \quad (13.33)$$

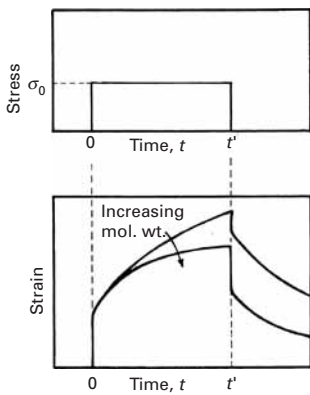


**Fig. 13.32** Strain response as a function of time for a glassy, viscoelastic polymer subjected to a constant stress  $\sigma_0$ . Increasing the molecular weight or degree of cross-linking tends to promote secondary bonding between chains and thus make the polymer more creep resistant.

If one plots a series of creep compliances as a function of time, both on logarithmic scales, over a range of temperature, one gets the curve shown in Figure 13.33(a). It turns out that such individual plots can be superposed by horizontal shifting (along the log-time axis) by an amount  $\log a_t$ , to obtain a master curve shown in Figure 13.33(b). In Figure 13.33(a), we use arrows to indicate the horizontal shift of data to obtain a master curve corresponding to a reference temperature of the polymer. This figure shows that, when creep compliance is measured at a series of temperatures, with the glass transition temperature  $T_g$  as the reference temperature, then curves above  $T_g$  are shifted to the right, while curves below  $T_g$  are shifted to the left.

As discussed earlier, a thermally activated process shows a dependence of its on temperature that can be described by an Arrhenius-type expression. When viscous flow occurs in a polymer, the network structure breaks and re-forms locally. The thermal energy for such viscous flow is available above the glass transition temperature  $T_g$ . Below  $T_g$ , the thermal energy is not high enough for the breaking and remaking of the bonds, and the material does not flow easily. In the viscoelastic range, time and temperature have similar effects on polymers. There are two easy ways of studying such behavior. In the first of these, we can impose a constant deformation on the polymer and follow the resultant stress. This will give us a stress relaxation modulus as a function of time. The other technique involves the application of a constant stress and measuring the deformation as a function of time. This will give us a curve of compliance vs. time. A very useful principle called time-temperature superposition allows us to take the data at one temperature and superimpose them on data taken at another temperature by a shift along the log-time axis. This principle is of great practical use, in as much as obtaining data over a full range of creep compliance or stress relaxation behavior can involve years. The principle allows one to shift data taken over shorter time spans, but at different temperatures, to obtain a master curve that covers longer time spans. Williams, Landel, and Ferry found that the logarithm of  $a_T$  (the time-shift factor) follows a simple expression, viz.,

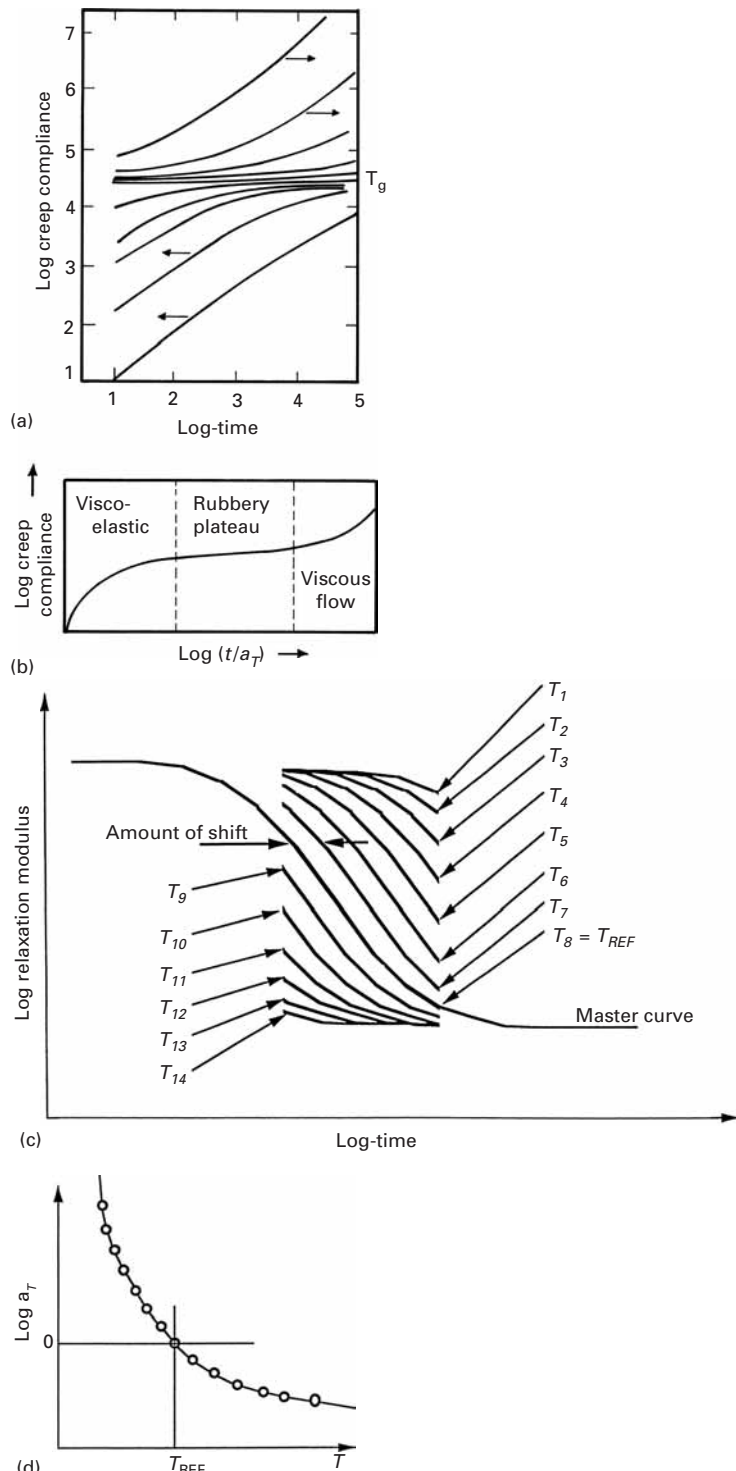
$$\log a_T = -C_1(T - T_s)/(C_2 + T - T_s),$$

where  $C_1$  and  $C_2$  are constants and  $T_s$  is a reference temperature for a given polymer.<sup>19</sup> If we take the reference temperature to be the glass transition temperature  $T_g$ , then  $C_1 = 17.5$  and  $C_2 = 52$  K. If the reference temperature  $T_s$  is taken to be about 50 °C above  $T_g$ , then  $C_1 = 20.4$  and  $C_2 = 101.6$  K.

The amount of shift can be calculated by the Williams-Landel-Ferry expression. The master curve for creep, obtained by superposing horizontally shifted curves, is shown in Figure 13.33(b). Another way of treating this problem is shown in Figure 13.33(c), where we plot

<sup>19</sup> M. L. Williams, R. F. Landel, and J. D. Ferry, *J. Amer. Chem. Soc.*, 77 (1955) 3701.

**Fig. I3.33** (a) A series of creep compliances vs. time, both on logarithmic scales, over a range of temperature. (b) The individual plots in (a) can be superposed by horizontal shifting (along the log-time axis) by an amount  $\log a_T$ , to obtain a master curve corresponding to a reference temperature  $T_g$  of the polymer. (c) Shift along the log-time scale to produce a master curve: modulus vs. time. (Courtesy of W. Knauss.) (d) "Experimentally" determined shift factor.



the stress relaxation modulus as a function of time, both on logarithmic scales. The “experimentally” determined time-shift factor, as a function of temperature, is shown in Figure 13.33(d).

Now recall the model in which spring and dash-pot are arranged in parallel, i.e., the Voigt model. The model is used to explain the stress relaxation behavior of a polymer. We impose a constant strain  $\varepsilon_0$  and follow the drop in stress  $\sigma(t)$  as a function of time. (See Figure 13.34.) Instead of a compliance term, we now have a stress relaxation modulus, given by

$$E(t) = \sigma(t)/\varepsilon_0.$$

In the case of stress relaxation also, one can obtain a master curve, as shown schematically in Figure 13.35. Also shown in the figure is the effect of cross-linking and molecular weight. Stress relaxation in polymers is of great practical significance when the polymers are used in applications involving gaskets and seals. At times, this effect can be exploited beneficially: for example, in a situation where residual stresses are not desirable, we can incorporate a polymer to undergo easy stress relaxation in response to residual stresses.

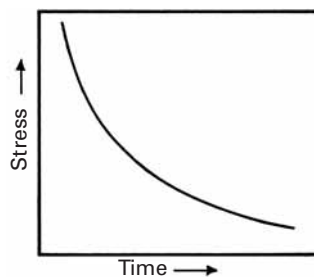


**Fig. 13.34** A constant imposed strain  $\varepsilon_0$  results in a drop in stress  $\sigma(t)$  as a function of time.

### Example 13.5

Data on stress relaxation modulus vs. time for polyisobutylene (also known as chewing gum) are shown in Figure E13.5(a). The data span a range of  $10^{-2}$  to  $10^2$  hours in time. Obtain the curve of the time-shift factor for a reference temperature of 298 K. Obtain a master curve for polyisobutylene based on time-temperature superposition of data.

**Solution:** By using the Williams-Landel-Ferry expression

$$\log a_T = -17.5(T - T_{\text{ref}})/[52 + (T - T_{\text{ref}})]$$

for a temperature range of  $-80$  °C to  $80$  °C, we obtain the curve of the time-shift factor vs. temperature shown in Figure E13.5(b). Using this time-shift curve, we superimpose the individual stress relaxation modulus curves given in the statement of the problem (Figure E13.5(a)), to obtain the master curve shown in Figure E13.5(c). Note that the time scale ranges from  $10^{-14}$  to  $10^2$  hours.

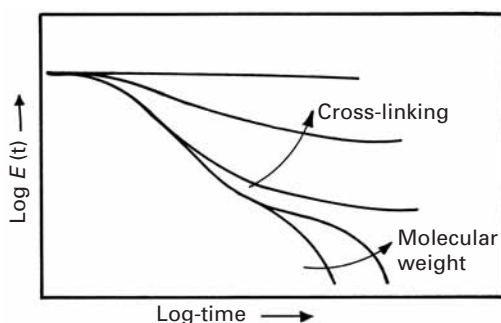


**Fig. 13.35** A master curve obtained in the case of stress relaxation, showing the variation in the reduced modulus as a function of time. Also shown is the effect of cross-linking and molecular weight.

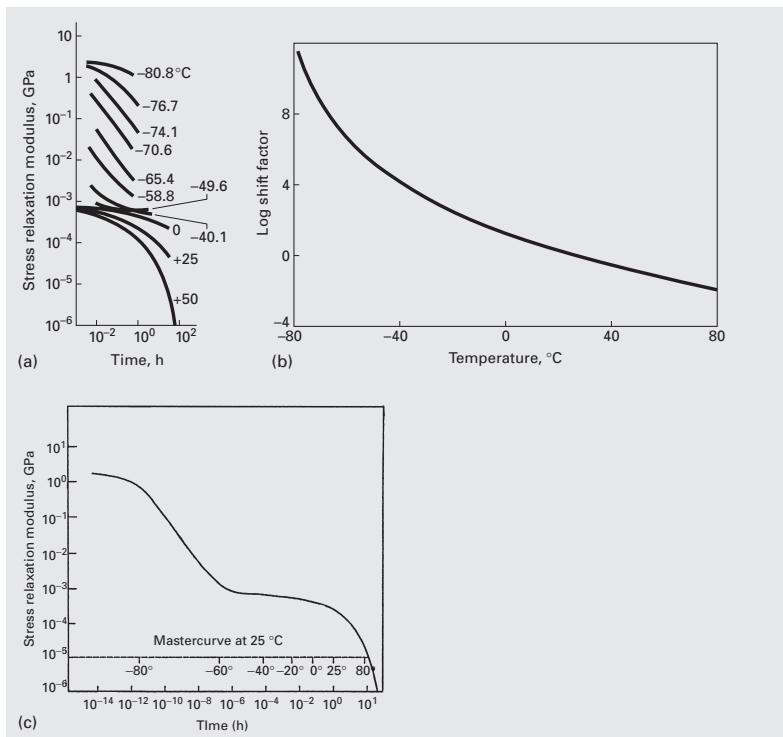


**Fig. E13.5** (a) Stress relaxation modulus; (b) time-shift factor; (c) master curve.  
(From E. Catsiff and A. V. Tobolsky, *J. Polymer Sci.*, 19 (1956) 111.)

### Example 13.6

The creep strain rate of a polymer is given by the expression

$$\dot{\varepsilon} = 4.5 \times 10^{11} \exp(-100 \text{ kJ}/RT),$$

where  $T$  is the temperature in kelvins and  $R$  is the universal gas constant. How much time will it take for a rod of this polymer to extend from 10 mm to 15 mm at 100 °C?

*Solution:*

$$\begin{aligned}\dot{\varepsilon} &= \Delta\varepsilon/\Delta t = 4.5 \times 10^{11} \exp[-100,000/(8.3 \times 373)] \\ &= 4.2 \times 10^{-3} \text{ s}^{-1}\end{aligned}$$

Hence,

$$\Delta t = 0.5 / (4.2 \times 10^{-3}) = 119 \text{ s.}$$

### Example 13.7

The activation energy for stress relaxation in a polymer is 50 kJ/mol. The relaxation time at 25 °C is 90 days. What is the relaxation time at 125 °C?

*Solution:*

$$\begin{aligned}1/\tau &= \frac{E}{\eta} = A \exp(-Q/RT), \\(1/\tau_{25})/(1/\tau_{125}) &= \exp(-Q/R298)/\exp(-Q/R398), \\\tau_{125} &= \tau_{25} \exp[(Q/R)(1/398 - 1/298)], \\\tau_{125} &= 90 \exp[((50 \times 10^3)/8.314)(1/398 - 1/298)], \\&= 90 \times 6.4 \times 10^{-3}, \\&= 0.57 \text{ day.}\end{aligned}$$

### Example 13.8 |

A nylon cord, used to tie a sack, has an initial stress of 5 MPa. If the relaxation time for this cord is 180 days, in how many days will the stress reduce to 1 MPa?

*Solution:*

$$\begin{aligned}\sigma &= \sigma_0 \exp(-t/\tau), \\1 \text{ MPa} &= 5(-t/180), \\t &= -180 \ln 1/5, \\t &= 290 \text{ days.}\end{aligned}$$

## 13.12 Diffusion-Related Phenomena in Electronic Materials

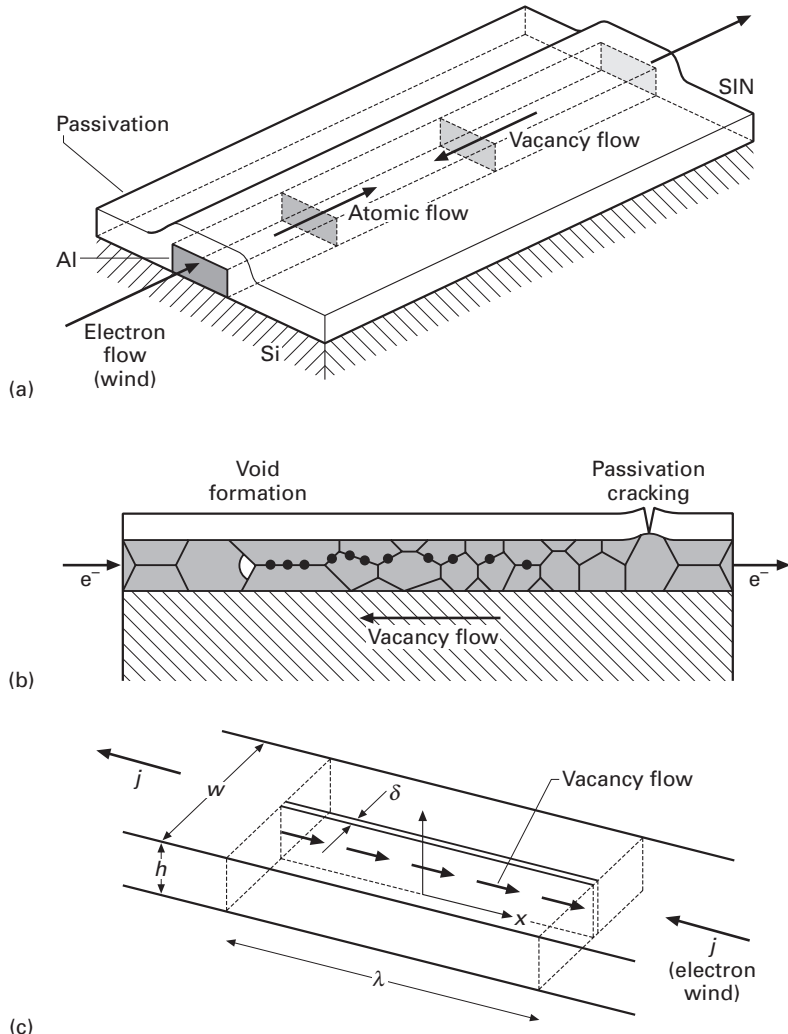
Interconnect lines in integrated circuits are subject to diffusional processes that can lead to void growth. These voids, in conjunction with stresses, may lead to failure. There are two mechanisms responsible for void growth:

- *Thermal stresses.* Figure 13.36(a) shows an interconnect. The core, which has a rectangular cross section, is the component carrying the electrical current. Electrical currents as high as  $10^{10} \text{ A/m}^2$  are carried by the metallic conductor (typically, aluminum). The conductor is covered by a passivation film (e.g. silicon nitride). The difference in thermal expansion coefficient between the two leads them to tensile stresses in the conductor. Assuming a rigid passivation layer, the stress in the conductor can be estimated from:

$$\sigma_t = 3\Delta\alpha\Delta T K, \quad (13.34)$$

where  $\Delta T$  is the temperature change following passivation,  $\Delta\alpha$  is the difference in thermal expansion coefficient between conductor and passivation layer, and  $K$  is the bulk modulus of the

**Fig. 13.36** Metal interconnect line covered by passivation layer subjected to electromigration; (a) overall scheme; (b) voids and cracks produced by thermal mismatch and electromigration; (c) basic scheme used in Nix-Arzt equation, which assumes grain-boundary diffusion of vacancies counterbalancing electron wind. (Adapted from W. D. Nix and E. Arzt, *Met. Trans.*, 23A (1992) 2007.)



conductor. Glaxner et al.<sup>20</sup> estimate that these hydrostatic (tensile) stresses can be as high as 500 MPa. Diffusion of vacancies, under these stresses, at a temperature of 200 °C (typical of the conductor) can lead to the formation of voids within the metal or cracks in the passivation layer.

- **Electromigration.** The high current densities in the metal interconnect lines produce an “electron wind.” This electron wind causes the migration of matter through, primarily, the diffusion of vacancies. The electron wind will produce an atomic flow in the same direction, with a vacancy flow in the opposite direction. The vacancy flow, which occurs principally along grain boundaries, is interrupted at transverse grain boundaries. The vacancies condense and form voids. This is shown in Figure 13.36(b).

<sup>20</sup> R. J. Glaxner, B. M. Clemens, and W. D. Nix, *J. Mater. Res.*, 12 (1997) 2081.

Figure 13.36(c) shows the flow of electrons and vacancies in a grain with length  $\lambda$ . Diffusion occurs primarily along grain boundaries because the grain-boundary diffusion coefficient,  $D_{gb}$ , is orders of magnitude higher than the lattice diffusion coefficients at temperatures below  $0.5T_m$ , where  $T_m$  is the melting point in kelvin. The thickness of the grain boundary is  $\delta$ . Nix and Arzt<sup>21</sup> developed the following equation for the stress due to electromigration:

$$\sigma_{NA} = \frac{1}{2} \frac{\lambda}{\Omega} eZ^* \rho j, \quad (13.35)$$

where  $\Omega$  is the atomic volume,  $\lambda$  is the grain-boundary length,  $\delta$  is the grain-boundary thickness,  $eZ^*$  is the effective charge of the metal ions,  $\rho$  is the resistance, and  $j$  is the current density.

### Example 13.9 |

Calculate the Nix–Arzt stress in an aluminum line if the current density is  $10^{10}$  A/m<sup>2</sup> and the grain size is 20  $\mu\text{m}$ .

Given:

$$eZ^* = 3.2 \times 10^{-18} \text{ coulombs},$$

$$\rho = 28 \times 10^{-9} \Omega\text{m},$$

$$\delta = 3 \times 10^{-10} \text{ m},$$

$$\Omega = 16.6 \text{ A}^3,$$

$$j = 1010 \text{ A/m}^2.$$

**Solution:** Inserting these values into Equation 13.33:

$$\sigma_{NA} = 520 \text{ MPa.}$$

This is indeed a high value.

## 13.13 | Superplasticity

Some metallic alloys and ceramics show a peculiar behavior called *superplasticity*. This is the ability to flow, in tension, to very large elongations. Figure 13.37 shows a dramatic illustration of superplastic behavior. The specimen was extended at a temperature of 413 K, and a total strain of 48.5 was reached without failure. The phenomenon of superplasticity was observed for the first time in 1934. A great deal of activity has taken place in the area since then, and superplastic forming has become a successful industrial process.

Superplasticity has been obtained in a number of alloy systems, including titanium alloys (Ti-6% Al-4% V), iron-based alloys, and

<sup>21</sup> W. D. Nix and E. Arzt, *Met. Trans.*, 32A (1992) 2007.

**Fig. 13.37** Superplastic tensile deformation in Pb–62% Sn eutectic alloy tested at 415 K and a strain rate of  $1.33 \times 10^{-4} \text{ s}^{-1}$ ; total strain of 48.5. (From M. M. I. Ahmed and T. G. Langdon, *Met. Trans. A*, 8 (1977) 1832.)



aluminum alloys. High-strength nickel-based superalloys have been found to exhibit superplastic behavior, and the process of “gatorizing” (supposedly named after an alligator living in the lake in front of the research institute) has been developed by Pratt and Whitney. The potential of superplastic forming is especially bright for titanium alloys, which are known to be very difficult to form, because of their HCP structure. Superplasticity has also been discovered in ceramics.

The basic reason that some materials can deform superplastically when others cannot is related to how they respond to changes in strain rate. The example of hot glass (above the transition temperature) comes to mind. We are all familiar with Coke bottles stretched to very high strains; these interesting items are sold in curio shops. Glass shows a Newtonian viscous behavior above a certain temperature. Fiberglass is formed in such a manner and can be pulled to extremely fine fibers. In a lamellar flow, Newtonian viscosity is defined by (see Equation 3.29)

$$\tau = \eta \frac{dv}{dy},$$

where  $dv/dy$  is the variation in velocity of the fluid with distance  $y$ ,  $\tau$  is the shear stress necessary to create the velocity gradient  $dv/dy$ , and  $\eta$  is the viscosity. The derivative  $dv/dy$  is equivalent to the shear strain rate  $\dot{\gamma}$ . (See Section 3.6.2.) Thus, we can write

$$\tau = \eta \dot{\gamma}. \quad (13.34)$$

The stress-versus-strain-rate relationship from many materials is not linear, but of the form (see Equation 3.23)

$$\sigma = K \dot{\varepsilon}^m, \quad (13.35)$$

where  $K$  and  $m$  are constants and  $m$  is called the strain-rate sensitivity. In general,  $m$  varies between 0.02 and 0.2, for homologous temperatures between 0 and 0.9 (90% of the melting point in K). Hence, one would have, at the most, an increase of 15% in the yield stress by doubling the strain rate. Comparing Equations 13.34 and 13.35, we see that a value of  $m = 1$  will give a Newtonian viscous solid. Such a material would not undergo tensile instability and could be stretched indefinitely. Figure 13.38(a) shows schematically how a high value of  $m$  will inhibit tensile instability (necking) and, consequently, enhance plasticity in tension. The specimen is being deformed, in tension, at a velocity  $v$ . The length increases from  $L_0$  to  $L_1$  and then to  $L_2$ . At  $L_2$ , necking starts. If the material has a high value of  $m$ , this instability

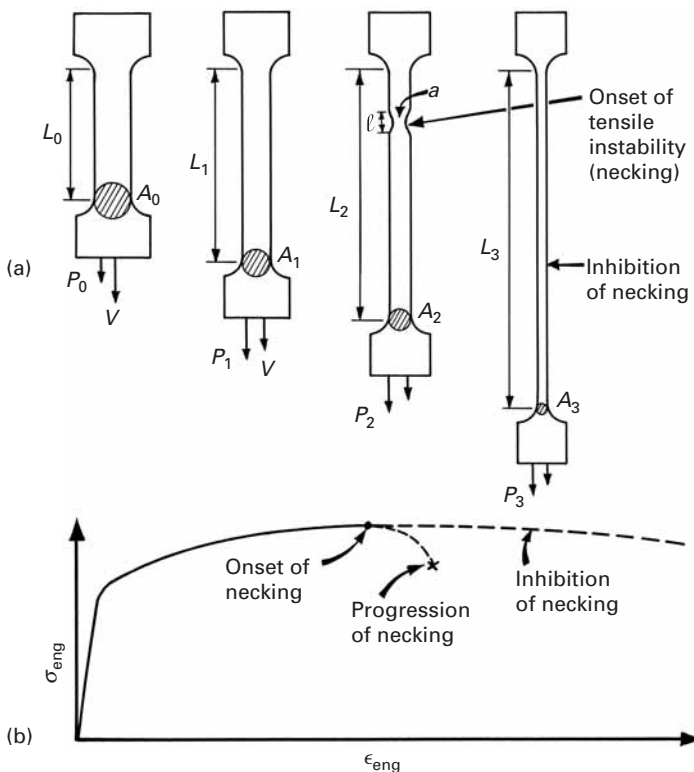


**Fig. 13.38** (a) Schematic representation of plastic deformation in tension with formation and inhibition of necking. (b) Engineering-stress–engineering-strain curves.

will be inhibited because of the localized strengthening effect. When the length is  $L_2$ , the strain rate over the specimen is

$$\dot{\varepsilon}_2 = \frac{v}{L_2}.$$

In the incipient neck region, which acts as a “minispecimen” embedded in the large specimen, one has

$$\dot{\varepsilon}'_2 = \frac{v}{\ell}.$$

Since  $\ell < L_2$ , one has  $\dot{\varepsilon}'_2 > \dot{\varepsilon}_2$ .

The strain rate sensitivity can be obtained from Equation 13.35 by applying that equation to two strain rates and eliminating  $K$ . When we do this, we obtain

$$m = \frac{\ln(\sigma'_2/\sigma_2)}{\ln(\dot{\varepsilon}'_2/\dot{\varepsilon}_2)}.$$

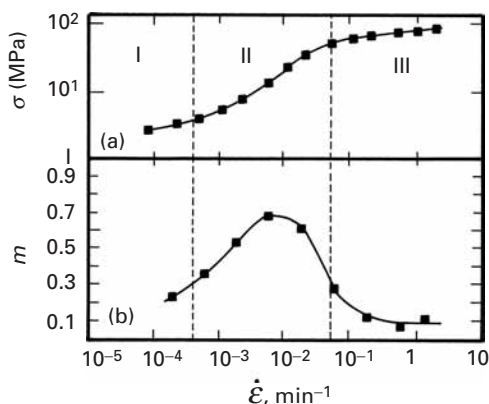
For a high value of  $m$ , the strength  $\sigma'_2$  in the neck region is much higher than  $\sigma_2$ , and further progression of plastic deformation at that region is halted. Mathematically,

$$\sigma'_2 > \frac{P_2}{a}.$$

When  $m$  is low,  $\sigma'_2$  is not sufficiently high, and we have

$$\sigma'_2 < \frac{P_2}{a}.$$

**Fig. 13.39** Strain-rate dependence of (a) stress and (b) strain-rate sensitivity for Mg-Al eutectic alloy tested at 350 °C (grain size 10 μm). (After D. Lee, *Acta Met.*, 17 (1969) 1057.)



$a$  is the cross-sectional area in the neck region. The deformation continues to concentrate itself at the neck, with the attendant reduction in area caused by the constancy of volume. This leads to failure. Figure 13.38(b) shows the two alternative paths beyond the maximum in the engineering-stress–engineering-strain curve. Thus, one concludes that superplasticity is the result of the inhibition of necking as a result of a high value of  $m$ .

Under certain conditions of temperature and strain rate, some metals and ceramics exhibit an enhancement of  $m$ . Curve (a) in Figure 13.39 shows the stress as a function of strain rate for an Mg-Al eutectic alloy tested at 350 °C. One can see that in region II, the stress rises more rapidly with strain rate. Curve (b) in the same figure shows the strain rate sensitivity  $m$  as a function of strain rate. The maximum,  $m = 0.6$ , occurs for a strain rate of  $10^{-2} \text{ s}^{-1}$ .  $m = \partial \ln \sigma / \partial \ln \dot{\epsilon}$  is the slope of curve (a) in the figure. Figure 13.40 shows the variation in  $\partial L / L_0$  (the tensile fracture strain) with  $\dot{\epsilon}$  for a Zr-22% Al alloy. The maxima (at the three temperatures) in  $\Delta L/L_0$  correspond roughly to the center of region II. Further proof of the effect of  $m$  on the extent of superplastic flow is provided by Figure 13.41, which contains data from several studies. Data for alloys of Fe, Mg, Pu, Pb-Sr, Ti, Zn, Zr are plotted, and the correlation is excellent. As  $m$  approaches unity,  $\Delta L/L_0$  reaches extraordinarily high values.

The microstructural requirement for a high value of  $m$  is a small grain size. The testing temperatures are usually above  $0.4T_m$ , where  $T_m$  is the absolute melting point, and the strain rates in which superplasticity is observed are usually intermediate ( $10^{-4} \text{ s}^{-1} < \dot{\epsilon} < 10 \text{ s}^{-1}$ ). Superplasticity is usually enhanced by thermal cycling, i.e., straining the material sequentially at two different temperatures. All alloys that show structural superplastic behavior have a very fine grain size (<10 μm). For these small grain sizes, and at the deformation temperatures, most of the plastic deformation takes place by grain-boundary sliding, and not by the conventional dislocation mechanisms in the interior of the grains. Specimens deformed to very large strains routinely exhibit an equiaxial grain structure, in contrast with

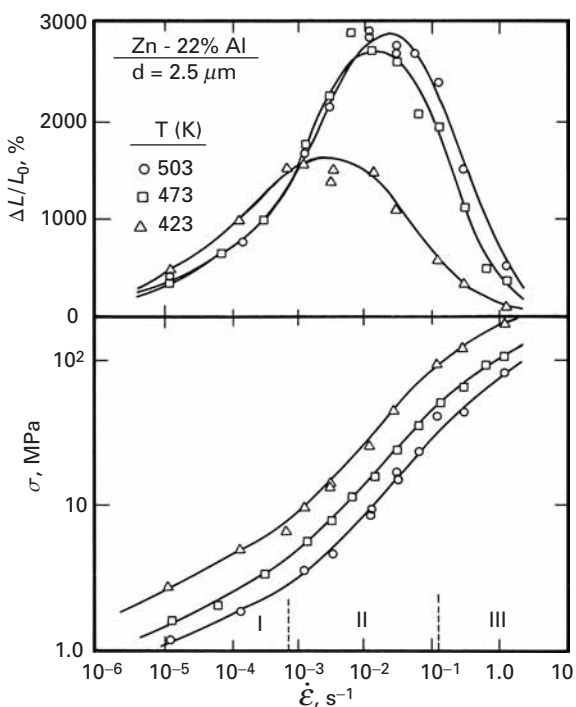


**Fig. 13.40** Tensile fracture strain and stress as a function of strain rate for Zr-22% Al alloy with 2.5- $\mu\text{m}$  grain size. (After F. A. Mohamed, M. M. I. Ahmed, and T. G. Langdon, *Met. Trans. A*, 8 (1977) 933.)

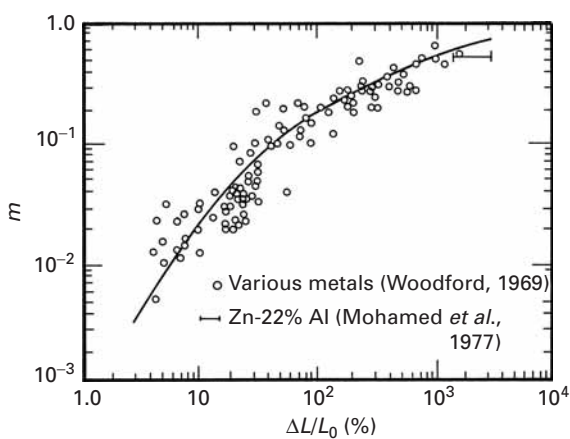


**Fig. 13.41** Effect of strain-rate sensitivity  $m$  on maximum tensile elongation for different alloys (Fe, Mg, Pu, Pb-Sr, Ti, Zn, Zr based). (From D. M. R. Taplin, G. L. Dunlop, and T. G. Langdon, *Ann. Rev. Mater. Sci.*, 9 (1979) 151.)

conventional deformation, in which the strain undergone by the individual grains is equal to the overall strain, and the grains assume an elongated shape. Grain-boundary sliding accounts for 50–70% of the overall strain. Superplastic materials may be likened to sand: the granules retain their shape with plastic deformation. In contrast to sand, however, superplastic materials do not have interstices between the grains. Thus, some plastic accommodation must occur as the grains slide past each other. The contribution of grain-boundary sliding to plastic deformation is more substantial the greater the grain-boundary surface per unit volume. Since the grain-boundary surface is inversely proportional to the grain size, this explains why the

**Table 13.2** Materials Exhibiting Very High Tensile Strains<sup>a</sup>

Material	Maximum strain (%)
Al–33% Cu eutectic	1,500
Al–6% Cu–0.5% Zr	1,200
Al–10.7% Zn–0.9% Mg–0.4% Zr	1,500
Bi–44% Sn eutectic	1,950
Cu–9.5% Al–4% Fe	800
Mg–33% Al eutectic	2,100
Mg–6% Zn–0.6% Zr	1,700
Pb–18% Cd eutectic	1,500
Pb–62% Sn eutectic	4,850
Ti–6% Al–4% V	1,000
Zn–22% Al eutectoid	2,900
Al(6061)–20% SiC (whiskers)	1,400
Partially stabilized zirconia	120
Lithium aluminosilicate	400
Cu–10% Al	5,500
Zirconia	350
Zirconia + SiO <sub>2</sub>	1,000

<sup>a</sup>Adapted from D. M. R. Taplin, G. L. Dunlap, and T. G. Langdon, *Ann. Rev. Mater. Sci.*, 9 (1979) 15.

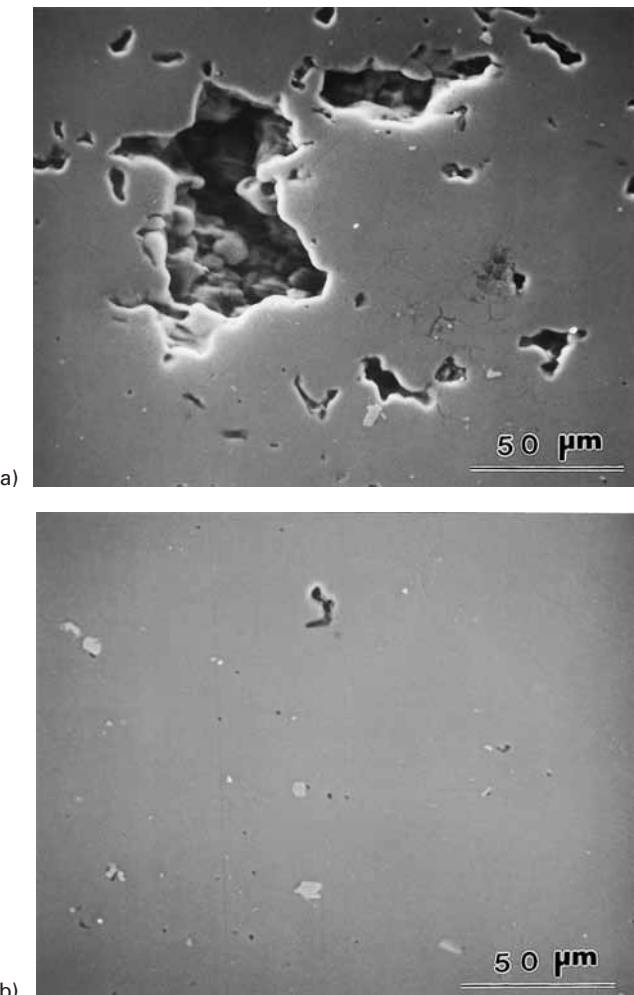
contribution of grain-boundary sliding is less important in materials with large grain sizes.

Table 13.2 shows the tensile elongation of a number of superplastic materials. It is interesting to note that superplasticity has been found in composites and ceramics. Sherby and co-workers obtained tensile elongations of 1,300% in an aluminum alloy/SiC whisker reinforced composite. The Sherby team used temperature cycling. These researchers also detected superplasticity in ultrahigh-carbon steel and were able to attribute the splendid properties of the Damascus sword to superplastic forming. Thus, the use of superplasticity is centuries old. For ceramics, superplasticity (in tension) is a technology with great potential. Wakai et al. obtained tensile elongations of 120% in an yttria-stabilized polycrystal containing 90% tetragonal zirconia and 10% cubic zirconia.<sup>22</sup> A grain size of 0.3 μm produced a strain rate sensitivity of  $m = 0.5$  at 1450 °C. This elongation was exceeded in work done by Nieh et al., who obtained a value of 350% at 1,550°C.<sup>23</sup> Nanocrystalline ceramics (Section 5.5) are especially attractive in this regard. Superplasticity was also obtained in an aluminosilicate and other ceramic systems.

One of the major problems in superplastic forming is the formation of voids at grain boundaries. Cavitation during superplastic

<sup>22</sup> F. Wakai, S. Sakaguchi, and Y. Matsuno, *Advanced Ceramic Materials*, 1(3) (1986) 259.

<sup>23</sup> T. G. Nieh, C. M. McNally, and J. Wadsworth, *Scripta Met.*, 22 (1988) 1297.



**Fig. 13.42** Cavitation in superplastically formed 7475-T6 aluminum alloy ( $\varepsilon = 3.5$ ) at  $475^\circ\text{C}$  and  $5 \times 10^{-4} \text{ s}^{-1}$ . (a) Atmospheric pressure. (b) Hydrostatic pressure  $P = 4 \text{ MPa}$ . (Courtesy of A. K. Mukherjee.)

forming results in a deterioration of the mechanical properties of parts formed by superplasticity. Cavities form because of incompatible deformation of adjacent grains and weaken the material. These voids can be reduced or eliminated by superimposing a hydrostatic stress upon the applied tensile stress. This is illustrated in Figure 13.42. The aluminum alloy shown exhibited considerable cavitation at a plastic strain of 350%, or 3.5. The application of a superimposed hydrostatic pressure of 4 MPa, through a gaseous medium, decreases the cavitation substantially. Otherwise, the cavitation would lead to premature failure. Figure 13.43(a) shows the effect of grain size on the elongation of an 7475 Al alloy. Figure 13.43(b) shows a number of specimens superplastically deformed up to failure. The initial specimen is at the bottom, and the effect of increasing the superimposed pressure is shown from bottom to top. The pressures (and elongations to failure) are, respectively, 330% (atmosphere), 720% (1.4 MPa); 830% (2.8 MPa), and 1330% (and no failure at 5.6 MPa).

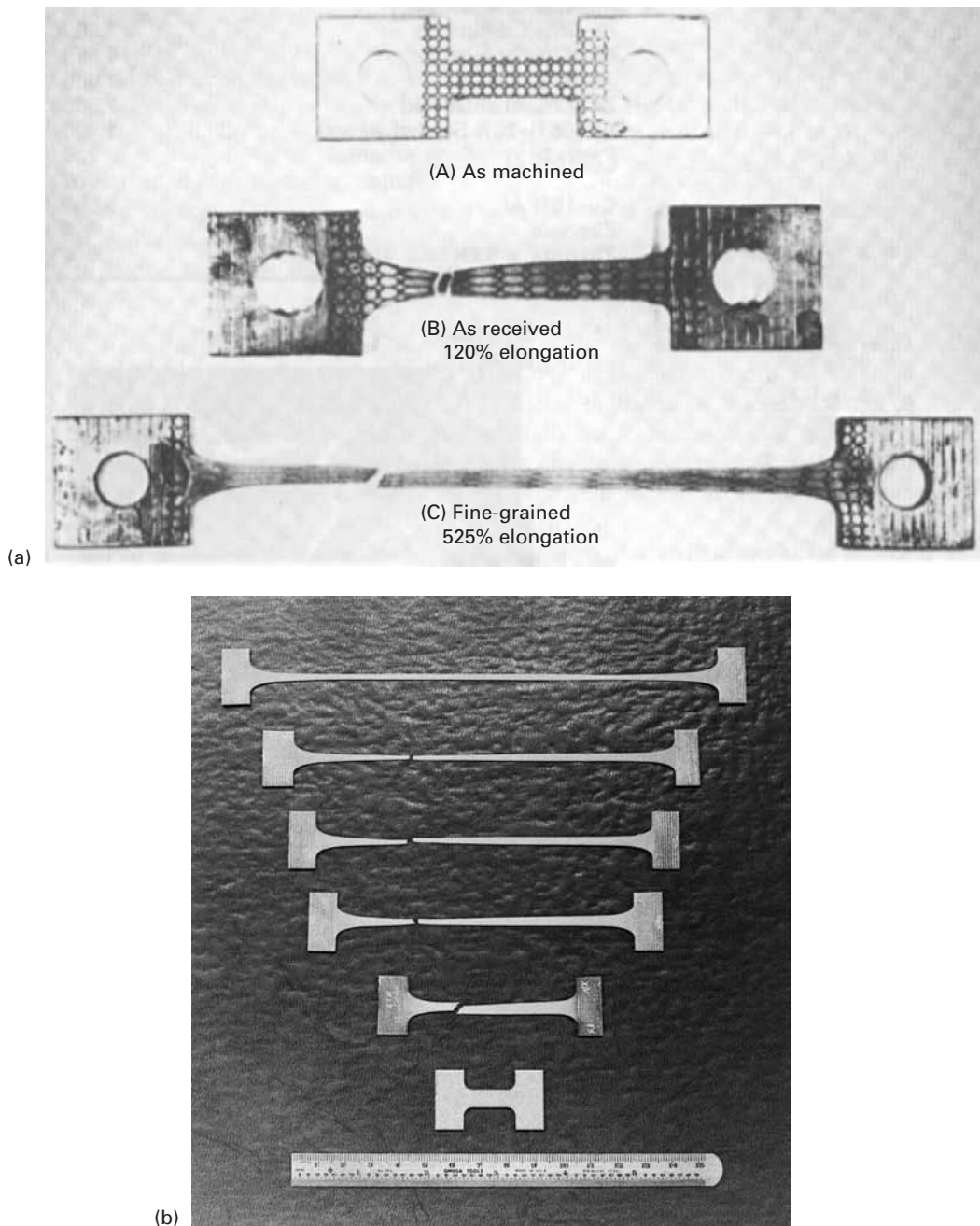


**Fig. 13.43** (a) Effect of grain size on elongation: (A) Initial configuration. (B) Large grains. (C) Fine grains ( $10 \mu\text{m}$ ) (Reprinted with permission from N. E. Paton, C. H. Hamilton, J. Wert, and M. Mahoney, *J. Metal*, 34 (1981) No. 8, 21.) (b) Failure strains increase with superimposed hydrostatic pressure (from 0 to 5.6 MPa). (Courtesy of A. K. Mukherjee.)

## Suggested Reading

- W. R. Cannon and T. G. Langdon. "Creep of Ceramics." *J. Mater. Sci.*, 18 (1983) 1 (Part 1); 23 (1988) 1 (Part 2).
- A. H. Chokshi, A. K. Mukherjee, and T. G. Langdon, "Superplasticity in Advanced Materials," *Matls. Sci and Eng. R: Reports*, 10 (1993) 237–274.
- A. H. Chokshi and T. G. Langdon. "Characteristics of Creep Deformation in Ceramics." *Matls. Sci. Techn.*, 7 (1991) 577.
- H. J. Frost and M. F. Ashby. *Deformation-Mechanism Maps*. Oxford: Pergamon Press, 1982.
- F. Garofalo. *Fundamentals of Creep and Creep Rupture in Metals*. New York, NY: Macmillan, 1965.
- J. Gittus. *Creep, Viscoelasticity and Creep Fracture in Solids*. New York, NY: Halsted Press (Wiley), 1975. *J. Eng. Mater. Technol.*, 101 (1979) 317.
- B. P. Kashyap, A. Arieli, and A. K. Mukherjee. "Microstructural Aspects of Superplasticity." *J. Mater. Sci.*, 20 (1985) 2661.
- M. E. Kassner and M. T. Perez-Prado, *Fundamentals of Creep in Metals and Alloys*. New York, NY: Elsevier, 2004.
- F. R. N. Nabarro, and H. L. de Villiers. *The Physics of Creep*. London: Taylor & Francis, 1995.
- J. P. Poirier. *Creep of Crystals: High Temperature Deformation Processes in Metals, Ceramics, and Minerals*. Cambridge, U.K.: Cambridge University Press, 1985.
- O. D. Sherby and P. M. Burke. "Mechanical Behavior of Crystalline Solids at Elevated Temperature." *Progr. Mater. Sci.*, 13 (1967) 325.
- J. Weertman, and J. R. Weertman. "Mechanical Properties, Strongly Temperature Dependent," in *Physical Metallurgy*, 4th ed., R. W. Cahn and P. Haasen. eds. New York, NY: Elsevier, 1995.

## Exercises

**13.1** A cylindrical specimen creeps at a constant rate during 10,000 hours when it is subjected to a constant load of 1,000 N. The initial diameter and length of the specimen are 10 and 200 mm, respectively, and the creep rate is  $10^{-8} \text{ h}^{-1}$ . Find:

- (a) The length of the specimen after  $10^4$ ,  $10^6$ , and  $10^8$  hours.
- (b) The true and engineering strains after these periods.
- (c) The true and engineering stresses after these periods.

**13.2** Give three reasons why the extrapolation of creep data obtained over a short period can be dangerous over long periods.

**13.3** By means of plots, show how isochronal stress-versus-strain curves can be constructed from creep curves for various stresses at a certain temperature.

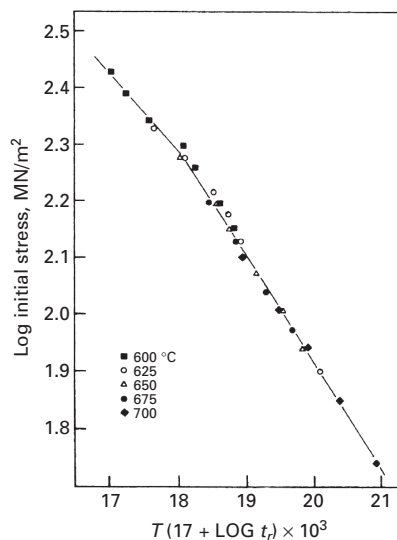
**13.4** Howson et al.<sup>24</sup> obtained the following stress-rupture results for the superalloy INCONEL MA 754 (a dispersion-strengthened alloy):

<sup>24</sup> T. E. Howson, D. A. Mervyn, and J. K. Tien, *Met. Trans.*, 11A (1980) 1609.

Temperature (°C)	Applied Stress (MPa)	Rupture Life (hours)
760	189.7	—
760	206.9	83.9
760	206.9	111.2
760	224.2	38.6
760	224.2	29.0
760	241.4	6.9
760	258.7	1.8
746	206.9	320.8
774	206.9	65.0
788	206.9	33.2
982	110.4	195.1
982	113.8	136.6
982	113.8	106.9
982	116.5	27.6
982	117.3	106.3
982	120.7	13.0
982	120.7	39.0
996	110.4	52.6
996	110.4	41.3
1010	110.4	20.3
1010	110.4	41.7
1024	110.4	9.4

- (a) Verify whether this alloy obeys a Larson–Miller relationship, and find  $C$ . Then prepare a master plot, assuming that it does.
- (b) Determine the predicted stress-rupture life if the alloy is stressed at 1,000 °C and 50 MPa.

**Fig. Ex13.5** Master plot for Larson–Miller parameter for AISI 316 stainless steel. (Courtesy of T. Silveira and S. N. Monteiro.)



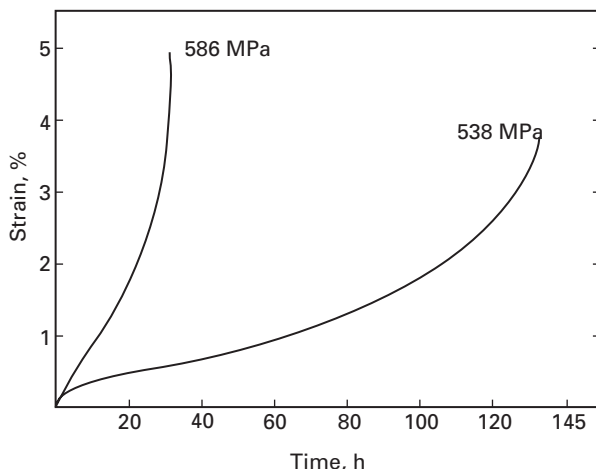


Fig. Ex13.8

13.5 What is the predicted stress-rupture life of AISI 316 steel (18% Cr, 8% Ni, 2–3% Mo) at 800 °C and 160 MPa? (See Figure Ex13.5.)

13.6 Verify whether the data of Exercise 13.5 obey the Manson–Haford correlation.

13.7 Assuming that pure silver creeps according to the Dorn equation, estimate the rupture time at 400 °C when the silver is subjected to a stress of 50 MPa, knowing that at 300 °C and at the same stress level the rupture time is 2,000 hours.

13.8 Howson et al.<sup>25</sup> studied the creep and stress-rupture response of oxide-dispersion-strengthened (ODS) superalloys produced by mechanical alloying. They determined that the activation energy for creep  $Q_c$  was 619 kJ/mol by conducting tests at a constant applied stress of 558.7 MPa at the three temperatures of 746, 760, and 774 °C.

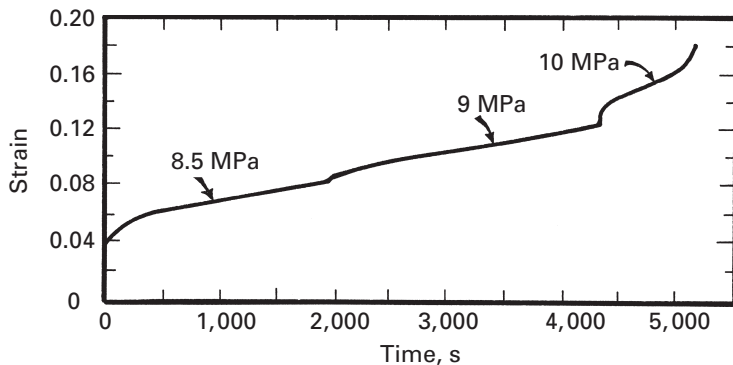
- (a) The results shown in Figure Ex13.8 were found for experimental alloy MA 6000 E at 760 °C. Estimate the value of  $n$ , and discuss this value in terms of the microstructure exhibited by the alloy (made by means of dispersion-strengthening by inert yttrium oxide dispersoids plus precipitation-strengthening by gamma prime).
- (b) By applying Equation 13.4, show how the activation energy can be found. Make the appropriate plot, and find the minimum creep rate at the aforementioned three temperatures. Note that the activation energy is given per mole.

13.9 In Exercise Ex13.9, verify how closely the Monkmon–Grant relationship is obeyed.

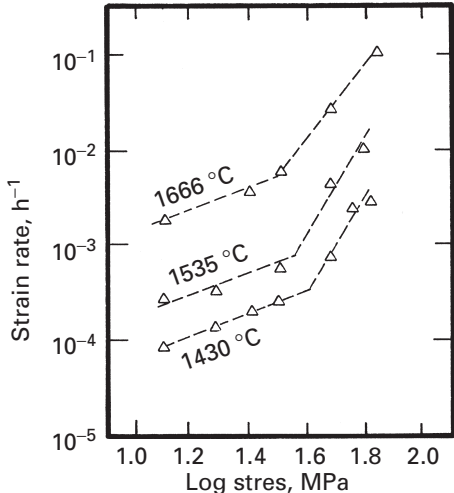
13.10 A lead-based alloy (melting point, 327.5 °C) was tested at ambient temperature (23 °C) and three different engineering stress levels: 8.5, 9, and 10 MPa. The curve that was obtained was shown in Figure Ex13.10.

- (a) From the temperature aspect, establish whether the room temperature is in the creep domain for Pb.
- (b) Obtain the minimum creep rates for the three stress levels.

<sup>25</sup> T. E. Howson, D. A. Mervyn, and J. K. Tien, *Met. Trans.*, 11A (1980) 1609.

**Fig. Ex13.10**

**Fig. Ex13.12** Steady-state creep behavior of  $\text{UO}_2$  can be divided into two regimens with different stress exponents. The transition stress between the regimens decreases with increasing temperature. (From L. E. Poteat and C. S. Yust, in *Ceramic Microstructures*, R. M. Fulrath and J. A. Pask, eds. (New York: John Wiley & Sons, 1968) 646.)



- (c) Obtain parameters for the curve at 8.5 MPa, as expressed by Equation 13.1.
- (d) Obtain the stress exponent in the Mukherjee–Bird–Dorn equation. Based on this value, what mechanism of creep do you expect?

13.11 Using the results from the previous problem, predict the minimum creep rate for the same material if the test would be carried out at 10 °C and stress levels of (a) 10 MPa and (b) 20 MPa. The self-diffusion coefficients for Pb are:

$$D = 5.24 \times 10^{-8} \text{ cm}^2 \cdot \text{h}^{-1} \text{ at } 250^\circ\text{C},$$

$$D = 2.92 \times 10^{-7} \text{ cm}^2 \cdot \text{h}^{-1} \text{ at } 285^\circ\text{C}.$$

13.12 Determine the slopes for the creep behavior of  $\text{UO}_2$ , shown in Figure Ex13.12. Discuss the deformation mechanisms in the two regions.

13.13 Tungsten is being used at half its melting point ( $T_m \approx 3,400^\circ\text{C}$ ) and a stress level of 160 MPa. An engineer suggests increasing the grain size by a factor of 4 as an effective means of reducing the creep rate.

- (a) Do you agree with the engineer? Why? What if the stress level were equal to 1.6 MPa?
- (b) What is the predicted increase in length of the specimen after 10,000 hours if the initial length is 10 cm?

(Hint: Use a Weertman–Ashby map.)

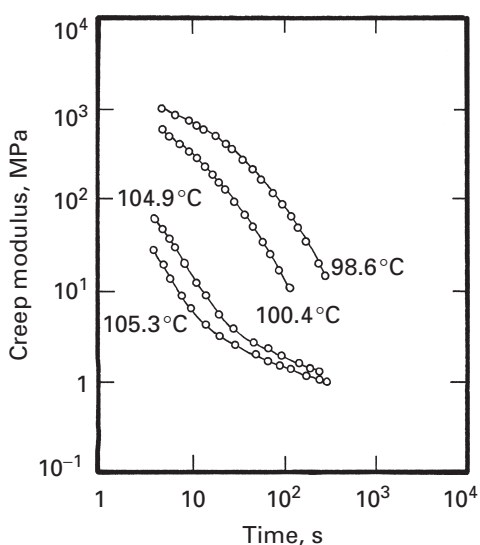


**Fig. Ex13.15** (After W. Kurz, J. P. Mercier, and G. Zambelli, *Introduction aux Sciences des Matériaux* (Lausanne, Switzerland: Presses, 1987), p. 287.)

13.14 Stress relaxation in a polymer results from molecular displacements. Thus, one would expect that the effect of temperature on stress relaxation would be similar to that of any other thermally activated process. As described in the text, an Arrhenius-type expression describes the temperature dependence of such phenomena. Thus, the relaxation time is the inverse rate, or

$$\frac{1}{\tau} \propto \exp(-Q/kT),$$

where the symbols have their usual significance. Describe how you would determine, from this expression, the activation energy  $Q$  of the molecular process causing the relaxation.

13.15 Curves of creep modulus (the inverse of creep compliance) vs. time for four different temperatures are shown in Figure Ex13.15. Obtain a master curve for the polymer at a reference temperature of 101.6 °C.

13.16 An amorphous polymer has a glass transition temperature of 100 °C. A creep modulus of 1 GPa was measured after 1 hour at 75 °C. Using the Williams-Landel-Ferry expression, determine the time required to reach this modulus at 50 °C.

13.17 The viscosity of an amorphous polymer is  $10^5$  Pa · s at 190 °C and  $2 \times 10^2$  Pa · s at 270 °C. At what temperature will the viscosity be  $10^9$  Pa · s?

13.18 What is the strain undergone by a polymer in tension at 67 °C for one minute if the polymer's strain-rate response is given by  $\dot{\epsilon} = 4.5 \times 10^{28} \exp(-200 \text{ kJ}/RT)$ ?

13.19 A nylon cord has an initial stress of 2 MPa and is used to tie a sack. If the relaxation time for this cord is 250 days, how many days will it take for the stress to drop to 0.1 MPa?

13.20 How much time will it take for a rod of polymer to extend from 20 mm to 30 mm at 120 °C if it is deformed at a strain rate  $\dot{\epsilon} = 4.5 \times 10^{11} \exp(-100 \text{ kJ}/RT)$ ?

**13.21** Find the initial stress for a nylon cord if the relaxation time for the cord is 100 days and in 50 days the stress is reduced to 1 MPa.

**13.22** (a) Determine the strain-rate sensitivity in the superplastic range for the alloys shown in Figures 13.39(a) and 13.40, and explain the values encountered. (b) Why does the maximum in ductility vary with temperature in Figure 13.40?

**13.23** Explain why the presence of voids decreases the maximum strain in superplastic deformation.

**13.24** A polymer has a viscosity of  $10^{12}$  Pa · s at 150 °C. If this polymer is subjected to a tensile stress of 100 MPa at that temperature, compute the deformation after 10 h. Assume the polymer to behave as a Maxwell solid. Take  $E = 5$  GPa, and use the equation  $E = \frac{\sigma}{E} + \frac{1}{3\eta}\sigma t$ .

**13.25** For a given polymer, the activation energy for stress relaxation was measured to be 10 kJ/mol. If the stress relaxation time for this polymer at room temperature is 3,600 s, what would be the relaxation time at 100 °C?

**13.26** In a laboratory experiment for potential creep deformation, it was found that the creep rate ( $\dot{\epsilon}$ ) of an alloy is 0.5% per hour at 780 °C and  $2.8 \times 10^{-2}$ % per hour at 650 °C.

- What is the activation energy for creep in the given temperature range?
- At a temperature of 550 °C, what is the estimated creep rate?

**13.27** A component used in a chemical plant is being used at 600 °C and stress of 25 MPa. The corresponding creep rate is:  $3 \times 10^{-12}$  s<sup>-1</sup>. If the stress is increased to 35 MPa and the temperature to 650 °C, what will be the corresponding creep rate?

Given:

$$\begin{aligned} Q &= 150 \text{ kJ/mol}, \\ n &= 4.5 \text{ (stress exponent)}. \end{aligned}$$

**13.28** Honey has a viscosity of 1.5 Pa · s at room temperature. If the activation energy of honey is 20 kJ/mol, what will be its viscosity at 0 °C?

**13.29** From the plot in Figure Ex13.29 on p. 711, determine the amount of strain that a titanium component will undergo if subjected to a stress of 30 MPa at a temperature of 700 °C for 1 hour.

Given:

$$\begin{aligned} D_0 &= 1 \text{ cm}^2 \text{ s}^{-1}, \\ G \text{ (shear modulus)} &= 43.8 \text{ GPa}, \\ Q &= 15 \text{ kJ/mol}, \\ b &= 0.3 \text{ nm}. \end{aligned}$$

**13.30** Give an example of the creep phenomenon in nature (without interference of human paws).

**13.31** Using the parameters in Figure 13.6, calculate the rupture time by the Larson–Miller equation: (a) at a temperature of 1089 K and stress of 100 MPa; (b) at a temperature of 1005 K and stress of 200 MPa; (c) at a temperature of 922 K and stress of 300 MPa.

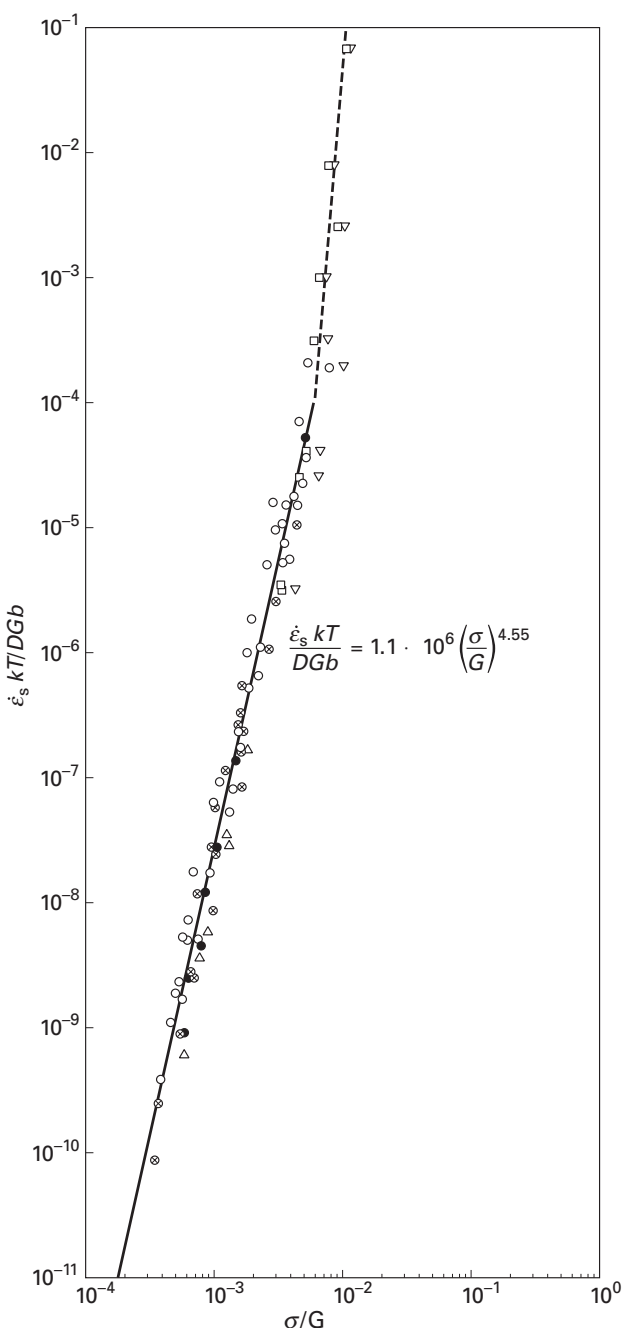


**Fig. Ex13.29** Plot of normalized strain rate  $\dot{\epsilon}_s kT / DGb$  versus normalized stress  $\sigma/G$  for the high-temperature plastic deformation of alpha titanium. (Adapted from H. Conrad, *Prog. Mater. Sci.*, 26 (1981) 375.)

13.32 At room temperature, the relaxation time for a polymer is 100 days. What will be its relaxation time if the activation energy is one-fourth of its current value?

13.33 Calculate the creep compliance for stainless steel with a relaxation time of 72 hours.

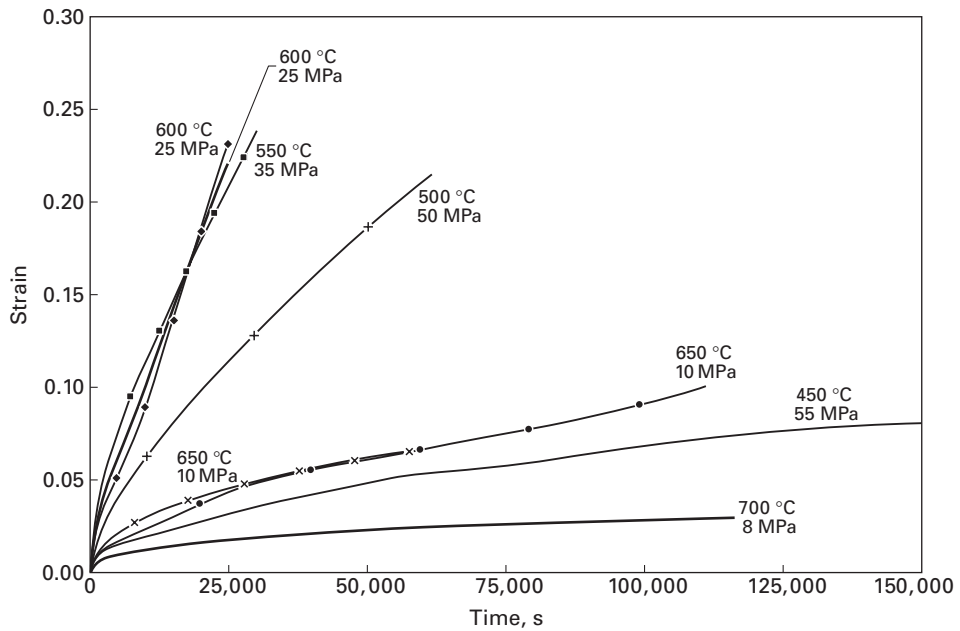


**Fig. Ex13.35** Creep curves for Zircaloy at different temperatures and stresses. (Courtesy of M. E. Kassner.)

13.34 Give an example of a superplastic material and find (and describe) an application for it. A web-engine search is recommended.

13.35 (a) From the different creep tests carried out on Zircaloy, Figure Ex13.35, determine the stress exponent. Given:

$$G(T) = 36.27 \text{ (GPa)} - 0.02T \text{ (°C)},$$

$$D_0 = 5 \times 10^{-4} \text{ m}^2/\text{s},$$

$$Q = 270 \text{ kJ/mol},$$

$$b = 3.23 \times 10^{-10} \text{ m}.$$

(b) Knowing the rupture time at 600 °C and 25 MPa is 10 hours, calculate the rupture time for the other conditions in Figure Ex13.35 using the Monkman–Grant equation.

---

## Chapter 14

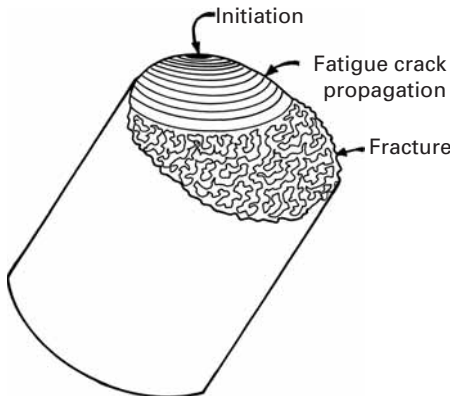
# Fatigue

### 14.1 | Introduction

There is some confusion in the literature about the terminology pertaining to fatigue. We define fatigue as a degradation of mechanical properties leading to failure of a material or a component under *cyclic* loading. This definition excludes the so-called phenomenon of static fatigue, which is sometimes used to describe stress corrosion cracking in glasses and ceramics in the presence of moisture. Brittle solids (glasses and crystalline ceramics) undergo subcritical crack growth in an aggressive environment under static loads. Silica-based glasses are especially susceptible to this kind of crack growth in the presence of moisture. If a glassy phase exists at grain boundaries and interfaces, it will be susceptible to such an attack. Thus, static fatigue is more appropriately a stress corrosion phenomenon, rather than a cyclic stress-related phenomenon.

In general, fatigue is a problem that affects any structural component or part that moves. Automobiles on roads, aircraft (principally the wings) in the air, ships on the high sea constantly battered by waves, nuclear reactors and turbines under cyclic temperature conditions (i.e., cyclic thermal stresses), and many other components in motion are examples in which the fatigue behavior of a material assumes a singular importance. It is estimated that 90% of service failures of metallic components that undergo movement of one form or another can be attributed to fatigue. Often, a fatigue fracture surface will show some easily identifiable macroscopic features, such as beach markings. Figure 14.1 shows a schematic of the fracture surface of, say, a steel shaft that failed in fatigue. The main features of this kind of failure are a fatigue crack initiation site, generally at the surface; a fatigue crack propagation region showing beach markings; and a fast-fracture region where the crack length exceeds a critical length. Typically, the failure under cyclic loading occurs at much lower stress levels than the strength under monotonic loading.

**Fig. 14.1** Schematic representation of a fatigue fracture surface in a steel shaft, showing the initiation region (usually at the surface), the propagation of fatigue crack (evidenced by beach markings), and catastrophic rupture when the crack length exceeds a critical value at the applied stress.



One can divide the study of cyclic behavior of materials into the following three classes:

- Stress-life approach
- Strain-life approach
- Fracture mechanics approach.

The stress-life approach is the oldest way of treating the cyclic fatigue data. It is useful when stresses and strains are mostly elastic. The main drawback of this approach is that we are unable to distinguish between the initiation and propagation phases of fatigue life. The strain-life approach is useful when there is a significant amount of plastic strain. The fatigue life is typically quite short under these conditions. In the fracture mechanics approach, we apply the basic ideas of fracture mechanics to cyclic fatigue, i.e., we use the cyclic stress intensity factor as the crack driver. It allows us to estimate the life spent in propagating a crack from an initial size to larger size or to the critical size corresponding to failure.

In this chapter, we present a basic description of the various aspects of fatigue in different materials, followed by a brief examination of the various fatigue-testing techniques.

## 14.2 Fatigue Parameters and S-N (Wöhler) Curves

We first define some important parameters that will be useful in the subsequent discussion of fatigue. These parameters, shown in Figure 14.2, are as follows:

$$\begin{aligned}
 \text{cyclic stress range} & \quad \Delta\sigma = \sigma_{\max} - \sigma_{\min}, \\
 \text{cyclic stress amplitude} & \quad \sigma_a = (\sigma_{\max} - \sigma_{\min})/2, \\
 \text{mean stress} & \quad \sigma_m = (\sigma_{\max} + \sigma_{\min})/2, \\
 \text{stress ratio} & \quad R = \sigma_{\min}/\sigma_{\max},
 \end{aligned}$$

where  $\sigma_{\max}$  and  $\sigma_{\min}$  are the maximum and minimum stress levels, respectively.

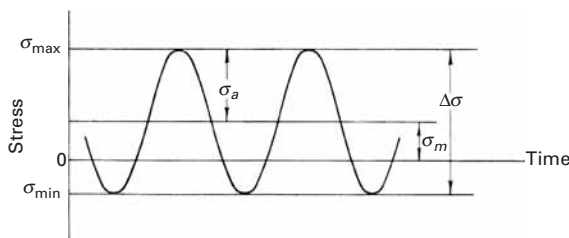
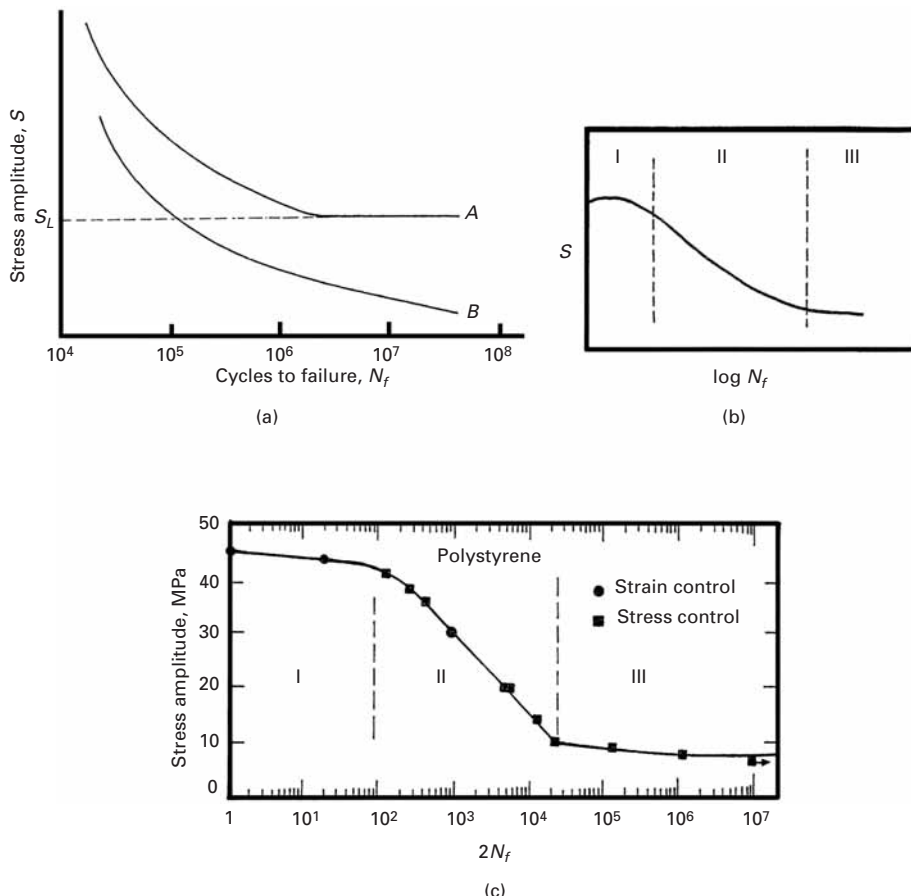


Fig. 14.2 Fatigue parameters.



Traditionally, the behavior of a material under fatigue is described by the S-N (or  $\sigma$ - $N$ ) curves (Figure 14.3), where  $S$  (or  $\sigma$ ) is the stress and  $N$  is the number of cycles to failure. Such an S-N curve is frequently called a *Wöhler curve*, after the German engineer who first observed that kind of fatigue behavior in railroad car wheels in the 1860s. For steels, in general, one observes a fatigue limit or endurance limit (curve A in Figure 14.3(a)), which represents a stress level below which the material does not fail and can be cycled indefinitely. Such an endurance limit does not exist for nonferrous metals (curve B in the figure). Polymeric materials show essentially similar S-N curves. Figure 14.3(b) shows a schematic of an S-N curve for a variety of polymers. Polymers that form crazes, such as polymethylmethacrylate (PMMA) and polystyrene (PS), may show a flattened portion in the very beginning, indicated as stage I in the figure. In region II, the stress is not

**Fig. 14.3** (a)  $S$  (stress)- $N$  (cycles to failure) curves. (A) Ferrous and (B) nonferrous metals;  $S_L$  is the endurance limit. (b) S-N curves for polymeric materials. Polymers that form crazes, such as polymethylmethacrylate (PMMA) and polystyrene (PS), may show a flattened portion in the very beginning, indicated as stage I. (c) An example of an actual S-N curve showing the three stages in the case of polystyrene.

high enough for crazes to form. Crazed regions are, of course, the sites of microcrack nucleation. They will form in the initial quarter of a tensile cycle in such materials. Recall that the crazes do not form in compression. Such a flat region does not exist for polymers that do not show craze formation, and the S-N curve for such polymers will be very similar to that of metals; that is, stage I is simply an extension of stage II. An example of an actual S-N curve showing the three stages in the case of polystyrene is presented in Figure 14.3(c). Polystyrene shows extensive crazing at room temperature. Polycarbonate, on the other hand, does not show crazing at room temperature, and its S-N curve does not show stage I. No such S-N curves are available for ceramics, although, as we shall see later in the chapter, stable subcritical crack propagation under cyclic fatigue can occur in ceramics. Note that the relationship between S and N is not a single-valued function, but serves to indicate a statistical tendency. Also, the fatigue life determined in terms of S-N curves cannot be separated into the initiation and propagation parts of fatigue. Figure 14.4 shows representative S-N curves for (a) metals and (b) polymers. It is apparent that the endurance life varies widely. There is a dramatic difference between, for instance, 1.2% C steel and gray cast iron.

### 14.3 | Fatigue Strength or Fatigue Life

Traditionally, fatigue life has been presented in the form of an S-N curve (Figure 14.3). With regard to this measure, *fatigue strength* refers to the capacity of a material to resist conditions of cyclic loading. However, in the presence of a measurable plastic deformation, materials respond differently to strain cycling than to stress cycling. Thus, one would expect that the fracture response of a material under cyclic conditions would show a similar difference. In this section, we treat fatigue life in terms of strength or strain versus number of cycles to failure  $N_f$  or number of reversals to failure,  $2N_f$ . It is convenient to consider separately the elastic and plastic components of strain. The elastic component can be readily described by means of a relation between the stress amplitude and the number of reversals (i.e., twice the number of cycles). This is called the Basquin<sup>1</sup> relationship. It may be expressed as:

$$\sigma_a = \sigma'_f (2N_f)^b.$$

Since the deformation is elastic, we can write:

$$\sigma_a = \frac{\Delta\sigma}{2} = \frac{\Delta\varepsilon_e E}{2}.$$

Thus:

$$\Delta\varepsilon_e / 2 = \sigma_a / E = (\sigma'_f / E)(2N_f)^b,$$

---

<sup>1</sup> O. H. Basquin, *Proc. Am. Soc. For Testing and Matls.*, 10 (1910) 625.

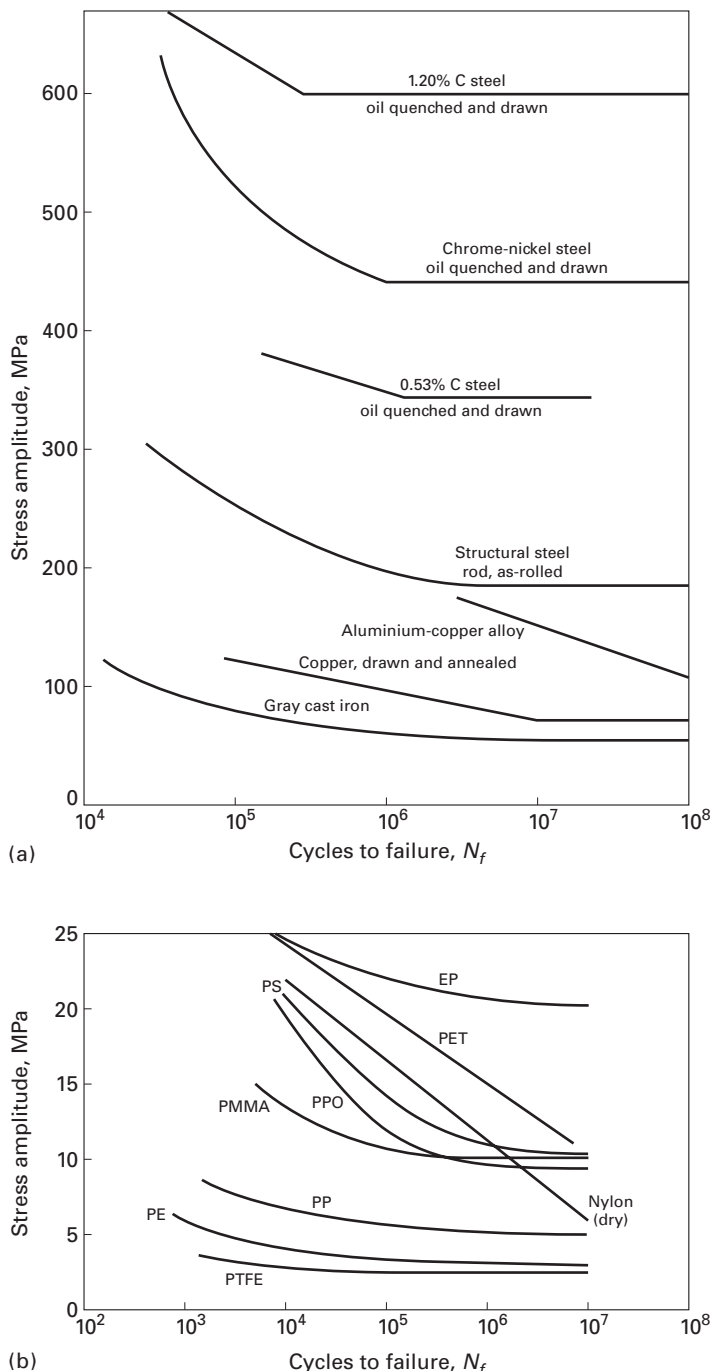
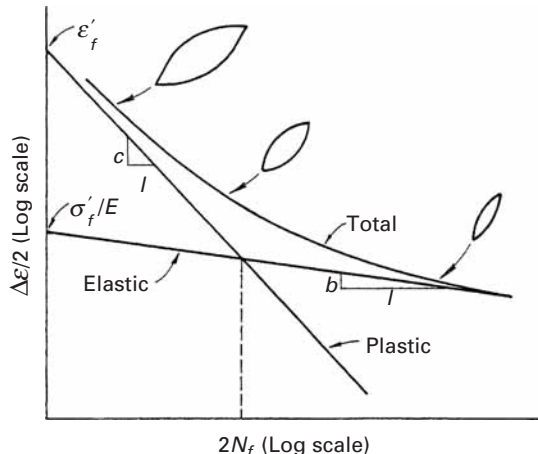


**Fig. 14.4** S-N curves for typical  
(a) metals and (b) polymers.

where  $\Delta\varepsilon_e/2$  is the elastic strain amplitude,  $\sigma_a$  is the true stress amplitude,  $\sigma'_f$  is the fatigue strength coefficient (equal to the stress intercept at  $2N_f = 1$ ),  $N_f$  is the number of cycles to failure, and  $b$  is the fatigue strength exponent. This relationship is an empirical representation of the S-N curve above the fatigue limit in Figure 14.3. On a log-log plot, it gives a straight line of slope  $b$ . One can see that the

**Fig. 14.5** Superposition of elastic and plastic curves gives the fatigue life in terms of total strain. (Adapted with permission from R. W. Landgraf, in *American Society for Testing and Materials, Special Technical Publication (ASTM STP) 467* (Philadelphia: ASTM, 1970), p. 3.)



two expressions are equivalent. In elastic deformation,  $\sigma_a/E$  is equal to the elastic strain amplitude,  $\Delta\epsilon_e/2$ .

The plastic strain component is better described by the Manson-Coffin relationship,<sup>2</sup>

$$\Delta\epsilon_p/2 = \sigma_a/E = \epsilon'_f(2N_f)^c,$$

where  $\Delta\epsilon_p/2$  is the amplitude of the plastic strain,  $\epsilon'_f$  is the ductility coefficient in fatigue (equal to the strain intercept at  $2N_f = 1$ ),  $2N_f$  is the number of reversals to failure, and  $c$  is the ductility exponent in fatigue. On a log-log plot, the Manson-Coffin relation gives a straight line of slope  $c$ . It has been observed that a smaller value of  $c$  results in a longer fatigue life. In the regimen of high-strain, low-cycle fatigue, the Manson-Coffin relation assumes great importance. Experimentally, it is frequently more convenient to control the total strain. In many structural components, the material in a critical place (say, at a notch root) may be subjected, essentially, to strain control conditions due to the elastic constraint of the surrounding material. For a material subjected to a total strain range of  $\Delta\epsilon_t$  (elastic and plastic strain), we can determine the fatigue strength by a superposition of the elastic and plastic strain components, i.e.,

$$\Delta\epsilon_t/2 = \Delta\epsilon_e/2 + \Delta\epsilon_p/2 = (\sigma'_f/E)(2N_f)^b + \epsilon'_f(2N_f)^c.$$

Thus, we expect that the curve of the fatigue life, in terms of total strain, will tend to the plastic curve at large total-strain amplitudes, whereas it will tend to the elastic curve at low total-strain amplitudes, as shown schematically in Figure 14.5. An example of such a behavior from a real material (an 18%-Ni maraging steel) is shown in Figure 14.6. The Manson-Coffin regimen is known as *low-cycle fatigue*, in which there is a discrete amount of plastic deformation in each cycle. The Basquin regimen is called *high-cycle fatigue*. The stresses are primarily

<sup>2</sup> L. F. Coffin, *Trans. ASME*, 76 (1954) 931; S. M. Manson and M. H. Hirschberg, in *Fatigue: An Interdisciplinary Approach* (Syracuse, NY: Syracuse University Press, 1964), p. 133.

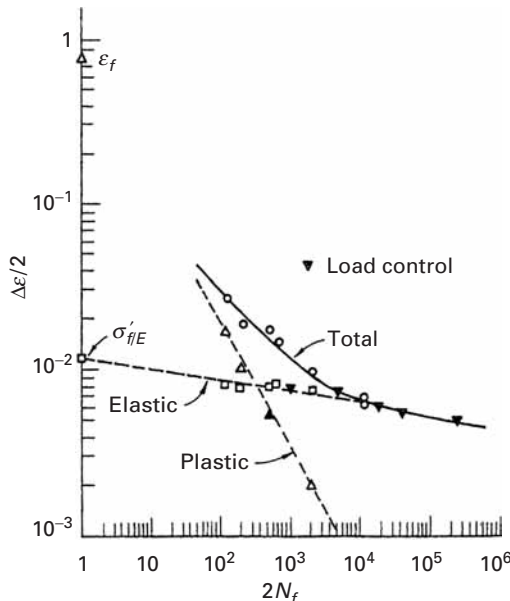


**Fig. 14.6** Fatigue life in terms of strain for an 18% Ni maraging steel. (Adapted with permission from R. W. Landgraf, in American Society for Testing and Materials, Special Technical Publication ASTM STP 467, (Philadelphia: ASTM, 1970), p. 3.)

elastic in this domain. The typical range of values for the exponents  $b$  (high-cycle fatigue) and  $c$  (low-cycle fatigue) are:

$$b : \frac{1}{8} \rightarrow \frac{1}{5} \text{ (Basquin exponent)},$$

$$c : 0.5 \rightarrow 0.6 \text{ (Manson-Coffin exponent)}.$$

## 14.4 | Effect of Mean Stress on Fatigue Life

The mean stress  $\sigma_m$  can have an important effect on the fatigue strength of a material. A simple and crude way to demonstrate the effect of  $\sigma_m$  would be to present S-N curves of a given material for different values of  $\sigma_m$  on the same graph. Figure 14.7 shows such curves schematically. Note that, for a given stress amplitude  $\sigma_a$ , as the mean stress increases, the fatigue life decreases.

We can describe the effect of  $\sigma_m$  in a very simple manner. Suppose that the limiting value of any combination of stresses is  $\sigma_f$ , the monotonic true fracture stress. We can think of other arbitrary limits, such as the ultimate tensile stress  $\sigma_{UTS}$  or the yield stress  $\sigma_y$ , but  $\sigma_f$  is the maximum allowable true stress. Figure 14.8(a) shows a schematic plot of alternating stress  $\sigma_a$  (or  $S$ ) versus  $\sigma_m$ . Note that, for  $\sigma_m = 0$ , the alternating stress  $\sigma_a$  is a maximum and equal to  $\sigma_f$ . For  $\sigma_a = \sigma_f$ , the fatigue life is simply one-fourth of a cycle. For an ideal material, one would expect the relationship  $\sigma_a + \sigma_m \leq \sigma_f$ , the limiting value of any combination of stresses, to be valid. Thus, one can expect a straight line to join points A and B in Figure 14.8(a). Cyclic loading is not possible to the right of line AB. Then, in the presence of a mean stress of, say,  $\sigma_f/3$ , we will have a maximum allowable stress equal to

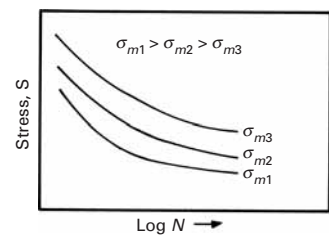


**Fig. 14.7** Effect of mean stress on S-N curves. The fatigue life decreases as the mean stress increases.

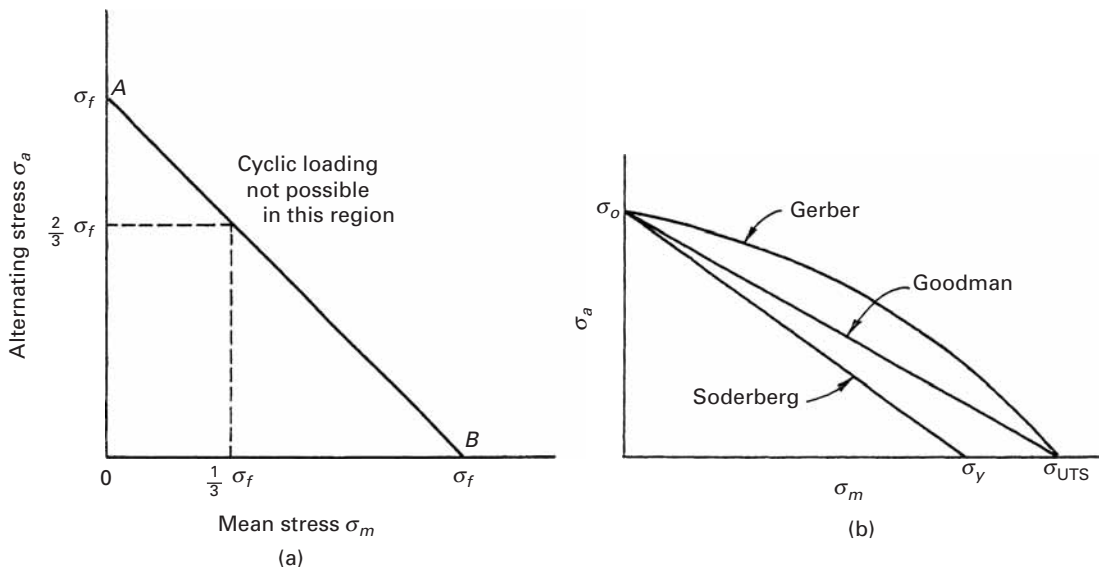


**Fig. 14.8** (a) Effect of mean stress on fatigue life. (b) Gerber, Goodman, and Soderberg diagrams, showing mean stress effect on fatigue life.

$2\sigma_f/3$ . Note that this description is an oversimplification of the real behavior of the material, in as much as it assumes that the damage produced in each cycle by cyclic plastic strain is independent and noncumulative.

Various empirical expressions have been proposed which take into account the effect of mean stress on fatigue life. Some of these are the following: Goodman's relationship, which assumes a linear effect of mean stress between  $\sigma_m = 0$  and  $\sigma_{UTS}$ :

$$\sigma_a = \sigma_0[1 - \sigma_m/\sigma_{UTS}].$$

Gerber's relationship, which assumes a parabolic effect of mean stress between  $\sigma_m = 0$  and  $\sigma_{UTS}$ :

$$\sigma_a = \sigma_0[1 - (\sigma_m/\sigma_{UTS})^2].$$

Soderberg's relationship, which assumes a linear effect of mean stress between  $\sigma_m = 0$  and  $\sigma_y$ :

$$\sigma_a = \sigma_0(1 - \sigma_m/\sigma_y).$$

In all these relationships,  $\sigma_m$  is the mean stress,  $\sigma_a$  is the fatigue strength in terms of stress amplitude when  $\sigma_m \neq 0$ ,  $\sigma_0$  is the fatigue strength in terms of stress amplitude when  $\sigma_m = 0$ ,  $\sigma_{UTS}$  is the monotonic ultimate tensile strength, and  $\sigma_y$  is the monotonic yield stress. Figure 14.8(b) shows the three relations schematically. Experimentally, it has been observed that the great majority of data falls between the Gerber and Goodman lines. Thus, the Goodman diagram represents a conservative estimate of the mean stress effect. Note that the three expressions involve uniaxial stresses. In most real-life situations, one encounters biaxial or triaxial situations. Hence, one needs to define stresses corresponding to  $\sigma_y$  or  $\sigma_{UTS}$  under multiaxial stress situations. A practical way around this is to use the concept of equivalent

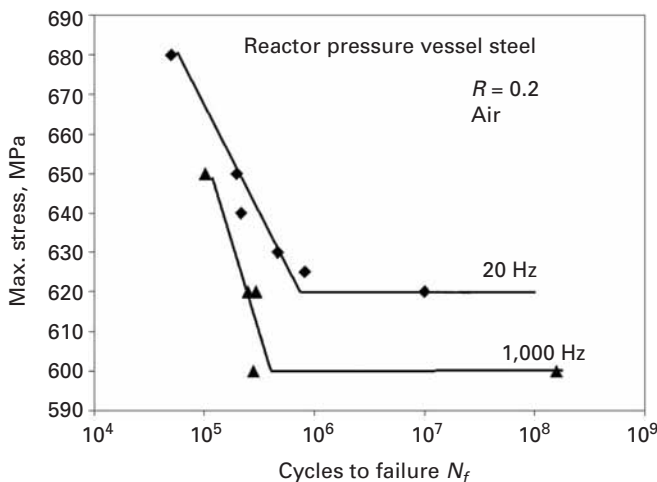


**Fig. 14.9** Effect of frequency on the fatigue life of a reactor pressure vessel steel. The fatigue life decreases at 1,000 Hz compared with that at 20 Hz. (Used with permission from P. K. Liaw, B. Yang, H. Tian et al., ASTM STP 1417 (West Conshohocken, PA: American Society for Testing and Materials, 2002.))

distortion energy – that is, to compute the distortion energy for uniaxial and multiaxial states and (a) assume that the cycling behavior of a material is equivalent when the material is cycled between two energy distortion values and (b) compute the maximum value of the mean stress by use of von Mises yield criterion. (See Chapter 3.) Then we can find the failure conditions for a given multiaxial stress state.

## 14.5 | Effect of Frequency

Frequency of cycling can have an effect on the fatigue behavior of a material. Figure 14.9 shows the S-N curves for a steel used for nuclear reactor pressure vessels at 20 Hz and 1,000 Hz. Note that increasing the test frequency from 20 Hz to 1,000 Hz resulted in lower fatigue life at a given stress level. The decrease of the fatigue life at higher frequencies is attributed to the temperature increase that results in the higher-frequency tests. We should mention that such high-frequency fatigue tests are done in very sophisticated machines. Special servovalves, activated by voice coils, allow frequencies of up to 1,000 Hz to be obtained. Typically, such a machine is housed in a separate, sound-proof room with a heat pump that allows cooling, thus preventing overheating of the servovalves.

## 14.6 | Cumulative Damage and Life Exhaustion

The discussion in the preceding sections was restricted to fatigue under simple conditions of constant amplitude, constant frequency, and so on. In real life, the service conditions are rarely so simple. Many components and structures are subject to a range of fluctuating loads, mean stress levels, and variable frequencies. Thus, it is of great importance to be able to predict the life of a component subjected to variable-amplitude conditions, starting from data obtained in simple

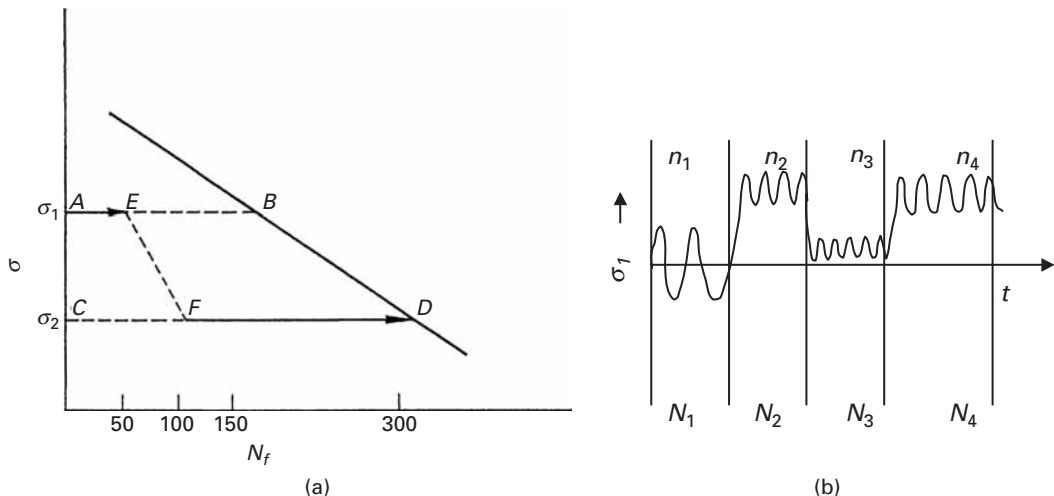


**Fig. 14.10** (a) Damage accumulation, in a high-to-low loading sequence. (Adapted with permission from B. I. Sandor, *Fundamentals of Cyclic Stress and Strain* (Madison, WI: University of Wisconsin Press, 1972).) (b) Sequence of block loadings at four different mean stresses and amplitudes.

constant-amplitude tests. The cumulative-damage theories attempt to do just that.

Basically, these theories consider fatigue to be a process of accumulating damage in a material until a certain maximum tolerable damage is reached. In other words, the phenomenon of fatigue is considered to be an exhaustion process of a material's inherent life (or ductility). A schematic fatigue life diagram, shown in Figure 14.10(a), elucidates the concept. At a constant stress of, say  $\sigma_1$ , the life of the material is 150 cycles, while at  $\sigma_2$  it is 300 cycles. According to the cumulative-damage theory, in going from A to B or C to D, we gradually exhaust the material's fatigue life. That is, at points A and C, 100% of life at that level is available, while at points B and D, the respective lives are completely exhausted. If fatigue damage does, indeed, accumulate in a linear manner, each cycle contributes the same amount of damage at a given stress level. For example, on cycling the material from A to E, we exhaust one-third of the fatigue life available at  $\sigma_1$ . If we now change the stress level to  $\sigma_2$ , then the percentage of life already exhausted at  $\sigma_1$  is equivalent to the percentage of life exhausted at  $\sigma_2$ . That is, one-third of fatigue life at  $\sigma_2$  is equivalent to one-third of fatigue life at  $\sigma_1$ . Thus, in descending from E to F, we get from 50 to 100 cycles, and, as only one-third of fatigue life was exhausted at  $\sigma_1$ , two-thirds of fatigue life – that is, 200 cycles – is still available at  $\sigma_2$ . The same kind of change can be described for a low-to high-stress traversal.

Figure 14.10(b) shows the sequence of cyclic loading periods, each one with a specific mean stress and stress amplitude. The number of cycles in the four blocks are  $n_1$ ,  $n_2$ ,  $n_3$ ,  $n_4$ , etc. The total life for each of these blocks is, respectively,  $N_1$ ,  $N_2$ ,  $N_3$ ,  $N_4$ , etc. We just add up the fractions. The parallel can be drawn with our health. If a person were to smoke during their entire life, their life expectancy would be, say 50 years. A totally healthy person would live 100 years. If somebody alternates between ten years of smoking and ten years of no smoking, the life expectancy would be shortened to 75.

This linear damage model does not concern itself with the physical picture of the fatigue damage. It does, however, give an empirical way of predicting the fatigue life after a complex loading sequence. The method is generally known as the *Palmgren-Miner rule* or, simply, *linear cumulative-damage theory*.<sup>3</sup> The Palmgren-Miner rule says that the sum of all life fractions is unity; that is,

$$\boxed{\sum_{i=1}^k n_i/N_i = 1, \quad \text{or}}$$

$$n_1/N_1 + n_2/N_2 + n_3/N_3 + n_4/N_4 + \dots n_k/N_k = 1, \quad (14.1)$$

where  $k$  is the number of stress levels in the block spectrum loading;  $N_1, N_2, \dots, N_i$  are the fatigue lives corresponding to stress levels  $\sigma_1, \sigma_2, \dots, \sigma_i$ , respectively; and,  $n_1, n_2, \dots, n_i$  are the number of cycles carried out at the respective stress levels. This rule is obeyed by a series of materials if the underlying assumptions are satisfied. The principal assumption is that the damage accumulation rate at any level does not depend on the prior loading history of the material; in other words, the damage per cycle is the same at the beginning or at the end of fatigue life, at a given stress level. This implies that the magnitude and direction of the change in amplitude (from low to high or high to low) do not have an effect on fatigue life. We also assume that in each block the loading is totally reversible (i.e.,  $\sigma_m = 0$ ). The validity of these assumptions is problematic. For example, it is quite likely that, for blocks identical in size and amplitude, a change in load from high to low would be much more dangerous than one from low to high: A crack initiated at high loads can continue to grow at low loads, whereas in the reverse case, at low loads, perhaps the crack would never have formed.

### Example 14.1

The S-N curve of a material is described by the relationship

$$\log N = 10(1 - S/\sigma_{\max}),$$

where  $N$  is the number of cycles to failure,  $S$  is the amplitude of the applied cyclic stress, and  $\sigma_{\max}$  is the monotonic fracture strength – i.e.,  $S = \sigma_{\max}$  at  $N = 1$ . A rotating component made of this material is subjected to  $10^4$  cycles at  $S = 0.5 \sigma_{\max}$ . If the cyclic load is now increased to  $S = 0.75 \sigma_{\max}$ , how many more cycles will the material withstand?

*Solution:*

For  $S = 0.5 \sigma_{\max}$ ,

$$\log N_1 = 10(1 - 0.5) = 5.$$

<sup>3</sup> A. Palmgren, Z. Ver. Dtsch. Ing., 53 (1924) 339; M. A. Miner, J. Appl. Mech., 12 (1945) 159.

Thus,

$$N_1 = 10^5 \text{ cycles.}$$

For  $S = 0.75 \sigma_{\max}$ ,

$$\log N_2 = 2.5.$$

So

$$N_2 = 316 \text{ cycles.}$$

Using Palmgren-Miner's rule, we have

$$n_1/N_1 + n_2/N_2 = 10^4/10^5 + n_2/316 = 1$$

or

$$n_2 = 284 \text{ cycles.}$$

### Example 14.2

A microalloyed steel was subjected to two fatigue tests at  $\pm 400$  MPa and  $\pm 250$  MPa. Failure occurred after  $2 \times 10^4$  and  $1.2 \times 10^6$  cycles, respectively, at these two stress levels. Making appropriate assumptions, estimate the fatigue life at  $\pm 300$  MPa of a part made from this steel that has already undergone  $2.5 \times 10^4$  cycles at  $\pm 350$  MPa.

**Solution:** We assume an equation of the form (other forms can also be assumed):

$$\begin{aligned} \Delta\sigma(N_f)^a &= c, \\ 800(2 \times 10^4)^a &= 500(1.2 \times 10^6)^a, \\ \frac{800}{500} &= 1.6 = \left(\frac{1.2 \times 10^6}{2 \times 10^4}\right)^a = (60)^a, \\ a &= 0.115, \\ c &= 800(2 \times 10^4)^{0.115} \text{ MPa} \\ &= 2,498 \text{ MPa}. \end{aligned}$$

At  $\pm 350$  MPa,

$$\begin{aligned} N_{f1} &= \left(\frac{c}{\Delta\sigma}\right)^{1/a} = \left(\frac{2,498}{700}\right)^{1/0.115} \\ &= (3.57)^{8.7} = 6.4 \times 10^4 \text{ cycles}. \end{aligned}$$

For  $2.5 \times 10^4$  cycles,

$$\frac{N_1}{N_{f1}} = \frac{2.5 \times 10^4}{6.4 \times 10^4} = 0.39.$$

At  $\pm 300$  MPa,

$$\begin{aligned} N_{f2} &= \left(\frac{c}{\Delta\sigma}\right)^{1/a} = \left(\frac{2,498}{600}\right)^{1/0.115} \\ &= (4.16)^{8.7} = 2.45 \times 10^5 \text{ cycles}. \end{aligned}$$

From Palmgren-Miner's rule,

$$\frac{N_1}{N_{f1}} + \frac{N_2}{N_{f2}} = 1,$$

$$\frac{N_2}{N_{f2}} = 1 - \frac{N_1}{N_{f1}} = 1 - 0.39 = 0.61.$$

Therefore,

$$N_2 = 0.61 \times N_{f2}$$

$$= 0.61 \times 2.45 \times 10^5$$

$$= 1.49 \times 10^5 \text{ cycles.}$$

## 14.7 | Mechanisms of Fatigue

In this section, we describe the physical mechanisms responsible for fatigue mechanisms – mainly, fatigue crack nucleation and propagation. We assume that our starting material does *not* have any pre-existing crack or cracklike defects. The fracture mechanics approach, focusing only on the propagation of preexisting cracks, will be examined in Section 14.8.

### 14.7.1 Fatigue Crack Nucleation

Fatigue cracks nucleate at singularities or discontinuities in most materials. Discontinuities may be on the surface or in the interior of the material. The singularities can be structural (such as inclusions or second-phase particles) or geometrical (such as scratches or steps). The explanation of preferential nucleation of fatigue cracks at surfaces perhaps resides in the fact that plastic deformation is easier there and that slip steps form on the surface. Slip steps alone can be responsible for initiating cracks, or they can interact with existing structural or geometric defects to produce cracks. Surface singularities may be present from the beginning or may develop during cyclic deformation, as, for example, the formation of intrusions and extrusions at what are called the persistent slip bands (PSBs) in metals. These bands were first observed in copper and nickel by Thompson *et al.*<sup>4</sup> They appeared after cyclic deformation and persisted even after electro-polishing. On retesting, slip bands appeared again in the same places. Later, the dislocation structure in the PSBs was investigated extensively. Figure 14.11(a) shows a TEM micrograph of a polycrystalline copper sample that was cycled to a total strain amplitude of  $6.4 \times 10^{-4}$  for  $3 \times 10^5$  cycles. Fatigue cycling was carried out in reverse bending at room temperature and at a frequency of 17 Hz. The thin foil was taken 73 μm below the surface. Two parallel PSBs (diagonally across the micrograph) embedded in a veined structure in polycrystalline

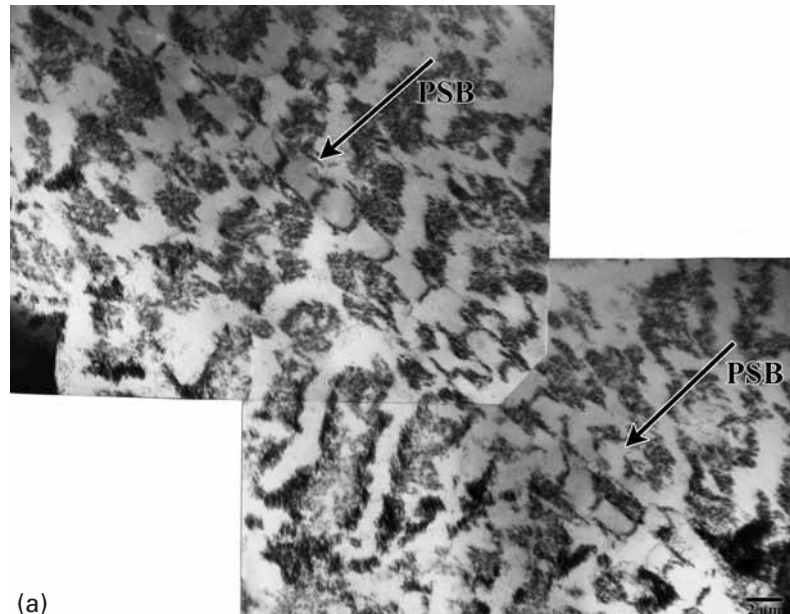
<sup>4</sup> N. Thompson, N. J. Wadsworth, and N. Louat, *Phil. Mag.*, 1 (1956) 113.

**Fig. 14.11** (a) Persistent slip bands in vein structure.

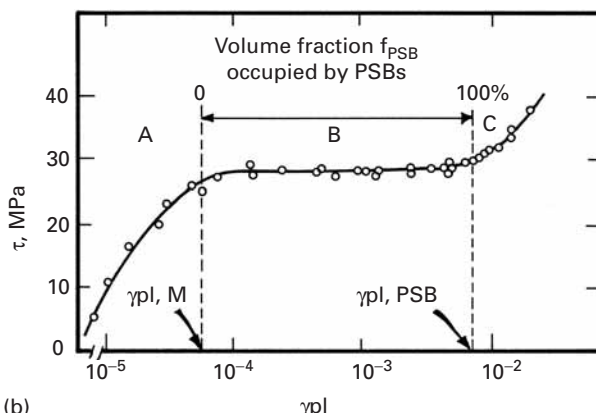
Polycrystalline copper fatigued at a total strain amplitude of  $6.4 \times 10^{-4}$  for  $3 \times 10^5$  cycles. Fatiguing carried out in reverse bending at room temperature and at a frequency of 17 Hz. The thin foil was taken 73  $\mu\text{m}$  below the surface. (Courtesy of J. R. Weertman and H. Shirai.)

(b) Cyclic shear stress,  $\tau$ , vs. plastic cyclic shear strain,  $\gamma_{pl}$ , curve for a single crystal of copper oriented for single slip. (After H. Mughrabi, *Mater. Sci. Eng.*, 33 (1978) 207.) The terms  $\gamma_{pl, M}$  and  $\gamma_{pl, PSB}$  refer to cyclic plastic shear strain in the matrix and persistent slip bands, respectively.

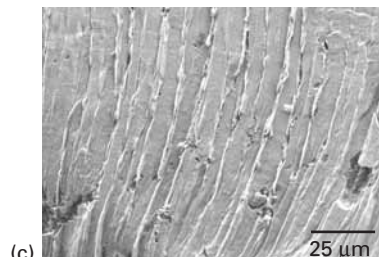
(c) Intrusions/extrusions in a tin-based solder due to thermal fatigue. (Courtesy of N. Chawla and R. Sidhu)



(a)



(b)



(c)

copper can be seen. The PSBs are clearly distinguished and consist of a series of parallel "hedges" (a ladder). These ladders are channels through which the dislocations move and produce intrusions and extrusions at the surface Figure 14.11(c). Stacking-fault energy and the concomitant ease or difficulty of cross-slip play an important role in

the development of the dislocation structure in the PSBs. Kuhlmann-Wilsdorf and Laird have discussed models for the formation of PSBs in metals.<sup>5</sup> They compared the deformation substructures produced by unidirectional and cyclic (fatigue) deformation and interpreted them in terms of the differences between the two modes of deformation. The principal differences are as follows:

1. Due to the much larger time spans of deformation in fatigue, the dislocation structures formed are much closer to the configurations having minimum energy than the ones generated by monotonic straining. That is, more stable dislocation arrays are observed after fatigue.
2. The oft-repeated to-and-fro motion in fatigue minimizes the buildup of surpluses of local Burgers vectors, which are fairly prevalent after unidirectional (monotonic) strain.
3. Much higher local dislocation densities are found in fatigued specimens.

The characteristic dislocation arrangements observed in FCC metals form in the following manner. In monocrystals, we first have uniform fine slip, followed by the formation of veins consisting of dense bundles of dislocation dipoles and other debris. After this, PSBs are formed. They occur with the onset of saturation and are often associated with slight work-softening. There also seems to be a threshold strain for PSB formation, equal to  $8 \times 10^{-5}$  in the case of copper monocrystals. When subjected to strain-controlled cycling, an initially annealed metal hardens at first and then attains a saturation stress. If we plot this saturation stress against the applied plastic strain, we get another type of cyclic stress-strain curve, an example of which is shown for a single crystal of copper oriented for single slip in Figure 14.11(b). The curve has three stages, one of which is a plateau region, and each stage is characterized by a distinct dislocation structure. At low strains in the plateau region, the structure consisted of a hard matrix containing a loop-patch dislocation structure and a soft PSB with dislocations in a ladderlike arrangement. At large strains in the plateau region (plastic shear strain greater than  $2 \times 10^{-3}$ ), most of the matrix phase and a part of the PSB had a well-developed mazelike structure. In the case of a polycrystal, the grains in the softest orientation and with not much constraint from their neighbors deform and harden by the accumulation of dislocations. An example of such a structure in a Cu-Ni polycrystal is shown in Figure 14.12. Dislocation walls form on {100} planes.

The interface between the PSB and the matrix represents a discontinuity in the density and distribution of dislocations. Hence, one would expect PSBs to be the preferential sites for fatigue crack nucleation. The surface of a metal subjected to cyclic stressing will have PSB extrusions and intrusions. Recall that monotonic loading of a

<sup>5</sup> D. Kuhlmann-Wilsdorf and C. Laird, *Mater. Sci. Eng.*, 27 (1977) 137; *Mater. Sci. Eng.*, 37 (1979) 111.

**Fig. 14.12** Well-developed maze structure, showing dislocation walls on {100} in Cu-Ni alloy fatigued to saturation. (From P. Charsley, *Mater. Sci. Eng.*, 47 (1981) 181.)

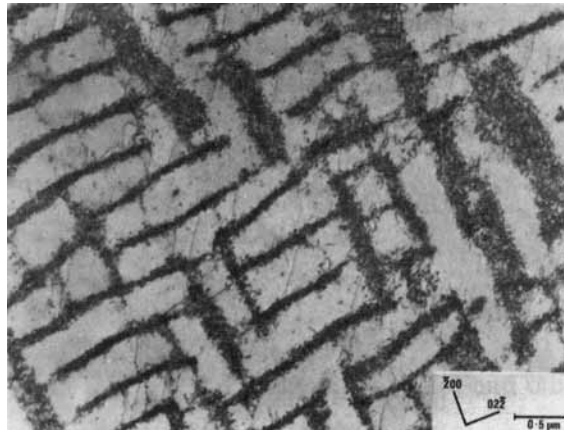
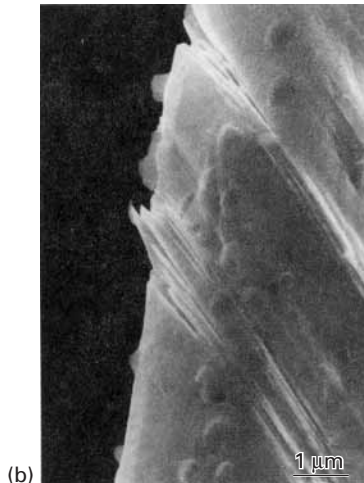
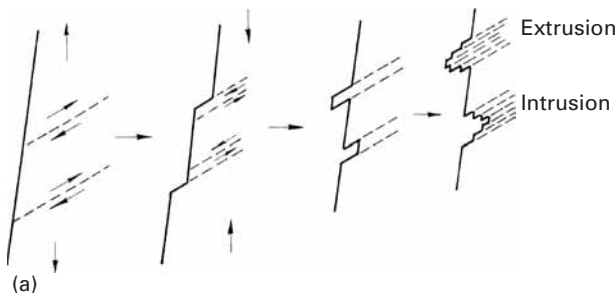
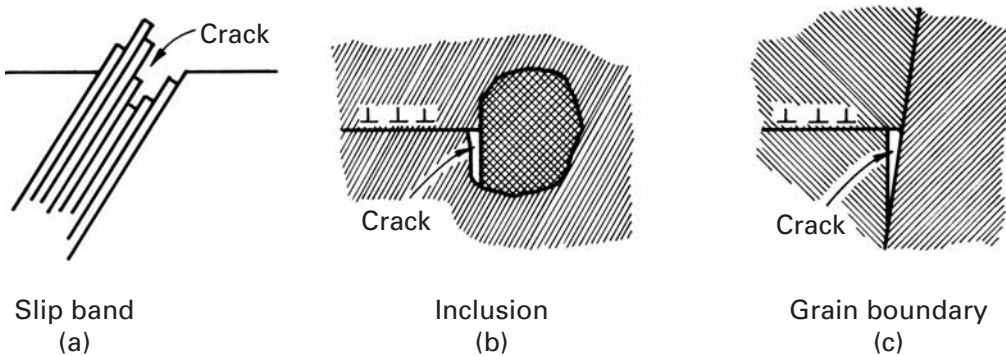


**Fig. 14.13** (a) Fatigue crack nucleation at slip bands. (b) SEM of extrusions and intrusions in a copper sheet. (Courtesy of M. Judelwicz and B. Ilschner.)



metal results in the formation of slip steps at the surface. On being subjected to cyclic loading, however, the surface of the metal will have intrusions and extrusions where PSBs emerge. A model for this form of nucleation is shown in Figure 14.13(a). During the loading part of the cycle, slip occurs on a favorably oriented plane, and during the unloading part of the cycle, reverse slip occurs on a parallel plane, because the slip on the original plane is inhibited owing to



Slip band

(a)

Inclusion

(b)

Grain boundary

(c)

hardening or, perhaps, the oxidation of the newly formed free surface. The first cyclic slip may create an extrusion or an intrusion at the surface. An intrusion may grow and form a crack by continued plastic deformation during subsequent cycles. An actual example of the formation of intrusions and extrusions in a sample of a copper sheet subjected to 15,000 cycles under a 60-MPa amplitude is shown in an SEM micrograph in Figure 14.13(b). Even during cyclic stressing in the tension-tension mode, this mechanism can function, as the plastic strain occurring at the peak load may lead to residual compressive stresses during the decreasing-load part of the cycle.

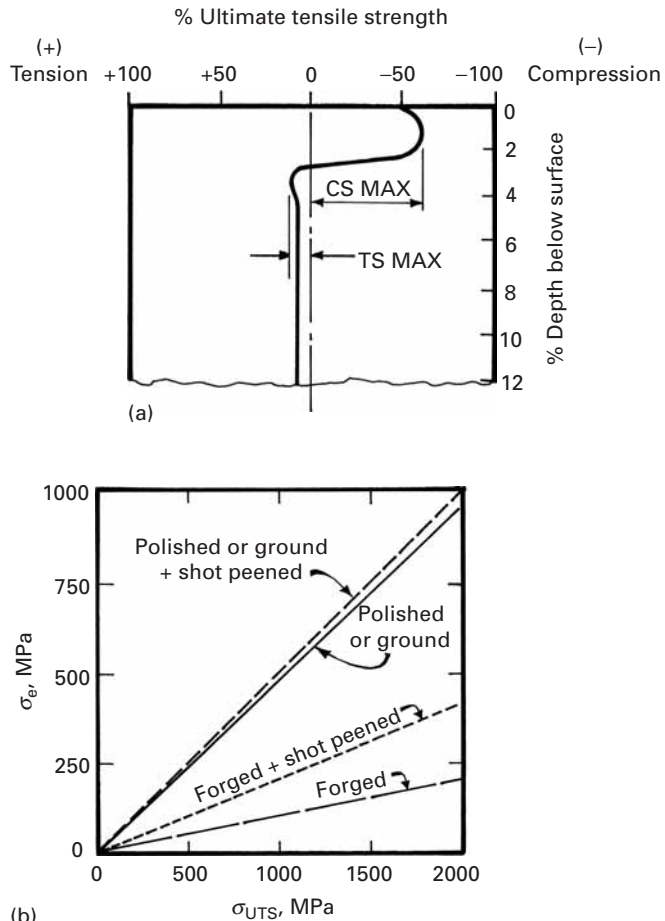
Such intrusions/extrusions owing to PSBs can form in ductile metals under the action of thermal fatigue as well. Thermal fatigue involves cyclic loading under thermal stresses. Such thermal stresses occur when a temperature change occurs, which leads to differential expansion in two components that are joined together. Figure 14.11(c) shows an interesting example of this in a tin-based solder in contact with copper; the two being subjected to temperature-induced thermal stress.

Twin boundaries can be important crack nucleation sites in hexagonal close-packed materials such as magnesium, titanium, etc., and their alloys. Inclusions and second-phase particles are commonly the dominant nucleation sites in materials of commercial purity – for example, aluminum, high-strength steels, and many polymers. Grain boundaries can become important nucleation sites at large strain amplitudes and at temperatures greater than about  $0.5T_m$ , where  $T_m$  is the melting point in kelvin, or in the presence of impurities that produce grain-boundary embrittlement (e.g., O<sub>2</sub> in iron). Some of these mechanisms are illustrated schematically in Figure 14.14.

Since most fatigue failures form at the surface of a material, the condition of the surface is very important. Indeed, polishing the surface can significantly increase the fatigue life of the material. A very important technological process to enhance fatigue life is *shot peening*, in which small metallic spheres are accelerated and hit the surface of the part. This bombardment by small particles puts the surface layer of a component in residual compression. This technique is used routinely in industry. Examples include compression coil springs in the automotive industry, wing skins for aircraft and other applications.

**Fig. 14.14** Some mechanisms of fatigue crack nucleation. (After J. C. Grosskreutz, Tech. Rep. AFML-TR-70-55 (Wright-Patterson AFB, OH: Air Force Materials Laboratory), 1970.)

**Fig. 14.15** (a) Residual stress profile generated by shot peening of a surface; CS and TS indicate compressive and tensile stress, respectively. (b) Effect of shot peening on fatigue life,  $\sigma_e$  of steels with different treatments as a function of ultimate tensile strength,  $\sigma_{UTS}$ . (After J. Y. Mann, *Fatigue of Materials* (Melbourne, Melbourne University Press, 1967).)



Compressive stresses in surface layers have been introduced by laser. The technique called laser peening, involves a laser system based on neodymium-doped glass. Figure 14.15(a) shows, in a schematic fashion, a surface layer under residual compressive stress due to the cold-working from shot peening. The interior is under a small tensile stress as a result. The effect of shot peening on the endurance limits of steels with different ultimate tensile strengths is shown in Figure 14.15(b). For the as-forged components, the endurance limit is approximately 15% of the ultimate tensile strengths. Shot peening doubles the endurance limit, although it becomes less effective once the part is polished or ground, because the endurance limit is considerably increased by that process.

#### 14.7.2 Fatigue Crack Propagation

At large stress amplitudes, a very large fraction (around 90%) of fatigue life is spent in the growth or propagation of a crack. For a component that contains a notch, this fraction becomes even larger. In as much as in most real structures cracklike imperfections are present, the crack propagation part can be a very important aspect of fatigue.

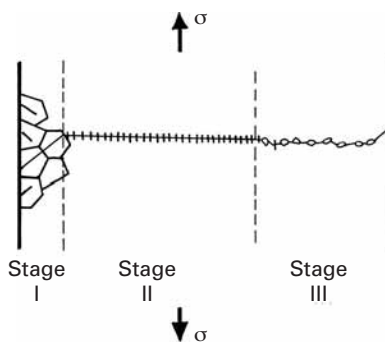
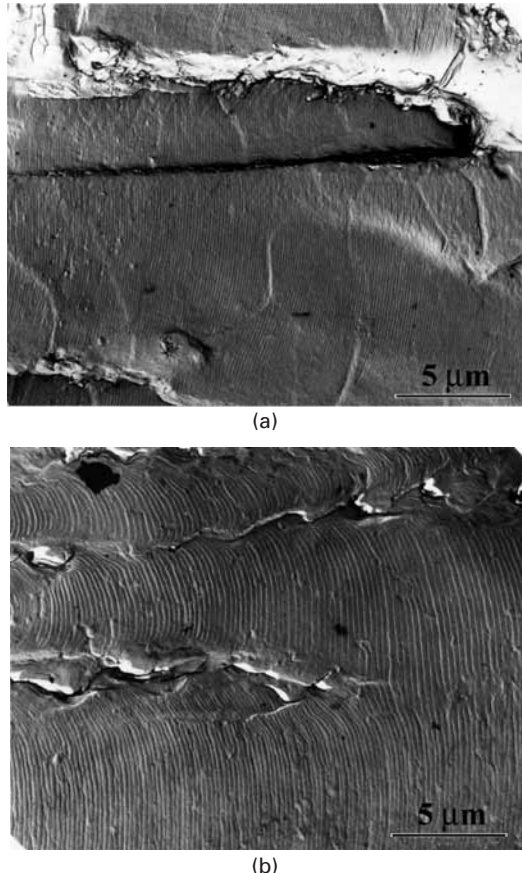


**Fig. 14.16** Stages I, II, and III of fatigue crack propagation.

A brief description of crack propagation, in terms of microstructural processes, follows. A few cracks nucleate at the surface and start propagating in a crystallographic shear mode (stage I) on planes oriented at approximately  $45^\circ$  to the stress axis. (See Figure 14.16.) During this stage, cracking occurs along the crystallographic slip planes, and the crack growth is on the order of a few micrometers or less per cycle. Little is known about crack propagation in this stage. Many consider the stage to be an extension of the nucleation process. Once a crack is initiated, say, at a slip band on the surface, it continues along the slip band until it encounters a grain boundary. These crystallographic cracks penetrate a few tenths of a millimeter in this mode. From there on, a dominant crack starts propagating in a direction perpendicular to the stress axis in the tensile mode. This is called stage II, and typically, the fracture surface shows striation markings. The ratio of the extent of stage I to stage II decreases with an increase in stress amplitude. The stress concentration at the tip of the crack causes local plastic deformation in a zone in front of the crack. With crack growth, the plastic zone increases in size until it becomes comparable to the thickness of the specimen. When this occurs, the plane-strain condition at the crack front in stage II does not exist any more, the crack plane undergoes a rotation, and the final part of rupture occurs in plane-stress or shear mode. This corresponds to Stage III, characterized by rapid crack propagation. Microscopic observations of fatigue fracture surfaces frequently show striations in stage II. Propagation occurs in a direction perpendicular to the tensile stress, and in a large number of metals and alloys (principally of Al and Cu), at high amplitudes, the fracture surface shows the characteristic striations. Such striations have been observed in polymers as well. Frequently, each striation is thought to represent one load cycle, and indeed, it has been observed by means of programmed amplitude fatigue tests that in many materials these striations do represent the crack front position in each cycle. An example of the variation in fatigue striations in a 2014-T6 aluminum alloy is presented in Figure 14.17. Figure 14.17(a) shows the striations in the early stage of fatigue life, while Figure 14.17(b) shows the striations in the late stage of cycling. Note the smaller striation spacing in the early stage, indicating a lower crack propagation rate than in the late stage. These micrographs

**Fig. 14.17** Fatigue striations in 2014-T6 aluminum alloy; two-stage carbon replica viewed in TEM. (a) Early stage. (b) Late stage. (Courtesy of J. Lankford.)



were taken in a TEM from a two-stage carbon replica of the surface of the aluminum alloy. The reason for this is that only TEM could provide the high-enough magnification for viewing the closely spaced striations in the early stage of fatigue. However, the reader is warned that such a correlation is not always available. If it were, one should be able to relate striation spacing to  $\Delta K$  (see Section 14.8) and obtain a one-to-one correspondence between the macroscopic growth rate and  $\Delta K$ . One cannot always do this, however, indicating that the crack front may have advanced by a combination of the formation of striations and other fracture mechanisms.

Care should be exercised in the interpretation of fatigue striations. It has been observed in an Fe-Si alloy that, whereas the fatigue striations were  $2 \mu\text{m}$  apart, the actual advance of the crack front per cycle was only  $10^{-9} \text{ m}$ , or 2,000 times smaller!<sup>6</sup> These results show that, under certain conditions, the crack front remains "dormant" for many cycles, while damage accumulates in the material. At a certain point, the crack advances discontinuously. This phenomenon is very common in polymers at low values of  $\Delta K$ . A craze forms gradually

<sup>6</sup> W. Yu, K. Esabul, and W. W. Gerberich, *Met. Trans., 15A* (1984) 889.

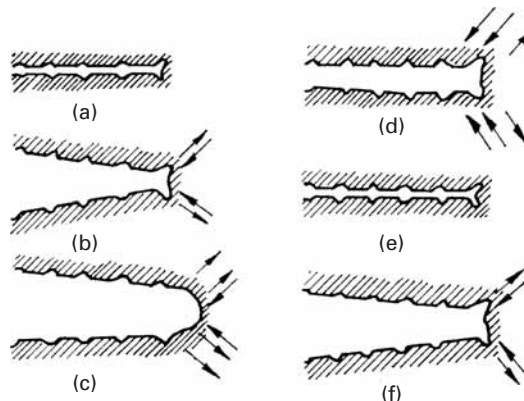


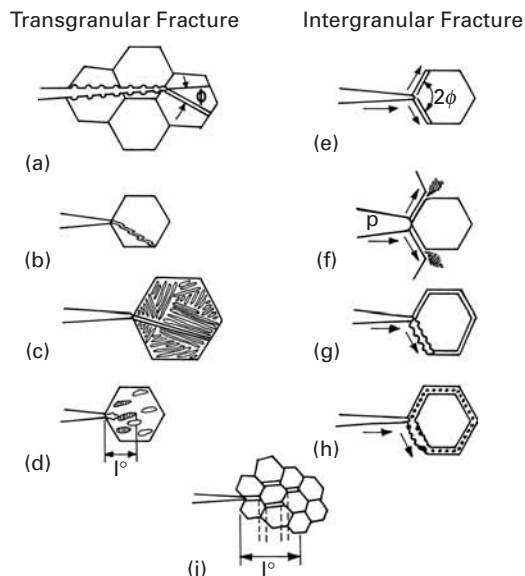
**Fig. 14.18** Fatigue crack growth by a plastic blunting mechanism. (a) Zero load. (b) Small tensile load. (c) Maximum tensile load. (d) Small compressive load. (e) Maximum compressive load. (f) Small tensile load. The loading axis is vertical (After C. Laird, in *Fatigue Crack Propagation*, ASTM STP 415 (Philadelphia: ASTM, 1967), p. 131.)

at the tip of the crack during fatigue. When the craze reaches a critical length, the crack advances through it. The process repeats itself periodically.

At higher values of  $\Delta K$ , striations become less important in the overall crack propagation rate. One model of fatigue crack growth by a striation mechanism is shown in Figure 14.18. This model involves repetitive blunting and sharpening of the crack front. Figure 14.18(a) shows the situation at zero load. During the tensile part of the load cycle, plastic strains at the crack tip cause localized slip on planes of maximum shear. (See Figure 14.18(b).) The situation at maximum tensile load is shown in Figure 14.18(c). The start of the compressive cycle is shown in Figure 14.18(d). The reversal of the loading direction, during compression, causes the crack faces to join (Figure 14.18(e)). However, the new surface created during the tensile part of the cycle is not completely “rehealed,” due to slip in the reverse direction. Depending on the material and the environment, a large part of slip during compression occurs on new slip planes, and the crack tip assumes a bent form with “ears,” as shown in Figure 14.18(e). At the end of the compression half of the cycle, the crack tip is resharpened, and the propagation sequence of the next cycle is restarted. (See Figure 14.18(f).) This model of plastic blunting and resharpening seems to be valid for any ductile material, including polymers. There is evidence that the crack propagates in a similar manner in stage I, but with only a group of slip planes at  $45^\circ$  operating. However, one must bear in mind that, although the presence of striations confirms a fatigue failure mechanism, an absence of striations does not necessarily preclude fatigue. In fact, a variety of other fracture modes are possible in fatigue. In single-phase materials, transgranular or intergranular fracture modes are possible, while any second phases that are present may lead to dual fracture modes. Figure 14.19 shows the various possible microscopic fracture modes in fatigue.

Fracture surfaces in polymers produced under fatigue conditions also show some characteristic features. Generally, two distinct regions are present: a region of smooth, slow crack growth surrounding the fracture initiation site and a rough region corresponding to rapid

**Fig. 14.19** Microscopic fracture modes in fatigue. (a) Ductile striations triggering cleavage. (b) Cyclic cleavage. (c)  $\alpha - \beta$  interface fracture. (d) Cleavage in an  $\alpha - \beta$  phase field. (e) Forked intergranular cracks in a hard matrix. (f) Forked intergranular cracks in a soft matrix. (g) Ductile intergranular striations. (h) Particle-nucleated ductile intergranular voids. (i) Discontinuous intergranular facets. (Adapted from W. W. Gerberich and N. R. Moody, in *Fatigue Mechanisms*, ASTM STP 675 (Philadelphia: ASTM, 1979) p. 292.)



crack growth. Sometimes, semicircular concentric bands are seen in the smooth region near the starting flaw. These bands are indicative of discontinuous crack growth, and the band width represents the extent of plastic zone or craze that developed ahead of the crack tip. Fracture surfaces produced by cyclic loading in polymers frequently show striations. There is some confusion on the use of the term *striation* in the literature on fatigue in polymers and metals. In metals, the term is used to denote markings on the fracture surface, without regard to any correlation between the striation spacing and the crack growth per cycle. In polymers, the term *striation* is used only when there is a one-to-one correlation between the striation spacing and the crack growth in each cycle. This stems from the fact that there are other types of discontinuous growth which result in fracture surface markings, but without any advance in the fatigue crack. In particular, in polymers there occur discontinuous growth bands (DGBs), which correspond to a burst of fatigue crack growth after some hundreds of fatigue cycles; that is, the crack tip remains stationary for some cycles and then undergoes an advance. DGBs resemble striations, but their spacing is much larger than the crack growth in a cycle. The formation of a DGB is thought to be due to the accumulation of damage ahead of the fatigue crack over many cycles, followed by a sudden jump by the crack. One model explains that a craze forms at the fatigue crack and that the crack initially grows along the craze-matrix interface, as shown in Figure 14.20, and then along the craze filled midrib until the crack is arrested. A repetition of this process results in the appearance of dark bands on the fracture surface. Thus, the DGBs represent the successive positions of crack tips that have been blunted, advanced, and arrested repeatedly.

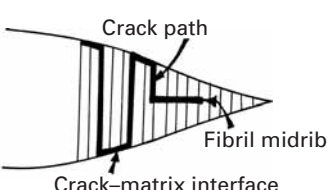


**Fig. 14.20** Discontinuous crack growth through a craze at the tip of a fatigue crack. (After L. Konczol, M. G. Schincker and W. Döll, *J. Mater. Sci.*, 19 (1984) 1604.)

## 14.8 Linear Elastic Fracture Mechanics Applied to Fatigue

The use of large monolithic structures has resulted in widespread application of fracture mechanics. In particular, the phenomenon of fatigue crack propagation can be analyzed in terms of linear elastic fracture mechanics. The basic assumption here is that cracks already exist in a structural component and that they will grow as the component gets used in service. In terms of fatigue crack growth studies, it is also implied that the fatigue life of a component is determined mostly by the crack growth under cyclic loading.

We can determine  $K_{Ic}$  or  $K_c$  for a given material in the laboratory and can use the data obtained to determine a failure locus in terms of a critical applied stress and a corresponding critical crack length, or vice versa. (See Figure 14.21.) For example, in Figure 14.21(a), we can observe that, for a given crack length  $a_1$ , there is a critical failure stress  $\sigma_1$  of the material. Conversely, for a given design stress  $\sigma_2$ , there is a critical crack length  $a_2$ . In principle, then, the region under the failure locus represents the safe region with respect to a catastrophic failure. Consider, for instance, a component containing a crack length of  $a_1$ , at a stress of  $\sigma_2$ , where  $\sigma_2 < \sigma_1$ . Under these

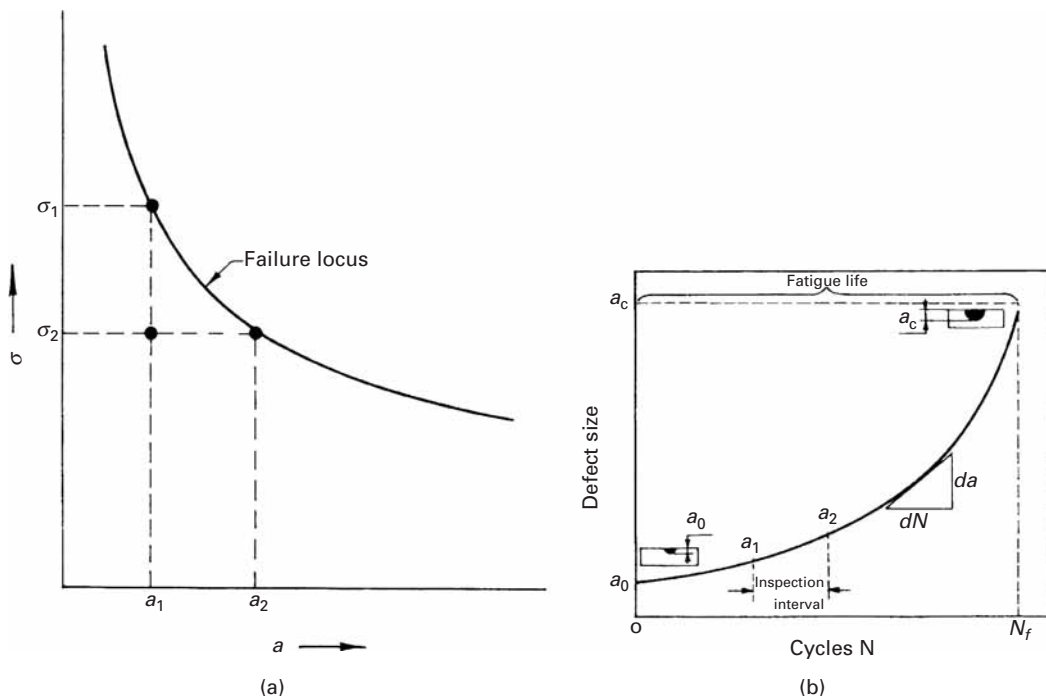


**Fig. 14.21** (a) Failure locus. (b) Schematic of crack length  $a$  as a function of number of cycles,  $N$ .

conditions, the component will be safe because  $a_1$  is smaller than the critical defect size  $a_2$ , which corresponds to the applied stress  $\sigma_2$ . This security is based, of course, on the assumption that loading is static and that the crack does not grow in service. But we know very well that cracks in structures do grow during service. An increase in crack length at  $\sigma_2$ , in service, from  $a_1$  to  $a_2$  will eventually lead to structural failure. Thus, although the fracture toughness of a material establishes the failure condition and the residual strength of a structural component, the component's service life or durability is mainly a function of its resistance to subcritical crack growth (i.e., its resistance to crack growth by fatigue, creep, stress corrosion, etc.).

As we pointed out in Chapter 7, linear elastic fracture mechanics accepts the preexistence of cracks in a structural member. The model for the crack tip is the same as that described for nonfatigue regimens. The material containing a crack, under tension, has a small plastic zone at the crack tip, and this plastic zone is surrounded by a rather large elastic region. This being so, we focus our attention on the propagation of cracks under conditions of fatigue. Once again – and it is worth repeating – we do not concern ourselves here with the crack nucleation problem under fatigue. Under cyclic loading, a dominant crack grows, as a function of the number of cycles, from an initial size  $a_0$  to a critical size  $a_c$ , corresponding to failure, as shown in Figure 14.21(b). The basic problem is thus reduced to one of characterizing the growth kinetics of the dominant crack in terms of an appropriate driving force. From there, one can estimate the service life and/or schedule inspection intervals under designed loading conditions and service environments. Since crack growth starts from the most highly stressed region at the crack tip, we characterize the driving force in terms of the stress intensity factors at the tip – that is, the range of the stress intensity factor  $\Delta K = K_{\max} - K_{\min}$ , where  $K_{\max}$  and  $K_{\min}$  are the maximum and minimum stress intensity factors corresponding to the maximum and minimum loads, respectively. The crack growth rate per cycle,  $da/dN$ , can then be expressed as a function of the cyclic stress intensity factor at the crack tip,  $\Delta K$ . Hence, if a mathematical equation describing the crack growth process and the appropriate boundary conditions is available, we can, in principle, compute the fatigue life (i.e., number of cycles to failure). Paris *et al.* proposed the following *empirical* relationship (known as the Paris-Erdogan relationship) for crack growth under cyclic conditions:<sup>7</sup>

$$\boxed{da/dN = c(\Delta K)^m} \quad (14.2)$$

Here,  $a$  is the crack length,  $N$  is the number of cycles,  $\Delta K$  is the cyclic stress intensity factor as defined earlier, and  $C$  and  $m$  are empirical constants that depend on the material, environment, and test conditions, such as the load ratio  $R$ , the test temperature, the waveform,

---

<sup>7</sup> P. C. Paris, M. P. Gomez, and W. P. Anderson, *The Trend in Engineering*, 13 (1961) 9; P. C. Paris and F. Erdogan, *J. Basic Eng., Trans. ASME*, 85 (1963) 528.

etc. Another empirical relation connecting the parameters  $C$  and  $m$  is

$$C = A/(\Delta K_0)^m$$

where  $A$  and  $K_0$  are some other material constants.

Since many variables affect the crack growth rate in fatigue, we can write, in a very general way,

$$da/dN = F(\Delta K, K_{\max}, R, \text{frequency, temperature, } \dots). \quad (14.3)$$

Clearly, one cannot obtain such an ideal and detailed characterization. In practice, one collects data under restricted conditions, but consistent with the applications in service. In principle, the rate equation 14.3 can be integrated to determine the service life  $N_f$ , or an appropriate inspection interval  $\Delta N$ , for a structural component. We have

$$N_f = \int_{a_0}^{a_f} \frac{da}{F(\Delta K, \dots)},$$

or

$$\Delta N = N_2 - N_1 = \int_{a_1}^{a_2} \frac{da}{F(\Delta K, \dots)}. \quad (14.4)$$

Rewriting, we get

$$N_f = \int_{K_{f\max}}^{K_{f\max}} \frac{dK}{(dK/da) F(\Delta K, \dots)}, \quad (14.5)$$

or

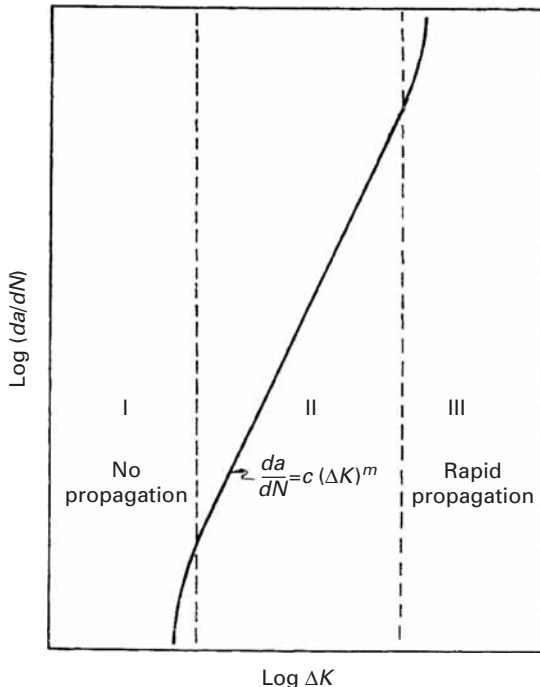
$$\Delta N = N_2 - N_1 = \int_{K_1}^{K_2} \frac{dK}{(dK/da) F(\Delta K, \dots)}. \quad (14.6)$$

If we plot the logarithm of the crack growth rate  $da/dN$  against the logarithm of the alternating stress intensity factor  $\Delta K = K_{\max} - K_{\min}$  at the crack tip, we get the kind of curve shown in Figure 14.22. The curve has a sigmoidal form with three regions. Region II is the one that shows the Paris-Erdogan type of power-law relation between  $da/dN$  and  $\Delta K$ . The power-law region connects the upper and lower limiting regions. The lower limit on the cyclic stress intensity factor in region I denotes a threshold value below which the crack does not propagate. This limit is called the *threshold cyclic stress intensity factor*  $\Delta K_{\text{th}}$ . The upper limit in region III indicates the conditions of accelerated crack growth rate associated with the start of final rupture.

Many researchers (see, for example, Suresh (1991) in the suggested reading) have discussed the primary operating mechanisms and the important variables in the three stages of fatigue crack propagation:

**Stage I:** In this stage, the average crack growth per cycle is less than a lattice spacing. Crack propagation mechanisms are characteristic of a discontinuous medium. The microstructure of

**Fig. 14.22** Schematic of crack propagation rate  $da/dN$  versus alternating stress intensity factor  $\Delta K$ .

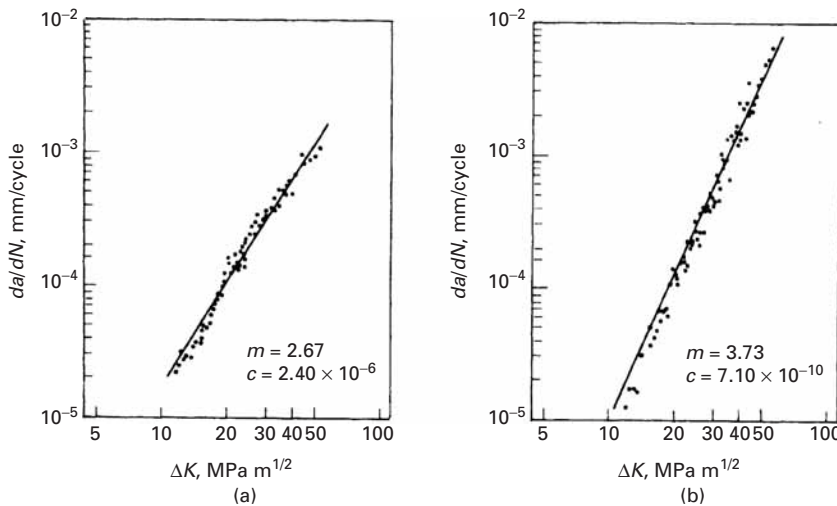


the material, the stress ratio  $R$ , and the environment have a large influence on the crack growth.

Stage II: This is the power-law regimen, where the Paris-Erdogan relationship applies. Crack propagation mechanisms in stage II are characteristic of a continuous medium. The influence of the microstructure,  $R$ , the environment, the thickness of the material, etc. on crack growth is small.

Stage III: Crack propagation mechanisms in this stage are similar to those in the static mode (cleavage, intergranular, microvoid coalescence, etc.) In stage III, the microstructure,  $R$ , and the thickness of the material have a large influence on crack growth, but the influence of the environment is small.

The Paris-Erdogan power relationship (Equation 14.2) describes the crack propagation rate in stage II for a variety of materials—polymers, metals, and ceramics. It is very useful because of its extreme simplicity. For example, it has been observed experimentally that data points in the form of  $\log (da/dN)$  versus  $\log \Delta K$  for a given material (with a constant microstructure) from three different samples—an edge crack in a compact-tension sample, a through-the-thickness central crack in a plate, and a plate containing a partial through-the-thickness crack—all fall on the same line. Also, there is experimental evidence that the stress level by itself does not influence the fatigue crack growth rate for levels below the general yielding stress. Thus, we can assume that the parameter  $\Delta K$  describes uniquely the crack growth rates for many engineering applications. However, rather gross



microstructural features of a material, such as the directionality imparted by aligned inclusions, can influence fatigue crack growth rates drastically, changing the value of  $m$  significantly. Figure 14.23 illustrates the directionality in the fatigue crack propagation rate in an AISI 4140 steel. The exponent  $m$  has a higher value in the transverse direction than in the longitudinal (rolling) direction, due to the presence of elongated inclusions.

### Example 14.3

Consider long crack propagation under fatigue. Develop an expression for the number of cycles,  $\Delta N$ , required for a crack to grow from an initial length  $a_i$  to a final length  $a_f$ . Given that  $\Delta K = Y \Delta \sigma \sqrt{\pi a}$  and  $da/dN = C \Delta K^m$ , where the symbols have their usual significance. Discuss the implications of the expression.

*Solution:*

$$\begin{aligned} da/dN &= C \Delta K^m, \\ \Delta N &= \int_{a_i}^{a_f} \frac{da}{C \Delta K^m} \\ &= \int_{a_i}^{a_f} \frac{da}{C (Y \Delta \sigma \sqrt{\pi})^m a^{m/2}} \\ &= \frac{a_f^{(1-m/2)} - a_i^{(1-m/2)}}{C (Y \Delta \sigma \sqrt{\pi})^m (1-m/2)} \\ &= \frac{1 - (a_i/a_f)^{m/2-1}}{C (Y \Delta \sigma \sqrt{\pi})^m (m/2-1)} \left( \frac{1}{a_f^{m/2} - 1} \right). \end{aligned}$$

The implications of the expression are that it is not valid for  $m = 2$  and that  $\Delta N$  is more sensitive to the initial crack length  $a_i$  than the final crack length  $a_f$ .

**Fig. 14.23** Fatigue crack

propagation in an AISI 4140 steel.  
(a) Longitudinal direction (parallel to rolling direction). (b) Transverse direction (perpendicular to rolling direction). (Reprinted with permission from E. G. T. De Simone, K. K. Chawla, and J. C. Miguez Suárez, Proc. 4th CBECIMAT (Florianópolis, Brazil, 1980), p. 345)

### Example 14.4

The fatigue crack markings shown in Figure E14.4 were found in a fractured part. Determine the time to rupture of this part if the loading frequency is 10 Hz, the maximum stress applied to the part is 300 MPa, and the minimum stress is zero. The initiation stage of the flaw is 50% of the life of the part.

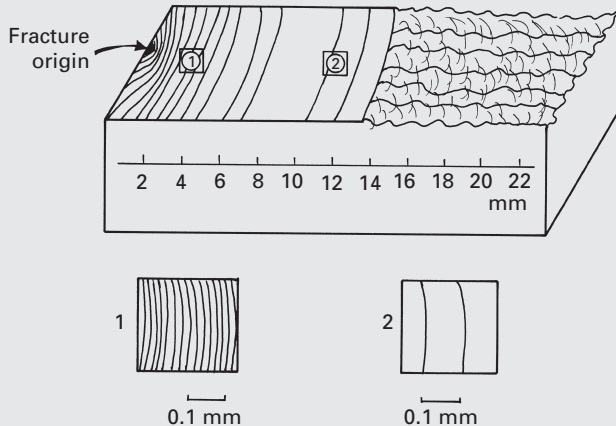


**Fig. E14.4**

**Solution:** We have

$$\left( \frac{da}{dN} \right)_1 = 0.016 \text{ mm}, \quad \left( \frac{da}{dN} \right)_2 = 0.1 \text{ mm}, \\ a_1 = 2 \text{ mm}, a_2 = 10 \text{ mm}.$$

Fracture occurs when  $a_f = 14 \text{ mm}$ . Assuming that we have plane strain,

$$K_{Ic} = 1.12\sigma\sqrt{\pi a} \\ = 1.12 \times 300\sqrt{\pi \times 0.014} \\ = 70 \text{ MPa m}^{1/2}.$$

We now find the parameters for the Paris equation:

$$\frac{da}{dN} = C(\Delta K)^m, \\ \Delta K_1 = 1.12\sigma\sqrt{\pi a_1} = 1.12 \times 300\sqrt{\pi \times 2 \times 10^{-3}} \\ = 26.6 \text{ MPa m}^{1/2}, \\ \Delta K_2 = 1.12\sigma\sqrt{\pi a_2} = 1.12 \times 300\sqrt{\pi \times 10 \times 10^{-3}} \\ = 59.55 \text{ MPa m}^{1/2}, \\ 0.016 \times 10^{-3} = C(26.6)^m, \\ 0.1 \times 10^{-3} = C(59.55)^m, \\ m = 2.27, \\ C = 0.94 \times 10^{-8},$$

$$\frac{da}{dN} = 0.94 \times 10^{-8} (\Delta K)^m = 0.94 \times 10^{-8} \times (1.12 \times 300 \sqrt{\pi a})^{2.27},$$

$$\frac{da}{a^{1.135}} = 0.019 \text{ dN.}$$

Integrating between the limits,  $a_f = 14 \text{ mm}$  and  $a_i = 0.02 \text{ mm}$ , we get:

$$\int_{a_i}^{a_f} \frac{da}{a^{1.135}} = \int_{0.02}^{14} \frac{da}{a^{1.135}} = 0.019 \int dN = 0.019N,$$

$$a_0 = 0.02 \text{ mm}$$

$$a_f = 14 \text{ mm}$$

$$0.019N = \frac{-1}{0.135 \times (14 \times 10^{-3})^{0.135}}$$

$$+ \frac{1}{0.135 \times (0.02 \times 10^{-3})^{0.135}}$$

Each cycle corresponds to 0.1 s, so

$$t = 0.1N$$

The total time is equal to the initiation time plus the propagation time:

$$t = 2t = 98.6 \times 2 \text{ s}$$

$$= 197.2 \text{ s.}$$

### Example 14.5

An aluminum alloy has a plane-strain fracture toughness  $K_{lc}$  of 50 MPa m<sup>1/2</sup>. A service engineer has detected a 1-mm-long crack in an automotive component made of this alloy. The component will be subjected to cyclic fatigue with  $\Delta\sigma = 100 \text{ MPa}$  with  $R = 0$ . How many more cycles can this component endure? Take  $K = 1.05 \sigma \sqrt{\pi a}$  and  $da/dN$  (mm/cycle) =  $1.5 \times 10^{-24} \Delta K^4$  (MPa m<sup>1/2</sup>)<sup>4</sup>.

**Solution:** The final crack length  $a_f$  can be obtained from  $K_{lc}$  with 100 MPa of applied stress:

$$K_{lc} = 50 = 1.05 \times 100 \times \sqrt{\pi a_f},$$

$$a_f = \left[ \frac{50}{1.05 \times 100 \sqrt{\pi}} \right]^2 \text{ m}$$

$$= 0.072 \text{ m}$$

$$= 72 \text{ mn.}$$

We thus have (being very careful with units!)

$$N_f = \frac{1}{(1.5 \times 10^{-24})(1.05^4)\pi^2(100)^4} \left[ \frac{1}{a_i} - \frac{1}{a_f} \right]$$

$$= \frac{10^{16}}{(1.5)(1.22)(9.87)} \left[ 1 - \frac{1}{72} \right] 10^3$$

$$= 10^{16}[0.055][0.986]$$

$$= 5.5 \times 10^{17} \text{ cycles.}$$

### Example 14.6

When subjected to fatigue under a  $\Delta\sigma = 140$  MPa, an alloy showed the following Paris-type fatigue crack propagation relationship:

$$\frac{da}{dN} (\text{m/cycle}) = 0.66 \times 10^{-8} (\Delta K)^{2.25}$$

where  $\Delta K$  is in  $\text{MPa m}^{1/2}$ . Estimate the number of cycles required for the crack to grow from 2 mm to 8.8 mm.

*Solution:*

$$\frac{da}{dN} = 0.66 \times 10^{-8} (1.12 \Delta\sigma \sqrt{\pi a})^{2.25},$$

$$a^{-1.125} da = 0.66 \times 10^{-8} (1.12)^{2.25} \times (140)^{2.25} (\pi)^{1.125} dN.$$

Integrating, we get

$$\int_{a_0}^{a_c} a^{-1.125} da = 2.0815 \times 10^{-3} \int_0^{N_f} dN,$$

$$N_f \times 2.0815 \times 10^{-3} = - \left[ \frac{a^{-0.125}}{0.125} \right]_{0.002}^{0.0088},$$

$$N_f = \frac{2.941}{2.0815 \times 10^{-3}} = 1.4129 \times 10^3 \text{ cycles},$$

or

$$N_f = 1,413 \text{ cycles.}$$

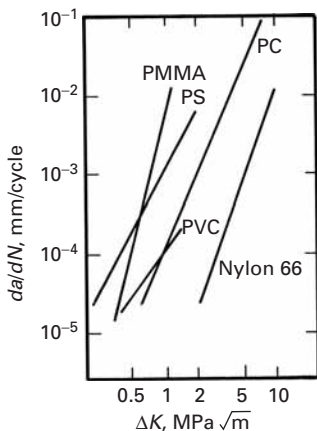


**Fig. 14.24** Fatigue crack propagation rates for a number of polymers. (After R. W. Hertzberg, J. A. Manson, and M. Skibo, *Polymer Eng. Sci.*, 15 (1975) 252.)

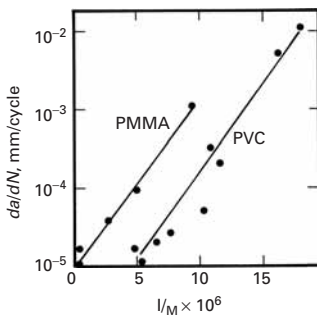


**Fig. 14.25** Variation in fatigue crack propagation rates, at fixed values of  $\Delta K$  ( $= 0.6 \text{ MPa m}^{1/2}$ ) and test frequency  $v$  ( $= 10 \text{ Hz}$ ), as a function of reciprocal of molecular weight for PMMA and PVC. (After S. L. Kim, M. Skibo, J. A. Manson, and R. W. Hertzberg, *Polymer Eng. Sci.*, 17 (1977) 194.)

A Paris–Erdogan type of relationship can be used to describe the fatigue crack propagation rate  $da/dN$  in polymers also. Figure 14.24 shows the fatigue crack rates as a function of  $\Delta K$  for a number of thermoplastic polymers. Note that semicrystalline nylon 66 is superior in resistance to fatigue crack growth than amorphous, but ductile, polymers such as polyvinyl chloride (PVC) and polycarbonate (PC), which in turn are superior to brittle, amorphous polymers such as PS and PMMA. The latter both show deformation by crazing. Metals such as aluminum alloy and steel (not shown in the figure) would have curves to the right of that of nylon. That is, polymers show a lower resistance to fatigue crack propagation than metals do: Unlike metals, the range of the exponent  $m$  for polymeric materials can be quite large, from 4 to 20.

The molecular weight of a polymer is a very important variable for a number of properties, including fatigue crack propagation. In general, as the molecular weight increases, the fatigue strength increases and the fatigue crack propagation rate decreases. Figure 14.25 shows the variation in the fatigue crack propagation rate in PMMA and PVC, at a constant value of  $\Delta K$  ( $0.6 \text{ MPa m}^{1/2}$ ) and at  $10 \text{ Hz}$ , as a function of  $1/M$ , where  $M$  is the molecular weight.

Earlier, it was thought that cyclic fatigue in ceramics did not occur, at least not in an inert atmosphere. This was based on the fact

that, in a ceramic, no dislocation-based plastic deformation occurred at the crack tip. Although dislocation plasticity is generally absent in ceramics, many ceramics show subcritical crack growth, under cyclic loading, at room temperature and at elevated temperatures. The deformation mechanisms under cyclic loading are generally different from those under static loading. While dislocation-based cyclic slip is responsible for fatigue in metals, phenomena such as micro-cracking, phase transformations, interfacial sliding, and creep can promote an inelastic constitutive response in brittle solids, leading to cycle fatigue. Work done by Suresh and coworkers, as well as others, on fatigue crack growth in a variety of brittle solids in compression, tension, and tension-compression fatigue shows that mechanical fatigue effects – that is, stable crack propagation – under cyclic fatigue conditions – can occur in ceramics at room temperature and in brittle solids as well.<sup>8</sup> Ewart and Suresh were the first ones to show such a cyclic fatigue effect in ceramics by subjecting them to cyclic compression. Researchers have used a variety of loading techniques to obtain fatigue crack growth data in ceramics under cyclic loading, such as four-point flexure, compact tension, and wedge-opening load specimens. Figure 14.26 shows the fatigue crack growth in an alumina sample (grain size  $\approx 10 \mu\text{m}$ ) subjected to tension-compression fatigue ( $R = -1$ ) at a frequency of 5 Hz, in terms of  $da/dN$  vs.  $K_{\max}$ , the maximum stress intensity factor. If we take  $\Delta K = K_{\max}$ , it is easy to see that the data correspond to a Paris-Erdogan type of power law,  $da/dN = C\Delta K^m$ . The figure also shows the data obtained from static loading in terms of crack growth per cycle. We use the relationship  $da/dN = (da/dt)/v$ , where  $v$  is the frequency, and plot this against the maximum stress intensity factor  $K_{\max}$  at which the static test was performed. The idea of putting the two curves together is to show that the crack growth rate in alumina under cyclic loading is much faster than that under static loading. S-N curves obtained in tension-tension cycling of fine-diameter alumina fiber also showed a distinct cyclic loading effect.<sup>9</sup> Work on fatigue growth rate in zirconia partially stabilized with magnesia also confirmed the cyclic fatigue effect.<sup>10</sup> One should note, however, that the values of  $m$  for ceramics in the Paris-Erdogan type of power law relationship range from 8 to 42, much higher than the 2–4 range for metals.

In many materials, such as intermetallics, composites, and ceramics, there are a number of additional mechanisms operating during cyclic fatigue. These mechanisms are responsible for R curve behavior. These mechanisms are classified as extrinsic and intrinsic. Figure 14.27 shows, in a schematic fashion, a few intrinsic and

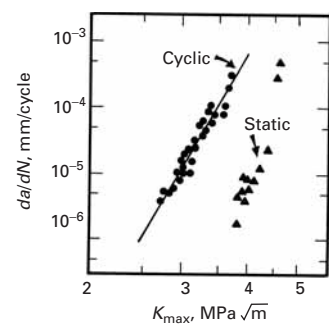


**Fig. 14.26** Fatigue crack growth rate  $da/dN$  in alumina as a function of the maximum stress intensity factor  $K_{\max}$  under fully reversed cyclic loads ( $v = 5 \text{ Hz}$ ). Also indicated are the rates of crack growth per cycle derived from static-load fracture data. (After M. J. Reece, F. Guiu, and M. F. R. Sammur, *J. Amer. Ceram. Soc.*, 72 (1989) 348.)

<sup>8</sup> L. Ewart and S. Suresh, *J. Mater. Sci.* 22 (1987) 1173; S. Suresh and J. R. Brockenbrough, *Acta Met.*, 36 (1988) 1455; M. J. Reece, F. Guiu, and M. F. R. Sammur, *J. Amer. Ceram. Soc.*, 72 (1989) 348; R. H. Dauskardt, D. B. Marshall, and R. O. Ritchie, *J. Amer. Ceram. Soc.* 73 (1990) 893.

<sup>9</sup> N. Chawla, M. Kerr, and K. K. Chawla, *J. Amer. Ceram. Soc.*, 88 (2005) 101.

<sup>10</sup> R. H. Dauskardt, D. B. Marshall, and R. O. Ritchie, *J. Amer. Ceram. Soc.*, 73 (1990) 893.

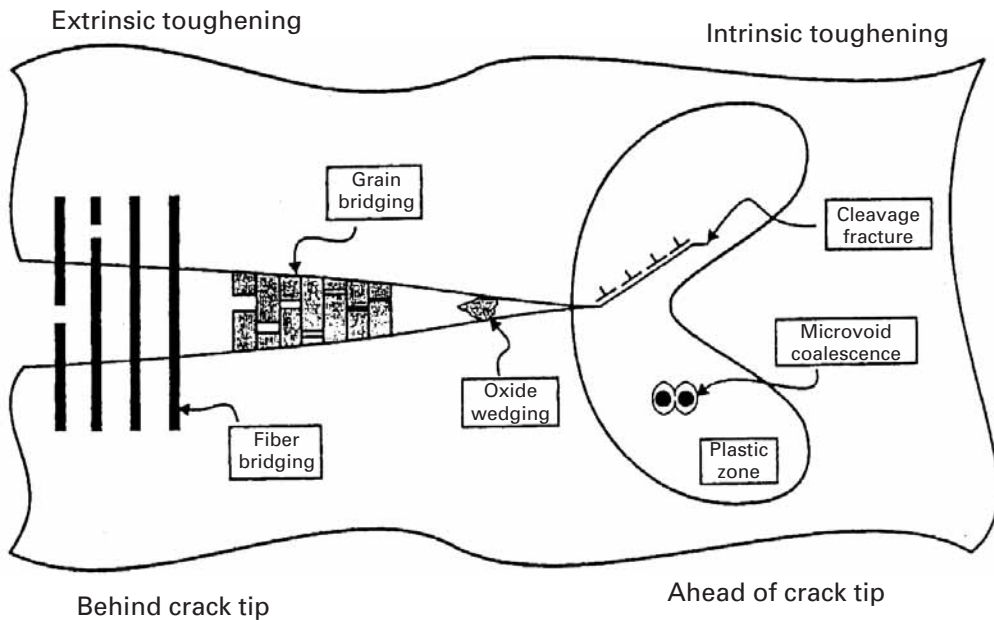


**Fig. 14.27** Intrinsic and extrinsic mechanisms of fatigue damage.  
(After R. O. Ritchie, *Int. J. Fracture*, 100 (1999) 55.)

extrinsic mechanisms. Intrinsic mechanisms operate ahead of the crack tip. Examples are void formation and coalescence, microcracks, plastic deformation, and phase transformations. Extrinsic mechanisms operate behind the crack tip. Extrinsic toughening mechanisms include fiber bridging (in the case of composites), grain bridging, phase transformations, microcrack toughening, and oxide wedging. Oxides formed on the cracked surface can dislodge themselves and act as microwedges along the crack, impeding it from closing completely on unloading. Thus, the stress amplitude is effectively decreased.

### 14.8.1 Fatigue of Biomaterials

A common type of fatigue damage in the body is called “stress fracture.” These are actually microcracks that form in bones from repeated stressing at excessive loads. Such is the case of long-distance runners whom experience stress fractures in the shins and feet. The body has a marvelous capacity of self-healing and rest usually alleviates the problem and allows the small cracks to close.

In the domain of biomaterials, most implants in the body undergo cyclic loading, which often results in failure. Hip and knee replacement joints, titanium posts in teeth implants, and mechanical heart valve prostheses are prone to fatigue. This problem is aggravated by the physiological environment, and environmental degradation can accelerate fatigue crack growth. For instance, the yield stress of the cobalt (62%)-chrome (28%) alloy used in biological applications is approximately 650 MPa. However, the endurance limit (for  $10^7$ - $10^8$  cycles) is in the 150–250 MPa range.

### Example 14.7

Estimate the number of cycles that a total hip replacement joint will experience in ten years.

**Solution:** A sedentary person walks approximately one hour per day. This corresponds to 5 km/day. Assuming that each step is equal to 780 mm (the student can verify this!) we have approximately 8,000 cycles/day, or  $2.9 \times 10^3$  cycles/year. Over a period of ten years, we would have approximately  $3 \times 10^4$  cycles.

Heart valve prostheses have been manufactured from titanium, cobalt-chromium alloys, and pyrolytic carbon. The problems encountered with metallic heart valves has led to the almost universal adoption of pyrolytic carbon or a pyrolytic carbon/graphite laminate. By 1996, over 600,000 of these valves had been installed. There are two types of commercial pyrolytic heart valves: a tilting-disc and a bileaflet design. Pyrolytic graphite exhibits a high biocompatibility and resistance to blood clotting. This aspect is of great importance, since blood clotting triggered by the immune response can lead to thromboembolism.

The human heart beats  $4 \times 10^7$  times per year. Both stress/life (S-N curves) and damage-tolerant approaches (Paris-Erdogan-type relationship) have been used to estimate the fatigue life of these valves. In the S-N analysis, pyrolytic graphite valves are designed for  $10^9$  cycles (with a failure rate less than one in 100,000). This represents 25 years. However, it is known that there is considerable scatter in the data. The damage-tolerant approach was implemented by Ritchie.<sup>11</sup> Different experiments carried out at  $\Delta K = 0.9 K_{\max}$  yielded the results shown in Figure 14.28. These plots show two striking characteristics:

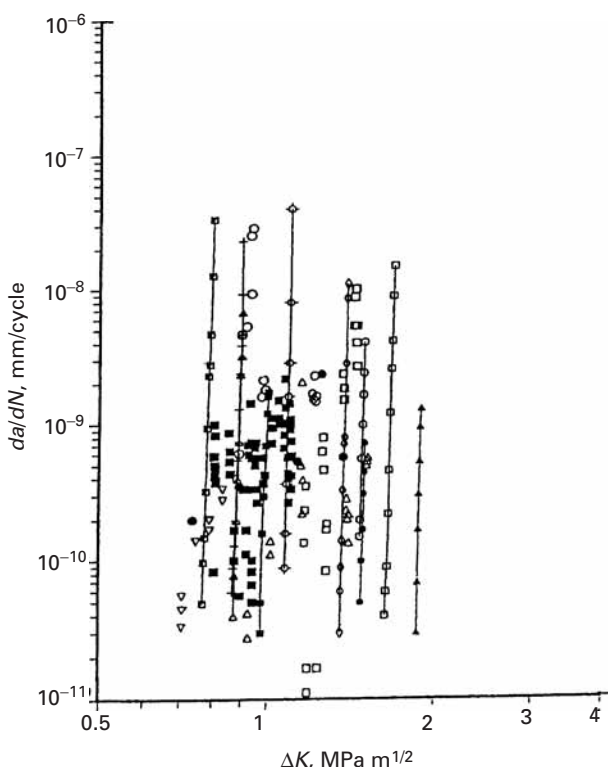
- The slope of the  $da/dN$  versus  $\Delta K$  plots,  $m$ , is extremely high: approximately 100. This behavior is also found in ceramics and signifies the following: once a preexisting cracks starts to grow, it rapidly increases in velocity and leads to failure. This is highly undesirable for applications, since the material is not forgiving.
- The growth behavior shows a large degree of scatter. The threshold stress intensity factor for which growth rates  $da/dN$  are on the order of  $10^{-11} \text{ m/cycle}$  vary from specimen to specimen, and one has:

$$0.7 \text{ MPa m}^{-1/2} \leq \Delta K_{th} \leq 2 \text{ MPa m}^{-1/2}.$$

These results illustrate the importance of a comprehensive fatigue evaluation of biomaterials. Although only 50 pyrolytic graphite heart valve prostheses had failed by 1996, the high value of  $m$  shows that a

<sup>11</sup> R. O. Ritchie, *J. Heart Valve Dis.*, 5 (1996) S9.

**Fig. 14.28** Fatigue crack propagation rates for pyrolytic-carbon coated graphite specimens in a physiological environment; leaflet and compact-tension specimens. (Adapted from R. O. Ritchie, *J. Heart Valve Dis.*, 5 (1996) S9.)



doubling of  $\Delta K$  (or the applied stress) leads to an increase in  $da/dN$  and reduction in life of 20 orders of magnitude. Thus, an accidental “nicking” of the pyrolytic graphite by a sharp scalpel during surgery can dramatically influence the life of the patient. The effect can be calculated through the Paris-Erdogan equation and is left to the curious student.

## 14.9 | Hysteretic Heating in Fatigue

An important aspect of fatigue behavior has to do with hysteretic heating. During each loading cycle, we get a hysteresis loop. The area of the loop represents the energy spent in the cycle. Most of the hysteretic energy is dissipated as heat, and if the material is not a good thermal conductor, as is the case with most polymers, then a temperature rise can occur. Such hysteretic heating and the resultant thermal softening can be important at high strain rates in most insulators. In extreme cases, the temperature rise can be large enough that the material fails by viscous flow or melting. Even room temperature can be quite high for polymers. It is convenient to examine the temperature effects in terms of the homologous temperature  $T_H$ . Thermally activated phenomena become operative in most materials at  $T_H > 0.4\text{--}0.5$ . Consider a thermoplastic polymer with a melting point of 300 °C. Taking room temperature to be 300 K, we find that

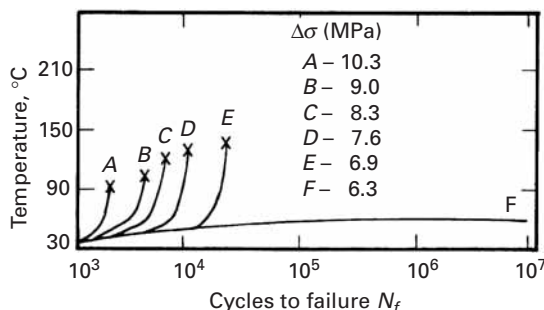


**Fig. 14.29** Effect of the applied stress range  $\Delta\sigma$  on temperature rise in PTFE subjected to stress-controlled fatigue. The symbol x denotes failure of the specimen. (After M. N. Riddell, G. P. Koo, and J. L. O'Toole, *Polymer Eng. Sci.* 6 (1966) 363.)

$T_H$  for this polymer is  $300/573 = 0.52$ . Thus, even a small increase in temperature above the ambient temperature will put such a polymer in the regimen where significant thermal softening can occur. Thermoplastics commonly have low thermal diffusivity and show nonlinear viscosity. The degree of thermal softening during fatigue will depend on the magnitude and frequency of the applied stress and on the viscoelastic characteristics of the polymer. It is easy to see that an appreciable rise in temperature can result at high stress amplitudes or frequencies. This can lead to a reduced fatigue life at frequencies greater than 10 Hz at room temperature. In fact, the ASTM standard specification D-671-71 calls for the measurement of the temperature at fatigue failure. If the temperature goes above the glass transition temperature of the polymer, thermal softening, fracture, and resolidification of the fractured material can occur.

The hysteretic temperature rise is a function of the dimensions of the specimen also. In a thinner specimen, a greater proportion of the heat generated will be lost to the environment. A thicker specimen, on the other hand, will retain a larger fraction of heat and thus show a lower fatigue endurance limit than a thinner specimen of the same material. Figure 14.29 shows the effect of applied stress on the temperature rise in polytetrafluoroethylene (PTFE) subjected to cycling at 30 Hz, at room temperature under stress control. The endurance limit  $\Delta\sigma_L$  for this material under these conditions is 6.5 MPa. For  $\Delta\sigma > \Delta\sigma_L$ , indicated by the curves marked A, B, C, D, and E in the figure, a rapid increase in temperature occurred with an increasing number of cycles. For  $\Delta\sigma < \Delta\sigma_L$ , represented by curve F in the figure, the temperature rise was not high enough to cause thermal softening.

Hysteretic heating effects during high-frequency fatigue have also been observed in continuous fiber-reinforced ceramic matrix composites.<sup>12</sup> Unlike the heating effect observed in polymers or polymer matrix composites, the origin of heating in ceramic matrix composites is the frictional sliding between two mating surfaces, such as a fiber-matrix interface or an interlaminar shear.

<sup>12</sup> See, for example, J. W. Holmes and C. Cho, *J. Amer. Ceram. Soc.*, 75 (1992) 929; N. Chawla, Y. K. Tur, J. W. Holmes, J. R. Barber, and A. Szweda, *J. Amer. Ceram. Soc.*, 81 (1998) 1221.

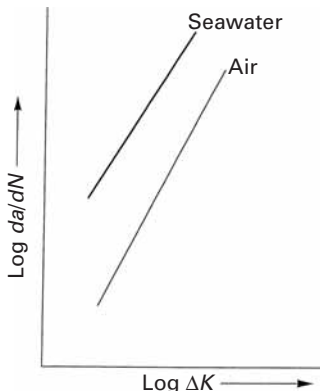


**Fig. 14.30** A schematic of fatigue crack propagation rate as a function of cyclic stress intensity factor in air and seawater. At any given  $\Delta K$ , the crack propagation rate is higher in seawater than in air.

## 14.10 Environmental Effects in Fatigue

Fatigue behavior of materials can be adversely affected by the environment (solid, liquid, or gaseous). We treat the topic of environmental effects on static mechanical properties of materials in Chapter 16. Here we wish to point out that an aggressive environment, under conditions involving cyclic fatigue, can hasten the nucleation of a surface crack and then propagate it to fracture. Such a phenomenon is also referred to as *corrosion fatigue*. Figure 14.30 shows schematically the fatigue crack propagation in a material subjected to cyclic fatigue in air and in seawater.

## 14.11 Fatigue Crack Closure

Under certain circumstances, surfaces of a fatigue crack can contact each other, and the crack will close even when the far-field stress field is still tensile. The crack does not reopen until a sufficiently high tensile stress is reached in the next loading cycle. This phenomenon, called *crack closure*, was said by a number of researchers to occur as result of crack-tip plasticity. As the applied stress on a material is increased, a plastic zone develops at the crack tip. (See Chapter 7.) As the crack grows, a plastically deformed zone is produced in its wake, while the material surrounding this zone is still elastic. The explanation of this phenomenon was that the plastically deformed zone caused the crack surfaces to close before zero stress was reached. However, for fatigue crack growth to occur, the crack must be fully open. Thus, premature contact between the crack surfaces – i.e., crack closure – results in a lowering of the crack driving force. It follows that one should use an effective stress intensity factor range,  $\Delta K_{\text{eff}}$ , rather than  $\Delta K$  in fatigue crack growth analysis. If the stress at which the crack is just open is  $\sigma_{\text{op}}$ , and the corresponding stress intensity factor is  $K_{\text{op}}$ , then we can define the effective cyclic stress intensity factor as

$$\Delta K_{\text{eff}} = K_{\max} - K_{\text{op}}.$$

Recall that the applied cyclic stress intensity factor is given by  $\Delta K = K_{\max} - K_{\min}$ , and that  $K_{\text{op}} > K_{\min}$ . Therefore, we will have

$$\Delta K > K_{\text{eff}}.$$

Elber proposed that  $\Delta K_{\text{eff}}$  explains the R effect on the fatigue crack growth rate.<sup>13</sup> At high values of R, the crack closure effect is small because  $K_{\text{op}}$  approaches  $K_{\min}$ , and  $\Delta K_{\text{eff}}$  becomes closer to  $\Delta K$ . Later, other explanations besides crack-tip plasticity were proposed for the crack closure effect. Among the various phenomena held to be responsible for crack closure are crack surface roughness, asperities in the

<sup>13</sup> W. Elber, Eng. Fract. Mech., 2 (1970) 37.

crack wake from oxides or corrosion products, viscous fluid, and phase transformation ahead of the crack tip. The oxide-induced crack closure is possible in a material that forms an oxide film on the surface easily. When such a material is subjected to cyclic stress near the threshold regimen at low load ratios ( $R$ ) and in a moist environment, corrosion products (i.e., oxides) of thickness comparable to the crack-tip opening displacements can build up at and near the tip. The oxide film continually breaks and forms behind the tip due to the crack surfaces coming together as a result of plasticity-induced closure and mode-I displacements characteristic of near-threshold crack growth. The crack closes at stress intensities above  $K_{\min}$ . This mechanism is less likely to operate in a dry, oxygen-free environment and high load ratios. (Plasticity-induced closure is small.) The formation of an oxide film is time dependent and not likely to occur at high frequencies. Roughness-induced crack closure is thought to occur when the fracture surface roughness is comparable in size to the crack-tip opening displacement (CTOD) and significant mode-II deformation occurs. In such a case, cracks can become wedge-closed at contact points above the crack faces. Crack closure causes an increase in stiffness and a decrease in compliance. High values of  $R$  result in less crack closure; that is,  $\Delta K_{\text{eff}}$  is closer to  $\Delta K$  for higher  $R$ .

## 14.12 | The Two-Parameter Approach

In a series of papers, Vasudevan *et al.* proposed a new, two-parametric approach to fatigue crack propagation.<sup>14</sup> Among the features of their approach are the following:

- It is not necessary to invoke crack closure to explain fatigue crack propagation.
- Plasticity at the crack tip cannot contribute to crack closure.
- Crack closure induced by oxide, corrosion, or roughness is very local and small.

There are five local parameters: the cyclic stress intensity factor  $\Delta K$ ; the maximum stress intensities  $K_{\max}$ ; the minimum stress intensity  $K_{\min}$ ; the mean cyclic stress intensity factor  $K_{\text{mean}}$ ; and the  $R$  ratio. Out of these five, Vasudevan *et al.* used the applied driving force  $\Delta K$  and the peak stress intensity  $K_{\max}$  as the two parameters that are *sufficient and necessary* to analyze fatigue crack propagation data. There are thus two threshold quantities, one in each of the two parameters: the alternating stress intensity factor  $\Delta K^*$  and  $K^*_{\max}$ . These two must be satisfied *simultaneously* for crack propagation to occur. Based on data available in the literature on a wide range of alloys, Vasudevan and colleagues constructed a fundamental fatigue threshold curve or a fatigue map, as shown in Figure 14.31. The fundamental curve is

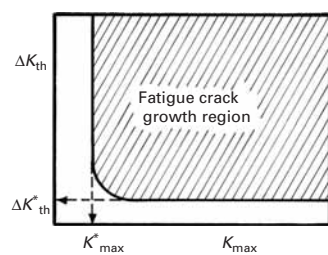


**Fig. 14.31** A fatigue threshold curve. (After A. K. Vasudevan, K. Sadananda, and N. Louat, *Mater. Sci. Eng.*, A188 (1994) 1.)

<sup>14</sup> See, for example, A. K. Vasudevan, K. Sadananda, and N. Louat, *Mater. Sci. Eng.*, A188 (1994) 1.

independent of testing and geometric parameters; it depends only on the material and environmental parameters. The shape and magnitude of such fundamental curves can vary, depending on the curve of  $\Delta K_{th}$  vs. the load ratio  $R$ . On the basis of these new concepts, Vasudevan *et al.* classified the fatigue crack growth data into five different classes, using the experimental data on  $\Delta K_{th}$  vs.  $R$ . Such a classification could provide a new basis for understanding the synergistic effects of various driving forces (mechanical, chemical, and microstructural) upon fatigue crack growth.

### 14.13 | The Short-Crack Problem in Fatigue

For long cracks, under conditions of applicability of linear elastic fracture mechanics (LEFM), there exists a threshold stress intensity range  $\Delta K_{th}$ , below which no fatigue crack growth occurs. The value of the cyclic threshold stress intensity depends on a variety of factors: the microstructure of the material; the test environment; the load ratio  $R$  ( $=\sigma_{min}/\sigma_{max} = K_{min}/K_{max}$ ); various crack-tip factors such as the amount of overload, cold work, etc.; experimental techniques; and the geometry of the specimen. It has been observed that *short* fatigue cracks, in metals and polymers, can propagate at rates different from those of the corresponding long fatigue cracks under the influence of the same driving force. Generally, for a given  $\Delta K$ , the growth rates of small cracks are higher than those of long cracks.<sup>15</sup> A *short crack* is a crack that is smaller than the microstructural unit of the materials; for instance, a crack of length equal to grain or precipitate size is a short crack. In practice, one finds that long cracks can be between 1 and 20 mm, while short cracks are smaller than 0.1 mm. The anomalous growth of short cracks is explained in Figure 14.32, a plot of  $\log da/dN$  vs.  $\log \Delta K$ . Long cracks do not grow below a constant threshold  $\Delta K_{th}$ . For long cracks, we have

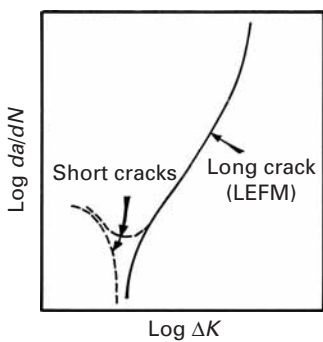


**Fig. 14.32** Fatigue crack growth rates for long and short cracks.

and the threshold  $\Delta K_{th}$  is a constant, as indicated in Fig. 14.32. This is in accord with LEFM, as  $K_I$  alone determines the stress state at the crack tip. However, in the short-crack regimen, cracks grow below this threshold value, as indicated by the deviation from the solid line in the figure. Short cracks propagate below the long-crack threshold ( $\Delta K_{th}$ ). The fatigue crack growth rate of short cracks decreases progressively, until a minimum in crack velocity occurs at a crack length on the order of the grain size; that is,  $a \approx d$ , where  $d$  is the grain size. This so-called short-crack anomaly arises when the crack size approaches the dimension of the microstructural feature (e.g., grain size, inclusions, etc.). Under such circumstances, homogeneity is lost, which is implicit in the LEFM treatment of the long crack.

<sup>15</sup> See, for example, R. A. Smith and K. J. Miller, *Int. J. Mech. Eng.*, 20 (1978) 201; S. Suresh and R. O. Ritchie, *Intl. Met. Rev.*, 29 (1984) 445.

Sadananda and Vasudevan have extended their two-parametric framework (see Section 14.12) to explain short-crack behavior.<sup>16</sup> According to these authors, a crack grows when both thresholds,  $\Delta K^*$  and  $K_{max}^*$ , are met simultaneously. A short crack is no exception, and for it to propagate, it must meet these requirements, too. The short crack is different from the long crack in terms of the internal stresses that it encounters: All short cracks grow in internal stress fields that accentuate the applied stress to the level at which the crack propagates. An important conclusion of Sadananda and Vasudevan's work is that a similitude between the long and short crack is maintained!

## 14.14 | Fatigue Testing

Among the reasons for carrying out fatigue testing on a material, we may include the need to develop a better understanding (fundamental or empirical) of the fatigue behavior of the material and the need to obtain more practical information on the fatigue response of a component or structure of the material. The fatigue test samples may thus range from tiny samples tested within, say, the specimen chamber of a scanning electron microscope to complete aircraft wings weighing many tons. It would be futile to try to include everything known about fatigue testing here; instead, we present some of the common techniques and point out some of their salient aspects.

### 14.14.1 Conventional Fatigue Tests

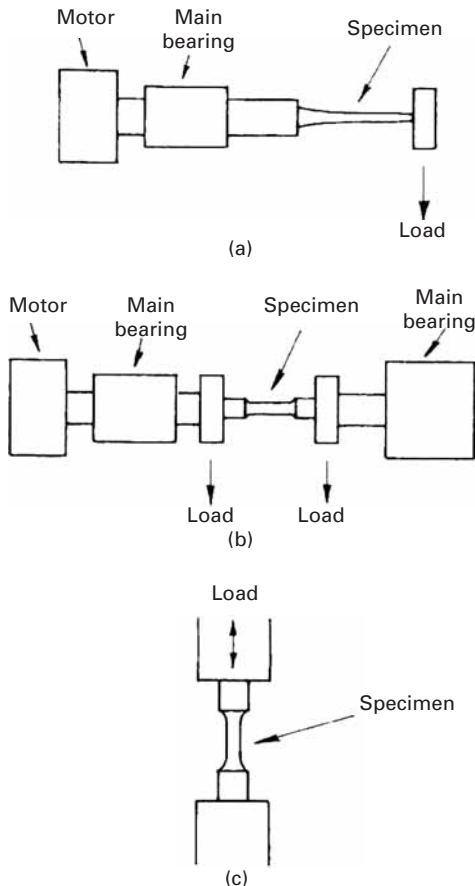
Conventionally, fatigue testing has been done by cycling a given material through ranges of stress amplitude and recording the number of cycles of failure. The results are reported in the form of S-N curves. There are two main types of loading: rotating bending tests and direct stress tests (Figure 14.33). In direct stress machines, the stress distribution over any cross section of the specimen is uniform, and we can easily apply a static mean tensile or compressive load (i.e., the  $R$  ratio may be varied). However, the more common and popular type of loading has been the rotating bending beam test, described next. Direct loading machines are discussed in Section 14.14.4.

### 14.14.2 Rotating Bending Machine

Rotating bending tests are perhaps one of the most simple and oldest types of fatigue test. They provide a simple method of determining fatigue properties at zero mean load by applying known bending moments to rotating round specimens. Commercially, many versions are available, the main difference being in the application of the load: at a single point, as in a cantilever loading machine, or by some kind of two- or four-point loading (Figure 14.33). In the latter case, the

<sup>16</sup> K. Sadananda and A. K. Vasudevan, in *Fatigue 96*, Berlin, May 6–10, 1996, (Oxford: Pergamon Press, 1996), p. 375; K. Sadananda and A. K. Vasudevan, in *Twenty-seventh National Symposium on Fracture Mechanics*, ASTM STP-1296, (West Conshohocken, PA: ASTM, 1996).

**Fig. 14.33** Various loading configurations used in fatigue testing. (a) In cantilever loading, the bending moment increases toward the fixed end. (b) In two-point beam loading, the bending moment is constant. (c) Pulsating tension, or tension-compression, axial loading.



bending moment is constant over the entire test section of the specimen, and thus, we use a specimen of constant diameter. In the cantilever type of loading machine, the specimen either has a narrow waist, so that the maximum bending stress occurs at the smallest diameter, or has a tapered cross section, such that the maximum bending stresses are constant at all cross-sections. The stress at a point on the surface of a rotating bending specimen varies sinusoidally between numerically equal maximum tensile and compressive values in every cycle. Assuming the specimen to be elastic, we have

$$\pm S = \frac{32M}{\pi d^3}, \quad (14.7)$$

where  $S$  is the maximum surface stress,  $M$  is the bending moment at the cross section under consideration, and  $d$  is the diameter of the specimen. In such a test we obtain the number of cycles to failure at a given stress level. The stress level  $S$  is continually reduced, and the number of cycles to failure,  $N_f$ , increases. A logarithmic scale is used for  $N$ , and we obtain an  $S$ - $N$  curve. In the case of ferrous materials, we generally attain a fatigue limit or endurance limit  $S_L$  (Figure 14.3). Cycling below  $S_L$  can be done indefinitely, without resulting in

failure of the material. Such an endurance limit is not encountered in nonferrous metals or polymers. In these cases, one sets an arbitrary number of cycles, say  $10^7$ , and takes the corresponding stress to be the fatigue life of the material.

#### 14.14.3 Statistical Analysis of S-N Curves

It has been observed that, if a sufficiently large number of identical specimens is fatigue tested at the same stress amplitude, a Gaussian or normal distribution describes the logarithm of the fatigue life distribution. Figure 14.34 shows a schematic S-N diagram with a log-normal distribution of lives at various stress levels. There is more of a spread in the lives of a group of specimens tested at a stress level greater than their fatigue limit than in the stress levels necessary to cause failure at a given life. The data from cyclic loading tests (whether rotating bending beam, pulsating tension, or axial tension-compression) must be analyzed statistically. The mean value  $\bar{x}$  and the standard deviation  $\sigma$  for a given set of data are given by

$$\bar{x} = \frac{\sum x}{n} \quad (14.8)$$

and

$$\sigma = \left[ \frac{\sum (x - \bar{x})^2}{n - 1} \right]^{1/2}, \quad (14.9)$$

where  $x$  is the cyclic life of the material at a given stress (the test value) and  $n$  is the number of test values (i.e., the number of samples tested to failure at a given stress). With these statistical parameters, one can obtain confidence limits for the probability of survival of the material. The anticipated fatigue life, with a desired level of confidence ( $C$ ) that at least  $P$  of the samples will not fail, may be written as

$$\text{anticipated life } (C, P) = \bar{x} - q\sigma. \quad (14.10)$$

where  $q$  is a function of  $C$ ,  $P$ , and the number of test samples used to determine  $\bar{x}$  and  $\sigma$ . The selection of a particular confidence limit depends on the importance of the component to the structural integrity of the material. The more important the component, the higher should be the confidence limit and the lower the stress. The  $q$  values for a given distribution are available in tabulated form in the literature. Table 14.1 presents the  $q$ -values, assuming a normal distribution. With anticipated life (Equation 14.10) and the  $q$  tables, we can develop a family of curves showing the probability of survival or failure of a component (Figure 14.35).

#### 14.14.4 Nonconventional Fatigue Testing

In the category of nonconventional fatigue testing, we include practically all modern fatigue testing other than that involving the determination of S-N curves. The machines used are direct loading machines. The drive system of the load train receives a time-dependent signal from the controls, converts it into a force, or

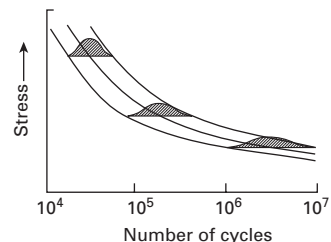


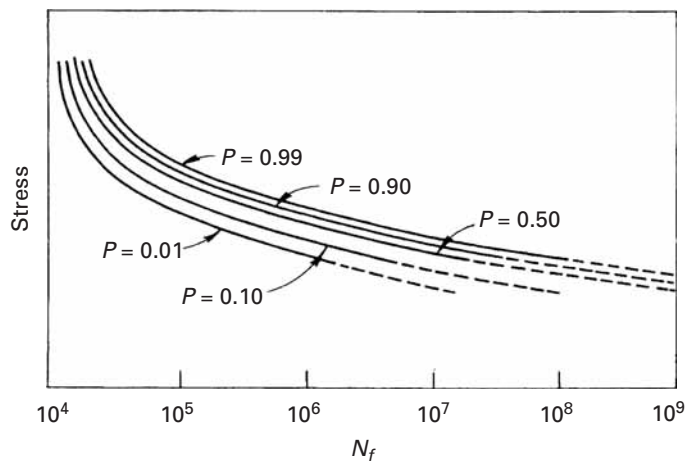
**Fig. 14.34** S-N curve showing log-normal distribution of lives at various stress levels.

**Table 14.1** *q-values for S-N Data, Assuming a Normal Distribution\**

$P(\%)$	75	90	95	99	99.9	75	90	95	99	99.9	
<i>n</i>	$C = 0.50$						$C = 0.75$				
4	0.739	1.419	1.830	2.601	3.464	1.256	2.134	2.680	3.726	4.910	
6	0.712	1.360	1.750	2.483	3.304	1.087	1.860	2.336	3.243	4.273	
8	0.701	1.337	1.719	2.436	3.239	1.010	1.740	2.190	3.042	4.008	
10	0.694	1.324	1.702	2.411	3.205	0.964	1.671	2.103	2.927	3.858	
12	0.691	1.316	1.691	2.395	3.183	0.933	1.624	2.048	2.851	3.760	
15	0.688	1.308	1.680	2.379	3.163	0.899	1.577	1.991	2.776	3.661	
18	0.685	1.303	1.674	2.370	3.150	0.846	1.544	1.951	2.723	3.595	
20	0.684	1.301	1.671	2.366	3.143	0.865	1.528	1.933	2.697	3.561	
25	0.682	1.297	1.666	2.357	3.132	0.842	1.496	1.895	2.647	3.497	
<i>n</i>	$C = 0.90$						$C = 0.95$				
4	1.972	3.187	3.957	5.437	7.128	2.619	4.163	5.145	7.042	9.215	
6	1.540	2.494	3.091	4.242	5.556	1.895	3.006	3.707	5.062	6.612	
8	1.360	2.219	2.755	3.783	4.955	1.617	2.582	3.188	4.353	5.686	
10	1.257	2.065	2.568	3.532	4.629	1.465	2.355	2.911	3.981	5.203	
12	1.188	1.966	2.448	3.371	4.420	1.366	2.210	2.736	3.747	4.900	
15	1.119	1.866	2.329	3.212	4.215	1.268	2.068	2.566	3.520	4.607	
18	1.071	1.800	2.249	3.106	4.078	1.200	1.974	2.453	3.370	4.415	
20	1.046	1.765	2.208	3.052	4.009	1.167	1.926	2.396	3.295	4.319	
25	0.999	1.702	2.132	2.952	3.882	1.103	1.838	2.292	3.158	4.143	

\*Reprinted with permission from ASTM STP No. 91 (Philadelphia: ASTM, 1963), p. 67.

**Fig. 14.35** Family of curves showing the probability of survival or failure of a component.



displacement-time excitation, and transfers this excitation to the fatigue specimen. The three common control parameters are force: deflection or displacement, and strain. For most constant-amplitude fatigue tests, a simple harmonic motion is programmed into the drive system. Electronic function generators are commonly used; they

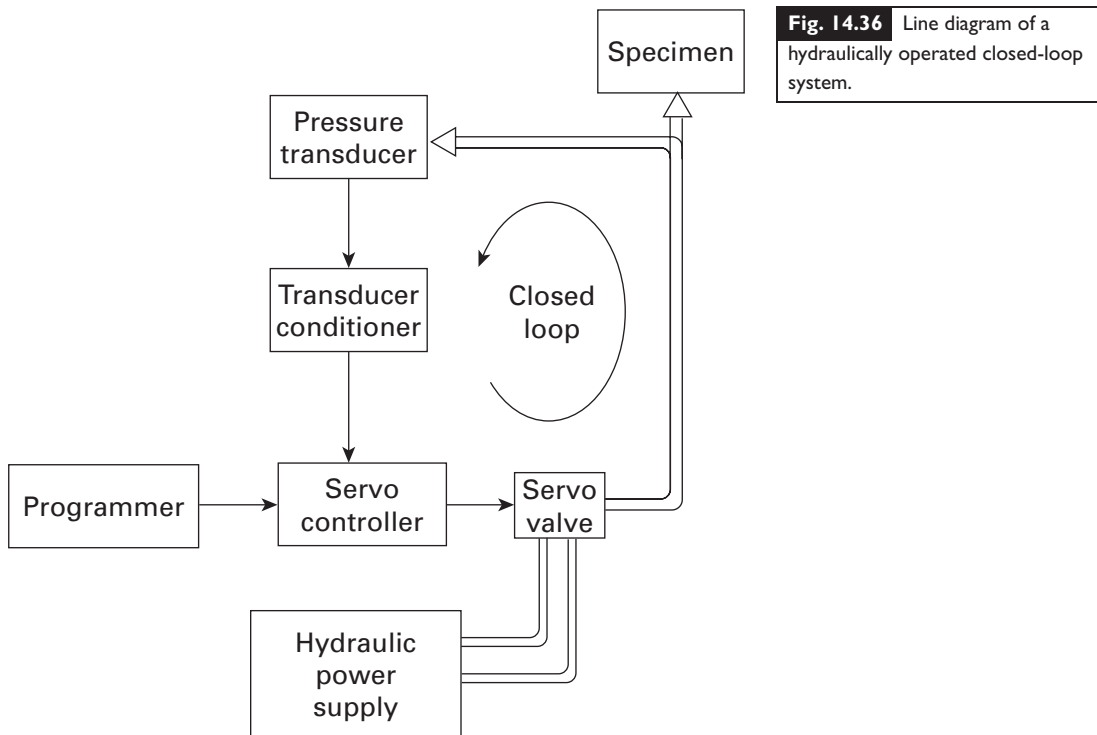


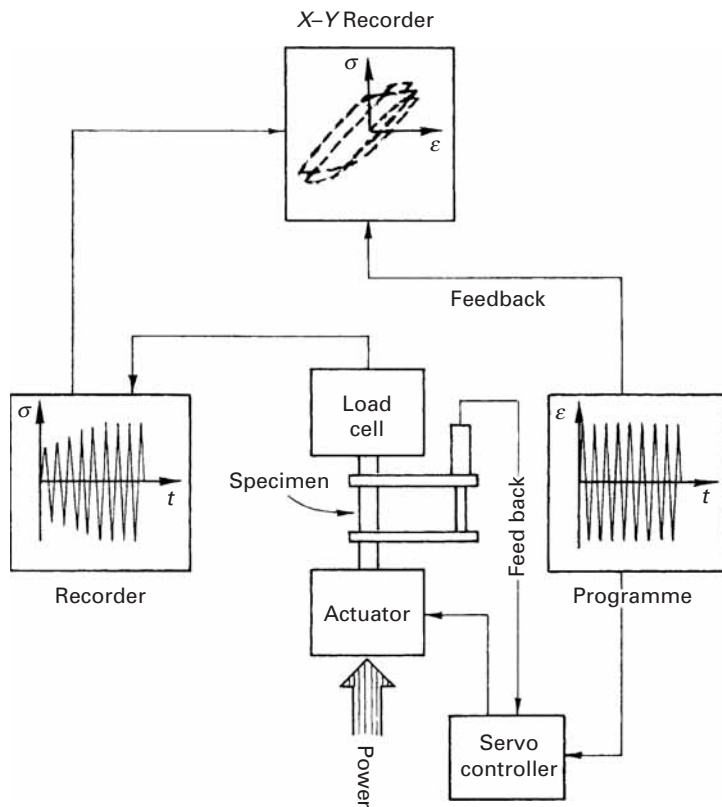
**Fig. 14.36** Line diagram of a hydraulically operated closed-loop system.

generate an electrical signal that varies with time in the way the fatigue control parameter is desired to vary with time. A variety of signals can be programmed – for example, constant amplitude, constant frequency, and zero mean stress; constant amplitude, constant frequency, with a non-zero-mean stress level; random loading; and so on.

#### 14.14.5 Servohydraulic Machines

Servohydraulically operated fatigue machines have become increasingly popular over the years. Figure 14.36 shows a line diagram of a servohydraulically operated closed-loop system. The load, applied through a hydraulic actuator, is measured by a load cell in series with the specimen. The amplified signal from the load cell is compared in a differential amplifier with the desired signal obtained from, say, a function generator. Thus, this system forms a closed-loop load control system. We can also have a displacement or strain control from a transducer or a strain gage on the specimen instead of the load cell. The actual value measured by a load cell, displacement transducer, or strain gage is continuously compared with the desired value and continuously corrected by the high-response electromagnetic servovalve. The energy is provided by a hydraulic power supply. The main advantage of such machines is a higher degree of flexibility. Larger specimen deflections are possible than are possible in electromechanical machines. Thus, we can test components involving large deflections, as well as conventional, stiff specimens. Another major advantage has to do with the versatility of the system in regard to the input

**Fig. 14.37** Block diagram of a low-cycle fatigue-testing system.



signal that can be used. Virtually any analog signal from a function generator, magnetic tape, or a random noise generator is acceptable. This enables us to use not only constant-amplitude waveforms or block-program spectrum loading, but also random waveforms, such as those obtained from actual service conditions. The upshot is that the materials or components can be subjected to more realistic fatigue testing. The main disadvantage of servohydraulic machines is, of course, that they require much higher power consumption than conventional devices.

#### 14.14.6 Low-Cycle Fatigue Tests

Under conditions of high nominal stresses (i.e., short lifetimes, less than  $10^4$  cycles), the constant-stress amplitude test gives only limited information. This is because rather large plastic strain components are involved in such cases. Under such conditions, the cyclic stress-strain curves obtained under strain control become more useful. Servohydraulic machines are generally used in a closed-loop mode. Figure 14.37 shows schematically a cyclic straining facility. Axial tension-compression is generally employed. We measure stress as a function of the number of strain reversals. Usually, stress and strain signals are fed to an X-Y recorder, and a complete hysteresis loop is obtained. The area of the loop is the plastic strain energy per cycle.

### Cyclic Stress-Strain Curves

We can obtain cyclic stress-strain curves by linking the tips of a series of hysteresis loops obtained from equivalent specimens tested at different plastic strain amplitudes ( $\Delta\varepsilon_p$ ). There are also methods of obtaining cyclic stress-strain curves from a single specimen. The hysteresis loop adjusts rather quickly following a sudden change in  $\Delta\varepsilon_p$ . Thus, we can obtain a cyclic stress-strain curve from one specimen tested at several strain amplitudes. This is called a *multiple-step test*. Another method is the *incremental step test* with one specimen. This method consists of gradually increasing the cyclic strain range until a cyclic strain of about  $\pm 1\%$  is attained. The strain range is then slowly reduced, and the procedure is repeated until the material is stabilized.

#### 14.14.7 Fatigue Crack Propagation Testing

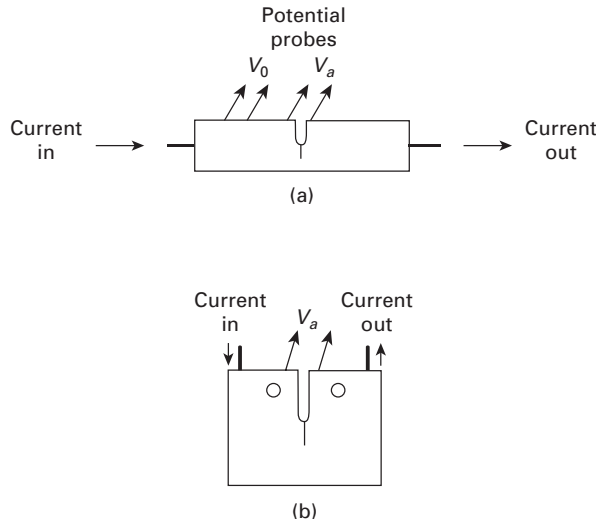
As pointed out earlier, the process of fatigue failure consists of the following two stages:

1. A certain number of cycles  $N_i$  in which a small crack is initiated. Some people include in this stage early growth of the microcrack to a somewhat larger crack.
2. Propagation of a major crack. Generally, this occurs in such a way that we are able to describe the propagation behavior by some kind of standard relationship, say, the Paris-Erdogan relation. There is a substage of this propagation stage wherein the final rupture occurs, namely, when the crack has reached a certain critical length for the material, the applied stress, and the test piece or structural component.

Much attention has been paid to the crack propagation behavior of materials in fatigue. Fatigue crack growth rates under service conditions can be of great importance, especially in determining inspection intervals. For example, wheels on large aircraft may have an ample safe lifetime after the appearance of detectable cracks. What we want to be sure of is that these cracks will not grow to a size that is critical for the part during the time available before the next periodic inspection.

Flat-sheet specimens are commonly chosen for crack propagation studies. The starter notch can be a side edge notch, a central through-the-thickness hole, or some other shape appropriate to the form of defects observed in service. These notches can be cut by a mechanical saw, electrical discharge machining, and so on. Usually, crack growth measurements are made after a small initial propagation in which there is an atomically sharp fatigue crack. The crack length is measured as a function of the number of cycles, and subsequent analysis is carried out in terms of fracture mechanics concepts. Synchronized strobe lighting can be used to illuminate the surface of the sample in order to provide a stable, vibration-free crack-length reading capability, or, in more sophisticated cases, a movie record can be obtained of the increase in the length of the crack. Traveling

**Fig. 14.38** Electric potential drop method for crack growth measurements. (a) Bend specimen. (b) Compact-tension specimen.  $V_a$  is the potential drop across the crack while  $V_0$  is some reference potential. The crack length is obtained as function of the normalized potential ( $V_a/V_0$ ). The sample is loaded by inserting pins in holes shown.



or stereo zoom microscopes are used in manual monitoring crack length. Such devices typically can read up to 0.01 mm. We may have scale markings photographically prepared on the sample or have a scale inserted in the ocular piece of the microscope. We can also use crack propagation gages, consisting of a series of 20 or 25 parallel, equally spaced resistance wires in the form of a grid. Crack length is measured by monitoring the overall change in resistance. In the electric potential drop method, a constant direct current is passed through the specimen containing a crack. The resistance of the specimen changes as the crack grows and is detected by measuring the potential drop across the mouth of the starter notch. Figure 14.38 shows the setup for a bend and a compact-tension specimen. As a crack is observed propagating, the number of cycles required for each increment is recorded, and a crack growth rate  $da/dN$  is computed from the curve of the crack length  $a$  versus the number of cycles  $N$ . The cyclic stress intensity factor at the crack tip ( $\Delta K$ ) may be computed from the crack length and the load. By plotting  $da/dN$  versus  $\Delta K$ , we can obtain the fatigue crack growth characteristics of the material.

## Suggested Reading

- J. M. Barsom and S. T. Rolfe. *Fracture and Fatigue Control in Structures*, 3rd ed. West Conshohocken, PA: ASTM, 1999.
- D. L. Davidson and J. Lankford, *Intl. Mater. Rev.*, 37 (1992) 65.
- A Guide for Fatigue Testing and the Statistical Analysis of Fatigue Data*. ASTM STP 91. Philadelphia, PA: ASTM, 1963.
- R. W. Hertzberg, and J. A. Manson. *Fatigue of Engineering Plastics*. New York, NY: Academic Press, 1980.
- J. G. Johnson. *The Statistical Treatment of Fatigue Experiments*. New York, NY: Elsevier, 1964.

- R. O. Ritchie, *Mater. Sci. Eng.*, 103 (1988) 15.  
 S. Suresh. *Fatigue of Materials*, 2nd ed. Cambridge, U. K.: Cambridge University Press, 1995.

## Exercises

**14.1** Many operations, such as machining, grinding, electroplating, and case-hardening, may induce residual stresses in a material. Discuss, in general terms, the effect of such residual stresses on the fatigue life of the material.

**14.2** A steel has the following properties:

Young's modulus  $E = 210$  GPa,  
 Monotonic fracture stress  $\sigma_f = 2.0$  GPa,  
 Monotonic strain at fracture  $\varepsilon_f = 0.6$ ,  
 Exponent  $b$  (cyclic) = 0.09;  $c$  (cyclic) = 0.06.

Compute the total strain that a bar of this steel will be subject to under cyclic straining before failing at 1,500 cycles.

**14.3** The low-cycle fatigue behavior of a material can be represented by

$$\sigma_L = \sigma_{UTS} N_f^{-0.1},$$

where  $\sigma_L$  is the endurance limit,  $\sigma_{UTS}$  is the ultimate tensile strength, and  $N_f$  is the number of cycles to failure. If  $\sigma_{UTS}$  for this material is 500 MPa, find its endurance limit. A sample of the material is subjected to block loading consisting of 40, 30, 20, and 10% of fatigue life at  $\sigma_L$ ,  $1.10\sigma_L$ ,  $1.2\sigma_L$ , and  $1.3\sigma_L$ , respectively. Use the Palmgren-Miner relationship to estimate the fatigue life of the sample under this block loading.

**14.4** A microalloyed steel was subjected to two fatigue tests at  $\pm 500$  MPa and  $\pm 300$  MPa. Failure occurred after  $10^3$  and  $10^5$  cycles, respectively, at these two stress levels. Making appropriate assumptions, estimate the fatigue life at  $\pm 400$  MPa of a part made from this steel that has already suffered  $10^4$  cycles at  $\pm 350$  MPa.

**14.5** The curve of crack growth rate  $da/dN$  vs. cyclic stress intensity  $\Delta K$  for a material in the Paris regimen is shown in Figure Ex14.5. Determine the parameters  $C$  and  $m$  for this material. (*Hint*: Take any two points on the straight portion of the curve, and determine the slope  $m$  of the line.)

**14.6** A steel has the following properties:

Yield stress  $\sigma_y = 700$  MPa,  
 Fracture toughness  $K_{Ic} = 165$  MPa  $m^{1/2}$ .

A plate of this steel containing a single edge crack was tested in fatigue under  $\Delta\sigma = 140$  MPa,  $R = 0.5$ , and  $a_0 = 2$  mm. It was observed experimentally that fatigue crack propagation in the steel could be described by the Paris-type relationship

$$\frac{da}{dN} \text{ (m/cycle)} = 0.66 \times 10^{-8} (\Delta K)^{2.25},$$

where  $\Delta K$  is measured in MPa  $m^{1/2}$ .

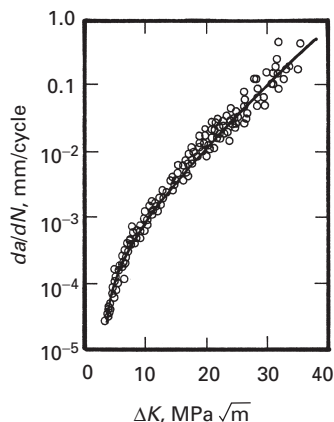
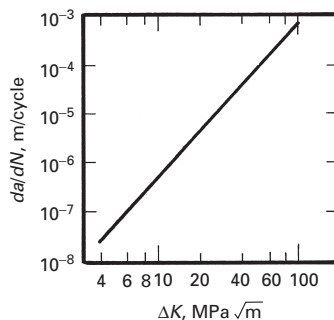


Fig. Ex14.5



**Fig. Ex14.7** Adapted from ASM Metals Handbook, 9th ed. (Metals Park, OH: ASM, 1986), p. 103.

- (a) What is the critical crack size  $a_c$  at  $\sigma_{\max}$ ?  
(b) Compute the fatigue life of the steel.

**14.7** Obtain the parameters for the Paris-type relationship for the data shown in Figure Ex14.7 for the aluminum alloy 7075-T6.

**14.8** For the 7075-T6 alloy in Exercise 14.7, determine the length of a crack after  $10^5$  cycles if the initial crack size was equal to 0.2 mm and the cyclic loading was such that, at the onset of fatigue,  $\Delta K = 10$  MPa  $m^{1/2}$ .

**14.9** Suppose that the fatigue life of a precracked specimen is totally occupied by crack propagation. If, in a certain case, the initial crack growth rate is given by

$$\frac{da}{dN} = C \Delta K^2$$

and  $\Delta K = 2\alpha \Delta\sigma \sqrt{\pi a}$ , show that

$$C = \frac{1}{4N \Delta\sigma^2 \alpha^2 \pi} \ln \frac{a_f}{a_0},$$

where  $\alpha$  is a constant  $N$  is the fatigue life,  $a_0$  is the initial crack length, and  $a_f$  is the final crack length, of the specimen.

**14.10** Fatigue crack propagation in a polymer can be described by the relationship

$$\frac{da}{dN} = 0.5 \times 10^6 \Delta K^{3.5},$$

where  $da/dN$  is in m/cycle and  $\Delta K$  is in MPa  $m^{1/2}$ . A sample with the following dimensions and a central through-the-thickness crack was subjected to fatigue under a maximum load of 200 N and a minimum load of zero:

thickness  $B = 10$  mm,  
width  $W = 50$  mm,  
crack length  $2a = 10$  mm.

Using an appropriate expression for  $\Delta K$  (see Chapter 7), calculate  $da/dN$  for this sample.

**14.11** (Design Problem) Estimate the life of a hip implant made of 304L stainless steel if it contains initial flaws with length  $2c = 200$   $\mu\text{m}$  and a height  $2a = 100$   $\mu\text{m}$ . Assume that the force applied on the artificial hip is

walking:  $3W$ ,  
running:  $7W$ ,

where  $W$  is the weight of the person. The fatigue response of 304L can be represented by

$$\frac{da}{dN} = 5.5 \times 10^{-9} \Delta K^3,$$

where  $da/dN$  is in mm/cycle and  $K$  is in MPa  $m^{1/2}$ . The person is assumed to

- (a) walk 3 hours per day  
(b) walk 3 hours and jog 20 minutes per day.

Make all necessary assumptions.

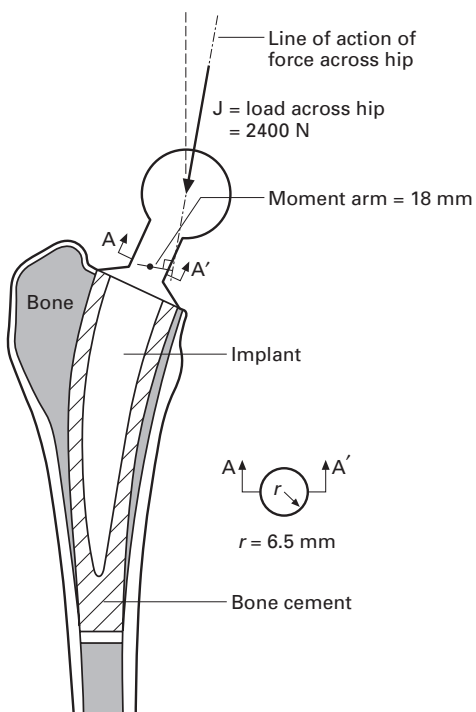


Fig. Ex14.11

**14.12** Assuming that fatigue failures are initiated at the “weakest link,” we may use the Weibull frequency distribution function to represent the fatigue lives of a group of specimens tested under identical conditions. We have

$$f(N) = \frac{b}{N_a - N_0} \left( \frac{N - N_0}{N_a - N_0} \right)^{b-1} \exp \left[ - \left( \frac{N - N_0}{N_a - N_0} \right)^b \right]$$

where  $N$  is the specimen’s fatigue life,  $N_0$  is the minimum life 0,  $N_a$  is the characteristic life at 36.8% survival of the population ( $36.8\% = 1/e$ , where  $e = 2.718$ ), and  $b$  is the shape parameter of the Weibull distribution curve. Letting  $x = (N - N_0)/(N_a - N_0)$ , plot frequency curves  $f(N)$  versus  $x$  for  $b = 1$ , 2, and 3.

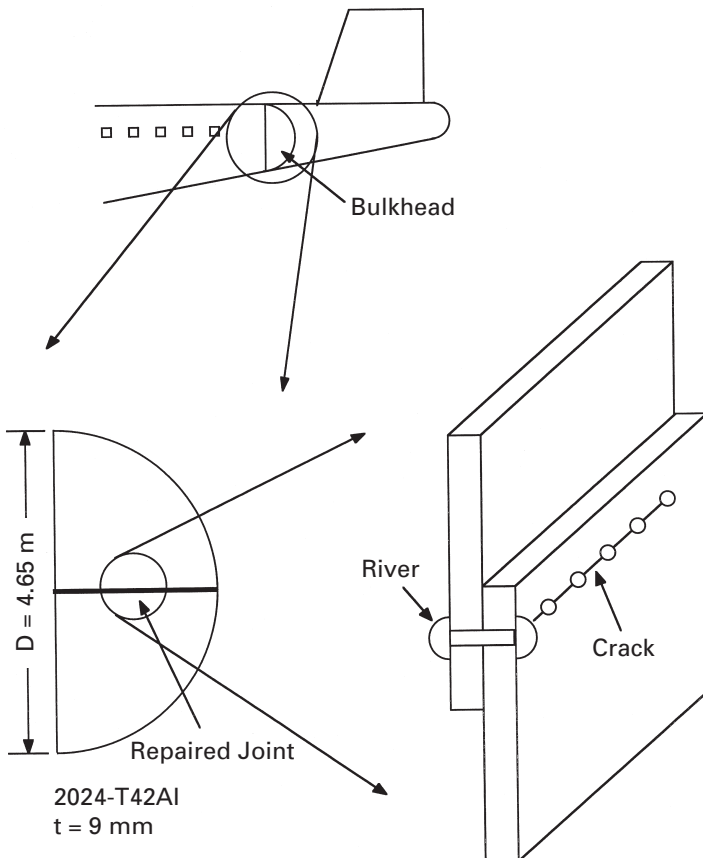
**14.13** Fatigue data are, generally, analyzed cumulatively to determine the survival percentage. The Weibull cumulative function for the fraction of population failing at  $N$  is an integration of the expression for  $f(N)$  in the preceding exercise. Show that this function is

$$F(N) = 1 - \exp \left[ - \left( \frac{N - N_0}{N_a - N_0} \right)^b \right].$$

Transform  $F$  into a straight-line relationship by taking the logarithm of the logarithm of the equation. Show how this relationship can be used on log-log paper for graphically fitting the Weibull cumulative distribution and for graphically estimating the parameters  $b$ ,  $N_0$ , and  $N_a$ .<sup>17</sup>

<sup>17</sup> See, for example, C. S. Yen, in *Metal Fatigue: Theory and Design*, A. F. Madayag, ed. (New York: Wiley, 1969), p. 140.

Fig. Ex14.14



**14.14** (Design Problem) One of the worst single aircraft accidents in history resulted in the loss of 520 lives. It was produced by the growth of a fatigue crack in the back of the bulkhead of a Boeing 747 plane. (See Figure Ex14.14.) The fatigue fracture was caused by a repair that replaced a double row of rivets by a single row in certain places. The accident occurred after the plane reached an altitude of 7,200 m. The atmospheric pressure decreases by 12 Pa for every meter increase in altitude.

- Calculate the stress cycle to which the pressurized cabin and bulkhead were subjected in each takeoff-landing sequence of the plane.
- Establish the critical crack length for which catastrophic growth would occur.
- Assuming that fatigue failure started at one of the rivet holes (which had a diameter of 12 mm) and that it propagated through subsequent holes, calculate the number of cycles necessary to bring down the "big bird," given the following data:

Paris relationship constants,  $C = 5 \times 10^{-8}$  and  $m = 3.6$ ,

$$\sigma_y = 310 \text{ MPa},$$

$$\sigma_{UTS} = 345 \text{ MPa}.$$

**14.15** An alloy steel plate is subjected to constant-amplitude uniaxial tension-compression fatigue. The stress amplitude is 100 MPa. The plate has a yield

strength of 1,500 MPa, a fracture toughness of 50 MPa m<sup>1/2</sup> and an edge crack of 0.5 mm. Estimate the number of fatigue cycles to cause fracture if  $da/dN$  (m/cycle) =  $1.5 \times 10^{-24} \Delta K^4$ , where the units of K are MPa m<sup>1/2</sup>. Use Y = 1 in the fracture toughness equation.

**14.16** A part is subjected to cyclic loading at 50 Hz. The stress intensity at the tip of a flaw is just above  $\Delta K_{th}$ , and  $da/dN$  is equal to  $10^{-8}$  mm/s. What is the length of crack after one week? Take  $m = 3$ .

**14.17** The low cycle fatigue of a metallic alloy can be described by the Coffin-Manson expression relating the number of cycles to failure,  $N_f$ , to plastic strain,  $\Delta\varepsilon_{pl}$ , as follows:

$$N_f^{0.5} \Delta\varepsilon_{pl} = 0.4.$$

Compute the number of cycles to failure if the alloy fails at a plastic strain of  $5 \times 10^{-3}$ .

**14.18** An alloy of titanium, Ti-6Al-4V, has a fracture toughness of 50 MPa m<sup>1/2</sup>. A plate of this material has a penny-shaped crack of diameter 10 mm. Take the yield stress of this alloy to be 980 MPa. What is the stress that can be applied in service to this plate without causing failure? Given:  $K = 2\sigma(a/\pi)^{1/2}$ .

**14.19** A 2024-T6 aluminum alloy used for the frame of an aircraft was tested in a Wöhler-type machine rotating at 400 rpm (sinusoidal stress variation, mean stress equal to zero). The following results were obtained:

stress range = 310 MPa;  $N = 10^4$  cycles;

stress range = 230 MPa;  $N = 10^7$  cycles.

Predict the life of the aircraft if it is in the air 16 hours per day and if it is subjected to the stress range of 180 MPa at the same frequency. The material obeys Basquin's law.

**14.20** Explain the effect on fatigue life of the following design and environmental factors:

- (a) A high polish surface finish.
- (b) A rivet hole.
- (c) Increasing the mean stress, but keeping the range constant.
- (d) A corrosive atmosphere.

**14.21** (Design Problem) On April 28, 1988, an Aloha Airlines Boeing 737, was flying from Hilo to Honolulu. As the airplane leveled at 8,000 m, both pilots heard a loud "clap" or "whooshing" sound followed by a wind noise behind them. The cockpit entry door was missing and that there was blue sky where the first-class ceiling had been. The plane was able to land. After the accident, a passenger stated that as she was boarding the airplane through the jet bridge at Hilo, she observed a longitudinal fuselage crack. The crack was in the upper row of rivets, about halfway between the cabin door and the edge of the jet bridge hood.

What is your interpretation on the cause of the accident? If the plane is pressurized, what is the critical crack length at an altitude of 8,000 m? Make all necessary assumptions and use sketches in your answer.

**14.22** A polymer has cycles to failure  $N_f$  as 50 when the stress amplitude is 43 MPa, and cycles to failure  $N_f$  as 5,000 when the stress amplitude

is 15 MPa. Estimate the cycles to failure when the stress amplitude is 20 MPa.

**14.23** An alloy has a Paris-type fatigue crack propagation relationship:

$$\frac{da}{dN} \text{ (m/cycle)} = 0.8 \times 10^{-6}(\Delta K)^2.$$

If it is subjected to fatigue under a stress amplitude  $\Delta\sigma = 100$  MPa, how long will the crack be after 1,000 cycles. Take the crack to be 0.5 mm.

**14.24** Calculate the mean stress for a titanium alloy with UTS = 1,140 MPa, yield stress 1,075 MPa, by the Goodman, Gerber, and Soderberg relationship. The stress amplitude is 120 MPa and  $\sigma_0 = 140$  MPa.

---

## Chapter 15

# Composite Materials

### 15.1 | Introduction

We can define a *composite* material as a material consisting of two or more physically and/or chemically distinct phases, suitably arranged or distributed. A composite material usually has characteristics that are not depicted by any of its components in isolation. Generally, the continuous phase is referred to as the *matrix*, while the distributed phase is called the *reinforcement*. Three items determine the characteristics of a composite: the reinforcement, the matrix, and the interface between them. In this chapter, we provide a brief survey of different types of composite materials, highlight some of their important features, and indicate their various applications.

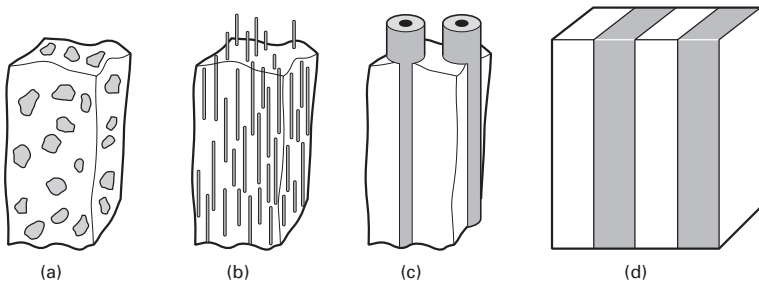
### 15.2 | Types of Composites

We may classify composites on the basis of the type of matrix employed in them – for example, polymer matrix composites (PMCs), metal matrix composites (MMCs), and ceramic matrix composites (CMCs). We may also classify composites on the basis of the type of reinforcement they employ (see Figure 15.1):

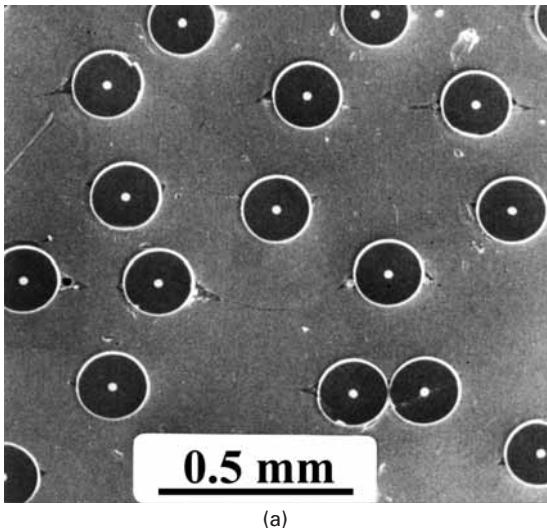
1. Particle reinforced composites.
2. Short fiber, or whisker reinforced, composites.
3. Continuous fiber, or sheet reinforced, MMCs.
4. Laminate composite.

Figure 15.2 shows typical microstructures of some composites: boron fiber/Al (Figure 15.2(a)), short alumina fiber/Al (Figure 15.2(b)), and NbC/Ni-Cr, an *in situ* (eutectic) composite (Figure 15.2(c)). Examples of microstructure of a silicon carbide particle (three different volume fractions) reinforced aluminium matrix are given in Figure 15.3. These were made by hot pressing of powders followed by hot extrusion. Note the preferential alignment of SiC particles in the extrusion direction.

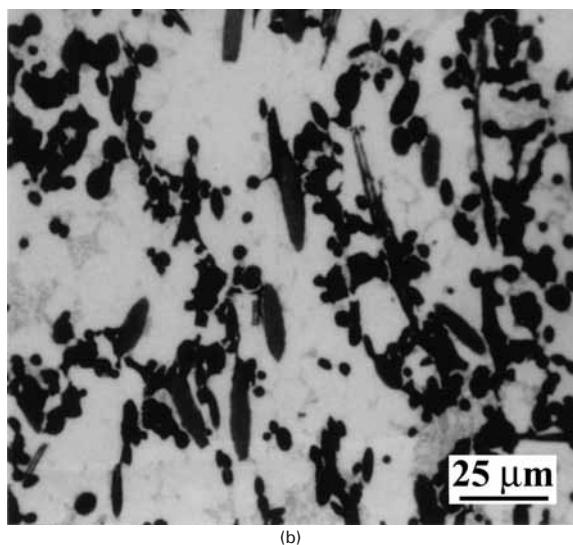
**Fig. 15.1** Different types of reinforcement for composites:  
(a) particle reinforcement;  
(b) short fiber reinforcement;  
(c) continuous fiber reinforcement;  
(d) laminate reinforcement



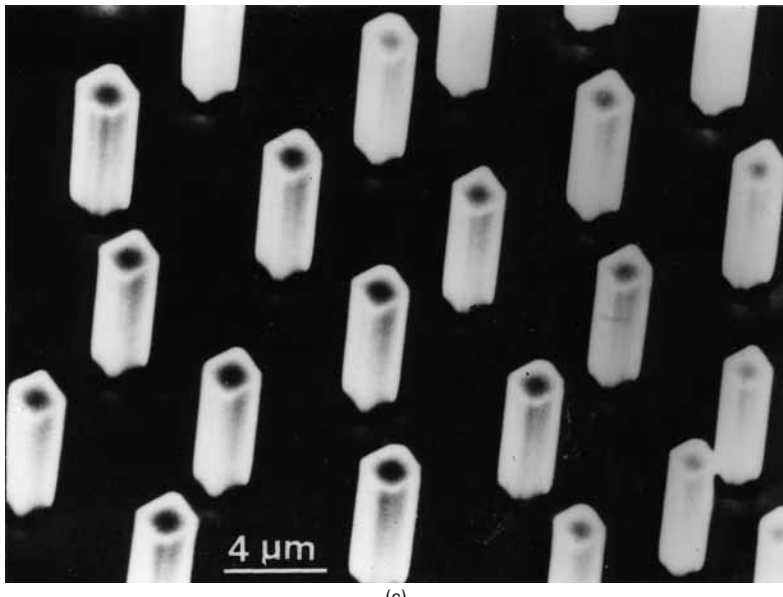
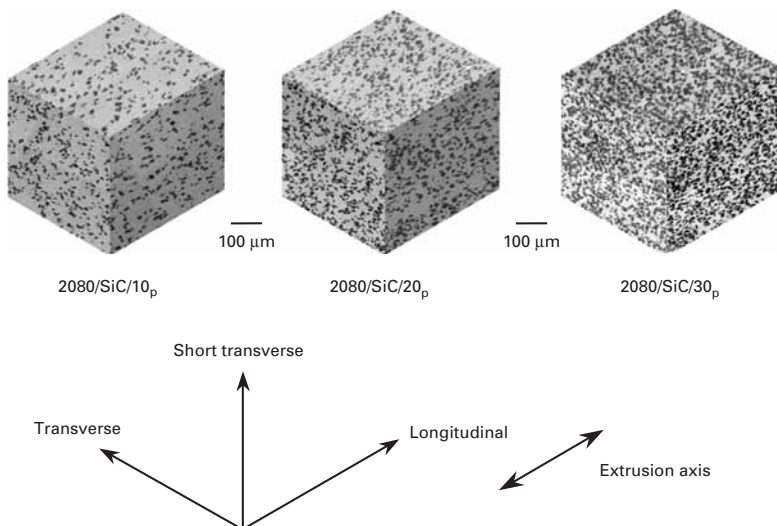
**Fig. 15.2** (a) Transverse section of a boron fiber reinforced aluminum composite.  $V_f = 10\%$ .  
(b) Section of a short alumina fiber/aluminum matrix composite.  
(c) Deeply etched transverse section of a eutectic composite showing NbC fibers in an Ni-Cr matrix. (Courtesy of S. P. Cooper and J. P. Billingham, GEC Turbine Generators Ltd, U.K.)



(a)



(b)

**Fig. 15.2** (cont.)

**Fig. 15.3** Microstructure of a silicon carbide particle (10, 20, and 30%, three different volume fractions) reinforced aluminium alloy (2080) matrix composites made by hot pressing of powders followed by hot extrusion. Note the preferential alignment of SiC particles in the extrusion direction. The number and subscript p indicate the volume fraction of SiC particles in the composites. (Courtesy of N. Chawla.)

## 15.3 Important Reinforcements and Matrix Materials

Many reinforcement materials are available in a variety of forms: continuous fibers, short fibers, whiskers, particles, etc. Some of the important ones are listed in Table 15.1, along with a summary of their salient characteristics. Reinforcements include organic fibers such as polyethylene and aramid, metallic fibers, and ceramic fibers and particles.

**Table 15.1** Properties of Some Important Reinforcement Fibers

Materials (Fibers)	Tensile Modulus (GPa)	Tensile Strength (GPa)	Density (g/cm <sup>3</sup> )
Alumina	350–380	1.7	3.9
Boron	415	3.5	2.5–2.6
SiC	300–400	2.8	2.8
E-Glass	71	1.8–3.0	2.5
Carbon P100 (pitch-based)	725	2.2	2.15
Carbon M60J (PAN-based)	585	3.8	1.94
Aramid	125	3.5	1.45
Polyethylene	110	3	0.97

A variety of materials – polymers (thermoset and thermoplastic), metals and their alloys, intermetallics, glasses, glass-ceramics, and crystalline ceramics – can be used as matrices. Most polymer matrix composites consist of cross-linked thermoset polymers such as epoxy, phenolic, and polyester resins. Cross-linked thermoset polymers have an amorphous structure. (See Chapter 1.) Phenolics have the advantage of being cheaper than epoxy and polyester resins. Their main disadvantage is that toxic by-products are liberated during the curing process. Cross-linking of polymer chains during curing in polyester and epoxy occurs by an addition mechanism, without any by-product produced. Glass fiber reinforced phenolic, polyester, or epoxy have been in use in a variety of automotive components. Epoxy resins have the added attractive feature that they can be partially cured to make fiber/epoxy prepgs, which are subsequently consolidated into a component, usually in an autoclave. A prepg is a thin lamina of unidirectional (or sometimes woven) fiber/polymer composite protected on both sides with easily removable separators. A typical unidirectional prepg comes in the form of a roll that is 300–1,500 mm wide, 0.125 mm thick, and 50–250 m long. Typically, the polymer content is approximately 35% by volume. It is not uncommon to use 50 or even more such plies in a component.

To a lesser extent than thermosets, thermoplastic resins such as poly(ether ether ketone) or PEEK and poly(phenylene sulfide), or polyamide, are used as matrix materials. PEEK is a high-performance semicrystalline thermoplastic that has been used as a matrix for carbon fibers. It is attractive as a polymeric matrix material because of its superior toughness and impact properties, compared to those of epoxies. Such properties are a function of the crystalline content and morphology of the thermoplastic.

There are many other important matrix materials. Among metallic matrix composite, we have aluminum and its alloys, mainly because of their low density and excellent strength, toughness, and resistance

to corrosion, as well as titanium alloys, magnesium alloys, copper, etc. Among intermetallic and ceramic matrix composites are a variety of intermetallic compounds such as molybdenum disilicide and aluminides of nickel and titanium, silica-based glasses, glass-ceramics, and crystalline ceramics such as alumina and silicon carbide.

### Example 15.1

Carbon black is frequently used as a particulate filler in polymers, both thermoplastic and thermoset. Describe some of the important effects of the addition of carbon black to polymers.

**Solution:** Carbon black is stronger than the polymer matrix; thus, we get a stronger and harder composite. Carbon black is also thermally more stable than the polymer matrix; therefore, its addition results in a thermally stable composite – that is, improved creep resistance. In addition, carbon black leads to an enhanced dimensional stability. (It has a higher modulus and lower expansion coefficient than the polymer.)

#### 15.3.1 Microstructural Aspects and Importance of the Matrix

The differential thermal expansion between the reinforcement and the metal matrix can introduce a high dislocation density in a metallic matrix, especially in the near-interface region of the matrix. This high matrix dislocation density, as well as the reinforcement-matrix interfaces, can provide high diffusivity paths in a composite. A semicrystalline thermoplastic matrix can have its crystallization kinetics altered by the presence of a reinforcement such as a carbon fiber. In the case of a ceramic matrix composite, the brittle matrix can undergo cracking in response to such thermal stresses. Thus, the characteristics of a matrix material are changed by the very process of making a composite. Such is not commonly the case with the reinforcement, however; only in rare instances of very high temperature processing, as, for example, in the case of a CMC, can the reinforcement also undergo a change in its microstructure. Hence, the matrix is much more than a mere medium or glue to hold the reinforcement, be that fibers, whiskers, or particles. Accordingly, it should be chosen after due consideration of its chemical compatibility and thermal mismatch with the reinforcement. Processing-induced chemical reactions and thermal stresses can cause changes in the microstructure of the matrix. These microstructural changes in the matrix, in turn, can affect the mechanical and physical behavior of the composite. The matrix strength in the composite (the *in situ* strength) will not be the same as that determined from a test of an unreinforced matrix sample in isolation, because the matrix is likely to suffer

several microstructural alterations during processing and, consequently, changes in its mechanical properties.

The final matrix microstructure is a function of the type, diameter, and distribution of the fiber, as well as conventional solidification parameters. For example, Mortensen et al. observed normal dendritic structure in the unreinforced region of the matrix of a silicon carbide fiber/Al-4.5% Cu matrix, while in the reinforced region, the dendritic morphology was controlled by the fiber distribution.<sup>1</sup> Second phase appeared preferentially at the fiber-matrix interface or in the narrow interfiber spaces. In short, the microstructure of the matrix in the fiber composite is likely to differ significantly from that of the unreinforced matrix material processed in an identical manner.

Porosity is a critical defect that is likely to be present in the matrix. Porosity can be highly deleterious to the overall performance of a composite. The main sources of porosity are any gas evolution, shrinkage occurring upon solidification, and, in the case of CMCs, incomplete elimination of any binder material. In a composite made by liquid infiltration of a preform, a high volume fraction of reinforcement may impede the flow of the liquid and inhibit any “bulk movement” of the semisolid matrix material. The desirability of having a low porosity in a PMC may be appreciated by the fact that the final stage in any PMC fabrication is called *debulking*, which serves to reduce the number of voids. A low quantity of voids is necessary for improved interlaminar shear strength. In the case of a CMC, made by sintering of glass or glass-ceramic powder and fibrous reinforcements, the reinforcements can form a network that impedes the transfer of mass required for sintering. Depending on the thermal expansion coefficients of the components, there is also the possibility of developing hydrostatic tensile stresses in the matrix that will counter the driving force for sintering. The following are some of the common structural defects in composites:

- Matrix-rich (fiber-poor) regions.
- Voids.
- Microcracks (which may form due to thermal mismatch between the components, curing stresses, or the absorption of moisture during processing).
- Debonded regions.
- Delaminated regions.
- Variations in fiber alignment.

---

## 15.4 | Interfaces in Composites

The interface region in a particular composite has a great deal of importance in determining the ultimate properties of the composite,

---

<sup>1</sup> A. Mortensen, M. N. Gungor, J. A. Cornic, and M. C. Flemings, *J. Met.*, 38 (Mar. 1986) 30.

essentially for two reasons: The interface occupies a very large area per unit volume in a composite, and, in general, the reinforcement and the matrix form a system that is not in thermodynamic equilibrium. We can define an interface as a boundary surface between two phases in which a discontinuity in one or more material parameters occurs. According to this definition, an interface is a bidimensional region across which a discontinuity occurs in one or more material parameters. In practice, there is always some volume associated with the interface region, and a gradual transition in material parameters occurs over the thickness of this interfacial zone. Some of the important parameters that can show a discontinuity at the interface are the elastic moduli, strength, chemical potential, coefficient of thermal expansion of the composite, and others. A discontinuity in chemical potential is likely to cause a chemical interaction, leading to an interdiffusion zone or the formation of a chemical compound at the interface. A discontinuity in the thermal expansion coefficient means that the interface will be in equilibrium only at the temperature at which the reinforcement and the matrix were brought into contact. At any other temperature, biaxial or triaxial stress fields will be present, because of the thermal mismatch between the components of a composite. Thermal stresses due to a thermal mismatch will generally have an expression of the form

$$\sigma = f(E, a, b, r) \Delta\alpha \Delta T, \quad (15.1)$$

where  $f(E, a, b, r)$  is a function of the elastic constants  $E$  and the geometric parameters  $a$ ,  $b$ , and  $r$ ;  $\Delta\alpha$  is the difference in the expansion coefficients of the components, and  $\Delta T$  is the change in temperature of the material. The term  $(\Delta\alpha\Delta T)$  is, of course, the thermal strain. (Detailed expressions for thermal stresses in composites can be found in textbooks on composites.<sup>2</sup>)

The reader can easily show that, for a given diameter and volume fraction of reinforcement, a fibrous composite will have a larger interfacial area than a particulate composite. The important point, however, is that the interfacial area in a composite increases with a decreasing reinforcement diameter. It is easy to visualize the interfacial area becoming very large for reinforcements less than 10–20  $\mu\text{m}$  in diameter. Since chemical and/or mechanical interactions between the reinforcement and the matrix occur at interfaces, an extremely large area of interface has an enormous importance in determining the final properties and performance of a composite.

#### 15.4.1 Crystallographic Nature of the Fiber–Matrix Interface

In crystallographic terms, ceramic–metal interfaces in composites are, generally, incoherent and high-energy interfaces. Accordingly, they can act as very efficient vacancy sinks and provide rapid diffusion

<sup>2</sup> See, for example, K. K. Chawla, *Composite Materials: Science and Engineering*, 2<sup>nd</sup> ed. (New York: Springer, 1998).

paths, segregation sites, and sites of heterogeneous precipitation, as well as sites for precipitate-free zones. Among the possible exceptions are some eutectic composites and the XD™ type of particulate composites. The *in situ* or eutectic composites do show semicoherent interfaces, that is, the lattice mismatch between the matrix phase and the reinforcement phase is accommodated by creating a network of dislocations. In general, interfaces in most composites are incoherent.

#### 15.4.2 Interfacial Bonding in Composites

Some bonding must exist between the reinforcement and the matrix for load transfer from matrix to fiber to occur. Neglecting any direct loading of the reinforcement, the applied load is transferred from the matrix to the reinforcement via a well-bonded interface. However, the degree of bonding desired in different types of composites is not the same. In general, one would like to have a strong interfacial bonding in the case of PMCs and MMCs, with which one aims at exploiting the high stiffness and load-bearing capacity of a fibrous reinforcement. In CMCs, on the other hand, one would like to have a weak interfacial bonding, so that an advancing crack gets deflected there rather than passing through unimpeded. This is because the main objective in CMCs is to enhance their toughness instead of their strength. Crack deflection, crack bridging by fiber, and fiber pullout lead to an increased toughness and a noncatastrophic failure.

An important parameter in regard to the interface is the wettability of reinforcement by the matrix. Wettability refers to the ability of a liquid to spread on a solid substrate. Frequently, the contact angle between a liquid drop and a solid substrate is taken as a measure of wettability, a contact angle of 0° indicating perfect wettability and a contact angle of 180° indicating no wettability. Wettability is only a measure of the possibility of attaining an intimate contact between a liquid and a solid. Good wetting is a necessary, but not sufficient, condition for strong bonding. One needs a good wetting even for purely mechanical bonding or weak van der Waals bonding; otherwise voids may form at the interface. Besides wettability, other important factors, such as chemical, mechanical, thermal, and structural factors, affect the nature of the bonding between reinforcement and matrix. As it happens, these factors frequently overlap, and it may not always be possible to isolate their effects.

In PMCs, the surfaces of fibers are generally treated to promote chemical or mechanical adhesion with the matrix. For example, glass fiber, a common reinforcement for a variety of polymeric resins, invariably has a treated surface. The treatment is called *sizing*. The size is applied to protect glass fiber from the environment, for ease of handling, and to avoid introducing surface defects into the material. Common sizes are starch gum, hydrogenated vegetable oil, gelatin, and polyvinyl alcohol. These sizes are removed before putting in resin matrix by heat cleaning at approximately 340 °C and washing. After cleaning, organometallic or organosilane coupling agents are applied. Organosilane compounds have the chemical formula,  $R-SiX_3$ , where X

typically is Cl and R is a resin-compatible group capable of interacting with hydroxylated silanes on the glass surface.

A mechanical keying effect between two surfaces can also contribute to bonding. Chawla and Metzger observed such mechanical bonding effects in alumina/aluminum, a metal-matrix composite system.<sup>3</sup> Bonding due to mechanical interlocking at a rough interface can be equally important in PMCs and CMCs. Carbon fibers are given an oxidation treatment to provide, among other things, a rough surface that aids in bonding with the polymer matrix.

### 15.4.3 Interfacial Interactions

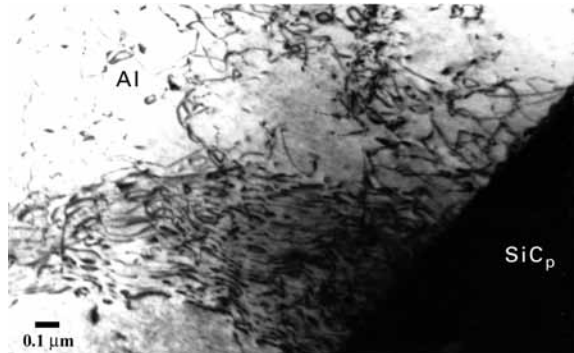
As mentioned earlier, most composite systems are nonequilibrium systems in the thermodynamic sense; that is, there exists a chemical potential gradient across the fiber-matrix interface. This means that, given favorable kinetic conditions (which, in practice, means a high enough temperature or long enough time), diffusion and/or chemical reactions will occur between the components. The interface layer(s) formed because of such a reaction will generally have characteristics different from those of either one of the components. At times, however, some controlled amount of reaction at the interface may be desirable for obtaining strong bonding between the fiber and the matrix, but too thick an interaction zone will adversely affect the properties of the composite. Metal and ceramic matrix composites are generally fabricated at high temperatures, because diffusion and chemical reaction kinetics are faster at elevated temperatures than at low temperatures.

A very important factor in regard to reinforcement-matrix compatibility has to do with the mismatch between the coefficient of thermal expansion of the reinforcement and that of the matrix. This thermal mismatch can lead to thermal stresses large enough to cause plastic deformation in a soft metallic matrix and cracking in a brittle ceramic or polymeric matrix. Plastic deformation in the metallic matrix leads to the introduction of defects such as dislocations, vacancies, etc., in the matrix, especially in the region near the interface. The introduction of such defects can and does affect the phenomena responsible for chemical reactions at the interface, as well as characteristics of the matrix such as the precipitation kinetics. Chawla and Metzger showed, in a definitive matter, the importance of thermal stresses in composites.<sup>4</sup> They used a large-diameter tungsten fiber, (225  $\mu\text{m}$ )/copper single-crystal matrix and low-fiber volume fractions. An etch-pitting technique was employed to observe dislocations in the matrix. The researchers observed that the dislocation density near the fiber was much higher than the dislocation density far away from the fiber. The enhanced dislocation density in the copper matrix near the fiber arose because of the plastic deformation

<sup>3</sup> K. K. Chawla and M. Metzger, in *Advances in Research on Strength and Fracture of Materials* 3 (New York: Pergamon Press, 1978), p. 1039.

<sup>4</sup> K. K. Chawla and M. Metzger, *J. Mater. Sci.*, 7 (1972) 34.

**Fig. 15.4** TEM micrograph showing dislocations in aluminum in the region near a silicon carbide particle ( $\text{SiC}_p$ ).



of the matrix, in response to the thermal stresses generated by the thermal mismatch between the fiber and the matrix. The existence of a plastically deformed zone containing a high dislocation density in the metallic matrix in the vicinity of the reinforcement was confirmed by transmission electron microscopy by a number of other researchers, both in fibrous and particulate metal matrix composites. Figure 15.4, a TEM micrograph, shows dislocations in an aluminum matrix near a particle of silicon carbide. Such high densities of defects in the metal matrix will, of course, lead to a different set of properties of the matrix. In nonprecipitation-hardening metals, this will simply cause a strengthening due to a higher dislocation density. In precipitation-hardenable matrix alloys, such as aluminum–copper, one would expect faster aging kinetics. Preferential precipitation at the reinforcement–matrix interface in an age-hardenable matrix has been observed by many researchers.

### Example 15.2

Ultrahigh-molecular-weight polyethylene (UHMWPE) fibers such as the Spectra fiber are very hard to bond with most matrix materials. Why?

**Solution:** High-modulus polyethylene fibers have a very highly oriented and extended chain structure. This high degree of crystallinity and a lack of polar surface do not allow good bonding of the fibers to most matrix materials. Indeed, the surface of such fibers must be treated with plasma to provide roughness or else a copolymer should be used to provide a polar surface, both of which approaches allow for bonding with the matrix. A similar problem exists, to varying degrees, with aramid and carbon fibers as well.

## 15.5 | Properties of Composites

We next describe some of the important properties of composites. In particular, we present expressions that allow us to predict the

properties of composites in terms of the properties of their components, their amounts, and their geometric distribution in the composite. We also discuss the limitations of such expressions.

### 15.5.1 Density and Heat Capacity

Density and heat capacity are two properties that may be predicted rather accurately by a rule-of-mixtures type of relationship, irrespective of the arrangement of one phase in another. The simple relationships predicting these properties of a composite are as follows.

#### Density

The density of a composite is given by the rule-of-mixture equation

$$\rho_c = \rho_m V_m + \rho_r V_r,$$

where  $\rho$  designates the density and  $V$  represents volume fraction, with the subscripts  $c$ ,  $m$ , and  $r$  denoting the composite, matrix, and reinforcement, respectively.

#### Heat capacity

The heat capacity of a composite is given by the expression

$$C_c = (C_m \rho_m V_m + C_r \rho_r V_r) / \rho_c,$$

where  $C$  denotes heat capacity and the other symbols have the significance given in the equation for density.

### 15.5.2 Elastic Moduli

The simplest model for predicting the elastic properties of a fiber/reinforced composite is shown in Figure 15.5. In the longitudinal direction, the composite is represented by a system of “action in parallel” (Figure 15.5(a)). For a load applied in the direction of the fibers, assuming equal deformation in the components, the two (or

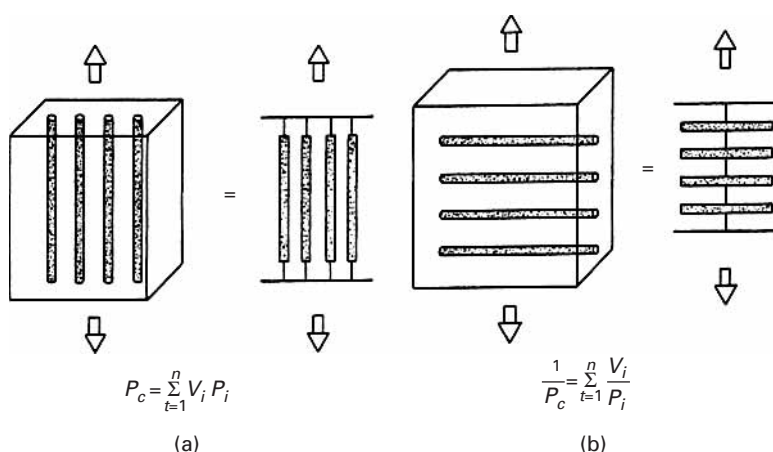


**Fig. 15.5** Simple composite models. (a) Longitudinal response (action in parallel). (b) Transverse response (action in series).

more) phases are viewed as being deformed in parallel. This is the classic case of Voigt's average, in which one has

$$P_c = \sum_{i=1}^n P_i V_i, \quad (15.2)$$

where  $P$  is a property,  $V$  denotes volume fraction, and the subscripts  $c$  and  $i$  indicate, respectively, the composite and the  $i$ th component of the total of  $n$  components. For the case under study,  $n = 2$ , and the property  $P$  is Young's modulus. We can write, in extended form,

$$E_c = E_f V_f + E_m V_m, \quad (15.3)$$

where the subscripts  $f$  and  $m$  indicate the fiber and matrix, respectively.

The elastic properties of such unidirectional composites in the transverse direction can be represented by a system of "action in series" (Figure 15.5(b)). Upon loading in a direction transverse to the fibers, then, we have equal stress in the components. This model is equivalent to Reuss's classic treatment. We may write

$$\frac{1}{P_c} = \sum_{i=1}^n \frac{V_i}{P_i}. \quad (15.4)$$

Once again, for the case of  $n = 2$ , and taking the property  $P$  to be Young's modulus, we obtain, for the composite,

$$\frac{1}{E_c} = \frac{V_f}{E_f} + \frac{V_m}{E_m}. \quad (15.5)$$

The simple relations expressed Equations 15.4 and 15.5 are commonly referred to as the "rule of mixtures." The reader is warned that this rule is nothing more than a first approximation; more elaborate models have been proposed. The following is a summary of various methods of obtaining composite properties.

- *The mechanics-of-materials method.* This deals with the specific geometric configuration of fibers in a matrix – for example, hexagonal, square, and rectangular – and we introduce large approximations in the resulting fields.
- *The self-consistent field method.* This method introduces approximations in the geometry of the phases. We represent the phase geometry by a single fiber embedded in a material whose properties are equivalent to those of a matrix or an average of a composite. The resulting stress field is thus simplified.
- *The variational calculus method.* This method focuses on the upper and lower limits of the properties of the composite and does not predict those properties directly. Only when the upper and the lower bounds coincide is a particular property determined. Frequently, however, the upper and lower bounds are well separated.
- *The numerical techniques method.* Here we use series expansion, numerical analysis, and finite-element techniques.

The variational calculus method does not give exact results, but provides upper and lower bounds. These results can be used only as indicators of the behavior of the material unless the upper and lower bounds are close enough. Fortunately, this is the case for longitudinal properties. Hill put rigorous limits on the value of  $E$  in terms of the bulk modulus in plane strain,  $k_p$ , Poisson's ratio  $\nu$ , and the shear modulus  $G$  of the two phases.<sup>5</sup> One notes that  $k_p$  is the modulus for lateral dilation with zero longitudinal strain ( $k_p$  is not equal to  $K$ ) and is given by

$$k_p = \frac{E}{2(1 - 2\nu)(1 + \nu)}.$$

According to Hill, the bounds on  $E_c$  are

$$\begin{aligned} \frac{4V_f V_m (\nu_m - \nu_f)^2}{V_f/k_{pm} + V_m/k_{pf} + 1/G_m} &\leq E_c - (E_f V_f + E_m V_m) \\ &\leq \frac{4V_f V_m (\nu_m - \nu_f)^2}{V_f/k_{pm} + V_m/k_{pf} + 1/G_f}. \end{aligned} \quad (15.6)$$

It is worth noting that this treatment of Hill does not have restrictions on the form of the fiber, the packing geometry, and so on. We can see, by putting in values in Equation 15.6, that the deviations from the rule of mixtures (Equation 15.3) are rather small, for all practical purposes. For example, take  $E_f/E_m = 100$ ,  $\nu_f = 0.25$ ,  $\nu_m = 0.4$ . Then the deviation of the Young's modulus of the composite from that predicted by the rule of mixtures is, at most, 2%. For a metallic fiber (e.g., tungsten in a copper matrix), the deviation is less than 1%. Of course, the rule of mixture becomes exact when  $\nu_f = \nu_m$ .

The transverse properties and the shear moduli are not amenable to such simple reductions. Indeed, they do not obey the rule of mixtures, even to the first approximation. The bounds on them are well spaced. Numerical analysis results show that the behavior of the composite depends on the form and packing of the fiber and on the spacing between fibers.

Unidirectionally reinforced, continuous fiber composites show a linear increase in their longitudinal Young's modulus as a function of the volume fraction of fiber. For materials with a low modulus, such as polymers and metals, reinforcement by high-modulus and high-strength ceramic fibers can result in a significant increase in the composite's elastic modulus and strength. Figure 15.6 shows an example of a linear increase in the longitudinal flexural modulus as a function of the volume fraction of fiber for a glass fiber-reinforced epoxy. In the case of CMCs, an increase in the elastic modulus or strength is rarely the objective, because most monolithic ceramics

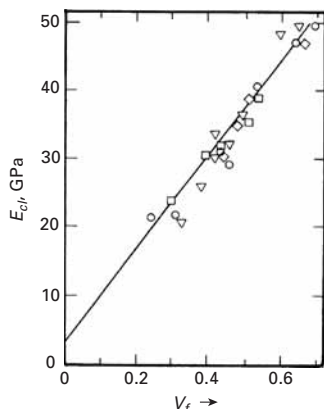


**Fig. 15.6** An example of a linear increase in the longitudinal flexural modulus of the composite,  $E_{cl}$ , as a function of the volume fraction of fiber for a glass fiber-reinforced epoxy. (After R. D. Adams and D. G. C. Bacon, *J. Comp. Mater.*, 7 (1973) 53.)

<sup>5</sup> R. Hill, *J. Mech. Phys. Solids*, 12 (1964) 199.

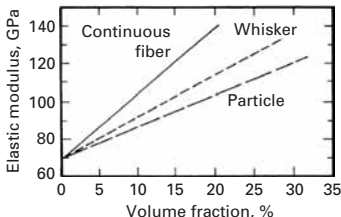


**Fig. 15.7** Schematic of increase in modulus in a composite with reinforcement volume fraction for a different form of reinforcement – continuous fiber, whisker, or particle. Note the loss of reinforcement efficiency as one goes from continuous fiber to particle.

already have very high modulus and strength. However, an increase in the elastic modulus and strength can be a welcome attribute for low-modulus matrix materials – for example, glasses, glass–ceramics, and some crystalline ceramics, such as MgO. Still, the main objective of continuous fiber reinforcement of ceramic matrix materials is to toughen them. In a manner similar to that in PMCs and MMCs, various glass matrix compositions reinforced with carbon fibers have been shown to increase in strength and modulus with the volume fraction of fiber, in accordance with the rule of mixtures. Young's modulus increases linearly with  $V_f$ , but at a higher  $V_f$  it may deviate from linearity, owing to porosity in the matrix and possible misalignment of the fibers.

Particle reinforcement also results in an increase in the modulus of the composite – much less, however, than that predicted by the rule of mixtures. This is understandable, in as much as the rule of mixtures is valid only for continuous fiber reinforcement. A schematic of the increase in modulus in a composite with volume fraction for the same reinforcement, but a different form of reinforcement – continuous fiber, whisker, or particle – is shown in Figure 15.7. This schematic shows the loss of reinforcement efficiency as one goes from continuous fiber to particle.

In sum, we can say that the increase in the longitudinal elastic modulus of a fibrous composite as a function of the reinforcement volume fraction is fairly straightforward. The modulus of a composite is reasonably independent of the reinforcement packing arrangement, as long as all the fibers are parallel. For discontinuous reinforcement, the modulus is also quite independent of the particle clustering, etc. The modulus of a composite does show a dependence on temperature, which enters the picture essentially through the dependence of the matrix modulus on temperature.

### Example 15.3

Consider a glass fiber-reinforced nylon composite. Let the volume fraction of the glass fiber be 65%. The density of glass is  $2.1 \text{ g cm}^{-3}$ , while that of nylon is  $1.15 \text{ g cm}^{-3}$ . Compute the density of the composite. Does it matter whether the glass fiber is continuous?

**Solution:** The density of the composite is given by

$$\rho_c = \rho_f V_f + \rho_m V_m = 0.65 \times 2.1 + 0.35 \times 1.15 = 1.76 \text{ g cm}^{-3}.$$

It does not matter what the exact form of the glass fiber is in the composite. In fact, it could be in the form of equiaxial particles. A rule-of-mixture type of expression is valid for density of all composites, irrespective of the precise geometrical distribution of phases.

**Example 15.4**

A carbon fiber reinforced epoxy composite consists of unidirectionally aligned fibers and has  $V_f = 65\%$ . Calculate the longitudinal and transverse Young's modulus of this composite.  $E_f = 200 \text{ GPa}$ ,  $E_m = 5 \text{ GPa}$ .

**Solution:** In the longitudinal direction, we have

$$\begin{aligned} E_{cl} &= V_f E_f + (1 - V_f) E_m \\ &= 0.65 \times 200 + 0.35 \times 5 \text{ GPa} \\ &= 131.75 \text{ GPa}. \end{aligned}$$

In the transverse direction, we have the expression

$$\frac{1}{E_{ct}} = \frac{V_f}{E_f} + \frac{1 - V_f}{E_m}.$$

Rearranging yields

$$\begin{aligned} E_{ct} &= \frac{E_f E_m}{E_f(1 - V_f) + E_m V_f} \\ &= \frac{200 \times 5}{200 \times 0.35 + 5 \times 0.65} \\ &= 13.65 \text{ GPa}. \end{aligned}$$

Note the high degree of anisotropy. In reality,  $E_{ct}$  will be less than the value calculated above because the transverse modulus of carbon fiber is about one-half of the longitudinal modulus value used in the example.

**Example 15.5**

Alumina particle (15 volume %) reinforced aluminum composite is used for making some special mountain bicycles. The density of alumina is  $3.97 \text{ g cm}^{-3}$ , while that of aluminum is  $2.7 \text{ g cm}^{-3}$ . Why is this composite used to make the mountain bicycle?

**Solution:** The alumina-aluminum composite will, of course, be slightly heavier than the unreinforced aluminum. The driving force for using the composite in this case is the enhanced stiffness:  $E_{\text{Al}_2\text{O}_3} = 380 \text{ GPa}$ , while  $E_{\text{Al}} = 70 \text{ GPa}$ . We can estimate the stiffness of the composite as

$$\begin{aligned} E_{\text{composite}} &= E_{\text{Al}_2\text{O}_3} V_{\text{Al}_2\text{O}_3} + E_{\text{Al}} V_{\text{Al}} \\ &= 380 \times 0.15 + 70 \times 0.85 \\ &= 57 + 59.50 = 116.50 \text{ GPa}. \end{aligned}$$

This estimate is somewhat higher than that realized in practice, because the expression is valid for an unidirectional fiber-reinforced composite, whereas the composite under consideration is a particulate composite. Even so, there is an almost 50% gain in stiffness by adding 15 volume % of alumina particles to aluminum.

### 15.5.3 Strength

Unlike elastic moduli, it is difficult to predict the strength of a composite by a simple rule-of-mixture type of relationship, because strength is a very structure-sensitive property. Specifically, for a composite containing continuous fibers and that is unidirectionally aligned and loaded in the fiber direction, the stress in the composite is written as

$$\sigma_c = \sigma_f V_f + \sigma_m V_m, \quad (15.7)$$

where  $\sigma$  is the axial stress,  $V$  is the volume fraction, and the subscripts  $c$ ,  $f$ , and  $m$  refer to the composite, fiber, and matrix, respectively. The reason that the rule of mixture does not work for properties such as strength, compared to its reasonable application in predicting properties such as Young's modulus in the longitudinal direction, is the following: The elastic modulus is a relatively structure-insensitive property, so, the response to an applied stress in the composite state is nothing but the volume-weighted average of the individual responses of the isolated components. Strength, on the contrary, is an extremely structure-sensitive property. Thus, synergism can occur in the composite state. Let us now consider the factors that may influence, in one way or the other, composite properties. First, the matrix or fiber structure may be altered during fabrication; and second, composite materials generally consist of two components whose thermomechanical properties are quite different. Hence, these materials suffer residual stresses and/or alterations in structure due to the internal stresses. The differential contraction that occurs when the material is cooled from the fabrication temperature to ambient temperature can lead to rather large thermal stresses, which, in turn, lead a soft metal matrix to undergo extensive plastic deformation. The deformation mode may also be influenced by rheological interaction between the components. The plastic constraint on the matrix due to the large difference in the Poisson's ratio of the matrix compared with that of the fiber, especially in the stage wherein the fiber deforms elastically while the matrix deforms plastically, can alter the stress state in the composite. Thus, the alteration in the microstructure of one or both of the components or the interaction between the components during straining can give rise to synergism in the strength properties of the composite. In view of this, the rule of mixture would be, in the best of the circumstances, a lower bound on the maximum stress of a composite.

Having made these observations about the applicability of the rule of mixture to the strength properties, we will still find it instructive to consider this lower bound on the mechanical behavior of the composite. We ignore any negative deviations from the rule of mixtures due to any misalignment of the fibers or due to the formation of a reaction product between fiber and matrix. Also, we assume that the components do not interact during straining and that these properties in the composite state are the same as those in the isolated state.

Then, for a series of composites with different fiber volume fractions,  $\sigma_c$  would be linearly dependent on  $V_f$ . Since  $V_f + V_m = 1$ , we can rewrite Equation 15.7 as

$$\sigma_c = \sigma_f V_f + \sigma_m(1 - V_f). \quad (15.8)$$

We can put certain restrictions on  $V_f$  in order to have real reinforcement. For this, a composite must have a certain minimum-fiber (continuous) volume fraction,  $V_{\min}$ . Assuming that the fibers are identical and uniform (that is, all of them have the same ultimate tensile strength), the ultimate strength of the composite will be attained, ideally, at a strain equal to the strain corresponding to the ultimate stress of the fiber. Then, we have

$$\sigma_{cu} = \sigma_{fu} V_f + \sigma'_m(1 - V_f), \quad V_f \geq V_{\min}, \quad (15.9)$$

where  $\sigma_{fu}$  is the ultimate tensile stress of the fiber in the composite and  $\sigma'_m$  is the matrix stress at the strain corresponding to the fiber's ultimate tensile stress. Note that  $\sigma'_m$  is to be determined from the stress-strain curve of the matrix alone; that is, it is the matrix flow stress at a strain in the matrix equal to the breaking strain of the fiber. As already indicated, we are assuming that matrix stress-strain behavior in the composite is the same as in isolation. At low volume fractions, if a work-hardened matrix can counterbalance the loss of load-carrying capacity as a result of fiber breakage, the matrix will control the strength of the composite. Assuming that all the fibers break at the same time, in order to have a real reinforcement effect, one must satisfy the relation

$$\sigma_{cu} = \sigma_{fu} V_f + \sigma'_m(1 - V_f) \geq \sigma_{mu}(1 - V_f), \quad (15.10)$$

where  $\sigma_{mu}$  is the ultimate tensile stress of the matrix. The equality in this expression serves to define the minimum fiber volume fraction,  $V_{\min}$ , that must be surpassed in order to have real reinforcement. In that case,

$$V_{\min} = \frac{\sigma_{mu} - \sigma'_m}{\sigma_{fu} + \sigma_{mu} - \sigma'_m}. \quad (15.11a)$$

The value of  $V_{\min}$  increases with decreasing fiber strength or increasing matrix strength.

In case we require that the composite strength should surpass the matrix ultimate stress, we can define a critical fiber volume fraction,  $V_{\text{crit}}$ , that must be exceeded.  $V_{\text{crit}}$  is given by the equation

$$\sigma_{cu} = \sigma_{fu} V_f + \sigma'_m(1 - V_f) \geq \sigma_{mu}.$$

In this case,

$$V_{\text{crit}} = \frac{\sigma_{mu} - \sigma'_m}{\sigma_{fu} - \sigma'_m}. \quad (15.11b)$$

$V_{\text{crit}}$  increases with increasing degree of matrix work-hardening ( $\sigma_{mu} - \sigma'_m$ ). Figure 15.8 shows graphically the determination of  $V_{\min}$  and  $V_{\text{crit}}$ . One notes that  $V_{\text{crit}}$  will always be greater than  $V_{\min}$ .

**Fig. 15.8** Determination of  $V_{\min}$  and  $V_{\text{crit}}$ .

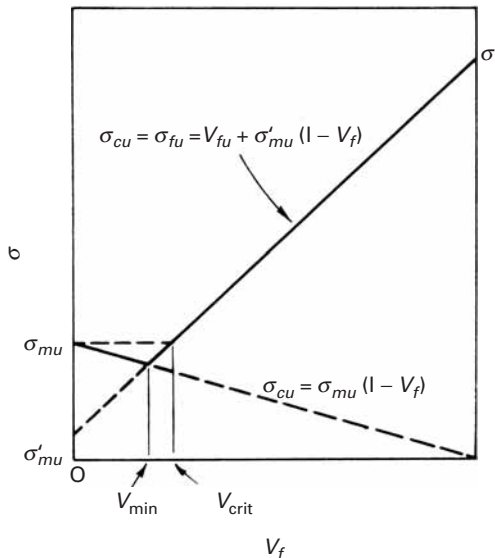
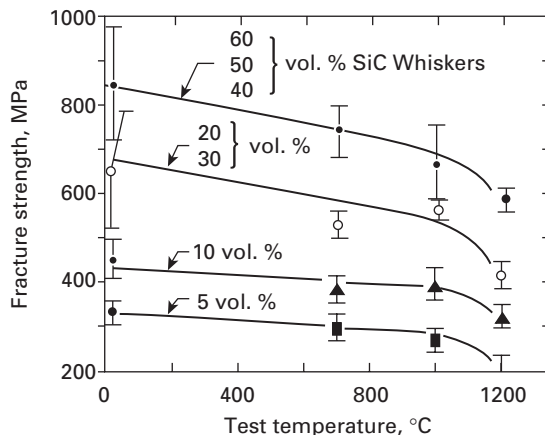


**Fig. 15.9** Increase in strength in silicon carbide whisker-alumina composites as a function of the whisker volume fraction and test temperature. (After G. C. Wei and P. F. Becher, *Am. Ceram. Soc. Bull.*, 64 (1985) 333.)



In general, by incorporating fibers, we can increase the strength of the composite in the longitudinal direction. The strengthening effect in the transverse direction is not significant. Particle reinforcement can result in a more isotropic strengthening, provided that we have a uniform distribution of particles. Carbon, aramid, and glass fibers are used in epoxies to obtain high-strength composites. Such PMCs, however, have a maximum use temperature of about 150 °C. Metal matrix composites, such as silicon carbide fiber in titanium, can take us to moderately high application temperatures. For applications requiring very high temperatures, we must resort to ceramic matrix composites. Silicon carbide whisker reinforced alumina composites show a good combination of mechanical and thermal properties: substantially improved strength, fracture toughness, thermal shock resistance, and high-temperature creep resistance over that of monolithic alumina. Figure 15.9 gives an example of the improvement in

strength in the silicon carbide whisker–alumina composites as a function of the whisker volume fraction and test temperature. Similar results have been obtained with silicon carbide whisker–reinforced silicon nitride composites.

Finally, we should mention the strength of *in situ* composites. In Figure 15.2(c), we showed the microstructure of an *in situ* composite. Such a composite is generally made by the unidirectional withdrawal of heat during the solidification of a eutectic alloy. This controlled solidification allows for one phase to appear in an aligned fibrous form in a matrix of the other phase. The strength  $\sigma$  of such an *in situ* metal matrix composites made by directional solidification of eutectic alloys is given by a relationship similar to the Hall–Petch relationship used for grain-boundary strengthening:<sup>6</sup>

$$\sigma = \sigma_0 + k\lambda^{-1/2}.$$

Here  $\sigma_0$  is a friction stress term,  $k$  is a material constant, and  $\lambda$  is the interfiber spacing between rods, or lamellae. It turns out that one can vary  $\lambda$  rather easily by controlling the solidification rate  $R$ , because  $\lambda^2R$  equals a constant. Thus, one can easily control the strength of these *in situ* composites.

### Example 15.6 |

Consider a uniaxial fiber-reinforced composite of aramid fibers in an epoxy matrix. The volume fraction of fibers is 60%. The composite is subjected to an axial strain of 0.1%. Compute the modulus and strength along the axial direction of the composite corresponding to this strain.

**Solution:** Both fiber and matrix deform elastically to a strain of 0.1%. Thus, we have

$$\begin{aligned}\text{longitudinal Young's modulus, } E_{cl} &= E_f V_f + E_m(1 - V_f) \\ &= 140 \times 0.6 + 5 \times 0.4 \\ &= 84 + 2 = 86 \text{ GPa},\end{aligned}$$

$$\begin{aligned}\text{longitudinal strength, } \sigma_{cl} &= \sigma_f V_f + \sigma'_m(1 - V_f) \\ &= eE_f V_f + eE_m(1 - V_f) \\ &= e(E_{cl}) = 0.001 \times 86 \text{ GPa}, \\ &= 86 \text{ MPa}.\end{aligned}$$

#### 15.5.4 Anisotropic Nature of Fiber Reinforced Composites

Fiber reinforced composites are highly anisotropic; in particular their mechanical properties are strongly dependent on direction. We derive an expression for the variation in the Young's modulus with the orientation of the fiber for a unidirectionally aligned composite.

<sup>6</sup> H. E. Cline, E. F. Walter, E. F. Koch, and L. M. Osika, *Acta Met.*, 19 (1971) 405.

The generalized Hooke's law may be written as (see Section 2.9)

$$\varepsilon_i = S_{ij}\sigma_j,$$

where  $\varepsilon_i$  is the strain,  $\sigma_j$  is the stress,  $S_{ij}$  is the compliance matrix, and  $i$  and  $j$  take values from 1 to 6, with summation indicated by a repeated suffix.

The compliances  $S_{11}$ ,  $S_{22}$ , and  $S_{33}$  are reciprocals of the generalized stiffness moduli, and it can be shown (see Chapter 2) that they transform with rotation about a principal axis, say, the  $x_3$ -axis, according to relations of the type

$$S'_{11} = m^4 S_{11} + n^4 S_{22} + m^2 n^2 (2S_{12} + S_{66}) + 2mn(m^2 S_{16} + n^2 S_{26}), \quad (15.13a)$$

where  $m = \cos \theta$ , and  $n = \sin \theta$ , in which  $\theta$  is the angle of rotation.

For the discriminating reader, we should point out that this equation follows from the transformation relationship for the fourth rank elasticity tensor:

$$S'_{ijkl} = \ell_{im} \ell_{jn} \ell_{ko} \ell_{lp} S'_{mnop}$$

where  $\ell_{im}$ ,  $\ell_{jn}$ ,  $\ell_{ko}$ , and  $\ell_{lp}$ , are the transformation coefficients. For  $S'_{1111}$ , we have

$$S'_{1111} = \ell_{lm} \ell_{ln} \ell_{lo} \ell_{lp} S'_{mnop}.$$

Care should be exercised when changing from the tensorial to matrix notation (see Section 2.9). For more details on such mathematical operations, the students should consult a text (for example, J. F. Nye. *Physical Properties of Crystals*. London: Oxford University Press, 1975). After converting to matrix notation we arrive at

$$S_{1111} = S_{11}; \quad S_{2222} = S_{22}; \quad 4S_{1212} = S_{66}; \quad 2S_{2212} = S_{26}.$$

For an orthotropic sheet material, such as a prepreg, for which the  $x_3$ -axis is normal to the plane of the sheet, we have  $S_{16} = S_{26} = 0$ ; then, assuming that the properties in the directions 1 and 2 are the same, Equation 15.13a becomes

$$\begin{aligned} S'_{11} &= (m^4 + n^4) S_{11} + m^2 n^2 (2S_{12} + S_{66}) \\ &= \frac{1}{2} S_{11} + \left( \frac{1}{2} S_{12} + \frac{1}{4} S_{66} \right) + \left[ \frac{1}{2} S_{11} - \left( \frac{1}{2} S_{12} + \frac{1}{4} S_{66} \right) \right] \cos^2 2\theta. \end{aligned}$$

Now let  $E_0$  and  $E_{45}$  be Young's modulus for  $\theta = 0^\circ$  and  $\theta = 45^\circ$ , respectively. Then  $S_{11} = 1/E_0$  and  $\frac{1}{2} S_{11} + \frac{1}{2} S_{12} + \frac{1}{4} S_{66} = 1/E_{45}$ . Using these relationships, we get

$$S' = \frac{1}{E_\theta} = \frac{1}{E_{45}} - \left( \frac{1}{E_{45}} - \frac{1}{E_0} \right) \cos^2 2\theta, \quad (15.13b)$$

where  $E_\theta$  is the modulus of the composite when the loading direction makes an angle  $\theta$  with the fiber direction.

We can also write the compliances  $S_{12}$  and  $S_{66}$  in terms of the shear modulus  $G$  and Poisson's ratio  $\nu$  for stresses applied in the

plane of the sheet in the directions 1 and 2. From this, we obtain the relationship

$$\frac{1}{2G} = \frac{1}{E_{45}} - \frac{1}{E_0} (1 - \nu).$$

### 15.5.5 Aging Response of Matrix in MMCs

We have pointed out that the microstructure of a metallic matrix is modified by the presence of a ceramic reinforcement (particle, whisker, or fiber). In particular, a higher dislocation density in the matrix metal or alloy than that in the unreinforced metal or alloy has been observed. The higher dislocation density in the matrix has its origin in the thermal mismatch ( $\Delta\alpha$ ) between the reinforcement and the metal matrix. For example, the thermal mismatch in the case of SiC-Al has a high value of  $21 \times 10^{-6} \text{ K}^{-1}$ , which will lead to thermal stress high enough to deform the matrix plastically and thus leave the matrix work-hardened. One expects that the quenching from the solutionizing temperature to room temperature, a change of about  $450^\circ \text{C}$ , will result in a large zone of matrix plastically deformed around each ceramic particle in which the dislocation density will be very high. This high dislocation density will tend to accelerate the aging kinetics of the matrix. Age-hardening treatment can contribute a considerable increment in strength to a precipitation-hardenable aluminum alloy composite. It should be borne in mind that the particle and whisker types of reinforcement, such as SiC, B<sub>4</sub>C, Al<sub>2</sub>O<sub>3</sub>, etc., are unaffected by the aging process. These particles, however, can affect the precipitation behavior of the matrix quite significantly. The dislocations generated by thermal mismatch form heterogeneous nucleation sites for the precipitates in the matrix during subsequent aging treatments. This in turn alters the precipitation kinetics in the matrix of the composite, compared to the precipitation kinetics in the unreinforced material. Most metal matrix composite work has involved *off-the-shelf* metallic alloys, especially in the case of particle reinforced metal matrix composites. It is important to bear in mind that in such cases using the standard heat treatment practices given in the manuals and handbooks for unreinforced alloys can lead to drastically different results.

### 15.5.6 Toughness

The toughness of a given composite depends on the following factors:

- Composition and microstructure of the matrix.
- Type, size, and orientation of the reinforcement.
- Any processing done on the composite, in so far as it affects microstructural variables (e.g., the distribution of the reinforcement, porosity, segregation, etc.).

Continuous fiber reinforced composites show anisotropy in toughness just as in other properties. The  $0^\circ$  and  $90^\circ$  arrangements of fibers result in two extremes of toughness, while the  $0^\circ/90^\circ$  arrangement

(i.e., alternating laminae of 0° and 90°) gives a sort of pseudo random arrangement with a reduced degree of anisotropy. Using fibers in the form of a braid can make the crack propagation toughness increase greatly due to extensive matrix deformation, crack branching, fiber bundle debonding, and pullout. The composition of the matrix can also have a significant effect on the toughness of a composite: The tougher the matrix, the tougher will be the composite. Thus, a thermoplastic matrix would be expected to provide a higher toughness than a thermoset matrix. In view of the importance of toughness enhancement in CMCs, we offer a summary of the rather extensive effort that has been expended in making tougher ceramics. Some of the approaches to enhancing the toughness of ceramics include the following:

- *Microcracking.* If microcracks form ahead of the main crack, they can cause crack branching, which in turn will distribute the strain energy over a large area. Such microcracking can thus decrease the stress intensity factor at the principal crack tip. Crack branching can also lead to enhanced toughness, because the stress required to drive a number of cracks is more than that required to drive a single crack.
- *Particle toughening.* The interaction between particles that do not undergo a phase transformation and a crack front can result in toughening due to crack bowing between particles, crack deflection at the particle, and crack bridging by ductile particles. Incremental increases in toughness can also result from an appropriate thermal mismatch between particles and the matrix. Taya *et al.* examined the effect of thermal residual stress in a TiB<sub>2</sub> particle reinforced silicon carbide matrix composite.<sup>7</sup> They attributed the increased crack growth resistance in the composite vis-a-vis the unreinforced SiC to the existence of compressive residual stress in the SiC matrix in the presence of TiB<sub>2</sub> particles.
- *Transformation toughening.* This involves a phase transformation of the second-phase particles at the crack tip with a shear and a dilatational component, thus reducing the tensile stress concentration at the tip. In particulate composites, such as alumina containing partially stabilized zirconia, the change in volume associated with the phase transformation in zirconia particles is exploited to obtain enhanced toughness. In a partially stabilized zirconia (e.g., ZrO<sub>2</sub> + Y<sub>2</sub>O<sub>3</sub>), the stress field at the crack tip can cause a stress-induced martensitic transformation in ZrO<sub>2</sub> from a tetragonal phase (*t*) to a monoclinic one (*m*); that is,



This transformation causes an expansion in volume (by approximately 4%) and a shear (0.16). The transformation in a particle at the crack tip results in stresses that tend to close the crack, and

---

<sup>7</sup> M. Taya, S. Hayashi, A. S. Kobayashi, and H. S. Yoon, *J. Am. Ceram. Soc.*, 73 (1990) 1382.

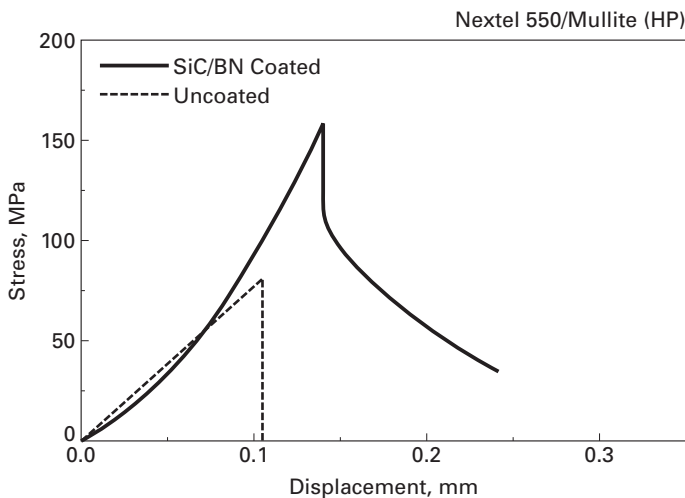


**Fig. 15.10** Stress vs. displacement curves for mullite fiber (Nextel 550)-mullite matrix in three-point bending. The uncoated one refers to the mullite-mullite composite with no interfacial coating, which shows a catastrophic failure. The composite with a double interfacial coating of SiC and BN shows a noncatastrophic failure. (Adapted from K. K. Chawla, Z. R. Xu, and J.-S. Ha, *J. Eur. Ceram. Soc.*, 16 (1996) 293.)

thus a portion of the energy that would go to fracture is spent in the stress-induced transformation. Also, the dilation in the transformed zone around a crack is opposed by the surrounding untransformed material, leading to compressive stresses that tend to close the crack. This results in increased toughness. The phenomenon of transformation toughening was discussed in Chapter 11. Transformation in the wake of a crack can result in a closure force that tends to resist the crack opening displacement. Crack deflection at zirconia particles can also contribute to toughness.

- **Fiber or whisker reinforcement.** Toughening by long fibers or whiskers can bring into play a series of energy-absorbing mechanisms in the fracture process of CMCs and thus allow these materials to tolerate damage.

It appears that the effectiveness of various toughening mechanisms for structural ceramics decreases in the following order: continuous fiber reinforcement; transformation toughening; whiskers, platelets, and particles; microcracking. Many researchers have shown that if we add continuous C or SiC fibers to a glass or ceramic matrix, we can obtain a stress-strain curve of the type shown in Figure 15.10. This curve has the following salient features:

- Damage-tolerant behavior in a composite consisting of two brittle components.
- Initial elastic behavior.
- At a stress  $\sigma_0$ , the brittle matrix cracks.
- The crack bypasses the fibers and leaves them bridging the crack.
- Under continued loading, we have regularly spaced cracks in the matrix, bridged by the fibers.
- Noncatastrophic failure occurs. Fiber pullout occurs after the peak load, followed by failure of the composite when the fibers fail.

The final failure of the composite does not occur catastrophically with the passage of a single crack; that is, *self-similar* crack propagation

does not occur. Thus, it is difficult to define an unambiguous fracture toughness value, such as a value for  $K_{Ic}$ .

Figure 15.10 shows the stress vs. displacement curves for mullite fiber (Nextel 550)-mullite matrix. The uncoated one refers to the mullite-mullite composite with no interfacial coating. This composite shows a catastrophic failure. The composite containing a double interfacial coating of SiC and BN shows a noncatastrophic behavior because of the energy expending mechanisms such as interfacial debonding, fiber pullout, etc. come into play during the fracture process. The interfacial coatings provide for easy crack deflection, interfacial debonding, and fiber pullout.

It has been amply demonstrated that incorporation of continuous fibers such as carbon, alumina, silicon carbide, and mullite fibers in brittle matrix materials (e.g., cement, glass, and glass-ceramic matrix) can result in toughening.<sup>8</sup> Not all of these failure mechanisms need operate simultaneously in a given fiber-matrix system, and often, in many composite systems, only one or two of the mechanisms will dominate the total fracture toughness. We discuss this topic further in Section 15.8.

## 15.6 | Load Transfer from Matrix to Fiber

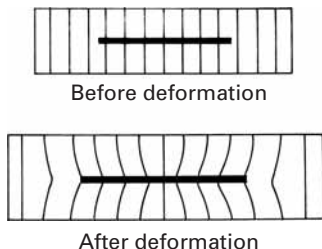


**Fig. 15.11** Perturbation of the matrix stress state due to the presence of fiber.

The matrix has the important function of transmitting the applied load to the fiber. Recall that we emphasized the idea that in fiber reinforced composites, the fibers are the principal load-carrying members. No direct loading of fibers from the ends is admitted. One imagines each fiber to be embedded inside a matrix continuum; the state of stress (and, consequently, that of strain) of the matrix is perturbed by the presence of the fiber (Figure 15.11). When the composite is loaded axially, the axial displacements in the fiber and in the matrix are locally different due to the different elastic moduli of the components. Macroscopically, the composite is deformed homogeneously.

### Example 15.7

The presence of voids in a composite is a serious, but commonly encountered, flaw. Suggest a simple method of determining the void content in a composite.

**Solution:** A simple method involves determining the density of the composite and getting an accurate estimate of values of the density of the reinforcement and matrix, most likely from the literature. We can write, for the volume of the voids in a composite,

$$V_v = V_c - (V_r + V_m)$$

<sup>8</sup> See, for example, K. K. Chawla, *Ceramic Matrix Composites*, 2nd ed. (Boston: Kluwer Academic, 2003).

where  $V$  is the volume and the subscripts,  $v$ ,  $c$ ,  $r$ , and  $m$  denote the void, composite, reinforcement, and matrix, respectively. Then, knowing the mass and density values, we can write

$$V_v = (M_c/\rho_c) - (V_m/\rho_r + M_m/\rho_m),$$

where  $M$  is the mass and  $\rho$  is the density, and the subscripts have the significance as before. The density of the composite can then be determined experimentally by Archimedes' method. The amount of reinforcement can be obtained by simply dissolving the matrix in a suitable chemical or by using a thermal method and weighing the residue.

Another simple method of determining the void content is by quantitative microstructural analysis.

The difference in the axial displacements in the fiber and the matrix implies that shear deformations are produced on planes parallel to the fiber axis and in the direction of this axis. These shear deformations are the means by which the applied load is distributed between the two components.

Let us consider the distribution of the longitudinal stress along the fiber-matrix interface. There are two distinct cases: (1) The matrix is elastic and the fiber is elastic, and (2) the matrix is plastic and the fiber is elastic.

### 15.6.1 Fiber and Matrix Elastic

We follow the treatment attributed to Cox.<sup>9</sup> Consider a fiber of length  $l$  embedded in a matrix subjected to a strain. Consider a point a distance  $x$  from one end of the fiber. It is assumed that (1) there exists a perfect contact between fiber and matrix (i.e., there is no sliding between them) and (2) Poisson's ratios of fiber and matrix are equal. Then the displacement of the point a distance  $x$  from one extremity of the fiber can be defined in the following manner;  $u$  is the displacement of point  $x$  in the presence of the fiber, and  $v$  is the displacement of the same point in the absence of the fiber.

The transfer of load from the matrix to the fiber may be written as

$$\frac{dP}{dx} = H(u - v), \quad (15.14a)$$

where  $P$  is the load on the fiber and  $H$  is a constant to be defined later. ( $H$  depends on the geometric arrangement of fibers, the matrix, and their moduli.)

Differentiating Equation 15.14, we obtain

$$\frac{d^2P}{dx^2} = H \left( \frac{du}{dx} - \frac{dv}{dx} \right). \quad (15.14b)$$

---

<sup>9</sup> H. L. Cox, *Brit. J. App. Phys.*, 3(1952) 72.

Now, it follows from the definition that

$$\begin{aligned}\frac{dv}{dx} &= \text{strain in matrix} = e, \\ \frac{du}{dx} &= \text{strain in fiber} = \frac{P}{A_f E_f},\end{aligned}\quad (15.15)$$

where  $A_f$  is the transverse-sectional area of the fiber. From Equations 15.14 and 15.15, we obtain

$$\frac{d^2P}{dx^2} = H \left( \frac{P}{A_f E_f} - e \right). \quad (15.16)$$

A solution of this differential equation is

$$P = E_f A_f e + S \sinh \beta x + T \cosh \beta x \quad (15.17)$$

where

$$\beta = \left( \frac{H}{A_f E_f} \right)^{1/2}. \quad (15.18)$$

The boundary conditions we need to evaluate the constants  $S$  and  $T$  are

$$P = 0 \text{ at } x = 0 \text{ and } x = \ell.$$

Putting in these values and using the “half-angle” trigonometric formulas, we get the equation

$$P = E_f A_f e \left\{ 1 - \frac{\cosh \beta[(\ell/2) - x]}{\cosh \beta(\ell/2)} \right\} \quad \text{for } 0 < x < \frac{\ell}{2}. \quad (15.19)$$

or

$$\sigma_f = \frac{P}{A_f} = E_f e \left\{ 1 - \frac{\cosh \beta[(\ell/2) - x]}{\cosh \beta(\ell/2)} \right\} \quad \text{for } 0 < x < \frac{\ell}{2}. \quad (15.20)$$

The maximum possible value of strain in the fiber is the imposed strain  $e$ , and thus, the maximum stress is  $eE_f$ . Hence, as long as we have a sufficiently long fiber, the stress in the fiber will increase from the two ends to a maximum value,  $\sigma_f^{\max} = E_f e$ . It can readily be shown that the average stress in the fiber will be

$$\bar{\sigma}_f = E_f e \left[ 1 - \frac{\tanh(\beta\ell/2)}{\beta\ell/2} \right]. \quad (15.21)$$

The variation in the shear stress  $\tau$  along the fiber-matrix interface is obtained by considering the equilibrium of forces acting over an element of fiber (with radius  $r_f$ ). Thus,

$$\frac{dP}{dx} dx = 2\pi r_f dx \tau. \quad (15.22)$$

$P$  is the tensile load on the fiber and is equal to  $\pi r_f^2 \sigma_f$ , so

$$\tau = \frac{1}{2\pi r_f} \frac{dP}{dx} = \frac{r_f}{2} \frac{d\sigma_f}{dx}, \quad (15.23)$$

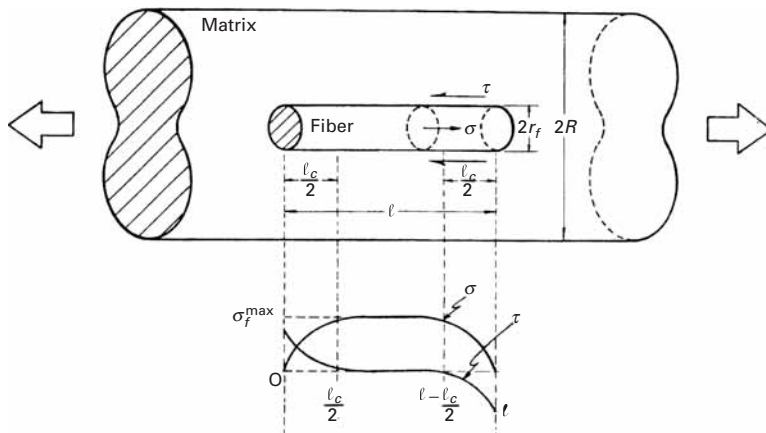


**Fig. 15.12** Load transfer to fiber. Variation in tensile stress  $\sigma$  in fiber and shear stress  $\tau$  along the interface with the fiber length  $\ell$ .

or

$$\tau = \frac{E_f r_f e \beta}{2} \frac{\sinh \beta[(\ell/2) - x]}{\cosh \beta(\ell/2)}. \quad (15.24)$$

The variation in  $\tau$  and  $\sigma_f$  with  $x$  is shown in Figure 15.12.

The shear stress  $\tau$  in Equation 15.24 will be the smaller of the following two shear stresses:

1. Strength of fiber-matrix interface in shear.
2. Shear yield stress of matrix.

Of these two shear stresses, the one that has a smaller value will control the load transfer phenomenon and should be used in Equation 15.24.

The constant  $H$  remains to be determined. An approximate value of  $H$  is derived next for a particular geometry. Let the fiber length  $\ell$  be much greater than the fiber radius  $r_f$ , and let  $2R$  be the average fiber spacing (center to center). Let  $\tau(r)$  be the shear stress in the direction of the fiber axis at a distance  $r$  from the axis. Then, at the fiber surface ( $r = r_f$ ),

$$\frac{dP}{dx} = -2\pi r_f \tau(r_f) = H(u - v).$$

Thus,

$$H = -\frac{2\pi r_f \tau(r_f)}{u - v}. \quad (15.25)$$

Let  $w$  be the real displacement in the matrix. Then at the fiber-matrix interface, without sliding,  $w = u$ . At a distance  $R$  from the center of a fiber,  $w = v$ . Considering equilibrium of forces on the matrix between  $r_f$  and  $R$ , we get

$$2\pi r \tau(r) = \text{constant} = 2\pi r_f \tau(r_f),$$

or

$$\tau(r) = \frac{\tau(r_f) r_f}{r}. \quad (15.26)$$

The shear strain  $\gamma$  in the matrix is given by  $\tau(r) = G_m r$ , where  $G_m$  is the matrix shear modulus. Then

$$\gamma = \frac{dw}{dr} = \frac{\tau(r)}{G_m} = \frac{\tau(r_f)r_f}{G_m r}. \quad (15.27)$$

Integrating from  $r_f$  to  $R$ , we get

$$\Delta w = \frac{\tau(r_f)r_f}{G_m} \ln\left(\frac{R}{r_f}\right). \quad (15.28)$$

But, by definition,

$$\Delta w = v - u = -(u - v). \quad (15.29)$$

Then

$$\frac{\tau(r_f)r_f}{u - v} = -\frac{G_m}{\ln(R/r_f)}. \quad (15.30)$$

From Equations 15.25 and 15.30, we get

$$H = \frac{2\pi G_m}{\ln(R/r_f)}, \quad (15.31)$$

and from Equation 15.18, we obtain an expression for the load transfer parameter:

$$\beta = \left( \frac{H}{E_f A_f} \right)^{1/2} = \left[ \frac{2\pi G_m}{E_f A_f \ln(R/r_f)} \right]^{1/2}. \quad (15.32)$$

Note that the greater the value of  $G_m/E_f$ , the more rapid is the increase in fiber stress from the two ends.

The foregoing analysis is an approximate one – particularly with regard to the evaluation of the load transfer parameter  $\beta$ . More exact analysis give similar results and differ only in the value of  $\beta$ . In all the analyses, however,  $\beta$  is proportional to  $\sqrt{G_m/E_f}$ , and the differences occur only in the term involving the fiber volume fraction,  $\ln(R/r_f)$ .

### 15.6.2 Fiber Elastic and Matrix Plastic

It should be clear from the preceding discussion that, in order to load high-strength fibers to their maximum strength in the matrix, the shear strength must correspondingly be large. A metallic matrix will flow plastically in response to the high shear stress developed. Should the fiber-matrix interface be weaker, it will fail first. Plastic deformation of a matrix implies that the shear stress at the fiber surface,  $\tau(r_f)$ , will never go above  $\tau_y$ , the matrix shear yield strength (ignoring any work-hardening effects). In such a case, we get, from an equilibrium of forces, the equation

$$\sigma_f \pi \frac{d^2}{4} = \tau_y \pi d \frac{\ell}{2},$$

or

$$\frac{\ell}{d} = \frac{\sigma_f}{2\tau_y}.$$

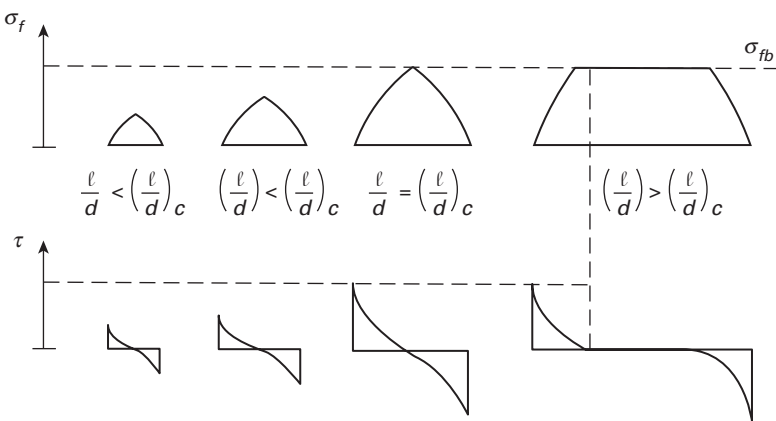


**Fig. 15.13** Variation in the fiber load transfer length as a function of the aspect ratio  $\ell/d$ .

We consider  $\ell/2$ , and not  $\ell$ , because the fiber is being loaded from both ends. If the fiber is sufficiently long, it should be possible to load it to its breaking stress,  $\sigma_{fb}$ , by means of load transfer through the matrix flowing plastically around it. Let  $(\ell/d)_c$  be the minimum fiber length-to-diameter ratio necessary to accomplish this. We call this ratio  $\ell/d$  the aspect ratio of the fiber and  $(\ell/d)_c$  the critical aspect ratio necessary to attain the breaking stress of the fiber,  $\sigma_{fb}$ . Then we can write

$$\left(\frac{\ell}{d}\right)_c = \frac{\sigma_{fb}}{2\tau_y}. \quad (15.33)$$

Or we can think of a critical fiber length  $\ell_c$  for a given fiber diameter  $d$ :

$$\frac{\ell_c}{d} = \frac{\sigma_{fb}}{2\tau_y}. \quad (15.34)$$

Thus, the fiber length  $\ell$  must be equal or greater than  $\ell_c$  for the fiber to be loaded to its maximum stress. If  $\ell < \ell_c$ , the matrix will flow plastically around the fiber and will load it to a stress in its central portion given by

$$\sigma_f = 2\tau_y \frac{\ell}{d} < \sigma_{fb}. \quad (15.35)$$

This is shown in Figure 15.13. An examination of the figure shows that, even for  $\ell/d > (\ell/d)_c$ , the average stress in the fiber will be less than the maximum stress to which it is loaded in its central region. In fact, we can write, for the average fiber stress,

$$\begin{aligned} \bar{\sigma}_f &= \frac{1}{\ell} \int_0^\ell \sigma_f dx \\ &= \frac{1}{\ell} [\sigma_f(\ell - \ell_c) + \phi \sigma_f \ell_c] \\ &= \frac{1}{\ell} [\sigma_f \ell - \ell_c (\sigma_f - \phi \sigma_f)], \end{aligned}$$

or

$$\bar{\sigma}_f = \sigma_f \left( 1 - \frac{1 - \phi}{\ell/\ell_c} \right), \quad (15.36)$$

where  $\phi\sigma_f$  is the average stress in the fiber over a portion  $\ell_c/2$  of its length at both the ends. We can thus regard  $\phi$  as a load transfer function where value will be precisely 0.5 for an ideally plastic matrix (i.e., the increase in stress in the fiber over the portion  $\ell_c/2$  will be linear).

### Example 15.8

- (a) Consider an alumina fiber reinforced polymer matrix composite. If the strength of the fiber is 1 GPa and the fiber-matrix interface has a shear strength of 10 MPa, compute the critical fiber length  $\ell_c$ . Take the diameter of the alumina fiber to be 10  $\mu\text{m}$ .
- (b) The composite in Part a is made of short (1-cm-long), but aligned, alumina fibers. Assuming that each fiber is loaded from both ends in a linear manner, compute the average stress in the fiber in this composite.

*Solution:* (a) Critical length:

$$\begin{aligned} \ell_c/d &= \sigma_{fb}/2\tau_i = 1,000/(2 \times 10) = 50, \\ \ell_c &= 50 \times 10 \mu\text{m} = 0.5\text{mm}. \end{aligned}$$

(b) Average fiber stress:

From the solution to Part a, we have

$$\begin{aligned} \ell/\ell_c &= 10/0.5 = 20, \\ \bar{\sigma}_f &= \sigma_f [1 - (1 - \phi)/(\ell/\ell_c)] \\ &= 1,000[1 - (1 - 0.5)/20] = 1,000(1 - 0.025) = 975 \text{ MPa}. \end{aligned}$$

## 15.7 | Fracture in Composites

Fracture is a complex subject, even in monolithic materials. (See Chapters 7–9.) Undoubtedly, it is even more complex in composite materials. A great variety of deformation modes can lead to failure in a composite. The operative failure mode will depend, among other things, on loading conditions and the particular composite system. The microstructure has a very important role in the mechanics of rupture of a composite. For example, the fiber diameter, its volume fraction and alignment, damage due to thermal stresses that may develop during fabrication or service – all these factors can contribute to, and directly influence, crack initiation and propagation. A multiplicity of failure modes can exist in a composite under different loading conditions.

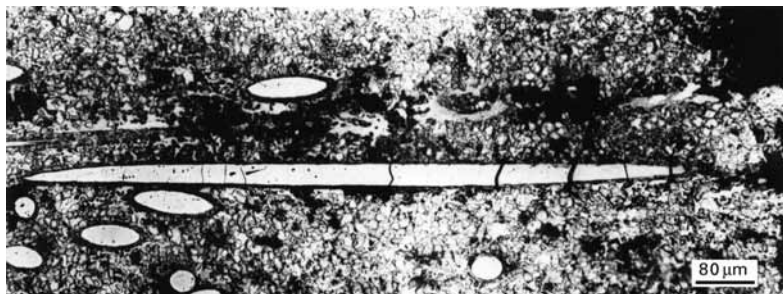


**Fig. 15.14** Optical micrograph showing multiple fracture of tungsten fibers in an Fe–Cu matrix.

### 15.7.1 Single and Multiple Fracture

In general, the two components of a composite will have different values of strain to fracture. When the component that has the smaller breaking strain fractures, the load carried by this component is thrown on to the other one. If the latter component, which has a higher strain to fracture, can bear the additional load, the composite will show multiple fracture of the brittle component (the one with smaller fracture strain); eventually, a particular transverse section of composite becomes so weak, that the composite is unable to carry the load any further, and it fails.

Let us consider the case of a fiber reinforced composite in which the fiber fracture strain is less than that of the matrix. Then the composite will show a single fracture when

$$\sigma_{fu} V_f > \sigma_{mu} V_m - \sigma'_m V_m, \quad (15.37)$$

where  $\sigma'_m$  is the matrix stress corresponding to the fiber fracture strain and  $\sigma_{fu}$  and  $\sigma_{mu}$  are the ultimate tensile stresses of the fiber and matrix, respectively. This equation says that when the fibers break, the matrix will not be in a condition to support the additional load, a condition that is commonly encountered in composites of high  $V_f$ , brittle fibers, and a ductile matrix. All the fibers break in more or less one plane, and the composite fails in that plane.

If, on the other hand, we have a system that satisfies the condition

$$\sigma_{fu} V_f < \sigma_{mu} V_m - \sigma'_m V_m, \quad (15.38)$$

the fibers will be broken into small segments until the matrix fracture strain is reached. An example of this type of breakage is shown in Figure 15.14, an optical micrograph of an Fe–Cu matrix containing a small volume fraction of W fibers.

In case the fibers have a fracture strain greater than that of the matrix (an epoxy resin reinforced with metallic wires), we would have a multiplicity of fractures in the matrix, and the condition for this may be written as

$$\sigma_{fu} V_f > \sigma_{mu} V_m - \sigma'_f V_f, \quad (15.39)$$

where  $\sigma'_f$  is now the fiber stress corresponding to the matrix fracture strain.

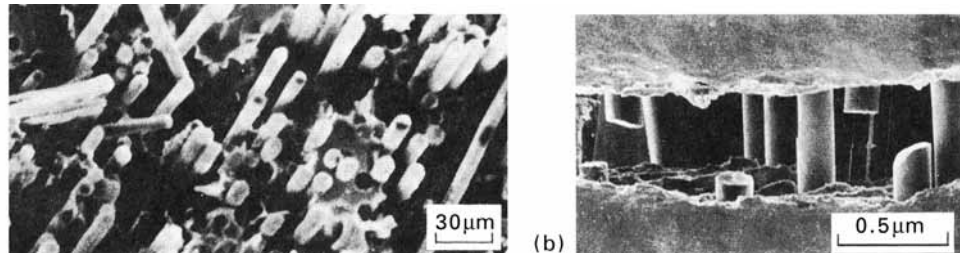


**Fig. 15.15** Scanning electron micrographs of fracture in composites, showing the fiber pullout phenomenon. (a) Carbon fiber/polyester. (b) Boron fiber/aluminum 6061.

### 15.7.2 Failure Modes in Composites

Two failure modes are commonly encountered in composites:

1. The fibers break in one plane, and, the soft matrix being unable to carry the load, the composite failure will occur in the plane of fiber fracture. This mode is more likely to be observed in composites that contain relatively high fiber volume fractions and fibers that are strong and brittle. The latter condition implies that the fibers do not show a distribution of strength with a large variance, but show a strength behavior that can be characterized by the Dirac delta function.
2. When the adhesion between fibers and matrix is not sufficiently strong, the fibers may be pulled out of the matrix before failure of the composite. This fiber pullout results in the fiber failure surface being nonplanar.

More commonly, a mixture of these two modes is found: fiber fracture together with fiber pullout. Fibers invariably have defects distributed along their lengths and thus can break in regions above or below the crack tip. This leads to separation between the fiber and the matrix and, consequently, to fiber pullout with the crack opening up. Examples are shown in Figure 15.15.

One of the attractive characteristics of composites is the possibility of obtaining an improved fracture toughness behavior together with high strength. Fracture toughness can be defined loosely as resistance to crack propagation. In a fibrous composite containing a crack transverse to the fibers, the crack propagation resistance can be increased by doing additional work by means of any or all of the following:

- Plastic deformation of the matrix.
- The presence of weak interfaces, fiber-matrix separation, and deflection of the crack.
- Fiber pullout.

It would appear that debonding of the fiber-matrix interface is a prerequisite for phenomena such as crack deflection, crack bridging by fibers, and fiber pullout. It is of interest to develop some criteria for interfacial debonding and crack deflection. Crack deflection at an interface between materials of identical elastic constants (i.e., the same material joined at an interface) has been analyzed on the basis of the strength of the interface. The deflection of the crack along

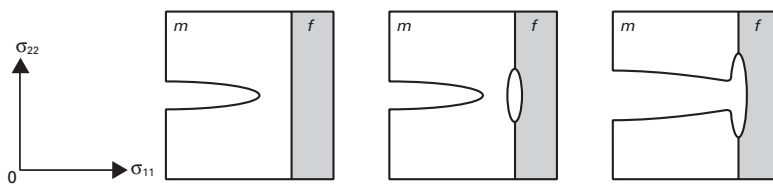


**Fig. 15.16** Fracture of weak interface in front of crack tip due to transverse tensile stress;  $m$  and  $f$  indicate the matrix and fiber, respectively. (After J. Cook and J. E. Gordon, Proc. Roy. Soc. (London), A 228 (1964) 508.)

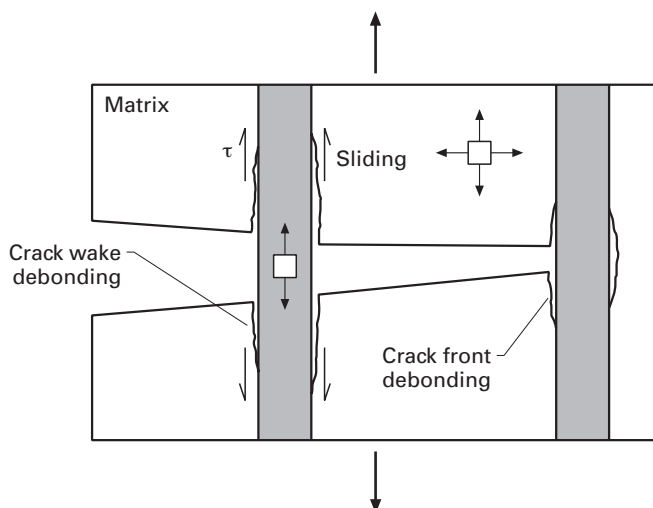


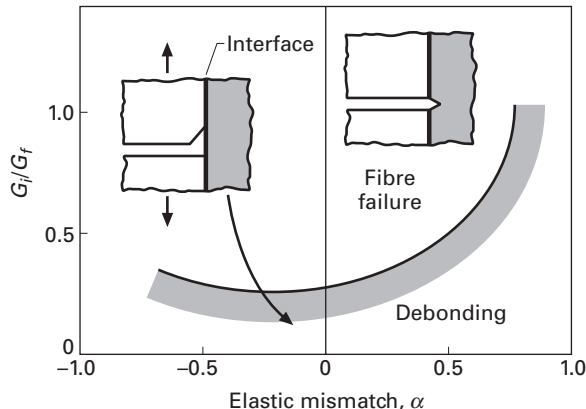
**Fig. 15.17** Crack front and crack wake debonding in a fiber reinforced composite.

an interface or the separation of the fiber-matrix interface is an interesting mechanism of augmenting the resistance to crack propagation in composites. Cook and Gordon analyzed the stress distribution in front of a crack tip and concluded that the maximum transverse tensile stress  $\sigma_{11}$  is about one-fifth of the maximum longitudinal tensile stress  $\sigma_{22}$ . They suggested, therefore, that when the ratio  $\sigma_{22}/\sigma_{11}$  is greater than 5, the fiber-matrix interface in front of the crack tip will fail under the influence of the transverse tensile stress, and the crack would be deflected  $90^\circ$  from its original direction. That way, the fiber-matrix interface would act as a crack arrester. This is shown schematically in Figure 15.16. The improvement in fracture toughness due to the presence of weak interfaces has been confirmed qualitatively.

Another treatment of this subject is based on a consideration of the fracture energy of the constituents.<sup>10</sup> Two materials that meet at an interface are more than likely to have *different* elastic constants. This mismatch in moduli causes shearing of the crack surfaces, which leads to a mixed-mode stress state in the vicinity of an interface crack tip involving both the tensile and shear components. This, in turn, results in a mixed-mode fracture, which can occur at the crack tip or in the wake of the crack. Figure 15.17 shows crack front and

<sup>10</sup> See M. Y. He and J. W. Hutchinson, J. App. Mech., 56 (1989) 270; A. G. Evans and D. B. Marshall, Acta Met., 37 (1989) 2567.

**Fig. 15.18** The ratio of the interface fracture toughness to that of fiber,  $G_i/G_f$ , vs. the elastic mismatch  $\alpha$ . Interfacial debonding occurs under the curve, while for conditions above the curve, the crack propagates through the interface.



crack wake debonding in a fiber reinforced composite. Because of the mixed-mode fracture, a single-parameter description by the critical stress intensity factor  $K_{lc}$  will not do; instead, one needs a more complex formalism of fracture mechanics to describe the situation. In this case, the parameter  $K$  becomes scale sensitive, but the critical strain energy release rate  $G_{lc}$  is not a scale-sensitive parameter.  $G$  is a function of the phase angle  $\psi$ , which, in turn, is a function of the normal and shear loading. For the opening mode, or mode I,  $\psi = 0^\circ$ , while for mode II,  $\psi = 90^\circ$ . One needs to specify both  $G$  and  $\psi$  to analyze the debonding at the interface. Without going into the details, we present here the final results of such an analysis, in the form of a plot of  $G_i/G_f$  vs.  $\alpha$ , where  $G_i$  is the mixed-mode interfacial fracture energy of the interface,  $G_f$  is the mode-I fracture energy of the fiber, and  $\alpha$  is a measure of the elastic mismatch between the matrix and the reinforcement, defined as

$$\alpha = \left( \frac{\bar{E}_1 - \bar{E}_2}{\bar{E}_1 + \bar{E}_2} \right), \quad (15.40)$$

where

$$\bar{E} = \frac{E}{1 - v^2}. \quad (15.41)$$

The plot in Figure 15.18 shows the conditions under which the crack will deflect along the interface or propagate through the interface into the fiber. For all values of  $G_i/G_f$  below the shaded boundary, interface debonding is predicted. For the special case of zero elastic mismatch (i.e., for  $\alpha = 0$ ), the fiber-matrix interface will debond for  $G_i/G_f$  less than about 0.25. Conversely, for  $G_i/G_f$  greater than 0.25, the crack will propagate across the fiber. In general, for elastic mismatch, with  $\alpha$  greater than zero, the minimum interfacial toughness required for interface debonding increases (i.e., high-modulus fibers tend to favor debonding). One shortcoming of this analysis is that it treats the fiber and matrix as isotropic materials; this is not always true, especially for carbon fiber.

Gupta *et al.*<sup>11</sup> derived strength and energy criteria for crack deflection at a fiber-matrix interface for several composite systems, taking due account of the anisotropic nature of the fiber. They used an experimental technique – spallation by means of a laser Doppler displacement interferometer – to measure the tensile strength of a planar interface. Through this technique, these researchers have tabulated the required values of the interface strength and fracture toughness for delamination in a number of ceramic, metal, intermetallic, and polymer matrix composites.

## 15.8 Some Fundamental Characteristics of Composites

Composite materials are not like any other common type of material. They are inherently different from monolithic materials, and consequently, these basic differences must be taken into account when one designs or fabricates any article from composite materials. In what follows, we give a brief description of some of the fundamental characteristics of composites.

### 15.8.1 Heterogeneity

Composite materials are inherently heterogeneous, consisting as they do of two components of different elastic moduli, different mechanical behavior, different expansion coefficients, and so on. For this reason, the analysis of, and the design procedures for, composite materials are quite intricate and complex, compared to those for ordinary materials. The structural properties of composites are functions of:

1. The properties of their components.
2. The geometric arrangement of their components.
3. The interface between the components.

Given two components, we can obtain a great variety of properties by manipulating items 2 and 3.

### 15.8.2 Anisotropy

In general, monolithic materials are reasonably isotropic; that is, their properties do not show any marked preference for any particular direction. The unidirectional composites are anisotropic due to their very nature. Once again, the analysis and design of composites should take into account this strong directionality of properties – properties that cannot be specified without any reference to some direction. Figure 15.19 shows, schematically, the elastic moduli of a monolithic material and a composite as a function of fiber orientation  $\theta$ . (See Section 15.5.4.) A monolithic material (e.g., Al) is an isotropic

<sup>11</sup> V. Gupta, J. Yuan, and D. Martinez, *J. Am. Ceram. Soc.*, 76 (1993) 305.

**Fig. 15.19** Schematic of variation in elastic moduli of a fiber composite and a monolithic material with the angle of reinforcement. (a)  $E_a$  is the axial Young's modulus (b)  $\nu_{at}$  is the principal Poisson's ratio, and (c)  $G_a$  is the axial shear modulus.

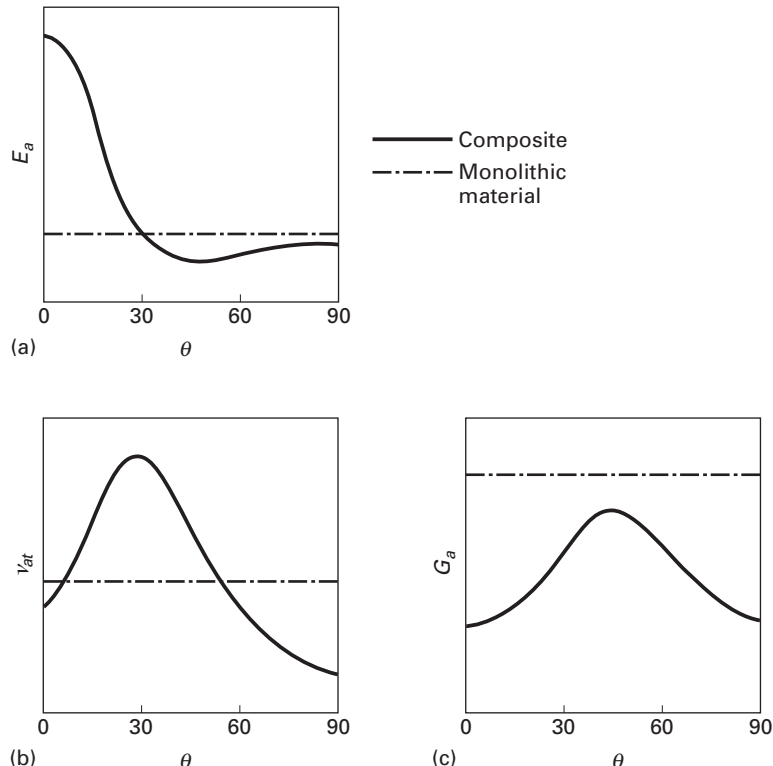
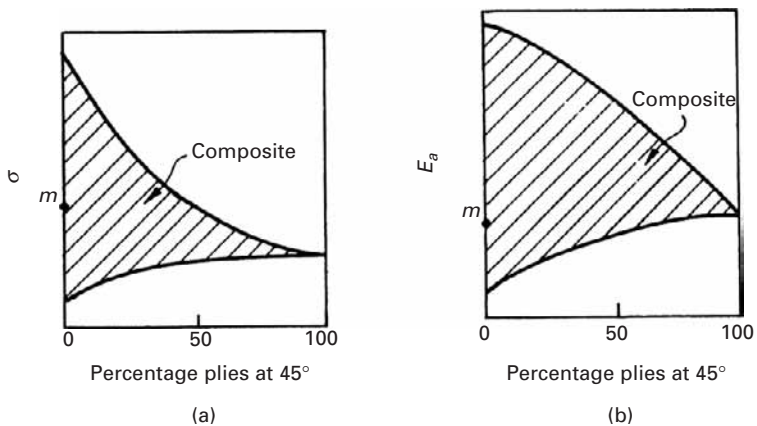


**Fig. 15.20** Schematic of a performance chart of a composite.



material; therefore, its moduli do not vary with the angle of testing, and the graphs are horizontal.

For an ordinary material (say, aluminum), the designer only needs to open a manual and find one unique value of strength or one unique value of the modulus of the material. But for fiber reinforced composite materials, the designer has to consult performance charts representing the strength and the modulus of the various composite systems. (See Figure 15.20.)

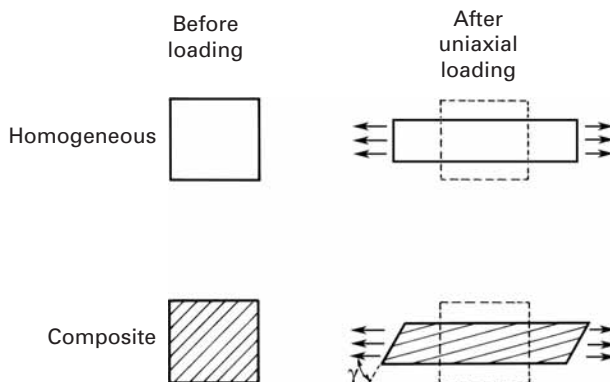


**Fig. 15.21** Shear coupling in a fiber composite

Ordinary materials, such as aluminum or steel, can be represented by a fixed point, indicated by  $m$  in Figure 15.20. For a composite material, however, there does not exist a unique combination of these properties. Instead, the composite contains a system of properties and must be represented by an area instead of a point. We call these graphs “carpet plots.” These plots give modulus or strength in terms of proportion of plies at different angles. The highest point on the graph represents the longitudinal properties of the composite, while the lowest point represents transverse properties. The important point to make is that, depending on the stacking of plies in a composite and the appropriate quantity of fiber, the characteristics of the composite can be varied. In other words, composites can be tailor-made, in accord with the final objective.

### 15.8.3 Shear Coupling

The properties of a composite are very sensitive functions of the fiber orientation. They display what is called *shear coupling*: shear strains produced by axial stress and axial strains produced by shear stress. (See Figure 15.21.) In response to a uniaxially applied load, an isotropic material produces only axial and transverse strains. In fiber reinforced composites, however, a shear strain  $\gamma$  is also produced in response to an axial load, because the fibers tend to align themselves in the direction of the applied load. This shear distortion can be eliminated if one makes a *cross-ply* composite – a composite containing an equal number of parallel fibers, alternately aligned at a given angle and at a complementary angle with respect to the loading axis (Figure 15.22). That is, we have the various layers in a composite arranged at  $\pm \theta$  degrees to the loading axis, and thus, the shear distortion due to one layer is compensated for by an equal and opposite shear distortion due to the other. However, this balance occurs only in two dimensions, whereas the real-life composites are three-dimensional materials. This leads to an “edge effect” in which the individual layers deform differently under tension and in the neighborhood of the free edges, giving rise to out-of-plane shear and bending. The stacking sequence of the various layers in the composite is important. For example, in a laminate composite consisting of fibers

**Fig. 15.22** Unidirectional and cross-plyed composites.

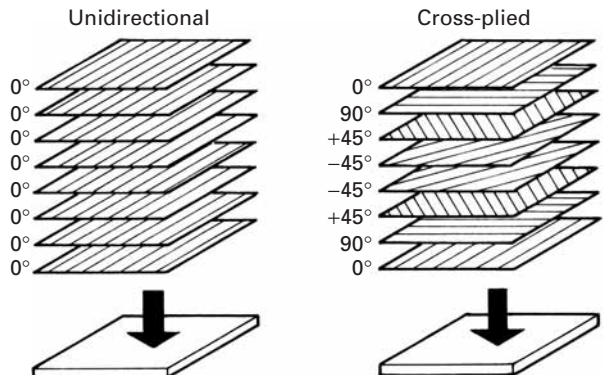
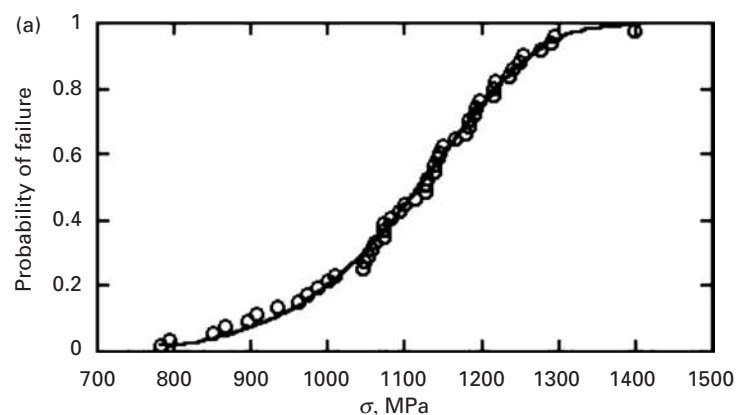


**Fig. 15.23** Probability of failure versus strength (Weibull) plot of tensile strength of a carbon fiber-epoxy composite. (Courtesy of B. Ataderro and V. Karbhari.)



at  $+90^\circ$ ,  $+45^\circ$ ,  $-45^\circ$ ,  $+45^\circ$ , and  $+90^\circ$ , subjected to an in-plane tensile stress, there occur compressive stresses in the direction of thickness, in the vicinity of the edges. Should the same composite have the sequence  $+45^\circ$ ,  $-45^\circ$ ,  $+90^\circ$ ,  $+90^\circ$ ,  $-45^\circ$ ,  $+45^\circ$ , however, these stresses in the direction of thickness are of a tensile nature and thus tend to delaminate the composite, clearly an undesirable effect.

#### 15.8.4 Statistical Variation in Strength

The strength of a composite can show significant variation from specimen to specimen. Thus, care has to be exercised when tests are conducted and strength is quoted. As an example, Figure 15.23 shows the results of 50 tensile tests carried out on a carbon fiber-epoxy matrix composite. The strength varied from 800 to 1400 MPa, a considerable spread. The Weibull modulus is 9.9, and  $\sigma_m$  is 1,160 MPa. The Weibull modulus is on the same order as the one for ceramics. The experimental results follow a Weibull distribution, which is represented by the continuous line in Figure 15.23.

## 15.9 Functionally Graded Materials

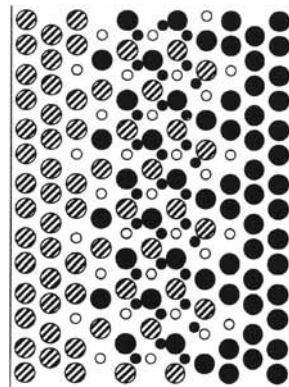
There is a good deal of interest in making materials that are graded in some respect. The gradient may be of the chemical composition, density, or coefficient of thermal expansion of the material, or it may involve microstructural features – for example, a particular arrangement of second-phase particles or fibers in a matrix. Such materials are called *functionally graded materials*, and the acronym FGM is commonly applied to them in the literature. Strictly speaking, though, the term “graded material” ought to be enough to convey the meaning; that is, the word “functionally” is redundant. The idea, however, is a very general one, viz., instead of having a step function, say, in composition at an interface, we should have a gradually varying composition from component A to component B. Figure 15.24 shows schematically the microstructure of a functionally graded material. Such a graded interface can be very useful in ameliorating high mechanical and thermal stresses. The concept of a functionally graded material is applicable to any material, polymer, metal, or ceramic.<sup>12</sup>

## 15.10 Applications

It is convenient to divide the applications of all composites into aerospace and nonaerospace categories. In the category of aerospace applications, low density coupled with other desirable features, such as a tailored thermal expansion and conductivity, and high stiffness and strength, are the main drivers. Performance, rather than cost, is an important item as well. We next give a brief description of various applications of composites.

### 15.10.1 Aerospace Applications

Reduction in the weight of a component is as major driving force for any application in the aerospace field. The Boeing 757 and 767 jets were the first large commercial aircraft to make widespread use of structural components made of PMCs. About 95% of the visible interior parts in Boeing 757 and 767 cabins are made from nonconventional materials. Most of the fuselage of a Boeing 787 is made of carbon/epoxy while a considerable part of Airbus 380 uses GLARE composites (see Sec. 15.11). One of the main reasons for the decision to use such materials was the steadily dropping price of carbon fibers. Similarly, there has been an increasing use of composites in aircraft, including helicopters, used by defense services. Weight and cost savings are the driving forces for these applications. Consider, for example, the Sikorsky H-69 helicopter. For this helicopter, manufacturing the conventional fuselage, of metal construction, is very labor intensive. In comparison, the composite fuselage, of carbon, aramid, and



● Ceramic                    ● Metal  
○ Micropore                 ● Additive

**Fig. 15.24** Schematic of a functionally graded material between a ceramic on the left-hand side and a metal on the right-hand side. Also shown are micropores and additives.

<sup>12</sup> See B. Ilschner, *J. Mech. Phys. Solids*, 44 (1996) 647; S. Suresh and A. Mortensen, *Intl. Mater. Rev.*, 42 (1997) 85.

glass fiber-epoxy, has much fewer parts, assemblies, and fasteners. PMCs are also lighter and cheaper to use than metals in the manufacture of fuselages. The use of lighter composites in aircraft results in energy savings: For a given aerodynamic configuration of an aircraft, there is a direct correlation between the weight of the airplane and fuel consumption. Weight savings resulting from the use of new, lighter materials lead to great increases in fuel economy.

In examining the applications of composites in space, it should be recognized that environment of space is not benign. Among the hazardous items that may be encountered in space are orbital debris, meteorites, and atomic oxygen. It appears that metal matrix composites can withstand the space environment better than polymer matrix composites. In the Hubble telescope, pitch-based continuous carbon fiber reinforced aluminum was used for waveguide booms because this composite is very light and has a high elastic modulus and a low coefficient of thermal expansion.

Other aerospace applications of MMCs involve the replacement of light, but toxic, beryllium by various composites. For example, in the U.S. Trident missile, beryllium has been replaced by an  $\text{SiC}_p/\text{Al}$  composite, which is also used in aircraft electronic equipment racks.

CMCs can lead to potential improvements in aircraft, helicopters, missiles, reentry modules of spacecraft, and other aerospace vehicles. Projected skin temperatures in future hypersonic aircraft are over 1600 °C. Other parts, such as radomes, nose tips, leading edges, and control surfaces, will have only slightly lower temperatures. Currently, one uses sacrificial, non-load-bearing thermal protection CMC materials on load-bearing components made of conventional materials. With the use of CMCs, one can have load-bearing components that are reusable at operating temperatures.

### 15.10.2 Nonaerospace Applications

Polymer composites based on aramid, carbon, and glass fibers are routinely used in civil construction and in marine and sporting goods. Applications in the sporting goods industry have burgeoned, all the way from tennis rackets to fishing poles to a whole variety of equipment used in downhill as well as cross-country skis, boots, poles, gloves, etc. The main advantages that the use of composites brings to the sporting goods industry are safety, less weight, and higher strength than conventional materials. Ski poles made of polymer composites are lighter and stiffer than aluminum poles. Frequently, hybrid composites are used, such as carbon fibers laid over a small sleeve of aramid.

Composites are also used in rifle stocks for biathlons because both weight and strength are important in the rifles, which may have to be carried over distances of up to 20 km.

The automobile industry is a major user of PMCs, mainly because of the cost advantage over other types of composites. One of the important applications of MMCs in the automotive area is in the diesel piston crown. This application involves the incorporation of

short fibers of alumina or alumina plus silica into the crown. The conventional diesel engine piston has an Al-Si casting alloy with a crown made of nickel cast iron. The replacement of the nickel cast iron by an aluminum matrix composite resulted in a lighter, more abrasion-resistant, and cheaper product. Yet another application of MMCs is in the automobile engine of the Honda *Prelude*. In the conventional automobile, the major part of the engine, and also the heaviest part, is the cast iron engine block. In the general quest for high performance combined with a light vehicle, the cast iron engine block has been replaced by light aluminum alloy in some automobiles, resulting in a weight reduction of 15–35 kg. But even in these aluminum engines, the liners are generally made of cast iron. This is because cast iron has superior sliding characteristics (pistons sliding in the cylindrical bores) than aluminum alloys do. The Honda Motor Company has developed an aluminum engine (used in the *Prelude*), with cylinder liners made of alumina- and carbon-fiber reinforced aluminum. The most important characteristic for this application is resistance against sliding. Seizure occurs when the coefficient of friction increases very rapidly. According to the researchers at Honda, a hybrid composite consisting of alumina and carbon fibers gave the best results. This was attributed to the self-lubricating properties of carbon fiber and the sliding resistance of alumina fiber. In composites containing only alumina fibers, when a scratch appeared, it easily worsened. In the case of hybrid alumina and carbon fibers in Al, the scratch did not grow. Particulate metal matrix composites – especially light ones such as aluminum and magnesium – also find applications in automotive and sporting goods. In this regard, it is important to remember that the price per kilogram becomes the driving force for the application.

An interesting application, led by 3M Co., involving continuous alumina fibers in aluminium matrix is in the form of a composite conductor, which is used in power-line cables. These new cables are capable of transmitting two or three times more electricity than the conventional power-line cables of the same diameter without additional weight or the need for more towers. The objective is to increase the amperage capacity of the existing power-line structures with no additional easements. Congestion is a key issue facing the power transmission grid in the USA. These new cables have a core that consists of composite (continuous alumina fiber in an aluminium matrix). The core is wrapped by aluminium-zirconium alloy conductor wires. Figure 15.25 shows the cross section of one such cable. This 3M conductor cable, also known as aluminum composite conductor reinforced (ACCR) cable, is light weight; consequently it sags less than the conventional power lines. It can be used to span difficult terrains such as wide rivers, lakes, or canyons. Because of their light weight, such cables are also able to withstand winter snow storms that cause accumulation of ice on the power lines, resulting in their snapping.

Copper-based composites having Nb, Ta, or Cr as the second phase in a discontinuous form are of interest for certain applications

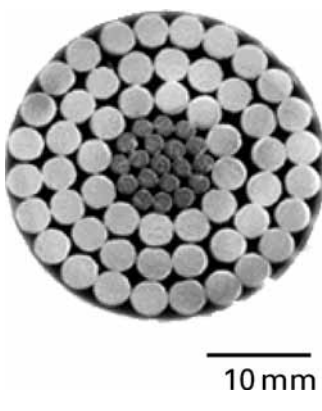


**Fig. 15.25** Cross section of an aluminium composite conductor reinforced (ACCR) cable. The central wires consist of continuous alumina fibers in an aluminium matrix composite while the outer wires are made of Al-Zr alloy. (Courtesy of 3M Co.)

requiring high thermal conductivity and high strength. Sometimes we refer to these composites as Cu-X composites, where X, which is insoluble in copper at room temperature, forms the second phase. One specific example is a high heat-flux application in the thrust chambers of rocket engines. Cu-X systems are very useful for processing such composites. At room temperature, the second phase appears in a dendritic form, which can be converted into a filamentary or ribbon form by mechanical working. Note that the ribbon morphology is thermodynamically unstable at high temperatures, because the ribbons tend to form spheroids with time, as a function of temperature.

Conventional commercial superconductors are referred to as *niobium-based superconductors* because Nb-Ti and Nb<sub>3</sub>Sn are superconducting materials. These conventional superconductors are nothing but copper matrix composites.

An area in which CMCs have found application is that of cutting tools. Silicon carbide whisker reinforced alumina (SiC<sub>w</sub>/Al<sub>2</sub>O<sub>3</sub>) is used as a cutting-tool insert for high-speed cutting of superalloys. For example, in the cutting of Inconel 718, SiC<sub>w</sub>/Al<sub>2</sub>O<sub>3</sub> composite tools perform three times better than conventional ceramic tools and eight times better than cemented carbides.

Carbon–carbon composites are used as implants, as well as for internal fixation of bone fractures, because of their excellent biocompatibility. They are also used for making molds for hot pressing. Carbon–carbon molds can withstand higher pressures and offer a longer service life than does polycrystalline graphite. However, their high cost limits them to aerospace and other specialty applications. The low oxidation resistance of carbon–carbon composites is a serious limitation, but is not a problem for short-term applications such as shields, rocket nozzles, and reentry vehicles.

---

## 15.11 | Laminated Composites

The abalone shell is a natural laminar or laminated composite based on CaCO<sub>3</sub>. It possesses unique strength and toughness properties. In Chapter 1 we showed a picture of the structure (Figure 1.30). The flexural strength of the abalone shell is approximately 80 MPa; in comparison, the flexural strength of monolithic CaCO<sub>3</sub> is close to 10 MPa. The fracture toughness of abalone is in the 4–10 MPa m<sup>1/2</sup> range, whereas that of CaCO<sub>3</sub> is approximately 1 MPa m<sup>1/2</sup>. Figure 15.26 shows the dramatic improvement in mechanical strength made possible by the organization of calcium carbonate into layers with thickness of approximately 0.5 μm. The same figure shows the improvement in properties obtained when Al<sub>2</sub>O<sub>3</sub> is arranged in layers with Al (Al<sub>2</sub>O<sub>3</sub>/Al) and when B<sub>4</sub>C is used to form a laminate with Al (B<sub>4</sub>C/Al).

Figure 15.27(a) shows the construction of tiles forming the nacreous portion of abalone. This structure resembles a “brick and

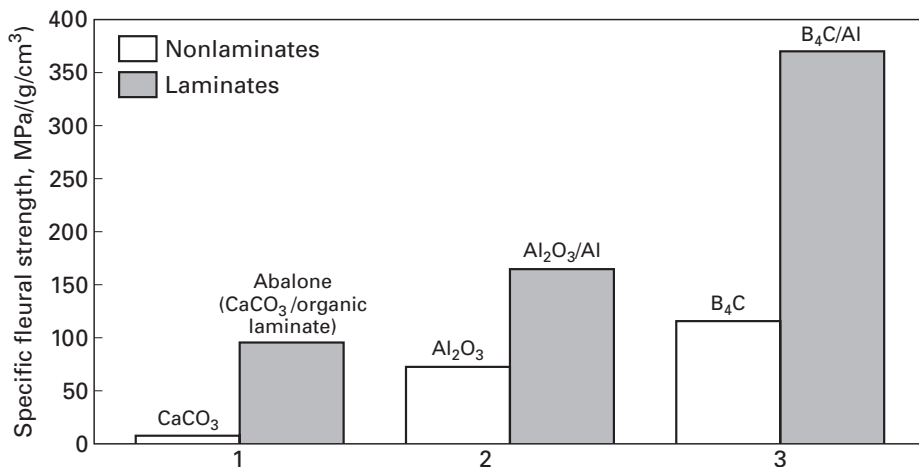
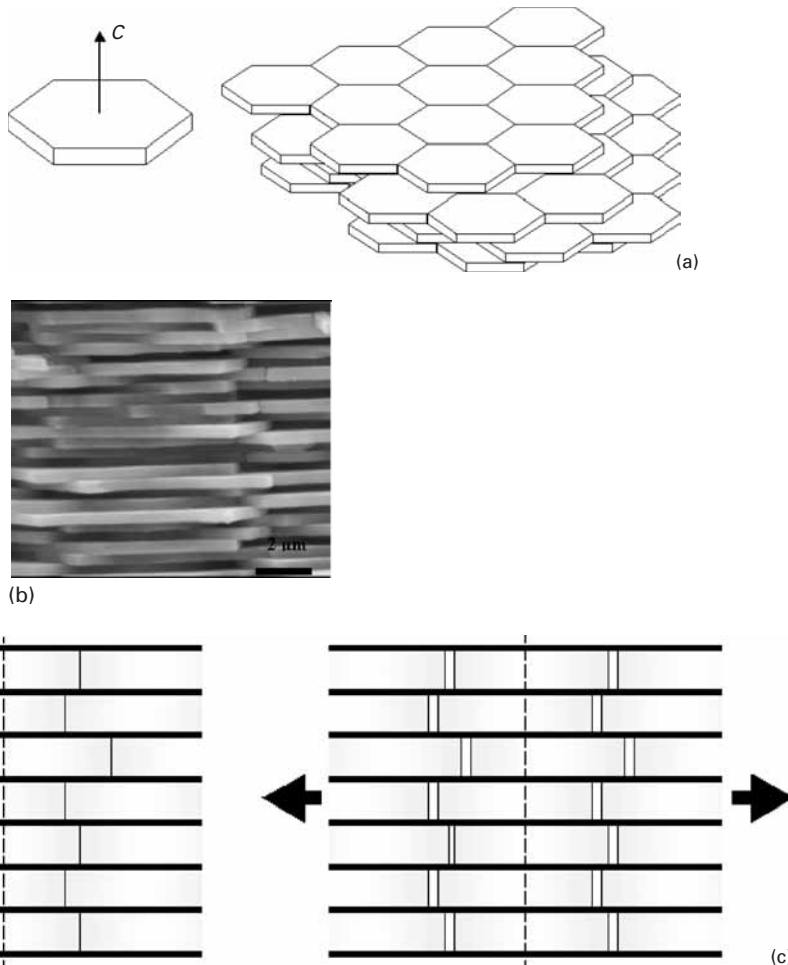


**Fig. 15.26** Flexural strength for selected monolithic and laminated materials. (Adapted from M. Sarikaya, *Micr. Res. Tech.*, 27 (1994) 371.)

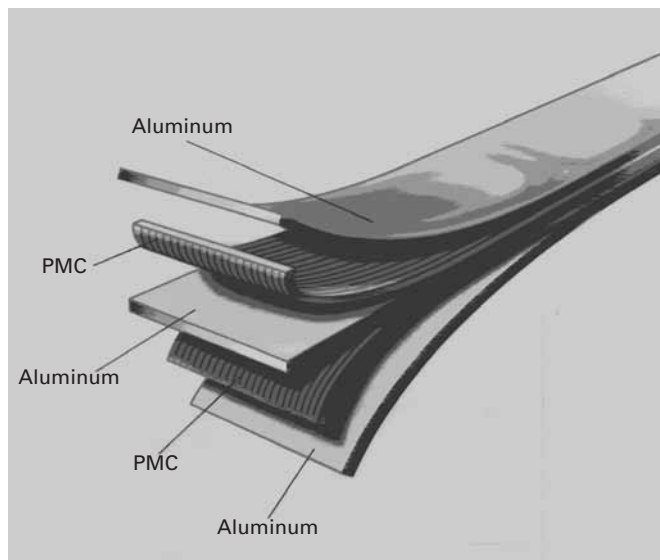
mortar” structure where aragonite (an orthorhombic form of  $\text{CaCO}_3$ ) is represented by “bricks” bound together by organic material (“mortar”). Again, the thick bands are made of aragonite and the thin layers in between the aragonite plates are an organic “glue.” This laminated structure of aragonite and organic material is the primary reason for the toughness of abalone. When abalone fractures under application of load, the resulting crack will follow a tortuous path that requires considerable energy to grow. Figure 15.27(b) shows the fracture surface. We see that the tiles are actually pulled out. These tiles slide past each other and the glue between them provides the resistance. This pullout action is shown in the sequence depicted in Figure 15.27(c).

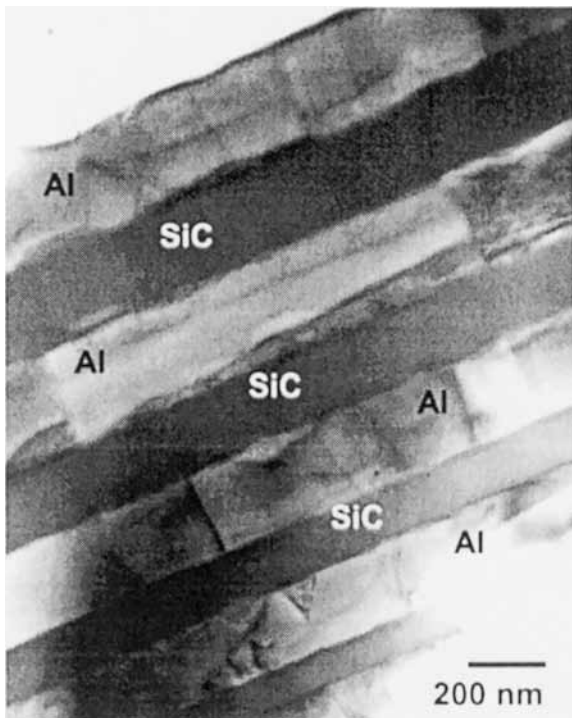
Several laminated composites are commercially available. A laminated composite made of two glass sheets bonded with poly(vinyl butyral), PVB, is used as a transparent safety glass material in a variety of applications, the most important being the automotive windshield. Bilayer or bimetallic composites are commonly used as switches. Some of the newer laminated composites are made by stacking alternate layers of a fiber reinforced polymer composite and monolithic metallic sheet. Examples include ARALL (aramid aluminum laminate) which consists of alternate layers of aramid fiber-epoxy and aluminum sheet and GLARE, which consists of alternate layers of glass fiber-epoxy and aluminum sheet. Figure 15.28 shows schematically such composites. They are also known as fiber metal laminates. Such composites have very high specific stiffness and strength. They are also more resistant to cyclic fatigue. Figure 15.29 shows the microstructure (SEM and TEM) of a laminated composite of aluminum and silicon carbide made by physical vapor deposition on a silicon substrate. It has mechanical properties vastly superior to those of individual components. These laminated composites are examples of bioinspired materials, where the same toughening principle is used as does nature in the abalone shell.

**Fig. 15.27** (a) Schematic showing an arrangement of tiles; (b) SEM of a fractured surface of abalone showing pullout of tiles; (c) schematic showing how pullout of tiles occurs through shear of organic layer that acts as glue. (Courtesy of A. Lin.)

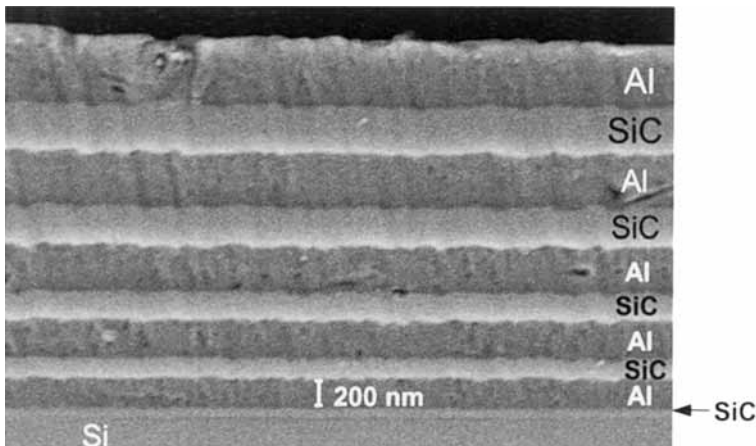


**Fig. 15.28** Schematic of a metal–polymer matrix composite (PMC) such as *Arall* or *Glare*.





(a)



(b)

**Fig. 15.29** Cross section of a laminate consisting of aluminum and silicon carbide: (a) SEM; (b) TEM. (From X. Deng, K. K. Chawla, M. Koopman, and J. P. Chu, *Adv. Eng. Mater.*, 7 (2005) 1.)

## Suggested Reading

- K. K. Chawla. *Composite Materials: Science and Engineering*, 2nd ed. New York, NY: Springer, 1998.
- K. K. Chawla. *Ceramic Matrix Composites*, 2nd ed. Boston, MA: Kluwer Academic, 1993.
- K. K. Chawla. *Fibrous Materials*. Cambridge, U.K.: Cambridge University Press, 1998.

- N. Chawla and K. K. Chawla, *Metal Matrix Composites*. New York, NY: Springer, 2006.
- T. W. Clyne and P. Withers. *Metal Matrix Composites*. Cambridge, U.K.: Cambridge University Press, 1994.
- L. N. Phillips, ed. *Design with Advanced Composite Materials*. London: The Design Council, 1989.
- S. Suresh, A. Needleman, and A. M. Mortensen, eds. *Fundamentals of Metal Matrix Composites*. Stoneham, MA: Butterworth-Heinemann, 1993.

## Exercises

**15.1** Describe some composite materials that occur in nature. Describe their structure and properties.

**15.2** To promote wettability and avoid interfacial reactions, protective coatings are sometimes applied to fibers. Any improvement in the behavior of a composite will depend on the stability of the layer of coating. The maximum time  $t$  for the dissolution of this layer can be estimated by the diffusion distance

$$x \approx \sqrt{Dt},$$

where  $D$  is the diffusivity of the matrix in the protective layer. Making an approximation that the matrix diffusion in the protective layer can be represented by self-diffusion, compute the time required for a 0.1-μm-thick protective layer on the fiber to be dissolved at  $T_m$  and  $0.75T_m$ , where  $T_m$  is the matrix melting point in kelvin. Assume a reasonable value of  $D$  for self-diffusion in metals, taking into account the variation in  $D$  with temperature.

**15.3** A fibrous form represents a higher energy form vis-a-vis a spherical form. Hence, a fibrous phase produced by unidirectional solidification of an eutectic will tend to form spheroids because such a change of shape results in a decrease in the surface energy of the material. Compute the energy released when a 10-cm-long, 20-μm-diameter fiber becomes spheroidal. The specific surface energy of the fibrous phase is 500 m Jm<sup>-2</sup>.

**15.4** One can obtain two-dimensional isotropy in a fiber composite plate by having randomly oriented fibers in the plane of the plate. Show that the average in-plane modulus is

$$\bar{E}_\theta = \frac{\int_0^{\pi/2} E_\theta d\theta}{\int_0^{\pi/2} d\theta}.$$

Plot  $E_\theta/E_{11}$  versus  $V_f$  for fiber reinforced composites with  $E_f/E_m = 1, 10$ , and 100.

**15.5** Consider a carbon fiber reinforced epoxy composite. The fibers are continuous, unidirectionally aligned and 60% by volume. The tensile strength of carbon fibers is 3 GPa, and the Young's modulus is 250 GPa. The tensile strength of the epoxy matrix is 50 MPa, and its Young's modulus is 3 GPa. Compute the Young's modulus and the tensile strength of the composite in the longitudinal direction.

**15.6** A steel wire of diameter 1.25 mm has an aluminum coating such that the composite wire has a diameter of 2.50 mm. Some other pertinent data

are as follows:

Property	Steel	Aluminum
Elastic modulus $E$	210 GPa	70 GPa
Yield stress $\sigma_y$	200 MPa	70 MPa
Poisson ratio $\nu$	0.3	0.3
Coefficient of thermal expansion (linear)	$11 \times 10^{-6} \text{ K}^{-1}$	$23 \times 10^{-6} \text{ K}^{-1}$

- (a) If the composite wire is loaded in tension, which of the two components will yield first? Why?
- (b) What tensile load can the composite wire support without undergoing plastic strain?
- (c) What is the elastic modulus of the composite wire?
- (d) What is the coefficient of thermal expansion of the composite wire?

15.7 A boron-aluminum composite has the following characteristics:

Unidirectional reinforcement,  
Fiber volume fraction  $V_f = 50\%$ ,  
Fiber length  $\ell = 0.1 \text{ m}$ ,  
Fiber diameter  $d = 100 \mu\text{m}$ ,  
Fiber ultimate stress  $\sigma_{fu} = 3 \text{ GPa}$ ,  
Fiber strain corresponding to  $\sigma_{fu}$ ,  $e_{fu} = 0.75\%$  (uniform elongation),  
Fiber Young's modulus  $E_f = 415 \text{ GPa}$ ,  
Matrix shear yield stress  $\tau_{ym} = 75 \text{ MPa}$ ,  
Matrix stress at  $e = e_{fu}$ ,  $\sigma'_m = 93 \text{ MPa}$ ,  
Matrix ultimate stress  $\sigma_{mu} = 200 \text{ MPa}$ .

Compute:

- (a) The critical fiber length  $\ell_c$  for the load transfer.
- (b) The ultimate tensile stress of the composite.
- (c)  $V_{\min}$  and  $V_{\text{crit}}$  for this composite system.

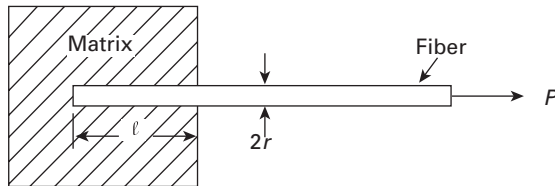
15.8 Determine Young's modulus for a steel fiber-aluminum matrix composite material, parallel and perpendicular to the fiber direction. The reinforcement steel has  $E = 210 \text{ GPa}$  and  $V_f = 0.3$ , and the aluminum matrix has  $E = 70 \text{ GPa}$  and  $V_m = 0.7$ .

15.9 An injection molded composite has short, aligned fibers. The fiber volume fraction is 40%. The length and diameter of the fibers are 500 and  $10 \mu\text{m}$ , respectively. Assume a square distribution of fibers in the cross section of the composite. The Young's modulus of the fiber and matrix are 230 and 3 GPa, respectively. The shear modulus of the matrix is 1 GPa. Compute the mean strength of this composite in the fiber direction.

15.10 A glass fiber reinforced polymer matrix composite has the following characteristics:

Fiber maximum strength = 2 GPa  
Interfacial shear strength = 50 MPa  
Fiber radius =  $10 \mu\text{m}$ .

Compute the critical fiber length for this system.

**Fig. Ex15.12**

**15.11** A unidirectionally reinforced fiber reinforced composite has the following characteristics:

$$\begin{aligned}E_f &= 380 \text{ GPa}, \\ \sigma_{fu} &= 3 \text{ GPa}, \\ V_f &= 0.4, \\ \tau_i &= 50 \text{ MPa}, \\ \text{fiber length } l &= 10 \text{ cm}, \\ \text{fiber diameter } d &= 15 \mu\text{m}.\end{aligned}$$

The matrix strength at fiber failure is = 200 MPa. Assuming that the fibers are aligned, compute the critical length for load transfer in this composite. If the load transfer coefficient  $\beta = 0.5$ , what is the strength of the composite along the fiber direction?

**15.12** Consider a fiber of radius  $r$  embedded up to a length  $\ell$  in a matrix. (See Figure Ex15.12.) When the fiber is pulled, the adhesion between the fiber and the matrix produces a shear stress  $\tau$  at the interface. In a composite system containing a fiber of fracture stress  $\sigma_f$  equal to eight times the maximum shear stress  $\tau_{\max}$  that the interface can bear, what fiber aspect ratio is required to break the fiber rather than pull it out?

**15.13** List some nonstructural applications of composite materials.<sup>13</sup>

**15.14** Bone is an excellent example of a natural composite. Describe the various components that make this composite.

**15.15** Describe mechanical characteristics of bone and its ability to repair.

**15.16** A glass fiber reinforced polypropylene composite has 65% by volume of fibers unidirectionally aligned.

- (a) Compute the weight fraction of glass fibers in this composite.
- (b) What is the density of this composite?
- (c) Compute the Young's modulus of the composite in a direction along the fiber and perpendicular to it.

**15.17** A composite is made of unidirectional carbon fibers embedded in an epoxy matrix.

- (a) Plot the Young's modulus as a function of the volume fraction of fibers parallel and perpendicular to the fiber direction.
- (b) If the continuous fibers are replaced by chopped fibers with random orientation, where do you expect that the elastic properties would lie? Indicate in the plot, given  $E_f = 390 \text{ GPa}$ ;  $E_m = 3 \text{ GPa}$ .
- (c) Name three applications for this composite.

---

<sup>13</sup> See M. B. Bever, P. E. Duwez, and W. A. Tiller, *Mater. Sci. Eng.*, 6 (1970) 149.

**15.18** A carbon fiber-epoxy composite has 70% fibers. Determine the elastic modulus of composite along the perpendicular to fiber direction. Compute the density of this composite.

Given:

$$\text{Density of carbon fibers} = 1.3 \text{ g/cm}^3,$$

$$\text{Density of epoxy} = 1.1 \text{ g/cm}^3,$$

$$E_c = 270 \text{ GPa},$$

$$E_e = 4 \text{ GPa}.$$

**15.19** A composite is made with discontinuous alumina fibers in an aluminum matrix. The fibers have a diameter of  $10 \mu\text{m}$ . If the volume fraction of fibers is 60%, what is the required length if we want the strength of composite to be equal to 50% of the same composite reinforced with continuous fibers.

Given:

$$\text{Fiber } E = 380 \text{ GPa},$$

$$\text{Fiber strength} = 1.7 \text{ GPa},$$

$$\text{Matrix strength} = 200 \text{ MPa}.$$

**15.20** A unidirectional reinforced composite has an aluminum matrix and steel fibers (40 vol%). Determine its strength.

Given:

$$\text{Aluminum: } \sigma = 100 + \varepsilon^{0.3} \text{ (in MPa),}$$

$$\text{Steel: } \sigma = 2.5 \text{ GPa.}$$

**15.21** Describe five applications of composites in sports equipment. Specify components of the composite.

**15.22** Metals can be joined by welding, riveting, and bolting. Is it possible to apply these processes to polymer matrix composites? Explain why, and present alternative means of joining composites.

**15.23** Give specific examples for the four different types of composites, and explain briefly the components involved (e.g. particle reinforced; short fiber reinforced, etc.).

**15.24** Give an example of a composite. Compare its mechanical properties with those of the reinforcements and matrix materials, respectively, and explain its advantages.

**15.25** Consider a steel and rayon-cord reinforced elastomer (rubber) with elastic moduli as shown in the table below.

Material	$E$ (MPa)
Rubber	13
Rayon	6,000
Steel	210,000

Calculate the elastic modulus for the two different composites, if the volume fraction of fiber (rayon or steel) is 0.3.

**15.26** Consider an elastomer matrix composite reinforced with steel cord (1 mm length and 0.5 mm diameter). What is the minimum fracture stress for the steel cord, if the interfacial shear strength is 20 MPa?

**15.27** Consider an aluminum–titanium laminated composite. Calculate the longitudinal and transverse Young's modulus of this composite if the volume fractions of the two metals are equal. Given  $E(\text{Ti}) = 116 \text{ GPa}$ ,  $E(\text{Al}) = 70 \text{ GPa}$ .

---

# Chapter 16

## Environmental Effects

### 16.1 | Introduction

Environment by its omnipresence, except perhaps in space, affects the behavior of all materials. Such effects can range from swelling in polymers to surface oxidation of metals and nonoxide ceramics to catastrophic failure of some materials under a combined action of stress and environment. Environmental degradation of materials is often referred to as corrosion. Such damage is generally time-dependent, i.e., one is able to predict it. Over time, however, environmental damage can become critical. There is, however, a more insidious corrosion problem which is time-independent. Examples of time-independent corrosion include stress corrosion cracking (SCC), environment induced embrittlement, etc. Such damage can occur at anytime, without much warning. There are many examples of such failures resulting in human and economic loss. Corrosion of structural components in aging aircraft is a serious problem. Just to cite one such example, a Boeing 737 belonging to Aloha Airlines, which flew inter island in Hawaii, lost a large portion of its upper fuselage at 7,500 m (24,000 feet) in the air. It turned out that the fuselage panels joined by rivets had corroded, which resulted in the mid-flight failure due to corrosion fatigue.

All materials (metals, ceramics, and polymers) show phenomena of premature failure or mechanical property degradation under certain combinations of stress and environment. We describe below the salient points in regard to environmental effects in different materials. We emphasize the role that the microstructure of a given material plays in this phenomenon, especially in environmentally assisted fracture.

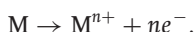
### 16.2 | Electrochemical Nature of Corrosion in Metals

Corrosion in metals, i.e., attack by an aggressive environment, is essentially electrochemical in nature. Fundamentally, there are two

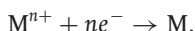
**Table 16.1** Galvanic Series of Some Metals and Alloys (in Seawater).

Pt	↑Cathodic
Au	
Graphite	
Ti	
Stainless steel (passivated)	
Cu–Ni alloys	
Bronze (Cu–Sn alloys)	
Cu	
Sn	
Pb	
Pb–Sn solders	
Stainless steel (activated)	
Cast Iron	
Steel	
Al alloys	
Al	
Zn	
Mg	↓Anodic

electrochemical reactions involved in the corrosion of a metal: oxidation and reduction. The reaction at the less noble metal is called oxidation or an anodic reaction (electrons are released in this reaction). In this case, the metal is the anode and it gets oxidized to an ion. We can write the reaction as:



At the more noble metal, one or more reduction or cathodic reactions, depending on the environment, can occur. Electrons are consumed in a cathodic reaction as per the following reaction:



Both these reactions occur simultaneously and at the same rate. If that were not so, there would occur a charge buildup in the metal.

One can classify the corrosion of metals in the following categories.

### 16.2.1 Galvanic Corrosion

Consider two different metals, say iron and copper, in electrical contact and exposed to an environment (i.e., an electrolyte such as water). The two dissimilar metals are said to form a *galvanic cell*. Metals and alloys can be conveniently ranked in terms of their relative reactivities to each other in an environment. Such a ranking is called the galvanic series. Table 16.1 lists some metals and alloys in the seawater environment. The metal that is less noble will corrode at the junction while the more noble one will be protected. In the example, iron will

corrode when it forms a galvanic cell with copper. The reader should note that the less noble metal is sacrificed.

Examples of such galvanic corrosion include steel screws suffering corrosion when in contact with brass in a marine environment. For example, if we have copper and steel in a water-heater, they will form a galvanic couple, and the steel will corrode. It should be pointed out that the rate of the corrosion is proportional to the ratio of the surface areas of the noble and less noble metals. Because the currents of the noble and less noble metal must be equal, therefore, if the less noble metal has a smaller surface area it will corrode very rapidly.

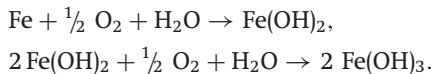
As a practical matter, we list some general recommendations to reduce galvanic corrosion.

- If dissimilar metals must be coupled, choose metals with similar activity.
- Avoid a small anode area.
- Electrically insulate the two metals.
- Use cathodic protection. This involves the use of a third metal that may be deliberately sacrificed. The less noble metal can be used as a sacrificial node to protect pipelines, ships, tanks, etc.

Stainless steels (Fe + Ni + 12% or more Cr) owe their corrosion resistance to a protective layer of chromium oxide. Such a coating protects the underlying metal from further corrosion.

### 16.2.2 Uniform Corrosion

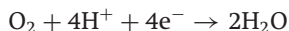
This type of corrosion occurs uniformly over the entire surface. Uniform corrosion is the least objectionable corrosion form because it is easy to predict. Examples of uniform corrosion include rusting of steel and tarnishing of silver. When iron is exposed to moist air, it corrodes. This is generally referred to as "rusting." The following chemical reactions are involved in rusting:



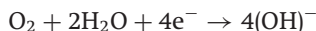
The rust consists of  $\text{Fe(OH)}_3$ , a hydrated oxide, which is cathodic in nature and insoluble in water.

### 16.2.3 Crevice corrosion

Initially metal corrodes uniformly. However, if there are holes on the surface for any reason, then solution in holes is stagnant so the oxygen concentration in the crevice solution is reduced by the following reactions:



for an acidic solution containing dissolved oxygen;



for neutral or basic solutions with dissolved oxygen.

This generates a potential difference between crevice and non-crevice regions, also called oxygen-concentration cells. The metal in contact with the most concentrated solution is the cathode and the metal in contact with the dilute solution (in the crevice) is the anode. The crevice (crack, depression, or a dent), where the oxygen concentration is relatively low, will corrode preferentially.

To reduce crevice corrosion, one should

- Avoid crevices in design, for example use welds rather than rivets.
- Flush crevices regularly.

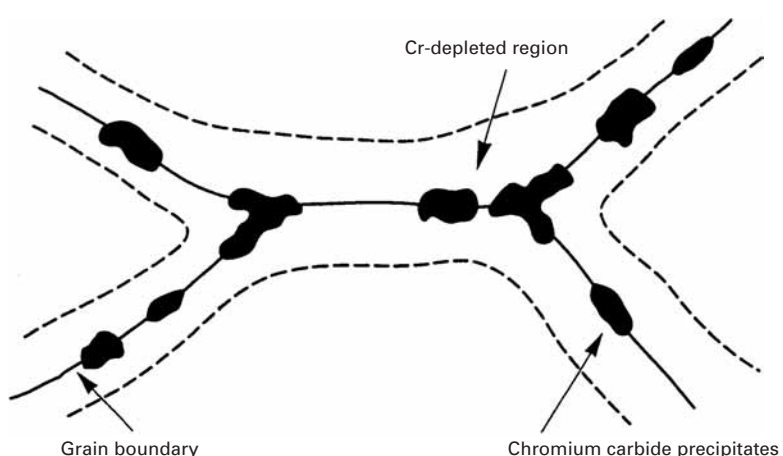
#### 16.2.4 Pitting Corrosion

This is another form of localized corrosion that involves the formation of small pits on the surface of a metal. Pits are likely to start at structural and/or compositional heterogeneities.

#### 16.2.5 Intergranular Corrosion

This type of corrosion, as suggested by the name, occurs along the grain boundaries. Generally, grain boundaries are energetically more active (i.e., anodic) than the grain interior. Recall that grain boundaries are regions of atomic disorder. Hence when exposed to an electrolyte the anodic grain boundaries dissolve preferentially and form a groove. A well known example of this is the phenomenon of *sensitization* in austenitic stainless steels. If austenitic stainless steels are heated to 500–800 °C for a long enough period, chromium carbide,  $\text{Cr}_{23}\text{C}_6$ , precipitates along grain boundaries. (See Figure 16.1.) This leaves the areas adjacent to the grain boundaries depleted in chromium. One needs at least 12% chromium for the stainless steel to be corrosion resistant. If the chromium content in regions adjacent to boundary falls below 12%, it will corrode preferentially. Some high strength aluminum alloys also show intergranular corrosion.

**Fig. 16.1** Sensitization of austenitic stainless steel. When austenitic stainless steels are heated to 500–800 °C for a long enough period, chromium carbide,  $\text{Cr}_{23}\text{C}_6$ , precipitates along grain boundaries, leaving the areas adjacent to the grain boundaries depleted in chromium and prone to corrosion.



### 16.2.6 Selective leaching

In this case, one element in an alloy dissolves preferentially. For example, zinc can leach out preferentially in a Cu-Zn brass.

### 16.2.7 Erosion-Corrosion

This type of corrosion involves a combination of chemical attack and mechanical abrasion, which is worse than either alone.

### 16.2.8 Radiation Damage

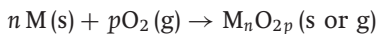
Damage can occur in metals when they are bombarded with energetic particles such as neutrons. Such damage includes formation of point defects, voids, compositional and/or microstructural changes. We have discussed this topic in Section 4.3.4. Suffice to reiterate here that among the property changes to which radiation damage can lead are: swelling, because of void formation; embrittlement, because of the generation of defects; and accelerated creep because of the formation of voids and bubbles.

### 16.2.9 Stress Corrosion

This type of degradation of a metal involves the combined action of stress and a specific corrosive medium. Failure occurs at stresses and corrosion levels where typically it would not occur alone. Residual stresses can also cause stress corrosion cracking. We describe the phenomenon of stress corrosion cracking below (Section 16.3) in some detail because of its importance.

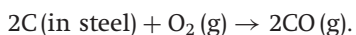
## 16.3 | Oxidation of Metals

The transformation of a metal into an oxide is accompanied by a reduction in energy, i.e., generally there is present a thermodynamic driving force for a metal to convert to what might be called its natural state. The natural state of metals (i.e., as they are found in nature) is one of compounds such as oxides, hydroxides, carbonates, silicates, sulfides, sulfates, etc. There are, of course, exceptions such as gold and platinum, which are called noble metals! Oxidation is sometimes referred to as dry corrosion. We can represent oxidation as a chemical reaction in the following manner:



where M represents a metal such as aluminum or a metalloid such as silicon.

Steel, which in its simplest form is an alloy of iron and carbon, can be decarburized in an oxygen environment as per the following reaction:



Some normally active metals become passive, i.e., lose their chemical reactivity and become inert by the formation of a highly adherent, thin oxide film on the surface that protects the metal from further corrosion. This phenomenon is called *passivity*. Examples of metals that passivate include Cr, Ni, Ti, Al. It is the chromium oxide film on the surface of stainless steel that makes the steel *stainless*, i.e., corrosion resistant. Similarly, aluminum oxide on aluminum provides a protective film. The important factor is whether the protective oxide scale that forms on the surface is protective or not? This feature can be determined by a parameter called Pilling–Bedworth ratio:

$$\text{Pilling–Bedworth ratio} = A_o \rho_o / A_m \rho_m,$$

where  $A_o$  is the atomic weight of the oxide,  $\rho_o$  is the density of the oxide,  $A_m$  is the atomic weight of the metal, and  $\rho_m$  is the density of the metal.

- For a protective oxide, the Pilling–Bedworth ratio is approximately 1.
- For a porous oxide, the Pilling–Bedworth ratio is less than 1.
- For a flaking oxide, the Pilling–Bedworth ratio is around 2 to 3.

Thermal mismatch between a metal and its oxide as represented by the difference in their coefficients of thermal expansion ( $\alpha_{\text{oxide}} - \alpha_{\text{metal}}$ ) is another important parameter.

If  $\alpha_{\text{oxide}} > \alpha_{\text{metal}}$ , the oxide will contract more than the underlying metal on cooling, putting the oxide layer in tension, which may crack. If  $\alpha_{\text{metal}} > \alpha_{\text{oxide}}$ , the metal substrate will contract more than the oxide on cooling, putting the oxide in compression, which may cause cracking or buckling of oxide and possible delamination.

If a continuous and adherent oxide film forms on the surface of a material in sufficient quantity to cover the surface, it may be used to protect the underlying material against further oxidation.

---

## 16.4 | Environmentally Assisted Fracture in Metals

Environmentally assisted fracture in metals can be classified under the following subheadings:

- stress corrosion cracking
- hydrogen damage
- liquid and solid metal embrittlement.

### 16.4.1 Stress Corrosion Cracking (SCC)

Generally, SCC is initiated by a rupture of the protective oxide film on the metal. This film rupture may occur because of a mechanical action or a chemical action of some species. Possible initiation sites of SCC include microscopic inhomogeneities such as local differences in

**Table 16.2** Some Important Alloy–Environment Combinations for SCC

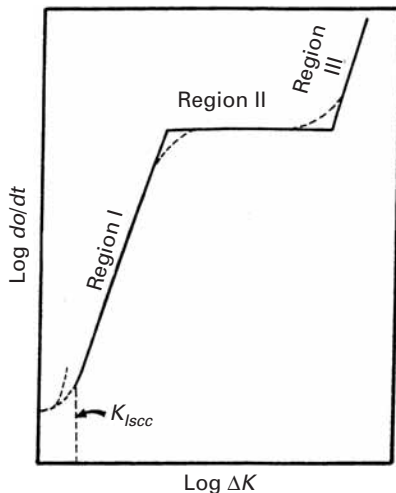
Alloys	Environments
Copper alloys	Ammonia, sulfur dioxide, oxygen
Austenitic stainless steels, Al alloys, Ti alloys, high strength steels	Chlorides and moisture
Low carbon steels	Hydrogen sulfide
Carbon steels	CO or CO <sub>2</sub> and moisture
Copper alloys	Oxides of nitrogen

chemical composition, amount of the corrosive species, and/or thickness of the protective film; and any stress concentration sites such as a preexisting gouge mark on the surface. Corrosion pits form at the rupture sites and cracking starts at the root of the pit. Electrochemical action maintains the sharpness of the crack tip, with corrosion continuing at the tip of a propagating crack. Bare metal under the protective film or passivated layer is exposed by the slip (i.e., plastic deformation) occurring at the crack tip. The new metal surface that is exposed becomes anodic with respect to adjacent areas that act cathodically. The corroding metal gets passivated again and the process of crack growth is repeated. The crack thus propagates in a stepwise manner in a transgranular or intergranular mode depending on the metal and environmental conditions. Characteristically, SCC shows branching, with the main crack growing in a direction perpendicular to the major tensile stress component and a low ductility.

As mentioned above, SCC occurs under the combined action of a tensile stress (applied or residual) and an aggressive environment. However, a specific metal–environment combination is required for SCC to occur. Examples include aluminum alloys–seawater, brass–ammonia, austenitic stainless steel–seawater, titanium–liquid nitrogen tetroxide (N<sub>2</sub>O<sub>4</sub>), etc. Table 16.2 summarizes some of the important metal–environment combinations.

The treatment of SCC in terms of linear elastic fracture mechanics (LEFM) analysis involves the use of crack-tip stress intensity factor as the dominant parameter controlling the crack growth under SCC conditions. Under a specific combination of a material and an aggressive environment, cracks can grow under a constant stress intensity factor  $K$  less than  $K_{Ic}$ , the fracture toughness. We then define  $K_{Iscc}$  as the threshold stress intensity value below which the crack propagation rate is negligible. One should add here the same warning in regard to the applicability of the linear fracture mechanics concepts as was done in the case of ordinary fracture in the absence of an aggressive environment; that is the size of the plastic zone at the crack tip must be small compared to the specimen dimensions for the application of LEFM to be valid. Crack growth velocity varies with the stress intensity factor,  $K$ . A schematic plot of  $\log da/dt$  vs. applied

**Fig. 16.2** Crack growth rate as function of the stress intensity factor under conditions of SCC.



stress intensity is shown in Figure 16.2. There are three regions in this curve:

- Region I: In this region the crack velocity depends on the stress intensity factor. The threshold stress intensity,  $K_{Isc}$ , below which the crack growth does not occur, is shown by a dashed line. Quite frequently, a true  $K_{Isc}$  does not exist. In such a case, we can define an operational  $K_{Isc}$  as that corresponding to a crack growth rate of  $10^{-9}$  or  $10^{-10} \text{ ms}^{-1}$ . Such an arbitrary value can be used to rate different alloys.
- Region II: The crack velocity in this region is independent of the stress intensity factor. The value at which this plateau region occurs is very specific to metal/environment combination and test conditions such as temperature.
- Region III: In this region the crack velocity becomes very fast as the crack-tip stress intensity factor approaches  $K_{Ic}$ . In this region, the crack velocity is mainly controlled by the stress intensity.

Figure 16.3 shows actual plots of log crack velocity vs. stress intensity factor for aluminum 7079 alloy in a potassium iodide solution for different temperatures.<sup>1</sup> Only data from regions I and II are shown in this figure. As the temperature increases, the curves shift upward, i.e., for a given stress intensity, the crack velocity increases with temperature. It should be clear to the reader that a knowledge of the full crack velocity versus stress intensity factor curve for a specific alloy in a specific environment will provide a better evaluation of the SCC resistance of the alloy in that particular environment. Similar three-region curves may be obtained under conditions of hydrogen damage and liquid metal embrittlement.

<sup>1</sup> M. O. Speidel, *Met. Trans.*, 6A (1975) 631.

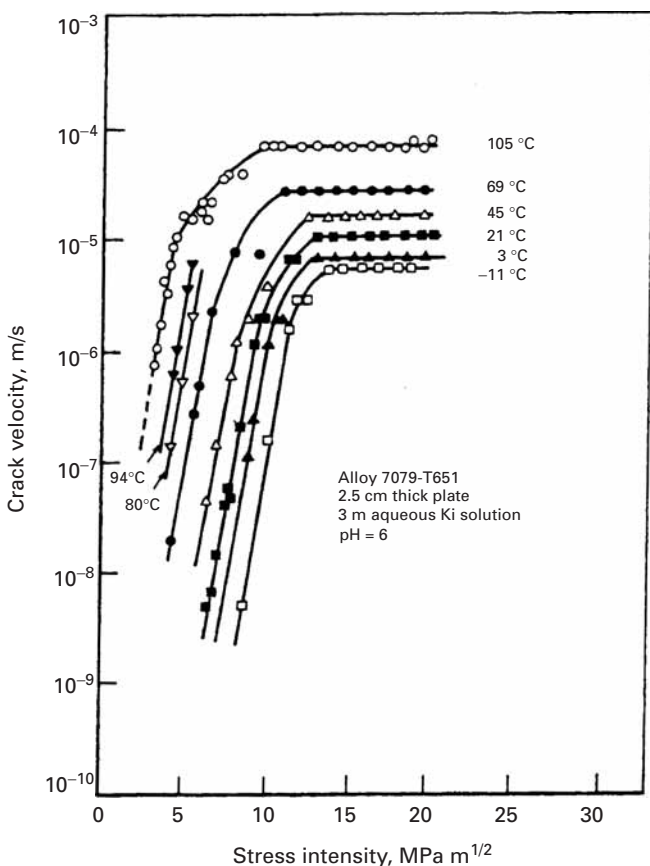
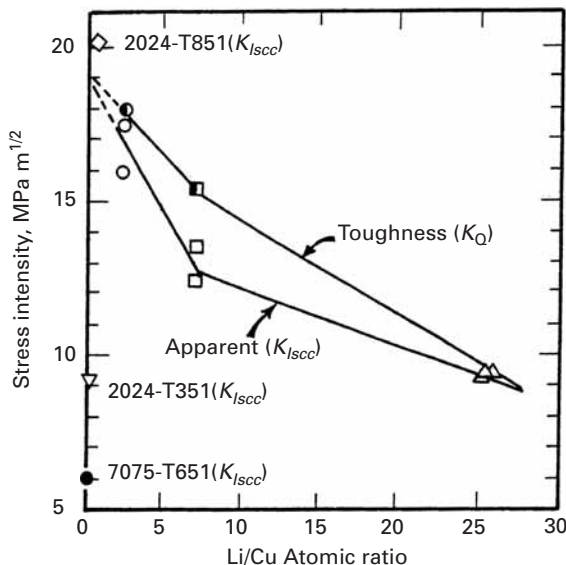


**Fig. 16.3** Log crack velocity vs. stress intensity factor for two aluminum alloys in a potassium iodide solution. Region III is not shown. (After M.O. Speidel, Met. Trans., 6A (1975) 631.)

### Effect of Material Variables on SCC

In general, high purity metals are less prone to SCC than alloys or impure metals. In particular, trace amounts of interstitial elements can have a very large effect. For example, nitrogen in excess of 500 ppm in austenitic stainless steel in chloride environments can be disastrous. The cracking in austenitic stainless steels is mainly transgranular, indicating that the effect of nitrogen must either be on the process of slip or the stability of the protective film. The grain size of the metal can also have a profound effect on its resistance to SCC. A smaller grain size is more resistant to SCC than a coarse one. Elongated grain structure commonly obtained in wrought aluminum alloys can cause a markedly anisotropic SCC behavior. For example, a sheet or plate of Al 7075-T6 shows high resistance against SCC when stressed in the rolling or long transverse direction but rather poor resistance against SCC in the plate thickness direction. The 7075-T7 temper, which has a lower strength than the T6 temper, can improve resistance against SCC in the through thickness direction. Generally, the aging treatment in aluminum alloys results in increasing their resistance against SCC. The 7XXX series of aluminum alloys (Al-Zn-Mg) show the best resistance against SCC when they are aged beyond the peak hardness, i.e., in the overaged condition.

**Fig. 16.4** Decrease in  $K_{Isc}$  with increasing (Li/Cu) ratio in an Al–Li–Cu–Zr alloy (T651 temper). The apparent toughness ( $K_Q$ ) also decreases with increasing (Li/Cu) ratio. (After A. K. Vasudevan, P. R. Ziman, S. Jha, and T. H. Sanders, in *Al-Li Alloys III* (London, The Institute of Metals, 1986), p. 303.)



Aluminum-lithium alloys are now used in the aerospace industry because of their enhanced modulus and low density (see Chapter 10). Generally, ternary or quaternary alloys are used. In particular, Al–Li–Cu–Zr alloys show quite an attractive combination of properties. It has been observed that the (Li/Cu) ratio can have significant effect on the precipitation sequence and consequently the resultant mechanical properties. The (Li/Cu) ratio also affects the stress corrosion resistance of the alloy. Figure 16.4 shows  $K_{Isc}$  in the T651 temper decreasing with increasing (Li/Cu) ratio.<sup>2</sup> The  $K_{Isc}$  values of 2024-T851 (peak aged) and 2024-T351 (underaged) are also included for comparative purposes. Also plotted is the apparent toughness ( $K_Q$ ) as function of (Li/Cu) ratio. It would appear that the loss of  $K_{Isc}$  is partly due to the loss of toughness of these alloys with increasing (Li/Cu). Low-Li alloys showed the transgranular cracking and crack branching while the high-Li alloys showed intergranular cracking.

#### 16.4.2 Hydrogen Damage in Metals

The presence of hydrogen in a material can cause serious damage to its performance. In addition to its great technological importance, the phenomenon of hydrogen damage has been a challenging basic research problem. One main reason for the damage caused by hydrogen in metals and alloys is the extremely small size of the hydrogen atom, which makes it move very fast in the metallic lattice. It is therefore not surprising that over the years a considerable research effort has gone into obtaining an understanding of the phenomenon, especially in metals and alloys. We provide below a short account of the hydrogen effects in various metals and alloys.

<sup>2</sup> A. K. Vasudevan, P. R. Ziman, S. Jha, and T. H. Sanders, in *Al-Li Alloys III* (London: The Institute of Metals, 1986), p. 303.

Some of the common sources of hydrogen in metals as well as some simple and straightforward remedies for the problem are as follows. Metals may absorb hydrogen during processing or service. For example, during melting and casting of metals, the hot metal can react with the raw materials or the humidity in air to form an oxide and hydrogen. The latter can be absorbed by the hot metal. This problem of hydrogen absorption by the liquid metal can be reduced by vacuum degassing processing. Atmospheric humidity can be a source of hydrogen in the arc welding of steels, while the electrode itself may absorb hydrogen during casting. Frequently, during some steps in the processing of a metal into a useful article, a chemical or electrochemical treatment is given. Nascent-hydrogen is released due to reaction of metal with acid during such a treatment. Most of it combines to form molecular hydrogen while the remainder will diffuse into the metal. Certain metals such as titanium, zirconium, etc. dissolve rather large quantities of hydrogen exothermally and form very brittle hydrides.

Quite frequently, in order to improve the corrosion resistance and/or for decorative purposes, electropolishing or plating of materials is carried out. Such finishing processes represent another important source of hydrogen entry into the base metal. In these finishing processes, hydrogen, together with the electroplated species, is deposited at the cathode. In such cases, it is thought by some that baking out at moderate temperatures after plating may help remove hydrogen. Others hold the view that the protective coating serves as a barrier to hydrogen removal during bakeout.

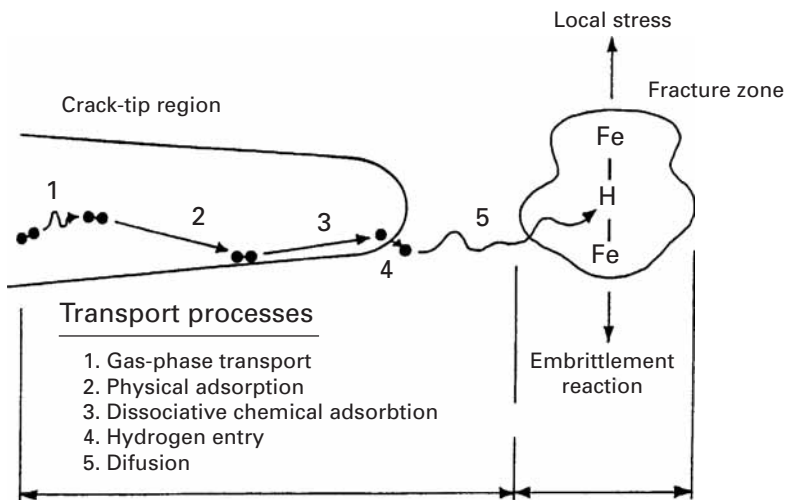
Aqueous corrosion is another common source of hydrogen for metals in service. Metal reacts with water to form an oxide (or a hydroxide) and atomic hydrogen, which is easily absorbed in the metal. In pressurized water nuclear reactors (PWR), water used for heat transfer can be an important source of hydrogen. Hydrogen embrittlement of zirconium alloy fuel cladding or of the pressure vessel itself can be a serious problem.

In the chemical and petrochemical industry, containers of chemicals (used for storage or as reaction chambers) can absorb hydrogen over a period of use. Natural gas containing  $H_2S$ , called sour gas, can cause hydrogen-induced cracking (HIC) in the pipeline steel. The sulfide ion is especially a problem species because it acts as a "surface poison" retarding the recombination of atomic hydrogen to form molecular hydrogen at the surface, leading to absorption of atomic hydrogen.

### Theories of Hydrogen Damage

No single model or theory is capable of explaining all the effects associated with the presence of hydrogen in different materials. However, almost all theories recognize that one of the most important attributes of hydrogen is that it diffuses very rapidly in most any material. For example, in steels hydrogen diffuses about  $10 \mu m$  per second at room temperature. This fast diffusion characteristic of

**Fig. 16.5** Schematic of the hydrogen transport processes at a crack tip in Fe and the embrittlement reaction. (After R. P. Gangloff and R. P. Wei, *Met. Trans. A*, 8A (1977) 1043.)



hydrogen stems partly from its extremely small size; hydrogen has the smallest atomic diameter among all the elements. In general, hydrogen tends to collect at defect sites in any material where it can produce high internal pressure, which can lead to cracking. There are certain special aspects of the hydrogen behavior in steels. Hydrogen has a very high mobility in the BCC lattice of Fe at ambient temperature. The comparative values of the diffusivity of hydrogen and nitrogen in the iron lattice at room temperature given below give a good idea of the extraordinarily high mobility of the hydrogen atom.<sup>3,4</sup>

$$D_H \text{ in Fe} \sim 10^{-2} \text{ m}^2 \text{ s}^{-1} \text{ at } 300 \text{ K}$$

$$D_N \text{ in Fe} \sim 10^{-12} \text{ m}^2 \text{ s}^{-1} \text{ at } 300 \text{ K.}$$

One can write for the local concentration of hydrogen in the BCC iron lattice as:<sup>5</sup>

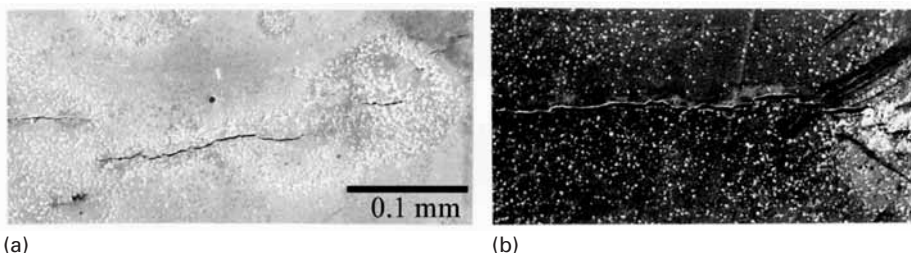
$$\ln \frac{C_H}{C_0} = \frac{\Omega \sigma_p}{RT},$$

where  $C_H$  is the local hydrogen concentration,  $C_0$  is the equilibrium hydrogen concentration in the unstressed lattice,  $\Omega$  is the molar volume of hydrogen in iron,  $\sigma_p$  is the hydrostatic stress ( $= \frac{\sigma_1 + \sigma_2 + \sigma_3}{3}$ ). Thus, in any nonuniformly stressed solid, there is a driving force for solute migration, which is a function of the solute atomic volume and the gradient in the hydrostatic stress component of the applied stress. Hydrogen segregates to regions of large hydrostatic tension. Figure 16.5 shows schematically the transport processes at a crack tip that eventually lead to the embrittlement reaction between the

<sup>3</sup> C. A. Wert, *Phys. Rev.*, 79 (1959) 601.

<sup>4</sup> R. A. Oriani, in *Fundamental Aspects of Stress Corrosion Cracking* (Houston, TX: NACE, 1969), p. 32.

<sup>5</sup> J. C. M. Li, R. A. Oriani, and L. W. Darken, *Z. Phys. Chem.* 49 (1966) 271.



(a) (b)

hydrogen and the metal, in this case iron.<sup>6</sup> This hydrogen transport process can be divided into the following steps:

- diffusion of hydrogen to the surface
- adsorption on the surface
- dissociation in the surface adsorption layer
- penetration through the surface
- diffusion into the bulk of the metal.

**Fig. 16.6** Stepwise cracking in a microalloyed steel after 24 h cathodic charging. (From K. K. Chawla, J. M. Rigsbee, and J. D. Woodhouse, *J. Mater. Sci.*, 21 (1986) 3777.)

Having given this very general picture of the effects of hydrogen in metals, we review briefly some of the specific theories that have been advanced to explain the phenomenon of hydrogen damage.

### Lattice Decohesion

A hydrogen-induced lattice decohesion can occur as originally proposed by Toriano.<sup>7</sup> Hydrogen diffuses into the triaxial tensile stress region at a crack tip, causing a localized reduction of the lattice cohesive strength. The concept is quite valid in very general terms. The exact mechanisms involved are, however, not clear.

### Pressure theory

Hydrogen atoms combine and precipitate as molecular hydrogen and cause internal pressure. When this internal pressure exceeds a critical value, HIC occurs. Because of the extremely high mobility of hydrogen in most lattices, segregation of absorbed hydrogen to regions of high expansion in the lattice, for example, internal voids and cracks, occurs easily. Large internal pressure would enhance void growth and crack propagation. A good example of this phenomenon is the blister formation in steels on cathodic charging. One would expect such cracking to vary with inclusion distribution. Figure 16.6 shows such hydrogen induced cracking in a microalloyed steel sample.<sup>8</sup> This extensive stepwise cracking resulted after cathodic charging for 24 hours. Such cracking or voiding is frequently associated with the presence of inclusions. Figure 16.7 shows an aluminum-based inclusion (possibly alumina) in the interior of a void produced by hydrogen charging.<sup>8</sup> The micrograph on the right in Figure 16.7 shows the mapping of aluminum, indicating an aluminum-based inclusion.

<sup>6</sup> R. P. Gangloff and R. P. Wei, *Met. Trans.*, 8A (1977) 1043.

<sup>7</sup> A. R. Toriano, *Trans. ASM*, 52 (1960) 54.

<sup>8</sup> K. K. Chawla, J. M. Rigsbee, and J. D. Woodhouse, *J. Mater. Sci.*, 21 (1986) 3777.

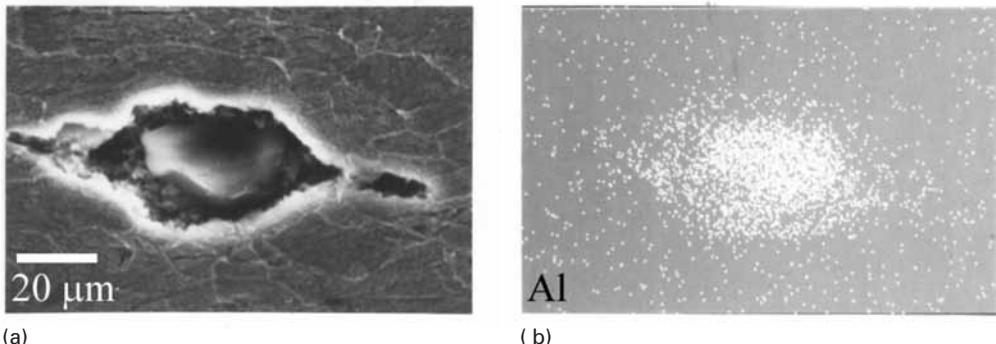


**Fig. 16.7** An aluminum-based inclusion in the interior of a void produced by hydrogen charging. (From K. K. Chawla, J. M. Rigsbee, and J. D. Woodhouse, *J. Mater. Sci.*, 21 (1986) 3777.)

The solubility of hydrogen is greatly influenced by the presence of lattice defects and impurities. For example, the solubility of hydrogen in a commercial steel at room temperature can be as much as 100% greater than that in a clean and well-annealed steel. Thus, although the solubility of hydrogen in iron is small, a large amount of it can be trapped rather easily at various defect sites.

Gas or oil containing  $H_2S$  can lead to sulfide stress corrosion cracking or hydrogen induced blistering in steel.<sup>9,10</sup> This form of HIC, also called *blistering*, is presumed to occur when hydrogen atoms generated in a wet, sour gas environment enter into the steel and precipitate at or around inclusions or other unfavorable microstructural sites. In this regard, manganese sulfide inclusions, elongated in the rolling direction, are perhaps the worst culprits. Hydrogen atoms, generated at the surface, penetrate and diffuse into the steel. These atoms are trapped at matrix-inclusion interfaces and at ferrite-(pearlite + bainite + martensite-austenite) interfaces.<sup>8</sup> Here it is appropriate to point out an important microstructural feature of in rolled low carbon steels. It is tacitly assumed that the solute atoms in a solid solution are uniformly distributed in the matrix. More often than not, it is not the case. Indendritic segregation of solutes starts during the freezing of alloys. Specifically, in Mn-C steels interdendritic segregation of Mn, followed by rolling, can result in pronounced banding. Pearlite layers in the microstructure coincide with the Mn segregation. Such a microstructure consisting of alternate layers of ferrite and pearlite is very anisotropic and susceptible to hydrogen induced cracking. In quenched and tempered steels, even high Mn steels do not show such segregation; these steels have superior resistance to HIC.

### Surface Energy

According to this theory, hydrogen is adsorbed on the free surfaces of a crack and reduces the surface energy. This results in a decrease in

<sup>9</sup> D. D. J. Thomas and K. R. Doble, in *Steels for Linepipe & Pipeline Fittings* (London: The Metals Society 1983), p. 22.

<sup>10</sup> T. Taira and Kobayashi, in *Steels for Linepipe & Pipeline Fittings*, (London: The Metals Society, 1983), p. 170.

the work of fracture as per the Griffith criterion. This theory, however, would not explain the reversible degradation attributed to hydrogen.

### Enhanced Plastic Flow

Beachem<sup>11</sup> proposed a hydrogen assisted cracking model in which hydrogen enhances dislocation motion. The hydrogen diffuses in front of the crack tip, increases the mobility of dislocations there and causes, locally, an enhanced plasticity. Figure 16.8 shows schematically this model. In the absence of hydrogen, a ductile metal fractures by microvoid coalescence within a large plastic zone at the crack tip, see Chapter 8. In the presence of hydrogen, however, locally plastic deformation becomes easier and crack growth occurs by severely localized deformation at the crack tip. This model has been supported experimentally by the work of Tabata and Birnbaum.<sup>12,13</sup> They used an *in situ* deformation stage in an environmental cell of a high voltage transmission electron microscope to investigate the effects of hydrogen on the behavior of dislocations in iron. It was observed that the introduction of hydrogen into the environmental cell increased the velocity of screw dislocations. This resulted in softening of the specimen in the early stages of deformation as the density of the mobile dislocations increased. In the later stages of deformation, this higher dislocation density may also contribute to work-hardening. These authors also studied the *in situ* fracture behavior of iron of different purities in the presence of hydrogen gas and observed that the presence of hydrogen enhanced fracture. The main conclusions of this work of are:

- Basic fracture mechanisms in iron in vacuum and in hydrogen atmosphere are the same, but the morphology of fracture is very different.
- Hydrogen enhanced fracture is caused by the localization of plasticity and by the enhancement of dislocation motion and generation in the presence of hydrogen, as first suggested by Beachem.<sup>11</sup>

### Hydride Formation

Certain metals such as Ti, Zr, V, Nb, Ta, Mg, Al, etc. could suffer hydrogen degradation by diffusion of hydrogen and reaction with the metal to form a hydride at the crack tip. The hydride phase, being brittle, cracks easily on continued loading. Crack arrest occurs when the crack tip reaches the matrix phase. New hydride phase forms and the cycle is repeated as shown schematically in Figure 16.9.<sup>14</sup> In pure iron, carbon and low alloy steels, a hydride phase is not formed or is unstable. This is attributed to the extremely low solubility of hydrogen in iron and steels. Other nonhydride forming systems include Mo, W, Cr, and their alloys.

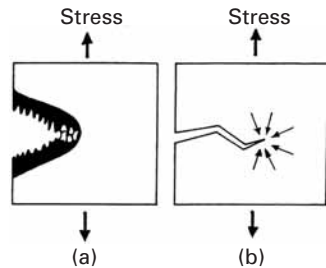


**Fig. 16.8** Schematic of crack growth in a high strength steel. (a) Without hydrogen, crack growth occurs by microvoid coalescence within a large plastic zone at the crack tip. (b) With hydrogen, plastic deformation becomes easy and crack growth occurs by severely localized deformation at the crack tip. (After C. D. Beachem, *Met. Trans.*, 3A (1972) 437.)

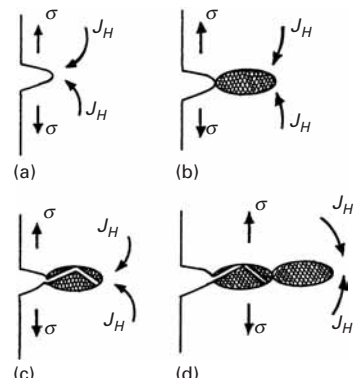


**Fig. 16.9** Hydrogen degradation due to hydride formation. (a) Under stress,  $\sigma$ , hydrogen diffuses indicated by flux  $J_H$ , to the crack tip. (b) A hydride phase forms at the crack tip. (c) The brittle hydride phase cracks easily on continued loading. (d) New hydride phase forms and the cycle is repeated. (After H. K. Birnbaum, in *Atomistics of Fracture* (New York, Plenum, 1983), p. 733.)

<sup>11</sup> C. D. Beachem, *Met. Trans.*, 3A (1972) 437.

<sup>12</sup> T. Tabata and H. K. Birnbaum, *Scripta Met.*, 17 (1983) 947.

<sup>13</sup> T. Tabata and H. K. Birnbaum, *Scripta Met.*, 18 (1984) 231.

<sup>14</sup> H. K. Birnbaum, in *Atomistics of Fracture*, (New York: Plenum, 1983), p. 733.

### Alleviating the Hydrogen Damage

While it is very difficult to provide simple recipes for alleviating the hydrogen damage in all the materials, we may list the following general guidelines as possible solutions:

- *Avoid entry of hydrogen.* This involves a control of the external environment, i.e., use of inhibitors or suitable alloying elements to protect the base metal surfaces against hydrogen ion discharge reaction.
- *Improve the material resistance to hydrogen damage.* An effective way of doing this is to modify the morphology and/or decrease the number of inclusions. Lowering the sulfur content (maximum S about 0.010%) is a very important item in inclusion content control. Because the elongated inclusions such as MnS stringers in steel are highly susceptible to hydrogen damage, inclusion shape control through use of rare earth metals is of great help. Modifying the alloy composition is yet another way. For example, chromium as an alloying element is very beneficial in steels. The reasons for this effect may be varied. The addition of chromium decreases the solubility of hydrogen in steels, perhaps, because chromium alters the electrochemical conditions on the surface of steel, enhances the oxidation of sulfur, or depresses adsorption of atomic hydrogen.

#### 16.4.3 Liquid and Solid Metal Embrittlement

Metals that fail in a ductile manner under normal conditions can fail in a very brittle fashion in the presence of certain active liquid or solid environments. This phenomenon has been variously referred to as *metal induced embrittlement* (MIE), *solid metal embrittlement* (SME), and *liquid metal embrittlement* (LME). LME of brasses and bronzes by mercury is a well known example. Gallium, which is a liquid at room temperature, causes a catastrophic failure in aluminum without any apparent diffusion. Carbon and low alloy steels are embrittled by cadmium. Amorphous metals are generally known to show excellent corrosion resistance, primarily because of the absence of grain boundaries and other defect sites. It has been observed, however, that several iron-based amorphous alloys show LME in the presence of Hg, Hg-In, or Sn<sub>6</sub>Pb<sub>4</sub>.<sup>15</sup>

LME is different from SCC in that positively and negatively charged ions in aqueous solution interact with solid metal in the SCC while, apparently, no electrochemical dissolution is involved in LME. There are certain prerequisites for LME to occur. The metals involved do not form any stable intermetallic compounds. The liquid metal must wet the solid metal and the metals do not have mutual solubility.

Among the models proposed to explain the phenomenon of LME are: reduction in surface energy of the solid metal by the

---

<sup>15</sup> S. Ashok, N. S. Stoloff, M. E. Glicksman, and T. Slayin, *Scripta Met.*, 15 (1981) 331.

adsorbing liquid metal species<sup>16</sup> and localized reduction of the strength of the atomic bonds at the crack tip by the embrittling species.<sup>16,17</sup> It would appear, however, that similar to the hydrogen effects in metals and alloys, different mechanisms seem to be responsible for LME under different conditions. For example, LME of many crystalline metals can be explained satisfactorily by enhanced shear or decohesion while solid metal induced embrittlement is accomplished by grain boundary penetration by the embrittling species. LME of amorphous metals, on the other hand, involves enhanced shear.

Finally, it should be pointed out to the reader that although the phenomenon of LME is generally considered as something undesirable, it is possible to use liquid metals, such as Pb-Sn eutectics, to facilitate drilling steels, titanium alloys, heat resistant Ni-Cr alloys. Increased drilling tool life and a better quality of the machined surface are improvements. Such beneficial effects have been known in nonmetallic fields for quite some time. For example, in the drilling of quartz rock, addition of  $\text{AlCl}_3$  to the water lubricant allows one to double the drilling speed without increasing the wear of the drilling bit.

## 16.5 | Environmental Effects in Polymers

Polymers can undergo a variety of changes due to environment, some of which can lead to severe embrittlement. Although polymers generally show good chemical resistance to various acids and alkalis, certain organic liquids and gases can affect their performance markedly. In particular, the fracture process can suffer rather drastic changes in the presence of certain environments. An example of such environmentally assisted fracture in polymers is that of polycarbonate, which fails at a low stress in a solution of sodium hydroxide in ethanol. Essentially, a specific combination of environment and stress results in a premature breakdown of the long-chain polymeric structure. Although our main concern in this section is the environmental effects on the mechanical behavior of polymers, it is worth pointing out that there is great interest in producing biodegradable polymers. This concern, of course, stems from the unsightly discarded plastic trash, which can be injurious to plant and human life. Yet another related topic, but which we shall not discuss in the book, is that of biocompatibility and stability of polymers in the body's environment, tissue-fluid interaction, etc.

Exposure to oxygen, moisture (ambient or otherwise) or other solvents, and ultraviolet radiation can lead to static fatigue or reduction in strain-to-failure. Swelling and/or dissolution are some of the most common phenomena. A liquid or solute molecule can diffuse in a polymer and cause swelling, leading to dimensional changes. Also the

<sup>16</sup> N. S. Stoloff and T. L. Johnston, *Acta Met.*, 11 (1963) 251.

<sup>17</sup> M. H. Kamdar, in *Adv. in Strength & Fracture*, Vol. 1 (Oxford, U.K.: Pergamon Press, 1977), p. 387.

liquid molecules push apart the chains so that secondary bonding is reduced and the polymer softens. The structural features responsible for such attack on polymers are the following.

- *Random Chain Scission:* The polymer breaks down at random points along the chain, with the attendant decrease in molecular weight and mechanical properties. The decrease in the molecular weight and/or changes the molecular weight distribution, can lead to a deterioration of the mechanical properties.
- *Successive Loss of Monomer Units:* This can occur at one extremity of the polymer chain and result in chain depolymerization. This is generally manifested in a gradual change in the molecular weight. Examples of such a phenomenon are exposure to different kinds of radiation, oxygen, ozone, etc. Rubber in the presence of ozone is particularly susceptible to this form of environmentally assisted failure. The ozone reacts at the surface of rubber and cracks nucleate and grow at low stress levels.

We provide below a brief description of different environmental effects in polymers.

### 16.5.1 Chemical or Solvent Attack

Thermoplastics can be dissolved by various organic solvents (e.g., xylene). Generally, the higher the molecular weight,  $M_w$ , the lower the solubility. For example, in a polymer having a distribution of various  $M_w$  fractions, the low  $M_w$  fractions can be dissolved and extracted by a solvent. Cross-linking of molecules, as in a thermoset, reduces solubility. Thus, a cross-linked epoxy is more resistant to chemicals than linear chain polymers such as polyethylene.

### 16.5.2 Swelling

Absorption of solvent molecules can be regarded as a form of solvent attack. Different polymers can absorb ambient moisture to different degrees. This phenomenon results in swelling of polymers and thus leads to dimensional changes. Such dimensional changes can be very important in polymers used as gaskets and seals. They also become important in polymer matrix composites, for example carbon fiber reinforced polymer. Because the polymer matrix will absorb moisture while the carbon fiber will not, there will result internal stresses due to a differential in swelling. One can get an idea of the seriousness of this problem by the following observation of carbon fiber reinforced polyimide composite. Polyimide is a high temperature polymer with a service temperature of 370 °C. However, retained moisture can result in a reduction of service temperature to 250 °C.

Generally, in monolithic polymers (i.e., not composites) swelling induced changes are reversible, i.e., the polymer will revert to its original dimensions when the absorbed molecule is removed. Moisture acts as a plasticizer, i.e., moisture absorption results in an increase impact toughness of a polymer while its strength decreases.

Swelling of a polymer can occur if a gas or a liquid permeates it. Typically, these swelling agents have small molecules and can easily penetrate the main polymeric network, where they reduce the cohesive force between the primary chains. Nylon, for example, can absorb moisture up to 1% of its weight, which can change its dimensions by about 1%. Moisture typically acts as a plasticizer, i.e., it lowers the glass transition temperature,  $T_g$ , of the polymer, with the result that deformation, crazing, and cracking occur at lower stress and strain values. If a polymer is uniformly swollen because of the permeation of a liquid, it will behave as a homogeneous polymer with a lower  $T_g$ . It should be pointed out that  $T_g$  of a polymer generally varies in a nonlinear manner with the plasticizer volume fraction. Figure 16.10 shows the glass transition temperature of polymethyl methacrylate (PMMA) as a function of the volume fraction of the plasticizer diethyl phthalate.<sup>18</sup> The solid line in the graph is given by:

$$[T_g - T_g^*]/[T_g - T] = 1 + r[1 - \phi]/\phi$$

where  $r = V_f/V = 0.5$ ,  $T_g^* = -65^\circ\text{C}$ ,  $V_f$  is the free volume,  $V$  is the total volume of the polymer, and the asterisks indicate the values for the plasticizer. At  $\phi = 1$ ,  $T_g = T$ , as expected. The absorption of the plasticizer facilitates the molecular motion. Generally, the plasticizer has a smaller molecule size but similar chemical structure to the polymer in which it penetrates. The plasticizer molecules separate the main chains and thus reduce the intermolecular forces, i.e., their presence makes it easier for the chains to slide past one another. However, more often than not, the swelling of the polymer is not uniform, because diffusion of liquid or gas in a polymer depends on many variables, such as the size of the diffusing molecule, the microstructure of the polymer, etc. Frequently, stresses are set up at the boundary between the part penetrated by the liquid and the unpenetrated part. One can easily imagine this phenomenon to be of great concern in polymer matrix composites. In general, polymers having high bond energies, high degree of crystallinity and cross-linking, etc. will show a reduced amount of swelling.

Figure 16.11 shows the decrease in tensile strength of injection-molded polyurethane when aged in distilled water at  $80^\circ\text{C}$  for thirty days.<sup>19</sup> Initially the decrease in strength with time is slow. After ten days of exposure to water, the rate accelerates. The increase in rate of loss of strength is because of the autocatalytic nature of the hydrolysis reaction.

### 16.5.3 Oxidation

Oxidation of polymers occurs throughout their life because it is impossible to avoid interaction with the oxygen in the atmosphere.

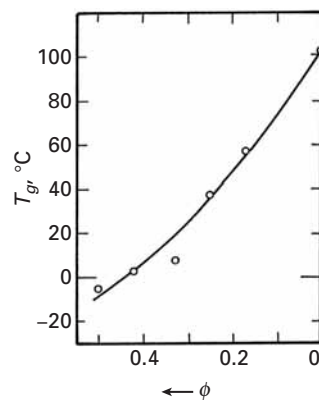
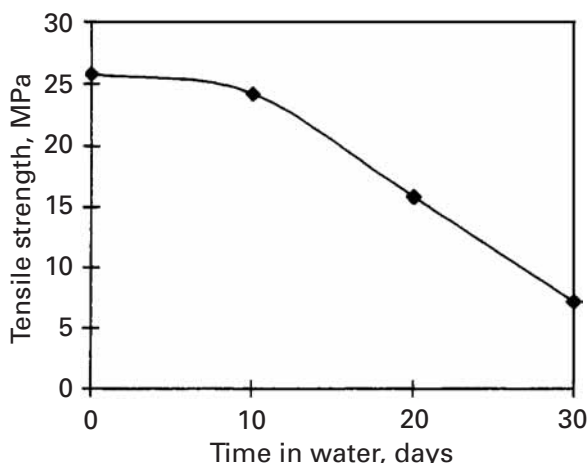


**Fig. 16.10** Decrease in glass transition temperature of polymethyl methacrylate as a function of increasing volume fraction of the plasticizer diethyl phthalate. (After F. N. Kelly and F. Bueche, *J. Polymer Sci.*, 50 (1961) 549.)

<sup>18</sup> F. N. Kelly and F. Bueche, *J. Polymer Sci.*, 50 (1961) 549.

<sup>19</sup> D. L. Faulkner, M. G. Wyzgorski, and M. E. Myers, in *The Effects of Hostile Environments on Coatings and Plastics*, D. P. Garner and G. A. Stahl (eds), American Chemical Society, Washington, DC, 1983.

**Fig. 16.11** Tensile strength loss of polyurethane aged in water at 80 °C. (After D. L. Faulkner, M. G. Wyzgoski, and M. E. Myers, in *The Effects of Hostile Environments on Coatings and Plastics*, D. P. Garner and G. A. Stahl, eds. (Washington, DC: American Chemical Society, 1983.)



More dangerous is ozone, sometimes present in the atmosphere but always in the outer space because ozone is much more reactive than oxygen. Oxygen can permeate a polymer and increase cross-linking, thereby decreasing its toughness and flexibility. Ozone attacks any elastomer with unsaturated bonds. This is especially important in rubbers and elastomers where cracking on the surface results after prolonged exposure to air. Most of us have experienced this type damage to the sidewalls of automobile tires.

#### 16.5.4 Radiation Damage

Radiation (ultraviolet, X-rays or other energetic particles such as neutrons) can lead to ionization, which can result in breaks in polymeric chains, called chain scission. (See Figure 16.12 for a schematic of this phenomenon.) Carbon–carbon (C–C) bonds form the backbone of polymers. Such bonds, however, can be ruptured by ultraviolet (UV) radiation. Rupture of molecular bonds in polymers (not in metals and ceramics) by UV radiation is commonly manifested as discoloration and loss of mechanical properties. Bond rupture can cause changes in molecular weight, degree of cross-linking, reaction with oxygen. Physical changes such as discoloration, surface embrittlement, cracking, and loss of strength are other manifestations of radiation damage in polymers. Effect of exposure to UV radiation on tensile strength of high density polyethylene is shown in Figure 16.13.<sup>20</sup> Tensile strength decreases with UV exposure time. UV exposure results in smaller molecules as well as a change in the molecular weight distribution,  $M_w$ . Consequently, mechanical properties such as strength are reduced. UV aids oxidation attack of a polymer. The term photodegradation is used to describe the damage caused by photooxidation and weathering, biodegradation, and hydrolysis. In an elastomer, there are many unsaturated double bonds along the carbon backbone.

<sup>20</sup> G. R. Rugger, in *Environmental Effects on Polymeric Materials*, vol. I, D. V. Rosato and R. T. Schwartz, eds. (New York: Interscience, 1968), p. 339.

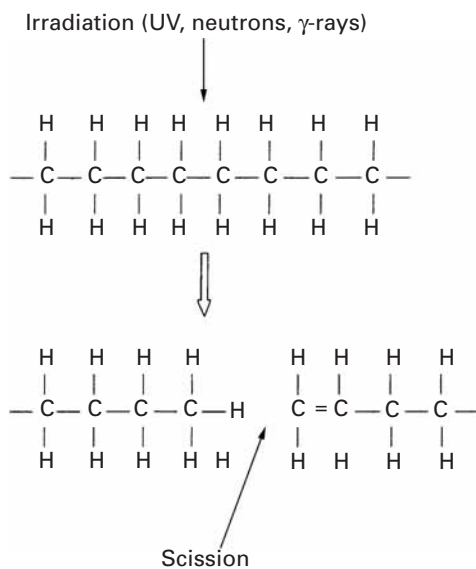


**Fig. 16.12** Effect of exposure to UV radiation on tensile strength of high density polyethylene. Tensile strength decreases with UV exposure time. (After G. R. Rugger, in *Environmental Effects on Polymeric Materials*, vol. I, D. V. Rosato and R. T. Schwartz, eds. (New York: Interscience, 1968, p. 339.)

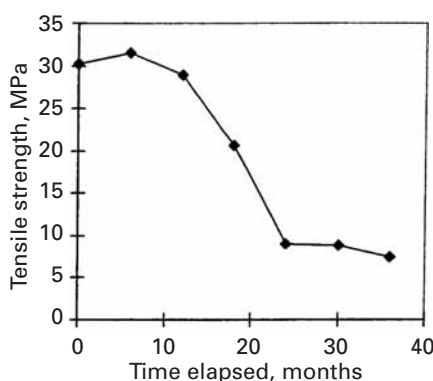


**Fig. 16.13** Decrease in tensile strength with exposure to UV radiation in high density polyethylene. (After G. R. Rugger, in *Environmental Effects on Polymeric Materials*, vol. I, D. V. Rosato and R. T. Schwartz, eds. (New York: Interscience, 1968, p. 339.)

Oxygen (or sulfur) may go to the unsaturated bond sites and provide crosslinking. Such an increase in cross-link density makes the tire strong. UV absorbing pigments (e.g., carbon black,  $\text{TiO}_2$ ) are commonly used to alleviate this problem.

### 16.5.5 Environmental Crazing

In general, environmentally induced crazes have a faster growth rate and grow to sizes much larger than those grown in inert environments. Certain organic liquids act as crazing and cracking agents. For example, the crazes shown in Figure 8.42 in a sample of polycarbonate, were produced under dead load in a specimen of polycarbonate immersed in alcohol, which is a good crazing agent. The problem, however, is much more complex than might appear at the first sight, particularly in glassy polymers. Organic liquids which act as cracking or crazing agents can also raise the toughness of the polymer, i.e., the crack propagation rate is slowed down. For example, cracks propagate in a stable manner in PMMA in air. In the presence of methanol, a crazing agent, cracks grow in a stick-slip manner reminiscent of the

behavior of thermosetting polymers in inert environments. The stick-slip mode of crack growth occurs in thermosets because of crack blunting due to shear yielding. In PMMA, however, the crazing agent causes multiple crazing at the crack tip and blunts the crack.<sup>21</sup> Thus, multiple craze formation can lead to an enhanced toughness.

Although the organic liquids can cause a reduction of the surface energy, it would appear that the plasticizing effects connected with the absorption of the crazing agents into the polymer on a molecular scale are more important. Most organic liquids generally diffuse rather slowly in a bulk polymer. The same organic liquids might penetrate rapidly in a craze and plasticize it. This is because the crazed volume in a polymer is highly porous and has a high surface area to volume ratio. Even a very short diffusion time can plasticize the drawn out polymer chains in the craze, i.e., a drop in the  $T_g$  will occur and it will become easier plastically to draw more polymer into fibrils at the craze surface.

#### 16.5.6 Alleviating the Environmental Damage in Polymers

Additives or coatings may be introduced to thermoplastic materials to promote resistance to certain adverse environmental affects. Additives are usually introduced during the mixing and processing of thermoplastics while coatings are applied after the thermoplastic has been consolidated or processed.

Antioxidants and stabilizers are added to polymers. A well known household example is butylated hydroxytoluol (BHT), which is added to food products to prevent oxidation. Antioxidants help a polymer retain its properties and thus provide a proper service life. Carbon black is a commonly used additive to stabilize polyolefins and other polymers against UV degradation. The UV resistance is very dependent on the amount, type, and particle size of the carbon black used. Carbon black particles of small size provide the greatest UV resistance but they tend to agglomerate into aggregates clusters.<sup>22</sup>

Antiozonants are additives that protect an elastomer against attack by ozone. Physical and chemical antiozonants (for example, derivatives of *p*-phenylenediamine (*p*-PDA) are used to protect rubber.

---

### 16.6 | Environmental Effects in Ceramics

Ceramics, especially the crystalline and fully dense variety, are quite inert compared to metals and polymers. This conventional wisdom about the refractoriness of ceramics notwithstanding, it turns out that moisture can be quite a damaging species, especially to silica-based glass. For example, identical glass fibers are three times stronger when tested in vacuum than in moist air. In vacuum, freshly drawn

---

<sup>21</sup> A. J. Kinloch and R. J. Young, *Fracture Behavior of Polymers*, (London: Elsevier, 1985), p. 79.

<sup>22</sup> W. L. Hawkins, M. A. Worthington, and F. H. Winslow, *Rubber Age*, 88 (1960) 279.

glass fibers can show strength as high as 14 GPa, among the strongest of all materials. Exposure to ambient air for periods of two to three weeks will reduce this strength to about 5 GPa. This effect has been known for a long time. American Indians would soak their flint stones in water before fracturing them for making arrowheads. Artisans would wet scratches made into glass with saliva prior to fracturing.

Figure 16.14 shows the effect of increasing vapor pressure of water on crack propagation in a Hertzian contact fracture test on soda-lime glass.<sup>23</sup> This figure shows the plot of crack velocity as a function of crack extension force for different vapor pressure values. Liquid water is the most active promoter of crack growth in glass, as indicated by line A in Figure 16.14. As the water vapor pressure decreases, the crack velocity vs. crack extension force curves shift to the right from B to E. Not unexpectedly, different chemicals have different effects.

Commonly, the fall in strength as a function of time in an aggressive environment in the ceramic literature is referred to as static fatigue. Figure 16.15 illustrates the phenomenon of static fatigue for glass, i.e., failure occurs under a constant applied stress lower than the tensile stress to cause failure. The drop in strength is greater under moist conditions than under dry conditions. Mechalske and Bunker<sup>24</sup> studied the effect of moisture on glass in detail. The phenomenon is referred to in the literature as *stress corrosion cracking of glass*. The water molecule can penetrate to the crack tip, where it attaches itself to the silica molecules (Figure 16.16(a)). The silica molecule hydrolyzes in the presence of moisture as per



As described in Chapter 1, the silica tetrahedra are the basic building blocks of the structure of glass. The water molecule, shown floating at the crack tip, attaches itself to two silica tetrahedra (Figure 16.16(b)). This decreases the bond strength of silica by about 20-fold and allows a much smaller applied stress to break the ring of silica tetrahedra. The process repeats itself; with water molecules penetrating the crack tip region and weakening the bonds as shown in Figure 16.16(c). A remarkable experimental evidence of this interaction of water with silica at the crack tip is shown in Figure 16.17. The low magnification optical micrograph shows a vivid proof of condensation caused by moisture at a crack tip in glass. The viscous nature of the crack-tip condensate indicates a chemical reaction between water and the glass. The effect of other molecules is not so drastic and depends on their size and reactivity.

Wiederhorn<sup>25</sup> modeled the effect of humidity on crack propagation velocity in a soda-lime glass. He treated the corrosion reaction at the crack tip to be an interfacially controlled process with

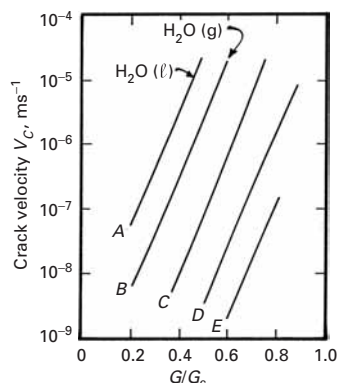


**Fig. 16.14** Crack velocity as a function of crack extension force for different vapor pressure values in a soda-lime glass. As the water vapor pressure decreases, the crack velocity vs. crack extension force curves shift to the right. Liquid water is the most active promoter of crack growth in glass, line A. (After M. V. Swain and B. R. Lawn, *Int. J. Fract. Mech.*, 9 (1973) 481.)

<sup>23</sup> M. V. Swain and B. R. Lawn, *Int. J. Fract. Mech.*, 9 (1973) 481.

<sup>24</sup> T. A. Mechalske and B. Bunker, *Sci. American*, 257 (No. 6) (1987) 122.

<sup>25</sup> S. M. Wiederhorn, *J. Amer. Ceram. Soc.*, 50 (1967) 407.

**Fig. 16.15** Schematic of static fatigue in fused silica and soda-lime glass. Although fused silica has a higher strength than soda-lime glass, both show a fall in strength as a function of time in an aggressive environment.

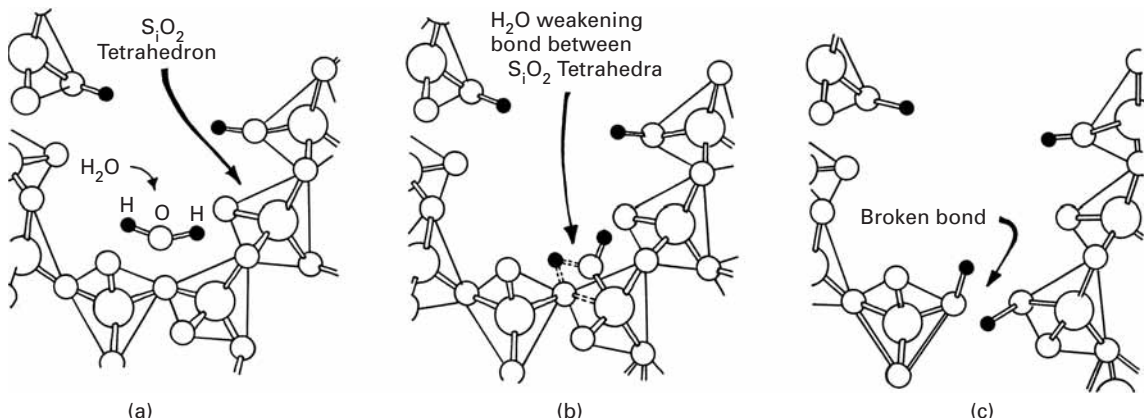
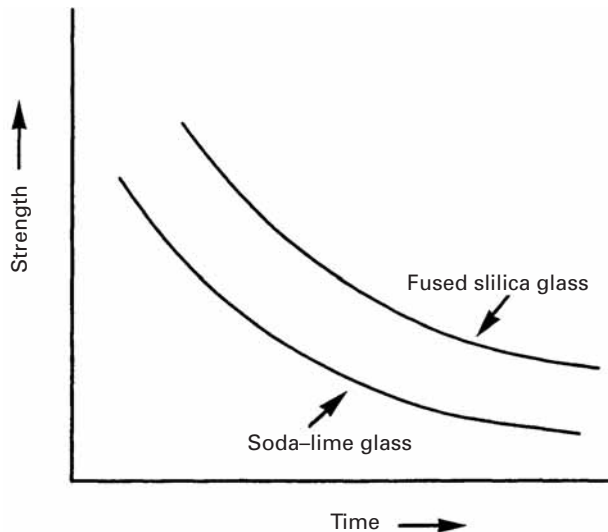
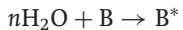


**Fig. 16.16** Interaction of the water molecule with silica at the crack tip. (a) The water molecule attaches itself to the silica molecules. (b) The water molecule, shown floating at the crack tip, attaches itself to two silica tetrahedra. (c) The process repeats itself, with water molecules penetrating the crack-tip region and weakening the bonds. (After T. A. Mechalske and B. Bunker, *Sci. American*, 257 (No. 6) (1987) 122.)

stress-dependent activation energy. The final expression for the crack velocity is

$$v = C \times^n \exp bK$$

where  $C$  is the mole fraction of water vapor at the crack tip,  $n$  is the number of water molecules of water reacting with a bond  $B$ :



and forming an activated complex  $B^*$ .  $K$  is the stress intensity factor and  $b$  is a constant. Thus, crack velocity,  $v$  increases as  $\exp bK$  and linearly with  $C$ . The factor  $C$  is a function of the water vapor pressure.

Alumina is also affected by the presence of moisture. Figure 16.18 shows the crack velocity as a function of applied force.<sup>26</sup> The test was done on a cantilever beam specimen at different relative humidities. The sapphire (single-crystal alumina) specimen was precracked along

<sup>26</sup> S. M. Wiederhorn, *Int. J. Fract. Mech.*, 4 (1968) 171.

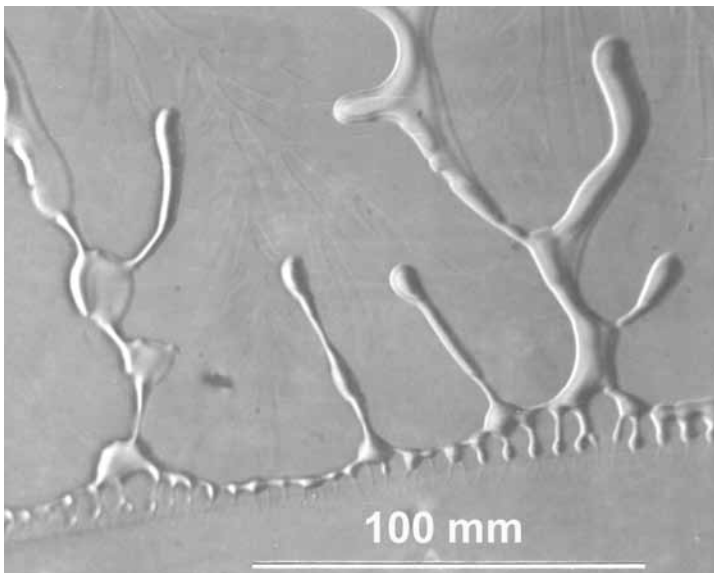


**Fig. 16.17** Condensation caused by moisture at a crack tip in glass. Note the viscous nature of the crack-tip condensate, indicating a chemical reaction between water and the glass. (Courtesy of S. Wiederhorn.)

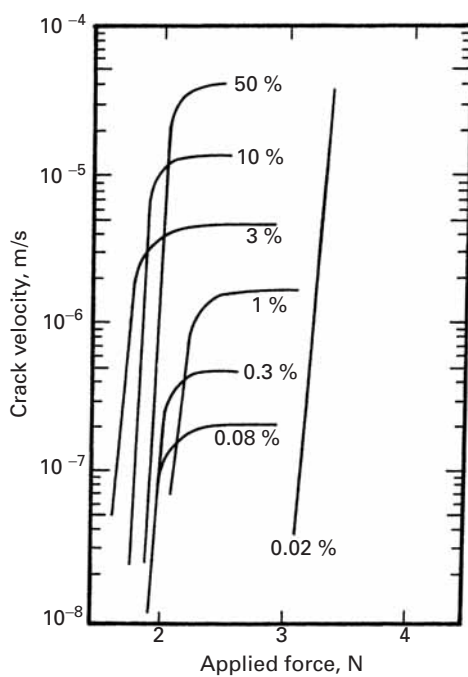


**Fig. 16.18** Crack velocity as a function of applied force in sapphire (single-crystal alumina) for different relative humidities. (After S. M. Wiederhorn, *Int. J. Fract. Mech.*, 4 (1968) 171.)

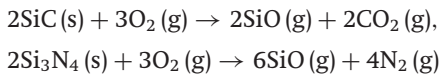
the (1011) rhombohedral plane. This is the plane that has the lowest surface energy in sapphire. The crack velocity values reach a plateau, the values of these plateaux increase with increasing humidity. The data points for 0.02% humidity are on a line that is nearly vertical.

### 16.6.1 Oxidation of Ceramics

Oxide ceramics such as alumina, mullite, silica, etc. are inherently stable in oxidizing atmospheres. That is the reason oxides such as silicates, aluminates, etc. are abundant in the earth's crust. Nonoxide

ceramics such silicon carbide, silicon nitride, molybdenum disilicide, etc. invariably have a surface layer. They tend to get oxidized at high temperatures in air.

One can represent the oxidation of structural ceramics such as SiC and  $\text{Si}_3\text{N}_4$  at low oxygen partial pressures ( $\leq 140 \text{ Pa}$ ) by the following reactions:



In a vacuum, or an inert atmosphere, silica can degrade by



Catastrophic oxidation can occur for some ceramics in the 300–700 °C range. In the literature this has been referred to as the *pesting* phenomenon.  $\text{MoSi}_2$  has excellent oxidation resistance outside the pesting range because a protective layer of  $\text{SiO}_2$  forms. This silica layer can protect  $\text{MoSi}_2$  to 1000 °C.

## Suggested Reading

- S. Al-Malaika, “Oxidative degradation and stabilisation of polymers,” *Intl. Mater. Rev.*, 48 (2003) 165.
- H. Arup and R. N. Parkins, (eds.), *Stress Corrosion*. Alphen aan den Rijn, The Netherlands: Sijhoff & Noordhoff, 1979.
- I. M. Bernstein and A. W. Thompson, eds. *Hydrogen Effects in Metals*. Warrendale, PA: TMS-AIME, 1981.
- M. R. Louthan, R. P. McNitt, and R. D. Sisson, eds. *Environmental Degradation of Engineering Materials in Hydrogen*. Blacksburg, VA: Virginia Tech Printing Dept., 1981.
- H. G. Nelson, in *Treatise on Materials Science and Technology*, vol. 25. New York, NY: Academic Press, 1983, p. 275.
- D. Talbot and J. Talbot, *Corrosion Science and Technology*. Boca Raton, FL: CRC Press, 1998.

## Exercises

**16.1** Steel products are commonly protected by chromium or zinc coatings. Based on the galvanic series, what difference would you expect in their ability to protect steel?

**16.2** Explain why a small anode/cathode area ratio will result in a higher corrosion rate.

**16.3** Alclad aluminum consists of a thin layer (5–10% of total thickness) of one Al alloy metallurgically bonded to the core alloy. Generally, the cladding layer is anodic to the core. Why?

**16.4** Tinplate (commonly used in the canning industry) is not plate or sheet of tin. It is actually a steel strip with a thin coating of tin. Discuss the pros and cons of using tin to protect steel.

**16.5** Describe how galvanizing (coating steel with zinc) works as a cathodic protection for steel.

**16.6** Describe some methods of protecting the inside of a metallic pipe against chemical attack.

**16.7** A form of corrosion called pitting corrosion can occur in aluminum in fresh water. As the name suggests, pits form on the surface of aluminum in this type of corrosion. The pit depth,  $d$  follows a cube root relationship time,  $t$ :

$$d = A t^{1/3}.$$

Normally, a  $5 \mu\text{m}$  thick  $\text{Al}_2\text{O}_3$  film forms on the surface of aluminum. If we double the thickness of the film, by what factor will the time to perforation increase?

**16.8** Structural ceramic materials such as  $\text{SiC}$ ,  $\text{Si}_3\text{N}_4$ ,  $\text{MoSi}_2$ , etc. oxidize in the presence of oxygen at high temperatures. Give the oxidation reactions and indicate how the reaction products serve to protect these materials from further oxidation. Does it have deleterious effect on the high temperature capability of these materials?

**16.9** A Ni-based superalloy has  $0.2 \mu\text{m}$  thick oxide layer. When placed in a burner rig to test for oxidation, it was observed to grow to  $0.3 \mu\text{m}$  in 1 h. If the superalloy follows a parabolic oxidation law ( $x^2 = a + bt$ , where  $x$  is the thickness,  $t$  is the time, and  $a$  and  $b$  are constants) what is the thickness after one week?

**16.10** The velocity of a crack in a material submerged in an aggressive medium such as humid air can be represented by:

$$V = \frac{da}{dt} = 0.5K_I^{20}.$$

Using the relationship  $K_I = \sigma \sqrt{\pi a}$ , compute the time to failure for this material.  $K_{Ic}$  for the material is  $5 \text{ MPa m}^{1/2}$ .

**16.11** For a silica-based glass, the following data are available for a  $V = A k_1^n$  type of relationship:

Relative humidity	Preexponential constant $A$	Crack velocity exponent $n$
10%	2.8	25
100%	4.0	22

Take  $K_{Ic} = 1 \text{ MPa m}^{1/2}$ . For a crack length  $a = 1 \text{ nm}$ , compute the fracture strength  $\sigma_c$  in an inert atmosphere. Then compute the lifetime of the material under  $0.3\sigma_c$  in 10% and 100% relative humidity.

**16.12** The stable, slow crack growth in a polymer in an aggressive environment can be represented by:

$$\frac{da}{dt} = 0.03K_I^2,$$

where  $a$  is the crack length in meters,  $t$  is the time in seconds, and  $K_I$  is the stress intensity factor in MPa m<sup>1/2</sup>.  $K_{Ic}$  for this polymer is 5 MPa m<sup>1/2</sup>. Calculate the time to failure under a constant applied stress of 50 MPa. Use  $K_I = \sigma\sqrt{\pi a}$ .

**16.13** It has been observed experimentally that, in cold-worked brass under stress-corrosion conditions, crack propagation is adequately described by:

$$\frac{da}{dt} = AK^2,$$

where  $A$  is a constant and the other symbols have their normal significance. Derive an expression for the time to failure of the material,  $t_f$ , in terms of  $A$ , the applied stress  $\sigma$ , the initial crack length  $a_0$ , and the critical stress intensity corresponding to  $a_f$  (i.e.,  $K_{Ic}$ ).

---

## Appendices

## UNIT CONVERSION FACTORS

*Length*

$1 \text{ m} = 10^{10} \text{ \AA} = 0.1 \text{ nm}$	$1 \text{ \AA} = 10^{-10} \text{ m}$
$1 \text{ mm} = 0.0394 \text{ in.}$	$1 \text{ in} = 25.4 \text{ mm}$
$1 \text{ cm} = 0.394 \text{ in.}$	$1 \text{ in} = 2.54 \text{ cm}$
$1 \text{ m} = 3.28 \text{ ft}$	$1 \text{ ft} = 0.3048 \text{ m}$

*Mass*

$1 \text{ Mg} = 10^3 \text{ kg}$	$1 \text{ kg} = 10^{-3} \text{ Mg}$
$1 \text{ kg} = 10^3 \text{ g}$	$1 \text{ g} = 10^{-3} \text{ kg}$
$1 \text{ kg} = 2.205 \text{ lb}_m$	$1 \text{ lb}_m = 0.4536 \text{ kg}$
$1 \text{ g} = 2.205 \times 10^{-3} \text{ lb}_m$	$1 \text{ lb}_m = 453.6 \text{ g}$

*Density*

$1 \text{ kg/m}^3 = 10^{-3} \text{ g/cm}^3$	$1 \text{ g/cm}^3 = 10^3 \text{ kg/m}^3$
$1 \text{ kg/m}^3 = 0.0624 \text{ lb}_m/\text{ft}^3$	$1 \text{ lb}_m/\text{ft}^3 = 16.02 \text{ kg/m}^3$
$1 \text{ g/cm}^3 = 62.4 \text{ lb}_m/\text{ft}^3$	$1 \text{ lb}_m/\text{ft}^3 = 1.602 \times 10^{-2} \text{ g/cm}^3$
$1 \text{ g/cm}^3 = 0.0361 \text{ lb}_m/\text{in.}^3$	$1 \text{ lb}_m/\text{in.}^3 = 27.7 \text{ g/cm}^3$

*Force*

$1 \text{ N} = 10^5 \text{ dynes}$	$1 \text{ dyne} = 10^{-5} \text{ N}$
$1 \text{ N} = 0.2248 \text{ lb}_f$	$1 \text{ lb}_f = 4.448 \text{ N}$

*Stress*

$1 \text{ MPa} = 145 \text{ psi}$	$1 \text{ psi} = 6.90 \times 10^{-3} \text{ MPa}$
$1 \text{ MPa} = 0.102 \text{ kg/mm}^2$	$1 \text{ kg/mm}^2 = 9.806 \text{ MPa}$
$1 \text{ Pa} = 10 \text{ dynes/cm}^2$	$1 \text{ dyne/cm}^2 = 0.10 \text{ Pa}$
$1 \text{ kg/mm}^2 = 1422 \text{ psi}$	$1 \text{ psi} = 7.03 \times 10^{-4} \text{ kg/mm}^2$

*Fracture Toughness*

$$1 \text{ psi in}^{1/2} = 1.099 \times 10^{-3} \text{ MPa m}^{1/2} \quad 1 \text{ MPa m}^{1/2} = 910 \text{ psi in}^{1/2}$$

*Energy*

$1 \text{ J} = 10^7 \text{ ergs}$	$1 \text{ erg} = 10^{-7} \text{ J}$
$1 \text{ J} = 6.24 \times 10^{18} \text{ eV}$	$1 \text{ eV} = 1.602 \times 10^{-19} \text{ J}$
$1 \text{ J} = 0.239 \text{ cal}$	$1 \text{ cal} = 4.184 \text{ J}$
$1 \text{ J} = 9.48 \times 10^{-4} \text{ Btu}$	$1 \text{ Btu} = 1054 \text{ J}$
$1 \text{ J} = 0.738 \text{ ft-lb}_f$	$1 \text{ ft-lb}_f = 1.356 \text{ J}$
$1 \text{ eV} = 3.83 \times 10^{-20} \text{ cal}$	$1 \text{ cal} = 2.61 \times 10^{19} \text{ eV}$
$1 \text{ cal} = 3.97 \times 10^{-3} \text{ Btu}$	$1 \text{ Btu} = 252.0 \text{ cal}$

*Power*

$1 \text{ W} = 0.239 \text{ cal/s}$	$1 \text{ cal/s} = 4.184 \text{ W}$
$1 \text{ W} = 3.414 \text{ Btu/h}$	$1 \text{ Btu/h} = 0.293 \text{ W}$
$1 \text{ cal/s} = 14.29 \text{ Btu/h}$	$1 \text{ Btu/h} = 0.070 \text{ cal/s}$

## UNIT CONVERSION FACTORS (cont.)

## Viscosity

$$1 \text{ Pa s} = 10 \text{ P}$$

$$1 \text{ P} = 0.1 \text{ Pa s}$$

## Temperature, T

$$T(\text{K}) = 273 + T(\text{°C})$$

$$T(\text{°C}) = T(\text{K}) - 273$$

$$T(\text{K}) = \frac{5}{9}[T(\text{°F}) - 32] + 273$$

$$T(\text{°F}) = \frac{9}{5}[T(\text{K}) - 273] + 32$$

$$T(\text{°C}) = \frac{9}{5}[T(\text{°F}) - 32]$$

$$T(\text{°F}) = \frac{9}{5}[T(\text{°C}) + 32]$$

## Specific Heat

$$1 \text{ J/kg-K} = 2.39 \times 10^{-4} \text{ cal/g-K}$$

$$1 \text{ cal/g-}^{\circ}\text{C} = 4184 \text{ J/kg-K}$$

$$1 \text{ J/kg-K} = 2.39 \times 10^{-4} \text{ Btu/lb}_m\text{-}^{\circ}\text{F}$$

$$1 \text{ Btu/lb}_m\text{-}^{\circ}\text{F} = 4184 \text{ J/kg-K}$$

$$1 \text{ cal/g-}^{\circ}\text{C} = 1.0 \text{ Btu/lb}_m\text{-}^{\circ}\text{F}$$

$$1 \text{ Btu/lb}_m\text{-}^{\circ}\text{F} = 1.0 \text{ cal/g-K}$$

## STANDARD PREFIXES, SYMBOLS, AND MULTIPLICATION FACTORS

Prefix	Symbol	Factor by Which Unit Has to Be Multiplied
Tera	T	$10^{12}$
Giga	G	$10^9$
Mega	M	$10^6$
Kilo	k	$10^3$
Hecto	h	$10^2$
Deca	da	$10^1$
Deci	d	$10^{-1}$
Centi	c	$10^{-2}$
Milli	m	$10^{-3}$
Micro	$\mu$	$10^{-6}$
Nano	n	$10^{-9}$
Pico	p	$10^{-12}$
Femto	f	$10^{-15}$
Atto	a	$10^{-18}$

## IMPORTANT CHARACTERISTICS OF SOME ELEMENTS

Symbol	Atomic Number	Atomic Weight (amu)	Density of Solid, 20 °C (g/cm³)	Crystal Structure, 20 °C	Atomic Radius (nm)	Ionic Radius (nm)	Most Common Valence	Melting Point (°C)
Al	13	26.98	2.70	FCC	0.143	0.053	3+	660.4
Ar	18	39.95	—	—	—	—	Inert	-189.2
Ba	56	137.33	3.5	BCC	0.217	0.136	2+	725
Be	4	9.012	1.85	HCP	0.114	0.035	2+	1278
B	5	10.81	2.34	Rhomb.	—	0.023	3+	2300
Br	35	79.90	—	—	—	0.196	1-	-7.2
Cd	48	112.41	8.65	HCP	0.149	0.095	2+	321
Ca	20	40.08	1.55	FCC	0.197	0.100	2+	839
C	6	12.011	2.25	Hex.	0.071	~0.016	4+	(sublimes at 3367)
Cs	55	132.91	1.87	BCC	0.265	0.170	1+	28.4
Cl	17	35.45	—	—	—	0.181	1-	-101
Cr	24	52.00	7.19	BCC	0.125	0.063	3+	1875
Co	27	58.93	8.9	HCP	0.125	0.072	2+	1495
Cu	29	63.55	8.96	FCC	0.128	0.096	1+	1084
F	9	19.00	—	—	—	0.133	1-	-220
Ga	31	69.72	5.90	Ortho.	0.122	0.062	3+	29.8
Ge	32	72.59	5.32	Dia. cubic	0.122	0.053	4+	937
Au	79	196.97	19.3	FCC	0.144	0.137	1+	1064
He	2	4.003	—	—	—	—	Inert	-272 (at 26 atm)
H	1	1.008	—	—	—	0.154	1+	-259
I	53	126.91	4.93	Ortho.	0.136	0.220	1-	114
Fe	26	55.85	7.87	BCC	0.124	0.077	2+	1538
Pb	82	207.2	11.35	FCC	0.175	0.120	2+	327
Li	3	6.94	0.534	BCC	0.152	0.068	1+	181
Mg	12	24.31	1.74	HCP	0.160	0.072	2+	649
Mn	25	54.94	7.44	Cubic	0.112	0.067	2+	1244
Hg	80	200.59	—	—	—	0.110	2+	-38.8
Mo	42	95.94	10.22	BCC	0.136	0.070	4+	2617
Ne	10	20.18	—	—	—	—	Inert	-248.7
Ni	28	58.69	8.90	FCC	0.125	0.069	2+	1453
Nb	41	92.91	8.57	BCC	0.143	0.069	5+	2468
N	7	14.007	—	—	—	0.01–0.02	5+	-209.9
O	8	16.00	—	—	—	0.140	2-	-218.4
P	15	30.97	1.82	Ortho.	0.109	0.035	5+	44.1
Pt	78	195.08	21.45	FCC	0.139	0.080	2+	1772
K	19	39.10	0.862	BCC	0.231	0.138	1+	63
Si	14	28.09	2.33	Dia. cubic	0.118	0.040	4+	1410
Ag	47	107.87	10.5	FCC	0.144	0.126	1+	962
Na	11	22.99	0.971	BCC	0.186	0.102	1+	98
S	16	32.06	2.07	Ortho.	0.106	0.184	2-	113
Sn	50	118.69	7.3	Tetra.	0.151	0.071	4+	232
Ti	22	47.88	4.51	HCP	0.145	0.068	4+	1668
W	74	183.85	19.3	BCC	0.137	0.070	4+	3410
V	23	50.94	6.1	BCC	0.132	0.059	5+	1890
Zn	30	65.39	7.13	HCP	0.133	0.074	2+	420
Zr	40	91.22	6.51	HCP	0.159	0.079	4+	1852

Adapted from W. D. Callister, *Materials Science and Engineering*. New York, NY John Wiley & Sons, 1997.

MECHANICAL PROPERTIES OF SOME IMPORTANT CERAMIC MATERIALS

	Weibull modulus	Flexural strength (MPa)	Young's modulus (GPa)	Poisson's ratio	Compressive strength (MPa)	Hardness (HV)	Tensile strength (MPa)	Fracture toughness (MPa m <sup>1/2</sup> )
Silicon Nitride	20	930	320	0.28	2100–3500	1800	350–415	6
Silicon Carbide	18	634	450	0.17	1035–1725	2300	390–450	43
Aluminum Nitride	10	200	320	0.22	1400–2100	1110	—	3
Tungsten Carbide	—	1930	627	0.21	2683	1600	344	—
Titanium Oxide	—	137	228	0.27	688	800	51.6	32
MgO stabilized Zirconia	—	620	200	0.3	1750	1200	352	11
Aluminum Oxide (98%)	10	300	340	0.22	2500	1800	150	4
Aluminum Oxide (99%)	10	400	370	0.22	3000	1800	180	4
Zirconia toughened alumina (ZTA)	13	912	285	0.25	—	1500	—	6.9
Boron Carbide	12	450	450	0.27	470	2700	—	30
Titanium Diboride	11	277	556	0.11	470	2700	—	6.9
Zirconia	15	800–1200	—	0.28	2000	1200	—	6–8

Note: the values given are indicative only

MECHANICAL PROPERTIES OF SOME IMPORTANT METALS AND ALLOYS								
Alloy	Density (kg/m <sup>3</sup> )	M.P. (°C)	Young's modulus (GPa)	Poisson's ratio	UTS (MPa)	Yield strength (MPa)	Strain-to- failure (%)	Fracture toughness MPa m <sup>1/2</sup>
Al 2024-T 85 I	2770	502	72.4	0.33	455	400	5	26.4
Al 7075-T 65 I	2810	477	72	0.33	570	505	11	24.2
Al 7178-T65 I	2830	477–629	73	0.33	605	540	10	23.1
Ti-6Al-4V (grade 5)	4430	1604–1660	113.8	0.342	1860	1480	14	55
Ti-3Al-2.5V (alpha annealed)	4480	1700	100	0.3	620	500	15	100
702 Zirconium	6500	1852	99.3	0.35	379	207	16	—
60–40 Soft solder	8600	183–190	30	0.4	53	—	—	—
Stainless steel 4340	7850	—	205	—	745	470	22	60.4
Stainless steel 304	8000	1400	193	0.29	505	215	70	—
Steel 5160	7850	—	205	—	724	275	17.2	—
Tool steel H 11 hot worked	7800	—	210	—	1990	1650	9	—
Maraging steel (18 Ni) (before aging)	8000	—	183	—	965	660	17	—
Maraging steel (18 Ni) (annealed & aged at 480 °C)	8080		200	—	1864	1737	17.4	—
Superalloy CoCrWNi	10000	—	—	—	860	310	10	—
Superalloy Fe based N08330 Ni	8000	—	—	—	586	276	40	—
Superalloy H-X Nickel	8220	—	—	—	690	276	40	—

Note: the values given are indicative only

**MECHANICAL PROPERTIES OF SOME IMPORTANT POLYMERIC MATERIALS**

	Density (g cm <sup>-3</sup> )	Young's modulus (MPa)	Tensile strength (MPa)	Strain-to- fracture (%)	Yield stress (MPa)	Yield strain	Rockwell hardness	Izod impact Energy J/m
<i>Thermoplastics</i>								
Cellulose acetate(soft)	1.27-1.34	593-1723	13-32	32-50	15-28	-	R49-R103	100-270
Cellulose acetate (hard)	1.27-1.34	1309-2757	31-58	6-40	28-52	-	R101-R123	3140-5060
Cellulose acetate butyrate (soft)	1.15-1.22	510-868	13-26	60-74	8.2-17	-	R59-R95	130-290
Cellulose acetate butyrate (hard)	1.19-1.25	1034-1378	34-46	38-54	24-42	-	R108-R117	38-130
Nylon 6/6	1.13-1.25	-	62-82	60-300	-	-	R108-R120	50-100
Polycarbonates (unfilled)	1.2	2000-2240	55-65	20-100	55-68	-	M70-M180	430-850
Polyethylene (low density)	0.91-0.925	96-260	6.9-9.6	400-700	7.5-11.7	20-40	-	-
Polyethylene (medium density)	0.926-0.941	240-620	8.2-24.1	50-600	10.3-17.9	10-20	R30-R50	26-850
Polyethylene (high density)	0.941-0.965	590-1110	21-37	15-100	16.5-34.4	5-10	M80-M105	80-1050
Methylmethacrylate (PMMA unmodified)	1.18-1.20	2410-3450	48-75	2-10	-	-	M6-32	-
Polypropylene (unmodified)	0.9	9.65-11.8	29-37	>220	33.8	15	93	53
Polypropylene (copolymer)	0.9	-	19-31	200-700	-	-	R50-R96	58-64
Polystyrene (unmodified)	1.04-1.08	2750-4140	34-68	1-2.5	-	-	M65-M85	13-32
PTFE (unmodified)	2.1-2.3	1030	31-41	250	29	10	J75-J95	130-210
<i>Thermosetting</i>								
Epoxy (unfilled)	1.115	2070	27-89	2-6	-	-	M75-M110	10-50
Melamine formaldehyde	1.47-1.52	8960	48-90	0.6-0.9	-	-	M110-M124	12-18
Polyester (glass fiber mat reinforced)	1.5-2.1	3450	206-344	.5-1.5	-	-	M80-M120	370-1600
Silicones (mineral filled)	1.8-2.8	-	20-27	-	-	-	M85-M95	13-18
Urea formaldehyde ( $\alpha$ -cellulose filled)	1.47-1.52	8970	37-89	0.6	-	-	E94-E97	12-20
ABS (high-heat resistant)	1.06-1.08	-	48-62	1-20	28-62	-	R110-R115	100-210

Note: the values given are indicative only



---

# Index

abalone 41, 806–8  
alpha-helix 49, 50  
aorta 242  
abductin 53  
activation energy 657, 661, 662, 665, 666, 673  
actin 4, 52  
active materials 57  
adhesion  
  thin films to substrates 552, 553  
adiabatic curve 394, 395  
adiabatic heating 192  
adiabatic shear bands 395, 396  
amino acids 48–50  
anelasticity 74, 120  
anisotropy 96, 213, 396, 799  
annealing point 197, 198  
antiphase boundary 624, 625, 628, 631  
ARALL *see* composites  
articular cartilage 137  
atactic polymer *see* polymer  
atomic point defects 25; *see also* point defects  
  
barreling 185, 186  
Bauschinger effect 187, 188  
Berg-Barrett topography 270  
beta sheet 49, 50  
biaxial test 162, 203, 208, 210, 212, 213, 230  
bicycle frame  
  materials 11–15  
biocompatibility 7  
Bioglass® 7  
bioimplants 42  
biological materials 40–57, 241–5  
biomaterials 40–56  
biomimetics 42  
blood vessels 134  
blue brittleness 570  
bone 242–5  
  cancellous 242–5  
  cortical 242–5  
Brale indenter *see* hardness  
branched polymers *see* polymers  
Bravais lattices 16, 17  
Bridgman's correction 174, 175, 185  
Brinell indenter *see* hardness

brittle materials 1, 2, 4, 7, 8, 41, 61, 205, 293, 412, 419 420, 422, 437, 443, 449–51, 474, 480–90, 494, 500–2, 507, 513  
bubble raft 196  
Budiansky and O'Connell equation 115, 118, 158  
bulk modulus 101, 150–2  
Burgers circuit *see* dislocation  
Burgers vector *see* dislocation  
  
cartilage 242  
  articular 137  
cascade 262, 263  
cavitation 472, 473, 657, 686, 687, 702, 70; *see also* void  
cellular materials 44–6, 639–45  
cellulose 53  
Charpy impact test 526–9  
Charpy impact instrumented test 531, 532  
Chevron notch test 547  
chitin 46, 54  
cleavage 406–8, 467, 480–5, 533  
Coble creep *see* creep  
coincidence site lattice *see* grain boundaries  
cold working 369, 370, 385  
collagen 51–5, 243  
compliance 97, 99, 101, 111, 112, 118, 119, 145  
composite(s) 7–9, 76, 117, 211  
  applications 803  
aging response of matrix 785  
anisotropic nature 783  
  applications 803  
fracture 795  
  single and multiple 795  
fundamental characteristics 799  
heat capacity 775  
importance of matrix 769  
laminated 42, 121, 637, 806–9  
  abalone, 41, 806–8  
  aluminum/silicon carbide 809  
  aramid aluminum (ARALL) 807, 808  
  glass aluminum (GLARE) 807, 808  
load transfer  
  fiber and matrix elastic 789  
fiber elastic and matrix plastic 792  
matrix materials 7, 67, 765–8  
  reinforcements 765–8, 770  
compressibility 101  
compression testing 183–6  
Considère's criterion 172, 229  
controlled rolling treatment 586  
corrosion 815–19  
  crevice 817  
electrochemical nature 815  
erosion 819  
galvanic 816, 817  
intergranular 818  
pitting 818  
stress 819  
uniform 817  
Cottrell atmosphere 562, 564, 601–4  
Cottrell theory 349  
crack  
  closure 748  
  extension force 434  
  nucleation 404, 468, 679  
  opening displacement 437  
  opening displacement testing 537  
  propagation 404, 730  
  propagation testing 75  
  propagation with plasticity 419  
  tip stress field 409, 423–7, 429, 444  
crack extension force *see* crack  
crack-tip opening modes 405, 423  
crazing 210, 508, 511, 734  
creep 653  
  Coble 660–70  
  compliance 690–3  
correlation and extrapolation methods 659  
  Larson-Miller 659–63  
  Manson-Haford 661–3  
  Sherby-Dorn 659, 661–3  
dislocation 670–3  
diffusion coefficient 657, 661, 662, 666, 673, 686  
electronic materials, in 695  
fracture 678–80  
mechanisms 665–70  
Monkman-Grant equation 661, 680, 681

- creep (*cont.*)  
 Mukherjee-Bird-Dorn equation 657–9  
 Nabarro-Herring 666–70  
 polymers, in 688–93  
   Maxwell model 689, 690  
   Voigt model 689, 690  
 power law 670–3  
 rafting 683, 684  
 relaxation time 689, 690  
 rocks, in 654  
 stress relaxation 690–3  
 cross slip 288, 302, 384  
 crowdion(s) 262  
 crystal structures 16–30
- DNA molecule 48, 140  
 optical trap 140  
 damage 262, 404  
 deep drawing 204, 229, 231  
 deformation energy density 77–9  
 deformation mechanism maps 676–8  
 density 3, 4, 8, 9, 27, 28, 30, 33, 36,  
   44, 45, 63, 768, 769, 775, 785,  
   803  
 diamond pyramid hardness *see*  
   hardness  
 diffusion coefficient 657, 661, 662,  
   666, 673, 686  
 dislocation (s)  
   Argon mechanism 195, 196  
   behavior 273  
   Burgers circuit 267–9, 272, 273  
   Burgers vector 196, 252, 267–9,  
   272, 273, 275, 276, 283–288,  
   291, 294–6, 301–4, 307, 308,  
   310  
 cells 288, 385, 388–91  
 climb 259, 270, 293, 297, 305, 312  
 deformation produced by 306  
 density 281, 298, 300, 307, 308,  
   379, 384–7, 390, 769, 774  
 energy 278, 296  
   ceramics, in 296  
   intermetallics, in 296  
 edge 259, 267–71, 273, 278, 280,  
   282, 296, 302–8, 313, 314  
 experimental observation of 270–3  
 emission 420  
 forest 304, 305, 312  
 Frank partial 288, 302  
 Frank’s rule 296  
 Frank-Read source 301, 302, 672  
 force required to bow 282
- Gilman model 196  
 glassy silica, in 196  
 glide 673  
 helical 270  
 intersection, of 304  
 Johnston-Gilman equation 313  
 jogs 259, 304–8  
 Kear-Wilsdorf lock  
 kinks 304–7  
 line tension 283  
 Lomer-Cottrell lock 289, 671  
 loops 283, 274  
 misfit 313–5  
 Orowan’s equation 306–8  
 Peach-Koehler equation 282–4, 310  
 Peierls-Nabarro stress 309, 310, 312  
 pileup 302–4  
 screw 34, 259, 267, 270, 273, 275–7,  
   280, 282, 301–6, 313  
 sessile 288  
 sources 298–302  
 stair rod 290, 291, 298  
 stair way 290, 291  
 stress field 275, 278, 280, 282, 296  
 structures 624  
   ceramics 293  
   electronic materials 313  
   various structures 284  
 tangles 288, 385  
 velocity 313
- dislocation-precipitate interaction 579  
 dispersion hardening 558, 559,  
   571–3, 576, 578, 588  
 dispersion strengthening *see*  
   dispersion hardening  
 draw ratio 127, 128  
 drop weight test 529–31  
 DS cast alloys 686  
 dual-phase steels 590  
 ductile material(s) 293, 421, 438, 443,  
   449, 450, 466, 469, 474, 480,  
   481, 484  
 ductile-brittle transition 481  
   temperature 272, 481, 485, 486  
 ductility 480, 634
- earing 232  
 edge dislocation *see* dislocation  
 elastic constants  
   biological materials 134  
   ceramics 111  
   electronic materials 143  
   materials 110
- metals 111  
 polymers 116, 119  
 polycrystals 107  
 unidirectional fiber reinforced  
   composites 102, 119, 120  
 elastic constants and bonding 145–55  
 elastic interaction 560  
 elastic modulus 77, 102, 117, 126,  
   134, 144, 145, 148, 149, 775  
 biaxial 144, 145  
 elastic properties  
   polycrystals 107–10  
   materials 110–120  
 elastic wave velocity 75, 77  
 elasticity 71  
   anisotropic 96–107  
   electronic materials 143–5  
   isotropic 99–101  
   nonlinear 126–33, 135, 136  
   rubber 126–33  
 elastin 53, 243  
 elastomer 121–8, 130–1  
 electronic materials 58, 59, 143–5,  
   695  
 electromigration 696, 697  
   interaction 147  
 environmental effects 404, 748,  
   815  
   ceramics 836–40  
   crazing 835, 836  
   intermetallics 638  
   metals 815–30  
   polymers 831–6  
     alleviating damage 836  
 Erichsen test 230, 232  
 extrusion(s) 161, 213, 231, 725–9
- facture mechanism maps 521, 676–8;  
*see also* Weertman-Ashby maps  
 failure criteria 199–214  
 failure modes in composites 796  
 fatigue  
   biomaterials 744–6  
   crack closure 748, 749  
   cumulative damage 721  
   crack nucleation 725  
   crack propagation 730–4  
   damage  
     cumulative 721–3  
     extrinsic mechanisms 744  
     intrinsic mechanisms 744  
   discontinuous crack growth 734  
   environmental effects 748  
   extrusions 725–9

- frequency, effect of 721  
 hysteretic heating 746, 747  
 intrusions 725–9  
 linear elastic fracture mechanics 733–44  
 life 716, 721  
 life exhaustion 721–23  
 mechanisms 725–34  
 mean stress, effect of 719–21  
 Palmgren-Miner rule 723  
 Paris-Erdogan equation 736–46  
 parameters 714  
 persistent slip bands 725–9  
 residual stress, effect of 729, 730  
 S-N (Wöhler) curves 714, 721  
 statistical analysis 753, 754  
 short crack problem 750, 751  
 shot peening 729, 730  
 strength 716  
 striations 731–4  
 two-parameter approach 749, 750  
 fatigue testing 751  
 conventional tests 751  
 rotating bending tests, 751, 752  
 servohydraulic machines 755, 756  
 flexure 454, 526, 540–4, 546  
 flexure test 540–4  
 flow criteria 169, 199  
 flow stress 161, 167, 174, 176, 177, 187, 188, 199–201, 204, 222–4  
 temperature, function of 312  
 fluidity 122  
 foams 621  
 syntactic 645  
 Focuser 262  
 forging 161, 369, 70, 395  
 formability 229–37  
 forming-limit curves 232  
 tests 230–7  
 Keeler-Goodwin diagrams 232–7  
 four-point bending 453, 542  
 fracture 794  
 biological materials 517  
 brittle 272, 466–9, 480, 484, 486, 507, 508  
 cleavage 480–6  
 ductile 421, 438, 443, 449, 466–8, 473–8, 481, 484, 487  
 environmentally assisted 820  
 Griffith criterion 406, 409, 410, 416–21, 443  
 intergranular 484, 522  
 mechanism maps 676–8
- mechanisms and morphologies 467  
 ceramics, in 487–94  
 glass, in 490  
 metals, in 468–74  
 modes 405, 423, 424, 458  
 polymers, in 468–70, 507–16  
 fracture toughness 405, 422, 447  
 ceramics 446–7  
 metals 447  
 parameters 434–45  
 polymers 447  
 fracture toughness tests 532  
 chevron notch test 547  
 crack opening displacement test 537, 538  
 double cantilever beam test 546, 547  
 double torsion test 546, 547  
 indentation test 549–51  
 J-integral test 538, 539  
 plane strain fracture toughness tests 532–7  
 free volume 209, 210  
 Frenkel defects 255  
 friction hill 187  
 Fukui test 230, 231  
 functionally graded materials 803  
 geometry of deformation 369–84  
 GLARE *see* composites  
 glass transition temperature 4, 30, 191, 194, 197  
 glasses 30, 193–6  
 metallic 193–6  
 Argon mechanism 196, 197  
 Gilman mechanism 196  
 plastic deformation 196  
 glassy polymers 189  
 graft copolymer 32, 33  
 grain boundary  
 coincidence site lattice 331–3  
 energy 328–33  
 variation with misorientation 330–2  
 ledges 330, 334–6, 350, 351  
 packing of polyhedral units 336  
 plastic deformation 322, 340, 345–9, 351, 352  
 sliding 675, 676  
 tilt 326  
 twist 326  
 triple junctions 334  
 grain boundary dislocations 334
- grain boundary sliding 358, 675  
 grain size  
 ASTM 323–5  
 strengthening 260, 345–8, 355, 357, 358, 494, 627  
 Griffith  
 criterion for crack propagation 409–21  
 failure criterion 206–8
- habit plane *see* martensitic transformation  
 Hall-Petch relationship 346–8, 355, 357, 358, 630  
 hardness 214–23  
 Brale indenter 215, 219  
 Brinell 216–18, 219  
 diamond pyramid 219, 220, 221  
 Knoop 222, 223  
 microindentation 221–3  
 nanoindentation 225–8  
 Rockwell 218–20  
 Vickers 219, 220–3
- Harper-Dorn equation *see* creep  
 heat resisting materials 681–8  
 high strength low alloy steels 586  
 Hooke's law 75, 144, 407  
 generalized 85–7  
 hot working 369, 370  
 hydride formation 829  
 hydrogen damage  
 metals 824–30  
 theories 825–30  
 hydroxyapatite 46, 48  
 hypotheses of LEFM 423  
 hysteretic heating 746, 747
- impact testing 525  
 imperfections in polymers 361  
 imperfections, point and line defects 251  
 implants 5–7  
 indentation tests for toughness 549–51  
 independent slip systems in polycrystals 384  
 Inglis equation 410, 413, 418, 419  
 instrumented Charpy impact test 531  
 interfaces in composites 770  
 interfacial defects 321  
 interfacial bonding 772  
 interlaminar shear strength test 543  
 intermetallics 621  
 gold-based 621, 624

- intermetallics (*cont.*)  
 ordered 622–7, 633  
 dislocation structure 624–7, 633  
 ductility 634  
 environmental effects 638  
 fatigue 631  
 Hall-Petch relationship 630  
 mechanical properties 627–34  
 macroalloying 636  
 microalloying 635  
 internal obstacles 353  
 interstitial defects 254–65, 295, 305,  
   558–62, 564, 565, 567–9  
 interstitial strengthening 564, 565,  
   567–9  
 intrusions 725–9  
 ion implantation 265  
 irradiation 263  
   voids due to 263  
 isotactic polymer 33  
 isotropic hardening 204  
 Izod test 526, 529
- J-integral 439  
   testing 538  
 jogs *see* dislocations  
 Johnson-Cook equation 167  
 Johnston-Gilman equation 313
- Kear-Wilsdorf lock *see* dislocation  
 Keeler-Goodwin diagrams *see*  
   formability  
 keratin 46, 52, 243  
 kinematic hardening 187, 204  
 kinks *see* dislocation  
 knock-on 263  
 Knoop indenter 222, 223  
 Kuhlmann-Wilsdorf theory of work  
   hardening 386, 388, 390, 391
- ladder polymer 32  
 laminated composites 806; *see also*  
   composites  
 Larson-Miller parameter *see* creep  
 ledges *see* grain boundary  
 Li theory for grain size  
   strengthening 350  
 limiting draw ratio 231  
 line defects *see* dislocation  
 line tension *see* dislocation  
 linear intercept 323–5  
 linear elastic fracture mechanics  
   (LEFM) 404, 421–48, 735–46,  
   750, 821–4
- linear polymers 32, 33  
 liquid metal embrittlement 830,  
   831  
 liquid crystal(s) 39–41  
 logarithmic decrement 125  
 Lomer-Cottrell lock *see* dislocation  
 loops *see* dislocation  
 loss modulus 124  
 loss tangent 125  
 low-cycle fatigue tests 756  
 Lüders band 566, 567  
 Ludwick-Hollomon equation 166
- macroindentation tests 216  
 Manson-Haferd parameter *see* creep  
 martensite  
   acicular 597, 598  
   lath 597, 598  
   lenticular 597  
   mechanical effects 603–8  
   morphologies 594–8  
   strength, of 600–3  
   structure 594–8  
   twinned 598, 599  
   *see also* martensitic transformation  
 martensitic transformation 594–613  
   ceramics, in 614–18  
   habit plane 600  
   systems 595  
   undistorted and unrotated plane  
     600
- materials  
   biological 134  
     artery 134, 135, 137  
     blood vessels 134  
     vein 134, 135  
     cartilage 137–40  
   mechanical properties, of 140–3,  
     241–5  
   composite 3–11  
   monolithic 3–11  
   structure 15–56  
   matrix materials 767–9, 774, 778
- maximum distortion energy  
   criterion 201–4  
 maximum shear stress criterion  
   (Tresca) 200–4  
 maximum stress criterion (Rankine)  
   200, 480  
 Maxwell model 689, 690  
 McClintock-Walsh criterion 207,  
   208  
 Meyers-Ashworth theory 351  
 microalloyed steels 585, 586
- microalloying 586  
 microhardness *see* microindentation  
   hardness  
 microindentation hardness tests  
   221  
 Miller indices 15–18  
 misorientation of grain boundary  
   322, 323, 326–30; *see also* grain  
   boundary  
 modulus *see* elastic modulus  
 Mohr circle 89–92  
 Mohr Coulomb failure criterion 206  
 molecular weight 36–8  
 Mooney-Rivlin equation 131, 132  
 Mukherjee-Bird-Dorn equation *see*  
   creep  
 muscle force 237–41  
 myosin 52, 54, 56
- Nabarro-Herring creep *see* creep  
 nano- and microstructure  
   biological materials, of 45  
 nanocrystalline materials 355–8  
 nanoindentation 225  
 nanotechnology 60, 61  
 nanotubes 60–1  
 necking 164, 171–6, 189, 191, 371  
 Newtonian viscosity *see* viscosity  
 NiTiNOL 608
- octahedral sites 255, 256, 295,  
   570
- Olsen test 230, 232  
 ordered alloys *see* intermetallics  
 Orowan's equation 306–8  
 orthotropic 98, 102, 117, 118, 784  
 oxidation  
   ceramics 839, 840  
   metals 819, 820  
   polymers 833, 834
- Palmgren-Miner rule *see* fatigue  
 Paris-Erdogan equation *see* fatigue  
 Peach-Koehler equation *see*  
   dislocation  
 Peierls-Nabarro stress *see* dislocation  
 persistent slip bands 725–9  
 pileup *see* dislocation  
 plane strain fracture toughness 405,  
   447  
   ceramics 447  
   metals 447  
   polymers 447
- plastic anisotropy 231

- plastic deformation  
  compression, in 183  
  glasses, of 193  
  polymers, of 188  
  tension, in 163
- plastic zone 534
- plastic zone size correction 428–31
- plasticity 161
- point defects 254, 259  
  equilibrium concentration of 256
- Poisson's ratio 83–5, 87, 101, 121, 169, 170
- pole figure 396
- polygonization 390
- polymers  
  atactic 33  
  block copolymers 32, 33  
  branched 32, 33, 35  
  crosslinked 32  
  defects 361–4  
  graft copolymers 32, 33  
  homopolymers 32, 33  
  isotactic 33  
  ladder 32  
  linear 32, 33, 35, 41  
  random copolymers 32, 33  
  syndiotactic 33  
  thermoplastic 33  
  thermoset 33, 514
- Porous materials 44, 639–50  
  plastic behavior 646–50
- post-yield fracture mechanics 448
- precipitation  
  microalloyed steels, in 585  
  precipitation hardening 558, 559, 571–5, 577, 578, 581–6, 590
- production of point defects 259
- prostheses  
  hip replacement 5–7  
  knee replacement 5–7
- proteins 47, 48
- pseudoelasticity 608–11
- punch-stretch tests 232
- quasicrystals 38, 39
- R curve 443
- radiation damage 261, 819, 834
- radiation effects 264, 265
- rafting 683, 684
- Rankine criterion 200, 480
- reduction in area 170, 172, 174
- reinforcements 767
- relationships among fracture  
  toughness parameters 444
- resilience 171
- resilin 53, 243
- Reuss average 107, 109, 110
- Rockwell *see* hardness
- rolling 161, 162, 176, 199, 204, 214, 231, 233
- temper 234
- rotating bending machine 751
- rubber elasticity 126–32
- Salganik equation 115, 118, 158
- Schmid factor 377, 381–4, 398
- Schmid law 377
- Schottky defects 255
- Seeger model 262, 263
- Seeger work hardening theory 388
- semicrystalline polymers 190
- sensitization 818
- serrated stress-strain curve 340, 568
- servohydraulic testing machine 163, 755
- sessile dislocation *see* dislocation
- shape memory effect 595, 608–13  
  polymers, in 614
- shear 80  
  banding 468, 511, 512  
  coupling 801  
  deformation 380  
  modulus 81, 102, 115, 154  
  pure 95, 96  
  yielding 210, 508
- Sherby-Dorn parameter *see* creep
- silicides 621–3
- silk 54, 243
- single crystal 34, 35, 383–6, 391, 395, 684–6
- skin 242
- slip 341–4  
  bands 383  
  conjugate 381, 382  
  critical 381, 382  
  cross 302, 381–5, 388  
  direction(s) 375, 376, 378, 380, 395  
  lines 383  
  markings 383  
  planes 384, 395  
  primary 381, 382, 384, 385, 388  
  systems 377, 378, 381, 382, 384, 385, 393
- smart materials 57
- S-N curves *see* fatigue
- Snoek effect 569
- softening mechanisms 392
- softening point 197, 198
- solid metal embrittlement 830, 831
- solid solution strengthening 558–70  
  mechanical effects 564–70
- spherulite(s) 35
- sponge spicule 56
- stacking fault 286–9, 291, 292, 297, 298, 303, 342, 343, 624, 626, 628, 634, 636
- stair rod dislocation *see* dislocation
- stamping 204, 229, 233, 236, 237, 369, 370
- statistical analysis  
  failure strength, of 448  
  S-N curves, of 753
- statistical variation in strength 802
- stereographic projections 373, 375, 381–4, 398
- stiffness 97, 99, 101, 111, 112, 118
- storage modulus 124
- strain  
  engineering 164–6, 171, 185  
  plane 87, 162, 418, 480, 532  
  point 197, 198  
  rate 197  
  shear 197  
    true 164–6, 170, 185
- strain aging 567
- strain energy density 77–9
- strain memory effect 608, 610–13
- strain rate effects 176, 189, 197, 310
- strain rate sensitivity 197
- strength 780
- strength of martensite 600
- strength of real materials 61
- stress 72–83  
  compressive 174  
    barreling 174  
    plastic deformation 174
- concentration 409
- concentration factor 409
- engineering 164–6, 171, 185
- hydrostatic 209–11  
  effect on yielding 209–11
- plane 86, 418
- residual 136, 137
- tensile 174  
  true 164–6, 170, 185
- uniaxial 86
- stress corrosion cracking (SCC) 820–4
- ceramics, in 837–9
- glass, in 837–9

- stress relaxation 688–94  
 modulus 693  
 stress required for slip 374  
 stress singularity at crack tip 458  
 stress-strain curves  
   idealized 165  
   tensile 171  
   parameters 171–6  
   polymers 188–91  
   strain rate effects 176–83  
   uniaxial 170, 171  
 stretching 229, 231, 235  
 striations *see* fatigue  
 structure  
   crystal 16–40  
     ceramics 25–30  
     hierarchical 3, 9–11, 45  
     liquid crystal 39, 40  
     metals 19–25  
     polymers 31–8  
     quasi-crystals 38, 39  
 subboundaries 389  
 subgrains 322, 389, 390  
 substitutional strengthening 564–6,  
   570  
 substitutional defects 558–61, 564–6,  
   570  
 superelasticity 608–13; *see also* shape  
   memory effect  
 superalloys 653, 654, 668, 681–4, 669  
 superplasticity 653–704  
 surface energy 360  
 swelling 832  
 Swift test 230, 231  
 SX cast alloys 636  
 syntactic foam 645, 646
- Taylor work hardening theory 386  
 Taylor-Orowan equation 306  
 tendon 9–10, 44, 51, 52  
 tensile curve parameters 171–6  
 tensile test 525  
 tetragonal distortion 560, 561  
 tetrahedral sites 255, 256, 264  
 texture 390, 395–8  
 texture strengthening 395–8  
 theoretical cleavage strength  
   406–8  
 theoretical tensile strength 406–8  
 theoretical shear strength 252–4
- thermal stress(es) 695, 696  
 thermoset *see* polymer  
 three-point bending 162  
   test 541  
 tilt boundaries 326  
 tissue  
   soft 9–11  
 torsion 81, 162  
 toucan beak 44–6  
 toughness 785  
   fiber reinforcement 787  
   microcracking 786  
   particle toughening 786  
   transformation toughening 786  
   importance in practice 445  
   polymers 513  
 transformation-induced plasticity  
   595  
 transformation toughening 595, 617,  
   618  
 Tresca criterion 201–4  
 tridimensional defects 358  
 TRIP steels 595, 606, 615  
 turbine 685  
 twin boundary(ies) 336  
   energy 332  
 twinning 341–4  
   direction(s) 332, 333, 339–41  
   plane(s) 332, 333, 349–51  
   plastic deformation 337, 339  
   serrated stress-strain curve 340  
   work-hardening 342  
 twist boundaries 326  
 two-parameter approach 749; *see also*  
   fatigue
- ultimate tensile strength 171  
 uniform elongation 171  
 upper yield point *see* yield point
- vacancy 254–63, 305  
 vacancy loops 275, 276, 282  
 Vickers 219, 220–3  
 viscoelasticity 71, 75, 120–5  
 viscosity 121–5, 192, 197, 198  
   glasses 197, 198  
   Newtonian 122  
   temperature, function of 197–9
- viscous flow 191–8  
   glasses, in 193–8
- Voce equation 166  
 void(s) 26, 255, 258, 262–5  
   radiation 262–5  
 Voigt average 107, 109  
 Voigt model 689, 690  
 volumetric defects 321, 358–60  
 von Mises criterion 201–4, 480, 721
- Wachtman-Mackenzie equation 113  
 Weibull statistical analysis 449–57  
 Weibull modulus 451  
 Weertman-Ashby maps 676–8  
 whiskers 61–3  
 Williams, Landel, and Ferry equation  
   691–3  
 wire drawing 174–6, 231, 345, 354  
 Wöhler curves 714  
 work hardening 342, 369, 371, 381,  
   389  
   coefficient 197  
   polycrystals, in 384, 389  
   Kuhlmann-Wilsdorf theory 386,  
   388, 390, 391  
   Seeger theory 388  
   Taylor theory 386–8  
 work softening 173  
 working of metals  
   cold 370, 371, 385  
   hot 370, 371
- yield criteria 199–214  
   polymers 209, 210  
   composites 211–13  
 yield point 171, 565–8  
   lower 565  
   upper 565–7  
 yield strength  
   orientation, function of 397  
 Young's modulus 75, 79, 81, 101–4,  
   107, 110, 111, 113, 115–21, 131,  
   145, 149, 150–4  
   orientation, function of 396, 397  
   porosity, effect of 113, 117  
   temperature, function of 153, 312
- Zachariasen model 196, 197  
 Zener anisotropy ratio 99  
 Zerilli-Armstrong equation 167  
 zirconia toughened alumina 617,  
   618